

Volume I  
**GENERAL  
ENGINEERING**

John R. Fanchi, Editor










**PETROLEUM  
ENGINEERING  
HANDBOOK**

Larry W. Lake, Editor-in-Chief

## Welcome to the *Petroleum Engineering Handbook*

How to use the *Handbook*:

-  Use to navigate forward and backward through the *Handbook*.
-  Press at any point to be taken back to the Contents page.
-  Perform a word or phrase search of the entire *Handbook*.
-  Press to launch the print dialog box.
-  View an extended list of chapter and section bookmarks.
-  View the Adobe® Reader® help file.
-  Press to exit out of the *Handbook*.

Use the tool bar at the bottom of the screen to jump to a specific page.



Uploaded by:

Ebooks Chemical Engineering

(<https://www.facebook.com/pages/Ebooks-Chemical-Engineering/238197077030>)

For More Books, softwares & tutorials Related to Chemical Engineering

Join Us

@facebook: <https://www.facebook.com/AllAboutChemicalEngineering>

@facebook: <https://www.facebook.com/groups/10436265147/>

@facebook: <https://www.facebook.com/pages/Ebooks-Chemical-Engineering/238197077030>

Volume I  
**GENERAL  
ENGINEERING**

John R. Fanchi, Editor



**PETROLEUM  
ENGINEERING  
HANDBOOK**

Larry W. Lake, Editor-in-Chief

**Petroleum Engineering Handbook**

*Larry W. Lake, Editor-in-Chief*

- I **General Engineering** *John R. Fanchi, Editor*
- II **Drilling Engineering** *Robert F. Mitchell, Editor*
- III **Facilities and Construction Engineering** *Kenneth E. Arnold, Editor*
- IV **Production Operations Engineering** *Joe Dunn Clegg, Editor*
- V **Reservoir Engineering and Petrophysics** *Edward D. Holstein, Editor*
- VI **Emerging and Peripheral Technologies** *H.R. Warner Jr., Editor*
- VII **Indexes and Standards**



SOCIETY OF PETROLEUM ENGINEERS

Volume I  
**GENERAL  
ENGINEERING**

John R. Fanchi, Editor



**PETROLEUM  
ENGINEERING  
HANDBOOK**

Larry W. Lake, Editor-in-Chief

# Petroleum Engineering Handbook

**Larry W. Lake**, Editor-in-Chief  
U. of Texas at Austin

Volume I

## General Engineering

**John R. Fanchi**, Editor  
Colorado School of Mines

Society of Petroleum Engineers



SOCIETY OF PETROLEUM ENGINEERS

Volume I  
**GENERAL  
ENGINEERING**

John R. Fanchi, Editor



**PETROLEUM  
ENGINEERING  
HANDBOOK**

Larry W. Lake, Editor-in-Chief

© Copyright 2006 Society of Petroleum Engineers

All rights reserved. No portion of this publication may be reproduced in any form or by any means, including electronic storage and retrieval systems, except by explicit, prior written permission of the publisher, except for brief passages excerpted for review and critical purposes.

Manufactured in the United States of America.

ISBN 978-1-55563-113-0

Society of Petroleum Engineers  
222 Palisades Creek Drive  
Richardson, TX 75080-2040 USA

<http://www.spe.org/store>  
[service@spe.org](mailto:service@spe.org)  
1.972.952.9393



SOCIETY OF PETROLEUM ENGINEERS



# PETROLEUM ENGINEERING HANDBOOK

Larry W. Lake, Editor-in-Chief

## Foreword

This 2006 version of SPE's *Petroleum Engineering Handbook* is the result of several years of effort by technical editors, copy editors, and authors. It is designed as a handbook rather than a basic text. As such, it will be of most benefit to those with some experience in the industry who require additional information and guidance in areas outside their areas of expertise. Authors for each of the more than 100 chapters were chosen carefully for their experience and expertise. The resulting product of their efforts represents the best current thinking on the various technical subjects covered in the *Handbook*.

The rate of growth in hydrocarbon extraction technology is continuing at the high level experienced in the last decades of the 20th century. As a result, any static compilation, such as this *Handbook*, will contain certain information that is out of date at the time of publication. However, many of the concepts and approaches presented will continue to be applicable in your studies, and, by documenting the technology in this way, it provides new professionals an insight into the many factors to be considered in assessing various aspects of a vibrant and dynamic industry.

The *Handbook* is a continuation of SPE's primary mission of technology transfer. Its direct descendents are the "Frick" *Handbook*, published in 1952, and the "Bradley" *Handbook*, published in 1987. This version is different from the previous in the following ways:

- It has multiple volumes in six different technical areas with more than 100 chapters.
- There is expanded coverage in several areas such as health, safety, and environment.
- It contains entirely new coverage on Drilling Engineering and Emerging and Peripheral Technologies.
- Electronic versions are available in addition to the standard bound volumes.

This *Handbook* has been a monumental undertaking that is the result of many people's efforts. I am pleased to single out the contributions of the six volume editors:

*General Engineering*—John R. Fanchi, Colorado School of Mines

*Drilling Engineering*—Robert F. Mitchell, Landmark Graphics Corp.

*Facilities and Construction Engineering*—Kenneth E. Arnold, AMEC Paragon

*Production Operations Engineering*—Joe D. Clegg, Shell Oil Co., retired

*Reservoir Engineering and Petrophysics*—Ed Holstein, Exxon Production Co., retired

*Emerging and Peripheral Technologies*—Hal R. Warner, Arco Oil and Gas, retired

It is to these individuals, along with the authors, the copy editors, and the SPE staff, that accolades for this effort belong. It has been my pleasure to work with and learn from them.

—Larry W. Lake



Volume I  
**GENERAL  
ENGINEERING**

John R. Fanchi, Editor



**PETROLEUM  
ENGINEERING  
HANDBOOK**

Larry W. Lake, Editor-in-Chief

## Preface

*General Engineering*, Volume I of the new *Petroleum Engineering Handbook*, has been designed to present material that is needed by all practicing petroleum engineers. It includes chapters on mathematics, properties of fluids, rock properties, rock/fluid interactions, economics, the law, and the social context of fossil energy.

The mathematics chapters of this volume are a major departure from previous editions. The mathematical tables presented in previous editions are now readily available using hand-held calculators or software on desktop computers. The mathematics chapters present mathematical topics that petroleum engineers need to better understand the literature and the software they use on a day-to-day basis. Topics such as vibrating systems, ordinary and partial differential equations, linear algebra and matrices, and Green's functions are introduced and references are provided for readers who would like to pursue the topics in more detail.

The discussion of fluid properties covers fluid sampling techniques; properties and correlations of oil, gas, condensate, and water; hydrocarbon phase behavior and phase diagrams for hydrocarbon systems; and the phase behavior of water/hydrocarbon systems. Two chapters consider the properties of waxes, asphaltenes, and crude oil emulsions.

Rock properties and rock/fluid interactions are discussed. The rock properties include bulk rock properties, such as porosity, elastic rock properties, and rock failure relationships. Measurement techniques and models of single-phase permeability are then presented, followed by a review of the properties that describe the interaction between rocks and fluids, notably relative permeability and capillary pressure.

In addition to mathematics, fluid properties, and rock properties, petroleum engineers need to understand economic and legal issues. Essential aspects of the economic and regulatory environment are addressed in the last section. A brief review of the role of fossil energy in the 21st century energy mix ends the volume.

I want to thank all of the authors who donated their time and expertise to the preparation of this volume.

—John R. Fanchi





## Contents

- 1 Mathematics of Vibrating Systems** - [click to view](#)  
*Alfred W. Eustes, III*
- 2 Mathematics of Fluid Flow** - [click to view](#)  
*John R. Fanchi*
- 3 Mathematics of Transient Analysis** - [click to view](#)  
*Erdal Ozkan*
- 4 Fluid Sampling** - [click to view](#)  
*John M. Williams and Sunil L. Kokal*
- 5 Gas Properties** - [click to view](#)  
*Brian F. Towler*
- 6 Oil System Correlations** - [click to view](#)  
*Robert P. Sutton*
- 7 Thermodynamics and Phase Behavior** - [click to view](#)  
*R.T. Johns*
- 8 Phase Diagrams** - [click to view](#)  
*F.M. Orr, Jr. and K. Jessen*
- 9 Asphaltenes and Waxes** - [click to view](#)  
*Long X. Nghiem and Bruce F. Kohse*
- 10 Properties of Produced Water** - [click to view](#)  
*David J. Blumer*
- 11 Phase Behavior of H<sub>2</sub>O + Hydrocarbon Systems** - [click to view](#)  
*E.D. Sloan*
- 12 Crude Oil Emulsions** - [click to view](#)  
*Sunil L. Kokal*
- 13 Rock Properties** - [click to view](#)  
*M. Batzle, D.-H. Han, and R. Hofmann*
- 14 Single-Phase Permeability** - [click to view](#)  
*Philip H. Nelson and Michael L. Batzle*
- 15 Relative Permeability and Capillary Pressure** - [click to view](#)  
*Richard L. Christiansen*
- 16 Petroleum Economics** - [click to view](#)  
*John D. Wright*
- 17 International Oil and Gas Law** - [click to view](#)  
*Mark D. Bingham, Scot W. Anderson,  
and Dustin M. Ammons*
- 18 The 21st Century Energy Mix** - [click to view](#)  
*John R. Fanchi*
- Author Index** - [click to view](#)
- Subject Index** - [click to view](#)



# Chapter 1

## Mathematics of Vibrating Systems

Alfred W. Eustes, III, SPE, Colorado School of Mines

### 1.1 Introduction

Many mathematical tools can be used to analyze vibrational systems. One of the first mathematical tools a neophyte engineer learns is calculus. The basics of limits, differentiation, and integration permeate all of engineering mathematics. This chapter offers a cursory review of these topics and uses the mathematics of vibrations to demonstrate how the concepts operate. For more specific information on all these topics, consult relevant sections of this Handbook.

Many of the mathematical tools engineers use to evaluate and predict behavior, such as vibrations, require equations that have continuously varying terms. Often, there are many terms regarding the rate of change, or the rate of change of the rate of change, and so forth, with respect to some basis. For example, a velocity is the rate of change of distance with respect to time. Acceleration is the rate of change of the velocity, which makes it the rate of change of the rate of change of distance with respect to time. Determining the solutions to these types of equations is the basis of differential calculus.

An equation with continuously varying terms is a differential equation. If only one basis is changing, then it is an ordinary differential equation (ODE); however, if two or more bases are changing, then it is a partial differential equation (PDE). An ODE uses the notation “d” and a PDE uses  $\partial$  to refer to change.

Understanding differentiation starts with an understanding of limits.

**1.1.1 Limits.** A graph is a useful method for determining how an equation behaves. The independent variable  $t$  in Eq. 1.1 determines how the dependent variable  $y$  behaves. The operators and constants in an equation specify this behavior. Fig. 1.1 shows the graph of Eq. 1.1, the distance of freefall over time with an initial velocity of zero. Down is considered negative in this equation:

$$y = \frac{-g_c t^2}{2} \dots\dots\dots (1.1)$$

The  $x$ -axis (abscissa) usually is the independent variable, and the  $y$ -axis (ordinate) usually is the dependent variable; however, many drilling charts hold an exception to this generality, in



Fig. 1.1—Graph of Eq. 1.1, the equation of free fall on earth.

that their ordinate often is the independent variable, and their abscissa is the dependent one. An example of such a drilling chart is the depth vs. time graph.

In Fig. 1.1, at the time of 3 seconds, the distance is -96.522 ft. A tangent line to the graph at 3 seconds is known as the slope (*A*) of the graph at that point. To quickly estimate the slope of the tangent, divide the rise ( $\Delta y$ ) by the run ( $\Delta t$ ), as shown in Eq. 1.2:

$$A = \frac{y_2 - y_1}{t_2 - t_1} = \frac{\Delta y}{\Delta t} \dots\dots\dots (1.2)$$

In this case, the tangent *y* value at 2 seconds is -48.261 ft and at 4 seconds is -241.305 ft. The slope then is:

$$A = \frac{-241.305 - -48.261}{4 - 2} = \frac{-193.044}{2} = -96.522 \dots\dots\dots (1.3)$$

Because the units in this case are ft/sec, this slope gives the velocity at that point. It is the rate of change of the distance with respect to time.

A limit is defined as the value of a function at a given point as that point is approached from either higher or lower values (often referred to as approaching from the left or right, respectively). The limit (*Y*) of Eq. 1.1 at 3 seconds is:

$$Y = \lim_{t \rightarrow 3} \frac{-g_c t^2}{2} \dots\dots\dots (1.4)$$

*Y* is known as the limit of the function. In this simple case, *Y* is the same regardless of whether *t* approaches 3 from the left or the right. This is not true in all cases, however (e.g., with a discontinuous function). In these cases, the limit can be determined analytically. One can also determine the limit using a graph such as in Fig. 1.1.

Limits have the following properties:

$$\text{If } \lim_{t \rightarrow z} f(t) = P \text{ and } \lim_{t \rightarrow z} g(t) = Q, \text{ then } \lim_{t \rightarrow z} [f(t) + g(t)] = P + Q, \dots\dots\dots (1.5)$$

$$\lim_{t \rightarrow z} r f(t) = r \left[ \lim_{t \rightarrow z} f(t) \right] = rP, \dots\dots\dots (1.6)$$

$$\lim_{t \rightarrow z} \frac{f(t)}{g(t)} = \frac{P}{Q}, \text{ as long as } Q \neq 0, \dots\dots\dots (1.7)$$

and

$$\lim_{t \rightarrow z} \sum_{j=0}^J r_j t^{J-j} = \sum_{j=0}^J r_j z^{J-j} \dots\dots\dots (1.8)$$

**1.1.2 Derivatives.** As noted earlier, the slope of graph of Eq. 1.1 at 3 seconds = -96.522 ft/sec and is the velocity (*v*) of free-fall at 3 seconds from release. This value is known as the first derivative of Eq. 1.1 at the value of 3. It is written as:

$$f'(t) = \frac{d}{dt} f(t) = \frac{d}{dt} y = \frac{dy}{dt} = v = -96.522 \dots\dots\dots (1.9)$$

and is defined as:

$$\frac{dy}{dt} = \lim_{\Delta t \rightarrow 0} \frac{f(t + \Delta t) - f(t)}{\Delta t} \dots\dots\dots (1.10)$$

As the limit of the value of  $\Delta t$  approaches zero, the solution converges to the first derivative. Derivatives have the following properties (*r* = constant).

$$\text{If } y = f(t) = r, \text{ then } \frac{dy}{dt} = f'(t) = 0. \dots\dots\dots (1.11)$$

$$\text{If } y = f(t) = r t^n, \text{ then } \frac{dy}{dt} = f'(t) = r n t^{n-1} \dots\dots\dots (1.12)$$

$$\text{If } y = f(t) = \sin (r t), \text{ then } \frac{dy}{dt} = f'(t) = r \cos (r t) \dots\dots\dots (1.13)$$

$$\text{If } y = f(t) = \cos (r t), \text{ then } \frac{dy}{dt} = f'(t) = -r \sin (r t) \dots\dots\dots (1.14)$$

$$\text{If } y = f(t) = e^{r t}, \text{ then } \frac{dy}{dt} = f'(t) = r e^{r t} \dots\dots\dots (1.15)$$

$$\text{If } y = f(t) = \ln (r t), \text{ then } \frac{dy}{dt} = f'(t) = \frac{1}{t} \dots\dots\dots (1.16)$$

In the case of Eq. 1.7, where  $Q = 0$ , L'Hopital's rule can help find the limit. This is shown in Eq. 1.17:

$$\lim_{t \rightarrow z^+} \frac{f(t)}{g(t)} = \lim_{t \rightarrow z^+} \frac{f'(t)}{g'(t)}, \text{ where } f(t) = g(t) = 0$$

or where  $f(t) = g(t) = \pm \infty \dots\dots\dots (1.17)$

Other rules regarding differentials are the following.

The linear superposition rule:

$$\text{If } f(t) = \sum_{j=1}^J f_j(t), \text{ then } f'(t) = \sum_{j=1}^J f_j'(t). \dots\dots\dots (1.18)$$

The product rule:

$$\frac{d}{dt}[f(t)g(t)] = f(t)\frac{d}{dt}g(t) + g(t)\frac{d}{dt}f(t). \dots\dots\dots (1.19)$$

The quotient rule:

$$\frac{d}{dt}\left[\frac{f(t)}{g(t)}\right] = \frac{1}{g(t)}\frac{d}{dt}f(t) - \frac{f(t)}{g(t)^2}\frac{d}{dt}g(t). \dots\dots\dots (1.20)$$

The chain rule (or function of a function):

$$\frac{dy}{dt} = \frac{dy}{dx} \frac{dx}{dt} \dots\dots\dots (1.21)$$

Multiple differentiations can be shown by

$$\frac{dy}{dt}\left[\frac{dy}{dt}f(t)\right] = \frac{d^2y}{dt^2}f(t) = f''(t), \dots\dots\dots (1.22)$$

and continued differentiations can be shown by

$$\left\{\frac{dy}{dt}\left[\frac{dy}{dt}\left(\frac{dy}{dt}f(t)\right)\right]\right\} = \frac{d^3y}{dt^3}f(t) = f'''(t). \dots\dots\dots (1.23)$$

A useful point to recognize is where a slope equals zero, which can correspond to a maximum, a minimum, or an inflection. To determine these points, determine a first derivative of an equation. Then, set this first-derivative equation to equal zero and solve for the basis (the unknown). To determine whether this point is a maximum, a minimum, or an inflection, determine the second derivative of that equation. If that value is negative, the point is a maximum; if it is positive, the point is a minimum; and if it is zero, the point is an inflection.

The graph of Eq. 1.24 (Fig. 1.2) is an example of this process:

$$y = t^3 - 5t^2 + 3t + 5. \dots\dots\dots (1.24)$$

The first derivative of Eq. 1.24 is:

$$\frac{dy}{dt} = 3t^2 - 10t + 3, \dots\dots\dots (1.25)$$

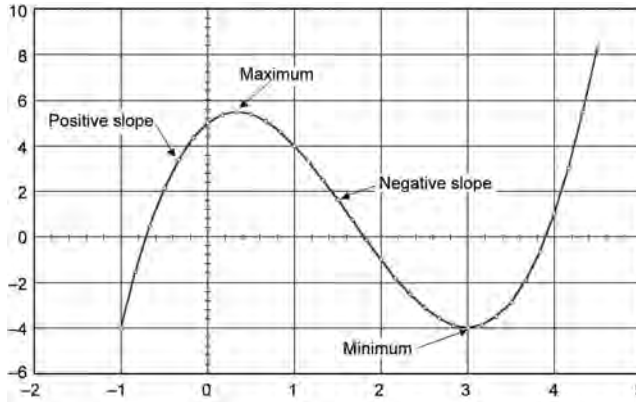


Fig. 1.2—Graph of Eq. 1.24, an example of slopes, minima, and maxima.

which, when set equal to zero, is a quadratic equation with two roots,  $t = 3$  and  $1/3$ . These two points correspond to the maximum and minimum points on the graph. To prove which is which, a second derivative is taken:

$$\frac{d^2y}{dt^2} = 6t - 10, \dots\dots\dots (1.26)$$

which at  $t = 3$  and  $1/3$  is equal to  $8$  and  $-8$ , respectively. This means that at  $t = 3$ , the function is at a minimum and at  $t = 1/3$ , the function is at a maximum.

The first differentiation of the equation of the position of a free-falling object starting at rest (Eq. 1.1) gives the slope of the graph, which, as noted, is the velocity:

$$\frac{dy}{dt} = v = g_c t \dots\dots\dots (1.27)$$

A second differentiation gives the change of the slope with respect to time (acceleration), and is:

$$\frac{d^2y}{dt^2} = g_c, \dots\dots\dots (1.28)$$

which is the acceleration caused by Earth’s gravity.

**1.1.3 Differential-Equation Solutions.** Solutions to differential equations solved in closed form can range from trivial to impossible. Numerical methods often are required. Nevertheless, some general strategies have been developed to solve differential equations.<sup>1,2,3</sup>

An ODE with only first derivatives is known as a first-order ODE. A second-order ODE has second and possibly first derivatives. The same reasoning applies to third order and beyond. Likewise, when a PDE has only first derivatives, it is a first-order PDE. The second and third orders and beyond are defined on the basis of their highest-order derivative.

This section has covered some of the basics of ODE and PDE mathematics. The reader is urged to review mathematical texts and handbooks for more details on this subject.

To illustrate some of the aforementioned principles of ODE and PDE mathematics, the rest of this chapter discusses examples within the subject of vibrations. Vibration mathematics has



Fig. 1.3—Excitation/response system for deterministic vibrations.

been chosen because vibrations are notorious for instigating drilling and production problems. The next section covers some basic information on the nature of vibrations, with subsequent sections devoted to some aspect of the mathematical models of vibrations.

**1.2 Introductory Thoughts About Vibrations**

The fundamental theories of vibration are not new. Indeed, Saint-Venant<sup>4</sup> published his theory on the vibrations of rods in 1867, and Love<sup>5</sup> published an entire treatise on vibration theory in 1926. The mathematics of vibration theory involves infinite series, complex functions, and Fourier integral transforms, and its physics involves Newtonian mechanics and stress analyses. Until recently, except under relatively simple conditions, the complexity of such mathematics had restrained the application of vibration theory to solving simple common problems. Now, however, state-of-the-art computers can perform these complex calculations in a reasonable time frame, making possible a wave of new studies.

**1.3 Vibration Theory**

A vibration is a fluctuating motion about an equilibrium state. There are two types of vibration: deterministic and random. A deterministic vibration is one that can be characterized precisely, whereas a random vibration only can be analyzed statistically. The vibration generated by a pumping unit is an example of a deterministic vibration, and an intermittent sticking problem within the same system is a random vibration.

In mechanical systems, deterministic vibrations are excitations that elicit a response from a system, as shown schematically in Fig. 1.3. In theory, as long as two of the three variables (excitation, system, and response) are known, the third one can be determined; however, the mathematics might be challenging. Most often, the response function is sought, so that the excitation function and the system must be known.

Vibration systems can be linear or nonlinear, and discrete or continuous (Fig. 1.4). In all cases, a vibration system can be in one, two, or three mutually orthogonal dimensions. A linear system is a system in which proportionality (Eq. 1.29) and superposition (Eq. 1.30) are true, that is, in which:

$$\text{If } E(t) \rightarrow R(t), \text{ then } rE(t) \rightarrow rR(t) \dots \dots \dots (1.29)$$

and

$$\begin{aligned} &\text{If } E_1(t) \rightarrow R_1(t) \text{ and } E_2(t) \rightarrow R_2(t), \\ &\text{then } E_1(t) + E_2(t) \rightarrow R_1(t) + R_2(t) \dots \dots \dots (1.30) \end{aligned}$$

When proportionality and superposition are not true, then the system is nonlinear.

A discrete system is one having a finite number of independent coordinates that can describe a system response. These independent coordinates are known as degrees of freedom (DOFs). If the motion of mass, either translational or rotational, of a vibrating system is a function of only one independent coordinate, then the system has one DOF. If two or more independent coordinates are required to describe one or both types of motion, then the system has two or more DOFs. If a system is continuous (an infinite set of independent coordinates is

	Linear	Nonlinear
Discrete	One DOF Two DOFs Three DOFs	One DOF Two DOFs Three DOFs
Continuous	1D, 2D, or 3D	1D, 2D, or 3D

Fig. 1.4—Vibration system classification.

	Absent	Present
Periodic	Free vibration	Forced vibration
Transient	Free vibration	Forced vibration

Fig. 1.5—Excitation function classification.

needed to describe the system response), it has an infinite number of DOFs. Because material structures all have a continuous nature, all systems have an infinite number of DOFs. Most systems have dominant DOFs; some even have a single dominant DOF. Such systems therefore can be characterized as discrete systems, which makes the mathematics more tractable.

If a system has a single DOF or set of DOFs in only one direction, it is a 1D system. If there are two mutually orthogonal directions for the DOF, it is a 2D system; and if there are three mutually orthogonal directions for the DOF, it is a 3D system.

As Fig. 1.5 shows, the excitation function can be periodic or transient, and absent or present. A periodic vibration is one that can be characterized mathematically as an indefinite repetition. A transient vibration is of finite length and is composed of waves that have a definite beginning and that eventually die out. These waves can be of extremely short duration or last for some time.

A standing wave is a vibration whose wave profile appears to be standing still, though actually the particles that make up the material are oscillating about an equilibrium position. Because of the geometry and boundary conditions of the material through which they are traveling, the waves and the reflected waves cancel and reinforce themselves over the same location in the material, which makes the wave profile appear not to be moving. The point at which no motion is occurring is a nodal point, or node. The point of maximum amplitude is the antinode.

In reality, all waves are transient in some way. If a wave is repeated over a longer time than it takes for a single wave to propagate through a material, then this series of waves can be called a vibration. All vibrations are transient, as well. If the vibration lasts longer than the time under analysis, then it can be characterized as infinite in length.

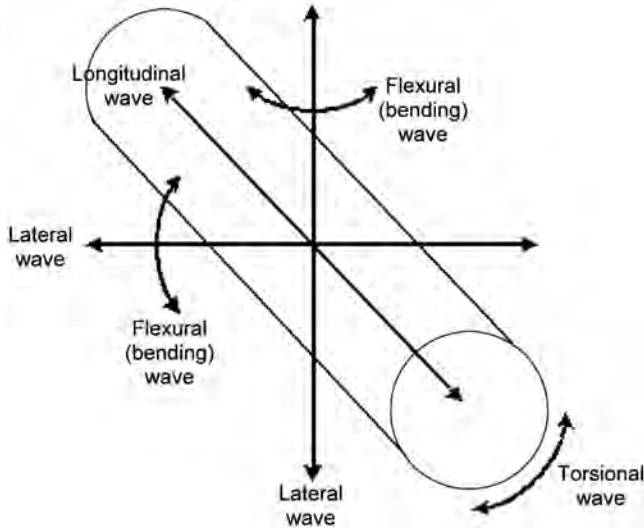


Fig. 1.6—Types of elastic waves.

When the excitation is present and is actively affecting the system within the analysis time frame, the response is called a forced vibration. The response of a system with an absent excitation function—one that is not present within the analysis time frame—is called a free vibration. As such, the system can be responding to the removal of an excitation function. For example, if the response of a mass and spring system is sought after the system has been pulled down and released, the original excitation function (the pulling force) is considered absent because the analysis is being performed after the release.

#### 1.4 Wave Propagation

The method by which a vibration travels through a system is known as wave propagation. When an external force is impressed on a real-world elastic body, the body does not react instantly over its entire length. The point immediately under the external force reacts first, and then the section just under that point reacts to the previous section's reaction, and so on. This series of reactions is called wave propagation because the reactions propagate through the body over a period of time at a specific velocity. If the rate of change of the external force is slow enough, static equilibrium analysis can model the reactions adequately for most engineering applications. This is called rigid-body analysis. If the external force changes rapidly, however, wave-propagation analysis is necessary to model the reactions effectively.

**1.4.1 Types of Waves.** There are many types of elastic waves. Some listed in this section are longitudinal, lateral, and bending waves.<sup>6</sup> Some of these are shown in [Fig. 1.6](#).

In longitudinal waves (also variously called compression/tension, axial, dilatational, and irrotational waves), the particles that make up the elastic medium are forced directly toward and away from each other, and the direction of the particles' motion is parallel to that of the wave motion. In most steels, longitudinal waves travel at  $\approx 16,800$  ft/sec. Longitudinal waves are not dispersive. This means that all the wave components that make up a longitudinal wave travel at the same velocity and, hence, do not separate (disperse).

In lateral waves (also known variously as shear, torsional, transverse, equivoluminal, and distortional waves), the particles slip beside each other, and move perpendicular to the direction of the wave motion. Because slipping uses more energy, lateral waves are slower. In steel, for example, they travel at 10,400 ft/sec. A rapidly changing torsional force on a section of



pipe will cause a lateral wave to propagate from the point of application to all other parts of the pipe. It propagates as an angular twist. Lateral waves are nondispersive and have a similar solution method as the longitudinal waves; however, shear or transverse waves are dispersive (i.e., the wave components that make up a shear wave travel at different velocities). Their wave components will disperse and “smear” the initial wave profile. This complicates the analysis significantly.

Bending waves (flexural waves) travel as a bend in a bar or plate and have longitudinal and lateral components. Rotary shears and moments of inertia complicate bending-wave analysis.

Wave-propagation studies in petroleum engineering areas generally have been confined to longitudinal, torsional, and lateral waves. Of these, longitudinal waves generally are easiest to model and are considered in this section. A compression wave is a stress wave in which the propagated stress is in compression. Likewise, a tension wave is a stress wave in which the propagated stress is in tension.

## 1.5 Wave Behavior

Wave velocity depends primarily on density and modulus of elasticity but also is affected by damping and frequency. For example, hitting one end of a long steel rod with a hammer will generate a longitudinal wave that compresses the particles of the steel. The wave’s length is set by the length of time that the hammer is in contact with the end of the rod, whereas its magnitude is set by the force of the hammer blow. As the wave moves along the rod, the steel within the length of the wave is compressed. After the wave passes, the steel returns to its unstressed state, though not necessarily in the same location as before the wave passage.

As another example, twisting (shearing) a steel rod will generate a shear wave. A shear wave moves along the rod more slowly than the longitudinal wave does. Similarly to the longitudinal wave discussed above, its length is set by the duration of the twisting action, whereas its magnitude is set by the torque from the twisting action.

Waves act independently, but the stresses they create can be additive. For example, two equal compression waves that are generated simultaneously by hammer blows at each end of a long steel rod will meet in the center of the rod, pass through one another, and then each continue along the rod as if the other never existed (independence). While the waves are passing each other, however, the compression in the steel will be twice (additive) that of either wave.

**1.5.1 Natural Frequencies and Resonance.** Everything has a natural frequency, a frequency at which it would vibrate were it given the energy to vibrate and left alone. For instance, the human body has a natural frequency of  $\approx 5$  cycles/sec. All drill and rod strings have a natural frequency that depends on the material properties and geometry. The material properties determine the wave velocity, and the geometry determines how waves are reflected and refracted.

During wave propagation, the wave eventually reaches an end of the material. Some of the wave will reflect back to its source. If the reflection reaches the source at the same time a new wave is generated, the two waves will combine and be synchronized in phase. Later, if those two waves’ reflections return to the source at the same time the next new wave is generated, all three waves will combine. This will continue for as long as waves are generated under these conditions, and the resultant wave will increase in amplitude, theoretically to infinity. This is called resonance. The frequency at which resonance occurs is the natural frequency or an integer multiple of that frequency (called a harmonic). If this wave reinforcement is allowed to continue, the system eventually will either self-destruct or fatigue to failure.

A continuous system contains an infinite number of natural frequencies, whereas a discrete single-degree-of-freedom (SDOF) system (e.g., a point mass on a massless spring) has only one natural frequency. If two point masses are connected using two springs, then there are two natural frequencies in this 2DOF system. In general, the number of DOFs in a system determines the number of natural frequencies it has, which means that any discrete system will have

a finite number of natural frequencies; however, in reality, there is an infinite number of natural frequencies because all systems are continuous. Some frequencies will have higher amplitudes than others. Such continuous systems with discrete higher-amplitude responses can be modeled with a discrete methodology.

**1.5.2 Damping.** Resonance energy does not reach an infinite value because of damping, the dissipation of energy over time or distance.<sup>7</sup> Without damping, or friction, the energy from vibrations would build until there is more energy than the structure can sustain, which can cause structural failure.

A wave propagating into a system adds energy to a system, whereas damping removes it. Generally, the dissipated energy from the vibration is converted to heat, and if damping does not take enough energy out of a system, the system can self-destruct from energy overload. The amount of energy in a system at a given time is reflected in the system's stress/strain level. The more stresses/strains in the system, the higher the energy level. Once the stresses reach a value greater than the yield strength of the system, yield failure is imminent. If the stresses are greater than the ultimate strength of the material, failure is immediate.

In the borehole, three distinctive types of damping occur: viscous, Coulomb, and hysteretic. Viscous damping occurs when the damping force generated is proportional to the velocity of the particles. Coulomb damping (also called dry friction) is the force generated by the movement of materials past one another, and it usually is proportional to the force normal to the materials' surfaces. The dynamic and static coefficients of friction are the proportionality constants. Hysteretic damping is the friction force generated by the relative motion of the internal planes of a material as a wave causes particle motion. Although this is true of all materials, some materials are viscoelastic (i.e., they show a much larger hysteretic effect than do others).

**Viscous Damping.** As noted above, viscous damping occurs when the damping force is proportional to the velocity of the particles. Viscous damping is shown by:

$$F_d = c \frac{dx}{dt} \dots\dots\dots (1.31)$$

One way that viscous damping arises in jarring analysis is from the interaction of a solid and liquid at their interface, such as where the steel contacts the liquid mud along the sides of a drillstring.

One method for determining the damping involves noting the decrement of acceleration over one vibration cycle.<sup>8</sup> An impulse is impressed on the drillstring to produce a wave. While the wave is decaying, the acceleration is measured and recorded multiple times at one location on the string and at the same phase (i.e., crest to crest). The time between recordings also is noted. These values are used in Eq. 1.32 to compute the damping coefficient ( $c$ ). Unfortunately, though, this method gives the total damping and does not distinguish between viscous and Coulomb damping.

$$c = 2 \frac{A_c E}{v_s^2 t} \ln \frac{\alpha_1}{\alpha_2} \dots\dots\dots (1.32)$$

**Coulomb Damping.** Coulomb damping is the friction that occurs when two dry surfaces slide over each other, and its force is a constant value that is independent of particle velocity and displacement, but dependent on the friction factor ( $\mu$ ) and the force normal to the friction surface. This value is:

$$F_f = \mu F_n \dots\dots\dots (1.33)$$

The Coulomb damping force always is of the opposite sign from that of the particle velocity, so that the damping force reverses when the particle velocity changes signs. This discontinuity makes it a nonlinear damping force, shown as:

$$F_f = \pm \left( \frac{dx}{dt} \right) \mu F_n \dots\dots\dots (1.34)$$

Nonlinearity makes a closed-form solution to an equation of motion difficult.

**Hysteretic Damping.** Hysteretic damping also is called structural damping because it arises from internal friction within a structure. A wave moves through a material because the atomic structure is reacting to an applied force. As the atoms of the structure move, energy is lost through the interaction of these atoms with their neighboring atoms. Hysteretic damping is the energy lost when atoms move relative to each other.

If a material had a perfectly linear stress/strain relationship, hysteretic damping would not occur. In reality, though, there is no such thing as a perfectly linear stress/strain curve. Two curves develop on the stress/strain diagram while a material is stressed and relieved. The center area between these two curves represents the energy lost to internal friction. (This hysteresis loop is the reason for the name of this damping type.) This variation can be small, but the amount of energy dissipated can be large because high-frequency vibrations can cause this loop to be repeated many, many times over a given time period.<sup>9</sup>

The hysteretic-damping value is highly dependent on a number of factors. One factor is the condition of the material (i.e., chemical composition, inhomogeneities, and property changes caused by thermal and stress histories). Another is the state of internal stress from initial and subsequent thermal and stress histories. Also, the type and variation of stress—axial, torsional, shear, and/or bending—affect the hysteretic-damping value.

A way of looking at hysteretic-damping force is to set it proportional to the particle velocity divided by the wave frequency. This is shown in Eq. 1.35.<sup>10</sup>

$$F_h = \frac{h}{\omega} \frac{dx}{dt} \dots\dots\dots (1.35)$$

**1.6 Equivalent Springs**

Many systems can be modeled as multiple springs. Such springs can be combined into a single, equivalent spring (Fig. 1.7). For parallel springs, the sum of the spring constants is equal to the equivalent spring constant (Eq. 1.36). For series springs, the reciprocal of the sum of the reciprocals of the spring constants is equal to the equivalent spring constant (Eq. 1.37). A linear spring oscillates in a single translational direction. A torsional spring oscillates with an angular twist (Eq. 1.38).

**1.7 Boundary and Initial Conditions**

The boundary conditions (how the ends of a system are attached) and initial condition (condition of the system at the start in time) are extremely important in vibration and wave propagation analysis. The specific solution of any ODE or PDE requires a set of boundary and/or initial conditions. Usually, a displacement (boundary condition) and an initial velocity (initial condition) are specified.

In wave propagation, the boundary conditions also dictate wave behavior. For example, a compression wave is reflected from a free end as a tension wave and from a fixed end as a compression wave. If two rods are connected at their ends and are of different geometry or material, then a fraction of the energy of the wave is reflected and the remaining portion of the energy is refracted at their connection. Other types of boundaries direct the system response by

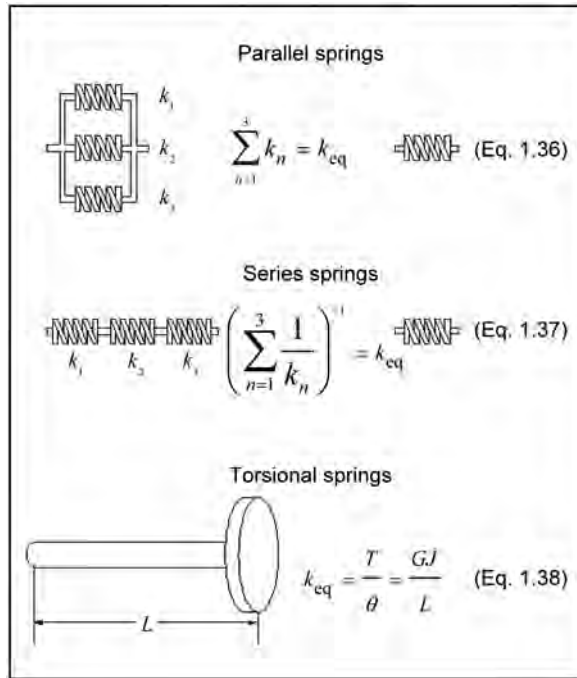


Fig. 1.7—Equivalent springs.

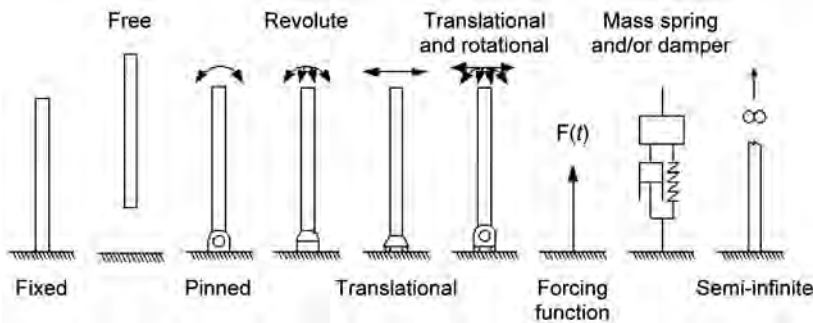


Fig. 1.8—Types of boundary conditions.

limiting the DOF. This includes boundary conditions of pinned, revolute, translational, translational and rotational; forcing function; mass spring and/or damper, and a semi-infinite connection. In addition, changes in material properties will affect the various constants and will cause wave-propagation reflections and refractions at the boundary between the properties. Fig. 1.8 shows some typical boundary conditions.

### 1.8 Mechanical Vibration Analysis

There are three components to mechanical vibration analysis: to determine the geometric compatibilities; to determine the constitutive (material properties) equations; and to determine the equilibrium condition.

The geometric compatibilities are the displacement constraints and connections. They also include the continuous properties, which state that the system does not separate into individual

pieces. (If it does, that is another problem altogether.) The constitutive equations represent the material properties, which include mass, damping, and spring coefficients. These constitutive equations include stress/strain relationships and Hooke’s law (Eqs. 1.39a and 1.39b):

$$\sigma = E\varepsilon \dots\dots\dots (1.39a)$$

or, in another form,

$$F = \frac{EA_c}{L}\Delta l \dots\dots\dots (1.39b)$$

The coefficient of  $\Delta l$  in Eq. 1.39b often is called the spring constant or stiffness constant.

The equilibrium condition is based on both static and dynamic conditions. A static equilibrium states that the sum of the forces acting on an object is equal to zero:

$$\sum F = 0 \dots\dots\dots (1.40)$$

A dynamic equilibrium is based on Newton’s second law and is the basis of many vibration analysis methods. The sum of the forces acting on an object is equal to its mass times the acceleration of the object. Other dynamic-equilibrium analysis includes virtual work methods and energy-balance methods (Hamilton’s principle).

Newton’s second law for a translational system is

$$\sum F = m\ddot{x} \dots\dots\dots (1.41)$$

and for torsional systems is

$$\sum T = I\ddot{\theta} \dots\dots\dots (1.42)$$

Newton’s second law can be rewritten in a form known as D’Alembert’s principle:

$$\sum F - m\ddot{x} = 0, \dots\dots\dots (1.43)$$

in which  $m\ddot{x}$  is treated as a force and is called an inertial force.

Some basic equations of vibration analysis are shown in **Table 1.1**.

**1.9 SDOF System**

An SDOF system is the most basic vibration analysis. The typical SDOF system is the classical linear oscillator (CLO), as shown in **Fig. 1.9**. It consists of a point mass, spring, and damper.

**1.9.1 Free Vibration Without Damping.** The first analysis is free vibration without damping. Using Newton’s second law and D’Alembert’s principle, the equation that describes free vibration without damping ( $c = 0$ ) is:

$$\sum F = kx, \dots\dots\dots (1.52)$$

which gives  $kx = m\ddot{x}$ , which when rearranged becomes:

$$m\ddot{x} + kx = 0 \dots\dots\dots (1.53)$$

<b>TABLE 1.1—VIBRATION NOTATION</b>	
<u>Item</u>	<u>Mathematical definition</u>
Period	$\tau = 1/f = 2\pi/\omega$ ..... (1.44)
Wavelength	$\lambda_w = 2\pi v_w/\omega = 2\pi/k_w$ ..... (1.45)
Cyclic frequency	$f = \omega/2\pi$ ..... (1.46)
Angular frequency	$\omega = 2\pi f$ ..... (1.47)
Wave phase	$\phi = k_w x - \omega t = \omega/v_w (x - v_w t) = 2\pi/\lambda_w (x - v_w t)$ ..... (1.48)
Phase velocity	$v_w = \omega/k_w = 2\pi\omega\lambda_w$ ..... (1.49)
Wave number	$k_w = 2\pi/\lambda_w = \omega/v_w$ ..... (1.50)
Group speed	$v_g = d\omega/dk_w$ ..... (1.51)

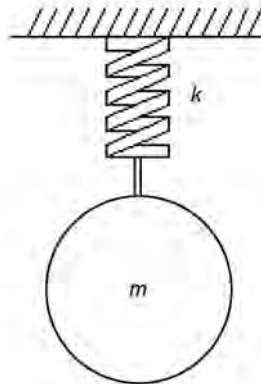


**Fig. 1.9—SDOF free and undamped CLO system.**

The solution to this differential equation is:

$$x = C_1 \sin \sqrt{\frac{k}{m}}t + C_2 \cos \sqrt{\frac{k}{m}}t \dots\dots\dots (1.54)$$

The constant multiplying the  $t$  is the natural frequency of the system and is:

$$\sqrt{\frac{k}{m}} = \omega_n \dots\dots\dots (1.55)$$

in radians/unit time. Multiplying by  $\frac{1}{2\pi}$  gives the natural frequency in cycles/unit time. When Eq. 1.55 is substituted into Eq. 1.54, the result is:

$$x = C_1 \sin \omega_n t + C_2 \cos \omega_n t. \dots\dots\dots (1.56)$$

The constants  $C_1$  and  $C_2$  are based on the initial and boundary conditions. If at time 0,  $x = x_0$  and  $\dot{x} = v_0$ , the initial location and velocity, respectively, the first coefficient is:

$$C_2 = x_0, \dots\dots\dots (1.57)$$

which is the initial location. Differentiating once gives:

$$\dot{x} = C_1 \omega_n \cos \omega_n t - C_2 \omega_n \sin \omega_n t, \dots\dots\dots (1.58)$$

which, when  $t = 0$ , gives the other coefficient:

$$C_1 = \frac{v_0}{\omega_n}, \dots\dots\dots (1.59)$$

which is based on the initial velocity. The entire equation then is:

$$x = x_0 \cos (\omega_n t) + \frac{v_0}{\omega_n} \sin (\omega_n t). \dots\dots\dots (1.60)$$

**Ex. 1.1** is an SDOF free and undamped CLO system.

**1.9.2 Free Vibration With Damping.** The second analysis of free vibration is with damping (**Fig. 1.10**). Using Newton’s second law, the equation that describes free vibration with damping ( $c \neq 0$ ) is:

$$\Sigma F = kx + c\dot{x}, \dots\dots\dots (1.61)$$

which is rearranged as before to get:

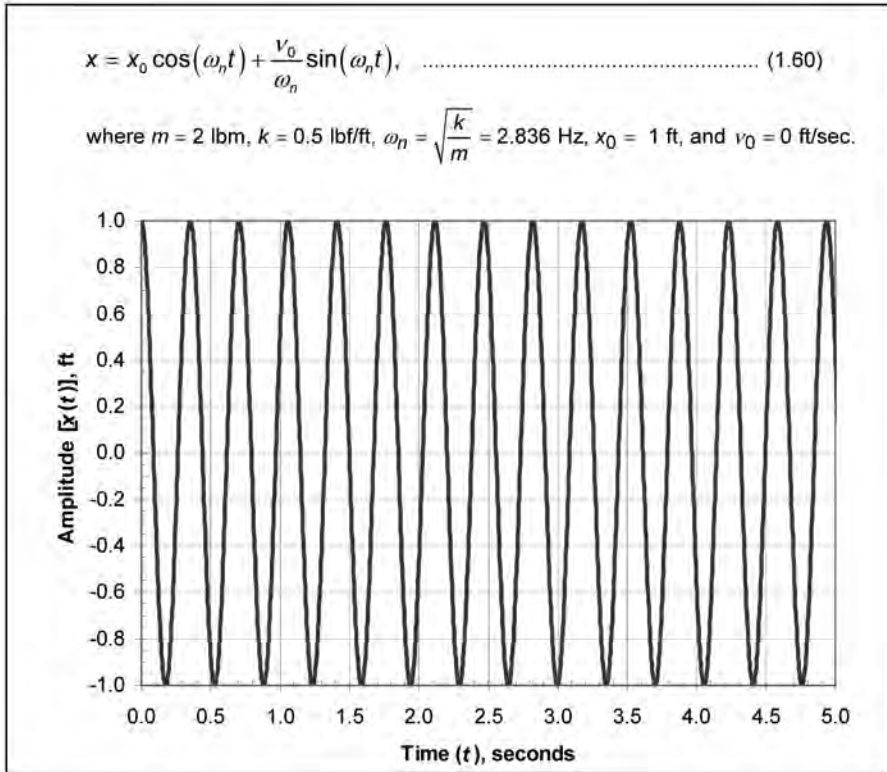
$$m\ddot{x} + c\dot{x} + kx = 0. \dots\dots\dots (1.62)$$

The general solution to this differential equation is:

$$x = C_1 e^{\frac{-c + (\sqrt{c^2 - 4mk})t}{2m}} + C_2 e^{\frac{-c - (\sqrt{c^2 - 4mk})t}{2m}}, \dots\dots\dots (1.63)$$

although the specific solution depends on the value under the square root. When  $c^2 - 4mk = 0$ , the system is critically damped. Another way to look at this critical damping point is:

$$c_{crit} = \sqrt{4mk} = 2m\omega_n. \dots\dots\dots (1.64)$$



**Example 1.1—SDOF free and undamped CLO system.**

Often, the damping coefficient is divided by the critical damping coefficient to get the critical damping ratio:

$$\frac{c}{2m\omega_n} = \frac{c}{c_{crit}} = \zeta, \dots\dots\dots (1.65)$$

If  $\zeta > 1$ , the system is underdamped. When disturbed, the system will experience an oscillating decay. If  $\zeta < 1$ , the system is overdamped and, when disturbed, will die out without oscillating. If  $\zeta = 1$ , the system is critically damped and also will not oscillate.

A useful simplifying equation is the “damped” natural frequency,  $\omega_d$ . It is:

$$\omega_d = \omega_n \sqrt{1 - \zeta^2} \dots\dots\dots (1.66)$$

If the system is underdamped, that is, if  $0 \leq \zeta < 1$ , the solution is:

$$x = e^{-\zeta\omega_n t} (C_1 \cos \omega_d t + C_2 \sin \omega_d t) \dots\dots\dots (1.67)$$

or



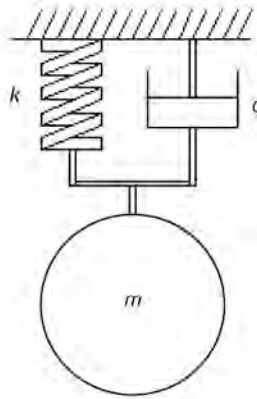


Fig. 1.10—SDOF free and damped CLO system.

$$x = \left(\sqrt{C_1^2 + C_2^2}\right)e^{-\zeta\omega_n t} \sin(\omega_d t + \Phi), \dots\dots\dots (1.68)$$

where  $\Phi = \tan^{-1} \frac{C_1}{C_2}$ . If the initial and boundary coefficients are the same as before, then the solution is:

$$x = e^{-\zeta\omega_n t} \left( x_0 \cos \omega_d t + \frac{v_0 + \zeta\omega_n x_0}{\omega_d} \sin \omega_d t \right) \dots\dots\dots (1.69)$$

or

$$x = \sqrt{x_0^2 + \left(\frac{v_0 + \zeta\omega_n x_0}{\omega_d}\right)^2} e^{-\zeta\omega_n t} \sin\left(\omega_d t + \tan^{-1} \frac{x_0 \omega_d}{v_0 + \zeta\omega_n x_0}\right) \dots\dots\dots (1.70)$$

**Ex. 1.2** is an SDOF free and underdamped CLO system.

If the system is overdamped, that is, if  $\zeta > 1$ , the solution is:

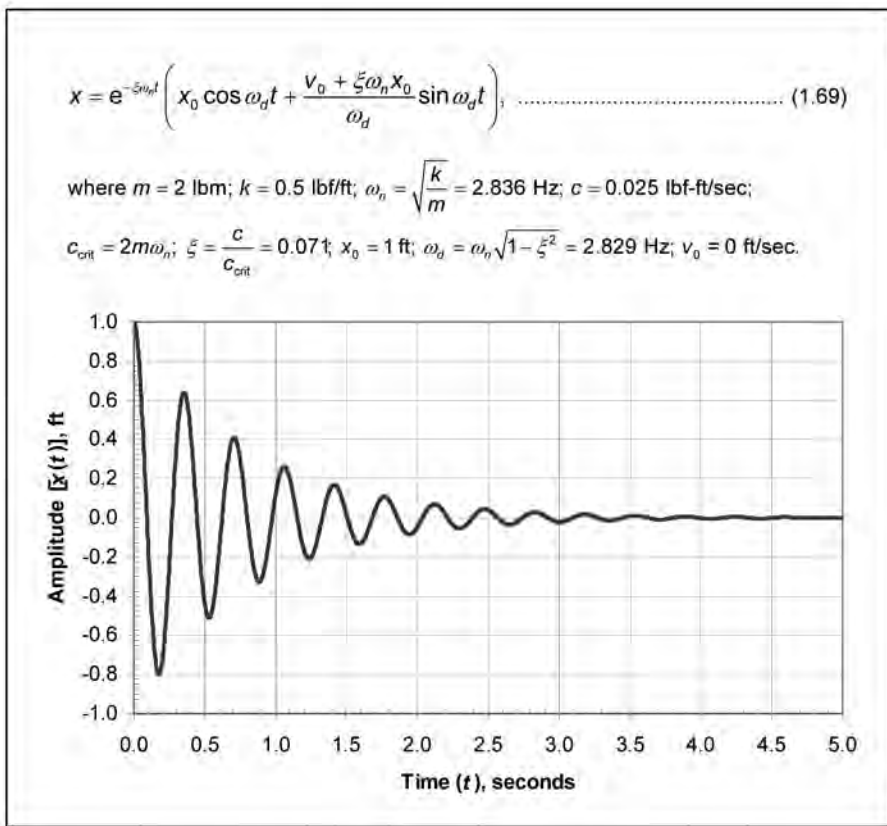
$$x = e^{-\zeta\omega_n t} (C_1 \cosh \omega_d t + C_2 \sinh \omega_d t), \dots\dots\dots (1.71)$$

but in this case,  $\omega_d = \omega_n \sqrt{\zeta^2 - 1}$ . The order changed because it was an imaginary number. With the same initial and boundary conditions as before, the solution is as before:

$$x = e^{-\zeta\omega_n t} \left( x_0 \cosh \omega_d t + \frac{v_0 + \zeta\omega_n x_0}{\omega_d} \sinh \omega_d t \right) \dots\dots\dots (1.72)$$

**Ex. 1.3** is an SDOF free and overdamped CLO system.

If the system is critically damped, that is, if  $\zeta = 1$ , the solution with the initial and boundary conditions is:



Example 1.2—SDOF free and underdamped CLO system.

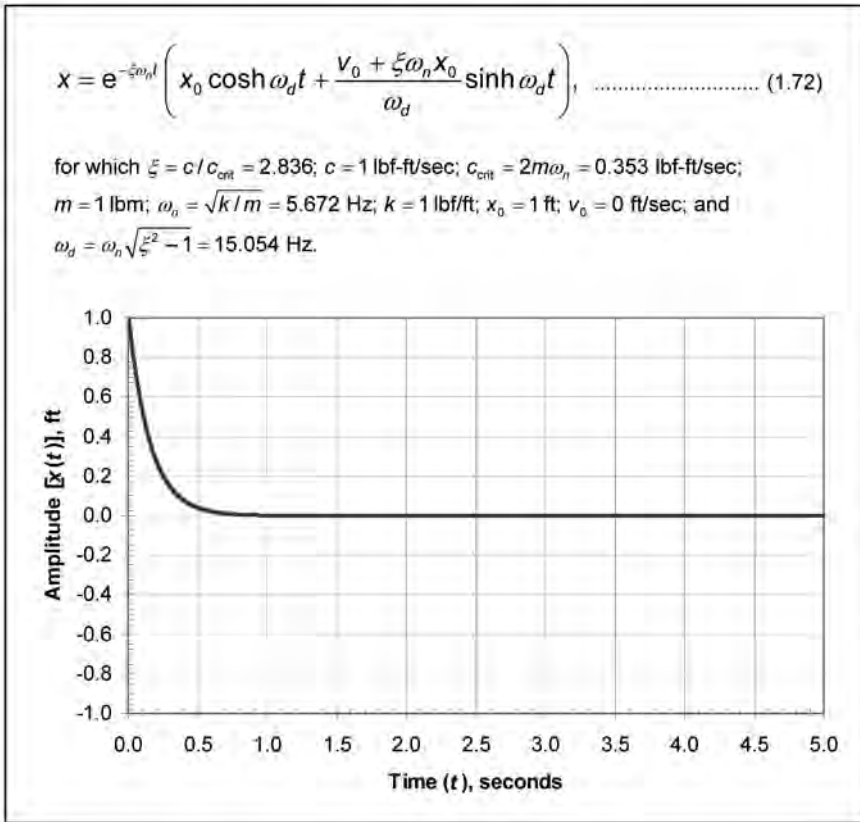
$$x = e^{-\omega_n t} [x_0 + (v_0 + \omega_n x_0)t]; \dots\dots\dots (1.73)$$

Ex. 1.4 is an SDOF free and critically damped CLO system.

**1.9.3 Forced Vibration Without Damping.** The next sets of systems have a forcing function driving the vibration. The first of these is a CLO without damping ( $c = 0$ ), as shown in Fig. 1.11. The equation of motion for this system with  $F = F_0 \sin \omega_f t$ , a sinusoidally varying force, using Newton’s second law, is:

$$m\ddot{x} + kx = F_0 \sin \omega_f t. \dots\dots\dots (1.74)$$

In this case, there are two terms in the solution, the homogenous or transient term, and the particular or steady-state term. The homogenous term is the same as in a free-vibration case and is solved by setting the forcing function to zero (that is, the free-vibration case, Eq. 1.60). If the same initial and boundary conditions are applied as before, the solution for the homogenous case is the same as before:



**Example 1.3—SDOF free and overdamped CLO system.**

$$x_h = x_0 \cos \omega_n t + \frac{v_0}{\omega_n} \sin \omega_n t. \dots\dots\dots (1.75)$$

The second term is the effect of the forcing function on the system. This is solved by assuming a particular solution and deriving it back:

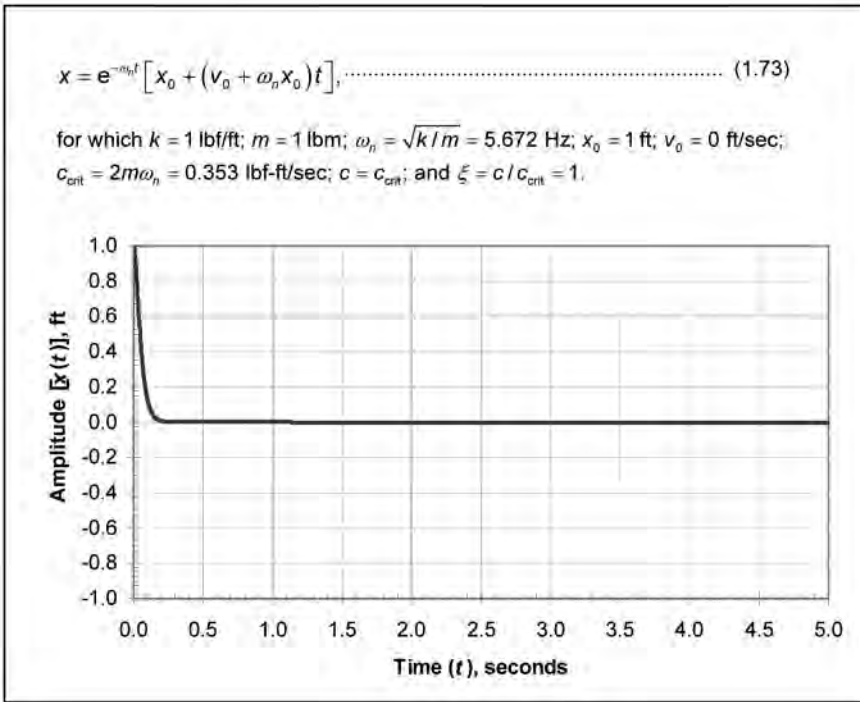
$$x_p = C_1 \sin \omega_f t + C_2 \cos \omega_f t. \dots\dots\dots (1.76)$$

$$\dot{x}_p = C_1 \omega_f \cos \omega_f t - C_2 \omega_f \sin \omega_f t. \dots\dots\dots (1.77)$$

$$\ddot{x}_p = -\omega_f^2 C_1 \sin \omega_f t - \omega_f^2 C_2 \cos \omega_f t. \dots\dots\dots (1.78)$$

Substituting the above equations into Eq. 1.74 gives:

$$m(-\omega_f^2 C_1 \sin \omega_f t - \omega_f^2 C_2 \cos \omega_f t)$$



Example 1.4—SDOF free and critically damped CLO system.

$$+k(C_1 \sin \omega_f t + C_2 \cos \omega_f t) = F_0 \sin \omega_f t. \dots \dots \dots (1.79)$$

Collecting the terms gives:

$$(k - m\omega_f^2)C_1 \sin \omega_f t + (k - m\omega_f^2)C_2 \cos \omega_f t = F_0 \sin \omega_f t. \dots \dots \dots (1.80)$$

Equating coefficients shows that:

$$C_1 = \frac{F_0}{k - m\omega_f^2} \dots \dots \dots (1.81)$$

and

$$C_2 = 0. \dots \dots \dots (1.82)$$

Therefore, the particular solution is:

$$x_p = \frac{F_0}{k - m\omega_f^2} \sin \omega_f t, \dots \dots \dots (1.83)$$

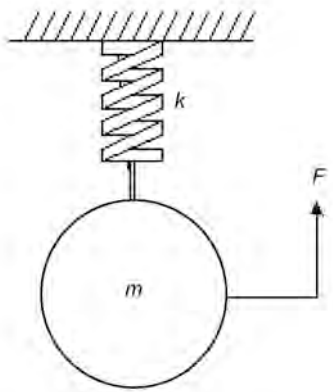


Fig. 1.11—SDOF forced and undamped CLO system.

which can be rewritten as:

$$x_p = \frac{F_0}{k} \left( \frac{1}{1 - \frac{\omega_f^2}{\omega_n^2}} \right) \sin \omega_f t, \dots\dots\dots (1.84)$$

where the reciprocal term in the parentheses sometimes is called the magnification factor. The total solution is:

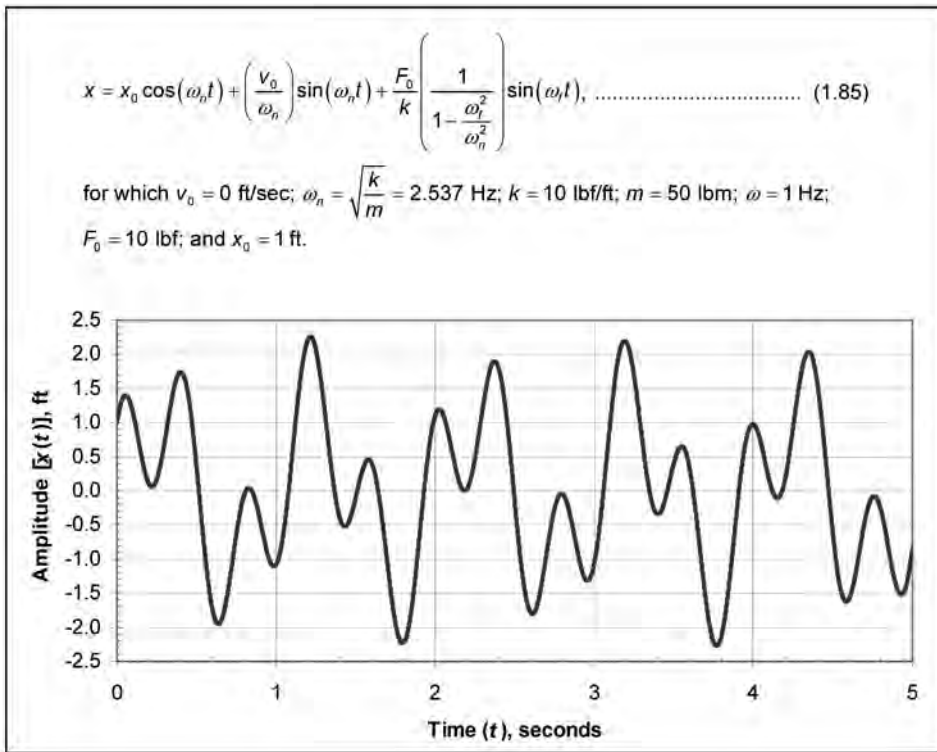
$$x = x_h + x_p = x_0 \cos(\omega_n t) + \left( \frac{v_0}{\omega_n} \right) \sin(\omega_n t) + \frac{F_0}{k} \left( \frac{1}{1 - \frac{\omega_f^2}{\omega_n^2}} \right) \sin(\omega_f t). \dots\dots\dots (1.85)$$

**Ex. 1.5** is an SDOF forced and undamped CLO system.

Note that when the forcing frequency,  $\omega_f$ , matches the natural frequency,  $\omega_n$ , the value of the coefficient is infinity. This is the resonance condition, and it can lead to excessively large displacements (see **Fig. 1.12**).

When the forcing frequency is close to but not at the natural frequency, a beating phenomenon occurs. This appears as a low frequency impressed over the frequency of the system. When the engines of a twin-engine aircraft are not quite synchronized, for example, one can hear a beating sound as a low-frequency pulse (the “wow-wow” throb). **Fig. 1.13** illustrates this beating phenomenon.

**1.9.4 Forced Vibration With Damping.** The second system with a forcing function driving the vibration is a CLO with damping ( $c \neq 0$ ), as shown in **Fig. 1.14**. The equation of motion for this system with the same force as before,  $F = F_0 \sin \omega t$ , is:



**Example 1.5—SDOF forced and undamped CLO system.**

$$m\ddot{x} + c\dot{x} + kx = F_0 \sin \omega_f t. \dots\dots\dots (1.86)$$

The solution has two parts, as before. It is similar to the last example, except for an additional damping term. The particular solution is solved similarly to the last example in Eqs. 1.76, 1.77, and 1.78. Differentiating and substituting into Eq. 1.86 gives:

$$m(-\omega_f^2 C_1 \sin \omega_f t - \omega_f^2 C_2 \cos \omega_f t) + c(C_1 \omega_f \cos \omega_f t - C_2 \omega_f \sin \omega_f t) + k(C_1 \sin \omega_f t + C_2 \cos \omega_f t) = F_0 \sin \omega_f t. \dots\dots\dots (1.87)$$

Rearranging gives:

$$\left[ (k - m\omega_f^2)C_1 - c\omega_f C_2 \right] \sin \omega_f t + \left[ c\omega_f C_1 + (k - m\omega_f^2)C_2 \right] \cos \omega_f t = F_0 \sin \omega_f t. \dots\dots\dots (1.88)$$

Equating coefficients as before yields:

$$(k - m\omega_f^2)C_1 - c\omega_f C_2 = F_0 \dots\dots\dots (1.89)$$

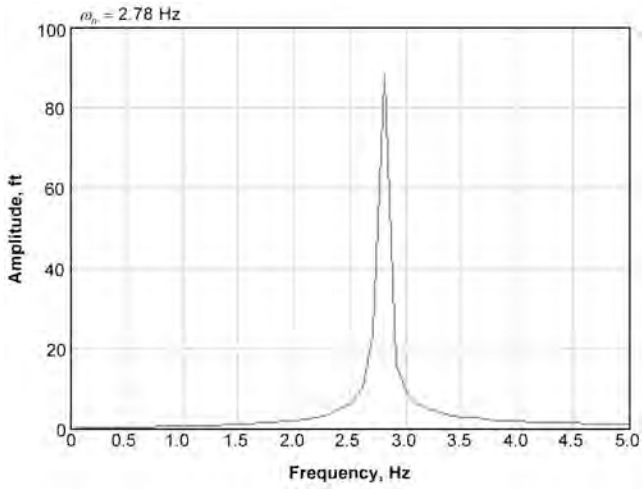


Fig. 1.12—SDOF resonance condition.

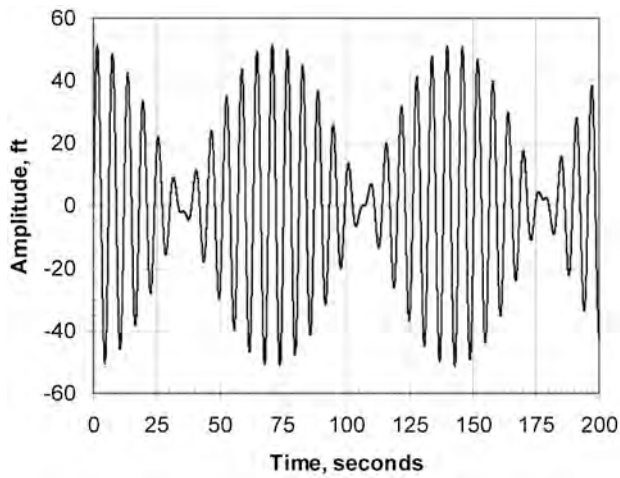


Fig. 1.13—SDOF beating phenomenon.

and

$$c\omega_f C_1 + (k - m\omega_f^2)C_2 = 0 \dots\dots\dots (1.90)$$

Solving for the constants gives:

$$C_1 = \frac{k\left(1 - \frac{\omega_f^2}{\omega_n^2}\right)F_0}{\left[k\left(1 - \frac{\omega_f^2}{\omega_n^2}\right)\right]^2 + c^2\omega_f^2} \dots\dots\dots (1.91)$$

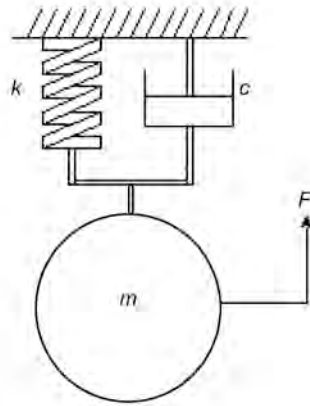


Fig. 1.14—SDOF forced and damped CLO system.

and

$$C_2 = \frac{-c\omega_f F_0}{\left[ k \left( 1 - \frac{\omega_f^2}{\omega_n^2} \right) \right]^2 + c^2 \omega_f^2}, \dots\dots\dots (1.92)$$

which gives the particular solution:

$$x_p = F_0 \left\{ \frac{k \left( 1 - \frac{\omega_f^2}{\omega_n^2} \right)}{\left[ k \left( 1 - \frac{\omega_f^2}{\omega_n^2} \right) \right]^2 + c^2 \omega_f^2} \sin \omega_f t + \frac{-c\omega_f}{\left[ k \left( 1 - \frac{\omega_f^2}{\omega_n^2} \right) \right]^2 + c^2 \omega_f^2} \cos \omega_f t \right\} \dots\dots\dots (1.93)$$

The total solution is homogenous and the particular solutions added together. In this case, if the same initial and boundary conditions are applied as before, the homogenous solution is the same as in the free-vibration case and is Eq. 1.69. The particular solution is Eq. 1.93 and is the effect of the forcing function on the system. As noted before, the critical damping coefficient dictates the behavior of the homogenous part of the solution.

Ex. 1.6 is an SDOF forced and underdamped CLO system.

**1.10 Two-Degree-of-Freedom (2DOF) Systems**

At the basic level, systems with two and more DOFs are similar to SDOF systems. In a 2DOF system, two independent equations of motion are required to define a system (e.g., a double CLO or a double pendulum), but the DOFs need not be the same. For example, a system could have a translational and a rotational DOF. As long as the equations of motion are independent of one other, it is a 2DOF system. These equations must be solved simultaneously.



$$x_h = \left\{ e^{-\zeta\omega_n t} \left[ x_0 \cos(\omega_d t) + \frac{v_0 + \zeta\omega_n x_0}{\omega_d} \sin(\omega_d t) \right] \right\}, \dots\dots\dots (1.69)$$

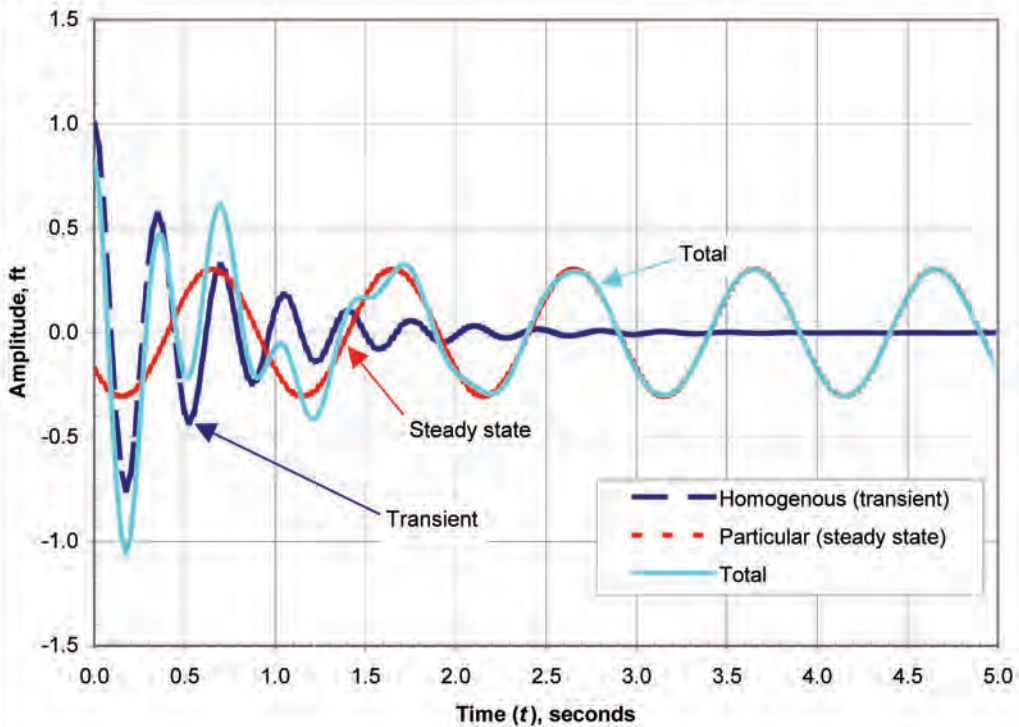
$$x_p = F_0 \left\{ \frac{k \left( 1 - \frac{\omega_f^2}{\omega_n^2} \right)}{\left[ k \left( 1 - \frac{\omega_f^2}{\omega_n^2} \right) \right]^2 + c^2 \omega_f^2} \sin(\omega_f t) + \frac{-c\omega_f}{\left[ k \left( 1 - \frac{\omega_f^2}{\omega_n^2} \right) \right]^2 + c^2 \omega_f^2} \cos(\omega_f t) \right\}, \dots\dots\dots (1.93)$$

and

$$X = X_h + X_p,$$

in which  $m = 2 \text{ lbm}$ ;  $k = 0.5 \text{ lbf/ft}$ ;  $\omega_n = \sqrt{\frac{k}{m}} = 2.836 \text{ Hz}$ ;  $c = 0.025 \text{ lbf-ft/sec}$ ;  $c_{crit} = 2m\omega_n$ ;

$\zeta = \frac{c}{c_{crit}} = 0.071$ ;  $x_0 = 1 \text{ ft}$ ;  $\omega_d = \omega_n \sqrt{1 - \zeta^2} = 2.829 \text{ Hz}$ ;  $v_0 = 0 \text{ ft/sec}$ ;  $F_0 = 1 \text{ lbf}$ , and  $\omega_f = 1 \text{ Hz}$ .



Example 1.6—SDOF forced and underdamped CLO system.

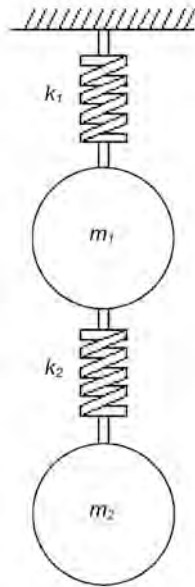


Fig. 1.15—2DOF free and undamped CLO system.

**1.10.1 Free Undamped 2DOF System.** As in the SDOF system, an undamped ( $c_1$  and  $c_2 = 0$ ) system will be developed first. Fig. 1.15 shows such a system. As before, Newton’s second law can determine the equations of motion. In the SDOF system, a solution in the form of sine and cosine was used. For the first 2DOF system, another valid form of a solution, a sine with a phase angle,  $\Phi$ , is used to show another solution form. The equation for mass 1 is

$$m_1 \ddot{x}_1 = -k_1 x_1 + k_2(x_2 - x_1) \dots\dots\dots (1.94)$$

and for mass 2 is

$$m_2 \ddot{x}_2 = -k_2(x_2 - x_1) \dots\dots\dots (1.95)$$

These two equations of motion must be solved simultaneously because they are coupled through the displacement terms,  $x_1$  and  $x_2$ . As before, a solution is assumed and substituted back into the equations of motion. The assumed solution is

$$x_1 = C_1 \sin (\omega t + \Phi) \dots\dots\dots (1.96)$$

and

$$x_2 = C_2 \sin (\omega t + \Phi), \dots\dots\dots (1.97)$$

for which the second differentiation is

$$\ddot{x}_1 = -\omega^2 C_1 \sin(\omega t + \Phi) \dots\dots\dots (1.98)$$

and

$$\ddot{x}_2 = -\omega^2 C_2 \sin(\omega t + \Phi) \dots\dots\dots (1.99)$$

Substituting back into the equations of motion and collecting terms, the result is:

$$(k_1 + k_2 - \omega^2 m_1)C_1 - k_2 C_2 = 0 \dots\dots\dots (1.100)$$

and

$$-k_2 C_1 + (k_2 - \omega^2 m_2)C_2 = 0 \dots\dots\dots (1.101)$$

The only way not to have a trivial solution ( $C_1$  and  $C_2 = 0$ ) to these equations is to have the determinate of the coefficients be zero:

$$\left| \begin{pmatrix} k_1 + k_2 - \omega^2 m_1 & -k_2 \\ -k_2 & k_2 - \omega^2 m_2 \end{pmatrix} \right| = 0 \dots\dots\dots (1.102)$$

Using linear algebra, the determinate is:

$$m_1 m_2 \omega^4 - [m_1 k_2 + m_2 (k_1 + k_2)] \omega^2 + k_1 k_2 = 0, \dots\dots\dots (1.103)$$

which is a quadratic equation in terms of the square of the natural frequencies,  $\omega^2$ . This solves to:

$$\omega^2 = \frac{m_1 k_2 + m_2 (k_1 + k_2) \pm \sqrt{[m_1 k_2 + m_2 (k_1 + k_2)]^2 - 4 m_1 m_2 k_1 k_2}}{2 m_1 m_2} \dots\dots\dots (1.104)$$

There are two roots to this equation, which means that there are two natural frequencies. The solution therefore must be in terms of the two frequencies. Substituting the first natural frequency back into the equation of motion solution gives the result of the first natural frequency:

$$(k_1 + k_2 - \omega_1^2 m_1)C_{11} - k_2 C_{21} = 0 \dots\dots\dots (1.105)$$

and

$$-k_2 C_{11} + (k_2 - \omega_1^2 m_2)C_{21} = 0 \dots\dots\dots (1.106)$$

The ratio of  $C_{11}$  to  $C_{21}$ , known as the mode shape, for the first natural frequency is:

$$\lambda_1 = \frac{C_{11}}{C_{21}} = \frac{k_2}{k_1 + k_2 + \omega_1^2 m_1} = \frac{k_2 - \omega_1^2 m_2}{k_2} \dots\dots\dots (1.107)$$

therefore,

$$C_{11} = \lambda_1 C_{21} \dots\dots\dots (1.108)$$

The first natural frequency motions then are:

$$x_1 = C_{11} \sin(\omega_1 t + \Phi_1) = \lambda_1 C_{21} \sin(\omega_1 t + \Phi_1) \dots\dots\dots (1.109)$$

and

$$x_2 = C_{21} \sin(\omega_1 t + \Phi_1) \dots\dots\dots (1.110)$$

The mode shape for the second natural frequency is:

$$\lambda_2 = \frac{C_{12}}{C_{22}} = \frac{k_2}{k_1 + k_2 + \omega_2^2 m_1} = \frac{k_2 - \omega_2^2 m_2}{k_2} \dots\dots\dots (1.111)$$

therefore,

$$C_{12} = \lambda_2 C_{22} \dots\dots\dots (1.112)$$

The second natural frequency motions then are:

$$x_1 = C_{12} \sin(\omega_2 t + \Phi_2) = \lambda_2 C_{22} \sin(\omega_2 t + \Phi_2) \dots\dots\dots (1.113)$$

and

$$x_2 = C_{22} \sin(\omega_2 t + \Phi_2) \dots\dots\dots (1.114)$$

The complete solution then is both displacements added into one equation:

$$x_1 = C_{11} \sin(\omega_1 t + \Phi_1) + C_{12} \sin(\omega_2 t + \Phi_2) + \lambda_1 C_{21} \sin(\omega_1 t + \Phi_1) + \lambda_2 C_{22} \sin(\omega_2 t + \Phi_2) \dots\dots\dots (1.115)$$

and

$$x_2 = C_{21} \sin(\omega_1 t + \Phi_1) + C_{22} \sin(\omega_2 t + \Phi_2) \dots\dots\dots (1.116)$$

The values of  $C_{11}$ ,  $C_{12}$ ,  $C_{21}$ ,  $C_{22}$ ,  $\Phi_1$ , and  $\Phi_2$  depend on the initial conditions and the mode shapes,  $\lambda_1$  and  $\lambda_2$ .

**Ex. 1.7** is a 2DOF free and undamped CLO system.

**1.10.2 Free Damped 2DOF System.** Adding damping complicates the equations considerably, but the procedure remains the same. In this case, it is easier to use linear algebra. Using the same model as before (see **Fig. 1.16**), but adding viscous dampers ( $c_1$  and  $c_2 \neq 0$ ), the equations of motion for the independent DOFs are determined for mass 1 as

Given that  $m_1 = 2 \text{ lbm}$ ,  $m_2 = 2 \text{ lbm}$ ,  $k_1 = 2 \text{ lbf/ft}$ ,  $k_2 = 2 \text{ lbf/ft}$ , determine the equations of motion for mass 1 and mass 2:

$$m_1 \ddot{x}_1 = -k_1 x_1 + k_2 (x_2 - x_1) \dots\dots\dots (1.94)$$

$$m_2 \ddot{x}_2 = -k_2 (x_2 - x_1) \dots\dots\dots (1.95)$$

Rearranging gives:

$$m_1 \ddot{x}_1 + (k_1 + k_2) x_1 - k_2 x_2 = 0 \dots\dots\dots (1.117)$$

$$m_2 \ddot{x}_2 - k_2 x_1 + k_2 x_2 = 0 \dots\dots\dots (1.118)$$

Assume a solution of the form  $x = C \sin(\omega t + \phi)$ :

$$x_1 = C_1 \sin(\omega t + \phi) \dots\dots\dots (1.96)$$

$$x_2 = C_2 \sin(\omega t + \phi) \dots\dots\dots (1.97)$$

which when differentiated twice gives

$$\ddot{x}_1 = -\omega^2 C_1 \sin(\omega t + \phi) \dots\dots\dots (1.98)$$

$$\ddot{x}_2 = -\omega^2 C_2 \sin(\omega t + \phi) \dots\dots\dots (1.99)$$

Substituting into the equations of motion gives:

$$-m_1 \omega^2 C_1 \sin(\omega t + \phi) + (k_1 + k_2) C_1 \sin(\omega t + \phi) - k_2 C_2 \sin(\omega t + \phi) = 0 \dots\dots\dots (1.119)$$

$$-m_2 \omega^2 C_2 \sin(\omega t + \phi) + k_2 C_2 \sin(\omega t + \phi) - k_2 C_1 \sin(\omega t + \phi) = 0 \dots\dots\dots (1.120)$$

which simplifies to

$$\begin{pmatrix} -m_1 \omega^2 + k_1 + k_2 & -k_2 \\ -k_2 & -m_2 \omega^2 + k_2 \end{pmatrix} \begin{pmatrix} C_1 \\ C_2 \end{pmatrix} \sin(\omega t + \phi) = 0 \dots\dots\dots (1.121)$$

The only nontrivial way these equations can equal zero is if the determinate of the coefficients is equal to zero. Therefore:

$$\begin{vmatrix} -m_1 \omega^2 + k_1 + k_2 & -k_2 \\ -k_2 & -m_2 \omega^2 + k_2 \end{vmatrix} = 0 \dots\dots\dots (1.102)$$

The solution is:

$$(-m_1 \omega^2 + k_1 + k_2)(-m_2 \omega^2 + k_2) - (-k_2)(-k_2) = 0 \dots\dots\dots (1.122)$$

which gives the characteristic equation

$$m_1 m_2 \omega^4 - [m_1 k_2 + m_2 (k_1 + k_2)] \omega^2 + k_1 k_2 = 0 \dots\dots\dots (1.103)$$

which is a quadratic function in terms of  $\omega^2$ . Therefore,  $\omega^2$  is equal to:

$$\omega^2 = \frac{-b \pm \sqrt{b^2 - 4ac}}{2a} = \frac{[m_1 k_2 + m_2 (k_1 + k_2)] \pm \sqrt{[m_1 k_2 + m_2 (k_1 + k_2)]^2 - 4m_1 m_2 k_1 k_2}}{2m_1 m_2} \dots\dots\dots (1.104)$$

which gives two solutions, which means two natural frequencies. In this example, the frequencies are  $\omega_1 = 9.178 \text{ Hz}$  and  $\omega_2 = 3.506 \text{ Hz}$ .

The shape functions are:

$$\lambda_1 = \frac{k_2}{k_1 + k_2 - \omega_1^2 m_1} = \frac{k_2 - \omega_1^2 m_2}{k_2} = -1.618 \dots\dots\dots (1.107)$$

$$\lambda_2 = \frac{k_2}{k_1 + k_2 - \omega_2^2 m_1} = \frac{k_2 - \omega_2^2 m_2}{k_2} = 0.618 \dots\dots\dots (1.111)$$

To determine the specific solutions, the boundary conditions must be applied. At time equal zero, they are  $x_1 = 1 \text{ ft}$ ,  $x_2 = 0 \text{ ft}$ ,  $v_1 = 0 \text{ ft/s}$ , and  $v_2 = 0 \text{ ft/s}$ . Applying these to the solution to the equations of motion gives:

$$x_1 = C_{11} \sin(\omega_1 t + \phi_1) + C_{12} \sin(\omega_2 t + \phi_2) = \lambda_1 C_{21} \sin(\phi_1) + \lambda_2 C_{22} \sin(\phi_2) \dots\dots\dots (1.123)$$

$$x_2 = C_{21} \sin(\omega_1 t + \phi_1) + C_{22} \sin(\omega_2 t + \phi_2) = C_{21} \sin(\phi_1) + C_{22} \sin(\phi_2) \dots\dots\dots (1.124)$$

$$v_1 = \omega_1 C_{11} \sin(\omega_1 t + \phi_1) + \omega_2 C_{12} \sin(\omega_2 t + \phi_2) = \lambda_1 \omega_1 C_{21} \sin(\phi_1) + \lambda_2 \omega_2 C_{22} \sin(\phi_2) \dots\dots\dots (1.125)$$

$$v_2 = \omega_1 C_{21} \sin(\omega_1 t + \phi_1) + \omega_2 C_{22} \sin(\omega_2 t + \phi_2) = \omega_1 C_{21} \sin(\phi_1) + \omega_2 C_{22} \sin(\phi_2) \dots\dots\dots (1.126)$$

which gives four unknowns for four independent equations. The simultaneous solution to the above set of equations is  $C_{21} = -0.447 \text{ ft}$ ,  $C_{22} = 0.447 \text{ ft}$ ,  $\phi_1 = 1.571 \text{ radians}$ , and  $\phi_2 = 1.571 \text{ radians}$ ; and further solutions give  $C_{11} = 0.724 \text{ ft}$  and  $C_{12} = 0.276 \text{ ft}$ .

The solution to the equations of motion is:

$$x_1 = 0.724 \sin[2\pi(9.178)t + 1.571] + 0.276 \sin[2\pi(3.506)t + 1.571] \text{ and}$$

$$x_2 = -0.447 \sin[2\pi(9.178)t + 1.571] + 0.447 \sin[2\pi(3.506)t + 1.571],$$

where  $2\pi$  is for conversion to radians.

Example 1.7—2DOF free and undamped CLO system.

$$m_1\ddot{x}_1 = -k_1x_1 + k_2(x_2 - x_1) - c_1\dot{x}_1 + c_2(\dot{x}_2 - \dot{x}_1) \dots\dots\dots (1.127)$$

and for mass 2 as

$$m_2\ddot{x}_2 = -k_2(x_2 - x_1) - c_2(\dot{x}_2 - \dot{x}_1) \dots\dots\dots (1.128)$$

This can be written in matrix form as

$$\begin{bmatrix} m_1 & 0 \\ 0 & m_2 \end{bmatrix} \begin{bmatrix} \ddot{x}_1 \\ \ddot{x}_2 \end{bmatrix} + \begin{bmatrix} c_1 + c_2 & -c_2 \\ -c_2 & c_2 \end{bmatrix} \begin{bmatrix} \dot{x}_1 \\ \dot{x}_2 \end{bmatrix} + \begin{bmatrix} k_1 + k_2 & -k_2 \\ -k_2 & k_2 \end{bmatrix} \begin{bmatrix} x_1 \\ x_2 \end{bmatrix} = \begin{bmatrix} 0 \\ 0 \end{bmatrix} \dots\dots\dots (1.129)$$

or as

$$\mathbf{M}\ddot{\mathbf{X}} + \mathbf{C}\dot{\mathbf{X}} + \mathbf{K}\mathbf{X} = \mathbf{0}, \dots\dots\dots (1.130)$$

where **M** = the mass matrix, **C** = the damping matrix, **K** = the stiffness matrix, **Ẍ** = the acceleration vector, **Ẋ** = the velocity vector, and **X** = the displacement vector, which are given as:

$$\mathbf{M} = \begin{bmatrix} m_1 & 0 \\ 0 & m_2 \end{bmatrix}, \dots\dots\dots (1.131)$$

$$\mathbf{C} = \begin{bmatrix} c_1 + c_2 & -c_2 \\ -c_2 & c_2 \end{bmatrix}, \dots\dots\dots (1.132)$$

$$\mathbf{K} = \begin{bmatrix} k_1 + k_2 & -k_2 \\ -k_2 & k_2 \end{bmatrix}, \dots\dots\dots (1.133)$$

$$\ddot{\mathbf{X}} = \begin{bmatrix} \ddot{x}_1 \\ \ddot{x}_2 \end{bmatrix}, \dots\dots\dots (1.134)$$

$$\dot{\mathbf{X}} = \begin{bmatrix} \dot{x}_1 \\ \dot{x}_2 \end{bmatrix}, \dots\dots\dots (1.135)$$

and

$$\mathbf{X} = \begin{bmatrix} x_1 \\ x_2 \end{bmatrix} \dots\dots\dots (1.136)$$

If the solution is assumed to be of the form

$$x = Ce^{\omega t}, \dots\dots\dots (1.137)$$

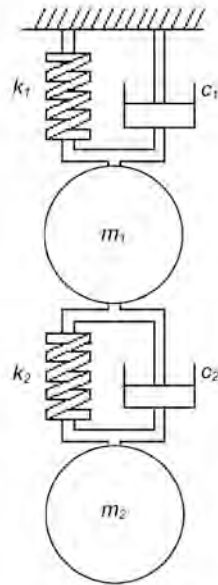


Fig. 1.16—2DOF free and damped CLO system.

then

$$\dot{x} = \omega C e^{\omega t} \dots\dots\dots (1.138)$$

and

$$\ddot{x} = \omega^2 C e^{\omega t} \dots\dots\dots (1.139)$$

Substituting back into the equation of motion, the result in matrix form is:

$$\omega^2 \mathbf{M} C e^{\omega t} + \omega \mathbf{C} C e^{\omega t} + \mathbf{K} C e^{\omega t} = 0, \dots\dots\dots (1.140a)$$

which can be rewritten as

$$(\omega^2 \mathbf{M} + \omega \mathbf{C} + \mathbf{K}) C e^{\omega t} = 0. \dots\dots\dots (1.140b)$$

Because time is always positive and a nontrivial solution is desired, the only way this equation is true is if the determinate of the coefficient of  $C e^{\omega t}$  is zero; that is, if

$$|\omega^2 \mathbf{M} + \omega \mathbf{C} + \mathbf{K}| = 0. \dots\dots\dots (1.141)$$

The determinate of Eq. 1.141 is a fourth-order polynomial in terms of  $a$ , which means that there are four roots. These roots can be:

Given  $m_1 = 2$  lbm,  $m_2 = 2$  lbm,  $c_1 = 0.1$  lbf-ft/sec,  $c_2 = 0.1$  lbf-ft/sec,  $k_1 = 2$  lbf/ft, and  $k_2 = 2$  lbf/ft, determine the equations of motion for mass 1 and mass 2:

$$m_1 \ddot{x}_1 = -k_1 x_1 + k_2 (x_2 - x_1) - c_1 \dot{x}_1 + c_2 (\dot{x}_2 - \dot{x}_1) \quad (1.127)$$

$$m_2 \ddot{x}_2 = -k_2 (x_2 - x_1) - c_2 (\dot{x}_2 - \dot{x}_1) \quad (1.128)$$

Rearranging gives:

$$m_1 \ddot{x}_1 + (c_1 + c_2) \dot{x}_1 - c_2 \dot{x}_2 + (k_1 + k_2) x_1 - k_2 x_2 = 0 \quad (1.142)$$

$$m_2 \ddot{x}_2 - c_2 \dot{x}_1 + c_2 \dot{x}_2 - k_2 x_1 + k_2 x_2 = 0 \quad (1.143)$$

Using linear algebra can simplify the notation. The mass matrix is

$$\mathbf{M} = \begin{pmatrix} m_1 & 0 \\ 0 & m_2 \end{pmatrix}, \quad (1.131)$$

the damping matrix is

$$\mathbf{C} = \begin{pmatrix} c_1 + c_2 & -c_2 \\ -c_2 & c_2 \end{pmatrix}, \quad (1.132)$$

the stiffness matrix is

$$\mathbf{K} = \begin{pmatrix} k_1 + k_2 & -k_2 \\ -k_2 & k_2 \end{pmatrix}, \quad (1.133)$$

the acceleration vector is

$$\ddot{\mathbf{x}} = \begin{pmatrix} \ddot{x}_1 \\ \ddot{x}_2 \end{pmatrix}, \quad (1.134)$$

the velocity vector is

$$\dot{\mathbf{x}} = \begin{pmatrix} \dot{x}_1 \\ \dot{x}_2 \end{pmatrix}, \quad (1.135)$$

and, finally, the displacement vector is

$$\mathbf{x} = \begin{pmatrix} x_1 \\ x_2 \end{pmatrix}, \quad (1.136)$$

which simplifies the basic equation of motion to

$$\mathbf{M}\ddot{\mathbf{x}} + \mathbf{C}\dot{\mathbf{x}} + \mathbf{K}\mathbf{x} = 0 \quad (1.130)$$

Assume a solution of the form  $\mathbf{x} = \mathbf{C}e^{i\omega t}$ :

$$x_1 = C_1 e^{i\omega t} \quad (1.144)$$

$$x_2 = C_2 e^{i\omega t}, \quad (1.145)$$

which, when differentiated once gives

$$\dot{x}_1 = i\omega C_1 e^{i\omega t} \quad (1.146)$$

$$\dot{x}_2 = i\omega C_2 e^{i\omega t}, \quad (1.147)$$

and when differentiated twice gives

$$\ddot{x}_1 = -\omega^2 C_1 e^{i\omega t} \quad (1.148)$$

$$\ddot{x}_2 = -\omega^2 C_2 e^{i\omega t}, \quad (1.149)$$

Substituting into the equations of motion gives:

$$(\omega^2 \mathbf{M} + i\omega \mathbf{C} + \mathbf{K}) \mathbf{C} e^{i\omega t} = 0, \quad (1.140b)$$

where

$$\mathbf{C} = \begin{pmatrix} C_1 \\ C_2 \end{pmatrix}. \quad (1.150)$$

### Example 1.8—2DOF free and damped CLO system.

1. Four real and negative roots.
2. Two sets of complex conjugates with negative real parts.
3. Two real and negative roots and one set of complex conjugates.



As in the previous example, the only nontrivial way this equation can equal zero is if the determinate of the coefficients is equal to zero. Therefore, completely spelled out, it becomes:

$$\begin{bmatrix} m_1\omega^2 + (c_1 + c_2)\omega + (k_1 + k_2) & -c_2\omega - k_2 \\ -c_2\omega - k_2 & m_2\omega^2 + c_2\omega + k_2 \end{bmatrix} = 0 \dots\dots\dots (1.151)$$

The solution gives the characteristic equation:

$$m_1m_2\omega^4 + [m_1c_2 + m_2(c_1 + c_2)]\omega^3 + [m_1k_2 + m_2(k_1 + k_2) + c_1c_2]\omega^2 + (c_1k_2 + c_2k_1)\omega + k_1k_2 = 0, \dots (1.152)$$

which is a fourth-order polynomial with four roots. The roots of this equation are:

$$\omega = \begin{bmatrix} -2.106 + 8.933i \\ -2.106 - 8.933i \\ -0.307 - 3.492i \\ -0.307 + 3.492i \end{bmatrix}$$

This is a case where the roots are pairs of complex conjugates. This gives a decaying exponential oscillating type of solution. If one takes the absolute value of  $\omega$ , the results are:

$$\omega = \begin{bmatrix} 9.178 \\ 9.178 \\ 3.506 \\ 3.506 \end{bmatrix} \text{ Hz,}$$

or two natural frequencies, as expected.

There are four shape functions:

$$\lambda = \begin{bmatrix} \frac{\omega_1 c_2 + k_2}{\omega_1^2 m_1 + \omega_1 (c_1 + c_2) + (k_1 + k_2)} \\ \frac{\omega_2 c_2 + k_2}{\omega_2^2 m_1 + \omega_2 (c_1 + c_2) + (k_1 + k_2)} \\ -\frac{\omega_3 c_2 + k_2}{\omega_3^2 m_1 + \omega_3 (c_1 + c_2) + (k_1 + k_2)} \\ \frac{\omega_4 c_2 + k_2}{\omega_4^2 m_1 + \omega_4 (c_1 + c_2) + (k_1 + k_2)} \end{bmatrix} = \begin{bmatrix} \frac{\omega_1^2 m_2 + \omega_1 c_2 + k_2}{\omega_1 c_2 + k_2} \\ \frac{\omega_2^2 m_2 + \omega_2 c_2 + k_2}{\omega_2 c_2 + k_2} \\ \frac{\omega_3^2 m_2 + \omega_3 c_2 + k_2}{\omega_3 c_2 + k_2} \\ \frac{\omega_4^2 m_2 + \omega_4 c_2 + k_2}{\omega_4 c_2 + k_2} \end{bmatrix} = \begin{bmatrix} -1.618 \\ -1.618 \\ 0.618 \\ 0.618 \end{bmatrix} \dots\dots\dots (1.153)$$

To determine the specific solutions, the boundary conditions must be applied. At time equal zero, they are:

$$x_1 = 1 \text{ ft, } x_2 = 0 \text{ ft, } v_1 = 0 \text{ ft/sec, } v_2 = 0 \text{ ft/sec}$$

Applied to the solution to the equations of motion, the displacements are

$$x_1 = C_{11}e^{i\omega t} + C_{12}e^{i\omega t} + C_{13}e^{i\omega t} + C_{14}e^{i\omega t} \dots\dots\dots (1.154)$$

$$x_2 = C_{21}e^{i\omega t} + C_{22}e^{i\omega t} + C_{23}e^{i\omega t} + C_{24}e^{i\omega t} \dots\dots\dots (1.155)$$

and the initial velocities are

$$v_1 = \omega_1 C_{11}e^{i\omega t} + \omega_2 C_{12}e^{i\omega t} + \omega_3 C_{13}e^{i\omega t} + \omega_4 C_{14}e^{i\omega t} \dots\dots\dots (1.156)$$

$$v_2 = \omega_1 C_{21}e^{i\omega t} + \omega_2 C_{22}e^{i\omega t} + \omega_3 C_{23}e^{i\omega t} + \omega_4 C_{24}e^{i\omega t} \dots\dots\dots (1.157)$$

These are eight unknowns for four equations. Further constraints include:

$$C_{11} = \lambda_1 C_{21}, C_{12} = \lambda_1 C_{22}, C_{13} = \lambda_1 C_{23}, \text{ and } C_{14} = \lambda_1 C_{24},$$

which gives eight unknowns for eight independent equations. The simultaneous solutions to the above set of equations are:

$$C_{11} = 0.362 - 0.085i, C_{12} = 0.362 + 0.085i, C_{13} = 0.138 + 0.012i, C_{14} = 0.138 - 0.012i, \\ C_{21} = -0.224 + 0.053i, C_{22} = -0.224 - 0.053i, C_{23} = 0.224 + 0.020i, \text{ and } C_{24} = 0.224 - 0.020i.$$

The solutions to the equations of motion are:

$$x_1 = (0.362 - 0.085i)e^{2\pi(-2.106 + 8.933i)t} + (0.362 + 0.085i)e^{2\pi(-2.106 - 8.933i)t} \\ + (0.138 + 0.012i)e^{2\pi(-0.307 - 3.492i)t} + (0.138 - 0.012i)e^{2\pi(-0.307 + 3.492i)t} \dots\dots\dots (1.158)$$

$$x_2 = (-0.224 + 0.053i)e^{2\pi(-2.106 + 8.933i)t} + (-0.224 - 0.053i)e^{2\pi(-2.106 - 8.933i)t} \\ + (0.224 + 0.020i)e^{2\pi(-0.307 - 3.492i)t} + (0.224 - 0.020i)e^{2\pi(-0.307 + 3.492i)t} \dots\dots\dots (1.159)$$

**Example 1.8—2DOF free and damped CLO system (continued).**

If number one is the case, then the result is an exponentially decaying motion without oscillation. It is similar to the overdamped case for an SDOF system. If number two is the case,

then the motions will be exponentially decaying oscillations for both DOFs. This is similar to the underdamped case for an SDOF system. Finally, for case number three, either condition can occur.

**Ex. 1.8** is a 2DOF free and underdamped CLO system.

More information on linear algebra can be found in Chap. 2 of this section of the Handbook.

**1.10.3 Forced Damped 2DOF System.** Adding forcing complicates the equations considerably yet again. The procedure is the same, however, and it is a matter of keeping the mathematics straight. Many texts are available to delve more deeply into this subject. For more information, please refer to Refs. 11 through 19.

**1.10.4 Multiple-DOF Systems.** The previous discussion of 2DOF systems points out how to handle any DOF system. The last example used matrix notation to define the system for the solution process. Multiple-DOF systems are solved similarly with the primary difference being the degree of the defining matrices is greater, as is the degree of difficulty in solving the system. The matrix will have the same number of rows and columns as the degree of freedom. There are other methods (e.g., finite-element modeling) that can be used to tackle the complexity of multiple-DOF systems.

**1.11 Continuous Systems**

If one continues to add DOFs, the limit at an infinite DOF defines a continuous system. The result becomes a PDE. The following is a brief description of the separation of variables method for solving a PDE.

**Fig. 1.17** shows a freebody diagram for axial and torsional systems. The axial system equations will be used to determine the solution of the equations of motion. Eq. 1.162 is the axial equation of motion:

$$m \frac{\partial^2 u}{\partial t^2} = A_c E \frac{\partial^2 u}{\partial x^2} - c \frac{\partial u}{\partial t} - mg_c, \dots\dots\dots (1.162)$$

where  $m \frac{\partial^2 u}{\partial t^2}$  = the inertial force,  $A_c E \frac{\partial^2 u}{\partial x^2}$  = the rate of strain change,  $mg_c$  = the static weight of the element, and  $c \frac{\partial u}{\partial t}$  = the force from viscous damping. This PDE, Eq. 1.162, can be solved using the separation of variables method. This is shown as:

$$U(x, t) = X(x)T(t). \dots\dots\dots (1.164)$$

The following solution assumption is made concerning the time function:

$$T(t) = e^{i\omega t} \dots\dots\dots (1.165)$$

This equation is substituted back into the assumed solution, which then is appropriately differentiated and substituted back into the equation of motion. The equation becomes

$$A_c E \frac{\partial^2 X(x)}{\partial x^2} e^{i\omega t} + (m\omega^2 - ci\omega)X(x)e^{i\omega t} = 0, \dots\dots\dots (1.166)$$

which is of the form

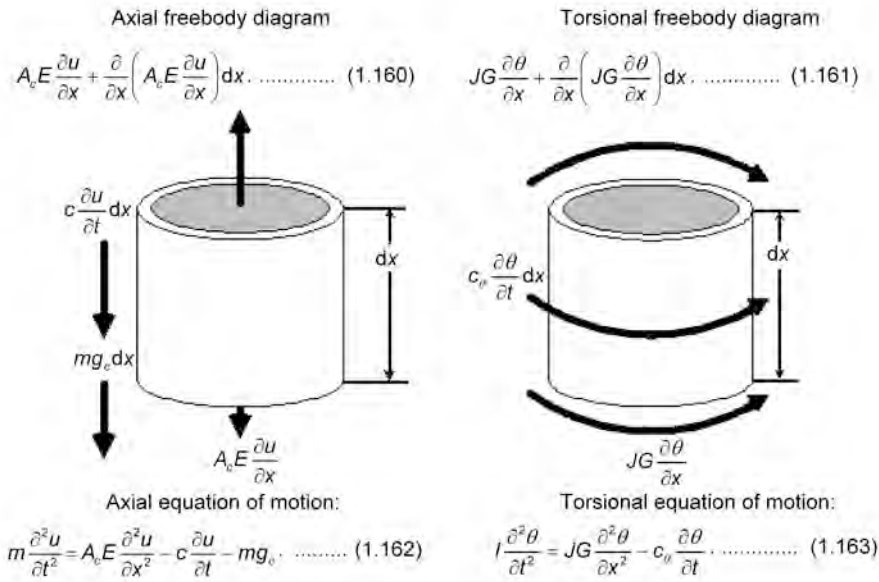


Fig. 1.17—Freebody diagrams for axial and torsional motion.

$$y'' + \varphi^2 y = 0 \dots \dots \dots (1.167)$$

The standard solution of this equation is:

$$X(x) = C_1 e^{-i\varphi x} + C_2 e^{i\varphi x} \dots \dots \dots (1.168)$$

The constants of integration,  $C_1$  and  $C_2$ , are determined by the initial and boundary conditions, and  $\varphi$  is a collection of the constants and is given by:

$$\varphi = \sqrt{\frac{m\omega^2 - ci\omega}{A_c E}} \dots \dots \dots (1.169)$$

Therefore, the total solution is:

$$U(x, t) = (C_1 e^{-i\varphi x} + C_2 e^{i\varphi x}) e^{i\omega t} \dots \dots \dots (1.170)$$

The solution to the torsional equation of motion is derived similarly to the axial equation, with the substitution of the appropriate variables and noting that there is no initial strain from gravity. The variables  $u$ ,  $m$ ,  $A_c$ ,  $E$ ,  $c$ ,  $\omega$ ,  $v_s$ , and  $\varphi$  are replaced by  $\theta$ ,  $I$ ,  $J$ ,  $G$ ,  $c_\theta$ ,  $\omega_\theta$ ,  $v_\theta$ , and  $\eta$ , respectively. The torsional equation of motion is:

$$I \frac{\partial^2 \theta}{\partial t^2} = JG \frac{\partial^2 \theta}{\partial x^2} - c_\theta \frac{\partial \theta}{\partial t} \dots \dots \dots (1.163)$$

This gives the solution as:

$$\theta(x, t) = \left[ (C_1 e^{-i\eta x} + C_2 e^{i\eta x}) e^{i\omega \theta t} \right] \dots\dots\dots (1.171)$$

Constants  $C_1$  and  $C_2$  are based on the initial and boundary conditions, and  $\eta$  is a collection of the constants and is given by:

$$\eta = \sqrt{\frac{\omega \theta^2}{v \theta^2} - \frac{i c \theta \omega \theta}{JG}} \dots\dots\dots (1.172)$$

where

$$v \theta = \sqrt{\frac{JG}{m \theta}} \dots\dots\dots (1.173)$$

and

$$m \theta = \frac{\rho A_c}{8} (d_o^2 - d_i^2) \dots\dots\dots (1.174)$$

**1.12 Wave Reflection From Various Geometric Boundaries**

As discussed early in the chapter, wave propagation is the movement of a distinct group of waves through some material in response to an external force.

A key point in wave-propagation studies is how waves interact with geometric discontinuities. What happens as a wave meets a fixed or free boundary condition? Also, what happens to a wave as it encounters a geometrical area change or a change in material properties?

There are two limiting boundary conditions for wave propagation: a fixed (pinned) end (zero displacement) and a free end (zero stress). A fixed end is a boundary condition in which there is zero displacement. According to wave theory, during a wave encounter with a fixed end, the stress at the fixed end doubles during the passage of the wave. A reflection of a stress wave will simply bounce back with the same sign. A compression wave will reflect as a compression wave and a tension wave will reflect as a tension wave. At a fixed end, because the displacement is zero, the particle velocity will be zero. The wave particle velocity amplitude is inverted during a reflection from a fixed end.

A free end is defined as a boundary condition free to move. The stress at the free end is always zero. The effects on stress and particle velocity caused by a free end are opposite of the effects on stress on a fixed end. A compression wave encountering a free end reflects as a tension wave, and a tension wave reflects as a compression wave. The wave particle velocity values double during an encounter with a free end and reflect with the same sign.

As a wave encounters a change in cross-sectional area, some of the wave is reflected and some is transmitted (refracted). The amplitudes and sign of the waves depend on the relative change in cross-sectional area. The equation that describes the effect on the incident force,  $F_i$ , of a cross-sectional-area, density, or modulus-of-elasticity change for the transmitted wave is

$$F_t = \frac{\sqrt{\frac{E_2 \rho_2}{E_1 \rho_1}}}{\sqrt{\frac{E_2 \rho_2}{E_1 \rho_1} \frac{A_{c2}}{A_{c1}} + 1}} F_i \dots\dots\dots (1.175)$$

and for the reflected wave is

$$F_r = \frac{\sqrt{\frac{E_2 \rho_2}{E_1 \rho_1} \frac{A_{c2}}{A_{c1}} - 1}}{\sqrt{\frac{E_2 \rho_2}{E_1 \rho_1} \frac{A_{c2}}{A_{c1}} + 1}} F_i \dots\dots\dots (1.176)$$

If an incident wave encounters a junction where the relative change in cross-sectional area is greater than 1 (a smaller area to a larger area), most of the wave will transmit through the junction. Some of the wave will reflect from the junction and will keep the same sign. For example, a compression wave will transmit through the junction and keep going as a somewhat-diminished compression wave. The part of the wave that is reflected is still a compression wave, but its amplitude is less than that of the wave that transmitted through the junction.

On the other hand, if an incident wave encounters a junction where the relative change in cross-sectional area is less than 1 (a larger area to a smaller area), most of the wave will reflect off the junction, but some of it will transmit through the junction and will keep the same sign. For example, a compression wave will transmit through the junction and keep going as a diminished compression wave. The reflected part of the wave is a tension wave whose absolute amplitude is greater than that of the compression wave that is transmitted through the junction.

As with most drillstrings, there are many geometric discontinuities (changes in cross-sectional area) that will cause part of the wave to refract and part to reflect. For example, drill collars to heavyweight drillpipe to drillpipe all are geometric discontinuities. Sometimes, too, there are material discontinuities—changes in material density or modulus of elasticity—that cause refractions and reflections. A third possible type of discontinuity is when there are different end-points. For example, if the pipe is stuck, one end can be modeled as stuck. If the pipe is hanging freely, such as with casing running, then the end is free.

More-detailed information on wave propagation can be found in [Refs. 20 through 25](#).

**Nomenclature**

- a* = acceleration, L/t<sup>2</sup>, ft/sec<sup>2</sup>
- A* = slope, dimensionless
- A<sub>c</sub>* = cross-sectional area, L<sup>2</sup>, in.<sup>2</sup>
- c* = axial damping coefficient, mL/t, lbf-ft/sec
- c<sub>crit</sub>* = critical damping coefficient, dimensionless
- c<sub>θ</sub>* = torsional damping coefficient, mL/t, lbf-sec/rad
- C* = constant of integration, various
- C** = damping matrix, mL/t, lbf-ft/sec
- d<sub>i</sub>* = inner diameter, L, in.
- d<sub>o</sub>* = outer diameter, L, in.
- E* = modulus of elasticity, m/Lt<sup>2</sup>, psia
- E(t)* = excitation function
- f* = cyclic frequency, 1/t, cycle/sec
- f(t)* = function of *t*
- f'(t)* = first differential function
- F* = axial force, mL/t<sup>2</sup>, lbf
- F<sub>d</sub>* = damping force, mL/t<sup>2</sup>, lbf
- F<sub>f</sub>* = friction force, mL/t<sup>2</sup>, lbf
- F<sub>h</sub>* = hysteretic force, mL/t<sup>2</sup>, lbf

- $F_i$  = incident force, mL/t<sup>2</sup>, lbf  
 $F_n$  = normal force, mL/t<sup>2</sup>, lbf  
 $F_r$  = reflected force, mL/t<sup>2</sup>, lbf  
 $F_t$  = transmitted force, mL/t<sup>2</sup>, lbf  
 $F_0$  = initial force, mL/t<sup>2</sup>, lbf  
 $g_c$  = gravitational constant, L/t<sup>2</sup>, 32.174 ft/sec<sup>2</sup>  
 $g(t)$  = function of  $t$   
 $g'(t)$  = first derivative of function of  $g(t)$   
 $G$  = shear modulus, m/Lt<sup>2</sup>, psia  
 $h$  = hysteretic factor, dimensionless  
 $i$  = imaginary operator  
 $I$  = second moment of inertia, L<sup>4</sup>, in.<sup>4</sup>  
 $j$  = iteration index  
 $J$  = polar moment, L<sup>3</sup>, in.<sup>3</sup>  
 $k$  = spring constant, m/t<sup>2</sup>, lbf/in.  
 $k_{eq}$  = equivalent spring constant, m/t<sup>2</sup>, lbf/in.  
 $k_w$  = wave number, 1/L, 1/ft  
 $\mathbf{K}$  = stiffness matrix, m/t<sup>2</sup>, lbf/in.  
 $L$  = total length, L, ft  
 $m$  = mass, m, lbm  
 $m_\theta$  = mass polar moment of inertia, mL, lbf-sec<sup>2</sup>  
 $\mathbf{M}$  = mass matrix, m, lbm  
 $n$  = exponent  
 $P$  = generic value  
 $Q$  = generic value  
 $r$  = generic constant  
 $r_j$  = iterated generic constant  
 $R(t)$  = response function  
 $t$  = time, seconds  
 $T$  = torque, mL<sup>2</sup>/t<sup>2</sup>, lbf-ft  
 $T(t)$  = displacement function in terms of time,  $t$   
 $u$  = displacement, L, in.  
 $U(x,t)$  = continuous displacement function, L, in.  
 $v$  = velocity, L/t, ft/sec  
 $v_g$  = group speed, L/t, ft/sec  
 $v_s$  = sonic velocity, L/t, ft/sec  
 $v_w$  = phase velocity, L/t, ft/sec  
 $v_0$  = initial velocity, L/t, ft/sec  
 $v_\theta$  = torsional sonic velocity, L/t, ft/sec  
 $x$  = displacement, L, in.  
 $x_h$  = homogeneous displacement, L, in.  
 $x_p$  = particular displacement, L, in.  
 $x_0$  = initial displacement, L, in.  
 $\dot{x}$  = first derivative with respect to time of displacement (velocity), L/t, ft/sec  
 $\dot{x}_p$  = particular velocity, L/t, ft/sec  
 $\ddot{x}$  = second derivative with respect to time of displacement (acceleration), L/t<sup>2</sup>, ft/sec<sup>2</sup>

- $\ddot{x}_p$  = particular acceleration, L/t<sup>2</sup>, ft/sec<sup>2</sup>  
 $X(x)$  = displacement function in terms of location  $x$   
 $\mathbf{X}$  = displacement vector  
 $\dot{\mathbf{X}}$  = velocity vector, L/t, ft/sec  
 $\ddot{\mathbf{X}}$  = acceleration vector, L/t<sup>2</sup>, ft/sec<sup>2</sup>  
 $y$  = dependent variable, various  
 $y_i$  = distance at point  $i$ , L, in.  
 $Y$  = limit value, various  
 $z$  = arbitrary constant, various  
 $\Delta l$  = change in length, L, in.  
 $\Delta t$  = change in time, t, seconds  
 $\Delta y$  = change in dependent variable, various  
 $\alpha$  = amplitude, various  
 $\epsilon$  = strain, L/L, in./in.  
 $\eta$  = convenient coefficient, 1/L, 1/ft  
 $\theta$  = twist, rad  
 $\ddot{\theta}$  = second derivative with respect to time of twist (acceleration) rad/sec<sup>2</sup>  
 $\lambda$  = mode shape, dimensionless  
 $\lambda_\omega$  = wavelength, L, in.  
 $\mu$  = friction factor, dimensionless  
 $\zeta$  = critical damping ratio, dimensionless  
 $\rho$  = density, m/L<sup>3</sup>, lbm/in.<sup>3</sup>  
 $\sigma$  = stress, m/Lt<sup>2</sup>, psia  
 $\Phi$  = phase angle, rad  
 $\omega$  = frequency, 1/t, Hz  
 $\omega_d$  = damped natural frequency, 1/t, Hz  
 $\omega_f$  = forcing frequency, 1/t, Hz  
 $\omega_n$  = natural frequency, 1/t, Hz  
 $\omega_\theta$  = twist natural frequency, 1/t, Hz  
 $\varphi$  = convenient coefficient, 1/L, 1/ft  
 $\tau$  = period, t, seconds

---

## References

1. Fanchi, J.: *Math Refresher for Scientists and Engineers*, John Wiley & Sons, New York City (1997).
2. Leithold, L.: *The Calculus with Analytic Geometry*, Harper and Row, New York City (1972).
3. Bird, J.O.: *Newnes Engineering Mathematics Pocket Book*, third edition, Newnes, Oxford, U.K. (2001).
4. de Saint-Venant, B.: *J. de Math. (Liouville)*, Ser.2, t.12, 1867.
5. Love, A.E.H.: *A Treatise on the Mathematical Theory of Elasticity*, fourth edition, Dover, New York City, 1926.
6. Meyers, M.A.: *Dynamic Behavior of Materials*, John Wiley & Sons, New York City (1994).
7. *Shock and Vibration Handbook*, third edition, C. Harris and C. Crede (eds.), McGraw-Hill Book Co. Inc., New York City (1988).
8. Dareing, D. and Livesay, B.: "Longitudinal and Angular Drillstring Vibration with Damping," *Trans. ASME, J. of Engineering for Industry* (1968) **90**, Series B, No. 4, 671.
9. Kolski, H.: *Stress Waves in Solids*, Dover Publications Inc., New York City (1963).
10. Doyle, J.F.: *Static And Dynamic Analysis Of Structures With an Emphasis on Mechanics and Computer Matrix Methods*, Kluwer Academic Publishers, Dordrecht, The Netherlands (1991).

11. Achenbach, J.D.: *Wave Propagation in Elastic Solids*, seventh edition, North-Holland Publishing Co./American Elsevier, Amsterdam/New York City (1973).
12. Clough, R.W. and Penzien, J.: *Dynamics of Structures*, McGraw-Hill Book Co. Inc., New York City (1975).
13. Den Hartog, J.P.: *Mechanical Vibrations*, Dover Publications Inc., New York City (1934).
14. Meirovitch, L.: *Elements of Vibration Analysis*, second edition, McGraw-Hill Book Co. Inc., New York City (1986).
15. Nashif, A.D., Jones, D.I.G., and Henderson, J.P.: *Vibration Damping*, John Wiley & Sons, New York City (1985).
16. Seto, W.: *Mechanical Vibrations*, McGraw-Hill Book Co. Inc., New York City (1964).
17. Shabana, A.A.: *Theory of Vibration, Volume I: An Introduction*, Springer-Verlag, New York City (1991).
18. Shabana, A.A.: *Theory of Vibration, Volume II: Discrete and Continuous Systems*, Springer-Verlag, New York City (1991).
19. Elmore, W.C. and Heald, M.A.: *Physics of Waves*, Dover Publications Inc., New York City (1969).
20. Hudson, J.A.: *The Excitation and Propagation of Elastic Waves*, Cambridge University Press, Cambridge, U.K. (1980).
21. Mal, A. and Singh, S.J.: *Deformation of Elastic Solids*, Prentice-Hall, Englewood Cliffs, New Jersey (1991).
22. Sharman, R.V.: *Vibrations and Waves*, Butterworth, London (1963).
23. Chin, W.C.: *Wave Propagation in Petroleum Engineering: Modern Applications to Drillstring Vibrations, Measurement-While-Drilling, Swab-Surge, and Geophysics*, Gulf Publishing, Houston (1994).
24. Tolstoy, I.: *Wave Propagation*, McGraw-Hill Book Co. Inc., New York City (1973).
25. Doyle, J.F.: *Wave Propagation in Structures: An FFT-Based Spectral Analysis Methodology*, Springer-Verlag New York Inc., New York City (1989).
26. Karl, J.H.: *An Introduction To Digital Signal Processing*, Academic Press Inc., San Diego, California (1989).
27. Ramirez, R.W.: *The FFT: Fundamentals and Concepts*, Prentice-Hall, Englewood Cliffs, New Jersey (1985).

---

## Suggested Reading

- Aarrestad, T.V and Kyllingstad, A.: "Measurements and Theoretical Models on Rig Suspension and the Effect on Drillstring Vibrations," paper SPE 19553 presented at the 1989 SPE Annual Technical Conference and Exhibition, San Antonio, Texas, 8–11 October.
- Aarrestad, T.V., Tonnesen, H.A., and Kyllingstad, A.: "Drillstring Vibrations: Comparison Between Theory and Experiments on a Full-Scale Research Drilling Rig," paper SPE 14760 presented at the 1986 IADC/SPE Drilling Conference, Dallas, 10–12 February.
- Besaisow, A.A. and Payne, M.L.: "A Study of Excitation Mechanisms and Resonances Inducing Bottomhole Assembly Vibrations," *SPEDE* (1988) 93.
- Booer, A.K. and Meehan, R.J.: "Drillstring Imaging: An Interpretation of Surface Drilling Vibrations," *SPEDC* (June 1992) 425.
- Brett, J.F.: "The Genesis of Bit-Induced Torsional Drillstring Vibrations," paper SPE 21943 presented at the 1991 SPE/IADC Drilling Conference, Amsterdam, 11–14 March.
- Broch, J.T.: *Mechanical Vibration and Shock Measurement*, Brüel & Kjær, Denmark (1984).
- Dareing, D.W.: "Drill Collar Length is a Major Factor in Vibration Control," *JPT* (April 1984) 637.
- Doyle, J.F.: "A Spectrally Formulated Finite Element For Longitudinal Wave Propagation," *The Intl. J. of Analytical and Experimental Modal Analysis* (January 1988) 1.
- Doyle, J.F.: "Application Of The Fast-Fourier Transform (FFT) To Wave-Propagation Problems," *The Intl. J. of Analytical and Experimental Modal Analysis* (October 1986) 18.



- Dubinsky, V.S.H., Henneuse, H.P., and Kirkman, M.A.: "Surface Monitoring of Downhole Vibrations; Russian, European, and American Approaches," paper SPE 24969 presented at the 1992 SPE European Petroleum Conference, Cannes, France, 16–18 November.
- Dufeyte, M. and Henneuse, H.: "Detection and Monitoring of the Slip-Stick Motion: Field Experiments," paper SPE 21945 presented at the 1991 SPE/IADC Drilling Conference, Amsterdam, 11–14 March.
- Dunayevsky, V.A., Abbassian, F., and Judzis, A.: "Dynamic Stability of Drillstrings Under Fluctuating Weight on Bit," *SPEDC* (June 1993) 84.
- Eustes, A.W.: "A Frequency Domain Approach to Drillstring Jarring Analysis," PhD dissertation, Colorado School of Mines, Golden, Colorado (1996).
- Eustes, A.W., Long R.C., and Mitchell, B.J.: "Core Bit Frequency Signatures," *Proc.*, ASME Energy-Sources Technology Conference & Exhibition (January 1995) 17.
- Eustes, A.W., Mitchell, B., and Stoner, M.: "Selection of Slim Hole Core Rods by Vibratory Analysis," *J. Energy Resources Technology*, ASME (1994) **116**, No. 4, 251.
- Fertis, D.G.: *Nonlinear Mechanics*, CRC Press, Boca Raton, Florida (1993).
- Fung, Y.C.: *Foundations of Solid Mechanics*, Prentice-Hall, Englewood Cliffs, New Jersey (1965).
- Gieck, K. and Gieck, R.: *Engineering Formulas*, sixth edition, McGraw-Hill Book Co. Inc., New York City (1990).
- Henneuse, H.: "Surface Detection of Vibrations and Drilling Optimization: Field Experience," paper SPE 23888 presented at the 1992 IADC/SPE Drilling Conference, New Orleans, 18–21 February.
- Karasudhi, P.: *Foundations of Solid Mechanics*, Kluwer Academic Publishers, Dordrecht, The Netherlands (1991).
- Kyllingstad, A. and Halsey, G.W.: "A Study of Slip/Stick Motion of the Bit," *SPEDE* (1988) 369.
- Lai, W.M., Rubin, D., and Krempl, E.: *Introduction to Continuum Mechanics*, Pergamon Press, Oxford, U.K. (1978).
- Macpherson, J.: "Vibration Signature of Roller Cone and PDC Bits," Baker Hughes INTEQ, Drilling Dynamics Technical Note (May 1993).
- Mitchell, B.: *Advanced Oilwell Drilling Engineering Handbook*, tenth edition, Mitchell Engineering, Golden, Colorado (1995).
- Moon, F.C.: *Chaotic Vibrations: An Introduction for Applied Scientists and Engineers*, John Wiley & Sons, New York City (1987).
- Paslay, P.R. *et al.*: "Detection of BHA Lateral Resonances While Drilling With Surface Longitudinal and Torsional Sensors," paper SPE 24583 presented at the 1992 SPE Annual Technical Conference and Exhibition, Washington, D.C., 4–7 October.
- Pestel, E. and Leckie, F.A.: *Matrix Methods in Elasto-Mechanics*, McGraw-Hill Book Co. Inc., New York City (1963).
- Randall, R.B.: *Frequency Analysis*, Brüel & Kjær, Denmark (1987).
- Rappold, K.: "Drilling Optimized with Surface Measurement of Downhole Vibrations," *Oil & Gas J.* (16 February 1993) 58.
- Rappold, K.: "Drilling Dynamics—Conclusion Drillstring Vibration Measurements Detect Bit Stick-Slip," *Oil & Gas J.* (1 March 1993) 66.
- Reddy, J.N.: *An Introduction To The Finite Element Method*, McGraw-Hill Book Co. Inc., New York City (1984).
- Skudrzyk, E.: *Simple and Complex Vibratory Systems*, Pennsylvania State U. Press, University Park, Pennsylvania (1968).
- Timoshenko, S. and Gere, J.: *Mechanics of Materials*, fourth edition, PWS Publishing Co., Boston (1990) 1–912.

Young, W.C.: *Roark's Formulas for Stress and Strain*, sixth edition, McGraw-Hill Book Co. Inc., New York City (1989).

Zienkiewicz, O.C. and Taylor, R.L.: *The Finite Element Method, Vol 1: Basic Formulation and Linear Problems*, fourth edition, McGraw-Hill Book Co. Inc., London, U.K. (1989).

### SI Metric Conversion Factors

cycle/sec	× 1.0*	E + 00	= Hz
ft	× 3.048*	E - 01	= m
ft <sup>2</sup>	× 9.290 304*	E - 02	= m <sup>2</sup>
in.	× 2.54*	E + 00	= cm
in. <sup>2</sup>	× 6.451 6*	E + 00	= cm <sup>2</sup>
in. <sup>3</sup>	× 1.638 706	E + 01	= cm <sup>3</sup>
in. <sup>4</sup>	× 4.162 314	E - 07	= m <sup>4</sup>
lbf	× 4.448 222	E + 00	= N
lbf-ft	× 1.355 818	E + 00	= N·m
lbf-sec <sup>2</sup>	4.448	E + 00	= N·s <sup>2</sup>
lbm	× 4.535 924	E - 01	= kg
psia	× 6.894 757	E + 00	= kPa
rad	× 1.00*	E + 00	= rad

\*Conversion factor is exact.

### Appendix—Glossary of Vibration Theory Terms

The **period** of a vibration is the time taken for a motion to repeat.

**Frequency** is the number of repeats per unit of time. This also is called a cyclic frequency. An angular frequency (sometimes called circular frequency) ( $\omega$ ) is measured in radians per unit time. Angular frequency is the product of  $2\pi$  and the cyclic frequency.<sup>7</sup>

The **amplitude** of a frequency is the difference between the maximum or minimum values of a sinusoidally varying quantity and its mean. A wave's crest is its maximum amplitude, and the trough is its minimum amplitude.

The **wave period** is the length of time it takes a wave to travel from crest to crest. The wave frequency is the inverse of the wave period.

The **wavelength** is the distance covered by one wave period.

The **phase angle** (abbreviated to "phase") of a wave is the fraction of the distance the wave has traveled relative to an arbitrary reference. The points at which the various waves cross the average amplitude line do not coincide unless the phase is zero. The phase is negative if the crossing occurs before the reference wave crossing, and positive if it occurs after the reference wave crossing.

**Phase velocity** is the velocity of a given point, as defined by the phase angle on a sinusoidal wave. When the phase velocity and the frequency remain constant, it is a nondispersing wave. If the phase velocity and the frequency are not constant, the wave disperses.

The **wave number** is the ratio of the wavelength to  $2\pi$ .<sup>10</sup> If this ratio is a real number, the wave will be a nondispersing wave (i.e., it will have a constant phase velocity for all its components and will retain its shape). If the wave number is complex, then the wave will be a dispersing wave (i.e., its components will have different phase velocities and it will not retain its shape and will disperse over time). All waves encountered in macroscopic reality are dispersing to some extent.

The **group speed** is the response of a wave's group of sinusoidal components, and is different from phase velocity. Group speed is important; the interaction of all the wave components in terms of wave number, amplitude, and frequency causes the appearance of a carrier wave of some wave number, amplitude, and frequency. This carrier wave is modulated by group waves that propagate at group speeds. In a nondispersing wave, the group speeds are the same as the

phase velocity of the wave components. In a dispersing wave, however, these group speeds can be different. If the group speeds are greater than the phase velocities, it will appear that a carrier wave originates at the back of the wave, propagates forward until it reaches the front of the wave, vanishes, and reappears at the back of the wave. If the group speeds are less than the phase velocities, it will appear that a carrier wave originates at the front of the wave, propagates backward until it reaches the back of the wave, vanishes, and reappears at the front of the wave. This can be visualized by thinking of a caterpillar's motion. The caterpillar's ripples appear to move backward, yet the caterpillar moves forward.<sup>24</sup> This is one reason the analysis of dispersing waves can be very complicated.

The **natural frequency** of a system is the frequency at which the system vibrates when free of any friction or forcing functions.

A **damped natural frequency** is a natural frequency with friction.

**Damping** is the dissipation of energy with time or distance. Several forms of damping are discussed in this chapter.

A **harmonic** is a frequency that is an integer multiple of a given frequency.

A **mode** is a particular harmonic frequency.

The **mode shape** is a pattern of the system assumed during a harmonic.

A **frequency spectrum** is a band of frequencies.

A **forcing function** is an external force that is acting on a vibrating system. This has the effect of modifying the vibrations that are experienced in the system, sometimes significantly. For example, in a rotating-drillstring system, the drill bit will impart a forcing vibration to the lower end of the string.

A **critical frequency** is a frequency at which amplitudes become unbounded. This occurs when the frequency of the system matches one of the natural frequencies.

The **critical rotary speed** is a rotary speed that coincides with one of the critical frequencies of the system.

**Resonance** occurs when the frequency of the forcing function is equal to one of the natural frequencies of the system.

A **stable** system returns to its former position after the removal of the force that disturbed the system. In pipe work, **stability** is involved with buckling, bending, and straightness of the pipe.

An **incident wave** is a wave going into a geometric or material discontinuity.

A **transmitted wave** is the portion of a wave that passes through a geometric or material discontinuity.

A **reflected wave** is the portion of a wave that does not pass through a geometric or material discontinuity.

**Impedance** is the ratio of a force-like quantity to a velocity-like quantity when the arguments of the real or imaginary parts of the quantities linearly increase with time. The reciprocal of impedance is **mobility**. If the mechanical impedance of two materials and their geometries are equal, then the maximum amount of energy will be transmitted at their intersection.

The **beating phenomenon** occurs when two harmonic waves of slightly different frequencies are impressed on a body. They are a periodic variation in vibration at a frequency that is the difference between two frequencies.

**Self-excited** vibrations occur when the forcing function is a function of the displacement, velocity, or acceleration of the system mass. If the energy gained from the self-excited vibrations is more than the system can absorb, the system will self-destruct.

A **standing wave** is a wave that appears to be standing still. There is no discernible beginning or end in time to the wave.

A **transient wave** is a wave that has a definite beginning and eventually dies out.

**Strain energy** is the energy gained by a mass as it is deformed.



## Chapter 2

# Mathematics of Fluid Flow

John R. Fanchi, Colorado School of Mines

### 2.1 Introduction

The purpose of this chapter is to review the mathematics of fluid flow. We limit our review to essential aspects of partial differential equations, vector analysis, numerical methods, matrices, and linear algebra. These topics are discussed in the context of two fluid flow applications: analysis of the convection/dispersion equation and diagonalization of the permeability tensor. For more details about the mathematics presented here, consult Refs. 1 through 4.

### 2.2 Partial Differential Equations

Partial differential equations (PDEs) are frequently encountered in petroleum engineering. We review basic concepts of PDEs by considering the relevant mathematical properties of the continuity equation.

**2.2.1 Continuity Equation.** Fluid flow through a volume can be described mathematically by the continuity equation. The continuity equation has many uses, and its derivation is provided to illustrate the construction of a partial differential equation from physical reasoning.<sup>5</sup> We begin by considering the flow illustrated in Fig. 2.1. The block in Fig. 2.1 has length ( $\Delta x$ ), width ( $\Delta y$ ), and depth ( $\Delta z$ ). Fluid flux ( $J$ ) is the rate of flow of mass per unit cross-sectional area normal to the direction of flow. The notation  $(J_x)_x$  denotes fluid flux in the  $x$  direction at location  $x$ . The cross-sectional area perpendicular to the flux direction is  $\Delta y \Delta z$ . Fluid flows into the block at  $x$  with fluid flux  $J_x$  and out of the block at  $x + \Delta x$  with fluid flux  $J_{x+\Delta x}$ . Applying the principle of conservation of mass, we have the mass balance, which is written as

$$\text{Mass in} - \text{mass out} = \text{mass accumulation} \dots\dots\dots (2.1)$$

The mass entering the block in time interval,  $\Delta t$ , for flux across the face of the block at  $x$  is

$$\left[ (J_x)_x \Delta y \Delta z \right] \Delta t = \text{mass in} \dots\dots\dots (2.2)$$

The mass leaving the block in time interval,  $\Delta t$ , across the face of the block at  $x + \Delta x$  is

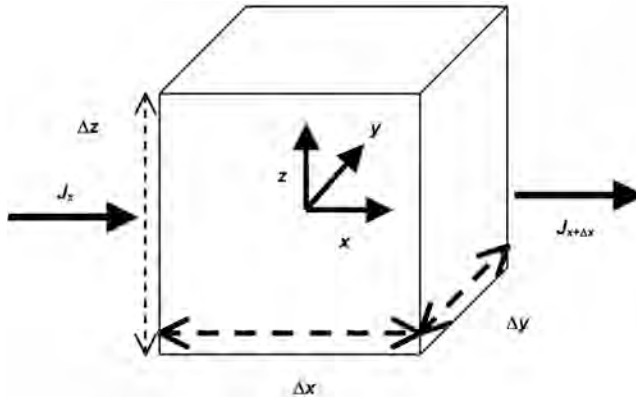


Fig. 2.1—Coordinate system for continuity equation.

$$\left[ (J_x)_{x+\Delta x} \Delta y \Delta z \right] \Delta t + q \Delta x \Delta y \Delta z \Delta t = \text{mass out}, \dots\dots\dots (2.3)$$

where we have added a source term  $q$ . Flow out of the block through  $q$  is represented by  $q > 0$ , and flow into the block is represented by  $q < 0$ . The source term,  $q$ , can represent a variety of important physical systems, including wells, aquifer support, fluid flow into a fracture system from matrix blocks in a naturally fractured reservoir, and gas flow into a cleat system from the coal in a coalbed.

Mass accumulation in the block is the change in concentration  $C$  of the mass in the block during the time interval  $\Delta t$ , where concentration,  $C$ , is defined as the total mass in the block divided by the block volume. The mass accumulation term is

$$\left[ (C)_{t+\Delta t} - (C)_t \right] \Delta x \Delta y \Delta z = \text{mass accumulation}, \dots\dots\dots (2.4)$$

where concentration is evaluated at times  $t$  and  $t + \Delta t$ .

Substituting Eqs. 2.2 through 2.4 into Eq. 2.1, dividing by  $\Delta x \Delta y \Delta z \Delta t$ , and rearranging gives

$$-\frac{(J_x)_{x+\Delta x} - (J_x)_x}{\Delta x} - q = \frac{(C)_{t+\Delta t} - (C)_t}{\Delta t} \dots\dots\dots (2.5)$$

In the limit as  $\Delta x \rightarrow 0$ ,  $\Delta t \rightarrow 0$ , the differences in Eq. 2.5 are replaced by partial derivatives. We assume the fluxes and concentrations are sufficiently smooth and continuous to allow the replacement of differences by partial derivatives. Eq. 2.5 becomes the continuity equation in one space dimension.

$$-\frac{\partial J_x}{\partial x} - q = \frac{\partial C}{\partial t} \dots\dots\dots (2.6)$$

Eq. 2.6 is an example of a partial differential equation.

**2.2.2 Partial Differential Equations.** PDEs are an extension of the concept of ordinary differential equations (ODEs). Unlike an ODE, which depends on only one independent variable, a PDE depends on two or more independent variables. In the previous example, Eq. 2.6 depends on two independent variables: one space dimension ( $x$ ) and time ( $t$ ). The order of Eq. 2.6 de-

depends on the form of concentration and flux. The order of a PDE is the order of the highest derivative that appears in the equation.

$$F\left\{x, y, \dots, \psi, \frac{\partial \psi}{\partial x}, \frac{\partial \psi}{\partial y}, \dots, \frac{\partial^2 \psi}{\partial x^2}, \frac{\partial^2 \psi}{\partial y^2}, \frac{\partial^2 \psi}{\partial x \partial y}, \dots\right\} = 0 \dots\dots\dots (2.7)$$

for a function ( $\psi$ ) of two or more independent variables  $\{x,y,\dots\}$ . A PDE is linear if it is first order in the unknown function and its partial derivatives, and the coefficients of the partial derivatives, are either constant or depend on the independent variables  $\{x,y,\dots\}$ . We illustrate these concepts by considering the continuity equation for flow of a fluid with density ( $\rho$ ), velocity ( $v_x$ ), and no source or sink terms. The concentration,  $C$ , and flux,  $J_x$ , for this example are

$$c = \rho;$$

$$J_x = \rho v_x;$$

and

$$q = 0. \dots\dots\dots (2.8)$$

Substituting Eq. 2.8 into Eq. 2.6 gives

$$\frac{\partial \rho}{\partial t} + \frac{\partial}{\partial x}(\rho v_x) = 0. \dots\dots\dots (2.9)$$

Eq. 2.9 is a linear, first-order PDE if density is the unknown function and velocity is constant. The situation is not so simple in more physically realistic systems.

Consider, for example, a slightly compressible fluid in which density is given by<sup>6</sup>

$$\rho = \rho_0 \exp [c_f(P - P_0)], \dots\dots\dots (2.10)$$

where  $P$  is pressure,  $c_f$  is fluid compressibility, and the subscript, 0, refers to a reference value of pressure. Assume, as well, that velocity is proportional to pressure gradient so that

$$v_x = \alpha \frac{\partial P}{\partial x}, \dots\dots\dots (2.11)$$

where  $\alpha$  is the proportionality constant. Substituting Eqs. 2.10 and 2.11 into Eq. 2.9 gives

$$\frac{\partial P}{\partial t} + \frac{\alpha}{c_f} \frac{\partial^2 P}{\partial x^2} + \alpha \left(\frac{\partial P}{\partial x}\right)^2 = 0. \dots\dots\dots (2.12)$$

Eq. 2.12 is a nonlinear, second-order PDE. It is second order because of the second-order partial derivative of pressure with respect to  $x$ , and it is nonlinear because of the square of the pressure gradient term.

Solutions of PDEs depend on the form of the PDEs and their associated boundary conditions. An important class of second-order PDEs has the form

TABLE 2.1—CLASSIFICATION SCHEME FOR SECOND-ORDER PDES		
PDE Type	Criterion	Example
Hyperbolic	$B^2 > AC$	Wave equation $\frac{\partial^2 \psi}{\partial x^2} - \frac{\partial^2 \psi}{\partial t^2} = 0$
Elliptic	$B^2 < AC$	Laplace equation $\frac{\partial^2 \psi}{\partial x^2} + \frac{\partial^2 \psi}{\partial y^2} = 0$
Parabolic	$B^2 = AC$	Heat equation $\frac{\partial^2 \psi}{\partial x^2} - \frac{\partial \psi}{\partial t} = 0$

$$A \frac{\partial^2 \psi(x, y)}{\partial x^2} + 2B \frac{\partial^2 \psi(x, y)}{\partial x \partial y} + C \frac{\partial^2 \psi(x, y)}{\partial y^2} = G, \dots\dots\dots (2.13)$$

where the functions  $\{A, B, C, G\}$  are known functions of two independent variables  $\{x, y\}$  and the first-order partial derivatives  $\partial \psi(x, y) / \partial x$  and  $\partial \psi(x, y) / \partial y$  in a region ( $R$ ) bounded by a surface ( $S$ ). The mathematical properties of the second-order PDEs depend on the relationship between the functions  $\{A, B, C, G\}$ . A classification scheme for second-order PDEs is given in **Table 2.1**.

Boundary conditions for second-order PDEs may be written as

$$\alpha(x, y)\psi(x, y) + \beta(x, y) \frac{\partial \psi(x, y)}{\partial n} = \gamma(x, y), \dots\dots\dots (2.14)$$

where  $\psi(x, y)$  is the unknown function of two independent variables  $\{x, y\}$ , and  $\partial \psi(x, y) / \partial n$  is the derivative normal to a boundary. The functions  $\{\alpha, \beta, \gamma\}$  are known functions of  $\{x, y\}$ . All of the functions and applicable derivatives are defined in a domain ( $R$ ) bounded by a surface ( $S$ ). A classification scheme for the boundary conditions of a second-order PDE is given in **Table 2.2**. The boundary conditions associated with the examples in **Table 2.1** are given in **Table 2.3**. The significance of PDE classification is considered further in the discussion of the convection/dispersion equation presented next.

**2.2.3 One-Dimensional (1D) Convection/Dispersion Equation.** The continuity equation is used to describe the mixing of one substance with another by writing flux in the form

$$J_x = C v - D \frac{\partial C}{\partial x} \dots\dots\dots (2.15)$$

The concentration,  $C$ , is the concentration of the solute in the solvent. The term  $v$  is the velocity of the solute, and  $D$  is the dispersion of the solute into the solvent. Substituting **Eq. 2.15** into **Eq. 2.6**, the 1D convection/dispersion equation without sources or sinks, gives



Name	Form	Comment
Dirichlet (first kind)	$\beta = 0$	$\psi$ specified at S
Neumann (second kind)	$\alpha = 0$	$\partial \psi (x,y) / \partial n$ specified at S
Cauchy	2 equations: $\alpha = 0$ in one and $\beta = 0$ in the other	
Robbins (third kind)	$\alpha$ and $\beta \neq 0$	

Example	PDE Type	Boundary Condition
Wave equation	Hyperbolic	Cauchy
Laplace equation	Elliptic	Dirichlet or Neumann
Heat equation	Parabolic	Dirichlet or Neumann

$$-\frac{\partial}{\partial x} \left( C v - D \frac{\partial C}{\partial x} \right) = \frac{\partial C}{\partial t} \dots\dots\dots (2.16)$$

If we assume that  $v$  and  $D$  are constant, Eq. 2.16 simplifies to the form

$$D \frac{\partial^2 C}{\partial x^2} - v \frac{\partial C}{\partial x} = \frac{\partial C}{\partial t} \dots\dots\dots (2.17)$$

Eq. 2.17 is the 1D convection/dispersion (C/D) equation. The dispersion term is  $D\partial^2C/\partial x^2$ , and the convection term is  $-v\partial C/\partial x$ . If the dispersion term is much larger than the convection term, the solution of Eq. 2.17 can be approximated by the solution of the equation

$$D \frac{\partial^2 C}{\partial x^2} = \frac{\partial C}{\partial t} \dots\dots\dots (2.18)$$

Eq. 2.18 is a parabolic PDE and behaves mathematically like a heat conduction equation. If the convection term is much larger than the dispersion term, the solution of Eq. 2.17 can be approximated by the solution of the equation.

$$-v \frac{\partial C}{\partial x} = \frac{\partial C}{\partial t} \dots\dots\dots (2.19)$$

Eq. 2.19 is a first-order hyperbolic PDE.

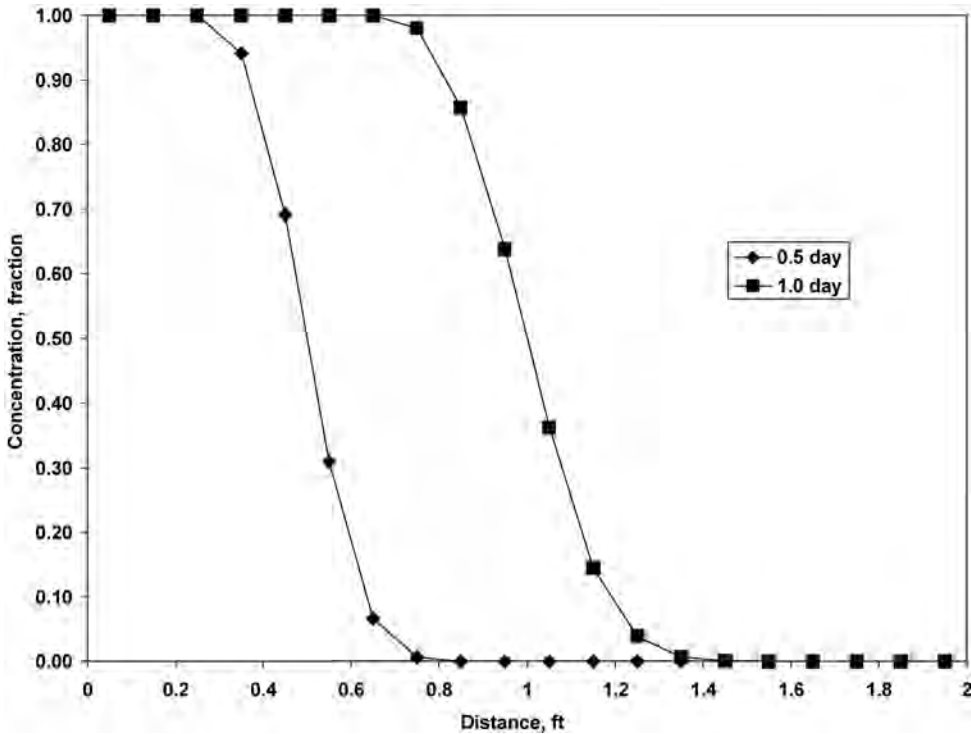


Fig. 2.2—Analytical solution of the 1D C/D equation.

A solution of the 1D C/D equation, given in Eq. 2.17, is obtained as follows. We assume that solute is moving in the  $x$ -direction with constant speed ( $v_x$ ). The concentration  $C(x,t)$  is a function of space and time. We must specify two boundary conditions and an initial condition for the concentration  $C(x,t)$  to solve the C/D equation. We impose the boundary conditions,  $C(0, t) = 1$  and  $C(\infty, t) = 0$ , for all time,  $t > 0$ , and the initial condition,  $C(x, 0) = 0$ , for all values of  $x > 0$ . The boundary condition,  $C(0, t) = 1$ , says that we are injecting 100% solute at  $x = 0$ , and the boundary condition,  $C(\infty, t) = 0$ , says that the solute never reaches the end of the flow path at  $x = \infty$ . The initial condition,  $C(x, 0) = 0$ , says that there is no solute in the solvent at the initial time,  $t = 0$ . The solution of the C/D equation is

$$C(x, t) = \frac{1}{2} \left[ \operatorname{erfc} \left( \frac{x - vt}{2\sqrt{Dt}} \right) + \exp \left( \frac{vx}{D} \right) \operatorname{erfc} \left( \frac{x - vt}{2\sqrt{Dt}} \right) \right], \dots\dots\dots (2.20)$$

where the complementary error function  $\operatorname{erfc}(y)$  is defined<sup>1</sup> as

$$\operatorname{erfc}(y) = 1 - \frac{2}{\sqrt{\pi}} \int_0^y \exp(-z^2) dz = 1 - \frac{2}{\sqrt{\pi}} \left[ y - \frac{y^3}{(1!)3} + \frac{y^5}{(2!)5} - \frac{y^7}{(3!)7} + \dots \right] \dots\dots\dots (2.21)$$

The integral in Eq. 2.21 can be solved using the series expansion on the right side of Eq. 2.21 or a numerical algorithm.<sup>7</sup> Eq. 2.20 is illustrated in Fig. 2.2 for physical parameters  $v = 1$  ft/day and  $D = 0.01$  ft<sup>2</sup>/day. This solution is used in Sec. 2.4 to evaluate a numerical solution of the C/D equation.

### 2.3 Vector Analysis

Fluid flow equations in two and three dimensions can be compactly represented using concepts from vector analysis. For example, the continuity equation in three space dimensions for the Cartesian coordinate system, shown in Fig. 2.1, is

$$-\frac{\partial J_x}{\partial x} - \frac{\partial J_y}{\partial y} - \frac{\partial J_z}{\partial z} - q = \frac{\partial C}{\partial t} \dots\dots\dots (2.22)$$

The flux terms ( $J_y$ ) and ( $J_z$ ) have meanings analogous to ( $J_x$ ) for flux in the  $y$  and  $z$  directions, respectively. If we write the components of flux as the flux vector  $\vec{J} = \{J_x, J_y, J_z\}$ , Eq. 2.22 can be written in vector notation as

$$-\nabla \cdot \vec{J} - q = \frac{\partial C}{\partial t}, \dots\dots\dots (2.23)$$

where the divergence of vector  $\vec{J} = \{J_x, J_y, J_z\}$ , in Cartesian coordinates, is

$$\nabla \cdot \vec{J} = \frac{\partial J_x}{\partial x} + \frac{\partial J_y}{\partial y} + \frac{\partial J_z}{\partial z} \dots\dots\dots (2.24)$$

The divergence operator  $\nabla \cdot$  is an example of an operator from vector analysis that determines the spatial variation of a vector or scalar field. Following Fanchi,<sup>4</sup> we first review the concepts of scalar and vector fields and then define gradient (grad), divergence (div), and curl operators.

**2.3.1 Scalar and Vector Fields.** We define scalar and vector fields in a Cartesian coordinate system with position vector

$$\vec{x} = x\hat{i} + y\hat{j} + z\hat{k}, \dots\dots\dots (2.25)$$

where  $\{\hat{i}, \hat{j}, \hat{k}\}$  are unit vectors defined along the orthogonal  $\{x,y,z\}$  coordinate axes. If we can associate a scalar function ( $f$ ) with every point in a region ( $R$ ), then the scalar field may be written as

$$f(x, y, z) = f(\vec{x}). \dots\dots\dots (2.26)$$

Examples of scalar fields include pressure, temperature, and saturation.

If, instead of a scalar function ( $f$ ), we can associate a vector  $\vec{v}$  with every point in the region ( $R$ ), we can construct a vector field of the form

$$\vec{v}(x, y, z) = \vec{v}(\vec{x}). \dots\dots\dots (2.27)$$

The vector field is a function that assigns a vector to every point in the region  $R$ . Examples of vector fields include the Darcy velocity field and seismic velocities.

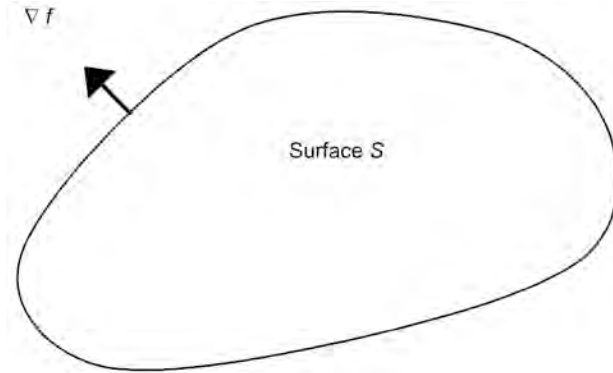


Fig. 2.3—Gradient  $\nabla f$  normal to surface S.

**2.3.2 Gradient, Divergence, and Curl.** The spatial variation of a scalar or vector field can be determined with the del operator  $\nabla$ . The del operator,  $\nabla$ , is defined in Cartesian coordinates as

$$\nabla \equiv \hat{i} \frac{\partial}{\partial x} + \hat{j} \frac{\partial}{\partial y} + \hat{k} \frac{\partial}{\partial z} \dots\dots\dots (2.28)$$

The gradient of a scalar field ( $f$ ) is obtained by operating on the scalar field with the del operator, thus

$$\text{grad } f = \nabla f \equiv \left( \hat{i} \frac{\partial}{\partial x} + \hat{j} \frac{\partial}{\partial y} + \hat{k} \frac{\partial}{\partial z} \right) f = \hat{i} \frac{\partial f}{\partial x} + \hat{j} \frac{\partial f}{\partial y} + \hat{k} \frac{\partial f}{\partial z} \dots\dots\dots (2.29)$$

The direction of the gradient of the scalar field ( $f$ ) evaluated at a point is oriented in the direction of maximum increase of the scalar field. In addition, the vector field,  $\nabla f$ , is perpendicular to a surface that corresponds to a constant value of the scalar field (Fig. 2.3).

Two outcomes are possible when the del operator is applied to a vector field. One outcome is to create a scalar, and the other is to create a vector. A scalar is obtained when we take the dot product of the del operator with a vector field ( $\vec{v}$ ). The result is the divergence of the vector field.

$$\begin{aligned} \text{Div } \vec{v} = \nabla \cdot \vec{v} &\equiv \left( \hat{i} \frac{\partial}{\partial x} + \hat{j} \frac{\partial}{\partial y} + \hat{k} \frac{\partial}{\partial z} \right) \cdot (v_x \hat{i} + v_y \hat{j} + v_z \hat{k}) \\ &= \frac{\partial v_x}{\partial x} + \frac{\partial v_y}{\partial y} + \frac{\partial v_z}{\partial z} \dots\dots\dots (2.30) \end{aligned}$$

A vector is obtained when we take the cross product of the del operator with a vector field ( $\vec{v}$ ). The result is the curl of the vector field  $\vec{v}$ .

$$\begin{aligned} \text{Curl } \vec{v} = \nabla \times \vec{v} &\equiv \left( \hat{i} \frac{\partial}{\partial x} + \hat{j} \frac{\partial}{\partial y} + \hat{k} \frac{\partial}{\partial z} \right) \times (v_x \hat{i} + v_y \hat{j} + v_z \hat{k}) \\ &= \hat{i} \left( \frac{\partial v_z}{\partial y} - \frac{\partial v_y}{\partial z} \right) + \hat{j} \left( \frac{\partial v_x}{\partial z} - \frac{\partial v_z}{\partial x} \right) + \hat{k} \left( \frac{\partial v_y}{\partial x} - \frac{\partial v_x}{\partial y} \right) \dots\dots\dots (2.31) \end{aligned}$$

The curl of the vector field  $\vec{v}$  is called the rotation of the vector field. It is a vector that is normal to the plane containing the vector field  $\vec{v}$ . The divergence of the gradient of a scalar field ( $f$ ) is

$$\nabla \times (\nabla f) \equiv \nabla^2 f = \frac{\partial^2 f}{\partial x^2} + \frac{\partial^2 f}{\partial y^2} + \frac{\partial^2 f}{\partial z^2}, \dots\dots\dots (2.32)$$

where we introduce the Laplacian operator,

$$\nabla^2 = \frac{\partial^2}{\partial x^2} + \frac{\partial^2}{\partial y^2} + \frac{\partial^2}{\partial z^2}, \dots\dots\dots (2.33)$$

in Cartesian coordinates.

The gradient, divergence, curl, and Laplacian operators arise in many PDEs that affect petroleum engineering. For example, a vector field  $\vec{v}$  is said to be irrotational if  $\text{curl } \vec{v} = 0$ , and it is said to be solenoidal if  $\text{div } \vec{v} = 0$ . These properties of the vector field are useful for analyzing the propagation of seismic waves. Another useful application of vector analysis is to the mathematical representation of fluid flow in two or three spatial dimensions. Two examples are presented next.

**2.3.3 Incompressible Flow.** Incompressible flow occurs when the density of a fluid is constant. In this case, the continuity equation for flow of a fluid with density ( $\rho$ ) and velocity ( $\vec{v}$ ) has concentration ( $C$ ) and flux ( $\vec{J}$ ) given by

$$C = \rho, \vec{J} = \rho \vec{v} \dots\dots\dots (2.34)$$

The concentration and density are scalar fields, and the velocity and flux are vector fields. The continuity equation without source or sink terms becomes

$$\frac{\partial \rho}{\partial t} + \nabla \cdot (\rho \vec{v}) = 0. \dots\dots\dots (2.35)$$

A more suitable form of the continuity equation for describing incompressible fluid flow is obtained by substituting the differential operator,

$$\frac{D}{Dt} = \frac{\partial}{\partial t} + \vec{v} \cdot \nabla, \dots\dots\dots (2.36)$$

into [Eq. 2.35](#) to obtain

$$\frac{D\rho}{Dt} + \rho \nabla \cdot \vec{v} = 0. \dots\dots\dots (2.37)$$

In the case of incompressible fluid flow, density is constant and [Eq. 2.37](#) reduces to

$$\nabla \cdot \vec{v} = 0. \dots\dots\dots (2.38)$$

Eq. 2.38 shows that the divergence of the velocity of a flowing, incompressible fluid is zero.

**2.3.4 Three-Dimensional (3D) Convection/Dispersion Equation.** The convection/dispersion equation in three dimensions is obtained by writing flux ( $\vec{J}$ ) in the multidimensional form

$$\vec{J} = C \vec{v} - D \nabla C \dots\dots\dots (2.39)$$

Substituting Eq. 2.39 into the 3D continuity equation gives

$$-\nabla \cdot C \vec{v} + \nabla \cdot D \nabla C - q = \frac{\partial C}{\partial t} \dots\dots\dots (2.40)$$

If we assume that  $\vec{v}$  and  $D$  are constant, we can simplify Eq. 2.40 to the form of

$$D \nabla^2 C - \vec{v} \cdot \nabla C - q = \frac{\partial C}{\partial t} \dots\dots\dots (2.41)$$

Eq. 2.41 is the 3D convection/dispersion equation. The term  $D \nabla^2 C$  is the dispersion term, and the term  $-\vec{v} \cdot \nabla C$  is the convection term.

**2.4 Numerical Methods**

Systems of nonlinear PDEs are needed to describe realistic multiphase, multidimensional flow in a reservoir. As a rule, these equations cannot be solved analytically; they must be solved with numerical methods. To illustrate the mathematics, we discuss the numerical solution of the 1D C/D equation.

$$D \frac{\partial^2 C}{\partial x^2} - v \frac{\partial C}{\partial x} = \frac{\partial C}{\partial t}, \dots\dots\dots (2.42)$$

as introduced in Sec. 2.2. As a reminder,  $v$  is velocity,  $D$  is dispersion, and  $C$  is concentration. Eq. 2.42 is a good example to use because it illustrates many useful numerical methods that can be compared with the analytical solution given by Eq. 2.20. We first introduce the concept of finite differences to convert Eq. 2.42 to an equation that can be solved numerically. We then present a numerical representation of Eq. 2.42 and illustrate its solution. For more details, you should consult the chapter on reservoir simulation in Vol. V, *Reservoir Engineering and Petrophysics*, as well as Refs. 8 through 14.

**2.4.1 Finite Differences.** One way to solve a PDE is to convert the PDE to finite-difference form. The finite-difference form is obtained by replacing the derivatives in the PDE with differences that are obtained from Taylor’s series. To illustrate the procedure, let us suppose that we know the function  $f(x)$  at two discrete points  $x = x_i$  and  $x = x_i + \Delta x$ , where  $\Delta x$  is an increment along the  $x$ -axis (Fig. 2.4). We can approximate the derivative  $df(x)/dx$  at  $x = x_i$  by solving the Taylor’s series,

$$f(x_i + \Delta x) = f(x_i) + \Delta x \left. \frac{df}{dx} \right|_{x=x_i} + \frac{(\Delta x)^2}{2!} \left. \frac{d^2 f}{dx^2} \right|_{x=x_i} + \frac{(\Delta x)^3}{3!} \left. \frac{d^3 f}{dx^3} \right|_{x=x_i} + \dots, \dots\dots (2.43)$$

for  $df(x)/dx$ . The result is

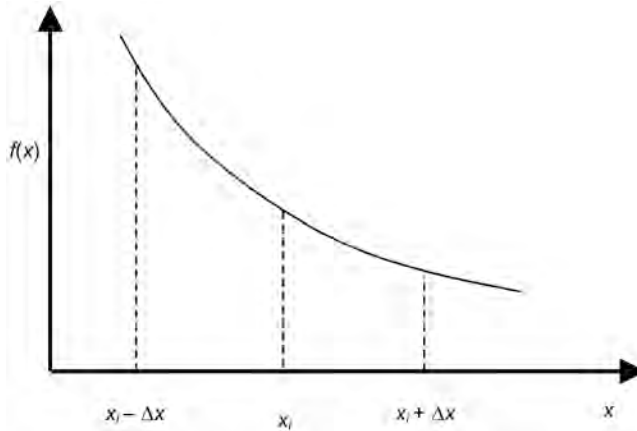


Fig. 2.4—Discrete points in the Taylor series expansion.

$$\left. \frac{df}{dx} \right|_{x=x_i} = \frac{f(x_i + \Delta x) - f(x_i)}{\Delta x} - E_T, \dots\dots\dots (2.44)$$

where  $E_T$  is the term

$$E_T = \frac{\Delta x}{2!} \left. \frac{d^2 f}{dx^2} \right|_{x=x_i} + \frac{(\Delta x)^2}{3!} \left. \frac{d^3 f}{dx^3} \right|_{x=x_i} + \dots\dots\dots (2.45)$$

If we neglect  $E_T$ , we obtain the finite-difference approximation of the first derivative.

$$\frac{df}{dx} \approx \frac{f(x_i + \Delta x) - f(x_i)}{\Delta x}. \dots\dots\dots (2.46)$$

Eq. 2.46 is an approximation because we are neglecting all of the terms in  $E_T$ , which is called the truncation error. In the limit as the increment  $\Delta x$  approaches zero, the truncation error approaches zero, and the finite difference approaches the definition of the derivative.

The finite difference in Eq. 2.46 is called a forward difference. Other differences are possible. Two that we use next are the backward difference,

$$\frac{df}{dx} \approx \frac{f(x_i) - f(x_i - \Delta x)}{\Delta x}, \dots\dots\dots (2.47)$$

and the centered difference,

$$\frac{df}{dx} \approx \frac{f(x_i + \Delta x) - f(x_i - \Delta x)}{2 \Delta x}. \dots\dots\dots (2.48)$$

Eqs. 2.46 through 2.48 are all derived from Taylor’s series.

**2.4.2 Illustration: Numerical Solution of the 1D C/D Equation.** We illustrate the application of finite differences in a fluid flow problem by considering a specific finite-difference represen-

tation of the 1D C/D equation. For a more detailed discussion of the numerical analysis of Eq. 2.42, see Chap. 4 of Ref. 8. In our example, we choose a backward difference for the time derivative in Eq. 2.42, a centered difference for the space derivative in the convection term, and a centered-in-time/centered-in-space difference for the dispersion term. Eq. 2.42 is converted from a PDE to the difference equation

$$D \frac{1}{2(\Delta x)^2} [C_{i+1}^{n+1} - 2C_i^{n+1} + C_{i-1}^{n+1} + C_{i+1}^n - 2C_i^n + C_{i-1}^n] - v \frac{1}{\Delta x} \left[ \frac{1}{2}(C_{i+1}^{n+1} - C_{i-1}^{n+1}) \right] = \frac{C_i^{n+1} - C_i^n}{\Delta t} \dots (2.49)$$

The subscripts of concentration  $C$  denote points in space, and the superscripts denote points in time. For example, the present time,  $t^n$ , is denoted by superscript  $n$  and future time  $t^{n+1}$  is denoted by  $n + 1$ . The time increment is  $\Delta t = t^{n+1} - t^n$ . Similarly, the space increment is  $\Delta x = x_{i+1} - x_i$ . The concentration at time  $t^{n+1}$  and spatial location  $x_i$  is denoted by  $C_i^{n+1}$ .

The future concentration distribution is found from the current concentration distribution by rearranging Eq. 2.49. We collect terms in  $C^{n+1}$  on the left-hand side and terms in  $C^n$  on the right-hand side, thus

$$C_i^{n+1} - \frac{D \Delta t}{2(\Delta x)^2} [C_{i+1}^{n+1} - 2C_i^{n+1} + C_{i-1}^{n+1}] + \frac{v \Delta t}{\Delta x} \left[ \frac{1}{2}(C_{i+1}^{n+1} - C_{i-1}^{n+1}) \right] = C_i^n + \frac{D \Delta t}{2(\Delta x)^2} (C_{i+1}^n - 2C_i^n + C_{i-1}^n) \dots (2.50)$$

Eq. 2.50 is now written in the form

$$a_i C_{i-1}^{n+1} + b_i C_i^{n+1} + c_i C_{i+1}^{n+1} = d_i \dots (2.51)$$

where the coefficients are

$$\begin{aligned} a_i &= -\frac{v \Delta t}{2 \Delta x} - \frac{D \Delta t}{2(\Delta x)^2}; \\ b_i &= 1 + \frac{D \Delta t}{(\Delta x)^2}; \\ c_i &= \frac{v \Delta t}{2 \Delta x} - \frac{D \Delta t}{2(\Delta x)^2}; \\ d_i &= C_i^n + \frac{D \Delta t}{2(\Delta x)^2} (C_{i+1}^n - 2C_i^n + C_{i-1}^n) \dots (2.52) \end{aligned}$$

All values of the variables in the coefficients are known at time  $t^n$ . If we assume that the spatial subscript is in the range  $1 \leq i \leq NX$ , the system of finite-difference equations becomes



$$\begin{bmatrix}
 b_1 & c_1 & 0 & 0 & 0 & \dots & 0 & 0 & 0 \\
 a_2 & b_2 & c_2 & 0 & 0 & \dots & 0 & 0 & 0 \\
 0 & a_3 & b_3 & c_3 & 0 & \dots & 0 & 0 & 0 \\
 \vdots & \vdots & \vdots & \vdots & \vdots & \ddots & \vdots & \vdots & \vdots \\
 0 & 0 & 0 & 0 & 0 & 0 & a_{NX-1} & b_{NX-1} & c_{NX-1} \\
 0 & 0 & 0 & 0 & 0 & 0 & 0 & a_{NX} & b_{NX}
 \end{bmatrix}
 \begin{bmatrix}
 C_1^{n+1} \\
 C_2^{n+1} \\
 C_3^{n+1} \\
 \vdots \\
 C_{NX-1}^{n+1} \\
 C_{NX}^{n+1}
 \end{bmatrix}
 =
 \begin{bmatrix}
 d_1 \\
 d_2 \\
 d_3 \\
 \vdots \\
 d_{NX-1} \\
 d_{NX}
 \end{bmatrix}
 \tag{2.53}$$

Eq. 2.53 can be written in matrix form as

$$\underline{M} \underline{C} = \underline{D}, \tag{2.54}$$

where  $\underline{M}$  is the  $NX \times NX$  matrix of coefficients,  $\underline{C}$  is the column vector of unknown concentrations at time  $t^{n+1}$ , and  $\underline{D}$  is the column vector of right-hand-side terms that depend on known concentrations at time  $t^n$ . Both column vectors  $\underline{C}$  and  $\underline{D}$  have  $NX$  elements.

The system of equations in Eq. 2.54 is called a tridiagonal system because it consists of three lines of nonzero diagonal elements centered about the main diagonal. All other elements are zero. Techniques for solving the tridiagonal system of equations, using the Thomas algorithm, are presented in Refs. 8 through 11 and Ref. 15. A solution of the set of equations for physical parameters  $v = 1$  ft/day and  $D = 0.01$  ft<sup>2</sup>/day and finite-difference parameters  $\Delta x = 0.1$  ft and  $\Delta t = 0.1$  day is shown in Fig. 2.5. The difference between the analytical solution and the numerical solution is because of numerical dispersion,<sup>8,16-17</sup> which is beyond the scope of this chapter. What interests us here is the appearance of matrices in the mathematics of fluid flow. Matrices are the subject of the next section.

### 2.5 Matrices and Linear Algebra

An example of a matrix was introduced in Sec. 2.4 for the 1D C/D equation. It is often easier to work with many fluid flow equations when they are expressed in terms of matrices. Our review follows the presentation in Ref. 4. We begin our discussion with an example of a matrix that is used later in this chapter, namely the matrix associated with the rotation of a coordinate system. We then summarize some important properties of matrices and determinants and review the concepts of eigenvalues and eigenvectors from linear algebra.

**2.5.1 Rotation of a Cartesian Coordinate System.** Fig. 2.6 illustrates a rotation of Cartesian coordinates from one set of orthogonal coordinates  $\{x_1, x_2\}$  to another set  $\{y_1, y_2\}$  by the angle  $\theta$ . The equations relating the coordinate systems are

$$\begin{aligned}
 y_1 &= x_1 \cos \theta + x_2 \sin \theta; \\
 y_2 &= -x_1 \sin \theta + x_2 \cos \theta. \tag{2.55}
 \end{aligned}$$

The set of equations in Eq. 2.55 has the matrix form

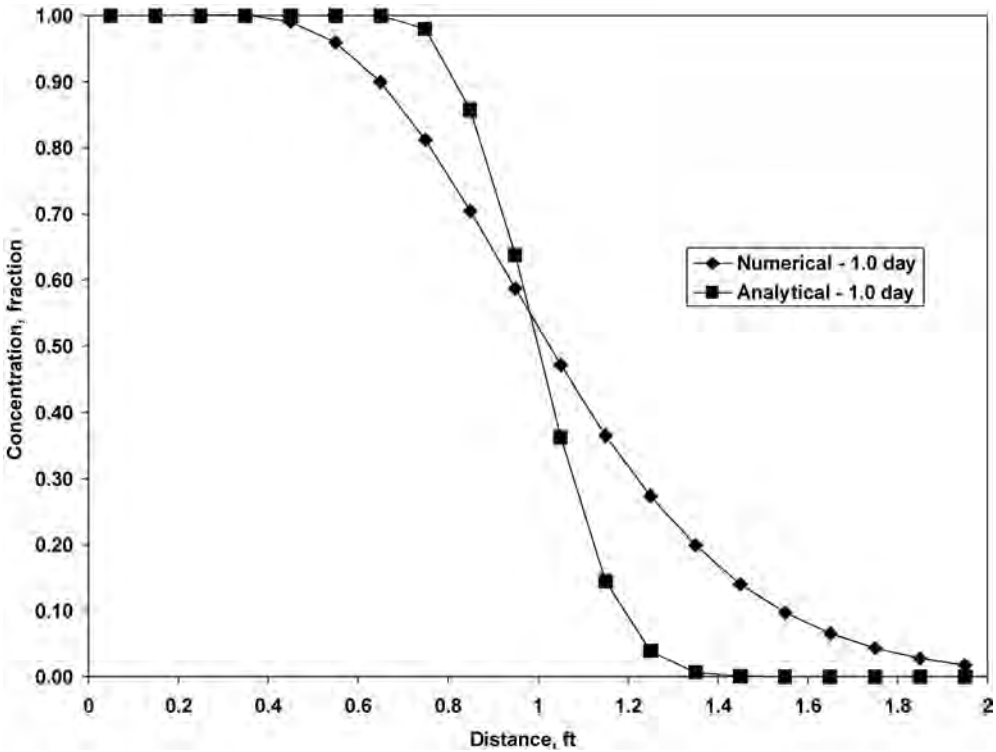


Fig. 2.5—Numerical solution of the 1D C/D equation.

$$\begin{bmatrix} y_1 \\ y_2 \end{bmatrix} = \begin{bmatrix} \cos \theta & \sin \theta \\ -\sin \theta & \cos \theta \end{bmatrix} \begin{bmatrix} x_1 \\ x_2 \end{bmatrix}, \dots\dots\dots (2.56)$$

which can be written as

$$\underline{y} = \underline{A}\underline{x} \dots\dots\dots (2.57)$$

The column vectors  $\underline{x}$  and  $\underline{y}$  are

$$\underline{y} = \begin{bmatrix} y_1 \\ y_2 \end{bmatrix} \text{ and } \underline{x} = \begin{bmatrix} x_1 \\ x_2 \end{bmatrix} \dots\dots\dots (2.58)$$

with two elements each, and the rotation matrix  $\underline{A}$  is the  $2 \times 2$  square matrix,

$$\underline{A} = \begin{bmatrix} \cos \theta & \sin \theta \\ -\sin \theta & \cos \theta \end{bmatrix} \dots\dots\dots (2.59)$$

**2.5.2 Properties of Matrices.** In general, a matrix with  $m$  rows and  $n$  columns has the order  $m \times n$  and is referred to as a  $m \times n$  matrix. The entry in the  $i^{\text{th}}$  row and  $j^{\text{th}}$  column of the

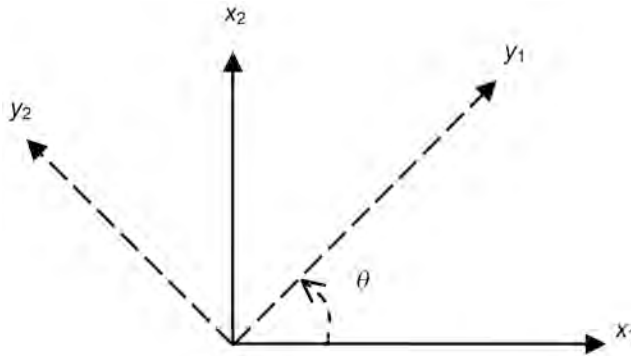


Fig. 2.6—Rotation of coordinate system.

matrix is the  $ij^{\text{th}}$  element of the matrix. If the number of rows equals the number of columns so that  $m = n$ , the matrix is called a square matrix. On the other hand, if  $m \neq n$ , the matrix is a rectangular matrix.

If the matrix has a single column so that  $n = 1$ , it is a column vector as in Eq. 2.58. If the matrix has a single row so that  $m = 1$ , it is a row vector. A row vector can be created from a column vector by taking the transpose of the column vector. For example, the transpose of the column vector  $\underline{x}$  in Eq. 2.58 may be written as

$$\underline{x}^T = \begin{bmatrix} x_1 \\ x_2 \end{bmatrix}^T = [x_1 \quad x_2], \dots\dots\dots (2.60)$$

where the superscript  $T$  denotes the transpose of the matrix. In general, we can write a  $m \times n$  matrix  $\underline{A}$  with a set of elements  $\{a_{ij} : i = 1, 2, \dots, n; j = 1, 2, \dots, m\}$  as

$$\underline{A} = [a_{ij}]. \dots\dots\dots (2.61)$$

The transpose of matrix  $\underline{A}$  is

$$\underline{A}^T = [a_{ij}]^T = [a_{ji}]. \dots\dots\dots (2.62)$$

The conjugate transpose of matrix  $\underline{A}$  is obtained by finding the complex conjugate of each element in  $\underline{A}$  and then taking the transpose of the matrix  $\underline{A}$ . This operation can be written as

$$\underline{A}^+ = [A^*]^T = [a_{ij}^*]^T = [a_{ji}^*], \dots\dots\dots (2.63)$$

where  $*$  denotes complex conjugation. Recall that the conjugate  $z^*$  of a complex number  $z$  is obtained by replacing the imaginary number  $i = \sqrt{-1}$  with  $-i = -\sqrt{-1}$  wherever it occurs. If all the elements of matrix  $\underline{A}$  are real, the conjugate transpose of matrix  $\underline{A}$  is equal to the transpose of matrix  $\underline{A}$ .

If the matrix  $\underline{\underline{A}}$  is a square matrix and the elements of matrix  $\underline{\underline{A}}$  satisfy the equality  $a_{ij} = a_{ji}$ , the matrix  $\underline{\underline{A}}$  is called a symmetric matrix. A square matrix  $\underline{\underline{A}}$  is Hermitian, or self-adjoint, if  $\underline{\underline{A}} = \underline{\underline{A}}^+$  (i.e., the matrix equals its conjugate transpose).

The set of elements  $\{a_{ii}\}$  of a square matrix  $\underline{\underline{A}}$  is the principal diagonal of the matrix. The elements  $\{a_{ji}\}$  with  $i \neq j$  are off-diagonal elements. The matrix  $\underline{\underline{A}}$  is a lower triangular matrix if  $a_{ij} = 0$  for  $i < j$ , and  $\underline{\underline{A}}$  is an upper triangular matrix if  $a_{ij} = 0$  for  $i > j$ . The matrix  $\underline{\underline{A}}$  is a diagonal matrix if  $a_{ij} = 0$  for  $i \neq j$ .

**2.5.3 Matrix Operations.** Suppose the matrices  $\underline{\underline{A}}$ ,  $\underline{\underline{B}}$ , and  $\underline{\underline{C}}$  with elements  $\{a_{ij}\}$ ,  $\{b_{ij}\}$ , and  $\{c_{ij}\}$  have the same order  $m \times n$ . We are using double underlines to denote matrices. Other notations are often used, such as boldface. The addition or subtraction of two matrices may be written as

$$\underline{\underline{A}} \pm \underline{\underline{B}} = \underline{\underline{C}}, \quad a_{ij} \pm b_{ij} = c_{ij} \dots\dots\dots (2.64)$$

The product of a matrix  $\underline{\underline{A}}$  with a number  $k$  may be written as

$$\underline{\underline{B}} = k\underline{\underline{A}}, \quad b_{ij} = k a_{ij} \dots\dots\dots (2.65)$$

The product of matrix  $\underline{\underline{A}}$  with order  $m \times n$  and matrix  $\underline{\underline{B}}$  with order  $n \times p$  is

$$\underline{\underline{C}} = \underline{\underline{A}}\underline{\underline{B}}, \quad c_{ij} = \sum_{q=1}^n a_{iq}b_{qj} \dots\dots\dots (2.66)$$

where matrix  $\underline{\underline{C}}$  has order  $m \times p$ . Notice that matrix multiplication is possible only if the number of columns in  $\underline{\underline{A}}$  equals the number of rows in  $\underline{\underline{B}}$ . This requirement is always satisfied for square matrices.

The transpose of the product of two square matrices  $\underline{\underline{A}}$  and  $\underline{\underline{B}}$  is

$$(\underline{\underline{A}}\underline{\underline{B}})^T = \underline{\underline{B}}^T \underline{\underline{A}}^T \dots\dots\dots (2.67)$$

and the adjoint of the product of two square matrices is

$$(\underline{\underline{A}}\underline{\underline{B}})^+ = \underline{\underline{B}}^+ \underline{\underline{A}}^+ \dots\dots\dots (2.68)$$

Notice that the product of two matrices may not be commutative (i.e.,  $\underline{\underline{A}}\underline{\underline{B}} \neq \underline{\underline{B}}\underline{\underline{A}}$  in general).

The identity matrix,  $\underline{\underline{I}}$ , is a square matrix with all off-diagonal elements equaling zero and all diagonal elements equaling one. The identity matrix preserves the identity of a square matrix  $\underline{\underline{A}}$  in matrix multiplication, thus

$$\underline{\underline{A}}\underline{\underline{I}} = \underline{\underline{I}}\underline{\underline{A}} = \underline{\underline{A}} \dots\dots\dots (2.69)$$

By contrast, a null matrix  $\underline{\underline{0}}$  is a matrix in which all elements are zero. In this case, the product of the null matrix with a matrix  $\underline{\underline{A}}$  is

$$\underline{\underline{A}}\underline{\underline{0}} = \underline{\underline{0}}\underline{\underline{A}} = \underline{\underline{0}} \dots\dots\dots (2.70)$$

The matrix,  $\underline{\underline{A}}$ , is singular if the product of matrix  $\underline{\underline{A}}$  with a column vector  $\underline{x}$  that has at least one nonzero element yields the null matrix; that is,  $\underline{\underline{A}}$  is singular if

$$\underline{\underline{A}}\underline{x} = \underline{\underline{0}}, \underline{x} \neq \underline{\underline{0}} \dots\dots\dots (2.71)$$

The concepts of identity matrix and matrix singularity are needed to define the inverse matrix. Suppose we have two square matrices  $\underline{\underline{A}}$  and  $\underline{\underline{B}}$  that satisfy the product

$$\underline{\underline{A}}\underline{\underline{B}} = \underline{\underline{B}}\underline{\underline{A}} = \underline{\underline{I}} \dots\dots\dots (2.72)$$

Notice that the matrices  $\underline{\underline{A}}$  and  $\underline{\underline{B}}$  commute. The matrix  $\underline{\underline{A}}$  is nonsingular, and the matrix  $\underline{\underline{B}}$  is the inverse of  $\underline{\underline{A}}$ , thus  $\underline{\underline{B}} = \underline{\underline{A}}^{-1}$ , where  $\underline{\underline{A}}^{-1}$  denotes the inverse of  $\underline{\underline{A}}$ . Eq. 2.72 can be written in terms of the inverse as

$$\underline{\underline{A}}\underline{\underline{A}}^{-1} = \underline{\underline{A}}^{-1}\underline{\underline{A}} = \underline{\underline{I}} \dots\dots\dots (2.73)$$

The inverse matrix is useful for solving systems of equations. For example, suppose we have a system of equations that satisfies

$$\underline{\underline{A}}\underline{x} = \underline{b}, \dots\dots\dots (2.74)$$

where the column vector  $\underline{b}$  and the matrix  $\underline{\underline{A}}$  are known, and the column vector  $\underline{x}$  contains a set of unknowns. Eq. 2.54 is an example for the 1D C/D equation. We can solve for  $\underline{x}$  in Eq. 2.74 by premultiplying Eq. 2.74 by  $\underline{\underline{A}}^{-1}$ . The result is

$$\underline{\underline{A}}^{-1}\underline{\underline{A}}\underline{x} = \underline{x} = \underline{\underline{A}}^{-1}\underline{b}. \dots\dots\dots (2.75)$$

Of course, we have to know  $\underline{\underline{A}}^{-1}$  to find  $\underline{x}$ . This leads us to a discussion of determinants.

**2.5.4 Determinants, Eigenvalues, and Eigenvectors.** The determinant (det) of a square matrix  $\underline{\underline{A}}$  is denoted by  $\det(\underline{\underline{A}})$  or  $|\underline{\underline{A}}|$ . Two examples of determinants are the determinants of a  $2 \times 2$  matrix and a  $3 \times 3$  matrix. The determinant of a  $2 \times 2$  matrix is

$$\det \begin{bmatrix} a_{11} & a_{12} \\ a_{21} & a_{22} \end{bmatrix} = a_{11}a_{22} - a_{21}a_{12}, \dots\dots\dots (2.76)$$

and the determinant of a  $3 \times 3$  matrix is

$$\det \begin{bmatrix} a_{11} & a_{12} & a_{13} \\ a_{21} & a_{22} & a_{23} \\ a_{31} & a_{32} & a_{33} \end{bmatrix} = a_{11}a_{22}a_{33} + a_{12}a_{23}a_{31} + a_{13}a_{21}a_{32}$$

$$-a_{31}a_{22}a_{13} - a_{32}a_{23}a_{11} - a_{33}a_{21}a_{12} \dots \dots \dots (2.77)$$

Determinants are useful for determining if an inverse matrix  $\underline{\underline{A}}^{-1}$  exists. Inverse matrices are needed to solve finite-difference equations representing fluid flow. The condition  $\det(\underline{\underline{A}}) \neq 0$  says that an inverse matrix  $\underline{\underline{A}}^{-1}$  exists, even though we may not know the elements of the inverse matrix. Determinants are also useful for determining eigenvalues and eigenvectors.

Eigenvalues and eigenvectors are useful for understanding the behavior of physical quantities that may be represented by a matrix. An example in fluid flow is permeability, which we discuss in more detail later in this chapter. First, we need to define the concepts of eigenvalue and eigenvector.

Eigenvalues are the values of  $\lambda$  in the eigenvalue equation

$$\underline{\underline{A}}\underline{\underline{x}} = \lambda \underline{\underline{x}}, \dots \dots \dots (2.78)$$

where  $\underline{\underline{A}}$  is an  $n \times n$  square matrix and  $\underline{\underline{x}}$  is a column vector with  $n$  rows. The eigenvalue equation may be written as

$$(\underline{\underline{A}} - \lambda \underline{\underline{I}})\underline{\underline{x}} = \underline{\underline{0}}, \dots \dots \dots (2.79)$$

where  $\underline{\underline{I}}$  is the  $n \times n$  identity matrix. Eq. 2.79 has nonzero solutions,  $\underline{\underline{x}}$ , if the eigenvalue,  $\lambda$ , is a characteristic root of  $\underline{\underline{A}}$ , that is,  $\lambda$  must be a solution of

$$\det(\underline{\underline{A}} - \lambda \underline{\underline{I}}) = 0 \dots \dots \dots (2.80)$$

Eq. 2.80 is the characteristic equation of  $\underline{\underline{A}}$ , and the  $n$  values of  $\lambda$  are the characteristic roots of the characteristic equation. The characteristic roots,  $\lambda$ , are obtained by expanding the determinant in Eq. 2.80 into an  $n$ th-degree polynomial and then solving for the  $n$  values of  $\lambda$ . These concepts are illustrated in the next section.

### 2.6 Diagonalizing the Permeability Tensor

The form of Darcy’s law that is most widely used in formulating fluid flow equations in reservoir simulators assumes that the coordinate system is aligned with the principal axes of the permeability tensor. The resulting diagonalized permeability greatly simplifies the fluid flow equations. The simplified equations are easier to code and can be solved with less computation time than fluid flow equations that include the full permeability tensor. Research in naturally-fractured-reservoir modeling,<sup>18</sup> geomechanics,<sup>19</sup> and upscaling<sup>20</sup> has demonstrated that the full permeability tensor is needed to correctly solve fluid flow problems in a variety of realistic settings. The mathematical procedure for diagonalizing the permeability tensor is presented here as an illustration of the mathematics discussed in Sec. 2.5. The relationship between the diagonalized-permeability-tensor assumption and grid orientation is discussed in Sec. 2.7. An understanding of the relationship between grid orientation and the permeability tensor can help us decide how to orient a fluid flow grid to most accurately represent the permeability distribution in a reservoir. The directional dependence of permeability and the permeability tensor are first introduced. The procedure for diagonalizing the permeability tensor is then presented.

**2.6.1 Darcy’s Law and the Permeability Tensor.** In one dimension, Darcy’s law says that flow rate is proportional to pressure gradient. This can be expressed in oilfield units for single-phase flow as

$$\vec{q} = -0.001127k \frac{A}{\mu} \frac{d\Phi}{dx}, \dots\dots\dots (2.81)$$

where  $\vec{q}$  is flow rate (B/D),  $x$  is length (ft),  $A$  is cross-sectional area (ft<sup>2</sup>),  $\mu$  is fluid viscosity (cp),  $k$  is permeability (md), and  $\Phi$  is the phase potential (psia).

$$\Phi = P - \gamma(\Delta z). \dots\dots\dots (2.82)$$

In Eq. 2.82,  $\Delta z$  is depth from a datum (ft),  $P$  is fluid pressure (psia), and  $\gamma$  is the pressure gradient associated with the gravity term (psia/ft). The form of Darcy’s law with full permeability tensor in Cartesian coordinate system  $\{x, y, z\}$  is

$$\begin{bmatrix} q_x \\ q_y \\ q_z \end{bmatrix} = -0.001127 \frac{A}{\mu} \begin{bmatrix} k_{xx} & k_{xy} & k_{xz} \\ k_{yx} & k_{yy} & k_{yz} \\ k_{zx} & k_{zy} & k_{zz} \end{bmatrix} \begin{bmatrix} \partial \Phi / \partial x \\ \partial \Phi / \partial y \\ \partial \Phi / \partial z \end{bmatrix}, \dots\dots\dots (2.83)$$

where we have treated the cross-sectional area,  $A$ , as a constant with respect to direction. Eq. 2.83 can be rewritten as either a dyadic equation,

$$\vec{q} = -0.001127 \frac{A}{\mu} \underline{\underline{k}} \cdot \nabla \Phi, \dots\dots\dots (2.84)$$

by treating permeability as a dyadic, or as a matrix equation,

$$\underline{\underline{q}} = \underline{\underline{k}} \underline{\underline{\Delta}}, \quad \underline{\underline{\Delta}} = -0.001127 \frac{A}{\mu} \begin{bmatrix} \partial \Phi / \partial x \\ \partial \Phi / \partial y \\ \partial \Phi / \partial z \end{bmatrix}, \dots\dots\dots (2.85)$$

by treating permeability as a matrix. We are interested here in the matrix representation.

The diagonal permeability elements  $\{k_{xx}, k_{yy}, k_{zz}\}$  represent the dependence of flow rate in one direction on pressure differences in the same direction. The off-diagonal permeability elements  $\{k_{xy}, k_{xz}, k_{yx}, k_{yz}, k_{zx}, k_{zy}\}$  account for the dependence of flow rate in one direction on pressure differences in orthogonal directions. Expanding Eq. 2.83 gives the corresponding set of three equations demonstrating this dependence.

$$\begin{aligned} q_x &= -0.001127 \frac{A}{\mu} \left( k_{xx} \frac{\partial \Phi}{\partial x} + k_{xy} \frac{\partial \Phi}{\partial y} + k_{xz} \frac{\partial \Phi}{\partial z} \right). \\ q_y &= -0.001127 \frac{A}{\mu} \left( k_{yx} \frac{\partial \Phi}{\partial x} + k_{yy} \frac{\partial \Phi}{\partial y} + k_{yz} \frac{\partial \Phi}{\partial z} \right). \\ q_z &= -0.001127 \frac{A}{\mu} \left( k_{zx} \frac{\partial \Phi}{\partial x} + k_{zy} \frac{\partial \Phi}{\partial y} + k_{zz} \frac{\partial \Phi}{\partial z} \right). \dots\dots\dots (2.86) \end{aligned}$$

**2.6.2 Similarity Transformations.** Eq. 2.85 relates flow rate ( $q$ ) and the pressure gradient term,  $\underline{\Lambda}$ . We can use a similarity transformation to diagonalize the matrix  $\underline{k}$  while preserving the form of the relationship between  $q$  and  $\underline{\Lambda}$ . Let us first show that a similarity transformation preserves the form of Eq. 2.85.

We begin by multiplying Eq. 2.85 on the left by  $\underline{A}$  to find

$$\underline{A}q = \underline{A}k\underline{\Lambda}, \dots\dots\dots (2.87)$$

where  $\underline{A}$  is a nonsingular,  $n \times n$  square matrix. Because  $\underline{A}$  is nonsingular, it is invertible; that is, it satisfies the equality

$$\underline{A}^{-1}\underline{A} = \underline{A}\underline{A}^{-1} = \underline{I}, \dots\dots\dots (2.88)$$

where  $\underline{I}$  is the  $n \times n$  identity matrix. Substituting Eq. 2.88 into Eq. 2.87 gives

$$\underline{A}q = \underline{A}k\underline{A}^{-1}\underline{A}\underline{\Lambda} \dots\dots\dots (2.89)$$

Defining the transformed matrices

$$\begin{aligned} q' &= \underline{A}q \text{ and} \\ \underline{\Lambda}' &= \underline{A}\underline{\Lambda}, \dots\dots\dots (2.90) \end{aligned}$$

and using the similarity transformation

$$\underline{k}' = \underline{A}k\underline{A}^{-1} \dots\dots\dots (2.91)$$

in Eq. 2.89 yields

$$q' = \underline{k}'\underline{\Lambda}' \dots\dots\dots (2.92)$$

Eq. 2.92 is the same form as Eq. 2.85.

**2.6.3 Matrix Diagonalization Procedure.** It is mathematically possible to find a coordinate system  $\{x', y', z'\}$  in which the permeability tensor has the diagonal form

$$\begin{bmatrix} k_{x'x'} & 0 & 0 \\ 0 & k_{y'y'} & 0 \\ 0 & 0 & k_{z'z'} \end{bmatrix}$$

We diagonalize the matrix  $\underline{k}$  by finding and applying a similarity transfor-

mation matrix  $\underline{A}$ . The procedure for finding a matrix  $\underline{A}$  that diagonalizes an  $n \times n$  matrix  $\underline{k}$  is as follows:<sup>4</sup>

- Find the eigenvalues  $\{\lambda_i; i = 1, \dots, n\}$  of  $\underline{k}$  from the eigenvalue equation  $\det(\underline{k} - \lambda\underline{I}) = 0$ .
- Find  $n$  linearly independent eigenvectors  $\{a_i; i = 1, \dots, n\}$ .
- Form the similarity transformation matrix  $\underline{A}$  with the eigenvectors as columns.



- Calculate the diagonalized matrix  $\underline{\underline{k}}'$ . The diagonal entries of  $\underline{\underline{k}}'$  are the eigenvalues corresponding to the eigenvectors  $\{\underline{a}_i : i = 1, \dots, n\}$ .

The coordinate axes  $\{x', y', z'\}$  are the principal axes of the diagonalized tensor, and the diagonal form of the permeability tensor is obtained by a principal-axis transformation. The flow equations along the principal axes are

$$\begin{aligned} q_{x'} &= -0.001127 \frac{A}{\mu} \left( k_{x'x'} \frac{\partial \Phi}{\partial x'} \right); \\ q_{y'} &= -0.001127 \frac{A}{\mu} \left( k_{y'y'} \frac{\partial \Phi}{\partial y'} \right); \\ q_{z'} &= -0.001127 \frac{A}{\mu} \left( k_{z'z'} \frac{\partial \Phi}{\partial z'} \right). \end{aligned} \quad \dots\dots\dots (2.93)$$

The form of the permeability tensor depends on the properties of the porous medium. If the medium is anisotropic, at least two elements of the diagonalized permeability tensor are not equal. If permeability does not depend on direction, then permeability is isotropic, and the elements of the diagonalized permeability tensor are equal, that is,

$$k_{x'x'} = k_{y'y'} = k_{z'z'} = k. \quad \dots\dots\dots (2.94)$$

If the magnitude of the elements of the permeability tensor varies from one point in the medium to another, the permeability tensor is heterogeneous; otherwise, permeability is homogeneous. The principal axes of the permeability tensor may also vary from point to point in the medium if permeability is heterogeneous.

**2.6.4 Diagonalizing a Symmetric  $2 \times 2$  Matrix.** The ideas previously presented are implemented by applying the matrix diagonalization algorithm to the  $2 \times 2$  symmetric matrix

$$\underline{\underline{k}} = \begin{bmatrix} k_{11} & k_{12} \\ k_{21} & k_{22} \end{bmatrix}, \quad \dots\dots\dots (2.95)$$

as viewed in the two-dimensional (2D) Cartesian coordinate system  $\underline{x} = \{x_1, x_2\}$  shown in Fig. 2.6. For this example, we require that the elements of  $\underline{\underline{k}}$  satisfy the relations

$$\begin{aligned} k_{11} &\neq k_{22} \\ k_{12} &= k_{21}. \end{aligned} \quad \dots\dots\dots (2.96)$$

The relation  $k_{12} = k_{21}$  for off-diagonal elements is necessary to assure that the matrix  $\underline{\underline{k}}$  is symmetric. The requirement that  $\underline{\underline{k}}$  is symmetric is important when we consider a coordinate transformation. To find the diagonal matrix  $\underline{\underline{k}}'$  corresponding to  $\underline{\underline{k}}$ , we must first solve the eigenvalue problem

$$\det[\underline{\underline{k}} - \lambda I] = 0. \quad \dots\dots\dots (2.97)$$

The two characteristic roots or eigenvalues  $\lambda_+$  and  $\lambda_-$  of Eq. 2.97 are the diagonal elements of the diagonalized  $2 \times 2$  matrix  $\underline{\underline{k}}'$ , thus

$$\underline{k}' = \begin{bmatrix} \lambda_+ & 0 \\ 0 & \lambda_- \end{bmatrix}, \dots\dots\dots (2.98)$$

where  $\lambda_+$  and  $\lambda_-$  are calculated as the solutions to the eigenvalue problem.

The eigenvalue problem is  $\det[\underline{k} - \lambda \underline{I}] = 0$ . Using Eq. 2.95 gives

$$\begin{vmatrix} k_{11} - \lambda & k_{12} \\ k_{21} & k_{22} - \lambda \end{vmatrix} = 0, \dots\dots\dots (2.99)$$

or

$$(k_{11} - \lambda)(k_{22} - \lambda) - k_{12}k_{21} = 0. \dots\dots\dots (2.100)$$

We expand the characteristic equation to get

$$k_{11}k_{22} - \lambda(k_{11} + k_{22}) + \lambda^2 - k_{12}^2 = 0. \dots\dots\dots (2.101)$$

The two eigenvalues are found from the quadratic equation to be

$$\lambda_{\pm} = \frac{1}{2}(k_{11} + k_{22}) \pm \frac{1}{2}[(k_{11} + k_{22})^2 - 4(k_{11}k_{22} - k_{12}^2)]^{\frac{1}{2}}. \dots\dots\dots (2.102)$$

The sum of the eigenvalues satisfies the relation

$$\lambda_+ + \lambda_- = k_{11} + k_{22}. \dots\dots\dots (2.103)$$

**2.6.5 Eigenvectors.** The matrix  $\underline{A}$  is composed of orthonormal eigenvectors ( $\underline{a}$ ) found from

$$\underline{k}\underline{a} = \lambda\underline{a}. \dots\dots\dots (2.104)$$

The basis vector,  $\underline{a}$ , satisfies

$$(\underline{k} - \lambda\underline{I})\underline{a} = 0. \dots\dots\dots (2.105)$$

with the identity matrix  $\underline{I}$ . Expanding Eq. 2.105 gives

$$\begin{aligned} (k_{11} - \lambda_+)a_1^+ + k_{12}a_2^+ &= 0; \\ k_{12}a_1^+ + (k_{22} - \lambda_+)a_2^+ &= 0. \dots\dots\dots (2.106) \end{aligned}$$

for the eigenvalue  $\lambda_+$ , and

$$(k_{11} - \lambda_-)a_1^- + k_{12}a_2^- = 0;$$

$$k_{12}a_1^- + (k_{22} - \lambda_-)a_2^- = 0 \dots\dots\dots (2.107)$$

for the eigenvalue  $\lambda_-$ . Rearranging Eq. 2.106 gives

$$a_1^+ = \frac{-k_{12}}{k_{11} - \lambda_+} a_2^+ \dots\dots\dots (2.108)$$

Eq. 2.108 and the normalization condition,

$$(a_1^+)^2 + (a_2^+)^2 = 1, \dots\dots\dots (2.109)$$

provide the two equations that are necessary for determining the components of  $\underline{a}^+$ ; thus,

$$a_2^+ = \left[ 1 + \frac{k_{12}^2}{(k_{11} - \lambda_+)^2} \right]^{-\frac{1}{2}} = \frac{k_{11} - \lambda_+}{[(k_{11} - \lambda_+)^2 + k_{12}^2]^{\frac{1}{2}}}, \dots\dots\dots (2.110)$$

and

$$a_1^+ = \frac{-k_{12}}{(k_{11} - \lambda_+)} \left[ 1 + \frac{k_{12}^2}{(k_{11} - \lambda_+)^2} \right]^{-\frac{1}{2}} = \frac{-k_{12}}{[(k_{11} - \lambda_+)^2 + k_{12}^2]^{\frac{1}{2}}} \dots\dots\dots (2.111)$$

Similar calculations for  $\underline{a}^-$  yield the results

$$a_1^- = \frac{-(k_{11} - \lambda_+)}{[(k_{11} - \lambda_+)^2 + k_{12}^2]^{\frac{1}{2}}}, \dots\dots\dots (2.112)$$

and

$$a_2^- = \frac{-k_{12}}{[(k_{11} - \lambda_+)^2 + k_{12}^2]^{\frac{1}{2}}}, \dots\dots\dots (2.113)$$

where the relation

$$k_{11} - \lambda_+ = -(k_{22} - \lambda_-), \dots\dots\dots (2.114)$$

from Eq. 2.103, has been used.

To show that  $\underline{a}^+$  and  $\underline{a}^-$  are orthogonal, we must show that

$$\underline{a}^+ \cdot \underline{a}^- = a_1^+ a_1^- + a_2^+ a_2^- = 0. \dots\dots\dots (2.115)$$

Substituting in the expressions for  $\underline{a}^+$  and  $\underline{a}^-$  gives

$$a_1^+ a_1^- + a_2^+ a_2^- = \frac{k_{12}(k_{11} - \lambda_+)}{(k_{11} - \lambda_+)^2 + k_{12}^2} - \frac{(k_{11} - \lambda_+)k_{12}}{(k_{11} - \lambda_+)^2 + k_{12}^2} = 0, \dots\dots\dots (2.116)$$

as expected.

**2.6.6 Coordinate Transformation.** We now use the orthonormal eigenvectors  $\underline{a}^+$  and  $\underline{a}^-$  to construct the transformation matrix  $\underline{\underline{A}}$ . According to the algorithm for diagonalizing a square matrix presented previously, we form  $\underline{\underline{A}}$  as

$$\underline{\underline{A}} = [\underline{a}^+, \underline{a}^-] = \begin{bmatrix} a_1^+ & a_1^- \\ a_2^+ & a_2^- \end{bmatrix}, \dots\dots\dots (2.117)$$

or

$$\underline{\underline{A}} = \frac{1}{[(k_{11} - \lambda_+)^2 + k_{12}^2]^{\frac{1}{2}}} \begin{bmatrix} -k_{12} & -(k_{11} - \lambda_+) \\ k_{11} - \lambda_+ & -k_{12} \end{bmatrix} \dots\dots\dots (2.118)$$

A coordinate vector in the transformed coordinate system  $\underline{y} = \{y_1, y_2\}$  is given by  $\underline{y} = \underline{\underline{A}}\underline{x}$ . Rewriting the matrix equation for coordinate transformations in algebraic form gives

$$\begin{aligned} y_1 &= a_1^+ x_1 + a_1^- x_2; \\ y_2 &= a_2^+ x_1 + a_2^- x_2; \dots\dots\dots (2.119) \end{aligned}$$

or

$$\begin{bmatrix} y_1 \\ y_2 \end{bmatrix} = \begin{bmatrix} a_1^+ & a_1^- \\ a_2^+ & a_2^- \end{bmatrix} \begin{bmatrix} x_1 \\ x_2 \end{bmatrix} \dots\dots\dots (2.120)$$

An angle ( $\theta$ ) can be associated with the linear transformation by writing the 2D coordinate transformation as

$$\begin{bmatrix} y_1 \\ y_2 \end{bmatrix} = \begin{bmatrix} \cos \theta & \sin \theta \\ -\sin \theta & \cos \theta \end{bmatrix} \begin{bmatrix} x_1 \\ x_2 \end{bmatrix} \dots\dots\dots (2.121)$$

The coordinate systems  $\underline{x} = \{x_1, x_2\}$  and  $\underline{y} = \{y_1, y_2\}$  are related by the counterclockwise rotation shown in Fig. 2.6.

Equating elements of the transformation matrix in Eqs. 2.120 and 2.121 gives

$$a_1^+ = a_2^- = \cos \theta, \dots\dots\dots (2.122)$$

and

$$a_2^+ = -a_1^- = -\sin \theta \dots\dots\dots (2.123)$$

The equalities  $a_1^+ = a_2^-$  and  $a_2^+ = -a_1^-$  are in agreement with Eqs. 2.110 through 2.113. The angle  $\theta$  may be found from either

$$\theta = \cos^{-1} a_1^+ \dots\dots\dots (2.124)$$

or

$$\theta = \sin^{-1} a_1^- \dots\dots\dots (2.125)$$

Note that the equality,

$$\cos^2 \theta + \sin^2 \theta = (a_1^+)^2 + (-a_2^+)^2 = (a_1^-)^2 + (a_2^-)^2 = 1, \dots\dots\dots (2.126)$$

demonstrates that the eigenvectors are orthonormal.

**2.7 Rotational Transformation of a 2 × 2 Permeability Tensor**

We want to calculate changes to the permeability tensor when we transform from a coordinate system  $\underline{y} = \{y_1, y_2\}$  where only the diagonal elements of a square matrix  $\underline{k}'$  are nonzero to a coordinate system  $\underline{x} = \{x_1, x_2\}$  in which a  $2 \times 2$  square matrix  $\underline{k}$  has nonzero off-diagonal elements. We do this by performing a similarity transformation on the matrix  $\underline{k}$ . The coordinate systems  $\underline{x} = \{x_1, x_2\}$  and  $\underline{y} = \{y_1, y_2\}$  are related by the similarity transformation matrix  $\underline{A}$  such that

$$\underline{y} = \underline{A}\underline{x}. \dots\dots\dots (2.127)$$

The two coordinate systems are shown in Fig. 2.6.

An angle ( $\theta$ ) is associated with the transformation in Eq. 2.127 by writing the 2D coordinate transformation as

$$\begin{bmatrix} y_1 \\ y_2 \end{bmatrix} = \begin{bmatrix} \cos \theta & \sin \theta \\ -\sin \theta & \cos \theta \end{bmatrix} \begin{bmatrix} x_1 \\ x_2 \end{bmatrix} \dots\dots\dots (2.128)$$

The coordinate systems  $\underline{x} = \{x_1, x_2\}$  and  $\underline{y} = \{y_1, y_2\}$  are related by the counterclockwise rotation shown in Fig. 2.6. We have an aligned coordinate system  $\underline{y} = \{y_1, y_2\}$  with the principal axes of the permeability tensor. The diagonal tensor in the coordinate system  $\underline{y} = \{y_1, y_2\}$  has the form

$$\underline{k}' = \begin{pmatrix} k_{\max} & 0 \\ 0 & k_T \end{pmatrix}, \dots\dots\dots (2.129)$$

where  $k_{\max}$  is the maximum permeability in the direction  $y_1$  and  $k_T$  is the permeability that is transverse to  $k_{\max}$  in the direction  $y_2$ . We want to know how the elements of the permeability tensor change if we transform to the different coordinate system  $\underline{x} = \{x_1, x_2\}$ .

The relationship between the elements of  $\underline{k}'$  and  $\underline{k}$  is

$$\underline{k}' = \underline{A} \underline{k} \underline{A}^{-1}, \dots\dots\dots (2.130)$$

where  $\underline{A}$  is

$$\underline{A} = \begin{bmatrix} \cos \theta & \sin \theta \\ -\sin \theta & \cos \theta \end{bmatrix} \dots\dots\dots (2.131)$$

If we multiply Eq. 2.130 from the left by  $\underline{A}^{-1}$  and from the right by  $\underline{A}$ , we obtain

$$\underline{k} = \underline{A}^{-1} \underline{k}' \underline{A}. \dots\dots\dots (2.132)$$

We find the elements of  $\underline{A}^{-1}$  by solving

$$\underline{A}^{-1} \underline{A} = \begin{bmatrix} a'_{11} & a'_{12} \\ a'_{21} & a'_{22} \end{bmatrix} \begin{bmatrix} \cos \theta & \sin \theta \\ -\sin \theta & \cos \theta \end{bmatrix} = \begin{bmatrix} 1 & 0 \\ 0 & 1 \end{bmatrix} \dots\dots\dots (2.133)$$

The result is

$$\underline{A}^{-1} = \begin{bmatrix} \cos \theta & -\sin \theta \\ \sin \theta & \cos \theta \end{bmatrix} = \underline{A}^T, \dots\dots\dots (2.134)$$

where  $\underline{A}^T$  is the transpose of  $\underline{A}$ . Substituting Eqs. 2.131 and 2.134 into 2.132 gives

$$\underline{k} = \begin{bmatrix} k_{\max} \cos^2 \theta + k_T \sin^2 \theta & k_{\max} \cos \theta \sin \theta - k_T \cos \theta \sin \theta \\ k_{\max} \sin \theta \cos \theta - k_T \sin \theta \cos \theta & k_{\max} \sin^2 \theta + k_T \cos^2 \theta \end{bmatrix} \\ = \begin{bmatrix} k_{11} & k_{12} \\ k_{21} & k_{22} \end{bmatrix} \dots\dots\dots (2.135)$$

We can use Eq. 2.135 to calculate the elements of  $\underline{k}$  for any rotation angle  $\theta$ . If the permeability is isotropic, we have  $k_{\max} = k_T = k_{\text{iso}}$  and Eq. 2.135 simplifies to the form

$$\underline{k} = \begin{bmatrix} k_{\text{iso}} & 0 \\ 0 & k_{\text{iso}} \end{bmatrix} \dots\dots\dots (2.136)$$

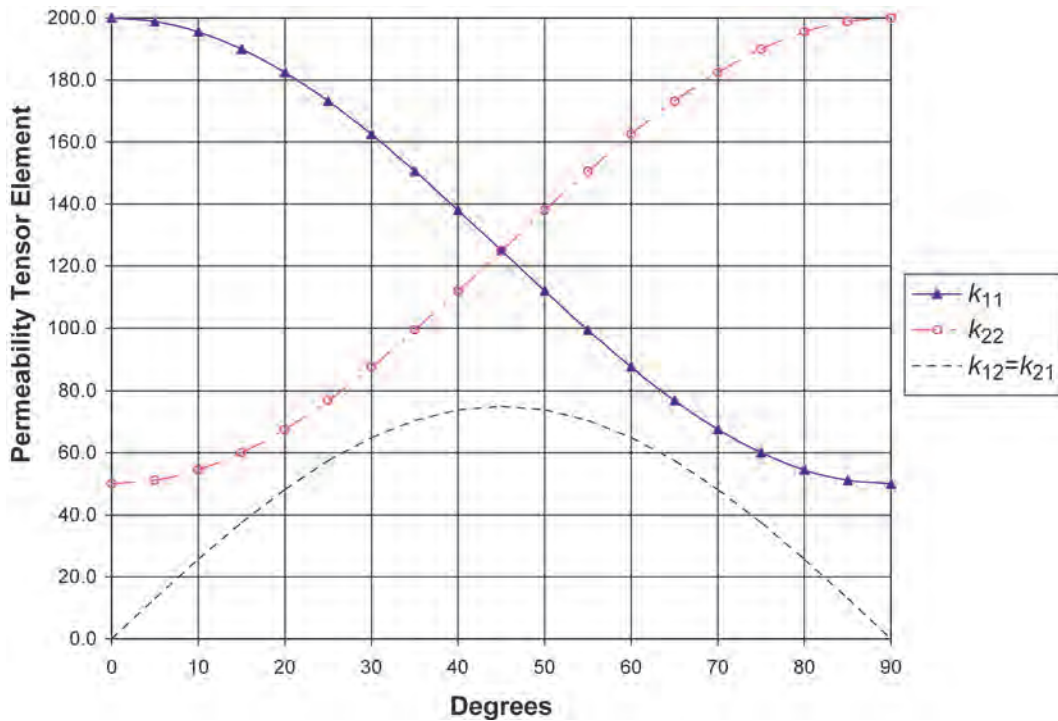


Fig. 2.7—Coordinate rotation in 2D.

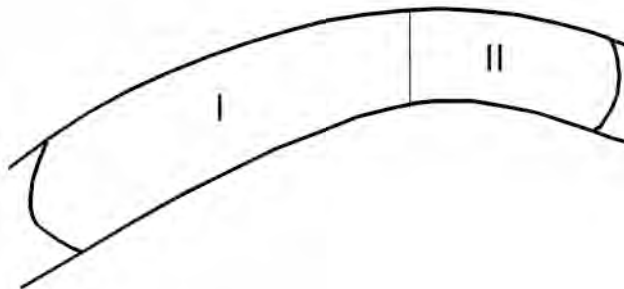


Fig. 2.8—Plan view of channel sand with two permeability regions.

In the special case of isotropic permeability, the orientation of the coordinate system does not affect the values of the elements of the permeability tensor.

Fig. 2.7 shows the results for an anisotropic case in which  $k_{max} = 200$  md and  $k_T = 50$  md. The values of elements  $k_{11}$ ,  $k_{12}$  and  $k_{22}$  of  $\underline{k}$  are presented in the figure. The off-diagonal terms satisfy the equality  $k_{12} = k_{21}$  for a symmetric matrix given in Eq. 2.96, so it is sufficient to show only  $k_{12}$ . The values of the diagonal elements change most as  $\theta$  approaches  $45^\circ$ , and the values of the off-diagonal elements are greatest at  $\theta = 45^\circ$ . A rotation of  $90^\circ$  recovers a diagonal permeability tensor, but  $k_{max}$  is now aligned along  $x_2$ , and  $k_T$  is aligned along  $x_1$ .

**2.7.1 Gridding a Channel Sand.** The ideas discussed are now considered in the context of a realistic application. Our problem is to find a coordinate system that lets us accurately model fluid flow in a channel sand with the two permeability regions in Fig. 2.8.

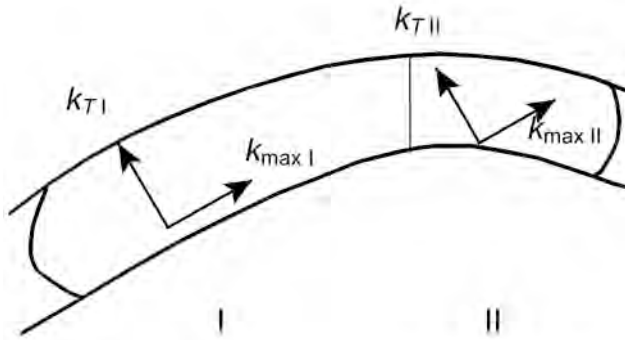


Fig. 2.9—Case A: homogeneous and anisotropic permeability.

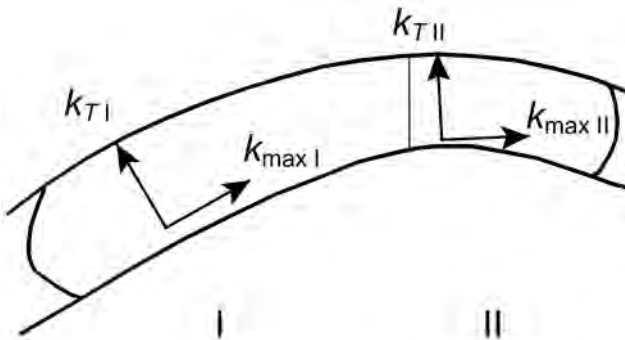


Fig. 2.10—Case B: heterogeneous and anisotropic permeability.

We can highlight important features of the relationship between grid orientation and the assumption of diagonalized permeability by assuming the permeability in each region is anisotropic with a maximum permeability  $k_{max}$  and a permeability  $k_T$  that is transverse to the direction of  $k_{max}$ . The diagonalized, anisotropic permeability tensor  $\underline{\underline{k'}}$  in the  $y_1$ - $y_2$  plane of a channel sand is the matrix

$$\underline{\underline{k'}} = \begin{bmatrix} k_{max} & 0 \\ 0 & k_T \end{bmatrix}, \dots\dots\dots (2.137)$$

and Darcy’s law for flow in the  $y_1$ - $y_2$  plane is

$$\begin{bmatrix} q_1 \\ q_2 \end{bmatrix} = -0.001127 \frac{A}{\mu} \begin{bmatrix} k_{max} & 0 \\ 0 & k_T \end{bmatrix} \begin{bmatrix} \frac{\partial \Phi}{\partial y_1} \\ \frac{\partial \Phi}{\partial y_2} \end{bmatrix} \dots\dots\dots (2.138)$$

Consider two cases. In Case A, permeability is homogeneous and anisotropic, and in Case B, permeability is heterogeneous and anisotropic. The two cases are illustrated in **Figs. 2.9 and 2.10**.



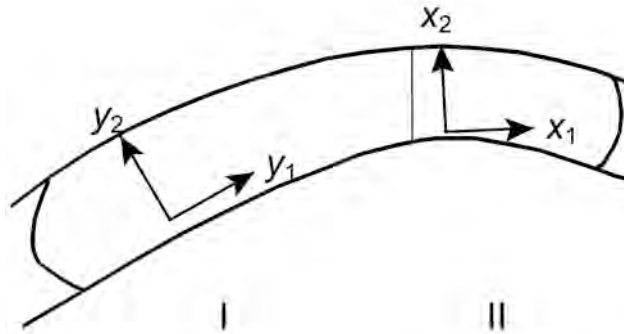


Fig. 2.11—Possible coordinate systems for grid orientation.

TABLE 2.4—SUMMARY OF GRID ORIENTATION ANALYSIS						
Case	Grid		Permeability Tensor		Formulation	
	Region I	Region II	Region I	Region II	Region I	Region II
A.1	$\underline{y} = \{y_1, y_2\}$	$\underline{y} = \{y_1, y_2\}$	ok	ok	ok	ok
A.2	$\underline{y} = \{y_1, y_2\}$	$\underline{x} = \{x_1, x_2\}$	ok	X	ok	X
A.3	$\underline{x} = \{x_1, x_2\}$	$\underline{y} = \{y_1, y_2\}$	X	ok	X	ok
A.4	$\underline{x} = \{x_1, x_2\}$	$\underline{x} = \{x_1, x_2\}$	X	X	X	X
B.1	$\underline{y} = \{y_1, y_2\}$	$\underline{y} = \{y_1, y_2\}$	ok	X	ok	X
B.2	$\underline{y} = \{y_1, y_2\}$	$\underline{x} = \{x_1, x_2\}$	ok	ok	ok	ok
B.3	$\underline{x} = \{x_1, x_2\}$	$\underline{y} = \{y_1, y_2\}$	X	X	X	X
B.4	$\underline{x} = \{x_1, x_2\}$	$\underline{x} = \{x_1, x_2\}$	X	ok	X	ok

Fig. 2.11 shows two possible coordinate systems for orienting the grid. Coordinate system  $\underline{y} = \{y_1, y_2\}$  is more closely aligned with the spatial orientation of Region I than coordinate system  $\underline{x} = \{x_1, x_2\}$ , while coordinate system  $\underline{x} = \{x_1, x_2\}$  is more closely aligned with the spatial orientation of Region II than coordinate system  $\underline{y} = \{y_1, y_2\}$ . The coordinate system  $\underline{y} = \{y_1, y_2\}$  is obtained by rotating the coordinate system  $\underline{x} = \{x_1, x_2\}$  through an angle  $\theta$  as in Fig. 2.6.

We consider four grid orientations for each case: (1) grid  $\underline{y} = \{y_1, y_2\}$  in Regions I and II; (2) grid  $\underline{y} = \{y_1, y_2\}$  in Region I and grid  $\underline{x} = \{x_1, x_2\}$  in Region II; (3) grid  $\underline{x} = \{x_1, x_2\}$  in Region I and grid  $\underline{y} = \{y_1, y_2\}$  in Region II; and (4) grid  $\underline{y} = \{y_1, y_2\}$  in Regions I and II. The grid orientation cases allow us to consider the effect of different coordinate systems on the permeability tensor in each region. We assume in our analysis that the reservoir simulator is a typical simulator with a formulation of fluid flow equations that uses Darcy’s law with a diagonal permeability tensor. We also assume the simulator allows different grid orientations in different regions of the model; otherwise, grid orientation cases 2 and 3 are not feasible. Our

analysis does not include multidimensional numerical dispersion,<sup>17</sup> which can also affect the accuracy of flow calculations. Results of the analysis are summarized in **Table 2.4**.

An “ok” in the “Permeability Tensor” column in **Table 2.4** indicates that the diagonal permeability tensor is aligned with the grid. An “X” indicates that the magnitudes of the diagonal terms in the permeability tensor must be corrected with **Eq. 2.135**. An “ok” in the “Formulation” column in **Table 2.4** indicates that the formulation of the fluid flow equations is correct. An “X” indicates that the formulation of the fluid flow equations is incorrect because the formulation does not include off-diagonal terms in the permeability tensor. Based on the results in **Table 2.4**, we observe that the grid orientation in Case A.1 provides the most faithful representation of the permeability tensor in Case A, and the grid orientation in Case B.2 provides the most faithful representation of the permeability tensor in Case B.

### Nomenclature

- $a_i, b_i, c_i, d_i$  = finite-difference coefficients, **Eq. 2.51**
- $a_{ij}, b_{ij}, c_{ij}$  = elements of matrices, **Eq. 2.64**
- $\underline{\underline{A}}, \underline{\underline{B}}, \underline{\underline{C}}$  = matrices, **Eq. 2.64**
- $\underline{\underline{A}}$  = rotation matrix, **Eq. 2.57**
- $\underline{\underline{A}}^T$  = transpose of matrix  $A$ , **Eq. 2.134**
- $A$  = cross-sectional area, **Eq. 2.81**
- $A, B, C, G$  = functions, **Eq. 2.13**
- $c_f$  = fluid compressibility, **Eq. 2.10**
- $\underline{C}$  = column vector of unknown concentrations at  $t^{n+1}$ , **Eq. 2.54**
- $\overline{C}$  = concentration, **Eq. 2.4**
- $D$  = dispersion of the solute into solvent, **Eq. 2.15**
- $\underline{D}$  = column vector of terms that depend on known concentrations at  $t^{n+1}$ , **Eq. 2.54**
- $E_T$  = truncation error, **Eq. 2.45**
- $f$  = scalar function, **Eq. 2.26**
- $\{\hat{i}, \hat{j}, \hat{k}\}$  = unit vectors in Cartesian coordinates, **Eq. 2.25**
- $\underline{\underline{I}}$  = identity matrix, **Eq. 2.69**
- $J_x, J_y, J_z$  = fluid flux in  $x$ -,  $y$ -,  $z$ -directions
- $\vec{J}$  = fluid flux vector, **Eq. 2.23**
- $(J_x)_x$  = fluid flux in  $x$ -direction at location  $x$
- $(J_y)_y$  = fluid flux in  $y$ -direction at location  $y$
- $(J_z)_z$  = fluid flux in  $z$ -direction at location  $z$
- $k$  = permeability matrix, **Eq. 2.85**
- $\overline{k}$  = permeability, **Eq. 2.81**
- $k_{\text{iso}}$  = isotropic permeability, **Eq. 2.136**
- $k_{\text{max}}$  = maximum permeability, **Eq. 2.129**
- $k_T$  = transverse permeability, **Eq. 2.129**
- $m, n$  = number of rows and columns, **Sec. 2.5.2**
- $\underline{\underline{M}}$  = matrix of coefficients, **Eq. 2.54**
- $\overline{P}$  = pressure, **Eq. 2.82**
- $\vec{q}, \underline{q}$  = flow rate, **Eqs. 2.81 and 2.85**
- $q$  = source term, **Eq. 2.3**
- $R$  = region
- $S$  = surface
- $t$  = time

- $t^n$  = present time  
 $t^{n+1}$  = future time  
 $\vec{v}$  = vector field, Eq. 2.27  
 $v$  = velocity of solute, Eq. 2.15  
 $v_x$  = speed in  $x$ -direction, Eq. 2.9  
 $\vec{x}$  = position vector, Eq. 2.25  
 $x, y, z$  = space dimensions  
 $x_i$  = discrete point in  $x$ -direction, Eq. 2.43  
 $\underline{x}, \underline{y}$  = column vectors, Eq. 2.121  
 $\alpha$  = proportionality constant, Eq. 2.11  
 $\{\alpha, \beta, \gamma\}$  = functions, Eq. 2.14  
 $\Delta t$  = time interval  
 $\Delta x$  = length  
 $\Delta y$  = width  
 $\Delta z$  = thickness  
 $\theta$  = angle, Eq. 2.55  
 $\lambda$  = eigenvalues, Eq. 2.78  
 $\mu$  = fluid viscosity, Eq. 2.81  
 $\rho$  = density, Eq. 2.8  
 $\underline{\Delta}$  = pressure gradient, Eq. 2.85  
 $\Phi$  = phase potential, Eq. 2.81  
 $\psi$  = function, Eq. 2.7

### Subscripts

- $i$  = discrete  $x$ -direction index  
 $i, j$  = matrix indices, Eq. 2.61  
 $i, j, k$  =  $x$ -,  $y$ -,  $z$ -direction indices  
 $NX$  = range of index, Eq. 2.53  
 $t$  = time index, Eq. 2.4  
 $x$  =  $x$ -direction index, Eq. 2.2  
 $0$  = reference value of pressure, Eq. 2.10

### Superscripts

- $*$  = complex conjugation  
 $T$  = transpose of matrix

---

## References

1. Kreyszig, E.: *Advanced Engineering Mathematics*, eighth edition, Wiley & Sons Inc., New York City (1999).
2. Collins, R.E.: *Mathematical Methods for Physicists and Engineers*, second corrected edition, Dover Publications, New York City (1999).
3. Chow, T.L.: *Mathematical Methods for Physicists: A Concise Introduction*, Cambridge U. Press, Cambridge (2000).
4. Fanchi, J.R.: *Math Refresher for Scientists and Engineers*, third edition, Wiley Interscience, New York City (2006).
5. Fanchi, J.R.: *Shared Earth Modeling*, Butterworth-Heinemann, Boston (2002).
6. Towler, B.F.: *Fundamental Principles of Reservoir Engineering*, SPE, Richardson, Texas (2002).
7. Abramowitz, M.A. and Stegun, I.A.: *Handbook of Mathematical Functions*, ninth printing, Dover Publications, New York City (1972).
8. Peaceman, D.W.: *Fundamentals of Numerical Reservoir Simulation*, Elsevier, Amsterdam (1977).

9. Aziz, K. and Settari, A.: *Petroleum Reservoir Simulation*, Applied Science Publications, London (1979).
10. Mattax, C.C. and Dalton, R.L.: *Reservoir Simulation*, Monograph Series, SPE, Richardson, Texas (1990) **13**.
11. Ertekin, T., Abou-Kassem, J.H., and King, J.R.: *Basic Applied Reservoir Simulation*, Textbook Series, SPE, Richardson, Texas (2001) **7**.
12. Munka, M. and Pápay, J.: *4D Numerical Modeling of Petroleum Reservoir Recovery*, Akadémiai Kiadó, Budapest (2001).
13. Fanchi, J.R.: *Principles of Applied Reservoir Simulation*, third edition, Butterworth-Heinemann, Boston (2006).
14. Fanchi, J.R.: *Integrated Flow Modeling*, Elsevier, Amsterdam (2000).
15. Chapra, S.C. and Canale, R.P.: *Numerical Methods for Engineers*, fourth edition, McGraw-Hill Book Co. Inc., Boston (2002).
16. Lantz, R.B.: "Quantitative Evaluation of Numerical Diffusion (Truncation Error)," *SPEJ* (September 1971) 315.
17. Fanchi, J.R.: "Multidimensional Numerical Dispersion," *SPEJ* (February 1983) 143.
18. Gupta, A., Penuela, G., and Avila, R.: "An Integrated Approach to the Determination of Permeability Tensors for Naturally Fractured Reservoirs," *J. Cdn. Pet. Tech.*, **40**, No. 12, 43.
19. Settari, A., Walters, D.A., and Behie, G.A.: "Use of Coupled Reservoir and Geomechanical Modeling for Integrated Reservoir Analysis and Management," *J. Cdn. Pet. Tech.*, **40**, No. 12, 55.
20. Young, L.C.: "Rigorous Treatment of Distorted Grids in 3D," *Proc.*, 15th SPE Symposium on Reservoir Simulation, Houston (1999).

### SI Metric Conversion Factors

bbbl	× 1.589 873	E – 01	= m <sup>3</sup>
cp	× 1.0*	E – 03	= Pa·s
ft	× 3.048*	E – 01	= m
ft <sup>2</sup>	× 9.290 304*	E – 02	= m <sup>2</sup>
psi	× 6.894 757	E + 00	= kPa

\*Conversion factor is exact.

# Chapter 3

## Mathematics of Transient Analysis

Erdal Ozkan, Colorado School of Mines

This chapter explains how fluid flow in porous media can be translated into a mathematical statement and how mathematical analysis can be used to answer transient-flow problems. This broad area is common to many other disciplines, such as heat conduction in solids and ground-water hydrology. The objective of this chapter is to introduce the fundamentals of transient analysis, present examples, and guide the interested reader to relevant references.

### 3.1 Introduction

Most physical phenomena in the domain of transient fluid flow in porous media can be described generally by partial differential equations (PDEs). With appropriate boundary conditions and sometimes with simplifying assumptions, the PDE leads to an initial boundary value problem (IBVP) that is solved to find a mathematical statement of the resulting flow in the porous medium. This section briefly discusses the statement of the IBVP for transient fluid flow in porous media.

**3.1.1 Equations of Transient Fluid Flow in Porous Media.** In essence, fluid motion in porous media can be specified by the knowledge of the velocity vector,  $\vec{v}$ , and the density of the fluid,  $\rho$ , as a function of the position  $(x, y, z)$  and time,  $t$ ; that is,  $\vec{v} = \vec{v}(x, y, z, t)$  and  $\rho = \rho(x, y, z, t)$ . Relative to the fixed Cartesian axes, the velocity vector can be written as

$$\vec{v} = v_x \vec{i}_x + v_y \vec{i}_y + v_z \vec{i}_z, \dots\dots\dots (3.1)$$

where  $v_x$ ,  $v_y$ , and  $v_z$  are the velocity components, and  $\vec{i}_x$ ,  $\vec{i}_y$ , and  $\vec{i}_z$  are the unit vectors in the  $x$ ,  $y$ , and  $z$  directions, respectively.

The physical law governing the macroscopic fluid-flow phenomena in porous media is the conservation of mass, which states that mass is neither created nor destroyed. The mathematical formula of this rule is developed by considering the flow through a fixed arbitrary closed surface,  $\Gamma$ , lying entirely within a porous medium of porosity  $\Phi$ , which is filled with a fluid of viscosity  $\mu$ . **Fig. 3.1** illustrates an arbitrary closed surface in porous medium.

The conservation of mass principle requires that the difference between the rates at which fluid enters and leaves the volume through its surface must equal the rate at which mass accumulates within the volume. The total mass within the volume at any time is given by

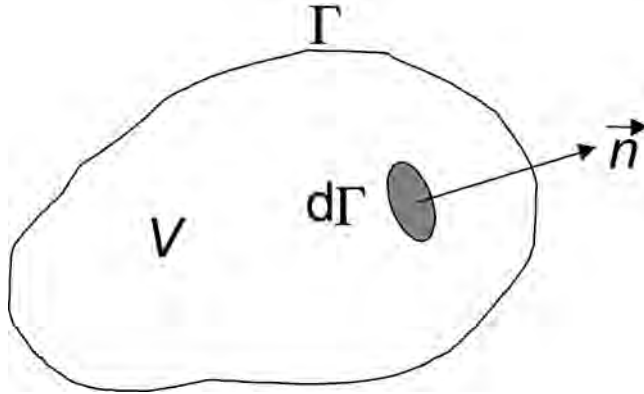


Fig. 3.1—Arbitrary closed surface  $\Gamma$  in porous medium.

$$M_g = \iiint_V \rho \Phi dV \dots\dots\dots (3.2)$$

Then, the time rate of change of mass within  $\Gamma$  is

$$\frac{dM_g}{dt} = \frac{d}{dt} \iiint_V \rho \Phi dV = \iiint_V \frac{\partial}{\partial t} (\rho \Phi) dV, \dots\dots\dots (3.3)$$

which, by the conservation of mass law, is equal to the rate at which mass enters  $V$  through the surface.

Consider the differential surface element,  $\vec{d}\Gamma$ , shown in Fig. 3.1. The mass entering the volume through  $d\Gamma$  at the normal velocity,  $\rho \vec{v} \cdot \vec{n}$ , in a time increment,  $\Delta t$ , is  $-\rho \vec{v} \cdot \vec{n} d\Gamma \Delta t$ , and the total mass of the fluid passing through  $\Gamma$  during  $\Delta t$  is

$$\Delta M_g = -\Delta t \oint_{\Gamma} \rho \vec{v} \cdot \vec{n} d\Gamma \dots\dots\dots (3.4)$$

The surface integral in Eq. 3.4 accounts for both influx and outflux through the surface of the volume; that is,  $\Delta M_g$  is the difference between the masses entering and leaving the control volume during the time increment,  $\Delta t$ . Then, the mass rate entering the volume,  $V$ , through its surface,  $\Gamma$ , can be written as

$$q = \lim_{\Delta t \rightarrow 0} \frac{\Delta M_g}{\Delta t} = \frac{dM_g}{dt} = -\oint_{\Gamma} \rho \vec{v} \cdot \vec{n} d\Gamma \dots\dots\dots (3.5)$$

By the principle of conservation of mass, equating the right sides of Eqs. 3.3 and 3.5 yields

$$\iiint_V \frac{\partial}{\partial t} (\rho \Phi) dV + \oint_{\Gamma} \rho \vec{v} \cdot \vec{n} d\Gamma \equiv 0 \dots\dots\dots (3.6)$$

A more useful relation is found with the divergence theorem, which states that the flux of  $\rho \vec{v}$  through the closed surface,  $\Gamma$ , is identical to the volume integral of  $\nabla \cdot (\rho \vec{v})$  (the divergence of  $\rho \vec{v}$ ) taken throughout  $V$ ; that is,

$$\oint_{\Gamma} \rho \vec{v} \cdot \vec{n} \, d\Gamma = \iiint_V \nabla \cdot (\rho \vec{v}) \, dV \dots\dots\dots (3.7)$$

Here,  $\nabla$  is the gradient operator, which in 3D Cartesian and cylindrical coordinates is given, respectively, by

$$\nabla \equiv \frac{\partial}{\partial x} \vec{i}_x + \frac{\partial}{\partial y} \vec{i}_y + \frac{\partial}{\partial z} \vec{i}_z \dots\dots\dots (3.8)$$

and

$$\nabla \equiv \frac{\partial}{\partial r} \vec{i}_r + \frac{1}{r} \frac{\partial}{\partial \theta} \vec{i}_\theta + \frac{\partial}{\partial z} \vec{i}_z \dots\dots\dots (3.9)$$

With the relation in Eq. 3.7, Eq. 3.6 can be recast into

$$\iiint_V \left[ \frac{\partial}{\partial t} (\rho \Phi) + \nabla \cdot \rho \vec{v} \right] dV \equiv 0 \dots\dots\dots (3.10)$$

If the functions involved in the argument of the integral in Eq. 3.10 are continuous, then the integral is identically zero if and only if its argument is zero (because the volume integral in Eq. 3.10 is identically zero for any arbitrarily chosen volume). Then, the following continuity equation can be obtained.

$$\frac{\partial}{\partial t} (\rho \Phi) + \nabla \cdot (\rho \vec{v}) = 0 \dots\dots\dots (3.11)$$

Eq. 3.11 is a PDE that is equivalent to the statement of the conservation of mass for fluid flow in porous media. For practical purposes, however, Eq. 3.11 is expressed in terms of pressure because density and velocity cannot be measured directly. To express density,  $\rho$ , and velocity,  $\vec{v}$ , in terms of pressure, we use an equation of state and a flux law, known as Darcy’s law, respectively.

The following definition of isothermal fluid compressibility,  $c$ , is a useful equation of state that relates density to pressure.

$$c = \left( \frac{1}{\rho} \frac{\partial \rho}{\partial p} \right)_T \dots\dots\dots (3.12)$$

If  $c$  is a constant (the compressibility of many reservoir liquids may be considered as constant), then Eq. 3.12 can be integrated to yield

$$\rho = \rho_0 \exp [c(p - p_0)], \dots\dots\dots (3.13)$$

where subscript 0 indicates the conditions at the datum. Similarly, the compressibility of the porous rock,  $c_f$ , is defined by

$$c_f = \frac{1}{\Phi} \frac{\partial \Phi}{\partial p}, \dots\dots\dots (3.14)$$

and the total system compressibility,  $c_t$ , is given by

$$c_t = c + c_f. \dots\dots\dots (3.15)$$

These definitions of compressibility help recast Eq. 3.11 in terms of pressure.

Darcy's law for fluid flow in porous media is a flux law. Neglecting the gravity effect, it is expressed by

$$\vec{v} = -\frac{k}{\mu} \nabla p. \dots\dots\dots (3.16)$$

In Eq. 3.16,  $\mu$  is the viscosity of the fluid, and  $k$  is the permeability tensor of the formation given by

$$k = \begin{pmatrix} k_{\alpha\alpha} & k_{\alpha\beta} & k_{\alpha\gamma} \\ k_{\beta\alpha} & k_{\beta\beta} & k_{\beta\gamma} \\ k_{\gamma\alpha} & k_{\gamma\beta} & k_{\gamma\gamma} \end{pmatrix}, \dots\dots\dots (3.17)$$

where  $\alpha$ ,  $\beta$ , and  $\gamma$  are the directions, and  $k_{ij}$  is the permeability in the  $i$  direction as a result of the pressure gradient in the  $j$  direction.

If Eqs. 3.13 through 3.16 are used in Eq. 3.11, an alternative statement of the conservation of mass principle for fluid flow in porous media is obtained:

$$\nabla \cdot \left( \frac{k}{\mu} \nabla p \right) + c \frac{k}{\mu} (\nabla p)^2 = \Phi c_t \frac{\partial p}{\partial t}. \dots\dots\dots (3.18)$$

Eq. 3.18 is the PDE that governs transient fluid flow in porous media. In the present form, Eq. 3.18 is not very useful in obtaining practical solutions because of the nonlinearity displayed in the second term of the left side. For liquid flow, the viscosity,  $\mu$ , is constant and Eq. 3.18 can be linearized by assuming that the pressure gradients,  $\nabla p$ , are small in the reservoir and the compressibility of the reservoir liquids,  $c$ , is on the order of  $10^{-5}$  or smaller. Then, the second term of the left side of Eq. 3.18 may be neglected compared with the remaining terms and the following linear expression is obtained:

$$\nabla \cdot (k \nabla p) = \Phi c_t \mu \frac{\partial p}{\partial t}. \dots\dots\dots (3.19)$$

Eq. 3.19 (or Eq. 3.18) is known as the diffusivity equation. As an example in Cartesian coordinates, assuming that the coordinate axes can be chosen in the directions of the principal permeabilities,  $k$ , in Eq. 3.19, may be represented by the following diagonal tensor:



$$k = \begin{pmatrix} k_x & 0 & 0 \\ 0 & k_y & 0 \\ 0 & 0 & k_z \end{pmatrix} \dots\dots\dots (3.20)$$

Then, Eq. 3.19 may be written as

$$k_x \frac{\partial^2 p}{\partial x^2} + k_y \frac{\partial^2 p}{\partial y^2} + k_z \frac{\partial^2 p}{\partial z^2} = \Phi c_t \mu \frac{\partial p}{\partial t} \dots\dots\dots (3.21)$$

If each coordinate,  $j = x, y,$  or  $z,$  is multiplied by  $\sqrt{k/k_j},$  where  $k$  may be chosen arbitrarily (to preserve the material balance,  $k$  is usually chosen to be  $\sqrt[3]{k_x k_y k_z},$  Eq. 3.21 may be transformed into the diffusion equation for an isotropic domain:

$$\eta \nabla^2 p - \frac{\partial p}{\partial t} = 0, \dots\dots\dots (3.22)$$

where  $\eta$  is the diffusivity constant defined by

$$\eta = \frac{k}{\Phi c_t \mu} \dots\dots\dots (3.23)$$

If the same transformation is also applied to the boundary conditions (see Sec. 3.1.2), the problems in anisotropic reservoirs may be transformed into those in isotropic reservoirs provided that the system is infinite or bounded by planes perpendicular to the principal axes of permeability. In all other cases, this transformation distorts the bounding surfaces.

For the flow of gases, the assumptions of small fluid compressibility and pressure gradient may not be appropriate and the  $c(\nabla p)^2$  term in Eq. 3.18 may not be negligible. In these cases, an expression similar to Eq. 3.21 may be obtained from Eq. 3.18 in terms of pseudopressure,  $m,$  as

$$k_x \frac{\partial^2 m}{\partial x^2} + k_y \frac{\partial^2 m}{\partial y^2} + k_z \frac{\partial^2 m}{\partial z^2} = \Phi c_t \mu \frac{\partial m}{\partial t} \dots\dots\dots (3.24)$$

Here, the pseudopressure is defined by<sup>1</sup>

$$m(p) = 2 \int_0^p \frac{p'}{\mu Z} dp', \dots\dots\dots (3.25)$$

where  $Z$  is the compressibility factor. To define a complete physical problem, Eq. 3.21 (or 3.24) should be subject to the initial and boundary conditions discussed in Sec. 3.1.2.

**3.1.2 Initial and Boundary Conditions.** The solution of the diffusivity equation (Eq. 3.19) should satisfy the initial condition in the porous medium. The initial condition is normally expressed in terms of a known pressure distribution at time zero; that is,

$$\lim_{t \rightarrow 0} p(x, y, z, t) = f(x, y, z). \dots\dots\dots (3.26)$$

The most common initial condition is the uniform pressure distribution in the entire porous medium; that is,  $f(x, y, z) = p_i$ .

The boundary conditions are specified at the inner (wellbore) and outer boundaries of the reservoir. These are usually in the form of prescribed flux or pressure at the boundaries. The condition of prescribed flux can be formulated as

$$\left( \frac{\partial p}{\partial n} \right)_{\Gamma} = g(t), \dots\dots\dots (3.27)$$

where  $\Gamma$  is the surface of the boundary, and  $n$  indicates the outward normal direction of the boundary surface. The prescribed flux condition may be used at the inner and outer boundaries of the reservoir. The most common use of the prescribed flux condition at the inner boundary is for the production at a constant rate. In this case, the function,  $g(t)$ , is related to a constant production rate,  $q$ . At the outer boundary, the prescribed flux condition is usually used to indicate impermeable boundaries [ $g(t)=0$ ] and leads to a pseudosteady state under the influence of boundaries.

For some applications, pressure may be specified at the inner and outer boundaries. In this case,

$$(p)_{\Gamma} = h(t). \dots\dots\dots (3.28)$$

When used at the inner boundary, this condition represents production at a constant pressure,  $p_{wf}$ ; that is,  $h(t) = p_{wf}$ . At the outer boundary, specified pressure,  $p_e$ , is usually a result of injection or influx from an adjacent aquifer, which usually leads to steady state in the reservoir.

It is also possible to have boundary conditions of mixed type. These usually correspond to interface conditions in porous media. Ref. 2 contains more details about the common boundary conditions for the diffusion equation.

**3.1.3 Assumptions and Limits.** Some assumptions have been made in the derivation of the diffusivity equation given by Eq. 3.19. These assumptions determine the limits of applicability of the solutions obtained from Eq. 3.19. One of the most important assumptions involved is the continuity of the properties involved in Eq. 3.19. (This was required to obtain Eq. 3.19 from the more general integral form in Eq. 3.10.) Therefore, sharp changes in the properties of the reservoir rock and fluid (such as faults and fluid banks) should be incorporated in the form of boundary or interface conditions in the solution of Eq. 3.19.

The second important assumption is that Darcy's law describes the flux in porous media. This assumption is valid at relatively low fluid velocities that may be appropriate to describe liquid flow. At high velocities (when Reynolds number based on average sand grain diameter approaches unity) such as those observed in gas reservoirs, Darcy's law is not valid.<sup>3</sup> In this case, Forchheimer's equation,<sup>4</sup> which accounts for the inertial effects, should be used. In petroleum engineering, it is a common practice to consider the additional pressure drop as a result of non-Darcy flow in the form of a pseudoskin because it is usually effective in a small vicinity of the wellbore. Therefore, in this chapter, we do not consider non-Darcy flow in the reservoir.

## 3.2 Bessel Functions

As Sec. 3.3 illustrates, the Laplace transform of the diffusion equation in radial coordinates yields a modified Bessel's equation, and its solutions are obtained in terms of modified Bessel

functions. This section introduces Bessel functions and discusses some of their properties to the extent that they are encountered in the solutions of more common petroleum engineering problems.

**3.2.1 Preliminary Definitions.** A differential equation of the type

$$\frac{d^2y}{dz^2} + \frac{1}{z} \frac{dy}{dz} + \frac{z^2 - v^2}{z^2} y = 0; \quad v \geq 0 \dots\dots\dots (3.29)$$

is called a Bessel’s equation of order  $v$ . A solution of Bessel’s equation of order  $v$  is called a Bessel function of order  $v$ . A differential equation of the type

$$\frac{d^2y}{dz^2} + \frac{1}{z} \frac{dy}{dz} + \frac{\lambda^2 z^2 - v^2}{z^2} y = 0; \quad v \geq 0 \dots\dots\dots (3.30)$$

is called a modified Bessel’s equation of order  $v$ . Eq. 3.30 is obtained by substituting  $\lambda z$  for  $z$  in Eq. 3.29. Of particular interest is the case in which  $\lambda=ki$  so that Eq. 3.30 becomes

$$\frac{d^2y}{dz^2} + \frac{1}{z} \frac{dy}{dz} - \frac{k^2 z^2 + v^2}{z^2} y = 0; \quad v \geq 0 \dots\dots\dots (3.31)$$

Eq. 3.31 is called the modified Bessel’s equation of order  $v$ . A solution of the modified Bessel’s equation of order  $v$  is called a modified Bessel function of order  $v$ .

**3.2.2 Solutions of Bessel’s Equations and Bessel Functions.** There are many methods of obtaining or constructing Bessel functions.<sup>5</sup> Only the final form of the Bessel functions that are of interest are presented here.

If  $v$  is not a positive integer, then the general solution of Bessel’s equation of order  $v$  (Eq. 3.29) is given by

$$y = AJ_v(z) + BJ_{-v}(z), \dots\dots\dots (3.32)$$

where  $A$  and  $B$  are arbitrary constants, and  $J_v(z)$  is the Bessel function of order  $v$  of the first kind given by

$$J_v(z) = \sum_{m=0}^{\infty} \frac{(-1)^m (z/2)^{v+2m}}{m! \Gamma(v+m+1)} \dots\dots\dots (3.33)$$

In Eq. 3.33,  $\Gamma(x)$  is the gamma function defined by

$$\Gamma(x) = \int_0^{\infty} e^{-t} t^{x-1} dt \dots\dots\dots (3.34)$$

If  $v$  is a positive integer,  $n$ , then  $J_v$  and  $J_{-v}$  are linearly dependent, and the solution of Eq. 3.29 is written as

$$y = AJ_n(z) + BY_n(z) \dots\dots\dots (3.35)$$

In Eq. 3.35,  $Y_n(z)$  is the Bessel function of order  $n$  of the second kind and is defined by

$$Y_n(z) = \lim_{\nu \rightarrow n} \left[ \frac{J_\nu(z) - (-1)^n J_{-\nu}(z)}{\nu - n} \right] \dots\dots\dots (3.36)$$

Similarly, if  $\nu$  is not a positive integer, the general solution of the modified Bessel’s equation of order  $\nu$  (Eq. 3.31) is given by

$$y = AI_\nu(kz) + BI_{-\nu}(kz), \dots\dots\dots (3.37)$$

where  $I_\nu(z)$  is the modified Bessel function of order  $\nu$  of the first kind defined by

$$I_\nu(z) = \sum_{m=0}^{\infty} \frac{(kz/2)^{\nu+2m}}{m! \Gamma(\nu+m+1)} \dots\dots\dots (3.38)$$

If  $\nu$  is a positive integer,  $n$ ,  $I_\nu$ , and  $I_{-\nu}$  are linearly dependent. The solution for this case is

$$y = AI_n(kz) + BK_n(kz), \dots\dots\dots (3.39)$$

where  $K_n(z)$  is the modified Bessel function of order  $n$  of the second kind and is defined by

$$K_n(z) = \lim_{\nu \rightarrow n} \left[ \frac{I_{-\nu}(z) - J_\nu(z)}{\nu - n} \right] \dots\dots\dots (3.40)$$

The modified Bessel functions of order zero and one are of special interest, and Sec. 3.2.3 discusses some of their special features.

**3.2.3 Modified Bessel Functions of Order Zero and One.** Modified Bessel functions of order zero and one are related to each other by the following relations:

$$\frac{dI_0(z)}{dz} = I_1(z) \dots\dots\dots (3.41)$$

and

$$\frac{dK_0(z)}{dz} = -K_1(z) \dots\dots\dots (3.42)$$

**Fig. 3.2** shows these functions graphically.

For small arguments, the following asymptotic expansions may be used for the modified Bessel functions of order zero and one:<sup>5</sup>

$$I_0(z) = \sum_{m=0}^{\infty} \frac{(z/2)^{2m}}{(m!)^2}, \dots\dots\dots (3.43)$$

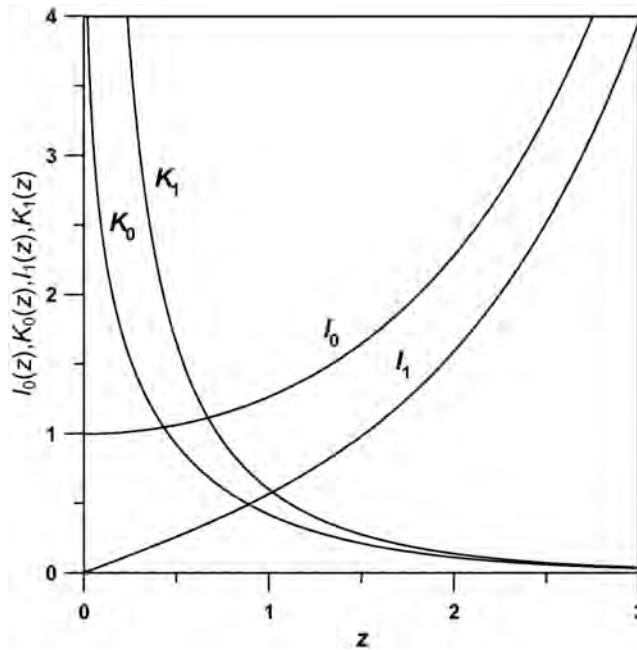


Fig. 3.2—Bessel functions of order zero and one.

$$I_1(z) = \sum_{m=0}^{\infty} \frac{2m(z/2)^{2m-1}}{(m!)^2}, \dots\dots\dots (3.44)$$

$$K_0(z) = -\left[ \ln\left(\frac{z}{2}\right) + \gamma \right] I_0(z) - \sum_{m=1}^{\infty} \frac{(z/2)^{2m}}{(m!)^2} \left( 1 + \frac{1}{2} + \frac{1}{3} + \dots + \frac{1}{k} \right), \dots\dots\dots (3.45)$$

where  $\gamma = 0.5772\dots$ , and

$$K_1(z) = \left[ \ln\left(\frac{z}{2}\right) - \gamma \right] I_1(z) + \frac{I_0(z)}{z} + \sum_{m=1}^{\infty} \frac{2m(z/2)^{2m}}{(2)^{2m}(m!)^2} \left( 1 + \frac{1}{2} + \frac{1}{3} + \dots + \frac{1}{k} \right), \dots\dots\dots (3.46)$$

Also, for large arguments, the following relations may be useful:

$$I_\nu(z) = \frac{e^z}{\sqrt{2\pi z}} \left[ 1 - \frac{(4\nu^2 - 1)}{8z} + \frac{(4\nu^2 - 1)(4\nu^2 - 9)}{2!(8z)^2} - \frac{(4\nu^2 - 1)(4\nu^2 - 9)(4\nu^2 - 25)}{3!(8z)^3} + \dots \right] \dots (3.47)$$

for  $|arg z| < \pi/2$ , and

$$K_\nu(z) = \sqrt{\frac{\pi}{2z}} e^{-z} \times \left[ 1 - \frac{(4\nu^2 - 1)}{8z} + \frac{(4\nu^2 - 1)(4\nu^2 - 9)}{2!(8z)^2} - \frac{(4\nu^2 - 1)(4\nu^2 - 9)(4\nu^2 - 25)}{3!(8z)^3} + \dots \right] \dots\dots\dots (3.48)$$

for  $|arg z| < 3\pi/2$ . On the basis of the relations given by Eqs. 3.43 through 3.48, the following limiting forms may be written:

$$\lim_{z \rightarrow 0} I_0(z) = 1, \dots\dots\dots (3.49)$$

$$\lim_{z \rightarrow \infty} I_0(z) = \infty, \dots\dots\dots (3.50)$$

$$\lim_{z \rightarrow 0} I_1(z) = 0, \dots\dots\dots (3.51)$$

$$\lim_{z \rightarrow \infty} I_1(z) = \infty, \dots\dots\dots (3.52)$$

$$\lim_{z \rightarrow 0} K_0(z) = -\ln(e^\gamma z / 2) \rightarrow \infty, \dots\dots\dots (3.53)$$

$$\lim_{z \rightarrow \infty} K_0(z) = 0, \dots\dots\dots (3.54)$$

$$\lim_{z \rightarrow 0} K_1(z) = \infty, \dots\dots\dots (3.55)$$

$$\lim_{z \rightarrow 0} z K_1(z) = 1, \dots\dots\dots (3.56)$$

and

$$\lim_{z \rightarrow \infty} K_1(z) = 0. \dots\dots\dots (3.57)$$

These relations are useful in the evaluation of the asymptotic behavior of transient-pressure solutions.

**3.3 Laplace Transformation**

Integral transforms are useful in solving differential equations. A special form of the linear integral transforms, known as the Laplace transformation, is particularly useful in the solution of the diffusion equation. The Laplace transformation of a function,  $F(t)$ , denoted by  $L\{F(t)\}$ , is defined by

$$L\{F(t)\} = \int_0^\infty e^{-st} F(t) dt, \dots\dots\dots (3.58)$$

where  $s$  is a number whose real part is positive and large enough for the integral in Eq. 3.58 to exist. In this chapter, a bar over the function indicates the image or the Laplace transform of the function; that is,

$$\bar{p}(s) = L\{p(t)\}. \dots\dots\dots (3.59)$$

**3.3.1 Fundamental Properties of the Laplace Transformation.** The following fundamental properties of the Laplace transformation are useful in the solution of common transient-flow problems.

**Transforms of Derivatives.**

$$L\left\{\frac{dp(x, y, z, t)}{dt}\right\} = s\bar{p}(x, y, z, s) - p(x, y, z, t = 0) \dots\dots\dots (3.60)$$

$$L\left\{\frac{d^n p(x, y, z, t)}{dt^n}\right\} = s^n \bar{p}(x, y, z, s) - s^{n-1} p(x, y, z, t = 0) - s^{n-2} \frac{dp(x, y, z, t)}{dt} \Big|_{t=0} - s^{n-3} \frac{d^2 p(x, y, z, t)}{dt^2} \Big|_{t=0} - \dots - \frac{d^{n-1} p(x, y, z, t)}{dt^{n-1}} \Big|_{t=0} \dots\dots\dots (3.61)$$

$$L\left\{\frac{d^n p(x, y, z, t)}{dx^n}\right\} = \frac{d^n \bar{p}(x, y, z, s)}{dx^n} \dots\dots\dots (3.62)$$

**Transforms of Integrals.**

$$L\left\{\int_0^t p(t') dt'\right\} = \frac{1}{s} \bar{p}(s) \dots\dots\dots (3.63)$$

**Substitution.**

$$L\{p(kt)\} = \frac{1}{k} \bar{p}\left(\frac{s}{k}\right) \text{ and } \dots\dots\dots (3.64)$$

$$L\{e^{-at} p(t)\} = \bar{p}(s + a), \dots\dots\dots (3.65)$$

where  $\bar{p}(s) = L\{p(t)\}$ .

**Translation.**

$$L\{H(t - t_0)p(t - t_0)\} = e^{-st_0} \bar{p}(s), \dots\dots\dots (3.66)$$

where  $H(t - t_0)$  is Heaviside's unit step function defined by

$$H(t - t_0) = \begin{cases} 0 & \text{for } t < t_0 \\ 1 & \text{for } t > t_0 \end{cases} \dots\dots\dots (3.67)$$

**Convolution.**

$$L\left\{\int_0^t p_1(\tau)p_2(t - \tau) d\tau\right\} = \bar{p}_1(s)\bar{p}_2(s) \dots\dots\dots (3.68)$$

**3.3.2 Inverse Laplace Transformation and Asymptotic Forms.** For the Laplace transform to be useful, the inverse Laplace transformation must be uniquely defined.  $L^{-1}$  denotes the inverse Laplace transform operator; that is,

$$p(t) = L^{-1}\{\bar{p}(s)\} \dots\dots\dots (3.69)$$

In this operation,  $p(t)$  represents the inverse (transform) of the Laplace domain function,  $\bar{p}(s)$ . A uniqueness theorem of the inversion guarantees that no two functions of the class  $\epsilon$  have the same Laplace transform.<sup>6</sup> The class  $\epsilon$  is defined as the set of sectionally continuous functions  $F(t)$  that are continuous on each bounded interval over the half line  $t > 0$  except at a finite number of points,  $t_i$ , where they are defined by

$$F(t_i) = \frac{1}{2}[F(t_i - 0) + F(t_i + 0)], \dots\dots\dots (3.70)$$

and  $|F(t)| < Me^{\alpha t}$  for any constants  $M$  and  $\alpha$ .

The most rigorous technique to find the inverse Laplace transform of a Laplace domain function is the use of the inversion integral,<sup>6</sup> but its discussion is outside the scope of this chapter. For petroleum engineering applications, a simple table look-up procedure is usually the first resort. **Table 3.1** shows an example table of Laplace transform pairs that may be used to find the Laplace transforms of real-space functions or the inverse Laplace transforms of the Laplace domain functions. Fairly large tables of Laplace transform pairs can be found in **Refs. 6 and 7**. The relations given in the Laplace transform tables may be extended to more complex functions with the fundamental properties of the Laplace transforms noted in **Sec. 3.3.1**.

When a simple analytical inversion is not possible, numerical inversion of a Laplace domain function is an alternate procedure. Many numerical inversion algorithms have been proposed in the literature. For the inversion of the transient-flow solutions in Laplace domain, the numerical inversion algorithm suggested by Stehfest<sup>8</sup> is the most popular algorithm.

The Stehfest algorithm is based on a stochastic process and suggests that an approximate value,  $p_a(T)$ , of the inverse of the Laplace domain function,  $\bar{p}(s)$ , may be obtained at time  $t = T$  by

$$p_a(T) = \frac{\ln 2}{T} \sum_{i=1}^N V_i \bar{p}(s)_{s=i \frac{\ln 2}{T}} \dots\dots\dots (3.71)$$

where

$$V_i = (-1)^{(N/2)+i} \sum_{k=(i+1)/2}^{\min(i, N/2)} \frac{k^{N/2}(2k)!}{[(N/2) - k]! k! (k - 1)! (i - k)! (2k - i)!} \dots\dots\dots (3.72)$$

In **Eqs. 3.71 and 3.72**,  $N$  is an even integer. Although, theoretically, the accuracy of the inversion should increase as  $N$  tends to infinity [ $p_a(T)$  should tend to  $p(T)$ ], the accuracy may be lost because of round-off errors when  $N$  becomes large. Normally, the optimum value of  $N$  is determined as a result of a numerical experiment. As a reference, however, the range of  $6 \leq N \leq 18$  covers the most common values of  $N$  for transient-flow problems. The Stehfest algorithm is not appropriate for the numerical inversion of oscillatory and discontinuous functions. In these cases, a more complex algorithm proposed by Crump<sup>9</sup> may be used.



TABLE 3.1—LAPLACE TRANSFORM PAIRS			
$F(t) = L^{-1}[f(s)]$	$(t > 0, \text{Re } s > 0)$	$L[F(t)] = f(s)$	$(t > 0, \text{Re } s > \alpha)$
$F(t)$		$\int_0^\infty e^{-st} F(t) dt$	
$a$		$a/s$	
$t^n$	$(n \text{ positive integer})$	$n!/s^{n+1}$	
$t^k$	$(k > 0)$	$\Gamma(k+1)/s^{k+1}$	
$1/t$		$\sqrt{\pi}/s$	
$e^{at}$		$1/(s-a)$	
$\sin at$		$a/(s^2 + a^2)$	
$\cos at$		$s/(s^2 + a^2)$	
$\sinh at$		$a/(s^2 - a^2)$	
$\cosh at$		$s/(s^2 - a^2)$	
$H(t-a)\theta$		$e^{-as}/s$	
$\{\exp[-a^2/(4t)]\}/\sqrt{\pi t}$	$(a \geq 0)$	$\exp(-a\sqrt{s})/\sqrt{s}$	
$\exp[-a^2/(4t)]/(2t)$	$(a \geq 0)$	$K_0(a\sqrt{s})$	
$\text{erf}[a/(2\sqrt{t})]$	$(a \geq 0)$	$[1 - \exp(-a\sqrt{s})]/s$	
$\ln t + \gamma$	$(\gamma = 0.5772\dots)$	$-(\ln s)/s$	

In some cases, obtaining asymptotic solutions for small and large values of time may be of interest. These asymptotic results may be obtained without inverting the full solution into the real-time domain. The limiting forms of the full solution as  $s \rightarrow \infty$  and  $s \rightarrow 0$  correspond to the limiting forms in the time domain for short and long time, respectively. The inversion of the limiting forms may be easier than the inversion of the full solution. [Examples 3.1](#) through [3.4](#) demonstrate the use of Laplace transformation in the solution of transient-flow problems.

**Example 3.1** Consider transient flow toward a fully penetrating vertical well in an infinite homogeneous reservoir of uniform thickness,  $h$ , and initial pressure,  $p_i$ .

*Solution.* This problem may be formulated most conveniently in the radial coordinates. The diffusivity equation governing fluid flow in porous media is given, in radial coordinates, by

$$\frac{1}{r} \frac{\partial}{\partial r} \left( r \frac{\partial \Delta p}{\partial r} \right) = \frac{1}{\eta} \frac{\partial \Delta p}{\partial t}, \dots\dots\dots (3.73)$$

where  $\Delta p = p_i - p$ . Eq. 3.73 is the same in absolute (cgs or SI) or Darcy units. (In field units, some conversion coefficients are involved in Eq. 3.73.) The initial condition is

$$\Delta p(r, t = 0) = 0, \dots\dots\dots (3.74)$$

which means that the pressure is uniform and equal to  $p_i$  initially throughout the reservoir. The outer boundary condition for an infinite reservoir is

$$\Delta p(r \rightarrow \infty, t) = 0, \dots\dots\dots (3.75)$$

which physically means that for any given time,  $t$ , there is a large enough distance,  $r$ , in the reservoir at which the initial pressure,  $p_i$ , has been preserved.

The inner boundary condition depends on the production conditions at the surface of the wellbore ( $r = r_w$ ). Assuming that the well is produced at a constant rate,  $q$ , for all times,

$$\left( r \frac{\partial \Delta p}{\partial r} \right)_{r=r_w} = - \frac{qB\mu}{2\pi k h} \dots\dots\dots (3.76)$$

The inner boundary condition given in Eq. 3.76 is simply a restatement of the flux law (Darcy's law given by Eq. 3.16) at the surface of the wellbore.

Eqs. 3.73 through 3.76 define the IBVP to be solved to obtain the transient-pressure distribution for the given system. Application of the Laplace transforms to Eq. 3.73 yields

$$\frac{1}{r} \frac{d}{dr} \left( r \frac{d\Delta \bar{p}}{dr} \right) = \frac{1}{r} \frac{d\Delta \bar{p}}{dr} + \frac{d^2 \Delta \bar{p}}{dr^2} = \frac{s}{\eta} \Delta \bar{p}, \dots\dots\dots (3.77)$$

or, rearranging, we obtain

$$\frac{1}{r} \frac{d\Delta \bar{p}}{dr} + \frac{d^2 \Delta \bar{p}}{dr^2} - \frac{s}{\eta} \Delta \bar{p} = 0. \dots\dots\dots (3.78)$$

In obtaining the right side of Eq. 3.77, the initial condition (Eq. 3.74) has been used. Similarly, Eqs. 3.75 and 3.76 are transformed into the following forms, respectively.

$$\Delta \bar{p}(r \rightarrow \infty, t) = 0, \dots\dots\dots (3.79)$$

and

$$\left( r \frac{d\Delta \bar{p}}{dr} \right)_{r=r_w} = - \frac{qB\mu}{2\pi k h s} \dots\dots\dots (3.80)$$

Comparing Eq. 3.78 with Eq. 3.31, we recognize Eq. 3.78 as the modified Bessel's equation of order zero. The solution of Eq. 3.78 may be written directly from Eq. 3.39 as

$$\Delta \bar{p}(s) = C_1 I_0(\sqrt{s/\eta} r) + C_2 K_0(\sqrt{s/\eta} r). \dots\dots\dots (3.81)$$

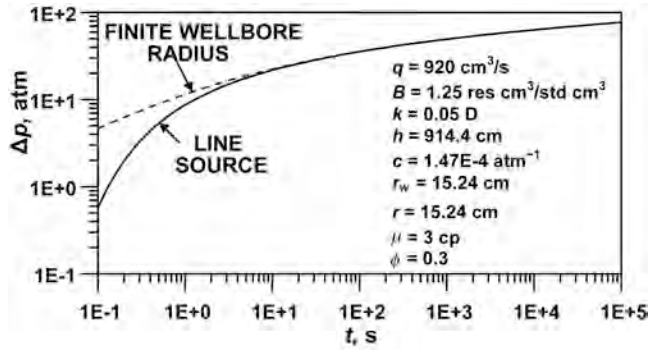


Fig. 3.3—Finite wellbore radius (Eq. 3.85) and line-source (Eq. 3.87 or 3.91) solutions for Example 3.1.

The constants  $C_1$  and  $C_2$  in Eq. 3.81 are obtained from the boundary conditions. The outer boundary condition (Eq. 3.79) indicates that  $C_1 = 0$  [because  $\lim_{x \rightarrow 0} I_0(x) = \infty$ , Eq. 3.79 is satisfied only if  $C_1 = 0$ ]; therefore,

$$\bar{\Delta p}(s) = C_2 K_0(\sqrt{s/\eta} r) \dots\dots\dots (3.82)$$

From Eqs. 3.80 and 3.82, we obtain

$$\left( r \frac{d\bar{\Delta p}}{dr} \right)_{r=r_w} = -C_2 \sqrt{s/\eta} r_w K_1(\sqrt{s/\eta} r_w) = -\frac{qB\mu}{2\pi k h s} \dots\dots\dots (3.83)$$

which yields

$$C_2 = \frac{qB\mu}{2\pi k h} \frac{1}{s \sqrt{s/\eta} r_w K_1(\sqrt{s/\eta} r_w)} \dots\dots\dots (3.84)$$

Then, the solution for the transient-pressure distribution is given, in the Laplace transform domain, by

$$\bar{\Delta p}(s) = \frac{qB\mu}{2\pi k h} \frac{K_0(\sqrt{s/\eta} r)}{s \sqrt{s/\eta} r_w K_1(\sqrt{s/\eta} r_w)} \dots\dots\dots (3.85)$$

To complete the solution of the problem, Eq. 3.85 should be inverted into the real-time domain. The real inversion of Eq. 3.85, however, is not available in terms of standard functions. One option is to use Stehfest’s numerical inversion algorithm<sup>8</sup> as discussed in Sec. 3.3.2. The dashed line in Fig. 3.3 represents the numerical inversion of the solution in Eq. 3.85. Another option is to find an approximate inversion. One of these asymptotic forms is known as the line-source solution and commonly used in transient-pressure analysis.

To obtain the line-source approximation of the solution given in Eq. 3.85, we assume that the radius of the wellbore is small compared with the other dimensions of the reservoir. Thus, if we assume  $r_w \rightarrow 0$  and use the relation given in Eq. 3.56, we obtain

$$\lim_{r_w \rightarrow 0} \sqrt{s/\eta} r_w K_1(\sqrt{s/\eta} r_w) = 1. \dots\dots\dots (3.86)$$

Using this relation in Eq. 3.85, we obtain the line-source solution in Laplace domain as

$$\bar{\Delta p}(s) = \frac{qB\mu}{2\pi kh} \frac{K_0(\sqrt{s/\eta} r)}{s} \dots\dots\dots (3.87)$$

The inversion of Eq. 3.87 can be accomplished by using a Laplace transform table. From Table 3.1 (or from the tables in Refs. 6 and 7), we have

$$L^{-1}\{K_0(k\sqrt{s})\} = \frac{1}{2t} \exp\left(-\frac{k^2}{4t}\right) \quad \text{for } k > 0. \dots\dots\dots (3.88)$$

With Eq. 3.88 and the Laplace transform property noted in Eq. 3.63, we obtain the following inversion of Eq. 3.87 in the real-time domain:

$$\Delta p(r, t) = \frac{qB\mu}{4\pi kh} \int_0^t \exp\left(-\frac{r^2}{4\eta t'}\right) \frac{dt'}{t'} \dots\dots\dots (3.89)$$

Making the substitution  $u = r^2/(4\eta t')$  and noting the definition of the exponential integral function,  $Ei(x)$ , given by

$$Ei(x) = - \int_{-x}^{\infty} \frac{e^{-u}}{u} du, \dots\dots\dots (3.90)$$

we obtain the line-source solution as

$$\Delta p(r, t) = - \frac{qB\mu}{4\pi kh} Ei\left(-\frac{r^2}{4\eta t}\right) \dots\dots\dots (3.91)$$

Fig. 3.3 shows a comparison of the results computed from Eq. 3.85 (finite-wellbore radius) and Eq. 3.91 (line source) for the data noted in the figure. The two solutions yield different results at early times but become the same at later times. In fact, it can be shown analytically that the long-time approximation of the finite-wellbore radius solution (Eq. 3.85) is the same as the line-source well solution. To show this, we note that the long-time approximation of the solution in the time domain corresponds to the limiting form of the solution in the Laplace domain as  $s \rightarrow 0$ . Then, with the property of the Bessel function given in Eq. 3.56, we can show that

$$\lim_{s \rightarrow 0} \bar{\Delta p}(s) = \frac{qB\mu}{2\pi kh} \frac{K_0(\sqrt{s/\eta} r)}{s \lim_{s \rightarrow 0} [\sqrt{s/\eta} r_w K_1(\sqrt{s/\eta} r_w)]} = \frac{qB\mu}{2\pi kh} \frac{K_0(\sqrt{s/\eta} r)}{s} \dots\dots\dots (3.92)$$

**Example 3.2** Consider transient flow as a result of constant-rate production from a fully penetrating vertical well in a closed cylindrical reservoir initially at uniform initial pressure,  $p_i$ .

*Solution.* Fluid flow in cylindrical porous media is described by the diffusion equation in radial coordinates given by

$$\frac{1}{r} \frac{\partial}{\partial r} \left( r \frac{\partial \Delta p}{\partial r} \right) = \frac{1}{\eta} \frac{\partial \Delta p}{\partial t} \dots\dots\dots (3.93)$$

The initial condition corresponding to the uniform pressure distribution equal to  $p_i$  is

$$\Delta p(r, t = 0) = 0, \dots\dots\dots (3.94)$$

and the inner boundary condition for a constant production rate,  $q$ , for all times is

$$\left( r \frac{\partial \Delta p}{\partial r} \right)_{r=r_w} = - \frac{qB\mu}{2\pi kh} \dots\dots\dots (3.95)$$

The closed outer boundary condition is represented mathematically by zero flux at the outer boundary ( $r = r_e$ ) that corresponds to

$$\left( \frac{\partial \Delta p}{\partial r} \right)_{r=r_e} = 0 \dots\dots\dots (3.96)$$

The Laplace transforms of Eqs. 3.93 through 3.96 yield, respectively,

$$\frac{1}{r} \frac{d\bar{\Delta p}}{dr} + \frac{d^2\bar{\Delta p}}{dr^2} - \frac{s}{\eta} \bar{\Delta p} = 0, \dots\dots\dots (3.97)$$

$$\left( r \frac{d\bar{\Delta p}}{dr} \right)_{r=r_w} = - \frac{qB\mu}{2\pi kh s}, \dots\dots\dots (3.98)$$

and

$$\left( \frac{d\bar{\Delta p}}{dr} \right)_{r=r_e} = 0 \dots\dots\dots (3.99)$$

(The initial condition given by Eq. 3.94 has been used to obtain Eq. 3.97.) Because Eq. 3.97 is the modified Bessel's equation of order zero, its general solution is given by

$$\bar{\Delta p}(s) = C_1 I_0(\sqrt{s/\eta} r) + C_2 K_0(\sqrt{s/\eta} r) \dots\dots\dots (3.100)$$

With the outer boundary condition given by Eq. 3.99, we obtain

$$\left( \frac{d\bar{\Delta p}}{dr} \right)_{r=r_e} = C_1 \sqrt{s/\eta} I_1(\sqrt{s/\eta} r_e) - C_2 \sqrt{s/\eta} K_1(\sqrt{s/\eta} r_e) = 0, \dots\dots\dots (3.101)$$

which yields

$$C_2 = C_1 \frac{I_1(\sqrt{s/\eta} r_e)}{K_1(\sqrt{s/\eta} r_e)} \dots\dots\dots (3.102)$$

and thus

$$\Delta \bar{p}(s) = C_1 \left[ I_0(\sqrt{s/\eta} r) + \frac{K_0(\sqrt{s/\eta} r) I_1(\sqrt{s/\eta} r_e)}{K_1(\sqrt{s/\eta} r_e)} \right] \dots\dots\dots (3.103)$$

Using the inner boundary condition given by Eq. 3.98 yields

$$\begin{aligned} \left( r \frac{d\Delta \bar{p}}{dr} \right)_{r=r_w} &= C_1 \left[ \sqrt{s/\eta} r_w I_1(\sqrt{s/\eta} r_w) - \frac{\sqrt{s/\eta} r_w K_1(\sqrt{s/\eta} r_w) I_1(\sqrt{s/\eta} r_e)}{K_1(\sqrt{s/\eta} r_e)} \right] \\ &= - \frac{qB\mu}{2\pi k h s} \dots\dots\dots (3.104) \end{aligned}$$

From Eqs. 3.102 and 3.104, we obtain the coefficients  $C_1$  and  $C_2$  as follows:

$$C_1 = \frac{qB\mu}{2\pi k h} \frac{K_1(\sqrt{s/\eta} r_e)}{s \sqrt{s/\eta} r_w \left[ I_1(\sqrt{s/\eta} r_e) K_1(\sqrt{s/\eta} r_w) - I_1(\sqrt{s/\eta} r_w) K_1(\sqrt{s/\eta} r_e) \right]} \dots\dots\dots (3.105)$$

and

$$C_2 = \frac{qB\mu}{2\pi k h} \frac{I_1(\sqrt{s/\eta} r_e)}{s \sqrt{s/\eta} r_w \left[ I_1(\sqrt{s/\eta} r_e) K_1(\sqrt{s/\eta} r_w) - I_1(\sqrt{s/\eta} r_w) K_1(\sqrt{s/\eta} r_e) \right]} \dots\dots\dots (3.106)$$

Substituting  $C_1$  and  $C_2$  into Eq. 3.100 yields

$$\Delta \bar{p}(s) = \frac{qB\mu}{2\pi k h} \frac{I_0(\sqrt{s/\eta} r) K_1(\sqrt{s/\eta} r_e) + I_1(\sqrt{s/\eta} r_e) K_0(\sqrt{s/\eta} r)}{s \sqrt{s/\eta} r_w \left[ I_1(\sqrt{s/\eta} r_e) K_1(\sqrt{s/\eta} r_w) - I_1(\sqrt{s/\eta} r_w) K_1(\sqrt{s/\eta} r_e) \right]} \dots\dots\dots (3.107)$$

The inverse of the solution given by Eq. 3.107 may not be found in the Laplace transform tables. van Everdingen and Hurst<sup>10</sup> provided the following analytical inversion of Eq. 3.107 with the inversion integral.

$$\Delta p(r, t) = \frac{qB\mu}{2\pi k h} \left( \frac{2}{r_e^2 - r_w^2} \left( \eta t - \frac{r^2}{4} \right) - \frac{r_e^2}{r_e^2 - r_w^2} \ln \frac{r}{r_w} - \frac{1}{4(r_e^2 - r_w^2)^2} \left( 3r_e^4 - 4r_e^4 \ln \frac{r_e}{r_w} - 2r_e^2 - 1 \right) \right)$$

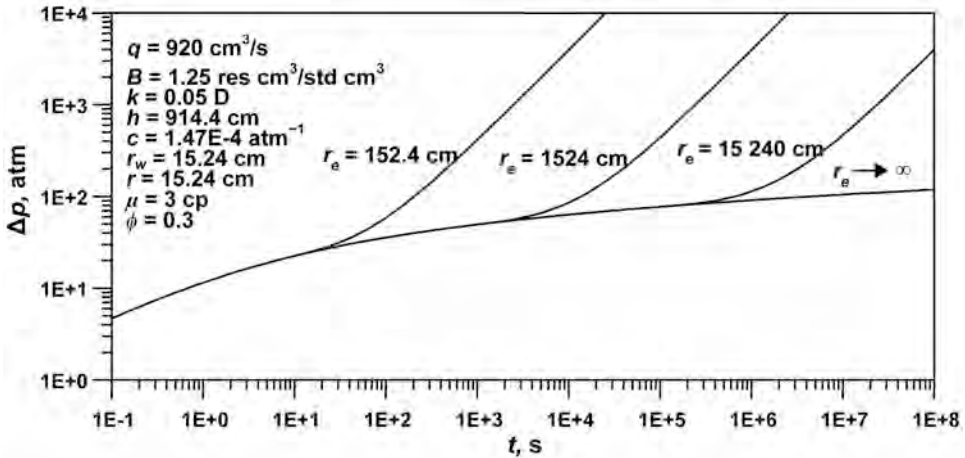


Fig. 3.4—Bounded reservoir solution (Eq. 3.107) for Example 3.2.

$$+ \pi \sum_{n=1}^{\infty} \frac{J_1^2\left(\beta_n \frac{r_e}{r_w}\right) \left[ J_1(\beta_n) Y_0\left(\beta_n \frac{r}{r_w}\right) - Y_1(\beta_n) J_0\left(\beta_n \frac{r}{r_w}\right) \right]}{\beta_n \left[ J_1^2\left(\beta_n \frac{r_e}{r_w}\right) - J_1^2(\beta_n) \right]} \exp\left(-\beta_n^2 \frac{\eta t}{r_w^2}\right) \dots \dots \dots (3.108)$$

In Eq. 3.108,  $\beta_1, \beta_2, \dots$  etc. are the roots of

$$Y_1(\beta_n) J_1\left(\beta_n \frac{r_e}{r_w}\right) - J_1(\beta_n) Y_1\left(\beta_n \frac{r_e}{r_w}\right) = 0 \dots \dots \dots (3.109)$$

The solution given in Eq. 3.107 may also be inverted numerically with the Stehfest algorithm.<sup>8</sup> Fig. 3.4 shows the results of the numerical inversion of Eq. 3.107.

**Example 3.3** Consider the flowing wellbore pressure of a fully penetrating vertical well with wellbore storage and skin in an infinite reservoir.

*Solution.* Revisit the case in Example 3.1 and add the effect of a skin zone around the wellbore. Assume that the constant production rate is specified at the surface so that the storage capacity of the wellbore needs to be taken into account. Before presenting the initial-boundary value problem, skin factor and surface production rate should be defined.

Using van Everdingen and Hurst’s thin-skin concept<sup>10</sup> (vanishingly small skin-zone radius), the skin factor is defined by

$$s_m = \frac{p(r_w +) - p_{wf}}{\left(r \frac{\partial p}{\partial r}\right)_{r=r_w}} = \frac{p(r_w +) - p_{wf}}{\frac{q_{sf} B \mu}{2\pi k h}}, \dots \dots \dots (3.110)$$

where  $q_{sf}$  is the sandface production rate,  $p(r_w +)$  denotes the reservoir pressure immediately outside the skin-zone boundary, and  $p_{wf}$  is the flowing wellbore pressure measured inside the wellbore. Rearranging Eq. 3.110, we obtain the following relation for the flowing wellbore pressure.

$$\Delta p_{wf} = \Delta p(r_w +) - s_m \left( r \frac{\partial \Delta p}{\partial r} \right)_{r=r_w} \dots\dots\dots (3.111)$$

When the production rate is specified at the surface, it is necessary to account for the fact that the wellbore can store and unload fluids. The surface production rate,  $q$ , is equal to the sum of the wellbore unloading rate,  $q_{wb}$ , and the sandface production rate,  $q_{sf}$ ; that is,

$$q = q_{wb} + q_{sf}, \dots\dots\dots (3.112)$$

where

$$q_{wb} = \frac{24C}{B} \frac{d\Delta p_{wf}}{dt} \dots\dots\dots (3.113)$$

and

$$q_{sf} = - \frac{2\pi kh}{B\mu} \left( r \frac{\partial \Delta p}{\partial r} \right)_{r=r_w} \dots\dots\dots (3.114)$$

In Eq. 3.113,  $C$  is the wellbore-storage coefficient. Substituting Eqs. 3.113 and 3.114 into Eq. 3.112, we obtain the following expression for the surface production rate.

$$\frac{24C}{B} \frac{d\Delta p_{wf}}{dt} - \frac{2\pi kh}{B\mu} \left( r \frac{\partial \Delta p}{\partial r} \right)_{r=r_w} = q \dots\dots\dots (3.115)$$

The mathematical statement of the problem under consideration is similar to that in Example 3.1, except that the inner-boundary condition should be replaced by Eq. 3.115, and Eq. 3.111 should be incorporated to account for the skin effect. The IBVP is defined by the following set of equations in the Laplace domain:

$$\frac{1}{r} \frac{d\bar{\Delta p}}{dr} + \frac{d^2 \bar{\Delta p}}{dr^2} - \frac{s}{\eta} \bar{\Delta p} = 0, \dots\dots\dots (3.116)$$

$$\bar{\Delta p}(r \rightarrow \infty, s) = 0, \dots\dots\dots (3.117)$$

$$\frac{24C}{B} s \bar{\Delta p}_{wf} - \frac{2\pi kh}{B\mu} \left( r \frac{d\bar{\Delta p}}{dr} \right)_{r=r_w} = \frac{q}{s}, \dots\dots\dots (3.118)$$

and

$$\bar{\Delta p}_{wf} = \bar{\Delta p}(r_w +) - s_m \left( r \frac{d\bar{\Delta p}}{dr} \right)_{r=r_w} \dots\dots\dots (3.119)$$

The general solution of Eq. 3.116 is

$$\bar{\Delta p}(s) = C_1 I_0(\sqrt{s/\eta} r) + C_2 K_0(\sqrt{s/\eta} r) \dots\dots\dots (3.120)$$



The condition in Eq. 3.117 requires that  $C_1 = 0$ ; therefore,

$$\Delta \bar{p}(s) = C_2 K_0(\sqrt{s/\eta} r) \dots \dots \dots (3.121)$$

The use of Eq. 3.121 in Eq. 3.119 yields

$$\Delta \bar{p}_{wf} = C_2 K_0(\sqrt{s/\eta} r_w +) + s_m C_2 \sqrt{s/\eta} r_w K_1(\sqrt{s/\eta} r_w) \dots \dots \dots (3.122)$$

From Eqs. 3.118, 3.121, and 3.122, we obtain

$$\begin{aligned} & \frac{24C}{B} C_2 s [K_0(\sqrt{s/\eta} r_w +) + s_m \sqrt{s/\eta} r_w K_1(\sqrt{s/\eta} r_w)] \\ & + \frac{2\pi k h}{B\mu} C_2 \sqrt{s/\eta} r_w K_1(\sqrt{s/\eta} r_w) = \frac{q}{s}, \dots \dots \dots (3.123) \end{aligned}$$

which yields

$$C_2 = \frac{qB\mu}{2\pi k h s} \times \left\{ \frac{1}{\sqrt{s/\eta} r_w K_1(\sqrt{s/\eta} r_w) + \frac{24C\mu}{2\pi k h} s [K_0(\sqrt{s/\eta} r_w +) + s_m \sqrt{s/\eta} r_w K_1(\sqrt{s/\eta} r_w)]} \right\} \dots \dots \dots (3.124)$$

Substituting Eq. 3.124 for  $C_2$  in Eq. 3.122, we obtain the solution for the transient-pressure distribution in the Laplace transform domain as

$$\Delta \bar{p}_{wf} = \frac{qB\mu}{2\pi k h s} \times \left\{ \frac{K_0(\sqrt{s/\eta} r_w +) + s_m \sqrt{s/\eta} r_w K_1(\sqrt{s/\eta} r_w)}{\sqrt{s/\eta} r_w K_1(\sqrt{s/\eta} r_w) + \frac{24C\mu}{2\pi k h} s [K_0(\sqrt{s/\eta} r_w +) + s_m \sqrt{s/\eta} r_w K_1(\sqrt{s/\eta} r_w)]} \right\} \dots \dots \dots (3.125)$$

The real inversion of the solution in Eq. 3.125 has been obtained by Agarwal *et al.*<sup>11</sup> with the inversion integral. It is also possible to invert Eq. 3.125 numerically. Fig. 3.5 shows the results of the numerical inversion of Eq. 3.125 with the Stehfest’s algorithm.<sup>8</sup> Also shown in Fig. 3.5 are the logarithmic derivatives of  $\Delta p_{wf}$ . These derivatives are computed by applying the Laplace transformation property given in Eq. 3.60 to Eq. 3.125 as follows:

$$L \left\{ \frac{d\Delta p_{wf}}{dt} \right\} = s \Delta \bar{p}_{wf} \dots \dots \dots (3.126)$$

Here, we have used  $\Delta p_{wf}(t = 0) = 0$ . To obtain the logarithmic derivatives, we simply note that

$$\frac{d\Delta p_{wf}}{d \ln t} = t \frac{d\Delta p_{wf}}{dt} \dots \dots \dots (3.127)$$

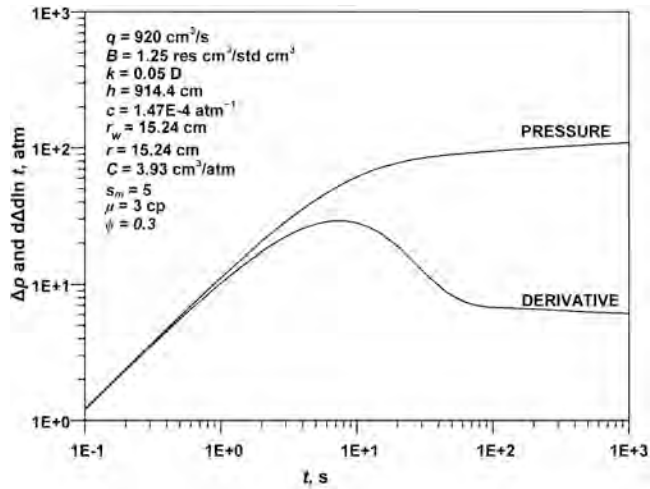


Fig. 3.5—Wellbore-storage and skin solution (Eq. 3.125) for Example 3.3.

**Example 3.4** Consider pressure buildup with wellbore storage and skin following a draw-down period at a constant rate in an infinite reservoir.

*Solution.* This example is similar to Example 3.3 except, at time  $t_p$ , the well is shut in and pressure buildup begins. The system of equations to define this problem is

$$\frac{1}{r} \frac{\partial}{\partial r} \left( r \frac{\partial \Delta p}{\partial r} \right) = \frac{1}{\eta} \frac{\partial \Delta p}{\partial t}, \dots\dots\dots (3.128)$$

$$\Delta p(r, t = 0) = 0, \dots\dots\dots (3.129)$$

$$\Delta p(r \rightarrow \infty, t) = 0, \dots\dots\dots (3.130)$$

$$\frac{24C}{B} \frac{d\Delta p_{wf}}{dt} - \frac{2\pi kh}{B\mu} \left( r \frac{\partial \Delta p}{\partial r} \right)_{r=r_w} = q[1 - H(t - t_p)], \dots\dots\dots (3.131)$$

where  $H(t - t_p)$  is Heaviside's unit function (Eq. 3.67), and

$$\Delta p_{wf} = \Delta p(r_w +) - s_m \left( r \frac{\partial \Delta p}{\partial r} \right)_{r=r_w} \dots\dots\dots (3.132)$$

The right side of the boundary condition in Eq. 3.131 accounts for a constant surface production rate,  $q$ , for  $0 < t < t_p$  and for shut in ( $q = 0$ ) for  $t > t_p$ . Taking the Laplace transforms of Eqs. 3.128 through 3.132, we obtain

$$\frac{1}{r} \frac{d\bar{\Delta p}}{dr} + \frac{d^2\bar{\Delta p}}{dr^2} - \frac{s}{\eta} \bar{\Delta p} = 0, \dots\dots\dots (3.133)$$

$$\bar{\Delta p}(r \rightarrow \infty, t) = 0, \dots\dots\dots (3.134)$$

$$\frac{24C}{B} s \Delta \bar{p}_{wf} - \frac{2\pi k h}{B\mu} \left( r \frac{d\Delta \bar{p}}{dr} \right)_{r=r_w} = \frac{q}{s} (1 - e^{-st} p), \dots\dots\dots (3.135)$$

and

$$\Delta \bar{p}_{wf} = \Delta \bar{p}(r_w +) - s_m \left( r \frac{d\Delta \bar{p}}{dr} \right)_{r=r_w} \dots\dots\dots (3.136)$$

The general solution of Eq. 3.133 is

$$\Delta \bar{p}(s) = C_1 I_0(\sqrt{s/\eta} r) + C_2 K_0(\sqrt{s/\eta} r). \dots\dots\dots (3.137)$$

The condition in Eq. 3.134 requires that  $C_1 = 0$ ; therefore,

$$\Delta \bar{p}(s) = C_2 K_0(\sqrt{s/\eta} r). \dots\dots\dots (3.138)$$

From Eqs. 3.138 and 3.136, we obtain

$$\Delta \bar{p}_{wf} = C_2 K_0(\sqrt{s/\eta} r_w +) + s_m C_2 \sqrt{s/\eta} r_w K_1(\sqrt{s/\eta} r_w). \dots\dots\dots (3.139)$$

Substituting the results of Eqs. 3.138 and 3.139 into Eq. 3.135, we have

$$\begin{aligned} & \frac{24C}{B} C_2 s [K_0(\sqrt{s/\eta} r_w +) + s_m \sqrt{s/\eta} r_w K_1(\sqrt{s/\eta} r_w)] \\ & + \frac{2\pi k h}{B\mu} C_2 \sqrt{s/\eta} r_w K_1(\sqrt{s/\eta} r_w) = \frac{q}{s} (1 - e^{-st} p), \dots\dots\dots (3.140) \end{aligned}$$

which yields

$$C_2 = \frac{qB\mu}{2\pi k h s} \times \left\{ \frac{1 - e^{-st} p}{\sqrt{s/\eta} r_w K_1(\sqrt{s/\eta} r_w) + \frac{24C\mu}{2\pi k h} s [K_0(\sqrt{s/\eta} r_w +) + s_m \sqrt{s/\eta} r_w K_1(\sqrt{s/\eta} r_w)]} \right\} \dots\dots\dots (3.141)$$

Substituting Eq. 3.141 into Eq. 3.139, we obtain the following solution in the Laplace transform domain, which covers both the drawdown and buildup periods.

$$\begin{aligned} \Delta \bar{p}_{wf} &= \frac{qB\mu}{2\pi k h s} \\ & \times \left\{ \frac{[K_0(\sqrt{s/\eta} r_w +) + s_m \sqrt{s/\eta} r_w K_1(\sqrt{s/\eta} r_w)] (1 - e^{-st} p)}{\sqrt{s/\eta} r_w K_1(\sqrt{s/\eta} r_w) + \frac{24C\mu}{2\pi k h} s [K_0(\sqrt{s/\eta} r_w +) + s_m \sqrt{s/\eta} r_w K_1(\sqrt{s/\eta} r_w)]} \right\} \dots\dots\dots (3.142) \end{aligned}$$

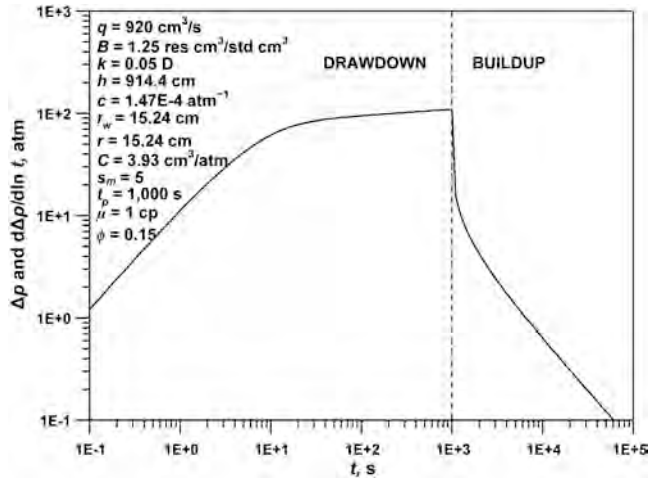


Fig. 3.6—Drawdown and buildup results with wellbore-storage and skin solution (Eq. 3.142) for Example 3.4.

The  $(1 - e^{-st_p})$  term contributed by the discontinuity at time  $t = t_p$  causes difficulties in the numerical inversion of the right side of Eq. 3.142 with the use of the Stehfest algorithm.<sup>8</sup> As suggested by Chen and Raghavan,<sup>12</sup> this problem may be solved by noting that

$$L^{-1}\left[\bar{f}(s)\left(1 - e^{-st_p}\right)\right] \Big|_t = L^{-1}\left[\bar{f}(s)\right] \Big|_t - L^{-1}\left[\bar{f}(s)\right] \Big|_{t-t_p}, \dots\dots\dots (3.143)$$

and applying the Stehfest algorithm term by term to the right side of Eq. 3.143. Fig. 3.6 shows sample results obtained by the numerical inversion of Eq. 3.142.

**3.4 Green’s Functions and Source Functions**

Green’s function and source functions are used to solve 2D and 3D transient-flow problems that may result from complex well geometries, such as partially penetrating vertical and inclined wells, hydraulically fractured wells, and horizontal wells. Before introducing these techniques, it is useful to clarify the terminology.

In our terminology, a source is a point, line, surface, or volume at which fluids are withdrawn from the reservoir. Strictly speaking, fluid withdrawal should be associated with a sink, and the injection of fluids should be related to a source. Here, however, the term source is used for both production and injection with the convention that a negative withdrawal rate indicates injection.

Green’s functions and source functions are closely related. A Green’s function is defined for a differential equation with specified boundary conditions (prescribed flux or pressure) and corresponds to an instantaneous point-source solution. A source function, on the other hand, is the solution of the given differential equation with specified boundary conditions and source geometry.

The details of the theory and application of Green’s function and source functions for the solution of transient-flow problems in porous media can be found in Ref. 2 and Refs. 13 through 20. A brief account of the use of these techniques is presented here, as well as an introduction of the fundamental solution and point-source concepts.

**3.4.1 Fundamental Solution of the Diffusion Equation.** The fundamental solution,  $\gamma_f(M, M', t, \tau)$ , of the diffusion equation for fluid flow in porous media satisfies the following differential equation:

$$\eta \nabla^2 \gamma_f(M, M', t, \tau) - \frac{\partial \gamma_f(M, M', t, \tau)}{\partial t} = -\delta(M, M', t, \tau), \dots\dots\dots (3.144)$$

where  $\delta(M, M', t, \tau)$  is a generalized (symbolic) function<sup>15</sup> called the Dirac delta function and is defined on the basis of its following properties:

$$\int_{t_1}^{t_2} \int_D \delta(M, M', t, \tau) dM' d\tau = \begin{cases} 1 & \text{for } t_1 < t, \tau < t_2 \text{ and } M, M' \text{ in } D \\ 0 & \text{otherwise} \end{cases}, \dots\dots\dots (3.145)$$

and

$$\int_{t_1}^{t_2} \int_D \delta(M, M', t, \tau) \varphi(M', \tau) dM' d\tau = \begin{cases} \varphi(M, t) & \text{for } t_1 < t, \tau < t_2 \text{ and } M, M' \text{ in } D \\ 0 & \text{otherwise} \end{cases} \dots\dots\dots (3.146)$$

The delta function is symmetric in  $M$  and  $M'$  and also in  $t$  and  $\tau$ . In this formulation, the delta function represents the symbolic density of a unit-strength, concentrated source located at  $M'$  and acting at time  $\tau$ . In physical terms, this source corresponds to an infinitesimally small well (located at point  $M'$ ) at which a finite amount of fluid is withdrawn (or injected) instantaneously (at time  $\tau$ ). Therefore, the solution of Eq. 3.144 (the fundamental solution) is also known as the instantaneous point-source solution. Formally, the point-source solution corresponds to the pressure drop,  $\Delta p = p_i - p$ , at a point  $M$  and time  $t$  in an infinite porous medium (reservoir) because of a point source of unit strength located at point  $M'$  and acting at  $\tau < t$ .

**3.4.2 The Source-Function Solutions of the Diffusion Equation.** The point-source solution was first introduced by Lord Kelvin<sup>16</sup> for the solution of heat conduction problems and was extensively discussed by Carslaw and Jaeger.<sup>14</sup> The point-source solution is usually obtained by finding the limiting form of the pressure drop resulting from a spherical source as the source volume vanishes. To demonstrate the derivation of the instantaneous point-source solution, consider the transient flow of a slightly compressible fluid of constant compressibility and viscosity toward a spherical source of radius  $r = a$  in an infinite, homogeneous, and isotropic porous medium. Because of the spherical symmetry of the physical problem, we can conveniently express the governing equation of fluid flow in porous media in spherical coordinates as

$$\frac{2}{r} \frac{\partial \Delta p}{\partial r} + \frac{\partial^2 \Delta p}{\partial r^2} = \frac{1}{\eta} \frac{\partial \Delta p}{\partial t} \quad \text{for } r > 0. \dots\dots\dots (3.147)$$

Assume that the initial pressure drop satisfies

$$\Delta p(r, t = 0) = \begin{cases} \Delta p_i & \text{for } 0 < r < a \\ 0 & \text{for } r > a \end{cases}, \dots\dots\dots (3.148)$$

and we have the condition that

$$\Delta p(r = 0, t) = 0. \dots\dots\dots (3.149)$$

On substitution of  $u = r\Delta p$ , Eqs. 3.147 through 3.149 become, respectively,

$$\frac{\partial u}{\partial t} = \eta \frac{\partial^2 u}{\partial r^2}, \dots\dots\dots (3.150)$$

$$u(r, t = 0) = \begin{cases} r\Delta p_i & \text{for } 0 < r < a \\ 0 & \text{for } r > a \end{cases}, \dots\dots\dots (3.151)$$

and

$$u(r = 0, t) = 0. \dots\dots\dots (3.152)$$

The solution of the problem described by Eqs. 3.150 through 3.152 is given by<sup>14</sup>

$$\Delta p = \frac{\Delta p_i}{2r\sqrt{\pi\eta t}} \exp\left(-\frac{r^2}{4\eta t}\right) \int_0^a r' \exp\left(-\frac{r'^2}{4\eta t}\right) \left[ \exp\left(\frac{rr'}{2\eta t}\right) - \exp\left(-\frac{rr'}{2\eta t}\right) \right] dr' \dots\dots\dots (3.153)$$

If we expand the exponential terms in the integrand in Eq. 3.153 in powers of  $r'$  and neglect the terms with powers higher than four, we obtain

$$\Delta p \approx \frac{4\pi a^3 \Delta p_i}{24(\pi\eta t)^{3/2}} \exp\left(-\frac{r^2}{4\eta t}\right) \left[ 1 + \left(\frac{a^2}{40\eta t}\right) \left(\frac{r^2}{\eta t} - 6\right) \right] \dots\dots\dots (3.154)$$

In Eq. 3.154,  $4\pi a^3/3=V$  where  $V$  is the volume of the spherical source. If  $\tilde{q}$  denotes the volume of the liquid released as a result of the change in the volume of the source,  $\Delta V$ , which is caused by the change in pressure,  $\Delta p_i$ , then  $\tilde{q} = -\Phi\Delta V$ . With the definition of compressibility,  $c = -(1/V)(\Delta V/\Delta p_i)$ , we obtain  $\tilde{q} = \Phi c V \Delta p_i$ . Then, we can show that

$$\frac{4\pi a^3}{3} \Delta p_i = \frac{\tilde{q}}{\Phi c} \dots\dots\dots (3.155)$$

Substituting Eq. 3.155 into Eq. 3.154, we obtain

$$\Delta p \approx \frac{\tilde{q}}{8\Phi c(\pi\eta t)^{3/2}} \exp\left(-\frac{r^2}{4\eta t}\right) \left[ 1 + \left(\frac{a^2}{40\eta t}\right) \left(\frac{r^2}{\eta t} - 6\right) \right] \dots\dots\dots (3.156)$$

If we let the radius of the spherical source,  $a$ , tend to zero while  $\tilde{q}$  remains constant, Eq. 3.156 yields the point-source solution in spherical coordinates given by

$$\Delta p = \frac{\tilde{q}}{8\Phi c(\pi\eta t)^{3/2}} \exp\left(-\frac{r^2}{4\eta t}\right) \dots\dots\dots (3.157)$$

This solution may be interpreted as the pressure drop at a distance  $r$  because of a volume of fluid,  $\tilde{q}$ , instantaneously withdrawn at  $r = 0$  and  $t = 0$ . Consistent with this interpretation,  $\tilde{q}/(\Phi c)$  is the strength of the source, which is the pressure drop in a unit volume of the porous medium caused by the instantaneous withdrawal of a volume of fluid,  $\tilde{q}$  (see Eq. 3.155).

**Instantaneous Point Source in an Infinite Reservoir.** Nisle<sup>21</sup> presented a more general solution for an instantaneous point source of strength  $\tilde{q}/(\Phi c)$  acting at  $t = \tau$  in an infinite, homogeneous, but anisotropic reservoir as

$$\Delta p(M, M', t - \tau) = \frac{\tilde{q}}{8\Phi c\sqrt{\eta_x\eta_y\eta_z}[\pi(t - \tau)]^{3/2}} \exp\left[-\frac{(M - M')^2/\tilde{\eta}}{4(t - \tau)}\right] \dots\dots\dots (3.158)$$

In Eq. 3.158,  $M$  and  $M'$  indicate the locations of the observation point and the source, respectively. For a 3D Cartesian coordinate system,  $M = (x, y, z)$ ,  $M' = (x', y', z')$ , and  $(M - M')^2/\tilde{\eta} = (x - x')^2/\eta_x + (y - y')^2/\eta_y + (z - z')^2/\eta_z$  with  $\eta_x$ ,  $\eta_y$ , and  $\eta_z$  representing the diffusivity constants (defined in Eq. 3.23) in the  $x$ ,  $y$ , and  $z$  directions, respectively.

**Continuous Point Source in an Infinite Reservoir.** If the fluid withdrawal is at a continuous rate,  $\tilde{q}(t)$ , from time 0 to  $t$ , then the pressure drop as a result of a continuous point source in an infinite reservoir is obtained by distributing the point sources of strength  $\tilde{q}(\tau)/(\Phi c)$  over a time interval  $0 \leq \tau \leq t$ . This is given by

$$\Delta p(M, M', t) = \frac{1}{\Phi c} \int_0^t \tilde{q}(\tau) S(M, M', t - \tau) d\tau, \dots\dots\dots (3.159)$$

where  $S(M, M', t - \tau)$  corresponds to a unit-strength [ $\tilde{q}/(\Phi c) = 1$ ], instantaneous point source in an infinite reservoir; that is,

$$S(M, M', t - \tau) = \frac{1}{8\sqrt{\eta_x\eta_y\eta_z}[\pi(t - \tau)]^{3/2}} \exp\left[-\frac{(M - M')^2/\tilde{\eta}}{4(t - \tau)}\right] \dots\dots\dots (3.160)$$

**Instantaneous and Continuous Line, Surface, and Volumetric Sources in an Infinite Reservoir.** Similarly, the distribution of instantaneous point sources of strength  $\tilde{q}(M')/(\Phi c)$  over a line, surface, or volume,  $\Gamma_w$ , in an infinite reservoir leads to the following solution corresponding to the pressure drop because of production from a line, surface, or volumetric source, respectively.

$$\Delta p(M, M', t - \tau) = \frac{1}{\Phi c} \int_{\Gamma_w} \tilde{q}(M'_w) S(M, M'_w, t - \tau) dM'_w \dots\dots\dots (3.161)$$

In Eq. 3.161,  $M_w$  indicates a point on the source ( $\Gamma_w$ ) and  $\tilde{q}(M_w)$  is the instantaneous withdrawal volume of fluids per unit length, area, or volume of the source, depending on the source geometry. For example, the pressure drop as a result of an infinite line source at  $x', y'$  and  $-\infty \leq z' \leq \infty$  may be obtained as follows:

$$\Delta p(x, x', y, y', t - \tau) = \frac{1}{8\Phi c \sqrt{\eta_x \eta_y \eta_z} [\pi(t - \tau)]^{3/2}} \exp \left[ -\frac{(x - x')^2 / \eta_x + (y - y')^2 / \eta_y}{4(t - \tau)} \right] \times \int_{-\infty}^{+\infty} \tilde{q}(x', y', z') \exp \left[ -\frac{(z - z')^2}{4\eta_z(t - \tau)} \right] dz' \dots\dots\dots (3.162)$$

If we assume that the flux is uniform along the line source and the source strength is unity [ $\tilde{q}(x', y', z') / (\Phi c) = \tilde{q} / (\Phi c) = 1$ ], then we can write the instantaneous, infinite line-source solution in an infinite reservoir as

$$S(x, x', y, y', t - \tau) = \frac{1}{4\pi \sqrt{\eta_x \eta_y} (t - \tau)} \exp \left[ -\frac{(x - x')^2 / \eta_x + (y - y')^2 / \eta_y}{4(t - \tau)} \right] \dots\dots\dots (3.163)$$

As another example, if we consider an instantaneous, infinite plane source at  $x = x', -\infty \leq y' \leq \infty$ , and  $-\infty \leq z' \leq \infty$  in an infinite reservoir, we can write

$$\Delta p(x, x', t - \tau) = \frac{1}{8\Phi c \sqrt{\eta_x \eta_y \eta_z} [\pi(t - \tau)]^{3/2}} \exp \left[ -\frac{(x - x')^2}{4\eta_x(t - \tau)} \right] \times \int_{-\infty}^{+\infty} \int_{-\infty}^{+\infty} \tilde{q}(x', y', z') \exp \left[ -\frac{(y - y')^2 / \eta_y + (z - z')^2 / \eta_z}{4(t - \tau)} \right] dy' dz', \dots\dots\dots (3.164)$$

which also leads to the following uniform-flux, unit-strength, instantaneous, infinite plane-source solution in an infinite reservoir:

$$S(x, x', t - \tau) = \frac{1}{2\sqrt{\pi \eta_x} (t - \tau)} \exp \left[ -\frac{(x - x')^2}{4\eta_x(t - \tau)} \right] \dots\dots\dots (3.165)$$

If the fluid withdrawal is at a continuous rate from time 0 to  $t$ , then the continuous line-, surface-, or volumetric-source solution for an infinite reservoir is given by

$$\Delta p(M, M', t) = \frac{1}{\Phi c} \int_0^t \int_{\Gamma_w} \tilde{q}(M'_w, \tau) S(M, M'_w, t - \tau) dM'_w d\tau \dots\dots\dots (3.166)$$

**Source Functions for Bounded Reservoirs.** The source solutions discussed previously can be extended to bounded reservoirs. The method of images provides a convenient means of generating the bounded-reservoir solutions with the use of the infinite reservoir solutions, especially when the reservoir boundaries consist of impermeable and constant-pressure planes. The method of images is an application of the principle of superposition, which states that if  $f_1$  and



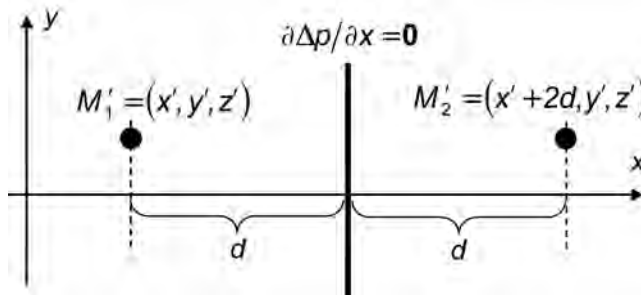


Fig. 3.7—Application of the method of images to generate the effect of a linear boundary.

$f_2$  are two linearly independent solutions of a linear PDE and  $c_1$  and  $c_2$  are two arbitrary constants, then  $f_3 = c_1 f_1 + c_2 f_2$  is also a solution of the PDE. Examples of source functions in bounded reservoirs are presented here.

**Instantaneous Point Source Near a Single Linear Boundary.** To generate the effect of an impermeable planar boundary at a distance  $d$  from a unit-strength, instantaneous point source in an infinite reservoir (see Fig. 3.7), we can apply the method of images to the instantaneous point-source solution given in Eq. 3.157 as

$$S(M, M', t - \tau) = \frac{1}{8\sqrt{\eta_x \eta_y \eta_z} [\pi(t - \tau)]^{3/2}} \exp \left[ -\frac{(y - y')^2 / \eta_y + (z - z')^2 / \eta_z}{4(t - \tau)} \right] \times \left\{ \exp \left[ -\frac{(x - x')^2}{4\eta_x(t - \tau)} \right] + \exp \left[ -\frac{(x - x' - 2d)^2}{4\eta_x(t - \tau)} \right] \right\} \dots \dots \dots (3.167)$$

It can be shown from Eq. 3.167 that  $(\partial S / \partial x)_{x=d} = 0$ ; that is, the bisector of the distance between the two sources is a no-flow boundary. Similarly, to generate the effect of a constant-pressure boundary, we use the method of images and the unit-strength, instantaneous point-source solution (Eq. 3.160) as follows:

$$S(M, M', t - \tau) = \frac{1}{8\sqrt{\eta_x \eta_y \eta_z} [\pi(t - \tau)]^{3/2}} \exp \left[ -\frac{(y - y')^2 / \eta_y + (z - z')^2 / \eta_z}{4(t - \tau)} \right] \times \left\{ \exp \left[ -\frac{(x - x')^2}{4\eta_x(t - \tau)} \right] - \exp \left[ -\frac{(x - x' - 2d)^2}{4\eta_x(t - \tau)} \right] \right\} \dots \dots \dots (3.168)$$

**Instantaneous Point Source in an Infinite-Slab Reservoir.** Using the method of images and considering the geometry shown in Col. A of Fig. 3.8, we can generate the solution for a unit-strength, instantaneous point source in an infinite-slab reservoir with impermeable boundaries at  $z = 0$  and  $h$ . The result is given by

$$S(M, M', t - \tau) = \frac{1}{8\sqrt{\eta_x \eta_y \eta_z} [\pi(t - \tau)]^{3/2}} \exp \left[ \frac{(x - x')^2 / \eta_x + (y - y')^2 / \eta_y}{4(t - \tau)} \right] \times \sum_{n=-\infty}^{+\infty} \left\{ \exp \left[ -\frac{(z - z' - 2nh)^2}{4\eta_z(t - \tau)} \right] + \exp \left[ -\frac{(z + z' - 2nh)^2}{4\eta_z(t - \tau)} \right] \right\}, \dots \dots \dots (3.169)$$

which, with Poisson’s summation formula given by<sup>14</sup>

$$\sum_{n=-\infty}^{+\infty} \exp \left[ -\frac{(\zeta - 2n\zeta_e)^2}{4t} \right] = \frac{\sqrt{\pi t}}{\zeta_e} \left[ 1 + 2 \sum_{n=1}^{\infty} \exp \left( -\frac{n^2 \pi^2 t}{\zeta_e^2} \right) \cos n\pi \frac{\zeta}{\zeta_e} \right], \dots\dots\dots (3.170)$$

may be transformed into

$$S(M, M', t - \tau) = \frac{1}{4\pi h \sqrt{\eta_x \eta_y} (t - \tau)} \exp \left[ -\frac{(x - x')^2 / \eta_x + (y - y')^2 / \eta_y}{4(t - \tau)} \right] \\ \times \left\{ 1 + 2 \sum_{n=1}^{\infty} \exp \left[ -\frac{n^2 \pi^2 \eta_z (t - \tau)}{h^2} \right] \left( \cos n\pi \frac{z}{h} \cos n\pi \frac{z'}{h} \right) \right\} \dots\dots\dots (3.171)$$

Following similar lines, if the slab boundaries at  $z = 0$  and  $h$  are at a constant pressure equal to  $p_b$ , we obtain

$$S(M, M', t - \tau) = \frac{\tilde{q}}{2\pi \Phi c h \sqrt{\eta_x \eta_y} (t - \tau)} \exp \left[ -\frac{(x - x')^2 / \eta_x + (y - y')^2 / \eta_y}{4(t - \tau)} \right] \\ \times \left\{ \sum_{n=1}^{\infty} \exp \left[ -\frac{n^2 \pi^2 \eta_z (t - \tau)}{h^2} \right] \left[ \sin n\pi \frac{z}{h} \sin n\pi \frac{z'}{h} \right] \right\} \dots\dots\dots (3.172)$$

Similarly, for the case in which the slab boundary at  $z = 0$  is impermeable while the boundary at  $z = h$  is at a constant pressure equal to  $p_b$ , the following solution may be derived:

$$S(M, M', t - \tau) = \frac{\tilde{q}}{2\pi \Phi c h \sqrt{\eta_x \eta_y} (t - \tau)} \exp \left[ -\frac{(x - x')^2 / \eta_x + (y - y')^2 / \eta_y}{4(t - \tau)} \right] \\ \times \left\{ \sum_{n=1}^{\infty} \exp \left[ -\frac{(2n - 1)^2 \pi^2 \eta_z (t - \tau)}{h^2} \right] \left[ \cos (2n - 1) \frac{\pi z}{2h} \cos (2n - 1) \frac{\pi z'}{2h} \right] \right\} \dots\dots\dots (3.173)$$

**Instantaneous Point Source in a Closed Parallelepiped.** The ideas used previously for slab reservoirs may be used to develop solutions for reservoirs bounded by planes in all three directions. For example, if the reservoir is bounded in all three directions (i.e.,  $0 \leq x \leq x_e$ ,  $0 \leq y \leq y_e$ , and  $0 \leq z \leq h$ ) and the bounding planes are impermeable, then we can use Eq. 3.157 and the method of images to write

$$S(M, M', t - \tau) = \frac{1}{8\sqrt{\eta_x \eta_y \eta_z} [\pi(t - \tau)]^{3/2}} \\ \times \sum_{n=-\infty}^{+\infty} \left\{ \exp \left[ -\frac{(x - x' - 2nx_e)^2}{4\eta_x(t - \tau)} \right] + \exp \left[ -\frac{(x + x' - 2nx_e)^2}{4\eta_x(t - \tau)} \right] \right\}$$

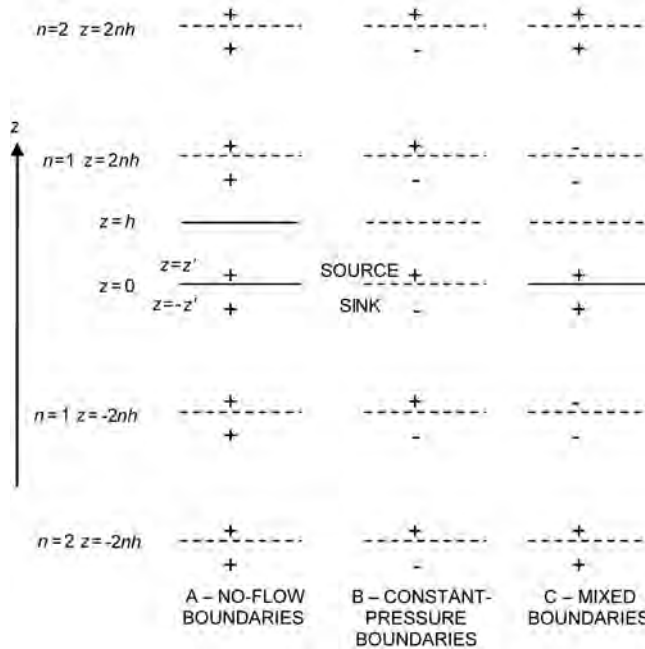


Fig. 3.8—Application of the method of images to generate the solutions for infinite-slab reservoirs.

$$\begin{aligned} & \times \sum_{n=-\infty}^{+\infty} \left\{ \exp \left[ -\frac{(y-y'-2ny_e)^2}{4\eta_y(t-\tau)} \right] + \exp \left[ -\frac{(y+y'-2ny_e)^2}{4\eta_y(t-\tau)} \right] \right\} \\ & \times \sum_{n=-\infty}^{+\infty} \left\{ \exp \left[ -\frac{(z-z'-2nh)^2}{4\eta_z(t-\tau)} \right] + \exp \left[ -\frac{(z+z'-2nh)^2}{4\eta_z(t-\tau)} \right] \right\}, \dots\dots\dots (3.174) \end{aligned}$$

which, with Poisson’s summation formula (Eq. 3.170), may be recast into the following form:

$$\begin{aligned} S(M, M', t - \tau) &= \frac{1}{x_e y_e h} \left\{ 1 + 2 \sum_{k=1}^{\infty} \exp \left[ -\frac{k^2 \pi^2 \eta_x (t - \tau)}{x_e^2} \right] \left( \cos k\pi \frac{x}{x_e} \cos k\pi \frac{x'}{x_e} \right) \right\} \\ & \times \left\{ 1 + 2 \sum_{m=1}^{\infty} \exp \left[ -\frac{m^2 \pi^2 \eta_y (t - \tau)}{y_e^2} \right] \left( \cos m\pi \frac{y}{y_e} \cos m\pi \frac{y'}{y_e} \right) \right\} \\ & \times \left\{ 1 + 2 \sum_{n=1}^{\infty} \exp \left[ -\frac{n^2 \pi^2 \eta_z (t - \tau)}{h^2} \right] \left( \cos n\pi \frac{z}{h} \cos n\pi \frac{z'}{h} \right) \right\} \dots\dots\dots (3.175) \end{aligned}$$

**Instantaneous Infinite-Plane Source in an Infinite-Slab Reservoir With Impermeable Boundaries.** The instantaneous point-source solutions of Eqs. 3.171 through 3.173 may be extended to different source geometries with Eq. 3.161. For example, the solution for an instantaneous infinite-plane source at  $z = z'$  in an infinite-slab reservoir with impermeable boundaries is obtained by substituting Eq. 3.171 for  $S$  in Eq. 3.161. This yields

$$\Delta p(M, t - \tau) = \frac{1}{\Phi c} \int_{-\infty}^{+\infty} \int_{-\infty}^{+\infty} \frac{\tilde{q}(x', y')}{4\pi h \sqrt{\eta_x \eta_y} (t - \tau)} \exp \left[ -\frac{(x - x')^2 / \eta_x + (y - y')^2 / \eta_y}{4(t - \tau)} \right] \\ \times \left\{ 1 + 2 \sum_{n=1}^{\infty} \exp \left[ -\frac{n^2 \pi^2 \eta_z (t - \tau)}{h^2} \right] \left( \cos n\pi \frac{z}{h} \cos n\pi \frac{z'}{h} \right) \right\} dx' dy' \dots (3.176)$$

Assuming a unit-strength, uniform-flux source [ $\tilde{q}(x', y') / (\Phi c) = \tilde{q} / (\Phi c) = 1$ ], we obtain the following instantaneous infinite-plane source solution in an infinite-slab reservoir with impermeable boundaries:

$$S(M, M', t - \tau) = \frac{1}{h} \left\{ 1 + 2 \sum_{n=1}^{\infty} \exp \left[ -\frac{n^2 \pi^2 \eta_z (t - \tau)}{h^2} \right] \left( \cos n\pi \frac{z}{h} \cos n\pi \frac{z'}{h} \right) \right\} \dots (3.177)$$

**Instantaneous Infinite-Slab Source in an Infinite-Slab Reservoir With Impermeable Boundaries.** Following similar lines, we can obtain the solution for an instantaneous, infinite-slab source of thickness,  $h_p$ , located at  $z = z_w$  ( $z_w$  is the  $z$ -coordinate of the midpoint of the slab source) in an infinite-slab reservoir with impermeable boundaries.

$$\Delta p(M, t - \tau) = \frac{1}{\Phi c} \int_{-\infty}^{+\infty} \int_{-\infty}^{+\infty} \int_{z_w - h_p}^{z_w + h_p} \frac{\tilde{q}(x', y', z')}{4\pi h \sqrt{\eta_x \eta_y} (t - \tau)} \exp \left[ -\frac{(x - x')^2 / \eta_x + (y - y')^2 / \eta_y}{4(t - \tau)} \right] \\ \times \left\{ 1 + 2 \sum_{n=1}^{\infty} \exp \left[ -\frac{n^2 \pi^2 \eta_z (t - \tau)}{h^2} \right] \left( \cos n\pi \frac{z}{h} \cos n\pi \frac{z'}{h} \right) \right\} dz' dx' dy' \dots (3.178)$$

If we assume a uniform-flux slab source [ $\tilde{q}(x', y', z') / (\Phi c) = \tilde{q} / (\Phi c) = 1$ ], then Eq. 3.178 yields

$$S(M, M', t - \tau) = \frac{h_p}{h} \left\{ 1 + \frac{4h}{\pi h_p} \sum_{n=1}^{\infty} \frac{1}{n} \exp \left[ -\frac{n^2 \pi^2 \eta_z (t - \tau)}{h^2} \right] \right. \\ \left. \times \left( \sin n\pi \frac{h_p}{2h} \cos n\pi \frac{z}{h} \cos n\pi \frac{z_w}{h} \right) \right\} \dots (3.179)$$

**Uniform-Flux, Continuous, Infinite-Slab Source in an Infinite-Slab Reservoir With Impermeable Boundaries.** Solutions for continuous plane and slab sources can be obtained as indicated by Eq. 3.159 (or Eq. 3.166). For example, the solution for a uniform-flux, continuous, infinite-slab source in an infinite-slab reservoir with impermeable top and bottom boundaries may be obtained by substituting the right side of Eq. 3.179 for  $S$  in Eq. 3.159 and is given by

$$\Delta p(M, t) = \frac{\tilde{q} h_p}{\Phi c h} \int_0^t \left[ 1 + \frac{4h}{\pi h_p} \sum_{n=1}^{\infty} \frac{1}{n} \exp \left( -\frac{n^2 \pi^2 \eta_z \tau}{h^2} \right) \right. \\ \left. \times \left( \sin n\pi \frac{h_p}{2h} \cos n\pi \frac{z}{h} \cos n\pi \frac{z_w}{h} \right) \right] d\tau \dots (3.180)$$

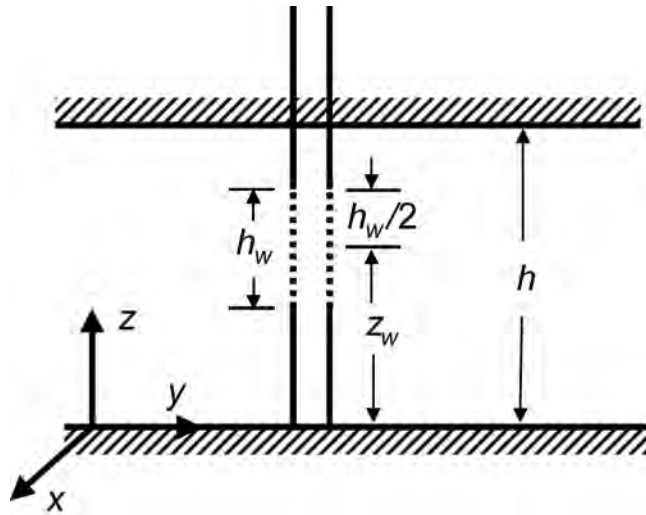


Fig. 3.9—Geometry of the well/reservoir system for a partially penetrating vertical well in an infinite-slab reservoir with impermeable boundaries for Example 3.5.

The same solution could have been obtained by substituting the unit-strength instantaneous point-source solution given by Eq. 3.171 for  $S$  in Eq. 3.166.

**Example 3.5** Consider transient flow toward a partially penetrating vertical well of penetration length,  $h_w$ , in an infinite, homogeneous, slab reservoir of uniform thickness,  $h$ , and initial pressure,  $p_i$ , with impermeable top and bottom boundaries.

*Solution.* Fig. 3.9 shows the geometry of the well and reservoir system of interest. The solution for this problem can be obtained by assuming that the well may be represented by a vertical line source. Then, starting with Eq. 3.166 and substituting the unit-strength, instantaneous point-source solution in an infinite-slab reservoir with impermeable boundaries [Eq. 3.171 with  $\tilde{q}/(\Phi c) = 1$ ] for  $S$ , we obtain

$$\Delta p(M, t) = \frac{1}{\Phi c} \int_0^{z_w+h_w/2} \int_{z_w-h_w/2}^{z_w+h_w/2} \frac{\tilde{q}(z', \tau)}{4\pi h \sqrt{\eta_x \eta_y} (t-\tau)} \exp \left[ -\frac{(x-x')^2/\eta_x + (y-y')^2/\eta_y}{4(t-\tau)} \right] \\ \times \left\{ 1 + 2 \sum_{n=1}^{\infty} \exp \left[ -\frac{n^2 \pi^2 \eta_z (t-\tau)}{h^2} \right] \left( \cos n\pi \frac{z}{h} \cos n\pi \frac{z'}{h} \right) \right\} dz' d\tau \dots \dots \dots (3.181)$$

If we assume that the strength of the source is uniformly distributed along its length (this physically corresponds to a uniform-flux distribution) and the production rate is constant over time [i.e.,  $\tilde{q}(z', \tau) = \tilde{q} = q/h_p$ , where  $q$  is the constant production rate of the well], then Eq. 3.181 yields

$$\Delta p(M, t) = \frac{q}{4\pi \Phi c h \sqrt{\eta_x \eta_y}} \int_0^t \exp \left[ -\frac{(x-x')^2/\eta_x + (y-y')^2/\eta_y}{4\tau} \right]$$

$$\times \left[ 1 + \frac{4h}{\pi h_w} \sum_{n=1}^{\infty} \frac{1}{n} \exp\left(-\frac{n^2 \pi^2 \eta_z \tau}{h^2}\right) \left( \sin n\pi \frac{h_w}{2h} \cos n\pi \frac{z}{h} \cos n\pi \frac{z_w}{h} \right) \right] \frac{d\tau}{\tau} \dots\dots\dots (3.182)$$

**3.4.3 The Use of Green’s Functions and Source Functions in Solving Unsteady-Flow Problems.**

As discussed in [Sec. 3.4.2](#), the conventional development of the source-function solutions uses the instantaneous point-source solution as the building block with the appropriate integration (superposition) in space and time. In 1973, Gringarten and Ramey<sup>13</sup> introduced the use of the source and Green’s function method to the petroleum engineering literature with a more efficient method of developing the source solutions. Specifically, they suggested the use of infinite-plane sources as the building block with Newman’s product method.<sup>22</sup> In this section, we discuss the use of Green’s functions and source functions in solving unsteady-flow problems in reservoirs.

Green’s function for transient flow in a porous medium is defined as the pressure at  $M(x, y, z)$  at time  $t$  because of an instantaneous point source of unit strength generated at point  $M'(x', y', z')$  at time  $\tau < t$  with the porous medium initially at zero pressure and the boundary of the medium kept at zero pressure or impermeable to flow.<sup>13,14</sup> If we let  $G(M, M', t - \tau)$  denote the Green’s function, then it should satisfy the diffusion equation; that is,

$$\frac{\partial G}{\partial t} = \eta \nabla^2 G \quad \text{for } t > \tau. \dots\dots\dots (3.183)$$

Because  $G$  is a function of  $t - \tau$ , it should also satisfy the adjoint diffusion equation,

$$\frac{\partial G}{\partial \tau} + \eta \nabla^2 G = 0 \quad \text{for } \tau < t. \dots\dots\dots (3.184)$$

Green’s function also has the following properties:<sup>13,14</sup>

1.  $G$  is symmetrical in the two points  $M$  and  $M'$ ; that is, Green’s function is invariant as the source and the observation points are interchanged.
2. As  $t \rightarrow \tau$ ,  $G$  vanishes at all points in the porous medium; that is,  $\lim_{t \rightarrow \tau} G(M, M', t - \tau) = 0$ , except at the source location,  $M = M'$ , where it becomes infinite, so that  $G$  satisfies the delta function property,

$$\lim_{t \rightarrow \tau} \int_D \varphi(M') G(M, M', t - \tau) dM' = \varphi(M), \dots\dots\dots (3.185)$$

where  $D$  indicates the domain of the porous medium, and  $\varphi(M)$  is any continuous function.

3. Because  $G$  corresponds to the pressure because of an instantaneous point source of unit strength, it satisfies

$$\int_D G(M, M', t - \tau) \partial M' = 1. \dots\dots\dots (3.186)$$

4.  $G$  or its normal derivative,  $\partial G / \partial n$ , vanishes at the boundary,  $\Gamma$ , of the porous medium. If the porous medium is infinite, then  $G$  vanishes as  $M$  or  $M' \rightarrow \infty$ .

Let  $p(M', \tau)$  be the pressure in the porous medium and  $G(M, M', t - \tau)$  be the Green's function. Let  $D$  denote the domain of the porous medium. Then,  $p$  and  $G$  satisfy the following differential equations:

$$\frac{\partial p}{\partial \tau} = \eta \nabla^2 p \quad \text{for } M' \text{ in } D \dots\dots\dots (3.187)$$

and

$$\frac{\partial G}{\partial \tau} = -\eta \nabla^2 G \quad \text{for } M, M' \text{ in } D \dots\dots\dots (3.188)$$

Then, we can write

$$\frac{\partial}{\partial \tau}(pG) = G \frac{\partial p}{\partial \tau} + p \frac{\partial G}{\partial \tau} = \eta(G \nabla^2 p - p \nabla^2 G) \dots\dots\dots (3.189)$$

or

$$\int_0^{t-\varepsilon} \int_D \frac{\partial}{\partial \tau}(pG) dM' d\tau = \eta \int_0^{t-\varepsilon} \int_D (G \nabla^2 p - p \nabla^2 G) dM' d\tau, \dots\dots\dots (3.190)$$

where  $\varepsilon$  is a small positive number. Changing the order of integration and applying the Green's theorem,

$$\int_D \nabla^2 f(M) dM = \int_\Gamma \frac{\partial f}{\partial n} d\Gamma, \dots\dots\dots (3.191)$$

where  $D$  and  $\Gamma$  indicate the volume and boundary surface of the domain, respectively;  $S$  denotes the points on the boundary; and  $\partial/\partial n$  indicates differentiation in the normal direction of the surface  $\Gamma$ ; we obtain

$$\int_D (pG)_{\tau=t-\varepsilon} dM' - \int_D (pG)_{\tau=0} dM' = \eta \int_0^{t-\varepsilon} \int_\Gamma \left( G \frac{\partial p}{\partial n} - p \frac{\partial G}{\partial n} \right) d\Gamma d\tau \dots\dots\dots (3.192)$$

Taking the limit as  $\varepsilon \rightarrow 0$  and noting the delta-function property of the Green's function (Eq. 3.185), Eq. 3.192 yields

$$p(M, t) = \int_D p_i(M') G(M, M', t) dM' + \eta \int_0^t \int_\Gamma \left( G \frac{\partial p}{\partial n} - p \frac{\partial G}{\partial n} \right) d\Gamma d\tau, \dots\dots\dots (3.193)$$

where  $p_i(M) = p(M, t = 0)$  is the initial pressure at point  $M$ .

In Eq. 3.193, the boundary of the porous medium consists of two surfaces: the inner boundary that corresponds to the surface of the wellbore,  $\Gamma_w$ , and the outer boundary of the reservoir,  $\Gamma_e$ . Eq. 3.193 may be written as

$$\begin{aligned}
 p(M, t) = & \int_D p_i(M')G(M, M', t) dM' + \eta \int_0^t \int_{\Gamma_w} \left( G \frac{\partial p}{\partial n} - p \frac{\partial G}{\partial n} \right) dM'_w d\tau \\
 & + \eta \int_0^t \int_{\Gamma_e} \left( G \frac{\partial p}{\partial n} - p \frac{\partial G}{\partial n} \right) dM'_e d\tau. \dots\dots\dots (3.194)
 \end{aligned}$$

As the fourth property of Green’s function noted previously requires, if the outer boundary of the reservoir is impermeable,  $[(\partial p / \partial n)_{\Gamma_e} = 0]$  or at infinity, then  $G$  vanishes at the outer boundary; that is,  $G(\Gamma_e) = 0$ . Thus, Eq. 3.194 becomes

$$p(M, t) = \int_D p_i(M')G(M, M', t) dM' + \eta \int_0^t \int_{\Gamma_w} \left( G \frac{\partial p}{\partial n} - p \frac{\partial G}{\partial n} \right) dM'_w d\tau. \dots\dots\dots (3.195)$$

Similarly, if the flux,  $(\partial p / \partial n)_{\Gamma_w}$ , is specified at the inner boundary, then the normal derivative of Green’s function,  $(\partial G / \partial n)_{\Gamma_w}$ , vanishes at that boundary. This yields

$$\int_D p_i(M')G(M, M', t) dM' - p(M, t) = -\eta \int_0^t \int_{\Gamma_w} G \frac{\partial p}{\partial n} dM'_w d\tau. \dots\dots\dots (3.196)$$

If the initial pressure,  $p_i$ , is uniform over the entire domain (porous medium),  $D$ , then, by the third property of Green’s function (Eq. 3.186), we should have

$$\int_D p_i(M')G(M, M', t) dM' = p_i. \dots\dots\dots (3.197)$$

Also, the flux law for porous medium (Darcy’s law) requires that the volume of fluid passing through the point,  $M'_w$ , on the inner-boundary surface,  $\Gamma_w$ , at time  $t$  be equal to

$$\tilde{q}(M'_w, t) = -\frac{k}{\mu} \frac{\partial p(M'_w, t)}{\partial n}. \dots\dots\dots (3.198)$$

The substitution of Eqs. 3.197 and 3.198 into Eq. 3.196 yields

$$\Delta p(M, t) = \frac{1}{\Phi c} \int_0^t \int_{\Gamma_w} \tilde{q}(M'_w, \tau) G(M, M'_w, t - \tau) dM'_w d\tau, \dots\dots\dots (3.199)$$

where  $\Delta p(M, t) = p_i - p(M, t)$ . Not surprisingly, Eq. 3.199 is the same as Eq. 3.166 because  $G$  in Eq. 3.199 is the instantaneous point-source solution of unit strength denoted by  $S$  in Eq. 3.166.

The expression given in Eq. 3.199 may be simplified further by assuming that the flux,  $\tilde{q}(M'_w, t)$ , is uniformly distributed on the inner-boundary surface (wellbore),  $\Gamma_w$ . This yields



$$\Delta p(M, t) = \frac{1}{\Phi c} \int_0^t \tilde{q}(\tau) S(M, M_w, t - \tau) d\tau, \dots\dots\dots (3.200)$$

where

$$S(M, M_w, t) = \int_{\Gamma_w} G(M, M'_w, t) dM'_w \dots\dots\dots (3.201)$$

The integration in the right side of Eq. 3.201 represents the distribution of instantaneous point sources over the length, area, or volume of the source (well), and *S* denotes the corresponding instantaneous source function. In Sec. 3.4.2, we discussed the conventional derivation of the source functions starting from the basic instantaneous point-source solution. Here, we discuss the use of infinite-plane sources as the building block with Newman’s product method.<sup>22</sup>

Newman’s product method<sup>22</sup> may be stated for transient-flow problems in porous media as follows:<sup>13</sup> if a well/reservoir system can be visualized as the intersection of 1D or 2D systems, then the instantaneous source or Green’s function for this well/reservoir system can be constructed by the product of the source or Green’s functions for the 1D and/or 2D systems. For example, an infinite line-source well at  $x = x', y = y',$  and  $-\infty \leq z' \leq +\infty$  in an infinite reservoir may be visualized as the intersection of two infinite, 1D plane sources; one at  $x = x', -\infty \leq y' \leq +\infty,$  and  $-\infty \leq z' \leq +\infty,$  and the other at  $-\infty \leq x' \leq +\infty, y = y',$  and  $-\infty \leq z' \leq +\infty.$  Then, the instantaneous source function for this infinite line-source well,  $S(x, x', y, y', t - \tau),$  may be obtained as the product of two infinite, 1D plane sources, given by

$$S(j, j', t - \tau) = \frac{1}{2\sqrt{\pi\eta_j(t - \tau)}} \exp \left[ -\frac{(j - j')^2}{4\eta_j(t - \tau)} \right] \quad \text{for } j = x \text{ or } y, \dots\dots\dots (3.202)$$

as follows

$$S(x, x', y, y', t - \tau) = \frac{1}{4\pi\sqrt{\eta_x\eta_y(t - \tau)}} \exp \left[ -\frac{(x - x')^2/\eta_x + (y - y')^2/\eta_y}{4(t - \tau)} \right] \dots\dots\dots (3.203)$$

As expected, this solution is the same as Eq. 3.163, which was obtained by integration of an instantaneous point source in an infinite reservoir. For a radially isotropic reservoir ( $\eta_x = \eta_y = \eta_z$ ), Eq. 3.203 yields

$$S(r, r', \theta, \theta', t - \tau) = \frac{1}{4\pi\eta_r(t - \tau)} \exp \left[ -\frac{d^2}{4\eta_r(t - \tau)} \right], \dots\dots\dots (3.204)$$

where *d* is the distance between the line source and the observation line in the *x-y* plane (see Fig. 3.10) and is given by

$$d^2 = (x - x')^2 + (y - y')^2 = r^2 + r'^2 - 2rr' \cos(\theta - \theta'). \dots\dots\dots (3.205)$$

Similarly, intersecting three infinite instantaneous plane sources (or a line source and a plane source), we can obtain the instantaneous point-source solution in an infinite reservoir as

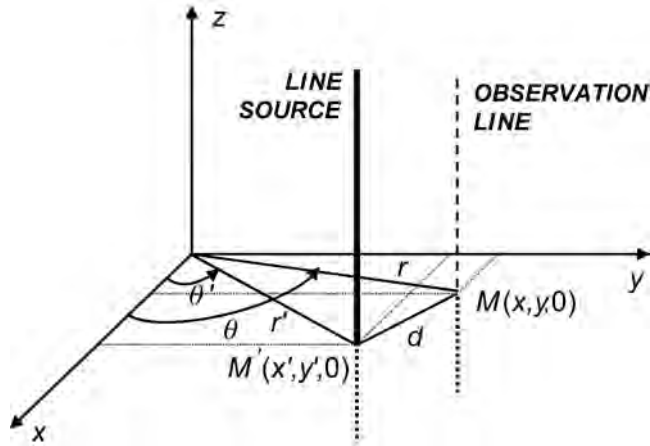


Fig. 3.10—Geometry of a line source in 3D Cartesian and radial coordinates.

$$S(x, x', y, y', z, z', t - \tau) = \frac{1}{8\sqrt{\eta_x \eta_y \eta_z} [\pi(t - \tau)]^{3/2}} \times \exp \left[ -\frac{(x - x')^2 / \eta_x + (y - y')^2 / \eta_y + (z - z')^2 / \eta_z}{4(t - \tau)} \right] \dots \dots \dots (3.206)$$

Instantaneous plane sources in slab reservoirs can be generated with the plane sources in infinite reservoirs and the method of images as discussed in [Sec. 3.4.2](#). Similarly, the instantaneous slab sources can be obtained by integrating plane sources over the thickness of the slab source (see [Sec. 3.4.2](#)). [Table 3.2](#), compiled from the work of Gringarten and Ramey,<sup>13</sup> presents the basic instantaneous source functions in infinite reservoirs, and [Table 3.3](#) shows the corresponding geometries of the source-reservoir systems. The basic instantaneous source functions given in [Table 3.3](#) may be used to construct the source functions that represent the appropriate well geometry by Newman’s product method.

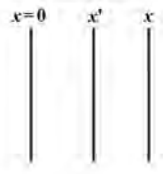
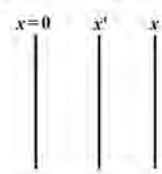
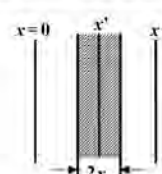
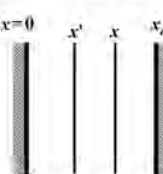
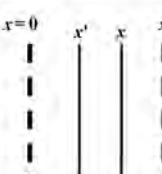
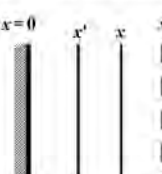
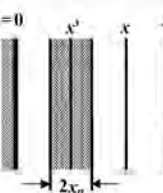
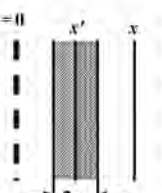
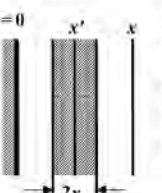
Gringarten and Ramey<sup>13</sup> have also presented the approximating forms of the instantaneous linear sources and the time ranges for these approximations to be valid. The approximate solutions are very useful in obtaining expressions for pressure distributions at early and late times and identifying the flow regimes during the corresponding time periods. [Table 3.4](#) presents the short- and long-time approximating forms for instantaneous linear sources and their time ranges. [Examples 3.6](#) and [3.7](#) present some applications of the product-solution method and the derivation of the approximate solutions for pressure distributions.

**Example 3.6** Consider transient flow toward a partially penetrating vertical fracture of vertical penetration  $h_f$  and horizontal penetration  $2x_f$  in an infinite, homogeneous, slab reservoir of uniform thickness,  $h$ , and initial pressure,  $p_i$ , with impermeable top and bottom boundaries.

*Solution.* [Fig. 3.11](#) shows the geometry of the well reservoir system of interest. Approximate the fracture by a vertical plane of height  $h_f$  and length  $2x_f$ . The corresponding source geometry may be visualized as the intersection of an infinite plane source at  $y = y'$  in an infinite reservoir (Source I in [Tables 3.2](#) and [3.3](#)), an infinite-slab source of thickness  $2x_f$  at  $x = x'$  in an infinite reservoir (Source IV), and an infinite-slab source of thickness  $h_p = h_f$  at  $z = z_w$  in an infinite-slab reservoir of thickness  $h$  (Source VIII). Then, by Newman’s product method, the appropriate source function is given by

<b>TABLE 3.2—BASIC INSTANTANEOUS SOURCE FUNCTIONS<sup>13</sup></b>	
<b>Infinite Reservoirs</b>	
I. Infinite-Plane Source	$\frac{1}{2\sqrt{\pi\eta_x(t-\tau)}} \exp\left[-\frac{(x-x')^2}{4\eta_x(t-\tau)}\right]$
II. Infinite-Line Source	$\frac{1}{4\pi\sqrt{\eta_x\eta_y(t-\tau)}} \exp\left[-\frac{(x-x')^2/\eta_x + (y-y')^2/\eta_y}{4(t-\tau)}\right] \text{ or}$ $\frac{1}{4\pi\eta_r(t-\tau)} \exp\left[-\frac{d^2}{4\eta_r(t-\tau)}\right] \quad \text{where} \quad \begin{aligned} d^2 &= (x-x')^2 + (y-y')^2 \\ d^2 &= r^2 + r'^2 - 2rr'\cos(\theta-\theta') \end{aligned}$
III. Point Source	$\frac{1}{8\sqrt{\eta_x\eta_y\eta_z}[\pi(t-\tau)]^{3/2}} \exp\left[-\frac{(x-x')^2/\eta_x + (y-y')^2/\eta_y + (z-z')^2/\eta_z}{4(t-\tau)}\right]$
IV. Infinite-Slab Source	$\frac{1}{2} \left[ \operatorname{erf} \frac{x_p + (x-x')}{2\sqrt{\eta_x(t-\tau)}} + \operatorname{erf} \frac{x_p - (x-x')}{2\sqrt{\eta_x(t-\tau)}} \right] \quad \text{where} \quad \operatorname{erf}(z) = \frac{2}{\sqrt{\pi}} \int_0^z \exp(-u^2) du$
<b>Infinite-Plane Sources in Infinite-Slab Reservoirs</b>	
V. Closed Boundaries	$\frac{1}{x_e} \left\{ 1 + 2 \sum_{n=1}^{\infty} \exp\left[-\frac{n^2\pi^2\eta_x(t-\tau)}{x_e^2}\right] \cos \frac{n\pi x'}{x_e} \cos \frac{n\pi x}{x_e} \right\}$
VI. Constant-Pressure Boundaries	$\frac{2}{x_e} \sum_{n=1}^{\infty} \exp\left[-\frac{n^2\pi^2\eta_x(t-\tau)}{x_e^2}\right] \sin \frac{n\pi x'}{x_e} \sin \frac{n\pi x}{x_e}$
VII. Mixed Boundaries	$\frac{2}{x_e} \sum_{n=1}^{\infty} \exp\left[-\frac{(2n+1)^2\pi^2\eta_x(t-\tau)}{x_e^2}\right] \cos \frac{(2n+1)\pi x'}{x_e} \cos \frac{(2n+1)\pi x}{x_e}$
<b>Infinite-Slab Sources in Infinite-Slab Reservoirs</b>	
VIII. Closed Boundaries	$\frac{2x_p}{x_e} \left\{ 1 + \frac{2x_e}{\pi x_p} \sum_{n=1}^{\infty} \frac{1}{n} \exp\left[-\frac{n^2\pi^2\eta_x(t-\tau)}{x_e^2}\right] \sin \frac{n\pi x_p}{x_e} \cos \frac{n\pi x'}{x_e} \cos \frac{n\pi x}{x_e} \right\}$
IX. Constant-Pressure Boundaries	$\frac{4}{\pi} \sum_{n=1}^{\infty} \frac{1}{n} \exp\left[-\frac{n^2\pi^2\eta_x(t-\tau)}{x_e^2}\right] \sin \frac{n\pi x_p}{x_e} \sin \frac{n\pi x'}{x_e} \sin \frac{n\pi x}{x_e}$
X. Mixed Boundaries	$\frac{8}{\pi} \sum_{n=1}^{\infty} \frac{1}{2n+1} \exp\left[-\frac{(2n+1)^2\pi^2\eta_x(t-\tau)}{x_e^2}\right] \sin \frac{(2n+1)\pi x_p}{2x_e} \cos \frac{(2n+1)\pi x'}{x_e} \cos \frac{(2n+1)\pi x}{x_e}$

$$S(x, x', y, y', z, z_w, t - \tau) = \frac{1}{2\sqrt{\pi\eta_y(t-\tau)}} \exp\left[-\frac{(y-y')^2}{4\eta_y(t-\tau)}\right]$$

<b>TABLE 3.3—SOURCE GEOMETRIES FOR BASIC INSTANTANEOUS SOURCE FUNCTIONS<sup>13</sup></b>		
Infinite Reservoirs		
I. Infinite-Plane Source	II. Infinite-Line Source	IV. Infinite-Slab Source
		
Infinite-Plane Sources in Infinite-Slab Reservoirs		
V. Closed Boundaries	VI. Constant-Pressure Boundaries	VII. Mixed Boundaries
		
Infinite-Slab Sources in Infinite-Slab Reservoirs		
VIII. Closed Boundaries	IX. Constant-Pressure Boundaries	X. Mixed Boundaries
		

$$\begin{aligned}
 & \times \frac{1}{2} \left[ \operatorname{erf} \frac{x_f + (x - x')}{2\sqrt{\eta_x(t - \tau)}} + \operatorname{erf} \frac{x_f - (x - x')}{2\sqrt{\eta_x(t - \tau)}} \right] \\
 & \times \frac{h_f}{h} \left\{ 1 + \frac{4h}{\pi h_f} \sum_{n=1}^{\infty} \frac{1}{n} \exp \left[ -\frac{n^2 \pi^2 \eta_z(t - \tau)}{h^2} \right] \sin \frac{n\pi h_f}{2h} \cos \frac{n\pi z_w}{h} \cos \frac{n\pi z}{h} \right\} \dots \dots \dots (3.207)
 \end{aligned}$$

Assuming that the production is at a constant rate,  $q = \tilde{q}(t) 2x_f h_f$  and using Eq. 3.207 for the source function,  $S$ , in Eq. 3.200, we obtain

$$\Delta p(x, y, z, t) = \frac{q}{8\Phi c x_f h \sqrt{\pi \eta_y}} \int_0^t \exp \left[ -\frac{(y - y')^2}{4\eta_y \tau} \right] \left[ \operatorname{erf} \frac{x_f + (x - x')}{2\sqrt{\eta_x \tau}} + \operatorname{erf} \frac{x_f - (x - x')}{2\sqrt{\eta_x \tau}} \right]$$

**TABLE 3.4—APPROXIMATE FORMS FOR INSTANTANEOUS LINEAR-SOURCE FUNCTIONS<sup>13</sup>**

Source Type	Space Limits or Boundary Conditions	Approximating Forms	Time Limits
<b>Early Times</b>			
V, VI, VII Plane Source in Slab Reservoir	All $x$	$\frac{1}{2\sqrt{\pi\eta_x(t-\tau)}} \exp\left[-\frac{(x-x')^2}{4\eta_x(t-\tau)}\right]$	
IV, VIII, IX, X Slab Source	Outside the source	0	$t \leq \delta^2/(20\eta_x)^*$
	Inside the source	1	
	On the source boundary	$\frac{1}{2}$	$t \leq x_f^2/(20\eta_x)$
<b>Early and Intermediate Times</b>			
VIII, IX, X Slab Source in Slab Reservoir	All boundary conditions	$\frac{1}{2} \left[ \operatorname{erf} \frac{x_p + (x-x')}{2\sqrt{\eta_x(t-\tau)}} + \operatorname{erf} \frac{x_p - (x-x')}{2\sqrt{\eta_x(t-\tau)}} \right]$	
<b>Late Times</b>			
V, VI, VII Plane Source in Slab Reservoir	Closed boundaries	$1/x_e$	$t \geq 5x_e^2/(\pi^2\eta_x)$
	Constant pressure boundaries	0	$t \geq 5x_e^2/(\pi^2\eta_x)$
	Mixed boundaries	0	$t \geq 20x_e^2/(\pi^2\eta_x)$
VIII, IX, X Slab Source in Slab Reservoir	Closed boundaries	$2x_p/x_e$	$t \geq 5x_e^2/(\pi^2\eta_x)$
	Constant pressure boundaries	0	$t \geq 5x_e^2/(\pi^2\eta_x)$
	Mixed boundaries	0	$t \geq 20x_e^2/(\pi^2\eta_x)$

\*  $\delta$  = nearest distance to the boundary.

$$\times \left[ 1 + \frac{4h}{\pi h_f} \sum_{n=1}^{\infty} \frac{1}{n} \exp\left(-\frac{n^2\pi^2\eta_z\tau}{h^2}\right) \sin \frac{n\pi h_f}{2h} \cos \frac{n\pi z_w}{h} \cos \frac{n\pi z}{h} \right] \frac{d\tau}{\sqrt{\tau}} \dots \dots \dots (3.208)$$

If the fracture penetrates the entire thickness of the reservoir (i.e.,  $h_f = h$ ) as shown in Fig. 3.12, then Eq. 3.208 yields

$$\Delta p(x, y, t) = \frac{q}{8\Phi c x_f h \sqrt{\pi\eta_y}} \times \int_0^t \exp\left[-\frac{(y-y')^2}{4\eta_y\tau}\right] \left[ \operatorname{erf} \frac{x_f + (x-x')}{2\sqrt{\eta_x\tau}} + \operatorname{erf} \frac{x_f - (x-x')}{2\sqrt{\eta_x\tau}} \right] \frac{d\tau}{\sqrt{\tau}} \dots \dots \dots (3.209)$$

The fully penetrating fracture solution given in Eq. 3.209 also could be obtained by constructing the source function as the product of an infinite plane source at  $y = y'$  in an infinite reservoir (Source I in Tables 3.2 and 3.3) and an infinite-slab source of thickness  $2x_f$  at  $x = x'$  in an infinite reservoir (Source IV). This source function then could be used in Eq. 3.200.

Fig. 3.13 presents an example of transient-pressure responses computed from Eq. 3.209. To obtain the results shown in Fig. 3.13, numerical integration has been used to evaluate the right side of Eq. 3.209. It is also of interest to obtain an early-time approximation for the solution

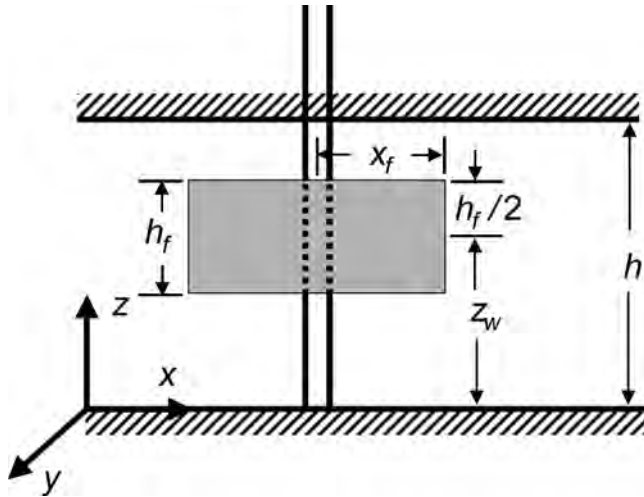


Fig. 3.11—Geometry of the well/reservoir system for a partially penetrating vertical fracture in an infinite-slab reservoir with impermeable boundaries for Example 3.6.

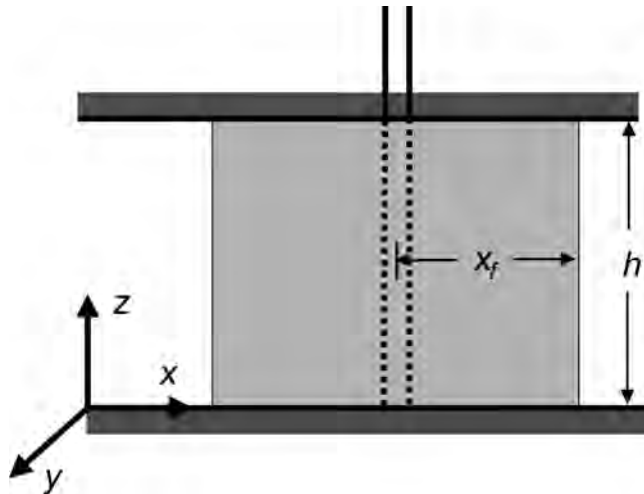


Fig. 3.12—A fully penetrating vertical fracture in an infinite-slab reservoir with impermeable boundaries.

given in Eq. 3.209. Substituting the early-time approximating forms for the slab sources in an infinite reservoir (approximations given in Table 3.4 for Source Functions IV and VIII), we obtain

$$S(x, x', y, y', z, z_w, t - \tau) = \frac{\alpha\beta}{2\sqrt{\pi\eta_y(t - \tau)}} \exp\left[-\frac{(y - y')^2}{4\eta_y(t - \tau)}\right], \dots\dots\dots (3.210)$$

where

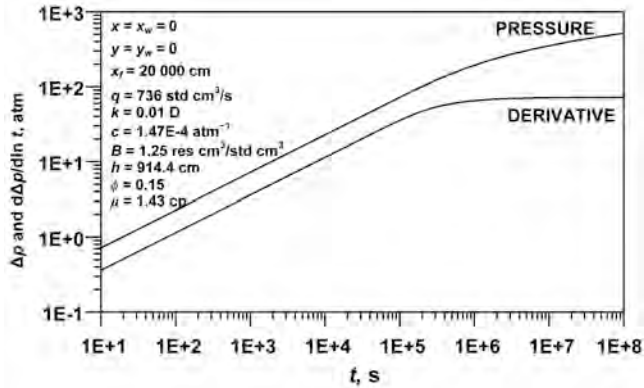


Fig. 3.13—Transient pressure responses of a uniform-flux fracture computed from Eq. 3.209.

$$\alpha = \begin{cases} 0 & \text{for } |z - z_w| > h_f/2 \\ 1 & \text{for } |z - z_w| < h_f/2 \\ 1/2 & \text{for } |z - z_w| = h_f/2 \end{cases} \dots\dots\dots (3.211)$$

and

$$\beta = \begin{cases} 0 & \text{for } |x - x'| > x_f \\ 1 & \text{for } |x - x'| < x_f \\ 1/2 & \text{for } |x - x'| = x_f \end{cases} \dots\dots\dots (3.212)$$

Assuming a constant production rate,  $q = \tilde{q}(t)2x_f h_f$ , and substituting the source function given by Eq. 3.210 in Eq. 3.200, we obtain

$$\Delta p(x, y, z, t) = \frac{q\alpha\beta}{2\Phi c x_f h_f \pi \eta_y} \left[ \sqrt{\pi \eta_y t} \exp\left(-\frac{y^2}{4\eta_y t}\right) - \frac{\pi}{2} y \operatorname{erfc}\left(\frac{y}{2\sqrt{\eta_y t}}\right) \right], \dots\dots\dots (3.213)$$

where  $\operatorname{erfc}(z)$  is the complementary error function defined by

$$\operatorname{erfc}(z) = 1 - \operatorname{erf}(z) = \frac{2}{\sqrt{\pi}} \int_x^\infty \exp(-u^2) du. \dots\dots\dots (3.214)$$

**Example 3.7** Consider transient flow toward a uniform-flux horizontal well of length  $L_h$  located at  $(x', y', z_w)$  in a closed, homogeneous, rectangular parallelepiped of dimensions  $0 \leq x \leq x_e$ ,  $0 \leq y \leq y_e$ ,  $0 \leq z \leq h$  and of initial pressure,  $p_i$ .

*Solution.* Fig. 3.14 shows the sketch of the horizontal-well/reservoir system considered in this example. If we approximate the horizontal well by a horizontal line source of length  $L_h$ , then the resulting source/reservoir system may be visualized as the intersection of three

sources: an infinite plane source at  $y = y'$  in an infinite-slab reservoir of thickness  $y_e$  with impermeable boundaries (Source V in Tables 3.2 and 3.3), an infinite-slab source of thickness  $L_h$  at  $x = x'$  in an infinite-slab reservoir of thickness  $x_e$  with impermeable boundaries (Source VI-II), and an infinite-plane source at  $z = z_w$  in an infinite-slab reservoir of thickness  $h$  with impermeable boundaries (Source V). Then, by Newman’s product method, the appropriate source function can be obtained as

$$\begin{aligned}
 S(x, x', y, y', z, z_w, t - \tau) = & \frac{1}{y_e} \left\{ 1 + 2 \sum_{m=1}^{\infty} \exp \left[ -\frac{m^2 \pi^2 \eta_y (t - \tau)}{y_e^2} \right] \cos \frac{m\pi y'}{y_e} \cos \frac{m\pi y}{y_e} \right\} \\
 & \times \frac{L_h}{x_e} \left\{ 1 + \frac{4x_e}{\pi L_h} \sum_{k=1}^{\infty} \frac{1}{k} \exp \left[ -\frac{k^2 \pi^2 \eta_x (t - \tau)}{x_e^2} \right] \sin \frac{k\pi L_h}{2x_e} \cos \frac{k\pi x'}{x_e} \cos \frac{k\pi x}{x_e} \right\} \\
 & \times \frac{1}{h} \left\{ 1 + 2 \sum_{n=1}^{\infty} \exp \left[ -\frac{n^2 \pi^2 \eta_z (t - \tau)}{h^2} \right] \cos \frac{n\pi z_w}{h} \cos \frac{n\pi z}{h} \right\} \dots\dots\dots (3.215)
 \end{aligned}$$

Assuming that the production is at a constant rate,  $q = \tilde{q}(t) L_h$ , and using Eq. 3.215 for the source function,  $S$ , in Eq. 3.200, we obtain

$$\begin{aligned}
 \Delta p(x, y, z, t) = & \frac{q}{\Phi c x_e y_e h} \int_0^t \left\{ 1 + 2 \sum_{m=1}^{\infty} \exp \left[ -\frac{m^2 \pi^2 \eta_y (t - \tau)}{y_e^2} \right] \cos \frac{m\pi y'}{y_e} \cos \frac{m\pi y}{y_e} \right\} \\
 & \times \left\{ 1 + \frac{4x_e}{\pi L_h} \sum_{k=1}^{\infty} \frac{1}{k} \exp \left[ -\frac{k^2 \pi^2 \eta_x (t - \tau)}{x_e^2} \right] \sin \frac{k\pi L_h}{2x_e} \cos \frac{k\pi x'}{x_e} \cos \frac{k\pi x}{x_e} \right\} \\
 & \times \left\{ 1 + 2 \sum_{n=1}^{\infty} \exp \left[ -\frac{n^2 \pi^2 \eta_z (t - \tau)}{h^2} \right] \cos \frac{n\pi z_w}{h} \cos \frac{n\pi z}{h} \right\} d\tau \dots\dots\dots (3.216)
 \end{aligned}$$

**Table 3.5** presents the pressure responses for a uniform-flux horizontal well in a closed square computed from Eq. 3.216. We may obtain a short-time approximation for Eq. 3.216 with the early-time approximations given in Table 3.4 for Source Functions V and VIII. This yields

$$\Delta p(x, y, z, t) = -\frac{q}{4\pi \Phi c \sqrt{\eta_y \eta_z} L_h} \text{Ei} \left[ -\frac{(y - y')^2 / \eta_y + (z - z_w)^2 / \eta_z}{4t} \right], \dots\dots\dots (3.217)$$

where  $\text{Ei}(-x)$  is the exponential integral function defined by Eq. 3.90. Eq. 3.217 indicates that the early-time flow is radial in the  $y$ - $z$  plane around the axis of the horizontal well. This solution corresponds to the time period during which none of the reservoir boundaries influence the pressure response.

It is also possible to obtain another approximation for Eq. 3.216 that covers the intermediate time-flow behavior. If we approximate the source function in the  $x$  direction (Source Function VIII) by its early and intermediate time approximation and the source function in the  $y$  direction (Source Function V) by its early time approximation given in Table 3.4, we obtain



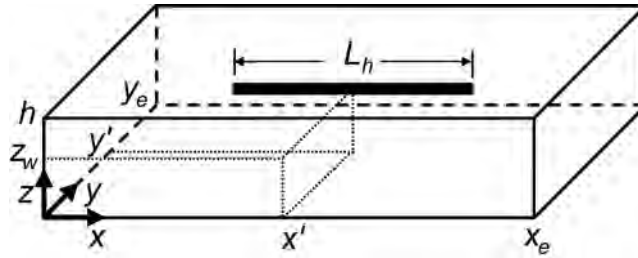


Fig. 3.14—A horizontal well in a closed rectangular parallelepiped (Example 3.7).

$$\begin{aligned} \Delta p(x, y, z, t) &= \frac{q}{4\sqrt{\pi\eta_y}\Phi_c L_h h} \int_0^t \exp\left[-\frac{(y-y')^2}{4\eta_y\tau}\right] \\ &\times \left[ \operatorname{erf} \frac{(L_h/2) + (x-x')}{2\sqrt{\eta_x\tau}} + \operatorname{erf} \frac{(L_h/2) - (x-x')}{2\sqrt{\eta_x\tau}} \right] \\ &\times \left\{ 1 + 2 \sum_{n=1}^{\infty} \exp\left(-\frac{n^2\pi^2\eta_z\tau}{h^2}\right) \cos \frac{n\pi z_w}{h} \cos \frac{n\pi z}{h} \right\} \frac{d\tau}{\sqrt{\tau}} \dots\dots\dots (3.218) \end{aligned}$$

This approximation should correspond to the time period during which the influence of the top and/or bottom boundaries may be evident but the lateral boundaries in the  $x$  and  $y$  directions do not have an influence on the pressure response. This solution also could have been obtained by assuming a laterally infinite reservoir. In this case, the source function would have been constructed as the product of three source functions: an infinite-plane source at  $y = y'$  in an infinite reservoir (Source I in Tables 3.2 and 3.3), an infinite-slab source of thickness  $L_h$  at  $x = x'$  in an infinite reservoir (Source IV), and an infinite-plane source at  $z = z_w$  in an infinite-slab reservoir of thickness  $h$  with impermeable boundaries (Source V).

**3.4.4 The Use of Source Functions in the Laplace Domain To Solve Unsteady-Flow Problems.**

There are many advantages of developing transient-flow solutions in the Laplace transform domain. For example, in the Laplace transform domain, Duhamel’s theorem<sup>23</sup> provides a convenient means of developing transient-flow solutions for variable-rate production problems using the solutions for the corresponding constant-rate production problem. Duhamel’s theorem states that if  $\Delta p$  and  $\Delta p_c$  denote the pressure drawdown corresponding to the variable production rate,  $q(t)$ , and the constant production rate,  $q_c$ , respectively, then

$$\Delta p(M, t) = \frac{1}{q_c} \int_0^t q(\tau) \frac{\partial \Delta p_c}{\partial \tau}(M, t - \tau) d\tau \dots\dots\dots (3.219)$$

Applying the Laplace transform converts the convolution integral in Eq. 3.219 to an algebraic expression, and Duhamel’s theorem is given in the Laplace transform domain as

$$\overline{\Delta p}(M, s) = s \frac{\overline{q}(s)}{q_c} \overline{\Delta p_c}(M, s) \dots\dots\dots (3.220)$$

**TABLE 3.5—UNIFORM-FLUX HORIZONTAL WELL IN A CLOSED SQUARE**

$$L\sqrt{k/k_z}/(2h) = 10, z_w/h = 0.5, r_w/h = 2 \times 10^{-3}$$

$$\eta = \sqrt[3]{\eta_x \eta_y \eta_z}, k = \sqrt[3]{k_x k_y k_z}, t_{AD} = \eta / x_e^2$$

$$x_{eD} = 2x_e \sqrt{k_x/k} / L_h$$

$$\frac{2\pi kh}{q\mu} \Delta p$$

$t_{AD}$	$x_{eD} = 2$	$x_{eD} = 4$	$x_{eD} = 10$	$x_{eD} = 20$
1.0E-4	0.2505	0.2897	0.3961	0.5733
2.0E-4	0.2684	0.3191	0.4695	0.7196
3.0E-4	0.2801	0.3416	0.5258	0.8293
5.0E-4	0.2981	0.3774	0.6152	0.9945
8.0E-4	0.3191	0.4194	0.7196	1.1704
1.0E-3	0.3309	0.4430	0.7775	1.2605
2.0E-3	0.3774	0.5359	0.9945	1.5617
3.0E-3	0.4130	0.6071	1.1450	1.7482
5.0E-3	0.4695	0.7196	1.3544	1.9904
8.0E-3	0.5359	0.8485	1.5617	2.2178
1.0E-2	0.5733	0.9187	1.6636	2.3268
2.0E-2	0.7202	1.1704	1.9904	2.8695
3.0E-2	0.8328	1.3372	2.1866	2.8695
5.0E-2	1.0124	1.5658	2.4380	3.1254
8.0E-2	1.2315	1.8078	2.6917	3.3803
1.0E-1	1.3646	1.9461	2.8325	3.5213
2.0E-1	1.9993	2.5846	3.4732	4.1619
3.0E-1	2.6274	3.2131	4.1011	4.7889
5.0E-1	3.8842	4.4694	5.3578	6.0470
8.0E-1	5.7692	6.3544	7.2428	7.9318
1.0E+0	7.0254	7.6115	8.4995	9.1887
2.0E+0	13.309	13.895	14.783	15.472
3.0E+0	19.592	20.179	21.067	21.755
5.0E+0	32.159	32.745	33.635	34.322
8.0E+0	51.012	51.594	52.479	53.171
1.0E+1	63.578	64.162	65.048	65.738

The simplicity of the expression given in Eq. 3.220 explains our interest in obtaining transient-flow solutions in the Laplace transform domain.

Another example to explain the convenience of the Laplace domain solutions is for the naturally fractured reservoirs. Common transient-flow models of naturally fractured reservoirs lead to the following differential equation in radial coordinates in the Laplace transform domain:<sup>2</sup>

$$\frac{1}{r_D} \frac{d}{dr_D} \left( r_D \frac{d\overline{\Delta p}_f}{dr_D} \right) - s f(s) \overline{\Delta p}_f = 0, \dots\dots\dots (3.221)$$

where the subscript  $f$  indicates the fracture property, and  $t_D$  and  $r_D$  are the dimensionless time and distance (as defined in Eqs. 3.230 and 3.234).

The naturally fractured reservoir function,  $f(s)$ , is a function of matrix and fracture properties and depends on the model chosen to represent the naturally fractured reservoir.<sup>2</sup> The corresponding differential equation for a homogeneous reservoir is obtained by setting  $f(s) = 1$  and is given by

$$\frac{1}{r_D^2} \frac{d}{dr_D} \left( r_D^2 \frac{d\bar{\Delta p}}{dr_D} \right) - s\bar{\Delta p} = 0 \dots\dots\dots (3.222)$$

The general solutions for Eqs. 3.221 and 3.222 are given, respectively, by

$$\bar{\Delta p}_f(s) = AI_0[\sqrt{s f(s)} r_D] + BK_0[\sqrt{s f(s)} r_D] \dots\dots\dots (3.223)$$

and

$$\bar{\Delta p}(s) = AI_0(\sqrt{s r_D}) + BK_0(\sqrt{s r_D}) \dots\dots\dots (3.224)$$

To obtain a solution for constant-rate production from an infinite reservoir, for example, the following boundary conditions are imposed:

$$\bar{\Delta p}_f(r_D \rightarrow \infty) = \bar{\Delta p}(r_D \rightarrow \infty) = 0 \dots\dots\dots (3.225)$$

and

$$\left( r_D \frac{d\bar{\Delta p}_f}{dr_D} \right)_{r_D=1} = \left( r_D \frac{d\bar{\Delta p}}{dr_D} \right)_{r_D=1} = -\frac{1}{s} \dots\dots\dots (3.226)$$

Then, it may be shown that

$$s\bar{\Delta p}_f[s f(s)] = [s\bar{\Delta p}(s)]_{s = s f(s)} \dots\dots\dots (3.227)$$

where the right side of Eq. 3.227 indicates the substitution of  $s f(s)$  for  $s$  in  $s\bar{\Delta p}(s)$ . This discussion demonstrates that it is possible to derive transient-flow solutions for naturally fractured reservoirs by following the same lines as those for the homogeneous reservoirs. Furthermore, if the solution for the corresponding homogeneous reservoir system is known in the Laplace transform domain, then the solution for the naturally fractured reservoir problem may be directly obtained from Eq. 3.227.

Obtaining the Laplace transforms of the Green's and source function solutions developed in the time domain with the methods explained in Secs. 3.4.2 and 3.4.3 usually poses a difficult problem. The problems arise mainly because of the use of the product method solution. For a specific class of functions, Chen *et al.*<sup>24</sup> presented a technique that may be used to apply the Laplace transform to the product-solution technique. For a more general procedure to develop source function solutions in the Laplace transform domain, however, the product solution technique should be avoided.<sup>20</sup>

Ozkan and Raghavan<sup>18,19</sup> have shown that it is more convenient to develop source-function solutions in the Laplace transform domain if the point-source solution is used as a building block. Then, other source geometries may be obtained by the superposition (integration) of the point sources along the length, surface, or volume of the source.

**Point-Source Solution in the Laplace Domain.** Consider the flow of a slightly compressible fluid in an infinite, naturally fractured reservoir. We can use the double-porosity model suggested by Barenblatt *et al.*<sup>25</sup> and Warren and Root<sup>26</sup> to develop the governing flow equations for naturally fractured reservoirs. The results, however, will be applicable to the model suggested by Kazemi<sup>27</sup> and de Swaan-O<sup>28</sup> with a simple modification.

Flow around a point source in an infinite porous medium may be expressed conveniently in spherical coordinates. The differential equations governing flow in a naturally fractured reservoir are given in spherical coordinates by

$$\frac{1}{r_D} \frac{\partial}{\partial r_D} \left( r_D \frac{\partial \Delta p_f}{\partial r_D} \right) = \omega \frac{\partial \Delta p_f}{\partial t_D} + (1 + \omega) \frac{\partial \Delta p_m}{\partial t_D} \dots\dots\dots (3.228)$$

and

$$\lambda (\Delta p_m - \Delta p_f) = -(1 - \omega) \frac{\partial \Delta p_m}{\partial t_D} \dots\dots\dots (3.229)$$

In Eqs. 3.228 and 3.229, subscripts *f* and *m* indicate the property of the fracture and matrix systems, respectively. Initial pressure, *p<sub>i</sub>*, is assumed to be uniform in the entire system; that is, *p<sub>f</sub>* = *p<sub>m</sub>* = *p<sub>i</sub>*. The dimensionless time, *t<sub>D</sub>*, is defined by

$$t_D = \eta t / \ell^2, \dots\dots\dots (3.230)$$

where *ℓ* is a characteristic length in the system, and

$$\eta = \frac{k_f}{[(V\Phi c_t)_f + (V\Phi c_t)_m] \mu} \dots\dots\dots (3.231)$$

The definitions of the other variables used in Eqs. 3.228 and 3.229 are

$$\omega = \frac{(V\Phi c_t)_f}{[(V\Phi c_t)_f + (V\Phi c_t)_m]}, \dots\dots\dots (3.232)$$

$$\lambda = \alpha \ell^2 k_m / k_f, \dots\dots\dots (3.233)$$

and

$$r_D = \sqrt{x_D^2 + y_D^2 + z_D^2} \dots\dots\dots (3.234)$$

where

$$\xi_D = \zeta \sqrt{k_f / k_{zf}} / \ell \quad \zeta = x, y, \text{ or } z \dots\dots\dots (3.235)$$

The initial and outer-boundary conditions are given, respectively, by

$$\Delta p_j(t_D = 0, r_D > 0) = 0; j = m, f \dots\dots\dots (3.236)$$

and

$$\Delta p_j(r_D \rightarrow \infty, t_D) = 0; j = m, f \dots\dots\dots (3.237)$$

The inner-boundary condition corresponding to the instantaneous withdrawal of an amount of fluid,  $\tilde{q}$ , at  $t = 0$  from a point source is obtained by considering the mass balance on a small sphere. If we require that at any time  $t = T > 0$ , the sum of the flux through the surface of a small sphere around the source location must equal the volume of the fluid,  $\tilde{q}$ , instantaneously withdrawn from the sphere at  $t = 0$ , we can write<sup>29</sup>

$$\int_0^T \left[ \lim_{\varepsilon \rightarrow 0^+} \frac{4\pi k_f}{\mu} \ell \left( r_D^2 \frac{\partial \Delta p_f}{\partial r_D} \right)_{r_D = \varepsilon} \right] dt = -\tilde{q} \dots\dots\dots (3.238)$$

Although the withdrawal of fluids from the sphere is instantaneous, the resulting flow in the porous medium, and the flux across the surface of the sphere, is continuous. Therefore, if  $q$  represents the total flux across the surface of the small sphere during the time interval  $0 \leq t \leq T$ , then the mass balance requires that the cumulative production (flux across the surface of the small sphere) at time  $T$  be equal to the instantaneous withdrawal volume of fluid from the sphere. That is,

$$\tilde{q} = \int_0^T q(t) dt \dots\dots\dots (3.239)$$

For the condition expressed in Eq. 3.239 to hold for every  $T \geq 0$ , we must have

$$q(t) = \tilde{q} \delta(t), \dots\dots\dots (3.240)$$

where  $\delta(t)$  is the Dirac delta function satisfying the properties expressed by Eqs. 3.185 and 3.186.

Using the results given by Eqs. 3.239 and 3.240 in Eq. 3.238, we obtain

$$\lim_{\varepsilon \rightarrow 0^+} \frac{4\pi k_f}{\mu} \ell \left( r_D^2 \frac{\partial \Delta p_f}{\partial r_D} \right)_{r_D = \varepsilon} = -\tilde{q} \delta(t) \dots\dots\dots (3.241)$$

The Laplace transform of Eqs. 3.228, 3.229, 3.237, and 3.241 yields

$$\frac{1}{r_D^2} \frac{d}{dr_D} \left( r_D^2 \frac{d\overline{\Delta p_f}}{dr_D} \right) - s f(s) \overline{\Delta p_f} = 0, \dots\dots\dots (3.242)$$

where

$$f(s) = [s\omega(1 - \omega) + \lambda] / [s(1 - \omega) + \lambda], \dots\dots\dots (3.243)$$

$$\overline{\Delta p}_f(r_D \rightarrow \infty) = 0, \dots\dots\dots (3.244)$$

and

$$\lim_{\epsilon \rightarrow 0^+} 4\pi\ell^3 \left( r_D^2 \frac{d\overline{\Delta p}_f}{dr_D} \right)_{r_D = \epsilon} = - \frac{\tilde{q}}{(V\Phi c_t)_f + (V\Phi c_t)_m} \dots\dots\dots (3.245)$$

In deriving these results, we have used the initial condition given by Eq. 3.236 and noted that

$$L\{\delta(t)\} = \int_0^\infty \exp(-st_D) \delta(t) dt_D = \frac{\eta}{\ell^2} \int_0^\infty \exp\left(-s \frac{\eta}{\ell^2} t\right) \delta(t) dt = \frac{\eta}{\ell^2} \dots\dots\dots (3.246)$$

In Eq. 3.245, the term  $\tilde{q} / [(V\Phi c_t)_f + (V\Phi c_t)_m]$  represents the strength of the source for the naturally fractured porous medium.

The solution of Eqs. 3.242, 3.244, and 3.245 yields the following solution for the pressure distribution in the reservoir, except at the source location (the origin), because of an instantaneous point source of strength  $\tilde{q} / [(V\Phi c_t)_f + (V\Phi c_t)_m]$  acting at  $t = 0$ :

$$\overline{\Delta p}_f = \frac{\tilde{q}}{(V\Phi c_t)_f + (V\Phi c_t)_m} \frac{\exp[-\sqrt{s f(s)} r_D]}{4\pi\ell^3 r_D} \dots\dots\dots (3.247)$$

If the source is located at  $x'_D, y'_D, z'_D$ , then, by translation, we can write

$$\overline{\Delta p}_f = \tilde{q} \overline{S}(R_D, s) / [(V\Phi c_t)_f + (V\Phi c_t)_m], \dots\dots\dots (3.248)$$

where

$$\overline{S}(R_D, s) = \exp[-\sqrt{s f(s)} R_D] / (4\pi\ell^3 R_D), \dots\dots\dots (3.249)$$

and

$$R_D = \sqrt{(x_D - x'_D)^2 + (y_D - y'_D)^2 + (z_D - z'_D)^2} \dots\dots\dots (3.250)$$

The instantaneous point-source solution for the model suggested by Barenblatt *et al.*<sup>25</sup> and Warren and Root<sup>26</sup> can also be used for the model suggested by Kazemi<sup>27</sup> and de Swaan-O,<sup>28</sup> provided that the appropriate  $f(s)$  function is invoked. To obtain the solution for a homogeneous reservoir,  $f(s)$  should be set to unity,  $V_f = 1$ , and  $V_m = 0$ .

If we consider continuous withdrawal of fluids from the point source, then, by the principle of superposition, we should have

**TABLE 3.6—LAPLACE DOMAIN SOLUTIONS FOR WELLS IN INFINITE-SLAB RESERVOIRS<sup>17</sup>**

Impermeable Boundaries at $z_D = 0$ and $h_D$	
$\tilde{x}_D = (x_D - x_{wD} - \alpha\sqrt{k/k_x}), \tilde{y}_D = (y_D - y_{wD}), \tilde{x}_f = x_f/\ell, \tilde{L}_h = L_h/(2\ell), \varepsilon_n = \sqrt{u + n^2\pi^2/h_D^2}$	
Well Type	Pressure Distribution, $\bar{\Delta p}$
Point Source $q = \tilde{q}$	$\frac{\tilde{q}\mu}{2\pi kh_D s} \left[ K_0(r_D\sqrt{u}) + 2 \sum_{n=1}^{\infty} K_0(r_D\varepsilon_n) \cos n\pi \frac{z}{h} \cos n\pi \frac{z'}{h} \right]$
Vertical Well $q = \tilde{q}h$	$\frac{\tilde{q}\mu h}{2\pi kh_D s} K_0(r_D\sqrt{u})$
Vertical Well Partial Penetration $q = \tilde{q}h_w$	$\frac{\tilde{q}\mu}{2\pi kh_D s} \left[ h_w K_0(r_D\sqrt{u}) + \frac{4h}{\pi} \sum_{n=1}^{\infty} \frac{1}{n} K_0(r_D\varepsilon_n) \sin n\pi \frac{h_w}{2h} \cos n\pi \frac{z}{h} \cos n\pi \frac{z'}{h} \right]$
Fractured Well $q = 2\tilde{q}h_x f$	$\frac{\tilde{q}\mu h}{2\pi kh_D s} \int_{-\tilde{x}_f}^{+\tilde{x}_f} K_0\left(\sqrt{\tilde{x}_D^2 + \tilde{y}_D^2} \sqrt{u}\right) d\alpha$
Fractured Well Partial Penetration $q = 2\tilde{q}h_x f$	$\frac{\tilde{q}\mu}{2\pi kh_D s} \left[ h_f \int_{-\tilde{x}_f}^{+\tilde{x}_f} K_0\left(\sqrt{\tilde{x}_D^2 + \tilde{y}_D^2} \sqrt{u}\right) d\alpha + \frac{4h}{\pi} \sum_{n=1}^{\infty} \frac{1}{n} \sin n\pi \frac{h_f}{2h} \cos n\pi \frac{z}{h} \cos n\pi \frac{z'}{h} \right. \\ \left. \times \int_{-\tilde{x}_f}^{+\tilde{x}_f} K_0\left(\sqrt{\tilde{x}_D^2 + \tilde{y}_D^2} \varepsilon_n\right) d\alpha \right]$
Horizontal Well $q = \tilde{q}L_h$	$\frac{\tilde{q}\mu}{2\pi kh_D s} \left[ \int_{-\tilde{L}_h}^{+\tilde{L}_h} K_0\left(\sqrt{\tilde{x}_D^2 + \tilde{y}_D^2} \sqrt{u}\right) d\alpha + 2 \sum_{n=1}^{\infty} \cos n\pi \frac{z}{h} \cos n\pi \frac{z'}{h} \int_{-\tilde{L}_h}^{+\tilde{L}_h} K_0\left(\sqrt{\tilde{x}_D^2 + \tilde{y}_D^2} \varepsilon_n\right) d\alpha \right]$
Constant-Pressure Boundaries at $z_D = 0$ and $h_D$	
$\tilde{x}_D = (x_D - x_{wD} - \alpha\sqrt{k/k_x}), \tilde{y}_D = (y_D - y_{wD}), \tilde{x}_f = x_f/\ell, \tilde{L}_h = L_h/(2\ell), \varepsilon_n = \sqrt{u + n^2\pi^2/h_D^2}$	
Well Type	Pressure Distribution, $\bar{\Delta p}$
Point Source $q = \tilde{q}$	$\frac{\tilde{q}\mu}{\pi kh_D s} \sum_{n=1}^{\infty} K_0(r_D\varepsilon_n) \sin n\pi \frac{z}{h} \sin n\pi \frac{z'}{h}$
Vertical Well Partial Penetration $q = \tilde{q}h_w$	$\frac{2\tilde{q}\mu h}{\pi^2 kh_D s} \sum_{n=1}^{\infty} \frac{1}{n} K_0(r_D\varepsilon_n) \sin n\pi \frac{h_w}{2h} \sin n\pi \frac{z}{h} \sin n\pi \frac{z'}{h}$
Fractured Well Partial Penetration $q = 2\tilde{q}h_x f$	$\frac{2\tilde{q}\mu h}{\pi^2 kh_D s} \sum_{n=1}^{\infty} \frac{1}{n} \sin n\pi \frac{h_w}{2h} \sin n\pi \frac{z}{h} \sin n\pi \frac{z'}{h} \int_{-\tilde{x}_f}^{+\tilde{x}_f} K_0\left(\sqrt{\tilde{x}_D^2 + \tilde{y}_D^2} \varepsilon_n\right) d\alpha$
Horizontal Well $q = \tilde{q}L_h$	$\frac{\tilde{q}\mu}{\pi kh_D s} \sum_{n=1}^{\infty} \sin n\pi \frac{z}{h} \sin n\pi \frac{z'}{h} \int_{-\tilde{L}_h}^{+\tilde{L}_h} K_0\left(\sqrt{\tilde{x}_D^2 + \tilde{y}_D^2} \varepsilon_n\right) d\alpha$

**TABLE 3.6—LAPLACE DOMAIN SOLUTIONS FOR WELLS IN INFINITE SLAB RESERVOIRS<sup>17</sup>**  
(continued)

Impermeable Boundary at $z_D = 0$ and Constant-Pressure Boundary at $z_D = h_D$	
$\tilde{x}_D = (x_D - x_{wD} - \alpha\sqrt{k/k_s}), \tilde{y}_D = (y_D - y_{wD}), \tilde{x}_f = x_f/\ell, \tilde{L}_h = L_h/(2\ell), \varepsilon_{2n-1} = \sqrt{u + (2n-1)^2\pi^2/h_D^2}$	
Well Type	Pressure Distribution, $\overline{\Delta p}$
Point Source $q = \tilde{q}$	$\frac{\tilde{q}\mu}{\pi k h_D s} \sum_{n=1}^{\infty} K_0(r_D \varepsilon_{2n-1}) \cos(2n-1) \frac{\pi z}{2h} \cos(2n-1) \frac{\pi z'}{2h}$
Vertical Well Partial Penetration $q = \tilde{q}h_w$	$\frac{4\tilde{q}\mu h}{\pi^2 k h_D s} \sum_{n=1}^{\infty} \frac{1}{(2n-1)} K_0(r_D \varepsilon_{2n-1}) \sin(2n-1) \frac{\pi h_w}{2h} \cos(2n-1) \frac{\pi z}{2h} \cos(2n-1) \frac{\pi z'}{2h}$
Fractured Well Partial Penetration $q = 2\tilde{q}h_f x_f$	$\frac{4\tilde{q}\mu h}{\pi^2 k h_D s} \sum_{n=1}^{\infty} \frac{1}{(2n-1)} \sin(2n-1) \frac{\pi h_f}{4h} \cos(2n-1) \frac{\pi z}{2h} \cos(2n-1) \frac{\pi z'}{2h}$ $\times \int_{-\tilde{y}_f}^{+\tilde{y}_f} K_0\left(\sqrt{\tilde{x}_D^2 + \tilde{y}_D^2} \varepsilon_{2n-1}\right) d\alpha$
Horizontal Well $q = \tilde{q}L_h$	$\frac{\tilde{q}\mu}{\pi k h_D s} \sum_{n=1}^{\infty} \cos(2n-1) \frac{\pi z}{2h} \cos(2n-1) \frac{\pi z'}{2h} \int_{-\tilde{L}_h}^{+\tilde{L}_h} K_0\left(\sqrt{\tilde{x}_D^2 + \tilde{y}_D^2} \varepsilon_{2n-1}\right) d\alpha$

$$\Delta p_f = \frac{1}{(V\Phi c_t)_f + (V\Phi c_t)_m} \int_0^t \tilde{q}(\tau) S(R_D, t_D - \tau) d\tau = \frac{\rho^2 \mu}{k_f} \int_0^{t_D} \tilde{q}(\tau_D) S(R_D, t_D - \tau_D) d\tau_D \dots (3.251)$$

The Laplace transform of Eq. 3.251 yields the following continuous point-source solution in an infinite reservoir:

$$\overline{\Delta p} = \frac{\tilde{q}\mu}{4\pi k \ell} \frac{\exp(-\sqrt{u}R_D)}{R_D}, \dots (3.252)$$

where we have substituted Eq. 3.249 for  $S$ , dropped the subscript  $f$ , and defined

$$u = s f(s). \dots (3.253)$$

**Line-, Surface-, and Volumetric-Source Solution in the Laplace Domain.** The point-source solution in the Laplace domain may be used to obtain the source solutions for different source geometries. If we define



$$G(x_D - x'_D, y_D - y'_D, z_D - z'_D, s) = \overline{\Delta p}_p / \tilde{q}, \dots\dots\dots (3.254)$$

where  $\Delta p_p$  represents the appropriate point-source solution, then, by the application of the superposition principle, the solution for the withdrawal of fluids from a line, surface, or volume,  $\Gamma_w$ , is given by

$$\overline{\Delta p} = \int_{\Gamma_w} \tilde{q}(x_{wD}, y_{wD}, z_{wD}) G(x_D - x_{wD}, y_D - y_{wD}, z_D - z_{wD}, s) dM_w \dots\dots\dots (3.255)$$

If we assume a uniform-flux distribution in time and over the length, surface, or volume of the source, then

$$\overline{\Delta p} = \frac{\tilde{q}}{s} \int_{\Gamma_w} G(x_D - x_{wD}, y_D - y_{wD}, z_D - z_{wD}, s) dM_w \dots\dots\dots (3.256)$$

The following presentation of the source function approach in the Laplace domain assumes that the flux distribution is uniform, and  $\tilde{q} = \tilde{q}/s$ . Also, the constant production rate from the length, area, or the volume of the source,  $\Gamma_w$ , is denoted by  $q$  so that  $\tilde{q} = q/\Gamma_w$ .

Only sources in infinite reservoirs have been considered so far. These solutions may be easily extended to bounded reservoirs. The following sections present some useful solutions for transient-flow problems in bounded porous media. The first group of solutions is for laterally infinite reservoirs bounded by parallel planes in the vertical direction (infinite-slab reservoirs). The second and third groups comprise the solutions for cylindrical and rectangular reservoirs, respectively.

**Solutions for Infinite-Slab Reservoirs.** In this section, we consider one of the most common reservoir geometries used in pressure-transient analysis of wells in porous media. It is assumed that the lateral boundaries of the reservoir are far enough not to influence the pressure response during the time period of interest. The top and bottom boundaries of the reservoir at  $z = 0$  and  $z = h$  are parallel planes and may be of impermeable, constant pressure, or mixed type. **Table 3.6** presents the solutions for the most common well geometries (point-source, vertical, fractured, and horizontal wells) in infinite-slab reservoirs. Next, we briefly discuss the derivation of these solutions.

Consider a point source in an infinite-slab reservoir with impermeable boundaries at the bottom,  $z = 0$ , and the top,  $z = h$ . To obtain the point-source solution for this case, we use the point-source solution in an infinite reservoir given by **Eq. 3.252** with the method of images. The result is given by

$$\overline{\Delta p} = \frac{\tilde{q}\mu}{4\pi k \ell s} \sum_{n=-\infty}^{+\infty} \left[ \exp\left(-\sqrt{u}\sqrt{r_D^2 + z_{D1}^2}\right) / \sqrt{r_D^2 + z_{D1}^2} + \exp\left(-\sqrt{u}\sqrt{r_D^2 + z_{D2}^2}\right) / \sqrt{r_D^2 + z_{D2}^2} \right], \dots\dots\dots (3.257)$$

where

$$r_D^2 = (x_D - x'_D)^2 + (y_D - y'_D)^2, \dots\dots\dots (3.258)$$

$$z_{D1} = z_D - z_{wD} - 2nh_D, \dots\dots\dots (3.259)$$

$$z_{D2} = z_D + z_{wD} - 2nh_D, \dots\dots\dots (3.260)$$

and

$$h_D = h\sqrt{k/k_z}/\ell. \dots\dots\dots (3.261)$$

The solution given in Eq. 3.257 is not very convenient for computational purposes. To obtain a computationally convenient form of the solution, we use the summation formula given by<sup>17,29</sup>

$$\sum_{n=-\infty}^{+\infty} \frac{\exp\left[-\sqrt{v}\sqrt{a^2 + (\xi - 2n\xi_e)^2}\right]}{\sqrt{a^2 + (\xi - 2n\xi_e)^2}} = \frac{1}{\xi_e} \left[ K_0(a\sqrt{v}) + 2 \sum_{n=1}^{\infty} K_0\left(a\sqrt{v + \frac{n^2\pi^2}{\xi_e^2}}\right) \cos n\pi \frac{\xi}{\xi_e} \right] \dots (3.262)$$

and recast Eq. 3.257 as

$$\overline{\Delta p} = \frac{\tilde{q}\mu}{2\pi k\ell h_D s} \left[ K_0(r_D\sqrt{u}) + 2 \sum_{n=1}^{\infty} K_0\left(r_D\sqrt{u + \frac{n^2\pi^2}{h_D^2}}\right) \cos n\pi \frac{z_D}{h_D} \cos n\pi \frac{z'_D}{h_D} \right] \dots\dots\dots (3.263)$$

The point-source solutions for infinite-slab reservoirs with constant pressure and mixed boundaries at the top and bottom are obtained in a similar manner<sup>17</sup> and are given in Table 3.6. The point-source solutions can be used with Eqs. 3.254 and 3.256 to generate the solutions for the other well geometries given in Table 3.6. For example, to generate the solution for a partially penetrating vertical line-source well of length  $h_w$  in an infinite-slab reservoir with impermeable slab boundaries, we integrate the right side of Eq. 3.263 from  $z_w - h_w / 2$  to  $z_w + h_w / 2$  with respect to  $z'$ , where  $z_w$  is the vertical coordinate of the midpoint of the open interval. If  $h_w = h$  (i.e., the well penetrates the entire thickness of the slab reservoir), then this procedure yields the solution for a fully penetrating vertical line-source well. The solution for a partially penetrating fracture of height  $h_f$  and half-length  $x_f$  is obtained if the point-source solution is integrated once with respect to  $z'$  from  $z_w - h_f / 2$  to  $z_w + h_f / 2$  and then with respect to  $x'$  from  $x_w - x_f$  to  $x_w + x_f$ , where  $x_w$  and  $z_w$  are the coordinates of the midpoint of the fracture. Similarly, the solution for a horizontal-line source well of length  $L_h$  is obtained by integrating the point-source solution with respect to  $x'$  from  $x_w - L_h / 2$  to  $x_w + L_h / 2$ , where  $x_w$  is the  $x$ -coordinate of the midpoint of the horizontal well.

**Solutions for Cylindrical Reservoir.** Solutions for cylindrical reservoirs may also be obtained by starting from the point-source solution in the Laplace transform domain. The Laplace domain solution for a point source located at  $r'_D, \theta', z'_D$  should satisfy the following diffusion equation in cylindrical coordinates.<sup>19</sup>

$$\frac{1}{r_D} \frac{d}{dr_D} \left( r_D \frac{d\overline{\Delta p}}{dr_D} \right) + \frac{1}{r_D^2} \frac{d^2\overline{\Delta p}}{d\theta^2} + \frac{d^2\overline{\Delta p}}{dz_D^2} - u\overline{\Delta p} = 0, \dots\dots\dots (3.264)$$

where

$$r_D = \sqrt{x_D^2 + y_D^2} \dots\dots\dots (3.265)$$

The point-source solution is also required to satisfy the following flux condition at the source location ( $r_D \rightarrow 0^+$ ,  $\theta = \theta'$ ,  $z_D = z'_D$ ):

$$\lim_{\varepsilon_D \rightarrow 0^+} \left( \lim_{r_D \rightarrow 0^+} \frac{2\pi k}{\mu \varepsilon_D} \varrho \int_{z'_D - \varepsilon_D/2}^{z'_D + \varepsilon_D/2} r_D \frac{d\overline{\Delta p}}{dr_D} dz'_D \right)_{\theta = \theta'} = -\frac{\tilde{q}}{s} \dots\dots\dots (3.266)$$

Assuming that the reservoir is bounded by a cylindrical surface at  $r_D = r_{eD}$  and by the parallel planes at  $z_D = 0$  and  $h_D$ , we should also impose the appropriate physical conditions at these boundaries.

We seek a point-source solution for a cylindrical reservoir in the following form:

$$\overline{\Delta p} = \overline{P} + \overline{Q} \dots\dots\dots (3.267)$$

In Eq. 3.267,  $\overline{P}$  is a solution of Eq. 3.264 that satisfies Eq. 3.266 and the boundary conditions at  $z_D = 0$  and  $h_D$ .  $\overline{P}$  may be chosen as one of the point-source solutions in an infinite-slab reservoir given in Table 3.6, depending on the conditions imposed at the boundaries at  $z_D = 0$  and  $h_D$ . If  $\overline{Q}$  is chosen such that it satisfies the boundary conditions at  $z_D = 0$  and  $h_D$ , its contribution to the flux vanishes at the source location, and  $\overline{P} + \overline{Q}$  satisfies the appropriate boundary condition at  $r_D = r_{eD}$ , then Eq. 3.267 should yield the point-source solution for a cylindrical reservoir with appropriate boundary conditions.

Consider the example of a closed cylindrical reservoir in which the boundary conditions are given by

$$\left( \frac{d\overline{\Delta p}}{dz_D} \right)_{z_D = 0, z_{eD}} = 0, \dots\dots\dots (3.268)$$

and

$$\left( \frac{d\overline{\Delta p}}{dr_D} \right)_{r_D = r_{eD}} = 0. \dots\dots\dots (3.269)$$

According to the boundary condition given by Eq. 3.268, we should choose  $\overline{P}$  as the point-source solution given in Table 3.6 (or by Eq. 3.263). Then, with the addition theorem for the Bessel function  $K_0(aR_D)$  given by<sup>14</sup>

$$K_0(aR_D) = \begin{cases} \sum_{k=-\infty}^{+\infty} I_k(ar_D)K_k(ar'_D) \cos k(\theta - \theta'); & \text{for } r_D < r'_D \\ \sum_{k=-\infty}^{+\infty} I_k(ar'_D)K_k(ar_D) \cos k(\theta - \theta'); & \text{for } r_D > r'_D \end{cases}, \dots\dots\dots (3.270)$$

where

$$R_D^2 = r_D^2 + r'^2_D - 2r_D r'_D \cos(\theta - \theta'), \dots\dots\dots (3.271)$$

we can write

$$\bar{P} = \frac{\tilde{q}\mu}{2\pi k\ell h_D s} \left\{ \sum_{k=-\infty}^{+\infty} I_k(\sqrt{ur_D}) K_k(\sqrt{ur'_D}) \cos k(\theta - \theta') + 2 \sum_{n=1}^{\infty} \cos n\pi \frac{z_D}{h_D} \cos n\pi \frac{z'_D}{h_D} \right. \\ \left. \times \left[ \sum_{k=-\infty}^{+\infty} I_k \left( \sqrt{u + \frac{n^2\pi^2}{h_D^2}} r_D \right) K_k \left( \sqrt{u + \frac{n^2\pi^2}{h_D^2}} r'_D \right) \cos k(\theta - \theta') \right] \right\} \dots\dots\dots (3.272)$$

for  $r_D < r'_D$ . If  $r_D > r'_D$ , we interchange  $r_D$  and  $r'_D$  in Eq. 3.272. If we choose  $\bar{Q}$  in Eq. 3.267 as

$$\bar{Q} = \frac{\tilde{q}\mu}{2\pi k\ell h_D s} \left\{ \sum_{k=-\infty}^{+\infty} a_k I_k(\sqrt{ur_D}) \cos k(\theta - \theta') + 2 \sum_{n=1}^{\infty} \cos n\pi \frac{z_D}{h_D} \cos n\pi \frac{z'_D}{h_D} \right. \\ \left. \times \left[ \sum_{k=-\infty}^{+\infty} b_k I_k \left( \sqrt{u + \frac{n^2\pi^2}{h_D^2}} r_D \right) \cos k(\theta - \theta') \right] \right\}, \dots\dots\dots (3.273)$$

where  $a_k$  and  $b_k$  are constants, then  $\bar{Q}$  satisfies the boundary condition given by Eq. 3.268, and the contribution of  $\bar{Q}$  to the flux at the source location vanishes. If we also choose the constants  $a_k$  and  $b_k$  in Eq. 3.273 as

$$a_k = -I_k(\sqrt{ur'_D}) K'_k(\sqrt{ur_{eD}}) / I'_k(\sqrt{ur_{eD}}) \dots\dots\dots (3.274)$$

and

$$b_k = -I_k \left( \sqrt{u + \frac{n^2\pi^2}{h_D^2}} r'_D \right) K'_k \left( \sqrt{u + \frac{n^2\pi^2}{h_D^2}} r_{eD} \right) / I'_k \left( \sqrt{u + \frac{n^2\pi^2}{h_D^2}} r_{eD} \right), \dots\dots\dots (3.275)$$

then  $\bar{\Delta p} = \bar{P} + \bar{Q}$  satisfies the impermeable boundary condition at  $r_D = r_{eD}$  given by Eq. 3.269. Thus, the point-source solution for a closed cylindrical reservoir is given by

$$\bar{\Delta p} = \frac{\tilde{q}\mu}{2\pi k\ell h_D s} \left\{ K_0(\sqrt{u}R_D) - \sum_{k=-\infty}^{+\infty} I_k(\sqrt{ur_D}) \frac{I_k(\sqrt{ur'_D}) K'_k(\sqrt{ur_{eD}})}{I'_k(\sqrt{ur_{eD}})} \cos k(\theta - \theta') \right. \\ \left. + 2 \sum_{n=1}^{\infty} \cos n\pi \frac{z_D}{h_D} \cos n\pi \frac{z'_D}{h_D} \left[ K_0 \left( \sqrt{u + \frac{n^2\pi^2}{h_D^2}} R_D \right) \right. \right. \\ \left. \left. - \sum_{k=-\infty}^{+\infty} I_k \left( \sqrt{u + \frac{n^2\pi^2}{h_D^2}} r_D \right) \frac{I_k \left( \sqrt{u + \frac{n^2\pi^2}{h_D^2}} r'_D \right) K'_k \left( \sqrt{u + \frac{n^2\pi^2}{h_D^2}} r_{eD} \right)}{I'_k \left( \sqrt{u + \frac{n^2\pi^2}{h_D^2}} r_{eD} \right)} \cos k(\theta - \theta') \right] \right\} \dots\dots\dots (3.276)$$

This solution procedure may be extended to the cases in which the boundaries are at constant pressure or of mixed type.<sup>19</sup> **Table 3.7** presents the point-source solutions for cylindrical reservoirs for all possible combinations of boundary conditions. Solutions for other source geometries in cylindrical reservoirs may be obtained by using the point-source solutions in **Table 3.7** in **Eq. 3.255** (or **Eq. 3.256**).

**Example 3.8** Consider a partially penetrating, uniform-flux fracture of height  $h_f$  and half-length  $x_f$  in an isotropic and closed cylindrical reservoir. The center of the fracture is at  $r' = 0$ ,  $\theta' = 0$ ,  $z' = z_w$ , and the fracture tips extend from  $(r' = x_f, \theta = \alpha + \pi)$  to  $(r' = x_f, \theta = \alpha)$ .

*Solution.* **Fig. 3.15** shows the geometry of the fracture/reservoir system considered in this example. The solution for this problem is obtained by first generating a partially penetrating line source and then using this line-source solution to generate the plane source. The solution for a partially penetrating line source at  $r'_D, \theta', z_w$  is obtained by integrating the corresponding point-source solution given in **Table 3.7** with respect to  $z'$  from  $z_w - h_f / 2$  to  $z_w + h_f / 2$  and is given by

$$\begin{aligned} \overline{\Delta p} = & \frac{\tilde{q}u h_f}{2\pi k \ell h_D s} \left\{ K_0(\sqrt{u}R_D) - \sum_{k=-\infty}^{+\infty} I_k(\sqrt{u}r_D) \frac{I_k(\sqrt{u}r'_D)K'_k(\sqrt{u}r_eD)}{I'_k(\sqrt{u}r_eD)} \cos k(\theta - \theta') \right. \\ & + \frac{4h}{\pi h_f} \sum_{n=1}^{\infty} \frac{1}{n} \sin n\pi \frac{h_f}{2h} \cos n\pi \frac{z_D}{h_D} \cos n\pi \frac{z_wD}{h_D} \\ & \left. \times \left[ K_0(\varepsilon_n R_D) - \sum_{k=-\infty}^{+\infty} I_k(\varepsilon_n r_D) \frac{I_k(\varepsilon_n r'_D)K'_k(\varepsilon_n r_eD)}{I'_k(\varepsilon_n r_eD)} \cos k(\theta - \theta') \right] \right\} \dots\dots\dots (3.277) \end{aligned}$$

To generate the solution for a partially penetrating plane source that represents the fracture, the partially penetrating line-source solution given in **Eq. 3.277** is integrated with respect to  $r'$  from 0 to  $x_f$  with  $\theta' = \alpha + \pi$  in the third quadrant and with  $\theta' = \alpha$  in the first quadrant. This procedure yields

$$\begin{aligned} \overline{\Delta p} = & \frac{\tilde{q}u h_f}{2\pi k h_D s} \left\{ \int_0^{x_f/\ell} K_0[\sqrt{u}\sqrt{r_D^2 + r'^2_D - 2r_D r'_D \cos(\theta - \alpha)}] dr'_D \right. \\ & + \int_0^{x_f/\ell} K_0[\sqrt{u}\sqrt{r_D^2 + r'^2_D - 2r_D r'_D \cos(\theta - \alpha - \pi)}] dr'_D \\ & - \sum_{k=-\infty}^{+\infty} [\cos k(\theta - \alpha) + \cos k(\theta - \alpha - \pi)] \frac{I_k(\sqrt{u}r_D)K'_k(\sqrt{u}r_eD)}{I'_k(\sqrt{u}r_eD)} \int_0^{x_f/\ell} I_k(\sqrt{u}r'_D) dr'_D \\ & + \frac{4h}{\pi h_f} \sum_{n=1}^{\infty} \frac{1}{n} \sin n\pi \frac{h_f}{2h} \cos n\pi \frac{z_D}{h_D} \cos n\pi \frac{z_wD}{h_D} \\ & \left. \times \left[ \int_0^{x_f/\ell} K_0[\varepsilon_n \sqrt{r_D^2 + r'^2_D - 2r_D r'_D \cos(\theta - \alpha)}] dr'_D \right. \right. \end{aligned}$$

**TABLE 3.7—LAPLACE DOMAIN SOLUTIONS FOR POINT-SOURCE WELLS  
IN CYLINDRICAL RESERVOIRS  
(after Raghavan and Ozkan<sup>19</sup>)**

Impermeable Boundary at $r_D = r_{eD}$	
$q = \tilde{q}, R_D^2 = r_D^2 + r_D'^2 - 2r_D r_D' \cos(\theta - \theta'), \varepsilon_n = \sqrt{u + n^2 \pi^2 / h_D^2}, \varepsilon_{2n-1} = \sqrt{u + (2n-1)^2 \pi^2 / h_D^2}$	
Condition	Pressure Distribution, $\bar{\Delta p}$
$\left. \frac{\partial \bar{\Delta p}}{\partial z_D} \right _{z_D=0, h_D} = 0$	$\frac{\tilde{q}\mu}{2\pi k \ell h_D s} \left\{ K_0(R_D \sqrt{u}) - \sum_{k=-\infty}^{+\infty} I_k(r_D \sqrt{u}) \frac{I_k(r_D' \sqrt{u}) K_k'(r_{eD} \sqrt{u})}{I_k'(r_{eD} \sqrt{u})} \cos k(\theta - \theta') \right.$ $\left. + 2 \sum_{n=1}^{\infty} \cos n\pi \frac{z_D}{h_D} \cos n\pi \frac{z_D'}{h_D} \left[ K_0(R_D \varepsilon_n) - \sum_{k=-\infty}^{+\infty} I_k(r_D \varepsilon_n) \frac{I_k(r_D' \varepsilon_n) K_k'(r_{eD} \varepsilon_n)}{I_k'(r_{eD} \varepsilon_n)} \cos k(\theta - \theta') \right] \right\}$
$\bar{\Delta p} \Big _{z_D=0, h_D} = 0$	$\frac{\tilde{q}\mu}{\pi k \ell h_D s} \sum_{n=1}^{\infty} \sin n\pi \frac{z_D}{h_D} \sin n\pi \frac{z_D'}{h_D} \left[ K_0(R_D \varepsilon_n) - \sum_{k=-\infty}^{+\infty} I_k(r_D \varepsilon_n) \frac{I_k(r_D' \varepsilon_n) K_k'(r_{eD} \varepsilon_n)}{I_k'(r_{eD} \varepsilon_n)} \cos k(\theta - \theta') \right]$
$\left. \frac{\partial \bar{\Delta p}}{\partial z_D} \right _{z_D=0} = 0$ and $\bar{\Delta p} \Big _{z_D=h_D} = 0$	$\frac{\tilde{q}\mu}{\pi k \ell h_D s} \sum_{n=1}^{\infty} \cos(2n-1) \frac{\pi z_D}{2h_D} \cos(2n-1) \frac{\pi z_D'}{2h_D}$ $\times \left[ K_0(R_D \varepsilon_{2n-1}) - \sum_{k=-\infty}^{+\infty} I_k(r_D \varepsilon_{2n-1}) \frac{I_k(r_D' \varepsilon_{2n-1}) K_k'(r_{eD} \varepsilon_{2n-1})}{I_k'(r_{eD} \varepsilon_{2n-1})} \cos k(\theta - \theta') \right]$
Constant-Pressure Boundary at $r_D = r_{eD}$	
$q = \tilde{q}, R_D^2 = r_D^2 + r_D'^2 - 2r_D r_D' \cos(\theta - \theta'), \varepsilon_n = \sqrt{u + n^2 \pi^2 / h_D^2}, \varepsilon_{2n-1} = \sqrt{u + (2n-1)^2 \pi^2 / h_D^2}$	
Condition	Pressure Distribution, $\bar{\Delta p}$
$\left. \frac{\partial \bar{\Delta p}}{\partial z_D} \right _{z_D=0, h_D} = 0$	$\frac{\tilde{q}\mu}{2\pi k \ell h_D s} \left\{ K_0(R_D \sqrt{u}) - \sum_{k=-\infty}^{+\infty} I_k(r_D \sqrt{u}) \frac{I_k(r_D' \sqrt{u}) K_k'(r_{eD} \sqrt{u})}{I_k(r_{eD} \sqrt{u})} \cos k(\theta - \theta') \right.$ $\left. + 2 \sum_{n=1}^{\infty} \cos n\pi \frac{z_D}{h_D} \cos n\pi \frac{z_D'}{h_D} \left[ K_0(R_D \varepsilon_n) - \sum_{k=-\infty}^{+\infty} I_k(r_D \varepsilon_n) \frac{I_k(r_D' \varepsilon_n) K_k'(r_{eD} \varepsilon_n)}{I_k(r_{eD} \varepsilon_n)} \cos k(\theta - \theta') \right] \right\}$
$\bar{\Delta p} \Big _{z_D=0, h_D} = 0$	$\frac{\tilde{q}\mu}{\pi k \ell h_D s} \sum_{n=1}^{\infty} \sin n\pi \frac{z_D}{h_D} \sin n\pi \frac{z_D'}{h_D} \left[ K_0(R_D \varepsilon_n) - \sum_{k=-\infty}^{+\infty} I_k(r_D \varepsilon_n) \frac{I_k(r_D' \varepsilon_n) K_k'(r_{eD} \varepsilon_n)}{I_k(r_{eD} \varepsilon_n)} \cos k(\theta - \theta') \right]$
$\left. \frac{\partial \bar{\Delta p}}{\partial z_D} \right _{z_D=0} = 0$ and $\bar{\Delta p} \Big _{z_D=h_D} = 0$	$\frac{\tilde{q}\mu}{\pi k \ell h_D s} \sum_{n=1}^{\infty} \cos(2n-1) \frac{\pi z_D}{2h_D} \cos(2n-1) \frac{\pi z_D'}{2h_D}$ $\times \left[ K_0(R_D \varepsilon_{2n-1}) - \sum_{k=-\infty}^{+\infty} I_k(r_D \varepsilon_{2n-1}) \frac{I_k(r_D' \varepsilon_{2n-1}) K_k'(r_{eD} \varepsilon_{2n-1})}{I_k(r_{eD} \varepsilon_{2n-1})} \cos k(\theta - \theta') \right]$

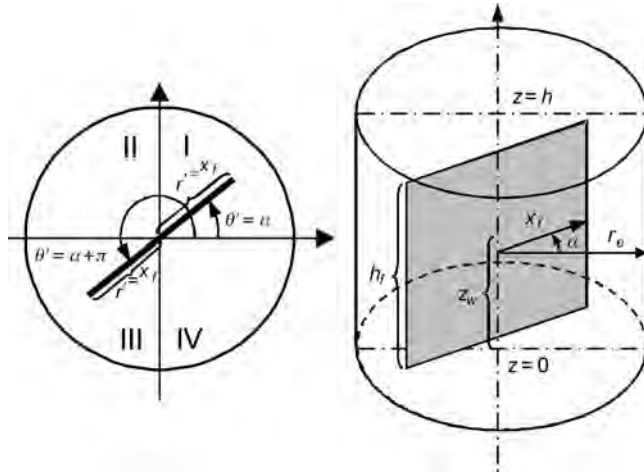


Fig. 3.15—Geometry of a partially penetrating fracture in a closed cylindrical reservoir (Example 3.8).

$$\begin{aligned}
 & + \int_0^{x_f/\ell} K_0 \left[ \epsilon_n \sqrt{r_D^2 + r'^2_D - 2r_D r'_D \cos(\theta - \alpha - \pi)} \right] dr'_D \\
 & - \sum_{k=-\infty}^{+\infty} \left[ \cos k(\theta - \alpha) + \cos k(\theta - \alpha - \pi) \right] \frac{I_k(\epsilon_n r_D) K'_k(\epsilon_n r_e D)}{I'_k(\epsilon_n r_e D)} \int_0^{x_f/\ell} I_k(\epsilon_n r'_D) dr'_D \Bigg\} \dots\dots (3.278)
 \end{aligned}$$

It is possible to obtain an alternate representation of the solution given in Eq. 3.278. With the addition theorem of the Bessel function  $K_0(x)$  given by Eq. 3.270, the solution in Eq. 3.277 may be written as

$$\begin{aligned}
 \overline{\Delta p} = \frac{\tilde{q}\mu h_f}{2\pi k \ell h_D s} & \left[ \sum_{k=-\infty}^{+\infty} F_k(\sqrt{u}) \cos k(\theta - \theta') + \frac{4h}{\pi h_f} \sum_{n=1}^{\infty} \frac{1}{n} \sin n\pi \frac{h_f}{2h} \cos n\pi \frac{z_D}{h_D} \cos n\pi \frac{z_w D}{h_D} \right. \\
 & \left. \times \sum_{k=-\infty}^{+\infty} F_k(\epsilon_n) \cos k(\theta - \theta') \right], \dots\dots\dots (3.279)
 \end{aligned}$$

where

$$F_k(\lambda) = \begin{cases} F_k(\lambda, r'_D, r_D) & \text{for } r_D \geq r'_D \\ F_k(\lambda, r_D, r'_D) & \text{for } r_D \leq r'_D \end{cases} \dots\dots\dots (3.280)$$

and

$$F_k(\lambda, a, b) = I_k(a\lambda) \left\{ \left[ K_k(b\lambda) I'_k(r_e D \lambda) - I_k(b\lambda) K'_k(r_e D \lambda) \right] / I'_k(r_e D \lambda) \right\} \dots\dots\dots (3.281)$$

The integration of the partially penetrating vertical well solution given in Eq. 3.279 with respect to  $r'$  from 0 to  $x_f$  (with  $\theta' = \alpha + \pi$  in the third quadrant and with  $\theta' = \alpha$  in the first quadrant) yields the following alternative form of the partially penetrating fracture solution:

$$\begin{aligned} \overline{\Delta p} = \frac{\tilde{q}\mu h_f}{2\pi k h_D s} & \left\{ \sum_{k=-\infty}^{+\infty} \left[ \cos k(\theta - \alpha - \pi) \int_0^{x_f/\ell} F_k(\sqrt{u}) dr'_D + \cos k(\theta - \alpha) \int_0^{x_f/\ell} F_k(\sqrt{u}) dr'_D \right] \right. \\ & + \frac{4h}{\pi h_f} \sum_{n=1}^{\infty} \frac{1}{n} \sin n\pi \frac{h_f}{2h} \cos n\pi \frac{z_D}{h_D} \cos n\pi \frac{z_w D}{h_D} \\ & \left. \times \sum_{k=-\infty}^{+\infty} \left[ \cos k(\theta - \alpha - \pi) \int_0^{x_f/\ell} F_k(\varepsilon_n) dr'_D + \cos k(\theta - \alpha) \int_0^{x_f/\ell} F_k(\varepsilon_n) dr'_D \right] \right\}, \dots\dots\dots (3.282) \end{aligned}$$

where

$$\int_0^{\beta} F_k(\lambda) dr'_D = \begin{cases} \int_0^{\beta} F_k(\lambda, r'_D, r_D) dr'_D & \text{for } r_D \geq x_f/\ell \\ \int_0^{r_D} F_k(\lambda, r'_D, r_D) dr'_D + \int_{r_D}^{\beta} F_k(\lambda, r_D, r'_D) dr'_D & \text{for } r_D \leq x_f/\ell \end{cases} \dots\dots\dots (3.283)$$

**Example 3.9** Consider a uniform-flux, horizontal line-source well of length  $L_h$  in an isotropic and closed cylindrical reservoir. The well extends from ( $r' = L_h/2, \theta = \alpha + \pi$ ) to ( $r' = L_h/2, \theta = \alpha$ ), and the center of the well is at  $r' = 0, \theta' = 0, z' = z_w$ .

*Solution.* The solution for a horizontal line-source well in a closed cylindrical reservoir is obtained by integrating the corresponding point-source solution in Table 3.7 with respect to  $r'$  from 0 to  $L_h/2$  with  $\theta' = \alpha + \pi$  in the third quadrant and with  $\theta' = \alpha$  in the first quadrant. The final form of the solution is given by

$$\begin{aligned} \overline{\Delta p} = \frac{\tilde{q}\mu}{2\pi k h_D s} & \left\{ \int_0^{L_h/(2\ell)} K_0[\sqrt{u}\sqrt{r_D^2 + r'^2_D - 2r_D r'_D \cos(\theta - \alpha)}] dr'_D \right. \\ & + \int_0^{L_h/(2\ell)} K_0[\sqrt{u}\sqrt{r_D^2 + r'^2_D - 2r_D r'_D \cos(\theta - \alpha - \pi)}] dr'_D \\ & - \sum_{k=-\infty}^{+\infty} [\cos k(\theta - \alpha) + \cos k(\theta - \alpha - \pi)] \frac{I_k(\sqrt{u}r_D) K'_k(\sqrt{u}r_{eD})}{I'_k(\sqrt{u}r_{eD})} \int_0^{L_h/(2\ell)} I_k(\sqrt{u}r'_D) dr'_D \\ & \left. + 2 \sum_{n=1}^{\infty} \cos n\pi \frac{z_D}{h_D} \cos n\pi \frac{z_w D}{h_D} \right\} \end{aligned}$$



$$\begin{aligned}
 & \times \left[ \int_0^{L_h/(2\ell)} K_0 \left[ \varepsilon_n \sqrt{r_D^2 + r'^2_D - 2r_D r'_D \cos(\theta - \alpha)} \right] dr'_D \right. \\
 & \left. + \int_0^{L_h/(2\ell)} K_0 \left[ \varepsilon_n \sqrt{r_D^2 + r'^2_D - 2r_D r'_D \cos(\theta - \alpha - \pi)} \right] dr'_D \right. \\
 & \left. - \sum_{k=-\infty}^{+\infty} \left[ \cos k(\theta - \alpha) + \cos k(\theta - \alpha - \pi) \right] \frac{I_k(\varepsilon_n r_D) K'_k(\varepsilon_n r_{eD})}{I'_k(\varepsilon_n r_{eD})} \int_0^{L_h/(2\ell)} I_k(\varepsilon_n r'_D) dr'_D \right] \dots \dots (3.284)
 \end{aligned}$$

**Solutions for Rectangular Parallelepiped Reservoir.** Solutions for rectangular parallelepiped reservoirs may also be obtained by starting from the point-source solution in the Laplace transform domain in an infinite reservoir and using the method of images to generate the effects of the planar boundaries. Although the formal procedure to obtain the solution is fairly easy, the use of the method of images in three directions ( $x, y, z$ ) yields triple infinite Fourier series, which may pose computational inconveniences. As an example, the solution for a continuous point source located at  $x', y', z'$  in a rectangular porous medium occupying the region  $0 < x < x_e, 0 < y < y_e,$  and  $0 < z < h$  is obtained by applying the method of images to the point-source solution given by Eq. 3.252:<sup>19,29</sup>

$$\begin{aligned}
 \overline{\Delta p} = \frac{\tilde{q}\mu}{4\pi k \ell s} & \sum_{k=-\infty}^{+\infty} \sum_{m=-\infty}^{+\infty} \sum_{n=-\infty}^{+\infty} (S_{1,1,1} + S_{2,1,1} + S_{1,2,1} \\
 & + S_{2,2,1} + S_{1,1,2} + S_{2,1,2} + S_{1,2,2} + S_{2,2,2}), \dots \dots \dots (3.285)
 \end{aligned}$$

where

$$\begin{aligned}
 S_{i,j,\ell} = \frac{\exp \left[ -\sqrt{u} \sqrt{(\tilde{x}_{Di} - 2kx_{eD})^2 + (\tilde{y}_{Dj} - 2my_{eD})^2 + (\tilde{z}_{D\ell} - 2nh_D)^2} \right]}{\sqrt{(\tilde{x}_{Di} - 2kx_{eD})^2 + (\tilde{y}_{Dj} - 2my_{eD})^2 + (\tilde{z}_{D\ell} - 2nh_D)^2}} \\
 \text{for } i, j, \ell = 1 \text{ or } 2, \dots \dots \dots (3.286)
 \end{aligned}$$

and

$$\tilde{x}_{Ds} = x_D + (-1)^s x_{wD} \quad \text{for } s = 1 \text{ or } 2, \dots \dots \dots (3.287)$$

$$\tilde{y}_{Ds} = y_D + (-1)^s y_{wD} \quad \text{for } s = 1 \text{ or } 2, \dots \dots \dots (3.288)$$

$$\tilde{z}_{Ds} = z_D + (-1)^s z_{wD} \quad \text{for } s = 1 \text{ or } 2, \dots \dots \dots (3.289)$$

Ref. 29 shows that the triple infinite sums in Eq. 3.285 may be reduced to double infinite sums with

$$\begin{aligned}
 \sum_{k=-\infty}^{+\infty} \sum_{m=-\infty}^{+\infty} \sum_{n=-\infty}^{+\infty} S = \frac{\pi}{2x_{eD}h_D} & \left\{ \frac{\cosh \sqrt{u}(y_{eD} - |\tilde{y}_D|)}{\sqrt{u} \sinh \sqrt{u}y_{eD}} \right. \\
 + 2 \sum_{k=1}^{\infty} \cos k\pi \frac{\tilde{x}_D}{x_{eD}} & \frac{\cosh \sqrt{u + \frac{\pi^2 k^2}{x_{eD}^2}}(y_{eD} - |\tilde{y}_D|)}{\sqrt{u + \frac{\pi^2 k^2}{x_{eD}^2}} \sinh \sqrt{u + \frac{\pi^2 k^2}{x_{eD}^2}}y_{eD}} \\
 + 2 \sum_{n=1}^{\infty} \cos n\pi \frac{\tilde{z}_D}{h_D} & \left[ \frac{\cosh \sqrt{u + \frac{\pi^2 n^2}{h_D^2}}(y_{eD} - |\tilde{y}_D|)}{\sqrt{u + \frac{\pi^2 n^2}{h_D^2}} \sinh \sqrt{u + \frac{\pi^2 n^2}{h_D^2}}y_{eD}} \right. \\
 \left. + 2 \sum_{k=1}^{\infty} \cos k\pi \frac{\tilde{x}_D}{x_{eD}} \frac{\cosh \sqrt{u + \frac{\pi^2 n^2}{h_D^2} + \frac{\pi^2 k^2}{x_{eD}^2}}(y_{eD} - |\tilde{y}_D|)}{\sqrt{u + \frac{\pi^2 n^2}{h_D^2} + \frac{\pi^2 k^2}{x_{eD}^2}} \sinh \sqrt{u + \frac{\pi^2 n^2}{h_D^2} + \frac{\pi^2 k^2}{x_{eD}^2}}y_{eD}} \right] & \left. \right\}, \dots\dots\dots (3.290)
 \end{aligned}$$

where

$$S = \frac{\exp \left[ -\sqrt{u} \sqrt{(\tilde{x}_D - 2kx_{eD})^2 + (\tilde{y}_D - 2my_{eD})^2 + (\tilde{z}_D - 2nh_D)^2} \right]}{\sqrt{(\tilde{x}_D - 2kx_{eD})^2 + (\tilde{y}_D - 2my_{eD})^2 + (\tilde{z}_D - 2nh_D)^2}} \dots\dots\dots (3.291)$$

The resulting continuous point-source solution for a closed rectangular reservoir is given by

$$\begin{aligned}
 \overline{\Delta p} = \frac{\tilde{q}\mu}{2k\ell x_{eD}s} & \left[ \frac{\cosh \sqrt{u}\tilde{y}_{D1} + \cosh \sqrt{u}\tilde{y}_{D2}}{\sqrt{u} \sinh \sqrt{u}y_{eD}} + 2 \sum_{k=1}^{\infty} \cos k\pi \frac{x_D}{x_{eD}} \cos k\pi \frac{x'_D}{x_{eD}} \right. \\
 \times \frac{\cosh \varepsilon_k \tilde{y}_{D1} + \cosh \varepsilon_k \tilde{y}_{D2}}{\varepsilon_k \sinh \varepsilon_k y_{eD}} & + 2 \sum_{n=1}^{\infty} \cos n\pi \frac{z_D}{h_D} \cos n\pi \frac{z'_D}{h_D} \left( \frac{\cosh \varepsilon_n \tilde{y}_{D1} + \cosh \varepsilon_n \tilde{y}_{D2}}{\varepsilon_n \sinh \varepsilon_n y_{eD}} \right. \\
 \left. + 2 \sum_{k=1}^{\infty} \cos k\pi \frac{x_D}{x_{eD}} \cos k\pi \frac{x'_D}{x_{eD}} \frac{\cosh \varepsilon_{k,n} \tilde{y}_{D1} + \cosh \varepsilon_{k,n} \tilde{y}_{D2}}{\varepsilon_{k,n} \sinh \varepsilon_{k,n} y_{eD}} \right) & \left. \right], \dots\dots\dots (3.292)
 \end{aligned}$$

where

$$\tilde{y}_{D1} = y_{eD} - |y_D - y'_D|, \dots\dots\dots (3.293)$$

$$\tilde{y}_{D2} = y_{eD} - (y_D + y'_D), \dots\dots\dots (3.294)$$

$$\varepsilon_n = \sqrt{u + n^2\pi^2/h_D^2}, \dots\dots\dots (3.295)$$

$$\varepsilon_k = \sqrt{u + k^2 \pi^2 / x_e^2} \dots\dots\dots (3.296)$$

and

$$\varepsilon_{k,n} = \sqrt{u + k^2 \pi^2 / x_e^2 + n^2 \pi^2 / h_D^2} \dots\dots\dots (3.297)$$

Following a procedure similar to the one explained here, it is possible to derive the point-source solutions in rectangular parallelepiped reservoirs for different combinations of boundary conditions.<sup>17,29</sup> **Table 3.8** gives these solutions, which may be used to derive the solutions for the other source geometries with Eq. 3.255 (or Eq. 3.256). **Examples 3.10** and **3.11** demonstrate the derivation of the solutions for the other source geometries in rectangular reservoirs.

**Example 3.10** Consider a fully penetrating vertical fracture of half-length  $x_f$  located at  $x' = x_w$  and  $y' = y_w$  in a closed rectangular reservoir.

*Solution.* Assuming uniform-flux distribution along the fracture surface, the solution for this problem is obtained by integrating the corresponding point-source solution in **Table 3.8**, first with respect to  $z'$  from 0 to  $h$  and then with respect to  $x'$  from  $x_w - x_f$  to  $x_w + x_f$ . The result is

$$\begin{aligned} \overline{\Delta p} = & \frac{\tilde{q}\mu h x_f}{k\ell x_e h_D s} \left( \frac{\cosh \sqrt{u} \tilde{y}_{D1} + \cosh \sqrt{u} \tilde{y}_{D2}}{\sqrt{u} \sinh \sqrt{u} y_{eD}} \right. \\ & \left. + \frac{2x_e}{\pi x_f} \sum_{k=1}^{\infty} \frac{1}{k} \sin k\pi \frac{x_f}{x_e} \cos k\pi \frac{x_w}{x_e} \cos k\pi \frac{x}{x_e} \frac{\cosh \varepsilon_k \tilde{y}_{D1} + \cosh \varepsilon_k \tilde{y}_{D2}}{\varepsilon_k \sinh \varepsilon_k y_{eD}} \right), \dots\dots\dots (3.298) \end{aligned}$$

where  $\tilde{y}_{D1}$ ,  $\tilde{y}_{D2}$ , and  $\varepsilon_k$  are given respectively by **Eqs. 3.293**, **3.294**, and **3.296**.

**Example 3.11** Consider a horizontal well of length  $L_h$  in the  $x$ -direction located at  $x' = x_w$ ,  $y' = y_w$ , and  $z' = z_w$  in a closed rectangular reservoir.

*Solution.* The solution for a horizontal line-source well is obtained by integrating the corresponding point-source solution in **Table 3.8**, with respect to  $x'$  from  $x_w - L_h / 2$  to  $x_w + L_h / 2$ , and is given by

$$\overline{\Delta p} = \overline{\Delta p}_1 + \overline{\Delta p}_2, \dots\dots\dots (3.299)$$

where

$$\begin{aligned} \overline{\Delta p}_1 = & \frac{\tilde{q}\mu L_h}{2k\ell x_e h_D s} \left( \frac{\cosh \sqrt{u} \tilde{y}_{D1} + \cosh \sqrt{u} \tilde{y}_{D2}}{\sqrt{u} \sinh \sqrt{u} y_{eD}} \right. \\ & \left. + \frac{4x_e}{\pi L_h} \sum_{k=1}^{\infty} \frac{1}{k} \sin k\pi \frac{L_h}{2x_e} \cos k\pi \frac{x_w}{x_e} \cos k\pi \frac{x}{x_e} \frac{\cosh \varepsilon_k \tilde{y}_{D1} + \cosh \varepsilon_k \tilde{y}_{D2}}{\varepsilon_k \sinh \varepsilon_k y_{eD}} \right) \dots\dots\dots (3.300) \end{aligned}$$

and

$$\overline{\Delta p}_2 = \frac{2\tilde{q}\mu L_h}{2k\ell x_e h_D s} \left[ \sum_{n=1}^{\infty} \cos n\pi \frac{z_D}{h_D} \cos n\pi \frac{z_w}{h_D} \left( \frac{\cosh \varepsilon_n \tilde{y}_{D1} + \cosh \varepsilon_n \tilde{y}_{D2}}{\varepsilon_n \sinh \varepsilon_n y_{eD}} \right) \right]$$

**TABLE 3.8—LAPLACE DOMAIN SOLUTIONS FOR POINT-SOURCE WELLS IN PARALLELEPIPED RESERVOIRS<sup>17</sup> (after Ozkan<sup>27</sup>)**

Impermeable Boundaries at  $z_D = 0$  and  $z_D = h_D$

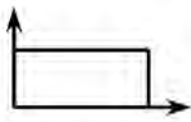
$$q = \tilde{q}, \tilde{y}_{D1} = y_{eD} - |y_D - y'_D|, \tilde{y}_{D2} = y_{eD} - (y_D + y'_D)$$

$$\varepsilon_n = \sqrt{u + n^2 \pi^2 / h_D^2}, \varepsilon_k = \sqrt{u + k^2 \pi^2 / x_{eD}^2}, \varepsilon_{k,n} = \sqrt{u + k^2 \pi^2 / x_{eD}^2 + n^2 \pi^2 / h_D^2}$$

$$\varepsilon_{2k-1} = \sqrt{u + (2k-1)^2 \pi^2 / x_{eD}^2}, \varepsilon_{2k-1,n} = \sqrt{u + (2k-1)^2 \pi^2 / x_{eD}^2 + n^2 \pi^2 / h_D^2}$$

Areal View

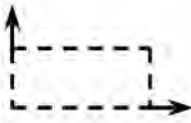
Pressure Distribution,  $\bar{\Delta p}$



$$\frac{\tilde{q}\mu}{2k\ell x_{eD} s} \left[ \frac{\cosh\sqrt{u}\tilde{y}_{D1} + \cosh\sqrt{u}\tilde{y}_{D2}}{\sqrt{u} \sinh\sqrt{u}y_{eD}} + 2 \sum_{k=1}^{\infty} \cos k\pi \frac{x_D}{x_{eD}} \cos k\pi \frac{x'_D}{x_{eD}} \right.$$

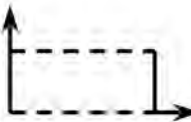
$$\times \frac{\cosh\varepsilon_k \tilde{y}_{D1} + \cosh\varepsilon_k \tilde{y}_{D2}}{\varepsilon_k \sinh\varepsilon_k y_{eD}} + 2 \sum_{n=1}^{\infty} \cos n\pi \frac{z_D}{h_D} \cos n\pi \frac{z'_D}{h_D} \left( \frac{\cosh\varepsilon_n \tilde{y}_{D1} + \cosh\varepsilon_n \tilde{y}_{D2}}{\varepsilon_n \sinh\varepsilon_n y_{eD}} \right.$$

$$\left. \left. + 2 \sum_{k=1}^{\infty} \cos k\pi \frac{x_D}{x_{eD}} \cos k\pi \frac{x'_D}{x_{eD}} \frac{\cosh\varepsilon_{k,n} \tilde{y}_{D1} + \cosh\varepsilon_{k,n} \tilde{y}_{D2}}{\varepsilon_{k,n} \sinh\varepsilon_{k,n} y_{eD}} \right) \right]$$



$$\frac{\tilde{q}\mu}{k\ell x_{eD} h_D s} \left( \sum_{k=1}^{\infty} \sin k\pi \frac{x_D}{x_{eD}} \sin k\pi \frac{x'_D}{x_{eD}} \frac{\cosh\varepsilon_k \tilde{y}_{D1} - \cosh\varepsilon_k \tilde{y}_{D2}}{\varepsilon_k \sinh\varepsilon_k y_{eD}} \right.$$

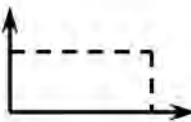
$$\left. + 2 \sum_{n=1}^{\infty} \cos n\pi \frac{z_D}{h_D} \cos n\pi \frac{z'_D}{h_D} \sum_{k=1}^{\infty} \sin k\pi \frac{x_D}{x_{eD}} \sin k\pi \frac{x'_D}{x_{eD}} \frac{\cosh\varepsilon_{k,n} \tilde{y}_{D1} - \cosh\varepsilon_{k,n} \tilde{y}_{D2}}{\varepsilon_{k,n} \sinh\varepsilon_{k,n} y_{eD}} \right)$$



$$\frac{\tilde{q}\mu}{2k\ell x_{eD} h_D s} \left[ \frac{\cosh\sqrt{u}\tilde{y}_{D1} + \cosh\sqrt{u}\tilde{y}_{D2}}{\sqrt{u} \sinh\sqrt{u}y_{eD}} + 2 \sum_{k=1}^{\infty} \cos k\pi \frac{x_D}{x_{eD}} \cos k\pi \frac{x'_D}{x_{eD}} \right.$$

$$\times \frac{\cosh\varepsilon_k \tilde{y}_{D1} - \cosh\varepsilon_k \tilde{y}_{D2}}{\varepsilon_k \sinh\varepsilon_k y_{eD}} + 2 \sum_{n=1}^{\infty} \cos n\pi \frac{z_D}{h_D} \cos n\pi \frac{z'_D}{h_D} \left( \frac{\cosh\varepsilon_n \tilde{y}_{D1} - \cosh\varepsilon_n \tilde{y}_{D2}}{\varepsilon_n \sinh\varepsilon_n y_{eD}} \right.$$

$$\left. \left. + 2 \sum_{k=1}^{\infty} \cos k\pi \frac{x_D}{x_{eD}} \cos k\pi \frac{x'_D}{x_{eD}} \frac{\cosh\varepsilon_{k,n} \tilde{y}_{D1} - \cosh\varepsilon_{k,n} \tilde{y}_{D2}}{\varepsilon_{k,n} \sinh\varepsilon_{k,n} y_{eD}} \right) \right]$$



$$\frac{\tilde{q}\mu}{k\ell x_{eD} h_D s} \left[ \sum_{k=1}^{\infty} \cos(2k-1) \frac{\pi x_D}{2x_{eD}} \cos(2k-1) \frac{\pi x'_D}{2x_{eD}} \left( \frac{\sinh\varepsilon_{2k-1} \tilde{y}_{D1} + \sinh\varepsilon_{2k-1} \tilde{y}_{D2}}{\varepsilon_{2k-1} \cosh\varepsilon_{2k-1} y_{eD}} \right. \right.$$

$$\left. \left. + 2 \sum_{n=1}^{\infty} \cos n\pi \frac{z_D}{h_D} \cos n\pi \frac{z'_D}{h_D} \frac{\sinh\varepsilon_{2k-1,n} \tilde{y}_{D1} + \sinh\varepsilon_{2k-1,n} \tilde{y}_{D2}}{\varepsilon_{2k-1,n} \cosh\varepsilon_{2k-1,n} y_{eD}} \right) \right]$$



$$\frac{\tilde{q}\mu}{k\ell x_{eD} h_D s} \left[ \sum_{k=1}^{\infty} \cos(2k-1) \frac{\pi x_D}{2x_{eD}} \cos(2k-1) \frac{\pi x'_D}{2x_{eD}} \left( \frac{\cosh\varepsilon_{2k-1} \tilde{y}_{D1} + \cosh\varepsilon_{2k-1} \tilde{y}_{D2}}{\varepsilon_{2k-1} \sinh\varepsilon_{2k-1} y_{eD}} \right. \right.$$

$$\left. \left. + 2 \sum_{n=1}^{\infty} \cos n\pi \frac{z_D}{h_D} \cos n\pi \frac{z'_D}{h_D} \frac{\cosh\varepsilon_{2k-1,n} \tilde{y}_{D1} + \cosh\varepsilon_{2k-1,n} \tilde{y}_{D2}}{\varepsilon_{2k-1,n} \sinh\varepsilon_{2k-1,n} y_{eD}} \right) \right]$$

**TABLE 3.8—LAPLACE DOMAIN SOLUTIONS FOR POINT-SOURCE WELLS IN PARALLELEPIPED RESERVOIRS<sup>17</sup> (after Ozkan<sup>27</sup>) (continued)**

Impermeable Boundaries at  $z_D = 0$  and  $z_D = h_D$

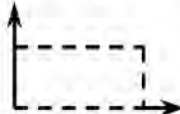
$$q = \tilde{q}, \tilde{y}_{D1} = y_{eD} - |y_D - y'_D|, \tilde{y}_{D2} = y_{eD} - (y_D + y'_D),$$

$$\varepsilon_n = \sqrt{u + n^2 \pi^2 / h_D^2}, \varepsilon_k = \sqrt{u + k^2 \pi^2 / x_{eD}^2}, \varepsilon_{k,n} = \sqrt{u + k^2 \pi^2 / x_{eD}^2 + n^2 \pi^2 / h_D^2},$$

$$\varepsilon_{2k-1} = \sqrt{u + (2k-1)^2 \pi^2 / x_{eD}^2}, \varepsilon_{2k-1,n} = \sqrt{u + (2k-1)^2 \pi^2 / x_{eD}^2 + n^2 \pi^2 / h_D^2}$$

Areal View

Pressure Distribution,  $\bar{\Delta p}$



$$\frac{\tilde{q}\mu}{klx_{eD}h_Ds} \left[ \sum_{k=1}^{\infty} \cos(2k-1) \frac{\pi x_D}{2x_{eD}} \cos(2k-1) \frac{\pi x'_D}{2x_{eD}} \left( \frac{\cosh \varepsilon_{2k-1} \tilde{y}_{D1} - \cosh \varepsilon_{2k-1} \tilde{y}_{D2}}{\varepsilon_{2k-1} \sinh \varepsilon_{2k-1} y_{eD}} \right) \right. \\ \left. + 2 \sum_{n=1}^{\infty} \cos n\pi \frac{z_D}{h_D} \cos n\pi \frac{z'_D}{h_D} \frac{\cosh \varepsilon_{2k-1,n} \tilde{y}_{D1} - \cosh \varepsilon_{2k-1,n} \tilde{y}_{D2}}{\varepsilon_{2k-1,n} \sinh \varepsilon_{2k-1,n} y_{eD}} \right]$$

Constant-Pressure Boundaries at  $z_D = 0$  and  $z_D = h_D$

$$q = \tilde{q}, \tilde{y}_{D1} = y_{eD} - |y_D - y'_D|, \tilde{y}_{D2} = y_{eD} - (y_D + y'_D),$$

$$\tilde{z}_{D1} = h_D - |z_D - z'_D|, \tilde{z}_{D2} = h_D - (z_D + z'_D),$$

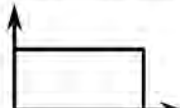
$$\varepsilon_n = \sqrt{u + n^2 \pi^2 / h_D^2}, \varepsilon_m = \sqrt{u + m^2 \pi^2 / y_{eD}^2}, \varepsilon_k = \sqrt{u + k^2 \pi^2 / x_{eD}^2}, \varepsilon_{k,n} = \sqrt{u + k^2 \pi^2 / x_{eD}^2 + n^2 \pi^2 / h_D^2},$$

$$\varepsilon_{k,m} = \sqrt{u + k^2 \pi^2 / x_{eD}^2 + m^2 \pi^2 / y_{eD}^2}, \varepsilon_{2k-1} = \sqrt{u + (2k-1)^2 \pi^2 / x_{eD}^2},$$

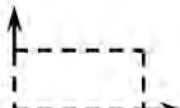
$$\varepsilon_{2k-1,n} = \sqrt{u + (2k-1)^2 \pi^2 / x_{eD}^2 + n^2 \pi^2 / h_D^2}, \varepsilon_{2k-1,m} = \sqrt{u + (2k-1)^2 \pi^2 / x_{eD}^2 + m^2 \pi^2 / y_{eD}^2}$$

Areal View

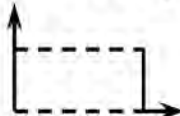
Pressure Distribution,  $\bar{\Delta p}$



$$\frac{\tilde{q}\mu}{2klx_{eD}y_{eD}s} \left[ \frac{\cosh \sqrt{u} \tilde{z}_{D1} - \cosh \sqrt{u} \tilde{z}_{D2}}{\sqrt{u} \sin h \sqrt{u} h_D} \right. \\ \left. + 2 \sum_{k=1}^{\infty} \cos k\pi \frac{x_D}{x_{eD}} \cos k\pi \frac{x'_D}{x_{eD}} \frac{\cosh \varepsilon_k \tilde{z}_{D1} - \cosh \varepsilon_k \tilde{z}_{D2}}{\varepsilon_k \sin h \varepsilon_k h_D} \right. \\ \left. + 2 \sum_{m=1}^{\infty} \cos m\pi \frac{y_D}{y_{eD}} \cos m\pi \frac{y'_D}{y_{eD}} \left( \frac{\cosh \varepsilon_m \tilde{z}_{D1} - \cosh \varepsilon_m \tilde{z}_{D2}}{\varepsilon_m \sinh \varepsilon_m h_D} \right) \right. \\ \left. + 2 \sum_{k=1}^{\infty} \cos k\pi \frac{x_D}{x_{eD}} \cos k\pi \frac{x'_D}{x_{eD}} \frac{\cosh \varepsilon_{k,m} \tilde{z}_{D1} + \cosh \varepsilon_{k,m} \tilde{z}_{D2}}{\varepsilon_{k,m} \sinh \varepsilon_{k,m} h_D} \right]$$



$$\frac{2\tilde{q}\mu}{klx_{eD}h_Ds} \left( \sum_{n=1}^{\infty} \sin n\pi \frac{z_D}{h_D} \sin n\pi \frac{z'_D}{h_D} \sum_{k=1}^{\infty} \sin k\pi \frac{x_D}{x_{eD}} \sin k\pi \frac{x'_D}{x_{eD}} \frac{\cosh \varepsilon_{k,n} \tilde{y}_{D1} - \cosh \varepsilon_{k,n} \tilde{y}_{D2}}{\varepsilon_{k,n} \sinh \varepsilon_{k,n} y_{eD}} \right)$$



$$\frac{\tilde{q}\mu}{klx_{eD}h_Ds} \left[ \sum_{n=1}^{\infty} \sin n\pi \frac{z_D}{h_D} \sin n\pi \frac{z'_D}{h_D} \left( \frac{\cosh \varepsilon_n \tilde{y}_{D1} - \cosh \varepsilon_n \tilde{y}_{D2}}{\varepsilon_n \sinh \varepsilon_n y_{eD}} \right) \right. \\ \left. + 2 \sum_{k=1}^{\infty} \cos k\pi \frac{x_D}{x_{eD}} \cos k\pi \frac{x'_D}{x_{eD}} \frac{\cosh \varepsilon_{k,n} \tilde{y}_{D1} - \cosh \varepsilon_{k,n} \tilde{y}_{D2}}{\varepsilon_{k,n} \sinh \varepsilon_{k,n} y_{eD}} \right]$$

**TABLE 3.8—LAPLACE DOMAIN SOLUTIONS FOR POINT-SOURCE WELLS IN PARALLELEPIPED RESERVOIRS<sup>17</sup>(after Ozkan<sup>27</sup>) (continued)**

Constant-Pressure Boundaries at $z_D = 0$ and $z_D = h_D$	
$q = \tilde{q}, \tilde{y}_{D1} = y_{eD} -  y_D - y'_D , \tilde{y}_{D2} = y_{eD} - (y_D + y'_D),$ $\tilde{z}_{D1} = h_D -  z_D - z'_D , \tilde{z}_{D2} = h_D - (z_D + z'_D),$ $\varepsilon_n = \sqrt{u + n^2 \pi^2 / h_D^2}, \varepsilon_m = \sqrt{u + m^2 \pi^2 / y_{eD}^2}, \varepsilon_k = \sqrt{u + k^2 \pi^2 / x_{eD}^2}, \varepsilon_{k,n} = \sqrt{u + k^2 \pi^2 / x_{eD}^2 + n^2 \pi^2 / h_D^2},$ $\varepsilon_{k,m} = \sqrt{u + k^2 \pi^2 / x_{eD}^2 + m^2 \pi^2 / y_{eD}^2}, \varepsilon_{2k-1} = \sqrt{u + (2k-1)^2 \pi^2 / x_{eD}^2},$ $\varepsilon_{2k-1,n} = \sqrt{u + (2k-1)^2 \pi^2 / x_{eD}^2 + n^2 \pi^2 / h_D^2}, \varepsilon_{2k-1,m} = \sqrt{u + (2k-1)^2 \pi^2 / x_{eD}^2 + m^2 \pi^2 / y_{eD}^2}$	
Areal View	Pressure Distribution, $\bar{\Delta p}$
	$\frac{2\tilde{q}\mu}{k\ell x_{eD} h_D s} \left( \sum_{n=1}^{\infty} \sin n\pi \frac{z_D}{h_D} \sin n\pi \frac{z'_D}{h_D} \sum_{k=1}^{\infty} \cos(2k-1) \frac{\pi x_D}{2x_{eD}} \cos(2k-1) \frac{\pi x'_D}{2x_{eD}} \right.$ $\left. \times \frac{\sinh \varepsilon_{2k-1,n} \tilde{y}_{D1} + \sinh \varepsilon_{2k-1,n} \tilde{y}_{D2}}{\varepsilon_{2k-1,n} \cosh \varepsilon_{2k-1,n} y_{eD}} \right)$
	$\frac{\tilde{q}\mu}{k\ell x_{eD} y_{eD} s} \left[ \sum_{k=1}^{\infty} \cos(2k-1) \frac{\pi x_D}{2x_{eD}} \cos(2k-1) \frac{\pi x'_D}{2x_{eD}} \left( \frac{\cosh \varepsilon_{2k-1} \tilde{z}_{D1} - \cosh \varepsilon_{2k-1} \tilde{z}_{D2}}{\varepsilon_{2k-1} \sinh \varepsilon_{2k-1} h_D} \right. \right.$ $\left. \left. + 2 \sum_{m=1}^{\infty} \cos m\pi \frac{y_D}{y_{eD}} \cos m\pi \frac{y'_D}{y_{eD}} \frac{\cosh \varepsilon_{2k-1,m} \tilde{z}_{D1} - \cosh \varepsilon_{2k-1,m} \tilde{z}_{D2}}{\varepsilon_{2k-1,m} \sinh \varepsilon_{2k-1,m} h_D} \right) \right]$
	$\frac{\tilde{q}\mu}{k\ell x_{eD} h_D s} \left[ \sum_{k=1}^{\infty} \cos(2k-1) \frac{\pi x_D}{2x_{eD}} \cos(2k-1) \frac{\pi x'_D}{2x_{eD}} \left( \frac{\cosh \varepsilon_{2k-1} \tilde{y}_{D1} - \cosh \varepsilon_{2k-1} \tilde{y}_{D2}}{\varepsilon_{2k-1} \sinh \varepsilon_{2k-1} y_{eD}} \right. \right.$ $\left. \left. + 2 \sum_{n=1}^{\infty} \sin n\pi \frac{z_D}{h_D} \sin n\pi \frac{z'_D}{h_D} \frac{\cosh \varepsilon_{2k-1,n} \tilde{y}_{D1} - \cosh \varepsilon_{2k-1,n} \tilde{y}_{D2}}{\varepsilon_{2k-1,n} \sinh \varepsilon_{2k-1,n} y_{eD}} \right) \right]$
Impermeable Boundary at $z_D = 0$ and Constant-Pressure Boundary at $z_D = h_D$	
$q = \tilde{q}, \tilde{y}_{D1} = y_{eD} -  y_D - y'_D , \tilde{y}_{D2} = y_{eD} - (y_D + y'_D),$ $\tilde{z}_{D1} = h_D -  z_D - z'_D , \tilde{z}_{D2} = h_D - (z_D + z'_D),$ $\varepsilon_{2n-1} = \sqrt{u + (2n-1)^2 \pi^2 / h_D^2}, \varepsilon_{2k-1} = \sqrt{u + (2k-1)^2 \pi^2 / x_{eD}^2}, \varepsilon_{k,2n-1} = \sqrt{u + k^2 \pi^2 / x_{eD}^2 + (2n-1)^2 \pi^2 / h_D^2},$ $\varepsilon_{2k-1,2n-1} = \sqrt{u + (2k-1)^2 \pi^2 / x_{eD}^2 + (2n-1)^2 \pi^2 / h_D^2}, \varepsilon_{2k-1,m} = \sqrt{u + (2k-1)^2 \pi^2 / x_{eD}^2 + m^2 \pi^2 / y_{eD}^2}$	
Areal View	Pressure Distribution, $\bar{\Delta p}$
	$\frac{\tilde{q}\mu}{k\ell x_{eD} h_D s} \left[ \sum_{n=1}^{\infty} \cos(2n-1) \frac{\pi z_D}{2h_D} \cos(2n-1) \frac{\pi z'_D}{2h_D} \left( \frac{\cosh \varepsilon_{2n-1} \tilde{y}_{D1} + \cosh \varepsilon_{2n-1} \tilde{y}_{D2}}{\varepsilon_{2n-1} \sinh \varepsilon_{2n-1} y_{eD}} \right. \right.$ $\left. \left. + 2 \sum_{k=1}^{\infty} \cos k\pi \frac{x_D}{x_{eD}} \cos k\pi \frac{x'_D}{x_{eD}} \frac{\cosh \varepsilon_{k,2n-1} \tilde{y}_{D1} + \cosh \varepsilon_{k,2n-1} \tilde{y}_{D2}}{\varepsilon_{k,2n-1} \sinh \varepsilon_{k,2n-1} y_{eD}} \right) \right]$

**TABLE 3.8—LAPLACE DOMAIN SOLUTIONS FOR POINT-SOURCE WELLS IN PARALLELEPIPED RESERVOIRS<sup>17</sup> (after Ozkan<sup>27</sup>) (continued)**

Impermeable Boundary at  $z_D = 0$  and Constant-Pressure Boundary at  $z_D = h_D$

$$q = \tilde{q}, \tilde{y}_{D1} = y_{eD} - |y'_D - y'_D|, \tilde{y}_{D2} = y_{eD} - (y_D + y'_D),$$

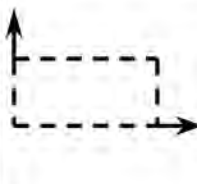
$$\tilde{z}_{D1} = h_D - |z_D - z'_D|, \tilde{z}_{D2} = h_D - (z_D + z'_D).$$

$$\varepsilon_{2n-1} = \sqrt{u + (2n-1)^2 \pi^2 / h_D^2}, \varepsilon_{2k-1} = \sqrt{u + (2k-1)^2 \pi^2 / x_{eD}^2}, \varepsilon_{k,2n-1} = \sqrt{u + k^2 \pi^2 / x_{eD}^2 + (2n-1)^2 \pi^2 / h_D^2},$$

$$\varepsilon_{2k-1,2n-1} = \sqrt{u + (2k-1)^2 \pi^2 / x_{eD}^2 + (2n-1)^2 \pi^2 / h_D^2}, \varepsilon_{2k-1,m} = \sqrt{u + (2k-1)^2 \pi^2 / x_{eD}^2 + m^2 \pi^2 / y_{eD}^2}.$$

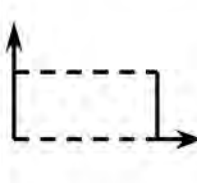
Areal View

Pressure Distribution,  $\Delta p$



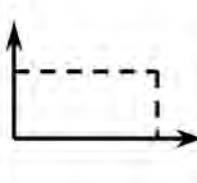
$$\frac{\tilde{q}\mu}{kLx_{eD}h_Ds} \left[ \sum_{n=1}^{\infty} \cos(2n-1) \frac{\pi z_D}{2h_D} \cos(2n-1) \frac{\pi z'_D}{2h_D} \left( \frac{\cosh \varepsilon_{2n-1} \tilde{y}_{D1} - \cosh \varepsilon_{2n-1} \tilde{y}_{D2}}{\varepsilon_{2n-1} \sinh \varepsilon_{2n-1} y_{eD}} \right) \right.$$

$$\left. + 2 \sum_{k=1}^{\infty} \sin k\pi \frac{x_D}{x_{eD}} \sin k\pi \frac{x'_D}{x_{eD}} \frac{\cosh \varepsilon_{k,2n-1} \tilde{y}_{D1} - \cosh \varepsilon_{k,2n-1} \tilde{y}_{D2}}{\varepsilon_{k,2n-1} \sinh \varepsilon_{k,2n-1} y_{eD}} \right]$$



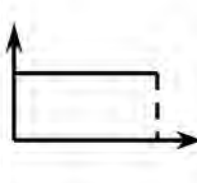
$$\frac{\tilde{q}\mu}{kLx_{eD}h_Ds} \left[ \sum_{n=1}^{\infty} \cos(2n-1) \frac{\pi z_D}{2h_D} \cos(2n-1) \frac{\pi z'_D}{2h_D} \left( \frac{\cosh \varepsilon_{2n-1} \tilde{y}_{D1} - \cosh \varepsilon_{2n-1} \tilde{y}_{D2}}{\varepsilon_{2n-1} \sinh \varepsilon_{2n-1} y_{eD}} \right) \right.$$

$$\left. + 2 \sum_{k=1}^{\infty} \cos k\pi \frac{x_D}{x_{eD}} \cos k\pi \frac{x'_D}{x_{eD}} \frac{\cosh \varepsilon_{k,2n-1} \tilde{y}_{D1} - \cosh \varepsilon_{k,2n-1} \tilde{y}_{D2}}{\varepsilon_{k,2n-1} \sinh \varepsilon_{k,2n-1} y_{eD}} \right]$$



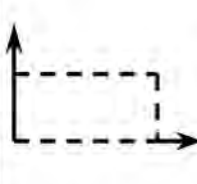
$$\frac{2\tilde{q}\mu}{kLx_{eD}h_Ds} \left[ \sum_{n=1}^{\infty} \cos(2n-1) \frac{\pi z_D}{2h_D} \cos(2n-1) \frac{\pi z'_D}{2h_D} \right.$$

$$\left. \sum_{k=1}^{\infty} \cos(2k-1) \frac{\pi x_D}{2x_{eD}} \cos(2k-1) \frac{\pi x'_D}{2x_{eD}} \frac{\sinh \varepsilon_{2k-1,2n-1} \tilde{y}_{D1} + \sinh \varepsilon_{2k-1,2n-1} \tilde{y}_{D2}}{\varepsilon_{2k-1,2n-1} \cosh \varepsilon_{2k-1,2n-1} y_{eD}} \right]$$



$$\frac{\tilde{q}\mu}{kLx_{eD}y_{eD}s} \left[ \sum_{k=1}^{\infty} \cos(2k-1) \frac{\pi x_D}{2x_{eD}} \cos(2k-1) \frac{\pi x'_D}{2x_{eD}} \left( \frac{\sinh \varepsilon_{2k-1} \tilde{z}_{D1} + \sinh \varepsilon_{2k-1} \tilde{z}_{D2}}{\varepsilon_{2k-1} \cosh \varepsilon_{2k-1} h_D} \right) \right.$$

$$\left. + 2 \sum_{m=1}^{\infty} \cos m\pi \frac{y_D}{y_{eD}} \cos m\pi \frac{y'_D}{y_{eD}} \frac{\sinh \varepsilon_{2k-1,m} \tilde{z}_{D1} + \sinh \varepsilon_{2k-1,m} \tilde{z}_{D2}}{\varepsilon_{2k-1,m} \cosh \varepsilon_{2k-1,m} h_D} \right]$$



$$\frac{2\tilde{q}\mu}{kLx_{eD}y_{eD}s} \left[ \sum_{k=1}^{\infty} \cos(2k-1) \frac{\pi x_D}{2x_{eD}} \cos(2k-1) \frac{\pi x'_D}{2x_{eD}} \right.$$

$$\left. \sum_{m=1}^{\infty} \sin m\pi \frac{y_D}{y_{eD}} \sin m\pi \frac{y'_D}{y_{eD}} \frac{\sinh \varepsilon_{2k-1,m} \tilde{z}_{D1} + \sinh \varepsilon_{2k-1,m} \tilde{z}_{D2}}{\varepsilon_{2k-1,m} \cosh \varepsilon_{2k-1,m} h_D} \right]$$

$$+ \frac{4x_e}{\pi L h} \sum_{k=1}^{\infty} \frac{1}{k} \sin k\pi \frac{L_h}{2x_e} \cos k\pi \frac{x_w}{x_e} \cos k\pi \frac{x}{x_e} \frac{\cosh \varepsilon_{k,n} \tilde{y}_{D1} + \cosh \varepsilon_{k,n} \tilde{y}_{D2}}{\varepsilon_{k,n} \sinh \varepsilon_{k,n} y_{eD}} \Bigg) \dots \dots \dots (3.301)$$

In Eq. 3.301,  $\tilde{y}_{D1}$ ,  $\tilde{y}_{D2}$ ,  $\varepsilon_n$ ,  $\varepsilon_k$ , and  $\varepsilon_{k,n}$  are given by Eqs. 3.293 through 3.297.

**Conversion From 3D to 2D Anisotropy.** The solutions previously presented assume that the reservoir is anisotropic in all three principal directions,  $x$ ,  $y$ , and  $z$  with  $k_x$ ,  $k_y$ , and  $k_z$  denoting the corresponding permeabilities. In these solutions, an equivalent isotropic permeability,  $k$ , has been defined by

$$k = \sqrt[3]{k_x k_y k_z} \dots\dots\dots (3.302)$$

For some applications, it may be more convenient to define an equivalent horizontal permeability by

$$k_h = \sqrt{k_x k_y} \dots\dots\dots (3.303)$$

and replace  $k$  in the solutions given in this section (Sec. 3.4.4) by  $k_h$ . Note that  $k$  takes place in the definition of the dimensionless time  $t_D$  (Eq. 3.230). Then, if we define a dimensionless time  $\tilde{t}_D$  based on  $k_h$ , the relation between  $\tilde{t}_D$  and  $t_D$  is given by

$$\tilde{t}_D = k_h t_D / k \dots\dots\dots (3.304)$$

Because in the solutions given in this section the Laplace transformation is with respect to  $t_D$ , conversion from 3D to 2D anisotropy requires the use of the following property of the Laplace transforms:

$$\overline{cF(cs)} = L\{F(t/c)\} \dots\dots\dots (3.305)$$

As an example, consider the solution for a horizontal well in an infinite-slab reservoir. Assuming that the midpoint of the well is the origin ( $x_{wD} = 0$ ,  $y_{wD} = 0$ ) and choosing the half-length of the horizontal well as the characteristic length (i.e.,  $\ell = L_h / 2$ ), the horizontal-well solution given in Table 3.6 may be written as

$$\begin{aligned} \overline{\Delta p} = & \frac{\tilde{q}\mu}{2\pi k h_D s} \left\{ \int_{-1}^{+1} K_0 \left[ \sqrt{(x_D - \alpha\sqrt{k/k_x})^2 + y_D^2} \sqrt{s f(s)} \right] d\alpha \right. \\ & \left. + 2 \sum_{n=1}^{\infty} \cos n\pi z_D \cos n\pi z_{wD} \int_{-1}^{+1} K_0 \left[ \sqrt{(x_D - \alpha\sqrt{k/k_x})^2 + y_D^2} \sqrt{s f(s) + \frac{n^2 \pi^2}{h_D^2}} \right] d\alpha \right\} \dots\dots\dots (3.306) \end{aligned}$$

In Eq. 3.306,  $s$  is the Laplace transform variable with respect to dimensionless time,  $t_D$ , based on  $k$  and

$$x_D = 2x\sqrt{k/k_x} / L_h, \dots\dots\dots (3.307)$$

$$y_D = 2y\sqrt{k/k_y} / L_h, \dots\dots\dots (3.308)$$

$$z_D = z / h, \dots\dots\dots (3.309)$$



and

$$h_D = 2h\sqrt{k/k_z}/L_h \dots\dots\dots (3.310)$$

If we define the following variables based on  $k_h$ ,

$$\tilde{x}_D = \sqrt{k_h/k}x_D, \dots\dots\dots (3.311)$$

$$\tilde{y}_D = \sqrt{k_h/k}y_D, \dots\dots\dots (3.312)$$

$$\tilde{h}_D = \sqrt{k_h/k}h_D, \dots\dots\dots (3.313)$$

and also note that

$$h_D = 2h\sqrt{k/k_z}/L_h = 2h\sqrt{k_x k_y/k}/(L_h k^{3/2}) = 2hk_h/(L_h k), \dots\dots\dots (3.314)$$

then, we may rearrange Eq. 3.306 in terms of the dimensionless variables based on  $k_h$  as

$$\begin{aligned} \overline{\Delta p}(k_h) &= \frac{\tilde{q}\mu(k/k_h)}{2\pi(2h/L_h)k_h(k/k_h)s} \left\{ \int_{-1}^{+1} K_0 \left[ \sqrt{(\tilde{x}_D - \alpha\sqrt{k_h/k_x})^2 + \tilde{y}_D^2} \sqrt{\frac{k}{k_h}} s \tilde{f}\left(\frac{k}{k_h}s\right) \right] d\alpha \right. \\ &+ 2 \sum_{n=1}^{\infty} \cos n\pi z_D \cos n\pi z_{wD} \int_{-1}^{+1} K_0 \left[ \sqrt{(\tilde{x}_D - \alpha\sqrt{k_h/k_x})^2 + \tilde{y}_D^2} \sqrt{\frac{k}{k_h}} s \tilde{f}\left(\frac{k}{k_h}s\right) + \frac{n^2\pi^2}{h_D^2} \right] d\alpha \left. \right\}, \dots\dots (3.315) \end{aligned}$$

where

$$\tilde{f}\left(\frac{k}{k_h}s\right) = \frac{(k/k_h)s\omega(1-\omega) + \tilde{\lambda}}{(k/k_h)s(1-\omega) + \tilde{\lambda}} \dots\dots\dots (3.316)$$

and

$$\tilde{\lambda} = k\lambda/k_h \dots\dots\dots (3.317)$$

If we compare Eqs. 3.306 and 3.315, we can show that

$$\overline{\Delta p}(k_h) = \frac{kh_D}{(2h/L_h)k_h} \left[ \frac{k}{k_h} \overline{\Delta p}\left(\frac{k}{k_h}s\right) \right] = \frac{kh_D}{(2h/L_h)k_h} L\{\Delta p(\tilde{t}_D)\}, \dots\dots\dots (3.318)$$

where we have used the relation given by Eq. 3.305. If we now define  $\tilde{s}$  as the Laplace transform variable with respect to  $\tilde{t}_D$ , we may write

$$\overline{\Delta p}(k_h) = \frac{kh_D}{(2h/L_h)k_h} \overline{\Delta p}(\tilde{s}). \dots\dots\dots (3.319)$$

With the relation given by Eq. 3.319 and Eq. 3.306, we obtain the following horizontal-well solution in terms of dimensionless variables based on  $k_h$ :

$$\begin{aligned} \overline{\Delta p}(k_h) = & \frac{\tilde{q}\mu}{2\pi(2h/L_h)k_h\tilde{s}} \left\{ \int_{-1}^{+1} K_0 \left[ \sqrt{(\tilde{x}_D - \alpha\sqrt{k_h/k_x})^2 + y_D^2} \sqrt{\tilde{s}f(\tilde{s})} \right] d\alpha \right. \\ & \left. + 2 \sum_{n=1}^{\infty} \cos n\pi z_D \cos n\pi z_w \int_{-1}^{+1} K_0 \left[ \sqrt{(\tilde{x}_D - \alpha\sqrt{k_h/k_x})^2 + y_D^2} \sqrt{\tilde{s}f(\tilde{s}) + \frac{n^2\pi^2}{h_D^2}} \right] d\alpha \right\} \dots\dots\dots (3.320) \end{aligned}$$

**Computational Considerations and Applications.** The numerical evaluation of the solutions given previously may be sometimes difficult, inefficient, or even impossible. Alternative computational forms of some of these solutions have been presented in Refs. 18, 19, and 29. Here, we present a summary of the alternative formulas to be used in the computation of the source functions in the Laplace transform domain. Some of these formulas are for computations at early or late times and may be useful to derive asymptotic approximations of the solutions during the corresponding time periods.

As Sec. 3.3.1 notes, the short- and long-time approximations of the solutions correspond to the limiting forms of the solution in the Laplace transform domain as  $s \rightarrow \infty$  and  $s \rightarrow 0$ , respectively. In the solutions given in this section, we have defined  $u = sf(s)$ . From elementary considerations, it is possible to show that the definition of  $f(s)$  given in Eq. 3.243 yields the following limiting forms:

$$\lim_{s \rightarrow \infty} u = \lim_{s \rightarrow \infty} sf(s) = s\omega \dots\dots\dots (3.321)$$

and

$$\lim_{s \rightarrow 0} u = \lim_{s \rightarrow 0} f(s) = s \dots\dots\dots (3.322)$$

These limiting forms are used in the derivation of the short- and long-time asymptotic approximations. In the following expressions, homogeneous reservoir solutions are obtained by substituting  $\omega = 1$ .

*The Integral.*

$$\bar{I} = \frac{1}{s} \int_a^b K_0 \left[ \sqrt{u} \sqrt{(x_D - \alpha)^2 + y_D^2} \right] d\alpha \dots\dots\dots (3.323)$$

This integral arises in the computation of many practical transient-pressure solutions and may not be numerically evaluated, especially as  $y_D \rightarrow 0$ ; however, the following alternate forms of the integral are numerically computable.<sup>19</sup>

$$\bar{I} = \frac{1}{s\sqrt{u}} \left[ \int_0^{\sqrt{u}(x_D - a)} K_0(\sqrt{\alpha^2 + uy_D^2}) d\alpha - \int_0^{\sqrt{u}(x_D - b)} K_0(\sqrt{\alpha^2 + uy_D^2}) d\alpha \right], \quad x_D \geq b; \dots\dots\dots (3.324)$$

$$\bar{I} = \frac{1}{s\sqrt{u}} \left[ \int_0^{\sqrt{u}(b-x_D)} K_0(\sqrt{\alpha^2 + uy_D^2}) d\alpha - \int_0^{\sqrt{u}(a-x_D)} K_0(\sqrt{\alpha^2 + uy_D^2}) d\alpha \right], \quad x_D \leq a; \dots\dots (3.325)$$

and

$$\bar{I} = \frac{1}{s\sqrt{u}} \left[ \int_0^{\sqrt{u}(x_D-a)} K_0(\sqrt{\alpha^2 + uy_D^2}) d\alpha + \int_0^{\sqrt{u}(b-x_D)} K_0(\sqrt{\alpha^2 + uy_D^2}) d\alpha \right], \quad a \leq x_D \leq b. \dots\dots (3.326)$$

The integrals in Eqs. 3.324 through 3.326 may be evaluated with the standard numerical integration algorithms for  $y_D \neq 0$ . For  $y_D = 0$ , the polynomial approximations given by Luke<sup>30</sup> or the following power series expansion given by Abramowitz and Stegun<sup>7</sup> may be used in the computation of the integrals in Eqs. 3.324 through 3.326:

$$\int_0^z K_0(\alpha) d\alpha = x \left\{ \sum_{k=0}^{\infty} \frac{(x/2)^{2k}}{(k!)^2(2k+1)} \left[ -\left( \ln \frac{x}{2} + 0.5772 \dots \right) + \sum_{n=1}^k \frac{1}{n} \right] + \sum_{k=0}^{\infty} \frac{(x/2)^{2k}}{(k!)^2(2k+1)^2} \right\} \dots\dots\dots (3.327)$$

For numerical computations and asymptotic evaluations, it may also be useful to note the following relations:<sup>19</sup>

$$\int_0^z K_0(\sqrt{\alpha^2 + c^2}) d\alpha = \frac{\pi}{2} \exp(-|c|) - \int_z^{\infty} K_0(\sqrt{\alpha^2 + c^2}) d\alpha, \dots\dots\dots (3.328)$$

and

$$\int_0^{\infty} K_0(\sqrt{\alpha^2 + c^2}) d\alpha = \frac{\pi}{2} \exp(-|c|). \dots\dots\dots (3.329)$$

It can be shown from Eqs. 3.328 and 3.329 that, for practical purposes, when  $z \geq 20$ , the right sides of Eqs. 3.327 and 3.328 may be approximated by  $\pi/2$  and  $\pi \exp(-|c|)/2$ , respectively.<sup>19,27</sup>

As Refs. 18, 19, and 29 show, it is possible to derive the following short- and long-time approximations (i.e., the limiting forms as  $s \rightarrow \infty$  and  $s \rightarrow 0$ , respectively) for the integral  $I$  given, respectively, by

$$\lim_{s \rightarrow \infty} \bar{I} = \frac{\pi\beta}{2\sqrt{\omega s}^{3/2}} \exp(-|y_D| \sqrt{\omega s}), \dots\dots\dots (3.330)$$

where

$$\beta = \begin{cases} 2 & \text{for } a < x_D < b \\ 1 & \text{for } x_D = a \text{ or } x_D = b \\ 0 & \text{for } x_D < a \text{ or } x_D > b \end{cases}, \dots\dots\dots (3.331)$$

and

$$\lim_{s \rightarrow 0} \bar{I} = \frac{b-a}{2s} (-\ln s + \ln 4 - 2\gamma + 2) + \frac{2}{s} \sigma(x_D, y_D, a, b), \dots\dots\dots (3.332)$$

where  $\gamma = 0.5772 \dots$  and

$$\begin{aligned} \sigma(x_D, y_D, a, b) = & \frac{1}{4} \{ (x_D - b) \ln [(x_D - b)^2 + y_D^2] - (x_D - a) \ln [(x_D - a)^2 + y_D^2] \} \\ & - \frac{y_D}{2} \left[ \arctan \left( \frac{x_D - a}{y_D} \right) - \arctan \left( \frac{x_D - b}{y_D} \right) \right]. \dots\dots\dots (3.333) \end{aligned}$$

It is also useful to note the real inversions of Eqs. 3.330 and 3.332 given, respectively, by

$$\lim_{t_D \rightarrow 0} I = \beta \left[ \sqrt{\pi t_D / \omega} \exp \left( -\frac{y_D^2}{4t_D / \omega} \right) - \frac{\pi}{2} |y_D| \operatorname{erfc} \left( \frac{|y_D|}{2\sqrt{t_D / \omega}} \right) \right] \dots\dots\dots (3.334)$$

and

$$\lim_{t_D \rightarrow \infty} I = \frac{b-a}{2} \left[ \ln \left( \frac{4t_D}{e^\gamma} \right) + 2 \right] + 2\sigma(x_D, y_D, a, b). \dots\dots\dots (3.335)$$

The Series  $\bar{S}_1$ .

$$\bar{S}_1 = \sum_{n=1}^{\infty} \frac{\cos n\pi z \cos n\pi z_w}{\sqrt{u + n^2 \pi^2 / h_D^2 + a^2}} \exp \left( -\sqrt{u + n^2 \pi^2 / h_D^2 + a^2} y_D \right) \text{ for } y_D \geq 0. \dots\dots\dots (3.336)$$

Two alternative expressions for the series  $S_1$  may be convenient for the large and small values of  $u$  (i.e., for short and long times).<sup>29</sup> When  $u$  is large,

$$\begin{aligned} \bar{S}_1 = & \frac{h_D}{2\pi} \sum_{n=-\infty}^{+\infty} \left\{ K_0 \left[ \sqrt{(z - z_w - 2n)^2 h_D^2 + y_D^2} \sqrt{u + a^2} \right] \right. \\ & \left. + K_0 \left[ \sqrt{(z + z_w - 2n)^2 h_D^2 + y_D^2} \sqrt{u + a^2} \right] - \frac{\exp \left( -\sqrt{u + a^2} y_D \right)}{2\sqrt{u + a^2}} \right\}, \dots\dots\dots (3.337) \end{aligned}$$

and when  $u + a^2 \ll n^2 \pi^2 / h_D^2$ ,

$$\begin{aligned} \bar{S}_1 = \sum_{n=1}^{\infty} \cos n\pi z \cos n\pi z_w & \left[ \frac{\exp\left(-\sqrt{u + n^2\pi^2/h_D^2 + a^2}y_D\right)}{\sqrt{u + n^2\pi^2/h_D^2 + a^2}} - \frac{\exp\left(-n\pi y_D/h_D\right)}{n\pi/h_D} \right] \\ & - \frac{h_D}{4\pi} \left\{ \ln \left[ 1 - 2 \exp\left(-\pi y_D/h_D\right) \cos \pi(z + z_w) + \exp\left(-2\pi y_D/h_D\right) \right] \right. \\ & \left. + \ln \left[ 1 - 2 \exp\left(-\pi y_D/h_D\right) \cos \pi(z - z_w) + \exp\left(-2\pi y_D/h_D\right) \right] \right\}, \dots\dots\dots (3.338) \end{aligned}$$

The Series  $\bar{S}_2$ .

$$\bar{S}_2 = \sum_{n=1}^{\infty} \frac{\sin n\pi z \sin n\pi z_w}{\sqrt{u + n^2\pi^2/h_D^2 + a^2}} \exp\left(-\sqrt{u + n^2\pi^2/h_D^2 + a^2}y_D\right) \text{ for } y_D \geq 0. \dots\dots\dots (3.339)$$

Alternative computational forms for the series  $S_2$  are given next.<sup>29</sup> When  $u$  is large,

$$\begin{aligned} \bar{S}_2 = \frac{h_D}{2\pi} \sum_{n=-\infty}^{+\infty} & \left\{ K_0 \left[ \sqrt{(z - z_w - 2n)^2 h_D^2 + y_D^2} \sqrt{u + a^2} \right] \right. \\ & \left. - K_0 \left[ \sqrt{(z + z_w - 2n)^2 h_D^2 + y_D^2} \sqrt{u + a^2} \right] \right\}, \dots\dots\dots (3.340) \end{aligned}$$

and when  $u + a^2 \ll n^2\pi^2/h_D^2$ ,

$$\begin{aligned} \bar{S}_2 = \sum_{n=1}^{\infty} \sin n\pi z \sin n\pi z_w & \left[ \frac{\exp\left(-\sqrt{u + n^2\pi^2/h_D^2 + a^2}y_D\right)}{\sqrt{u + n^2\pi^2/h_D^2 + a^2}} - \frac{\exp\left(-n\pi y_D/h_D\right)}{n\pi/h_D} \right] \\ & - \frac{h_D}{4\pi} \ln \frac{1 - 2 \exp\left(-\pi y_D/h_D\right) \cos \pi(z + z_w) + \exp\left(-2\pi y_D/h_D\right)}{1 - 2 \exp\left(-\pi y_D/h_D\right) \cos \pi(z - z_w) + \exp\left(-2\pi y_D/h_D\right)} \dots\dots\dots (3.341) \end{aligned}$$

The Series  $\bar{S}_3$ .

$$\begin{aligned} \bar{S}_3 = \sum_{n=1}^{\infty} \frac{\cos(2n-1)\frac{\pi}{2}z \cos(2n-1)\frac{\pi}{2}z_w}{\sqrt{u + (2n-1)^2\pi^2/(4h_D^2) + a^2}} & \exp\left[-\sqrt{u + (2n-1)^2\pi^2/(4h_D^2) + a^2}y_D\right] \\ & \text{for } y_D \geq 0. \dots\dots\dots (3.342) \end{aligned}$$

The following alternative forms for the series  $\bar{S}_3$  may be convenient for the large and small values of  $u$  (i.e., for short and long times).<sup>29</sup> When  $u$  is large,

$$\begin{aligned} \bar{S}_3 = \frac{h_D}{2\pi} \sum_{n=-\infty}^{+\infty} (-1)^n & \left\{ K_0 \left[ \sqrt{(z - z_w - 2n)^2 h_D^2 + y_D^2} \sqrt{u + a^2} \right] \right. \\ & \left. + K_0 \left[ \sqrt{(z + z_w - 2n)^2 h_D^2 + y_D^2} \sqrt{u + a^2} \right] \right\}, \dots\dots\dots (3.343) \end{aligned}$$

and when  $u + a^2 \ll (2n - 1)^2 \pi^2/(4h_D^2)$ ,

$$\begin{aligned} \bar{S}_3 &= \sum_{n=1}^{\infty} \cos(2n-1)\frac{\pi}{2}z \cos(2n-1)\frac{\pi}{2}z_w \\ &\times \left\{ \frac{\exp\left[-\sqrt{u+(2n-1)^2\pi^2/(4h_D^2)+a^2}y_D\right]}{\sqrt{u+(2n-1)^2\pi^2/(4h_D^2)+a^2}} - \frac{\exp\left[-(2n-1)\pi y_D/(2h_D)\right]}{(2n-1)\pi/(2h_D)} \right\} \\ &+ \frac{h_D}{4\pi} \left\{ \ln \frac{1+2\exp\left[-\pi y_D/(2h_D)\right] \cos\frac{\pi}{2}(z+z_w) + \exp(-\pi y_D/h_D)}{1-2\exp\left[-\pi y_D/(2h_D)\right] \cos\frac{\pi}{2}(z+z_w) + \exp(-\pi y_D/h_D)} \right. \\ &\left. + \ln \frac{1+2\exp\left[-\pi y_D/(2h_D)\right] \cos\frac{\pi}{2}(z-z_w) + \exp(-\pi y_D/h_D)}{1-2\exp\left[-\pi y_D/(2h_D)\right] \cos\frac{\pi}{2}(z-z_w) + \exp(-\pi y_D/h_D)} \right\} \dots\dots\dots (3.344) \end{aligned}$$

The Series  $\bar{F}$ .

$$\bar{F} = \frac{1}{s} \sum_{n=1}^{\infty} \cos n\pi z_D \cos n\pi z'_D \int_a^b K_0\left[\varepsilon_n \sqrt{(x_D - \alpha)^2 + y_D^2}\right] d\alpha, \dots\dots\dots (3.345)$$

where

$$\varepsilon_n = \sqrt{u + n^2\pi^2/h_D^2} \dots\dots\dots (3.346)$$

The series  $\bar{F}$  may be written in the following forms with the use of Eqs. 3.324 through 3.326.

$$\begin{aligned} \bar{F} &= \frac{1}{s} \sum_{n=1}^{\infty} \frac{\cos n\pi z_D \cos n\pi z'_D}{\varepsilon_n} \\ &\times \left[ \int_0^{\varepsilon_n(x_D - a)} K_0(\sqrt{\alpha^2 + \varepsilon_n^2 y_D^2}) d\alpha - \int_0^{\varepsilon_n(x_D - b)} K_0(\sqrt{\alpha^2 + \varepsilon_n^2 y_D^2}) d\alpha \right]^{x_D \geq b}, \dots\dots\dots (3.347) \end{aligned}$$

$$\begin{aligned} \bar{F} &= \frac{1}{s} \sum_{n=1}^{\infty} \frac{\cos n\pi z_D \cos n\pi z'_D}{\varepsilon_n} \\ &\times \left[ \int_0^{\varepsilon_n(b - x_D)} K_0(\sqrt{\alpha^2 + \varepsilon_n^2 y_D^2}) d\alpha - \int_0^{\varepsilon_n(a - x_D)} K_0(\sqrt{\alpha^2 + \varepsilon_n^2 y_D^2}) d\alpha \right]^{x_D \leq a}, \dots\dots\dots (3.348) \end{aligned}$$

and

$$\bar{F} = \frac{1}{s} \sum_{n=1}^{\infty} \frac{\cos n\pi z_D \cos n\pi z'_D}{\varepsilon_n}$$

$$\times \left[ \int_0^{\varepsilon_n(x_D - a)} K_0(\sqrt{\alpha^2 + \varepsilon_n^2 y_D^2}) d\alpha + \int_0^{\varepsilon_n(b - x_D)} K_0(\sqrt{\alpha^2 + \varepsilon_n^2 y_D^2}) d\alpha \right]^{a \leq x_D \leq b} \dots\dots\dots (3.349)$$

The computation of the series in Eqs. 3.347 and 3.348 should not pose numerical difficulties; however, the series in Eq. 3.349 converges slowly. With the relation given in Eq. 3.328, we may write Eq. 3.349 as<sup>29</sup>

$$\bar{F}(a \leq x_D \leq b) = \bar{F}_1 - \frac{1}{s} \sum_{n=1}^{\infty} \frac{\cos n\pi z_D \cos n\pi z'_D}{\varepsilon_n} \times \left[ \int_{\varepsilon_n(x_D - a)}^{\infty} K_0(\sqrt{\alpha^2 + \varepsilon_n^2 y_D^2}) d\alpha + \int_{\varepsilon_n(b - x_D)}^{\infty} K_0(\sqrt{\alpha^2 + \varepsilon_n^2 y_D^2}) d\alpha \right], \dots\dots\dots (3.350)$$

where

$$\bar{F}_1 = \frac{\pi}{s} \sum_{n=1}^{\infty} \frac{\cos n\pi z_D \cos n\pi z'_D}{\varepsilon_n} \exp(-\varepsilon_n |y_D|). \dots\dots\dots (3.351)$$

Before discussing the computation of the series given in Eq. 3.351, we first discuss the derivation of the asymptotic approximations for the series  $\bar{F}$ . When  $s$  is large (small times),  $\bar{F}$  may be approximated by<sup>29</sup>

$$\lim_{s \rightarrow \infty} \bar{F} = \frac{\beta h_D}{4s} \sum_{n=-\infty}^{+\infty} \left\{ K_0[\sqrt{(z_D + z'_D - 2n)^2 h_D^2 + y_D^2} \sqrt{\omega s}] + K_0[\sqrt{(z_D - z'_D - 2n)^2 h_D^2 + y_D^2} \sqrt{\omega s}] \right\} - \pi\beta \exp(-\sqrt{\omega s} |y_D|) / (4s^{3/2} \sqrt{\omega}), \dots\dots\dots (3.352)$$

where  $\beta$  is given by Eq. 3.331. If  $s$  is sufficiently large, then Eq. 3.352 may be further approximated by

$$\lim_{s \rightarrow \infty} \bar{F} = \frac{\beta h_D}{4s} K_0[\sqrt{(z_D - z'_D)^2 h_D^2 + y_D^2} \sqrt{\omega s}] - \frac{\pi\beta \exp(-\sqrt{\omega s} |y_D|)}{4s^{3/2} \sqrt{\omega}}. \dots\dots\dots (3.353)$$

The inverse Laplace transform of Eq. 3.353 yields

$$\lim_{t_D \rightarrow 0} F = -\frac{\beta h_D}{8} Ei \left[ -\frac{(z_D - z'_D)^2 h_D^2 + y_D^2}{4t_D/\omega} \right] - \frac{\beta}{2} \left[ \sqrt{\frac{\pi t_D}{\omega}} \exp\left(-\frac{y_D^2}{4t_D/\omega}\right) - \frac{\pi}{2} |y_D| \operatorname{erfc}\left(\frac{|y_D|}{2\sqrt{t_D/\omega}}\right) \right]. \dots\dots\dots (3.354)$$

For small  $s$  (large times), depending on the value of  $x_D$ ,  $\bar{F}$  may be approximated by one of the following equations:<sup>29</sup>

$$\lim_{s \rightarrow 0} \bar{F} = \frac{h_D}{\pi s} \sum_{n=1}^{\infty} \frac{\cos n\pi z_D \cos n\pi z'_D}{n}$$

$$\times \left[ \int_0^{n\pi(x_D - a)/h_D} K_0(\sqrt{\alpha^2 + n^2 \pi^2 y_D^2 / h_D^2}) d\alpha - \int_0^{n\pi(x_D - b)/h_D} K_0(\sqrt{\alpha^2 + n^2 \pi^2 y_D^2 / h_D^2}) d\alpha \right]^{x_D \geq b}, \dots (3.355)$$

$$\lim_{s \rightarrow 0} \bar{F} = \frac{h_D}{\pi s} \sum_{n=1}^{\infty} \frac{\cos n\pi z_D \cos n\pi z'_D}{n}$$

$$\times \left[ \int_0^{n\pi(b - x_D)/h_D} K_0(\sqrt{\alpha^2 + n^2 \pi^2 y_D^2 / h_D^2}) d\alpha - \int_0^{n\pi(a - x_D)/h_D} K_0(\sqrt{\alpha^2 + n^2 \pi^2 y_D^2 / h_D^2}) d\alpha \right]^{x_D \leq a}, \dots (3.356)$$

and

$$\lim_{s \rightarrow 0} \bar{F} = \lim_{s \rightarrow 0} \bar{F}_1 - \frac{h_D}{\pi s} \sum_{n=1}^{\infty} \frac{\cos n\pi z_D \cos n\pi z'_D}{n}$$

$$\times \left[ \int_{n\pi(x_D - a)/h_D}^{\infty} K_0(\sqrt{\alpha^2 + n^2 \pi^2 y_D^2 / h_D^2}) d\alpha \right.$$

$$\left. + \int_{n\pi(b - x_D)/h_D}^{\infty} K_0(\sqrt{\alpha^2 + n^2 \pi^2 y_D^2 / h_D^2}) d\alpha \right]^{a \leq x_D \leq b}, \dots (3.357)$$

where  $\lim_{s \rightarrow 0} \bar{F}_1$  is given by Eq. 3.364.

The Series  $\bar{F}_1$ .

$$\bar{F}_1 = \frac{\pi}{s} \sum_{n=1}^{\infty} \frac{\cos n\pi z_D \cos n\pi z'_D}{\varepsilon_n} \exp(-\varepsilon_n |y_D|), \dots (3.358)$$

where

$$\varepsilon_n = \sqrt{u + n^2 \pi^2 / h_D^2} \dots (3.346)$$

With the relations given in Eqs. 3.337 and 3.338, the following alternative forms for the series  $\bar{F}_1$  may be obtained, respectively, for the large and small values of  $s$  (i.e., for short and long times).<sup>29</sup> When  $u$  is large,

$$\bar{F}_1 = \frac{h_D}{2s} \sum_{n=-\infty}^{+\infty} \left\{ K_0 \left[ \sqrt{(z_D - z'_D - 2n)^2 h_D^2 + y_D^2 u} \right] \right.$$

$$\left. + K_0 \left[ \sqrt{(z_D + z'_D - 2n)^2 h_D^2 + y_D^2 u} \right] - \pi \exp(-\sqrt{u} |y_D|) / (2s\sqrt{u}) \right\}, \dots (3.359)$$



and when  $u \ll n^2\pi^2/h^2_D$ ,

$$\begin{aligned} \lim_{s \rightarrow 0} \bar{F}_1 &= \frac{\pi}{s} \sum_{n=1}^{\infty} \cos n\pi z_D \cos n\pi z'_D \left[ \frac{\exp(-\varepsilon_n |y_D|)}{\varepsilon_n} - \frac{\exp(-n\pi |y_D|/h_D)}{n\pi/h_D} \right] \\ &\quad - \frac{h_D}{4s} \left\{ \ln \left[ 1 - 2 \exp(-\pi |y_D|/h_D) \cos \pi(z + z_w) + \exp(-2\pi |y_D|/h_D) \right] \right. \\ &\quad \left. + \ln \left[ 1 - 2 \exp(-\pi |y_D|/h_D) \cos \pi(z - z_w) + \exp(-2\pi |y_D|/h_D) \right] \right\} \dots\dots\dots (3.360) \end{aligned}$$

It is also possible to derive asymptotic approximations for the series  $\bar{F}_1$ . When  $s$  is large (small times),  $\bar{F}_1$  may be approximated by<sup>29</sup>

$$\begin{aligned} \lim_{s \rightarrow \infty} \bar{F}_1 &= \frac{h_D}{2s} \sum_{n=-\infty}^{+\infty} \left\{ K_0 \left[ \sqrt{(z_D + z'_D - 2n)^2 h_D^2 + y_D^2} \sqrt{\omega s} \right] \right. \\ &\quad \left. + K_0 \left[ \sqrt{(z_D - z'_D - 2n)^2 h_D^2 + y_D^2} \sqrt{\omega s} \right] - \pi \exp(-\sqrt{\omega s} |y_D|) / (2s^{3/2} \sqrt{\omega}) \right\} \dots\dots\dots (3.361) \end{aligned}$$

If  $s$  is sufficiently large, then Eq. 3.361 may be further approximated by

$$\lim_{s \rightarrow \infty} \bar{F}_1 = \frac{h_D}{2s} K_0 \left[ \sqrt{(z_D - z'_D)^2 h_D^2 + y_D^2} \sqrt{\omega s} \right] - \pi \exp(-\sqrt{\omega s} |y_D|) / (2s^{3/2} \sqrt{\omega}) \dots\dots\dots (3.362)$$

The inverse Laplace transform of Eq. 3.362 yields

$$\begin{aligned} \lim_{s \rightarrow 0} \bar{F}_1 &= -\frac{h_D}{4} Ei \left[ -\frac{(z_D - z'_D)^2 h_D^2 + y_D^2}{4t_D/\omega} \right] \\ &\quad + \sqrt{\frac{\pi t_D}{\omega}} \exp\left(-\frac{y_D^2}{4t_D/\omega}\right) + \frac{\pi}{2} |y_D| \operatorname{erfc}\left(\frac{|y_D|}{2\sqrt{t_D/\omega}}\right) \dots\dots\dots (3.363) \end{aligned}$$

For small  $s$  (large times),  $\bar{F}_1$  may be approximated by<sup>29</sup>

$$\begin{aligned} \lim_{s \rightarrow 0} \bar{F}_1 &= -\frac{h_D}{4s} \left\{ \ln \left[ 1 - 2 \exp(-\pi |y_D|/h_D) \cos \pi(z + z_w) + \exp(-2\pi |y_D|/h_D) \right] \right. \\ &\quad \left. + \ln \left[ 1 - 2 \exp(-\pi |y_D|/h_D) \cos \pi(z - z_w) + \exp(-2\pi |y_D|/h_D) \right] \right\} \dots\dots\dots (3.364) \end{aligned}$$

The Ratio  $\bar{R}_1$ .

$$\bar{R}_1 = \frac{\cosh \sqrt{a}(y_{eD} - \tilde{y}_D)}{\sinh \sqrt{a} y_{eD}} \dots\dots\dots (3.365)$$

By elementary considerations, the ratio  $\bar{R}_1$  may be written as<sup>29</sup>

$$\bar{R}_1 = \left\{ \exp(-\sqrt{a}\tilde{y}_D) + \exp[-\sqrt{a}(2y_{eD} - \tilde{y}_D)] \right\} \left[ 1 + \sum_{m=1}^{\infty} \exp(-2m\sqrt{a}y_{eD}) \right] \dots\dots\dots (3.366)$$

The expression given in Eq. 3.366 provides computational advantages when  $s$  is small (time is large).

**Example 3.12** Consider a fully penetrating, uniform-flux fracture of half-length  $x_f$  located at  $x'=0, y'=0$  in an infinite-slab reservoir with closed top and bottom boundaries.

*Solution.* Table 3.6 gives the solution for this problem. For simplicity, assuming an isotropic reservoir, choosing the characteristic length as  $\ell = x_f$  and noting that  $q = 2\tilde{q}h x_f$ , the solution becomes

$$\frac{2\pi k h}{q\mu} \overline{\Delta p} = \frac{1}{2s} \int_{-1}^{+1} K_0 \left[ \sqrt{(x_D - \alpha)^2 + y_D^2} \sqrt{u} \right] d\alpha \dots\dots\dots (3.367)$$

First consider the numerical evaluation of Eq. 3.367. We note from Eqs. 3.324 through 3.326 that Eq. 3.367 may be written in one of the following forms, depending on the value of  $x_D$ .

$$\frac{2\pi k h}{q\mu} \overline{\Delta p} = \frac{1}{2s\sqrt{u}} \left[ \int_0^{\sqrt{u}(x_D+1)} K_0(\sqrt{\alpha^2 + uy_D^2}) d\alpha - \int_0^{\sqrt{u}(x_D-1)} K_0(\sqrt{\alpha^2 + uy_D^2}) d\alpha \right] \quad x_D \geq 1, \dots (3.368)$$

$$\frac{2\pi k h}{q\mu} \overline{\Delta p} = \frac{1}{2s\sqrt{u}} \left[ \int_0^{\sqrt{u}(1-x_D)} K_0(\sqrt{\alpha^2 + uy_D^2}) d\alpha - \int_0^{\sqrt{u}(-1-x_D)} K_0(\sqrt{\alpha^2 + uy_D^2}) d\alpha \right] \quad x_D \leq -1, \dots\dots\dots (3.369)$$

and

$$\frac{2\pi k h}{q\mu} \overline{\Delta p} = \frac{1}{2s\sqrt{u}} \left[ \int_0^{\sqrt{u}(x_D+1)} K_0(\sqrt{\alpha^2 + uy_D^2}) d\alpha + \int_0^{\sqrt{u}(1-x_D)} K_0(\sqrt{\alpha^2 + uy_D^2}) d\alpha \right] \quad -1 \leq x_D \leq +1 \dots\dots\dots (3.370)$$

The numerical evaluation of the integrals in Eqs. 3.368 through 3.370 for  $y_D \neq 0$  should be straightforward with the use of the standard numerical integration algorithms. For  $y_D = 0$ , the polynomial approximations given by Luke<sup>30</sup> or the power series expansion given by Eq. 3.327 should be useful.

The short- and long-time asymptotic approximations of the fracture solution are also obtained by applying the relations given by Eqs. 3.330 and 3.332, respectively, to the right side of Eq. 3.367. This procedure yields, for short times,

$$\lim_{s \rightarrow \infty} \frac{2\pi k h}{q\mu} \overline{\Delta p} = \frac{\pi\beta}{4\sqrt{\omega s}^{3/2}} \exp(-|y_D| \sqrt{\omega s}), \dots\dots\dots (3.371)$$

or, in real-time domain,

$$\lim_{t_D \rightarrow 0} \frac{2\pi k h}{q\mu} \Delta p = \frac{\beta}{2} \left[ \sqrt{\pi t_D / \omega} \exp\left(-\frac{y_D^2}{4t_D / \omega}\right) - \frac{\pi}{2} |y_D| \operatorname{erfc}\left(\frac{|y_D|}{2\sqrt{t_D / \omega}}\right) \right], \dots\dots\dots (3.372)$$

where  $\beta$  is given by Eq. 3.331 with  $a = -1$  and  $b = +1$ . At long times, the following asymptotic approximation may be used:

$$\lim_{s \rightarrow 0} \frac{2\pi k h}{q\mu} \overline{\Delta p} = \frac{1}{2s} (-\ln s + \ln 4 - 2\gamma + 2) + \frac{1}{s} \sigma(x_D, y_D, -1, +1), \dots\dots\dots (3.373)$$

or, in real-time domain,

$$\lim_{t_D \rightarrow \infty} \frac{2\pi k h}{q\mu} \Delta p = \frac{1}{2} \left[ \ln\left(\frac{4t_D}{e^\gamma}\right) + 2 \right] + \sigma(x_D, y_D, -1, +1), \dots\dots\dots (3.374)$$

where  $\gamma = 0.5772 \dots$  and  $\sigma(x_D, y_D, -1, +1)$  is given by Eq. 3.333.

**Example 3.13** Consider a horizontal well of length  $L_h$  located at  $x' = 0, y' = 0$ , and  $z' = z_w$  in an infinite-slab reservoir with closed top and bottom boundaries.

*Solution.* Table 3.6 gives the horizontal-well solution for an infinite-slab reservoir with impermeable boundaries. Assuming an isotropic reservoir, choosing the characteristic length as  $\ell = L_h / 2$  and noting that  $q = \tilde{q}L_h$ , the solution may be written as

$$\frac{2\pi k h}{q\mu} \overline{\Delta p} = \frac{2\pi k h}{q\mu} \overline{\Delta p}_f + \overline{F}, \dots\dots\dots (3.375)$$

where  $2\pi k h \overline{\Delta p}_f / (q\mu)$  is the fracture solution given by the right side of Eq. 3.367 and  $\overline{F}$  is given by

$$\overline{F} = \frac{1}{s} \sum_{n=1}^{\infty} \cos n\pi \tilde{z}_D \cos n\pi \tilde{z}_{wD} \int_{-1}^{+1} K_0 \left[ \sqrt{(x_D - \alpha)^2 + y_D^2} \varepsilon_n \right] d\alpha, \dots\dots\dots (3.376)$$

with

$$\varepsilon_n = \sqrt{u + n^2 \pi^2 / h_D^2}, \dots\dots\dots (3.346)$$

$$\tilde{z}_D = z / h, \dots\dots\dots (3.377)$$

and

$$\tilde{z}_{wD} = z_w / h. \dots\dots\dots (3.378)$$

The computation of the first term in the right side of Eq. 3.375 [ $2\pi kh\overline{\Delta p}_f/(q\mu)$ ] is the same as the computation of the fracture solution given by Eq. 3.367 and has been discussed in Example 3.12. The computational form of the second term ( $\overline{F}$ ) in the right side of Eq. 3.375 is given by Eqs. 3.347 through 3.350. Of particular interest is the case for  $-1 \leq x_D \leq +1$ . In this case, from Eqs. 3.350 and 3.351, we have

$$\overline{F}(-1 \leq x_D \leq +1) = \overline{F}_1 - \frac{1}{s} \sum_{n=1}^{\infty} \frac{\cos n\pi\tilde{z}_D \cos n\pi\tilde{z}_{wD}}{\varepsilon_n} \times \left[ \int_{\varepsilon_n(x_D+1)}^{\infty} K_0(\sqrt{\alpha^2 + \varepsilon_n^2 y_D^2}) d\alpha + \int_{\varepsilon_n(1-x_D)}^{\infty} K_0(\sqrt{\alpha^2 + \varepsilon_n^2 y_D^2}) d\alpha \right], \dots\dots\dots (3.379)$$

where

$$\overline{F}_1 = \frac{\pi}{s} \sum_{n=1}^{\infty} \frac{\cos n\pi\tilde{z}_D \cos n\pi\tilde{z}_{wD}}{\varepsilon_n} \exp(-\varepsilon_n |y_D|). \dots\dots\dots (3.380)$$

The computational considerations for the series  $\overline{F}_1$  have been discussed previously.

Next, we consider the short- and long-time approximations of the horizontal-well solution given by Eq. 3.375. To obtain a short-time approximation, we substitute the asymptotic expressions for  $2\pi kh\overline{\Delta p}_f/(q\mu)$  and  $\overline{F}$  as  $s \rightarrow \infty$  given, respectively, by Eqs. 3.371 and 3.353. This yields

$$\lim_{s \rightarrow \infty} \frac{2\pi kh}{q\mu} \overline{\Delta p} = \frac{\beta h_D}{4s} K_0 \left[ \sqrt{(\tilde{z}_D - \tilde{z}_{wD})^2 h_D^2 + y_D^2} \sqrt{\omega s} \right], \dots\dots\dots (3.381)$$

where  $\beta$  is given by Eq. 3.331. The inverse Laplace transform of Eq. 3.381 is given by

$$\lim_{t_D \rightarrow 0} \frac{2\pi kh}{q\mu} \Delta p = -\frac{\beta h_D}{8} Ei \left[ -\frac{(\tilde{z}_D - \tilde{z}_{wD})^2 h_D^2 + y_D^2}{4t_D/\omega} \right]. \dots\dots\dots (3.382)$$

To obtain the long-time approximation of Eq. 3.375, we substitute the asymptotic expressions for  $2\pi kh\overline{\Delta p}_f/(q\mu)$  and  $\overline{F}$  as  $s \rightarrow \infty$  given, respectively, by Eq. 3.374 and Eqs. 3.355 through 3.357. Of particular interest is the case for  $-1 \leq x_D \leq +1$ , where we have

$$\begin{aligned} \lim_{s \rightarrow 0} \frac{2\pi kh}{q\mu} \overline{\Delta p} &= \frac{1}{2s} (-\ln s + \ln 4 - 2\gamma + 2) + \frac{1}{s} \sigma(x_D, y_D, -1, +1) \\ &- \frac{h_D}{4s} \left\{ \ln \left[ 1 - 2 \exp(-\pi |y_D|/h_D) \cos \pi(\tilde{z}_D + \tilde{z}_{wD}) + \exp(-2\pi |y_D|/h_D) \right] \right. \\ &+ \left. \ln \left[ 1 - 2 \exp(-\pi |y_D|/h_D) \cos \pi(\tilde{z}_D - \tilde{z}_{wD}) + \exp(-2\pi |y_D|/h_D) \right] \right\} \\ &- \frac{h_D}{\pi s} \sum_{n=1}^{\infty} \frac{\cos n\pi\tilde{z}_D \cos n\pi\tilde{z}_{wD}}{n} \end{aligned}$$

$$\times \left[ \int_{n\pi(x_D+1)/h_D}^{\infty} K_0(\sqrt{\alpha^2 + n^2\pi^2 y_D^2 / h_D^2}) d\alpha + \int_{n\pi(1-x_D)/h_D}^{\infty} K_0(\sqrt{\alpha^2 + n^2\pi^2 y_D^2 / h_D^2}) d\alpha \right], \dots (3.383)$$

where  $\gamma = 0.5772 \dots$  and  $\sigma(x_D, y_D, -1, +1)$  is given by Eq. 3.333. The inverse Laplace transform of Eq. 3.383 yields

$$\begin{aligned} \lim_{t_D \rightarrow \infty} \frac{2\pi k h}{q\mu} \Delta p &= \frac{1}{2} \left[ \ln \left( \frac{4t_D}{e^\gamma} \right) + 2 \right] + \sigma(x_D, y_D, -1, +1) \\ &+ \ln \left\{ \left[ 1 - 2 \exp(-\pi |y_D| / h_D) \cos \pi(\tilde{z}_D - \tilde{z}_{wD}) + \exp(-2\pi |y_D| / h_D) \right] \right\} \\ &\quad - \frac{h_D}{\pi} \sum_{n=1}^{\infty} \frac{\cos n\pi\tilde{z}_D \cos n\pi\tilde{z}_{wD}}{n} \\ &- \frac{h_D}{4} \left\{ \ln \left[ 1 - 2 \exp(-\pi |y_D| / h_D) \cos \pi(\tilde{z}_D + \tilde{z}_{wD}) + \exp(-2\pi |y_D| / h_D) \right] \right\} \\ &\times \left[ \int_{n\pi(x_D+1)/h_D}^{\infty} K_0(\sqrt{\alpha^2 + n^2\pi^2 y_D^2 / h_D^2}) d\alpha + \int_{n\pi(1-x_D)/h_D}^{\infty} K_0(\sqrt{\alpha^2 + n^2\pi^2 y_D^2 / h_D^2}) d\alpha \right], \dots (3.384) \end{aligned}$$

**Example 3.14** Consider a fully penetrating, uniform-flux fracture of half-length  $x_f$  in an isotropic and closed cylindrical reservoir. The center of the fracture is at  $r' = 0, \theta = 0$  and the fracture tips extend from  $(r' = x_f, \theta = \alpha + \pi)$  to  $(r' = x_f, \theta = \alpha)$ .

*Solution.* The solution for this problem has been obtained in Eq. 3.278 in Example 3.8 with  $h_w = h$ . Choosing the characteristic length as  $\ell = x_f$  and noting that  $q = 2\tilde{q}h x_f$ , the solution is given by

$$\begin{aligned} \frac{2\pi k h}{q\mu} \overline{\Delta p} &= \frac{1}{2s} \left\{ \int_0^1 K_0 \left[ \sqrt{u} \sqrt{r_D^2 + r'^2_D - 2r_D r'_D \cos(\theta - \alpha)} \right] dr'_D \right. \\ &\quad \left. + \int_0^1 K_0 \left[ \sqrt{u} \sqrt{r_D^2 + r'^2_D - 2r_D r'_D \cos(\theta - \alpha - \pi)} \right] dr'_D \right. \\ &\quad \left. - \sum_{k=-\infty}^{+\infty} \left[ \cos k(\theta - \alpha) + \cos k(\theta - \alpha - \pi) \right] \frac{I_k(\sqrt{ur_D}) K'_k(\sqrt{ur_{eD}})}{I'_k(\sqrt{ur_{eD}})} \int_0^1 I_k(\sqrt{ur'_D}) dr'_D \right\}, \dots (3.385) \end{aligned}$$

For the computation of the pressure responses at the center of the fracture ( $r_D = 0$ ), Eq. 3.385 simplifies to

$$\frac{2\pi k h}{q\mu} \overline{\Delta p} = \frac{1}{s} \int_0^1 \left[ K_0(\sqrt{ur'_D}) + I_0(\sqrt{ur'_D}) K_1(\sqrt{ur_{eD}}) / I_1(\sqrt{ur_{eD}}) \right] dr'_D, \dots (3.386)$$

It is also possible to find a very good approximation for Eq. 3.385, especially when  $r_{eD}$  is large. If we assume<sup>19</sup>

$$(-1)^n K'_k(\sqrt{ur_{eD}}) / I'_k(\sqrt{ur_{eD}}) = K'_0(\sqrt{ur_{eD}}) / I'_0(\sqrt{ur_{eD}}), \dots (3.387)$$

and use the following relation<sup>4</sup>

$$I_0[\sqrt{u}\sqrt{r_D^2 + r'^2_D - 2r_D r'_D \cos(\theta - \theta')}] = \sum_{n=-\infty}^{+\infty} (-1)^n I_n(\sqrt{ur_D}) I_n(\sqrt{ur'_D}) \cos n(\theta - \theta'), \dots (3.388)$$

then Eq. 3.385 may be written as

$$\begin{aligned} \frac{2\pi k h}{q\mu} \overline{\Delta p} &= \frac{1}{2s} \left\{ \int_0^1 K_0[\sqrt{u}\sqrt{r_D^2 + r'^2_D - 2r_D r'_D \cos(\theta - \alpha)}] dr'_D \right. \\ &\quad \left. + \int_0^1 K_0[\sqrt{u}\sqrt{r_D^2 + r'^2_D - 2r_D r'_D \cos(\theta - \alpha - \pi)}] dr'_D \right\} \\ &+ \frac{1}{2s} \frac{K_1(\sqrt{ur_{eD}})}{I_1(\sqrt{ur_{eD}})} \left\{ \int_0^1 I_0[\sqrt{u}\sqrt{r_D^2 + r'^2_D - 2r_D r'_D \cos(\theta - \alpha)}] dr'_D \right. \\ &\quad \left. + \int_0^1 I_0[\sqrt{u}\sqrt{r_D^2 + r'^2_D - 2r_D r'_D \cos(\theta - \alpha - \pi)}] dr'_D \right\} \dots (3.389) \end{aligned}$$

Because<sup>19</sup>

$$\begin{aligned} \int_{-\cos \alpha}^{+\cos \alpha} Z(\sqrt{u}\hat{R}_D) d\xi &= \int_0^1 Z[\sqrt{u}\sqrt{r_D^2 + r'^2_D - 2r_D r'_D \cos(\theta - \alpha)}] dr'_D \\ &+ \int_0^1 Z[\sqrt{u}\sqrt{r_D^2 + r'^2_D - 2r_D r'_D \cos(\theta - \alpha - \pi)}] dr'_D, \dots (3.390) \end{aligned}$$

where

$$\hat{R}_D = (x_D - x'_D - \xi)^2 + (y_D - y'_D - \xi \tan \alpha), \dots (3.391)$$

Eq. 3.389 may also be written as

$$\frac{2\pi k h}{q\mu} \overline{\Delta p} = \frac{1}{2s} \int_{-\cos \alpha}^{+\cos \alpha} [K_0(\sqrt{u}\hat{R}_D) + I_0(\sqrt{u}\hat{R}_D) K_1(\sqrt{ur_{eD}}) / I_1(\sqrt{ur_{eD}})] d\xi, \dots (3.392)$$

Although the assumption given in Eq. 3.387 may not be justified by itself, the solution given in Eq. 3.392 is a very good approximation for Eq. 3.385, especially when  $r_{eD}$  is large. For a fracture at the center of the cylindrical drainage region, Eq. 3.392 simplifies to

$$\frac{2\pi kh}{q\mu} \overline{\Delta p} = \frac{1}{2s} \int_{-1}^{+1} \left\{ K_0 \left[ \sqrt{u} \sqrt{(x_D - \xi)^2 + y_D^2} \right] d\xi + I_0 \left[ \sqrt{u} \sqrt{(x_D - \xi)^2 + y_D^2} \right] K_1(\sqrt{ur_{eD}}) / I_1(\sqrt{ur_{eD}}) \right\} d\xi \dots (3.393)$$

It is also possible to obtain short- and long-time approximations for the solution given in Eq. 3.393. For short times,  $u \rightarrow \infty$  and the second term in the argument of the integral in Eq. 3.393 becomes negligible compared with the first term. Then, Eq. 3.393 reduces to the solution for an infinite-slab reservoir given by Eq. 3.367, of which the short-time approximation has been discussed in Example 3.12.

To obtain a long-time approximation, we evaluate Eq. 3.393 at the limit as  $s \rightarrow 0$  ( $u \rightarrow s$ ). As shown in Sec. 3.2.3, for small arguments we may approximate the Bessel functions in Eq. 3.393 by

$$K_0(z) = - \ln (e^\gamma z / 2), \dots (3.394)$$

$$K_1(z) = 1 / z + (z / 2) [ \ln (e^\gamma z / 2) - 1 / 2 ], \dots (3.395)$$

$$I_0(z) = 1 + z^2 / 4, \dots (3.396)$$

and

$$I_1(z) = z / 2 + z^3 / 16, \dots (3.397)$$

where  $\gamma = 0.5772 \dots$ . With Eqs. 3.394 through 3.397 and by neglecting the terms of the order  $s^{3/2}$ , we may write<sup>29</sup>

$$\lim_{s \rightarrow 0} [ K_0(\sqrt{s\tilde{r}_D}) + I_0(\sqrt{s\tilde{r}_D}) K_1(\sqrt{s r_{eD}}) / I_1(\sqrt{s r_{eD}}) ] = \frac{2}{r_{eD}^2 s} + \ln \frac{r_{eD}}{\tilde{r}_D} - \frac{3}{4} + \frac{\tilde{r}_D^2}{2r_{eD}^2} \dots (3.398)$$

If we substitute the right side of Eq. 3.398 into Eq. 3.393, we obtain

$$\lim_{s \rightarrow 0} \frac{2\pi kh}{q\mu} \overline{\Delta p} = \frac{2}{r_{eD}^2 s^2} + \frac{1}{s} \left( \ln r_{eD} - \frac{3}{4} \right) + \frac{1 + \sigma(x_D, y_D, -1, +1)}{s} + \frac{\delta(x_D, y_D, r_{eD})}{s}, \dots (3.399)$$

where  $\sigma(x_D, y_D, -1, +1)$  is given by Eq. 3.333 and

$$\delta(x_D, y_D, r_{eD}) = y_D^2 / (2r_{eD}^2) + [(x_D - 1)^3 - (x_D + 1)^3] / (12r_{eD}^2) \dots (3.400)$$

The inverse Laplace transform of Eq. 3.399 yields the following long-time approximation for a uniform-flux fracture at the center of a closed square:

$$\lim_{t \rightarrow \infty} \frac{2\pi kh}{q\mu} \overline{\Delta p} = \frac{2t_D}{r_{eD}^2} + \ln r_{eD} - \frac{3}{4} + 1 + \sigma(x_D, y_D, -1, +1) + \delta(x_D, y_D, r_{eD}) \dots \dots \dots (3.401)$$

**Example 3.15** Consider a fully penetrating, uniform-flux fracture of half-length  $x_f$  in an isotropic and closed parallelepiped reservoir of dimensions  $x_e \times y_e \times h$ . The fracture is parallel to the  $x$  axis and centered at  $x_w, y_w, z_w$ .

*Solution.* The solution for this problem has been obtained in [Example 3.10](#) and, by choosing  $\ell = x_f$ , is given by

$$\begin{aligned} \overline{p_{Df}} = \frac{2\pi kh}{q\mu} \overline{\Delta p}_1 = \frac{\pi}{x_{eD} s} & \left\{ \frac{\cosh \sqrt{u}(y_{eD} - |y_D - y_{wD}|) + \cosh \sqrt{u}[y_{eD} - (y_D + y_{wD})]}{\sqrt{u} \sinh \sqrt{u} y_{eD}} \right. \\ & + \frac{2x_{eD}}{\pi} \sum_{k=1}^{\infty} \frac{1}{k} \sin k\pi \frac{1}{x_{eD}} \cos k\pi \frac{x_{wD}}{x_{eD}} \cos k\pi \frac{x_D}{x_{eD}} \\ & \left. \times \frac{\cosh \varepsilon_k(y_{eD} - |y_D - y_{wD}|) + \cosh \varepsilon_k[y_{eD} - (y_D + y_{wD})]}{\varepsilon_k \sinh \varepsilon_k y_{eD}} \right\}, \dots \dots \dots (3.402) \end{aligned}$$

where

$$\varepsilon_k = \sqrt{u + k^2 \pi^2 / x_{eD}^2} \dots \dots \dots (3.403)$$

The computation of the ratios of the hyperbolic functions in [Eq. 3.402](#) may be difficult, especially when their arguments approach zero or infinity. When  $s$  is small (long times), [Eq. 3.366](#) should be useful to compute the ratios of the hyperbolic functions. When  $s$  is large (small times), with [Eq. 3.366](#) the solution given in [Eq. 3.402](#) may be written as<sup>29</sup>

$$\overline{p_{Df}} = \overline{p_{D1}} + \overline{p_{Db1}} + \overline{p_{Db2}}, \dots \dots \dots (3.404)$$

where

$$\begin{aligned} \overline{p_{D1}} &= \frac{2}{s} \sum_{k=1}^{\infty} \frac{1}{k} \sin k\pi \frac{1}{x_{eD}} \cos k\pi \frac{x_D}{x_{eD}} \cos k\pi \frac{x_{wD}}{x_{eD}} \frac{\exp(-\varepsilon_k |y_D - y_{wD}|)}{\varepsilon_k} \\ &= \frac{\pi}{x_{eD} s} \sum_{k=1}^{\infty} \int_{x_{wD}-1}^{x_{wD}+1} \cos k\pi \frac{x_D}{x_{eD}} \cos k\pi \frac{x'_D}{x_{eD}} \frac{\exp(-\varepsilon_k |y_D - y_{wD}|)}{\varepsilon_k} dx'_D \\ &= \frac{1}{2s} \int_{-1}^{+1} \sum_{k=-\infty}^{+\infty} \left\{ K_0 \left[ \sqrt{(x_D - x_{wD} - 2kx_{eD} - a)^2 + (y_D - y_{wD})^2} \sqrt{u} \right] \right. \\ &\quad \left. + K_0 \left[ \sqrt{(x_D + x_{wD} - 2kx_{eD} - a)^2 + (y_D - y_{wD})^2} \sqrt{u} \right] \right\} da \\ &\quad - \pi \exp(-\sqrt{u} |y_D - y_{wD}|) / (x_{eD} s \sqrt{u}), \dots \dots \dots (3.405) \end{aligned}$$



$$\begin{aligned} \bar{p}_{Db1} = & \frac{\pi}{x_{eD}s\sqrt{u}} \left\{ \exp[-\sqrt{u}(y_D + y_{wD})] + \exp[-\sqrt{u}(2y_{eD} - y_D - y_{wD})] \right. \\ & + \exp(-\sqrt{u} | y_D - y_{wD} |) + \exp[-\sqrt{u}(2y_{eD} - | y_D - y_{wD} |)] \left. \right\} \\ & \times \left[ 1 + \sum_{m=1}^{\infty} \exp(-2m\sqrt{u}y_{eD}) \right], \dots\dots\dots (3.406) \end{aligned}$$

and

$$\begin{aligned} \bar{p}_{Db2} = & \frac{2}{s} \sum_{k=1}^{\infty} \frac{1}{k\varepsilon_k} \sin k\pi \frac{1}{x_{eD}} \cos k\pi \frac{x_D}{x_{eD}} \cos k\pi \frac{x_{wD}}{x_{eD}} \\ & \times \left\{ \exp[-\varepsilon_k(y_D + y_{wD})] + \exp[-\varepsilon_k(2y_{eD} - y_D - y_{wD})] \right. \\ & + \exp(-\varepsilon_k | y_D - y_{wD} |) + \exp[-\varepsilon_k(2y_{eD} - | y_D - y_{wD} |)] \left. \right\} \\ & \times \left[ 1 + \sum_{m=1}^{\infty} \exp(-2m\varepsilon_k y_{eD}) \right] \dots\dots\dots (3.407) \end{aligned}$$

The last equality in Eq. 3.405 follows from the relation given by Eq. 3.349. The expression given in Eq. 3.405 may also be written as

$$\bar{p}_{D1} = \bar{p}_{Di} + \bar{p}_{Db3}, \dots\dots\dots (3.408)$$

where

$$\bar{p}_{Di} = \frac{1}{2s} \int_{-1}^{+1} K_0 \left[ \sqrt{(x_D - x_{wD} - \alpha)^2 + (y_D - y_{wD})^2} \sqrt{u} \right] d\alpha, \dots\dots\dots (3.409)$$

and

$$\begin{aligned} \bar{p}_{Db3} = & \frac{1}{2s} \int_{-1}^{+1} K_0 \left[ \sqrt{(x_D + x_{wD} - \alpha)^2 + (y_D - y_{wD})^2} \sqrt{u} \right] d\alpha \\ & + \frac{1}{2s} \sum_{k=1}^{+\infty} \int_{-1}^{+1} \left\{ K_0 \left[ \sqrt{(x_D - x_{wD} - 2kx_{eD} - \alpha)^2 + (y_D - y_{wD})^2} \sqrt{u} \right] \right. \\ & + K_0 \left[ \sqrt{(x_D + x_{wD} - 2kx_{eD} - \alpha)^2 + (y_D - y_{wD})^2} \sqrt{u} \right] \\ & + K_0 \left[ \sqrt{(x_D - x_{wD} + 2kx_{eD} - \alpha)^2 + (y_D - y_{wD})^2} \sqrt{u} \right] \\ & \left. + K_0 \left[ \sqrt{(x_D + x_{wD} + 2kx_{eD} - \alpha)^2 + (y_D - y_{wD})^2} \sqrt{u} \right] \right\} d\alpha \\ & - \pi \exp(-\sqrt{u} | y_D - y_{wD} |) / (x_{eD}s\sqrt{u}), \dots\dots\dots (3.410) \end{aligned}$$

Therefore, the solution given by Eq. 3.402 may be written as follows for computation at early times (for large values of *s*):

$$\bar{p}_{Df} = \bar{p}_{Di} + \bar{p}_{Db}, \dots\dots\dots (3.411)$$

where  $\bar{p}_{Di}$  is given by Eq. 3.409 and corresponds to the solution for a fractured well in an infinite-slab reservoir (see Eq. 3.367 in Example 3.12) and  $\bar{p}_{Db}$  represents the contribution of the lateral boundaries and is given by

$$\bar{p}_{Db} = \bar{p}_{Db1} + \bar{p}_{Db2} + \bar{p}_{Db3} \dots\dots\dots (3.412)$$

In Eq. 3.412,  $\bar{p}_{Db1}$ ,  $\bar{p}_{Db2}$ , and  $\bar{p}_{Db3}$  are given, respectively, by Eqs. 3.406, 3.407, and 3.410. The integrals appearing in Eqs. 3.409 and 3.410 may be evaluated by following the lines outlined by Eqs. 3.324 through 3.326.

It is also possible to derive short- and long-time approximations for the fracture solution in a closed rectangular parallelepiped. The short-time approximation corresponds to the limit of the solution as  $s \rightarrow \infty$ . It can be easily shown that the  $\bar{p}_{Db}$  term in Eq. 3.411 becomes negligible compared with the  $\bar{p}_{Di}$  term for which a short-time approximation has been obtained in Example 3.12 (see Eqs. 3.371 and 3.372).

To obtain a long-time approximation (small values of  $s$ ), the solution given in Eq. 3.402 may be written as<sup>27</sup>

$$\bar{p}_{Df} = H + \frac{2}{s} \sum_{k=1}^{\infty} \frac{1}{k} \sin k\pi \frac{1}{x_{eD}} \cos k\pi \frac{x_{wD}}{x_{eD}} \cos k\pi \frac{x_D}{x_{eD}} \times \frac{\cosh \varepsilon_k (y_{eD} - |y_D - y_{wD}|) + \cosh \varepsilon_k [y_{eD} - (y_D + y_{wD})]}{\varepsilon_k \sinh \varepsilon_k y_{eD}}, \dots\dots\dots (3.413)$$

where

$$H = \frac{\pi}{x_{eD} s} \left\{ \frac{\cosh \sqrt{u} (y_{eD} - |y_D - y_{wD}|) + \cosh \sqrt{u} [y_{eD} - (y_D + y_{wD})]}{\sqrt{u} \sinh \sqrt{u} y_{eD}} \right\} = \frac{2\pi}{x_{eD} y_{eD} s u} + \frac{2\pi}{x_{eD} y_{eD} s} \sum_{m=1}^{\infty} \frac{1}{\varepsilon_m^2} \left( \cos m\pi \frac{y_D - y_{wD}}{y_{eD}} + \cos m\pi \frac{y_D + y_{wD}}{y_{eD}} \right), \dots\dots\dots (3.414)$$

and

$$\varepsilon_m = \sqrt{u + m^2 \pi^2 / y_{eD}^2} \dots\dots\dots (3.415)$$

The second equality in Eq. 3.414 results from<sup>31</sup>

$$\sum_{k=1}^{\infty} \frac{\cos kx}{k^2 + a^2} = \frac{\pi}{2a} \frac{\cosh a(\pi - x)}{\sinh a\pi} - \frac{1}{2a^2}, \quad 0 \leq x \leq 2\pi \dots\dots\dots (3.416)$$

For small values of  $s$ , replacing  $u$  by  $s$  and  $s + \alpha$  by  $\alpha$ , and with<sup>31</sup>

$$\sum_{k=1}^{\infty} \frac{\cos kx}{k^2} = \frac{\pi^2}{6} - \frac{\pi x}{2} + \frac{x^2}{4}, \quad 0 \leq x \leq 2\pi, \dots\dots\dots (3.417)$$

the term  $H$  given by Eq. 3.414 may be approximated by

$$\begin{aligned} \lim_{s \rightarrow 0} H &= \frac{2\pi}{x_{eD}y_{eD}s^2} + \frac{2y_{eD}}{\pi x_{eD}s} \sum_{m=1}^{\infty} \frac{1}{m^2} \left( \cos m\pi \frac{y_D - y_{wD}}{y_{eD}} + \cos m\pi \frac{y_D + y_{wD}}{y_{eD}} \right) \\ &= \frac{2\pi}{x_{eD}y_{eD}s^2} + \frac{2\pi y_{eD}}{x_{eD}s^2} \left[ \frac{1}{3} - \frac{|y_D - y_{wD}| + y_D + y_{wD}}{2y_{eD}} + \frac{(y_D - y_{wD})^2 + (y_D + y_{wD})^2}{4y_{eD}^2} \right] \dots (3.418) \end{aligned}$$

The long-time approximation of the second term in Eq. 3.413 is obtained by assuming  $u \ll k^2\pi^2/x_{eD}^2$  and taking the inverse Laplace transform of the resulting expressions; therefore, we can obtain the following long-time approximation

$$\begin{aligned} \lim_{t \rightarrow \infty} p_{Df} &= \frac{2\pi t_D}{x_{eD}y_{eD}} + \frac{2\pi y_{eD}}{x_{eD}} \left[ \frac{1}{3} - \frac{|y_D - y_{wD}| + y_D + y_{wD}}{2y_{eD}} + \frac{(y_D - y_{wD})^2 + (y_D + y_{wD})^2}{4y_{eD}^2} \right] \\ &\quad + \frac{2x_{eD}}{\pi} \sum_{k=1}^{\infty} \frac{1}{k^2} \sin k\pi \frac{1}{x_{eD}} \cos k\pi \frac{x_{wD}}{x_{eD}} \cos k\pi \frac{x_D}{x_{eD}} \\ &\quad \times \frac{\cosh \varepsilon_k (y_{eD} - |y_D - y_{wD}|) + \cosh \varepsilon_k [y_{eD} - (y_D + y_{wD})]}{\sinh k\pi \frac{y_{eD}}{x_{eD}}} \dots\dots\dots (3.419) \end{aligned}$$

**Example 3.16** Consider a uniform-flux horizontal well of length  $L_h$  in an isotropic and closed parallelepiped reservoir of dimensions  $x_e \times y_e \times h$ . The center of the well is at  $x_w, y_w, z_w$ , and the well is parallel to the  $x$  axis.

*Solution.* The solution for this problem was obtained in Example 3.11 and, by choosing  $\ell = L_h / 2$ , is given by

$$\frac{2\pi kh}{q\mu} \overline{\Delta p} = \overline{p}_{Df} + \overline{F}_1, \dots\dots\dots (3.420)$$

where  $\overline{p}_{Df}$  is the solution discussed in Example 3.15, and  $\overline{F}_1$  is given by

$$\begin{aligned} \overline{F}_1 &= \frac{2\pi}{x_{eD}s} \sum_{n=1}^{\infty} \cos n\pi \tilde{z}_D \cos n\pi \tilde{z}_{wD} \\ &\quad \times \left\{ \frac{\cosh \varepsilon_n (y_{eD} - |y_D - y_{wD}|) + \cosh \varepsilon_n [y_{eD} - (y_D + y_{wD})]}{\varepsilon_n \sinh \varepsilon_n y_{eD}} \right\} \\ &\quad + \frac{4}{s} \sum_{n=1}^{\infty} \cos n\pi \tilde{z}_D \cos n\pi \tilde{z}_{wD} \sum_{k=1}^{\infty} \frac{1}{k} \sin k\pi \frac{1}{x_{eD}} \cos k\pi \frac{x_{wD}}{x_{eD}} \cos k\pi \frac{x_D}{x_{eD}} \end{aligned}$$

$$\times \left\{ \frac{\cosh \varepsilon_{k,n}(y_{eD} - |y_D - y_{wD}|) + \cosh \varepsilon_{k,n}[y_{eD} - (y_D + y_{wD})]}{\varepsilon_{k,n} \sinh \varepsilon_{k,n} y_{eD}} \right\} \dots\dots\dots (3.421)$$

In Eq. 3.421,  $\tilde{z}_D$  and  $\tilde{z}_{wD}$  are given by Eqs. 3.377 and 3.378, respectively,

$$\varepsilon_n = \sqrt{u + n^2 \pi^2 / h_D^2} \dots\dots\dots (3.346)$$

and

$$\varepsilon_{k,n} = \sqrt{u + k^2 \pi^2 / x_{eD}^2 + n^2 \pi^2 / h_D^2} \dots\dots\dots (3.422)$$

The computation and the asymptotic approximations of the  $\bar{p}_{Df}$  term have been discussed in Example 3.15. To compute the  $\bar{F}_1$  term for long times (small  $s$ ), the relation for the ratios of the hyperbolic functions given by Eq. 3.366 should be useful. For computations at short times (large values of  $s$ ), following the lines similar to those in Example 3.15, the  $\bar{F}_1$  term in Eq. 3.421 may be written as

$$\bar{F}_1 = \bar{F} + \bar{F}_b \dots\dots\dots (3.423)$$

where

$$\bar{F} = \frac{1}{s} \sum_{n=1}^{\infty} \cos n\pi\tilde{z}_D \cos n\pi\tilde{z}_{wD} \int_{-1}^{+1} K_0 \left[ \sqrt{(x_D - x_{wD} - \alpha)^2 + (y_D - y_{wD})^2} \varepsilon_n \right] d\alpha \dots\dots\dots (3.424)$$

$$\bar{F}_b = \bar{F}_{b1} + \bar{F}_{b2} + \bar{F}_{b3} \dots\dots\dots (3.425)$$

$$\begin{aligned} \bar{F}_{b1} = & \frac{2\pi}{x_{eD} s} \sum_{n=1}^{\infty} \frac{1}{\varepsilon_n} \cos n\pi\tilde{z}_D \cos n\pi\tilde{z}_{wD} \left\{ \exp[-\varepsilon_n(y_D + y_{wD})] + \exp[-\varepsilon_n(2y_{eD} - y_D - y_{wD})] \right. \\ & + \exp[-\varepsilon_n(2y_{eD} - |y_D - y_{wD}|)] \left. \left[ 1 + \sum_{m=1}^{\infty} \exp(-2m\varepsilon_n y_{eD}) \right] \right. \\ & \left. + \exp(-\varepsilon_n |y_D - y_{wD}|) \sum_{m=1}^{\infty} \exp(-2m\varepsilon_n y_{eD}) \right\} \dots\dots\dots (3.426) \end{aligned}$$

$$\begin{aligned} \bar{F}_{b2} = & \frac{4}{s} \sum_{n=1}^{\infty} \cos n\pi\tilde{z}_D \cos n\pi\tilde{z}_{wD} \sum_{k=1}^{\infty} \frac{1}{\varepsilon_{k,n} k} \sin k\pi \frac{1}{x_{eD}} \cos k\pi \frac{x_D}{h_D} \cos k\pi \frac{x_{wD}}{h_D} \\ & \times \left\{ \left\{ \exp[-\varepsilon_{k,n}(y_D + y_{wD})] + \exp[-\varepsilon_{k,n}(2y_{eD} - y_D - y_{wD})] \right. \right. \\ & \left. \left. + \exp[-\varepsilon_{k,n}(2y_{eD} - |y_D - y_{wD}|)] \right\} \left[ 1 + \sum_{m=1}^{\infty} \exp(-2m\varepsilon_{k,n} y_{eD}) \right] \right\} \end{aligned}$$

$$+ \exp(-\varepsilon_{k,n} |y_D - y_{wD}|) \sum_{m=1}^{\infty} \exp(-2m\varepsilon_{k,n} y_{eD}) \Big\}, \dots\dots\dots (3.427)$$

and

$$\begin{aligned} \bar{F}_{b3} &= \frac{1}{s} \sum_{n=1}^{\infty} \cos n\pi\tilde{z}_D \cos n\pi\tilde{z}_{wD} \\ &\times \left\{ \int_{-1}^{+1} K_0 \left[ \sqrt{(x_D + x_{wD} - \alpha)^2 + (y_D - y_{wD})^2} \varepsilon_n \right] d\alpha \right. \\ &+ \sum_{k=1}^{+\infty} \int_{-1}^{+1} \left\{ K_0 \left[ \sqrt{(x_D - x_{wD} - 2kx_{eD} - \alpha)^2 + (y_D - y_{wD})^2} \varepsilon_n \right] \right. \\ &\quad + K_0 \left[ \sqrt{(x_D + x_{wD} - 2kx_{eD} - \alpha)^2 + (y_D - y_{wD})^2} \varepsilon_n \right] \\ &\quad + K_0 \left[ \sqrt{(x_D - x_{wD} + 2kx_{eD} - \alpha)^2 + (y_D - y_{wD})^2} \varepsilon_n \right] \\ &\quad \left. \left. + K_0 \left[ \sqrt{(x_D + x_{wD} + 2kx_{eD} - \alpha)^2 + (y_D - y_{wD})^2} \varepsilon_n \right] \right\} d\alpha \right\} \dots\dots\dots (3.428) \end{aligned}$$

The computational form of the  $\bar{F}$  term in Eq. 3.424 is obtained by applying the relations given by Eqs. 3.347 through 3.350 and Eq. 3.328. Of particular interest is the case for  $-1 \leq x_D \leq +1$  and  $y_D = y_{wD}$  given by

$$\begin{aligned} \bar{F}(-1 \leq x_D \leq +1) &= \bar{F}_1 - \frac{1}{s} \sum_{n=1}^{\infty} \frac{1}{\varepsilon_n} \cos n\pi\tilde{z}_D \cos n\pi\tilde{z}_{wD} \\ &\times \left[ \int_{\varepsilon_n(x_D - x_{wD} + 1)}^{\infty} K_0(\alpha) d\alpha + \int_{\varepsilon_n(1 - x_D + x_{wD})}^{\infty} K_0(\alpha) d\alpha \right], \dots\dots\dots (3.429) \end{aligned}$$

where

$$\bar{F}_1 = \frac{\pi}{s} \sum_{n=1}^{\infty} \frac{\cos n\pi\tilde{z}_D \cos n\pi\tilde{z}_{wD}}{\varepsilon_n} \exp(-\varepsilon_n |y_D|), \dots\dots\dots (3.430)$$

which can be written as follows by using the relation given in Eq. 3.337:

$$\bar{F}_1 = \frac{h_D}{2s} \sum_{n=-\infty}^{+\infty} \left[ K_0 \left( \left| \tilde{z}_D - \tilde{z}_{wD} - 2n \right| h_D \sqrt{u} \right) + K_0 \left( \left| \tilde{z}_D + \tilde{z}_{wD} - 2n \right| h_D \sqrt{u} \right) - \frac{\pi}{2s\sqrt{u}} \right] \dots (3.431)$$

Similarly, for  $-1 \leq x_D \leq +1$  and  $y_D = y_{wD}$ , the  $\bar{F}_{b3}$  term given in Eq. 3.428 may be written as

$$\bar{F}_{b3} = \frac{1}{s} \sum_{n=1}^{\infty} \frac{1}{\varepsilon_n} \cos n\pi\tilde{z}_D \cos n\pi\tilde{z}_{wD} \left\{ Ki_1 \left[ (x_D + x_{wD} + 1) \varepsilon_n \right] - Ki_1 \left[ (x_D + x_{wD} - 1) \varepsilon_n \right] \right.$$

$$\begin{aligned}
 & + \sum_{k=1}^{+\infty} \left\{ Ki_1 \left[ (2kx_{eD} - x_D + x_{wD} + 1) \varepsilon_n \right] - Ki_1 \left[ (2kx_{eD} - x_D + x_{wD} - 1) \varepsilon_n \right] \right. \\
 & \quad + Ki_1 \left[ (2kx_{eD} - x_D - x_{wD} + 1) \varepsilon_n \right] - Ki_1 \left[ (2kx_{eD} - x_D - x_{wD} - 1) \varepsilon_n \right] \\
 & \quad + Ki_1 \left[ (2kx_{eD} + x_D - x_{wD} + 1) \varepsilon_n \right] - Ki_1 \left[ (2kx_{eD} + x_D - x_{wD} - 1) \varepsilon_n \right] \\
 & \left. + Ki_1 \left[ (2kx_{eD} + x_D + x_{wD} + 1) \varepsilon_n \right] - Ki_1 \left[ (2kx_{eD} + x_D + x_{wD} - 1) \varepsilon_n \right] \right\}, \dots \dots \dots (3.432)
 \end{aligned}$$

where

$$Ki_1(x) = \int_x^\infty K_0(\alpha) d\alpha. \dots \dots \dots (3.433)$$

Example 3.15 discussed the short- and long-time approximations of the  $\bar{p}_{Df}$  term in Eq. 3.420. A small-time approximation for  $\bar{F}_1$  given by Eq. 3.423 is obtained with  $u = \omega s$  and by noting that as  $s \rightarrow \infty$ ,  $\bar{F} + \bar{F}_b \approx \bar{F}$ . Then, substituting the short-time approximations for  $\bar{p}_{Df}$  and  $\bar{F}$  given, respectively, by Eqs. 3.371 and 3.353 into Eq. 3.420, the following short-time approximation is obtained:<sup>27</sup>

$$\lim_{s \rightarrow \infty} \frac{2\pi kh}{q\mu} \bar{\Delta p} = \frac{\beta h_D}{4s} K_0 \left[ \sqrt{(\tilde{z}_D - \tilde{z}_{wD})^2 h_D^2 + (y_D - y_{wD})^2} \sqrt{\omega s} \right], \dots \dots \dots (3.434)$$

where  $\beta$  is given by Eq. 3.331. The inverse Laplace transform of Eq. 3.434 yields

$$\lim_{t \rightarrow 0} \frac{2\pi kh}{q\mu} \bar{\Delta p} = -\frac{\beta h_D}{8} Ei \left[ \frac{(\tilde{z}_D - \tilde{z}_{wD})^2 h_D^2 + (y_D - y_{wD})^2}{4t_D / \omega} \right]. \dots \dots \dots (3.435)$$

The long-time approximation of Eq. 3.420 is obtained by substituting the long-time approximations of  $\bar{p}_{Df}$  and  $\bar{F}_1$ . The long time-approximation of  $\bar{p}_{Df}$  is obtained in Example 3.15 (see Eq. 3.413 through 3.419). The long-time approximation of  $\bar{F}_1$  is obtained by evaluating the right side of Eq. 3.421 as  $s \rightarrow 0$  ( $u \rightarrow 0$ ) and is given by

$$\begin{aligned}
 \bar{F}_1 &= \frac{2h_D}{x_{eD}} \sum_{n=1}^{\infty} \frac{1}{n} \cos n\pi\tilde{z}_D \cos n\pi\tilde{z}_{wD} \\
 & \times \left\{ \frac{\cosh \lambda_n (y_{eD} - |y_D - y_{wD}|) + \cosh \lambda_n [y_{eD} - (y_D + y_{wD})]}{\lambda_n \sinh \lambda_n y_{eD}} \right\} \\
 & + \frac{4}{s} \sum_{n=1}^{\infty} \cos n\pi\tilde{z}_D \cos n\pi\tilde{z}_{wD} \sum_{k=1}^{\infty} \frac{1}{k} \sin k\pi \frac{1}{x_{eD}} \cos k\pi \frac{x_{wD}}{x_{eD}} \cos k\pi \frac{x_D}{x_{eD}} \\
 & \times \left\{ \frac{\cosh \lambda_{k,n} (y_{eD} - |y_D - y_{wD}|) + \cosh \lambda_{k,n} [y_{eD} - (y_D + y_{wD})]}{\lambda_{k,n} \sinh \lambda_{k,n} y_{eD}} \right\}, \dots \dots \dots (3.436)
 \end{aligned}$$

where

$$\lambda_n = n\pi / h_D \dots\dots\dots (3.437)$$

and

$$\lambda_{k, n} = k\pi / x_{eD} + n\pi / h_D \dots\dots\dots (3.438)$$

Thus, the long-time approximation Eq. 3.420 is given by

$$\frac{2\pi k h}{q\mu} \Delta p = p_{Df} + F_1, \dots\dots\dots (3.439)$$

where  $p_{Df}$  and  $F_1$  are given, respectively, by Eqs. 3.419 and 3.436. For computational purposes, however,  $F_1$  may be replaced by

$$F_1 = F + F_{b1} + F_{b2} + F_{b3} \dots\dots\dots (3.440)$$

In Eq. 3.440,  $F$ ,  $F_{b1}$ ,  $F_{b2}$ , and  $F_{b3}$  are given, respectively, by

$$F = \sum_{n=1}^{\infty} \cos n\tilde{\pi}z_D \cos n\tilde{\pi}z_{wD} \int_{-1}^{+1} K_0 \left[ \lambda_n \sqrt{(x_D - x_{wD} - \alpha)^2 + (y_D - y_{wD})^2} \right] d\alpha, \dots\dots\dots (3.441)$$

$$F_{b1} = \frac{2h_D}{x_{eD}} \sum_{n=1}^{\infty} \frac{1}{n} \cos n\tilde{\pi}z_D \cos n\tilde{\pi}z_{wD} \left\{ \left\{ \exp \left[ -\lambda_n (y_D + y_{wD}) \right] + \exp \left[ -\lambda_n (2y_{eD} - y_D - y_{wD}) \right] \right. \right. \\ \left. \left. + \exp \left[ -\lambda_n (2y_{eD} - |y_D - y_{wD}|) \right] \right\} \left[ 1 + \sum_{m=1}^{\infty} \exp \left( -2m\lambda_n y_{eD} \right) \right] \right. \\ \left. + \exp \left( -\lambda_n |y_D - y_{wD}| \right) \sum_{m=1}^{\infty} \exp \left( -2m\lambda_n y_{eD} \right) \right\}, \dots\dots\dots (3.442)$$

$$F_{b2} = 4 \sum_{n=1}^{\infty} \cos n\tilde{\pi}z_D \cos n\tilde{\pi}z_{wD} \sum_{k=1}^{\infty} \frac{1}{\lambda_{k, n} k} \sin k\pi \frac{1}{x_{eD}} \cos k\pi \frac{x_D}{h_D} \cos k\pi \frac{x_{wD}}{h_D} \\ \left\{ \left\{ \exp \left[ -\lambda_{k, n} (y_D + y_{wD}) \right] + \exp \left[ -\lambda_{k, n} (2y_{eD} - y_D - y_{wD}) \right] \right. \right. \\ \left. \left. + \exp \left[ -\lambda_{k, n} (2y_{eD} - |y_D - y_{wD}|) \right] \right\} \left[ 1 + \sum_{m=1}^{\infty} \exp \left( -2m\lambda_{k, n} y_{eD} \right) \right] \right. \\ \left. + \exp \left( -\lambda_{k, n} |y_D - y_{wD}| \right) \sum_{m=1}^{\infty} \exp \left( -2m\lambda_{k, n} y_{eD} \right) \right\}, \dots\dots\dots (3.443)$$

and

$$F_{b3} = \frac{1}{2} \sum_{n=1}^{\infty} \cos n\tilde{\pi}z_D \cos n\tilde{\pi}z_{wD}$$

$$\begin{aligned}
& \times \left\{ \int_{-1}^{+1} K_0 \left[ \sqrt{(x_D + x_{wD} - \alpha)^2 + (y_D - y_{wD})^2} \lambda_n \right] d\alpha \right. \\
& + \sum_{k=1}^{+\infty} \int_{-1}^{+1} \left\{ K_0 \left[ \sqrt{(x_D - x_{wD} - 2kx_{eD} - \alpha)^2 + (y_D - y_{wD})^2} \lambda_n \right] \right. \\
& \quad + K_0 \left[ \sqrt{(x_D + x_{wD} - 2kx_{eD} - \alpha)^2 + (y_D - y_{wD})^2} \lambda_n \right] \\
& \quad + K_0 \left[ \sqrt{(x_D - x_{wD} + 2kx_{eD} - \alpha)^2 + (y_D - y_{wD})^2} \lambda_n \right] \\
& \left. \left. + K_0 \left[ \sqrt{(x_D + x_{wD} + 2kx_{eD} - \alpha)^2 + (y_D - y_{wD})^2} \lambda_n \right] \right\} d\alpha \right\} \dots\dots\dots (3.444)
\end{aligned}$$

When computing the integrals and the trigonometric series, the relations given by Eqs. 3.324 through 3.326 and 3.345 through 3.350 are useful.

### Nomenclature

- $a$  = radius of the spherical source,  $L$
- $B$  = formation volume factor, res cm<sup>3</sup>/std cm<sup>3</sup>
- $c$  = fluid compressibility, atm<sup>-1</sup>
- $c_f$  = formation compressibility, atm<sup>-1</sup>
- $c_t$  = total compressibility, atm<sup>-1</sup>
- $C$  = wellbore-storage coefficient, cm<sup>3</sup>/atm
- $d$  = distance to a linear boundary, cm
- $D$  = domain
- $Ei(x)$  = exponential integral function
- $f(s)$  = naturally fractured reservoir function
- $\tilde{f}(s)$  = naturally fractured reservoir function based on  $\tilde{s}$
- $\bar{f}(s)$  = Laplace transform of a function  $f(t)$
- $G$  = Green's function
- $h$  = formation thickness, cm
- $\tilde{h}_D$  = dimensionless thickness, Eq. 3.313
- $h_D$  = dimensionless thickness, Eq. 3.314
- $h_f$  = fracture height (vertical penetration), cm
- $h_p$  = slab thickness, cm
- $h_w$  = well length (penetration), cm
- $H(x - x')$  = Heaviside's unit step function
- $\vec{i}_\zeta$  = unit normal vector in the  $\zeta$  direction,  $\zeta = x, y, z, r, \theta$
- $I_\nu(x)$  = modified Bessel function of the first kind of order  $\nu$
- $I'_\nu(x)$  = derivative of  $I_\nu(x)$
- $J_\nu(x)$  = Bessel function of the first kind of order  $\nu$
- $k$  = isotropic permeability, md
- $k_f$  = fracture permeability, md
- $k_h$  = equivalent horizontal permeability, md
- $k_{ij}$  = permeability in  $i$ -direction as a result of pressure gradient in  $j$ -direction, md



- $k_{\zeta}$  = permeability in  $\zeta$ -direction,  $\zeta = x, y, z$ , md  
 $k_{\zeta f}$  = fracture permeability in  $\zeta$ -direction,  $\zeta = x, y, z$ , md  
 $Ki_1(x)$  = first integral of  $K_0(z)$   
 $K_n(x)$  = modified Bessel function of the second kind of order  $n$   
 $K'_n(x)$  = derivative of  $K_n(x)$   
 $\ell$  = characteristic length of the system, cm  
 $L$  = Laplace transform operator  
 $L^{-1}$  = inverse Laplace transform operator  
 $L_h$  = horizontal-well length, cm  
 $m$  = pseudopressure, atm<sup>2</sup>/cp  
 $M_g$  = mass, g  
 $M$  = point in space  
 $M'$  = source point in space  
 $M_w$  = point in  $\Gamma_w$   
 $M'_w$  = source point in  $\Gamma_w$   
 $n$  = outward normal direction of the boundary surface  
 $\vec{n}$  = normal vector  
 $N$  = even integer in Stehfest's algorithm  
 $p$  = pressure, atm  
 $p_c$  = pressure for constant production rate,  $q_c$ , atm  
 $\bar{p}$  = dimensionless fracture pressure  
 $p_{Df}$   
 $p_e$  = external boundary pressure, atm  
 $p_f$  = fracture pressure, atm  
 $p_{fi}$  = initial pressure in fracture system, atm  
 $p_i$  = initial pressure, atm  
 $p_j$  = pressure in medium  $j, j=m, f$ , atm  
 $p_m$  = matrix pressure, atm  
 $p_{mi}$  = initial pressure in matrix system, atm  
 $p_{wf}$  = flowing wellbore pressure, atm  
 $\bar{p}(s)$  = Laplace transform of  $p(t)$   
 $p(t)$  = inverse of the Laplace domain function  
 $p_a(T)$  = approximate inverse of  $\bar{p}(s)$  at  $t=T$ , atm  
 $q$  = production rate, cm<sup>3</sup>/s  
 $\tilde{q}$  = instantaneous production rate for a point source, cm<sup>3</sup>/s  
 $q_c$  = constant production rate, cm<sup>3</sup>/s  
 $q_{sf}$  = sandface production rate, cm<sup>3</sup>/s  
 $q_{wb}$  = wellbore production rate as a result of storage, cm<sup>3</sup>/s  
 $r$  = radial coordinate and distance, cm  
 $r'$  = source coordinate in  $r$ -direction, cm  
 $r_e$  = external radius of the reservoir, cm  
 $r_w$  = wellbore radius, cm  
 $R$  = distance in 3D coordinates, cm

- $R_D$  = dimensionless radial distance in cylindrical coordinates  
 $s$  = Laplace transform parameter  
 $\tilde{s}$  = Laplace transform parameter based on  $\tilde{t}_p$   
 $s_m$  = skin factor  
 $S$  = source function  
 $t$  = time, s  
 $\tilde{t}_D$  = dimensionless time based on  $k_h$   
 $t_{AD}$  = dimensionless time based on area  
 $t_p$  = producing time, s  
 $T$  = Temperature, °C  
 $u$  =  $sf(s)$   
 $\vec{v}$  = velocity vector  
 $v_\xi$  = velocity component in the  $\xi$  direction,  $\xi = x, y, z, r, \theta$ , cm/s  
 $V$  = volume, cm<sup>3</sup>  
 $V_i$  = constant in Stehfest's algorithm  
 $V_f$  = fraction of the volume occupied by fractures  
 $V_m$  = fraction of the volume occupied by matrix  
 $x$  = distance in  $x$ -direction, cm  
 $x'$  = source coordinate in  $x$ -direction, cm  
 $x_e$  = distance to the external boundary in  $x$ -direction, cm  
 $x_p$  = half slab thickness, cm  
 $x_f$  = fracture half-length, cm  
 $\tilde{x}_f$  = dimensionless fracture half-length  
 $x_w$  = well coordinate in  $x$ -direction, cm  
 $y$  = distance in  $y$ -direction, cm  
 $y'$  = source coordinate in  $y$ -direction, cm  
 $y_e$  = distance to the external boundary in  $y$ -direction, cm  
 $y_w$  = well coordinate in  $y$ -direction, cm  
 $Y_n(x)$  = Bessel function of the second kind of order  $n$   
 $z$  = distance in  $z$ -direction, cm  
 $z'$  = source coordinate in  $z$ -direction, cm  
 $\tilde{z}_D$  = dimensionless distance in  $z$ -direction, [Eq. 3.377](#)  
 $z_w$  = well coordinate in  $z$ -direction, cm  
 $\tilde{z}_{wD}$  = dimensionless well coordinate in  $z$ -direction, [Eq. 3.378](#)  
 $Z$  = compressibility factor  
 $\alpha$  = permeability direction, [Eq. 3.17](#)  
 $\beta$  = permeability direction, [Eq. 3.17](#)  
 $\Gamma$  = boundary surface, cm<sup>2</sup>  
 $\Gamma_e$  = external boundary surface  
 $\Gamma_w$  = length, surface, or volume of the source  
 $\Gamma(x)$  = Gamma function  
 $\gamma$  = Euler's constant ( $\gamma = 0.5772\dots$ )  
 $\gamma$  = permeability direction, [Eq. 3.17](#)  
 $\gamma_f$  = fundamental solution of diffusion equation

$\Delta$	=	difference operator
$\delta(x)$	=	Dirac delta function
$\eta$	=	diffusivity constant
$\eta_i$	=	diffusivity constant in $i$ direction, $i = x, y, z,$ or $r$
$\theta$	=	angle from positive $x$ -direction, degrees radian
$\theta'$	=	source coordinate in $\theta$ -direction, degrees radian
$\lambda$	=	transfer coefficient for a naturally fractured reservoir
$\tilde{\lambda}$	=	$\lambda$ based on $k_h$
$\mu$	=	viscosity, cp
$\rho$	=	density, g/cm <sup>3</sup>
$\tau$	=	time, s
$\Phi$	=	porosity, fraction
$\phi(M)$	=	any continuous function
$\omega$	=	storativity ratio for a naturally fractured reservoir

### Subscripts and Superscripts

D	=	dimensionless
$f$	=	fracture
i	=	initial
$m$	=	matrix
w	=	wellbore
$\bar{L}$	=	Laplace transform indicator

---

## References

1. Al-Hussainy, R., Ramey, H.J. Jr., and Crawford, P.B.: "The Flow of Real Gases Through Porous Media," *JPT* (May 1966) 624.
2. Raghavan, R.: *Well Test Analysis*, Prentice Hall Petroleum Engineering Series, Englewood Cliffs, New Jersey (1993) 28–31, 336–435.
3. Fancher, G.H., Lewis, J.A., and Barnes, K.B.: "Some Physical Characteristics of Oil Sands," Mineral Industries Experimental Station Circular, *Pennsylvania State College Bull.* (1933) **12**, 322–333.
4. Forchheimer, P.: "Wasserbewegung durch Boden," *Zeitschrift des Vereins Deutscher Ingenieure* (1901) **45**, 1782–1788.
5. Watson, G.N.: *A Treatise on the Theory of Bessel Functions*, Cambridge U. Press, Cambridge, U.K. (1944).
6. Churchill, R.V.: *Operational Mathematics*, McGraw-Hill Book Co. Inc., New York City (1972) 2.
7. Abramowitz, M. and Stegun, I.A.: *Handbook of Mathematical Functions*, Dover Publications Inc., New York City (1972) 1020–1029.
8. Stehfest, H.: "Numerical Inversion of Laplace Transforms," *Communications of the ACM* (1970) **13**, No. 1, 47.
9. Crump, K.S.: "Numerical Inversion of Laplace Transforms Using a Fourier Series Approximation," *J. of the ACM* (1976) **233**, 89.
10. van Everdingen, A.F. and Hurst, W.: "The Application of the Laplace Transformation to Flow Problems in Reservoirs," *Trans.*, AIME (1953) **198**, 171.
11. Agarwal, R.G., Al-Hussainy, R., and Ramey, H.J. Jr.: "An Investigation of Wellbore Storage and Skin Effect in Unsteady Liquid Flow: I. Analytical Treatment," *SPEJ* (September 1970) 279.
12. Chen, C.C. and Raghavan, R.: "An Approach to Handle Discontinuities by the Stehfest Algorithm," *SPEJ* (December 1996) 363.
13. Gringarten, A.C. and Ramey, H.J. Jr.: "The Use of Source and Green's Functions in Solving Unsteady-Flow Problems in Reservoirs," *SPEJ* (October 1973) 285.

14. Carslaw, H.S. and Jaeger, J.C.: *Conduction of Heat in Solids*, Oxford U. Press, Oxford, U.K. (1959) 353–386.
15. Stakgold, I.: *Green's Functions and Boundary Value Problems*, John Wiley & Sons, New York City (1979) 86–104.
16. Kelvin, W.T.: *Mathematical and Physical Papers*, Vol. II, Cambridge U. Press, Cambridge, U.K. (1884) 41.
17. Ozkan, E. and Raghavan, R.: “New Solutions for Well-Test-Analysis Problems: Part 1—Analytical Considerations,” *SPEFE* (September 1991) 359.
18. Ozkan, E. and Raghavan, R.: “New Solutions for Well-Test-Analysis Problems: Part 2—Computational Considerations and Applications,” *SPEFE* (September 1991) 369.
19. Raghavan, R. and Ozkan, E.: *A Method for Computing Unsteady Flows in Porous Media*, Longman Scientific & Technical, Essex, U.K. (1994).
20. Raghavan, R.: “The Method of Sources and Sinks—A Perspective,” *SPE Memorial Series*, Richardson, Texas (1995) **1**, 135.
21. Nisle, R.G.: “The Effect of Partial Penetration on Pressure Build-Up in Oil Wells,” *Trans.*, AIME (1958) **213**, 85.
22. Newman, A.B.: “Heating and Cooling Rectangular and Cylindrical Solids,” *Industrial and Engineering Chemistry* (1936) **28**, 545.
23. Duhamel, J.M.C.: “Mémoire sur la méthode générale relative au mouvement de la chaleur dans les corps solides prolongé dans les milieux dont la température varie avec le temps,” *J. de Ec. Polyt.*, Paris (1833) **14**, 20.
24. Chen, H.-Y., Poston, S.W., and Raghavan, R.: “An Application of the Product-Solution Principle for Instantaneous Source and Green's Functions,” *SPEFE* (June 1991) 161.
25. Barenblatt, G.E., Zheltov, I.P., and Kochina, I.N.: “Basic Concepts in the Theory of Homogeneous Liquids in Fissured Rocks,” *J. of Appl. Math. Mech.* (1960) **24**, No. 5, 1286.
26. Warren, J.E. and Root, P.J.: “The Behavior of Naturally Fractured Reservoirs,” *SPEJ* (September 1963) 245; *Trans.*, AIME, **228**.
27. Kazemi, H.: “Pressure Transient Analysis of Naturally Fractured Reservoirs with Uniform Fracture Distribution,” *SPEJ* (December 1969) 451; *Trans.*, AIME, **246**.
28. de Swaan-O., A.: “Analytical Solutions for Determining Naturally Fractured Reservoir Properties by Well Testing,” *SPEJ* (June 1976) 117; *Trans.*, AIME, **261**.
29. Ozkan, E.: “Performance of Horizontal Wells,” PhD dissertation, U. of Tulsa, Tulsa (1988).
30. Luke, Y.L.: *Integrals of Bessel Functions*, McGraw-Hill Book Co. Inc., New York City (1962) 64–66.
31. Gradshteyn, I.S. and Ryzhik, I.M.: *Table of Integrals, Series, and Products*, Academic Press Inc., Orlando, Florida (1980) 40.

### SI Metric Conversion Factors

atm	× 1.013 250*	E + 05	= Pa
cp	× 1.0*	E – 03	= Pa·s
in.	× 2.54*	E + 00	= cm
in. <sup>2</sup>	× 6.451 6*	E + 00	= cm <sup>2</sup>
°F	(°F–32)/1.8		= °C
ft	× 3.048*	E – 01	= m

\*Conversion factor is exact.

## Chapter 4

# Fluid Sampling

John M. Williams\* and Sunil L. Kokal, Saudi Aramco

### 4.1 Introduction

Many general petroleum engineering texts have sections covering the measurement of phase behavior or pressure/volume/temperature (PVT) analysis, but few have detailed descriptions of fluid-sampling practices. This chapter covers the sampling of all produced reservoir fluids. It is intended to provide an overview of sampling methods, guidelines for selecting suitable methods, and detailed procedures for the most common practices.

An enormous range of reservoir fluids exists, and this means that the limited measurements of produced oil and gas properties that can be made in the field are far from adequate to provide the detailed characterization that modern petroleum engineering requires. In addition to PVT analysis, of fundamental importance to reservoir management, measurements relating to corrosion potential, solids formation, and nonhydrocarbon constituents have the potential to produce serious effects on the design of production facilities, on compatibility with pipeline transport, on product sales value, on refinery maintenance costs, and on reservoir asset values in general. The lack of such data could easily represent more risk than that tolerated when the decision to perform sampling and laboratory studies is taken. Examples of the financial impact of errors in fluid-property measurements are given elsewhere.<sup>1</sup> Fluid samples are thus required to enable advanced physical and chemical analyses to be carried out in specialized laboratories. Samples must be collected from a wide range of locations, including separators, pipelines, tanks, wellbores, and the formation itself. This chapter primarily targets the sampling of fluids under pressures above atmospheric, where numerous tools and procedures have been developed that are essentially specific to the petroleum industry. Best practices are proposed for fluid sampling, reporting of data, and quality control of samples.

Reservoir-fluid-property measurements derive from a complicated series of processes relying both on the operation of equipment and the performance of people, so the scope for errors is very significant. The overriding challenge in fluid sampling is that of ensuring that the fluid entering the sample container is representative of the bulk fluid being sampled. It is equally important that the sample remains representative during handling and storage, until all required measurements have been completed. Although thorough sample-checking procedures can identify some of the most obvious problems, there is never absolute certainty that the fluid under

---

\* Now with The Petroleum Inst., Abu Dhabi, UAE.

study is truly representative of the reservoir fluid. On occasion, laboratory measurements can show that a fluid is definitely not representative (e.g., saturation pressure is significantly higher than reservoir pressure), but even here the problem could lie with errors in field measurement data rather than with the samples themselves. Thus, it is essential that all the necessary precautions are taken to prevent poor samples from leading to erroneous physical-property measurements.

**Fig. 4.1** is a schematic diagram illustrating some of the most common sources of error in relation to the collection of production samples and data in the field. Perhaps the most important, yet often misunderstood, phase of any sampling program is that of well conditioning. A poorly conditioned well may still be producing drilling-mud filtrate, workover fluids, or reaction products and, in extreme cases, such materials may remain even after months of production. A conflicting aim of well conditioning is to avoid excessive pressure drawdown and the creation of a large region of two-phase reservoir fluid around the wellbore, which may be difficult to remove. This is especially important in the case of gas/condensate reservoirs, of which many are found at their saturation pressures. The sampling program must ensure that appropriate procedures are used to ensure that samples are taken under the best conditions.

Measurements of reactive or nonhydrocarbon components of reservoir fluids are complicated by the potential for loss through reaction or adsorption in contact with the production tubing or with sample-bottle walls, especially during long storage periods. On-site measurements can be very important if performed and recorded properly.

The schematic in **Fig. 4.1** emphasizes sampling activities in cased-hole wells, but pressurized samples are also obtained with formation-test tools in openhole wells. Here, contamination by mud filtrate or excessive pressure decrease (drawdown) during sampling means that it may not be possible to obtain quality PVT samples. Contamination by oil-based mud (OBM) is especially problematic.<sup>2</sup> Sampling from tanks or pipelines also requires that care be taken to ensure that the fluid is representative of the location or condition required to be studied.

Not only may errors in the field mean that samples are not fully representative of the reservoir fluid, but even good fluid samples may be studied under invalid conditions. Pressure and temperature errors can influence measurements and their interpretation, but it is especially errors in gas/oil ratio (GOR) that can have a major influence on a PVT study. Even basic data, such as sampling date and time, if not recorded or erroneous, can reduce the value of samples, even to the point of making measurements meaningless.

## 4.2 General Guidelines for Setting Up a Sampling Program

The specific requirements for samples and laboratory studies naturally will depend on the state of knowledge about a prospect. Thus, it may be advisable to perform extensive sampling and a complete suite of laboratory measurements on a wildcat well when nothing is previously known about the reservoir; this may provide the only fluid data on which to base future exploration work. However, the early wells in a field may not provide the best samples because drilling and workover practices will not have been optimized, and the wells' response to testing programs may require changes that are detrimental to fluid sampling. It may then be necessary to repeat some analyses during the appraisal stage, typically when wells will yield samples that are more representative of likely production. In contrast, sampling late in the appraisal phase may be needed only on occasions when surface measurements indicate unexpected fluid character.

The composition of subsurface water commonly changes laterally, as well as with depth, in the same aquifer. Changes may be brought about by the intrusion of other waters and by discharge from and recharge to the aquifer. It is thus difficult to obtain a representative sample of a given subsurface body of water. Any one sample is a very small part of the total mass, which may vary widely in composition. Therefore, it is generally necessary to obtain and analyze many samples. Also, the samples may change with time as gases come out of solution and

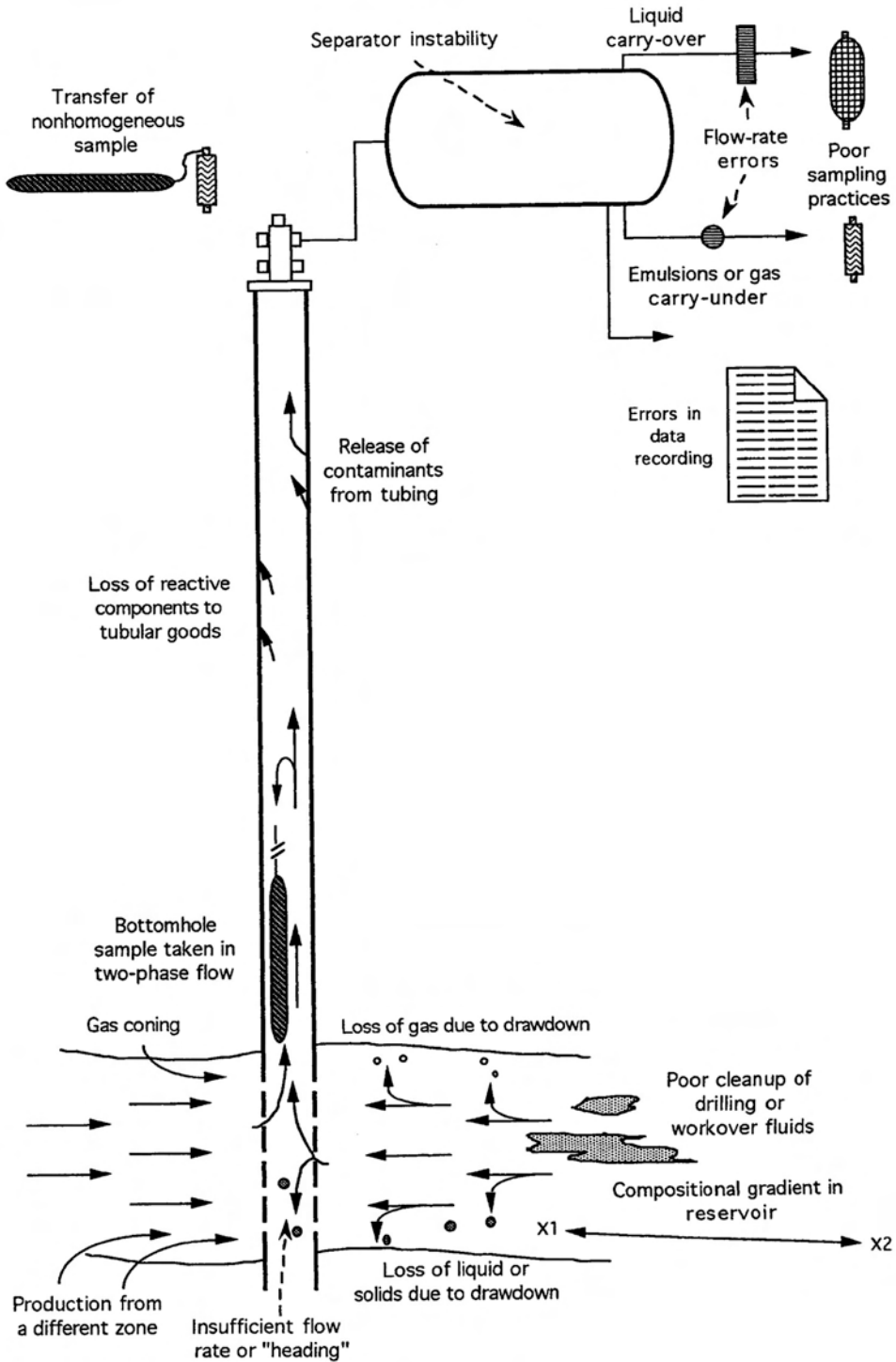


Fig. 4.1—A schematic view of wellsite sampling and measurement errors.<sup>1</sup>

supersaturated solutions produce precipitates. Sampling sites should be selected, if possible, to fit into a comprehensive network to cover an oil-productive geologic basin. There is a tendency

TABLE 4.1—RECOMMENDED FLUID-PROPERTY MEASUREMENTS

Measurement	Application(s)	Method(s)	Timing
Basic PVT study with saturation pressure, PV study, differential vaporization and viscosity for oils, separation tests	Reservoir engineering, well-test interpretation, production facility design, etc.	PVT laboratory with window cell for gas/condensate work	All exploration wells; appraisal wells for more accurate study or if composition is variable over the field
Hydrogen sulfide (H <sub>2</sub> S) content of gases	Safety, corrosion, treatment-plant design, etc.	On site through indicator tubes, monitors, or portable GC*; in laboratory as part of routine PVT study	All wells, at intervals covering the duration of the test
Reservoir-fluid composition, calorific value	Equation-of-state modeling for reservoir, production and PVT validation, sales specification	Part of routine PVT laboratory study; on-site analysis of fluids possible by GC	All exploration wells; appraisal wells for more accurate data or if fluid varies
GOR or condensate/gas ratio, liquid and gas stream gravities	Well-test monitoring, PVT sample, recombination process plant and pipeline design	Well-test separator measurements (can be confirmed by laboratory study)	All wells; can help identify fluid variation and confirm need for appraisal well samples
Water analysis	Log interpretation, corrosion potential, scale formation	On-site salinity and pH, full analysis in a laboratory	All exploration wells producing water; others as required
Heavy-metals content of hydrocarbon liquids	Refinery (catalyst poisons), power-plant emissions control	Laboratory analysis by AAS* or ICP*; part crude-oil assay	All exploration wells; appraisal wells if concentrations vary
Hydrate potential	Production facility design, etc.	Modeling based on water content of gas; special laboratory studies if warranted	All gas or condensate exploration wells; appraisal wells if composition varies
Mercaptans (hydrocarbon derivatives of H <sub>2</sub> S)	Processing needs, sales specification	GC analysis using a special detector; on site through indicator tubes (interferences)	All exploration wells in which H <sub>2</sub> S is detected; appraisal wells if composition varies
Sulfur content	Processing, sales specification	Various laboratory techniques available	All exploration wells; others as required
Other nonhydrocarbons such as carbon dioxide (CO <sub>2</sub> ), helium, nitrogen	Corrosion (CO <sub>2</sub> ), processing needs, helium recovery, sales specification	Laboratory or portable GC using thermal-conductivity detector and different carrier gas	All exploration wells; appraisal wells for more accurate study or if composition varies
Corrosion potential	Well completion, process plant and pipeline design	Complete laboratory water analysis needed	All exploration wells producing water; others as required
Mercury in gas	Safety, corrosion, sales quality	On-site indicator tubes, gold film detector, "adsorption samples" for laboratory	All exploration wells; appraisal wells if detected or if composition variable



**TABLE 4.1—RECOMMENDED FLUID-PROPERTY MEASUREMENTS (continued)**

Measurement	Application(s)	Method(s)	Timing
Stable isotopes in water	Origin of oilfield brines	Laboratory measurements	Producing wells flowing significant volumes of water
Radioactive element production or scaling	Safety, process design, sales specification	Specialized on-site measurements for radon (decay), others in laboratory	All exploration wells; on-site measurement if radon suspected; other wells as needed
Wax and asphaltene content	Production facility design, pipeline compatibility	Laboratory tests on oils and condensates as appropriate	All exploration wells; appraisal wells if content is variable
Refinery assay, paraffin/naphthene/aromatic analysis (PNA)	Sales specification, refinery use	Including large-scale distillation, PNA measurement	During appraisal stage if required
Biomarkers	Geochemistry, reservoir engineering	<i>n</i> -alkanes (GC); 13-C isotopes, hopanes/steranes by GCMS*	All exploration wells; other wells where fluids are sampled
Interfacial-tension measurements	Reservoir engineering, production facility design	Specialized PVT laboratory studies	Only after laboratory studies show high retrograde liquid level
Methanol content of condensate	Sales specification	Laboratory GC or other method	Exploration wells if methanol is used to prevent hydrates
Sulfate-reducing bacteria (SRB), organic acids	Corrosion, reservoir souring, drilling- or completion-fluid contamination	On-site SRB kit or accurate laboratory tests	All aqueous fluids used in or produced from wells

\*Abbreviations: GC = gas chromatography, AAS = atomic absorption spectroscopy, ICP = inductively coupled plasma emission spectroscopy, GCMS = gas chromatography mass spectrometry

for some oilfield waters to become more diluted as the oil reservoir is produced. Such dilution may result from the movement of water from adjacent compacting clay beds into the petroleum reservoir as pressure declines with the continued removal of oil and brine. The composition of oilfield water varies with the position within the geologic structure from which it is obtained. In some cases, the salinity will increase up-structure to a maximum at the point of oil/water contact.

The first priority in developing a sampling program, whether extensive or limited, is to establish exactly what measurements are required. **Table 4.1** gives a wide range of the measurements that are typically considered for exploration wells. This can be used as a checklist, together with direct contacts with users in other functions, to identify specific requirements for sampling and on-site measurements. Generally, it is advisable to plan to perform all applicable measurements unless sufficient information is already available from earlier tests of other wells. The fact that a measurement proves to be “normal,” or an unwanted component is not detected, should not be regarded as a waste of resources because it can still provide essential information, especially if data are different on other wells or changes are identified during production. On-site measurements are recommended for all reactive components because concentrations may change with time (e.g., during a well test), and losses frequently occur during

sample transport and storage. [Table 4.1](#) is not a comprehensive list, and other measurements will be required in certain locations and for specific purposes.

Having decided which fluid measurements are required, it is necessary to set up a suitable sampling program, taking into account the cost of the work, the quality and quantity of samples and subsequent measurements, the urgency with which data are required, and the application of safe practices. The program should specify who has overall responsibility if a change is required in the program, as often occurs. Sampling programs should not be developed in isolation from the other objectives of a well test because there is direct conflict in some cases, such as when the well test requires large drawdowns for gas/condensate fluids as part of flow-capacity tests. Thus, in the case of a well test, the overall plan should include the following: (a) establish the production potential, (b) determine the permeability, (c) determine the skin, and (d) collect fluid samples. Each objective should be defined in sufficient detail so that all parties involved are fully aware of their obligations, thus increasing the likelihood of achieving the objective. Objectives must be realistic and must allow for possible changes. In the case of fluid sampling and on-site analyses, the following sorts of questions should be considered in deciding the detailed sampling objectives: (1) How much information is available on the likely reservoir fluid? (2) What types of fluid sampling will be best? (3) What is the most suitable well-cleanup and -conditioning procedure, and how can this be integrated with other well-test objectives? (4) How many samples are needed, and do partners need duplicates? (5) When is the ideal time to take samples? (6) Will on-site analyses be required? (7) Who will perform sampling and analysis duties?

Fluid-sampling operations are often left to service-company personnel, but because significant variation in levels of competence exists within the industry and within service companies themselves, it is recommended either to use specialist laboratory personnel or to supervise the service-company operations closely.

General guidelines for choosing reservoir-fluid-sampling methods and sample quantities required are summarized in [Table 4.2](#). Regardless of the actual volumes mentioned, you should collect at least two separate samples of each fluid, referred to as duplicate or replicate samples. This reduces the chance of losing information if one of the samples leaks or is accidentally damaged during laboratory operations, and it allows a comparison between the samples as part of the quality-control procedures.

Surface-separator sampling is the most common technique, but the reservoir-fluid sample recombined in the laboratory is subject to errors in the measured GOR and any imprecision in the laboratory recombination procedure. Downhole samples (or wellhead samples) are not affected by such inaccuracies but require the fluid to be in monophasic condition when sampled; this can be confirmed definitively only afterward in the laboratory. Also, there is general reluctance to attempt downhole sampling in gas/condensate reservoirs because many are saturated, and the phases are likely to segregate in the wellbore. The ideal situation for a laboratory is to receive both surface and downhole samples because a choice is then available, and a good idea can be obtained of how representative the resulting fluid is.

In certain circumstances, it can be good practice to collect “backup” fluid samples at the earliest opportunity during a production test, even if a well has not cleaned up properly. If the test has to be aborted for some reason [well bridging, unexpected levels of hydrogen sulfide ( $H_2S$ ), etc.], the backup samples may be of great value, even if they are not 100% representative. If the test is completed successfully, the backup samples can be discarded to avoid the cost of unnecessary shipment and testing.

If sampling is part of a long-term monitoring program, such as those required by government authorities or those forming part of custody-transfer contracts, the methods defined in the appropriate documentation or contracts must be followed as closely as possible, even if this constitutes differences with the procedures or recommendations in this text or in the industry

TABLE 4.2—GUIDELINES FOR RESERVOIR-FLUID SAMPLING

Type of Sample	Comments	Quantity Required
Surface separator	This method should be used routinely for all well tests in which fluids are produced into a separator. It can be used as the principal method or as a backup or cross check for other methods.	Minimum of two gas samples of 20-L volume; plus two liquid samples of 500 cm <sup>3</sup> (more gas may be needed at pressures below 100 psia)
Downhole or bottomhole	This method is recommended for all reservoir oils and may be successful with undersaturated gas/condensate fluids. Take backup surface samples in case fluid is diphasic downhole.	Minimum of two fluid samples (three, if possible) of approximately 500 cm <sup>3</sup>
Wellhead	For dry gases or highly undersaturated fluids from high-pressure/high-temperature wells. This method can avoid downhole sampling costs. Take backup surface samples in case fluid is diphasic at the wellhead.	Minimum of two fluid samples of approximately 500 cm <sup>3</sup> for oils or high-pressure gas fluids; standard 20-L gas bottles can be used for low-pressure, dry-gas wells
Stock tank	Samples should be taken by flashing separator liquid or from a source of clean stock-tank liquid.	Two cans of 1-L volume or more, depending on tests required [possibly collect a jerrycan (a portable, sealed container holding 20 L of liquid) full of stock-tank oil].
Water	Samples should be collected from the water sight glass or clean sample tap on the water flowline.	Two glass or plastic bottles of 250-cm <sup>3</sup> volume or more, depending on tests required

standards cited here. Full use of this text and appropriate industry standards should, of course, be made in setting up new procedures and contracts that require long-term sampling and measurement programs.

If there is concern about whether the fluid is homogeneous in a flow line or tank, the best approach is to take samples from different locations and compare them. In a liquid flow line, take samples from the top and bottom; in a tank, take samples at different depths. If samples are indeed different, it is advisable to locate a better sampling point (e.g., where there is sufficient turbulence to homogenize the fluid). Failing this, the only solution may be to mix the samples together in an attempt to provide a representative average fluid. If, however, the purpose of the sampling is to study the nonhomogeneity, then separate samples should be taken accordingly.

When samples are collected from drillstem tests (DSTs), which do not involve surface production, the limited volume of fluid produced from the reservoir may be insufficient to remove mud filtrate or other contaminated or changed fluid. Thus, even samples collected from the last fluid that enters the drillstem may not be truly representative. This is especially the case for formation-water samples, which are more widely susceptible to contamination from drilling fluids, well-completion fluids, cements, tracing fluids, and acids, which contain many different chemicals. The most representative formation-water samples are usually those obtained after the oil well has produced for a period of time and all extraneous fluids adjacent to the wellbore have been flushed out.

In some cases, fluid sampling may be made on short notice in response to a problem, with the intention of identifying the cause and preventing any recurrence. Here, it is essential to record all the operating conditions and any changes that may have contributed to the problem.

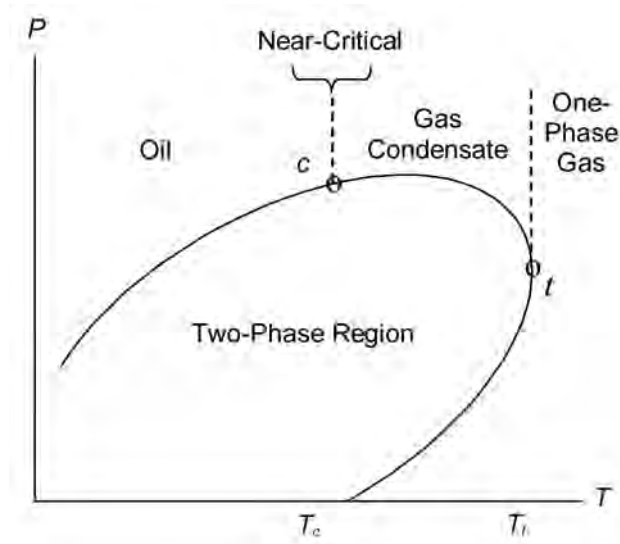


Fig. 4.2—A generalized phase diagram for reservoir fluids.

Also, it can be useful to collect a reference sample when operation is normal, if this is possible (e.g., a sporadic problem or a similar installation not affected), to allow comparisons. Laboratory personnel also should be contacted regarding the sample needs and the types of analyses that could be performed.

### 4.3 Reservoir-Fluid Type

One of the principal variables in reservoir-fluid sampling is the type of reservoir fluid present. This is rarely known with certainty and, in exploration wells, may be completely unknown at the start of testing. Determining the exact nature of a reservoir fluid is, of course, a key objective of sampling and laboratory study. Fig. 4.2 shows the relation between the major classes of hydrocarbon reservoir fluid in terms of a generalized phase diagram. Although the shape of the phase diagram is specific to the actual fluid composition, it is the reservoir temperature compared to the temperature  $T_c$  of the critical point ( $T_c$  determines if the fluid is an oil or a gas). When the reservoir temperature is lower than  $T_c$ , the fluid is an oil and will exhibit a bubble-point when pressure is reduced into the two-phase region. If the reservoir-fluid temperature is above  $T_c$ , the fluid is a gas and will either show gas/condensate behavior and a dewpoint on pressure reduction or, if the reservoir temperature is also above the cricondentherm  $T_t$ , the fluid will behave as a one-phase gas with no liquid formation in the reservoir on pressure reduction. If the fluid exists in the reservoir at or close to its critical temperature, it is classified as a critical or near-critical fluid. These fluids exhibit neither bubblepoint nor dewpoint, but on pressure reduction into the two-phase region, they immediately form a system comprising large proportions of both gas and liquid (e.g., 60% gas and 40% liquid by volume).

The reservoir pressure determines whether the fluid is at the boundary of the two-phase region (and referred to as saturated) or at a higher pressure than the two-phase region (and referred to as undersaturated). Saturated fluids will immediately enter the two-phase region when a well produces fluid because of the reduction of pressure in the well and near-wellbore region. More details on phase diagrams are available in the General Engineering section of this Handbook.

Both the reservoir-fluid type and the saturation condition influence the way fluid samples must be collected, yet this information can be estimated only at the time of the sampling pro-

gram and is especially uncertain when fluids are close to the boundaries between the different types. Numerous correlations are available for estimating reservoir-fluid type and condition from produced-fluid flow rates and properties measured at the wellsite (such as those developed by Standing<sup>3</sup> and those given elsewhere in this Handbook), but you should be careful in using these methods, especially when the fluid properties differ significantly from those used to develop the correlation. For this reason, it is good practice to allow for significant error in the reservoir-fluid character when designing and implementing sampling programs.

#### 4.4 Well Conditioning

The best way to prepare a well for sampling is dependent on the reservoir-fluid type, as indicated earlier. With the exception of one-phase gas reservoirs, prolonged production will cause all reservoirs to reach saturation conditions, thus bringing about changes in the fluid composition throughout the reservoir. When this happens, there is no longer any possibility of obtaining truly representative fluid samples. Thus, although in one-phase gas reservoirs (and for a certain length of time in undersaturated reservoirs), the fluid will remain unchanged during pressure depletion—the true nature of the fluid will be unknown until samples actually have been analyzed in a laboratory—it is strongly recommended to take samples at the earliest opportunity in the life of a well.

Both in openhole and in cased-hole completions, the best depth or production interval for sampling will be as far away as possible from gas/oil, gas/water, and oil/water transition zones to reduce the chances of coning. Every attempt should be made to test zones individually because commingled production may be difficult to detect and is impossible to correct in the laboratory.

The possible influence of any matrix-treatment chemicals on sampling programs should be evaluated, and treatment schedules should be modified accordingly. Problems such as the liberation of carbon dioxide (CO<sub>2</sub>) or H<sub>2</sub>S after acid treatments are possible, as is the release of other components such as metal ions, and these could affect analyses. On the other hand, sampling after an acid treatment has been properly cleaned up has the probable advantage of reduced drawdown in the near-wellbore region.

Because of the enormous variety of constraints, there can be no definitive guidelines for well conditioning. The first phase of conditioning involves the cleanup, in which the well is flowed to the surface to remove any solids resulting from perforating activities, drilling mud or completion fluids in the well, and mud filtrate or workover fluids that may remain in the formation near the wellbore. Here, the production rate must provide a sufficient flow velocity in the production string to lift solids, hydrocarbon liquids, and water to the surface, but conditioning is typically performed at the maximum rate, as this reduces the total length of the cleanup period.

The cleanup period typically lasts from a few hours to 24 hours, and progress is monitored by regular measurements of flowing wellhead pressure, basic sediment and water (BS&W), and other parameters. At the end of the cleanup period, production may be diverted through the separator to check its operation. This is an ideal moment to take backup samples.

Depending on the fluid type, significant differences can exist in conditioning procedures, which attempt to control or eliminate any modified reservoir fluid so that fluid entering the well is identical to that in the reservoir. For an unknown fluid, one of the most important considerations is the need to interpret the response of the well to different flow conditions and then develop the final sampling program during the test itself on the basis of this information. If initial production indicates an oil, the best approach is to evaluate the response of surface GOR to changes in production rate. As long as representative reservoir fluid enters the wellbore and is carried to the surface, and the same separator operating conditions of temperature and pressure are maintained, the GOR should remain stable for different choke sizes. A GOR that changes significantly between choke sizes is indicative of nonrepresentative production either caused by two-phase flow effects in the near-wellbore region or possibly by commingled

production of more than one reservoir fluid (e.g., oil zone and gas cap), and production should be choked back until GOR no longer changes with choke size.

If, however the reservoir contains a saturated gas condensate, extra flow periods will simply compound the condensate-buildup problem, so sampling at the earliest stable rate is probably advisable. In fact, some modeling work<sup>4</sup> has shown that when an important ring or bank of condensate has built up in the reservoir, it may be possible to produce at reasonably high rates with an apparently stable GOR while producing fluid that is not representative of the original reservoir fluid. At very high flow rates, the GOR may appear to increase as a result of liquid carry-over in the separator gas stream.

Gas wells that have a small flow velocity will exhibit liquid “slippage” in the tubing and heading or unstable flow rates at the surface. Several methods of establishing the required minimum flow rate are available, of which an industry nomogram<sup>5</sup> has been used extensively. In very-low-permeability, saturated gas/condensate reservoirs, it may not be possible to lift condensate from the well without creating a major pressure drawdown in the reservoir and causing nonrepresentative fluid to enter the wellbore. The best approach here is to select a small tubing diameter before the test so that the minimum lift velocity can be achieved with a low flow rate and, thus, reduced drawdown.

In highly undersaturated reservoirs, it is possible to take downhole samples while the reservoir is producing, provided that the downhole flowing pressure is greater than the fluid saturation pressure. In many cases, however, the saturation pressure will be unknown or cannot be estimated with sufficient accuracy; then, the best recommendation for downhole sampling in an oil reservoir is to sample when shut in, as for reservoirs that are at or close to saturation pressure. Before downhole sampling with the well shut in, it is necessary to allow pressure to build up near to static and then to purge fresh reservoir fluid at a low rate to replace any “changed” fluid in the wellbore or in the near-wellbore region. The most suitable time for downhole sampling during the well test is probably after the initial cleanup and buildup, but an alternative is at the very end of the test if a long buildup is part of the test plan.

On a different aspect of well conditioning, the use of OBM during drilling operations can lead to contamination of the near-wellbore region, and any subsequent contamination of fluid samples by base oil may not be identified. This is unlikely to pose a problem if the well is properly cleaned up, but it can result in significant contamination if samples are collected using an openhole formation tester in which only small volumes are purged. It is thus best if lost circulation can be minimized during drilling and ideal if only water-based muds are used.

If surface-separator sampling is planned, another form of conditioning can be necessary if chemicals are in use. Injection of methanol or glycol upstream of the separator can be used to prevent gas-hydrate formation, and the injection of antifoaming agents and demulsifiers may be required in oil reservoir fluids. If possible, any such injection should be stopped before separator samples are taken, and enough time should be allowed for such potential contaminants to be purged from the separator (e.g., by waiting at least five times the residence time). Residence times can be derived from the nomogram given in the chapter on Design of Two- and Three-Phase Separators in the Facilities and Construction Engineering section of this Handbook.

Separator conditions themselves also have an influence on sampling operations. Separator temperature can be controlled only by changing the production rate or by the use of a heater, but there is generally more flexibility in the separator pressure, which can be set at any value not exceeding the choke downstream pressure limit for critical flow (or the working pressure of the separator, if it is lower). The advantages of using the highest-acceptable separator pressure include more intermediate components being in the liquid (increasing the liquid flow rate somewhat), more gas in sample bottles because of the increased pressure, and generally a leaner gas stream with less condensation on cooling. Although service companies may be reluctant to operate separators at higher pressures, these benefits can be important for the quality of fluid

measurements. For low-GOR oil production, a lower separator pressure may be advisable because it can significantly increase the gas flow rate and improve its measurement accuracy. Separator liquid levels also can be adjusted in many separators; lower levels increase gas residence time and thus can reduce carry-over problems for gas wells, whereas higher levels increase oil residence time, which can reduce emulsion or foaming problems.

In view of the concerns presented above, the current best practices for conditioning a well for sampling should include the following steps. Complementary details of guidelines can be found elsewhere.<sup>1,6</sup>

For oil reservoirs:

- Clean up the well until wellhead pressure and BS&W stabilize.
  - For surface sampling, reduce the flow rate in steps until the separator GOR does not change between choke sizes, then stabilize separator conditions and take separator samples.
  - For downhole sampling, shut in the well and build up to static pressure; produce at a low rate for long enough to remove all changed material in the near-wellbore region, and briefly shut in.
  - Finally, purge fluid past the sampler in the well at a bleed rate and shut in before sampling (this step may be omitted if downhole fluid is known to be monophasic).
- For gas/condensate reservoirs:
- Clean up the well until wellhead pressure and BS&W stabilize, then flow the well at the lowest flow rate that will lift liquids up the tubing.
  - For surface sampling, stabilize separator conditions and take separator samples.
  - For downhole sampling (undersaturated reservoir with monophasic flow downhole), collect downhole samples.

Recommendations for well conditioning in a near-critical-fluid reservoir are not widely available, both because these reservoirs are fairly rare and because there is no sure way of identifying the situation from surface measurements. A rule of thumb is that reservoirs with near-critical fluids often exhibit separator GORs in the region of 4,000 scf/bbl (700 m<sup>3</sup>/m<sup>3</sup>), but there are no well-established GOR ranges for the near-critical region, and correlations are rarely applicable in this area. Because pressure drawdown can result in major changes in the reservoir fluid, it is advisable to perform sampling at the earliest moment (a good practice for all reservoir types) and to condition the well by flowing it at successively slower rates to remove all nonrepresentative hydrocarbon phases as far as possible. However, it may be difficult to establish when the well is adequately conditioned because the surface GOR may change only slightly with different quantities of downhole phases, and expert advice should be sought to evaluate all the observations.

#### 4.5 Selection and Preparation of Sampling Equipment

Equipment planning must start as soon as the sampling program is defined to ensure that all necessary equipment will be available and checked well in advance of the sampling operation. For pressurized sampling operations, metal cylinders are invariably used, almost always with valves at each end that facilitate filling, transfer, and cleaning operations. For downhole samples and separator liquid samples, the sampling procedure requires maintaining pressure on the sample while the sample cylinder is filled. Achieving this by draining mercury from a full cylinder<sup>7</sup> has been largely discontinued owing to the safety and environmental concerns with mercury. The industry is now using piston cylinders, which have an internal piston to separate the sample part of the chamber from the hydraulic fluid (commonly a mixture of water and ethylene glycol). Maintenance of the piston cylinders is more complicated because the piston seals must be in excellent condition to prevent the occurrence of internal leaks.

Cylinders are commonly made from stainless steel or titanium, the latter being significantly lighter and offering better resistance to H<sub>2</sub>S (while being incompatible with mercury). Aluminum cylinders are in common use because larger volumes of sample are generally required,

and the cylinder weight is a concern. Cylinders with internal coatings, such as Teflon<sup>®\*</sup>, are also used occasionally. The wide variety of materials used for pressurized sampling demonstrates the fact that there is no perfect solution to the problems of resistance to corrosion, sample preservation, volume, and weight. All cylinders must be provided with plugs for the valves, endcaps to protect the valves, and storage containers to facilitate handling and to protect cylinders during transport. It is good practice to plug and label cylinders when they have been prepared for sampling to avoid any confusion when at the job site.

For atmospheric samples, containers that are used for water samples include polyethylene, other plastics, hard rubber, metal cans, and borosilicate glass, but the choice should be based on the measurements that will be performed on the samples. For stock-tank hydrocarbon liquids, glass or plastic containers are more resistant to corrosive components and are generally preferred for smaller volumes. Although plastic containers are more robust, they can contaminate samples with plasticizers, and glass bottles must be used for storing stock-tank samples intended for geochemical analysis. Glass containers must be well protected against the risk of breakage.

For water samples, glass will adsorb various ions such as iron and manganese and may contribute boron or silica to the aqueous sample, so its use should be avoided if ionic analyses are required. Plastic and hard rubber containers are not suitable if the sample is to be analyzed to determine its organic content, and a metal container is often used if the sample is to be analyzed for dissolved hydrocarbons such as benzene. Otherwise, a polyethylene bottle is probably the most satisfactory container, especially if the sample is to be stored for some time before analysis. Also, a plastic container is less likely to break than is glass if a water sample is transported in freezing temperatures. However, not all polyethylenes are acceptable because some contain relatively high amounts of metal contributed by catalysts in their manufacture. The approximate metal content of the plastic can be determined by a qualitative emission spectrographic technique.

In addition to sample containers, sampling equipment must include fittings, valves, gauges, and lines to enable samples to be recovered safely from the required location. Trained personnel must be assigned to collect samples. They should have copies of the sampling program and field procedures, the prepared forms for recording data, and a supply of labels. All sampling equipment must have been previously pressure tested and be clean and dry. Downhole-sampling equipment such as production samplers and formation-test samplers are extremely sophisticated and must be prepared by specialists. Great care must be taken with maintenance, cleaning, and assembly to ensure the maximum chance of correct operation and the minimum chance of contamination or other nonrepresentative sampling.

#### **4.6 Pressurized Hydrocarbon Fluid-Sampling Procedures**

The procedures covered here apply to reservoir fluids or production streams above ambient pressure, and they are highly specific to the petroleum industry. The American Petroleum Inst. publishes a detailed recommended practice,<sup>6</sup> which is the most complete industry standard covering the sampling of pressurized hydrocarbon fluids. It should be consulted for additional information to that presented here. The choice of sampling method depends on the reservoir-fluid type; this has been explained in the guidelines mentioned above. Here, the various methods have been subdivided into downhole- or surface-sampling methods. The former obviously apply to a specific well, whereas the latter can be used for wells, gathering stations, or other surface facilities.

---

\* Trademark of DuPont Corp., Wilmington, Delaware



Although here, “hydrocarbon” is intended to mean fluids containing hydrocarbons and non-hydrocarbons but no (or only small) quantities of water, techniques in this section also can be applied to the sampling of pressurized water fluids, though this is not very common.

**4.6.1 Production Downhole Sampling.** Production downhole sampling, also referred to as bottomhole sampling, involves running a special sampling tool into the well on wireline so that a sample of the fluid in the well can be collected under the increased pressure of the fluid column. Careful well conditioning is necessary, as described earlier, to ensure that the fluid is in monophasic condition. Modern samplers are triggered either by a timer or a mechanical clock in the tool itself, or by an electric signal conveyed by electric line. The former system is more common, being able to be run with any wireline unit, but it has the inconvenience of needing a preset delay to allow the tool and well to be set up for sampling. The sampler should be lowered into the well until it is a short distance above the upper limit of the perforated interval (unless there are mechanical limitations that prevent the tool from reaching this depth) to collect a sample that is representative of all the produced intervals. Various drillstem and tubing-conveyed installations are available for downhole samplers, which allow them to be operated without the use of wireline. These can allow samples to be collected downhole in high-risk wells in which wireline operations are not permitted.

One advantage of downhole sampling is that it can be performed without a separator at the well. There are several problems that can occur in downhole sampling: the fluid around the sampler may be in two-phase condition, or it may have segregated in the wellbore; a mechanical problem can lead to incorrect opening or closing of the device; the fluid may be contaminated with water or drilling mud; or the sample may not be made fully homogeneous before transfer into a shipping bottle. Use of a pressure survey may help check the whereabouts of any interfaces in the wellbore, but lack of an interface does not guarantee that the fluid present has not lost any material in the form of condensation or wax or asphaltene precipitation.

It is common practice for downhole samples to be transferred at the wellsite, as this allows a measure of the quality of the sample to be obtained, and can allow additional sampling runs to be made in most cases (if needed) while still at the wellsite. This approach also can reduce rental charges for the downhole samplers if supplied by a service company. Because it is difficult either to transfer the entire downhole sample (such that it need not be homogeneous) or to make it fully homogeneous (and just transfer a portion), the best practice is to try to achieve both objectives. Samplers with moving metal parts to facilitate mixing are now fairly common and are preferred. General recommendations to be followed for downhole sampling are given in [Table 4.3](#).

Downhole samples are commonly transferred to shipping bottles at the wellsite, and the following subsection describes a method suitable for most production downhole samples and many formation-test samples. This step-by-step method is reproduced from *RP 44* (where it appears as Section 6.2.5)<sup>6</sup> by kind permission of the American Petroleum Inst. (API). It may need to be modified according to the actual type of transfer equipment available.

**API RP 44 Method for Sample Transfer to Shipping Container.** If the sampler itself is not used to transport the sample to the laboratory, the sample must be transferred to a transfer container for shipping or transport. Whatever vessel is used, it must have an adequate pressure rating and be certified to meet all applicable shipping regulations. Further, the shipping cylinders must be cleaned thoroughly; this is particularly important to avoid contamination of the sample from trace amounts of heavy components remaining in the cylinder from previous use.

The primary concern in transferring a downhole sample to a shipping container is to maintain the integrity of the sample during the transfer operation. This requires that the fluid in the sampler be maintained in a single-phase condition during the entire sample-transfer process or, if the fluid is in a two-phase condition, that the entire contents of the sampler be transferred. (The sampler should be heated if wax or asphaltenes are present.) If only a portion of a two-

**TABLE 4.3—RECOMMENDATIONS FOR DOWNHOLE SAMPLING**

1. Use downhole samplers that open and close downhole rather than samplers that are open when run in.
2. It is preferable to choose piston samplers with a capacity less than that of sample bottles (e.g., 500 cm<sup>3</sup> to permit entire transfer into a 600-cm<sup>3</sup> sample bottle) and that contain a mechanical agitating device.
3. The sampler should be properly maintained, clean, and dry before use.
4. All available information should be considered in attempting to sample representative, monophasic fluid.
5. Sampler contents should be made monophasic and homogeneous by applying pressure and mixing the contents (rocking through 180° from the vertical) before transfer.
6. Pressure and volume measurements may enable an apparent bubblepoint to be observed that can be used to compare duplicate samples, or a rough compressibility value may be calculated to help identify the sampler contents.
7. If there is a possibility of high wax content, the sampler should be heated or thermally insulated to reduce cooling before transfer.
8. Sampling runs must be repeated as necessary to obtain a minimum of two (and preferably three) apparently representative samples.
9. A completed sampling-data sheet must be included with each sample bottle when it is placed in the shipping container.

phase sample is transferred, the fluid transferred to the shipping container will differ from the original sample because the two phases in the sampler almost certainly cannot be transferred in the proportions that exist in the sampler. Because valid transfer is crucial to sample quality, the preferred procedure is to maintain the fluid in a single-phase state and transfer it in its entirety. An important consideration is that pressurizing the sample may produce a single-phase condition but may not homogenize the sample; thus, thorough agitation (by rocking the cylinder) during the process is important.

In addition, the sample composition must not be altered either by (a) leaks of hydraulic fluid across the piston of piston-type samplers or (b) by selective absorption of components from the sample into a transfer fluid (e.g., water or glycol) in cases in which the transfer fluid is in direct contact with the sample. The latter is a particular problem in samples containing CO<sub>2</sub> or H<sub>2</sub>S, which are very soluble in the transfer fluid.

At all stages of the transfer process, the pressure must be maintained substantially higher than the sample saturation pressure. **Fig. 4.3** shows a schematic diagram of a transfer apparatus for piston-type samplers and transport containers. The 1966 Edition 1 of API *RP 44*<sup>7</sup> should be consulted for transfer apparatus involving direct contact between the sample and mercury (as the hydraulic fluid).

The transfer procedure is as follows.

1. Use the pump to fill all lines between valves B and F with hydraulic fluid (refer to **Fig. 4.3**). This can be done by loosening the fittings at these valves and pumping until hydraulic fluid appears, then tightening each fitting. *Note: Valves A and B and F, G, and H may be integral parts of the sampler and transfer container, respectively, depending on the design of these vessels. Also, valve H and its line may be arranged somewhat differently from Fig. 4.3 so that valve H simply “tees” into the line from valve A to valve G.*
2. With valves A, D, E, and F closed and valve C open, slightly open valve B and note the opening pressure of the sampler. Valve B is often hydraulically or spring-actuated in cases in which it is part of the sampler; if so, use the pump to raise the pressure until valve B just opens, and record the opening pressure.
3. Open valve G and evacuate through valve H the line between valves G and A, including the sample side of the transfer container.

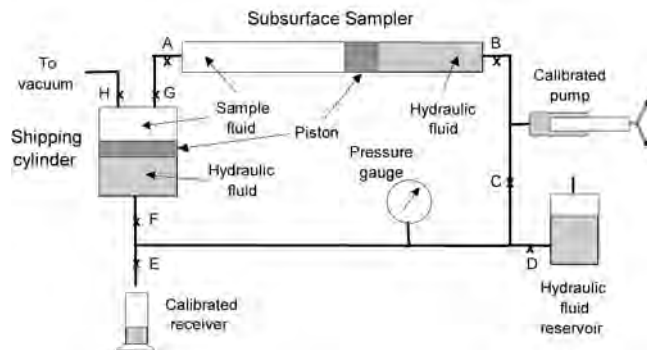


Fig. 4.3—Diagram of sample transfer apparatus.

4. Close valve H.

5. Open valve F and use the pump to bring the hydraulic oil pressure in both the sampler and the shipping container to a pressure well above the saturation pressure of the sample.

6. Slightly open valve A and fill the line between that valve and the upper face of the piston in the shipping container with sample fluid, using the pump to keep the pressure on the gauge well above the saturation pressure during this transfer process.

7. Close valve C, then slightly open valve D, allowing hydraulic fluid to drain slowly into the hydraulic oil reservoir (open to atmospheric pressure) as fluid flows from the sampler to the shipping container. Use the calibrated pump to (a) keep the pressure in the sampler above the saturation pressure and to (b) keep track of the amount of sample transferred. When the desired amount of sample has been transferred, close valve D, then close valves A and G.

8. Before the transferred sample can be shipped, a vapor space must be created in the shipping container. To do this, slightly open valve E and allow hydraulic oil to drain from the shipping container into an open calibrated receiver. Close valve E, then valve F, when the volume of hydraulic fluid in the receiver equals 10% of the volume of the shipping container. This will result in a 10% vapor space (“ullage” or “outage”) in the shipping container. Such a void volume is required for safety because very high pressures can result if the temperature increases even slightly in a totally liquid-filled, closed vessel. *Note: Special sample cylinders with an auxiliary gas cap are available for samples that must be retained in single-phase (monophasic) condition.*

9. Close valve B if it is not self-sealing. Open valve C, then valve D, to relieve pressure in the pump. At this point, the sampler and shipping (transfer) vessel can be disconnected from the transfer apparatus.

**4.6.2 Downhole Sampling With Formation Testers.** The collection of reservoir-fluid samples by formation-test tools was originally a secondary benefit of their use for the measurement of pore pressures. Formation-test tools can obtain reservoir-fluid samples without any production to the surface. The tool is typically run into an openhole well containing drilling mud or completion fluid to a specific depth, and a probe is forced against the formation, providing a seal and allowing formation fluid to flow into the tool. Modern formation testers generally can be equipped with numerous devices designed specifically to enable samples of reservoir fluid to be collected in a series of sample chambers. These tools offer the advantage of the ability to collect samples without performing a DST with fluid flow to the surface, and they are especially useful in obtaining fluids from a number of discrete depths, thus helping identify possible fluid gradients. However, the principal disadvantage is the limited cleanup that is possible, resulting in various levels of contamination by drilling-mud filtrate. These problems have been

reduced by developments allowing the pumping of significant volumes of fluid into the well and the monitoring of the quality of the fluid flowing into the tool. Nevertheless, samples collected almost always contain some contamination (both from mud filtrate and from small quantities of water used to fill connecting lines when the tool is prepared), but when the drilling mud is water-based, such contamination can be separated in the laboratory, and it is a significant concern only when sampled fluids contain soluble components such as  $H_2S$  and  $CO_2$ . When sampling in wells that have been drilled with OBM, contamination is more difficult to detect and impossible to remove physically. Advanced spectroscopic detection systems have been developed for formation-test tools, but the industry is now beginning to accept that there always will be problems with formation-test sample contamination where OBMs have been used, and laboratories have developed various methods for evaluating the level of contamination and for estimating the true physical properties of uncontaminated reservoir fluid.<sup>8</sup> In fact, this problem is not limited to formation-test samples because in some cases, production testing may not fully clean up OBM filtrate, especially if there have been significant losses during drilling.

Formation-test tools are extremely sophisticated and must be run by specially trained engineers and wireline operators. In addition, significant differences exist between the tools available from the various service companies, and technological developments are occurring all the time, so specific operating details will not be given here. However, in addition to the well preparation described earlier, a number of recommendations can be made for the sampling process:

- Planning must optimize the match between tool capability and sampling and analysis needs.
- Sample sizes collected should be compatible with storage containers so that individual samples can be transferred in their entirety.
- Sample chambers containing mixing devices are to be preferred because they facilitate sample homogenization before transfer; where possible, duplicate samples should be taken from each depth sampled.
- To determine depth gradients, samples should be collected from at least three different depths spanning the reservoir interval; when available, fluid-quality monitors should be used to evaluate cleanup of the fluid entering the tool.
- The fluid-sampling rate should be adjusted where possible to minimize pressure draw-down, unless downhole bubblepoint measurement or estimation are available that allow higher sampling rates to be used with confidence.
- If OBM was used in drilling, collect a sample of the mud that has been used most recently, and contact a laboratory that will analyze the samples to establish which fluid samples are needed; for some correction techniques, samples are required from the same depth with different levels of filtrate contamination.
- Use of the formation-tester pump to compress collected samples (sometimes referred to as “overpressuring”) may help reduce the effects of cooling, but it should not be used if final pressures are to be used as a measure of sample quality. If phase segregation on cooling must be avoided, single-phase sample chambers should be selected as described below.
- If fluid pumpout into the well is not possible (e.g., for safety reasons— $H_2S$ , low overbalance, etc.), large sample chambers should be used at the start of sampling to serve as “dump” chambers, allowing better-quality samples to be collected afterward.
- The depth and sampling time must be recorded together with the serial number of each chamber.
- If possible, avoid using OBM when drilling, or switch to water-based mud for probable hydrocarbon-bearing intervals. Handling and transfer of formation-test samples should be along the lines described above for production-test downhole samples.

**4.6.3 Single-Phase Sampling.** Downhole samples cool down as they are pulled out of the well, and the associated fall in pressure will usually result in the sample entering the two-phase region, thus necessitating homogenization before transfer. Special versions of downhole samplers now available, known as single-phase or monophasic samplers, use the release of gas pressure behind an additional piston to maintain a downhole sample above reservoir pressure while it is brought to the surface. This design of sampler is especially used for reservoir fluids likely to precipitate asphaltenes, which are very susceptible to pressure reduction and difficult to homogenize. For other fluids, single-phase samplers facilitate sample transfer and reduce the chance of the transferred fluid not being representative of the fluid in the sampler. One disadvantage of the one-phase sampler is that a “bubblepoint check” cannot be performed on site because the gas buffer will mask sample behavior. One solution to this limitation is to run a conventional sampler in tandem to permit a quality check on one of the samples in the field.

Although the single-phase sampler will prevent the formation of a gas phase in most cases, it does not prevent the formation of a wax phase in waxy reservoir fluids, which commonly occurs with cooling. A sampler with a heated chamber is available but has not been used widely. Also, gas/condensate fluids undergo significant shrinkage on cooling, and single-phase samplers may not prevent the formation of condensate in the sample chamber. Single-phase versions of formation-tester sample chambers are also available.

**4.6.4 Other Downhole-Sampling Tools.** Various other tools can be used to collect downhole fluid samples, such as DST chambers, but thought must be given to the problems in recovering a valid sample from the tool, and preference must be given to configurations that allow samples to be homogenized, transferred under pressure, and preferably contained in a single storage cylinder. Industry practice now favors the use of standard wireline samplers conveyed into the well as part of the DST tool.

**4.6.5 Separator Sampling.** Surface sampling primarily involves sampling individual gas and liquid streams from a production separator or similar installation, and it is by far the most common method of sampling pressurized hydrocarbon fluids. The operation of oil and gas separators is covered in detail elsewhere in this Handbook. Usually, the objective of separator sampling is to obtain a fluid representative of the production of one well that enters the separator in its entirety, but the method also can be used to obtain a fluid representing commingled production from a number of wells into a single gas/oil separation plant. In either case, the objective is to collect separate samples of the gas and liquid exiting the separator and to measure the separate flow rates of the two phases and obtain the GOR. Although the two phases are never in perfect equilibrium, providing that the two samples are representative of the separate flows, it is possible to mix the two samples together in the same proportion in which they are produced to obtain a recombined sample that represents the fluid entering the separator.

Some of the biggest errors affecting fluid samples are related to the measurement of separator-gas and -liquid flow rates, which are crucial for the recombination process in the laboratory. Good accuracy is often considered to be in the region of 5%, but the figure can be much worse, for example, if there is carry-over of liquid in the gas exit stream (or carry-under of gas in an oil with foaming tendencies). Problems are especially common for gas-well production tests, where very high flow rates can be used, and special techniques are available for trying to measure liquid carry-over in such situations. However, the best approach involves proper sizing and adjustment of the separator for the production rate. Another important source of error in this domain involves confusion over whether liquid flow rates are reported at separator conditions or at tank conditions; this has serious implications for gas/condensate fluids in which the separator-liquid shrinkage is typically much larger than in the case of an oil.

Although broad guidelines were given above concerning the volumes of samples that should be collected, special attention should be given when collecting gas samples from separa-

Separator Gas Volume To Be Collected as a Function of Pressure, GOR, and Oil Volume  
(For Oil Reservoir Fluid Recombination)

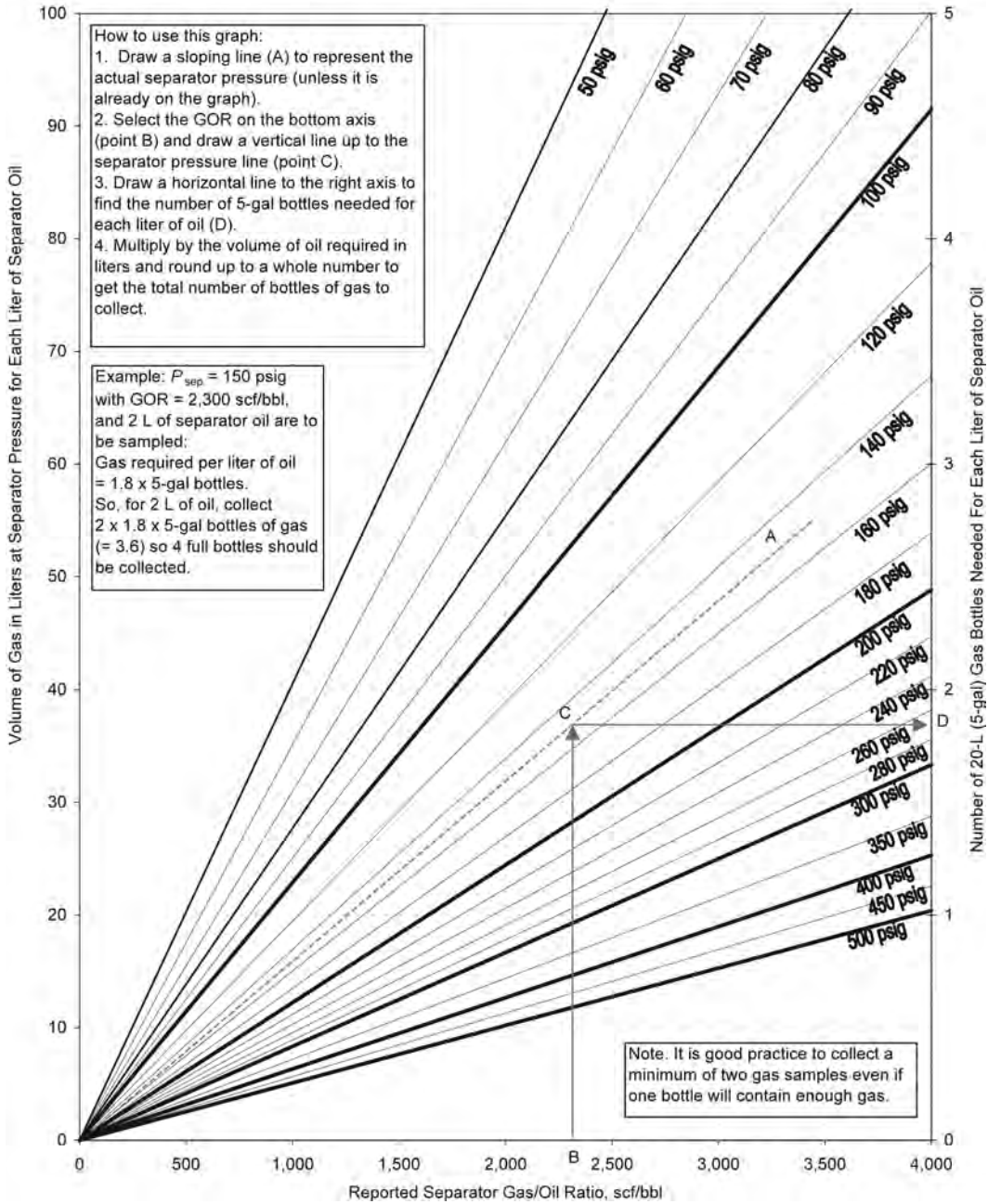


Fig. 4.4—Separator-gas volume to be collected as a function of pressure, GOR, and oil volume.

tors operating at low pressures because the lower density may result in the collection of insufficient weight of gas. Fig. 4.4 enables the required volume of gas to be estimated simply as a function of separator pressure, GOR, and the volume of liquid that is required. This chart is reproduced with the kind permission of Saudi Aramco.

TABLE 4.4—SURFACE-SAMPLING GUIDELINES

1. Sampling containers and equipment must be clean and dry.
2. The working pressure and temperature of the equipment must be at least equal to the pressure and temperature of the fluid to be sampled.
3. All sampling lines and pipework must be purged with at least three times their volume of fresh fluid before each sampling session.
4. Liquid samples are to be collected where possible by the use of piston bottles; the hydraulic fluid should be water or a 50% glycol/water mixture.
5. Liquid samples must be collected while controlling the pressure drop in the sample line to the minimum that will allow the sample bottle to be filled within 30 minutes or less; a volume of not more than 90% of the bottle capacity is to be collected, unless the bottle uses an integral gas buffer.
6. Sample pressure should be measured at the outlet end of the bottle to ensure that it is filling properly, and piston displacement should be monitored through the volume of hydraulic fluid collected.
7. A gas cap of at least 10% of the bottle capacity should be created for liquid samples by the release of additional hydraulic fluid.
8. Gas samples should be collected in evacuated bottles, with the vacuum being "topped up" on site if possible.
9. The gas-sampling rate should be selected to minimize cooling and reduce the likelihood of condensation occurring and being left in the sample lines.
10. Valves must be plugged and tagged before shipment.
11. A completed sampling-data sheet must be included with each sample bottle when it is placed in the shipping container.
12. In very important wells, or if there is a risk that the well test will be aborted, it is good practice to take some backup samples as early as possible (before rates are fully stable, and even before the well has cleaned up properly).

In line with current trends in the oil industry, this work recommends using evacuated bottles for gases and piston bottles for liquids and avoiding any use of mercury in sampling operations. At extremely low temperatures, piston bottles have been reported to leak past the piston seal, so sampling under such conditions should be avoided if possible. If these methods cannot be used, then repeated purging (a minimum of five times) should be used for gas samples, and the displacement of brine should be used for liquid samples unless high H<sub>2</sub>S or CO<sub>2</sub> levels are present, in which case it is preferable to use separator water saturated with gas if it is available. The principal guidelines to be followed for surface sampling are given in [Table 4.4](#).

The following two subsections describe the two most common separator-sampling methods in detail.

**API RP 44 Gas Method No. 1: Filling an Evacuated Container.** The following step-by-step method is reproduced from *RP 44* (where it appears as Section 6.3.7.1)<sup>6</sup> by kind permission of API.

This method is especially simple and accurate. The principal undesirable feature of the method is the requirement that the vessel be evacuated before its transport to the sampling point (with possible loss of vacuum during transport), or that a vacuum pump be provided at the wellsite. Testing pre-evacuated vessels for adequate vacuum at the time of sampling should be done only by personnel well trained in vacuum-testing procedures because improper testing often leads to loss of vacuum or introduction of air into the sample vessel. (Collecting an additional sample may be preferable to vacuum testing.) A clean, evacuated container should never be purged with separator gas and re-evacuated in the field because any liquid that condenses in the container during the purge may not totally re-evaporate during evacuation in the field.

Sample collection is accomplished by the following steps:

1. Locate an appropriate sample source valve A (see Fig. 4.5) on the separator from which the desired sample can be collected. Clean any debris from valve A; open the valve briefly to blow it out, and then close it.

2. Connect the fitting on the flexible tubing of the sampling rig securely to valve A on the separator. Open the line valve B, and open the purge valve C.

3. If a vacuum pump is available and personnel are qualified in vacuum techniques, connect the sample inlet valve D on the sample container to the fitting on the sampling rig, as shown in Fig. 4.5. Connect the vacuum pump to valve C, open valve C and valve B to evacuate the sampling rig, then close valve C and disconnect the pump. Slowly reopen valve A completely to establish full separator pressure on the entire sampling rig from valve A to valve D, and proceed to Step 6.

4. If a vacuum pump is not available, open valves B and C, then open and close valve A in one quick burst to purge air from the sampling rig, and quickly close valve B. Slowly reopen valve A completely to establish full separator pressure on the entire sampling rig from valve A to valve B.

5. Connect the sample inlet valve D on the sample container to the fitting on the sampling rig, as shown in Fig. 4.5. Open valve C, then open and close valve B in one quick burst to purge air from the line connecting valves B and D, and close valve C promptly. *Note: Use a long vent line on valve C if  $H_2S$  is present.* Reopen valve B to establish full separator pressure on the entire sampling rig from valve A to valve D.

6. Cautiously crack open valve D, while carefully monitoring the pressure gauge, and fill the container slowly. Continuously adjust valve D as needed to keep full pressure on the pressure gauge. Filling a large container can take as long as 20 minutes. The progress of the filling process can be monitored by listening for a hissing sound at valve D (and in the container) and by monitoring the pressure gauge. When you think that the container is full, open valve D further while listening to the container and monitoring the pressure gauge.

7. When the container is full, close valve D, and then close valve B.

8. Slightly open valve C to bleed the connections between valves B and D to atmospheric pressure. *Note: The line from valve A to valve B, including the pressure gauge, is still under full pressure. Use a long vent line on valve C if  $H_2S$  is present.*

9. Disconnect the sample container. This is the last step in collecting the first sample. The apparatus is now ready for collecting additional samples by repeating Steps 5–8.

10. Following collection of the last sample, close valve A securely, then open valve B (and valve C, if it is not already open) to bleed pressure from all parts of the line and sampling rig before disconnecting the line from valve A. *Note: Use a long vent line on valve C if  $H_2S$  is present.*

11. Insert sealing plugs into the valves on each sample container; then check the valves for leaks by immersing them in water or painting them with soap solution. Before inserting the sealing plugs, the threads should be lubricated by stretching Teflon® tape into the threads or by applying pipe dope. After a container is determined to be leak-free, it should be tagged and otherwise prepared for storage or transit.

**API RP 44 Oil Method No. 3: Filling a Piston-Type Container.** The following step-by-step method is reproduced from RP 44 (where it appears as Section 6.3.8.3)<sup>6</sup> by kind permission of API. It refers to the same sampling rig as that used for the gas-sampling method above, though the sample cylinder will contain a piston, and valve E will represent the hydraulic-fluid connection, as indicated in Fig. 4.6. Some steps in this procedure may need modification depending on exact equipment design; this is notable for sample cylinders, which have an additional purge valve at the sample inlet end of the cylinder.



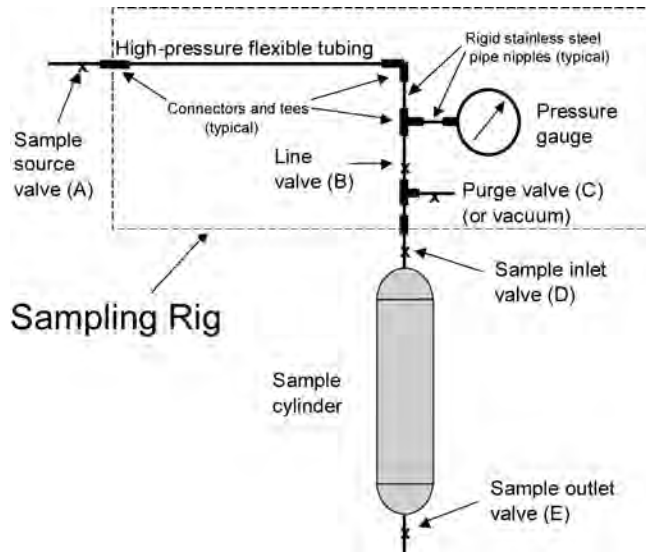


Fig. 4.5—Diagram of a sampling apparatus.

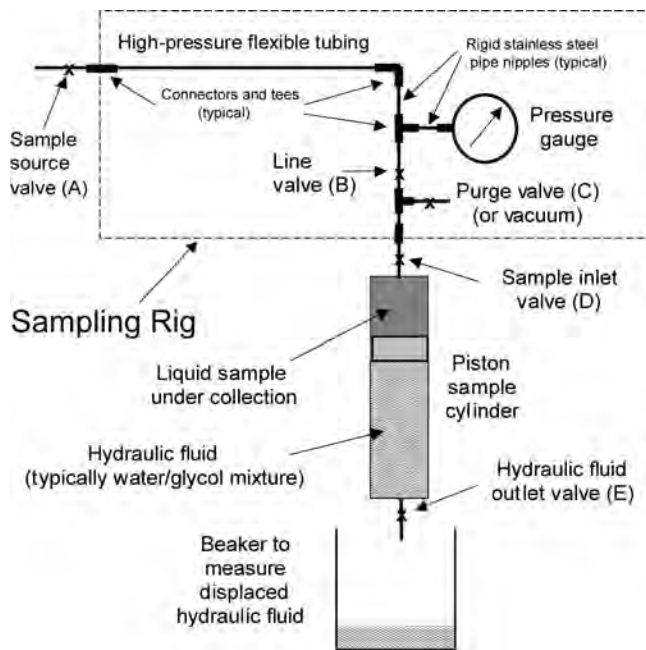


Fig. 4.6—Diagram of a liquid-sampling apparatus.

This is a preferred method for nonmercury liquid-sample collection. It has the advantage that the liquid sample can be kept at the saturation pressure throughout the collection process, which avoids gas breakout from the sample. In addition, the sample does not come into contact with any other fluids during sampling or during transfer in the laboratory. The undesirable feature of the method is that with sample containers, the potential for contamination with hydraulic fluid exists if the seal on the piston leaks. (Water can be used as the hydraulic fluid to

minimize the possibility of contamination, but the operator should first check with the manufacturer to ensure that water will not damage the container.)

If a piston-type container is being used, hydraulic fluid must be preloaded behind the piston so that the piston position is fully toward the sampling end. A danger is that inexperienced personnel may not know this and may attempt to use this type of container without a proper fill of hydraulic fluid and without proper hydraulic-pressure support on the piston seal. In such a case, full pressure will not be maintained on the separator oil during sampling, and the process essentially will be the same as filling an empty container, except that the seal on the piston might leak. The manufacturer's instructions should be consulted to ensure that the operation of the piston-type container is completely understood before commencing the sampling operation.

The procedure is as follows:

1. Locate an appropriate sample source valve A on the separator (see Fig. 4.6) from which the desired oil sample can be collected. Clean any debris from valve A, hold a rag over the valve (or attach a temporary purge line connected to a suitable container), open valve A slowly, purge sufficient oil through the valve, and then close valve A. Remove the rag or temporary purge line. *Note: Use a long vent line if  $H_2S$  is present.*

2. Connect the fitting on the flexible tubing of the sampling rig (see Fig. 4.6) securely to valve A on the separator. Open the line valve B, and open the purge valve C.

3. If a vacuum pump is available and personnel are qualified in vacuum techniques, connect the sample inlet valve D on the sample container to the fitting on the sampling rig, as shown in Fig. 4.6. Connect the vacuum pump to valve C, open valve C and valve B to evacuate the sampling rig, and then close valve B. Slowly reopen valve A completely to establish full separator pressure on the entire sampling rig from valve A to valve B. Open valve D to evacuate the connection and the small dead volume in the container (the internal volume between valve D and the face of the piston when the piston position is at the sampling end), then close valve C and disconnect the pump. Slowly reopen valve B completely to establish full separator pressure on the entire system from valve A through valve D to the face of the piston in the container, and proceed to Step 6. Be sure that valve D is completely open.

4. If a vacuum pump is not available, close valve B and open valve A slowly (the pressure on the gauge should rise to the separator pressure). Close valve A, attach a purge line at the end of the rig below valve C, close valve C, and open valve B to let the pressure deplete to atmospheric. Close valve B, then slowly reopen valve A completely. Slightly open valve B, and slowly purge a volume of oil equivalent to several times the volume of the sampling rig, collecting the purged oil in a suitable container (maintain full separator pressure on the pressure gauge during this purge). Close valve B, and remove the purge line. Full separator pressure should now be on the entire sampling rig from valve A to valve B.

5. Connect the sample inlet valve D on the sample container to the fitting on the sampling rig, as shown in Fig. 4.6, and attach a purge line at the end of valve C. Open valve D, close valve C, and open valve B slowly to pressure up the connection with the container and any dead volume in the sample container. Close valve B, and open valve C to let the pressure deplete to atmospheric. Close valve C, then slowly reopen valve B completely. Slightly open valve C, and slowly purge a volume of oil equivalent to several times the volume of the connection, collecting the purged oil in a suitable container (maintain full separator pressure on the pressure gauge during this purge). Close valve C, and remove the purge line. Full separator pressure should now be on the entire sampling rig from valve A through valve D to the face of the piston in the sample container. Be sure that valve D is completely open. *Note: This method is not perfect because the oil in the dead volume in the sample container has not been purged under pressure. However, if the piston position is fully toward the sampling end of the container, the amount of oil in the dead volume will be negligible.*

6. Cautiously crack open sample outlet valve E while carefully monitoring the pressure gauge, and allow the sample fluid to slowly displace the preload hydraulic oil into a suitable collection vessel. Continuously adjust valve E as needed to be sure that the rate of sample collection is sufficiently slow so that full separator pressure is maintained on the sample side of the piston (as indicated by the pressure gauge). The sampling operation can be ended when a desired volume of sample is collected (as indicated by a given volume of hydraulic fluid being displaced to the collection vessel). The operation must be stopped with at least enough preload liquid left in the container to provide the “outage” required in Step 7. Close valves E, D, and B, in that order. (If the container has a magnetic indicator to show the position of the piston, then nitrogen gas can be used as the hydraulic fluid behind the piston, and Step 7 can be eliminated so long as approximately 10% volume of nitrogen remains on the hydraulic side of the piston.)

7. Open valve E slightly (with valve D closed), and drain into the collection vessel a volume of hydraulic oil equal to approximately 10% of the container volume. This will create the necessary vapor space in the container without altering the overall composition of the oil sample. (Be sure to leave at least some hydraulic oil behind the piston so that there is pressure support on the seal and very little pressure drop across the seal). Close valve E securely.

8. Slightly open valve C to bleed the connections between valves B and D to atmospheric pressure. *Note: The line from valve A to B, including the pressure gauge, is still under pressure. Use a long vent line if  $H_2S$  is present.*

9. Disconnect the sample container. This is the last step for the first sample and leaves the apparatus ready for collection of additional samples by repeating Steps 5–8.

10. Following collection of the last sample, close valve A securely, then open valve B (and valve C, if it is not already open) to bleed pressure from all parts of the line and sampling rig before disconnecting the line from source valve A.

11. Wipe the valves on the sample container clean and inspect for any signs of leakage. After a container is determined to be leak-free, insert plugs in the valves, then tag the container and otherwise prepare it for storage or transit. Before inserting the sealing plugs, the threads should be lubricated by stretching Teflon<sup>®</sup> tape into the threads or by applying pipe dope.

**4.6.6 Wellhead Sampling.** Wellhead sampling, more commonly known as flowline sampling, involves the collection of a fluid sample at the surface from the wellhead itself or from the flowline or upstream side of the choke manifold, provided that the fluid is still in one-phase condition. This option is restricted to wells producing dry gas, very-low-GOR oils, and some high-pressure/high-temperature reservoir fluids. Dry-gas wellhead samples can be collected as for gas sampling from a separator, whereas wellhead sampling of other or unknown fluids should be performed as for separator liquids. However, all equipment must be compatible with maximum wellhead pressure, and as the state of the fluid is not usually known with certainty, separator sampling also should be performed if possible, as a backup.

**4.6.7 Isokinetic Sampling.** Isokinetic sampling, also known as split-stream sampling, involves collecting samples from well production in two-phase flow, using a small side stream to allow the two-phase fluid to be collected and measured in laboratory scale equipment at the wellsite. There are two principal challenges in this approach: controlling the side stream so that it is removed from the main flow at identical velocity (hence the term *isokinetic*) to avoid disproportionate sampling of the two phases, and ensuring that the flow is turbulent upstream of the sampling probe so that the minor phase is finely distributed in the major phase. Although this special type of sampling has been used for more than 60 years, mainly for sampling gas/condensate production, many still consider it to be at the development stage,<sup>2</sup> and it has never achieved wide acceptance. A more recent development of isokinetic sampling involves sampling of the exit gas stream from a separator and calculation of a figure for separator

efficiency. This efficiency is then used to modify the GOR used for recombining separator samples, but it should be compared to the separator efficiencies reported elsewhere in this Handbook.

#### 4.7 Nonpressurized Hydrocarbon Fluid-Sampling Procedures

The sampling of nonpressurized or atmospheric-pressure hydrocarbon fluids from lines is relatively simple to perform, but attention must be paid to the need to purge sampling lines and pipework with at least three times their volume of fresh fluid before each sampling session. This is especially important in some installations and processing facilities, where the sampling point may be at the end of a “dead-leg” or trap in which fluid has collected or stagnated over a long period of time. In general, oil or condensate samples should be collected from a sample tap on the side of the line or the top of the line to avoid any water or sediment that may have accumulated at the bottom of the line. Atmospheric gas samples are rarely collected, but if they are required, they should be collected in evacuated chambers to minimize contamination by air.

Atmospheric hydrocarbon samples also may be collected from pressurized lines or from samples collected in pressurized chambers, such as downhole samples. Usually, this will involve the release of gas and the collection of oil or condensate. Because the separation procedure that releases gas is dependent on the temperature and pressure (which may be above atmospheric if the liquid is collected in a closed trap), the properties of samples collected in this way may vary. Also, because the fluid in a sample chamber may already be in two-phase condition (or may have segregated), liquid from the entire sample should be collected to minimize uncertainty in the sample quality.

Sampling from tanks is complicated by the need to collect samples from various depths to allow for any property changes or segregation that may exist. The procedure given next is a traditional method used for measuring and testing a field tank of crude oil, frequently referred to as “running” when related to custody-transfer transactions. It was published as API Standard 2500 but is no longer available. The method is reproduced here with the permission of the American Petroleum Inst. It is intended to support operations still using this method, or methods derived from it, and serve as a guideline to engineers setting up similar methods. Detailed descriptions of individual calibration and measurement methods are available in the API *Manual of Petroleum Measurement Standards* (MPMS),<sup>9</sup> which represents all branches of the petroleum industry and is the recognized standard for downstream measurement methods.

##### 4.7.1 Procedure for Typical Measuring, Sampling, and Testing of a Tank of Oil.

1. The tank is vertical, nonpressurized, and has a fixed roof with side outlets; it is to be gauged by the innage method (a process to determine the depth of liquid in a tank, which is measured from the surface of the liquid to the tank bottom or to a fixed datum plate).

2. The oil viscosity is less than 100 Saybolt seconds at 100°F and is a liquid at atmospheric temperature and pressure.

3. A cup-case thermometer is used to read the temperature of the oil in the tank.

4. A thief is used to obtain fluid samples from the tank. (A “thief” is an industry term for a bottom-closure, core-type sampler used to secure samples from chosen depths in storage tanks.)

5. The API gravity scale hydrometer test method is used to determine the API gravity of the oil; the temperature of the oil has to be near 60°F ( $\pm 5^\circ\text{F}$ ).

6. The water and sediment in the oil are to be determined by the centrifuge method with a 203-mm (8-in.) cone-shaped tube.

The following outline gives the sequence of steps to be taken and the key points to be noted at each step.

1. Isolate the tank to be checked.

2. Use safety precautions and fresh air bottles if an H<sub>2</sub>S hazard exists.  
3. Ground yourself to a stair railing or tank shell before reaching the top. This prevents static-electrical discharge in a hazardous area.

4. Stand to the side of the hatch when opening it to permit wind to blow gas away from you.

5. Measure the temperature: suspend a thermometer in the oil tank. The thermometer should be 12 in. or more from the tank shell and must be immersed in oil for 5 minutes.

Use an American Soc. for Testing and Materials (ASTM)-approved, wood-back or corrosion-resistant metal cup case. If atmospheric temperature differs by more than 20°F from that of the liquid in the tank, the cup case should be given at least two preliminary immersions. Empty the cup case after each immersion.

Rapidly withdraw the thermometer and read and record the temperature to the nearest 1°F.

*Note: The number of temperature measurements varies with the depth of the liquid.*

In a tank containing more than 15 ft of liquid, three measurements should be taken: (1) 3 ft below the top surface of the liquid, (2) in the middle of the liquid, and (3) 3 ft above the bottom of the liquid.

In a tank containing 10 to 15 ft of liquid, two measurements should be taken: (1) 3 ft below the top surface of the liquid, and (2) 3 ft above the bottom surface of the liquid. In a tank containing less than 10 ft of liquid, one measurement should be taken in the middle of the liquid. For tanks over 10 ft high with a capacity of less than 5,000 bbl, one measurement in the middle of the liquid should be taken.

6. With a thief, take sample(s) for a BS&W centrifuge test. Note: The number of samples to be taken for BS&W determination varies.

In tanks larger than 1,000-bbl capacity that contain more than 15 ft of liquid, equal-volume samples should be taken (1) 6 in. below the top of the liquid, (2) at the middle of the liquid, and (3) at the outlet connection of the merchantable oil, in the order named. This method also may be used in tanks up to and including a capacity of 1,000 bbl.

In a tank larger than 1,000-bbl capacity that contains more than 10 ft and up to 15 ft of liquid, equal-volume samples should be taken (1) 6 in. below the top surface of the liquid and (2) at the outlet connection of the merchantable oil, in the order named. This method may be used on tanks up to and including a capacity of 1,000 bbl.

In a tank larger than 1,000-bbl capacity that contains 10 ft or less of liquid, one sample may be taken in the middle of the column of liquid.

7. Place the BS&W composite sample in a sample container. The sample should be a blend of the upper, middle, and lower samples (if three samples were required), containing equal parts from the samples taken.

8. Seal the sample container. In the lower 48 states, with the exception of California, the sample is ready to be tested for BS&W, as described in Step 17. In California, the container should be labeled and delivered to the laboratory for BS&W determination. (*Note: These U.S. state references were part of the original standard.*)

9. With a thief, take a sample for gravity determination. The sample should be taken midway between the oil surface and the pipeline connection. Hang the thief in the hatch. Remove bubbles, and place the hydrometer in the oil sample.

10. Determine and record the sample temperature to the nearest 0.5°F. The hydrometer must float away from the wall of the cylinder; the temperature of the surrounding media should not change more than 5°F.

Depress the hydrometer two scale divisions and release. Read the hydrometer to the nearest 0.05°API on a scale at which surface or liquid cuts scale.

11. Read and record the sample temperature to the nearest 0.5°F. Repeat the gravity reading if the temperature of the sample before and after the gravity reading has changed more than 1°F. Apply any relevant correction to the observed hydrometer reading (correction scale on

bulb) to the nearest 0.1°API. Record the mean temperature reading observed before and after the final hydrometer reading to the nearest 1°F.

*Note: Hydrometer scale readings at temperatures other than calibration temperatures (60°F) should not be considered more than scale readings because the hydrometer bulb changes with temperature.*

12. Convert the relevant corrected value to standard temperatures. Use API MPMS Chapter 11.1 (Table 5A)<sup>9</sup> for crude oils.

13. Take the bottom thief sample for BS&W height. Lower the clean, dry thief slowly into the oil to the desired depth, trip the thief, and raise it slowly to avoid agitation. When the sample is taken, the top of the thief must be 2 in. above the bottom of the pipeline connections.

14. Determine and record BS&W height in the tank. Pour the remaining thief sample over a test glass until contamination appears. Measure and record (as the BS&W height) the distance from the bottom of the thief to the top of the contamination in the thief. If BS&W height is less than 4 in. from the bottom of the pipeline connection, do not run the tank.

15. Gauge the tank. Do not gauge a boiling or foaming tank. Use steel innage tape with an innage plumb bob. Always make contact between the gauge line and the hatch while running tape into the tank.

Gauge the tank only at the reference point on the gauging hatch. On tanks of 1,000-bbl capacity or less, read to the nearest 1/4 in. On tanks of 1,000 bbl or more, read to the nearest 1/8 in. Record the reading immediately; repeat until two identical gauges are obtained.

16. Saturate solvent with water. Toluene is approved solvent; it is flammable and toxic. Care should be taken when using toluene.

Fill a 1-qt or 1-L glass bottle with a screw top with 700 to 800 mL of toluene. Add 25 mL of either distilled or tap water. Screw the cap on; shake vigorously for 30 seconds. Loosen the cap; place the bottle in a bath for 30 minutes. Maintain the bath at a constant temperature of 140 ±5°F. Remove, tighten the cap, and shake vigorously for 30 seconds. Repeat three times.

Allow the bottle of water/toluene mixture to sit in the bath for 48 hours before using. Be sure that no free water is left in the bottle.

17. Shake the sample container until the sample is well mixed. Fill two 203-mm (8-in.) cone-shaped centrifuge tubes with 50 mL of sample. Use a pipette to add 50 mL of toluene. Toluene should be water saturated at 140°F. Read the top of the meniscus at both the 50- and 100-mL marks. Add a 0.2-mL demulsifier if necessary for a clean break in the oil/water contact.

Stopper the tube tightly; invert the tube 10 times to ensure that oil and solvent are uniformly mixed.

18. Loosen the stopper slightly. Immerse the tube to the 100-mL mark in a bath for 15 minutes. The bath must maintain a temperature of 140 ±5°F; by contract agreement, the bath temperature may be 120 ±5°F.

Remove the tube from the bath and tighten the stopper. Invert the tube 10 times to ensure that oil and solvent are uniformly mixed.

19. Place the tubes in trunnion cups on opposite sides of the centrifuge. Spin for 10 minutes while maintaining minimum relative centrifuge force of 600.

Following the spinning, read and record the combined volume of water and sediment at the bottom of each tube. Read to the nearest 0.05 mL for oil from 0.1- to 1-mL graduation. Read to the nearest 0.1 mL above 1-mL graduation. Estimate to the nearest 0.025 mL below 0.1-mL graduation.

Return the tube to the centrifuge without agitation. Spin for 10 minutes at the same rate. Repeat this operation until the combined volume of water and sediment remains constant on two consecutive readings.

20. Record the final volume of water and sediment in each tube. The sum of the two admissible readings is the vol% of water and sediment in the sample.

After the tank has been run, the following closing data should be obtained.

21. Closing oil temperature: no closing temperature is necessary on tanks of 5,000 bbl or less; on tanks of 5,000 bbl or more, always read to the nearest 1°F.

22. Obtain a closing gauge reading at the same point and in the same manner as the opening gauge reading.

23. Obtain the bottom thief. If the BS&W level is lower than the opening gauge, report this to a supervisor.

More information concerning the specific measurement methods referred to here can be found in the API MPMS.<sup>9</sup> The manual is being updated continually, and care should be taken that the current standard or chapter is used. Identification of the appropriate section can be made using the publication catalog on the API website (<http://www.api.org/cat/>).

#### 4.8 Oilfield Waters

Oilfield waters are often referred to as brines, especially when they contain significant quantities of dissolved salts. They also frequently contain dissolved gases (more details are available elsewhere in this Handbook) and may contain small quantities of the heavier hydrocarbons found in oils. Water can be present in a surface separator during production, either from liquid water in the zone being tested or by condensation from water vapor in the produced gas, or possibly from both. Water from aquifers or seawater may also need to be analyzed in connection with water-injection activities.

The analysis of oilfield waters has a wide range of applications, including identifying the origin of produced water, characterizing aquifer properties, interpreting wireline-log measurements, predicting formation damage from water incompatibility, investigating scaling tendencies in surface and downhole equipment, monitoring fluid movement in reservoirs, identifying the presence of bacteria, evaluating disposal options and environmental compliance, and predicting and monitoring corrosion. Water analyses also can be useful in diagnosing and correcting numerous oilfield operating problems.

API publishes *Recommended Practice 45*,<sup>10</sup> which contains information on the applications of oilfield-water analyses and gives recommendations for the proper collection, preservation, and labeling of oilfield-water samples. *RP 45* also gives a description of numerous analytical methods and recommends appropriate reporting formats for analytical results. This publication should be consulted for more information about specific analytical methods and any special sampling or storage requirements linked to such methods. Numerous analytical methods are also available as ASTM standards.<sup>11</sup>

When sampling and analysis are part of a long-term monitoring program, such as those required by government authorities or those forming part of custody-transfer contracts, the methods defined in the appropriate documentation or contracts must be followed as closely as possible, even if this constitutes differences with the procedures or recommendations in this text or with the industry standards cited here. However, the guidelines provided here should be taken into consideration before contracts are drafted or when existing contracts are renewed.

If samples are to be collected for the measurement of trace components, biological species, or reactive chemicals that are likely to be affected by storage, container material, or ambient conditions, on-site analyses should be considered. API *RP 45* lists the following measurements that should be carried out immediately in the field after sampling and filtering oilfield waters: (1) pH, (2) temperature, (3) alkalinity, (4) dissolved oxygen, (5) CO<sub>2</sub>, (6) H<sub>2</sub>S, and (7) total and soluble iron. Other measurements or preparations to be performed in the field include (8) turbidity on an unfiltered sample, (9) total suspended solids with at least primary filtration and washing performed in the field, (10) bacteria with filtering and/or culturing in the field, and incubation and counting performed in the laboratory. Biological determinations are outside the scope of this document but are covered in detail elsewhere.<sup>12,13</sup>

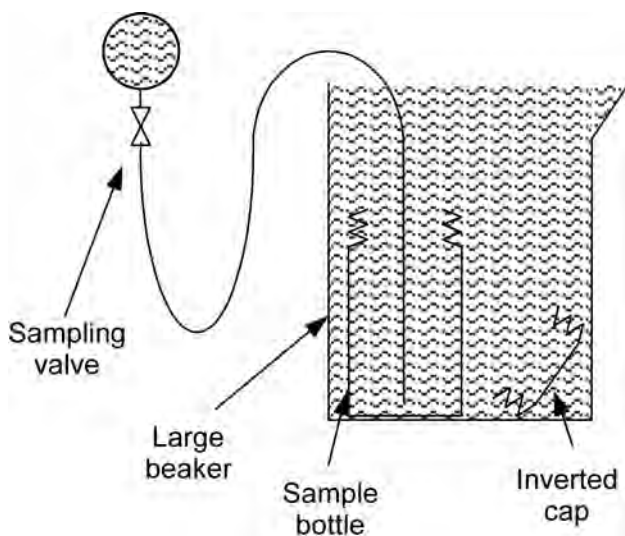


Fig. 4.7—Water-sampling method to avoid air.

For many other analyses, special preparation and preservation measures are required to be performed in the field. This can involve acidification with various acids, addition of other chemicals, refrigeration [ideally 39°F (4°C)], and storage in the dark. If there is any uncertainty concerning sample storage conditions, the laboratory that will perform the analyses should be consulted for advice. If no information is available, it is advisable to keep samples cool and out of the sunlight.

For a DST that does not flow to the surface, great care must be taken to determine if the test has flowed sufficient fluid to allow representative reservoir brine into the tool. The best practice is to sample the water after each stand of pipe is removed. Normally, the total-dissolved-solids content will increase downward and become constant when pure formation water is obtained. A test that flows water will give even higher assurance of an uncontaminated sample. If only one DST water sample is taken for analysis, it should be taken just above the tool because this is the last water to enter the tool and is least likely to show contamination.

Surface sampling is commonly used to obtain a sample of formation water from a sampling valve at the wellhead or another sampling point. A plastic or rubber tube can be used to transfer the sample from the sample valve into the container. Fig. 4.7 shows a simple method of excluding air when sampling water in this way. After purging the sample valve and line to remove any foreign material, water is delivered to the bottom of the sample bottle, which is placed in a large, much taller beaker until the water fills the beaker and overflows. Then, the cap is immersed in the beaker and inverted to eliminate air bubbles before removing the delivery tube and closing the sample bottle under water. This technique cannot be used when acid or other preservatives must be added to the sample.

An alternative sampling technique for use when a clean source of water is available is shown in Fig. 4.8. Here, once the sample point and line have been purged, the sample is collected in the sample cylinder by closing the two valves. This system should not be used to collect pressurized water samples.

In many producing wells, it may be impossible to locate a suitable sampling point free from oil or gas, such as for pumping wellheads in which the brine will surge out in heads and be mixed with oil. In such situations, a larger container equipped with a sampling tap near the bottom can be used as a surge tank or oil/water separator. Such a device is shown in Fig. 4.9. This method will serve to obtain samples that are relatively oil-free.



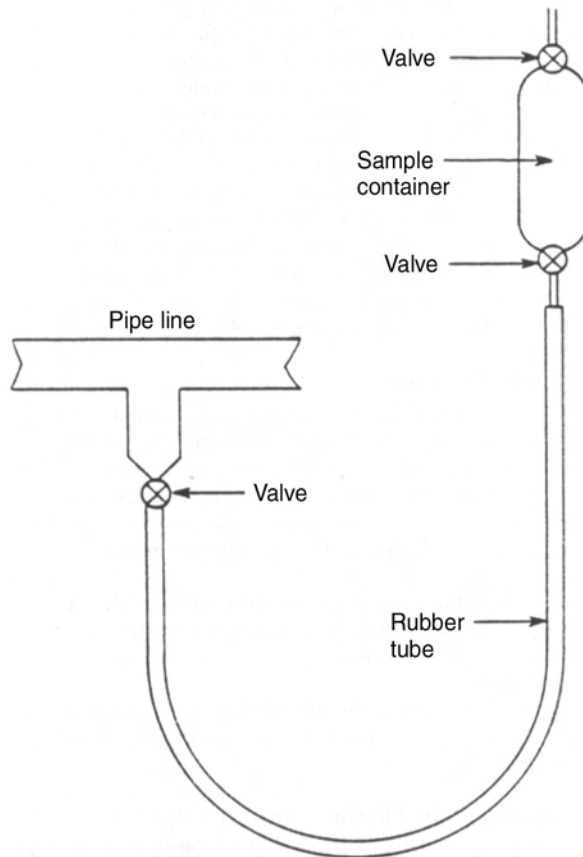


Fig. 4.8—An alternative method for collecting air-free water samples.

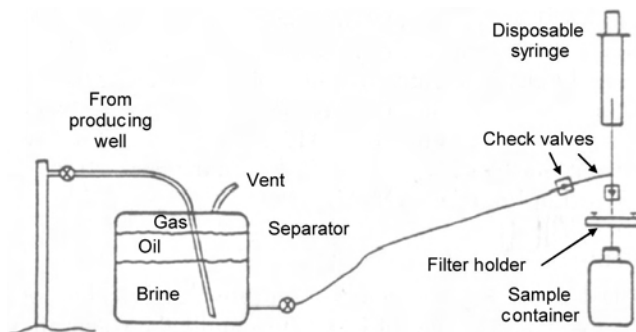


Fig. 4.9—Oil/water separator and water-sample filtering system.

For some measurements, it is necessary to obtain a field-filtered sample. The filtering system shown in Fig. 4.9 is simple and economical and can be used for various applications. It consists of a 50-mL disposable syringe, two check valves, and an inline disk-filter holder. The filter holder takes size 47-mm-diameter, 0.45- $\mu\text{m}$  pore-size filters, with the option of including various prefilters. The syringe fill line should be connected to a source of brine free from oil or gas, either directly to a suitable sample point or to the brine outlet from a suitable separa-

tion vessel, as shown in Fig. 4.9. The brine is drawn through the inlet line into the syringe and then forced through the filter into the collection bottle. The check valves allow the syringe to be used as a pump for filling the collection bottle without needing to open and close valves. If the filter becomes clogged, it can be replaced in a few minutes. Approximately 2 minutes are required to collect 250 mL of sample. Usually two samples are taken, with the one being acidified to pH 3 or less with concentrated hydrochloric or nitric acid. The system can be cleaned easily or flushed with brine to prevent contamination.

If pressurized water samples are required, most of the procedures described previously for pressurized hydrocarbon fluids can be used, including downhole sampling. Piston sample bottles are essential because the sample cannot be collected by the displacement of water or brine.

#### 4.9 Sampling-Data Measurement and Recording

In the same way that laboratory measurements require representative samples to be meaningful, the samples themselves must be supported by accurate data to provide a unique identification and to record all important production and sampling parameters that will be used in checking the sample and (in many cases) in determining the exact measurements that will be performed. This section reviews the importance of data measurement and provides guidelines for recording and validating the necessary data.

Provided that flowmeters and pressure gauges are properly sized for a measurement, so that readings are not made at the low end of the measurement range, random errors are generally small. Systematic errors are a major concern, however, for all measurements, deriving from sensor malfunction, poor (or lack of) calibration, and human error in general; the latter item can include both errors in recording and reporting data and those deriving from the use of computer-based acquisition systems (e.g., entry of erroneous calibration data, incorrect sensor connections, and even software bugs). Although systematic errors are comparatively rare, their magnitude can be significant. In fact, on some occasions, errors are identified only when measured values are so large that the values become ridiculous.

The GOR is considered to be the most important measurement for separator samples, and it is dependent on errors in both the gas flow rate and the oil flow rate, which are measured separately. New techniques have seen limited application to reduce errors in GOR, such as the injection of a standard marker chemical upstream of the separator and measurements of the concentrations in the separated gas and liquid streams. Also, use of various carry-over measurement techniques has been made, such as the isokinetic approach described briefly earlier. However, significant improvements can be achieved simply by proper sizing, calibration, and recording.

In production testing, gas flow rate itself is widely measured by the orifice meter. This system has been in use for a long time, but new standards have been issued more recently that improve gas rate calculations.<sup>14</sup> The orifice meter relies on a range of coefficients or factors to calculate the flow rate from the differential pressure measured across the orifice. Many of these factors are derived from on-site measurements of the gas. The measurement accuracy can be improved by ensuring that the orifice plate has been sized correctly for the flow so that it falls within 30 to 70% of full range (or higher, if there is no chance of going off scale). Likely additional sources of error come from what could be considered mechanical factors, such as the physical condition of the orifice plate itself; waxy deposits or damage will change the flow performance and can lead to significant errors. An obvious but commonly overlooked potential error concerns not the condition of the orifice, but the recording of the orifice size. An oversight here can have serious implications not only for fluid analysis but for well-test interpretation. Errors in the differential-pressure measurement derive primarily from poor calibration of the recording instrument or from liquid buildup in the lines that have not been purged. The orifice meter pressure-base factor is a common source of errors because variations do exist between the reference pressure and temperature used for gas measurements (e.g., a variation

between 100 kPa and 14.7 psia is an increase of 1.4%). Thus, it is essential that reference conditions are quoted correctly. The actual source of gas gravity and supercompressibility factors ( $F_g$  and  $F_{pv}$ ) is usually not important for fluid studies because accurate values are commonly calculated in the laboratory on the basis of compositional analysis of the gas sample, but it is necessary to know exactly which values were used to correct gas flow rate to the new values. To ensure the highest accuracy in gas flow-rate measurement, a check should be made that all the meter factors are determined and used correctly. Approximate flow rates can be derived from the choke setting, and a comparison should identify any major error in the orifice meter calculation.

Condensate or oil flow rates are normally measured by a positive displacement meter that is placed in the outlet line from the separator upstream of the flow control valve. The most common error derives from incomplete reporting of the measurement conditions for the oil rate, especially whether the oil flow is measured at separator or at stock-tank conditions, and the meter factors and shrinkage values that should be applied if stock-tank rates are reported. The most likely causes of error in the measurement itself are poor calibration, worn seals (allowing liquid to bypass the measuring element), or the release of gas leading to high-volume, two-phase measurement. The latter problem can be treated by the installation of a “gas eliminator,” which is effectively a tiny separator before the meter. Gas breakout in the meter may be signaled by sudden flow-rate fluctuations, whereas stable foams with some oils (occasionally referred to as “carry-under”) may be less obvious and may require antifoaming agents to overcome. Any water and sediment in the oil flow should be determined by the BS&W measurement and corrected for accordingly. It is good practice to size the flowmeter according to the expected flow rate, as recommended for gas flows. Flow rates also should be checked by gauging the stock tank regularly.

BS&W measurement is performed by centrifuging a sample of liquid mixed with solvent; although relative error in the measurement can be very important at low BS&W, measurement accuracy is generally adequate for the purposes of flow-rate correction. Of more concern is whether the sample used for the measurement is representative, so samples should be taken from the top and bottom of the liquid flowline, and a comparison should be made.

The shrinkage factor, used to relate separator-liquid volumes to stock-tank conditions, depends on a differential liberation of gas and may give different values from the true flash process as separator liquid enters the tank stage. In normal circumstances, it is thus much better to rely on a separator flow rate measured with a calibrated meter than to use the tank flow rate corrected according to the shrinkage tester. In the worst case, with no reliable liquid flow rates at separator conditions, an experimental shrinkage factor must be determined in the laboratory and used with the average tank flow rate to obtain the necessary rate.

Further details of proper oil- and gas-measurement practices are available elsewhere in this Handbook and in other sources.<sup>1,2</sup> **Table 4.5** provides a checklist that can ensure that surface-measurement data are as reliable as possible. Other surface measurements should be validated in similar fashion; for example, wellhead pressures should be measured with a dead-weight tester or with a pressure gauge that has been calibrated recently.

Among the downhole measurements, it is the reservoir temperature that is the most important for fluid studies because this is the temperature at which reservoir-fluid-property measurements will be made. In addition, pressures, gradients (density, pressure, and temperature), and, indeed, the depth at which these measurements are made are all important in validating samples and in interpreting laboratory measurements. Downhole temperature and pressure gauges should be calibrated, under well conditions if possible, and adequate time allowed for temperatures to stabilize if fluid production or injection has influenced downhole temperatures. Good knowledge of temperatures in a reservoir may only be available once measurements have been made in several wells.

TABLE 4.5—WELL-TEST CHECKLIST FOR IMPROVED GOR ACCURACY

Check Required	Identification	Action to be Taken
Orifice plate size and condition	Routine check	Inspect orifice plate size and condition with service engineer on entry/removal.
	Poor correlation with choke setting	
Orifice meter factor	Routine check	Check that the meter factor is recorded and used correctly. Note any changes.
	Poor correlation with choke setting	
Differential-pressure gauge	Routine check	Purge lines regularly.
	Poor correlation with choke setting	Calibrate gauge if necessary.
Liquid flowmeter factor	Routine check	Verify based on tank rate and shrinkage. Recalibrate as soon as feasible, if needed.
	Poor correlation with stock-tank gauging	
Liquid flow rate	Poor correlation with stock-tank gauging	Check for gas liberation in flowline or "carry-under." If no cure is possible, rely on stock-tank rate.
	Rate fluctuations	
Separator temperature	Routine check with portable thermometer	Investigate differences of 1°C or more, and replace sensor or record offset.
	Apparent mismatch with other data	
Separation efficiency	Misting or liquid carry-over in gas streams	Reduce flow rate, or reduce liquid level if possible. Try to estimate carry-over rate, and record for reference.
	Observations by sampling crew; increase in GOR with flow rate at high rates	
Separator pressure	Routine check to be made at atmospheric pressure (15 psia or 0 psig) and separator test pressure; mismatch observed	Calibrate against field dead-weight tester (retrospectively, if only option), replace pressure gauge or sensor, record any changes.

Note: In all cases in which a measurement problem is identified, the change should be recorded and an estimate given of the correction needed to earlier readings. This correction then can be applied retrospectively

The data listed in [Tables 4.6 and 4.7](#) must be considered essential if fluid samples are to be studied properly in the laboratory. These data are the absolute minimum needed for valid laboratory studies. Every attempt should be made to provide all the information requested on sampling sheets. An independent check at the wellsite is advisable to ensure that sampling personnel have achieved this need. Many additional measurements are of value in sample validation, and measurement trends with time are important in monitoring well behavior (such as during cleanup or when evaluating the effect of changes in production). To enable a proper check to be made of well conditioning, separator stability, and data recorded on the sampling sheets, it is recommended that a full copy of the well-test report (or records of production data for production facilities) be sent to the laboratory that will be working on the samples.

Water can be produced in a surface separator—either from liquid water in the zone being tested or by condensation from water vapor in the produced gas, or possibly from both—and can affect measurement accuracy. The effect of water on gas gravity (and, thus, the gas flow rate) is currently ignored because it is not routinely measured either in the field or in the laboratory. In most cases, this is an acceptable approach, but in separators operating at high temperatures and low pressures, the water content of the gas stream can reach significant proportions (for further details, refer to the nomogram<sup>15</sup> "Water content of hydrocarbon gas").

**TABLE 4.6—ESSENTIAL SAMPLING DATA FOR SEPARATOR SAMPLES**

1. Sample-bottle or container number, sample type, and sampling point.
2. Well location, reservoir, and test references (such as producing interval).
3. Date and time the sampling was performed.
4. Operator references.
5. Report of any unusual observations or problems taking the sample, or any signs of contamination.
6. Static reservoir temperature at middle of perforations.
7. Static reservoir pressure at middle of perforated interval.
8. Separator-gas flow rate at standard conditions.
9. Standard conditions (pressure and temperature) used for the gas flow rate.
10. Value used for the gas gravity in the gas flow-rate calculation.
11. Value used for the  $F_{pv}$  factor ( $1/\sqrt{Z}$ ).
12. Either the liquid flow rate at separator conditions (preferably) or the liquid flow rate at stock-tank conditions and the measured shrinkage factor.
13. Separator pressure and temperature.
14. Bottle numbers for corresponding gas or liquid samples.
15. Report of the use of any chemicals to combat hydrate formation or foaming.
16. Name, company, and telephone number of sampling operator.
17. Sample containers themselves must be labeled with the information in Items 1, 2, and 3 together with any additional information needed to provide unique identification.

Water production can have more serious consequences if separator-liquid flow rates are not properly corrected for BS&W measurements.

The data in **Table 4.8** should be recorded for the sampling of water from a well. Similar data should be recorded for water samples taken from other installations or facilities.

## 4.10 Quality Control of Samples

**4.10.1 Selecting Samples for Study.** This is an area in which there have been significant improvements in recent years, with significantly more details of quality-control tests being reported by laboratories, yet only limited information has been published on the aspect of fluid sampling.<sup>16</sup> This section highlights the principal controls that should be performed and gives guidelines for selecting which samples are most likely to be representative. Newer concerns involve the quality of formation-test samples from wells drilled with OBM. Because of the wide range of fluids and sampling conditions, comparison of duplicate (or, more correctly, replicate) samples is generally the best method of evaluating whether the sample is representative.

The primary objectives must be selection of a fluid that is most representative of the reservoir fluid and identification of any serious quality problems related to the samples or the sampling data; these problems must be communicated to the client before proceeding with the fluid study.

Poor sample quality can arise from such sources as sampling nonrepresentative fluid, human error during sampling or field transfers, contaminated sample containers, and leaks during shipment.

For separator-gas samples, the quality checks that should be made when the sample bottles have been heated to, or slightly above, separator temperature are (1) determination of opening

**TABLE 4.7—ESSENTIAL SAMPLING DATA FOR DOWNHOLE SAMPLES**

1. Sample-bottle or container number, sample type, and sampling point.
2. Well location, reservoir, and test references (such as producing interval).
3. Date and time the sampling was performed.
4. Operator references.
5. Report of any unusual observations or problems taking the sample, or any signs of contamination.
6. Static reservoir temperature at middle of perforated interval, or at sampling depth for formation samples.
7. Static reservoir pressure at middle of perforated interval, or at sampling depth for formation samples.
8. Initial opening pressure and temperature if sample was transferred in the field.
9. Apparent bubblepoint (if any) and transfer pressure if transferred.
10. Bottle or chamber numbers for associated downhole samples.
11. Type of drilling fluid used if formation samples were recovered (collect a sample of any OBM used).
12. Name, company, and telephone number of sampling operator.
13. Sample containers themselves must be labeled with the information in Items 1, 2, and 3 together with any additional information needed to provide unique identification.

**TABLE 4.8—ESSENTIAL SAMPLING DATA FOR WATER SAMPLES**

1. Sample-bottle or container number, sample type, and sampling point.
2. Well location, reservoir, and test references (such as producing interval).
3. Date and time the sampling was performed.
4. Operator references.
5. Report of any unusual observations or problems taking the sample, or any signs of contamination.
6. Static reservoir temperature at middle of perforations.
7. Gas, hydrocarbon-liquid, and water flow rates.
8. Sample-point pressure and temperature.
9. Bottle numbers for associated samples.
10. Report of the use of any chemicals and their injection rates.
11. Any on-site measurements made on the sample or sample stream.
12. Name, company, and telephone number of sampling operator.
13. Sample containers themselves must be labeled or tagged with the information in Items 1, 2, and 3 together with any additional information needed to provide unique identification.

pressure; (2) compositional analysis, including air content; and (3) determination of residual liquids, possibly from carry-over.

Separator liquids transported with a gas cap must be homogenized by pressurization and agitation. In this instance, the controls that must be performed are (1) determination of initial opening pressure; (2) determination of bubblepoint pressure at ambient or (preferably) separator temperature; (3) a check for presence of sediments or an aqueous phase; and, when feasible, (4) flash separation to give GOR, shrinkage, gas gravity, or composition.

Downhole samples should be checked in the same way, except that bubblepoint pressure can be measured at either ambient or reservoir temperature. Measurement at reservoir temperature takes longer but is preferable for comparisons with downhole static or flowing pressures.

Ambient bubblepoint-pressure estimates are often available from field transfers, but they should be used only as a guide because thorough mixing of the sample may not be achieved during recompression, and temperatures may be unstable. In downhole samples of a highly volatile oil or a gas condensate, no “break point” will be seen on the recompression curve, and a saturation pressure must be determined in a windowed PVT cell.

The following are parameters that should be used, in order of preference, when a sample is selected on the basis of sample quality alone (i.e., when samples are essentially duplicates collected at the same time and under the same conditions): (1) an adequate sample volume or pressure; (2) a downhole sample bubblepoint pressure lower than downhole pressure during sampling; (3) contamination levels lower than, or similar to, duplicate samples; (4) bottle opening pressures that agree with sampling data (i.e., leaks are unlikely); (5) surface sample bubblepoint pressures that agree with separator data; (6) a close correlation between laboratory measurements on duplicate samples; and (7) one sample that represents “average” properties of duplicates.

For gas and oil samples collected from a separator, if at all possible, production test reports or other documentation should be studied in addition to the sampling sheets that normally accompany samples because a high proportion of sampling sheets contain inconsistencies. Data should be studied with the following objectives: (1) to identify what well or plant conditioning has been performed; (2) to look for the stability of gas and liquid rates when the surface samples were taken and, possibly, to calculate averages at the time the samples were taken; (3) to ensure that the GOR is based on oil flow rate at separator conditions; (4) to determine which gas gravity and nonideality ( $Z$ ) factors were used, as well as the reference pressure and temperature; and (5) to verify reservoir temperature and static pressure.

If all samples meet the quality criteria, the choice can be made on the basis of field data alone, although the selection tends to be a compromise in some cases. Both operator and laboratory personnel must be involved in these choices. Primary emphasis should be given to (1) samples collected after proper well conditioning, (2) surface oil and gas samples taken simultaneously or close together, (3) a downhole sample that was collected above its bubblepoint that compares well with the bubblepoint pressure for duplicate samples, (4) a good downhole sample in preference to a recombined surface sample, and (5) a recombined surface sample if doubt exists about the quality of downhole samples. In cases in which downhole samples have been backed up by surface samples (an excellent practice), creation of a recombined surface sample from the best surface samples might be worthwhile, especially if there are only one or two downhole samples that appear to be valid. This allows comparison of the recombined surface sample with the downhole samples. In fact, in important wells, complete analyses of the two types of reservoir-fluid samples might be useful. Such an approach can give a high level of confidence in the data and could provide a crosscheck of separator GORs.

All validation data and analyses do not need to be included in the report when laboratory measurements are reported, but it is good practice to use a minimum of one page to explain sample selection and to detail any quality or field-data problems. This information can be of major value to engineers using the measured data.

Wells drilled with OBM are particularly problematic for formation-test-tool sample quality, and many research and development (R&D) centers worldwide are working on correction techniques. **Figs. 4.10 and 4.11** demonstrate the sort of contamination that can occur; because the base oil is miscible with reservoir oil, it is impossible to remove this contamination from samples. It is essential to perform “fingerprint”-type gas chromatography (GC) analyses as a minimum quality control on formation-test samples to provide a qualitative indication of contamination, and even on production-test samples for which thorough cleanup may not have been achieved.

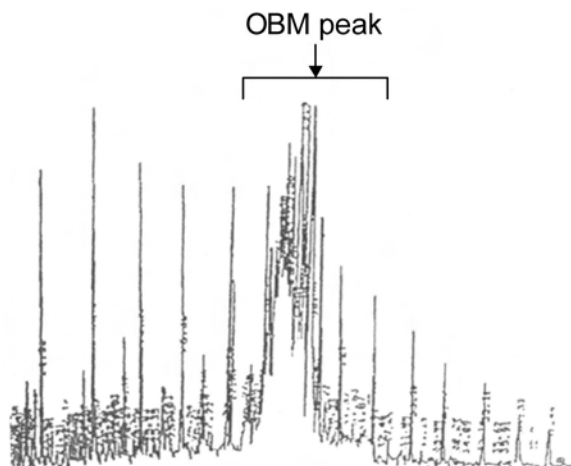


Fig. 4.10—Chromatogram showing broad OBM peak.

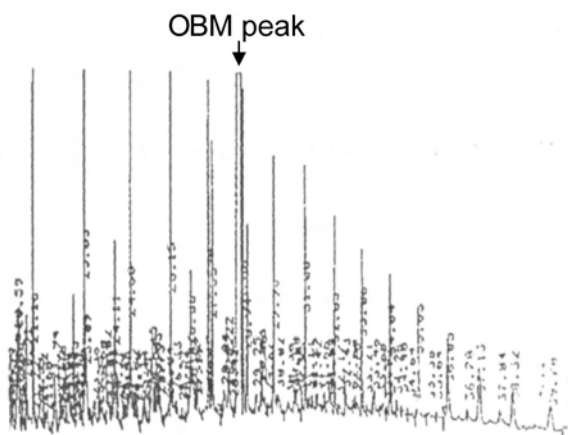


Fig. 4.11—Chromatogram showing narrow OBM peak.

Special correction techniques are increasingly used within the oil industry, and because these techniques vary between organizations and laboratories, sample selection should be done only after considering which method to use. Many companies are forced to use oil-based drilling muds to manage drilling costs in water-sensitive formations, and the added expense of handling contaminated samples (and the risk associated with poorer-quality data) must be used to evaluate the overall economic balance.

For water samples, comparisons of duplicates also give a good indication of quality. Where fluid concentration may be stabilizing (e.g., at the end of a cleanup), sequential samples should be used to look for compositional trends and thus to help decide if representative fluid has been sampled. For some sampling procedures involving trapping or precipitation of particular components, it is highly recommended to use blank “samples,” which undergo exactly the same treatment and storage as the actual sample and provide a reference measurement to assist with the interpretation of laboratory measurements. More details are available in API *RP 45*.<sup>10</sup>



**TABLE 4.9—QUALITY-CONTROL STEPS FOR COMPOSITIONAL ANALYSIS BY GC**

1. All chromatographs should be recalibrated on a regular basis (commonly daily).
2. A check with a calibration gas or well-defined reference gas should be made before and after each analysis or series of analyses.
3. Each chromatogram should be visually inspected to ensure that peaks have been properly identified and quantified by the integration software.
4. Any unusually large peaks identified in chromatograms should be checked and reported, as this may be an indication of the presence of a solvent or other contaminant in the sample, or of a very unusual hydrocarbon distribution.
5. If an unusually high concentration of a nonhydrocarbon component is determined (typically using a thermal-conductivity detector), the measurement should be verified either by analyzing a standard gas with a similar concentration of the component or by using an independent measurement technique (e.g., length-of-stain tubes).
6. All analyses should be run in duplicate, unless a duplicate-sample analysis can serve the purpose of a check.

Although this chapter concentrates on sampling rather than on analytical measurements, it is worth providing simple quality-control guidelines for GC here. This is because of the importance of GC analytical techniques both in the quality-control procedures described above and, increasingly, in on-site measurements and because simple guidelines of the sort given in [Table 4.9](#) are not widely reported.

**4.10.2 Selecting Fluid Samples for Storage.** Decisions concerning sample storage involve the following constraints: (1) discarding samples may prevent future measurements or checking of dubious results; (2) long-term storage of pressurized samples may incur very high rental costs; (3) sample-bottle purchase involves higher “short-term” cost (instead of long-term rental charges) but may sidestep the issue of deciding on a long-term storage policy; and (4) long-term storage requires a safe storage area and a catalog to be maintained (subcontracting is an option to be considered by producers).

One policy could be to keep duplicate samples for a short length of time on a rental basis and then to transfer minimum sample quantities into bottles purchased specifically for long-term storage. In all cases, it is advisable to budget for long-term storage within the project costs.

A good approach is for the laboratory report to recommend which samples should be kept or discarded on the basis of the quality checks and the study itself. An initial selection can be made at the end of the study, or even at the quality-control stage, if useless samples are identified. Then, the “customer” can respond on the basis of this information and the other needs of the project.

Further measurements may be warranted for a number of reasons: doubts about initial measurements; measurements required at different temperature or pressure conditions; advanced PVT measurements that are deemed necessary (interfacial tension, phase diagram, etc.); new analytical techniques that are developed before the reservoir is developed; or an asset purchase or joint venture that changes needs or requires independent measurements.

Because of the complexity of the heavy components in reservoir fluids, it is impossible to make an adequate synthetic mixture based on the liquid composition determined. It is thus good practice to store at least 1L of stock-tank liquid. This can be stored cheaply in a low-pressure closed container, but it also could be blended with a synthetic gas mixture (based on separator-gas and stock-tank gas analyses) to recreate a sample close to the original fluid composition, if further work was eventually required on the reservoir fluid itself.

A small volume (e.g., 100 cm<sup>3</sup>) of separator gas should be stored under pressure in case more-accurate or new analytical measurements are required on the gas later. For a downhole sample, a flash separation can be made at a convenient pressure to generate a suitable gas sample for storage.

Note that the quantities specified above are recommended in the case that no further laboratory measurements are anticipated. If further work appears likely, appropriate quantities of samples should be stored in addition to these minimum volumes.

This work recommends that a suitable sample-storage policy be identified and implemented in operating companies.

#### 4.11 Hazards

No text covering fluid sampling would be complete without reference to the numerous hazards that must be considered when establishing safe working practices and sampling programs. Like many areas of the petroleum industry, if not managed properly, hazards can lead to equipment damage or loss, personal injury, and even death. Common hazards include the following (though this list is not exhaustive and may not cover unusual locations or special operating practices).

**Hydrogen Sulfide (H<sub>2</sub>S).** This poisonous chemical is present in numerous hydrocarbon reservoirs and can be present both in gas streams and dissolved in hydrocarbon liquids. Although H<sub>2</sub>S is recognizable by its smell at the low parts per million (ppm) level, above approximately 100 ppm the human nose becomes insensitive to the gas, and personnel could easily be exposed to lethal levels of H<sub>2</sub>S (700 ppm can lead to instant death) if proper safety equipment is not in use. Safety measures should range from automatic alarm systems, personal monitors, and evacuation equipment to positive-pressure breathing systems, depending on the exact nature of the risk.

**High Pressures.** Fluid sampling frequently involves pressures up to 10,000 psi (700 bar), and even higher pressures are becoming increasingly common. Basic precautions should involve careful checking that equipment has a working pressure rating compatible with the maximum pressure that can be encountered at a sampling point (beware that flowing streams can produce a “hammer” effect when valves are closed suddenly), routine wearing of eye protection, and releasing of pressure before tightening leaking connections and attaching the ends of lines used to vent pressure.

**Flammable Materials.** Reservoir-fluid samples contain combustible hydrocarbons, so care must be taken to eliminate all sources of ignition from areas in which samples are collected or stored, especially where hydrocarbons are released during the purging of lines. Equipment must never be pressurized with oxygen or air (e.g., to clear blockages), as this can result in autoignition of heavy hydrocarbons (the “diesel” effect).

**Solvents.** Cleaning agents may contain dangerous compounds such as chlorinated solvents, and indeed, produced fluids may contain benzene. Breathing of vapors and skin contact with solvents should be avoided as much as possible. Solvents should be used as efficiently as possible, and all waste materials should be stored in closed containers before proper disposal.

**Transport and Storage.** Physical shocks are common during transport, so sample containers should be shipped with connecting ports plugged and exposed valves protected by endcaps. Liquid-filled containers are at risk of developing high pressures when heated; the best protection is to collect samples so that the liquid is in two-phase condition, with a gas cap representing approximately 10% of the capacity, or to use sample containers with a special separate gas cap. Rupture disks can be used to provide similar protection, but there is an increased risk of sample loss and venting of hazardous material.

**Other Hazards.** Examples of other dangers that sampling personnel must be aware of include offshore operations (special survival training is available), lack of oxygen in enclosed areas where large volumes of gases can be vented (notably nitrogen, but other gases such as

hydrocarbons are an equal danger), and the toxicity of mercury, still used in some sampling operations.

Personnel who are not trained to work safely in the presence of these or other hazards must not undertake fluid-sampling activities. Assistance in properly managing all hazards should be obtained from qualified safety specialists.

## 4.12 Special Topics in Fluid Sampling

**4.12.1 Sampling of Crude-Oil Emulsions.** Samples of emulsions may be required for several reasons, including verifying crude specifications, evaluating the performance of emulsion-treating systems, or for laboratory testing such as choice of demulsifiers and optimum concentration. Emulsions frequently must be sampled under pressure, and special procedures must be used to obtain representative samples. For crude specification testing, it is not important to maintain the integrity of the water droplets; however, the sample location point may be critical. In general, samples should not be withdrawn from the bottom of the pipe or vessel, where free water may accumulate, affecting the BS&W reading and, thus, the validity of the sample. In addition, the sample should not be withdrawn from the top of the vessel or pipe, as it is likely to contain primarily oil. The best position in the pipe to take an emulsion sample is from the side at approximately midheight, preferably with a sampling probe (often known as a “quill”). Choosing a sampling point at which there is turbulence and high fluid velocity in the pipe may also avoid problems caused by segregation and ensure that the sample is homogeneous.

As for all sampling activities, every effort should be made to obtain representative samples. When sampling from pressurized lines and vessels, care should be taken to ensure that emulsification does not occur during the sampling process itself. For example, samples obtained at the wellhead or production headers may show a high percentage of emulsion (as a consequence of the sampling as the sample was depressurized into the sample container), whereas the actual oil and water inside the piping may or may not be in the form of an emulsion. Also, emulsions exhibit a wide range of stability, so samples of emulsions collected in the field may separate partially or even totally during shipment to the laboratory.

The best sampling procedure to use for samples from pressurized sources, without further emulsification of the liquids, is the technique based on a floating-piston cylinder, as described in [Section 4.6.5](#). A setup similar to that in [Fig. 4.6](#) is used, with the hydraulic section of the cylinder filled with a pressurizing fluid (e.g., a glycol/water mixture or a synthetic oil) and the top of the cylinder evacuated. Purging of the sample line can be made but should be carried out at a bleed rate. The sample collection should be performed slowly to obtain the sample with a minimum pressure drop between the cylinder and the sampling point. Alternative methods use a simple sample cylinder (without any floating piston), which is initially filled with water (or mercury). Once the pressurized sample is captured, the cylinder can be depressurized, if required, by removing further quantities of hydraulic fluid extremely slowly with little effect on the sample.

In situations in which sampling into a pressurized container is not possible, the best method to take an emulsion sample is to bleed the sample line very slowly into the sample container. The idea is to minimize shear and reduce emulsification that may be caused by the sampling procedures. Emulsions are covered in more detail elsewhere in this Handbook.

**4.12.2 Waxy and Asphaltenic Fluids.** Great care should be taken in sampling fluids that have potential for the precipitation of wax or asphaltenes because loss of a solid or flocculated phase during sampling or handling will produce fluids that are no longer representative. Because these tendencies may not be recognized until the samples are being studied, the same precautions are advisable for all fluids that have not been characterized previously in detail.

Asphaltene problems in particular are difficult to predict owing to a poor correlation between asphaltene concentration and flocculation tendency. Because of the difficulty of homogenizing fluids containing flocculated asphaltenes, it is highly recommended that downhole samples be collected using single-phase samplers with the pressure raised well above reservoir pressure by the nitrogen charge. Separator oils and atmospheric oils generally suffer from limited asphaltene deposition problems because they contain very few of the light hydrocarbons that contribute to flocculation.

Paraffinic or waxy crude oils can be extremely difficult to sample, with separator liquids occasionally solidifying in sampling lines and equipment, and the use of heated, short, large-diameter sampling lines is recommended. At downhole temperatures, sampling is generally easier, and limited availability of heated sampling tools exists. Single-phase sampling tools can be used, especially if asphaltene and wax problems may occur, but pressure maintenance alone will not prevent wax precipitation on cooling, as this is strongly dependent on temperature. Though rarer, gas/condensate reservoirs can also produce liquids that show wax-forming tendencies, which require special handling procedures.

Sample bottles containing movable mixing devices are recommended in all these cases, as returning samples to original sampling conditions and agitating for a lengthy period (e.g., overnight) gives the highest chance of recovering representative samples from samplers or sampling cylinders.

**4.12.3 On-Site Measurements.** It is worth giving some details of common on-site measurements because they must be performed on representative samples or sample streams and are frequently included in sampling programs.

The most common on-site gas analysis method is the “length-of-stain” detector tubes (often called “sniffer” tubes or Drager tubes, after one of the suppliers) used primarily for H<sub>2</sub>S but available for CO<sub>2</sub> and a wide range of other gases and vapors. This method is relatively simple to use, and principal errors derive from incorrect use of response factors or stroke counts. The ASTM has a number of standards that apply to this method,<sup>17–19</sup> and all propose a sampling system based on a modified polythene wash bottle (or equivalent setup) to ensure that measurements are performed on a representative sample stream. Flexible tubing is connected from a control valve at the sample point to the wash-bottle delivery tube, and the screw cap is removed (or perforated). Then, the control valve is opened slightly to allow gas to flow into the bottom of the wash bottle, which purges air out of the top. After purging for at least 3 minutes, the length-of-stain detector can be inserted through the top of the wash bottle and the pump operated to perform the measurement. This arrangement ensures that the gas sampled is at atmospheric pressure. Detector tubes have a limited life and should not be used beyond the date limit. Care must be taken to avoid contacting any liquids with the end of the tube. An alternative approach used a gas bag, which must be made from an inert material and purged completely at least five times immediately before the measurement. In some circumstances, gas concentrations above the detector-tube limit can be estimated by using fewer or fractional pump strokes, but such practices must be recorded clearly to help interpret measurements. For reactive species like H<sub>2</sub>S, there is significant justification for making on-site concentration measurements by two independent techniques, as this provides on-site quality assurance.<sup>20</sup>

Portable gas chromatographs are becoming more common at the wellsite, and they bring the advantage of early characterization of gas composition, together with an identification of most nonhydrocarbons present (depending on the carrier gas used). However, such instruments are accurate only when operated by trained personnel and when properly calibrated. Also, the additional cost of the service must be justified, though this could occur in the following cases: (1) high nitrogen or helium is anticipated, (2) early decisions must be made on the basis of gas sales value, (3) variable nonhydrocarbon concentrations occur within a field and will contribute

to property mapping or be used to determine if fluid sampling is required, or (4) sample transport logistics mean that laboratory analyses may take a very long time.

The possibility of sulfate-reducing bacteria (SRB) contaminating completion fluids and even souring the reservoir itself represents a significant risk, and tests on site or sampling for SRB are recommended to identify and address potential problems. Tests that give a negative result can be particularly helpful in identifying the origin of SRB development later in the life of a field.

Many additional analytical measurements can now be performed on site because there is a wide variety of portable chemical test kits available, especially for water analysis. However, suitably trained operators are essential.

**4.12.4 Drilling-Mud Gas.** During drilling operations, returning drilling mud is commonly monitored for the presence of hydrocarbons, both for formation-evaluation purposes and for safety concerns. Generally, hydrocarbons are extracted from the mud to provide an air sample containing hydrocarbons, and as the extraction technique is dependent on equipment design and installation, measured compositions are rarely quantitatively representative of the concentrations in the drilling mud. This limitation is commonly accounted for by the use of hydrocarbon ratios when interpreting drilling-mud hydrocarbon analyses and logs, but it has been shown<sup>21</sup> that effective quantitative measurements can be obtained with careful location of the mud-sampling point, the use of a special extraction device, and care to account for losses of hydrocarbon gas from the return line before the mud-sampling point. Mud logging is covered in detail elsewhere in this Handbook.

**4.12.5 Water-Cut Measurements.** Downhole sampling can be used as a means to measure water cut in producing oil wells, especially when there are no separation facilities or suitable measuring instruments at the wellsite or when measurements with depth are required as an alternative to (or validation for) production logs. In these cases, the well should be flowing at normal producing conditions, unless the purpose of the sampling is to investigate the water cut at other production conditions. As in all cases in which sampling is attempted from two-phase flow, there is the potential for preferential collection of one of the phases; this is especially likely if the two phases are not well distributed. It may be advisable to set the sampler to collect the sample in the shortest time to minimize any segregation. Care also should be taken in high-angle well sections, where the sampler will lie in the lowest part and is likely to sample water preferentially.

For a measurement of total water cut, it is advisable to sample from a depth a moderate distance [e.g., 20 ft (6 m)] above the top of the perforated interval. Also, it is good practice to take a number of separate samples under identical flow conditions to allow evaluation of the repeatability of water-cut measurements. Good agreement between replicate samples, although not absolute proof, gives high confidence in the reliability of the measurements, whereas significant variation is a clear sign of unrepresentative sampling or of variable water cut in the fluids entering the wellbore. Sampling from a range of depths both above and within the perforated interval in a well can provide more-detailed information on water production, but it does not give production-rate information on its own.

Volumetric measurement of water cut should ideally be made on site so that repeat measurements can be made as required. If emulsion is present in the sampled fluid, this should be given time to break, or suitable chemicals should be used to demulsify the sample before the definitive water-cut measurement.

## 4.13 Conclusions

Optimizing costs in all petroleum-industry activities continues to have a major effect on sampling operations, with competition between production testing and formation-test-tool opera-

tions leading to widespread industry acceptance of lower-quality fluid samples from the latter. A key challenge at present is to get better-quality formation-test-tool samples not simply by advanced tool capability but by better planning and preparation for the test. Increasing efforts to obtain reservoir information from short well cleanups is also putting pressure on fluid-sampling operations, but in some cases (such as on-site measurements), this change in emphasis may provide opportunities for measurements that otherwise would not be available.

Multiphase metering is likely to have an increasing impact on sampling operations because the accuracy of flow-rate measurement is seen to be improving, and the economic benefits of avoiding the use of separators will be major. However, even with significant development of special sampling approaches (such as isokinetic sampling), it seems unlikely that the same quality of samples will be available as with traditional separator methods.

Among the major developments in the past 10 to 15 years is the progress toward the worldwide elimination of the use of mercury in fluid-sampling operations, producing significant improvements in personnel safety and environmental protection. Efforts must continue to achieve better management of sampling programs and cost-efficient sample storage, despite the difficult challenge of trying to assign monetary values to fluid samples and the measurements made on them.

Specific technical developments that can be anticipated are a greater use of automatic surface-sampling systems, introduction of equipment better designed to preserve reactive samples such as fluids containing  $H_2S$ , an increase in gas/condensate downhole sampling and in use of downhole sampler technology (such as heated chambers for sampling waxy fluids), and downhole measurement of simplified composition and physical properties such as bubblepoint.

With the tremendous pace of the development and functionality of new downhole tools, there is a need for speedy updating of industry standards documentation to allow broad dissemination of new sampling knowledge and practices; however, it is clear that this is not a role readily filled by traditional standards organizations such as API. Working groups and forums involving service companies and operators may provide the best prospect of developing standards updates, which can be published in peer-reviewed petroleum engineering journals.

### Nomenclature

- $F_g$  = gas gravity meter factor defined as  $\sqrt{1/G}$
- $F_{pv}$  = gas supercompressibility meter factor defined as  $\sqrt{1/Z}$
- $G$  = gas gravity
- $P_{sep}$  = separator pressure
- $T_c$  = critical temperature
- $T_i$  = cricondentherm
- $Z$  = gas nonideality (or compressibility) factor

---

### References

1. Moffatt, B.J. and Williams, J.M.: "Identifying and Meeting the Key Needs for Reservoir Fluid Properties: A Multi-Disciplinary Approach," paper SPE 49067 prepared for presentation at the 1998 SPE Annual Technical Conference and Exhibition, New Orleans, 27–30 September.
2. Williams, J.M.: "Fluid Sampling Under Adverse Conditions," *Revue de l'Institut Français du Pétrole* (May–June 1998) **53**, No. 3, 355.
3. Standing, M.B.: "Volumetric and Phase Behavior of Oil Field Hydrocarbon Systems," SPE, Richardson, Texas (1951) 10–19.
4. McCain, W.D. Jr. and Alexander, R.A.: "Sampling Gas-Condensate Wells," *SPE* (August 1992) 358; *Trans.*, AIME, **293**.
5. Turner, R.G., Hubbard, M.G., and Dukler, A.E.: "Analysis and Prediction of Minimum Flow Rate for the Continuous Removal of Liquids from Gas Wells," *Trans.*, AIME (1969) **246**, 1475.

6. *RP 44, Recommended Practice for Sampling Petroleum Reservoir Fluids*, second edition, API, Washington, DC (2003).
7. *RP 44, Recommended Practice for Sampling Petroleum Reservoir Fluids*, first edition, API, Washington, DC (1966).
8. Hy-Billiot, J. *et al.*: “Getting the Best From Formation Tester Sampling,” paper SPE 77771 presented at the 2002 SPE Annual Technical Conference and Exhibition, San Antonio, Texas, 29 September–2 October.
9. *Manual of Petroleum Measurement Standards*, API, Washington, DC (1974–present).
10. *RP 45, Recommended Practice for Analysis of Oil-Field Waters*, third edition, API, Washington, DC (1998).
11. “Water and Environmental Technology,” Section 11, Annual Book of ASTM Standards, American Soc. for Testing and Materials, West Conshohocken, Pennsylvania (2002).
12. TM0194-94, “Field Monitoring of Bacterial Growth in Oilfield Systems,” NACE Intl., Houston.
13. *RP 38, Recommended Practice for Biological Analysis of Subsurface Injection Waters*, third edition, API, Washington, DC (1975).
14. Teyssandier, R.G. and Beaty, R.: “New Orifice Meter Standards Improve Gas Calculations,” *Oil & Gas J.* (11 January 1993) 40.
15. *Engineering Data Book*, Gas Processors Suppliers Assn., Tulsa (1987) Vol. II, Fig. 20-3.
16. Williams, J.M.: “Getting the Best out of Fluid Samples,” *JPT* (September 1994) 752.
17. “Standard Test Method for Hydrogen Sulfide in Natural Gas Using Length-of-Stain Detector Tubes,” D-4810, American Soc. for Testing and Materials, West Conshohocken, Pennsylvania (June 1988).
18. “Standard Test Method for Carbon Dioxide in Natural Gas Using Length-of-Stain Detector Tubes,” D-4984, American Soc. for Testing and Materials, West Conshohocken, Pennsylvania (November 1989).
19. “Standard Test Method for Water Vapor in Natural Gas Using Length-of-Stain Detector Tubes,” D-4888, American Soc. for Testing and Materials, West Conshohocken, Pennsylvania (February 1989).
20. Williams, J.M.: “Getting Reliable On-Site H<sub>2</sub>S and CO<sub>2</sub> Concentrations for Anti-Corrosion Measures in Gas Wells,” paper SPE 81495 presented at the 2003 SPE Middle East Oil Show and Conference, Bahrain, 9–12 June.
21. Roberts, G.L., Kelessidis, V.C., and Williams, J.M.: “New System Provides Continuous Quantitative Analysis of Gas Concentration in the Mud During Drilling,” *SPEDE* (September 1991) 219.

### SI Metric Conversion Factors

°API	141.5/(131.5+°API)		= g/cm <sup>3</sup>
bar ×	1.0*	E + 05	= Pa
bbl ×	1.589 873	E – 01	= m <sup>3</sup>
ft ×	3.048*	E – 01	= m
ft <sup>3</sup> ×	2.831 685	E – 02	= m <sup>3</sup>
°F	(°F – 32)/1.8		= °C
in. <sup>3</sup> ×	1.638 706	E + 01	= cm <sup>3</sup>
psi ×	6.894 757	E + 00	= kPa

\*Conversion factor is exact.





## Chapter 5

### Gas Properties

Brian F. Towler, U. of Wyoming

#### 5.1 Molecular Weight

Molecules of a particular chemical species are composed of groups of atoms that always combine according to a specific formula. The chemical formula and the international atomic weight table provide us with a scale for determining the weight ratios of all atoms combined in any molecule. The molecular weight,  $M$ , of a molecule is simply the sum of all the atomic weights of its constituent atoms. It follows, then, that the number of molecules in a given mass of material is inversely proportional to its molecular weight. Therefore, when masses of different materials have the same ratio as their molecular weights, the number of molecules present is equal. For instance, 2 lbm hydrogen contains the same number of molecules as 16 lbm methane. For this reason, it is convenient to define the unit “lbm mol” as a mass of the material in pounds equal to its molecular weight. Similarly, a “g mol” is its mass in grams. One lbm mol or one g mol of any compound, therefore, represents a fixed number of molecules. This number for the g mol was determined in 1998 by the U.S. Natl. Inst. of Standards and Technology to be  $6.02214199 \times 10^{23}$ . The number of significant digits shown is the accuracy to which it has been determined experimentally.

#### 5.2 Ideal Gas

The kinetic theory of gases postulates that a gas is composed of a large number of very small discrete particles. These particles can be shown to be identified with molecules. For an ideal gas, the volume of these particles is assumed to be so small that it is negligible compared with the total volume occupied by the gas. It is assumed also that these particles or molecules have neither attractive nor repulsive forces between them. The average energy of the particles or molecules can be shown to be a function of temperature only. Thus, the kinetic energy,  $E_k$ , is independent of molecule type or size. Because kinetic energy is related to mass and velocity by  $E_k = \frac{1}{2}mv^2$ , it follows that small molecules (less mass) must travel faster than large molecules (more mass) when both are at the same temperature. Molecules are considered to be moving in all directions in a random manner as a result of frequent collisions with one another and with the walls of the containing vessel. The collisions with the walls create the pressure exerted by the gas. Thus, as the volume occupied by the gas is decreased, the collisions of the particles with the walls are more frequent, and an increase in pressure results. It is a statement of

Boyle's law that this increase in pressure is inversely proportional to the change in volume at constant temperature:

$$\frac{V_1}{V_2} = \frac{p_2}{p_1}, \dots\dots\dots (5.1)$$

where  $p$  is the absolute pressure and  $V$  is the volume.

Further, if the temperature is increased, the velocity of the molecules and, therefore, the energy with which they strike the walls of the containing vessel will be increased, resulting in a rise in pressure. To maintain the pressure constant while heating a gas, the volume must be increased in proportion to the change in absolute temperature. This is a statement of Charles' law,

$$\frac{V_1}{V_2} = \frac{T_1}{T_2}, \dots\dots\dots (5.2)$$

where  $T$  is the absolute temperature and  $p$  is constant.

From a historical viewpoint, the observations of Boyle and Charles in no small degree led to the establishment of the kinetic theory of gases, rather than vice versa. It follows from this discussion that, at zero degrees absolute, the kinetic energy of an ideal gas, as well as its volume and pressure, would be zero. This agrees with the definition of absolute zero, which is the temperature at which all the molecules present have zero kinetic energy.

Because the kinetic energy of a molecule depends only on temperature, and not on size or type of molecule, equal molecular quantities of different gases at the same pressure and temperature would occupy equal volumes. The volume occupied by an ideal gas therefore depends on three things: temperature, pressure, and number of molecules (moles) present. It does not depend on the type of molecule present. The ideal-gas law, which is actually a combination of Boyle's and Charles' laws, is a statement of this fact:

$$pV = nRT, \dots\dots\dots (5.3)$$

where  $p$  = pressure,  $V$  = volume,  $n$  = number of moles,  $R$  = gas-law constant, and  $T$  = absolute temperature.

The gas-law constant,  $R$ , is a proportionality constant that depends only on the units of  $p$ ,  $V$ ,  $n$ , and  $T$ . **Tables 5.1a through 5.1c** present different values of  $R$  for the various units of these parameters. The value of the gas constant is experimental, and more-accurate values are reported occasionally. The values in **Tables 5.1a through 5.1c** are based on the values reported by Moldover *et al.*<sup>1</sup> Their value was determined from measurements of the speed of sound in argon as a function of pressure at the temperature of the triple point of water. Note that because  $pV$  has the units of energy, the value of  $R$  is typically given in units of energy per mole per absolute temperature unit [e.g., the appropriate SI value for  $R$  is 8.31447 J/(g mol-K), and the appropriate British gravitational (sometimes called the American customary units) value for  $R$  is 1,545.35 ft-lbf/(lb-mol<sup>o</sup>R)]. However, sometimes pressure and volume units are more appropriate, such as  $R = 10.7316$  (psia-ft<sup>3</sup>)/(lb mol-<sup>o</sup>R).

### 5.3 Critical Temperature and Pressure

Typical pressure/volume/temperature (PVT) relationships for a pure fluid are illustrated in **Fig. 5.1**. The curve segment B-C-D defines the limits of vapor/liquid coexistence, with B-C being the bubblepoint curve of the liquid and C-D being the dewpoint curve of the vapor. Any com-

TABLE 5.1A—GAS-CONSTANT VALUES BASED ON ENERGY UNITS

	<u>g mol Kelvin</u>	<u>lb mol Kelvin</u>	<u>g mol Rankine</u>	<u>lb mol Rankine</u>
Btu	0.0078806	3.57458	0.00437811	1.98588
cal	1.98588	900.779	1.10327	500.433
Chu	0.00437811	1.98588	0.00243228	1.10327
erg	$8.31447 \times 10^7$	$3.77138 \times 10^{10}$	$4.61915 \times 10^7$	$2.09521 \times 10^{10}$
lbf-ft	6.13244	2781.63	3.40691	1545.35
hp-hr	$3.09719 \times 10^{-6}$	0.00140486	$1.72066 \times 10^{-6}$	0.000780479
J	8.31447	3771.38	4.61915	2095.21
kcal	0.00198588	0.900779	0.00110327	0.500433
kgf-m	0.847840	384.574	0.471022	213.652
kJ	0.00831447	3.77138	0.00461915	2.09521
kW-hr	$2.30958 \times 10^{-6}$	0.00104761	$1.28310 \times 10^{-6}$	0.000582003
N-m	8.31447	3771.38	4.61915	2095.21

Chu = Celsius heat unit (1 Chu = 1899.18 J); erg = a unit of energy (1 erg =  $10^{-7}$  J); hp-hr = horsepower/hour.

bination of temperature, pressure, and volume above that line segment indicates that the fluid exists in a single phase. At low temperatures and pressures, the properties of equilibrium vapors and liquids are extremely different (e.g., the density of a gas is low, while that of a liquid is relatively high). As the pressure and temperature are increased along the coexistence curves, liquid density, viscosity, and other properties generally decrease while vapor density and viscosity generally increase. Thus, the difference in the physical properties of the coexisting phases decreases. These changes continue as the temperature and pressure are raised until a point is reached at which the properties of the equilibrium vapor and liquid become equal. The temperature, pressure, and volume at this point are called the “critical” values for that species. Location C on Fig. 5.1 is the critical point. The critical temperature and pressure are unique values for each species and are useful in correlating physical properties. Critical constants for some of the commonly occurring hydrocarbons and other components of natural gas can be found in Table 5.2.

#### 5.4 Specific Gravity (Relative Density)

The specific gravity of a gas,  $\gamma$ , is the ratio of the density of the gas at standard pressure and temperature to the density of air at the same standard pressure and temperature. The standard temperature is usually 60°F, and the standard pressure is usually 14.696 psia. However, slightly different standards are sometimes used in different locations and in different units. The ideal-gas laws can be used to show that the specific gravity (ratio of densities) is also equal to the ratio of the molecular weights. By convention, specific gravities of all gases at all pressures are

TABLE 5.1B—GAS-CONSTANT VALUES BASED ON PRESSURE AND VOLUME UNITS

	cm <sup>3</sup>	L	m <sup>3</sup>	ft <sup>3</sup>	in. <sup>3</sup>
atm	82.0575	0.0820575	$8.20575 \times 10^{-5}$	0.00289783	5.00745
bar	83.1447	0.0831447	$8.31447 \times 10^{-5}$	0.00293623	5.0738
ft H <sub>2</sub> O	2781.63	2.78163	0.00278163	0.0982323	169.745
in. H <sub>2</sub> O	33379.5	33.3795	0.0333795	1.17879	2036.94
in. Hg	2455.27	2.45527	0.00245527	0.086707	149.83
kgf/cm <sup>2</sup>	84.784	0.084784	$8.4784 \times 10^{-5}$	0.00299412	5.17384
kPa	8314.47	8.31447	0.00831447	0.293623	507.38
lb/ft <sup>2</sup>	173651	173.651	0.173651	6.13244	10596.9
mbar	83144.7	83.1447	0.0831447	2.93623	5073.8
m H <sub>2</sub> O	847.84	0.84784	0.00084784	0.0299412	51.7384
mm H <sub>2</sub> O	847840	847.84	0.84784	29.9412	51738.4
mm Hg	62363.8	62.3638	0.0623638	2.20236	3805.68
Pa	$8.31447 \times 10^6$	8314.47	8.31447	293.623	507380
psi	1205.91	1.20591	0.00120591	0.0425864	73.5893

This table is based on g mol and Kelvin temperature units.

usually set equal to the ratio of the molecular weight of the gas to that of air (28.967). Although specific gravity is used throughout this chapter, this traditional term is not used under the SI system; it has been replaced by “relative density.”

### 5.5 Mole Fraction and Apparent Molecular Weight of Gas Mixtures

The analysis of a gas mixture can be expressed in terms of a mole fraction,  $y_i$ , of each component, which is the ratio of the number of moles of a given component to the total number of moles present. Analyses also can be expressed in terms of the volume, weight, or pressure fraction of each component present. Under limited conditions, where gaseous mixtures conform reasonably well to the ideal-gas laws, the mole fraction can be shown to be equal to the volume fraction but not to the weight fraction. The apparent molecular weight of a gas mixture is equal to the sum of the mole fraction times the molecular weight of each component.

### 5.6 Specific Gravity of Gas Mixtures

The specific gravity ( $\gamma_g$ ) of a gas mixture is the ratio of the density of the gas mixture to that of air. It is measured easily at the wellhead in the field and therefore is used as an indication of the composition of the gas. As mentioned earlier, the specific gravity of gas is proportional to its molecular weight ( $M_g$ ) if it is measured at low pressures where gas behavior approaches

TABLE 5.1C—GAS-CONSTANT VALUES BASED ON PRESSURE AND VOLUME UNITS

	cm <sup>3</sup>	L	m <sup>3</sup>	ft <sup>3</sup>	in. <sup>3</sup>
atm	20678.1	20.6781	0.0206781	0.730241	1261.86
bar	20952.1	20.9521	0.0209521	0.739917	1278.58
ft H <sub>2</sub> O	700958	700.958	0.700958	24.7541	42775.1
in. H <sub>2</sub> O	8.41150 × 10 <sup>6</sup>	8411.50	8.41150	297.049	513301
in. Hg	618717	618.717	0.618717	21.8498	37756.5
kgf/cm <sup>2</sup>	21365.2	21.3652	0.0213652	0.754505	1303.79
kPa	2.09521 × 10 <sup>6</sup>	2095.21	2.09521	73.9917	127858
lbf/ft <sup>2</sup>	4.37594 × 10 <sup>7</sup>	43759.4	43.7594	1545.35	2.67036 × 10 <sup>6</sup>
mbar	2.09521 × 10 <sup>7</sup>	20952.1	20.9521	739.917	1.27858 × 10 <sup>6</sup>
m H <sub>2</sub> O	213652	213.652	0.213652	7.54505	13037.9
mm H <sub>2</sub> O	2.13652 × 10 <sup>6</sup>	213652	213.652	7545.05	1.30379 × 10 <sup>7</sup>
mm Hg	1.57154 × 10 <sup>7</sup>	15715.4	15.7154	554.985	959014
Pa	2.09521 × 10 <sup>9</sup>	2.09521 × 10 <sup>6</sup>	2095.21	73991.7	1.27858 × 10 <sup>6</sup>
psi	303885	303.885	0.303885	10.7316	18544.2

This table is based on lb mol and Rankine temperature units.

ideality. Specific gravity also has been used to correlate other physical properties of natural gases. To do this, it is necessary to assume that the analyses of gases vary regularly with their gravities. Because this assumption is only an approximation and is known to do poorly for gases with appreciable nonhydrocarbon content, it should be used only in the absence of a complete analysis or of correlations based on a complete analysis of the gas.

### 5.7 Dalton's Law

The partial pressure of a gas in a mixture of gases is defined as the pressure that the gas would exert if it alone were present at the same temperature and volume as the mixture. Dalton's law states that the sum of the partial pressures of the gases in a mixture is equal to the total pressure of the mixture. This law can be shown to be true if the ideal-gas laws apply.

### 5.8 Amagat's Law

The partial volume of a gas in a mixture of gases is defined as the volume that the gas would occupy if it alone were present at the same temperature and pressure as the mixture of the gases. If the ideal-gas laws hold, then Amagat's law (that the sum of the partial volumes is equal to the total volume) also must be true.

TABLE 5.2—SOME PHYSICAL CONSTANTS OF HYDROCARBONS

Number	Compound	Formula	Molecular Weight	Vapor Pressure (100°F, psia)	Pressure (psia)	Critical Constants		Gas Density (60°F, 14.696 psia)
						Temperature (°F)	Volume (ft <sup>3</sup> /lbm)	
1	methane	CH <sub>4</sub>	16.043	-5000	667.8	-116.68	0.0988	59.1
2	ethane	C <sub>2</sub> H <sub>6</sub>	30.07	-800	707.8	90.1	0.0788	37.48
3	propane	C <sub>3</sub> H <sub>8</sub>	44.097	188	616.3	206.01	0.0737	36.49
4	<i>n</i> -butane	C <sub>4</sub> H <sub>10</sub>	58.124	51.54	550.7	-305.62	0.0703	31.80
5	isobutane	C <sub>4</sub> H <sub>10</sub>	58.124	72.39	529.1	274.96	0.0724	30.65
6	<i>n</i> -pentane	C <sub>5</sub> H <sub>12</sub>	72.151	15.575	488.6	385.6	0.0674	27.67
7	isopentane	C <sub>5</sub> H <sub>12</sub>	72.151	20.4444	490.4	369.03	0.0679	27.38
8	neopentane	C <sub>5</sub> H <sub>12</sub>	72.151	36.66	464	321.08	0.0673	26.16
9	<i>n</i> -hexane	C <sub>6</sub> H <sub>14</sub>	86.178	4.96	436.9	453.6	0.06887	24.38
10	2-methylpentane	C <sub>6</sub> H <sub>14</sub>	86.178	6.767	436.6	435.74	0.0682	24.16
11	3-methylpentane	C <sub>6</sub> H <sub>14</sub>	86.178	6.103	453.1	448.2	0.0682	24.56
12	neohexane	C <sub>6</sub> H <sub>14</sub>	86.178	9.859	446.9	420.04	0.0668	24.02
13	2,3-dimethylbutane	C <sub>6</sub> H <sub>14</sub>	86.178	7.406	453.5	440	0.0665	24.47
14	<i>n</i> -heptane	C <sub>7</sub> H <sub>16</sub>	100.205	1.62	396.8	512.7	0.069	21.73
15	2-methylhexane	C <sub>7</sub> H <sub>16</sub>	100.205	2.2719	396.5	494.89	0.0673	21.56
16	3-methylhexane	C <sub>7</sub> H <sub>16</sub>	100.205	2.131	408.1	503.67	0.0646	21.84
17	3-ethylpentane	C <sub>7</sub> H <sub>16</sub>	100.205	2.013	419.3	513.36	0.0665	22.19
18	2,2-dimethylpentane	C <sub>7</sub> H <sub>16</sub>	100.205	3.494	402.2	477.12	0.0665	21.41
19	2,4-dimethylpentane	C <sub>7</sub> H <sub>16</sub>	100.205	3.293	397	475.84	0.0668	21.39
20	3,3-dimethylpentane	C <sub>7</sub> H <sub>16</sub>	100.205	2.774	427.1	505.74	0.0662	22.03
21	triptane	C <sub>7</sub> H <sub>16</sub>	100.205	3.375	428.4	496.33	0.0636	21.93
22	<i>n</i> -octane	C <sub>8</sub> H <sub>18</sub>	114.232	0.537	360.6	564.1	0.069	19.58
23	diisobutyl	C <sub>8</sub> H <sub>18</sub>	114.232	1.1017	360.6	530.31	0.0676	19.33
24	isooctane	C <sub>8</sub> H <sub>18</sub>	114.232	1.709	372.5	519.33	0.0657	19.28
25	<i>n</i> -nonane	C <sub>9</sub> H <sub>20</sub>	128.259	0.1796	331.8	610.54	0.0684	17.81
26	<i>n</i> -decane	C <sub>10</sub> H <sub>22</sub>	142.286	0.0609	304.4	651.6	0.0679	16.32
27	cyclopentane	C <sub>5</sub> H <sub>10</sub>	70.135	9.914	653	461.6	0.0594	33.85
28	methylcyclopentane	C <sub>6</sub> H <sub>12</sub>	84.162	4.503	549	499.24	0.0607	28.33
29	cyclohexane	C <sub>6</sub> H <sub>12</sub>	84.162	3.266	590.9	536.6	0.0589	29.45
30	methylcyclohexane	C <sub>7</sub> H <sub>14</sub>	98.189	1.6093	503.6	570.15	0.0601	24.92
31	ethylene	C <sub>2</sub> H <sub>4</sub>	28.054	-	731.1	48.56	0.0748	-
32	propene	C <sub>3</sub> H <sub>6</sub>	42.081	227.6	667.2	197.06	0.0689	39.25
33	1-butene	C <sub>4</sub> H <sub>8</sub>	56.108	62.1	583.5	295.48	0.0686	33.91
34	<i>cis</i> -2-butene	C <sub>4</sub> H <sub>8</sub>	56.108	45.95	612.1	324.37	0.0668	35.36
35	<i>trans</i> -2-butene	C <sub>4</sub> H <sub>8</sub>	56.108	49.94	587.1	311.86	0.0679	34.40
36	isobutene	C <sub>4</sub> H <sub>8</sub>	56.108	63.64	580	292.55	0.0682	33.86
37	1-pentene	C <sub>5</sub> H <sub>10</sub>	70.135	19.117	591.8	-376.93	0.0676	29.13
38	1,2-butadiene	C <sub>4</sub> H <sub>6</sub>	54.092	36.5	-653	-340	-0.0649	38.4
39	1,3-butadiene	C <sub>4</sub> H <sub>6</sub>	54.092	59.4	628	305	0.0655	36.69
40	isoprene	C <sub>5</sub> H <sub>8</sub>	68.119	16.68	-558.4	-412	-0.065	31.87
41	acetylene	C <sub>2</sub> H <sub>2</sub>	26.038	-	890.4	95.32	0.0695	-
42	benzene	C <sub>6</sub> H <sub>6</sub>	78.114	3.225	710.4	552.22	0.0525	35.82
43	toluene	C <sub>6</sub> H <sub>5</sub> -CH <sub>3</sub>	92.141	1.033	595.5	605.57	0.0549	29.94
44	ethylbenzene	C <sub>8</sub> H <sub>10</sub>	106.168	0.376	523.4	651.29	0.0565	25.97
45	<i>o</i> -xylene	C <sub>8</sub> H <sub>10</sub>	106.168	0.263	541.6	674.92	0.0557	26.36
46	<i>m</i> -xylene	C <sub>8</sub> H <sub>10</sub>	106.168	0.325	512.9	651.02	0.0567	25.88
47	<i>p</i> -xylene	C <sub>8</sub> H <sub>10</sub>	106.168	0.3424	509.2	649.54	0.057	25.8
48	styrene	C <sub>8</sub> H <sub>8</sub>	104.152	0.238	580	706	0.0541	27.68
49	isopropylbenzene	C <sub>9</sub> H <sub>12</sub>	120.195	0.188	465.4	676.3	0.0572	22.8
50	methyl alcohol	CH <sub>3</sub> O	32.042	4.63	1,174.40	463.08	0.0589	78.61
51	ethyl alcohol	C <sub>2</sub> H <sub>5</sub> O	46.069	2.125	925.3	465.39	0.058	54.36
52	carbon monoxide	CO	28.01	-	507.5	-220.4	0.0532	-
53	carbon dioxide	CO <sub>2</sub>	44.01	-	1,071.00	87.87	0.0342	59.78
54	hydrogen sulfide	H <sub>2</sub> S	34.076	387.1	1,306.00	212.6	0.046	73.07
55	sulfur dioxide	SO <sub>2</sub>	64.059	85.46	1,145.00	315.8	0.0306	69.01
56	ammonia	NH <sub>3</sub>	17.031	211.9	1,636.00	270.4	0.0681	114.71
57	air	N <sub>2</sub> O <sub>2</sub>	28.964	-	546.9	-221.4	0.0517	-
58	hydrogen	H <sub>2</sub>	2.016	-	188.1	-399.9	0.5164	-
59	oxygen	O <sub>2</sub>	31.999	-	736.9	-181.2	0.0367	-
60	nitrogen	N <sub>2</sub>	28.013	-	493	-232.7	0.0516	-
61	chlorine	Cl <sub>2</sub>	70.906	154.9	1,118.40	291	0.028	63.53
62	water	H <sub>2</sub> O	18.015	0.9495	3,207.90	705.5	0.0509	175.6

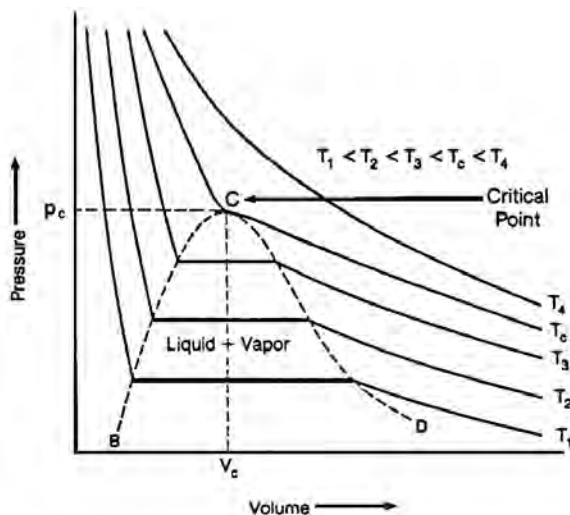


Fig. 5.1—A typical pressure/volume diagram for pure components.

### 5.9 Real Gases

At low pressures and relatively high temperatures, the volume of most gases is so large that the volume of the molecules themselves may be neglected. Also, the distance between molecules is so great that the presence of even fairly strong attractive or repulsive forces is not sufficient to affect the behavior in the gas state. However, as the pressure is increased, the total volume occupied by the gas becomes small enough that the volume of the molecules themselves is appreciable and must be considered. Also, under these conditions, the distance between the molecules is decreased to the point at which the attractive or repulsive forces between the molecules become important. This behavior negates the assumptions required for ideal-gas behavior, and serious errors are observed when comparing experimental volumes to those calculated with the ideal-gas law. Consequently, a real-gas law was formulated (in terms of a correction to the ideal-gas law) by use of a proportionality term.

### 5.10 Real-Gas Law

The volume of a real gas is usually less than what the volume of an ideal gas would be at the same temperature and pressure; hence, a real gas is said to be supercompressible. The ratio of the real volume to the ideal volume, which is a measure of the amount that the gas deviates from perfect behavior, is called the supercompressibility factor, sometimes shortened to the compressibility factor. It is also called the gas-deviation factor and given the symbol  $z$ . The gas-deviation factor is by definition the ratio of the volume actually occupied by a gas at a given pressure and temperature to the volume it would occupy if it behaved ideally, or:

$$z = \frac{\text{Actual volume of gas at specified } T \text{ and } p}{\text{Ideal volume of gas at same } T \text{ and } p} \dots\dots\dots (5.4)$$

Note that the numerator and denominator of Eq. 5.4 refer to the same mass. (This equation for the  $z$  factor is also used for liquids.) Thus, the real-gas equation of state is written:

$$pV = znRT \dots\dots\dots (5.5)$$

The gas-deviation factor,  $z$ , is close to 1 at low pressures and high temperatures, which means that the gas behaves as an ideal gas at these conditions. At standard or atmospheric conditions, the gas  $z$  factor is always approximately 1. As the pressure increases, the  $z$  factor first decreases to a minimum, which is approximately 0.27 for the critical temperature and critical pressure. For temperatures of 1.5 times the critical temperature, the minimum  $z$  factor is approximately 0.77, and for temperatures of twice the critical temperature, the minimum  $z$  factor is 0.937. At high pressures, the  $z$  factor increases above 1, where the gas is no longer supercompressible. At these conditions, the specific volume of the gas is becoming so small, and the distance between molecules is much smaller, so that the density is more strongly affected by the volume occupied by the individual molecules. Hence, the  $z$  factor continues to increase above unity as the pressure increases.

Tables of compressibility factors are available for most pure gases as functions of temperature and pressure. Compressibility factors for mixtures (or unknown pure compounds) are measured easily in a Burnett<sup>2</sup> apparatus or a variable-volume PVT equilibrium cell. The gas-deviation factor,  $z$ , is determined by measuring the volume of a sample of the natural gas at a specific pressure and temperature, then measuring the volume of the same quantity of gas at atmospheric pressure and at a temperature sufficiently high so that the hydrocarbon mixture is in the vapor phase. Tables of compressibility factors are available for most pure gases as functions of temperature and pressure. Excellent correlations are also available for the calculation of compressibility factors. For this reason, compressibility factors are no longer routinely measured on dry-gas mixtures or on most of the leaner wet gases. Rich-gas/condensate systems require other equilibrium studies, and compressibility factors can be obtained routinely from these data.

If the gas-deviation factor is not measured, it may be estimated from correlations. The correlations depend on the pseudoreduced temperature and pressure, which in turn depend on the pseudocritical temperature and pseudocritical pressure. The pseudocritical temperature and pseudocritical pressure normally can be defined most simply as the molal average critical temperature and pressure of the mixture components. Thus,

$$p_{pc} = \sum y_i p_{ci} \quad \text{and} \quad T_{pc} = \sum y_i T_{ci}, \dots \dots \dots (5.6)$$

where  $p_{pc}$  = pseudocritical pressure of the gas mixture,  $T_{pc}$  = pseudocritical temperature of the gas mixture,  $p_{ci}$  = critical pressure of component  $i$  in the gas mixture,  $T_{ci}$  = critical temperature of component  $i$  in the gas mixture, and  $y_i$  = mole fraction of component  $i$  in the gas mixture. These relations are known as Kay's rule after W.B. Kay,<sup>3</sup> who first suggested their use.

The pseudocritical temperature and pressure are not the actual critical temperature and pressure of the mixture but represent the values that must be used for the purpose of comparing corresponding states of different gases on the  $z$ -factor chart (**Fig 5.2**). It has been found to approximate the convergence of the lines of constant volume on a pressure/temperature diagram.

Sutton<sup>4</sup> found that Kay's rules for the determination of pseudocritical properties did not give accurate results for higher-molecular-weight mixtures of hydrocarbon gases. He found that they resulted in errors in the  $z$  factor as high as 15%. Instead, Sutton<sup>4</sup> proposed a modification of a method first proposed by Stewart *et al.*<sup>5</sup> Sutton's<sup>4</sup> method is to first define and determine the pseudocritical properties of the  $C_{7+}$  fraction, then calculate the pseudocritical properties of the mixture as follows:

$$F_j = \frac{1}{3} \left( \frac{y T_c}{p_c} \right)_{C_{7+}} + \frac{2}{3} \left( y \sqrt{\frac{T_c}{p_c}} \right)_{C_{7+}} \dots \dots \dots (5.7)$$



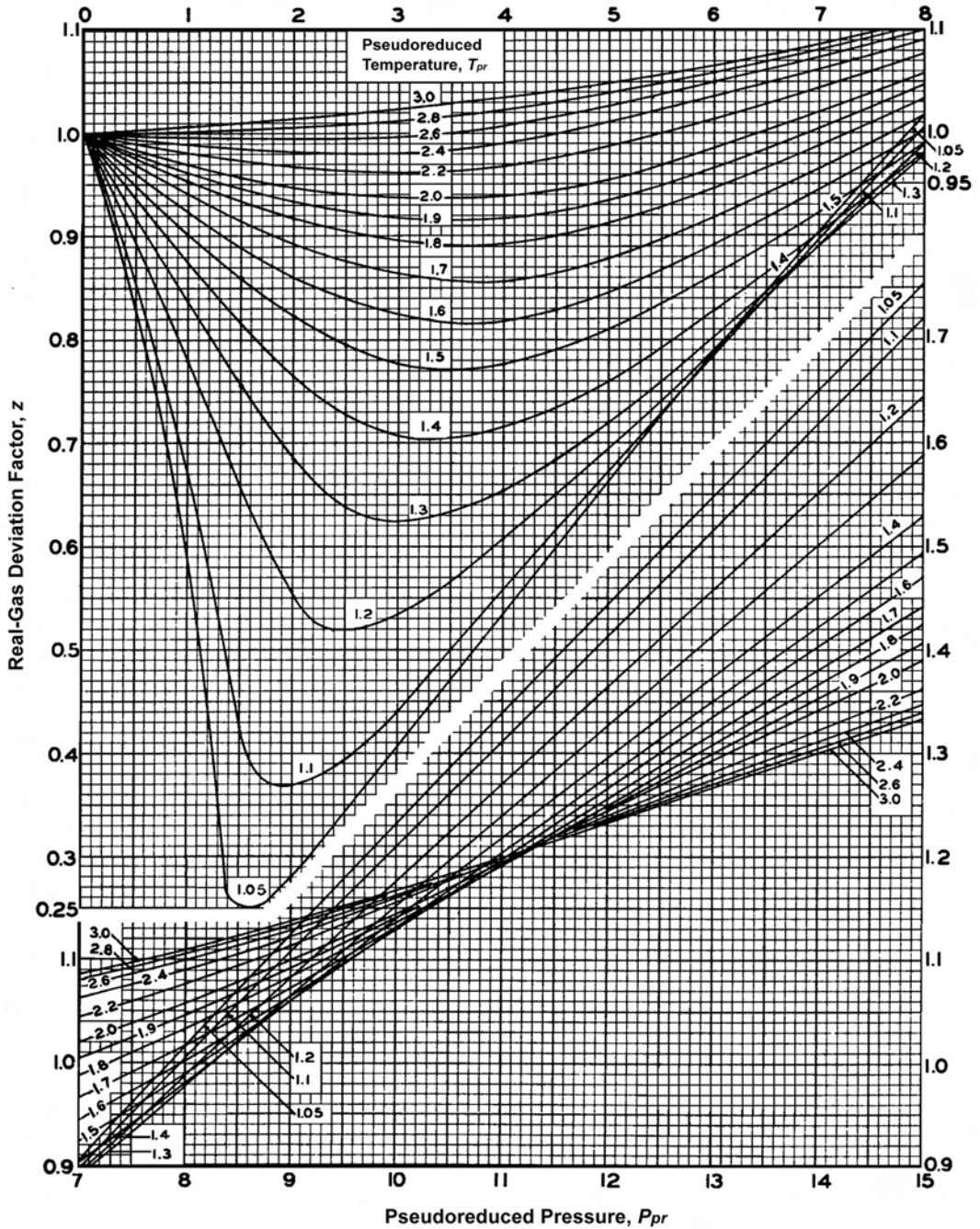


Fig. 5.2—Gas-deviation-factor chart for natural gases (from Standing and Katz<sup>6</sup>).

$$J = \frac{1}{3} \sum_{i=1}^n \left( \frac{y_i T_{ci}}{P_{ci}} \right) + \frac{2}{3} \left[ \sum_{i=1}^n \left( y_i \sqrt{\frac{T_{ci}}{P_{ci}}} \right) \right]^2 - 0.6081F_j - 1.1235F_j^2 + 14.004F_j y_{C7+} - 64.434F_j y_{C7+}^2 \dots \dots \dots (5.8)$$

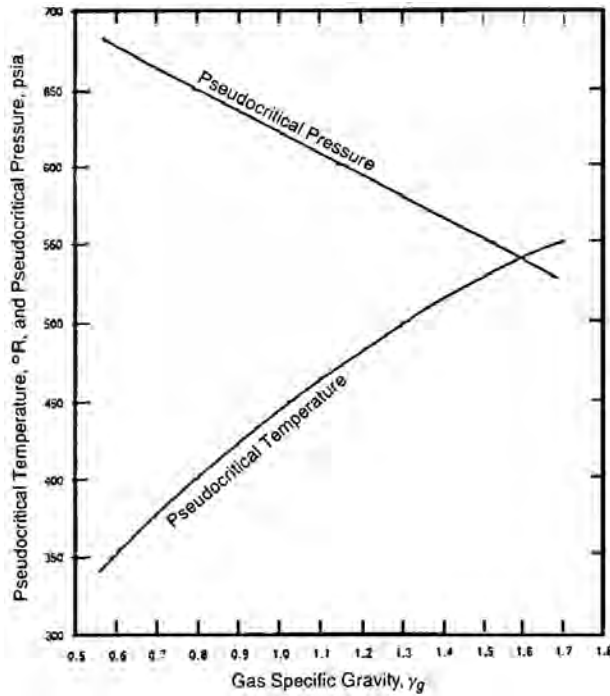


Fig. 5.3—Pseudocritical properties of methane-based natural gases (from Sutton<sup>4</sup>).

$$F_K = \left( \frac{T_c}{\sqrt{p_c}} \right)_{C_{7+}} \left( 0.3129y_{C_{7+}} - 4.8156y_{C_{7+}}^2 + 27.3751y_{C_{7+}}^3 \right) \dots\dots\dots (5.9)$$

$$K = \sum_{i=1}^n \left( \frac{y_i T_{ci}}{\sqrt{p_{ci}}} \right) - F_K \dots\dots\dots (5.10)$$

$$T_{pc} = \frac{K^2}{J} \dots\dots\dots (5.11)$$

$$p_{pc} = \frac{T_{pc}}{J} \dots\dots\dots (5.12)$$

If the composition of the gas is unknown, then a correlation to estimate pseudocritical temperature and pseudocritical pressure values from the specific gravity is used. There are several different correlations available, but Fig. 5.3 was developed by Sutton<sup>4</sup> on the basis of 264 different gas samples. Sutton also used regression analysis on the raw data to obtain the following second-order fit for the pseudocritical properties of hydrocarbon mixtures:

$$p_{pc} = 756.8 - 131.07\gamma_g - 3.6\gamma_g^2 \dots\dots\dots (5.13)$$

$$T_{pc} = 169.2 + 349.5\gamma_g - 74.0\gamma_g^2 \dots\dots\dots (5.14)$$

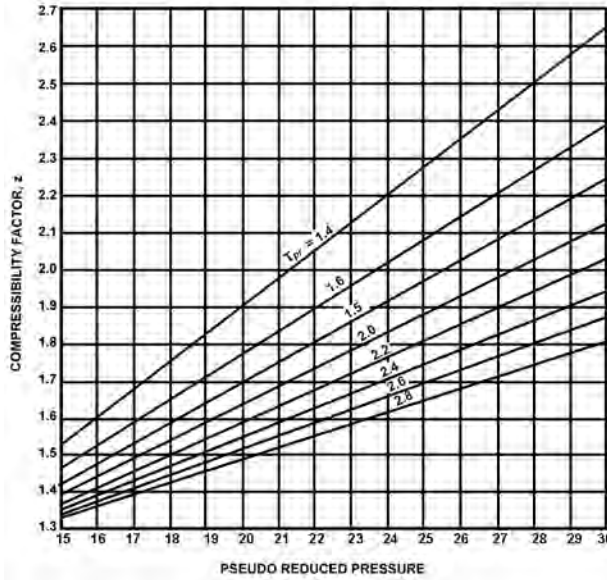


Fig. 5.4—Gas-deviation factors for natural gases at pressures of 10,000 to 20,000 psia.<sup>7</sup>

These equations and Fig 5.3 are valid over the range of specific-gas gravities with which Sutton<sup>4</sup> worked:  $0.57 < \gamma_g < 1.68$ . Using the obtained pseudocritical values, the pseudoreduced pressure and temperature are calculated using

$$p_r = \frac{p}{p_{pc}}$$

and  $T_r = \frac{T}{T_{pc}}$  ..... (5.15)

The gas-deviation factor is then found by using the well-known correlation chart of Fig. 5.2, originally developed by Standing and Katz.<sup>6</sup> Compressibility factors of high-pressure natural gases (10,000 to 20,000 psia) may be obtained from Fig. 5.4, which was developed by Katz *et al.*<sup>7</sup> Figs. 5.5 and 5.6 may be used for low-pressure applications after Brown *et al.*<sup>8</sup>

Dranchuk and Abou-Kassem<sup>9</sup> fitted an equation of state to the data of Standing and Katz,<sup>6</sup> which is more convenient for estimating the gas-deviation factor in computer programs and spreadsheets. Hall and Yarborough<sup>10</sup> also have published an alternative equation of state. The Dranchuk and Abou-Kassem<sup>9</sup> equation of state is based on the generalized Starling equation of state and is expressed as follows:

$$z = 1 + \left( A_1 + \frac{A_2}{T_r} + \frac{A_3}{T_r^3} + \frac{A_4}{T_r^4} + \frac{A_5}{T_r^5} \right) \rho_r + \left( A_6 + \frac{A_7}{T_r} + \frac{A_8}{T_r^2} \right) \rho_r^2 - A_9 \left( \frac{A_7}{T_r} + \frac{A_8}{T_r^2} \right) \rho_r^5 + A_{10} (1 + A_{11} \rho_r^2) \left( \frac{\rho_r^2}{T_r^3} \right) \exp(-A_{11} \rho_r^2), \dots (5.16)$$

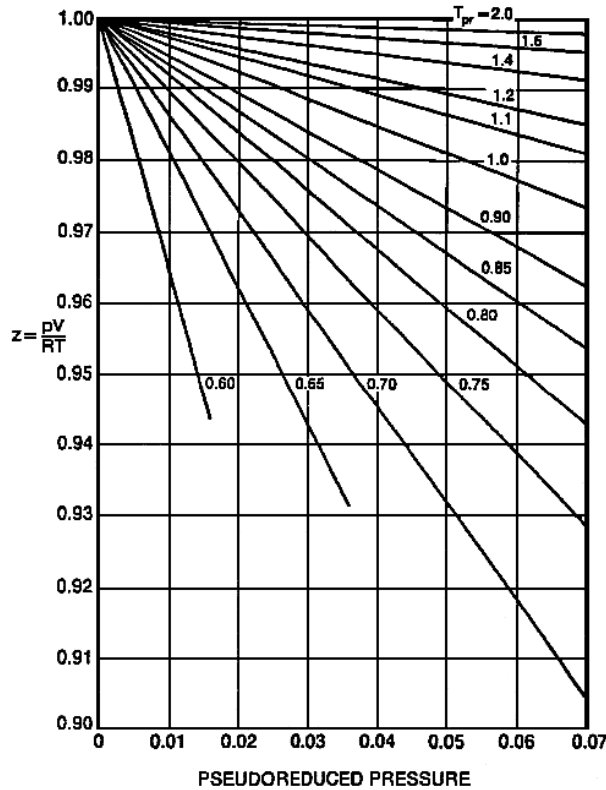


Fig. 5.5—Gas-deviation-factor chart for natural gases near atmospheric pressure.<sup>8</sup>

where  $\rho_r = \frac{0.27 p_r}{(z T_r)}$  and where the constants  $A_1$  through  $A_{11}$  are as follows:  $A_1 = 0.3265$ ;  $A_2 = -1.0700$ ;  $A_3 = -0.5339$ ;  $A_4 = 0.01569$ ;  $A_5 = -0.05165$ ;  $A_6 = 0.5475$ ;  $A_7 = -0.7361$ ;  $A_8 = 0.1844$ ;  $A_9 = 0.1056$ ;  $A_{10} = 0.6134$ ; and  $A_{11} = 0.7210$ .

Dranchuk and Abou-Kassem<sup>9</sup> found an average absolute error of 0.486% in their equation, with a standard deviation of 0.00747 over ranges of pseudoreduced pressure and temperature of  $0.2 < p_{pr} < 30$ ;  $1.0 < T_{pr} < 3.0$ ; and for  $p_{pr} < 1.0$  with  $0.7 < T_{pr} < 1.0$ .

Dranchuk and Abou-Kassem<sup>9</sup> also found that this equation and other equations of state give unacceptable results near the critical temperature for  $T_{pr} = 1.0$  and  $p_{pr} > 1.0$ , so these equations are not recommended in this range.

Because the parameter  $z$  is embedded in  $\rho_r$ , an iterative solution is necessary to solve the Dranchuk and Abou-Kassem equation of state, but this can be programmed. An example of this is provided by Dranchuk and Abou-Kassem.<sup>9</sup> The equation also can be solved on a spreadsheet using the nonlinear-equation-solver option, which is discussed in more detail elsewhere.<sup>11</sup> Nonlinear equation solvers are also set up specifically to solve these equations easily.

The  $z$ -factor chart of Standing and Katz (Fig 5.2) and the pseudocritical property-calculation methods of Sutton<sup>4</sup> are valid only for mixtures of hydrocarbon gases. Wichert and Aziz<sup>12</sup> have developed a correlation to account for inaccuracies in the Standing and Katz chart when the gas contains significant fractions of acid gases, specifically carbon dioxide ( $\text{CO}_2$ ) and hydrogen sulfide ( $\text{H}_2\text{S}$ ). The Wichert and Aziz<sup>12</sup> correlation modifies the values of the pseudocritical temperature and pressure of the gas. Once the modified pseudocritical properties are obtained,

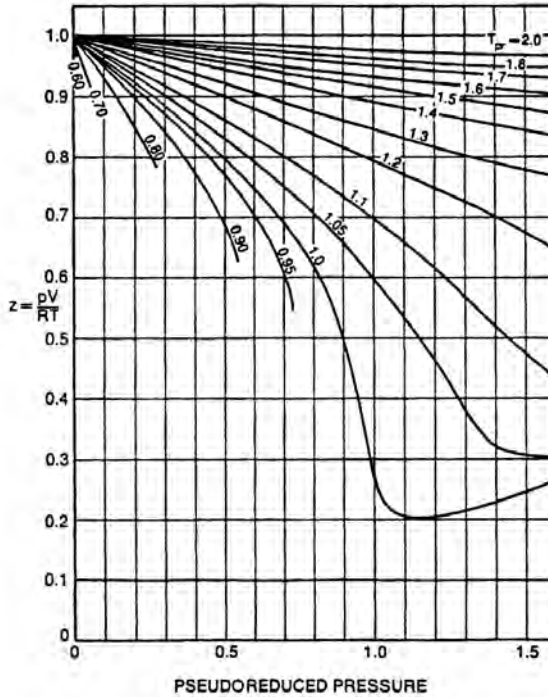


Fig. 5.6—Gas-deviation-factor chart for natural gases at low reduced pressure.<sup>8</sup>

they are used to calculate pseudoreduced properties, and the  $z$  factor is determined from Fig. 5.2 or Eq. 5.10. The Wichert and Aziz<sup>12</sup> correlation first calculates a deviation parameter  $\epsilon$ :

$$\epsilon = 120(A^{0.9} - A^{1.6}) + 15(B^{0.5} - B^4), \dots\dots\dots (5.17)$$

where  $A$  = the sum of the mole fractions of CO<sub>2</sub> and H<sub>2</sub>S in the gas mixture and  $B$  = the mole fraction of H<sub>2</sub>S in the gas mixture. Then, the value of  $\epsilon$  is used to determine the modified pseudocritical properties as follows:

$$T'_{pc} = T_{pc} - \epsilon \dots\dots\dots (5.18)$$

$$\text{and } p'_{pc} = \frac{p_{pc} T'_{pc}}{T_{pc} - B(1 - B)\epsilon} \dots\dots\dots (5.19)$$

The correlation is valid only in units of  $T$  in R and  $p$  in psia. It is applicable to concentrations of CO<sub>2</sub> < 54.4 mol% and H<sub>2</sub>S < 73.8 mol%. Note that  $\epsilon$  also has units of R. The correction factor,  $\epsilon$ , has been plotted against H<sub>2</sub>S and CO<sub>2</sub> concentrations in Fig. 5.7 for convenience. Note that maximum correction occurs around  $A = B = 47\%$  or 47% H<sub>2</sub>S concentration and 0% CO<sub>2</sub> concentration. Wichert and Aziz<sup>12</sup> found their correlation to have an average absolute error of 0.97% over the following ranges of data: 154 psia <  $p$  < 7,026 psia and 40°F <  $T$  < 300°F.

Piper *et al.*<sup>13</sup> have also adapted the Stewart *et al.*<sup>5</sup> method to develop equations that can be used to calculate the pseudocritical properties of natural gas mixtures that contain nitrogen

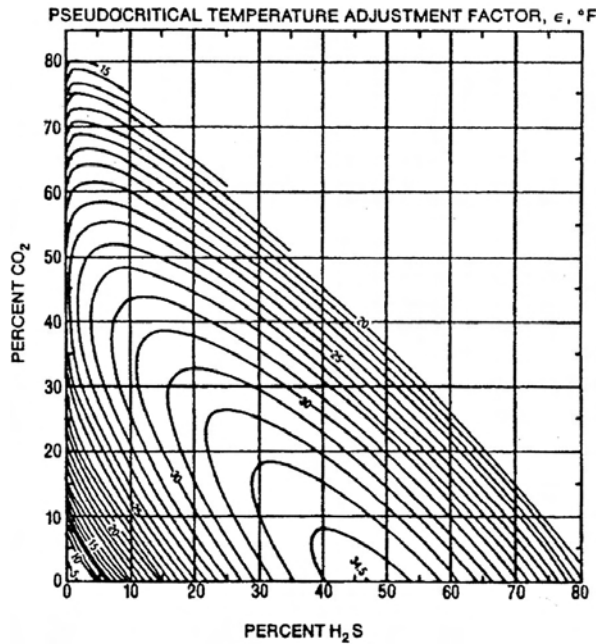


Fig. 5.7—Pseudocritical-temperature-adjustment factor,<sup>12</sup> ε, °F.

(N<sub>2</sub>), CO<sub>2</sub>, and H<sub>2</sub>S without making a separate correction. There are two sets of equations, depending on whether the composition or the specific gravity is known. When the gas composition is used, the following equations are developed on the basis of 896 data points:

$$J = \alpha_0 + \sum_{i=1}^3 \alpha_i \left( \frac{y_i T_{ci}}{p_{ci}} \right) + \alpha_4 \sum_{j=1}^6 y_j \frac{T_{cj}}{p_{cj}} + \alpha_6 y_{C7+} M_{C7+} + \alpha_7 (y_{C7+} M_{C7+})^2 \dots (5.20)$$

$$\text{and } K = \beta_0 + \sum_{i=1}^3 \beta_i \left( \frac{y_i T_{ci}}{\sqrt{p_{ci}}} \right) + \beta_4 \sum_{j=1}^6 y_j \frac{T_{cj}}{\sqrt{p_{cj}}} + \beta_6 y_{C7+} M_{C7+} + \beta_7 (y_{C7+} M_{C7+})^2, \dots (5.21)$$

where  $y_i$  are the contaminant compositions  $\{y_{H_2S}, y_{CO_2}, y_{N_2}\}$  and  $y_j$  are the hydrocarbon compositions  $\{y_{C_1}, y_{C_2}, y_{C_3}, y_{C_4}, y_{C_5}, y_{C_6}\}$ , and  $\alpha_i$  and  $\beta_i$  are as given in **Table 5.3**.

If the composition of the hydrocarbons is unknown but the specific gravity and the nonhydrocarbon compositions are known, the following equations for  $J$  and  $K$  were developed by Piper *et al.*<sup>13</sup> on the basis of 1,482 data points:

$$J = 0.11582 - 0.45820 y_{H_2S} \left( \frac{T_c}{p_c} \right)_{H_2S} - 0.90348 y_{CO_2} \left( \frac{T_c}{p_c} \right)_{CO_2} - 0.66026 y_{N_2} \left( \frac{T_c}{p_c} \right)_{N_2} + 0.70729 \gamma_g - 0.099397 \gamma_g^2 \dots (5.22)$$

and

$i$	$\alpha_i$	$\beta_i$
0	0.052073	-0.39741
1	1.0160	1.0503
2	0.86961	0.96592
3	0.72646	0.78569
4	0.85101	0.98211
5	0.0	0.0
6	0.020818	0.45536
7	-0.0001506	-0.0037684

$$\begin{aligned}
 K = & 3.8216 - 0.06534y_{\text{H}_2\text{S}}\left(\frac{T_c}{\sqrt{p_c}}\right)_{\text{H}_2\text{S}} - 0.42113y_{\text{CO}_2}\left(\frac{T_c}{\sqrt{p_c}}\right)_{\text{CO}_2} - 0.91249y_{\text{N}_2}\left(\frac{T_c}{\sqrt{p_c}}\right)_{\text{N}_2} \\
 & + 17.438\gamma_g - 3.2191\gamma_g^2 \dots\dots\dots (5.23)
 \end{aligned}$$

Then, the pseudocritical properties can be calculated from  $J$  and  $K$  in Eqs. 5.11 and 5.12.

**Example 5.1** Calculation of the  $z$  Factor for Sour Gas. Using (a) the Sutton<sup>4</sup> correlation and the Wichert and Aziz<sup>12</sup> correction, and (b) the method of Piper *et al.*,<sup>13</sup> calculate the  $z$  factor for a gas with the following properties and conditions:

$\gamma_g = 0.7$ ,  $\text{H}_2\text{S} = 7\%$ , and  $\text{CO}_2 = 10\%$ ;  $p = 2,010$  psia and  $T = 75^\circ\text{F}$ .

*Solution.* (a) First, calculate the pseudocritical properties.

$$\begin{aligned}
 p_{pc} &= 756.8 - 131.07\gamma_g - 3.6\gamma_g^2 \\
 &= 756.8 - (131.07)(0.7) - (3.6)(0.7^2) \\
 &= 663.29 \text{ psia.}
 \end{aligned}$$

$$\begin{aligned}
 T_{pc} &= 169.2 + 349.5\gamma_g - 74.0\gamma_g^2 \\
 &= 169.2 + (349.5)(0.7) - (74.0)(0.7^2) \\
 &= 377.59^\circ \text{ R.}
 \end{aligned}$$

Next, calculate the adjustments to the pseudocritical properties using the Wichert and Aziz<sup>12</sup> parameters.

$$\begin{aligned}
 \varepsilon &= 120(A^{0.9} - A^{1.6}) + 15(B^{0.5} - B^4) \\
 &= (120)(0.17^{0.9} - 0.17^{1.6}) + (15)(0.07^{0.5} - 0.07^4) \\
 &= 21.278^\circ \text{ R.} \\
 T'_{pc} &= T_{pc} - \varepsilon = 377.59 - 21.278 = 356.31^\circ \text{ R}
 \end{aligned}$$

$$p'_{pc} = \frac{p_{pc} T'_{pc}}{T_{pc} - B(1-B)\epsilon} = \frac{(663.29 \text{ psia})(356.31^\circ \text{ R})}{377.59^\circ \text{ R} - (0.07)(0.93)(21.278^\circ \text{ R})} = 628.21 \text{ psia.}$$

Next, calculate the pseudoreduced properties:

$$p_r = \frac{p}{p'_{pc}} = \frac{2,010 \text{ psia}}{628.21 \text{ psia}} = 3.1995$$

$$\text{and } T_r = \frac{(75 + 459.67)^\circ \text{ R}}{356.31^\circ \text{ R}} = 1.5006.$$

Finally, looking up the  $z$ -factor chart (Fig 5.2) gives  $z = 0.772$ .

(b) Using the method of Piper *et al.*,<sup>13</sup>

$$J = 0.11582 - 0.45820y_{\text{H}_2\text{S}}\left(\frac{T_c}{p_c}\right)_{\text{H}_2\text{S}} - 0.90348y_{\text{CO}_2}\left(\frac{T_c}{p_c}\right)_{\text{CO}_2} - 0.66026y_{\text{N}_2}\left(\frac{T_c}{p_c}\right)_{\text{N}_2}$$

$$+ 0.70729\gamma_g - 0.099397\gamma_g^2$$

$$= 0.11582 - (0.45820)\left(0.07\right)\left(\frac{672.3^\circ \text{ R}}{1,306 \text{ psia}}\right) - (0.90348)\left(0.1\right)\left(\frac{547.5^\circ \text{ R}}{1,071 \text{ psia}}\right)$$

$$+ (0.70729)(0.7) - (0.099397)(0.7^2)$$

$$= 0.4995^\circ \text{ R (in.}^2\text{) / lbf.}$$

$$K = 3.8216 - 0.06534y_{\text{H}_2\text{S}}\left(\frac{T_c}{\sqrt{p_c}}\right)_{\text{H}_2\text{S}} - 0.42113y_{\text{CO}_2}\left(\frac{T_c}{\sqrt{p_c}}\right)_{\text{CO}_2} - 0.91249y_{\text{N}_2}\left(\frac{T_c}{\sqrt{p_c}}\right)_{\text{N}_2}$$

$$+ 17.438\gamma_g - 3.2191\gamma_g^2$$

$$= 3.8216 - (0.06534)(0.07)\left(\frac{672.3^\circ \text{ R}}{\sqrt{1,306 \text{ psia}}}\right) - 0.42113y_{\text{CO}_2}\left(\frac{547.5^\circ \text{ R}}{\sqrt{1,071 \text{ psia}}}\right)$$

$$+ (17.438)(0.7) - (3.2191)(0.7^2)$$

$$= 13.661^\circ \text{ R (in.) / lbf}^{0.5}.$$

$$T_{pc} = \frac{K^2}{J} = \frac{13.661^{2\circ} \text{ R}^2 \text{ in.}^2 / \text{lbf}}{0.4995^\circ \text{ R in.}^2 / \text{lbf}} = 373.6^\circ \text{ R}$$

$$p_{pc} = \frac{T_{pc}}{J} = \frac{373.6}{0.4995} = 747.9 \text{ psia.}$$

The pseudoreduced properties are then:

$$p_r = \frac{p}{p_{pc}} = \frac{2,010 \text{ psia}}{747.9 \text{ psia}} = 2.687$$

$$\text{and } T_r = \frac{T}{T_{pc}} = \frac{(75 + 459.67)^\circ \text{ R}}{373.6^\circ \text{ R}} = 1.431.$$

Finally, looking up the  $z$ -factor chart (Fig 5.3) gives  $z = 0.745$ .



The two methods give results that differ by 3.6% of the smaller value ( $z = 0.745$ ), which is within the range of accuracy of either method. Because the method of Piper *et al.*<sup>13</sup> is based on a larger data set and has integrated the nonhydrocarbon compositions into the method, it is likely to be more accurate.

**5.11 Gas Density and Formation Volume Factor**

The formation volume factor of gas is defined as the ratio of the volume of gas at the reservoir temperature and pressure to the volume at the standard or surface temperature and pressure ( $p_s$  and  $T_s$ ). It is given the symbol  $B_g$  and is often expressed in either cubic feet of reservoir volume per standard cubic foot of gas or barrels of reservoir volume per standard cubic foot of gas. The gas-deviation factor is unity at standard conditions; hence, the equation for the gas formation volume factor can be calculated using the real gas equation:

$$B_g = \frac{V_R}{V_{sc}} = \frac{znRT}{p} \frac{p_{sc}}{z_{sc}nRT_{sc}} = \frac{p_{sc}zT}{T_{sc}p} \dots\dots\dots (5.24)$$

The  $n$  divides out here because both volumes refer to the same quantity of mass.

When  $p_s$  is 1 atm (14.696 psia or 101.325 kPa) and  $T_s$  is 60°F (519.67°R or 288.71°K), this equation can be written in three well-known standard forms:

$$\begin{aligned} B_g &= 0.0282793 \frac{zT}{p} \text{ rcf / scf} \\ &= 0.00503676 \frac{zT}{p} \text{ RB / scf} \\ &= 0.350958 \frac{zT}{p} \text{ Rm}^3 / \text{Sm}^3, \dots\dots\dots (5.25) \end{aligned}$$

where rcf/scf = reservoir cubic feet per standard cubic feet, RB = reservoir barrels, and Rm<sup>3</sup>/Sm<sup>3</sup> = reservoir cubic meters per standard cubic meters. The formation volume factor is always in units of reservoir volumes per standard volumes.

The three forms in Eq. 5.25 are for specific units. In the first two equation forms, the pressure is in psia and the temperature is in °R. In the third form, the pressure is in kPa and the temperature is in K.

The density of a reservoir gas is defined as the mass of the gas divided by its reservoir volume, so it can also be derived and calculated from the real-gas law:

$$\rho_g = \frac{m_g}{V_R} = \frac{nM_g}{znRT/p} = \frac{nM_{air}\gamma_g}{znRT/p} = \frac{28.967\gamma_g p}{zRT} \dots\dots\dots (5.26)$$

**5.12 Isothermal Compressibility of Gases**

The isothermal gas compressibility,  $c_g$ , is a useful concept that is used extensively in determining the compressible properties of the reservoir. The isothermal compressibility is also the reciprocal of the bulk modulus of elasticity. Gas usually is the most compressible medium in the reservoir; however, care should be taken so that it is not confused with the gas-deviation factor,  $z$ , which is sometimes called the compressibility factor.

The isothermal gas compressibility is defined as:

$$c_g = -\frac{1}{V_g} \left( \frac{\partial V_g}{\partial p} \right)_T \dots\dots\dots (5.27)$$

An expression in terms of  $z$  and  $p$  for the compressibility can be derived from the real-gas law (Eq. 5.5):

$$\left( \frac{\partial V_g}{\partial p} \right)_T = \frac{nRT}{p} \left( \frac{\partial z}{\partial p} \right)_T - \frac{znRT}{p^2} = \left( \frac{znRT}{p} \right) \frac{1}{z} \frac{dz}{dp} - \left( \frac{znRT}{p} \right) \frac{1}{p} \dots\dots\dots (5.28)$$

From the real-gas equation of state,

$$\frac{1}{V_g} = \frac{p}{znRT}$$

and  $\frac{1}{V_g} \left( \frac{\partial V_g}{\partial p} \right)_T = \frac{1}{z} \frac{dz}{dp} - \frac{1}{p}; \dots\dots\dots (5.29)$

hence,

$$c_g = \frac{1}{p} - \frac{1}{z} \left( \frac{\partial z}{\partial p} \right)_T \dots\dots\dots (5.30)$$

For gases at low pressures, the second term is small, and the isothermal compressibility can be approximated by  $c_g \approx 1/p$ . Eq. 5.30 is not particularly convenient for determining the gas compressibility because in Fig 5.2 and Eq. 5.16,  $z$  is not actually expressed as a function of  $p$  but of  $p_r$ . However, Eq. 5.30 can be made more convenient when written in terms of a dimensionless, pseudoreduced gas compressibility defined as

$$c_r = c_g p_{pc} \dots\dots\dots (5.31)$$

Multiplying Eq. 5.30 through by the pseudocritical pressure gives

$$c_r = c_g p_{pc} = \frac{1}{p_r} - \frac{1}{z} \left( \frac{\partial z}{\partial p_r} \right)_{T_r} \dots\dots\dots (5.32)$$

Charts of the pseudoreduced gas compressibility have been published by Trube<sup>14</sup> and by Mattar *et al.*,<sup>15</sup> and two of these are shown in Figs 5.8 and 5.9. Mattar *et al.*<sup>15</sup> also developed an analytical expression for calculating the pseudoreduced compressibility; that expression is

$$c_r = \frac{1}{p_r} - \frac{0.27}{z^2 T_r} \left[ \frac{\left( \frac{\partial z}{\partial p_r} \right)_{T_r}}{1 + \left( \frac{\rho_r}{z} \right) \left( \frac{\partial z}{\partial \rho_r} \right)_{T_r}} \right] \dots\dots\dots (5.33)$$

Taking the derivative of Eq. 5.10, the following is obtained:

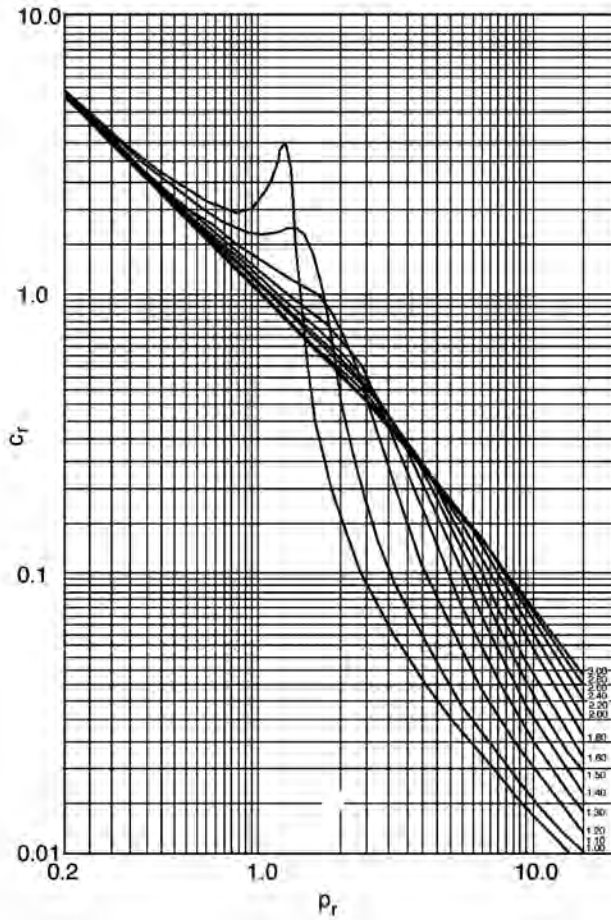


Fig. 5.8—Pseudoreduced-compressibility chart for  $3.0 \geq T_r \geq 1.05$  and  $15.0 \geq p_r \geq 0.2$  (from Mattar *et al.*<sup>15</sup>).

$$\left(\frac{\partial z}{\partial \rho_r}\right)_{T_R} = \left(A_1 + \frac{A_2}{T_r} + \frac{A_3}{T_r^3} + \frac{A_4}{T_r^4} + \frac{A_5}{T_r^5}\right) + 2\left(A_6 + \frac{A_7}{T_r} + \frac{A_8}{T_r^2}\right)\rho_r - 5A_9\left(\frac{A_7}{T_r} + \frac{A_8}{T_r^2}\right)\rho_r^4 + [1 + A_{11}\rho_r^2 - (A_{11}\rho_r^2)^2]\left(\frac{2A_{10}\rho_r}{T_r^3}\right)\exp(-A_{11}\rho_r^2) \dots (5.34)$$

Parameters  $A_1$  through  $A_{11}$  are defined after Eq. 5.16. Eq. 5.34 can then be substituted into Eq. 5.33, and the pseudoreduced gas compressibility can be calculated. Then, if the pseudoreduced gas compressibility is divided by the pseudocritical pressure, the gas compressibility is obtained analytically. Either the graphical method or the analytical method can be used, but the analytical method is easier to apply in a spreadsheet, nonlinear solver, or other computer program.

There is also a close relationship between the formation volume factor of gas and the isothermal gas compressibility. It can easily be shown that

$$c_g = -\frac{1}{B_g} \left(\frac{\partial B_g}{\partial p}\right)_T \dots (5.35)$$

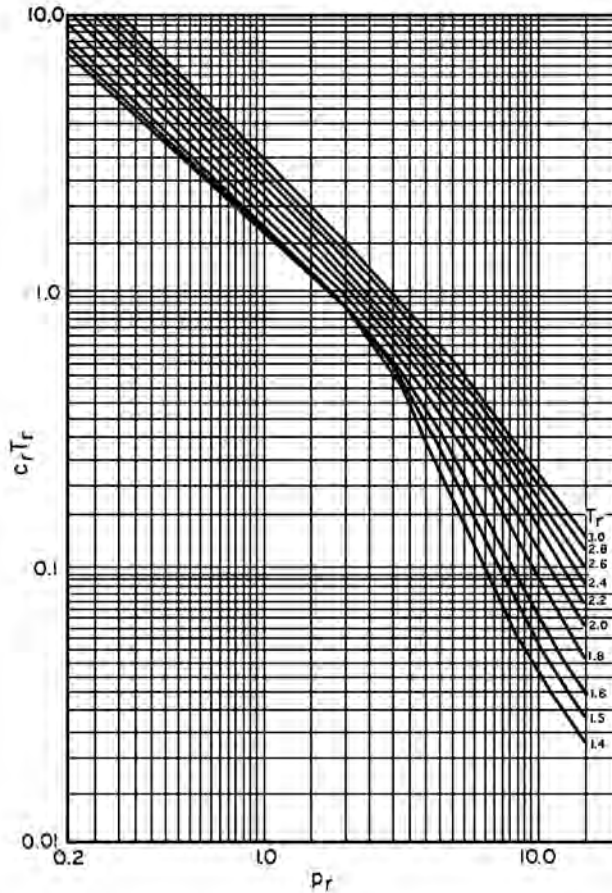


Fig. 5.9—Pseudoreduced-compressibility chart for  $3.0 \geq T_r \geq 1.4$  and  $15.0 \geq p_r \geq 0.2$  (from Mattar *et al.*<sup>15</sup>).

**5.13 Gas Viscosity**

Just as the compressibility of natural gas is much greater than that of oil, water, or rock, the viscosity of natural gas is usually several orders of magnitude smaller than oil or water. This makes gas much more mobile in the reservoir than either oil or water. Reliable correlation charts are available to estimate gas viscosity. Carr *et al.*<sup>16</sup> have developed charts (Figs. 5.10 through 5.13) that are the most widely used for estimating the viscosity of natural gas from the pseudoreduced critical temperature and pressure. Fig. 5.10 gives the viscosities for individual components. Fig. 5.11 gives the viscosities for gas at the desired temperature and atmospheric pressure based on the temperature and specific gravity or molecular weight. The viscosity of gas mixtures at one atmosphere and reservoir temperature can either be read from Fig. 5.11 or determined from the gas-mixture composition with Eq. 5.36.

$$\mu_{ga} = \frac{\sum_{i=1}^N y_i \mu_i \sqrt{M_{gi}}}{\sum_{i=1}^N y_i \sqrt{M_{gi}}}, \dots\dots\dots (5.36)$$

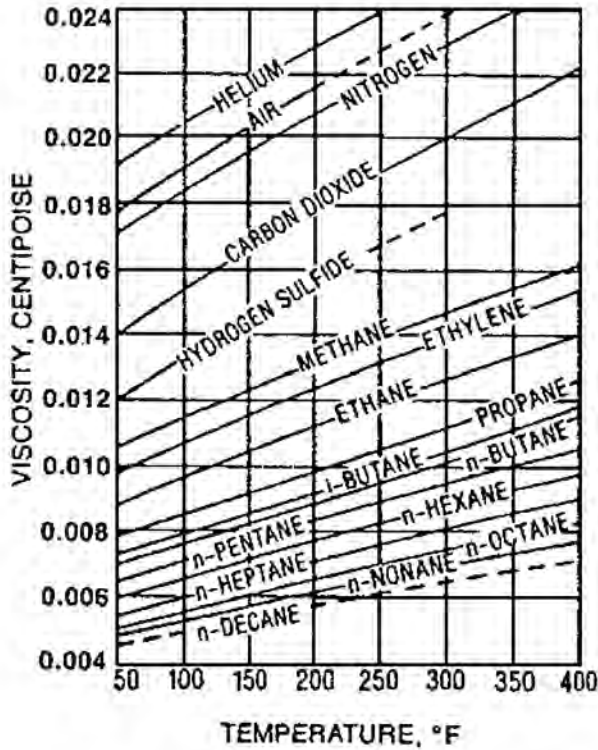


Fig. 5.10—Viscosity of pure hydrocarbons at 1 atm (from Carr *et al.*<sup>16</sup>).

where  $\mu_{ga}$  = viscosity of the gas mixture at the desired temperature and atmospheric pressure;  $y_i$  = mole fraction of the  $i$ th component;  $\mu_i$  = viscosity of the  $i$ th component of the gas mixture at the desired temperature and atmospheric pressure (obtained from Fig. 5.10);  $M_{gi}$  = molecular weight of the  $i$ th component of the gas mixture; and  $N$  = number of components in the gas mixture.

This viscosity is then multiplied by the viscosity ratio (from Fig. 5.12 or Fig. 5.13) to obtain the viscosity at reservoir temperature and pressure. Note that Figs. 5.12 and 5.13 (from Carr *et al.*<sup>16</sup>) are based on pseudocritical properties determined with Kay’s rules. It would not be correct, then, to use the methods of Sutton<sup>4</sup> or Piper *et al.*<sup>13</sup> to calculate the pseudocritical properties for use with those charts. However, Kay’s rules require a full gas composition. If only specific gravity is known, then the pseudocritical properties would have to be obtained from Fig. 5.3 or Eqs. 5.13 and 5.14. The inserts of Fig. 5.11 are corrections to be added to the atmospheric viscosity when the gas contains N<sub>2</sub>, CO<sub>2</sub>, and H<sub>2</sub>S.

Lee *et al.*<sup>17</sup> developed a useful analytical method that gives a good estimate of gas viscosity for most natural gases. This method lends itself for use in computer programs and spreadsheets. The method uses the gas temperature, pressure,  $z$  factor, and molecular weight, which have to be measured or calculated; the density can be measured or calculated as well. The equations of Lee *et al.*<sup>17</sup> are for specific units as noted below and are as follows:

$$\mu_g = K_1 \exp(X\rho^Y), \dots\dots\dots (5.37)$$

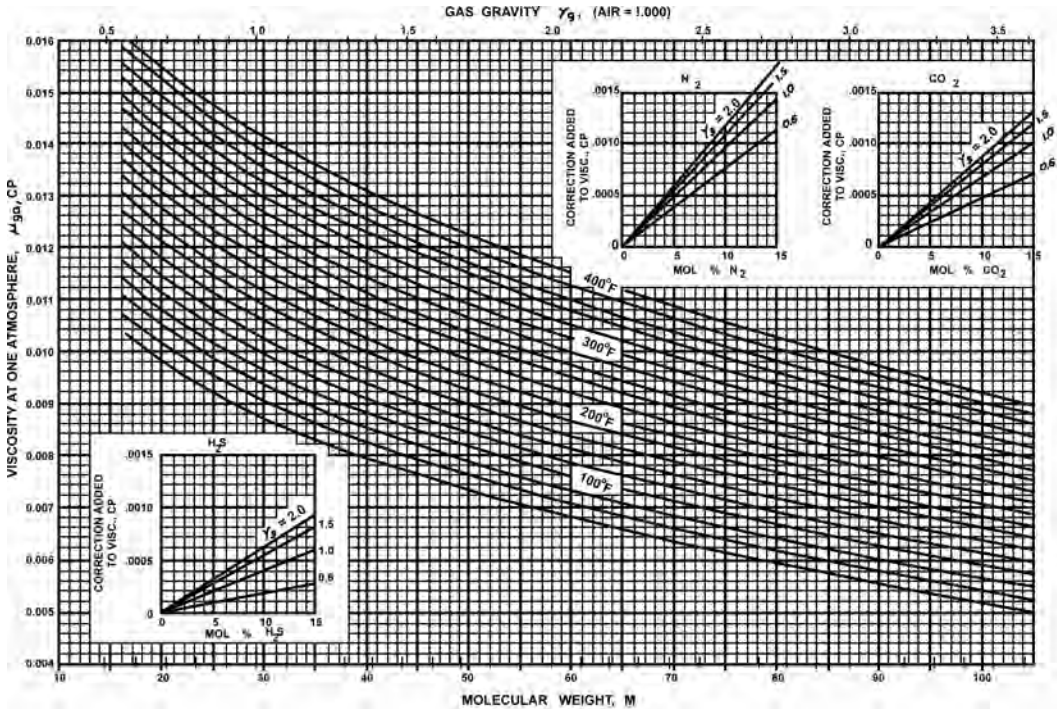


Fig. 5.11—Viscosity of natural gases at 1 atm (from Carr *et al.*<sup>16</sup>).

where  $\rho = \frac{pM_g}{zRT} = 0.00149406 \frac{pM_g}{zT}$ ,  $K_1 = \frac{(0.00094 + 2 \times 10^{-6} M_g) T^{1.5}}{(209 + 19M_g + T)}$ ,  $X = 3.5 + \frac{986}{T} + 0.01M_g$ , and  $Y = 2.4 - 0.2X$  and where  $\mu_g$  = gas viscosity, cp;  $\rho$  = gas density, g/cm<sup>3</sup>;  $p$  = pressure, psia;  $T$  = temperature, °R; and  $M_g$  = gas molecular weight =  $28.967\gamma_g$ .

For the data from which the correlation was developed, the standard deviation in the calculated gas viscosity was 2.7%, and the maximum deviation was 9%. The ranges of variables used in the correlation were 100 psia <  $p$  < 8,000 psia, 100 <  $T$  (°F) < 340, and 0.90 < CO<sub>2</sub> (mol %) < 3.20 and 0.0 < N<sub>2</sub> (mol%) < 4.80. In using these equations, it is important either to measure the density or to ensure that the  $z$ -factor calculation has included the effect of N<sub>2</sub>, CO<sub>2</sub>, and H<sub>2</sub>S using the method of Wichert and Aziz.<sup>12</sup> The equations of Lee *et al.*<sup>17</sup> were originally written to give the viscosity in micropoise, but the modified form above gives the viscosity in the more commonly used centipoise. This viscosity unit (cp) is also easily converted to the SI unit of Pa·s by dividing by 1,000.

**Example 5.2 Properties of Natural Gas.** For the gas in Example 5.1, find the (a) density, (b) formation volume factor, (c) viscosity, and (d) isothermal compressibility.

*Solution.*

(a) The density is calculated from Eq. 5.14:

$$\rho_g = \frac{28.967\gamma_g p}{zRT} = \frac{\left[ \frac{(28.967)(0.7) \text{ lbm}}{\text{lb mol}} \right] (2,010 \text{ psia})}{(0.772) \left( 10.732 \frac{\text{lb mol} \cdot \text{psia}}{\text{ft}^3 \cdot \text{R}} \right) (75 + 459.67)^\circ \text{R}} = 9.20 \frac{\text{lbm}}{\text{ft}^3}$$

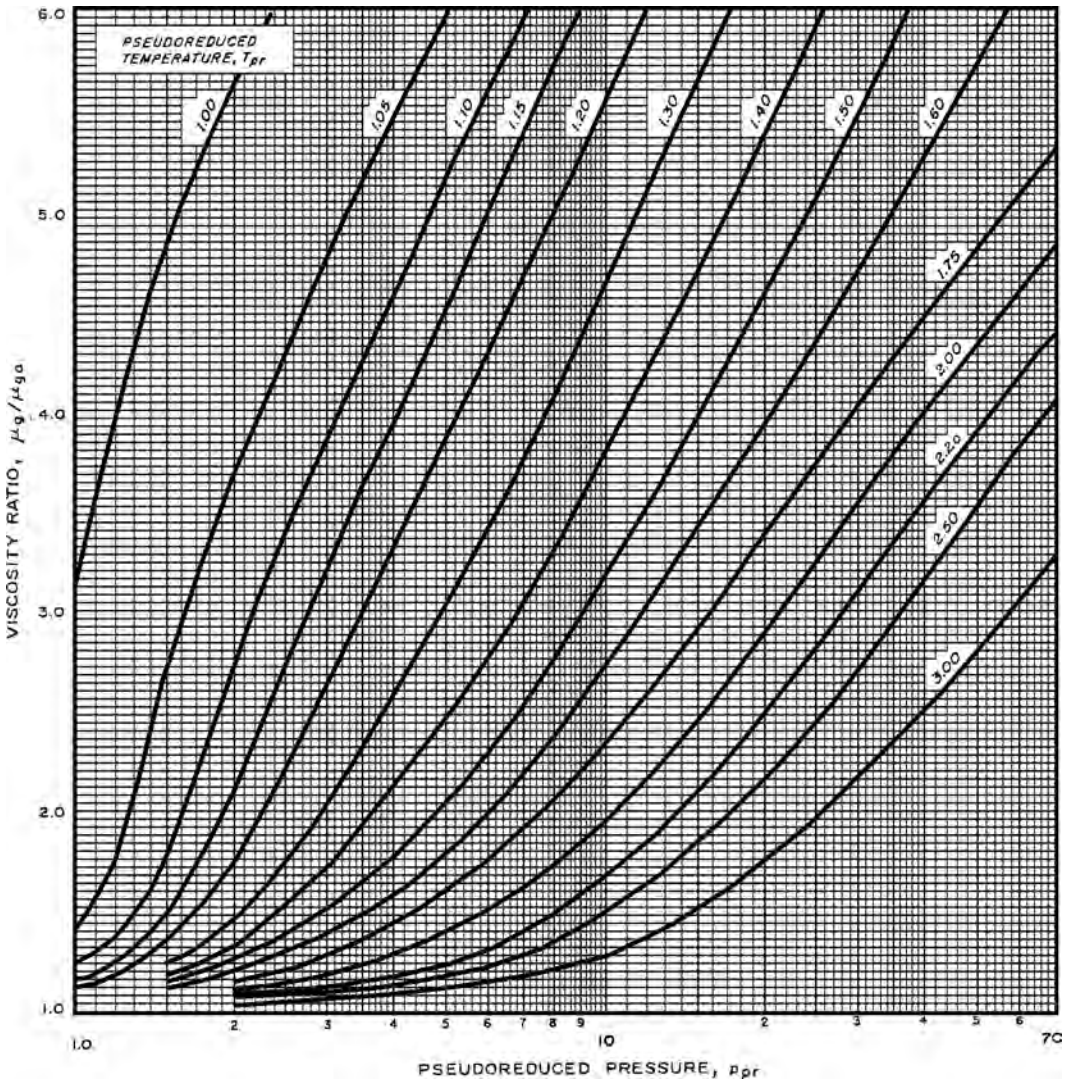


Fig. 5.12—Effect of temperature and pressure on viscosity of natural gases (from Carr *et al.*<sup>16</sup>).

(b) The formation volume factor is calculated from Eq. 5.13:

$$B_g = 0.028793 \frac{zT}{p} = 0.028793 \frac{0.772(75 + 459.67)^\circ R}{2,010 \text{ psia}} = 0.00581 \frac{\text{ft}^3}{\text{scf}}$$

(c) The viscosity is determined using the charts of Carr *et al.*<sup>16</sup> in Figs. 5.10 through 5.13. First, the viscosity for  $M_g = (0.7)(28.967) = 20.3$  at  $p = 1 \text{ atm}$  and  $T = 75^\circ\text{F}$  is read from Fig. 5.11. This gives 0.0102 cp, but corrections are needed for the acid gases. The correction for 10% CO<sub>2</sub> is 0.0005 cp, and the correction for 7% H<sub>2</sub>S is 0.0002 cp. Hence, this gives  $\mu_{ga} = 0.0109 \text{ cp}$ .

Next, the ratio of  $\mu_g/\mu_{ga}$  is read from Fig. 5.13, which gives  $\mu_g/\mu_{ga} = 1.55$ . Hence,  $\mu_g = (1.55)(0.0109 \text{ cp}) = 0.0169 \text{ cp}$ .

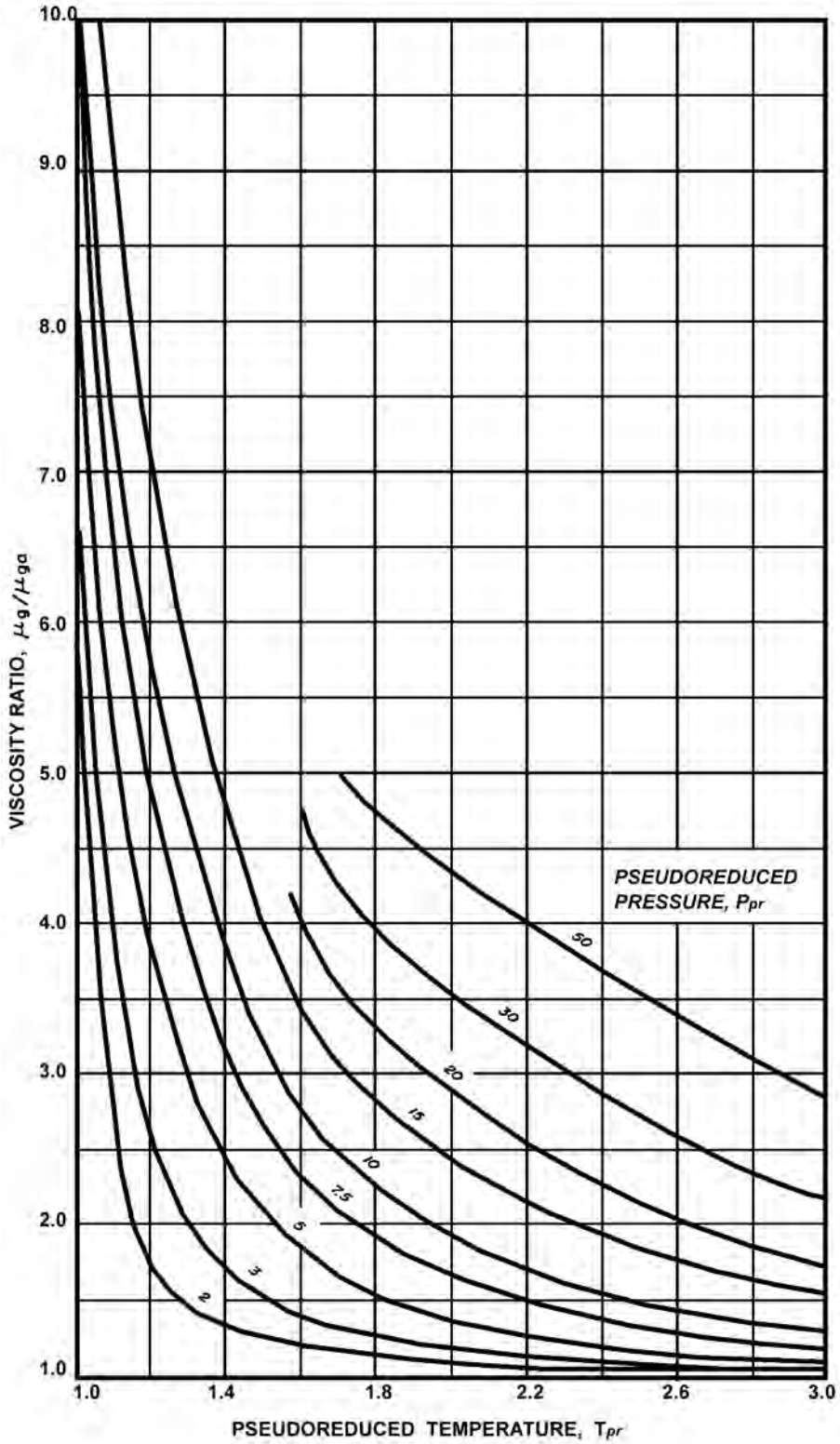


Fig. 5.13—Effect of temperature and pressure on viscosity of natural gases (from Carr *et al.*<sup>16</sup>).



(d) The compressibility is determined by first reading Fig. 5.8 or Fig. 5.9 for the previously calculated values of  $p_r = 3.200$  and  $T_r = 1.500$  to give  $c_r T_r = 0.5$ . Because  $T_r = 1.500$  then  $c_r = 0.5/1.5 = 0.3333$ . Because  $c_r = c_g p_{pc}$ ,

$$c_g = c_r / p_{pc} = 0.3333 / 628.21$$

$$c_g = 5.306 \times 10^{-4} \text{psi}^{-1}.$$

### 5.14 Real-Gas Pseudopotential

In the analysis of gas reservoirs, well-test analysis, gas flow in pipes, and other calculations can be made more accurate by the use of the real-gas pseudopotential. This is because the  $z$  factor and viscosity that appear in such equations along with pressure terms are dependent on pressure. Consequently, the integral of pressure divided by the  $z$  factor and viscosity is defined as a separate parameter called the real-gas pseudopotential and is designated here as  $\psi(p)$ .

$$\psi(p) = 2 \int_{p_o}^p \frac{p}{\mu z} dp, \dots\dots\dots (5.38)$$

where  $p_o$  is some arbitrary low base pressure (typically atmospheric pressure). This integral is usually evaluated numerically using values of  $z$  and  $\mu$  for the particular gas at a particular temperature. Then, the pseudopotential is tabulated as a function of pressure and temperature. Illustrations of the calculation and use of the real-gas pseudopotential are provided elsewhere in this *Handbook*.

### 5.15 Vapor Pressure

At a given temperature, the vapor pressure of a pure compound is the pressure at which vapor and liquid coexist at equilibrium. The term “vapor pressure” should be used only with pure compounds and is usually considered as a liquid (rather than a gas) property. For a pure compound, there is only one vapor pressure at any temperature. A plot of these pressures for various temperatures is shown in Fig. 5.14 for *n*-butane. The temperature at which the vapor pressure is equal to 1 atm (14.696 psia or 101.32 kPa) is known as the normal boiling point.

**5.15.1 The Clapeyron Equation.** The Clapeyron equation gives a rigorous quantitative relationship between vapor pressure and temperature:

$$\frac{dp_v}{dT} = \frac{L_v}{T\Delta V}, \dots\dots\dots (5.39)$$

where  $p_v$ =vapor pressure,  $T$ =absolute temperature,  $\Delta V$ =increase in volume caused by vaporizing 1 mole, and  $L_v$ =molal latent heat of vaporization.

Assuming ideal-gas behavior of the vapor and neglecting the liquid volume, the Clapeyron equation can be simplified over a small temperature range to give the approximation

$$\frac{d(\ln p_v)}{dT} = \frac{L_v}{RT^2}, \dots\dots\dots (5.40)$$

which is known as the Clausius-Clapeyron equation. Integrating this equation gives

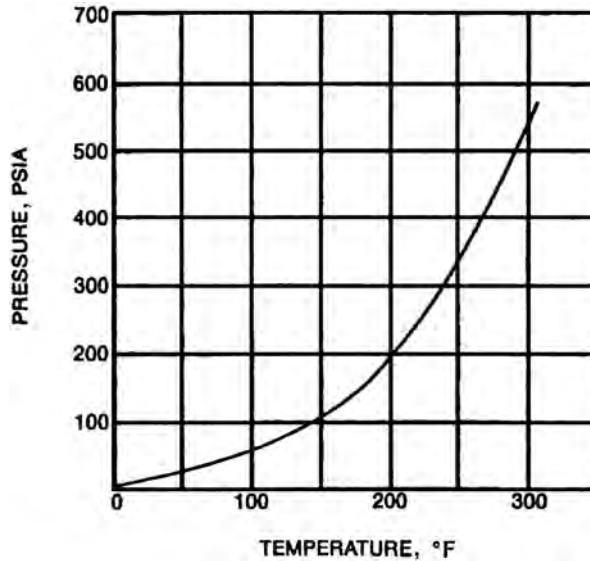


Fig. 5.14—Vapor pressure of *n*-butane.

$$\int d(\ln p_v) = \int \frac{L_v}{RT^2} dT = \ln p_v = \frac{L_v}{RT} + b, \dots\dots\dots (5.41)$$

where  $b$  is a constant of integration that depends on the particular fluid and the data range. This equation suggests that a plot of logarithm of vapor pressure against the reciprocal of the absolute temperature would approximate a straight line. Such a plot is useful in interpolating and extrapolating data over short ranges. However, the shape of this relationship for a real substance over a significant temperature range is more S-shaped than straight. Therefore, the use of the Clausius-Clapeyron equation is not recommended when other methods are available, except over short temperature ranges in regions where the ideal-gas law is valid.

**5.15.2 Cox Chart.** Cox<sup>18</sup> further improved the method of estimating vapor pressure by plotting the logarithm of vapor pressure against an arbitrary temperature scale. The vapor-pressure/temperature plot forms a straight line, at least for the reference compound (and usually for most of the materials related to the reference compound). This is especially true for petroleum hydrocarbons. A Cox chart, using water as a reference material, is shown in Fig. 5.15. In addition to forming nearly straight lines, compounds of the same family appear to converge on a single point. Thus, it is necessary to know only vapor pressure at one temperature to estimate the position of the vapor-pressure line. This approach is very useful and can be much better than the previous method. Its accuracy is dependent to a large degree on the readability of the chart.

**5.15.3 Calingart and Davis Equation.** The Cox chart was fit with a three-parameter function by Calingart and Davis.<sup>19</sup> Their equation is

$$\ln p_v = A - \frac{B}{T - C}, \dots\dots\dots (5.42)$$

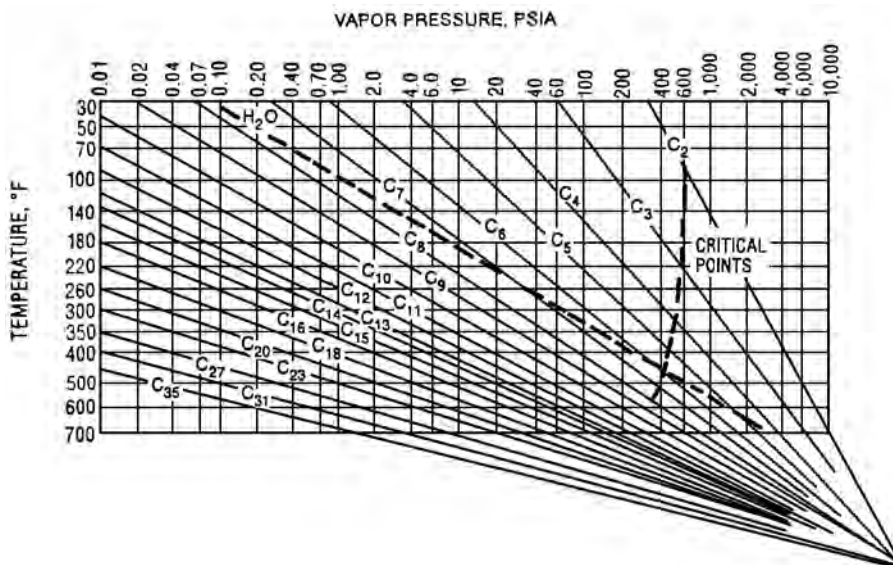


Fig. 5.15—Cox chart for normal paraffin hydrocarbons.<sup>18</sup>

where  $A$  and  $B$  are empirical constants and, for compounds boiling between 32 and 212°F,  $C$  is a constant with a value of 43 when  $T$  is in K and a value of 77.4 when  $T$  is in °R. This equation generally is known as the Antoine<sup>20</sup> equation because Antoine proposed one of a very similar nature that used 13 K for the constant  $C$ . Knowledge of the vapor pressure at two temperatures will fix  $A$  and  $B$  and permit approximations of vapor pressures at other temperatures. Generally, the Antoine approach can be expected to have less than 2% error and is the preferred approach if the vapor pressure is expected to be less than 1,500 mm Hg (200 kPa) and if the constants are available.

**5.15.4 Lee-Kesler Equation.** Vapor pressures also can be calculated by corresponding-states principles. The most common expansions of the Clapeyron equation lead to a two-parameter expression. Pitzer *et al.*<sup>21</sup> extended the expansion to contain three parameters:

$$\ln(p_{vr}) = f^0(T_r) + \omega f^1(T_r), \dots\dots\dots (5.43)$$

where  $p_{vr}$  is the reduced vapor pressure (vapor pressure/critical pressure),  $f^0$  and  $f^1$  are functions of reduced temperature, and  $\omega$  is the acentric factor.

Lee and Kesler<sup>22</sup> have expressed  $f^0$  and  $f^1$  in analytical forms:

$$f^0 = 5.92714 - \frac{6.09648}{T_r} - \left(1.28862\right) \ln T_r + 0.169347(T_r)^6 \dots\dots\dots (5.44)$$

and

$$f^1 = 15.2518 - \frac{15.6875}{T_r} - \left(13.4721\right) \ln T_r + 0.43577(T_r)^6, \dots\dots\dots (5.45)$$

$i$	$y_i$	$M_i$	$y_i M_i$
C <sub>1</sub>	0.8319	16.04	13.344
C <sub>2</sub>	0.0848	30.07	2.55
C <sub>3</sub>	0.0437	44.1	1.927
<i>i</i> -C <sub>4</sub>	0.0076	58.12	0.442
<i>n</i> -C <sub>4</sub>	0.0168	58.12	0.976
<i>i</i> -C <sub>5</sub>	0.0057	72.15	0.411
<i>n</i> -C <sub>5</sub>	0.0032	72.15	0.231
C <sub>6</sub>	0.0063	86.18	0.543
Total	1		20.424

which can be solved easily by computer or spreadsheet. Lee-Kesler<sup>22</sup> is the preferred method of calculation but should be used only for nonpolar liquids.

The advent of computers, calculators, and spreadsheets makes the use of approximations and charts much less advantageous than it was before the 1970s. Values of acentric factors can be found in Poling *et al.*,<sup>23</sup> who also presented many other available vapor-pressure correlations and calculation techniques, with comments about their advantages and limitations.

### 5.16 Further Example Problems

**Example 5.3** Calculate the relative density (specific gravity) of natural gas with the following composition (all compositions are in mol%):

- C<sub>1</sub> = 83.19%
- C<sub>2</sub> = 8.48%
- C<sub>3</sub> = 4.37%
- i*-C<sub>4</sub> = 0.76%
- n*-C<sub>4</sub> = 1.68%
- i*-C<sub>5</sub> = 0.57%
- n*-C<sub>5</sub> = 0.32%
- C<sub>6</sub> = 0.63%
- Total = 100%

**Solution.** First, calculate the apparent mole weight from the information presented in [Table 5.4](#).

$$M_g = \sum y_i M_i = 20.424.$$

$$\gamma_g = M_g / M_a = \sum y_i M_i / 28.967 = 20.424 / 28.967 = 0.705,$$

where the molecular weight of air,  $M_a$ , is 28.967.

$i$	$y_i$	$p_{ci}$ (psia)	$T_{ci}$ (°R)	$y_i T_{ci} / p_{ci}$	$y_i T_{ci} / \sqrt{p_{ci}}$
C <sub>1</sub>	0.8319	667.8	342.99	0.42727	11.04153
C <sub>2</sub>	0.0848	707.8	549.77	0.06587	1.75235
C <sub>3</sub>	0.0437	616.3	665.68	0.04720	1.17179
$i$ -C <sub>4</sub>	0.0076	550.7	765.29	0.01056	0.24785
$n$ -C <sub>4</sub>	0.0168	529.1	734.63	0.02333	0.53655
$i$ -C <sub>5</sub>	0.0057	490.4	828.7	0.00963	0.21330
$n$ -C <sub>5</sub>	0.0032	488.6	845.27	0.00554	0.12237
C <sub>6</sub>	0.0063	436.9	913.27	0.01317	0.27526
Total	1			0.60257	15.36101

**Example 5.4** Calculate the actual density of the same mixture at 1,525 psia and 75°F (a) using Kay's<sup>3</sup> rules, (b) Sutton's<sup>4</sup> correlation, and (c) the Piper *et al.*<sup>13</sup> correlation.

*Solution.* The density is calculated from

$$\rho_g = \frac{M_g p}{zRT},$$

where  $p = 1,525$  psia,  $M_g = 20.424$ ,  $R = 10.7316$  (psia-ft<sup>3</sup>)/(lbm mol°R), and  $T = 75^\circ\text{F} + 459.67 = 534.67^\circ\text{R}$ , and  $z$  must be obtained from Fig. 5.3.

(a) Calculate  $z_g$  from the known composition in Table 5.5.

Using Kay's<sup>3</sup> rules, we obtain from the known gas composition:

$$T_{pc} = \sum y_i T_i = 393.8^\circ\text{R},$$

$$T_{pr} = 534.67/393.8 = 1.3577,$$

$$p_{pc} = \sum y_i p_{ci} = 662.88 \text{ psia},$$

$$p_{pr} = p/p_{pc} = 1,525/662.88 = 2.301,$$

and from Fig. 5.3,  $z_g = 0.71$ .

(b) From Sutton's<sup>4</sup> gas gravity method,  $\gamma_g = 0.705$ ; then, we obtain from Eqs. 5.7 and 5.8 that

$$\begin{aligned} p_{pc} &= 756.8 - 131.07\gamma_g - 3.6\gamma_g^2 \\ &= 756.8 - (131.07)(0.705) - (3.6)(0.705^2) \\ &= 662.6 \text{ psia.} \end{aligned}$$

$$\begin{aligned} T_{pc} &= 169.2 + 349.5\gamma_g - 74.0\gamma_g^2 \\ &= 169.2 + (349.5) - (0.705) - (74.0)(0.705^2) \\ &= 378.8^\circ \text{R.} \end{aligned}$$

This gives

$$p_{pr} = \frac{p}{p_{pc}} = \frac{1,525 \text{ psia}}{662.6 \text{ psia}} = 2.302$$

$$\text{and } T_{pr} = \frac{T}{T_{pc}} = \frac{534.67 \text{ R}}{378.8 \text{ R}} = 1.411.$$

From Fig. 5.3, we obtain  $z_g = 0.745$ .

(c) Using the Piper *et al.*<sup>13</sup> method, we first calculate  $J$  and  $K$  using

$$J = \alpha_0 + \alpha_4 \sum_{j=1}^6 y_j \frac{T_{cj}}{p_{cj}}$$

$$\text{and } K = \beta_0 + \beta_4 \sum_{j=1}^6 y_j \frac{T_{cj}}{\sqrt{p_{cj}}}.$$

The details of the calculations are found in Table 5.5.

Then,

$$J = 0.052073 + (0.85101)(0.60257)$$

$$= 0.56486^\circ \text{ R-in.}^2 / \text{lbf.}$$

$$K = -0.39741 + (0.98211)(15.36101)$$

$$= 14.68879^\circ \text{ R-in.} / \text{lbf}^{0.5}.$$

$$T_{pc} = \frac{K^2}{J} = \frac{14.68879^2}{0.56486} = 381.97^\circ \text{ R.}$$

$$p_{pc} = \frac{T_{pc}}{J} = \frac{381.97}{0.56486} = 676.22 \text{ psia.}$$

$$p_r = \frac{p}{p_{pc}} = 1525 \Big| 676.22 = 2.255$$

$$\text{and } T_r = \frac{T}{T_{pc}} = 534.67 \Big| 381.97 = 1.400.$$

Finally, looking up the  $z$ -factor chart (Fig. 5.3) gives  $z = 0.745$ .

*Conclusion.* Even though the Sutton<sup>4</sup> correlation and the Piper *et al.*<sup>13</sup> correlation gave slightly different critical properties, the  $z$  factors from those two methods are the same. Kay's<sup>3</sup> rule gives a value that is 4.6% lower, but the result using Sutton's<sup>4</sup> correlation and the Piper *et al.*<sup>13</sup> correlation has been shown to be more accurate. The density is then given by

$$\rho = \frac{pM_g}{zRT} = \frac{(1,525)(20.424)}{(0.745)(10.7316)(534.67)} = 7.286 \text{ lbm} / \text{ft}^3 = 116.8 \text{ kg} / \text{m}^3.$$

**Example 5.5** Calculate the  $z$  factor for the reservoir fluid in Table 5.6 at 307°F and 6,098 psia.

The experimental value is  $z = 0.998$ .

*Solution.* Using the Piper *et al.*<sup>13</sup> method, we first calculate  $J$  and  $K$  using

TABLE 5.6—VALUES FOR EXAMPLE PROBLEM 5

	Mole Fraction	$T_c$ (°R)	$p_c$ (psia)	$M_g$
Nitrogen	0.1186	226.97	493	28.02
Methane	0.3836	342.99	667.8	16.04
Carbon dioxide	0.0849	547.54	1071	44.01
Ethane	0.0629	549.77	707.8	30.07
Hydrogen sulfide	0.2419	672.27	1306	34.08
Propane	0.0261	665.68	616.3	44.09
<i>i</i> -butane	0.0123	765.29	550.7	58.12
<i>n</i> -butane	0.0154	734.63	529.1	58.12
<i>i</i> -pentane	0.0051	828.7	490.4	72.15
<i>n</i> -pentane	0.0052	845.27	488.6	72.15
Hexanes	0.0067	913.27	436.9	86.17
Heptanes plus	0.0373	1,116	453	119

$$J = \alpha_0 + \sum_{i=1}^3 \alpha_i \left( \frac{y_i T_{ci}}{p_{ci}} \right) + \alpha_4 \sum_{j=1}^6 y_j \frac{T_{cj}}{p_{cj}} + \alpha_6 y_{C7+} M_{C7+} + \alpha_7 (y_{C7+} M_{C7+})^2$$

$$\text{and } K = \beta_0 + \sum_{i=1}^3 \beta_i \left( \frac{y_i T_{ci}}{\sqrt{p_{ci}}} \right) + \beta_4 \sum_{j=1}^6 y_j \frac{T_{cj}}{\sqrt{p_{cj}}} + \beta_6 y_{C7+} M_{C7+} + \beta_7 (y_{C7+} M_{C7+})^2.$$

The details of the calculation are in [Table 5.7](#).

Then,

$$\begin{aligned} J &= \alpha_0 + \sum_{i=1}^3 \alpha_i \left( \frac{y_i T_{ci}}{p_{ci}} \right) + \alpha_4 \sum_{j=1}^6 y_j \frac{T_{cj}}{p_{cj}} + \alpha_6 y_{C7+} M_{C7+} + \alpha_7 (y_{C7+} M_{C7+})^2 \\ &= 0.052073 + (1.106)(0.12452) + (0.86961)(0.0434) + (0.72646)(0.0546) + (0.85101)(0.34416) \\ &\quad + (0.020818)(4.4387) - (0.0001506)(4.4387^2) \\ &= 0.63832^\circ \text{R}(\text{in.}^2)/\text{lbf}. \end{aligned}$$

$$\begin{aligned} K &= \beta_0 + \sum_{i=1}^3 \beta_i \left( \frac{y_i T_{ci}}{\sqrt{p_{ci}}} \right) + \beta_4 \sum_{j=1}^6 y_j \frac{T_{cj}}{\sqrt{p_{cj}}} + \beta_6 y_{C7+} M_{C7+} + \beta_7 (y_{C7+} M_{C7+})^2 \\ &= -0.39741 + (1.0503)(4.50) + (0.96592)(1.4205) + (0.78569)(1.2124) + (0.98211)(8.666) \\ &\quad + (0.45536)(4.4387) - (0.0037684)(4.4387^2) \\ &= 17.372^\circ \text{R}(\text{in.})/\text{lbf}^{0.5}. \end{aligned}$$

TABLE 5.7—DETAILS OF THE CALCULATION FOR THE SOLUTION OF EXAMPLE PROBLEM 5

	$y_i M_g$	$y_i T_{ci} / p_{ci}$	$y_i T_{ci} / \sqrt{p_{ci}}$
Nitrogen	3.3232	0.0546	1.2124
Methane	6.1529	0.19702	5.0914
Carbon dioxide	3.7364	0.0434	1.4205
Ethane	1.8914	0.04886	1.2998
Hydrogen sulfide	8.2439	0.12452	4.5000
Propane	1.1507	0.02819	0.6999
<i>i</i> -butane	0.7149	0.01709	0.4011
<i>n</i> -butane	0.8950	0.02138	0.4918
<i>i</i> -pentane	0.3680	0.00862	0.1909
<i>n</i> -pentane	0.3752	0.009	0.1988
Hexanes	0.5773	0.01401	0.2927
Heptanes plus	4.4387	0.09189	1.9558

$$T_{pc} = \frac{K^2}{J} = \frac{17.37166^2}{0.63832} = 472.76^\circ \text{R}$$

$$p_{pc} = \frac{T_{pc}}{J} = \frac{472.76}{0.63832} = 740.64 \text{ psia,}$$

$$p_r = \frac{p}{p_{pc}} = 6098 / 740.64 = 8.233,$$

$$\text{and } T_r = \frac{T}{T_{pc}} = 766.67 / 472.76 = 1.622.$$

Finally, looking up the  $z$ -factor chart (Fig. 5.3) gives  $z = 1.02$ . This represents a 2% error with the experimental value.

**Example 5.6** Calculate the viscosity at 150°F (609.67°R) and 2,012 psia for the gas of the composition shown in Table 5.8.

*Solution (by the Carr et al.<sup>16</sup> Method).* First, calculate the pseudocritical properties using Kay's<sup>3</sup> rules. The charts of Carr et al.<sup>16</sup> are based on pseudocritical properties determined with Kay's rules; it would not be correct, then, to use the methods of Sutton<sup>4</sup> or Piper et al.<sup>13</sup> to calculate the pseudocritical properties for use with the viscosity calculation. The details are in Table 5.9.



	$y_i$	$M_g$	$T_c$ ( $^{\circ}\text{R}$ )	$p_c$ (psia)
Nitrogen	0.158	28.02	226.97	493
Methane	0.739	16.04	342.99	667.8
Ethane	0.061	30.07	549.77	707.8
Propane	0.034	44.09	665.68	616.3
<i>i</i> -butane	0.002	58.12	765.29	550.7
<i>n</i> -butane	0.006	58.12	734.63	529.1

$$\begin{aligned}
 J &= \alpha_0 + \alpha_3 y_{\text{N}_2} \frac{T_{c\text{N}_2}}{p_{c\text{N}_2}} + \alpha_4 \sum_{j=1}^6 y_j \frac{T_{c j}}{p_{c j}} \\
 &= 0.052073 + (0.72646)(0.072741) + (0.85101)(0.474774) \\
 &= 0.50895^{\circ} \text{R}(\text{in.}^2)/\text{lbf}.
 \end{aligned}$$

$$\begin{aligned}
 K &= \beta_0 + \beta_3 y_{\text{N}_2} \frac{T_{c\text{N}_2}}{\sqrt{p_{c\text{N}_2}}} + \beta_4 \sum_{j=1}^6 y_j \frac{T_{c j}}{\sqrt{p_{c j}}} \\
 &= -0.39741 + (0.78569)(1.61511) + (0.98211)(12.2376) \\
 &= 12.8902^{\circ} \text{R}(\text{in.})/\text{lbf}^{0.5}.
 \end{aligned}$$

$$T_{pc} = \frac{K^2}{J} = \frac{12.8902^2}{0.50895} = 326.47^{\circ} \text{R}.$$

$$p_{pc} = \frac{T_{pc}}{J} = \frac{326.47}{0.50895} = 641.45 \text{ psia}.$$

$$p_r = \frac{p}{p_{pc}} = \frac{2012}{638.08} = 3.145$$

$$\text{and } T_r = \frac{T}{T_{pc}} = \frac{609.67}{351.44} = 1.735.$$

These parameters are then used to determine the viscosity at 1 atm. First, the viscosity for  $M_g = 20.079$  at  $p = 1$  atm and  $T = 150^{\circ}\text{F}$  is read from Fig. 5.11. This gives  $\mu_{ga} = 0.0114$  cp, but a correction is needed for the nitrogen. The correction for 15.8%  $\text{N}_2$  is 0.0013 cp. Hence, this gives  $\mu_{ga} = 0.0127$  cp.

Next, the ratio of  $\mu_g/\mu_{ga}$  is read from Fig. 5.13 using the pseudoreduced properties calculated above, which gives  $\mu_g/\mu_{ga} = 1.32$ . Hence,  $\mu_g = (1.32)(0.0127) = 0.0168$  cp. This represents a 2.5% error from the experimentally determined value of 0.0172 cp.

*Solution (by the Lee et al.<sup>17</sup> Method).* In this method, the  $z$  factor is required; this is most accurately determined with the Piper et al.<sup>13</sup> method, the details of which are in Table 5.10.

TABLE 5.9—DETAILS OF THE SOLUTION FOR EXAMPLE PROBLEM 6 (CARR <i>et al.</i> <sup>16</sup> METHOD)				
<i>i</i>	<i>y<sub>i</sub></i>	<i>y<sub>i</sub>M<sub>g</sub></i>	<i>y<sub>i</sub>T<sub>ci</sub></i>	<i>y<sub>i</sub>P<sub>ci</sub></i>
Nitrogen	0.158	4.42716	35.86126	77.894
Methane	0.739	11.85356	253.4696	493.5042
Ethane	0.061	1.83427	33.53597	43.1758
Propane	0.034	1.49906	22.63312	20.9542
<i>i</i> -butane	0.002	0.11624	1.53058	1.1014
<i>n</i> -butane	0.006	0.34872	4.40778	3.1746
Total	1	20.079	351.4383	639.8042

$$\begin{aligned}
 J &= \alpha_0 + \alpha_3 y_{N_2} \frac{T_{cN_2}}{P_{cN_2}} + \alpha_4 \sum_{j=1}^6 y_j \frac{T_{cj}}{P_{cj}} \\
 &= 0.052073 + (0.72646)(0.072741) + (0.85101)(0.474774) \\
 &= 0.50895 \frac{^{\circ}\text{R}(\text{in.}^2)}{\text{lb}^{\text{f}}}.
 \end{aligned}$$

$$\begin{aligned}
 K &= \beta_0 + \beta_3 y_{N_2} \frac{T_{cN_2}}{\sqrt{P_{cN_2}}} + \beta_4 \sum_{j=1}^6 y_j \frac{T_{cj}}{\sqrt{P_{cj}}} \\
 &= -0.39741 + (0.78569)(1.61511) + (0.98211)(12.2376) \\
 &= 12.8902 \frac{^{\circ}\text{R}(\text{in.})}{\text{lb}^{\text{f}0.5}}.
 \end{aligned}$$

$$T_{pc} = \frac{K^2}{J} = \frac{12.8902^2}{0.50895} = 326.47^{\circ}\text{R},$$

$$p_{pc} = \frac{T_{pc}}{J} = \frac{326.47}{0.50895} = 641.45 \text{ psia},$$

$$p_r = \frac{p}{p_{pc}} = \frac{2012 \text{ psia}}{641.45 \text{ psia}} = 3.1366,$$

$$\text{and } T_r = \frac{T}{T_{pc}} = \frac{609.67 \text{ R}}{326.47 \text{ R}} = 1.8675.$$

Look up the chart of Fig. 5.3, which gives a value of  $z = 0.91$ ; then,

TABLE 5.10—DETAILS OF THE SOLUTION FOR EXAMPLE PROBLEM 6 (LEE <i>et al.</i> <sup>17</sup> METHOD)				
<i>i</i>	<i>y<sub>i</sub></i>	<i>y<sub>i</sub>M<sub>g</sub></i>	<i>y<sub>i</sub>T<sub>ci</sub>/p<sub>ci</sub></i>	<i>y<sub>i</sub> T<sub>ci</sub>/√p<sub>ci</sub></i>
Nitrogen	0.158	4.42716	0.072741	1.61511
Methane	0.739	11.85356	0.379559	9.808502
Ethane	0.061	1.83427	0.047381	1.260537
Propane	0.034	1.49906	0.036724	0.911692
<i>i</i> -butane	0.002	0.11624	0.002779	0.065223
<i>n</i> -butane	0.006	0.34872	0.008331	0.191624
Total	1	20.079		

$$\rho = \frac{pM_g}{zRT} = \frac{(0.00149406)(2012)(20.079)}{(0.91)(609.67)} = 0.11025 \text{ g/cm}^3.$$

$$K_1 = \frac{(0.00094 + 2 \times 10^{-6} M_g) T^{1.5}}{209 + 19M_g + T}$$

$$= \frac{(0.00094 + 2 \times 10^{-6})(20.079)(609.67^{1.5})}{209 + (19)(20.079) + 609.67} = 0.012294 \text{ cp.}$$

$$X = 3.5 + \frac{986}{T} + 0.01M_g$$

$$= 3.5 + \frac{986}{609.67} + (0.01)(20.079) = 5.3181.$$

$$Y = 2.4 - 0.2X = 2.4 - (0.2)(5.3181) = 1.3364.$$

$$\mu_g = K_1 \exp(X\rho^Y) = 0.012294 \exp[(5.3181)(0.11025^{1.3364})] = 0.01625 \text{ cp.}$$

This method gives a value that is 5.5% less than the experimentally determined value of 0.0172 cp.

**Example 5.7** The vapor pressure of pure hexane as a function of temperature is 54.04 kPa at 50°C and 188.76 kPa at 90°C. Estimate the vapor pressure of hexane at 100°C, using all the methods outlined previously.

*Solution: Clausius-Clapeyron.* The Clausius-Clapeyron equation can be solved graphically by plotting a log of vapor pressure vs. reciprocal absolute temperature and extrapolating. It also can be solved by slopes fitting an equation of the form  $\log(p_v) = c/T + b$  to the two data points. Because the other three methods must be done in American customary units, the Clausius-Clapeyron method also will be converted to those units.

$$T_1 = 50^\circ\text{C} = 122^\circ\text{F} = 581.67^\circ\text{R},$$

$$1/T_1 = 0.0017192^\circ\text{R}^{-1},$$

$$T_2 = 90^\circ\text{C} = 653.67^\circ\text{R},$$

$$1/T_2 = 0.0015298^\circ\text{R}^{-1},$$

$$p_v \text{ at } T_1 = 54.04 \text{ kPa} = 7.8374 \text{ psia},$$

$$\log p_v = 0.89417,$$

$p_v$  at  $T_2 = 188.76 \text{ kPa} = 27.3773 \text{ psia}$ ,  
 $\log p_v = 1.43739$ ,  
 $\Delta \log p_v = -0.543195$ ,  
 $1/T_1 - 1/T_2 = 0.00018936$ ,  
 and  $c = \text{slope} = -0.543195/0.00018936$   
 $= -2868.52^\circ\text{R}$ .  
 Solving for  $b$ ,  $\log p_v = -2868.52/T + b$  yields  
 $b = 5.8257$ ,  
 $T_3 = 100^\circ\text{C} = 212^\circ\text{F} = 671.67^\circ\text{R}$ ,  
 and  $1/T_3 = 0.0014888$ .  
 Solving for  $p_v$  at  $100^\circ\text{C}$  yields

$$\begin{aligned}
 \log p_v &= -2868.52/T + 5.8257 \\
 &= -2868.52(0.0014888) + 5.8257 \\
 &= 1.555;
 \end{aligned}$$

hence,  $p_v = 35.89 \text{ psia} = 247.46 \text{ kPa}$ .

Alternatively, if the vapor pressure at  $70^\circ\text{C}$  is  $105.37 \text{ kPa}$  and is known, you can use the  $70$  to  $90^\circ\text{C}$  temperature differential to calculate the slope and intercept and ultimately calculate  $p_v = 35.79 \text{ psia} = 246.79 \text{ kPa}$ .

*Solution: Cox Chart.*<sup>18</sup> From Fig. 5.15, the vapor pressure at  $100^\circ\text{C}$  can be approximated between 35 and 36 psia. A larger chart is required for more-precise readings.

*Solution: The Calingart and Davis or Antoine Equation.* This can be used by obtaining the Antoine constants from Poling *et al.*<sup>23</sup> For *n*-hexane, with temperature in K, these constants are  $A = 15.8366$ ,  $B = 2697.55$ , and  $C = -48.78$ . Then,

$$\ln p_v = A - \frac{B}{T - C} = 15.8366 - \frac{2697.55}{373 - 48.78} = 3.60233,$$

and  $p_v = 36.68 \text{ psia} = 252.73 \text{ kPa}$ .

*Solution: Lee-Kesler.* The use of the Lee-Kesler<sup>22</sup> equation requires  $p_c$ ,  $T_c$ , and  $\omega$  for *n*-hexane. These can be obtained from Table 5.2.

$p_c = 436.9 \text{ psia} (29.7 \text{ atm})$ ,  
 $T_c = 453.7^\circ\text{F}$  or  $913.3^\circ\text{R}$  or  $507.4 \text{ K}$ ,  
 and  $\omega = 0.3007$ .  
 For  $100^\circ\text{C}$ ,  
 $T_r = 0.7351$ ,  
 $(T_r)^6 = 0.15782$ ,  
 $\ln T_r = -0.30775$ ,

$$\begin{aligned}
 f^0 &= 5.92714 - (6.09648/0.7351) + 1.28862(0.30775) + 0.169347(0.15782) \\
 &= -1.94296,
 \end{aligned}$$

$$\begin{aligned}
 \text{and } f^1 &= 15.2518 - (15.6875/0.7351) + 13.4721(0.30775) + 0.43577(0.15782) \\
 &= -1.87402,
 \end{aligned}$$

$$\begin{aligned}\ln p_{vr} &= -1.94296 + (0.3007)(-1.87402) \\ &= -2.50648, \\ p_{vr} &= \frac{p_v}{p_c} = 0.0816,\end{aligned}$$

and  $p_v = (0.0816)(29.7) = 2.4235 \text{ atm} = 35.62 \text{ psia} = 245.6 \text{ kPa}$ .

*Experimental Value.* 35.69 psia = 246.1 kPa.

*Conclusions.* Lee-Kesler gives the best answer, but the Clausius-Clapeyron method is also very accurate to within 0.17 psi, which is typical if the extrapolation is close to the appropriate range.

## Nomenclature

- $a$  = constant characteristic of the fluid
- $a_i$  = empirical constant for substance  $i$
- $a_{ij}$  = mixture parameter
- $a_m$  = parameter  $a$  characteristic
- $a(T)$  = functional relationship
- $A$  = sum of the mole fractions of  $\text{CO}_2$  and  $\text{H}_2\text{S}$  in the gas mixture
- $b$  = constant characteristic of the fluid
- $b_i$  = empirical constant for substance  $i$
- $b_m$  = parameter  $b$  for mixture
- $B$  = mole fraction of  $\text{H}_2\text{S}$  in the gas mixture
- $B_g$  = gas formation volume factor (RB/scf or  $\text{Rm}^3/\text{Sm}^3$ )
- $c$  = empirical constant
- $c_g$  = coefficient of isothermal compressibility
- $c_r$  = dimensionless pseudoreduced gas compressibility
- $C$  = constant with a value of 43 when the temperature is in K, and a value of 77.4 when the temperature is in  $^\circ\text{R}$
- $d$  = empirical constant
- $d_i$  = empirical constant for substance  $i$
- $D_o$  = empirical constant
- $e$  = viscosity parameter
- $E_k$  = kinetic energy, J
- $E_o$  = empirical constant
- $f^0, f^1$  = functions of reduced temperature
- $F_j$  = parameter in the Stewart *et al.*<sup>5</sup> equations (Eqs. 5.9 and 5.10),  $\text{K}\cdot\text{Pa}^{-1/2}$
- $J$  = parameter in the Stewart *et al.*<sup>5</sup> equations (Eqs. 5.9 and 5.10),  $\text{K}\cdot\text{Pa}^{-1}$
- $K$  = parameter in the Stewart *et al.*<sup>5</sup> equations (Eqs. 5.9 and 5.10),  $\text{K}\cdot\text{Pa}^{-1/2}$
- $K_l$  = parameter in the Lee *et al.*<sup>16</sup> viscosity (Eq. 5.37), cp
- $K_{ij}$  = constant for each binary pair when used for mixtures
- $L_v$  = molal latent heat of vaporization, J
- $m$  = mass, kg
- $m_g$  = mass of gas, kg
- $M$  = molecular weight
- $M_a$  = molecular weight of air

- $M_{C_{7+}}$  = molecular weight of  $C_{7+}$  fraction  
 $M_g$  = average molecular weight of gas mixture  
 $n$  = number of moles  
 $N$  = number of components in the gas mixture  
 $p$  = absolute pressure, Pa  
 $p_c$  = critical pressure, Pa  
 $p_{ci}$  = critical pressure of component  $i$  in a gas mixture, Pa  
 $p_o$  = base pressure for real-gas pseudopotential, typically atmospheric pressure, Pa  
 $p_{pc}$  = pseudocritical pressure of a gas mixture, Pa  
 $p_r$  = reduced pressure  
 $p_{rc}$  = pressure at reservoir conditions, Pa  
 $p_{sc}$  = pressure at standard conditions, Pa  
 $p_v$  = vapor pressure, Pa  
 $p_{vr}$  = reduced vapor pressure (vapor pressure/critical pressure)  
 $R$  = gas-law constant, J/(g mol-K)  
 $t$  = ratio of critical to absolute temperature  
 $T$  = absolute temperature, K  
 $T_c$  = critical temperature, K  
 $T_{ci}$  = critical temperature of component  $i$  in a gas mixture, K  
 $T_{pc}$  = corrected pseudocritical temperature, K  
 $T_r$  = reduced temperature  
 $T_{rc}$  = temperature at reservoir conditions, K  
 $T_{sc}$  = temperature at standard conditions, K  
 $u^*$  = correlating parameter  
 $v$  = velocity, m/s  
 $V$  = volume,  $m^3$   
 $V_c$  = critical volume,  $m^3$   
 $V_{cC_{7+}}$  = critical volume of  $C_{7+}$  fraction,  $m^3$   
 $V_g$  = volume of gas,  $m^3$   
 $V_M$  = molar volume,  $m^3$   
 $V_r$  = reduced volume  
 $V_{rc}$  = volume at reservoir conditions,  $m^3$   
 $V_R$  = volume of gas at reservoir temperature and pressure,  $m^3$   
 $V_{sc}$  = volume at standard conditions,  $m^3$   
 $x_i$  = mole fraction of component  $i$  in a liquid  
 $X$  = parameter used to calculate  $Y$   
 $y_i$  = mole fraction of component  $i$  in a gas mixture  
 $Y$  = parameter in [Eq. 5.37](#)  
 $z$  = compressibility factor (gas-deviation factor)  
 $z_{rc}$  = compressibility factor at reservoir conditions  
 $z_{sc}$  = compressibility factor at standard conditions  
 $\rho_M$  = molar density  
 $\rho_{pc}$  = relative density of  $C_{7+}$  fraction  
 $\varepsilon$  = temperature-correction factor for acid gases, K  
 $\omega$  = acentric factor  
 $\gamma_g$  = specific gravity for gas

- $\mu$  = viscosity, Pa·s  
 $\mu_{ga}$  = viscosity of gas mixture at desired temperature and atmospheric pressure, Pa·s  
 $\rho_g$  = density of gas, kg/m<sup>3</sup>  
 $\rho_r$  = dimensionless density of gas in Eq. 5.16 =  $0.27 p_r/(zT_r)$   
 $\psi$  = real-gas pseudopotential defined by Eq. 5.38  
 $\psi(p)$  = real-gas pseudopotential

## References

- Moldover, M.R. *et al.*: "Measurement of the universal gas constant  $R$  using a spherical acoustic resonator," *J. Res. NBS* (1988) **93**, No. 2, 85.
- Burnett, E.S.: "Compressibility Determinations without Volume Measurements," *J. Applied Mechanics* (December 1936) **3**, A136–40.
- Kay, W.B.: "Density of Hydrocarbon Gases at High Temperature and Pressure," *Ind. Eng. Chem.* (September 1936) **28**, 1014–1019.
- Sutton, R.P.: "Compressibility Factors for High-Molecular-Weight Reservoir Gases," paper SPE 14265 presented at the 1985 SPE Annual Technical Conference and Exhibition, Las Vegas, Nevada, 22–25 September.
- Stewart, W.F., Burkhardt, S.F., and Voo, D.: "Prediction of Pseudocritical Parameters for Mixtures," presented at the 1959 AIChE meeting, Kansas City, Missouri, 18 May.
- Standing, M.B. and Katz, D.L.: "Density of Natural Gases," *Trans., AIME* (1942) **146**, 140.
- Katz, D.L. *et al.*: *Handbook of Natural Gas Engineering*, McGraw-Hill Book Co. Inc., New York City (1959).
- Brown, G.G. *et al.*: "Natural Gasoline and the Volatile Hydrocarbons," Natural Gas Assn. of America, Tulsa (1948).
- Dranchuk, P.M. and Abou-Kassem, J.H.: "Calculation of Z Factors for Natural Gases Using Equations of State," *J. Cdn. Pet. Tech.* (July–September 1975) **14**, No. 3, 34.
- Hall, K.R. and Yarborough, L.: "A New Equation of State for Z-Factor Calculations," *Oil & Gas J.* (18 June 1973) **71**, No. 25, 82.
- Towler, B.F.: *Fundamental Principles of Reservoir Engineering*, Textbook Series, SPE, Richardson, Texas (2002) **8**.
- Wichert, E. and Aziz, K.: "Calculate Z's for Sour Gases," *Hydrocarbon Processing* (May 1972) **51**, 119.
- Piper, L.D., McCain, W.D. Jr., and Corredor, J.H.: "Compressibility Factors for Naturally Occurring Petroleum Gases," paper SPE 26668 presented at the 1993 SPE Annual Technical Conference and Exhibition, Houston, 3–6 October.
- Trube, A.S.: "Compressibility of Natural Gases," *Trans., AIME* (1957) **210**, 355.
- Mattar, L., Brar, G.S., and Aziz, K.: "Compressibility of Natural Gases," *J. Cdn. Pet. Tech.* (October–December 1975) **14**, No. 4, 77.
- Carr, N.L., Kobayashi, R., and Burrows, D.B.: "Viscosity of Hydrocarbon Gases Under Pressure," *Trans., AIME* (1954) **201**, 264.
- Lee, A.L., Gonzalez, M.H., and Eakin, B.E.: "The Viscosity of Natural Gases," *JPT* (August 1966) **997**; *Trans., AIME*, **237**.
- Cox, E.R.: "Pressure Temperature Chart for Hydrocarbon Vapors," *Ind. Eng. Chem.* (1923) **15**, No. 4, 592.
- Calingeart, G. and Davis, D.S.: "Pressure Temperature Charts Extended Ranges," *Ind. Eng. Chem.* (1925) **17**, No. 12, 1287.
- Antoine, C.: *Chem. Reviews* (1888) **107**, 836–50.
- Pitzer, K.S. *et al.*: "The Volumetric and Thermodynamic Properties of Fluids. II. Compressibility Factor, Vapor Pressure and Entropy of Vaporization," *J. American Chemical Soc.* (1955) **77**, 3433.
- Lee, B.I. and Kesler, M.G.: "A Generalized Thermodynamic Correlation Based on Three-Parameter Corresponding States," *AIChE J.* (May 1975) **21**, 510.

23. Poling, B.E., Prausnitz, J.M., and O'Connell, J.P.: *The Properties of Gases and Liquids*, fifth edition, McGraw-Hill Book Co. Inc., New York City (2001).

### SI Metric Conversion Factors

$^{\circ}\text{API}$	$141.5/(131.5+^{\circ}\text{API})$		$= \text{g/cm}^3$
atm $\times$	$1.013\ 250^*$	E+05	$= \text{Pa}$
bar $\times$	$1.0^*$	E+05	$= \text{Pa}$
bbl $\times$	$1.589\ 873$	E-01	$= \text{m}^3$
cp $\times$	$1.0^*$	E-03	$= \text{Pa}\cdot\text{s}$
Darcy $\times$	$9.869\ 233$	E-01	$= \mu\text{m}^2$
dyne $\times$	$1.0^*$	E-02	$= \text{mN}$
dyne/cm <sup>2</sup> $\times$	$1.0^*$	E-01	$= \text{Pa}$
ft $\times$	$3.048^*$	E-01	$= \text{m}$
ft <sup>2</sup> $\times$	$9.290\ 304^*$	E-02	$= \text{m}^2$
ft <sup>3</sup> $\times$	$2.831\ 685$	E-02	$= \text{m}^3$
ft-lbf $\times$	$1.355\ 818$		$= \text{J}$
$^{\circ}\text{F}$	$(^{\circ}\text{F}-32)/1.8$		$= ^{\circ}\text{C}$
$^{\circ}\text{F}$	$(^{\circ}\text{F}+459.67)/1.8$		$= \text{K}$
hp-hr $\times$	$2.684\ 520$	E+06	$= \text{J}$
in. $\times$	$2.54^*$	E+00	$= \text{cm}$
in. <sup>2</sup> $\times$	$6.451\ 6^*$	E+00	$= \text{cm}^2$
in. <sup>3</sup> $\times$	$1.638\ 706$	E+00	$= \text{cm}^3$
kW-hr $\times$	$3.6$	E+06	$= \text{J}$
lbf $\times$	$4.448\ 222$	E+00	$= \text{N}$
lbf/in. <sup>2</sup> $\times$	$6.894\ 757$	E+03	$= \text{Pa}$
lbf-s/ft <sup>2</sup> $\times$	$4.788\ 026$	E+01	$= \text{Pa}\cdot\text{s}$
lbm $\times$	$4.535\ 924$	E-01	$= \text{kg}$
mile $\times$	$1.609\ 344$	E+00	$= \text{km}$
N·m			$= \text{J}$
psi $\times$	$6.894\ 757$	E+00	$= \text{kPa}$
$^{\circ}\text{R}/1.8$			$= \text{K}$

\*Conversion factor is exact.



## Chapter 6

# Oil System Correlations

Robert P. Sutton, Marathon Oil Co.

### 6.1 Introduction

The calculation of reserves in an oil reservoir or the determination of its performance requires knowledge of the fluid's physical properties at elevated pressure and temperature. Of primary importance are those properties including bubblepoint pressure, solution gas/oil ratio (GOR), and formation volume factor (FVF). In addition, viscosity and surface tension must be determined for calculations involving the flow of oil through pipe or porous media. Ideally, these properties are determined from laboratory studies designed to duplicate the conditions of interest; however, experimental data are quite often unavailable because representative samples cannot be obtained or the producing horizon does not warrant the expense of an in-depth reservoir fluid study. In these cases, pressure-volume-temperature (PVT) properties must be determined by analogy or through the use of empirically derived correlations. This chapter reviews methods for the determination of bubblepoint pressure, solution GOR, oil FVF, isothermal compressibility, dead (gas-free) oil viscosity, gas-saturated (bubblepoint) oil viscosity, undersaturated oil viscosity, and gas/oil, oil/water, and gas/water surface tension. **Table 6.1** (Refs. 1 through 28) summarizes the recommended methods for general use determination of each property. These recommendations are based on the correlation performance derived from a common data set or the author's experiences drawn from using various correlations for a number of years. In Appendix A, **Tables A-1 through A-12** (Refs. 29 through 65) contain a comprehensive and descriptive list of available correlations because specific applications could require the use of methods other than those listed in **Table 6.1**.

During the last 60 years, several correlations have been proposed for determining PVT properties. The most widely used correlations treat the oil and gas phases as a two-component system. Only the pressure, temperature, specific gravity, and relative amount of each component are used to characterize the oil's PVT properties. Crude oil systems from various oil-producing regions of the world were used in the development of the correlations. These crude oils can exhibit regional trends in chemical composition, placing them into one of the following groups: paraffinic, naphthenic, or aromatic. Because of the differences in composition, correlations developed from regional samples, predominantly of one chemical base, may not provide satisfactory results when applied to crude oils from other regions.

Hydrocarbons are classified according to the structure of the molecule.<sup>66</sup> Paraffin hydrocarbons are characterized by open or straight chains joined by single bonds. Examples are

TABLE 6.1—RECOMMENDED PVT CORRELATIONS FOR GENERAL USE

Property	Method
Bubblepoint pressure	Lasater, <sup>1</sup> Al-Shammasi, <sup>2</sup> or Velarde <sup>3</sup>
Formation volume factor	Al-Marhoun, <sup>4</sup> Al-Shammasi, Farshad, <sup>5</sup> or Kartoatmodjo <sup>6-8</sup>
Isothermal compressibility	Dindoruk and Christman, <sup>9</sup> Petrosky, <sup>10,11</sup> or Farshad
Dead oil viscosity	Glasø, <sup>12</sup> Bergman, <sup>13,14</sup> or Fitzgerald <sup>15,16</sup>
Gas-saturated oil viscosity	Chew and Connally <sup>17,18</sup> or Beggs and Robinson <sup>19</sup>
Undersaturated oil viscosity	Beal, <sup>20,21</sup> Kouzel, <sup>22</sup> or Vazquez and Beggs <sup>23,24</sup>
Gas/oil surface tension	Abdul-Majeed <sup>25</sup> or Baker and Swerdloff <sup>26,27</sup>
Water/hydrocarbon surface tension	Firoozabadi and Ramey <sup>28</sup>

methane, ethane, propane, and decane. Isomers of these compounds, which contain branched chains, are also included as paraffins. The first four members of the series are gaseous at room temperature and pressure. Compounds ranging from pentane (C<sub>5</sub>H<sub>12</sub>) through heptadecane (C<sub>17</sub>H<sub>36</sub>) are liquids, while the heavier members are colorless, wax-like solids. Unsaturated hydrocarbons, which consist of olefins, diolefins, and acetylenes, have double and triple bonds in the molecule. These compounds are highly reactive and are not normally present to any great extent in crude oil. Naphthene hydrocarbons are ringed molecules and are also called cycloparaffins. These compounds, like the paraffins, are saturated and very stable. They make up a second primary constituent of crude oil. Aromatic hydrocarbons are also cyclic but are derivatives of benzene. The rings are characterized by alternating double bonds and, in contrast to olefins, are quite stable, though not as stable as paraffins. Crude oils are complex mixtures of these hydrocarbons. Oils containing primarily paraffin hydrocarbons are called paraffin-based or paraffinic. Traditional examples are Pennsylvania grade crude oils. Naphthenic-based crudes contain a large percentage of cycloparaffins in the heavy components. Examples of this type of crude come from the United States midcontinent region. Highly aromatic crudes are less common but are still found around the world.<sup>67</sup> Crude oils tend to be a mixture of paraffins-naphthenes-aromatics, with paraffins and naphthenes the predominant species. Fig. 6.1, although not complete, shows a distribution of crude oil samples obtained worldwide. Geochemical analyses provided the crude's chemical nature.

Resins and asphaltenes may also be present in crude oil.<sup>69,70</sup> Resins and asphaltenes are the colored and black components found in oil and are made up of relatively high-molecular-weight, polar, polycyclic, aromatic ring compounds. Pure asphaltenes are nonvolatile, dry, solid, black powders, while resins are heavy liquids or sticky solids with the same volatility as similarly sized hydrocarbons. High-molecular-weight resins tend to be red in color, while lighter resins are less colored. Asphaltenes do not dissolve in crude oil but exist as a colloidal suspension. They are soluble in aromatic compounds such as xylene, but will precipitate in the presence of light paraffinic compounds such as pentane. Resins, on the other hand, are readily soluble in oil.

No crude oil has ever been completely separated into its individual components, although many components can be identified. Table 6.2 lists the more important compounds in a sample of Oklahoma crude. A total of 141 compounds were identified in this oil sample that account for 44% of the total crude volume. Despite this complexity, several properties relevant to petroleum engineers can be determined from black oil PVT correlations.

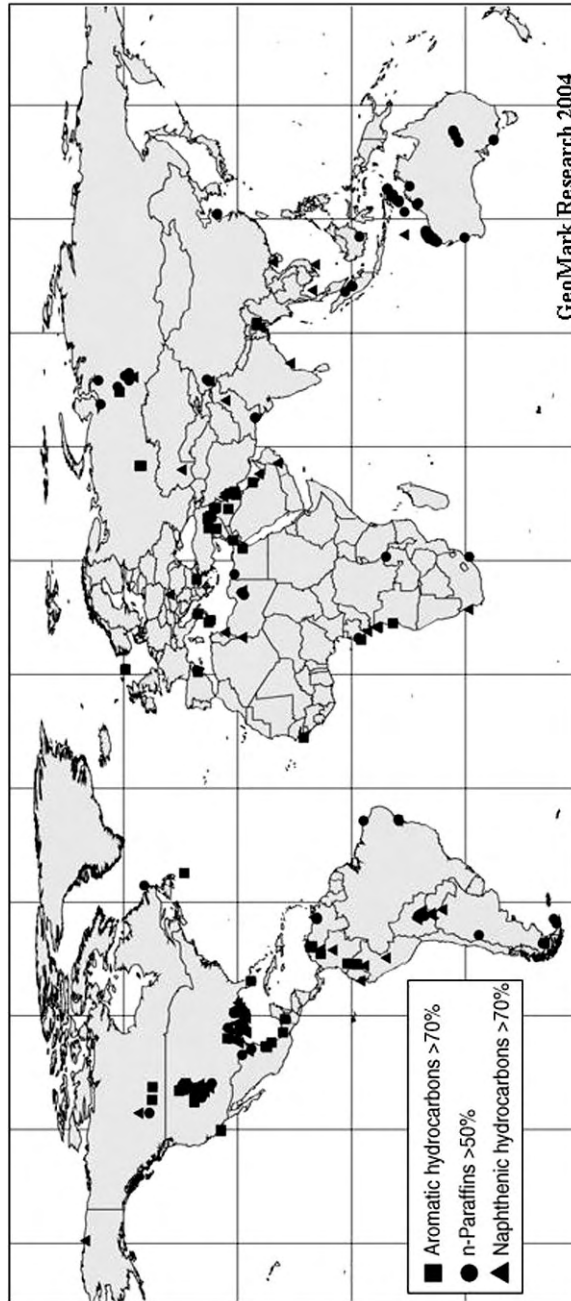


Fig. 6.1—Chemical nature of crude oils found worldwide (after Reservoir Fluid Database<sup>68</sup>).

### 6.2 Crude Oil Characterization

Crude oil characterization has long been an area of concern in refining; however, the need to identify the chemical nature of crude has gained importance in upstream operations. Traditionally, this has been done by simply stating the crude oil gravity. The petroleum industry uses API gravity as the preferred gravity scale, which is related to specific gravity as

**TABLE 6.2—EXAMPLE OF DETAILED CRUDE OIL COMPOSITION<sup>66</sup>**

Paraffins	Naphthenes	Aromatics
All normal paraffins to C <sub>10</sub> H <sub>22</sub>	Cyclopentane	Benzene
Isobutane	Cyclohexane	Toluene
2-Methylbutane	Methylcyclopentane	Ethylbenzene
2,3-Dimethylbutane	1,1-Dimethylcyclopentane	Xylene
2-Methylpentane	Methylcyclohexane	1,2,4-Trimethylbenzene
3-Methylpentane	1,3-Dimethylcyclohexane	
2-Methylhexane	1,2,4-Trimethylcyclohexane	
3-Methylhexane		
2-Methylheptane		
2,6-Dimethylheptane		
2-Methyloctane		

$$\gamma_{API} = \frac{141.5}{\gamma_o} - 131.5 \dots\dots\dots (6.1)$$

Whitson<sup>71</sup> has suggested use of the Watson<sup>72,73</sup> characterization factor as a means of further characterizing crude oils and components. In 1933, Watson and Nelson introduced a ratio between the mean average boiling point and specific gravity that could be used to indicate the chemical nature of hydrocarbon fractions and, therefore, could be used as a correlative factor. Characterization factors are calculated with

$$K_w = \frac{T_b^{1/3}}{\gamma_o} \dots\dots\dots (6.2)$$

Characterization factors are useful because they remain reasonably constant for chemically similar hydrocarbons. A characterization factor of 12.5 or greater indicates a hydrocarbon compound predominantly paraffinic in nature. Lower values of this factor indicate hydrocarbons with more naphthenic or aromatic components. Highly aromatic hydrocarbons exhibit values of 10.0 or less; therefore, the Watson characterization factor provides a means of determining the paraffinicity of a crude oil. Using work from Riazi and Daubert,<sup>74</sup> Whitson<sup>71</sup> developed the following relationship in terms of molecular weight and specific gravity.

$$K_w = 4.5579 M_o^{0.15178} \gamma_o^{-0.84573} \dots\dots\dots (6.3)$$

**Table 6.3** provides values of Watson characterization factors for selected pure components classified as paraffins, naphthenes, or aromatics. The characterization factor values provide insight into their use.

Crude oils typically have characterization factors ranging from 11 to 12.5. **Table 6.4** was derived from assay data available in the public domain. It samples crudes from around the world and can be used to provide insight into PVT behavior on a regional basis.

The properties of the heptanes-plus fraction in the stock tank crude oil are an additional source that can provide insight into the Watson characterization factor. It is important to ac-

**TABLE 6.3—WATSON CHARACTERIZATION FACTORS FOR SELECTED COMPOUNDS**

Series	Compound	Formula	Boiling Point Temperature (°R)	Molecular Weight	Specific Gravity	Watson Characterization Factor
Paraffins	n-Hexane	C <sub>6</sub> H <sub>14</sub>	615.4	86.178	0.6640	12.8
	2-Methylpentane	C <sub>6</sub> H <sub>14</sub>	600.1	86.178	0.6579	12.8
	n-Heptane	C <sub>7</sub> H <sub>16</sub>	668.8	100.205	0.6882	12.7
Naphthenes	Cyclohexane	C <sub>6</sub> H <sub>12</sub>	637.0	84.162	0.7834	11.0
	Methylcyclohexane	C <sub>7</sub> H <sub>14</sub>	673.4	98.189	0.7740	11.3
Aromatics	Benzene	C <sub>6</sub> H <sub>6</sub>	635.8	78.114	0.8844	9.7
	Toluene	C <sub>7</sub> H <sub>8</sub>	690.8	92.141	0.8718	10.1

count for the lighter paraffin components found in the oil to arrive at the characterization factor for the entire crude.

Fig. 6.2 depicts a relationship between crude oil gravity and characterization parameter. While not definitive, it can be observed that lower gravity crudes tend to be more naphthenic, while higher-gravity crudes tend to be more paraffinic.

**6.3 Bubblepoint Pressure**

Tables A-1 and A-2 summarize correlations of bubblepoint. Since Standing’s<sup>29</sup> correlation appeared in 1947, more than 30 methods have been proposed. Many of these were developed during the last 15 years. The effective use of the correlations lies in an understanding of their development, along with knowledge of their limitations. These equations can be expressed functionally as

$$p_b = f(T, \gamma_{API}, \gamma_g, R_s) \dots\dots\dots (6.4)$$

Solution GOR is determined by rearranging any given correlation equation. Recent studies<sup>75-78</sup> provide statistical analyses for bubblepoint-pressure correlations and provide recommendations based on their findings; however, none of these references examines the full set of correlations. Al-Shammasi<sup>2</sup> compiled a databank of 1,243 data points from the literature. This was supplemented by 133 samples available from a GeoMark Research database,<sup>68</sup> bringing the total number of data points to 1,376. These data were then used to rank the bubblepoint pressure correlations. Table 6.5 summarizes the ranges of data found in this compilation and the distribution. Fig. 6.3 shows the distribution of data used to prepare PVT correlations.

Table 6.6 summarizes correlation performance. The results are sorted by absolute average relative error, which provided a means to rank the methods.

The data were further grouped to examine the impact of crude oil gravity and GOR on the consistency of the correlations. Methods proposed by Lasater,<sup>1</sup> Al-Shammasi,<sup>2</sup> and Velarde *et al.*<sup>3</sup> showed reliability over a wide range of conditions. The author has experienced good results from both the Standing<sup>21,29</sup> and Glasø<sup>12</sup> correlations, although they may not have ranked highly with this data set. Fig. 6.4 depicts these correlations for comparison.

Fig. 6.5 graphically summarizes the results of all 32 bubblepoint pressure correlations for varying GOR, a 35°API crude oil, a hydrocarbon gas gravity of 0.65, and a temperature of 150°F. Individual methods are unlabeled because it is the envelope and range of answers that are of interest. Some information concerning correlation trends can be gathered from the outliers.

TABLE 6.4—SAMPLE OF WORLDWIDE CRUDE OIL PROPERTIES<sup>50</sup>

Reservoir	Area	Country	API	$K_w$
Boscan	Zulia	Venezuela	9.5	11.65
Kern River	California	U.S.A.	10.7	11.15
Quitman	Mississippi	U.S.A.	12.7	11.85
Vermilion		Canada	14.0	11.32
Bachaquero	Zulia	Venezuela	14.0	11.40
Quiyarah		Iraq	14.4	11.71
Santa María	California	U.S.A.	15.4	11.48
Lloydminster		Canada	16.2	11.35
Quiquire	Monagas	Venezuela	17.2	11.22
Tarakan	Kalimantan	Indonesia	18.0	10.92
Klamono		New Guinea	18.0	11.20
Kuito		Angola	19.0	11.60
Alba		U.K.	19.4	11.70
Casabe	Antioquia	Colombia	20.5	11.48
Smackover	Arkansas	U.S.A.	20.5	11.55
Coalinga (East)	California	U.S.A.	20.7	11.24
Duri	Sumatra	Indonesia	20.8	12.00
Naranjos		Mexico	21.6	11.90
Tatums	Oklahoma	U.S.A.	22.1	11.69
Miranda	Texas	U.S.A.	22.5	11.13
Wafra	Neutral Zone	Middle East	24.2	11.82
Talco	Texas	U.S.A.	24.4	11.94
La Rosa	Zulia	Venezuela	25.3	11.70
Limau	Sumatra	Indonesia	26.0	11.50
Quatif		Saudi Arabia	27.4	11.92
Amelia	Texas	U.S.A.	28.2	11.51
Mara	Zulia	Venezuela	29.5	11.98
Poza Rica		Mexico	30.7	11.95
Coalinga	California	U.S.A.	31.1	11.58
Kuwait		Kuwait	31.4	11.93
Elk Basin	Wyoming	U.S.A.	31.5	11.64
Coco		Republic of Congo	31.6	12.20
Kalimantan (waxy)	Kalimantan	Indonesia	32.0	11.35
Monument	Minnesota	U.S.A.	32.1	11.56
Jusepin	Monagas	Venezuela	32.4	11.80
West Texas	Texas	U.S.A.	32.5	11.75
Cabinda		Angola	32.5	12.20
South Louisiana	Louisiana	U.S.A.	33.3	11.87
Aaconsib	Zulia	Venezuela	33.5	12.01
San Joaquin Valley	California	U.S.A.	33.6	11.66
Healdton	Oklahoma	U.S.A.	33.6	11.88
Barco (heavy)		Colombia	33.8	11.95
Escravos		Nigeria	34.2	11.70
Redwater	Alberta	Canada	34.3	11.83

TABLE 6.4—SAMPLE OF WORLDWIDE CRUDE OIL PROPERTIES<sup>50</sup> (continued)

Reservoir	Area	Country	API	$K_w$
El Dorado	Kansas	U.S.A.	34.4	11.88
Dammam		Saudi Arabia	34.9	11.94
Pennington		Nigeria	35.0	11.70
Minas	Sumatra	Indonesia	35.0	12.60
Medanito		Argentina	35.1	12.20
Rincon		Argentina	35.8	11.80
Hibernia	Offshore	Canada	35.8	11.90
Seria (waxy)	Brunei	Borneo	36.0	11.50
Agha Jari	Khuzistan	Iran	36.0	11.81
Salt Creek	Wyoming	U.S.A.	36.2	11.83
Abqaiq		Saudi Arabia	36.5	12.00
Kirkuk		Iraq	36.6	11.92
Sprayberry	Texas	U.S.A.	37.2	11.85
Kitina		Republic of Congo	37.2	12.20
Oklahoma City	Oklahoma	U.S.A.	37.3	12.06
Kettleman	California	U.S.A.	37.5	11.67
Barrow Island		Asia	37.7	11.70
Guara (light)	Anzoátegui	Venezuela	37.7	11.75
Statfjord		U.K.-Norway	38.2	12.00
East Texas	Texas	U.S.A.	38.4	11.89
Quatif	Zone D	Saudi Arabia	38.6	12.00
Nemba		Angola	38.7	12.20
Louden	Illinois	U.S.A.	38.8	11.84
Nanghai Light		South China Sea	39.7	12.40
Gwinville	Mississippi	U.S.A.	39.9	12.22
Draugen		Norway	40.2	11.80
Michigan	Michigan	U.S.A.	40.2	12.16
Leduc	Alberta	Canada	40.4	11.84
Thevenard Island		Asia	40.7	11.90
Santa Elena		Ecuador	41.0	11.91
Benchamas		Gulf of Thailand	41.3	12.60
Edmond	Oklahoma	U.S.A.	41.5	11.95
Turner Valley	Alberta	Canada	41.7	11.82
Tantawan		Gulf of Thailand	41.8	12.50
Magallanes		Chile	41.9	12.00
Williston	North Dakota	U.S.A.	42.0	11.79
Scurry County	Texas	U.S.A.	42.0	11.85
Farmers Valley	Pennsylvania	U.S.A.	42.4	12.20
Rodessa	Louisiana	U.S.A.	42.8	12.22
Santa Rosa	Anzoátegui	Venezuela	44.2	11.84
Atlanta (limestone)	Arkansas	U.S.A.	44.5	12.05
Kutubu Light		New Guinea	44.7	12.20
Grass Creek	Wyoming	U.S.A.	45.8	11.81
Djambi (NIAM)	Sumatra	Indonesia	46.0	11.80
N'Kossa		Republic of Congo	46.5	12.10

Reservoir	Area	Country	API	$K_w$
Tengiz		Kazakhstan	47.2	12.40
Chase	Kansas	U.S.A.	48.1	11.91
Cossack		Australia	48.2	12.00
Barco (light)		Colombia	48.7	12.04
Pegasus County	Texas	U.S.A.	52.3	12.39
El Roble	Anzoátegui	Venezuela	54.6	11.85
Santa Anita		Bolivia	57.0	12.08
Northwest Shelf		Australia	60.3	12.30

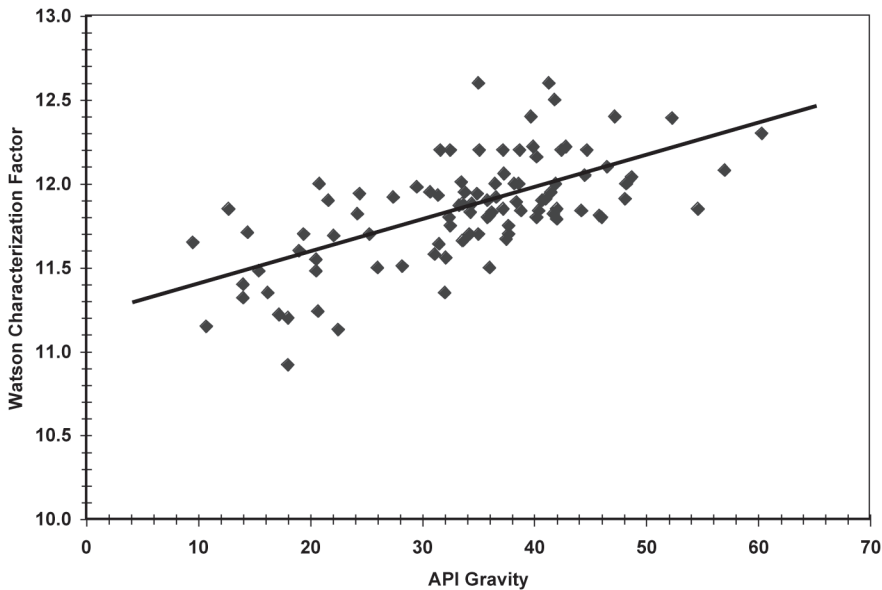


Fig. 6.2—Typical characterization factors for various crude oil gravities.

Owolabi's<sup>33</sup> method for Alaska Cook Inlet Basin crude oil systems, shown in Fig. 6.5, illustrates the impact of gas impurities on the correlation. This crude oil system is characterized by GORs in the range 200 to 300 scf/STB and nitrogen contents of 5 to 15%. The limited range of GORs combined with the nitrogen in the surface gas results in a correlation that predicts rather large values of bubblepoint pressure when extrapolated to higher GORs. This illustrates the pitfalls of developing a correlation from a limited set of data and further defines the importance of understanding the range of applicability for any given correlation. The method may be perfectly valid within a limited range of conditions; however, the equations that define the method may not be suitable for extrapolation.

This example also illustrates the importance of adjusting the calculated bubblepoint pressure for the effects of gas impurities. For the most part, bubblepoint-pressure correlations have been established with little or no impurities in the gas. Owolabi recognized the importance of these impurities and their impact on the calculated results. Methods to adjust the calculated



TABLE 6.5—DATA RANGES USED FOR BUBBLEPOINT PRESSURE AND OIL FVF CORRELATION EVALUATION			
Property	Minimum	Maximum	Average
Bubblepoint pressure, psia	32	10,326	2,041
Temperature, °F	58	342	185
FVF, bbl/STB	1,023	2,952	1,349
Solution GOR, scf/STB	6	3,448	592
Crude oil gravity, °API	6.0	63.7	34.1
Gas specific gravity	0.511	3.445	1.005

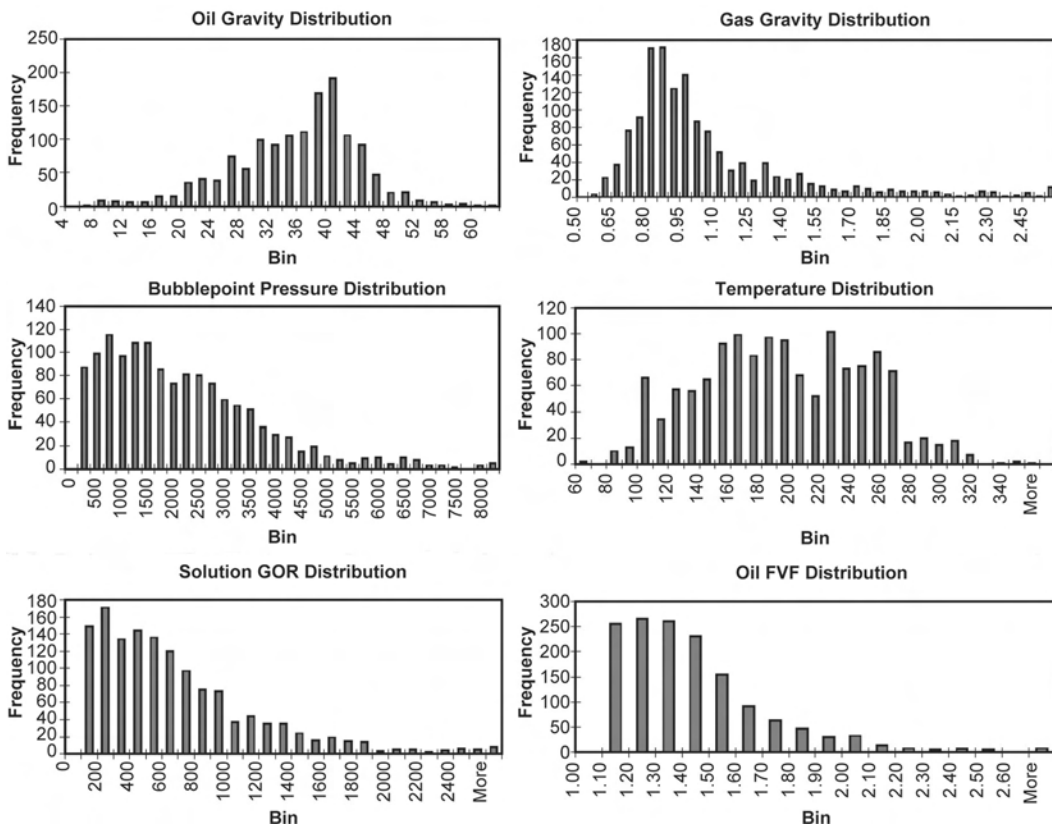


Fig. 6.3—Distribution of data used to prepare PVT correlations.

bubblepoint pressure for gas impurities have been developed and should be used. [Sec. 6.4](#) covers these methods.

It is instructive to focus on the large spread in the range of correlations presented in [Fig. 6.5](#). The correlations form a core envelope of results that coincide with variations expected because of the chemical nature of the crude oil. Correlations with results residing above and below the core envelope were ignored, and the difference between high and low results was determined as shown in [Fig. 6.6](#).

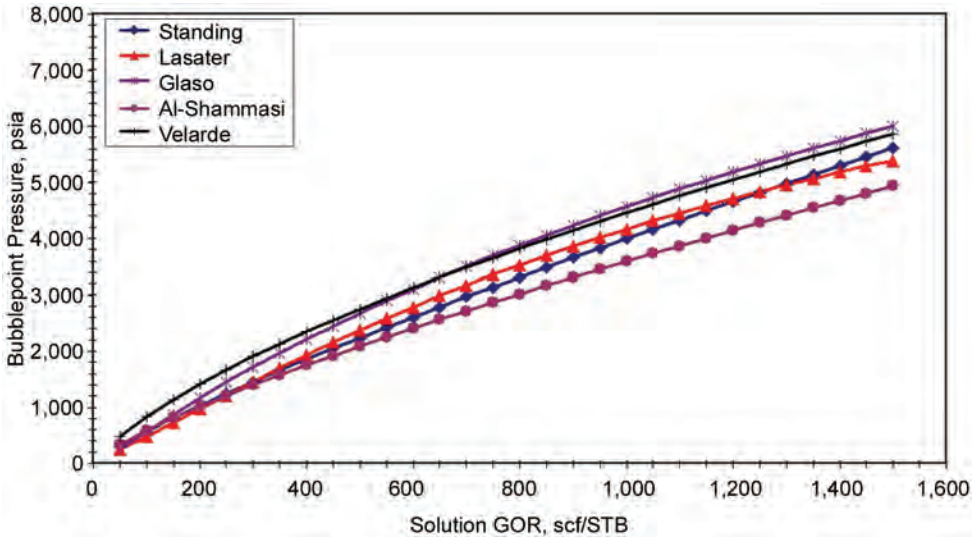


Fig. 6.4—Selected bubblepoint pressure correlations.

Correlations using only API gravity to define the crude oil component do not adequately describe the chemical nature of the crude oil. Lasater’s method relies on a relationship relating crude oil gravity and molecular weight. Whitson’s Watson characterization factor equation can be used to examine this relationship. Lasater reported that the oil gravity/molecular weight relationship corresponded to a Watson characterization factor of 11.8; however, on closer examination, the correlation is representative of paraffinic oil with a Watson characterization factor of approximately 12.2, as Fig. 6.7 shows. Whitson and Brulé<sup>13</sup> recommended that Cragoe’s<sup>79</sup> relationship to determine molecular weight from API gravity be used to determine crude molecular weight.

$$M_o = \frac{6,084}{\gamma_{API} - 5.9} \dots\dots\dots (6.5)$$

First published in 1929, this equation is generally used with condensates and is applicable over the range of 20 to 80°API. It should not be used outside this range. A Watson characterization factor of 11.8 is defined by Cragoe’s relationship over the API gravity range 30 to 40. Whitson’s work with North Sea crudes that have a characterization factor of 11.9 supports this recommendation. A more general recommendation is to use Whitson’s equation to determine the molecular weight from the Watson characterization factor and oil specific gravity. This adds the dimension of crude oil chemical nature to the estimate of fluid properties using correlations. Lasater developed a correlation between a bubblepoint pressure factor,  $p_b \gamma_g / T$ , and the mole fraction of gas dissolved in the oil, which is depicted in Fig. 6.8. The equation fit to the data has been modified to provide better performance of the correlation at high GOR conditions. Lasater’s method is summarized in its entirety in Tables A-1 and A-2.

Whitson and Brulé offered a modification to Glasø’s correlation to account for changes in characterization factor. Glasø’s correlation was developed from North Sea crude oils with a Watson characterization factor of 11.9. The proposed modification is

$$\gamma_{o_c} = \gamma_{o_m} (K_w / 11.9)^{1.1824} \dots\dots\dots (6.6)$$

**TABLE 6.6—STATISTICAL SUMMARY OF BUBBLEPOINT PRESSURE CORRELATION PERFORMANCE**

Correlation	ARE* (%)	Standard Deviation (%)	AARE** (%)	Standard Deviation (%)
Al-Shammasi	1.56	24.17	17.75	16.47
Velarde	-3.90	27.76	19.26	20.36
Lasater	-5.40	27.23	19.38	19.88
Standing	3.23	33.80	20.25	27.24
Levitán and Murtha	10.51	36.13	21.79	30.67
Glasø-Volatile Oil	-12.27	26.18	22.14	18.58
Vazquez and Beggs	12.95	36.50	22.68	31.39
Al-Marhoun <sup>36</sup>	-0.97	35.61	22.77	27.38
Hasan	11.80	39.57	22.97	34.30
Agip	13.67	35.20	23.05	29.91
Al-Marhoun <sup>34</sup>	-4.11	35.58	23.64	26.91
Al-Najjar <i>et al.</i>	-5.15	36.51	23.90	28.07
Glasø	12.21	33.28	24.33	25.78
Dindoruk and Christman	-0.31	34.71	24.71	24.37
Kartoatmodjo and Schmidt	13.12	42.06	25.27	36.09
Dokla and Osman	0.33	36.84	25.91	26.18
Farshad <i>et al.</i>	-15.38	34.08	26.34	26.54
Labedi	8.98	47.28	28.96	38.44
Almehaideb	-2.50	47.41	30.27	36.56
Elsharkawy	-14.44	40.38	30.36	30.29
Khairy <i>et al.</i>	5.76	54.24	31.46	44.55
De Ghetto	22.42	67.17	33.53	62.37
Petrosky	-19.38	44.58	36.03	32.63
Owolabi ANS	22.03	50.20	37.17	40.30
Macary <i>et al.</i>	25.41	64.76	38.95	57.63
Elam	32.16	72.34	39.85	68.40
Asgarpour <i>et al.</i> Nisku	29.73	81.10	41.68	75.65
Obomanu and Okpobiri	-44.99	29.21	48.44	23.04
Asgarpour <i>et al.</i> Leduc	58.74	162.52	75.01	155.67
Asgarpour <i>et al.</i> Cardium	62.82	164.24	75.69	158.72
Owolabi CIB	82.74	98.52	92.64	89.28
Omar and Todd	222.89	2537.08	233.94	2536.08

\*ARE = average relative error =  $\frac{100}{N} \sum_{i=1}^N \frac{X_{i,calc} - X_{i,meas}}{X_{i,meas}}$

\*\*AARE = average absolute relative error =  $\frac{100}{N} \sum_{i=1}^N \left| \frac{X_{i,calc} - X_{i,meas}}{X_{i,meas}} \right|$

**Fig. 6.9** depicts the effect of changing the Watson characterization factor on bubblepoint pressure for the Lasater and Glasø correlations. The range in bubblepoint pressure solutions is comparable to the range exhibited in Fig. 6.6. Clearly, the addition of Watson characterization

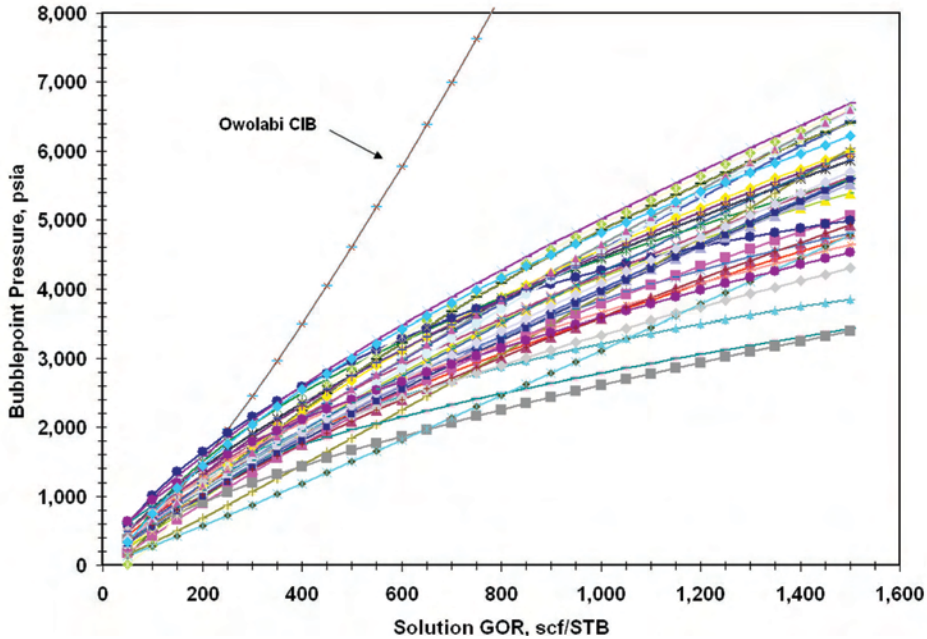


Fig. 6.5—Bubblepoint pressure relationship with solution GOR.

factor to correlation of bubblepoint pressure offers increased flexibility in the use of a correlation on a worldwide basis. Whitson and Brulé present graphs detailing the relationship between bubblepoint pressure and characterization that show bubblepoint pressure declining with an increase in characterization factor. Their analysis procedure also allows for changing API gravity and GOR. By allowing these two quantities to vary, their evaluation shows the converse of Fig. 6.9.

A correlation is an equation or method fit to specific data groups to provide the relationship between dependent and independent variables. Properly defined, the variables cover a wide range of conditions, enabling the correlation to properly represent the physical processes being modeled. Formulation of the equations is important because they are routinely extrapolated outside the range used for their development. Some correlations have been developed with multiple equations for various ranges of crude oil gravity. Normally, 30°API is selected as a point at which the equations change. Discontinuities in relationships can arise as a result of using multiple equations. Other methods show nonphysical trends. Care must be exercised in the use of these methods for “general use” calculations over a wide range of conditions.

Correlations proposed by Vazquez and Beggs,<sup>23,24</sup> Al-Najjar *et al.*,<sup>38</sup> Kartoatmodjo and Schmidt,<sup>6–8</sup> De Ghetto *et al.*,<sup>44,45</sup> and Elsharkawy and Alikhan<sup>47</sup> use multiple equations to cover the range of API gravities. These methods often exhibit discontinuities across the boundaries. The method of Dokla and Osman<sup>39</sup> shows virtually no sensitivity to crude oil gravity. Bubblepoint pressure should increase with rising temperature. Methods proposed by Dokla and Osman, Almehaideb,<sup>46</sup> Elsharkawy and Dindoruk, and Christman<sup>9</sup> show a decrease. Bubblepoint pressure should decrease with increasing gas gravity. Methods proposed by Asgarpour *et al.*<sup>37</sup> (for the Cardium/Viking and D2/Leduc formations) and Elsharkawy are insensitive to gas gravity or show increasing bubblepoint pressure with increasing gas gravity. Omar and Todd's<sup>41,42</sup> correlation shows a parabolic trend that is inaccurate for high gas gravities. This

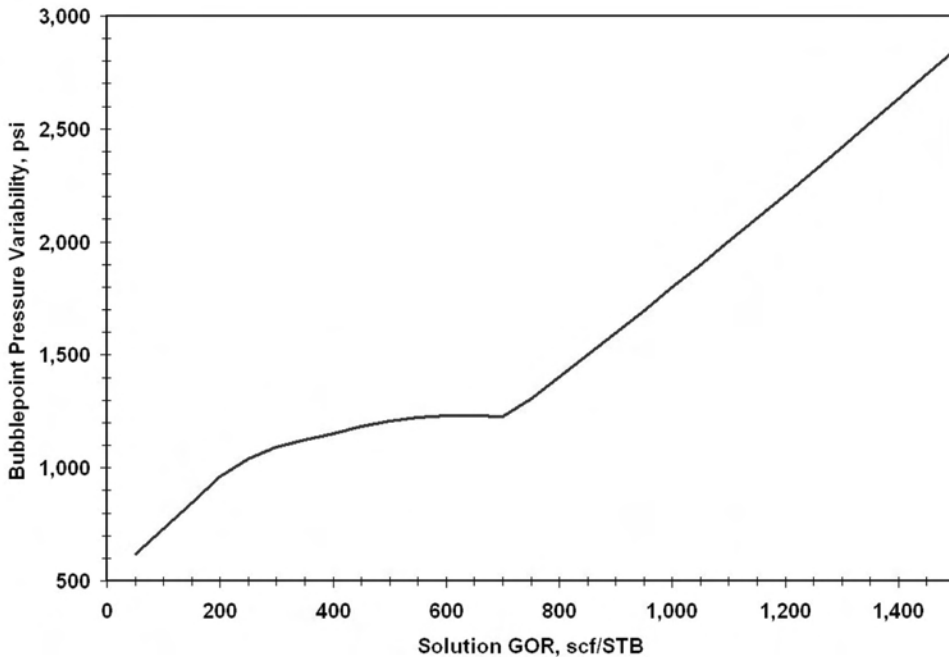


Fig. 6.6—Variability defined by bubblepoint pressure correlations.

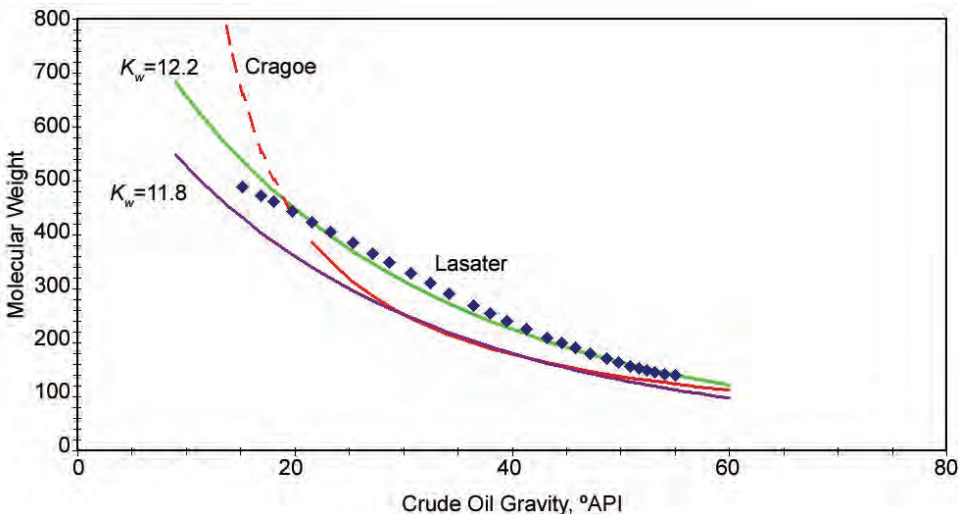


Fig. 6.7—Effective molecular weight related to tank-oil gravity.

method should be avoided for crude oil systems with gas-specific gravities greater than 1.10. **Figs. 6.10 through 6.12** show these results graphically.

Additionally, several other correlations have been found to exhibit undesirable tendencies. At atmospheric pressure where solution GOR is zero, Petrosky and Farshad<sup>10,11</sup> determines a value of 50 to 100 scf/STB. Dindoruk and Christman provided separate equations for GOR and bubblepoint pressure because of their complexity. Both equations provide nearly identical re-

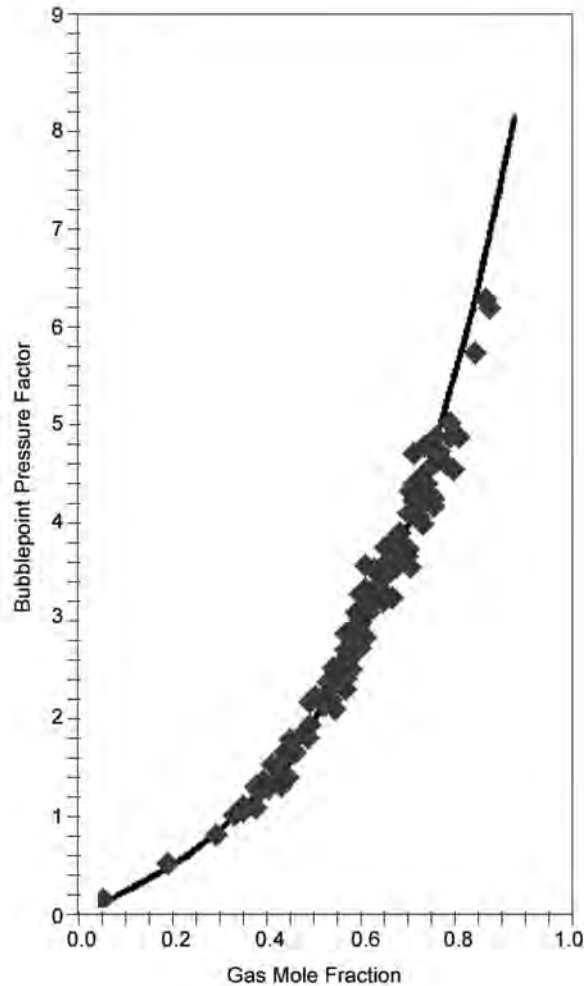


Fig. 6.8—Bubblepoint pressure factor correlation with gas mole fraction.

sults for low GOR systems. For higher GOR systems (e.g., greater than 2,000 scf/STB), their GOR equation provides more realistic results; therefore, when using the Dindoruk and Christman method, their equation for solution GOR is recommended. For calculating bubblepoint pressure, this equation must be solved with numerical methods because of its formulation. Correlations proposed by Owolabi<sup>33</sup> and Hasan *et al.*<sup>43</sup> are undefined at pressures less than 55 psia, while Al-Marhoun's<sup>34</sup> method, published in 1985, has an upper pressure limit of 5,348 psia because of the formulation of the equations.

In summary, correlations are often incorporated into computer programs in which they can easily be used for conditions outside the range intended for the method. Some methods are well behaved and provide reasonable results when extrapolated. Other methods should only be used within the bounds defined by the data used in the development of the correlation.

#### 6.4 Nonhydrocarbon Gas Effects

Nonhydrocarbon gases typically found in crude oil systems are nitrogen, carbon dioxide, and hydrogen sulfide. The bubblepoint pressure correlations (with the exception of Owolabi,<sup>33</sup> Al-

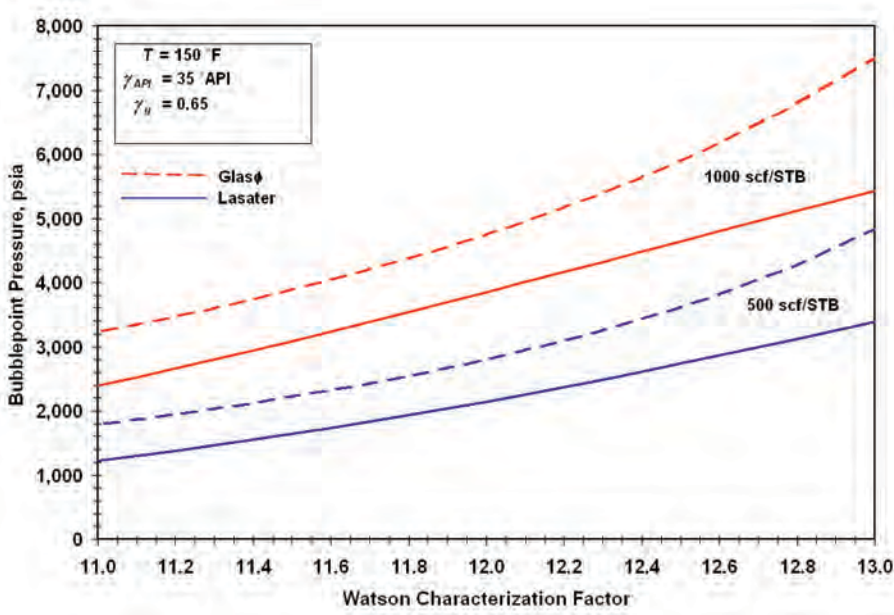


Fig. 6.9—Effect of characterization factor on bubblepoint pressure.

Marhoun,<sup>34,36</sup> and Dokla and Osman<sup>39</sup>) were developed with crude oil systems that did not contain significant amounts of impurities in the gas phase. Work by Jacobson,<sup>80</sup> Glasø,<sup>12</sup> and Owolabi point out the need for procedures to modify the calculated bubblepoint pressure for these impurities. Nitrogen does not readily dissolve in crude oil, resulting in an increase in bubblepoint pressure. On the other hand, carbon dioxide and hydrogen sulfide are more soluble in crude oil than natural gas, which has the effect of lowering bubblepoint pressure. Jacobson evaluated 110 crude oil PVT samples containing up to 14% nitrogen and found that a correction factor need only be based on the nitrogen content of the gas and the temperature of the mixture. An equation to account for the effects of nitrogen on bubblepoint pressure was developed.

$$\frac{P_{bN_2}}{P_{bh}} = 1.1585 + 2.86 y_{N_2} - 1.07 \times 10^{-3} T \dots\dots\dots (6.7)$$

Glasø examined the effects of nitrogen, carbon dioxide, and hydrogen sulfide on bubblepoint pressure and developed corrections for each impurity. The correction for nitrogen content is a function of nitrogen content in the gas, temperature, and crude oil gravity.

$$\frac{P_{bN_2}}{P_{bh}} = 1.0 + [(-2.65 \times 10^{-4} \gamma_{API} + 5.5 \times 10^{-3})T + (0.0931 \gamma_{API} - 0.8295)] y_{N_2} \\ + [(1.954 \times 10^{-11} \gamma_{API}^{4.699})T + (0.027 \gamma_{API} - 2.366)] y_{N_2}^2 \dots\dots\dots (6.8)$$

The correction for carbon dioxide is a function of carbon dioxide content and temperature,

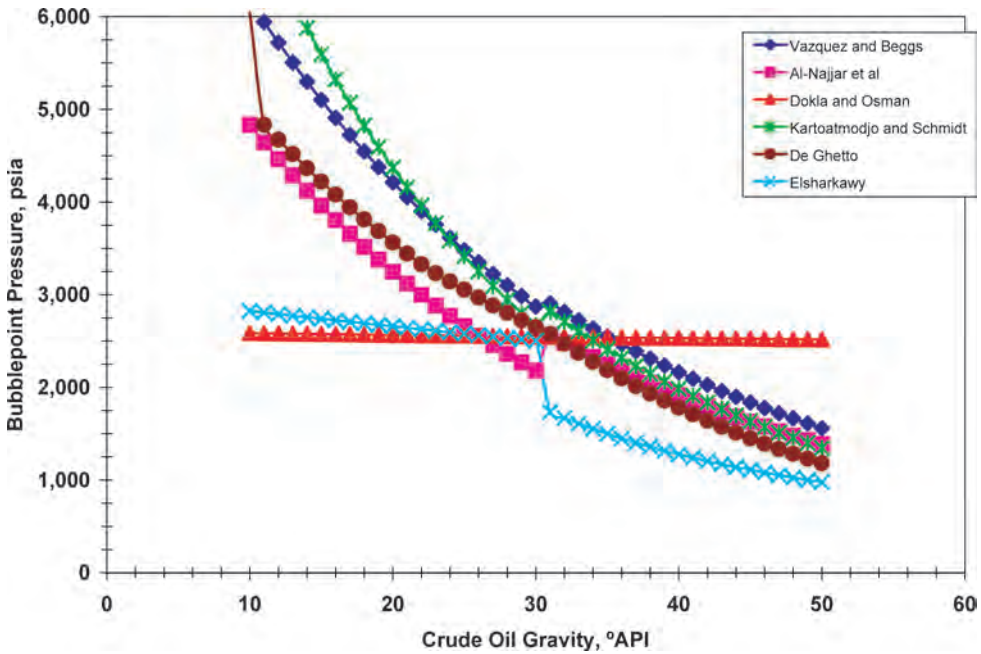


Fig. 6.10—Example of correlation discontinuities—API gravity.

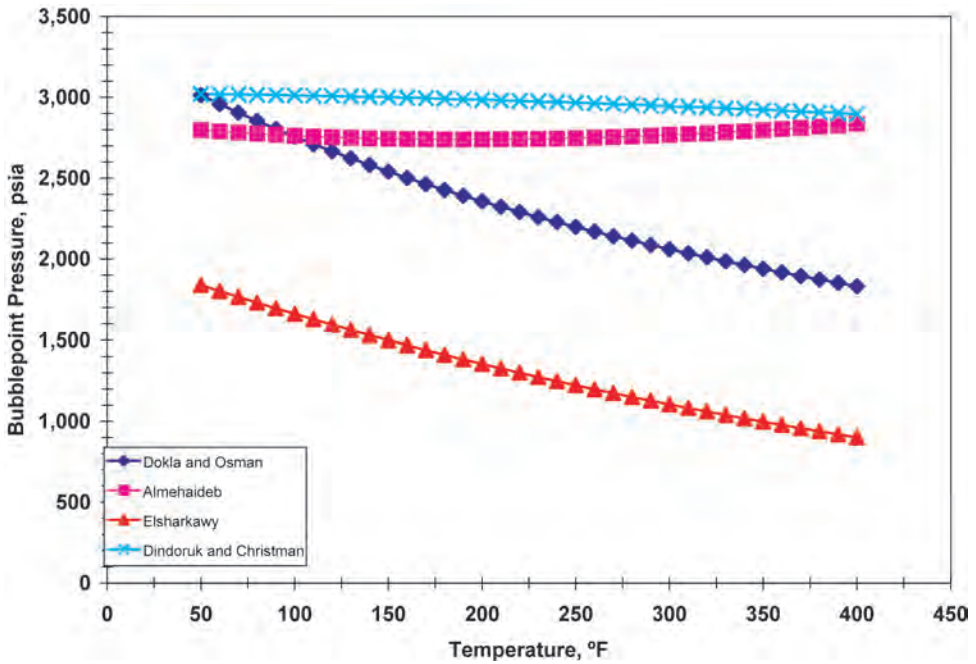


Fig. 6.11—Correlations exhibiting nonphysical trends with temperature.

$$\frac{P_{bCO_2}}{P_{bh}} = 1.0 - 693.8 y_{CO_2} T^{-1.553}, \dots\dots\dots (6.9)$$



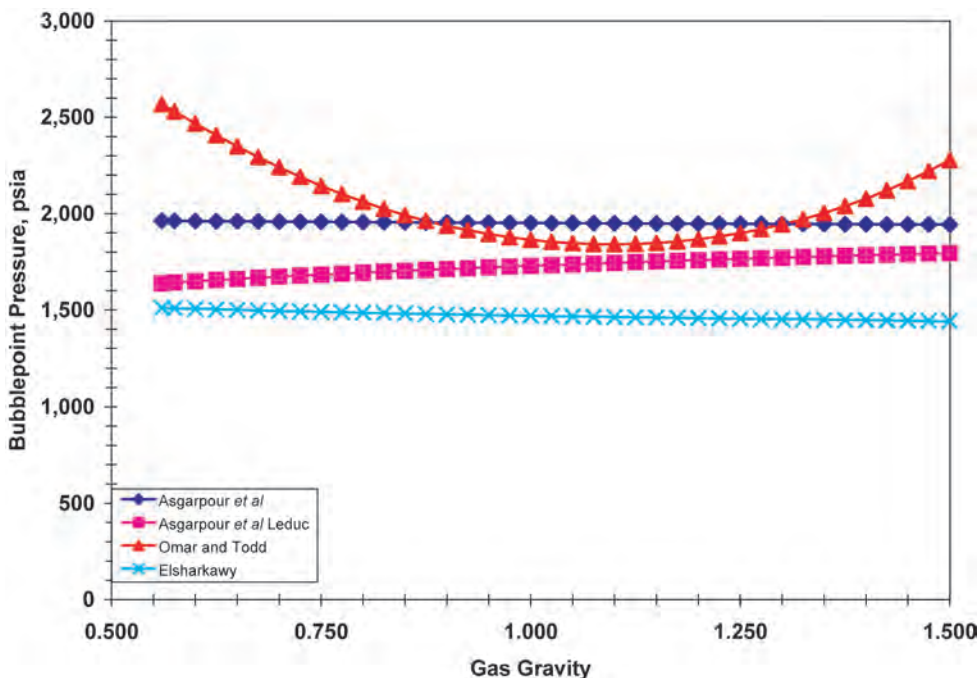


Fig. 6.12—Correlations exhibiting nonphysical trends with solution gas gravity.

while the correction for hydrogen sulfide was found to be a function of hydrogen sulfide content in the surface gas and crude oil gravity.

$$\frac{P_{bH_2S}}{P_{bh}} = 1.0 - (0.9035 + 0.0015 \gamma_{API}) y_{H_2S} + 0.019 (45 - \gamma_{API}) y_{H_2S}^2 \dots \dots \dots (6.10)$$

Figs. 6.13 through 6.15 depict these corrections. Owolabi found that Jacobson’s method was superior for correcting the calculated bubblepoint pressure for the nitrogen content in Cook Inlet crude oil systems. Jacobson’s method was derived from measured data containing less than 14% nitrogen, while Glasø’s data covered systems with nearly 20% nitrogen. Glasø’s correction factors for carbon dioxide and hydrogen sulfide used measured data containing impurities of 20 and 40%, respectively.

**6.5 Solution GOR**

This property is determined by rearranging the equations for calculating bubblepoint pressure as discussed in Secs. 6.3 and 6.4.

**6.6 Formation Volume Factor**

The oil FVF relates the volume of oil at stock-tank conditions to the volume of oil at elevated pressure and temperature. Values typically range from approximately 1.0 bbl/STB for crude oil systems containing little or no solution gas to nearly 3.0 bbl/STB for highly volatile oils. Tables A-3 and A-4 summarize thirty correlations for saturated crude oil systems that have been identified in the literature. For saturated systems, gas is liberated as pressure is reduced below the bubblepoint. This results in a corresponding shrinkage in oil volume, as shown for all of the methods in Fig. 6.16. The rather large number of correlations preclude the identification of individual methods. The results show a relatively narrow range of oil FVF values determined

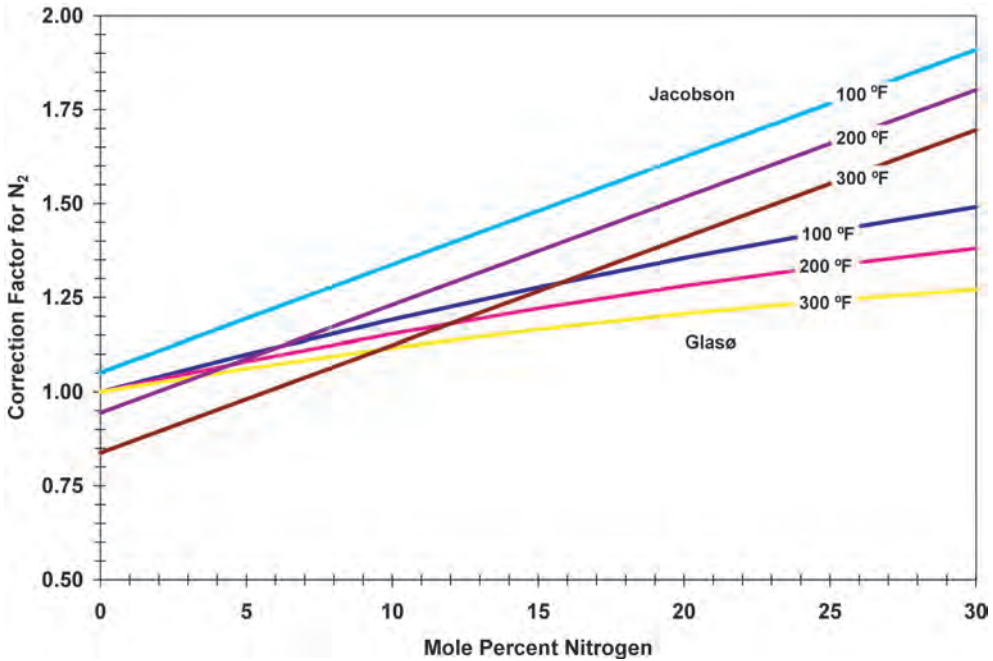


Fig. 6.13—Nitrogen bubblepoint pressure correlations factor.

by all of the correlation methods. These correlations determine FVF based on the following function.

$$B_{ob} = f(T, \gamma_{API}, \gamma_g, R_s) \dots\dots\dots (6.11)$$

Solution GOR accounts for the largest change in FVF. Increases in temperature, crude oil gravity, and gas gravity provide a small increase in FVF.

Recent studies<sup>75-77,81</sup> provide statistical analyses for bubblepoint oil FVF correlations and provide recommendations based on their findings; however, none of these references examines the full set of correlations. Al-Shammasi<sup>2</sup> compiled a databank of 1,345 data points from the literature that was combined with 133 data points from the GeoMark Research database<sup>68</sup> to yield a total of 1,478 data points. These data were used to rank the accuracy of the oil FVF correlations. The ranges and distribution of these data can be found in Table 6.5 and Fig. 6.3. Table 6.7 summarizes correlation performance. The results are sorted by absolute average relative error, which provides a means to rank the methods.

The data were further grouped to examine the impact of crude oil gravity and GOR on consistency of the correlations. Methods proposed by Al-Marhoun,<sup>4</sup> Al-Shammasi,<sup>2</sup> Farshad *et al.*,<sup>5</sup> and Kartoatmodjo and Schmidt<sup>6-8</sup> showed reliability over a wide range of conditions. The author has experienced good results from both the Standing<sup>50</sup> and Glasø<sup>12</sup> correlations, although they may not have ranked highly with this data set. Fig. 6.17 summarizes these methods.

The correlations were tested against the other parameters used in the derivation of the methods: crude oil API gravity, gas gravity, and temperature. Several methods use multiple equations valid for specified ranges of crude oil gravity. Discontinuities, which are summarized in Fig. 6.18, can result from the use of this technique to develop a correlation. Furthermore, FVF should increase with increasing API gravity. Fig. 6.18 shows methods that exhibit nonphysical results.

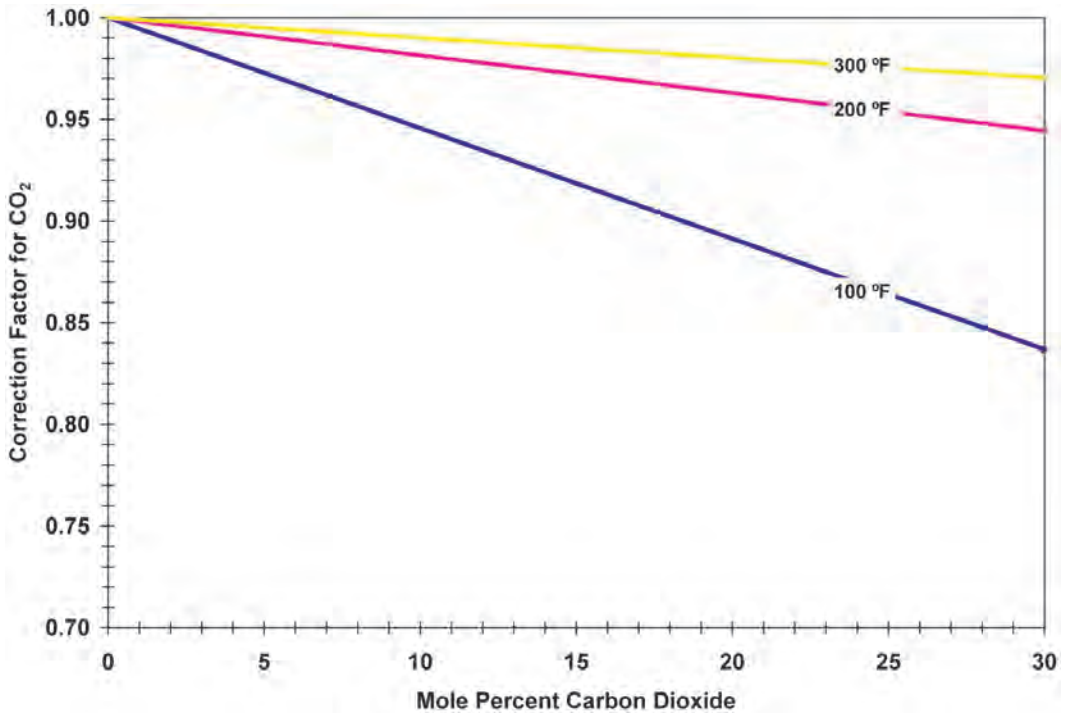


Fig. 6.14—Carbon dioxide bubblepoint pressure correction factor.

FVF should increase with increasing solution gas gravity. Fig. 6.19 shows that a number of correlations predict results opposite to this trend. Correlations listed in Figs. 6.18 and 6.19 should be used with caution to avoid problems associated with discontinuities or nonphysical behavior. Limitations imposed by data used in the correlation’s development should be followed.

**6.7 Isothermal Compressibility**

The isothermal compressibility of undersaturated oil is defined as

$$c_o = -\frac{1}{V} \left( \frac{\partial V}{\partial p} \right)_T = -\frac{1}{B_o} \left( \frac{\partial B_o}{\partial p} \right)_T, \dots\dots\dots (6.12)$$

which reflects the change in volume with change in pressure under constant temperature conditions. Below the bubblepoint pressure, oil isothermal compressibility is defined from oil and gas properties to account for gas coming out of solution. The corresponding saturated oil compressibility is

$$c_o = -\frac{1}{B_o} \left[ \left( \frac{\partial B_o}{\partial p} \right)_T - B_g \left( \frac{\partial R_s}{\partial p} \right)_T \right] \dots\dots\dots (6.13)$$

Above bubblepoint pressure, oil volume changes as a function of isothermal compressibility only. Tables A-5 and A-6 summarize the correlations developed to predict this property. Oil FVFs for undersaturated crude oil are determined as a function of bubblepoint FVF, isothermal compressibility, and pressure above bubblepoint from

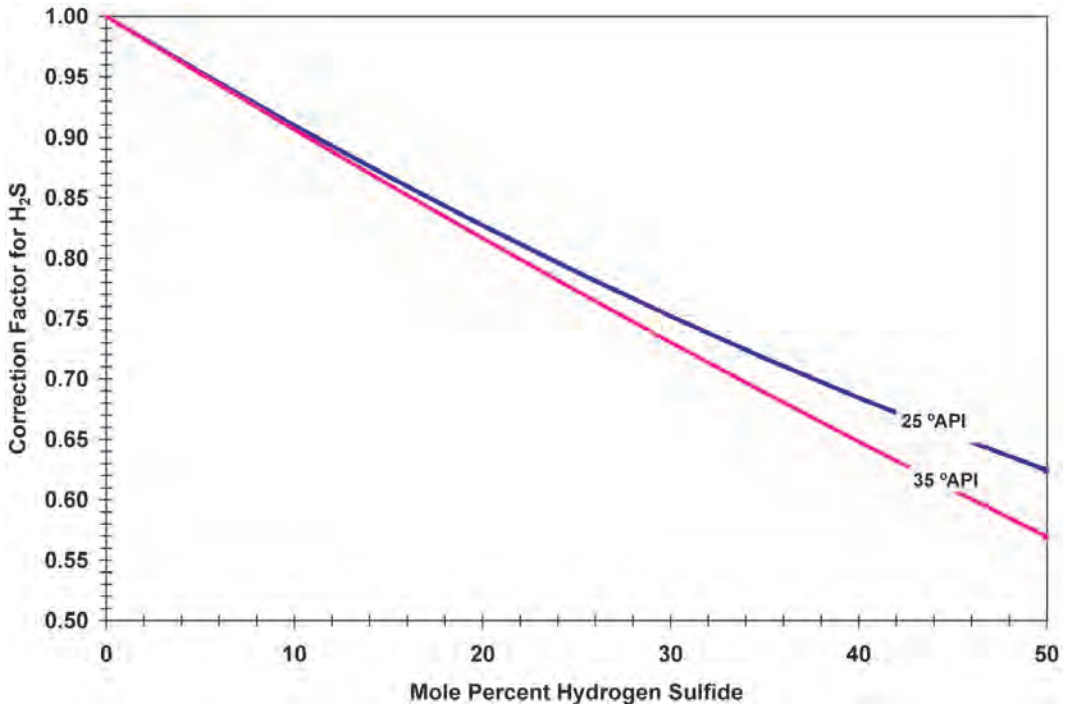


Fig. 6.15—Hydrogen sulfide bubblepoint pressure correction factor.

$$B_o = B_{ob} e^{[c_o(p_b - p)]} \dots\dots\dots (6.14)$$

A total of 141 data points were available from the GeoMark PVT database.<sup>68</sup> Geographically, these samples were obtained from the Gulf of Mexico and the Gulf of Suez. **Table 6.8** provides a summary of the data. This data was used to evaluate and rank the performance of the isothermal compressibility correlations. **Table 6.9** provides the results. Data in the table have been sorted by absolute average relative error, which provides a means to rank the methods. **Fig. 6.20** graphically shows isothermal compressibility vs. pressure.

Methods proposed by Standing<sup>13</sup> and Ahmed<sup>52</sup> exhibit excessive changes in compressibility compared with the other methods and can determine results that are physically unreal. **Fig. 6.21** shows how isothermal compressibility changes with crude oil gravity. As oil gravity increases, isothermal compressibility should increase. Results predicted by Ahmed, Al-Marhoun,<sup>4</sup> De Ghetto *et al.*,<sup>44,45</sup> and Elsharkawy and Alikhan<sup>47</sup> do not properly model the phenomena. De Ghetto *et al.* proposed a method that uses several equations covering various API gravity ranges. This technique results in discontinuities in predicted properties as the equations change. **Fig. 6.22** shows the change in isothermal compressibility with solution GOR. Varying this property also results in varying the bubblepoint pressure. To illustrate this effect, isothermal compressibility is determined at 1,000 psi above a variable saturation pressure. Results from methods proposed by Petrosky and Farshad,<sup>10,11</sup> Kartoatmodjo and Schmidt,<sup>6-8</sup> and Dindoruk and Christman<sup>9</sup> are undefined for solution GORs of zero. Methods proposed by Ahmed, Al-Marhoun, and Kartoatmodjo produce unphysical results with changing GOR.

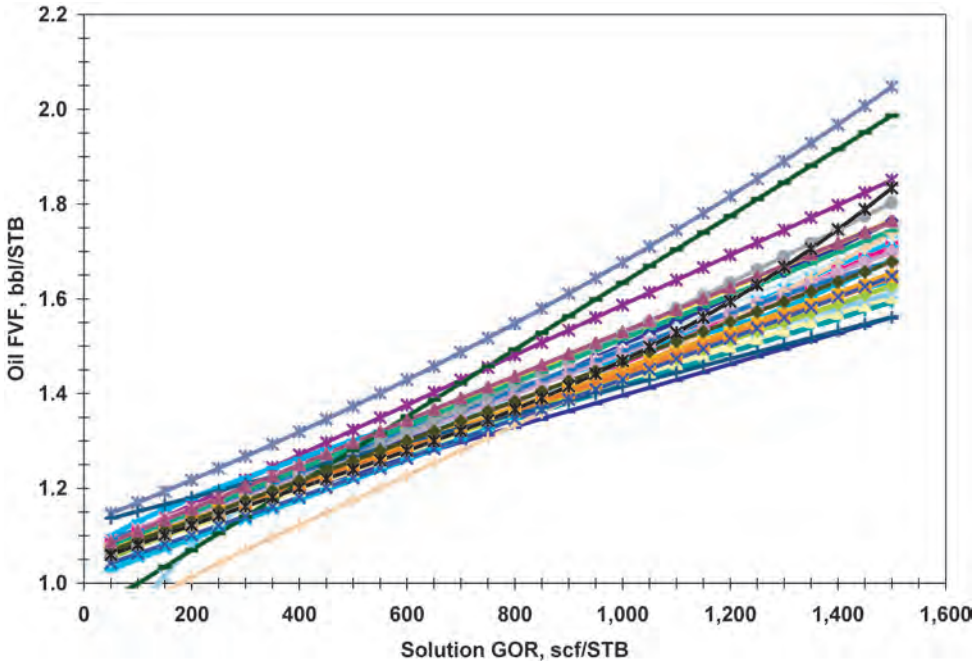


Fig. 6.16—Gas saturated oil FVF correlation results vs. solution GOR.

**6.8 Density**

The physical property density is the ratio between mass and volume. The density of crude oil can be determined from specific gravity of the crude oil, the solution gas gravity, the solution GOR, and the oil FVF.<sup>82</sup> Under any condition, density will be defined by

$$\rho_o = \frac{W_o + W_g}{V_o + \Delta V_g} \dots\dots\dots (6.15)$$

Stated more rigorously with PVT properties, this relationship becomes

$$\rho_o = \frac{62.42796 \gamma_o + 0.0136 \gamma_g R_s}{B_o} \dots\dots\dots (6.16)$$

This is valid for all pressure and temperature conditions for which the PVT properties are determined. As expressed, this equation provides density with the units of lbm/ft<sup>3</sup>.

**6.9 Viscosity**

Absolute viscosity provides a measure of a fluid’s internal resistance to flow. Any calculation involving the movement of fluids requires a value of viscosity. This parameter is required for conditions ranging from surface gathering systems to the reservoir. Therefore, correlations can then be expected to evaluate viscosity for temperatures ranging from 35 to 300°F. Fluids that exhibit viscosity behavior independent of shear rate are described as being Newtonian fluids. Viscosity correlations discussed in this chapter apply to Newtonian fluids.

The principal factors affecting viscosity are oil composition, temperature, dissolved gas, and pressure. Typically, oil composition is described by API gravity only. As discussed earlier in

TABLE 6.7—STATISTICAL SUMMARY OF OIL FVF CORRELATION PERFORMANCE

Correlation	ARE* (%)	Standard Deviation (%)	AARE** (%)	Standard Deviation (%)
Al-Marhoun <sup>4</sup>	0.03	2.83	1.74	2.23
Al-Shammasi	0.17	2.85	1.79	2.22
Farshad <i>et al.</i>	-0.84	2.81	1.95	2.18
Kartoatmodjo and Schmidt	-0.49	2.91	1.97	2.20
Al-Marhoun <sup>3b</sup>	-0.58	3.11	2.11	2.36
Velarde	-1.44	3.43	2.42	2.82
Al-Najjar <i>et al.</i>	0.80	3.34	2.44	2.43
Petrosky	0.99	3.76	2.52	2.97
Standing	1.08	3.73	2.54	2.93
Elsharkawy	1.54	3.29	2.55	2.59
Elam	1.80	3.86	2.69	3.30
Glasø	-1.52	3.53	2.86	2.56
Levitan and Murtha	-0.44	4.45	3.10	3.22
Asgarpour <i>et al.</i> Leduc	1.32	4.37	3.24	3.22
Owolabi CIB	-1.87	4.34	3.31	3.37
Abdul-Majeed and Salman	-1.62	5.17	3.35	4.26
Omar and Todd	-1.79	4.79	3.35	3.86
Labedi	1.68	4.12	3.42	2.86
Vazquez and Beggs	-2.49	5.05	3.61	4.33
Dokla and Osman	-0.21	4.85	3.66	3.18
Asgarpour <i>et al.</i> Cardium	-1.89	4.30	3.70	2.90
Ahmed	-2.22	6.24	3.80	5.42
Owolabi ANS	-2.73	4.88	3.99	3.92
Dindoruk and Christman	0.96	6.33	4.02	4.98
Almehaideb	0.02	5.37	4.24	3.29
Obomanu and Okpobiri	2.61	5.21	4.26	3.97
Al-Marhoun <sup>3d</sup>	-0.46	6.30	4.39	4.54
Asgarpour <i>et al.</i> Nisku	-2.40	5.95	4.76	4.30
Khairy <i>et al.</i>	2.82	6.48	5.42	4.54
Macary <i>et al.</i>	8.39	6.59	8.78	6.05

$$*ARE = \text{average relative error} = \frac{100}{N} \sum_{i=1}^N \frac{X_{i,calc} - X_{i,meas}}{X_{i,meas}}$$

$$**AARE = \text{average absolute relative error} = \frac{100}{N} \sum_{i=1}^N \left| \frac{X_{i,calc} - X_{i,meas}}{X_{i,meas}} \right|$$

this chapter, this is a shortcoming. The use of both the API gravity and the Watson characterization factor provides a more complete description of the oil. **Table 6.10** shows an example for a 35° API gravity oil that points out the relationship of viscosity and chemical makeup recalling a characterization factor of 12.5 is reflective of highly paraffinic oils, while a value of 11.0 is indicative of a naphthenic oil. Clearly, chemical composition, in addition to API gravi-

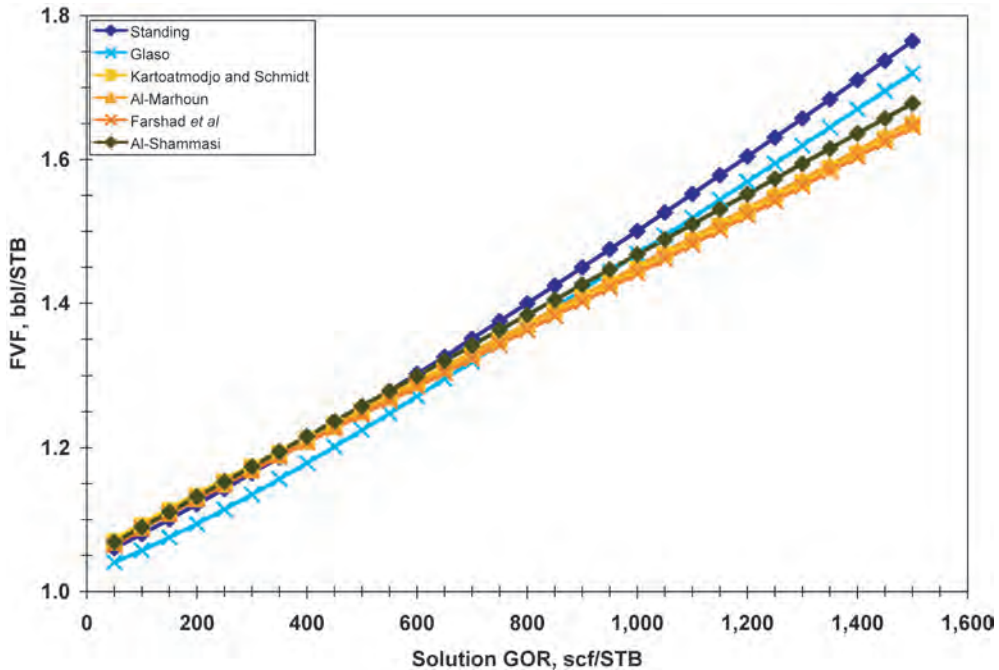


Fig. 6.17—Selected oil FVF correlations.

ty, plays a role in the viscosity behavior of crude oil. Fig. 6.23 shows the effect of crude oil characterization factor on dead oil viscosity. In general, viscosity characteristics are predictable. Viscosity increases with decreases in crude oil API gravity (assuming a constant Watson characterization factor) and decreases in temperature. The effect of solution gas is to reduce viscosity. Above saturation pressure, viscosity increases almost linearly with pressure. Fig. 6.24 provides the typical shape of reservoir oil viscosity at constant temperature.

Viscosity calculations for live reservoir oils require a multistep process involving separate correlations for each step of the process. Dead or gas-free oil viscosity is determined as a function of crude oil API gravity and temperature. The viscosity of the gas saturated oil is found as a function of dead oil viscosity and solution GOR. Undersaturated oil viscosity is determined as a function of gas saturated oil viscosity and pressure above saturation pressure.

Figs. 6.25 and 6.26 summarize all of the dead oil viscosity correlations described in Tables A-7 and A-8. The results provided by Fig. 6.26 show that the method proposed by Standing<sup>94</sup> is not suited for crude oil with gravities less than 28°API. Al-Kafaji *et al.*'s<sup>59</sup> method is unsuited for crudes with gravities less than 15°API, while Bennison's<sup>62</sup> method, developed primarily for low API gravity North Sea crudes, is not suited for gravities greater than 30°API.

Fig. 6.27 provides an annotated list of the most commonly used methods. The results illustrate the trend for dead oil viscosity and temperature. As temperature decreases, viscosity increases. At temperatures below 75°F, the method of Beggs and Robinson<sup>19</sup> significantly overpredicts viscosity while Standing's method actually shows a decrease in viscosity. These tendencies make these methods unsuitable for use in the temperature range associated with pipelines. Beal's<sup>20,21</sup> method was developed from observations of dead oil viscosity at 100 and 200°F and has a tendency to underpredict viscosity at high temperature. Dead oil viscosity correlations are somewhat inaccurate because they fail to take into account the chemical nature of the crude oil. Only methods developed by Standing<sup>13</sup> and Fitzgerald<sup>15,16,61</sup> take into account the

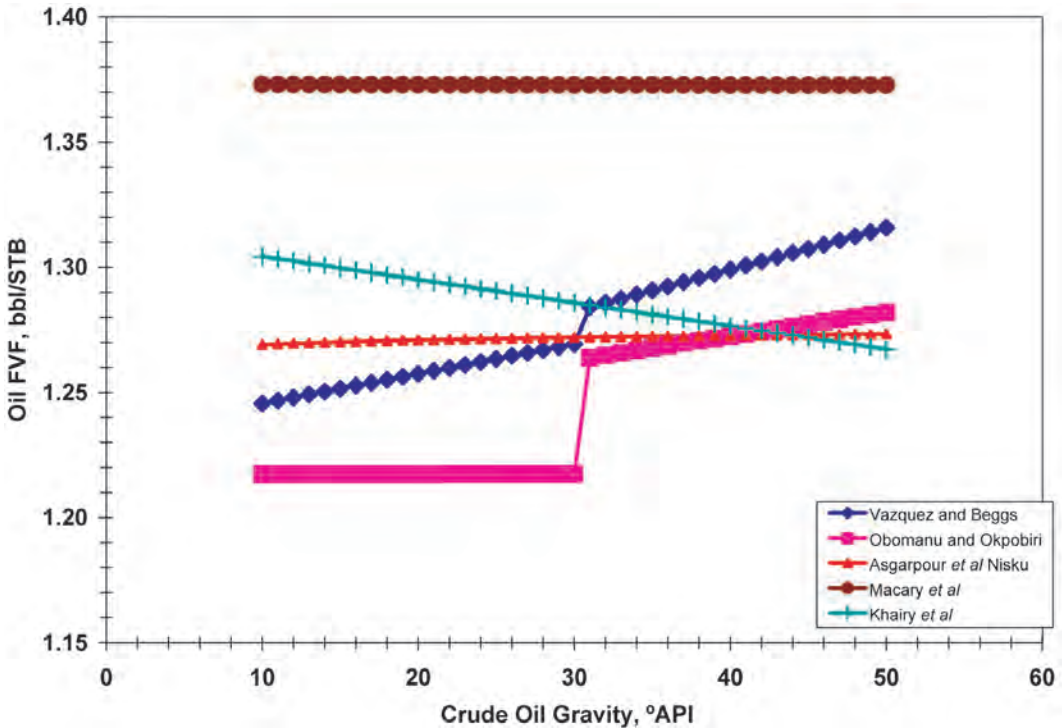


Fig. 6.18—Oil FVF vs. crude oil API gravity.

chemical nature of crude oil through use of the Watson characterization factor. Fitzgerald’s method was developed over a wide range of conditions, as detailed in Tables A-7 and A-8, and is the most versatile method suitable for general use of the correlations listed in that table. Fig. 6.28 provides the area of applicability for Fitzgerald’s method.

Andrade’s<sup>55,56</sup> method is based on the observation that the logarithm of viscosity plotted vs. reciprocal absolute temperature forms a linear relationship from somewhat above the normal boiling point to near the freezing point of the oil, as Fig. 6.29 shows. Andrade’s method is applied through the use of measured dead oil viscosity data points taken at low pressure and two or more temperatures. Data should be acquired at temperatures over the range of interest. This method is recommended when measured dead oil viscosity data are available.

Tables A-9 and A-10 provide a complete summary of the bubblepoint oil viscosity methods. Correlations for bubblepoint oil viscosity typically take the form proposed by Chew and Connally.<sup>17</sup> This method forms a correlation with dead oil viscosity and solution GOR where A and B are determined as functions of solution GOR.

$$\mu_{ob} = A\mu_{od}^B \dots\dots\dots (6.17)$$

Figs. 6.30 and 6.31 shows the correlations for the A and B parameters developed by various authors. Fig. 6.32 shows the effect of the A and B correlation parameters on the prediction of viscosity. This plot was developed with a dead oil viscosity value of 1.0 cp so the effect of solution GOR could be examined. Correlations proposed by Labedi,<sup>31,57</sup> Khan *et al.*,<sup>64</sup> and Almeida<sup>46</sup> do not specifically use dead oil viscosity and solution GOR and were not included in this plot.



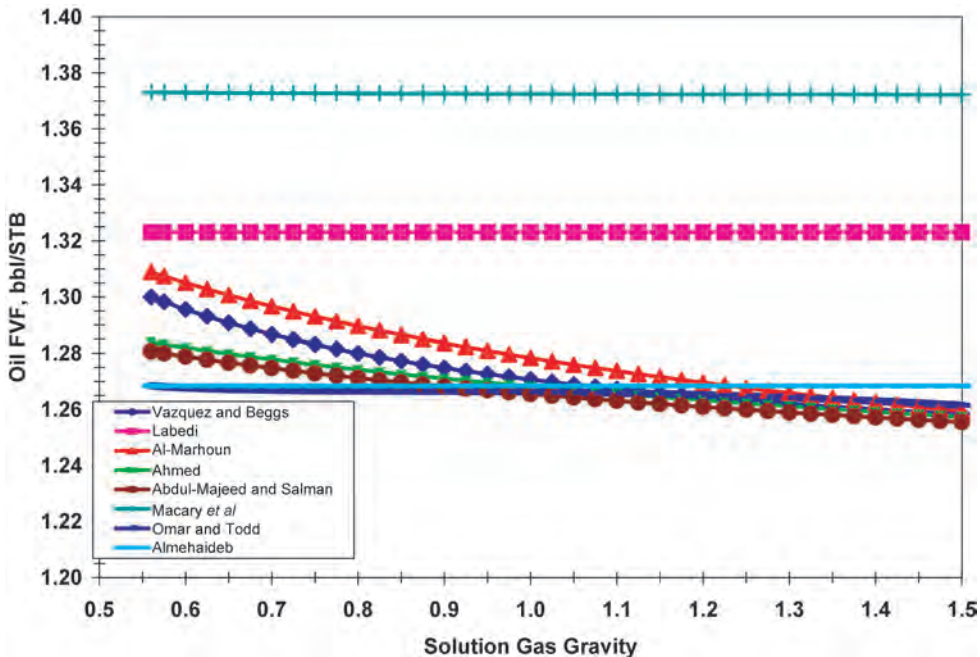


Fig. 6.19—Oil FVF vs. solution gas gravity.

Property	Minimum	Maximum	Average
Bubblepoint pressure, psia	430	10,326	4,239
Temperature, °F	90	266	172
Isothermal compressibility, $\text{psi}^{-1} \times 10^{-6}$	5.17	38.70	13.21
Solution GOR, scf/STB	77	3,448	1,045
Crude oil gravity, °API	15.5	41.9	31.7
Gas specific gravity	0.60	1.202	0.774

When pressure increases above bubblepoint, the oil becomes undersaturated. In this region, oil viscosity increases nearly linearly with pressure. Tables A-11 and A-12 provide correlations for modeling undersaturated oil viscosity. Fig. 6.33 presents a visual comparison of the methods.

### 6.10 Surface Tension

Interfacial or surface tension exists when two phases are present. These phases can be gas/oil, oil/water, or gas/water. Surface tension is the force that holds the surface of a particular phase together and is normally measured in dynes/cm. The surface tension between gas and crude oil ranges from near zero to approximately 34 dynes/cm. It is a function of pressure, temperature, and the composition of each phase. Two forms of correlations for calculating gas/oil surface tension have been developed. The first form is a pseudocompositional black oil approach. Two components, gas and oil, are identified, and techniques used with compositional models are used to calculate surface tension. The second approach uses empirical correlations to determine surface tension. Black oil correlations may provide less than accurate results because of the

**TABLE 6.9—STATISTICAL SUMMARY OF ISOTHERMAL COMPRESSIBILITY CORRELATION PERFORMANCE**

Correlation	ARE* (%)	Standard Deviation (%)	AARE** (%)	Standard Deviation (%)
Dindoruk and Christman	-3.45	15.60	11.35	11.21
Petrosky	6.76	17.26	12.44	13.72
Farshad <i>et al.</i>	-5.08	18.15	15.35	10.87
Almehaideb	0.72	28.05	17.12	22.19
Labedi	8.82	25.59	18.91	19.31
Agip	5.84	25.89	19.19	18.26
Vazquez and Beggs	12.73	25.00	21.30	18.21
Calhoun	10.08	25.61	21.94	16.54
Al-Mahoun	10.21	41.38	22.10	36.41
Elsharkawy	-10.21	27.17	22.90	17.75
Trube	-12.21	30.65	27.43	18.22
Kartoatmodjo and Schmidt	-15.86	31.74	27.90	21.84
De Ghetto	18.86	42.37	33.27	32.23
Standing	46.60	34.96	48.75	31.85
Ahmed	30.32	99.44	69.80	76.86

\*ARE = average relative error =  $\frac{100}{N} \sum_{i=1}^N \frac{X_{i\text{calc}} - X_{i\text{meas}}}{X_{i\text{meas}}}$

\*\*AARE = average absolute relative error =  $\frac{100}{N} \sum_{i=1}^N \left| \frac{X_{i\text{calc}} - X_{i\text{meas}}}{X_{i\text{meas}}} \right|$

simplified characterization of the crude oil. Generally, the heavy end components of a crude oil may be made of asphaltic and surface active materials that have a measurable effect on surface tension.

With the compositional approach, surface tension is determined from the following equation proposed by Weinaug and Katz.<sup>83</sup>

$$\sigma_{go}^{1/4} = \sum_{i=1}^N P_i \left( x_i \frac{\rho_o}{M_o} - y_i \frac{\rho_g}{M_g} \right), \dots\dots\dots (6.18)$$

where the density terms are defined with units of g/cm<sup>3</sup>. *P<sub>i</sub>* is the parachor of each component. This property is a characteristic of pure components and is determined from surface tension measurements where the density of the gas and liquid phases are known. Fig. 6.34 provides a relationship between parachors and molecular weight.

In 1973, Ramey<sup>85</sup> proposed a pseudocompositional method for calculating surface tension. The two components are oil and gas. Gas is free to dissolve in the oil phase, and oil is free to vaporize in the gas phase, which makes this method more versatile than the other methods discussed in this chapter. The Weinaug-Katz equation is modified as

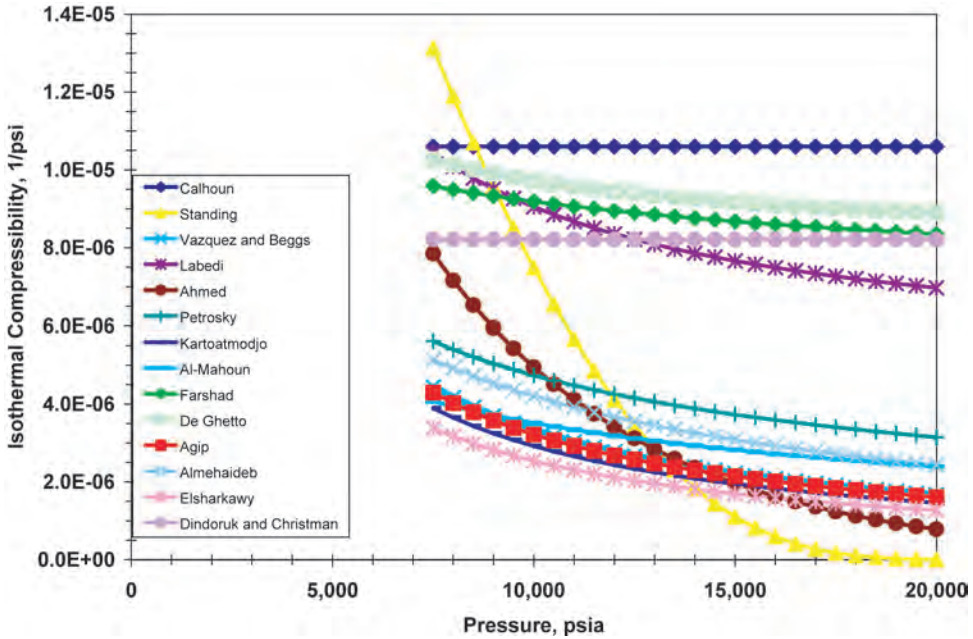


Fig. 6.20—Isothermal compressibility vs. pressure.

$$\sigma_{go}^v = P_o \left( x_o \frac{\rho_o}{M_{og}} - y_o \frac{\rho_g}{M_{go}} \right) - P_g \left( x_g \frac{\rho_o}{M_{og}} - y_g \frac{\rho_g}{M_{go}} \right), \dots\dots\dots (6.19)$$

where the oil mole fraction in the oil phase is defined as

$$x_o = \left[ 1 + \frac{7.521 \times 10^{-6} R_s M_o}{\gamma_o} \right]^{-1}, \dots\dots\dots (6.20)$$

and the gas mole fraction in oil is

$$x_g = 1 - x_o. \dots\dots\dots (6.21)$$

The mole fraction of oil and gas in the gas phase is

$$y_o = \left[ 1 + \frac{7.521 \times 10^{-6} M_o}{\gamma_o r_v} \right]^{-1}, \dots\dots\dots (6.22)$$

and

$$y_g = 1 - y_o. \dots\dots\dots (6.23)$$

The traditional assumption used with the black oil approach is that the oil vaporized in the gas phase,  $r_v$ , is zero. In this instance,  $y_o=0$  and  $y_g=1$ , which simplifies Eqs. 6.22 and 6.23.

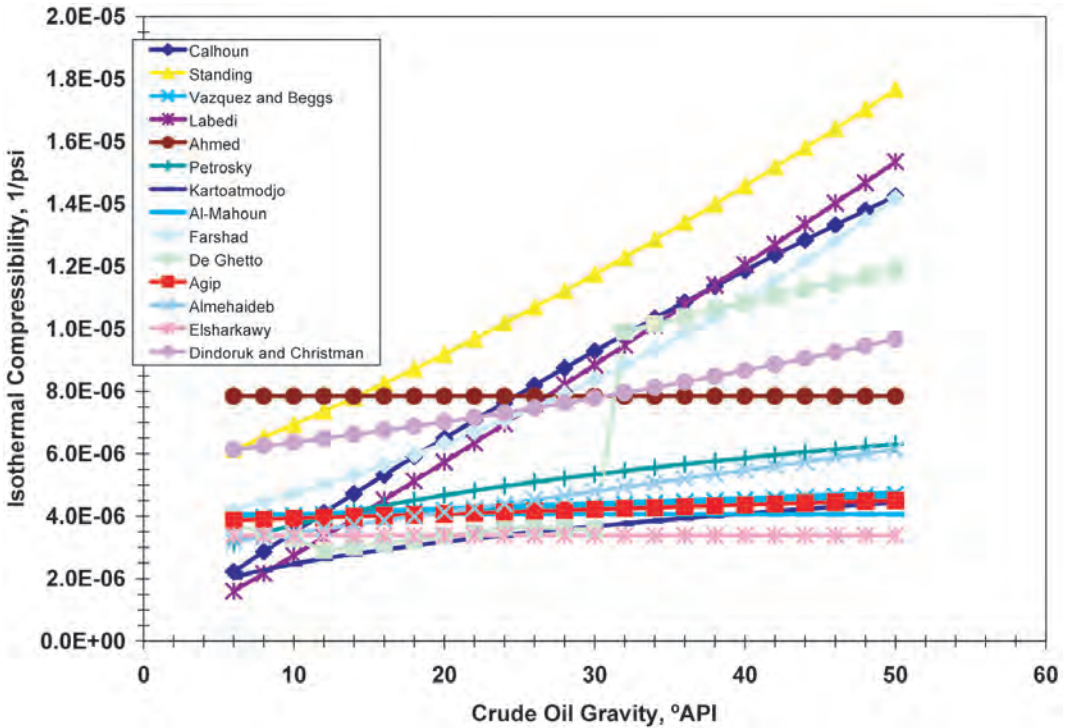


Fig. 6.21—Isothermal compressibility vs. crude oil gravity.

The average molecular weights of the oil and gas phases are defined as

$$M_{og} = x_o M_o + x_g M_g, \dots\dots\dots (6.24)$$

and

$$M_{go} = y_o M_o + y_g M_g \dots\dots\dots (6.25)$$

Liquid and gas densities are defined with units of g/cm<sup>3</sup>:

$$\rho_o = \frac{\gamma_o + 2.179 \times 10^{-4} \gamma_g R_s}{B_o}, \dots\dots\dots (6.26)$$

and

$$\rho_g = 9.3184 \times 10^{-2} \frac{p M_{go}}{ZT} \dots\dots\dots (6.27)$$

Whitson and Brulé<sup>13</sup> suggested the following parachor equations, which reproduce the graphical methods suggested by Ramey:

$$P_o = (2.376 + 0.0102 \gamma_{API}) M_o, \dots\dots\dots (6.28)$$

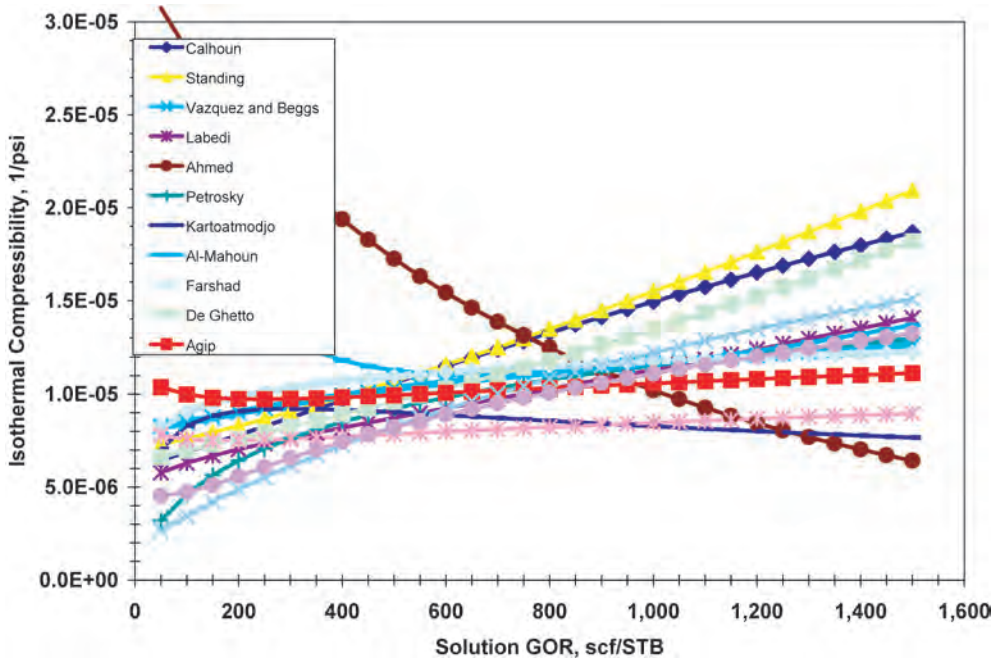


Fig. 6.22—Isothermal compressibility vs. solution GOR.

and

$$P_g = 25.2 + 2.86 M_g \dots\dots\dots (6.29)$$

In 1989, Asheim<sup>86</sup> presented another pseudocompositional correlation for surface tension. With the assumption that no oil vaporizes into the gas phase, the resulting equation is

$$\sigma_{go}^{1/4} = P_o \frac{\gamma_o}{M_o B_o} + 1.493 \times 10^{-3} P_g \left( \frac{R_s}{5.614583 B_o} - \frac{1}{B_g} \right), \dots\dots\dots (6.30)$$

where the gas FVF,  $B_g$ , is defined as

$$B_g = \frac{p_{sc} Z(T + 459.67)}{p(T_{sc} + 459.67)} \dots\dots\dots (6.31)$$

Asheim proposed the following equations to calculate the parachors for the oil and gas phases.

$$P_o = 2.40 M_o + 40 \dots\dots\dots (6.32)$$

$$P_g = 2.79 M_g + 40 \dots\dots\dots (6.33)$$

While this method appears different from that proposed by Ramey, it is identical for the Ramey case in which no oil vaporizes into the gas phase. This method differs from Ramey’s method only by the definition of the oil and gas parachors.

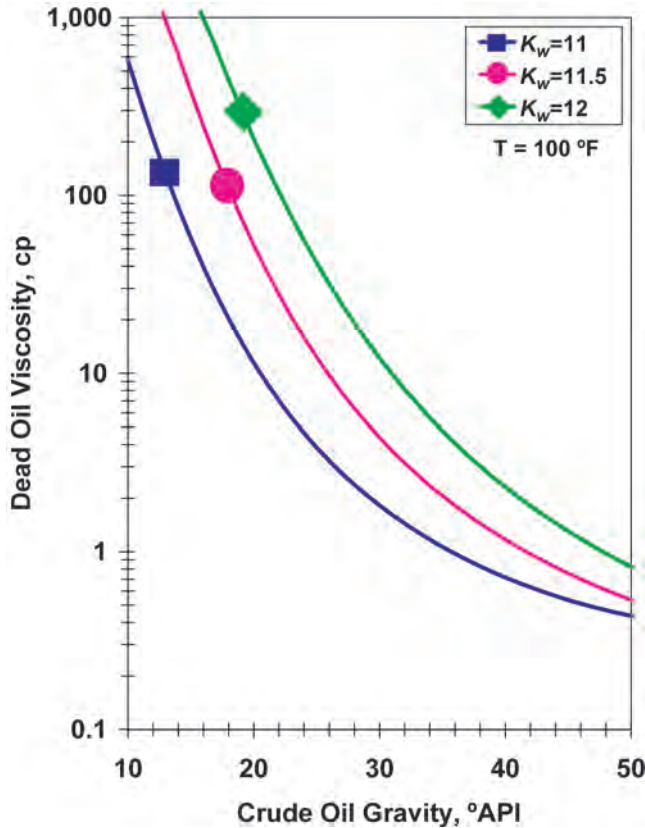


Fig. 6.23—Dead oil viscosity vs. API gravity and Watson characterization factor.

The Baker and Swerdloff<sup>26,27</sup> method was published in 1955. It was presented in the form of graphs for estimating gas/oil surface tension (Fig. 6.35). Equations to calculate the dead oil surface tension at 68 and 100°F are

$$\sigma_{od_{68}} = 39 - 0.2571 \gamma_{API} \dots\dots\dots (6.34)$$

and

$$\sigma_{od_{100}} = 37.5 - 0.2571 \gamma_{API} \dots\dots\dots (6.35)$$

Beggs<sup>87</sup> suggests that for temperatures greater than 100°F, the value calculated for 100°F should be used. Similarly, if the temperature is less than 68°F, the value calculated for 68°F should be used. For intermediate temperatures, surface tension is derived by linear interpolation as described by

$$\sigma_{od} = \sigma_{od_{68}} - \frac{(T - 68)(\sigma_{od_{68}} - \sigma_{od_{100}})}{32} \dots\dots\dots (6.36)$$

TABLE 6.10—VARIATION IN VISCOSITY WITH CHARACTERIZATION FACTOR <sup>50</sup>		
Temperature (°F)	Watson Characterization Factor	Viscosity (cp)
100	11.2	1.3
	11.5	2.0
	11.8	3.0
	12.1	5.5
200	11.2	0.6
	11.5	0.85
	11.8	1.2
	12.1	1.9

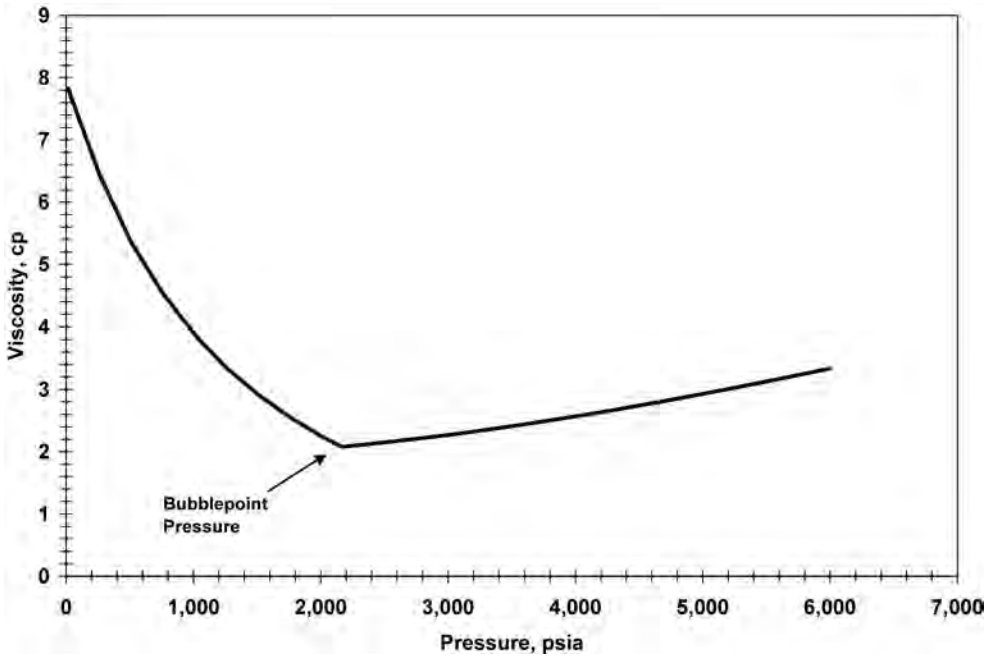


Fig. 6.24—Typical oil viscosity curve.

At pressures greater than atmospheric pressure, gas is dissolved in the oil, which reduces surface tension. Baker and Swerdloff provided the graphical correction factor shown in Fig. 6.36, which can be reproduced mathematically by

$$\left(\frac{\sigma_{go}}{\sigma_{od}}\right) = e^{(-8.6306 \times 10^{-4} p)} \dots\dots\dots (6.37)$$

The live oil surface tension is then derived from

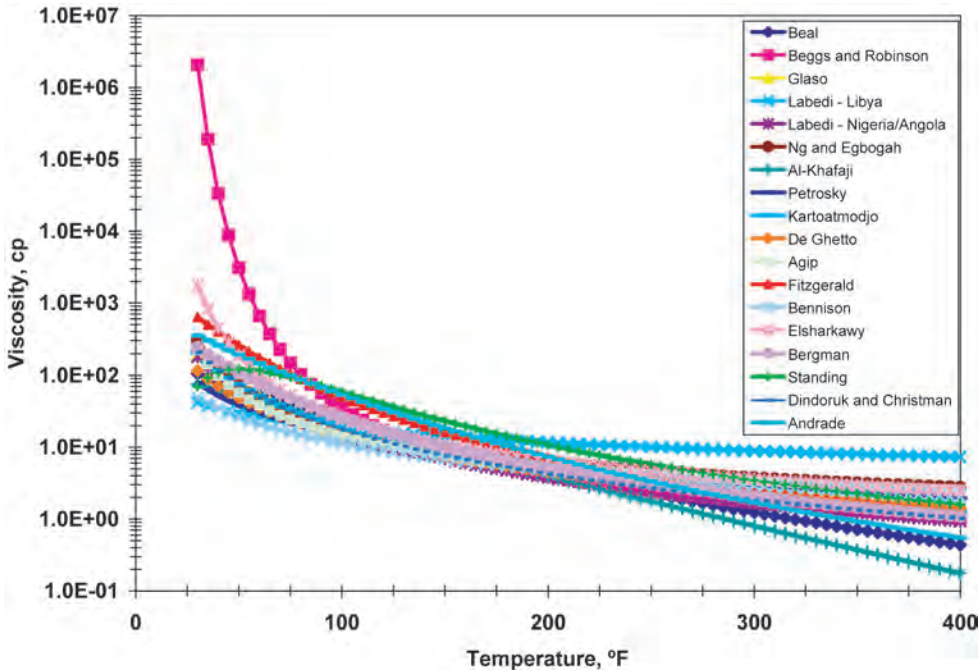


Fig. 6.25—Dead oil viscosity correlations vs. temperature.

$$\sigma_{go} = \sigma_{od} \left( \frac{\sigma_{go}}{\sigma_{od}} \right) \dots\dots\dots (6.38)$$

In 2000, Abdul-Majeed<sup>25</sup> presented an update to Baker and Swerdloff’s correlation. Surface tension data from 18 crude oils covering the temperature range 60 to 130°F was used to derive Eq. 6.39, which Fig. 6.37 shows graphically.

$$\sigma_{od} = (1.17013 - 1.694 \times 10^{-3} T)(38.085 - 0.259 \gamma_{API}) \dots\dots\dots (6.39)$$

Data acquired from 42 crude oil/gas systems was used to develop the live oil correction factor. These data, shown graphically in Fig. 6.38, can be represented by

$$\left( \frac{\sigma_{go}}{\sigma_{od}} \right) = 0.056379 + 0.94362 e^{(-3.8491 \times 10^{-3} R_s)} \dots\dots\dots (6.40)$$

As with the Baker and Swerdloff method, the live oil surface tension is given by Eq. 6.38. Table 6.11 shows the statistics provided by Abdul-Majeed comparing the results of the proposed method with the Baker and Swerdloff method. Fig. 6.39 shows a comparison of the four methods for calculating surface tension.

**6.11 Water-Hydrocarbon Surface Tension**

The surface tension of a water-hydrocarbon system varies from approximately 72 dynes/cm for water/gas systems to 20 to 40 dynes/cm for water/oil systems at atmospheric conditions. In 1973, Ramey<sup>85</sup> published methods to evaluate the surface tension of water-hydrocarbon mix-



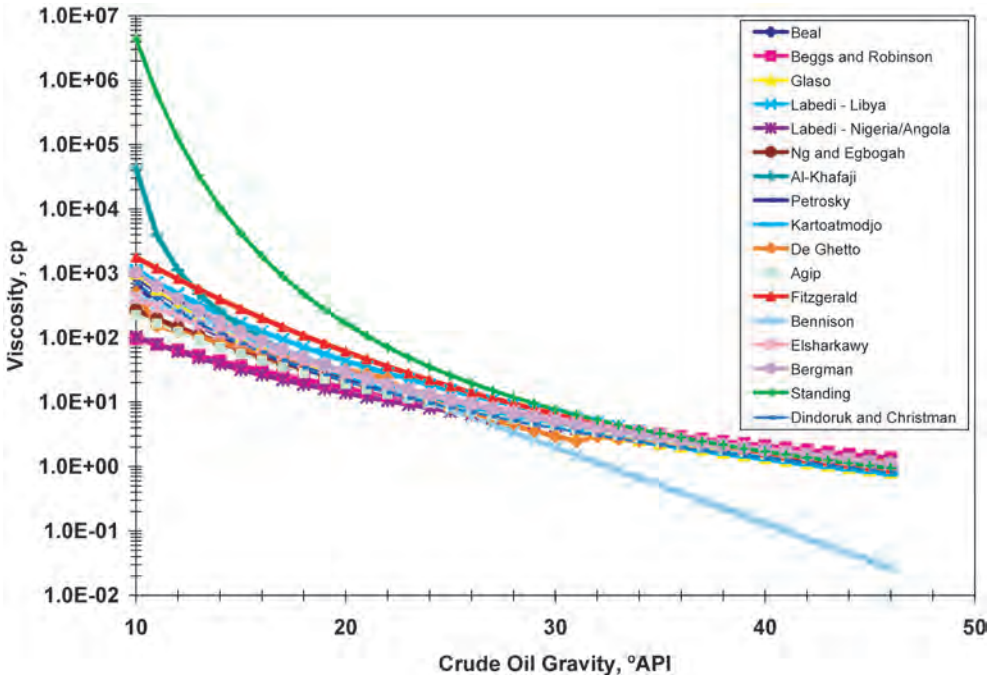


Fig. 6.26—Dead oil viscosity vs. API gravity.

tures. Unfortunately, this work was for liquid hydrocarbons and did not extend into the gas-phase region. A later publication by Firoozabadi and Ramey<sup>28</sup> provided a more generalized correlation suitable for use with gas and liquid hydrocarbons. Surface tension data from pure components ranging from n-dodecane to methane were plotted as shown in Fig. 6.40. The surface tension function used for the y-axis is

$$\left( \frac{\sigma_{hw}^{0.25}}{\rho_w - \rho_h} \right) T_r^{0.3125}, \dots\dots\dots (6.41)$$

while the density difference between the water and hydrocarbon phase is plotted on the x-axis. The data in Fig. 6.40 can be represented by

$$\left( \frac{\sigma_{hw}^{0.25}}{\rho_w - \rho_h} \right) T_r^{0.3125} = 1.58 + \frac{1.76}{\rho_w - \rho_h} \dots\dots\dots (6.42)$$

Solving for surface tension, the relationship becomes

$$\sigma_{hw} = \left[ \frac{1.58(\rho_w - \rho_h) + 1.76}{T_r^{0.3125}} \right]^4 \dots\dots\dots (6.43)$$

This equation requires that the pseudocritical temperature of the oil and gas phases be calculated to evaluate reduced temperature. Riazi's<sup>74</sup> relationship for liquid hydrocarbons can be modified to yield

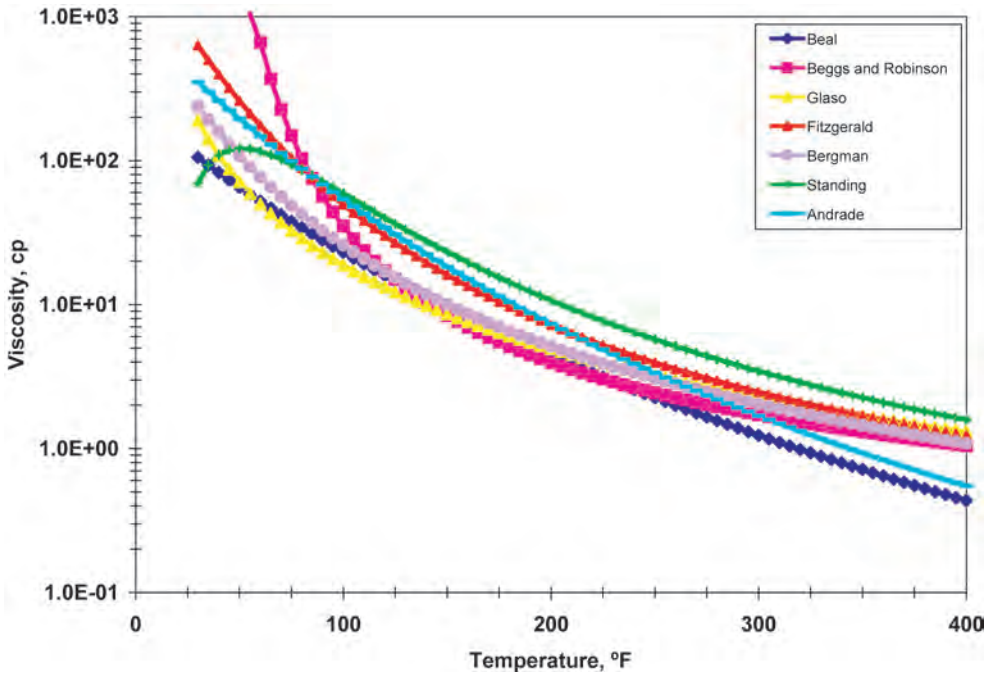


Fig. 6.27—Annotated list of commonly used dead oil viscosity correlations.

$$T_{co} = 24.2787 K_w^{1.76544} \gamma_o^{2.12504} \dots\dots\dots (6.44)$$

Sutton's<sup>89</sup> equation for pseudocritical temperature can be used for the gas phase:

$$T_{cg} = 169.2 + 349.5 \gamma_{ghc} - 74.0 \gamma_{ghc}^2 \dots\dots\dots (6.45)$$

When the pressure increases and gas dissolves into the oil phase, the composition of that phase changes. The pseudocritical temperature of the mixture can be evaluated by calculating the mole fraction of each component present in the oil. For the oil component, we have

$$x_o = \left[ 1 + \frac{7.521 \times 10^{-6} R_s M_o}{\gamma_o} \right]^{-1}, \dots\dots\dots (6.46)$$

while the gas mole fraction in oil is

$$x_g = 1 - x_o \dots\dots\dots (6.47)$$

The pseudocritical temperature of the mixture is then the mole fraction weighted average pseudocritical temperature of each component:

$$T_{cm} = x_o T_{co} + x_g T_{cg} \dots\dots\dots (6.48)$$

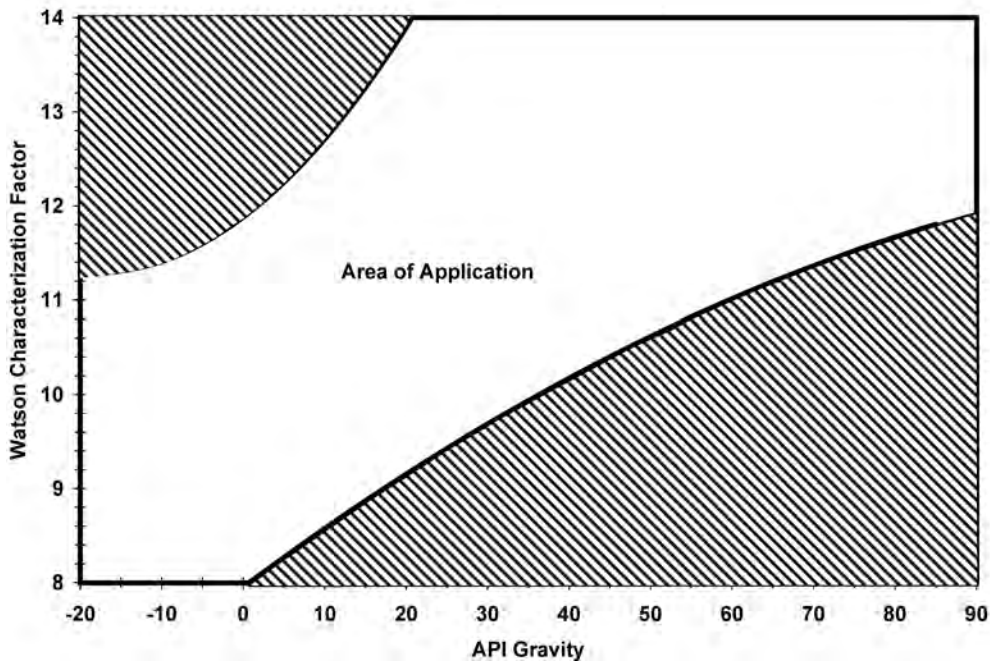


Fig. 6.28—Area of applicability for Fitzgerald’s correlation. (Reproduced courtesy of the American Petroleum Institute.<sup>16</sup>)

This work serves as a guide for estimating the surface tension between water and hydrocarbons. Firoozabadi and Ramey recommended that a single point measurement for oil water systems be obtained so that the curve in Fig. 6.40 could be appropriately adjusted. Fig. 6.41 shows an example of results for oil/water and gas/water systems derived from this method.

For methane-brine systems, Standing<sup>13</sup> has indicated that the surface tension will increase according to Fig. 6.42. The relationship in Fig. 6.42 can be approximated by

$$\sigma_{cor} = 3.44 \times 10^{-5} C_{sw} \dots\dots\dots (6.49)$$

**Example 6.1** Determine the PVT properties for a United States midcontinental crude oil and natural gas system with properties listed in Table 6.12. Table 6.13 lists the correlations to be used. Measured data are provided for comparison with the calculated results. For correlations that rely on other correlations, these data illustrate the effects of error propagation in the calculations.

*Solution.* Determine the crude oil specific gravity,

$$\gamma_o = \frac{141.5}{\gamma_{API} + 131.5} = \frac{141.5}{37.9 + 131.5} = 0.8353, \dots\dots\dots (6.50)$$

and molecular weight,

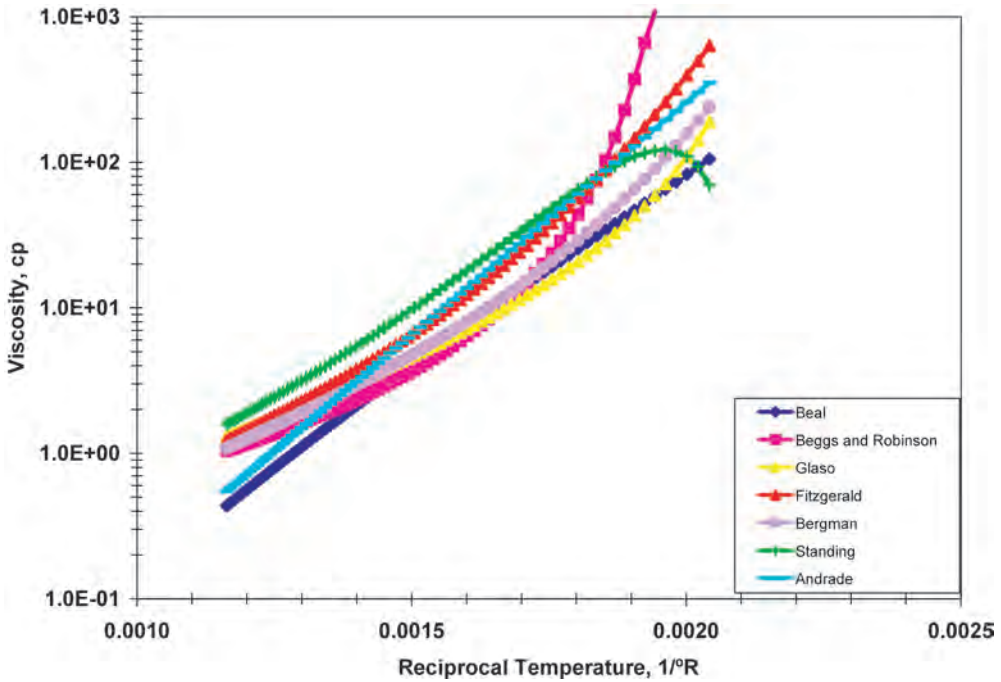


Fig. 6.29—Dead oil viscosity vs. reciprocal absolute temperature.

$$M_o = \left( \frac{K_w \gamma_o^{0.84573}}{4.5579} \right)^{6.58848} = \left( \frac{11.8 \times 0.8498^{0.84573}}{4.5579} \right)^{6.58848} = 193 \dots \dots \dots (6.51)$$

Bubblepoint Pressure—Lasater. Calculate the gas mole fraction in the oil,

$$x_g = \left[ 1 + \frac{\gamma_o}{7.521 \times 10^{-6} R_s M_o} \right]^{-1} = \left[ 1 + \frac{0.8353}{7.521 \times 10^{-6} \times 769 \times 193} \right]^{-1} = 0.572, \dots (6.52)$$

and the Lasater bubblepoint pressure factor,

$$p_f = e^{\left( \frac{(x_g - 0.15649)}{0.33705} \right)} - 0.59162 = e^{\left( \frac{(0.572 - 0.15649)}{0.33705} \right)} - 0.59162 = 2.843, \dots \dots \dots (6.53)$$

with Lasater’s relationship between bubblepoint pressure factor and bubblepoint pressure,

$$p_b = \frac{p_f (T + 459.67)}{\gamma_g} = \frac{2.843 (120 + 459.67)}{0.804} = 2,050 \text{ psia} \dots \dots \dots (6.54)$$

For comparison, Standing = 2,316 psia, Glasø = 2,725 psia, Al-Shammasi = 2,421 psia, and Velardi = 2,411 psia.

Modify the calculated bubblepoint pressure to account for the effects of nitrogen in the surface gas with Jacobson’s equation.

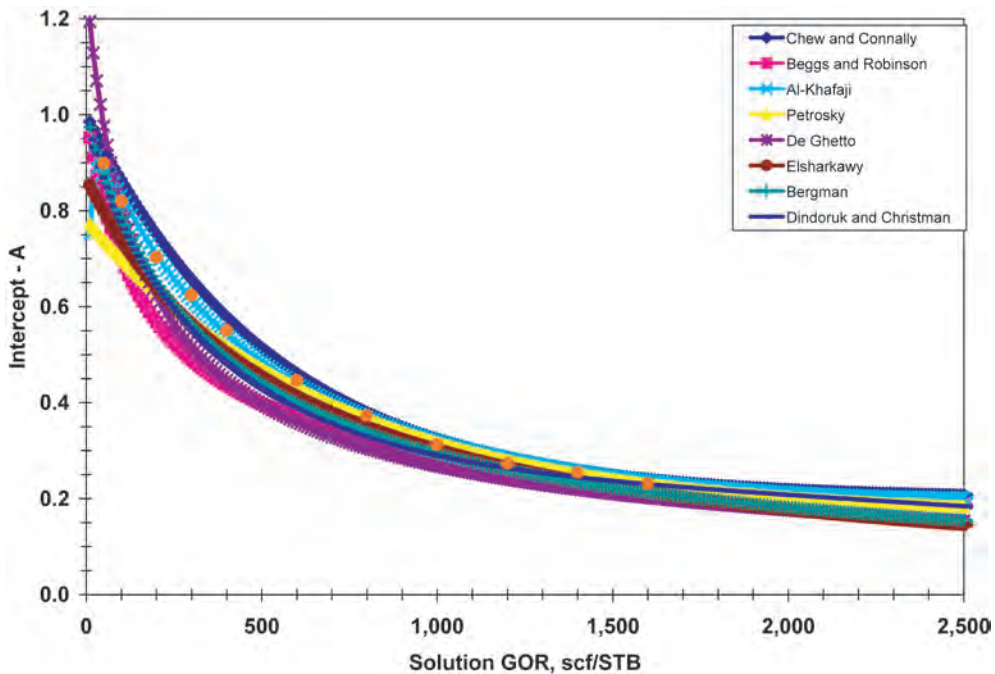


Fig. 6.30—Bubblepoint viscosity correlation parameter A.

$$\begin{aligned} \frac{p_{bN_2}}{p_{bh}} &= 1.1585 + 2.86 y_{N_2} - 1.07 \times 10^{-3} T \\ &= 1.1585 + 2.86 \times 0.0238 - 1.07 \times 10^{-3} \times 120 = 1.098 \dots \dots \dots (6.7) \end{aligned}$$

Therefore, the bubblepoint pressure should be increased by 9.8% to 2,251 psia. The measured bubblepoint pressure was reported to be 2,479 psia.

Bubblepoint Oil FVF—Al-Shammasi.

$$\begin{aligned} B_{ob} &= 1 + 5.53 \times 10^{-7} R_s (T - 60) + \frac{1.81 \times 10^{-4} R_s}{\gamma_o} + \frac{4.49 \times 10^{-4} (T - 60)}{\gamma_o} \\ &\quad + \frac{2.06 \times 10^{-4} R_s \gamma_g}{\gamma_o} \dots \dots \dots (6.55) \\ &= 1 + 5.53 \times 10^{-7} \times 769 \times (120 - 60) + \frac{1.81 \times 10^{-4} \times 769}{0.8353} \\ &\quad + \frac{4.49 \times 10^{-4} (120 - 60)}{0.8353} + \frac{2.06 \times 10^{-4} \times 769 \times 0.804}{0.8353} \\ &= 1.377 \text{ bbl/STB.} \end{aligned}$$

For comparison (in bbl/STB), Standing = 1.410, Glasø = 1.386, Al-Marhoun<sup>10</sup> = 1.364, Farshad = 1.364, and Kartoatmodjo = 1.358. The measured bubblepoint oil FVF is 1.398 bbl/STB.

Isothermal Oil Compressibility—Farshad.

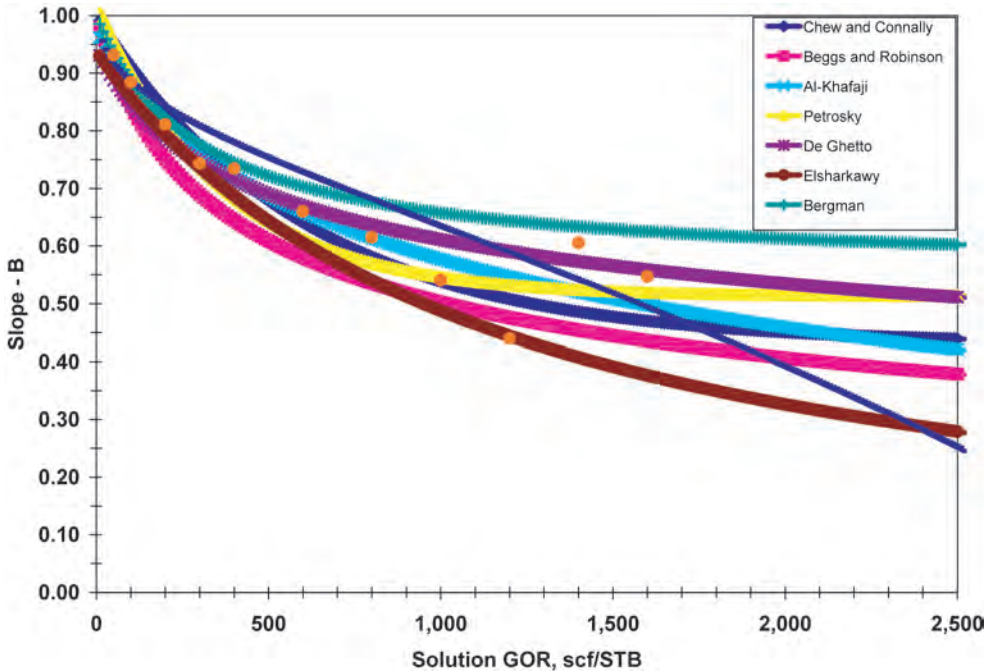


Fig. 6.31—Bubblepoint viscosity correlation parameter B.

$$X = R_s^{0.1982} T^{0.6685} \gamma_g^{-0.21435} \gamma_{API}^{1.0116} p^{-0.1616} \dots\dots\dots (6.56)$$

$$= 769^{0.1982} 120^{0.6685} 0.804^{-0.21435} 37.9^{1.0116} 4500^{-0.1616} = 974.59.$$

$$c_o = 10^{(-5.4531 + 5.03 \times 10^{-4} X - 3.5 \times 10^{-8} X^2)} \dots\dots\dots (6.57)$$

$$= 10^{(-5.4531 + 5.03 \times 10^{-4} 974.59 - 3.5 \times 10^{-8} 974.59^2)} = 10.09 \times 10^{-6} \text{ psi}^{-1}.$$

The measured isothermal compressibility is  $11.06 \times 10^{-6} \text{ psi}^{-1}$ .

Undersaturated Oil FVF. With the results from Lasater’s method for bubblepoint pressure, Al-Shammasi’s method for bubblepoint oil FVF, and Farshad’s equation for isothermal compressibility, the undersaturated oil FVF is given by

$$B_o = B_{ob} e^{[c_o(p_b - p)]} \dots\dots\dots (6.14)$$

$$= 1.377 e^{[(10.09 \times 10^{-6})^{-1} (2,251 - 4,500)]} = 1.346 \text{ bbl / STB},$$

which compares to a measured value of 1.367 bbl/STB. Because this calculation uses the results from multiple correlations, individual correlation error compounds and propagates through to the final result. The calculated value is 1.367 bbl/STB with the actual bubblepoint value of 1.398 bbl/STB; therefore, the accuracy of the bubblepoint FVF is primarily affected by the accuracy of the undersaturated FVF.

Oil Density.

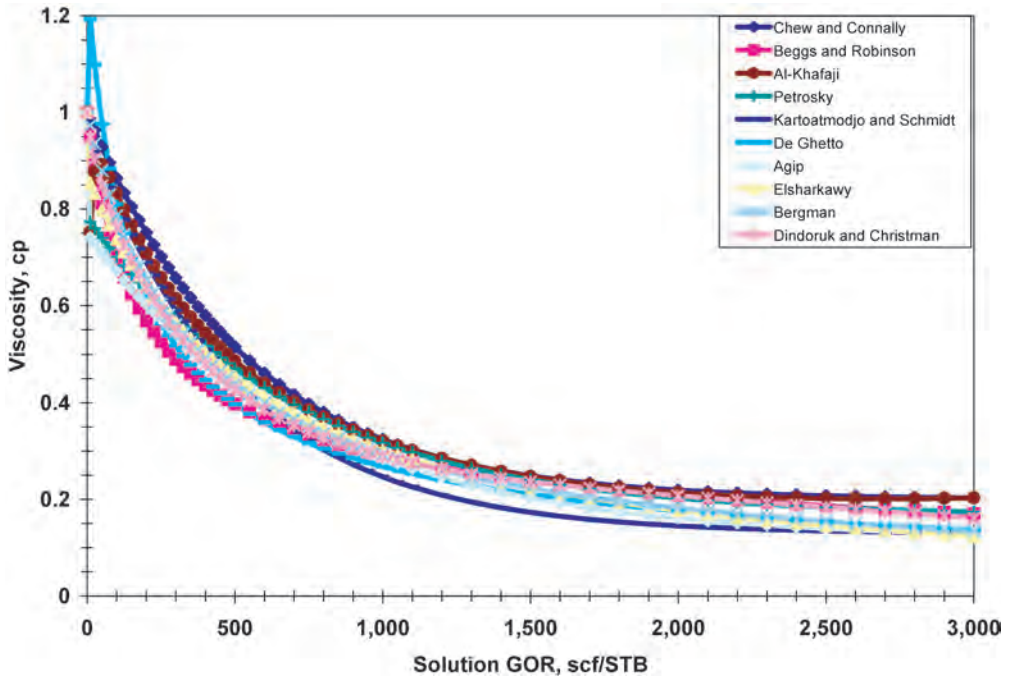


Fig. 6.32—Bubblepoint oil viscosity vs. solution GOR.

$$\rho_o = \frac{62.42796 \gamma_o + 0.0136 \gamma_g R_s}{B_o} \dots\dots\dots (6.16)$$

$$= \frac{62.42796 \times 0.8353 + 0.0136 \times 0.804 \times 769}{1.346} = 45.0 \text{ lbm/ft}^3.$$

Dead Oil Viscosity—Glasø.

$$\mu_{od} = \left( \frac{3.141 \times 10^{10}}{T^{3.444}} \right) \log(\gamma_{API})^{[10.313 \log(T) - 36.447]} \dots\dots\dots (6.58)$$

$$= \left( \frac{3.141 \times 10^{10}}{120^{3.444}} \right) \log(37.9)^{[10.313 \log(120) - 36.447]} = 2.30 \text{ cp.}$$

For comparison, Fitzgerald = 1.808 cp, and Bergman = 2.851 cp. The measured dead oil viscosity is 1.67 cp.

Bubblepoint Oil Viscosity—Chew and Connally.

$$A = 0.20 + \frac{0.80}{10^{(0.00081 R_s)}} = 0.20 + \frac{0.80}{10^{(0.00081 \times 769)}} = 0.3906 \dots\dots\dots (6.59)$$

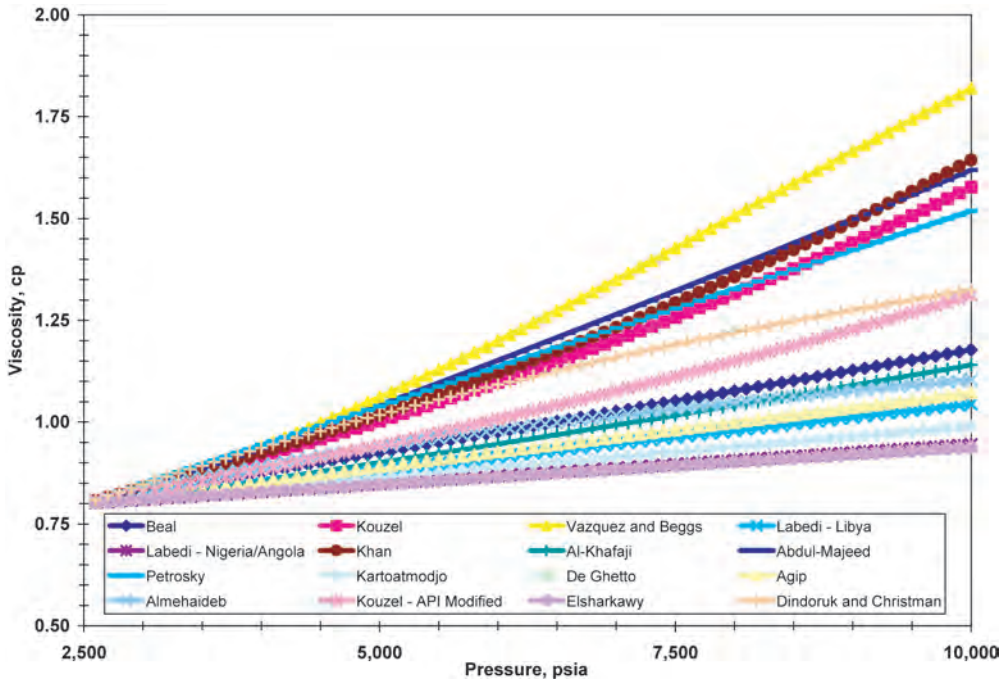


Fig. 6.33—Undersaturated oil viscosity vs. pressure.

$$B = 0.43 + \frac{0.57}{10^{(0.00072 R_s)}} = 0.43 + \frac{0.57}{10^{(0.00072 \times 769)}} = 0.5893 \dots\dots\dots (6.60)$$

$$\mu_{ob} = A\mu_{od}^B = 0.3906 \times 2.30^{0.5893} = 0.638 \text{ cp} \dots\dots\dots (6.17)$$

For comparison, Beggs and Robinson = 0.515 cp. The measured viscosity at bubblepoint is 0.401 cp.

Undersaturated Oil Viscosity—Vazquez and Beggs.

$$\begin{aligned} \mu_o &= \mu_{ob} \left( \frac{p}{p_b} \right)^{2.6 p^{1.187} 10^{(-3.9 \times 10^{-5} p - 5)}} \dots\dots\dots (6.61) \\ &= 0.638 \left( \frac{4500}{2251} \right)^{2.6 \times 4500^{1.187} 10^{(-3.9 \times 10^{-5} \times 4500 - 5)}} = 0.828 \text{ cp.} \end{aligned}$$

For comparison, Beal = 0.730 cp and Kouzel = 0.778 cp. The measured value is 0.475 cp. This example illustrates the steps necessary to calculate oil viscosity requiring correlations for dead oil viscosity, bubblepoint viscosity, undersaturated viscosity, and bubblepoint pressure/solution GOR. Errors in individual correlations can compound and propagate through to the resulting answer. For instance, if the measured bubblepoint viscosity is used in Eq. 6.61, the result is 0.52 cp—much closer to the measured value. Therefore, care should be exercised in the selection of accurate correlations for individual properties.

Gas/Oil Surface Tension—Abdul-Majeed. Calculate the dead oil surface tension.



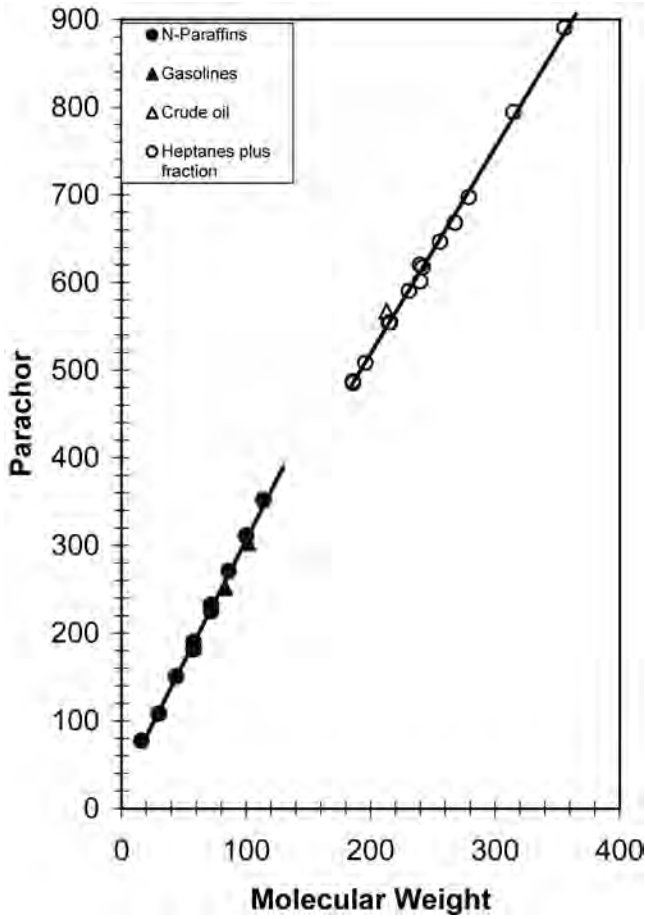


Fig. 6.34—Hydrocarbon parachors.<sup>84</sup>

$$\sigma_{od} = (1.17013 - 1.694 \times 10^{-3}T)(38.085 - 0.259\gamma_{API}) \dots\dots\dots (6.39)$$

$$= (1.17013 - 1.694 \times 10^{-3} \times 120)(38.085 - 0.259 \times 37.9) = 27.3 \text{ dynes/cm.}$$

Determine the live oil adjustment factor.

$$\left(\frac{\sigma_{go}}{\sigma_{od}}\right) = 0.056379 + 0.94362 e^{(-3.8491 \times 10^{-3} R_s)} \dots\dots\dots (6.40)$$

$$= 0.056379 + 0.94362 e^{(-3.8491 \times 10^{-3} \times 769)} = 0.105.$$

Calculate the live gas/oil surface tension.

$$\sigma_{go} = \sigma_{od} \left(\frac{\sigma_{go}}{\sigma_{od}}\right) \dots\dots\dots (6.38)$$

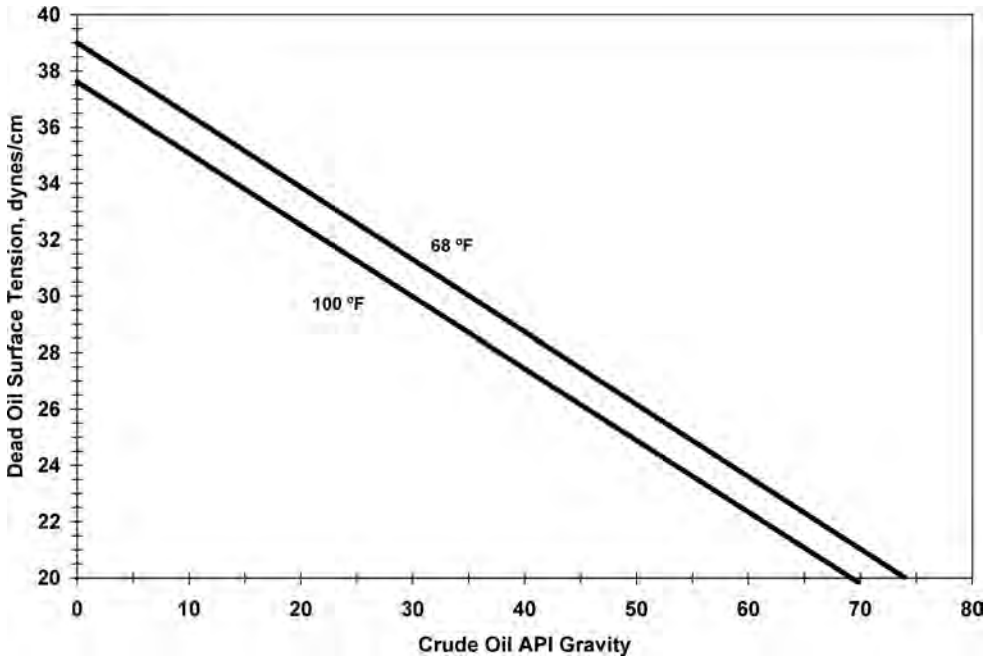


Fig. 6.35—Surface tension of crude oil at atmospheric pressure (after Baker and Swerdloff<sup>27</sup>).

$$= 27.3 \times 0.105 = 2.88 \text{ dynes/cm.}$$

For comparison, Baker and Swerdloff = 4.73 dynes/cm.

Water/Oil Surface Tension—Firoozabadi and Ramey. Calculate the pseudocritical temperature of the dead oil.

$$T_{co} = 24.2787 K_w^{1.76544} \gamma_o^{2.12504} \dots\dots\dots (6.44)$$

$$= 24.2787 \times 11.8^{1.76544} 0.8353^{2.12504} = 1292.7^\circ \text{ R.}$$

Calculate the pseudocritical temperature of the gas.

$$T_{cg} = 169.2 + 349.5 \gamma_{ghc} - 74.0 \gamma_{ghc}^2 \dots\dots\dots (6.45)$$

$$= 169.2 + 349.5 \times 0.804 - 74.0 \times 0.804^2 = 402.4^\circ \text{ R.}$$

Calculate the pseudocritical temperature of the live gas/oil mixture.

$$T_{cm} = x_o T_{co} + x_g T_{cg}$$

$$= (1 - 0.572) 1292.7 + 0.572 \times 402.4 = 783^\circ \text{ R.} \dots\dots\dots (6.48)$$

Convert oil density units from lbm/ft<sup>3</sup> to g/cm<sup>3</sup>.

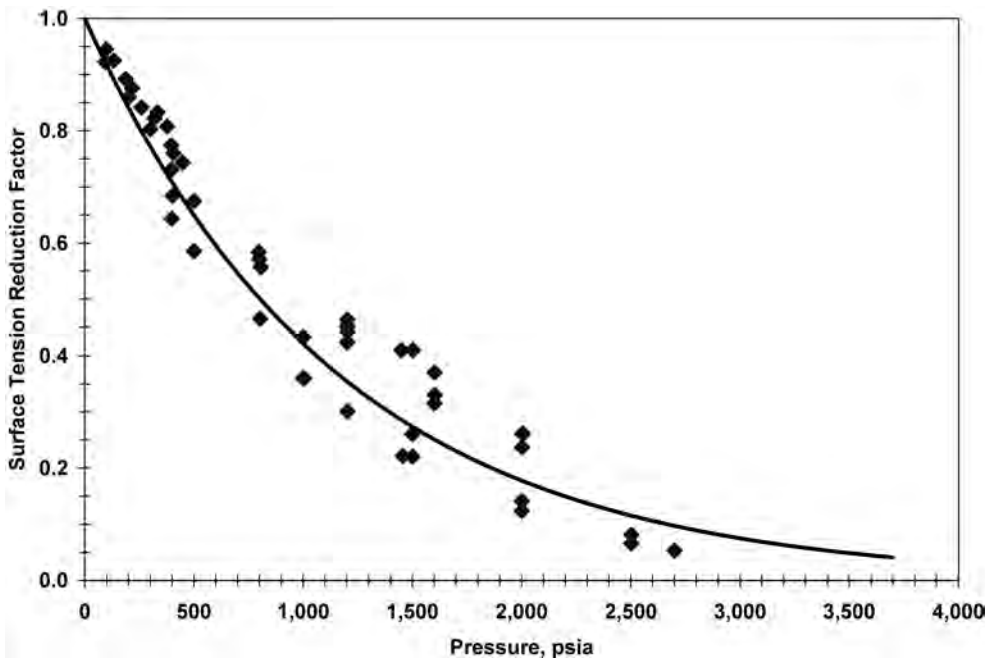


Fig. 6.36—Effect of solution gas on crude oil surface tension (after Baker and Swerdloff<sup>27</sup>).

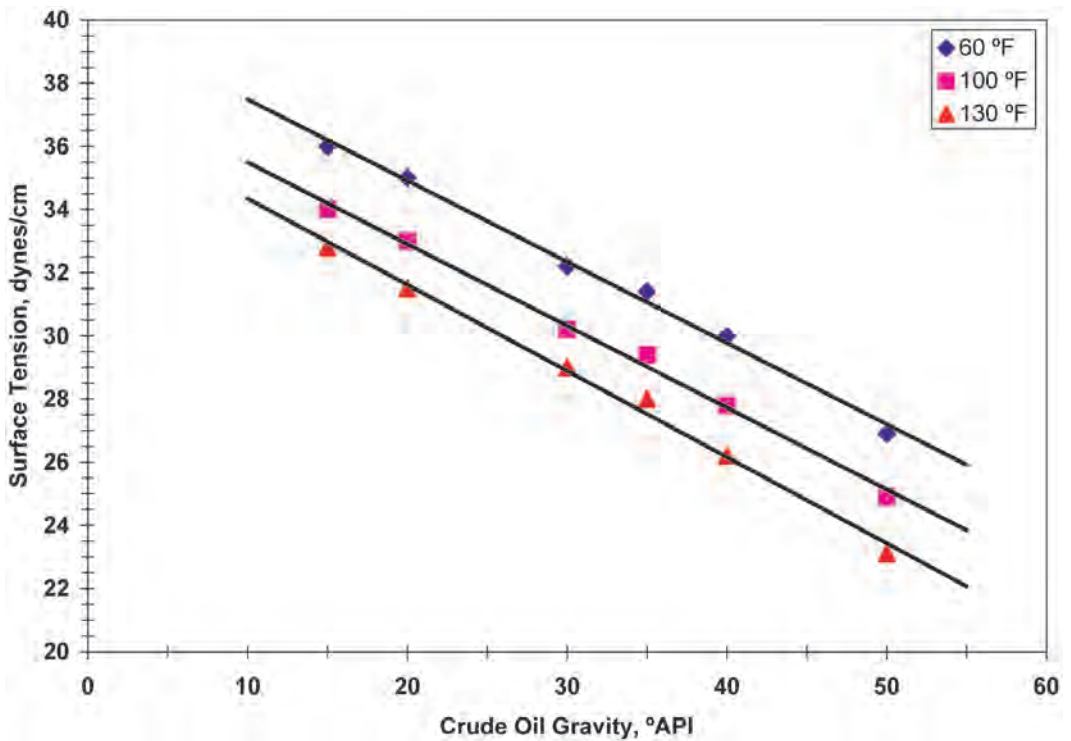


Fig. 6.37—Surface tension of crude oil at atmospheric pressure. (Reprinted from *J. of Petroleum Science and Engineering*, Vol. 27, Abdul-Majeed and Abu Al-Soof, “Estimation of Gas-Oil Surface Tension,” 197, Copyright 2000, with permission from Elsevier.)

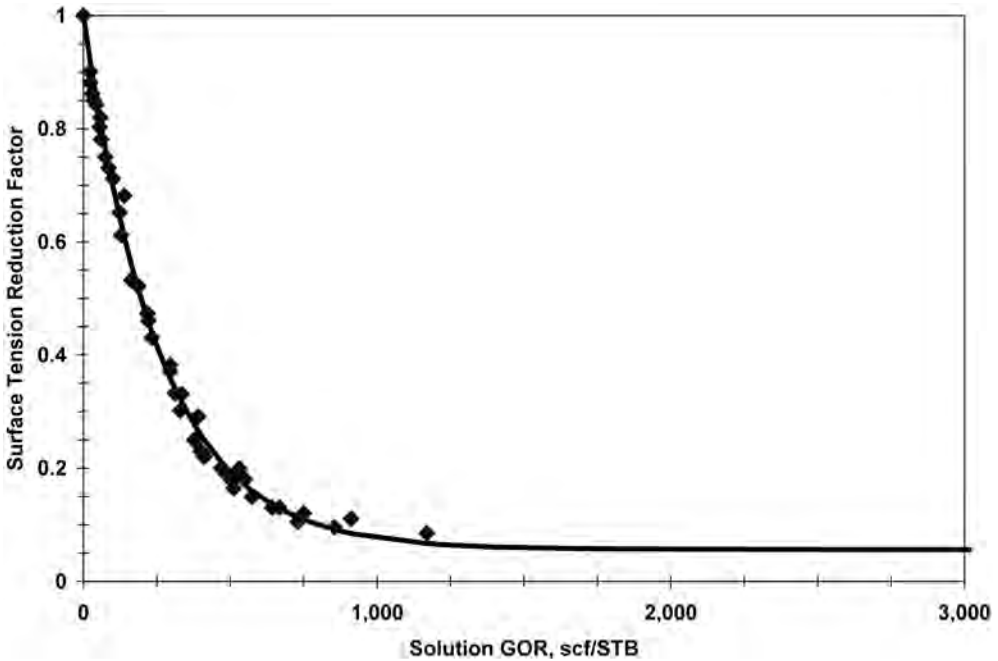


Fig. 6.38—Effect of solution gas on surface tension of crude oils. (Reprinted from *J. of Petroleum Science and Engineering*, Vol. 27, Abdul-Majeed and Abu Al-Soof, “Estimation of Gas-Oil Surface Tension,” 197, Copyright 2000, with permission from Elsevier.)

$$\rho_h = \frac{\rho_o}{62.42796} = 0.7206 \text{ g/cm}^3 \dots\dots\dots (6.62)$$

Calculate the surface tension between the oil and water phases.

$$\sigma_{hw} = \left[ \frac{1.58(\rho_w - \rho_h) + 1.76}{T_r^{0.3125}} \right]^4 \dots\dots\dots (6.43)$$

$$= \left[ \frac{1.58(1.000 - 0.7206) + 1.76}{\left( \frac{(120 + 459.67)}{783} \right)^{0.3125}} \right]^4 = 34.2 \text{ dynes/cm.}$$

**TABLE 6.11—STATISTICAL SUMMARY OF SURFACE TENSION CORRELATIONS**  
 (Reprinted from *J. of Petroleum Science and Engineering*, Vol. 27, Abdul-Majeed and Abu Al-Soof, "Estimation of Gas-Oil Surface Tension," 197, Copyright 2000, with permission from Elsevier.)

Correlation	Average Error (%)	Average Absolute Error (%)	Standard Deviation
Baker and Swerdloff	1.12	16.25	21.7
Abdul-Majeed	0.64	7.28	9.77

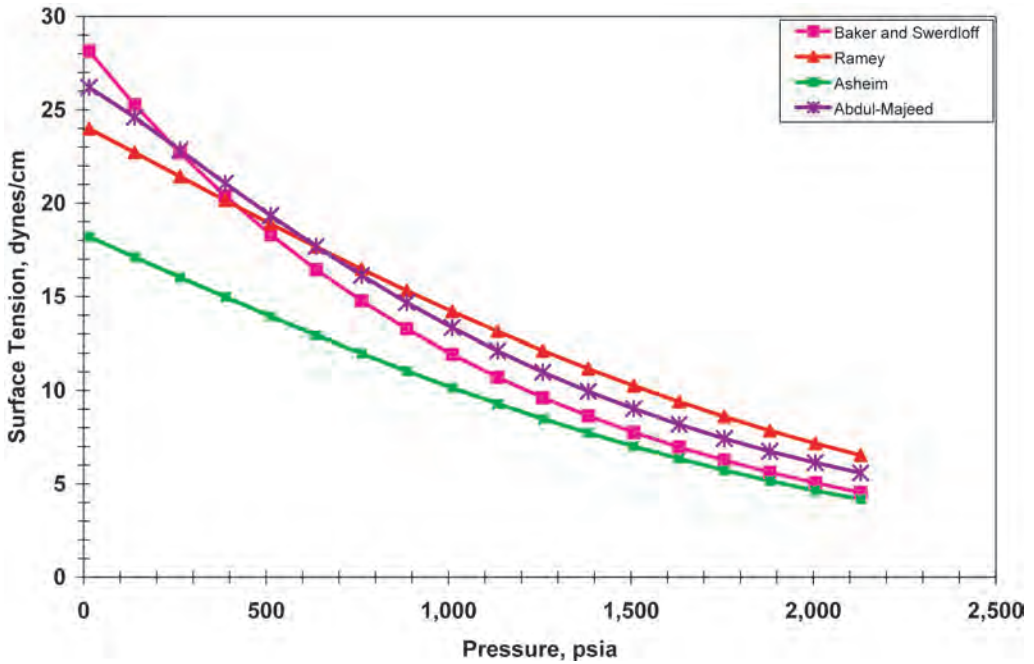


Fig. 6.39—Comparison of surface tension calculation methods.

TABLE 6.12—PROPERTIES FOR EXAMPLE 6.1	
Property	Value
Crude oil gravity, °API	37.9
Watson characterization factor	11.8
Gas specific gravity	0.804
Nitrogen content in the surface gas, mole %	2.38
GOR, scf/STB	769
Pressure, psia	4,500
Temperature, °F	120

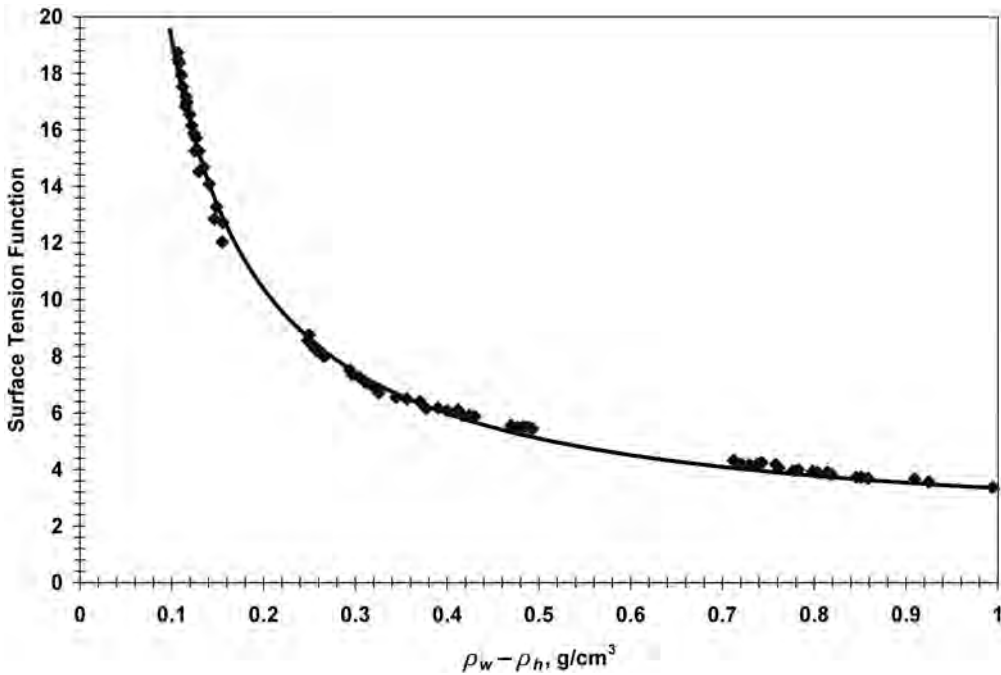


Fig. 6.40—Generalized correlation for water/hydrocarbon surface tension. [This material is being used with permission from the Petroleum Society. The author thanks the Petroleum Society for the use of this material and reminds recipients that no other copies may be made without the expressed written consent of the Petroleum Society. Firoozabadi, A. and Ramey, H.J.: "Surface Tension of Water-Hydrocarbon Systems at Reservoir Conditions," *Journal of Canadian Petroleum Technology* (May-June 1988) 41.]

TABLE 6.13—CORRELATIONS FOR EXAMPLE 6.1	
Property	Correlation
Bubblepoint pressure	Lasater
Nitrogen correction to bubblepoint	Jacobson
Oil FVF	Al-Shammasi
Isothermal compressibility	Farshad
Viscosity	Glasø, Chew and Connally, Vazquez and Beggs
Surface tension at bubblepoint	Abdul-Majeed
Oil/water interfacial tension	Firoozabadi and Ramey

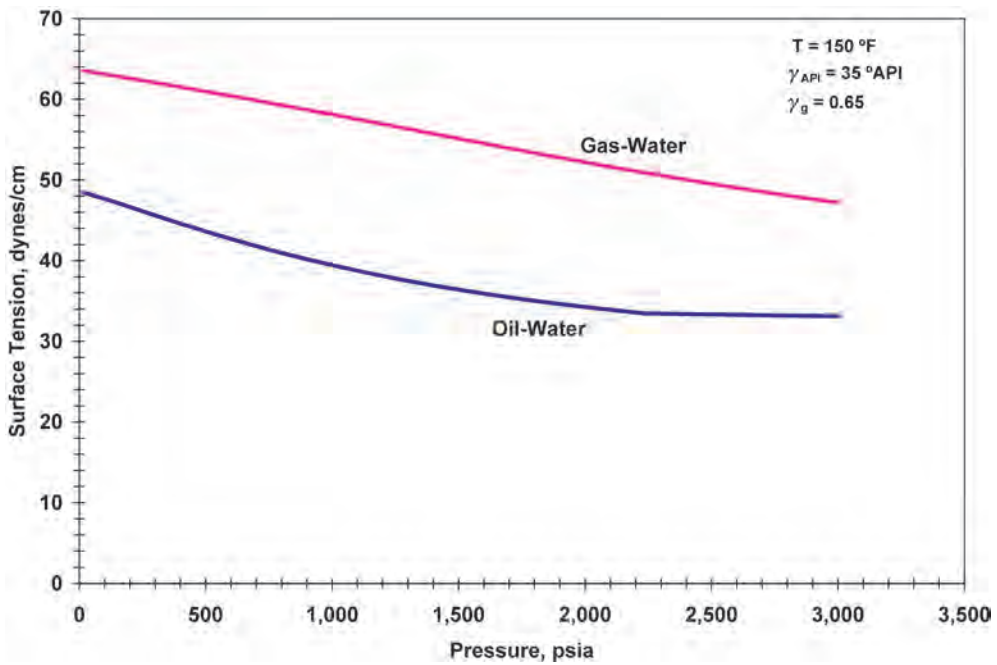


Fig. 6.41—Water/hydrocarbon surface tension.

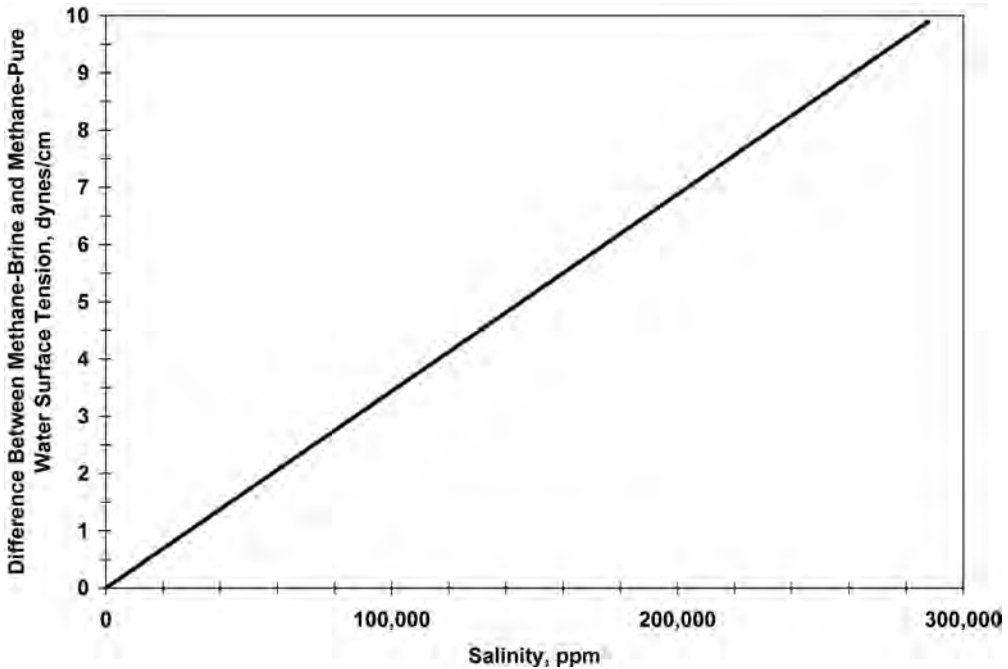


Fig. 6.42—Methane/brine surface tension correlation.<sup>13</sup>

## Nomenclature

- $B_g$  = gas FVF, ft<sup>3</sup>/scf  
 $B_o$  = oil FVF, bbl/STB  
 $B_{ob}$  = oil formation volume at bubblepoint pressure, bbl/STB  
 $c_o$  = oil isothermal compressibility, Lt<sup>2</sup>/m, psi<sup>-1</sup>  
 $c_{ob}$  = oil isothermal compressibility at bubblepoint, Lt<sup>2</sup>/m, psi<sup>-1</sup>  
 $C_{sw}$  = salt concentration in water, ppm  
 $K_w$  = Watson characterization factor, °R<sup>1/3</sup>  
 $M_g$  = gas molecular weight, m, lbm/lbm mol  
 $M_{go}$  = gas/oil mixture molecular weight, m, lbm/lbm mol  
 $M_o$  = oil molecular weight, m, lbm/lbm mol  
 $M_{og}$  = oil-gas mixture molecular weight, m, lbm/lbm mol  
 $p$  = pressure, m/Lt<sup>2</sup>, psia  
 $p_b$  = bubblepoint pressure, m/Lt<sup>2</sup>, psia  
 $p_{bCO_2}$  = bubblepoint pressure of oil with CO<sub>2</sub> present in surface gas, m/Lt<sup>2</sup>, psia  
 $p_{bH_2S}$  = bubblepoint pressure of oil with H<sub>2</sub>S present in surface gas, m/Lt<sup>2</sup>, psia  
 $p_{bN_2}$  = bubblepoint pressure of oil with N<sub>2</sub> present in surface gas, m/Lt<sup>2</sup>, psia  
 $p_{bh}$  = bubblepoint pressure of oil without nonhydrocarbons, m/Lt<sup>2</sup>, psia  
 $p_f$  = bubblepoint pressure factor, psia/°R  
 $p_r$  = pressure ratio (fraction of bubblepoint pressure)  
 $p_{sc}$  = pressure at standard conditions, m/Lt<sup>2</sup>, psia  
 $p_{sp}$  = separator pressure, m/Lt<sup>2</sup>, psia  
 $P$  = parachor  
 $P_g$  = gas parachor  
 $P_i^g$  = parachor of each component



- $P_o$  = oil parachor  
 $r_v$  = vaporized oil/gas ratio, STB/scf  
 $R_s$  = solution GOR, scf/STB  
 $R_{sb}$  = solution GOR at bubblepoint conditions, scf/STB  
 $T$  = temperature, T, °F  
 $T_{abs}$  = temperature, T, °R  
 $T_b$  = mean average boiling point temperature, T, °R  
 $T_{cg}$  = gas pseudocritical temperature, T, °R  
 $T_{cm}$  = mixture pseudocritical temperature, T, °R  
 $T_{co}$  = oil pseudocritical temperature, T, °R  
 $T_r$  = reduced temperature, T  
 $T_{sc}$  = temperature at standard conditions, T, °F  
 $T_{sp}$  = separator temperature, T, °F  
 $\nu_{100}$  = kinematic viscosity at 100°F, L<sup>2</sup>/t, cs  
 $\nu_{210}$  = kinematic viscosity at 200°F, L<sup>2</sup>/t, cs  
 $V$  = volume, L<sup>3</sup>  
 $V_o$  = volume of crude oil, L<sup>3</sup>  
 $W_g$  = weight of dissolved gas, m  
 $W_o$  = weight of crude oil, m  
 $x_g$  = gas “component” mole fraction in oil  
 $x_i$  = component  $i$  mole fraction in oil phase  
 $x_o$  = oil “component” mole fraction in oil  
 $X_i$  = calculated value in ARE and AARE calculations  
 $X_i$  = measured value in ARE and AARE calculations  
 $y_{CO_2}$  = mole fraction CO<sub>2</sub> in surface gas  
 $y_g$  = gas “component” mole fraction in gas  
 $y_{H_2S}$  = mole fraction H<sub>2</sub>S in surface gas  
 $y_i$  = component  $i$  mole fraction in gas phase  
 $y_{N_2}$  = mole fraction N<sub>2</sub> in surface gas  
 $y_o$  = oil “component” mole fraction in gas  
 $y_{oc}$  = corrected oil “component” mole fraction in gas  
 $y_{om}$  = measured oil “component” mole fraction in gas  
 $Z$  = gas compressibility factor  
 $\gamma_{API}$  = oil API gravity  
 $\gamma_g$  = gas specific gravity, air=1  
 $\gamma_{gc}$  = gas specific gravity adjusted for separator conditions, air=1  
 $\gamma_{ghc}$  = gas specific gravity of hydrocarbon components in a gas mixture, air=1  
 $\gamma_{gs}$  = separator gas specific gravity, air=1  
 $\gamma_o$  = oil specific gravity  
 $\gamma_{oc}$  = “corrected” oil specific gravity  
 $\gamma_{om}$  = measured oil specific gravity  
 $\Delta V_g$  = change in volume as a result of dissolved gas, L<sup>3</sup>  
 $\Delta \rho_p$  = adjustment to liquid density because of pressure, m/L<sup>3</sup>, lbm/ft<sup>3</sup>  
 $\Delta \rho_T$  = adjustment to liquid density because of temperature, m/L<sup>3</sup>, lbm/ft<sup>3</sup>  
 $\mu_o$  = oil viscosity, m/Lt, cp  
 $\mu_{ob}$  = bubblepoint oil viscosity, m/Lt, cp  
 $\mu_{od}$  = dead oil viscosity, m/Lt, cp  
 $\rho_a$  = apparent liquid density of solution gas, m/L<sup>3</sup>, lbm/ft<sup>3</sup>

- $\rho_g$  = gas density, m/L<sup>3</sup>, lbm/ft<sup>3</sup>  
 $\rho_h$  = hydrocarbon density, m/L<sup>3</sup>, g/cm<sup>3</sup>  
 $\rho_o$  = oil density, m/L<sup>3</sup>, lbm/ft<sup>3</sup>  
 $\rho_{ob}$  = bubblepoint oil density, m/L<sup>3</sup>, lbm/ft<sup>3</sup>  
 $\rho_{po}$  = pseudoliquid density, m/L<sup>3</sup>, lbm/ft<sup>3</sup>  
 $\rho_w$  = water density, m/L<sup>3</sup>, g/cm<sup>3</sup>  
 $\sigma_{cor}$  = water salinity correction for gas/water surface tension, m/t<sup>2</sup>, dynes/cm  
 $\sigma_{hw}$  = hydrocarbon/water surface tension, m/t<sup>2</sup>, dynes/cm  
 $\sigma_{go}$  = gas/oil surface tension, m/t<sup>2</sup>, dynes/cm  
 $\sigma_{od}$  = dead oil surface tension, m/t<sup>2</sup>, dynes/cm  
 $\sigma_{od_{68}}$  = dead oil surface tension at 68°F, m/t<sup>2</sup>, dynes/cm  
 $\sigma_{od_{100}}$  = dead oil surface tension at 100°F, m/t<sup>2</sup>, dynes/cm

---

## References

1. Lasater, J.A.: "Bubble Point Pressure Correlation," *Trans., AIME* (1958) **213**, 379.
2. Al-Shammasi, A.A.: "A Review of Bubblepoint Pressure and Oil Formation Volume Factor Correlations," *SPEREE* (April 2001) 146.
3. Velarde, J., Blasingame, T.A., and McCain, W.D. Jr.: "Correlation of Black Oil Properties At Pressures Below Bubble Point Pressure—A New Approach," paper 97-93 presented at 1997 Annual CIM Petroleum Soc. Technical Meeting, Calgary, 8–11 June.
4. Al-Marhoun, M.A.: "New Correlations For Formation Volume Factors of Oil And Gas Mixtures," *J. Cdn. Pet. Tech.* (March 1992) 22.
5. Farshad, F.F. *et al.*: "Empirical PVT Correlations For Colombian Crude Oils," paper SPE 36105 presented at the 1996 SPE Latin American and Caribbean Petroleum Engineering Conference, Port of Spain, Trinidad and Tobago, 23–26 April.
6. Kartoatmodjo, R.S.T.: "New Correlations for Estimating Hydrocarbon Liquid Properties," MS thesis, U. of Tulsa, Tulsa (1990).
7. Kartoatmodjo, R.S.T. and Schmidt, Z.: "New Correlations For Crude Oil Physical Properties," unsolicited paper SPE 23556 (September 1991).
8. Kartoatmodjo, R.S.T. and Schmidt Z.: "Large Data Bank Improves Crude Physical Property Correlations," *Oil and Gas J.* (4 July 1994) 51.
9. Dindoruk, B. and Christman, P.G.: "PVT Properties and Viscosity Correlations for Gulf of Mexico Oils," paper SPE 71633 presented at the 2001 SPE Annual Technical Conference and Exhibition, New Orleans, 30 September–3 October.
10. Petrosky, G.E. Jr.: "PVT Correlations for Gulf of Mexico Crude Oils," MS thesis, U. of Southwestern Louisiana, Lafayette, Louisiana (1990).
11. Petrosky, G.E. Jr. and Farshad, F.F.: "Pressure-Volume-Temperature Correlations For Gulf of Mexico Crude Oils," *SPEREE* (October 1998) 416.
12. Glasø, Ø.: "Generalized Pressure-Volume-Temperature Correlations," *JPT* (May 1980) 785.
13. Whitson, C.H. and Brulé, M.R.: *Phase Behavior*, first edition, SPE, Richardson, Texas (2000) Chap. 3.
14. Bergman, D.F.: "Don't Forget Viscosity," presented at the 2004 Petroleum Technology Transfer Council Annual Reservoir Engineering Symposium, Lafayette, Louisiana, 2 December.
15. Fitzgerald, D.J.: "A Predictive Method for Estimating the Viscosity of Undefined Hydrocarbon Liquid Mixtures," MS thesis, Pennsylvania State U. (1994).
16. *API Technical Data Book—Petroleum Refining*, sixth edition, API, Washington, DC (April 1997) Chap. 11.
17. Chew, J. and Connally, C.A. Jr.: "A Viscosity Correlation for Gas-Saturated Crude Oils," *Trans., AIME* (1959) **216**, 23.
18. Aziz, K., Govier, C.W., and Fogarasi, M.: "Pressure Drop in Wells Producing Oil and Gas," *J. Cdn. Pet. Tech.* (July–September 1972) 38.

19. Beggs, H.D. and Robinson, J.R.: "Estimating the Viscosity of Crude Oil Systems," *JPT* (September 1975) 1140.
20. Beal, C.: "The Viscosity of Air, Water, Natural Gas, Crude Oil and Its Associated Gases at Oil Field Temperatures and Pressures," *Oil and Gas Property Evaluation and Reserve Estimates*, SPE Reprint Series No. 3, SPE, Richardson, Texas (1970) 114–127.
21. Standing, M.B.: *Volumetric and Phase Behavior of Oil Hydrocarbon Systems*, ninth edition, SPE, Dallas (1981).
22. Kouzel, B.: "How Pressure Affects Liquid Viscosity," *Hydrocarbon Processing* (March 1965) 120.
23. Vazquez, M.E.: "Correlations for Fluid Physical Property Prediction," MS thesis, U. of Tulsa, Tulsa (1976).
24. Vazquez, M.E. and Beggs, H.D.: "Correlations for Fluid Physical Property Prediction," *JPT* (June 1980) 968.
25. Abdul-Majeed, G.H. and Abu Al-Soof, N.B.: "Estimation of Gas-Oil Surface Tension," *J. of Petroleum Science and Engineering* (2000) 197.
26. Baker, O. and Swerdloff, W.: "Calculation of Surface Tension 3—Calculating Parachor Values," *Oil & Gas J.* (5 December 1955) 141.
27. Baker, O. and Swerdloff, W.: "Calculation of Surface Tension 6—Finding Surface Tension of Hydrocarbon Liquids," *Oil & Gas J.* (2 January 1956) 125.
28. Firoozabadi, A. and Ramey, H.J.: "Surface Tension of Water-Hydrocarbon Systems at Reservoir Conditions," *J. Cdn. Pet. Tech.* (May–June 1988) 41.
29. Standing, M.B.: "A Pressure-Volume-Temperature Correlation For Mixtures of California Oils and Gases," *Drill. and Prod. Prac.*, API (1947) 275.
30. Elam, F.M.: "Prediction of Bubble Point Pressures and Formation Volume Factors from Field Data," MS thesis, U. of Texas at Austin, Austin, Texas (1957).
31. Labedi, R.M.: "PVT Correlations of the African Crudes," PhD thesis, Colorado School of Mines, Golden, Colorado (May 1982).
32. Labedi, R.M.: "Use of Production Data To Estimate The Saturation Pressure, Solution GOR and Chemical Composition of Reservoir Fluids," paper SPE 21164 presented at the 1990 SPE Latin American Petroleum Engineering Conference, Rio De Janeiro, 14–19 October.
33. Owolabi, O.O.: "Reservoir Fluid Properties of Alaskan Crudes," MS thesis, U. of Alaska, Fairbanks, Alaska (May 1984).
34. Al-Marhoun, M.A.: "Pressure-Volume-Temperature Correlations for Saudi Crude Oils," paper SPE 13718 presented at the 1985 SPE Middle East Oil Technical Conference and Exhibition, Bahrain, 11–14 March.
35. Obomanu, D.A. and Okpobiri, G.A.: "Correlating The PVT Properties of Nigerian Crudes," *J. of Energy Resources Technology; Trans.*, ASME (December 1987) 214.
36. Al-Marhoun, M.A.: "PVT Correlations for Middle East Crude Oils," *JPT* (May 1988) 650.
37. Asgarpour, S. et. al.: "Pressure-Volume-Temperature Correlations For Western Canadian Gases And Oils," *J. Cdn. Pet. Tech.* (July–August 1989) 103.
38. Al-Najjar, H.S., Al-Soof, N.B.A., and Al-Khalisy, K.M.: "Correlations For Bubble-Point Pressures, Gas Oil Ratios And Formation Volume Factors For Iraqi Crude Oils," *J. of Petroleum Research* (June 1988) 13.
39. Dokla, M.E. and Osman, M.E.: "Correlation of PVT Properties For UAE (United Arab Emirates) Crudes," *SPEFE* (March 1992) 41.
40. Macary, S.M. and El-Batanoney, M.H.: "Derivation of PVT Correlations for the Gulf of Suez Crude Oils," *Proc.*, 1992 EGPC Petroleum Exploration and Production Conference (1992) 374.
41. Omar, M.I. and Todd, A.C.: "Development of New Modified Black Oil Correlations For Malaysian Crudes," paper SPE 25338 presented at the 1993 SPE Asia Pacific Oil and Gas Conference, Singapore, 8–10 February.
42. Omar, M.I., Daud, M.E., and Raja, D.M.A.: "New Correlation For Determining Bubble Point Oil FVF (Formation Volume Factor)," paper presented at the 1993 Asian Council Petroleum Conference, Bangkok, Thailand, 2–6 November.
43. Hasan, M., Lestari and Inawati: "PVT Correlations for Indonesian Crude Oils," *Proc.*, Indonesian Petroleum Assn., 1993 Annual Convention, IPA93-2.1-070.

44. De Ghetto, G., Paone, F., and Villa, M.: "Reliability Analysis on PVT Correlations," paper SPE 28904 presented at the 1994 SPE European Petroleum Conference in London, 25–27 October.
45. De Ghetto, G., Paone, F., and Villa, M.: "Pressure-Volume-Temperature Correlations for Heavy and Extra Heavy Oils," paper SPE 30316 presented at the 1995 SPE International Heavy Oil Symposium, Calgary, 19–21 June.
46. Almehaideb, R.A.: "Improved PVT Correlations for UAE Crude Oils," paper SPE 37691 presented at the 1997 SPE Middle East Oil Conference and Exhibition in Manama, Bahrain, 17–20 March.
47. Elsharkawy, A.M. and Alikhan, A.A.: "Correlations For Predicting Solution Gas/Oil Ratio, Oil Formation Volume Factor, And Undersaturated Oil Compressibility," *J. of Petroleum Science and Engineering* (May 1997) 291.
48. Khairy, M., El-Tayeb, S., and Hamdallah, M.: "PVT Correlations Developed for Egyptian Crudes," *Oil and Gas J.* (4 May 1998) 114.
49. Levitan, L.L. and Murtha, M.: "New Correlations Estimate Pb, FVF," *Oil and Gas J.* (8 March 1999) 70.
50. Frick, T.C.: *Petroleum Production Handbook, Volume II*, SPE of AIME, Dallas (1962) Chaps. 18 and 19.
51. Labedi, R.M.: "Use of Production Data To Estimate Volume Factor, Density And Compressibility of Reservoir Fluids," *J. of Petroleum Science and Engineering* (September 1990) 375.
52. Ahmed, T.H.: *Hydrocarbon Phase Behavior*, Gulf Publishing, Houston (1989).
53. Abdul-Majeed, G.H. and Salman, N.H.: "An Empirical Correlation For Oil FVF (Formation Volume Factor) Prediction," *J. Cdn. Pet. Tech.* (November–December 1988) 118.
54. Calhoun, J.C. Jr.: *Fundamentals of Reservoir Engineering*, U. of Oklahoma Press, Norman, Oklahoma (1947) 35.
55. Andrade, E.N. da C.: "The Viscosity of Liquids," *Nature* (1930) **125**, 309.
56. Reid, R.C., Prausnitz, J.M., and Sherwood, T.K.: *The Properties of Gases and Liquids*, third edition, McGraw-Hill Book Co. (1977) 435–439.
57. Labedi, R.M.: "Improved Correlations For Predicting The Viscosity of Light Crudes," *J. of Petroleum Science and Engineering* (October 1992) 221.
58. Egbogah, E.O. and Ng, J.T.H.: "An Improved Temperature-Viscosity Correlation For Crude Oil Systems," paper 83-34-32 presented at 1983 Annual CIM Petroleum Soc. and Canadian Assn. Drilling Engineering Technical Meeting, Banff, Canada, 10–13 May.
59. Al-Khafaji, A.H., Abdul-Majeed, G.H., and Hassoon, S.F.: "Viscosity Correlation For Dead, Live And Undersaturated Crude Oils," *J. of Petroleum Research* (December 1987) 1.
60. Petrosky, G.E. Jr. and Farshad, F.F.: "Viscosity Correlations for Gulf of Mexico Crude Oils," paper SPE 29468 presented at the 1995 SPE Production Operations Symposium, Oklahoma City, Oklahoma, 2–4 October.
61. Sutton, R.P. and Farshad, F.F.: "Evaluation of Empirically Derived PVT Properties for Gulf of Mexico Crude Oils," *SPE* (February 1990) 79.
62. Bennison, T.: "Prediction of Heavy Oil Viscosity," presented at the 1998 IBC Heavy Oil Field Development Conference, London, 2–4 December.
63. Elsharkawy, A.M. and Alikhan, A.A.: "Models For Predicting The Viscosity of Middle East Crude Oils," *Fuel* (June 1999) 891–903.
64. Khan, S.A. *et al.*: "Viscosity Correlations for Saudi Arabian Crude Oils," paper SPE 15720 presented at the 1987 SPE Middle East Oil Show, Bahrain, 7–10 March.
65. Abdul-Majeed, G.H., Kattan, R.R., and Salman, N.H.: "New Correlation for Estimating the Viscosity of Undersaturated Crude Oils," *J. Cdn. Pet. Tech.* (May–June 1990) 80.
66. Burcik, E.J.: *Properties of Petroleum Reservoir Fluids*, John Wiley and Sons Inc., New York, New York (1957) Chap 1.
67. Pirson, S.J.: *Oil Reservoir Engineering*, Robert E. Krieger Publishing Co., Huntington, New York (1977) 303–304.
68. *Reservoir Fluid Database*, GeoMark Research Inc., Houston (2003).
69. Allen, T.O. and Roberts, A.P.: *Production Operations: Well Completions, Workover, and Stimulation*, Vol. 2, second edition, Oil and Gas Consultants Intl. Inc., Tulsa (1982) Chap. 2.
70. McCain, W.D. Jr.: *The Properties of Petroleum Fluids*, second edition, PennWell Publishing Co., Tulsa (1990).

71. Whitson, C.H.: “Characterizing Hydrocarbon Plus Fractions,” *SPEJ* (August 1983) 683.
72. Watson, K.M. and Nelson, E.F.: “Improved Methods for Approximating Critical and Thermal Properties of Petroleum,” *Industrial and Engineering Chemistry* (1933) 880.
73. Watson, K.M., Nelson, E.F., and Murphy, G.B.: “Characterization of Petroleum Fractions,” *Industrial and Engineering Chemistry* (1935) 1460.
74. Riazi, M.R. and Daubert, T.E.: “Simplify Property Predictions,” *Hydrocarbon Processing* (March 1980) 115.
75. Elsharkawy, A.M., Elgibaly, A.A., and Alikhan, A.A.: “Assessment of the PVT Correlations for Predicting the Properties of Kuwaiti Crude Oils,” *J. of Petroleum Science and Engineering* (1995) 219.
76. Mahmood, M.A. and Al-Marhoun, M.A.: “Evaluation of Empirically Derived PVT Properties for Pakistani Crude Oils,” *J. of Petroleum Science and Engineering* (1996) 275.
77. Robertson, C.J.: “Comparison of Revised PVT Properties with Published Correlations,” Marathon Oil Co. Internal Report, Houston (April 1983).
78. Valkó, P.P. and McCain W.D. Jr.: “Reservoir Oil Bubblepoint Pressures Revisited: Solution Gas-Oil Ratios and Surface Specific Gravities,” *J. of Petroleum Science and Engineering* (2003) 153.
79. Cragoe, C.S.: “Thermodynamic Properties of Petroleum Products,” Bureau of Standards, U.S. Dept. of Commerce (1929) Miscellaneous Pub. No. 97, 22.
80. Jacobson, H.A.: “The Effect of Nitrogen on Reservoir Fluid Saturation Pressure,” *J. Cdn. Pet. Tech.* (July–September 1967) 101.
81. Al-Fattah, S.M. and Al-Marhoun, M.A.: “Evaluation of Empirical Correlations For Bubblepoint Oil Formation Volume Factor,” *J. of Petroleum Science and Engineering* (September 1994) 341.
82. Beggs, H.D. and Brill, J.P.: *Two Phase Flow in Pipes*, 3rd ed., 2nd printing, U. of Tulsa, Tulsa (December 1977).
83. Weinaug, C.F. and Katz, D.L.: “Surface Tensions of Methane-Propane Mixtures,” *Industrial and Engineering Chemistry* (February 1943) 239.
84. Katz, D.L., Monroe, R.R., and Trainer, R.R.: “Surface Tension of Crude Oils Containing Dissolved Gases,” *Petroleum Technology* (September 1943) 1.
85. Ramey, H.J. Jr.: “Correlations of Surface and Interfacial Tensions of Reservoir Fluids,” unsolicited paper SPE 4429 (1973).
86. Asheim, H.: “Extension of the Black-Oil Model To Predict Interfacial Tension,” paper SPE 19383 available from SPE, Richardson, Texas (1989).
87. Bradley, H.B.: *Petroleum Engineering Handbook*, SPE, Richardson, Texas (1987) Chap. 22.
88. Sutton, R.P.: “Compressibility Factors for High-Molecular-Weight Reservoir Gases,” paper SPE 14265 presented at the 1985 SPE Annual Technical Conference and Exhibition, Las Vegas, Nevada, 22–25 September.

### Conversion Factors

°API	141.5/(131.5+°API)		= g/cm <sup>3</sup>
bbbl ×	1.589 873	E-01	= m <sup>3</sup>
cp ×	1.0*	E-03	= Pa·s
Cs ×	1.0*	E-06	= m <sup>2</sup> /s
dyne ×	1.0*	E-02	= mN
ft <sup>3</sup> ×	2.831 685	E-02	= m <sup>3</sup>
°F	(°F-32)/1.8		= °C
in. ×	2.54*	E+00	= cm
lbm ×	4.535 924	E-01	= kg
psi ×	6.894 757	E+00	= kPa

\*Conversion factor is exact.

## Appendix

TABLE A-1—BUBBLEPOINT PRESSURE CORRELATIONS															
Author	Publication Date	Correlation	Origin												
Standing <sup>21,29</sup>	1947	$p_b = 18.2 \left[ \left( \frac{R_s}{\gamma_g} \right)^{0.831} 10^{(0.00091 T - 0.0118 \gamma_{API}) - 1.4} \right]$	California												
Elam <sup>30</sup>	1957	$p_b = \frac{R_s^{0.702}}{\gamma_g^{0.514}} e^{(0.00348 T - 0.0282 \gamma_{API} + 3.58)}$	Texas												
Lasater <sup>1</sup>	1958	$p_b = \frac{p_f(T + 459.67)}{\gamma_g}$ $x_g = \left[ 1 + \frac{\gamma_a}{7.521 \times 10^{-6} R_s M_a} \right]^{-1}$ $p_f = e^{\left( \frac{x_g - 0.15649}{0.33705} \right) - 0.59162}$	Midcontinent U.S.												
Vazquez and Beggs <sup>23,24</sup>	1976	$p_b = \left[ A \left( \frac{R_s}{\gamma_{gc}} \right) 10^{\left( \frac{B \gamma_{gc}}{T + 459.67} \right) C} \right]$ $\gamma_{gc} = \gamma_g \left[ 1 + (0.5912 \times 10^{-4}) \gamma_{API} T_{sp} \log \left( \frac{p_{sp}}{114.7} \right) \right]$	Worldwide												
<table border="1"> <thead> <tr> <th>Coefficient</th> <th><math>\gamma_{API} \leq 30</math></th> <th><math>\gamma_{API} &gt; 30</math></th> </tr> </thead> <tbody> <tr> <td>A</td> <td>27.64</td> <td>56.06</td> </tr> <tr> <td>B</td> <td>-11.172</td> <td>-10.393</td> </tr> <tr> <td>C</td> <td>0.9143</td> <td>0.8425</td> </tr> </tbody> </table>				Coefficient	$\gamma_{API} \leq 30$	$\gamma_{API} > 30$	A	27.64	56.06	B	-11.172	-10.393	C	0.9143	0.8425
Coefficient	$\gamma_{API} \leq 30$	$\gamma_{API} > 30$													
A	27.64	56.06													
B	-11.172	-10.393													
C	0.9143	0.8425													
Glasø <sup>12</sup>	1980	nonvolatile oils $X = \left( \frac{R_s}{\gamma_g} \right)^{0.816} \left( \frac{T^{0.172}}{\gamma_{API}^{0.989}} \right)$ volatile oils $X = \left( \frac{R_s}{\gamma_g} \right)^{0.816} \left( \frac{T^{0.130}}{\gamma_{API}^{0.989}} \right)$ $p_b = 1.7669 + 1.7447 \log X - 0.30218 (\log X)^2$	North Sea												
Labedi <sup>31,32</sup>	1982	$p_b = \frac{6.0001}{\gamma_{ga}} \left[ \frac{R_s^{0.6714} \left( \frac{T}{\gamma_{API}} \right)^{0.7097} T_{sp}^{0.08929}}{10^{(7.995 \times 10^{-5} R_s)}} \right]$	Libya, Nigeria, and Angola												
Owolabi <sup>33</sup>	1984	$p_b = 55.0 + 0.8643 \left[ \left( \frac{R_s}{\gamma_g} \right)^{1.253} \frac{T^{0.172}}{\gamma_{API}^{0.178}} \right]$	Alaska Cook Inlet												
Owolabi <sup>33</sup>	1984	$p_b = -987.56359 + 179.58816 \left[ \left( \frac{R_s}{\gamma_g} \right)^{0.4808266} \frac{T^{0.09353150}}{\gamma_{API}^{0.16048320}} \right]$	Alaska North Slope												
Al-Marhoun <sup>34</sup>	1985	$X = R_s^{0.722569} \frac{\gamma_a^{3.046590}}{\gamma_g^{1.879109}} (T + 459.67)^{1.302347}$ $p_b = -64.13891 + 7.02362 \times 10^{-3} X - 2.278475 \times 10^{-9} X^2$ where $11,309.1 < X < 1,541,298.4$	Saudi Arabia												

TABLE A-1—BUBBLEPOINT PRESSURE CORRELATIONS (continued)

Author	Publication Date	Correlation	Origin																								
Obomanu and Okpobin <sup>35</sup>	1987	$p_b = \left( \frac{R_s T^{0.497} 10^{0.011}}{1.01136371 \gamma_g^{2.15} \gamma_{API}^{1.27}} \right)^{1.0782}$	Nigeria																								
Al-Marhoun <sup>36</sup>	1988	$p_b = \frac{5.38088 \times 10^{-3} R_s^{0.715082} \gamma_g^{3.1457} (T + 459.67)^{1.32657}}{\gamma_g^{1.87784}}$	Saudi Arabia																								
Asgarpour <i>et al.</i> <sup>37</sup>	1988	$p_b = a_1 \gamma_g^{a_2} \gamma_{API}^{a_3} T^{a_4} \left( \frac{R_s}{5.614583} \right)^{a_5}$ where T has units of °C	Canada																								
<table border="1"> <thead> <tr> <th>Coefficient</th> <th>Cardium/Viking</th> <th>D-2/Nisku</th> <th>D-3/Leduc</th> </tr> </thead> <tbody> <tr> <td>a<sub>1</sub></td> <td>70.9815</td> <td>83.7883</td> <td>193.770</td> </tr> <tr> <td>a<sub>2</sub></td> <td>-0.0101</td> <td>-0.4114</td> <td>0.0928</td> </tr> <tr> <td>a<sub>3</sub></td> <td>-0.2514</td> <td>-0.2697</td> <td>-1.1369</td> </tr> <tr> <td>a<sub>4</sub></td> <td>0.4593</td> <td>0.2810</td> <td>0.7899</td> </tr> <tr> <td>a<sub>5</sub></td> <td>0.5093</td> <td>0.8259</td> <td>0.6519</td> </tr> </tbody> </table>				Coefficient	Cardium/Viking	D-2/Nisku	D-3/Leduc	a <sub>1</sub>	70.9815	83.7883	193.770	a <sub>2</sub>	-0.0101	-0.4114	0.0928	a <sub>3</sub>	-0.2514	-0.2697	-1.1369	a <sub>4</sub>	0.4593	0.2810	0.7899	a <sub>5</sub>	0.5093	0.8259	0.6519
Coefficient	Cardium/Viking	D-2/Nisku	D-3/Leduc																								
a <sub>1</sub>	70.9815	83.7883	193.770																								
a <sub>2</sub>	-0.0101	-0.4114	0.0928																								
a <sub>3</sub>	-0.2514	-0.2697	-1.1369																								
a <sub>4</sub>	0.4593	0.2810	0.7899																								
a <sub>5</sub>	0.5093	0.8259	0.6519																								
Al-Najjar, Al-Soof, and Al-Khalisy <sup>38</sup>	1988	$p_b = a_1 \left( \frac{R_s}{\gamma_g} \right)^{a_2} e^{a_3 \left[ \frac{\gamma_{API}}{(T + 459.67)} \right]}$	Iraq																								
<table border="1"> <thead> <tr> <th>Coefficient</th> <th><math>\gamma_{API} \leq 30</math></th> <th><math>\gamma_{API} &gt; 30</math></th> </tr> </thead> <tbody> <tr> <td>A</td> <td>7.920</td> <td>30.910</td> </tr> <tr> <td>B</td> <td>1.025</td> <td>0.816</td> </tr> <tr> <td>C</td> <td>-24.244</td> <td>-19.748</td> </tr> </tbody> </table>				Coefficient	$\gamma_{API} \leq 30$	$\gamma_{API} > 30$	A	7.920	30.910	B	1.025	0.816	C	-24.244	-19.748												
Coefficient	$\gamma_{API} \leq 30$	$\gamma_{API} > 30$																									
A	7.920	30.910																									
B	1.025	0.816																									
C	-24.244	-19.748																									
Dokla and Osman <sup>39</sup>	1990	$p_b = \frac{8363.86 R_s^{0.734047} \gamma_w^{0.107091}}{\gamma_w^{1.010849} (T + 459.67)^{0.022364}}$	United Arab Emirates																								
Petrosky <sup>10,11</sup>	1990	$p_b = 112.727 \left[ \frac{R_s^{0.571421}}{\gamma_g^{0.8439} 10^{[7.916 \times 10^{-3} \gamma_{API}^{1.06} - 4.561 \times 10^{-4} T^{1.0511]}} \right] = 12.340$	Gulf of Mexico																								
Kartoatmodjo and Schmidt <sup>6,b</sup>	1991	$p_b = \left[ \frac{R_s}{A \gamma_w^{0.4} 10^{[ \frac{\gamma_{API}}{(T + 459.67)} ]}} \right]^{0.1}$ $\gamma_w = \gamma_g \left[ 1 + 0.1595 \frac{\gamma_{API}^{0.4078}}{T^{0.2466}} \log \left( \frac{p_g}{114.7} \right) \right]$	Indonesia, North America, Middle East, and Latin America																								
<table border="1"> <thead> <tr> <th>Coefficient</th> <th><math>\gamma_{API} \leq 30</math></th> <th><math>\gamma_{API} &gt; 30</math></th> </tr> </thead> <tbody> <tr> <td>A</td> <td>0.05958</td> <td>0.03150</td> </tr> <tr> <td>B</td> <td>0.7972</td> <td>0.7587</td> </tr> <tr> <td>C</td> <td>13.1405</td> <td>11.289</td> </tr> <tr> <td>D</td> <td>0.998602</td> <td>0.914328</td> </tr> </tbody> </table>				Coefficient	$\gamma_{API} \leq 30$	$\gamma_{API} > 30$	A	0.05958	0.03150	B	0.7972	0.7587	C	13.1405	11.289	D	0.998602	0.914328									
Coefficient	$\gamma_{API} \leq 30$	$\gamma_{API} > 30$																									
A	0.05958	0.03150																									
B	0.7972	0.7587																									
C	13.1405	11.289																									
D	0.998602	0.914328																									
Farshad <sup>5</sup>	1992	$p_b = 64.14 \left[ \frac{R_s^{0.6343}}{\gamma_g^{1.15036} 10^{[7.97 \times 10^{-3} \gamma_{API} - 1.35 \times 10^{-4} T]}} \right] - 7.2818$	Columbia																								
Macary <sup>40</sup>	1992	$p_b = 204.257 e^{[7.7 \times 10^{-3} T - 9.7 \times 10^{-4} \gamma_{API} - 0.0003 \gamma_g]} (R_s^{0.51} - 4.7927)$	Gulf of Suez Egypt																								

TABLE A-1—BUBBLEPOINT PRESSURE CORRELATIONS (continued)

Author	Publication Date	Correlation	Origin
Omar and Todd <sup>41,42</sup>	1993	$X = 1.4256 - 0.2608 B_v - 0.4596 \gamma_g + 0.04481 B_v^2 + 0.2360 \gamma_g^2 - \frac{0.1077}{\gamma_g B_v}$ $p_b = 18.2 \left[ \left( \frac{R_v}{\gamma_g} \right)^X 10^{(0.00091 T - 0.0125 \gamma_{API})} - 1.4 \right]$	Malaysia
Hasan <sup>43</sup>	1993	$p_b = 18.3 \left[ \left( \frac{R_v}{\gamma_g} \right)^{0.87} 10^{(0.00091 T - 0.0125 \gamma_{API})} + 2.2 \right]$	Indonesia
De Ghetto <sup>44,45</sup>	1994	<p>Extra heavy oil (<math>^{\circ}\text{API} \leq 10</math>)</p> $p_b = 10.7025 \left( \frac{R_v}{\gamma_g} \right)^{0.8986} 10^{(0.00156 T - 0.00169 \gamma_{API})}$ <p>Heavy oil (<math>10 &lt; ^{\circ}\text{API} \leq 22.3</math>)</p> $p_b = \left[ \frac{56.434 R_v}{\gamma_{gc} 10^{\left[ \frac{10.9267 \gamma_{API}}{(T + 459.67)} \right]}} \right]^{-0.8294}$ <p>Medium oil (<math>22.3 &lt; ^{\circ}\text{API} \leq 31.1</math>)</p> $p_b = \left( \frac{R_v}{0.10084 \gamma_{gc}^{0.2556} 10^{\left[ \frac{7.4576 \gamma_{API}}{(T + 459.67)} \right]}} \right)^{1.0134}$ <p>Light oil (<math>^{\circ}\text{API} &gt; 31.1</math>)</p> $p_b = \left( \frac{R_v}{0.01347 \gamma_{gc}^{0.3873} 10^{\left[ \frac{12.753 \gamma_{API}}{(T + 459.67)} \right]}} \right)^{0.8536}$ <p>Agip Model</p> $p_b = \left( \frac{37.966 R_v}{\gamma_{gc} 10^{\left[ \frac{9.441 \gamma_{API}}{(T + 459.67)} \right]}} \right)^{0.8669}$	Mediterranean Basin, Africa, Persian Gulf, and North Sea
Almehaideb <sup>46</sup>	1997	$p_b = -620.592 + 6.23087 R_v \frac{\gamma_{API}}{\gamma_g B_v^{1.38559}} + 2.89868 T$ <p>where</p> $B_v = 1.122018 + \frac{1.410 \times 10^{-6} R_v T}{\gamma_{API}^2}$	United Arab Emirates



TABLE A-1—BUBBLEPOINT PRESSURE CORRELATIONS (continued)			
Author	Publication Date	Correlation	Origin
Elsharkawy <sup>47</sup>	1997	for $\gamma_{API} > 30$ $p_b = \left[ \frac{R_s}{\gamma_g^{0.04439} \gamma_{API}^{1.1394} 10^{(6.392 - 10^{-4} T - 2.188)}} \right]^{1.0551194}$ for $\gamma_{API} \leq 30$ $p_b = \left[ \frac{R_s}{\gamma_g^{(0.4636 \gamma_{API} / T - 1.2179)}} \right]^{-0.847271}$	Kuwait
Khairy <sup>48</sup>	1998	$p_b = 49.3647 \frac{R_s^{0.5774} T^{0.0041}}{\gamma_g^{1.4676} \gamma_{API}^{1.0303}}$	Egypt
Al-Shammasi <sup>2</sup>	1999	$p_b = \frac{\gamma_w^{5.527215} [\gamma_g R_s (T + 459.67)]^{0.781210}}{e^{(1.041408 p_c \gamma_s)}}$	Worldwide
Levitan and Murtha <sup>49</sup>	1999	$p_b = 14.7 \left( \frac{R_s}{\gamma_g} \right)^{0.85} \gamma_w^5 \left( \frac{T + 459.67}{519.67} \right)^{1.5}$	na
Velarde <sup>3</sup>	1999	$p_b = 1091.47 \left[ \frac{R_s^{0.081465} 10^{(0.013098 T^{0.30297} - 0.25 \cdot 10^{-4} \gamma_{API}^{1.70423})}}{\gamma_g^{0.161488}} - 0.740152 \right]^{0.454891}$ $A = 9.73 \times 10^{-7} \gamma_g^{1.1672608} \gamma_{API}^{-0.929870} T^{0.247235} p_b^{1.056052}$ $B = 0.022339 \gamma_g^{-1.004750} \gamma_{API}^{-0.337711} T^{0.132795} p_b^{0.302065}$ $C = 0.725167 \gamma_g^{-1.485480} \gamma_{API}^{-0.164741} T^{-0.091230} p_b^{0.047094}$ $p_c = \frac{p}{p_b}$ $R_s = R_{sb} [A p_c^B + (1 - A) p_c^C]$	na
Dindoruk and Christman <sup>9</sup>	2001	$A = \frac{1.42828 \times 10^{-10} T^{2.844501797} - 6.74896 \times 10^{-4} \gamma_{API}^{1.225226436}}{(0.033383304 + 2 \gamma_g^{0.084226069} R_s^{-0.272945957})^2}$ $p_b = 1.86997927 \left( \frac{R_s^{1.221486524} 10^d}{\gamma_g^{1.370508349}} + 0.011688308 \right)$ $A = \frac{4.86996 \times 10^{-6} \gamma_{API}^{5.730982539} + 9.9251 \times 10^{-3} T^{1.776179364}}{(44.2500268 + 2 \gamma_{API}^{2.702889206} p_b^{-0.744335673})^2}$ $R_s = \left[ \left( \frac{p_b}{3.35975497} + 28.10133245 \right) \gamma_g^{1.57905016} 10^d \right]^{-0.928131344}$	Gulf of Mexico

TABLE A-2—ADDITIONAL INFORMATION FOR BUBBLEPOINT PRESSURE CORRELATIONS

Author	No. of Data Points	$p_b$ Range (psia)	$T$ Range (°F)	$R_g$ Range (scf/STB)	API Range	$\gamma_g$ Range	AAE* (%)	ASD** (%)	AAAE† (%)
Standing <sup>21,29</sup>	105	130 to 7,000	100 to 258	20 to 1,425	16.5 to 63.8	0.59 to 0.95	4.8	na	na
Elam <sup>30</sup>	231	168 to 4,595	85 to 245	11 to 1,597	19 to 53	0.56 to 1.95	13.6	na	na
Lasater <sup>1</sup>	158	48 to 5,780	82 to 272	3 to 2,905	17.9 to 51.1	0.57 to 1.2	3.8	na	na
Vazquez and Beggs <sup>23,24</sup>	6,004	15 to 6,055	75 to 294	0 to 2,199	15.3 to 59.3	0.51 to 1.35	-0.7	na	na
Glase <sup>32</sup>	41	165 to 7,142	80 to 280	90 to 2,637	22.3 to 48.1	0.65 to 1.28	1.28	6.98	na
Labedi <sup>31,32</sup>	247	121 to 6,557	100 to 306	12 to 3,366	22.9 to 52.0	0.579 to 1.251	-0.48	9.93	na
Owolabi <sup>33</sup>	7	515 to 1,802	152 to 180	140 to 309	32.7 to 35.3	0.853 to 1.094	0.79	5.03	4.22
Owolabi <sup>33</sup>	20	2,480 to 4,507	145 to 220	341 to 850	18.9 to 28.4	0.663 to 0.759	-2.41	4.78	3.75
Al-Marhoun <sup>34</sup>	200	107 to 4,315	75 to 240	24 to 1,901	14.3 to 44.6	0.752 to 1.367	1.844	10.968	7.449
Obomanu and Okpobiri <sup>35</sup>	503	na	na	na	15.0 to 43.0	na	-0.086	0.067	2.19
Al-Marhoun <sup>36</sup>	160	20 to 3,573	74 to 240	26 to 1,602	19.4 to 44.6	0.75 to 1.37	0.03	4.536	3.66
Asgarpour et al <sup>37</sup>	1,500	291 to 3,997	94 to 224	135 to 2,107	23.2 to 51.0	0.655 to 1.586	‡,§,^	na	na
Al-Najjar, Al-Soof, and Al-Khalisy <sup>38</sup>	223	580 to 4,181	160 to 242	139 to 2,408	17.0 to 44.0	0.572 to 1.319	1.39	17.06	13.87
Dokla and Osma <sup>39</sup>	51	590 to 4,640	190 to 275	181 to 2,266	282.40.3	0.80 to 1.29	0.45	10.378	7.61
Petrosky <sup>10,11</sup>	90	1,574 to 6,523	114 to 288	217 to 1,406	16.3 to 45.0	0.58 to 0.86	-0.17	2.56	3.28
Kartoatmodjo and Schmidt <sup>6,8</sup>	5,392	15 to 6,055	75 to 320	0 to 2,890	14.4 to 58.9	0.38 to 1.71	3.34	na	20.17
Farshad <sup>5</sup>	43	32 to 4,138	95 to 260	6 to 1,645	18.0 to 44.9	0.66 to 1.73	1.91	9.8	na
Macary <sup>40</sup>	90	1,200 to 4,600	130 to 290	200 to 1,200	25 to 40	0.70 to 1.00	0.52	na	7.04
Omar and Todd <sup>41,42</sup>	93	790 to 3,851	125 to 280	142 to 1,440	26.6 to 53.2	0.61 to 1.32	na	9.7	7.29
Hasan <sup>43</sup>	95	55 to 4,765	118 to 320	1 to 1,520	22.3 to 57.6	0.66 to 1.798	-0.6	24.9	18.6
De Ghetto <sup>44,45</sup>	195	107 to 6,614	81 to 342	9 to 3,299	6 to 56.8	0.624 to 1.789	b	c	na
Almehaideb <sup>46</sup>	62	501 to 4,822	190 to 306	128 to 3,871	30.9 to 48.6	0.75 to 1.12	na	6.56	4.997
Elsharkawy <sup>47</sup>	175	302 to 4,375	39 to 1,586	130 to 250	19.9 to 42.76	0.663 to 1.268	0.44	10.73	7.87
Khairy <sup>48</sup>	39	236 to 4,930	120 to 282	16 to 4,589	30.7 to 54.3	0.675 to 1.417	-1.556	17.63	14.15
Al-Shammasi <sup>2</sup>	1,243	32 to 7,127	74 to 342	6 to 3,299	6.0 to 63.7	0.51 to 3.44	na	17.17	17.85
Levitan and Murtha <sup>49</sup>	na	na	na	na	na	na	na	na	na
Velarde <sup>3</sup>	728 <sup>D</sup> 2,097 <sup>E</sup>	70 to 6,700 <sup>D</sup> 106 to 5,312 <sup>E</sup>	74 to 327 <sup>D</sup> 70 to 307 <sup>E</sup>	10 to 1,870 <sup>D</sup> 102 to 1,808 <sup>E</sup>	12 to 55 <sup>D</sup> 11.6 to 53.4 <sup>E</sup>	0.556 to 1.367 <sup>D</sup> 0.561 to 1.101 <sup>E</sup>	0.6	na	11.5 <sup>D</sup> 10.5 <sup>E</sup>
Dindoruk and Chrstman <sup>9</sup>	104	926 to 12,230	117 to 276	133 to 3,050	14.7 to 40.0	0.6017 to 1.027	-0.27	7.51	5.7

\*AAE = author average error; \*\*ASD = author standard deviation; †AAAE = author average absolute error; ‡Cardium/Viking=6.86; §D-2/Nisku=6.67; ^D-3/Leduc=14.14; ^extra heavy=6.5, heavy=17.0, medium=8.8, light=15.2 Agip=18.3; ^extra heavy=4.5, heavy=11.3, medium=9.1, light=13.8, Agip=12.5; <sup>D</sup>data for bubblepoint pressure; <sup>E</sup>data for GOR.

**TABLE A-3—OIL FORMATION VOLUME FACTOR CORRELATIONS**

Author	Publication Date	Correlation	Origin												
Standing <sup>29,50</sup>	1947	$B_{ob} = 0.972 + 1.47 \times 10^{-4} \left[ R_s \left( \frac{\gamma_g}{\gamma_o} \right)^{0.5} + 1.25T \right]^{1.175}$	California												
Elam <sup>30</sup>	1957	$B_{ob} = e^{\left[ -0.0355 + 3.55 \times 10^{-4} R_s \left( \frac{\gamma_g}{\gamma_o} \right)^{0.5} + 7.1 \times 10^{-4} T \right]}$	Texas												
Vazquez and Beggs <sup>23,24</sup>	1976	$B_{ob} = 1 + a_1 R_s + (T - 60) \left( \frac{\gamma_{API}}{\gamma_{gr}} \right) (a_2 + a_3 R_s)$	Worldwide												
		<table border="1"> <thead> <tr> <th>Coefficient</th> <th><math>\gamma_{API} \leq 30</math></th> <th><math>\gamma_{API} &gt; 30</math></th> </tr> </thead> <tbody> <tr> <td><math>a_1</math></td> <td><math>4.677 \times 10^{-4}</math></td> <td><math>4.670 \times 10^{-4}</math></td> </tr> <tr> <td><math>a_2</math></td> <td><math>1.751 \times 10^{-5}</math></td> <td><math>1.100 \times 10^{-5}</math></td> </tr> <tr> <td><math>a_3</math></td> <td><math>-1.8106 \times 10^{-8}</math></td> <td><math>1.337 \times 10^{-9}</math></td> </tr> </tbody> </table>	Coefficient	$\gamma_{API} \leq 30$	$\gamma_{API} > 30$	$a_1$	$4.677 \times 10^{-4}$	$4.670 \times 10^{-4}$	$a_2$	$1.751 \times 10^{-5}$	$1.100 \times 10^{-5}$	$a_3$	$-1.8106 \times 10^{-8}$	$1.337 \times 10^{-9}$	
Coefficient	$\gamma_{API} \leq 30$	$\gamma_{API} > 30$													
$a_1$	$4.677 \times 10^{-4}$	$4.670 \times 10^{-4}$													
$a_2$	$1.751 \times 10^{-5}$	$1.100 \times 10^{-5}$													
$a_3$	$-1.8106 \times 10^{-8}$	$1.337 \times 10^{-9}$													
Glase <sup>12</sup>	1980	$X = R_s \left( \frac{\gamma_g}{\gamma_o} \right)^{0.526} + 0.968T$ $\log(B_{ob} - 1) = -6.58511 + 2.91329 \log X - 0.27683(\log X)^2$	North Sea												
Labedi <sup>31,51</sup>	1982	$B_{ob} = 0.9976 + 5.273 \times 10^{-4} R_{sb} + 2.6636 \times 10^{-8} (T - 60) \left( \frac{\gamma_{API} P_{gr}}{P_{gr}} \right) + 1.6982 \times 10^{-5} \gamma_{API} (T - 60)$ black oil formulation where $B_{ob} \leq 1.758$ $X_1 = \frac{3.61 R_{sb}^{0.4625} B_{ob}^{13.398} P_{sp}^{0.0775}}{10^{(3.231 B_{ob})}}$ $B_o = B_{ob} - X_1 \left( 1 - \frac{P}{P_b} \right)$ volatile oil formulation where $B_o > 1.758$ $X_2 = 1.6339 - 9.152 \times 10^{-4} R_{sb} + 1.584 \times 10^{-7} R_{sb}^2$ $B_o = B_{ob} - \left( 1 - \frac{P}{P_b} \right)^{X_2}$	Libya, Nigeria, and Angola												
Owolabi <sup>33</sup>	1984	$B_{ob} = 0.9871 + 4.0689 \times 10^{-4} \left[ R_s \left( \frac{\gamma_g}{\gamma_o} \right)^{0.526} + 1.25T \right]$	Alaska Cook Inlet												
Owolabi <sup>33</sup>	1984	$B_{ob} = 0.9957 + 3.7921 \times 10^{-4} \left[ R_s \left( \frac{\gamma_g}{\gamma_o} \right)^{0.526} + 1.25T \right]$	Alaska North Slope												
Al-Marhoun <sup>34</sup>	1985	$X = R_s^{0.501538} \gamma_g^{-0.145526} \gamma_o^{-5.220726}$ $B_{ob} = 0.574095 + 7.723532 \times 10^{-4} (T + 459.67) + 2.454005 \times 10^{-3} X + 3.727676 \times 10^{-5} X^2$	Saudi Arabia												
Obomanu and Okpobiri <sup>35</sup>	1987	If $\gamma_o < 0.876$ $B_{ob} = 0.3321 + 1.404154 \times 10^{-3} R_s + 4.1588128 \times 10^{-4} R_s \frac{\gamma_g}{\gamma_o} + 1.15861 \times 10^{-5} (T + 459.67)$ If $\gamma_o \geq 0.876$ $B_{ob} = 1.0232 + 2.725 \times 10^{-3} \left[ R_s \left( \frac{\gamma_g}{\gamma_o} + T \right) \right]^{0.79}$	Nigeria												

**TABLE A-3—OIL FORMATION VOLUME FACTOR CORRELATIONS (continued)**

Author	Publication Date	Correlation	Origin																																								
Al-Marhoun <sup>36</sup>	1988	$X = R_s^{0.742390} \gamma_g^{0.321294} \gamma_o^{-1.202040}$ $B_{ob} = 0.497069 + 8.62963 \times 10^{-4} (T + 459.67) + 1.82594 \times 10^{-3} X + 3.18099 \times 10^{-6} X^2$	Saudi Arabia																																								
Asgarpour <sup>37</sup>	1988	$X = a_1 \gamma_g^{a_2} \gamma_{API}^{a_3} T^{a_4} \left( \frac{R_s}{5.614583} \right)^{a_5}$ <p>where T has units of °C</p> $B_{ob} = a_6 + a_7 X + a_8 X^2 + a_9 X^3$ <table border="1" style="margin-left: auto; margin-right: auto;"> <thead> <tr> <th>Coefficient</th> <th>Cardium/Viking</th> <th>D-2/Nisku</th> <th>D-3/Leduc</th> </tr> </thead> <tbody> <tr> <td>a<sub>1</sub></td> <td>0.1203</td> <td>0.251</td> <td>0.1941</td> </tr> <tr> <td>a<sub>2</sub></td> <td>0.0645</td> <td>0.0724</td> <td>0.0136</td> </tr> <tr> <td>a<sub>3</sub></td> <td>0.2452</td> <td>2.75 × 10<sup>-5</sup></td> <td>0.0912</td> </tr> <tr> <td>a<sub>4</sub></td> <td>0.1118</td> <td>0.1538</td> <td>0.159</td> </tr> <tr> <td>a<sub>5</sub></td> <td>0.2321</td> <td>0.2235</td> <td>0.211</td> </tr> <tr> <td>a<sub>6</sub></td> <td>1.3420</td> <td>-2.3211</td> <td>0.8603</td> </tr> <tr> <td>a<sub>7</sub></td> <td>-0.5811</td> <td>7.039</td> <td>0.7341</td> </tr> <tr> <td>a<sub>8</sub></td> <td>0.1830</td> <td>-5.0060</td> <td>-0.9378</td> </tr> <tr> <td>a<sub>9</sub></td> <td>0.1656</td> <td>1.330</td> <td>0.4686</td> </tr> </tbody> </table>	Coefficient	Cardium/Viking	D-2/Nisku	D-3/Leduc	a <sub>1</sub>	0.1203	0.251	0.1941	a <sub>2</sub>	0.0645	0.0724	0.0136	a <sub>3</sub>	0.2452	2.75 × 10 <sup>-5</sup>	0.0912	a <sub>4</sub>	0.1118	0.1538	0.159	a <sub>5</sub>	0.2321	0.2235	0.211	a <sub>6</sub>	1.3420	-2.3211	0.8603	a <sub>7</sub>	-0.5811	7.039	0.7341	a <sub>8</sub>	0.1830	-5.0060	-0.9378	a <sub>9</sub>	0.1656	1.330	0.4686	Canada
Coefficient	Cardium/Viking	D-2/Nisku	D-3/Leduc																																								
a <sub>1</sub>	0.1203	0.251	0.1941																																								
a <sub>2</sub>	0.0645	0.0724	0.0136																																								
a <sub>3</sub>	0.2452	2.75 × 10 <sup>-5</sup>	0.0912																																								
a <sub>4</sub>	0.1118	0.1538	0.159																																								
a <sub>5</sub>	0.2321	0.2235	0.211																																								
a <sub>6</sub>	1.3420	-2.3211	0.8603																																								
a <sub>7</sub>	-0.5811	7.039	0.7341																																								
a <sub>8</sub>	0.1830	-5.0060	-0.9378																																								
a <sub>9</sub>	0.1656	1.330	0.4686																																								
Al-Najjar et al. <sup>38</sup>	1988	$B_{ob} = 0.96325 + 4.9 \times 10^{-4} \left[ R_s \left( \frac{\gamma_g}{\gamma_o} \right)^{0.5} + 1.25 T \right]$	Iraq																																								
Ahmed <sup>52</sup>	1988	$B_{ob} = -0.12869353 + R_s^{0.023484804} \frac{\gamma_{API}^{0.015906573}}{\gamma_g^{0.021946351}} - 4.5243973 \times 10^{-4} T + 3.9063637 \times 10^{-6} T^2 - \frac{5.5542509}{T} - 5.7603220 \times 10^{-6} p - 3.9528992 \times 10^{-6} p^2 + \frac{16.289473}{p} + 3.8718887 \times 10^{-4} R_1 + 7.0703685 \times 10^{-8} R_1^2 - \frac{1.4358395}{R_1}$	na																																								
Abdul-Majeed and Salman <sup>53</sup>	1988	$X = \frac{R_s^{1.20}}{\gamma_g^{0.1470} \gamma_o^{5.2220}}$ $B_{ob} = 0.9657876 + 4.8141 \times 10^{-5} X - 6.89870 \times 10^{-10} X^2 + 7.73 \times 10^{-4} T$	Iraq																																								
Dokla and Osman <sup>39</sup>	1990	$X = R_s^{0.773572} \frac{\gamma_g^{0.404020}}{\gamma_o^{0.882605}}$ $B_{ob} = 4.31935 \times 10^{-2} + 1.56667 \times 10^{-3} (T + 459.67) + 1.39775 \times 10^{-3} X + 3.80525 \times 10^{-6} X^2$	United Arab Emirates																																								
Petrosky <sup>10,11</sup>	1990	$B_{ob} = 1.0113 + 7.2046 \times 10^{-5} \left( \frac{R_s^{0.3738} \gamma_g^{0.2914}}{\gamma_o^{0.6265}} + 0.24626 T^{0.5171} \right)^{1.0926}$	Gulf of Mexico																																								
Kartoatmodjo and Schmidt <sup>6-8</sup>	1991	$B_{ob} = 0.98496 + 1.0 \times 10^{-4} \left( \frac{R_s^{0.755} \gamma_g^{0.25}}{\gamma_o^{1.5}} + 0.45 T \right)^{1.3}$ $\gamma_{gc} = \gamma_g \left[ 1 + 0.1595 \frac{\gamma_{API}^{0.4078}}{T^{0.2466}} \log \left( \frac{-P_{sp}}{114.7} \right) \right]$	Indonesia, North America, Middle East and Latin America																																								

TABLE A-3—OIL FORMATION VOLUME FACTOR CORRELATIONS (continued)

Author	Publication Date	Correlation	Origin
Al-Marhoun <sup>4</sup>	1992	$B_{oh} = 1.0 + 1.77342 \times 10^{-3} R_s + 2.20163 \times 10^{-4} R_s \frac{\gamma_g}{\gamma_o} +$ $4.29258 \times 10^{-6} R_s (T - 60)(1 - \gamma_o) + 5.28707 \times 10^{-4} (T - 60)$	Middle East and North America
Farshad <sup>5</sup>	1992	$X = R_s^{0.5950} \frac{\gamma_o^{0.2360}}{\gamma_o^{1.3202}} + 0.0976 T$ $B_{oh} = 1.0 + 10^{[-2.6541 + 0.5576 \log(\gamma_o) + 0.1333 \log(X\gamma)]}$	Columbia
Macary <sup>40</sup>	1992	$B_{oh} = (1.0031 + 0.0008T)e^{\left(\frac{0.0004R_s + 0.0006\gamma_g}{\gamma_o}\right)}$	Gulf of Suez/Egypt
Omar and Todd <sup>41,42</sup>	1993	$X = 1.1663 + 7.62 \times 10^{-4} \frac{\gamma_{API}}{\gamma_g} - 0.0339 \gamma_g$ $B_{oh} = 0.972 + 1.47 \times 10^{-4} \left[ R_s \left( \frac{\gamma_g}{\gamma_o} \right)^{0.5} + 1.25 T \right]^X$	Malaysia
Almehaideb <sup>46</sup>	1997	$B_{oh} = 1.122018 + \frac{1.41 \times 10^{-6} R_s T}{\gamma_o^2}$	United Arab Emirates
Elsharkawy <sup>47</sup>	1997	$B_{oh} = 1 + 4.0428 \times 10^{-4} R_s + 6.3802 \times 10^{-4} (T - 60) +$ $7.8 \times 10^{-7} R_s (T - 60) \frac{\gamma_g}{\gamma_o}$	Kuwait
Khairy <sup>48</sup>	1998	$B_{oh} = 0.773413 + 7.05341 \times 10^{-4} R_s + 0.18669 \gamma_g -$ $9.2589 \times 10^{-4} \gamma_{API} + 4.41 \times 10^{-4} T$	Egypt
Al-Shammasi <sup>2</sup>	1999	$B_{oh} = 1 + 5.53 \times 10^{-7} R_s (T - 60) + \frac{1.81 \times 10^{-4} R_s}{\gamma_o} +$ $\frac{4.49 \times 10^{-4} (T - 60)}{\gamma_o} + \frac{2.06 \times 10^{-4} R_s \gamma_g}{\gamma_o}$	Worldwide
Levitan and Murtha <sup>49</sup>	1999	$B_{oh} = 1.0 + 0.0005 R_s \left( \frac{\gamma_g}{\gamma_o} \right)^{0.25} + \frac{0.2(T - 60)}{519.67 \gamma_g \gamma_o}$	na

TABLE A-3—OIL FORMATION VOLUME FACTOR CORRELATIONS (continued)

Author	Publication Date	Correlation	Origin
Velarde <sup>3</sup>	1999	<p>trial estimate of <math>\rho_{po}</math></p> $\rho_{po} = 52.8 - 0.01 R_s$ <p>calculate <math>\rho_a</math></p> $\rho_a = -49.8930 + 85.0149 \gamma_{gs} - 3.70373 \gamma_{gs} \rho_{po} +$ $0.047982 \gamma_{gs} \rho_{po}^2 + 2.98914 \rho_{po} - 0.035689 \rho_{po}^2$ <p>then calculate <math>\rho_{po}</math>, iterate until convergence is obtained</p> $\rho_{po} = \frac{R_s \gamma_{gs} + 4600 \gamma_o}{73.71 + R_s \frac{\gamma_{gs}}{\rho_a}}$ $\Delta \rho_p = \left( 0.167 + 16.181 \times 10^{-0.0425 \rho_{po}} \right) \left( \frac{p}{1000} \right) -$ $0.01 \left( 0.299 + 263 \times 10^{-0.0603 \rho_{po}} \right) \left( \frac{p}{1000} \right)^2$ $\Delta \rho_T = \left[ \left( 0.00302 + 1.505 (\rho_{po} + \Delta \rho_p)^{-0.951} \right) (T - 60)^{0.938} + \right.$ $\left. \left[ 0.0216 - 0.0233 \times 10^{-0.0161 (\rho_{po} + \Delta \rho_p)} \right] (T - 60)^{0.475} \right]$ $\rho_o = \rho_{po} + \Delta \rho_p - \Delta \rho_T$ $B_{ob} = \frac{62.42797 \gamma_o + 0.01357 R_s \gamma_g}{\rho_o}$	na
Dindoruk and Christman <sup>9</sup>	2001	$X = \frac{\left[ \frac{R_s^{2.510755}}{\gamma_g^{4.852538} \gamma_o^{11.8335}} + 1.365428 \times 10^5 (T - 60)^{2.25288} + 10.0719 R_s \right]^{-0.4450849}}{\left[ 5.352624 + 2 R_s^{-0.6309052} \gamma_g^{-0.9000749} (T - 60) \right]^2}$ $B_{ob} = 0.9871766 + 7.865146 \times 10^{-4} X + 2.689173 \times 10^{-6} X^2 +$ $1.100001 \times 10^{-5} (T - 60) \frac{\gamma_{API}}{\gamma_g}$	Gulf of Mexico

TABLE A-4—ADDITIONAL INFORMATION FOR OIL FORMATION VOLUME FACTOR CORRELATIONS									
Author	No. of Data Points	$B_o$ Range (Bbl/STB)	T Range (°F)	$R_o$ Range (scf/STB)	API Range	$\gamma_g$ Range	AAE (%)	ASD (%)	AAAE (%)
Standing <sup>29,50</sup>	105	1.024 to 2.15	100 to 258	20 to 1,425	16.5 to 63.8	0.59 to 0.95	1.17	na	na
Elam <sup>30</sup>	205	1.019 to 2.115	85 to 245	11 to 1,597	19.0 to 53.0	0.562 to 1.950	2.2	na	na
Vazquez and Beggs <sup>23,24</sup>	6,004	1.028 to 2.226	75 to 294	0 to 2,199	15.3 to 59.3	0.511 to 1.35	-0.4	na	na
Glasø <sup>12</sup>	41	1.032 to 2.588	80 to 280	90 to 2,637	22.3 to 48.1	0.65 to 1.28	-0.43	2.18	na
Labedi <sup>31,51</sup>	331	1.047 to 2.925	100 to 306	10 to 3,366	22.91 to 52.0	na	-0.077	2.82	na
Owolabi <sup>33</sup>	7	1.129 to 1.205	152 to 180	140 to 309	32.7 to 35.3	0.853 to 1.094	0.059	0.199	0.158
Owolabi <sup>33</sup>	20	1.167 to 1.399	145 to 220	341 to 850	18.9 to 28.4	0.663 to 0.759	-0.185	0.789	0.632
Al-Marhoun <sup>34</sup>	200	1.02 to 2.42	75 to 240	24 to 1,901	14.3 to 44.6	0.752 to 1.367	-0.055	2.607	1.861
Obomanu and Okpobiri <sup>35</sup>	503	na	na	na	15.0 to 43.0	na	-0.114* -0.026**	0.042* 0.018**	2.178* 1.178**
Al-Marhoun <sup>36</sup>	160	1.032 to 1.997	74 to 240	26 to 1,602	19.4 to 44.6	0.75 to 1.37	-0.01	1.18	0.88
Asgarpour <sup>37</sup>	1,500	1.05 to 2.30	94 to 224	135 to 2,107	23.2 to 51.0	0.655 to 1.577	†,‡,§	na	na
Al-Najjar <sup>38</sup>	223	na	160 to 242	139 to 2,408	17.0 to 44.0	0.572 to 1.319	-0.54	3.22	1.98
Ahmed <sup>52</sup>	na	na	na	na	na	na	na	na	na
Abdul-Majeed and Salman <sup>53</sup>	420	1.028 to 2.042	75 to 290	0 to 1,664	9.5 to 59.5	0.51 to 1.35	-0.24	1.91	1.4
Dokla and Osman <sup>39</sup>	51	1.216 to 2.493	190 to 275	181 to 2,266	28.2 to 40.3	0.80 to 1.29	0.023	1.681	1.225
Petrosky <sup>10,11</sup>	90	1.118 to 1.623	114 to 288	217 to 1,406	16.3 to 45.0	0.58 to 0.85	-0.01	0.58	0.64
Kartoatmodjo and Schmidt <sup>6-6</sup>	5,392	1.022 to 2.747	75 to 320	0 to 2,890	14.4 to 58.9	0.38 to 1.71	-0.104	na	2.025
Al-Marhoun <sup>4</sup>	4,012	1.010 to 2.960	75 to 300	0 to 3,265	9.5 to 55.9	0.575 to 2.52	0	0.6787	0.57
Farshad <sup>5</sup>	107	1.060 to 2.064	95 to 280	6 to 1,645	18.0 to 44.9	0.66 to 1.7	0.0028	0.0338	0.02
Macary <sup>40</sup>	90	1.20 to 2.00	130 to 290	200 to 1,200	25 to 40	0.70 to 1.00	0.52	7.04	na
Omar and Todd <sup>41,42</sup>	93	1.085 to 1.954	125 to 280	142 to 1,440	26.6 to 53.2	0.612 to 1.32	na	1.88	1.44
Almehaideb <sup>46</sup>	62	1.142 to 3.562	190 to 306	128 to 3,871	30.9 to 48.6	0.75 to 1.12	na	5.17	1.35
Elsharkawy <sup>47</sup>	171	1.076 to 1.969	130 to 250	39 to 1,586	19.9 to 42.76	0.663 to 1.268	0.12	1.96	1.43
Khairy <sup>48</sup>	39	1.064 to 4.42	120 to 282	16 to 4,569	30.7 to 54.3	0.675 to 1.417	0.1521	4.1	3.27
Al-Shammasi <sup>2</sup>	1,345	1.02 to 2.916	74 to 342	6.0 to 3,299	6.0 to 63.7	0.51 to 3.44	na	2.27	1.806
Levitan and Murtha <sup>49</sup>	na	na	na	na	na	na	na	na	na
Velarde <sup>3</sup>	2,097	1.040 to 2.082	70 to 307	102 to 1,808	11.6 to 53.4	0.561 to 1.101	na	na	1.74
Dindoruk and Christman <sup>8</sup>	99	1.085 to 2.738	117 to 276	133 to 3,050	14.7 to 40.0	0.6017 to 1.027	-0.11	3.17	2.00

\* $\gamma_g < 0.876$ ; \*\* $\gamma_g \geq 0.876$ ; †Cardium/Viking=1.90; ‡D-2/Nisku=1.18; §D-3/Leduc=1.84.

TABLE A-5—ISOTHERMAL COMPRESSIBILITY CORRELATIONS

Author	Publication Date	Correlation	Origin
Calhoun <sup>54</sup>	1947	$c_o = \frac{(68.399 - 99.967 \gamma_{ob} + 28.852 \gamma_{ob}^2)}{1 \times 10^6}$	na
Standing <sup>13</sup>	1974	$c_o = 10^{-6} e^{\left[ \frac{p_o + 4.347 \times 10^{-3} (p - p_h) - 79.1}{7.141 \times 10^{-4} (p - p_h) - 12.938} \right]}$	na
Vazquez and Beggs <sup>23,24</sup>	1976	$c_o = \frac{5R_s + 17.2T - 1180\gamma_{gc} + 12.61\gamma_{API} - 1.433}{10^5 p}$	Worldwide
Labedi <sup>31,51</sup>	1982	$c_{ob} = 10^{-7.902} B_{ob}^{1.3221} \gamma_{API}^{1.0507} T^{0.5369}$ at pressures above bubblepoint $c_o = c_{ob} - \left( 10^{-8.202} B_{ob}^{2.9650} T^{1.2194} \left( 1 - \frac{p_h}{p} \right) \right)$	Libya, Nigeria, and Angola
Ahmed <sup>52</sup>	1988	$c_o = \frac{e^{(-1.8473 \times 10^{-4} p)}}{24841.0822 + 14.07428745 R_s}$	na
Petrosky <sup>10,11</sup>	1990	$c_o = \frac{1.705 \times 10^{-7} R_s^{0.69357} \gamma_g^{0.1885} \gamma_{API}^{0.3272} T^{0.6729}}{p^{0.5906}}$	Gulf of Mexico
Kartoatmodjo and Schmidt <sup>6-8</sup>	1991	$c_o = \frac{10^{(0.83415 + 0.5002 \log(R_s) + 0.3613 \log(\gamma_{API}) + 0.7606 \log(T) - 0.35505 \log(\gamma_{gc}))}}{10^6 p}$	Indonesia, North America, Middle East, and Latin America
Al-Mahoun <sup>4</sup>	1992	$X = -1.3668 \times 10^{-5} R_s - 1.95682 \times 10^{-8} R_s^2 + 2.408026 \times 10^{-2} \gamma_{gc} - 9.26019 \times 10^{-8} (T + 459.67)^2$ $c_o = \frac{X \ln\left(\frac{p}{p_h}\right)}{(p_h - p)}$	Middle East and North America
Farshad <sup>5</sup>	1992	$X = R_s^{0.1982} T^{0.6685} \gamma_g^{-0.21435} \gamma_{API}^{1.0116} p^{-0.1610}$ $c_o = 10^{(-5.4531 + 5.03 \times 10^{-4} X - 3.5 \times 10^{-8} X^2)}$	Columbia
De Ghetto <sup>44,45</sup>	1994	Extra heavy oil ( $^{\circ}\text{API} \leq 10$ ) $c_o = \frac{-889.6 + 3.1374 R_s + 20T - 627.3 \gamma_{gc} - 81.4476 \gamma_{API}}{10^5 p}$ Heavy oil ( $10 < ^{\circ}\text{API} \leq 22.3$ ) $c_o = \frac{2.9646 R_s + 25.5439 T - 1230.5 \gamma_{gc} + 41.91 \gamma_{API} - 2841.8}{10^5 p}$ Medium oil ( $22.3 < ^{\circ}\text{API} \leq 31.1$ ) $c_o = \frac{2.2246 R_{ob} + 26.0644 T - 2080.823 \gamma_{gc} - 9.6807 \gamma_{API} - 705.288}{10^5 p}$ Light oil ( $^{\circ}\text{API} > 31.1$ ) $c_o = \frac{B_{ob}^{1.8789} \gamma_{API}^{-0.3646} T^{0.1966}}{10^{6.1646}} - \left( 1 - \frac{p_h}{p} \right) \frac{B_{ob}^{2.9392} T^{1.349}}{10^{8.98}}$ Agip Model $c_o = \frac{4.133 R_{ob} + 22.12 T - 1323.8 \gamma_{gc} + 10.5 \gamma_{API} - 1682.8}{10^5 p}$	Mediterranean Basin, Africa, Persian Gulf, and North Sea



TABLE A-5—ISOTHERMAL COMPRESSIBILITY CORRELATIONS (continued)

Author	Publication Date	Correlation	Origin
Almehaideb <sup>46</sup>	1997	$c_o = \frac{-70603.2 + 98.404 R_s + 378,266 T - 6102.03 \gamma_g + 755,345 \gamma_{API}}{10^6 (p + 3755.53)}$	United Arab Emirates
Elsharkawy <sup>47</sup>	1997	$c_o = \frac{-27321 + 33.784 R_s + 238.81 T}{10^6 p}$	Kuwait
Dindoruk and Christman <sup>9</sup>	2001	$X_1 = \frac{R_s^{0.980922372} \gamma_g^{0.021003077}}{\gamma_o^{0.338486128}} + 20.00006358 (T - 60)^{0.300001059} -$ $0.876813622 R_s$ $X_2 = \frac{X_1^{1.759732076}}{\left( 2.749114986 + \frac{2 R_s^{-1.713572145}}{\gamma_g^{0.999932841}} (T - 60) \right)^2}$ $c_o = 10^{-6} \left( 4.487462368 + 0.005197040 X_2 + 1.258 \times 10^{-5} X_2^2 \right)$	Gulf of Mexico

TABLE A-6—ADDITIONAL INFORMATION FOR ISOTHERMAL COMPRESSIBILITY CORRELATIONS

Author	No. of Data Points	$c_0$ Range ( $10^6 \text{ psi}^{-1}$ )	$T$ Range ( $^{\circ}\text{F}$ )	$R_s$ Range (scf/STB)	API Range	$\gamma_p$ Range	AAE* (%)	ASD** (%)	AAAE† (%)
Calhoun <sup>64</sup>	na	na	na	na	na	na	na	na	na
Standing <sup>13</sup>	na	na	na	na	na	na	na	na	na
Vazquez and Beggs <sup>23,24</sup>	4,486	na	na	9 to 2,199	15.3 to 59.5	0.511 to 1.351	na	na	na
Labedi <sup>31,51</sup>	267	5.81 to 57.04	128 to 306	na	na	na	-0.036	8.36	na
Ahmed <sup>52</sup>	245	na	na	na	na	na	na	na	na
Petrosky <sup>10,11</sup>	304	3.507 to 24.65	114 to 288	217 to 1,406	16.3 to 45.0	0.578 to 0.852	-0.17	11.32	6.66
Kartoatmodjo and Schmidt <sup>6-8</sup>	3,588	2.701 to 127.4	75 to 320	0 to 2,890	14.4 to 59.0	na	0.301	na	23.67
Al-Mahoun <sup>4</sup>	3,711	na	75 to 240	1 to 3,113	10.4 to 49.2	0.657 to 1.588	na	na	na
Farshad <sup>5</sup>	726	2 to 34	95 to 260	6 to 1,758	13.7 to 46.5	0.59 to 1.731	-6.86	32.5	20.21
De Ghetto <sup>44,45</sup>	195	3.02 to 43	81 to 342	8 to 2,986	6.0 to 56.8	na	‡	§	na
Almehaideb <sup>48</sup>	244	na	190 to 306	128 to 3,871	30.9 to 48.6	0.746 to 1.116	na	13.33	9.88
Elsharkawy <sup>47</sup>	423	3.62 to 29.18	120 to 243	367 to 1,568	24.5 to 39.8	0.807 to 1.234	-5.36	22.74	15.23
Dindoruk and Christman <sup>9</sup>	99	5.02 to 31.91	117 to 276	133 to 3,050	14.7 to 40.0	0.6017 to 1.027	-0.85	8.95	6.21

\*AAE=author average error; \*\*ASD=author standard deviation; †AAAE=author average absolute error; ‡extra heavy=8.5, heavy=15.6, medium=12.5, light=8.5, and Agip=17.5; §extra heavy=5.0, heavy=10.7, medium=11.8, light=6.8, Agip=13.9

TABLE A-7—DEAD OIL VISCOSITY CORRELATIONS			
Author	Publication Date	Correlation	Origin
Andrade <sup>55,56</sup>	1930	$\mu_{od} = A 10^{\left[\frac{B}{T} (T + 459.67)\right]}$	na
Beal <sup>20,21</sup>	1946	$X = e^{-\left[2.302585 \left(0.43 + \frac{8.33}{\gamma_{API}}\right)\right]}$ $\mu_{od} = \left(0.32 + \frac{1.8 \times 10^7}{\gamma_{API}^{4.53}}\right) \left(\frac{360}{T + 200}\right)^X$	U.S.A
Beggs and Robinson <sup>19</sup>	1975	$X = 10^{(3.0324 - 0.02023 \gamma_{API}) T^{-1.163}}$ $\mu_{od} = 10^X - 1.0$	na
Glasø <sup>12</sup>	1980	$\mu_{od} = \left(\frac{3.141 \times 10^{10}}{T^{3.444}}\right) \log(\gamma_{API})^{[0.317 \log(T) - 36.447]}$	North Sea
Labedi <sup>31,57</sup>	1982	$\mu_{od} = 10^{9.224 \gamma_{API}^{-4.7013} T^{-0.6739}}$	Libya
Labedi <sup>31</sup>	1982	$\mu_{od} = 10^{9.37 \gamma_{API}^{-2.92} T^{-2.0356}}$	Nigeria and Angola
Egbogah and Ng <sup>58</sup>	1983	$X = 10^{\left[1.8653 - 2.5086 \times 10^{-2} \gamma_{API} - 0.8641 \log(T)\right]}$ $\mu_{od} = 10^X - 1.0$	na
Al-Khafaji <sup>59</sup>	1987	$\mu_{od} = 10^{\left[\frac{4.9563 - 0.00488 T}{(\gamma_{API} + T/30 - 14.29)^{2.766}}\right]}$	na
Petrosky <sup>10,60</sup>	1990	$\mu_{od} = \frac{2.3511 \times 10^7}{T^{2.10255}} \log(\gamma_{API})^{[4.59388 \log(T) - 22.82792]}$	Gulf of Mexico
Kartoatmodjo and Schmidt <sup>6-8</sup>	1991	$\mu_{od} = \frac{1.6 \times 10^9}{T^{2.8177}} \log(\gamma_{API})^{[5.7526 \log(T) - 26.9718]}$	Indonesia, North America, Middle East, and Latin America
De Ghetto <sup>44,45</sup>	1994	Extra heavy oil ( $^{\circ}\text{API} \leq 10$ ) $X = 10^{\left[1.90296 - 1.2619 \times 10^{-2} \gamma_{API} - 0.61748 \log(T)\right]}$ Heavy oil ( $10 < ^{\circ}\text{API} \leq 22.3$ ) $X = 10^{\left[2.06492 - 1.79 \times 10^{-2} \gamma_{API} - 0.70226 \log(T)\right]}$ Light oil ( $^{\circ}\text{API} > 31.1$ ) $X = 10^{\left[1.67083 - 1.7628 \times 10^{-2} \gamma_{API} - 0.61304 \log(T)\right]}$ for each evaluation of $X$ $\mu_{od} = 10^X - 1.0$ Medium oil ( $22.3 < ^{\circ}\text{API} \leq 31.1$ ) $\mu_{od} = \frac{220.15 \times 10^9}{T^{3.5560}} \log(\gamma_{API})^{[12.5428 \log(T) - 45.7874]}$ Agip Model $X = 10^{\left[1.8515 - 2.5548 \times 10^{-3} \gamma_{API} - 0.56238 \log(T)\right]}$ $\mu_{od} = 10^X - 1.0$	Mediterranean Basin, Africa, Persian Gulf, and North Sea

TABLE A-7—DEAD OIL VISCOSITY CORRELATIONS (continued)

Author	Publication Date	Correlation	Origin
Fitzgerald <sup>15,16,61</sup>	1997	$A_1 = 34.931 - 8.84387 \times 10^{-2} T_b + 6.73513 \times 10^{-5} T_b^2 - 1.01394 \times 10^{-8} T_b^3$ $A_2 = -2.92649 + 6.98405 \times 10^{-3} T_b - 5.09947 \times 10^{-6} T_b^2 + 7.49378 \times 10^{-10} T_b^3$ $\log X_1 = A_1 + A_2 K_w$ $\log X_2 = -1.35579 + 8.16059 \times 10^{-4} T_b + 8.38505 \times 10^{-7} T_b^2$ $v_{100} = X_1 + X_2$ $\log v_{210} = -1.92353 + 2.41071 \times 10^{-4} T_b + 0.51130 \log(T_b v_{100})$ $X_3 = v_{100} + 0.7 + e^{(-1.47 - 1.84 v_{100} - 0.51 v_{100}^2)}$ $X_4 = v_{210} + 0.7 + e^{(-1.47 - 1.84 v_{210} - 0.51 v_{210}^2)}$ $X_5 = \frac{[\log \log(X_3) - \log \log(X_4)]}{[\log(559.67) - \log(669.67)]}$ $\log(X_6) = 10 [\log \log(X_3) + X_5 (\log(T + 459.67) - \log(559.67))]$ $\mu_{od} = \left\{ \gamma_o - 4.6 \times 10^{-4} (T - 60) \right\} \times \left\{ X_6 - 0.7 - e^{[-0.7487 - 3.295(X_6 - 0.7) + 0.6119(X_6 - 0.7)^2 - 0.3193(X_6 - 0.7)^3]} \right\}$	Saudi Arabia, Iran, Iraq, Kuwait, Libya, North Sea, U.S.A., Indonesia, Soviet Union, Romania, and South America
Bennison <sup>52</sup>	1998	$\mu_{od} = 10^{(-0.8021 \gamma_{API} + 23.8765)} T^{(0.31458 \gamma_{API} - 9.21592)}$	North Sea
Elsharkawy <sup>63</sup>	1999	$X = 10^{[2.16924 - 0.02525 \gamma_{API} - 0.68875 \log(T)]}$ $\mu_{od} = 10^X - 1.0$	Middle East
Bergman <sup>13,14</sup>	2000	$X = e^{[22.53 - 0.194 \gamma_{API} + 0.00033 \gamma_{API}^2 - (3.2 - 0.0185 \gamma_{API}) \log(T + 310)]}$ $\mu_{od} = e^X - 1.0$	na
Standing <sup>13</sup>	2000	$\log(\mu_{od} / \rho_o) = \frac{1}{X_3 [K_w - (8.24 / \gamma_o)] + 1.639 X_2 - 1.059} - 2.17$ <p>where</p> $X_1 = 1 + 8.69 \log[(T + 459.67) / 559.67]$ $X_2 = 1 + 0.544 \log[(T + 459.67) / 559.67]$ $X_3 = -0.1285 \frac{(2.87 X_1 - 1) \gamma_o}{2.87 X_1 - \gamma_o}$ $\rho_o = \frac{\gamma_o}{1 + 0.000321(T - 60) 10^{(0.00462 \gamma_{API})}}$	na
Dindoruk and Christman <sup>9</sup>	2001	$\mu_{od} = \frac{a_5 T^{a_4} \log(\gamma_{API})^{[a_6 \log(T) + a_5]}}{a_5 \rho_b^{a_6} + a_7 R_s^{a_6}}$ <p>where</p> $a_1 = 14.505357625 \quad a_5 = -3.1461171 \times 10^{-9}$ $a_2 = -44.868655416 \quad a_6 = 1.517652716$ $a_3 = 9.36579 \times 10^9 \quad a_7 = 0.010433654$ $a_4 = -4.194017808 \quad a_8 = -0.000776880$	Gulf of Mexico

TABLE A-8—ADDITIONAL INFORMATION FOR DEAD OIL VISCOSITY CORRELATIONS

Author	No. of Data Points	$\mu_{ed}$ Range (cp)	T Range (°F)	API Range	AAE* (%)	ASD** (%)	AAAE† (%)
Andrade <sup>55,56</sup>	na	na	na	na	na	na	na
Beal <sup>20,21</sup>	753	0.865 to 1,550	98 to 250	10.1 to 52.5	24.2	na	na
Beggs and Robinson <sup>19</sup>	460	na	70 to 295	16.0 to 58.0	-0.64	13.53	na
Glasø <sup>12</sup>	29	0.616 to 39.10	50 to 300	20.1 to 48.1	na	na	na
Labedi <sup>31,57</sup>	91	0.66 to 4.79	100 to 306	32.2 to 48.0	-2.61	23.06	na
Labedi <sup>31</sup>	29	0.72 to 21.15	104 to 221	25.5 to 45.5	-5.87	33.03	na
Egbogah and Ng <sup>56</sup>	394	na	59 to 176	5.0 to 58.0	-5.13	55.51	na
Al-Khafaji <sup>59</sup>	350	na	60 to 300	15.0 to 51.0	-2.4	4.8	3.2
Petrosky <sup>10,60</sup>	118	0.725 to 10.25	114 to 288	25.4 to 46.1	-3.48	16.4	12.38
Kartoatmodjo and Schmidt <sup>5-8</sup>	661	0.506 to 682.0	80 to 320	14.4 to 59.0	-13.16	na	39.61
De Ghetto <sup>44,45</sup>	195	0.46 to 1,386.9	81 to 342	6.0 to 56.8	‡	§	na
Fitzgerald <sup>15,16,61</sup>	7,267	0.3 to 30,000 cst	-30 to 500	-2 to 71.5	-3.77	na	14.08
Bennison <sup>62</sup>	16	6.4 to 8,396	39 to 300	11.1 to 19.7	na	na	16.0
Eisharkawy <sup>63</sup>	254	0.6 to 33.7	100 to 300	19.9 to 48	-2.5	25.8	19.3
Bergman <sup>13,14</sup>	na	na	na	na	na	na	na
Standing <sup>13</sup>	na	na	na	na	na	na	na
Dindoruk and Christman <sup>9</sup>	95	0.896 to 62.63	121 to 276	17.4 to 40.0	-2.86	16.74	12.62

\*AAE=author average error; \*\*ASD=author standard deviation; †AAAE=author average absolute error; ‡extra heavy=17.4, heavy=37.8, medium=35.1, light=21.6, Agip=30.7; §extra heavy=8.9, heavy=21.9, medium=22.8, light=15.6, Agip=20.0.

TABLE A-9—GAS SATURATED OIL VISCOSITY CORRELATIONS

Author	Publication Date	Correlation	Origin
Chew and Connally <sup>17,18</sup>	1959	$A = 0.20 + \frac{0.80}{10^{(0.00081 R_s)}}$ $B = 0.43 + \frac{0.57}{10^{(0.00072 R_s)}}$	U.S.A., Canada, and South America
Beggs and Robinson <sup>19</sup>	1975	$A = \frac{10.715}{(R_s + 100)^{0.315}}$ $B = \frac{5.44}{(R_s + 150)^{0.338}}$	na
Labedi <sup>31,57</sup>	1982	$\mu_{ob} = \frac{10^{(2.344 - 0.035427 R_s)} \mu_{od}^{0.6447}}{p_b^{0.426}}$ <p>at <math>p &lt; p_b</math></p> $\mu_o = \frac{\mu_{ob}}{1 - (10^{-3.876} p_b^{0.5423} \gamma_{API}^{1.1302}) (1 - p/p_b)}$	Libya
Labedi <sup>31</sup>	1982	$\mu_{ob} = \frac{1.303 \mu_{od}^{0.8479}}{10^{(2.133 \times 10^{-4} p_b)}}$ <p>at <math>p &lt; p_b</math></p> $\mu_o = \frac{\mu_{ob}}{1 - (0.2861 \times 10^{(1.076 \times 10^{-4} p_b)}) (1 - p/p_b)}$	Nigeria and Angola
Khan <sup>54</sup>	1987	$\mu_{ob} = \frac{0.09 \gamma_g^{0.5}}{R_{ob}^{1/3} \left[ \frac{(T + 459.67)}{459.67} \right]^{4.5} (1 - \gamma_g)^3}$ <p>if <math>p &lt; p_b</math></p> $\mu_o = \frac{\mu_{ob} e^{[2.5 \times 10^{-4} (p - p_b)]}}{(p/p_b)^{0.14}}$	Saudi Arabia
Al-Khafaji <sup>59</sup>	1987	$X_1 = \log(R_s)$ $A = 0.247 + 0.2824 X_1 + 0.5657 X_1^2 - 0.4065 X_1^3 + 0.0631 X_1^4$ $B = 0.894 + 0.0546 X_1 + 0.07667 X_1^2 - 0.0736 X_1^3 + 0.01008 X_1^4$	na
Petrosky <sup>10,60</sup>	1990	$A = 0.1651 + \frac{0.6165}{10^{(6.0866 \times 10^{-4} R_s)}}$ $B = 0.5131 + \frac{0.5109}{10^{(1.1831 \times 10^{-3} R_s)}}$	Gulf of Mexico
Kartoatmodjo and Schmidt <sup>6-6</sup>	1991	$X_1 = 0.43 + 0.5165 \times 10^{(-8.1 \times 10^{-4} R_s)}$ $X_2 = \left[ 0.2001 + 0.8428 \times 10^{(-8.45 \times 10^{-4} R_s)} \right] \mu_{od}^{X_1}$ $\mu_{ob} = -0.06821 + 0.9824 X_2 + 4.034 \times 10^{-4} X_2^2$	Indonesia, North America, Middle East, and Latin America

**TABLE A-9—GAS SATURATED OIL VISCOSITY CORRELATIONS (continued)**

Author	Publication Date	Correlation	Origin
De Ghetto <sup>44,45</sup>	1994	Extra heavy oil ( $^{\circ}\text{API} \leq 10$ )	Mediterranean Basin, Africa, Persian Gulf, and North Sea
		$X_1 = 0.5798 + 0.3432 \times 10^{(-8.1 \times 10^{-4} R_s)}$	
		$X_2 = \left[ -0.0335 + 1.0785 \times 10^{(-8.45 \times 10^{-4} R_s)} \right] \mu_{od}^{X_1}$	
		$\mu_{ob} = 2.3945 + 0.8927 X_2 + 1.567 \times 10^{-3} X_2^2$	
		Heavy oil ( $10 < ^{\circ}\text{API} \leq 22.3$ )	
		$X_1 = 0.4731 + 0.5158 \times 10^{(-8.1 \times 10^{-4} R_s)}$	
		$X_2 = \left[ 0.2478 + 0.6114 \times 10^{(-8.45 \times 10^{-4} R_s)} \right] \mu_{od}^{X_1}$	
		$\mu_{ob} = -0.6311 + 1.078 X_2 - 3.653 \times 10^{-3} X_2^2$	
		Medium oil ( $22.3 < ^{\circ}\text{API} \leq 31.1$ )	
		$X_1 = 0.3855 + 0.5664 \times 10^{(-8.1 \times 10^{-4} R_s)}$	
		$X_2 = \left[ 0.2038 + 0.8591 \times 10^{(-8.45 \times 10^{-4} R_s)} \right] \mu_{od}^{X_1}$	
		$\mu_{ob} = 0.0132 + 0.9821 X_2 - 5.215 \times 10^{-3} X_2^2$	
Light oil ( $^{\circ}\text{API} > 31.1$ )			
$A = \frac{25.1921}{(R_s + 100)^{0.6487}}$	$\mu_{ob} = A \mu_{od}^B$		
$B = \frac{2.7516}{(R_s + 150)^{0.2135}}$			
Agip Model			
$X_1 = 0.172 + 0.7881 \times 10^{(-3.96 \times 10^{-4} R_s)}$			
$X_2 = \left[ 0.1615 + 0.7024 \times 10^{(-5.83 \times 10^{-4} R_s)} \right] \mu_{od}^{X_1}$			
$\mu_{ob} = -0.032124 + 0.9289 X_2 - 2.865 \times 10^{-2} X_2^2$			
Almehaideb <sup>46</sup>	1997	$\mu_{ob} = \frac{6.59927 \times 10^5}{R_s^{0.597627} T^{0.941624} \gamma_R^{0.555208} \gamma_{API}^{1.487449}}$	United Arab Emirates
Eisharkawy <sup>63</sup>	1999	$A = \frac{1241.932}{(R_s + 641.026)^{1.12410}}$	Middle East
$B = \frac{1768.841}{(R_s + 1180.335)^{1.06622}}$	$\mu_{ob} = A \mu_{od}^B$		
Bergman <sup>13,14</sup>	2000	$A = e^{[4.768 - 0.8359 \ln(R_s + 200)]}$	na
$B = 0.555 + \frac{133.5}{R_s + 300}$	$\mu_{ob} = A \mu_{od}^B$		
Dindoruk and Christman <sup>9</sup>	2001	$A = \frac{a_1}{e^{(a_2 R_s)}} + \frac{a_3 R_s^{a_4}}{e^{(a_5 R_s)}}$	Gulf of Mexico
$B = \frac{a_6}{e^{(a_7 R_s)}} + \frac{a_8 R_s^{a_9}}{e^{(a_{10} R_s)}}$	$\mu_{ob} = A \mu_{od}^B$		
where			
$a_1 = 1.0$	$a_6 = 1.0$		
$a_2 = 4.740729 \times 10^{-4}$	$a_7 = -2.191172 \times 10^{-3}$		
$a_3 = -1.023451 \times 10^{-3}$	$a_8 = -1.660981 \times 10^{-2}$		
$a_4 = 6.600358 \times 10^{-1}$	$a_9 = 4.233179 \times 10^{-1}$		
$a_5 = 1.075080 \times 10^{-3}$	$a_{10} = -2.273945 \times 10^{-4}$		

TABLE A-10—ADDITIONAL INFORMATION FOR GAS SATURATED OIL VISCOSITY CORRELATIONS

Author	No. of Data Points	$\mu_{ob}$ Range (cp)	$R_s$ Range (scf/STB)	AAE* (%)	ASD** (%)	AAAE† (%)
Chew and Connally <sup>17,18</sup>	2,257	na	51 to 3,544	na	na	na
Beggs and Robinson <sup>19</sup>	2,073	na	20 to 2,070	-1.83	27.25	na
Labedi <sup>31,32</sup>	91	0.115 to 3.72	na	-2.38	22.81	na
Labedi <sup>31</sup>	31	0.098 to 10.9	na	-2.3	24.23	na
Khan <sup>64</sup>	1,841	0.13 to 77.4	24 to 1,901	-0.941	7.201	5,157
Al-Khafaji <sup>59</sup>	72	na	0 to 2,100	1.8	2.8	2.7
Petrosky <sup>10,60</sup>	864	0.21 to 7.40	21 to 1,885	-3.12	19.66	14.47
Kartoatmodjo and Schmidt <sup>6-8</sup>	5,321	0.096 to 586.0	0 to 2,890	0.08	na	16.08
De Ghetto <sup>44,45</sup>	195	0.07 to 295.9	9 to 3,299	‡	§	na
Almehaideb <sup>46</sup>	57	na	128 to 3,871	na	16.26	13
Elsharkawy <sup>53</sup>	254	0.05 to 20.89	10 to 3,600	2.8	25.7	18.6
Bergman <sup>13,14</sup>	na	na	na	na	na	na
Dindoruk and Christman <sup>3</sup>	95	0.161 to 8.7	133 to 3,050	-3.05	17.29	13.2

\*AAE=author average error; \*\*ASD=author standard deviation; †AAAE=author average absolute error; ‡extra heavy=12.6, heavy=11.8, medium=11.9, light=15.2, Agip=13.9; §extra heavy=10.0, heavy=9.9, medium=9.8, light=14.8, Agip=10.8.



TABLE A-11—UNDERSATURATED OIL VISCOSITY CORRELATIONS

Author	Publication Date	Correlation	Origin
Beal <sup>20,21</sup>	1946	$\mu_o = \mu_{ob} + [0.001(p - p_b)](0.024 \mu_{ob}^{1.6} + 0.038 \mu_{ob}^{0.56})$	U.S.A.
Kouzel <sup>22</sup>	1965	$\mu_o = \mu_{ob} 10^{\left[ \frac{(p-p_b)(0.02339+0.01638 \mu_{ob}^{0.10})}{1000} \right]}$	na
Vazquez and Beggs <sup>23,24</sup>	1976	$\mu_o = \mu_{ob} \left( \frac{p}{p_b} \right)^{\left[ 2.6 p_b^{3.169} 10^{(3.9 \times 10^{-5} p_b^{-1.5})} \right]}$	Worldwide
Labedi <sup>31,57</sup>	1982	$\mu_o = \mu_{ob} + \frac{\mu_{od}^{0.9036} p_b^{0.6151}}{10^{(2.488 + 0.01976 \gamma_{API})}} \left( \frac{p}{p_b} - 1 \right)$	Libya
Labedi <sup>31</sup>	1982	$\mu_o = \mu_{ob} + 0.0483 \mu_{od}^{0.7574} \left( \frac{p}{p_b} - 1 \right)$	Nigeria and Angola
Khan <sup>64</sup>	1987	$\mu_o = \mu_{ob} e^{9.6 \times 10^{-3}(p-p_b)}$	Saudi Arabia
Al-Khafaji <sup>59</sup>	1987	$X = -0.3806 - 0.1845 \gamma_{API} + 0.004034 \gamma_{API}^2 - 3.716 \times 10^{-5} \gamma_{API}^3$ $\mu_o = \mu_{ob} + 10^{[X + 1.11 \log[0.07031(p-p_b)]]}$	na
Abdul-Majeed <sup>65</sup>	1990	$X = 1.9311 - 0.89941 (\ln R_s) - 0.001194 \gamma_{API}^2 + 0.0092545 \gamma_{API} (\ln R_s)$ $\mu_o = \mu_{ob} + 1000 \times 10^{[X - 5.2106 + 1.11 \log[6.8945757(p-p_b)]]}$	North America and Middle East
Petrosky <sup>10,60</sup>	1990	$X_1 = \log(\mu_{ob})$ $X_2 = -1.0146 + 1.3322 X_1 - 0.4876 X_1^2 - 1.15036 X_1^3$ $\mu_o = \mu_{ob} + 1.3449 \times 10^{-3} (p - p_b) 10^{X_2}$	Gulf of Mexico
Kartoatmodjo and Schmidt <sup>6-6</sup>	1991	$\mu_o = 1.00081 \mu_{ob} + 1.127 \times 10^{-3} (p - p_b)$ $\left( -6.517 \times 10^{-3} \mu_{ob}^{1.8148} + 0.0038 \mu_{ob}^{1.59} \right)$	Indonesia, North America, Middle East, and Latin America
De Ghetto <sup>44,45</sup>	1994	Extra heavy oil ( $^{\circ}\text{API} \leq 10$ ) $\mu_o = \mu_{ob} - \left( 1 - \frac{p}{p_b} \right) \frac{10^{-2.19} \mu_{od}^{1.055} p_b^{0.3132}}{10^{(0.0099 \gamma_{API})}}$ Heavy oil ( $10 < ^{\circ}\text{API} \leq 22.3$ ) $\mu_o = 0.9886 \mu_{ob} + 0.002763 (p - p_b) \times$ $\left( -0.01153 \mu_{ob}^{1.7933} + 0.0316 \mu_{ob}^{1.5939} \right)$ Medium and light oil ( $^{\circ}\text{API} > 22.3$ ) $\mu_o = \mu_{ob} - \left( 1 - \frac{p}{p_b} \right) \frac{10^{-3.8055} \mu_{od}^{1.4131} p_b^{0.6957}}{10^{(-0.00288 \gamma_{API})}}$ Agip Model $\mu_o = \mu_{ob} - \left( 1 - \frac{p}{p_b} \right) \frac{10^{-1.9} \mu_{od}^{0.7423} p_b^{0.5026}}{10^{(0.0243 \gamma_{API})}}$	Mediterranean Basin, Africa, Persian Gulf, and North Sea
Almehaideb <sup>46</sup>	1997	$\mu_o = \mu_{ob} \left( \frac{p}{p_b} \right)^{(0.134819 + 1.94345 \times 10^{-4} R_s - 1.93106 \times 10^{-9} R_s^2)}$	United Arab Emirates

TABLE A-11—UNDERSATURATED OIL VISCOSITY CORRELATIONS (continued)			
Author	Publication Date	Correlation	Origin
Kouzel—API Modified <sup>15</sup>	1997	$\mu_o = \mu_{ob} 10^{\left( \frac{(p-p_b)(-0.0102+0.04042\mu_o^{0.61})}{1000} \right)}$	na
Elsharkawy <sup>63</sup>	1999	$\mu_o = \mu_{ob} \mp \frac{10^{-2.0771(p-p_b)} \mu_{ob}^{1.19279}}{\mu_{ob}^{0.40712} p_b^{0.7941}}$	Middle East
Dindoruk and Christman <sup>9</sup>	2001	$X = a_1 + a_2 \log(\mu_{ob}) + a_3 \log(R_s) + a_4 \mu_{ob} \log(R_s) + a_5 (p - p_b)$ $\mu_o = \mu_{ob} + a_6 (p - p_b) 10^X$ <p>where</p> $a_1 = 0.776644115 \quad a_4 = 0.009147711$ $a_2 = 0.987658646 \quad a_5 = -0.000019111$ $a_3 = -0.190564677 \quad a_6 = 0.000063340$	Gulf of Mexico

**TABLE A-12—ADDITIONAL INFORMATION FOR UNDERSATURATED  
OIL VISCOSITY CORRELATIONS**

Author	No. of Data Points	$\mu_o$ Range (cp)	$\mu_{ob}$ Range (cp)	$\rho$ Range (psia)	$P_b$ Range (psia)	AAE* (%)	ASD** (%)	AAAE <sup>†</sup> (%)
Beal <sup>20,21</sup>	26	0.16 to 315	0.142 to 127	na	na	2.7	na	na
Kouzel <sup>22</sup>	95	1.78 to 202	1.22 to 134	423 to 6,015	14.7	-4.8	12.4	10.7
Vazquez and Beggs <sup>23,24</sup>	3,593	0.117 to 148	na	126 to 9,500	na	-7.541	na	na
Labedi <sup>31,57</sup>	91	na	0.115 to 3.72	na	60 to 6,358	-3.1	27.19	na
Labedi <sup>31</sup>	31	na	0.098 to 10.9	na	715 to 4,794	-6.8	41.07	na
Khan <sup>64</sup>	1,503	0.13 to 71.0	0.13 to 77.4	na	107 to 4,315	0.094	2.999	1.915
Al-Khafaji <sup>59</sup>	210	0.093 to 7.139	na	na	na	0.0578	0.713	0.44
Abdul-Majeed <sup>65</sup>	253	0.096 to 28.5	0.093 to 20.5	na	498 to 4,864	-0.0193	1.978	1.188
Petrosky <sup>10,60</sup>	404	0.22 to 4.09	0.211 to 3.546	1,600 to 10,250	1,574 to 9,552	-0.19	4.22	2.91
Kartoatmodjo and Schmidt <sup>6-8</sup>	3,588	0.168 to 517.03	0.168 to 184.86	25 to 6,015	25 to 4,775	-4.29	na	6.88
De Ghetto <sup>44,45</sup>	195	.13 to 354.6	na	na	na	‡	§	na
Almehaideb <sup>46</sup>	328	na	na	na	na	na	4.07	2.885
Kouzel—API Modified <sup>16</sup>	1,279	na	na	na	na	9.5	na	na
Elsharkawy <sup>63</sup>	254	0.2 to 5.7	na	1,287 to 10,000	na	-0.9	6.2	4.9
Dindoruk and Christman <sup>9</sup>	95	0.211 to 10.6	0.161 to 8.7	na	926 to 12,230	-0.83	8.42	5.99

\*AAE=author average error; \*\*ASD=author standard deviation; †AAAE=author average absolute error; ‡extra heavy=4.0, heavy=6.0, medium=3.5, light=6.3, Agip=6.4; §extra heavy=3.4, heavy=7.2, medium=3.7, light=16.8, Agip=6.6.



# Chapter 7

## Thermodynamics and Phase Behavior

R.T. Johns, U. of Texas at Austin

### 7.1 Introduction

Phase behavior describes the complex interaction between physically distinct, separable portions of matter called phases that are in contact with each other. Typical phases are solids, liquids, and vapors. Phase behavior plays a vital role in many petroleum applications, such as enhanced oil recovery, compositional simulation, geochemical behavior, wellbore stability, geothermal energy, environmental cleanup, multiphase flow in wellbores and pipes, and surface facilities.

Thermodynamics, which is central to understanding phase behavior, is the study of energy and its transformations. Using thermodynamics, we can follow the energy changes that occur during phase changes and predict the outcome of a process. Thermodynamics began as the study of heat applied to steam power but was substantially broadened by Gibbs in the middle to late 1800s. Gibbs' most significant contribution was the development of phase-equilibrium thermodynamics applied to multicomponent mixtures, particularly the concept of chemical potential.<sup>1</sup> The concept of chemical potential leads to the result that, at equilibrium, the chemical potential of each component must be the same in all phases ( $\mu_{iL} = \mu_{iV}$ ).

Phase-equilibrium thermodynamics seeks to determine properties such as temperature, pressure, and phase compositions that establish themselves once all tendencies for further change have disappeared. This chapter reviews the fundamentals of phase-equilibrium thermodynamics used in petroleum applications, especially those that require liquid-vapor phase behavior.<sup>2-7</sup> The next chapter in this section of the Handbook illustrates phase behavior through diagrams.

### 7.2 Fundamental Ideas and Problem Statement

**Fig. 7.1** is a schematic showing a closed container of liquid and vapor. Given constant and known temperature, pressure, and overall compositions ( $z_i$  where  $i = 1, \dots, n_c$ ) at equilibrium, the fundamental task is to quantify the molar fractions of the phases ( $L, V$ ) and compositions of the vapor ( $y_i$  where  $i = 1, \dots, n_c$ ) and liquid phases ( $x_i$  where  $i = 1, \dots, n_c$ ) that form at equilibrium. The phases are assumed to be homogeneous, in which intensive parameters such as pressure, temperature, density, viscosity, and phase compositions are uniform throughout the phase. (Thus, gravity effects are not typically considered.) Intensive properties are those that are independent of the amount of the phases (e.g., phase density, pressure, and temperature). Alternatively, extensive properties depend on the amount of the phases (e.g., total volume and

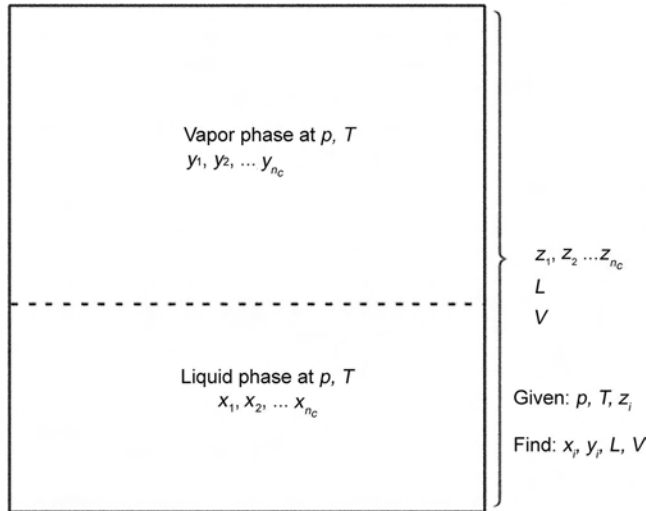


**Fig. 7.1—Vapor-liquid equilibrium at constant pressure, temperature, and overall composition. A dashed line shows a distinct interface between the two phases.**

moles of liquid). Intensive properties can be determined as the ratio of two extensive properties; for example, molar density is the number of moles divided by the total volume.

The overall compositions and phase compositions in Fig. 7.1 are written as mole fractions, which are defined by

$$z_i = \frac{\text{moles of component } i \text{ in all phases}}{\text{total moles of all phases}},$$

and

$$y_i = \frac{\text{moles of component } i \text{ in the vapor}}{\text{total moles of vapor}},$$

where  $\sum_{i=1}^{n_c} z_i = 1.0$  for the container,  $\sum_{i=1}^{n_c} x_i = 1.0$  for liquid, and  $\sum_{i=1}^{n_c} y_i = 1.0$  for vapor. The relative amounts of the phases are defined by the phase mole fractions,

$$L = \frac{\text{moles of the liquid phase}}{\text{total moles of all phases}},$$

and

$$V = \frac{\text{moles of the vapor phase}}{\text{total moles of all phases}},$$

where  $L + V = 1$ . The phase molar fractions are not saturations, although they could be converted to saturations from the phase densities. The molar fractions of the phases are related to the overall and phase compositions by

$$L = \frac{z_i - y_i}{x_i - y_i} \dots \dots \dots (7.1)$$

Thus, once the overall compositions and phase compositions are known, the phase molar fractions,  $L$  and  $V$ , are also known.

**7.2.1 Gibbs Phase Rule and Duhem's Theorem.** The Gibbs phase rule and Duhem's theorem assure us that the problem illustrated in Fig. 7.1 can be solved. Ideas and theories from thermodynamics are based on observations. Gibbs, for example, observed that the equilibrium intensive state of the system is fully known once the pressure, temperature, and phase compositions are specified. The number of intensive properties that we would like to know is, therefore,  $2 + n_c n_p$ , where  $n_p$  is the number of phases (for vapor/liquid equilibrium,  $n_p$  is two). These intensive properties can only be determined if a sufficient number of equations are available or if some of them are explicitly specified. An inventory of equations shows that there are  $n_p$  summation equations (i.e., the phase mole fractions for each phase sum to 1.0) and  $n_c(n_p - 1)$  equilibrium relations, for a total of  $n_p + n_c(n_p - 1)$  equations. The equilibrium relations could be given as  $K$ -values ( $K_i = \frac{y_i}{x_i}$ ), which relate the component liquid and vapor mole fractions or, as described later, chemical potential criteria for equilibrium (i.e.,  $\mu_{iL} = \mu_{iV}$ ).

The Gibbs phase rule says that the degrees of freedom are  $2 + n_c - n_p$ , which is the difference between the number of required intensive properties (unknowns) and the number of relations (equations). The Gibbs phase rule is only practically useful for a small number of components but does offer significant insight into the maximum number of phases that can form as well as how many intensive properties can be independently specified.

For example, suppose that only one phase ( $n_p = 1$ ) is present at equilibrium in a system containing a pure fluid ( $n_c = 1$ ). The Gibbs phase rule says that only two intensive properties can be specified (degrees of freedom are two). We cannot specify three or more intensive properties for this case, but we are free to choose which intensive properties are set. Typically, we would choose temperature and pressure. The choice of intensive properties is not completely arbitrary, for only properties related to an individual phase can be selected. Thus, properties such as the overall density of the two-phase system or the phase molar fractions,  $L$  and  $V$ , cannot be used to reduce the degrees of freedom.

Suppose next that three equilibrium phases exist in the pure fluid (i.e., the triple point). For this case, the degrees of freedom are zero, and no intensive properties can be specified. That is, the intensive properties, such as temperature and pressure, are determined and are not arbitrary at the triple point. Four phases in equilibrium with each other are not allowed by the Gibbs phase rule (neither are they observed experimentally).

Duhem's theorem is another rule, similar to the phase rule, but it specifies when both the extensive and intensive states of the system are determined. The theorem states that for any closed system containing specified moles of  $n_c$  components (from which the overall compositions can be calculated), the equilibrium state is completely determined when any two independent properties are fixed. The two independent properties may be either intensive or extensive; however, the maximum number of independent intensive properties that can be specified is given by the Gibbs phase rule. For example, when the degrees of freedom are one, at least one of the two variables must be extensive. When the degrees of freedom are zero, both must be extensive. Thus, the combination of the Gibbs phase rule and Duhem's theorem shows that the extensive and intensive state of the two-phase problem in Fig. 7.1 can be determined when the temperature, pressure, and moles of all the components are specified. For a pure component

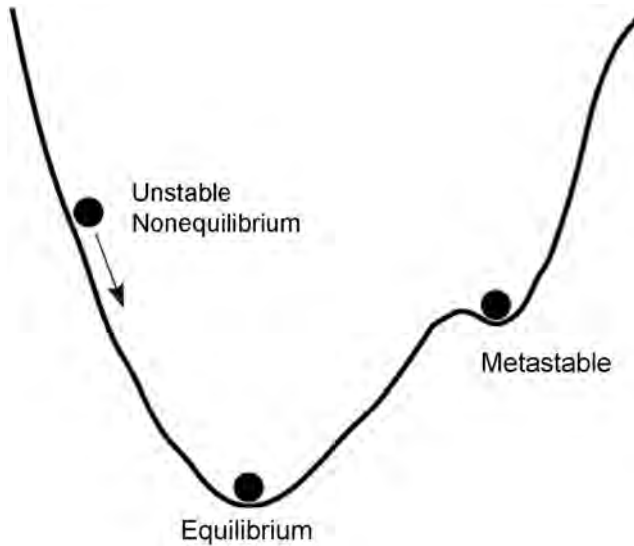


Fig. 7.2—Potential states of a system illustrated by a ball rolling down a hill.

system, the intensive and extensive state of the system is determined when the temperature, pressure, and the total number of moles are given.

**7.2.2 Equilibrium, Stability, and Reversible Thermodynamic Systems.** Thermodynamics is a macroscopic viewpoint in that it concerns itself with the properties of a system, such as temperature and density. Thermodynamics predicts the nature of a new equilibrium state—not the rate at which that state is reached. One of the characteristics of equilibrium is that the thermodynamic properties are time invariant. Furthermore, once equilibrium is reached, the process or pathway that led to equilibrium cannot be determined.

The equilibrium state is always time invariant, whether it is dynamic or static. A dynamic equilibrium process is a steady-state process, in which the properties change spatially but not temporally. A static process, while having the appearance of reaching a static state on a macroscopic scale (such as that shown in Fig. 7.1), is anything but static on a microscopic scale. Molecules from the liquid phase continue to move into the vapor phase and vice versa, but the rates of energy and mass transfer are equal, giving the appearance of equilibrium on a macroscopic scale. Indeed, this is exactly the definition for equilibrium embodied by the chemical potential criterion  $\mu_{iL} = \mu_{iV}$ .

The criterion of time invariance is a necessary, but not sufficient, condition for equilibrium. Some systems can exist in metastable states that are time invariant. For example, at the Earth's surface, diamonds are in a metastable state of pure carbon, whereas graphite is the equilibrium state. Fig. 7.2 illustrates the concept of equilibrium vs. metastable or unstable (nonequilibrium) states by considering a ball rolling down a hill into a valley. When the ball is on the side of the hill, it is unstable and will roll down the slope because of gravitational forces; this is an unstable process. The ball, however, if initially trapped in a small depression on the side of the hill, will not roll down the hill; this is a metastable state. Lacking any additional energy, the ball will stay in the metastable position. If the depression is removed, or the ball is slightly moved, the ball will roll down the hill until it reaches the lowest position, which corresponds to the lowest gravitational potential energy or equilibrium position.

Later on, we will find that a definition for equilibrium is when the Gibbs free energy of the system is the lowest value possible, and this is how one can recognize unstable or metastable



states from the true equilibrium. Generally, equilibrium states that arise naturally are stable to small disturbances. On the flip side, metastable equilibrium states, which are not stable to small disturbances, do not occur often in nature. Our mathematical description of equilibrium, however, will exhibit these unstable and metastable states, so we must be able to recognize them.

Processes of interest to us are often not time invariant, and it would appear that equilibrium thermodynamics is not very useful. For example, we typically run transient simulations to estimate the recovery of reservoir oil by injection of a gas. The concept of local equilibrium and reversibility are used to overcome this apparent limitation of thermodynamics. Equilibrium at a point in a reservoir, termed local equilibrium, often applies when internal relaxation processes are rapid with respect to the rate at which changes are imposed on the system. That is, equilibrium thermodynamics can be applied over small volumes of the reservoir, even though pressure and other gradients remain in the reservoir. In reservoir simulation, the small volumes are gridblocks, although the size of the gridblocks must be sufficiently small so that good accuracy is obtained.

The concept of reversibility of a process is also important. A reversible process proceeds in sufficiently small steps so that it is essentially in equilibrium at any given time (i.e., the process at a point in the reservoir proceeds in a succession of local equilibrium steps). A process is reversible when its direction can be reversed at any point by an infinitesimal change in external conditions.

The concept of reversibility is, in a sense, the temporal equivalent to the spatial concept of local equilibrium. Thus, the concepts of local equilibrium and reversibility allow the application of equilibrium thermodynamics to real systems, which are invariably nonequilibrium at large scales. For most cases, very little accuracy is lost in making such assumptions.

### 7.3 Fundamental Equations

Relatively few ideas and equations are used to solve the phase behavior problem illustrated in Fig. 7.1. The most fundamental idea in thermodynamics is the conservation of total energy, which is termed “the first law of thermodynamics.” The first law is based on our every day observation that for any change of thermodynamic properties, total energy, which includes internal, potential, kinetic, heat, and work, is conserved. The second fundamental idea in thermodynamics is the total entropy balance or “the second law of thermodynamics.” Entropy is a thermodynamic property that expresses the unidirectional nature of a process and, in some sense, is “nature’s clock.” For example, a cup of hot coffee at room temperature cools down instead of heating up. The conservation of total mass is also used to constrain thermodynamic processes.

These equations are applied to a thermodynamic system. A thermodynamic system is defined as that part of the universe we are considering—for example, the inside of the container in Fig. 7.1. Everything else is called the surroundings. A system may be related to its surroundings in a variety of ways, depending on whether mass or energy (in the form of heat or work) is exchanged (see Fig. 7.3). When no heat or mass is transferred, and no work is done on or by the surroundings, the system is referred to as an “isolated” system. When only energy is exchanged between the system and surroundings, the system is “closed.” Last, the system is “open” when both mass and energy are exchanged between the system and its surroundings. No work is allowed on or by an isolated system, and its boundaries are therefore rigid.

A thermodynamic state is given by its thermodynamic properties (e.g., pressure, density, enthalpy, temperature, internal energy, entropy, and other properties). All of these are state functions that depend only on the present state reached (point conditions)—not the path that the system took to reach that state. For example, if methane is heated, compressed, and then returned to its initial volume and temperature, the methane will have exactly the same pressure as before, independent of how it was heated or compressed. The usefulness of state functions

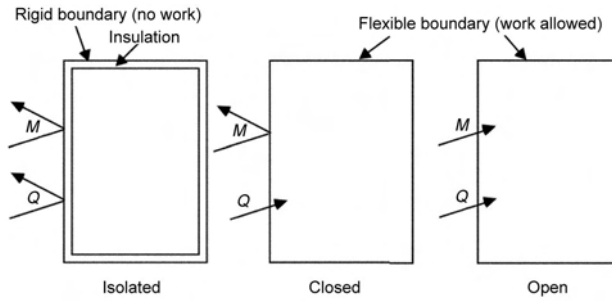


Fig. 7.3—Three types of thermodynamic systems. *M* indicates mass, and *Q* indicates heat.

is the simplest possible path can be selected for the calculation of the change in a state function; that is, we would likely choose a reversible path that consists of isothermal or isobaric steps.

In contrast to state functions such as entropy or pressure, heat and work are not thermodynamic properties but depend on the nature or path of the process that the system undergoes. A different path will give a different amount of work and heat.

**7.3.1 First Law of Thermodynamics.** We begin with the first law of thermodynamics applied to an open thermodynamic system. As illustrated in Fig. 7.3, an open system allows mass and energy to flow into or out of the system. We make the following assumptions and definitions:

1. Mass flows into or out of the system along one boundary of the system. The mass flow rate into the system is positive, whereas flow rates out of the system to the surroundings are negative.

2. Mass can carry internal energy into or out of the system. We neglect kinetic and potential energy carried by the mass. This is often a good assumption when the fluid is not moving near the speed of sound, the change in height over the system is not large, or the system temperature variations are not large.

3. The only types of work that are present are expansion/compression of the system and flow work. The boundaries of the system can expand or contract. Thus, work can be done by the system on the surroundings or vice versa. Work is positive when the surroundings do work on the system (i.e., the system contracts). The mass that enters or exits the system also does work—sometimes called flow work or pressure work.

4. We neglect potential energy and kinetic energy changes within the system.

5. Energy in the form of heat might enter or leave the system across the system boundaries. Heat transfer is positive when heat is exchanged from the surroundings to the system.

Before proceeding, we must define internal energy. Internal energy of a substance is the sum of the potential energy arising from chemical bonds of atoms and electrons and the sum of the kinetic energy of the atoms and molecules. The microscopic kinetic energy is sometimes called thermal energy, which is proportional to temperature.

With this definition, a total macroscopic energy balance in the system, at an instantaneous point in time, gives

$$\left( \begin{array}{c} \text{Rate of accumulation of total} \\ \text{energy within the system} \end{array} \right) = \left( \begin{array}{c} \text{Net rate of transport of total} \\ \text{energy into the system} \end{array} \right), \dots\dots\dots (7.2)$$

where

$$\left( \begin{array}{c} \text{Rate of accumulation of total} \\ \text{energy within the system} \end{array} \right) = \frac{d(nU)}{dt}, \dots\dots\dots (7.3)$$

and  $nU$ , the total internal energy, is equal to the total energy within the system by assumption four previously discussed. The property,  $U$ , is the molar internal energy (total energy/mole). Eq. 7.3 shows that when work or heat is added to the system, the molecular activity increases, causing the total internal energy to increase; that is,  $\frac{d(nU)}{dt} > 0$ .

The term on the right side of Eq. 7.2 contains three terms: mass influx into the system that carries energy; heat transfer into the system; and compression work done by the surroundings on the system. Because we neglect potential and kinetic energy of the mass that flows into the system (assumption two), the energy associated with the mass influx into the system is simply  $U\dot{n}$ , where  $\dot{n}$  is the molar flow rate. Based on assumption one, there is only one molar flow rate into the system. The rate of heat flow from the surroundings across the system boundaries into the system is given by  $\dot{Q}$ . Compression (or expansion) of the system boundaries causes work on the system denoted by  $\dot{W}$ . Substitution of these terms into Eq. 7.2 gives

$$\frac{d(nU)}{dt} = U\dot{n} + \dot{Q} + \dot{W}, \dots\dots\dots (7.4)$$

where the left side refers to energy within the system and the right side to energy that flows across the system boundaries into the system.

The two types of work considered are expansion/compression work and flow work (assumption three). From physics, work is performed whenever a force acts over a distance. Thus, the differential mechanical work that results from a differential displacement  $d\vec{l}$  is given by  $dW = \vec{F} \cdot d\vec{l}$ . For expansion/compression work, the external force is equal to an external pressure supplied by the surroundings multiplied by the corresponding area along the boundary of the system.

In Cartesian coordinates,  $dW = -p_{\text{ext}}(A_x dx + A_y dy + A_z dz)$ , where the external pressure is constant along the boundary of the system.  $A_x$  is the area normal to the  $x$ -coordinate that is being displaced, and so forth. The minus sign indicates that work is positive if the displacement is negative (i.e., an external force compresses the system). The expression for the differential work can be simplified further as  $dW = -p_{\text{ext}}d(nV)$ , where  $nV$  is the total volume and  $V$  is the molar volume (volume/mole). The rate of work is  $\dot{W} = -p_{\text{ext}}\frac{d(nV)}{dt}$ . This equation applies to any arbitrarily shaped system.

For example, consider a rectangular box that expands differentially into the surroundings on three sides, as illustrated in Fig 7.4. Here,  $A_x \approx yz$ ,  $A_y \approx xz$ , and  $A_z \approx xy$ , where the differential cross terms are neglected. The differential work is, therefore,  $dW = -p_{\text{ext}}(yzdx + xzdy + xydz)$ , provided the external pressure is the same on all faces of the box. The differential displacement volume is equal to  $d(nV) = d(xyz) = yzdx + xzdy + xydz$ , which gives the desired result. In this example, the differential work is negative because the system does work on the surroundings. The example also illustrates that even though the system expands into the surroundings, the work is always related to the external pressure. If the external pressure is zero, no work will be done by the system because the surroundings will offer no resistance.

Flow work is done by mass that enters or exits the system. A flowing fluid element does work on the fluid ahead of it, and the fluid behind it does work on that fluid element. Flow work, for example, turns the turbine shaft of a hydroelectric power plant. For one-dimensional

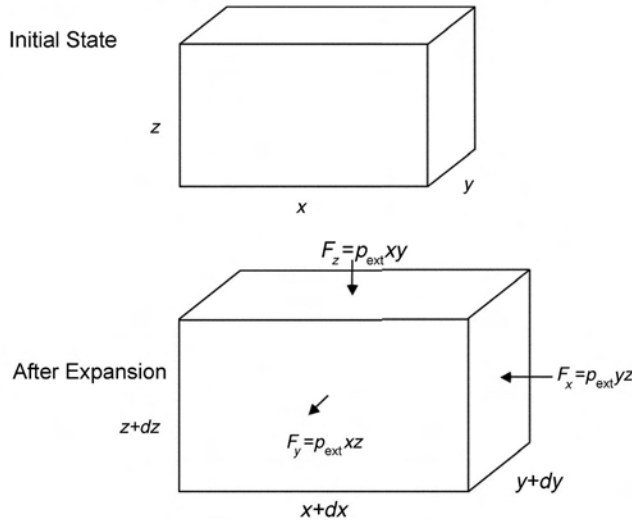


Fig. 7.4—The expansion of a rectangular system into the surroundings.

(1D) inflow or outflow of fluid, the instantaneous rate of flow work is  $\dot{W} = F \frac{dl}{dt} = p_{\text{ext}} Au = \frac{p_{\text{ext}}}{\rho} \dot{n} = p_{\text{ext}} V \dot{n}$ , where  $u$  is the velocity of the fluid;  $\rho$  is the molar density (i.e., inverse of  $V$ ); and the molar flow rate is  $\dot{n} = \rho Au$ . Flow work is positive when the fluid is entering the system; that is, the surroundings do work on the system.

For reversible displacements, the pressure in the system must equal the external pressure,  $p = p_{\text{ext}}$ , supplied by the surroundings, so the system and surroundings are always in equilibrium. With the assumption of reversibility, the total rate of work (expansion/compression work plus flow work) becomes  $\dot{W} = pV\dot{n} - p \frac{d(nV)}{dt}$ . Eq. 7.4 is then written as

$$\frac{d(nU)}{dt} = U\dot{n} + \dot{Q} + pV\dot{n} - p \frac{d(nV)}{dt} \dots\dots\dots (7.5)$$

Eq. 7.5 can be simplified by defining the enthalpy,  $H = U + pV$ . The definition for enthalpy is defined strictly for mathematical convenience. For liquids and solids at low pressures, we often take  $H = U$  because the product  $pV$  is small compared to  $U$  (the molar volume of the condensed phases is also small). Combining the first and third terms on the right side of Eq. 7.5 gives

$$\frac{d(nU)}{dt} = H\dot{n} + \dot{Q} - p \frac{d(nV)}{dt} \dots\dots\dots (7.6)$$

Eq. 7.6 can be written in thermodynamic shorthand as

$$d(nU) = Hdn + dQ - pd(nV) \dots\dots\dots (7.7)$$

For closed systems,  $dn = 0$  (the total moles in the system is constant), and Eq. 7.7 becomes

$$d(nU) = dQ - pd(nV).$$

For isolated systems,  $dn = 0$ ,  $dQ = 0$ , and  $d(nV) = 0$ ; therefore, Eq. 7.7 reduces to

$$d(nU) = 0, \dots\dots\dots (7.8)$$

which shows that the total internal energy of an isolated system is constant ( $nU = \text{constant}$ ).

**7.3.2 Second Law of Thermodynamics.** Conservation of total mass and energy are insufficient to solve many phase-equilibrium problems. Processes that satisfy these conservation equations may not be physically possible; that is, the process of a cold cup of coffee spontaneously heating up on your dinner table would satisfy the first law of thermodynamics but has a near zero probability to occur. Processes have a natural direction to them in that spontaneous processes tend to dissipate gradients (e.g., Darcy's law for pressure gradients and Fick's law for concentration gradients) in the system until equilibrium is reached. A system that is not subject to forced flows of mass or energy from its surroundings will evolve to a time-invariant state that is uniform or composed of uniform subsystems—the equilibrium state. The second law of thermodynamics introduces a new thermodynamic property, entropy, and provides a mathematical statement that describes this unidirectional nature of processes.

The second law also has implications for the efficiency of processes. Heat and work are not of the same quality in that work can be efficiently converted to thermal energy (e.g., frictional heat losses), but thermal energy can be only partially converted into mechanical energy (e.g., steam power plants). Thus, work is a more valuable form of energy than heat—work has a high quality. Furthermore, energy at higher temperatures is more useful than energy at lower temperatures. For example, the ocean contains an immense amount of energy, but it is not very useful because of its low temperature. Energy is degraded when heat transfers from one system to another of lower temperature. Entropy is a measure of the energy degradation or disorder of the system.

Entropy is a thermodynamic property just like temperature and pressure. Entropy is a state function, in which changes during a reversible process in a closed system are given by the ratio  $Q/T$ . Entropy increases as  $T$  decreases or  $Q$  increases.

Entropy is related to the likelihood that equilibrium will be reached. Entropy is best understood by examining a very simple example at the microscopic scale. Fig. 7.5 shows the initial state of a hypothetical closed system that contains four molecules. The system is initially partitioned into two halves, such that the molecules from one half cannot move into the other half. One molecule is in the left subsystem and three are in another, thus, the pressures are not initially the same. Each subsystem has only one possible configuration—the initial state. Thus, the subsystems are well ordered, and entropy is initially small.

When the partition is removed, however, the molecules from each subsystem are free to move into the other half of the system, and a total of 16 different configurations are possible, as shown in Fig. 7.5. Because each of these configurations is equally likely, the probability that the system will be found in its original configuration is only  $1/16$  (i.e.,  $2^{-4}$ ). The system is more likely to contain two molecules in each subsystem (probability of  $6/16$  or  $3/8$ ), which is the equilibrium state—the most disordered state. Entropy is related to the maximum number of possible configurations of the system, and thus, the entropy after the partition is removed has increased. The configurations could also be arrangements of energy quanta, instead of molecular arrangements, as in this example.

Although the original configuration for four molecules is not improbable, real systems contain many more molecules. For example, if one mole of a gas were present in the system ( $6.0 \times 10^{23}$  molecules), the likelihood that the system would be found in its initial state would be very unlikely ( $2^{-6} \times 10^{23}$ ). However, the probability that the system would contain a similar

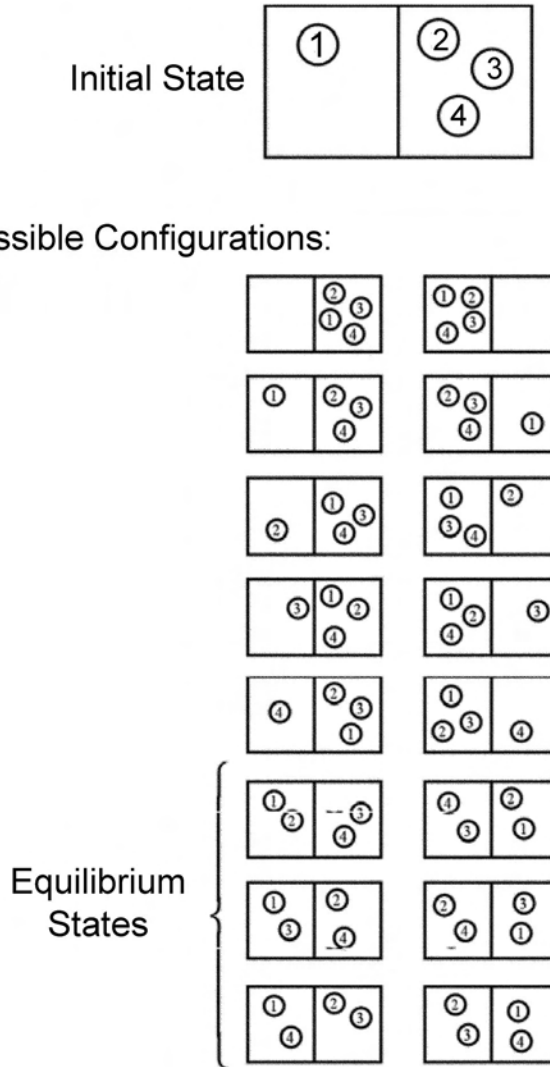


Fig. 7.5—Illustration of entropy for a closed composite system with four molecules (after Smith *et al.*<sup>5</sup>). The molecules on each side of the partition are initially constrained by a partition. After the partition is removed, the molecules are free to move around the entire system by Brownian motion. Equilibrium is the most likely final state.

number of molecules on each side would be near 1.0 (i.e., the pressure would be equal throughout the closed system).

The steps to write the entropy balance for an open system are similar to those for the first law of thermodynamics. We allow for the following:

1. Mass flows into or out of the system at only one location on the boundary of the system. The mass flow rate into the system is positive, whereas flow rates out of the system to the surroundings are negative.

2. Mass can carry entropy into or out of the system. The rate of entropy transfer into the system by mass flow is given by  $S\dot{n}$ .

3. Energy in the form of heat may enter or leave the system across the system boundaries at a specified exterior temperature,  $T$ . Heat transfer is positive when heat is exchanged from

the surroundings to the system. Entropy,  $Q/T$ , is transferred from the surroundings to the system during heat transfer. The rate of entropy transfer into the system by heat transfer is therefore  $\frac{\dot{Q}}{T}$ .

4. The temperature at the boundary or exterior of the system is equal to the temperature within the system (i.e., the heat transfer process is reversible).

5. Unlike total energy or mass, entropy is generated within a system that is not in equilibrium. Entropy generation is related to irreversibilities in the system such as temperature gradients, pressure gradients, or concentration gradients. The second law of thermodynamics states that entropy generation is always positive.

With these assumptions and definitions, the entropy balance is

$$\frac{d(nS)}{dt} = S\dot{n} + \frac{\dot{Q}}{T} + \dot{S}_G, \dots\dots\dots (7.9)$$

where the term on the left is the change in total entropy within the system ( $S$  is entropy/mole), and the first two terms on the right are the net rate of total entropy transported into or out of the system by mass and heat transfer. The last term is the internal generation rate of entropy within the system. In thermodynamic shorthand, the entropy balance can be written as

$$d(nS) = Sdn + \frac{dQ}{T} + dS_G. \dots\dots\dots (7.10)$$

For closed systems ( $dn = 0$ ), the entropy balance becomes  $d(nS) = \frac{dQ}{T} + dS_G$ . For isolated systems ( $dn = 0$  and  $dQ = 0$ ), the entropy balance is

$$d(nS) = dS_G. \dots\dots\dots (7.11)$$

In an isolated system at equilibrium, the total entropy cannot change with time. Thus, the generation of entropy must be zero at equilibrium ( $dS_G = 0$ ), which we stated previously. Away from equilibrium, entropy generation is positive ( $dS_G > 0$ ), which implies that entropy, in an isolated system, increases with time and reaches a maximum at equilibrium.

Why is entropy generation positive away from equilibrium? Consider an isolated system that is composed of two open subsystems  $A$  and  $B$ .<sup>4</sup> Heat is exchanged only from the high temperature subsystem  $A$  to the low temperature subsystem  $B$ . Thus, the rate of heat transfer is  $\dot{Q}_A = -\dot{Q}_B = -h(T_A - T_B)$ , where  $h$  is a constant heat-transfer coefficient. Each subsystem is well mixed so that  $T$  is always uniform [i.e., no internal gradients exist, and subsystems  $A$  and  $B$  must pass through a succession of equilibrium states (i.e., the process is reversible and  $\dot{S}_{GA} = \dot{S}_{GB} = 0$ )]. From Eq. 7.9 and the expressions for the rate of heat transfer, the entropy

balance for subsystem  $A$  is  $\frac{d(nS_A)}{dt} = \frac{\dot{Q}_A}{T_A} = -h\left(\frac{T_A - T_B}{T_A}\right)$ , and for subsystem  $B$ ,

$$\frac{d(nS_B)}{dt} = \frac{\dot{Q}_B}{T_B} = h\left(\frac{T_A - T_B}{T_B}\right).$$

For the isolated system not in equilibrium, the entropy balance is  $\frac{d(nS)}{dt} = \dot{S}_G$ . Furthermore, the total entropy,  $nS$ , is an extensive property so that  $nS = n_A S_A + n_B S_B$ . The entropy generation term of the combined system is therefore given by  $\dot{S}_G = \frac{h(T_A - T_B)^2}{T_A T_B}$ . Because absolute

temperatures are positive and the heat transfer coefficient is positive, this result demonstrates that entropy generation is always positive away from equilibrium. At equilibrium  $T_A = T_B$ , and the entropy generation term is zero, as stated before. Furthermore, the rate of entropy generation is proportional to the square of the gradients (temperature difference in this case). If the temperature gradients are kept small with time (infinitesimal equilibrium steps), entropy generation remains near zero.

A process is reversible if it occurs with small gradients (i.e., consists of a succession of infinitesimal equilibrium steps). Thus,  $dS_G = 0$  for a reversible process, and from Eq. 7.10,

$$d(nS) = Sdn + \frac{dQ_{rev}}{T} \dots\dots\dots (7.12)$$

For a closed system that undergoes a reversible process, Eq. 7.12 reduces to  $dQ_{rev} = Td(nS)$ .

In summary, the second law of thermodynamics states that the rate of entropy generation within a system must be greater than or equal to zero. A process for which the rate of generation of entropy is always zero is a reversible process. A large rate of entropy generation corresponds to greater process irreversibilities.

**7.3.3 Fundamental Property Relations and Equilibrium Conditions.** We would like to calculate thermodynamic properties and the equilibrium state from a simplified mathematical model, called an equation-of-state (EOS). To do this, we need equations that relate thermodynamic quantities in terms of pressure, molar volume, and temperature data (PVT data), and we want to eliminate any path dependence by eliminating all properties that are not state functions. Substitution of Eq. 7.10 into Eq. 7.7 by elimination of  $dQ$  (a path dependent quantity) and selection of a reversible path (such that  $dS_G = 0$ ) gives

$$d(nU) = Hdn + Td(nS) - TSdn - pd(nV) \dots\dots\dots (7.13)$$

All of the properties in Eq. 7.13 are state functions; thus, Eq. 7.13 is independent of the path or process. After combining like terms, Eq. 7.13 becomes

$$d(nU) = Gdn + Td(nS) - pd(nV), \dots\dots\dots (7.14)$$

where  $G \equiv H - TS$  is defined as the molar Gibbs energy. For a closed system ( $dn = 0$ ), Eq. 7.14 becomes

$$d(nU) = Td(nS) - pd(nV) \dots\dots\dots (7.15)$$

Eqs. 7.14 and 7.15 are examples of fundamental property relations. Other fundamental property relations are possible. For example, differentiation of the definition for total Gibbs energy gives  $d(nG) = d(nH) - Td(nS) - (nS)dT$ . Similarly, differentiation of the total enthalpy gives  $d(nH) = d(nU) + pd(nV) + (nV)dp$ . Substitution of these relations into Eq. 7.14 (or Eq. 7.15) by elimination of the enthalpy term gives the fundamental property relation for the total Gibbs free energy of a closed system as

$$d(nG) = (nV)dp - (nS)dT, \dots\dots\dots (7.16)$$

or, for an open system,

$$d(nG) = (nV)dp - (nS)dT + Gdn \dots\dots\dots (7.17)$$



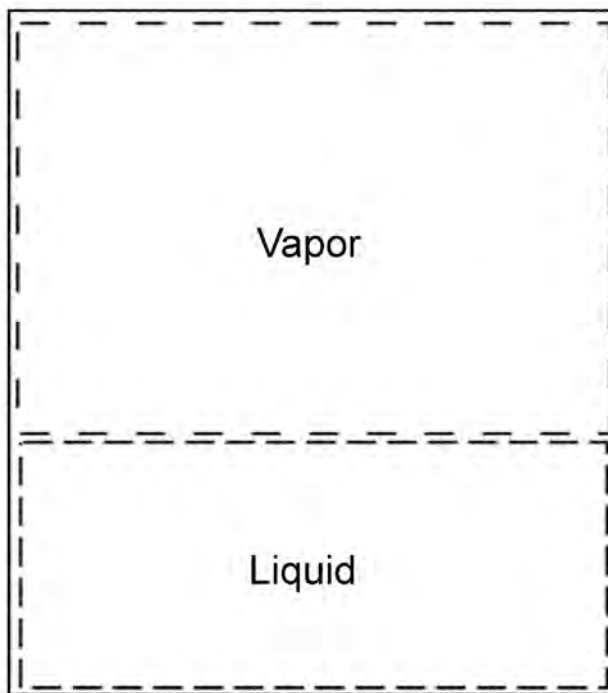


**Fig. 7.6—Isolated system with two open subsystems.** The subsystems correspond to the vapor and liquid phases as shown by the dashed lines. The solid line is the boundary of the isolated system.

**Equilibrium Criteria for Single-Component Liquid/Vapor Systems.** Consider an isolated system of a pure fluid with two phases, vapor and liquid. Initially, the temperature, pressure, and other properties of the two phases are not in equilibrium. **Fig. 7.6** illustrates the composite isolated system in which each phase is treated as a subsystem.

We begin by writing the differential entropy change from **Eq. 7.14** for each open subsystem. The vapor phase equation is

$$d(nS)_V = \frac{d(nU)_V}{T_V} + \frac{p_V}{T_V} d(nV)_V - \frac{G_V}{T_V} dn_V, \dots\dots\dots (7.18)$$

and for the liquid phase,

$$d(nS)_L = \frac{d(nU)_L}{T_L} + \frac{p_L}{T_L} d(nV)_L - \frac{G_L}{T_L} dn_L, \dots\dots\dots (7.19)$$

The change in the total entropy of the isolated system can be written as the summation of **Eqs. 7.18** and **7.19**. The result is

$$d(nS) = \frac{d(nU)_V}{T_V} + \frac{d(nU)_L}{T_L} + \frac{p_V}{T_V} d(nV)_V + \frac{p_L}{T_L} d(nV)_L - \frac{G_V}{T_V} dn_V - \frac{G_L}{T_L} dn_L, \dots\dots\dots (7.20)$$

For an isolated system, the change in the total internal energy is zero (see Eq. 7.8), as is the change in the total mass and volume. Thus,  $dn_L = -dn_V$ ,  $d(nU)_L = -d(nU)_V$ , and  $d(nV)_L = -d(nV)_V$ . The differential entropy change for an isolated system at equilibrium must also be zero (see Eq. 7.11). Eq. 7.20 becomes

$$0 = \left(\frac{1}{T_L} - \frac{1}{T_V}\right)d(nU)_L + \left(\frac{p_L}{T_L} - \frac{p_V}{T_V}\right)d(nV)_L + \left(\frac{G_V}{T_V} - \frac{G_L}{T_L}\right)dn_L.$$

Because changes in internal energy, volume, and mass of the liquid phase can be arbitrarily set (i.e., are independent), we must have at equilibrium that  $\left(\frac{1}{T_L} - \frac{1}{T_V}\right) = \left(\frac{p_L}{T_L} - \frac{p_V}{T_V}\right) = \left(\frac{G_V}{T_V} - \frac{G_L}{T_L}\right) = 0$ . Thus, at equilibrium,  $T_L = T_V$ ,  $p_L = p_V$ , and  $G_L = G_V$ . The first two equilibrium criteria are obvious. The equilibrium condition that the Gibbs free energy of the phases is equal is not as obvious.

Other systems lead to similar equilibrium conditions. For example, for a closed system at constant pressure and temperature ( $dp = 0$ ,  $dT = 0$ ) the fundamental property relation from Eq. 7.16 becomes  $d(nG) = 0$ . Thus, the equilibrium criterion here is that the Gibbs free energy must be a minimum. This criterion also leads to the equality of the Gibbs free energy of both phases at equilibrium,  $G_L = G_V$ .

*Fugacity of a Pure Fluid.* Fugacity criterion is often used as a substitute for the Gibbs free-energy criterion. The definition for fugacity comes from an analogue with ideal gases that is derived for a closed system under isothermal conditions. Eq. 7.16 for an isothermal process ( $dT = 0$ ) is

$$d(nG) = (nV)dp. \dots\dots\dots (7.21)$$

For an ideal gas,  $V = \frac{RT}{p}$ , and Eq. 7.21 becomes

$$d(nG)^{ig} = \frac{nRT}{p} dp = nRT d(\ln p). \dots\dots\dots (7.22)$$

Fugacity is defined by analogy for a fluid that is not ideal. That is, we define the fugacity,  $f$ , based on a comparison with Eq. 7.22, which is written as

$$d(nG) = nRT d(\ln f). \dots\dots\dots (7.23)$$

Eq. 7.23 shows that the value for fugacity is whatever is required to give the correct behavior of the real fluid. More exactly, fugacity measures how the Gibbs free energy of a real fluid deviates from that of an ideal gas. Fugacity has units of pressure, and for an ideal gas the fugacity is equal to the pressure (compare Eqs. 7.23 and 7.22).

We showed that at equilibrium for a pure fluid  $G_L = G_V$ . By integration of Eq. 7.23 under isothermal conditions, the Gibbs free-energy criterion implies that the fugacity of the liquid and vapor phases must also be equal at equilibrium. That is, at equilibrium for a pure fluid,

$$f_L = f_V. \dots\dots\dots (7.24)$$

We would like an expression for fugacity in terms of our convenient quantities of pressure, molar volume, and temperature, so that an EOS can be used. Substitution of Eq. 7.21 into Eq. 7.23 gives

$$V dp = RT d(\ln f).$$

Subtraction of  $\frac{RT dp}{p}$  from both sides and some algebraic rearrangement gives

$$d\left(\ln \frac{f}{p}\right) = -\frac{1}{RT}\left(\frac{RT}{p} - V\right) dp.$$

Finally, integration from a reference state of zero pressure (ideal gas state) to the actual pressure gives

$$\ln \frac{f}{p} = \ln \left(\frac{f}{p}\right)_{p=0} - \frac{1}{RT} \int_0^P \left(\frac{RT}{p} - V\right) dp.$$

From the definition of fugacity,  $\lim_{p \rightarrow 0} \frac{f}{p} = 1$  (i.e., the fugacity is equal to the pressure for an ideal gas), we have

$$\ln \frac{f}{p} = \ln \phi = -\frac{1}{RT} \int_0^P \left(\frac{RT}{p} - V\right) dP = \int_0^P (Z-1) \frac{dP}{P}, \dots\dots\dots (7.25)$$

where  $\phi = \frac{f}{p}$  is known as the fugacity coefficient, and  $Z = \frac{PV}{RT}$  is the compressibility factor. The fugacity coefficient is therefore equal to 1.0 for an ideal gas. Eq. 7.25 requires knowing the compressibility factor as a function of pressure.

Models for compressibility factor, such as a cubic EOS, however, are typically not explicit functions of pressure. A more convenient form would be to transform the integral with respect to pressure to one with respect to volume. Eq. 7.25 can be transformed to

$$\ln \frac{f}{P} = \frac{1}{RT} \int_{\infty}^V \left(\frac{RT}{V} - P\right) dV - \ln Z + (Z-1). \dots\dots\dots (7.26)$$

The importance of Eq. 7.26 is that the fugacity can be calculated if the molar volume, temperature, and pressure are known over the full range of molar volumes from  $V$  to  $\infty$ . Typically, sufficient laboratory data ( $p, V, T$ ) is not available, and mathematical models, such as cubic EOS, are used. We will use Eqs. 7.24 and 7.26 in Sec. 7.4 to calculate the intensive and extensive state of a pure fluid at equilibrium using a cubic EOS.

**Equilibrium Criteria for Multicomponent Liquid/Vapor Systems.** The procedure to determine the equilibrium criterion for multicomponent systems is similar to that used for pure fluids. We consider a closed system with a multicomponent mixture of  $n$  moles as illustrated in Fig. 7.1. Transfer of mass from one phase to the other is allowed, but the overall system is closed, such that the overall composition of the system is constant. Given the overall composi-

tions ( $z_i$ ), pressure, and temperature, we seek to determine the amount of liquid and vapor present at equilibrium, as well as the component mole fractions for the phases ( $x_i$  and  $y_i$ ).

As before, the closed system consists of two subsystems, the liquid and vapor phases (see Fig. 7.6). The primary difference between the derivation for pure fluids and the derivation for multiple components is that the fundamental property relations for the open system must be modified to include mass transfer of different components. That is, we must compute the change in the total Gibbs energy of the liquid phase as small amounts of each component ( $dn_i$ ) are transferred from the vapor phase to the liquid phase (or vice versa for the vapor phase). For example, Eq. 7.17 becomes

$$d(nG) = (nV)dp - (nS)dT + \bar{G}_1 dn_1 + \bar{G}_2 dn_2 + \dots + \bar{G}_{n_c} dn_{n_c} = (nV)dp - (nS)dT + \sum_{i=1}^{n_c} \bar{G}_i dn_i, \dots \dots \dots (7.27)$$

where  $\bar{G}_i$  is the molar Gibbs free energy added to the liquid phase when  $dn_i$  moles are added to it. The partial molar Gibbs energy  $\bar{G}_i$  is also named the chemical potential,  $\mu_i = \bar{G}_i = \left( \frac{\partial(nG)}{\partial n_i} \right)_{T, p, n_j \neq i}$ . The chemical potential measures how much Gibbs energy is added to a mixture when  $dn_i$  is added to it.<sup>1</sup> Thus, Eq. 7.27 is commonly written as

$$d(nG)_L = (nV)_L dp - (nS)_L dT + \sum_{i=1}^{n_c} \mu_{iL} dn_{iL}$$

for the liquid phase, and

$$d(nG)_V = (nV)_V dp - (nS)_V dT + \sum_{i=1}^{n_c} \mu_{iV} dn_{iV}$$

for the vapor phase. As for pure fluids, these two equations are added to obtain the differential total Gibbs energy of the entire closed system. Because the differential total Gibbs free energy of the closed system must be zero when pressure and temperature are constant, we obtain

$$d(nG) = d(nG)_L + d(nG)_V = \sum_{i=1}^{n_c} (\mu_{iL} dn_{iL} + \mu_{iV} dn_{iV}) = 0. \dots \dots \dots (7.28)$$

Conservation of mass requires that any component that enters a phase must have come from the other phase so that  $dn_{iL} = -dn_{iV}$ , and upon substitution into Eq. 7.28,

$$\sum_{i=1}^{n_c} (\mu_{iL} - \mu_{iV}) dn_{iL} = 0.$$

Because the  $dn_i$  are independent and arbitrary, we must have at equilibrium

$$\mu_{iL} = \mu_{iV}, \quad \text{for } i = 1, \dots, n_c. \dots \dots \dots (7.29)$$

Eq. 7.29 says that at equilibrium the chemical potential of a component in the liquid phase must be equal to the chemical potential of the same component in the vapor phase. This equilibrium criterion reduces to  $G_L = G_V$  for the case of a pure fluid.

*Fugacity of a Component in a Mixture.* The equilibrium criterion expressed as component fugacities is often used instead of chemical potentials. The reason for this is primarily one of convenience because component fugacity has units of pressure. Just as for pure fluids, the fugacity of a component is defined as an analogue to an ideal gas mixture.

Consider an ideal gas mixture at a temperature  $T$ . The pressure for  $n$  moles is  $p = \frac{nRT}{nV}$ . In this mixture, each component has  $n_i$  moles. If  $n_i$  moles of each component in this mixture occupy the same total volume alone at the same temperature, the pressure would be  $p_i = \frac{n_i RT}{nV} = \frac{y_i RT}{V}$ . Division of this result by the pressure gives the partial pressure of a component in an ideal gas mixture. That is,  $p_i = y_i p$ , where  $y_i = \frac{n_i}{n}$  is the vapor molar fraction of each component. The sum of the partial pressures equals the pressure  $p = \sum_{i=1}^{n_c} y_i p_i$ .

For an ideal pure gas at constant temperature, we had  $dG_i^{ig} = \frac{RT}{p} dp = RT d \ln p$  (see Eq. 7.22). It follows, therefore, that the partial molar Gibbs energy of a component should be evaluated at the partial pressure, or

$$d\bar{G}_i^{ig} = RT d \ln p_i = RT d \ln (y_i p) \dots\dots\dots (7.30)$$

For a real mixture (not an ideal gas or solution), the component fugacity is defined by analogue with Eq. 7.30.

$$d\bar{G}_i = d\mu_i = RT d \ln \hat{f}_i, \dots\dots\dots (7.31)$$

where  $\hat{f}_i$  is the fugacity of component  $i$  in a mixture. The component fugacity for real fluids is sometimes referred to as a corrected partial pressure. Comparison of Eqs. 7.30 and 7.31 show that for ideal mixtures,  $\hat{f}_i = y_i p$ . From the integration of Eq. 7.31 and the use of the equilibrium criteria of Eq. 7.29, we obtain the equilibrium criteria for component fugacities as

$$\hat{f}_{iL} = \hat{f}_{iV}, \text{ for } i = 1, \dots, n_c \dots\dots\dots (7.32)$$

Eq. 7.32 is often used instead of the equality of chemical potentials to determine equilibrium.

To calculate component fugacities of a real mixture, we subtract the chemical potential for component  $i$  in an ideal gas (Eq. 7.30) from both sides of Eq. 7.31. The result is

$$d\mu_i - d\mu_i^{ig} = RT d \ln \frac{\hat{f}_i}{y_i p} = RT d \ln \hat{\phi}_i, \dots\dots\dots (7.33)$$

where  $\hat{\phi}_i = \frac{\hat{f}_i}{y_i p}$  is the component fugacity coefficient. Eq. 7.33 is used to calculate the deviation of the component fugacity from ideal behavior (this is also known as the residual partial Gibbs energy of component  $i$ ). Integration of Eq. 7.33 from zero pressure to the actual pressure gives  $\mu_i = RT \ln \hat{\phi}_i$ , where the chemical potential is zero and the component fugacity

Pure Fluid:	Multicomponent Mixture
$dG^{ig} = RTd \ln p \Rightarrow$ (ideal gas) .	$d\bar{G}_i^{ig} = d\mu_i^{ig} = RTd \ln y_i p \Rightarrow$ (ideal gas) .
$dG = RTd \ln f \Rightarrow$ (real fluid) .	$d\bar{G}_i = d\mu_i = RTd \ln \bar{f}_i \Rightarrow$ (real fluid) .
$\lim_{p \rightarrow 0} \left( \frac{f}{p} \right) = \lim_{p \rightarrow 0} \phi = 1$ .	$\lim_{p \rightarrow 0} \left( \frac{\bar{f}_i}{y_i p} \right) = \lim_{p \rightarrow 0} \hat{\phi}_i = 1$ .
$\ln \frac{f}{p} = \int_0^p [Z - 1] \frac{dp}{p}$ .	$\ln \frac{\bar{f}_i}{y_i p} = \int_0^p [\bar{Z}_i - 1] \frac{dp}{p}$ .
$G_L = G_V$ at equilibrium .	$\bar{G}_{iL} = \mu_{iL} = \bar{G}_{iV} = \mu_{iV}$ at equilibrium .
$\bar{f}_L = \bar{f}_V$ at equilibrium .	$\bar{f}_{iL} = \bar{f}_{iV}$ at equilibrium .

coefficient is 1.0 at zero pressure (the mixture is ideal at zero pressure). From Eqs. 7.21 and 7.22 and the definition of fugacity, we obtain using calculus:

$$\ln \hat{\phi}_i = \int_0^p (\bar{Z}_i - 1) \frac{dp}{p}, \dots\dots\dots (7.34)$$

where  $\bar{Z}_i = \left[ \frac{\partial(nZ)}{\partial n_i} \right]_{T, P, n_j \neq i}$  is the partial molar compressibility factor.

Eq. 7.34 is similar in form to Eq. 7.25 for a pure fluid. Table 7.1 compares the fundamental equilibrium equations for pure and multicomponent fluids. Because cubic EOS represent Z as an explicit function of V and not Z as a function of p, Eq. 7.34 is often rearranged to

$$\ln \hat{\phi}_i = - \int_{\infty}^V \left[ \left( \frac{\partial(nZ)}{\partial n_i} \right)_{T, n_V, n_j \neq i} - 1 \right] \frac{dV}{V} - \ln Z. \dots\dots\dots (7.35)$$

Eq. 7.35 shows that the fugacity of a component in a mixture can be calculated when the molar volume, temperature, pressure, and compositions are known over the full range of molar volumes from V to ∞. Sufficient laboratory data is typically not available for the integration and an EOS must be used. We will use Eqs. 7.32 and 7.35 in Sec. 7.5 to calculate the intensive and extensive state of a multicomponent mixture at equilibrium using a cubic EOS.

**7.4 Volumetric Properties of Pure Fluids**

The phase behavior of a typical pure fluid can be represented on a pressure-temperature diagram, as illustrated in Fig. 7.7. From the Gibbs phase rule (Sec. 7.2.1), the number of degrees of freedom are 3 - n<sub>p</sub>, which means that one, two, or three phases can be present at equilibrium. For simplicity, these phases are shown as a solid, liquid, and a vapor, although numerous additional solid and liquid phases are possible, as long as no more than three of those phases coexist at equilibrium at the same temperature and pressure. Water, for example, has nine different solid phases, each of which has a different crystalline structure.<sup>6</sup> At the pressure and temperature of the Earth’s surface, however, we experience only one solid, liquid, and vapor phase of water.

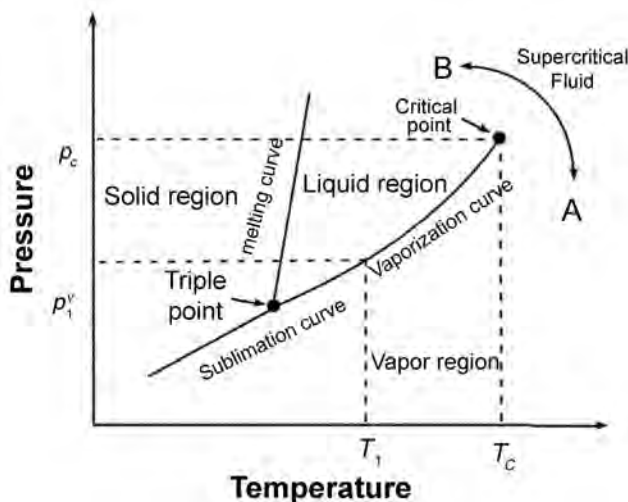


Fig. 7.7—Illustration of a pressure-temperature diagram for a pure fluid. The path indicated from point A, a vapor, to point B, a liquid, would never encounter an interface.

According to the Gibbs phase rule, there are no degrees of freedom when three phases are in equilibrium. This necessarily implies that three phases must be in equilibrium only at one temperature and pressure; this is the triple point indicated in Fig. 7.7. That is, we are not free to choose the temperature and pressure at which three phases can coexist. The temperature and pressure of the triple point are determined.

For two phases, however, the degrees of freedom are one, and we can set either the temperature or the pressure, but not both. Once the temperature is specified, the pressure is determined. Thus, two equilibrium phases are represented by curves on a pressure-temperature diagram. The sublimation curve gives the locus of points where solid and vapor are in equilibrium; the melting or fusion curve gives the locus of points where solid and liquid are in equilibrium; and the vaporization or saturation curve gives the locus of points where the liquid and vapor are in equilibrium. The pressure along the vaporization curve is called the vapor or saturation pressure. For example, the pure fluid at temperature  $T_1$  in Fig. 7.7 has a vapor pressure of  $p_1^v$ .

A single solid, liquid, or vapor phase can exist over a range of temperatures and pressures (degrees of freedom are two). This is indicated in Fig. 7.7 by the three single-phase regions of solid, liquid, and vapor.

When the temperature and pressure along the vaporization curve is increased to the critical pressure,  $p_c$ , and temperature,  $T_c$ , the interface between the liquid and vapor phases becomes indistinct. This occurs at the critical point shown in Fig. 7.7. Beyond the critical point, fluids become “supercritical” and no phase interface is visible. For example, the vapor at point “A” in Fig. 7.7 would become more liquid-like as the pressure and temperature are varied along the semicircle to point “B,” a liquid. The fluid would never exhibit two phases during the process, as identified by an interface. Because there is no actual boundary that defines the supercritical region, fluids should be described in terms of liquid-like or vapor-like.

One important characteristic of critical fluids is that thermodynamic properties approach each other; that is, the densities/viscosities of the vapor and liquid phases become the same at the critical point. We often inject supercritical fluids, such as carbon dioxide, into reservoirs so that, as the supercritical fluid and the reservoir fluid mix, phase interfaces disappear, facilitating production of hydrocarbon components previously not recovered (see the chapter on steam

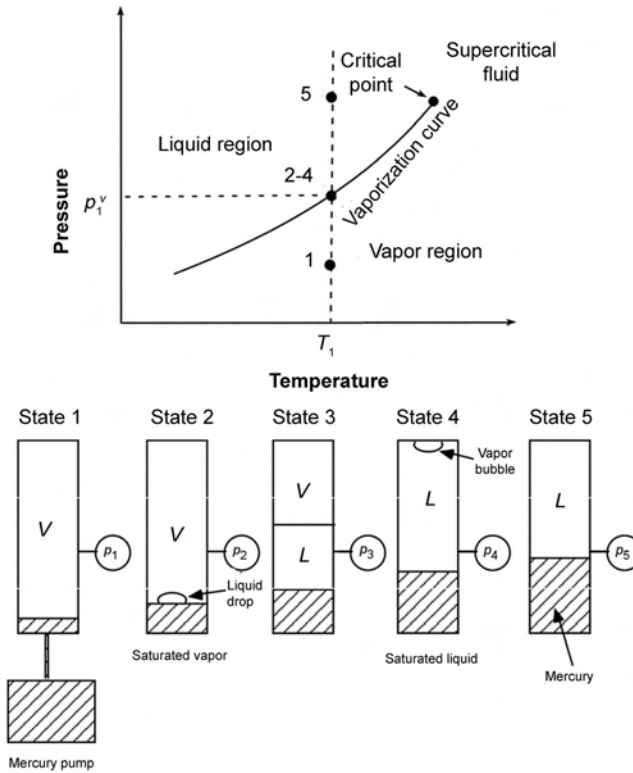


Fig. 7.8—PVT experiment of a pure fluid along an isotherm in a closed system (constant composition expansion). The pressures for states two through four are equal to the vapor pressure,  $p_1^v$ , in Fig. 7.7.

injection in the Reservoir Engineering and Petrophysics section of this Handbook). Thus, an accurate characterization of critical behavior is very important.

A pressure-temperature diagram contains no information about molar volume—just phase boundaries. Consider an experiment in a closed system that is held at constant temperature (ignoring the solid phase). The experiment is designed to measure pressure as the volume is changed and is generally referred to as a PVT experiment. Fig. 7.8 illustrates several phase behavior states that occur in a PVT experiment. The chapter on phase diagrams in this section of the Handbook outlines similar experiments for multicomponent mixtures. The steps in the PVT experiment for a pure fluid are listed next.

1. Place a known amount of a single-component fluid in a constant temperature PVT cell at vapor state one, illustrated in Fig. 7.8. The molar volume of the fluid can be calculated from 
$$V^V = \frac{\text{total moles in cell}}{(\text{volume of cell} - \text{mercury volume injected})}$$
. Measure the pressure.

2. Inject a volume of mercury into the cell. Calculate  $V^V$  again, and monitor the corresponding pressure change. Because vapor is highly compressible and the mercury is highly incompressible, the pressure change with decreasing molar volume of the vapor phase will be relatively small. The fluid remains a vapor.

3. Continue to inject mercury until the vapor becomes saturated at state two. At this pressure (the vapor pressure,  $p_1^v$ , in Fig. 7.7), a small amount of liquid forms (for multicomponent mixtures, this is the dew point). Calculate the saturated  $V^V$ , and measure the pressure.

4. Continue to inject mercury to state three, where the molar fractions of vapor and liquid are about equal. The pressure is constant at the vapor pressure  $p_1^v$ , corresponding to tempera-



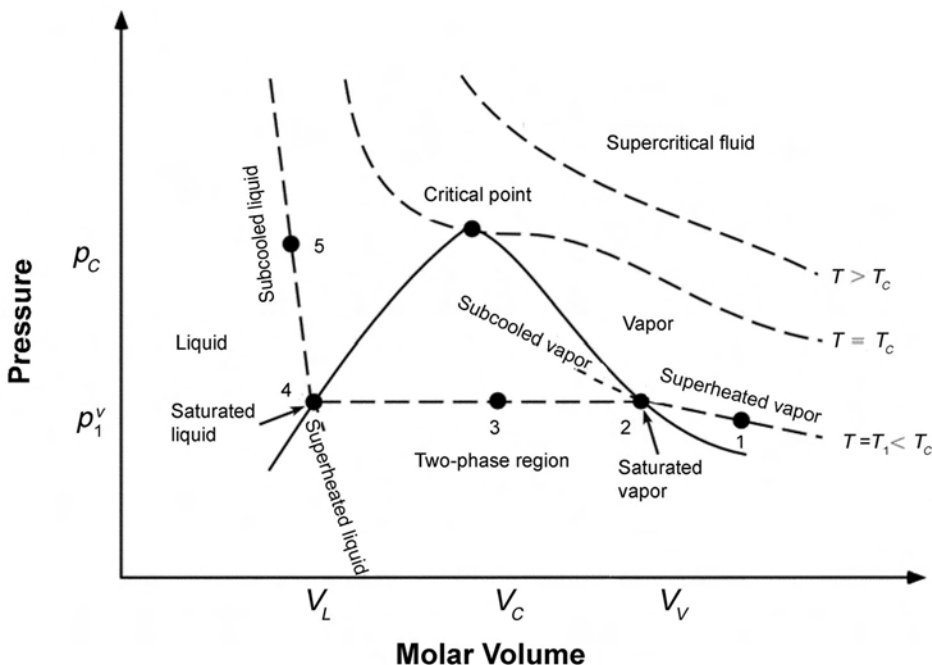


Fig. 7.9—Illustration of a pressure-volume diagram for a pure fluid in a closed system. The isotherm for  $T_1$  corresponds approximately to the same temperature in Figs. 7.7 and 7.8.

ture  $T_1$ . The pressure is constant because the temperature is constant (i.e., the degrees of freedom from the Gibbs phase rule are one for two phases in equilibrium; thus, the pressure is fixed if the temperature is constant). Because the pressure does not change with decreasing molar volume, the compressibility of the closed system is infinite.

5. Continue to inject mercury to state four until only a small drop of vapor remains (for multicomponent mixtures, this is the bubble point). Calculate the saturated liquid molar volume,  $V_L$ .

6. Continue mercury injection to state five and calculate  $V_L$ , while monitoring the pressure. During this step, the fluid remains a liquid, and the pressure rises very quickly for small changes in the molar volume. The pressure rises quickly with decreasing molar volume because liquids are nearly incompressible compared to vapors.

The PVT process just described generates an isotherm on a pressure-volume diagram, as illustrated in Fig. 7.9. States one through five correspond to those in the isothermal PVT experiment. A vapor pressure dome or two-phase envelope outlines the two-phase region. Along the left boundary of the dome, the liquid is completely saturated, for any reduction in pressure would cause a bubble of vapor to form. Along the right boundary of the dome, the vapor is saturated. To the left of the dome the liquid is subcooled, whereas to the right of the dome, the vapor is superheated. Two metastable states have been observed within the two-phase region: superheated liquid and subcooled vapor. These states are unlikely to exist in a reservoir where nucleation is always present (see Ref. 2 on nucleation).

From the Gibbs phase rule, the pressure within the two-phase region along the  $T_1$  isotherm remains at its corresponding vapor pressure as molar volume changes from states two to four (i.e.,  $V_V$  to  $V_L$ ).  $V_V$  in Fig. 7.9 is the molar volume of the saturated vapor, whereas  $V_L$  is the saturated liquid molar volume.  $V_C$  is the molar volume of the fluid at its critical point.

The critical point, in which the molar volumes of the liquid and vapor become equal, is at the apex of the dome in Fig. 7.9. The critical point must be at the apex because the isotherms in the two-phase region are horizontal, as required by the Gibbs phase rule. Thus, the slope and the inflection point of the isotherm at the critical temperature must be zero. For isotherms where  $T > T_C$ , the molar volume (inverse of molar density) changes continuously from vapor-like values to liquid-like values as the pressure increases.

The isothermal compressibility of the fluid is given by the inverse of the slopes of the isotherms. For isotherms where  $T < T_C$ , the slope is small in the superheated vapor region, indicating that the fluid compressibility is large. The slope is large in the subcooled liquid region, indicating that the fluid is nearly incompressible. At the boundary of the two-phase dome, the isothermal compressibility is discontinuous and is equal to infinity (zero slope). Compressibility is infinite in the two-phase region because, as the system volume is decreased, some of the vapor molecules, which occupy more space, are condensed into the denser liquid phase in which they occupy less space.

For a two-phase mixture at constant temperature, such as that shown by state three in Fig. 7.9, the molar phase volumes,  $V_V$  and  $V_L$ , do not change as the volume of the closed system changes. This occurs because the pressure is constant in the two-phase region for a pure fluid. Thus, as the volume is changed, the molar densities of the vapor and liquid phases do not change, but only the molar fractions (or amounts) of the phases change. The overall density of the two-phase mixture will change as the closed system is compressed or expanded.

For example, consider state three in the two-phase region at a temperature of  $T_1$ . The vapor molar density is  $\frac{1}{V_V}$  (at state two), whereas the liquid molar density is  $\frac{1}{V_L}$  (at state four). The mole fraction of vapor at state two is  $V$ . Extensive parameters, such as the total molar volume of the two-phase mixture, can be calculated by

$$V_T = \frac{\text{total volume of closed system}}{\text{total moles in closed system}} = V_L(1 - V) + V_V V. \quad (7.36)$$

For total molar enthalpy,

$$H_T = \frac{\text{total enthalpy of closed system}}{\text{total moles in closed system}} = H_L(1 - V) + H_V V, \quad (7.37)$$

where  $H_L$  is the molar enthalpy of the saturated liquid, and  $H_V$  is the molar enthalpy of the saturated vapor. Eqs. 7.36 and 7.37 can be solved for  $V$  as

$$V = \frac{V_T - V_L}{V_V - V_L} = \frac{H_T - H_L}{H_V - H_L}. \quad (7.38)$$

Eq. 7.38 is known as a lever rule. The fluid quality is the molar volume fraction  $V$  as a percentage. An illustration of quality lines is given in Fig. 7.10. A quality of 100% is a saturated vapor. State three in Fig. 7.10 has a quality of about 60%.

**7.4.1 Phase Behavior Models of Pure Fluids.** An accurate characterization of phase behavior is critical to the prediction of oil recovery. Often, sufficient PVT experimental data is not available, and mathematical models that are “tuned” to experimental data are needed. EOS calculations are used for this purpose. EOS models are typically easy to implement in a numerical simulator.

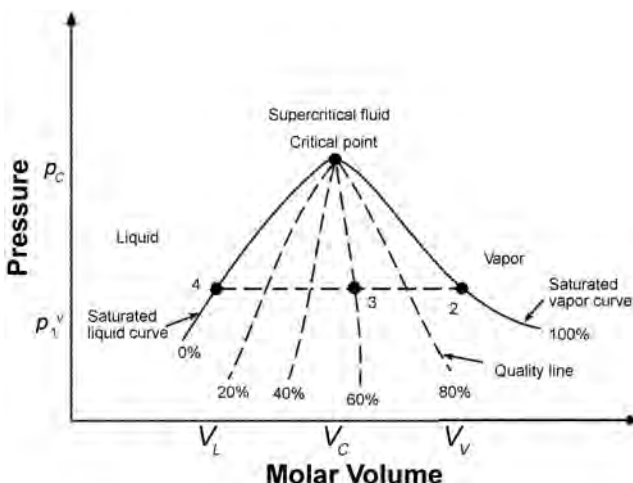


Fig. 7.10—Quality lines within the two-phase region on a pressure-volume diagram.

One of the first EOS was Boyle’s and Charles’s law. These laws were combined into the ideal gas equation we use today,  $pV = RT$ . The ideal gas equation is generally satisfactory for vapors at pressures below a few atmospheres. Numerous other types of EOS were developed through the years,<sup>5</sup> but the most widely used EOS type in the petroleum industry is the cubic EOS.

Van der Waals developed the first cubic EOS. Unlike the ideal gas equation, which is limited to low pressure vapors, the van der Waals EOS attempted to provide good phase behavior estimates for both liquids and vapors by using only one equation. He also developed the principle of corresponding states, which is frequently used in the petroleum industry today. Numerous cubic EOS models are available today that give better accuracy than the van der Waals’ EOS. The two most widely used cubic EOS are the Peng-Robinson EOS<sup>8</sup> and modified versions of the Redlich-Kwong EOS.<sup>9,10</sup>

Prediction of the phase behavior of real reservoir fluids is difficult because of the complex interaction of molecules. Intermolecular forces of attraction and repulsion determine thermodynamic properties for any mixture of molecules. The attraction forces allow fluids to form liquid and solid phases, whereas repulsions are responsible for resistance to compression.

The accuracy of any EOS depends on its ability to model the attractions and repulsions between molecules over a wide range of temperatures and pressures. EOS models are empirical in that they do not attempt to model the detailed physics but only the cumulative effect in terms of a small number of empirical parameters. Generally, EOS models are more accurate when attractions are small, which explains why water, a polar substance, is more difficult to model.

**Ideal Gas Equation.** The simplest and most fundamental EOS is the ideal gas equation, in which the pressure, volume, and temperature of a fluid are related by

$$pV = RT \dots\dots\dots (7.39)$$

As stated previously, the behavior of a gas may be approximated by Eq. 7.39 if the pressure is relatively low (i.e., less than a few atmospheres). A gas is ideal if molecular interactions are negligible, something that could only occur at zero pressure. Thus, molecular interactions are negligible at zero pressure; therefore, thermodynamic properties, such as the molar internal energy of an ideal gas, are only a function of temperature.

**Real Fluid Equation.** Most fluids are not ideal. Real fluids, whether vapor or liquid, can be defined by the compressibility factor

$$Z = \frac{pV}{RT} \dots\dots\dots (7.40)$$

Intensive thermodynamic properties, such as the molar internal energy, are a function of both temperature and pressure for a real fluid. A common mistake is to believe that Eq. 7.40 is only applicable to gases. Eq. 7.40 will be used later in this chapter to represent the behavior of any phase, whether liquid or vapor.

**Coefficient of Isothermal and Isobaric Compressibility.** For a single-phase fluid, we often employ very simple equations-of-state that describe the relationships between pressure, temperature, and molar volume. As stated previously, molar volume is a state function—it is not determined by the process or path taken to that state. Thus, for every temperature and pressure, there corresponds only one value of molar volume, and hence, we can write an equation that describes differential changes in molar volume as

$$dV = \left(\frac{\partial V}{\partial T}\right)_p dT + \left(\frac{\partial V}{\partial p}\right)_T dp \dots\dots\dots (7.41)$$

Division of Eq. 7.41 by the molar volume gives

$$\frac{dV}{V} = c_p dT - c dp, \dots\dots\dots (7.42)$$

where  $c = -\frac{1}{V}\left(\frac{\partial V}{\partial p}\right)_T$  is the isothermal compressibility of the fluid, and  $c_p = \frac{1}{V}\left(\frac{\partial V}{\partial T}\right)_p$  is the isobaric compressibility of the fluid. The minus sign is introduced, per convention, to make the compressibilities positive.

Eq. 7.42 describes the fractional change in the molar volume for small changes in temperature and pressure. Because reservoirs are usually thought to be isothermal, the isothermal compressibility is most often used in reservoir engineering. It is often written in terms of density or formation volume factor (FVF) as

$$c = -\frac{1}{V}\left(\frac{\partial V}{\partial p}\right)_T = \frac{1}{\rho}\left(\frac{\partial \rho}{\partial p}\right)_T = -\frac{1}{B}\left(\frac{\partial B}{\partial p}\right)_T$$

Several special cases of Eq. 7.42 are useful to consider. First, when the volume under consideration is closed ( $dV = 0$ ), Eq. 7.42 gives  $dp = \frac{c_p}{c} dT$ . Under the assumption of constant compressibilities, this result can be integrated to  $\Delta p = \frac{c_p}{c} \Delta T$ , which gives the pressure change in a closed volume resulting from a temperature change.

Second, when the process is isothermal, Eq. 7.42 reduces to  $\frac{dV}{V} = -c dp$ . This result can be integrated under the assumption of constant compressibility to obtain

$$\ln\left(\frac{V}{V_o}\right) = -c(p - p_o), \dots\dots\dots (7.43)$$

where subscript  $o$  is a reference state. Eq. 7.43 is often referred to as the EOS for a constant compressibility fluid. It can be rewritten in a more familiar form as  $V = V_o e^{-c(p-p_o)}$  or  $\rho = \rho_o e^{c(p-p_o)}$ . This result is often used in well testing.

Third, when the compressibility of the fluid is both constant and small, and the pressure change is not too large, the exponential term in Eq. 7.43 can be simplified so that  $V = V_o(1 - c\Delta p)$  or  $\rho = \rho_o(1 + c\Delta p)$ . This result is often referred to as the EOS for a fluid with a slight, but constant, compressibility.

Last, substitution of the definition of compressibility factor (Eq. 7.40) into Eq. 7.42 gives

$$c = \frac{1}{p} - \frac{1}{Z} \left( \frac{\partial Z}{\partial p} \right)_T \dots\dots\dots (7.44)$$

Eq. 7.44 is exact, whether the fluid is a vapor or liquid. For an ideal gas, the compressibility factor is constant and equal to 1.0, and Eq. 7.44 reduces to  $c = \frac{1}{p}$ . Thus, the isothermal compressibility for an ideal gas is inversely proportional to pressure.

**Cubic Equations-of-State.** The van der Waals EOS was the first EOS capable of representing both the liquid and vapor. The van der Waals EOS, however, is not used because of its lack of accuracy near critical points. The Peng-Robinson EOS and a modified version of the Redlich-Kwong EOS are generally used (see Table 7.2 for comparison). Nevertheless, the simplicity of the van der Waals EOS makes it useful in demonstrating several key concepts.

As for other cubic EOS, the van der Waals EOS describes the pressure as a function of molar volume and temperature, which is written as

$$p = \frac{RT}{V-b} - \frac{a}{V^2}, \dots\dots\dots (7.45)$$

where  $b$  is the repulsion parameter, and  $a$  is the attraction parameter. The first term on the right side of Eq. 7.45 attempts to represent the pressure deviation from an ideal gas that results from molecules occupying and competing for space. The effective volume available for movement of the molecules (on a molar basis) is  $V - b$ —not  $V$ , as it would be for an ideal gas. Thus,  $b$  represents the smallest possible volume that one mole of molecules can occupy (no space would exist between the molecules).

As  $V$  approaches  $b$ , the denominator in the first term on the right side becomes small so that pressure increases very rapidly. Because  $b$  is based on the effective molecule size, the value for  $b$  will change with the nature of the pure fluid and will determine the lower boundary for the region of interest on a pressure-volume diagram (i.e., the physical region of interest is only where  $V > b$ ).

The second term on the right side of Eq. 7.45 accounts for the attractive forces between molecules. The attractive forces will be proportional to the square of the number of molecules present and, thus,  $\frac{1}{V^2}$  on a macroscopic scale. The proportionality constant,  $a$ , depends on the nature and strength of the forces between the molecules and, therefore, the fluid type. As  $V$  becomes large, the contribution of the attractive forces becomes small, and the second term on the right side of Eq. 7.45 becomes negligible. Under these conditions, the van der Waals EOS approaches the ideal gas equation (Eq. 7.39). This is also true for the other EOS in Table 7.2.

The van der Waals EOS can be rewritten in cubic form as

	Equation-of-State	Constant Parameters
van der Waals	$p = \frac{RT}{V-b} - \frac{a}{V^2}$	$a = \frac{27R^2T_c^2}{64p_c}$ $b = \frac{RT_c}{8p_c}$ $Z_c = 0.375$
Redlich-Kwong	$p = \frac{RT}{V-b} - \frac{a\alpha}{V(V+b)}$ <p>where <math>\alpha = \frac{1}{T_R^{0.5}}</math></p>	$a = \frac{0.42748R^2T_c^2}{p_c}$ $b = \frac{0.08664RT_c}{p_c}$ $Z_c = 0.333$
Soave Redlich-Kwong	$p = \frac{RT}{V-b} - \frac{a\alpha}{V(V+b)}$ <p>where</p> $\alpha = \left(1 + (0.48508 + 1.55171\omega - 0.15613\omega^2)(1 - T_R^{0.5})\right)^2$	$a = \frac{0.42748R^2T_c^2}{p_c}$ $b = \frac{0.08664RT_c}{p_c}$ $Z_c = 0.333$
Peng-Robinson	$p = \frac{RT}{V-b} - \frac{a\alpha}{V(V+b) + b(V-b)}$ <p>where, for <math>\omega &lt; 0.5</math>,</p> $\alpha = \left(1 + (0.37464 + 1.54226\omega - 0.26992\omega^2)(1 - T_R^{0.5})\right)^2$ <p>and, for <math>\omega &gt; 0.5</math>,</p> $\alpha = \left(1 + (0.37964 + 1.4850\omega - 0.16442\omega^2 + 0.016667\omega^3)(1 - T_R^{0.5})\right)^2$	$a = \frac{0.45724R^2T_c^2}{p_c}$ $b = \frac{0.07780RT_c}{p_c}$ $Z_c = 0.307$

$$V^3 - \left(b + \frac{RT}{p}\right)V^2 + \frac{aV}{p} - \frac{ab}{p} = 0, \dots\dots\dots (7.46)$$

or in terms of the compressibility factor,

$$Z^3 - \left(1 + \frac{bp}{RT}\right)Z^2 + \frac{ap}{(RT)^2}Z - \frac{abp^2}{(RT)^3} = 0.$$

*Determination of a and b From van der Waals EOS.* We previously demonstrated that an isotherm on a pressure-volume diagram must have zero slope at the critical point. There is also an inflection point there. Thus, any cubic EOS must be constrained by

$$\left(\frac{\partial p}{\partial V}\right)_{T_c} = \left(\frac{\partial^2 p}{\partial V^2}\right)_{T_c} = 0. \dots\dots\dots (7.47)$$

Eq. 7.47 consists of two equations that can be solved simultaneously to determine the unknowns,  $a$  and  $b$ . This procedure can be somewhat tedious, especially for more advanced cubic EOS.

A simpler method is to recognize that Eq. 7.47 implies that only one volume root of the cubic EOS exists at the critical point. Mathematically, this can be expressed as  $(V - V_C)^3 = 0$ , which upon expansion is  $V^3 - 3V_C V^2 + 3V_C^2 V - V_C^3 = 0$ . Comparison of this expansion to Eq. 7.48 term by term at the critical point gives  $-3V_C = -\left(b + \frac{RT_C}{p_C}\right)$ ,  $3V_C^2 = \frac{a}{p_C}$ , and  $-V_C^3 = -\frac{ab}{p_C}$ . These three relationships are easily solved to obtain  $a$  and  $b$  in terms of only the critical pressure and temperature, as well as to determine the relationship between critical parameters. That is,  $a = \frac{27R^2 T_C^2}{64p_C}$ ;  $b = \frac{RT_C}{8p_C}$ ; and  $Z_C = \frac{p_C V_C}{RT_C} = \frac{3}{8}$ . A similar procedure can be used for any cubic EOS.

The result shows that the critical compressibility factor is constant and is independent of the fluid. This is true for the other cubic EOS models in Table 7.2. For the van der Waals EOS, we obtained  $Z_C = \frac{3}{8} = 0.375$ . In reality, the critical compressibility factor is not constant for different fluids and is generally smaller than 0.3. For example, water has a critical compressibility of about 0.23, and that of carbon dioxide is 0.27. The poor match of the van der Waals EOS at the critical point explains why it is not used today. Both the Redlich-Kwong EOS and the Peng-Robinson EOS have critical compressibilities closer to measured values (see Table 7.2).

A constant critical compressibility factor means that only two of the three critical properties can be satisfied at the critical point. For example, if critical pressure and temperature are specified, the critical volume will not be correctly predicted. For the van der Waals EOS,  $V_C = \frac{3}{8} \frac{RT_C}{p_C}$ . Thus, when the critical pressure and temperature are specified, the critical volume or critical density of the fluid is likely in error. In general, liquid densities predicted by cubic EOS exhibit greater error than do vapor densities. Ref. 2 gives a good description of how density predictions can be improved using volume translation parameters.

We determined  $a$  and  $b$  only at the critical point. Their values could be different away from the critical point and could be functions of temperature. Therefore, in general,  $a = \frac{27R^2 T_C^2}{64p_C} \alpha$ , and  $b = \frac{RT_C}{8p_C} \beta$ , where  $\alpha$  and  $\beta$  are functions of temperature; these functions must approach 1.0 at the critical point. For most cubic EOS,  $\beta$  is taken to be 1.0, and  $\alpha$  is adjusted to give the correct vapor pressure (see Table 7.2).

*Construction of Pressure-Volume Diagram From Cubic EOS.* Once  $a$  and  $b$  are defined, a cubic EOS can be used to generate the pressure-volume diagram, as illustrated in Fig. 7.9. From the Gibbs phase rule, there is only one degree of freedom within the two-phase region for pure fluids. We assume that temperature has been specified but not the pressure. Our goal, therefore, is to solve for the vapor pressure, given temperature and the critical properties of the fluid.

The procedure used to estimate  $a$  and  $b$  ensures that the cubic EOS gives the experimentally measured shapes of the isotherms for temperatures greater than or equal to the critical point. Fig. 7.11 illustrates the isotherms generated from a cubic EOS. As shown by the loop in the curve, cubic EOS can have three roots for isotherms below the critical temperature. The loop is not physical because the pressure must be constant in the two-phase region.

The nonphysical condition must be removed to achieve the correct physical response in the two-phase region. That is, the loop within the two-phase region must be discarded and replaced

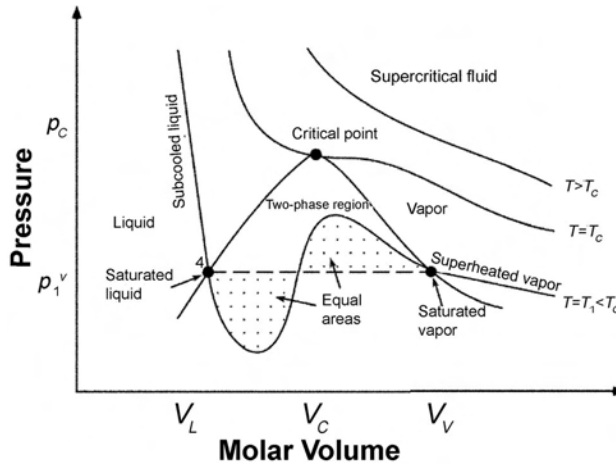


**Fig. 7.11—Isotherms with a cubic EOS are shown for three different temperatures. The isotherm below the critical temperature does not give the physically-correct result within the two-phase region because pressure should be constant there. The dashed line indicates the correct isotherm in the two-phase region. The areas above and below the dashed line should be equal when the pressure is equal to the equilibrium vapor pressure (Maxwell’s equal-area rule).**

by the correct vapor pressure. The procedure is relatively simple. Within the two-phase region, there are three roots along an isotherm. At the vapor pressure, the root with the largest molar volume is taken to be the molar volume of the saturated vapor  $V_V$ , whereas the smallest root is  $V_L$ . The middle root is discarded because choosing that root would lead to unstable phases (see Sec. 7.2.2). The middle root is clearly nonphysical in that it is located on the isotherm where  $(\frac{\partial p}{\partial V})_T > 0$  (i.e., pressure increases as density decreases).

*Principle of Corresponding States.* Correlations for reservoir fluids, such as the generalized compressibility factor charts for natural gases, use reduced temperature, pressure, and volume, where  $T_R = \frac{T}{T_C}$ ,  $p_R = \frac{p}{p_C}$ , and  $V_R = \frac{V}{V_C}$ . A cubic EOS shows why these parameters give good correlations. For example, substitution of the reduced parameters into the van der Waals EOS (Eq. 7.45), along with the definitions of  $a$  and  $b$ , gives

$$p_R = \frac{8T_R}{3V_R - 1} - \frac{3}{V_R^2} \dots\dots\dots (7.48)$$

Eq. 7.48 is dimensionless and is often called the reduced form of the van der Waals EOS. The reduced form leads directly to the principle of corresponding states. The two-parameter principle of corresponding states says that all fluids, when compared at the same reduced temperature and pressure, have approximately the same compressibility factor, and all deviate from ideal-gas behavior by about the same degree. The reduced compressibility factor is given by  $\frac{Z}{Z_C} = \frac{p_R V_R}{RT_R}$ . Because  $Z_C$  is constant for a cubic EOS, the compressibility factor is constant for the same reduced temperature and pressure (reduced volume is related to reduced pressure and temperature through Eq. 7.48).

The principle of corresponding states is a powerful idea even though it is only qualitatively correct. Experiments show that  $Z_C$  is not constant for different fluids. Nevertheless, it demonstrates that, to obtain reasonable estimates of fluid properties, only the reduced pressure and



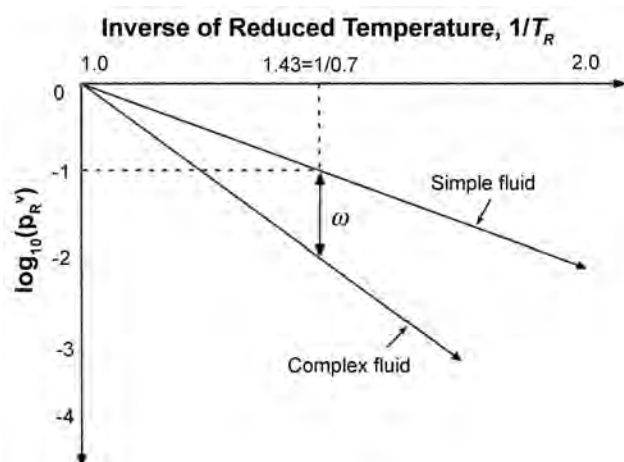


**Fig. 7.12—Estimation of acentric factor (after Smith *et al.*<sup>5</sup>). Simple fluids collapse to a single curve. The deviation of complex fluids from simple fluids is measured by the acentric factor,  $\omega$ . The deviation (or acentric factor) is determined at a reduced temperature of 0.70.**

temperature must be known. This is why most fluid correlations use reduced temperature and pressure.

In reality, fluids can deviate from the principle of corresponding states. Pitzer noted that a plot of  $\frac{1}{T_R}$  vs.  $\log_{10} p_R^v$  for simple fluids (molecules that are roughly spherical in shape such as the Noble gases) collapse onto a straight line (see Fig. 7.12). The parameter,  $p_R^v$ , is the reduced pressure at the vapor pressure. Other more complex and nonspherical molecules such as hydrocarbon-chained molecules, however, do not plot on that same line. Thus, Pitzer defined an additional correlation variable called the acentric factor, where

$$\omega = -1.0 - \log_{10}(p_R^v) \Big|_{T_R=0.7} = \log_{10} \left[ \frac{p_C}{10(p^v)_{T_R=0.7}} \right].$$

The acentric factor measures the deviation of complex fluids from the simple fluids at a reduced temperature of 0.70 (see Fig. 7.12). Hydrocarbons with longer chains generally have greater acentric factors. For example, methane has an acentric factor of 0.008, while *n*-butane has an acentric factor of 0.193.

Because the acentric factor is simple to measure, it is often used to improve phase-behavior calculations from cubic EOS. The three-parameter principle of corresponding states is that a fluid will have about the same compressibility factor as another fluid, if the reduced pressure, reduced temperature, and acentric factors are similar.

*Calculation of Vapor Pressure.* Although the shape of an isotherm from a cubic EOS can be made qualitatively correct, the problem remains that the vapor pressure is unknown for a given temperature. The vapor pressure is determined using the equilibrium criterion of Eq. 7.24. For example, substitution of the Soave Redlich-Kwong EOS into Eq. 7.25 and subsequent integration gives the fugacity as a function of pressure, molar volume, and temperature. That is,

$$f = p \exp \left[ \ln \left( \frac{V}{V-b} \right) + \left( \frac{aa}{RTb} \right) \ln \left( \frac{V}{V+b} \right) + Z - 1 - \ln Z \right].$$

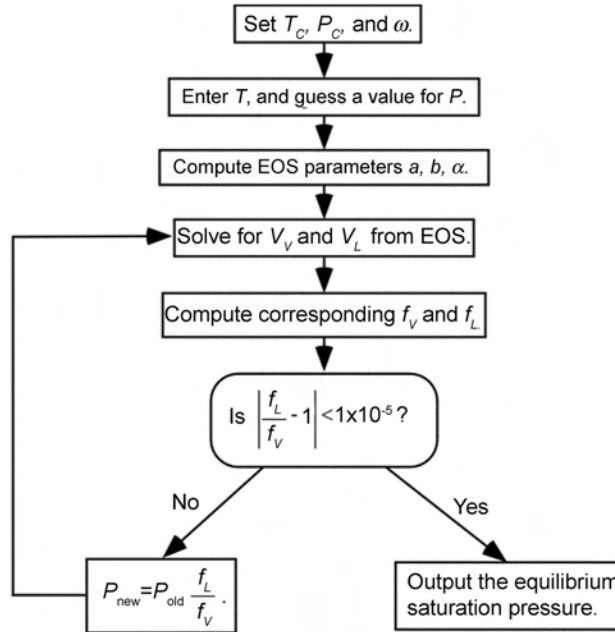


Fig. 7.13—Procedure for determination of vapor pressure for a pure fluid.

The fugacity of the vapor is computed using the molar volume of the vapor phase,  $V_V$ , whereas the liquid fugacity is determined using  $V_L$ . Thus, the fugacity for the vapor phase from the Soave Redlich-Kwong EOS is

$$f_V = p \exp \left[ \ln \left( \frac{V_V}{V_V - b} \right) + \left( \frac{a\alpha}{RTb} \right) \ln \left( \frac{V_V}{V_V + b} \right) + Z_V - 1 - \ln Z_V \right], \dots\dots\dots (7.49)$$

where  $Z_V = \frac{pV_V}{RT}$ ; and for the liquid phase,

$$f_L = p \exp \left[ \ln \left( \frac{V_L}{V_L - b} \right) + \left( \frac{a\alpha}{RTb} \right) \ln \left( \frac{V_L}{V_L + b} \right) + Z_L - 1 - \ln Z_L \right], \dots\dots\dots (7.50)$$

where  $Z_L = \frac{pV_L}{RT}$ .

The problem of calculating the vapor pressure reduces to finding the pressure that gives the required phase molar volumes so that the fugacities of the phases are equal. Fig. 7.13 illustrates the procedure. The procedure works well as long as the initial guess for the pressure is in the range of the cubic EOS where three roots exist (i.e., the pressure is within the loop of the cubic EOS). If the pressure is above the critical pressure, only one root exists for the molar volume. This is also true if the pressure is below the minimum value of the loop (the minimum pressure of the loop could be negative).

For a pure fluid, the vapor pressure can also be determined graphically with Maxwell’s equal area construction. Fig. 7.11 shows that the vapor pressure is the pressure required so that the areas bounded by the vapor pressure line and the loop of the cubic EOS must be equal. The equal area construction results from the equality of Gibbs energy (or fugacities). This

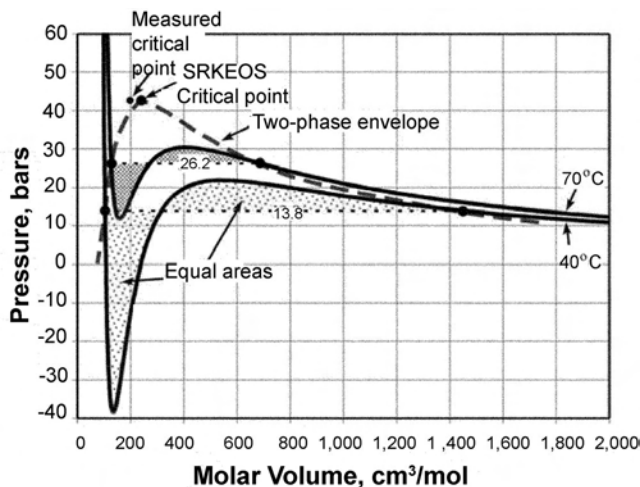


Fig. 7.14—Example calculation of two-phase envelope for propane using the SRKEOS (Soave-Redlich-Kwong Equation-of-State). The solid lines are the isotherms at 40 and 70°C. The vapor pressures are labeled on the narrow-dashed lines. The critical point, calculated with the SRKEOS, is compared to the experimentally measured critical point for propane. The two-phase envelope connects the equilibrium liquid and vapor molar volumes.

method is less accurate but serves as a useful check to the calculated vapor pressure. Ref. 2 outlines Maxwell's construction method in detail for pure fluids and mixtures.

*Example Calculation of Two-Phase Envelope.* This section demonstrates a calculation of vapor pressure and the two-phase envelope for a pure fluid using the procedure outlined in Fig. 7.13. Propane is selected as the pure fluid at a temperature of 40°C (313°K). We also select the Soave-Redlich-Kwong EOS to model the phase behavior. The properties for propane are a critical temperature of 370°K; a critical pressure of 42.5 bars; and an acentric factor of 0.152. The gas constant in consistent units is 83.1 cm<sup>3</sup>-bar/mol/K.

With these values, the parameter “a” in Table 7.2 is calculated to be 9.51E6 cm<sup>6</sup>-bar/mol<sup>2</sup>, and parameter “b” is 62.7 cm<sup>3</sup>/mol. The value for  $\alpha$  from Table 7.2 is found to be 1.05 (the reduced temperature at 40°C is 0.913). Fig. 7.14 shows the isotherm at 40°C calculated with the SRKEOS.

Based on the calculated isotherm, we select an initial value of 10 bars for the vapor pressure. Any value within the S-loop of the isotherm would be satisfactory as an initial guess for the vapor pressure. A vapor pressure of 13.8 bars is calculated with the iteration procedure of Fig. 7.13. The calculated vapor pressure is the pressure at which the fugacities of the vapor and liquid phases are equal (illustrated in Figs. 7.11 and 7.14 by the Maxwell equal-area rule). The fugacities are 11.3 bars at the vapor pressure, which are calculated with Eqs. 7.49 and 7.50. The equilibrium liquid molar volume is 105 cm<sup>3</sup>/mol, and the vapor molar volume is 1462 cm<sup>3</sup>/mol.

Fig. 7.14 also illustrates the phase behavior with the SRKEOS at a higher temperature of 70° C. The calculated vapor pressure at this temperature is 26.2 bars. The equilibrium liquid molar volume is 128 cm<sup>3</sup>/mol, and the vapor molar volume is 691 cm<sup>3</sup>/mol. Thus, as the temperature is increased, the size of the two-phase region shrinks. Fig. 7.14 shows the two-phase envelope that connects the liquid and vapor molar volumes. At the critical temperature, the two-phase region disappears.

The values for vapor pressure and molar volumes are calculated parameters only. Using the critical temperature and pressure, the critical volume from the SRKEOS is approximately 241 cm<sup>3</sup>/mol ( $Z_C = 1/3$  always for the SRKEOS). The actual critical volume from experimental

data is 200 cm<sup>3</sup>/mol, which is about 20 percent smaller than the calculated value. Ref. 2 outlines a more complex method to improve the calculated match of cubic EOS to experimental data.

### 7.5 Volumetric Properties of Mixtures

The interaction of the different molecules in a mixture causes behavior not observed in pure fluids. The chapter on phase diagrams in this section of the handbook describes the volumetric behavior of mixtures. Sec. 7.5 presents the basic procedure to predict the equilibrium phase behavior of mixtures by a cubic EOS. More detailed information can be found in many sources, including Refs. 2 and 7.

The thermodynamic properties of a mixture can be calculated with the same EOS for a pure fluid, with some modifications. The primary difference is that the mixture molar volume for a phase is calculated with EOS constants and temperature-dependent functions of the phase molar composition, either  $x_i$  or  $y_i$ . For example, the Soave Redlich-Kwong EOS written for a mixture is

$$p = \frac{RT}{V_m - b_m} - \frac{(a\alpha)_m}{V_m(V_m + b_m)},$$

where subscript  $m$  indicates a mixture property. The mixture properties are calculated with mixing rules that are often linear or quadratic functions of the phase mole fractions. For example, for the liquid phase, the mixing rule for the product,  $a\alpha$ , is often the quadratic equation,

$$(a\alpha)_m = \sum_{i=1}^{n_c} \sum_{j=1}^{n_c} x_i x_j (a\alpha)_{ij},$$

where  $(a\alpha)_{ij} = (1 - k_{ij})\sqrt{(a\alpha)_i(a\alpha)_j}$ . The parameters  $k_{ij}$  are called binary interaction parameters. Binary interaction parameters are constants that are determined by fitting the cubic EOS to experimental PVT data. The mixing rule for  $a\alpha$  is theoretically justified from virial EOS, which are discussed in Refs. 2 through 7. For  $b_m$ , the linear relationship,  $b_m = \sum_{i=1}^{n_c} x_i b_i$ , is often used.

For equilibrium calculations, the fugacity of every component in each phase must be calculated. Eq. 7.35 is used for this purpose. For example, substitution of the Soave Redlich-Kwong EOS into Eq. 7.35 gives the fugacity of a component in the liquid phase, which is written as

$$\hat{f}_{iL} = p \exp \left\{ \ln \left( \frac{V_{mL}}{V_{mL} - b_{mL}} \right) + \frac{b_i}{V_{mL} - b_{mL}} + \left( \frac{2 \sum_{j=1}^{n_c} x_j (a\alpha)_{ij}}{RT b_{mL}} \right) \ln \left( \frac{V_{mL}}{V_{mL} + b_{mL}} \right) + \frac{b_i (a\alpha)_{mL}}{RT b_{mL}^2} \left[ \ln \left( \frac{V_{mL} + b_{mL}}{V_{mL}} \right) - \frac{b_{mL}}{V_{mL} + b_{mL}} \right] - \ln \left( \frac{Z_L}{x_i} \right) \right\}, \dots \quad (7.51)$$

where  $Z_L = \frac{pV_{mL}}{RT}$ . A similar equation is written for the vapor phase, where  $x_i$  is replaced by  $y_i$ , and superscript  $L$  is replaced by  $V$ .

**7.5.1 Procedure for Equilibrium Calculations of a Mixture.** The procedure for equilibrium calculations of a potential two-phase mixture is more complex than that of a pure fluid. For an equilibrium flash calculation, the pressure and temperature and overall mole fractions are specified (i.e., pressure and temperature are now independent, as specified by the Gibbs phase rule). The general procedure for a flash calculation is discussed next.

1. Make an initial guess of the  $K$ -values, where  $K_i = \frac{y_i}{x_i}$ . When the guess of the  $K$ -values is near the equilibrium solution, the procedure will converge rapidly. If the guess is not good, the procedure might not converge at all. Most EOS programs use some empirical correlation to estimate the phase mole fractions based on  $K$ -values. The Wilson equation<sup>11</sup> is often used,

$$\text{where } K_i = \frac{y_i}{x_i} = \frac{\exp \left[ 5.37 \left( 1 + \omega_i \right) \left( 1 - \frac{1}{T r_i} \right) \right]}{P_{Ri}}$$

2. Calculate  $x_i$  and  $y_i$  with the Rachford-Rice procedure.<sup>12</sup> Once the  $K$ -values for each component are specified, the Rachford-Rice procedure is used to estimate the phase mole fractions. A material balance on each component gives  $z_i = Lx_i + (1-L)y_i$ , where  $L$  is the mole fraction liquid (see Eq. 7.1). Substitution of  $y_i = K_i x_i$  into the material balance equation gives, upon

rearrangement,  $x_i = \frac{z_i}{L + (1-L)K_i}$  or alternatively  $y_i = \frac{K_i z_i}{L + (1-L)K_i}$ . Substitution of these expres-

sions into the function  $F(L) = \sum_{i=1}^n x_i - \sum_{i=1}^n y_i = 0$  gives  $F(L) = \sum_{i=1}^n \frac{(1-K_i)z_i}{L + (1-L)K_i} = 0$ . This is a nonlinear equation that can best be solved by a simple Newton-Raphson iteration, where for

each iteration the new value of the liquid mole fraction is found from  $L^{\text{new}} = L^{\text{old}} - \frac{F(L^{\text{old}})}{\left(\frac{dF}{dL}\right)_{L^{\text{old}}}}$ .

For the first iteration, choose  $L = 0.5$  and iterate until  $\left(\frac{L^{\text{new}}}{L^{\text{old}}} - 1\right) < 10^{-5}$ .

3. Calculate the cubic EOS parameters (e.g.,  $a_m$  and  $b_m$ ). This step is very straightforward and depends on the selected EOS and its associated mixing rules. The critical temperatures, pressures, and acentric factors for each component are needed to calculate the EOS parameters.

4. Solve the cubic EOS for the phase molar volumes  $V_{mL}$  and  $V_{mV}$ . This step requires solution of the cubic EOS for the compressibility factor,  $Z$ , of the vapor and liquid (or alternatively for  $V_V$  and  $V_L$ ). Because the compositions of the vapor and liquid are different, two separate solutions for the roots of the cubic EOS are required. A cubic equation-solver or iteration method should be used to obtain the roots of the EOS.

The procedure for this step is more complex than for a pure fluid because six roots of the cubic EOS are calculated (i.e., three roots for the liquid and three for the vapor). The middle root for the vapor and liquid are discarded because that solution leads to unstable phases, similar to pure fluids. One of the remaining two liquid roots is paired with one of the other vapor roots to calculate component fugacities and equilibrium. If the wrong root pairing is selected, the solution could be false in that an unstable or metastable solution could be obtained. The correct equilibrium solution is the one that minimizes the total Gibbs energy compared with the other possible root-pairings. Refs. 2 and 7 provide a good description of how to select the liquid and vapor roots so that the total Gibbs energy of the two-phase mixture is minimized. For most cases, the correct root for the liquid is the one that gives the smallest molar volume, and the correct root for the vapor is the one that gives the largest molar volume.

Refs. 2 and 7 also examine using stability analyses to determine whether a mixture will form three phases instead of just one or two phases. The chapter on phase diagrams in this

section of the handbook discusses the formation of three equilibrium phases in CO<sub>2</sub>/crude oil systems.

5. Calculate the component fugacities of each component in each phase,  $\hat{f}_{iV}$  and  $\hat{f}_{iL}$ . The selected cubic EOS is used to determine an expression for the fugacity of a component in a phase (see Eq. 7.51 for example).

6. Check to see if equilibrium has been reached. A good criterion is  $\left(\frac{\hat{f}_{iV}}{\hat{f}_{iL}} - 1\right) < 10^{-5}$  for all components. If the criteria are satisfied, equilibrium has been obtained. The correct equilibrium solution is found when  $\hat{f}_{iL} = \hat{f}_{iV}$  for each component. Because the solution is never found exactly, we accept the solution if  $\left(\frac{\hat{f}_{iV}}{\hat{f}_{iL}} - 1\right) < 10^{-5}$  for each component. The tolerance of  $10^{-5}$  can be decreased if better accuracy is required.

7. If the criteria have not been satisfied, the  $K$ -values should be updated and steps two through six repeated. This step is also very important; it affects both the rate of convergence and whether the iteration converges at all. One procedure that works well is the simple successive substitution scheme that relies on the fact that  $\hat{\phi}_{iV} = \frac{\hat{f}_{iV}}{y_i p}$  and  $\hat{\phi}_{iL} = \frac{\hat{f}_{iL}}{x_i p}$  for each component.

Therefore,  $\frac{\hat{\phi}_{iL}}{\hat{\phi}_{iV}} = \frac{\hat{f}_{iL} y_i}{\hat{f}_{iV} x_i}$ . At equilibrium, the component fugacities are equal so that

$\frac{\hat{\phi}_{iL}}{\hat{\phi}_{iV}} = \frac{y_i}{x_i} = K_i$ . We can use this ratio to estimate new  $K$ -values from the old ones. That is,

$K_i^{\text{new}} = \frac{\hat{f}_{iL}}{\hat{f}_{iV}} K_i^{\text{old}}$ . Once the new  $K$ -values are determined, steps two through six are repeated until convergence in step six is achieved. Convergence from successive substitutions can be slow near the critical region. Other methods may be required when convergence is slow.<sup>2</sup>

## 7.6 Characterization of In-Situ Fluids

Phase behavior calculations require that all components and their properties be specified. Crude oils, however, typically have hundreds of components, making the EOS procedure in Sec. 7.5 computationally intensive. Thus, components are often lumped into pseudocomponents to approximate the in-situ fluid characterization. The characterization usually takes the following three steps:

1. The hydrocarbon components in the in-situ fluid are analyzed using analytical techniques, such as chromatography or distillation. New analytical techniques often give a reliable analysis for hydrocarbon components up to C<sub>30</sub>, instead of the traditional C<sub>7</sub>. Properties for hydrocarbon components greater than C<sub>30</sub> are reported as a C<sub>30+</sub> fraction.

2. The measured components are separated and lumped into a minimum number of pseudocomponents. The chosen number of pseudocomponents is often a result of the measured fluid characterization and the degree of accuracy required (see step three). The properties and selection of the pseudocomponents are determined using a variety of methods as reported in Ref. 7. The required pseudocomponent properties are those needed for the cubic EOS calculations, such as critical temperature, pressure, and acentric factor.

3. The pseudocomponent properties are adjusted to match all available phase behavior data (e.g., PVT reports). This process, which typically uses nonlinear regression, is known as EOS tuning. EOS tuning is needed because of the inherent uncertainty in the properties estimated from step two, especially for the heavier components. Binary interaction parameters are typically the first parameters to be adjusted, although all of the parameters may need some tuning.

The number of pseudocomponents may need to be increased from step two to obtain a good fit of the calculated phase behavior with the measured phase behavior data.

The selection of pseudocomponents and their property values are likely not unique, as is often the case when numerous model parameters are estimated by fitting measured data with nonlinear regression. Care should be taken to avoid estimates in the pseudocomponent properties that are unphysical and to reduce the number of parameters. Furthermore, the final EOS characterization is most accurate in the range of the measured phase behavior data. Phase behavior data should be collected that covers, as much as possible, the conditions that occur in the reservoir. The characterization should be updated when new data becomes available.

Finally, fluid characterizations may vary from one location in the reservoir to another. In such cases, multiple EOS characterizations might be required. Compositional variations can occur for a variety of reasons. For example, gravity can cause vertical compositional gradients, where heavier components become more concentrated at greater depths. Refs. 2, 13, and 14 provide examples of gravitational concentration gradients. Variations caused by thermal gradients are also discussed in Ref. 2.

### Nomenclature

$a$	= constant parameter in cubic EOS in Table 7.2, pressure-volume <sup>2</sup> , Pa-m <sup>6</sup>
$A$	= area normal to specified direction, m <sup>2</sup>
$b$	= constant parameter in cubic EOS in Table 7.2, volume/mole, m <sup>3</sup> /mole
$B$	= formation volume factor of the fluid, volume/volume
$c$	= isothermal compressibility of a fluid, 1/pressure, 1/Pa
$c_p$	= isobaric compressibility of a fluid, 1/pressure, 1/Pa
$f$	= fugacity of a pure fluid, pressure, Pa
$\hat{f}_i$	= fugacity of a component in a mixture, mole <sup>2</sup> -pressure/mole <sup>2</sup> , Pa
$F$	= external force on one side of system, energy/length, J/m
$\vec{F}$	= external force vector of surroundings on system, energy/length, J/m
$G$	= molar Gibbs free energy, energy/mole, J/mole
$h$	= heat transfer coefficient, energy/temperature/time, J/(Kelvin-sec)
$H$	= molar enthalpy of fluid, energy/mole, J/mole
$k$	= binary interaction parameter, dimensionless
$K_i$	= $K$ -value of $i^{\text{th}}$ component, $y_i/x_i$ , dimensionless
$\vec{l}$	= displacement vector of system, length, m
$L$	= liquid mole fraction, moles liquid/total moles, dimensionless
$M$	= net mass transferred, mass, moles
$n$	= total moles of all components, moles
$n_c$	= number of components
$n_p$	= number of phases
$p$	= pressure, force/area, Pa
$Q$	= net heat transferred, energy, J
$R$	= gas constant, pressure-volume/temperature/mole, Pa-m <sup>3</sup> /(Kelvin-mole)
$S$	= molar entropy of fluid, entropy/mole, J/(Kelvin-mole)
$t$	= time, seconds
$T$	= temperature, Kelvin
$u$	= velocity of fluid, length/time, m/sec
$U$	= molar internal energy, energy/mole, J/mole
$V$	= vapor mole fraction, moles vapor/total moles, dimensionless or molar volume of fluid, volume/mole, m <sup>3</sup> /mole
$W$	= net work performed, energy, J
$x$	= $x$ -coordinate, length, m

- $x_i$  = mole fraction of  $i^{\text{th}}$  component in liquid, moles  $i^{\text{th}}$  component in liquid/total moles liquid, dimensionless  
 $y$  =  $y$ -coordinate, length, m  
 $y_i$  = mole fraction of  $i^{\text{th}}$  component in vapor, moles  $i^{\text{th}}$  component in vapor/total moles vapor, dimensionless  
 $z$  =  $z$ -coordinate, length, m  
 $z_i$  = overall mole fraction of  $i^{\text{th}}$  component, moles  $i^{\text{th}}$  component/total moles, dimensionless  
 $Z$  = compressibility factor of a fluid, dimensionless  
 $\alpha$  = temperature dependence function in cubic EOS in [Table 7.2](#), dimensionless  
 $\beta$  = temperature dependence function in cubic EOS, typically set to 1.0, dimensionless  
 $\mu_i$  = chemical potential of  $i^{\text{th}}$  component, energy/mole, J/mole  
 $\rho$  = molar density of fluid, moles/volume, mole/m<sup>3</sup>  
 $\varphi$  = fugacity coefficient for a pure fluid, pressure/pressure, dimensionless  
 $\varphi_i$  = fugacity coefficient for a component in a mixture, mole<sup>2</sup>-pressure/mole<sup>2</sup>-pressure, dimensionless  
 $\omega$  = acentric factor, dimensionless

### Subscripts

- $A$  = open subsystem A  
 $B$  = open subsystem B  
 $C$  = state is at critical point  
 ext = external to system  
 $G$  = generated quantity within system  
 $i$  =  $i^{\text{th}}$  component  
 $j$  =  $j^{\text{th}}$  component  
 $L$  = liquid  
 $m$  = mixture  
 $o$  = reference state  
 rev = reversible process  
 $R$  = reduced parameter, ratio of quantity/critical value, dimensionless  
 $T$  = total  
 $v$  = vapor pressure  
 $V$  = vapor  
 $x$  = direction is along  $x$ -coordinate  
 $y$  = direction is along  $y$ -coordinate  
 $z$  = direction is along  $z$ -coordinate

### Superscripts

- $ig$  = ideal gas  
 $L$  = liquid  
 $v$  = vapor pressure  
 $V$  = vapor

---

## References

1. Gibbs, J.W.: *The Scientific Papers of J. Willard Gibbs*, H.A. Bumstead and R.G. Van Name (eds.), Longmans, Green and Co., London (1906), reprinted Dover, New York (1961).



2. Firoozabadi, A.: *Thermodynamics of Hydrocarbon Reservoirs*, McGraw-Hill Book Co. Inc., New York City (1999) 355.
3. Prausnitz, J.M., Lichtenthaler, R.N., and de Azevedo, E.G.: *Molecular Thermodynamics of Fluid-Phase Equilibria*, third edition, Prentice Hall, New Jersey (1999).
4. Sandler, S.I.: *Chemical and Engineering Thermodynamics*, third edition, John Wiley & Sons, New York City (2000).
5. Smith, J.M., Van Ness, H.C., and Abbott, M.M.: *Chemical Engineering Thermodynamics*, sixth edition, McGraw-Hill Book Co. Inc., New York City (2001) 787.
6. Walas, S.M.: *Phase Equilibria in Chemical Engineering*, Butterworth Publishings, Boston (1985) 671.
7. Whitson, C.H., and Brule, M.R.: *Phase Behavior*, Monograph Series, SPE, Richardson, Texas (2000) **20**.
8. Peng, D. and Robinson, D.B.: "A New Two-Constant Equation-of-State," *Industrial & Engineering Chemistry Fundamentals* (1976) **15**, No.1, 59.
9. Redlich, O. and Kwong, J.N.S.: "On the Thermodynamics of Solutions, V. An Equation-of-State. Fugacities of Gaseous Solutions," *Chemical Reviews* (1949) **44**, 233.
10. Soave, G.: "Equilibrium Constants from a Modified Redlich-Kwong Equation-of-state," *Chemical Engineering Science* (1972) **27**, No. 6, 1197.
11. Wilson, G.M.: "A Modified Redlich-Kwong Equation-of-State, Application to General Physical Data Calculations," paper 15c presented at the 1969 AIChE Natl. Meeting, Cleveland, Ohio, 4–7 May.
12. Rachford, H.H. and Rice, J.D.: "Procedure for Use of Electrical Digital Computers in Calculating Flash Vaporization Hydrocarbon Equilibrium," *JPT* (October 1952) 10; *Trans., AIME*, **195**.
13. Sage, B.H. and Lacey, W.N., "Gravitational Concentration Gradients in Static Columns of Hydrocarbon Fluids," *Trans., AIME* (1939) **132**, 120–131.
14. Schulte, A.M.: "Compositional Variations Within a Hydrocarbon Column due to Gravity," paper SPE 9235 presented at the 1980 SPE Annual Technical Conference and Exhibition, Dallas, 21–24 September.

### SI Metric Conversion Factors

bar	× 1.0*	E + 05	= Pa
ft	× 3.048*	E – 01	= m
ft <sup>2</sup>	× 9.290 304*	E – 02	= m <sup>2</sup>
ft/sec	× 3.048	E – 01	= m/s
°F	(°F – 32)/1.8		= °C
kelvin	(K – 273.15)		= °C

\*Conversion factor is exact.



## Chapter 8

# Phase Diagrams

F.M. Orr, Jr. and K. Jessen, Stanford U.

### 8.1 Introduction

Petroleum reservoir fluids are complex mixtures containing many hydrocarbon components that range in size from light gases such as methane ( $C_1$ ) and ethane ( $C_2$ ) to very large hydrocarbon molecules containing 40 or more carbon atoms. Nonhydrocarbon components such as nitrogen,  $H_2S$ , or  $CO_2$  also may be present. Water, of course, is present in essentially all reservoirs. At a given temperature and pressure, the components distribute between the solid, liquid, and vapor phases present in a reservoir. A phase is the portion of a system that is homogeneous, is bounded by a surface, and is physically separable from other phases. Equilibrium phase diagrams offer convenient representations of the ranges of temperature, pressure, and composition within which various combinations of phases coexist. Phase behavior plays an important role in a variety of reservoir engineering applications, ranging from pressure maintenance to separator design to enhanced oil recovery (EOR) processes. This chapter reviews the fundamentals of phase diagrams used in such applications. Additional material on the role of phase equilibrium in petroleum/reservoir engineering can be found in [Refs. 1 and 2](#).

### 8.2 Phase Diagrams for a Single Component

[Fig. 8.1](#) summarizes the phase behavior of a single component. The saturation curves shown in [Fig. 8.1](#) indicate the temperatures and pressures at which phase changes occur. At temperatures below the triple point, the component forms a vapor phase if the pressure is below that indicated by the sublimation curve and forms a solid phase at pressures above the curve. At pressures and temperatures lying on the sublimation curve, solid and vapor can coexist. At pressures and temperatures on the melting curve, solid and liquid are in equilibrium. At higher temperatures, liquid and vapor can coexist along the vaporization or vapor-pressure curve. If the pressure is greater than the vapor pressure, a liquid forms; if the pressure is lower than the vapor pressure, a vapor forms. The vapor-pressure curve terminates at the critical point. At temperatures above the critical temperature,  $T_c$ , a single phase forms over the entire range of pressures. For a single component, the critical temperature is the maximum temperature at which two phases can exist. Critical temperatures of hydrocarbons vary widely. Small hydrocarbon molecules have low critical temperatures, while large hydrocarbon molecules have much higher critical temperatures. Critical pressures generally decline as the molecular size increases. For instance, the

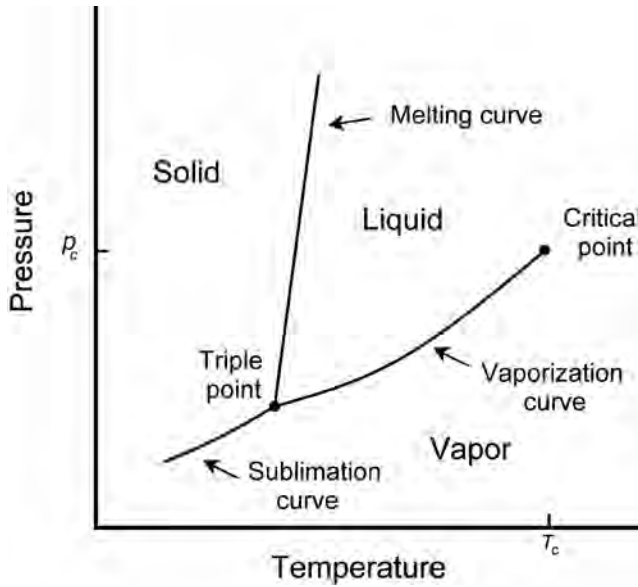


Fig. 8.1—Phase behavior of a pure component.

critical temperature and pressure of  $C_1$  are  $-117^\circ\text{F}$  and 668 psia; for decane, the values are  $652^\circ\text{F}$  and 304 psia.

For many reservoir engineering applications, liquid/vapor equilibrium is of greatest interest, although liquid/liquid equilibria are important in some EOR processes. Solid/liquid phase changes, such as asphaltene or paraffin precipitation (see the chapter on crude oil emulsions in this volume), occasionally occur in petroleum production operations.

Fig. 8.2 shows typical volumetric behavior of a single component in the range of temperatures and pressures near the vapor-pressure curve in Fig. 8.1. If the substance under consideration is placed in a pressure cell at constant temperature,  $T_1$ , below  $T_c$  and at a low pressure (point A, for instance), it forms a vapor phase of high volume (low density). If the volume of the sample is decreased with the temperature held constant, the pressure rises. When the pressure reaches  $p_v(T_1)$ , the sample begins to condense. The pressure remains constant (see Sec. 8.3) at the vapor pressure until the sample volume is reduced from the saturated vapor volume ( $V_V$ ) to that of the saturated liquid ( $V_L$ ). With further reductions in volume, the pressure rises again as the liquid phase is compressed. Small decreases in volume give rise to large pressure increases in the liquid phase because of the low compressibility of liquids. At a fixed temperature,  $T_2$ , above the critical temperature, no phase change is observed over the full range of volumes and pressures. Instead, the sample can be compressed from high volume (low density) and low pressure to low volume (high density) and high pressure with only one phase present.

### 8.3 The Phase Rule

The number of components present in a system determines the maximum number of phases that can coexist at fixed temperature and pressure. The phase rule of Gibbs states that the number of independent variables that must be specified to determine the intensive state of the system is given by

$$F = 2 + n_c - n_p - N_c, \dots\dots\dots (8.1)$$

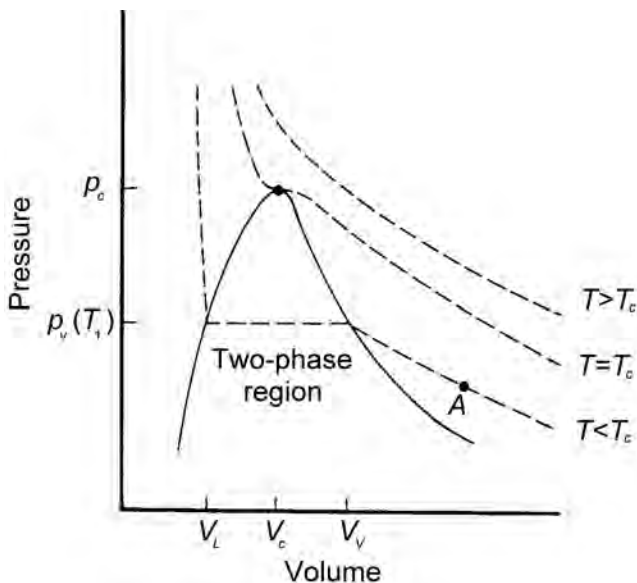


Fig. 8.2—Volumetric behavior of a pure component in the vapor/liquid region.

where  $F$  is the number of degrees of freedom,  $n_c$  is the number of components,  $n_p$  is the number of phases, and  $N_c$  is the number of constraints (e.g., chemical reactions). For a single-component system, the maximum number of phases occurs when there are no constraints ( $N_c = 0$ ) and no degrees of freedom ( $F = 0$ ). Thus, the maximum number of possible phases is three. Therefore, if three phases coexist in equilibrium (possible only at the triple point), the pressure and temperature are fixed. If only two phases are present in a pure component system, then either the temperature or the pressure can be chosen. Once one is chosen, the other is determined. If the two phases are vapor and liquid, for example, choice of the temperature determines the vapor pressure at that temperature. These permitted pressure/temperature values lie on the vapor-pressure curve in Fig. 8.1.

In a binary system, two phases can exist over a range of temperatures and pressures. The number of degrees of freedom is calculated by

$$F = 2 - N_c; \dots\dots\dots (8.2)$$

therefore, both the temperature and pressure can be chosen, although there is no guarantee that two phases will occur at a specific choice of  $T$  and  $p$ .

For multicomponent systems, the phase rule provides little guidance because the number of phases is always far less than the maximum number that can occur. However, for typical applications, the temperature, pressure, and overall composition of a system are known in advance. This allows the number of phases in the system to be predicted by stability analysis, as described in the chapter on phase behavior in this volume. Secs. 8.4 through 8.8 introduce the types of phase diagrams that can be used to portray the thermodynamic phenomena that play important roles in oil and gas production.

**8.4 Binary Phase Diagrams**

Fig. 8.3 is a pressure-composition (p-x-y) phase diagram that shows typical vapor/liquid phase behavior for a binary system at a fixed temperature below the critical temperature of both components. At pressures below the vapor pressure of Component 2,  $p_{v2}$ , any mixture of the two

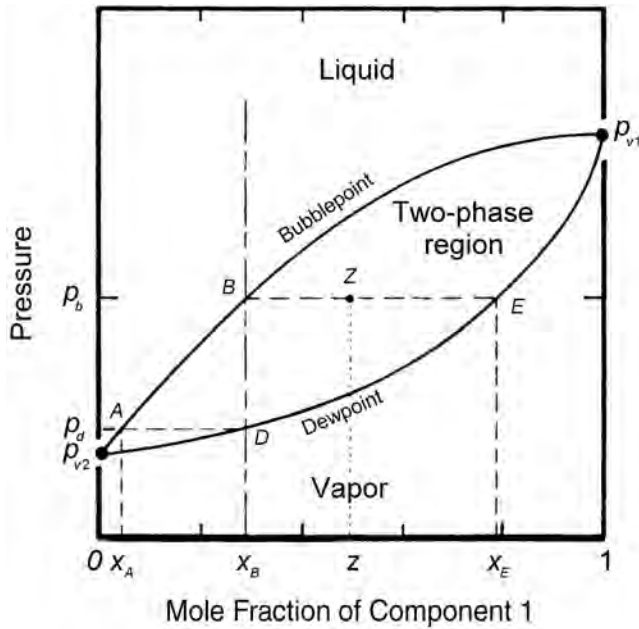


Fig. 8.3—Pressure-composition diagram for a binary mixture at a temperature below the critical temperature of both components.

components forms a single vapor phase. At pressures between  $p_{v1}$  and  $p_{v2}$ , two phases can coexist for some compositions. For instance, at pressure  $p_b$ , two phases will occur if the mole fraction of Component 1 lies between  $x_B$  and  $x_E$ . If the mixture composition is  $x_B$ , it will be all liquid; if the mixture composition is  $x_E$ , it will be all vapor. At constant temperature and pressure, the line connecting a liquid phase and a vapor phase in equilibrium is known as a tie line. In binary phase diagrams such as Fig. 8.3, the tie lines are always horizontal because the two phases are in equilibrium at a fixed pressure. For 1 mole of mixture of overall composition,  $z$ , between  $x_B$  and  $x_E$ , the number of moles of liquid phase is

$$L = \frac{x_E - z}{x_E - x_B} \dots\dots\dots (8.3)$$

Eq. 8.3 is an inverse lever rule because it is equivalent to a statement concerning the distances along a tie line from the overall composition to the liquid and vapor compositions. Thus, the amount of liquid is proportional to the distance from the overall composition to the vapor composition, divided by the length of the tie line.

Phase diagrams such as Fig. 8.3 can be determined experimentally by placing a mixture of fixed overall composition in a high-pressure cell and measuring the pressures at which phases appear and disappear. For example, a mixture of composition  $x_B$  would show the behavior indicated qualitatively in Fig. 8.4. At a pressure less than  $p_d$  (Fig. 8.3), the mixture is a vapor. If the mixture is compressed by injecting mercury into the cell, the first liquid, which has composition  $x_A$ , appears at the dewpoint pressure,  $p_d$ . As the pressure is increased further, the volume of liquid grows as more and more of the vapor phase condenses. The last vapor of composition  $x_E$  disappears at the bubblepoint pressure,  $p_b$ .

If the system temperature is above the critical temperature of one of the components, the phase diagram is similar to that shown in Fig. 8.5. At the higher temperature, the two-phase

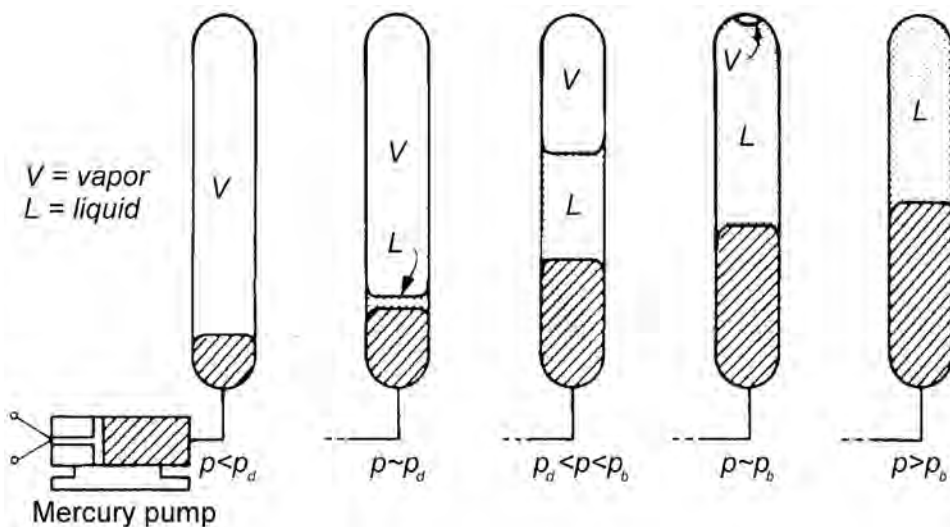


**Fig. 8.4—Volumetric behavior of a binary mixture at constant temperature that shows a bubblepoint pressure.**

region no longer extends to the pure Component 1 side of the diagram. Instead, there is a critical point,  $C$ , at which liquid and vapor phases are identical. The critical point occurs at the maximum pressure of the two-phase region. The volumetric behavior of mixtures containing less Component 1 than the critical mixture,  $x_c$ , is like that shown in Fig. 8.4. Fig. 8.6 shows the volumetric behavior of mixtures containing more Component 1. Compression of the mixture of composition  $x_2$  (in Fig. 8.5) leads to the appearance of liquid phase of composition  $x_1$  when pressure  $p_{d1}$  is reached. The volume of liquid first grows and then declines with increasing pressure. The liquid phase disappears again when pressure  $p_{d2}$  is reached. Such behavior is called “retrograde vaporization” or “retrograde condensation” if the pressure is decreasing.

If the system temperature is exactly equal to the critical temperature of Component 1, the critical point on the binary pressure-composition phase diagram is positioned at a Component 1 mole fraction of 1.0. Fig. 8.7 shows the behavior of the two-phase regions as the temperature rises. As the temperature increases, the critical point moves to lower concentrations of Component 1. As the critical temperature of Component 2 is approached, the two-phase region shrinks, disappearing altogether when the critical temperature is reached.

Fig. 8.8 shows a typical locus of critical temperatures and pressures for a pair of hydrocarbons. The critical locus shown in Fig. 8.8 is the projection of the critical curve in Fig. 8.7 onto the  $p$ - $T$  plane. Thus, each point on the critical locus represents a critical mixture of different composition, although composition information is not shown on this diagram. For temperatures between the critical temperature of Component 1 and Component 2, the critical pressure of the mixtures can be much higher than the critical pressure of either component. Thus, two phases can coexist at pressures much greater than the critical pressure of either component. If the difference in molecular weight of the two components is large, the critical locus may reach very high pressures. Fig. 8.9 gives critical loci for some hydrocarbon pairs.<sup>3</sup>

The binary phase diagrams reviewed here are those most commonly encountered. However, more complex phase diagrams involving liquid/liquid and liquid/liquid/vapor equilibria do occur in hydrocarbon systems at very low temperatures (well outside the range of conditions encountered in reservoirs or surface separators) and in  $\text{CO}_2$ /crude oil systems at temperatures below approximately  $50^\circ\text{C}$ . See Refs. 4 and 5 for reviews of such phase behavior.

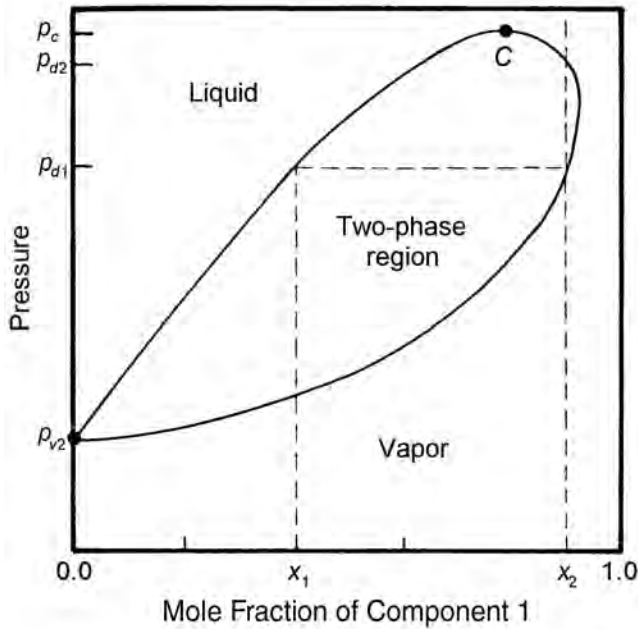


Fig. 8.5—Pressure-composition phase diagram for a binary mixture at a temperature above the critical temperature of Component 1.

### 8.5 Ternary Phase Diagrams

Phase behavior of mixtures containing three components is represented conveniently on a triangular diagram such as those shown in Fig. 8.10. Such diagrams are based on the property of equilateral triangles that the sum of the perpendicular distances from any point to each side of the diagram is a constant equal to the length of any of the sides. Thus, the composition of a point in the interior of the triangle can be calculated as

$$x_1 = \frac{L_1}{L_T}, \quad x_2 = \frac{L_2}{L_T}, \quad x_3 = \frac{L_3}{L_T}, \dots \dots \dots (8.4)$$

where

$$L_T = L_1 + L_2 + L_3, \dots \dots \dots (8.5)$$

Several other useful properties of triangular diagrams are a consequence of this fact. For mixtures along any line parallel to a side of the diagram, the fraction of the component of the corner opposite to that side is constant (Fig. 8.10b). In addition, mixtures lying on any line connecting a corner with the opposite side contain a constant ratio of the components at the ends of the side (Fig. 8.10c). Finally, mixtures of any two compositions, such as A and B in Fig. 8.10d, lie on a straight line connecting the two points on the ternary diagram. Compositions represented on a ternary diagram can be expressed in volume, mass, or mole fractions. For vapor/liquid equilibrium diagrams, mole fractions are most commonly used.

Fig. 8.11 shows the typical features of a ternary phase diagram for a system that forms a liquid and a vapor at fixed temperature and pressure. Mixtures with overall compositions that lie inside the binodal curve will split into liquid and vapor. Tie lines connect compositions of



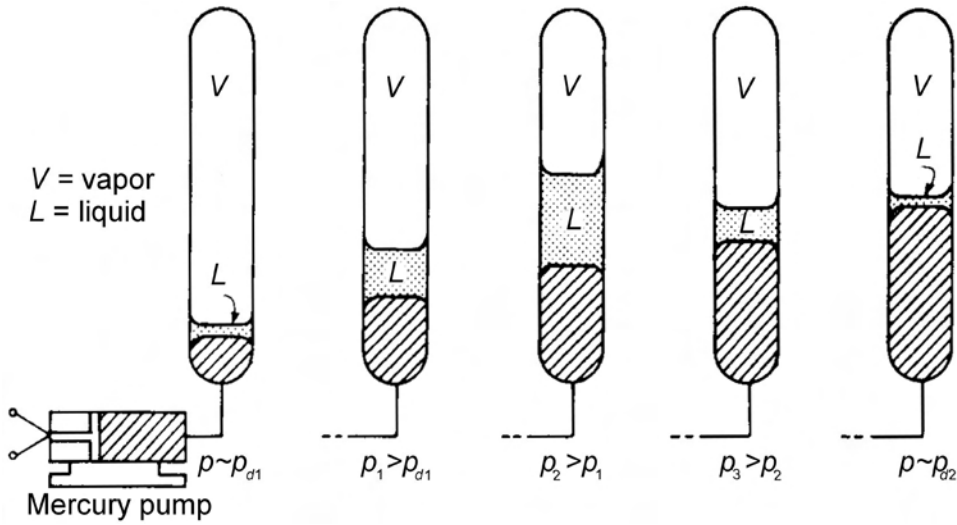


Fig. 8.6—Volumetric behavior of a binary mixture at constant temperature showing retrograde condensation.

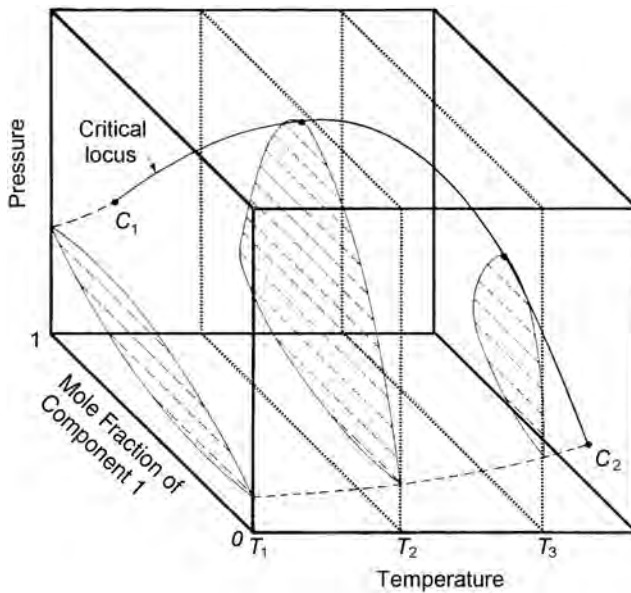


Fig. 8.7—Regions of temperature, pressure, and composition for which two phases occur in a binary liquid/vapor system.

liquid and vapor phases in equilibrium. Any mixture with an overall composition along a tie line gives the same liquid and vapor compositions. Only the amounts of liquid and vapor change as the overall composition changes from the liquid side of the binodal curve to the vapor side. If the mole fractions of Component  $i$  in the liquid, vapor, and overall mixture are  $x_i$ ,  $y_i$ , and  $z_i$ , the fraction of the total moles in the mixture in the liquid phase is given by

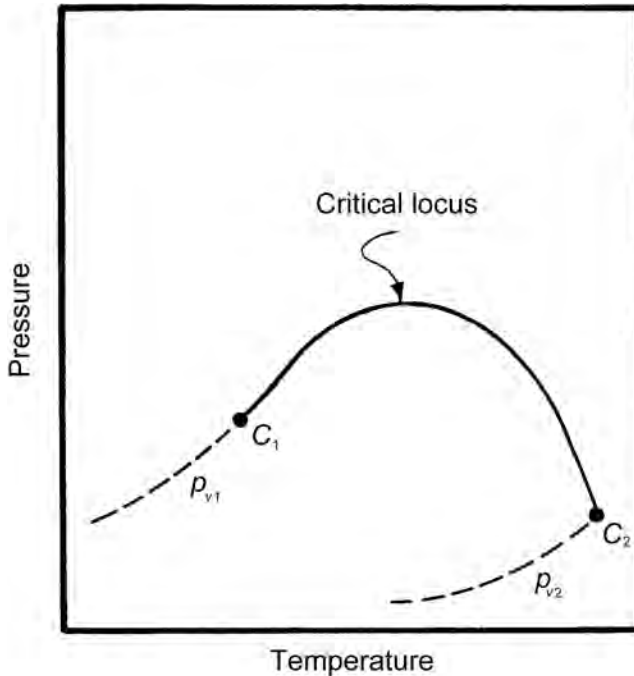


Fig. 8.8—Pressure-temperature diagram: a projection of the vapor-pressure ( $p_{v1}$  and  $p_{v2}$ ) curves and locus of critical points for binary mixtures. Points  $C_1$  and  $C_2$  are the critical points of the pure components.

$$L = \frac{y_i - z_i}{y_i - x_i} \dots \dots \dots (8.6)$$

Eq. 8.6 is another lever rule similar to that described for binary diagrams. The liquid and vapor portions of the binodal curve meet at the plait point, a critical point at which the liquid and vapor phases are identical. Thus, the plait-point mixture has a critical temperature and pressure equal to the conditions for which the diagram is plotted. Depending on the pressure, temperature, and components, a plait point may or may not be present.

Any one ternary diagram is given for fixed temperature and pressure. As either the temperature or pressure is varied, the location of the binodal curve and slopes of the tie lines may change. Fig. 8.12 shows the effect of increasing pressure on ternary phase diagrams for mixtures of  $C_1$ , butane ( $C_4$ ), and decane ( $C_{10}$ ) at 160°F.<sup>6,7</sup> The sides of the ternary diagram represent a binary system; therefore, the ternary diagram includes whatever binary tie lines exist at the temperature and pressure of the diagram. Fig. 8.13 shows the corresponding binary phase diagrams for the  $C_1$ - $C_4$  and  $C_1$ - $C_{10}$  pairs. The  $C_4$ - $C_{10}$  pair is not shown because it forms two phases only below the vapor pressure of  $C_4$ , approximately 120 psia at 160°F (see Fig. 8.9).

As Fig. 8.12 shows, at 1,000 psia the two-phase region is a band that stretches from the  $C_1$ - $C_{10}$  side of the diagram to the tie line on the  $C_1$ - $C_4$  side. If the pressure is increased above 1,000 psia, the liquid composition line shifts to higher methane concentrations; methane is more soluble in both  $C_4$  and  $C_{10}$  at the higher pressure (see Fig. 8.13). The two-phase region detaches from the  $C_1$ - $C_4$  side of the diagram at the critical pressure of the  $C_1$ - $C_4$  pair (approximately 1,800 psia). As the pressure increases above that critical pressure, the plait point moves into the interior of the diagram (Fig. 8.12, lower diagrams). With further increases in pressure,

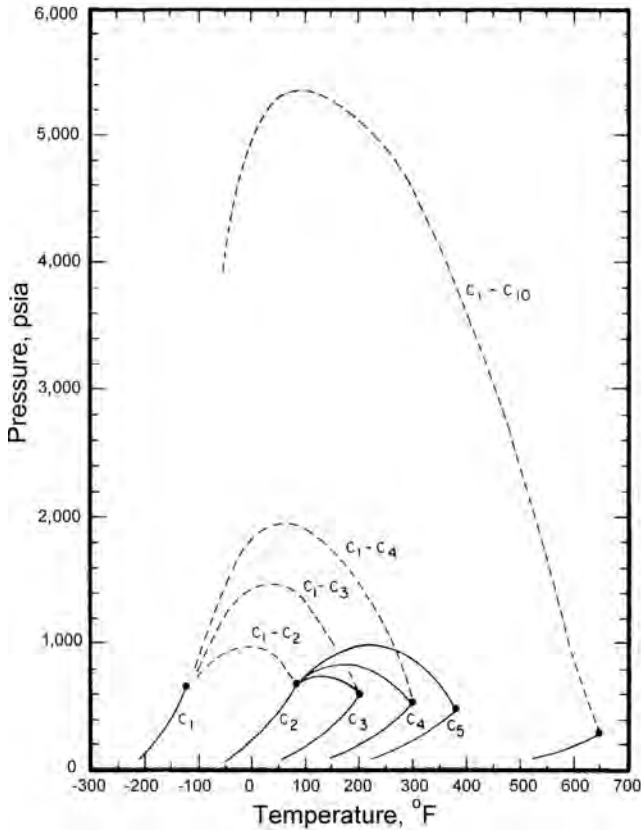


Fig. 8.9—Vapor-pressure curves for light hydrocarbons and critical loci for selected hydrocarbon pairs.

the two-phase region continues to shrink. It would disappear completely from the diagram if the pressure reached the critical pressure of the C<sub>1</sub>–C<sub>10</sub> system at 160°F (nearly 5,200 psia).

According to the phase rule, three phases may coexist at a fixed temperature and pressure for some ternary systems. Fig. 8.14 shows the general structure of such systems. The three-phase region (3Φ) on a ternary diagram is represented as a triangle in Fig. 8.14. Any overall composition lying within the three-phase region splits into the same three phases (I, II and III). Only the amounts of each phase change as the overall composition varies within the three-phase region. Given 1 mole of an overall mixture in the three-phase region, the geometrical relations

$$\beta_I = \frac{a}{a + b}, \quad \beta_{II} = \frac{c}{c + d}, \quad \text{and} \quad \beta_{III} = \frac{e}{e + f} \dots\dots\dots (8.7)$$

$$\text{with } \sum_{i=I}^{III} \beta_i = 1 \dots\dots\dots (8.8)$$

determine the fraction of each phase. The edges of the three-phase region are tie lines for the associated two-phase (2Φ) regions; thus, there is a two-phase region adjacent to each of the sides of the three-phase triangle. Three-phase regions can exist in several phase diagrams applied in the design of EOR processes. Examples are discussed in Secs. 8.7 and 8.8.

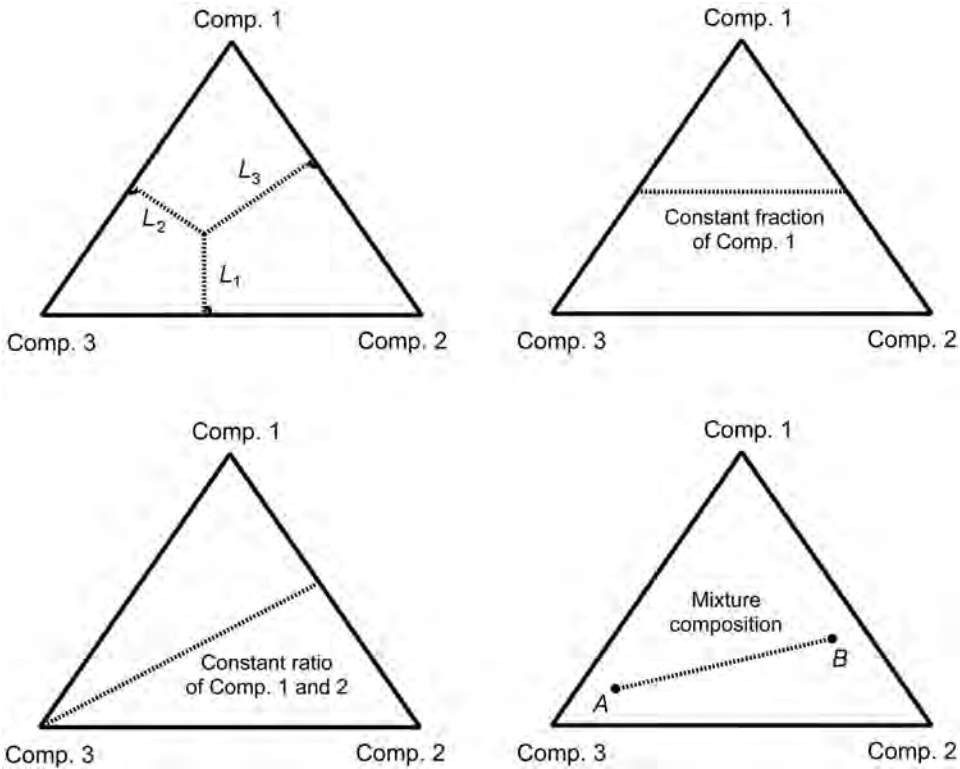


Fig. 8.10—Properties of ternary diagrams.

## 8.6 Quaternary Phase Diagrams

Phase diagrams for systems with four components can be represented conveniently on a tetrahedral diagram like that shown in Fig. 8.15a, which shows a quaternary phase diagram calculated with the Peng-Robinson<sup>8</sup> equation of state for mixtures of methane ( $C_1$ ),  $C_3$ ,  $C_6$ , and hexadecane ( $C_{16}$ ) at 200°F and 2,000 psia. These phase diagrams have a property similar to that of ternary diagrams: the sum of the lengths of perpendicular lines drawn from a composition point in the interior of the diagram to the four faces of the diagram is a constant length. Hence, the fractions of four components can be represented by an extension of Eq. 8.4 to four components.

The faces of the quaternary diagram are ternary phase diagrams. Fig. 8.15b shows the ternary diagram for the ternary methane ( $C_1$ )/hexane ( $C_6$ )/hexadecane ( $C_{16}$ ) system, which is the bottom face of the quaternary diagram. The two-phase region is a band across the diagram, and there is no critical point on that face. Fig. 8.15c shows the  $C_1/C_3/C_{16}$  system, which is the left face of the quaternary diagram. That ternary system does have a critical point. While the ternary diagram for  $C_1/C_3/C_6$  is not shown separately, it is qualitatively similar to the diagram for the  $C_1/C_3/C_{16}$  system in Fig. 8.15c.

The two-phase region in the interior of the quaternary diagram is a 3D region of composition space bounded by the ternary two-phase regions on the faces. Within that region, every mixture composition forms two phases, and each composition point lies on a tie line that connects equilibrium vapor and liquid compositions. A vertical slice through the two-phase region is shown in Fig. 8.15a, along with a few tie lines that lie in the interior of the diagram. The mole fraction of liquid phase is still calculated with Eq. 8.6, which applies to systems with any number of components.

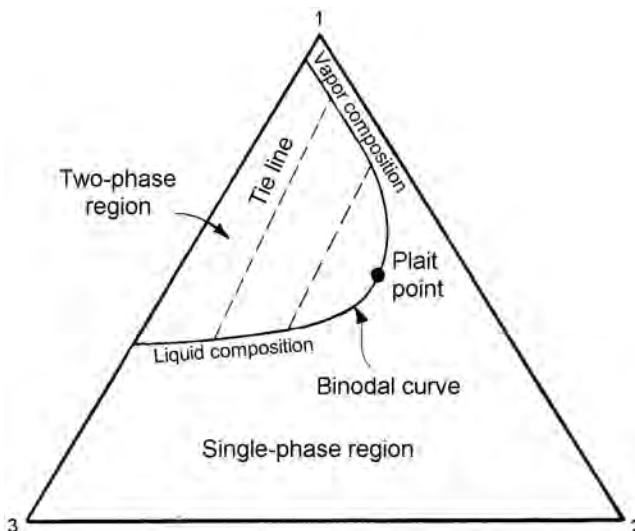


Fig. 8.11—Ternary phase diagram at a constant temperature and pressure for a system that forms a liquid and a vapor.

The boundary of the two-phase region in the interior of the quaternary diagram is divided into two parts: a surface that includes all the vapor-phase compositions and a corresponding surface of liquid-phase compositions. The dividing line between the liquid and vapor surfaces is a critical locus (the dotted line in Fig. 8.15c) that connects the critical point in the  $C_1/C_3/C_{16}$  face (Fig. 8.15a) with the critical point in the  $C_1/C_3/C_6$  face. The critical locus is a set of compositions at which the liquid and vapor phases have identical compositions and properties. The compositions and limiting tie lines on the critical locus play important roles in the description of EOR processes (see Sec. 8.8).

### 8.7 Reservoir Fluid Systems

Real reservoir fluids contain many more than two, three, or four components; therefore, phase-composition data can no longer be represented with two, three or four coordinates. Instead, phase diagrams that give more limited information are used. Fig. 8.16 shows a pressure-temperature phase diagram for a multicomponent mixture; it gives the region of temperatures and pressures at which the mixture forms two phases. The analog of Fig. 8.16 for a binary system can be obtained by taking a slice at constant mole fraction of Component 1 through the diagram in Fig. 8.7. Also given are contours of liquid-volume fractions, which indicate the fraction of total sample volume occupied by the liquid phase; however, Fig. 8.16 does not give any compositional information. In general, the compositions of coexisting liquid and vapor will be different at each temperature and pressure.

At temperatures below the critical temperature (point C), a sample of the mixture described in Fig. 8.16 splits into two phases at the bubblepoint pressure (Fig. 8.4) when the pressure is reduced from a high level. At temperatures above the critical temperature, dewpoints are observed (Fig. 8.6). In this multicomponent system, the critical temperature is no longer the maximum temperature at which two phases can exist. The critical point is the temperature and pressure at which the phase compositions and all phase properties are identical.

The bubblepoint, dewpoint, and single-phase regions shown in Fig. 8.16 are sometimes used to classify reservoirs. At temperatures greater than the cricondentherm, which is the maximum temperature for the formation of two phases, only one phase occurs at any pressure. For

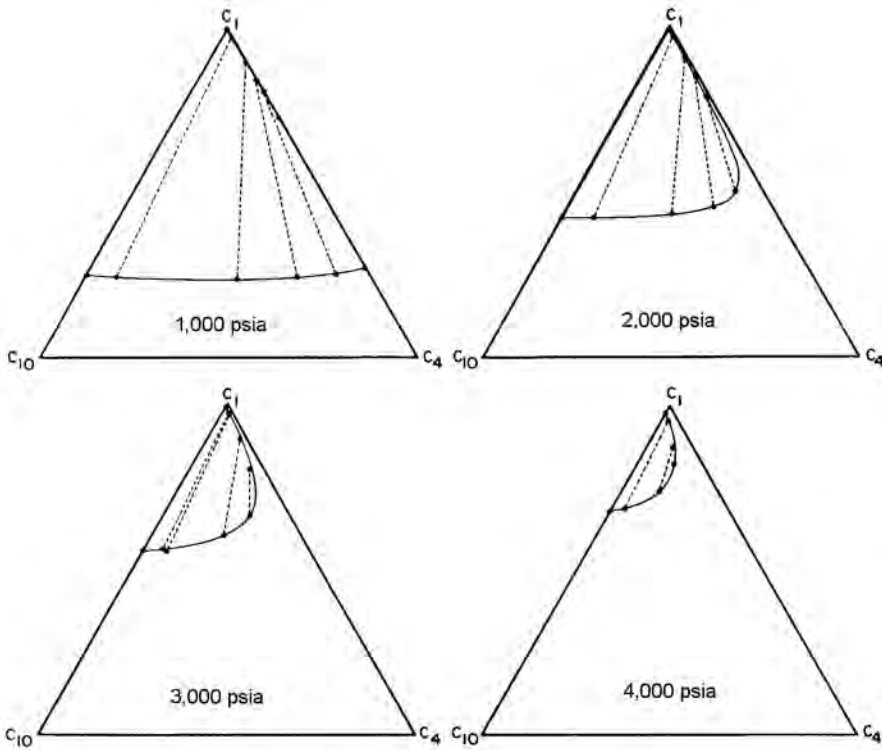


Fig. 8.12—Ternary phase diagram for the methane/butane/decane system at 160°F.

instance, if the hydrocarbon mixture in Fig. 8.16 were to occur in a reservoir at temperature  $T_A$  and pressure  $p_A$  (point A), a decline in pressure at approximately constant temperature caused by removal of fluid from the reservoir would not cause the formation of a second phase.

While the fluid in the reservoir remains a single phase, the produced gas splits into two phases as it cools and expands to surface temperature and pressure at point A'. Thus, some condensate would be collected at the surface even though only one phase is present in the formation. The amount of condensate collected depends on the operating conditions of the separator. The lower the temperature at a given pressure, the larger the volume of condensate collected (Fig. 8.16).

Dewpoint reservoirs are those for which the reservoir temperature lies between the critical temperature and the cricondetherm for the reservoir fluid. Production of fluid from a reservoir starting at point B in Fig. 8.16 causes liquid to appear in the reservoir when the dewpoint pressure is reached. As the pressure declines further, the saturation of liquid increases because of retrograde condensation. Because the saturation of liquid is low, only the vapor phase flows to producing wells. Thus, the overall composition of the fluid remaining in the reservoir changes continuously.

The phase diagram shown in Fig. 8.16 is for the original composition only. The preferential removal of light hydrocarbon components in the vapor phase generates new hydrocarbon mixtures, which have a greater fraction of the heavier hydrocarbons. Differential liberation experiments, in which a sample of the reservoir fluid initially at high pressure is expanded through a sequence of pressures, can be used to investigate the magnitude of the effect of pressure reduction on the vapor composition. At each pressure, a portion of the vapor is removed and analyzed. These experiments simulate what happens when condensate is left behind in the reser-

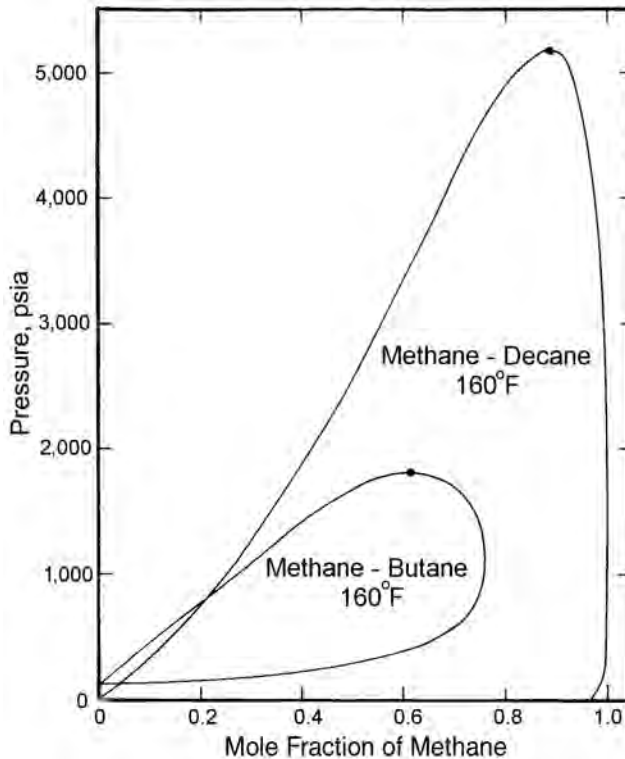


**Fig. 8.13—Pressure-composition phase diagram for methane/butane and methane/decane binary systems at 160°F.**

voir as the pressure declines. See Ref. 9 for more details on pressure/volume/temperature experiments.

As the reservoir fluid becomes heavier, the boundary of the two-phase region in a diagram like Fig. 8.16 shifts to higher temperatures. Thus, the composition change also acts to drive the system toward higher liquid condensation. Such reservoirs are candidates for pressure maintenance by lean gas injection to limit the retrograde loss of condensate or for gas cycling to vaporize and recover some of the liquid hydrocarbons.

Bubblepoint reservoirs are those in which the temperature is less than the critical temperature of the reservoir fluid (point D in Fig. 8.16). These reservoirs are sometimes called undersaturated because the fraction of light components present in the oil is too low for a gas phase to form at that temperature and pressure. Isothermal pressure reduction causes the appearance of a vapor phase at the bubblepoint pressure. Because the compressibility of the liquid phase is much lower than that of a vapor, the pressure in the reservoir declines rapidly during production in the single-phase region. The appearance of the much more compressible vapor phase reduces the rate of pressure decline. The volume of vapor present in the reservoir grows rapidly with reduction of reservoir pressure below the bubblepoint.

Because the vapor viscosity is much lower than the liquid viscosity and the gas relative permeability goes up markedly with increasing gas saturation, the vapor phase flows more easily. Hence, the produced gas/oil ratio climbs rapidly. Again, pressure maintenance by water-drive, water injection, or gas injection can improve oil recovery substantially over the 10 to 20% recovery typical of pressure depletion in these solution-gas-drive reservoirs. As in dew-

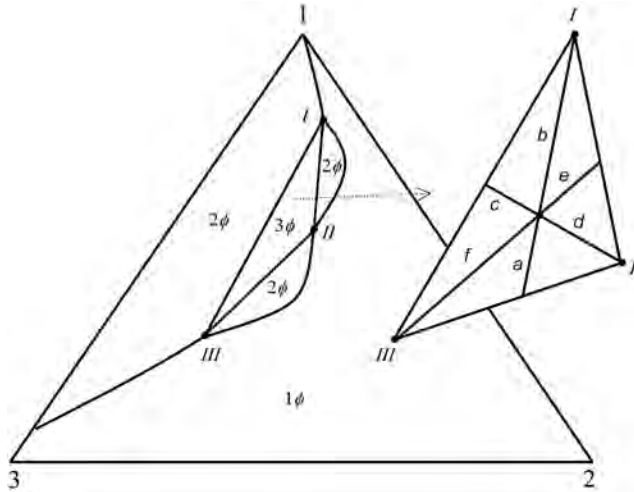


Fig. 8.14—Generic ternary phase diagram with three-phase region.

point reservoirs, the composition of the reservoir fluid changes continuously once the two-phase region is reached.

There is, of course, no reason why initial reservoir temperatures and pressures cannot lie within the two-phase region. Oil reservoirs with gas caps and gas reservoirs with some liquids present are common. There also can be considerable variation in the initial composition of the reservoir fluid. The discussion of single-phase, dewpoint, and bubblepoint reservoirs is based on a phase diagram for one fluid composition. Even for one fluid, all the types of behavior occur over a range of temperatures. In actual reservoir settings, the composition of the reservoir fluid correlates with depth and temperature. Deeper reservoirs usually contain lighter oils.<sup>10</sup>

Fig. 8.17 shows the relationships between oil gravity and depth for two basins. The higher temperatures of deeper reservoirs alter the original hydrocarbon mixtures to produce lighter hydrocarbons over geologic time.<sup>10</sup> Low oil gravity, low temperature, and relatively small amounts of dissolved gas all combine to produce bubblepoint reservoirs. High oil gravity, high temperatures, and a high concentration of light components produce dewpoint or condensate systems.

## 8.8 Phase Diagrams for EOR Processes

Phase behavior plays an important role in a variety of EOR processes. Such processes are designed to overcome, in one way or another, the capillary forces that act to trap oil during waterflooding. Interpretation of phase diagrams is particularly important in the design of surfactant/polymer processes and gas-injection processes.

**8.8.1 Surfactant/Polymer Floods.** In surfactant/polymer displacement processes, the effects of capillary forces are reduced by injection of surfactant solutions that contain molecules with oil- and water-soluble portions. Such molecules migrate to the oil/water interface and reduce the interfacial tension, thereby reducing the magnitude of the capillary forces that resist movement of trapped oil.

Fig. 8.18<sup>11</sup> shows phase diagrams typical of those used to describe the behavior of surfactant systems. In these ternary diagrams, the components shown are no longer true thermodynamic components because they are mixtures. A crude oil contains hundreds of components, and the brine and surfactant pseudocomponents also may be complex mixtures. The simplified rep-



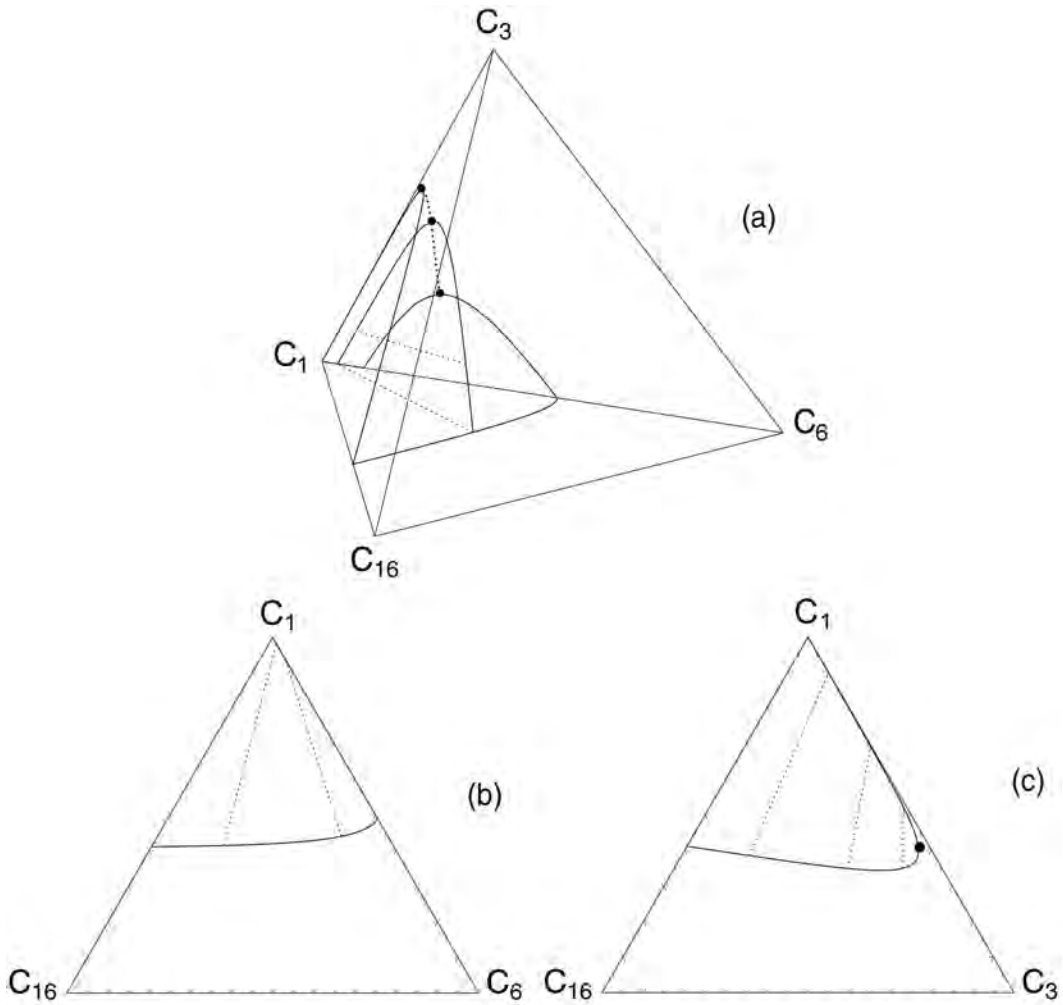


Fig. 8.15—Properties of the quaternary phase diagram.

resentation, however, has obvious advantages for describing phase behavior, and it is reasonably accurate as long as each pseudocomponent has approximately the same composition in each phase. In Fig. 8.18a, for instance, the “oil” pseudocomponent can appear in an oil-rich phase or in a phase containing mostly surfactant and brine. If the oil solubilized into the surfactant/brine phase is nearly the same mixture of hydrocarbons as the original “oil,” then the representation in terms of pseudocomponents is reasonable. The compositions shown in Fig. 8.18 are in volume fractions. An inverse lever rule similar to Eqs. 8.3 and 8.6 gives the relationship between the volumes of the two phases for a given overall composition, as Fig. 8.18 illustrates.

Fig. 8.18a is a phase diagram for the liquid/liquid equilibrium behavior typical of mixtures of brines of low salinity with oil. If there is no surfactant present, the oil and brine are immiscible; mixture compositions on the base of the diagram split into essentially “pure” brine in equilibrium with “pure” oil. The addition of surfactant causes some oil to be solubilized into a microemulsion rich in brine. That phase is in equilibrium with a phase containing nearly pure oil. Thus, in the low-salinity brine, the surfactant partitions into the brine phase, solubilizing

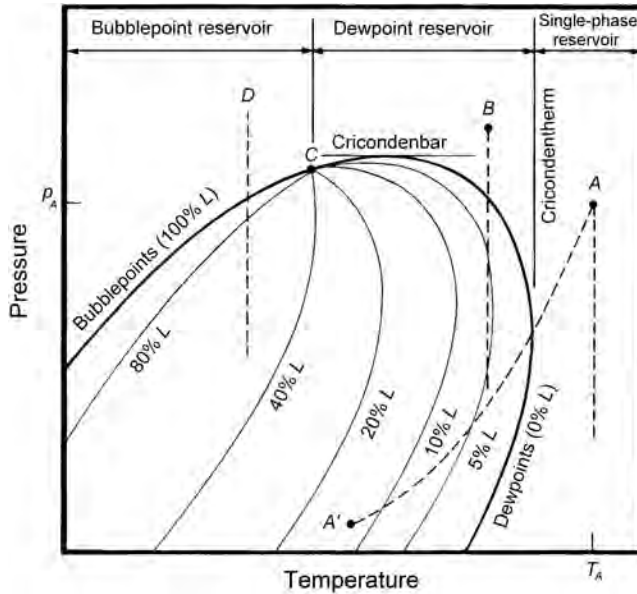


Fig. 8.16—Pressure-temperature phase diagram (phase envelope) for a mixture of fixed composition.

some oil. The plait point in Fig. 8.18a lies close to the oil corner of the diagram. Because only two phases occur and the tie lines all have negative slope, such phase is often called Type II(-).

Phase diagrams for high-salinity brines are often similar to Fig. 8.18b. In the high-salinity systems, the surfactant partitions into the oil phase and solubilizes water into an oil-external microemulsion. In this case, the plait point is close to the brine apex on the ternary diagram. For intermediate salinities, the phase behavior can be more complex, as Fig. 8.18c shows. A triangular three-phase region occurs (see Fig. 8.14) for which the phases are a brine-rich phase, an oil-rich phase, and a microemulsion phase. There is a two-phase region adjacent to each of the sides of the three-phase triangle. In Fig. 8.18c, the two-phase region at low surfactant concentrations is too small to show on the diagram. It must be present, however, because oil and brine form only two phases in the absence of surfactant.

**8.8.2 Gas-Injection Processes.** Miscible displacement processes are designed to eliminate interfaces between the oil and the displacing phase, thereby removing the effects of capillary forces between the injected fluid and the oil. Unfortunately, fluids that are strictly miscible with oil are too expensive for general use. Instead, fluids such as  $C_1$ ,  $C_1$  enriched with intermediate hydrocarbons,  $CO_2$ , or nitrogen are injected, and the required miscible-displacing fluid is generated by mixing the injected fluid with oil in the reservoir. Phase behavior of gas/oil systems is often summarized in pressure-composition ( $p$ - $x$ ) diagrams.

Fig. 8.19 is an example of a  $p$ - $x$  diagram for mixtures of  $CO_2$  (containing a small amount of  $C_1$  contamination) with crude oil from the Rangely field.<sup>12</sup> The behavior of binary mixtures of  $CO_2$  with a particular oil is reported for a fixed temperature; therefore, the oil is represented as a single pseudocomponent. The bubblepoint and dewpoint pressures, the regions of pressure and composition for which two or more phases exist, and information about the volume fractions of the phases are indicated. However, the diagrams provide no information about the compositions of the phases in equilibrium.

Fig. 8.20 illustrates the reason for the absence of composition data and gives data reported by Metcalfe and Yarborough<sup>13</sup> for a ternary system of  $CO_2$ ,  $C_4$ , and  $C_{10}$ . Binary-phase data for

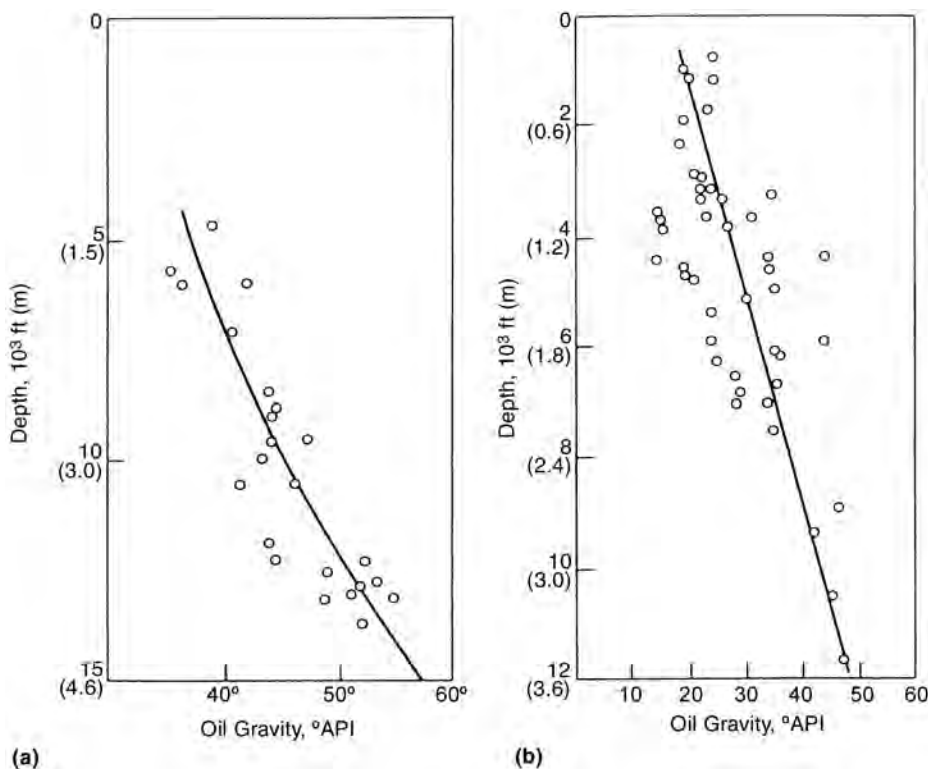


**Fig. 8.17—Increase in °API gravity with depth: (a) Ordovician Ellenberger reservoirs in Delaware Val Verde basin and (b) Pennsylvanian Tensleep reservoirs in Wyoming.**

the  $\text{CO}_2\text{-C}_4$ <sup>14</sup> and  $\text{CO}_2\text{-C}_{10}$ <sup>15</sup> systems also are included. Fig. 8.20 shows a triangular solid within which all possible compositions (mole fractions) of  $\text{CO}_2\text{-C}_4\text{-C}_{10}$  mixtures for pressures between 400 and 2,000 psia are contained. The two-phase region is bounded by a surface that connects the binary-phase envelope for the  $\text{CO}_2\text{-C}_{10}$  binary pair to that on the  $\text{CO}_2\text{-C}_4$  side of the diagram. That surface is divided into two parts—liquid compositions and vapor compositions.

Tie lines connect the compositions of liquid and vapor phases in equilibrium at a fixed pressure. Thus, the ternary phase diagram for  $\text{CO}_2\text{-C}_4\text{-C}_{10}$  mixtures at any pressure is just a constant pressure (horizontal) slice through the triangular prism. Several such slices at different pressures are shown in Fig. 8.20. At pressures below the critical pressure of  $\text{CO}_2\text{-C}_4$  mixtures (1,184 psia), both  $\text{CO}_2\text{-C}_{10}$  and  $\text{CO}_2\text{-C}_4$  mixtures form two phases for some range of  $\text{CO}_2$  concentrations. At 400 and 800 psia, the two-phase region is a band across the diagram. Above the critical pressure of  $\text{CO}_2\text{-C}_4$  mixtures,  $\text{CO}_2$  is miscible with  $\text{C}_4$  and ternary slices at higher pressures show a continuous binodal curve on which the locus of liquid compositions meets that of vapor compositions at a plait point. The locus of plait points connects the critical points of the two binary pairs.

To see the effect of representing the phase behavior of a ternary system on a pseudobinary diagram, consider a  $p\text{-}x$  diagram for “oil” composed of 70 mol%  $\text{C}_{10}$  and 30 mol%  $\text{C}_4$ . At any fixed pressure, the mixtures of  $\text{CO}_2$  and oil, which would be investigated in an experiment to determine a  $p\text{-}x$  diagram, lie on a straight line (the dilution line), which connects the original oil composition with the  $\text{CO}_2$  apex. Thus, a  $p\text{-}x$  diagram for this system is a vertical slice through the triangular prism shown in Fig. 8.20. The saturation pressures on a  $p\text{-}x$  diagram are those at which the dilution plane intersects the surface that bounds the two-phase region. Bub-

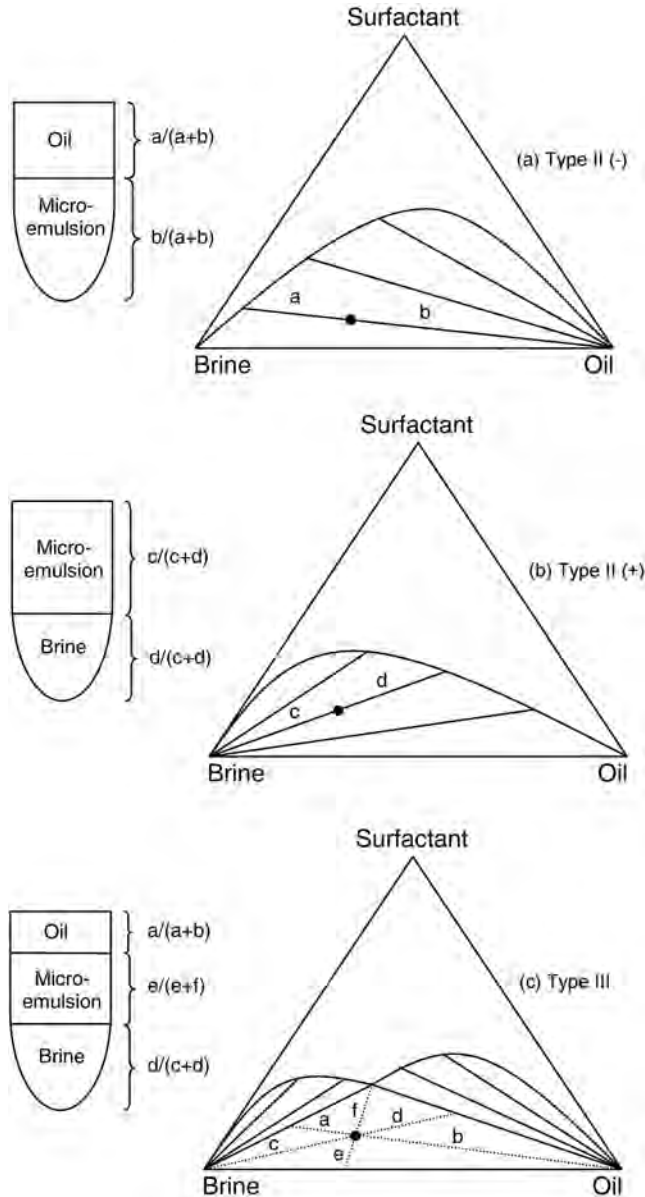


Fig. 8.18—Ternary representation of phase diagrams.<sup>11</sup>

blebpoint pressures occur where the dilution plane intersects the liquid composition side of the two-phase surface, while dewpoint pressures occur at the intersection with vapor compositions. Comparison of the phase envelope on the resulting  $p$ - $x$  diagram with binary phase diagrams yields the following observations.

- Tie lines do not, in general, lie in the dilution plane; they pierce that plane. This means that the composition of vapor in equilibrium with a bubblepoint mixture on the  $p$ - $x$  diagram is not the same as that of the dewpoint mixture at the same pressure.

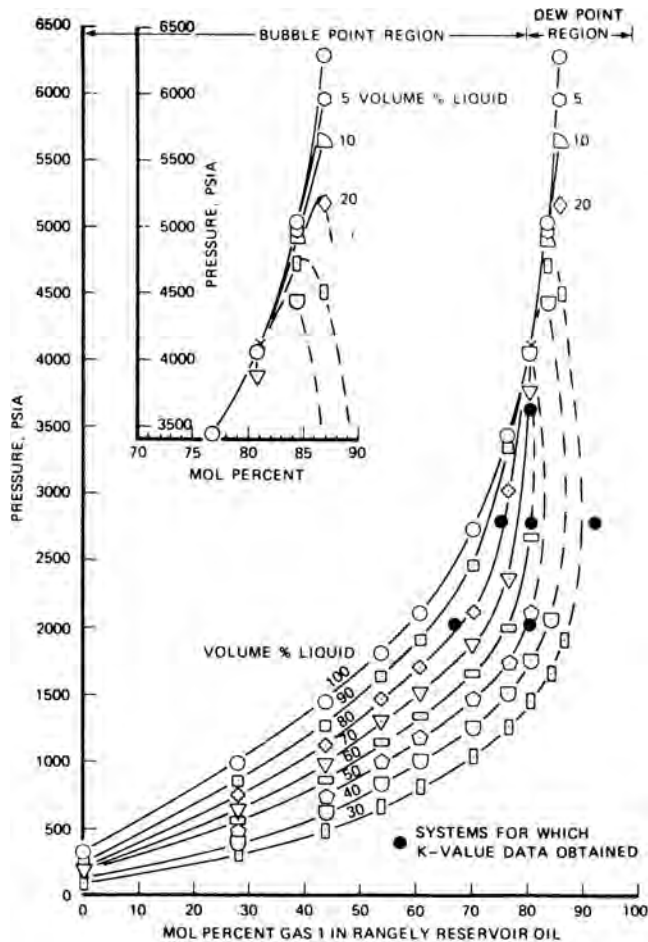


Fig. 8.19—Pressure-composition diagram. Gas 1 system for Rangely oil: 95% CO<sub>2</sub> and 5% CH<sub>4</sub> gas system at 160°F.

• The critical point on the  $p$ - $x$  diagram occurs where the locus of critical points pierces the dilution plane. It is not, in general, at the maximum saturation pressure on the  $p$ - $x$  diagram. The maximum pressure occurs where the binodal curve in a horizontal slice is tangent to the dilution plane. The critical point on the  $p$ - $x$  diagram can lie on either side of the maximum pressure, depending on the position of locus of plait points on the two-phase surface.

It is apparent from Fig. 8.20 that the composition of the original oil has a strong influence on the shape of the saturation-pressure curve and on the location of the critical point on the  $p$ - $x$  diagram. If the oil had been richer in C<sub>4</sub>, the critical pressure and maximum pressure both would have been lower. Thus, it should be anticipated that the appearance of  $p$ - $x$  diagrams for CO<sub>2</sub>/crude oil systems should depend on the composition of the oil.

Figs. 8.19 and 8.21 illustrate the complexity of phase behavior observed for CO<sub>2</sub>/crude oil systems. Fig. 8.19 gives the behavior of mixtures of CO<sub>2</sub> (with approximately 5% C<sub>1</sub> as a contaminant) with Rangely crude oil at 160°F. The oil has a bubblepoint pressure of approximately 350 psia. Mixtures containing up to approximately 80 mol% CO<sub>2</sub> (+ C<sub>1</sub>) show bubblepoints, while those containing more CO<sub>2</sub> show dewpoints. At the relatively high temperature of the

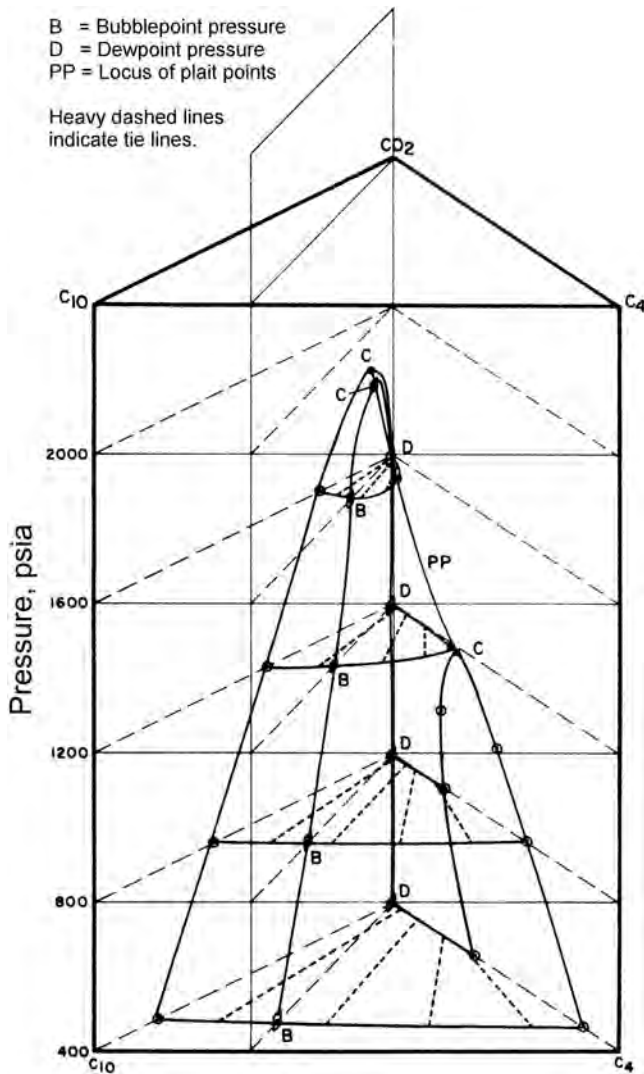


Fig. 8.20—Phase behavior of  $\text{CO}_2$ - $\text{C}_4$ - $\text{C}_{10}$  mixtures at  $160^\circ\text{F}$ .

Rangely field, only two phases, a liquid and a vapor, form. At lower temperatures, more complex phase behavior can occur.

Fig. 8.21 shows the behavior of mixtures of an oil containing no dissolved gas from the Wasson field<sup>4</sup> with  $\text{CO}_2$ . At  $90^\circ\text{F}$  and  $105^\circ\text{F}$ , the mixtures form a liquid and a vapor at low pressures and two liquid phases at high pressures and high  $\text{CO}_2$  concentrations. They form three phases, two liquids and a vapor, for a small range of pressures at high  $\text{CO}_2$  concentrations. The liquid/liquid and liquid/liquid/vapor behavior disappears if the temperature is high enough. At  $120^\circ\text{F}$  (Fig. 8.21c), the three-phase region disappears. For the systems studied to date,  $120^\circ\text{F}$  appears to be a reasonable estimate of the maximum temperature for liquid/liquid/vapor separations. See Refs. 4 and 5 for detailed discussions of such phase behavior. Well-characterized ternary systems that display similar behavior are described by Larsen *et al.*,<sup>16</sup> who report ternary diagrams like Fig. 8.14 for  $\text{CO}_2$ /hydrocarbon systems.

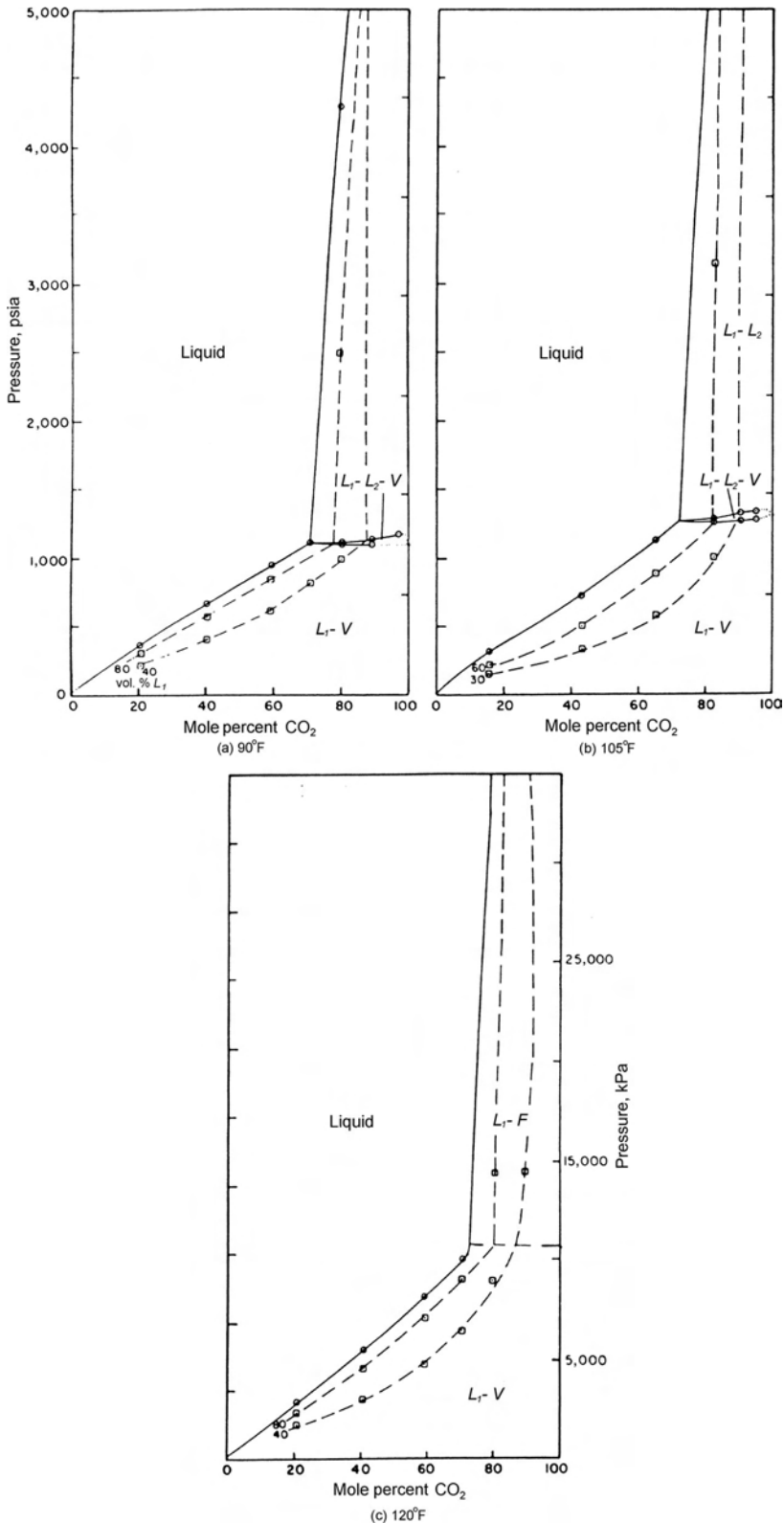


Fig. 8.21— $p-x$  diagrams for mixtures of  $\text{CO}_2$  with Wasson oil, where  $L_1$  is liquid phase (oil rich),  $L_2$  is liquid phase 2 ( $\text{CO}_2$ -rich phase), and  $V$  is the vapor phase. Dashed lines indicate constant volume fraction of  $L_1$  phase.

**8.8.3 Multicontact Miscibility in Gas-Injection Processes.** Phase diagrams of the types described here are often used to represent miscible gas-injection processes. The simplest form of miscibility is first contact miscibility. It occurs when a given gas is injected into oil at a temperature and pressure at which any mixture of the oil and gas result in a single-phase fluid. For an oil/gas pair to be first contact miscible, the dilution line, which connects the oil composition and the gas composition, cannot intersect the two-phase region. The lowest pressure at which first contact miscibility can occur is the pressure at which the dilution line is tangent to the two-phase boundary; therefore, this pressure is referred to as the first contact miscibility pressure. However, multicontact miscibility can develop at pressures lower, often substantially lower, than the first contact miscibility pressure.

For ternary systems, two mechanisms can lead to the development of a multicontact miscible displacement: vaporizing drives and condensing drives. Fig. 8.22a demonstrates the features of a vaporizing drive for the displacement of a  $C_6$ – $C_{16}$  mixture ( $O_1$ ) by pure  $C_1$ . The displacement composition path traverses the two-phase region along two key tie lines in compositional space: the tie line that extends through the injected gas composition (the injection tie line) and the tie line that extends through the initial oil composition (the initial tie line).<sup>17,18</sup> As the pressure is increased, the two-phase region shrinks and, at some point, one of the key tie lines become a critical tie line (a tie line that is tangent to the two-phase region at a critical point).

Fig. 8.22b demonstrates the features of a condensing gas drive for a  $C_1$ – $C_3$  mixture displacing oil consisting of  $C_1$  and  $C_{16}$ . In this case, the injection tie line is closer to the critical point, and as the pressure is increased, it is the first to become a critical tie line. For both cases, the pressure at which one of the key tie lines become a critical tie line is known as the minimum miscibility pressure (MMP).<sup>18</sup> Thus, in three-component systems, a displacement can be multicontact miscible only if one of the two key tie lines is a critical tie line. If it is the initial oil tie line that is critical, the displacement is a vaporizing drive, and if the injection gas tie line is the critical tie line, the displacement is a condensing drive.

For four-component systems, the displacement path has been shown to include a third key tie line referred to as the crossover tie line.<sup>19</sup> Fig. 8.22c shows the crossover tie line. Just as in the ternary displacements, miscibility develops when any one of the key tie lines reduces to a critical point. If the pressure in Fig. 8.22c is increased, the crossover tie line will become a critical tie line before either the initial or injection tie lines. Hence, the existence of the crossover tie line introduces a third mechanism for the development of multicontact miscibility. This mechanism is known as the combined condensing/vaporizing drive.<sup>20,21</sup> Fig. 8.22c shows that the displacement composition path for a four-component system in which a mixture of  $C_1$  and  $C_3$  displaces an oil containing  $C_1$ ,  $C_6$ , and  $C_{16}$  includes a vaporizing segment connected to a condensing segment by the crossover tie line.

With each additional component added to the displacement process, another crossover tie line is added to the displacement composition path. The MMP for such multicomponent gas-injection processes can be determined by locating the key tie lines and calculating the length of these tie lines as the pressure is increased. The MMP is the pressure at which one of the key tie lines has zero length. Fig. 8.23<sup>22</sup> reports the result of such a calculation for a 15-component fluid description. In this system, the injection gas contains 11 components and is rich in  $C_1$  but includes  $N_2$ ,  $CO_2$ , and hydrocarbons up to  $C_7$ . The eighth crossover tie line becomes a critical tie line at the MMP of 5,350 psia. Displacements that display the combined condensing/vaporizing mechanism are common in oilfield fluid systems.



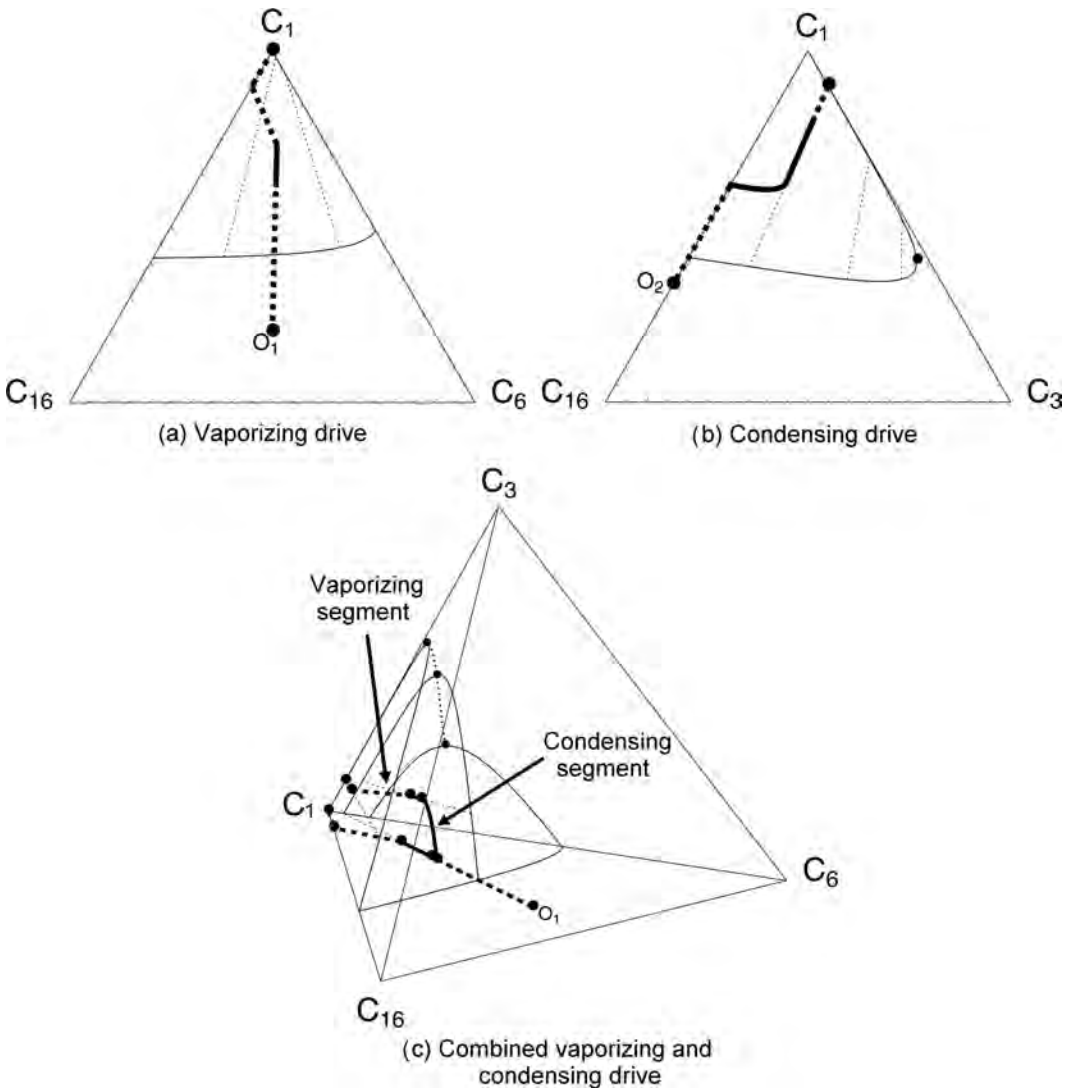


Fig. 8.22—Condensing and vaporizing segments in gas-injection processes.

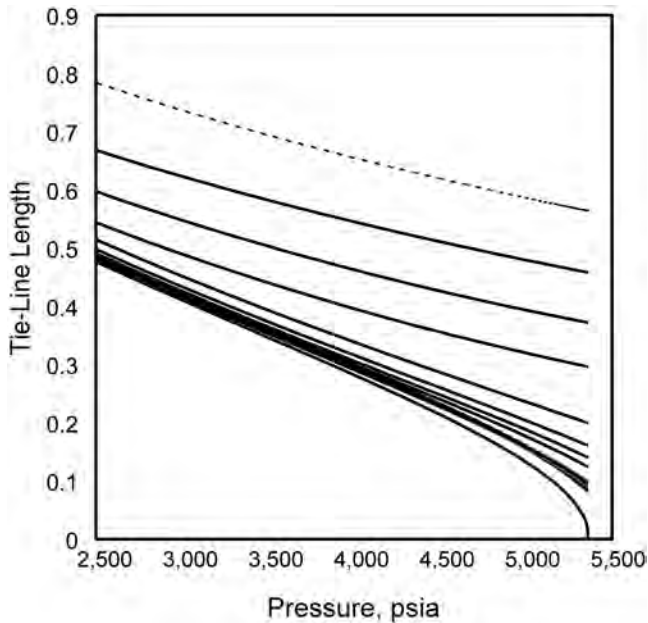


Fig. 8.23—Tie-line length vs. pressure for a multicomponent gas-injection process.

### Nomenclature

- $a$  = length of line  $a$  in Fig. 8.14
- $b$  = length of line  $b$  in Fig. 8.14
- $c$  = length of line  $c$  in Fig. 8.14
- $C$  = critical point
- $d$  = length of line  $d$  in Fig. 8.14
- $e$  = length of line  $e$  in Fig. 8.14
- $f$  = length of line  $f$  in Fig. 8.14
- $F$  = number of degrees of freedom
- $i$  = component  $i$
- $L$  = liquid phase
- $L_k$  = perpendicular distance from a given point to side in an equilateral triangle  
( $k=1, 2, 3$ )
- $L_T$  = side length in equilateral triangle
- $n_c$  = number of components
- $n_p$  = number of phases
- $N_c$  = number of constraints
- $p$  = pressure, m/Lt<sup>2</sup>, psi
- $p_A$  = pressure at point A, m/Lt<sup>2</sup>, psi
- $p_b$  = bubblepoint pressure, m/Lt<sup>2</sup>, psi
- $p_c$  = critical pressure, m/Lt<sup>2</sup>, psi
- $p_d$  = dewpoint pressure of mixture  $x_B$ , m/Lt<sup>2</sup>, psi
- $p_{d1}$  = lower dewpoint pressure mixture  $x^2$ , m/Lt<sup>2</sup>, psi
- $p_{d2}$  = upper dewpoint pressure mixture  $x^2$ , m/Lt<sup>2</sup>, psi
- $p_t$  = total pressure, m/Lt<sup>2</sup>, psi
- $p_v$  = vapor pressure, m/Lt<sup>2</sup>, psi

- $p_{v1}$  = saturation pressure of pure component 1, m/Lt<sup>2</sup>, psi  
 $p_{v2}$  = saturation pressure of pure component 2, m/Lt<sup>2</sup>, psi  
 $T$  = temperature, T, K  
 $T_1$  = constant temperature below  $T_c$ , T, K  
 $T_2$  = constant temperature above  $T_c$ , T, K  
 $T_A$  = temperature at point A, T, K  
 $T_c$  = critical temperature, T, K  
 $V$  = vapor  
 $V_c$  = critical volume, L<sup>3</sup>, ft<sup>3</sup>  
 $V_L$  = saturated liquid volume, L<sup>3</sup>, ft<sup>3</sup>  
 $V_V$  = saturated vapor volume, L<sup>3</sup>, ft<sup>3</sup>  
 $x_1$  = mole fraction of component 1  
 $x_2$  = mole fraction of component 2  
 $x_3$  = mole fraction of component 3  
 $x_A$  = saturated liquid composition at  $p_d$   
 $x_B$  = saturated vapor composition at  $p_d$   
 $x_C$  = critical mixture  
 $x_E$  = vapor phase composition in equilibrium with  $x_B$  from overall mixture  $z$   
 $x_i$  = mole fraction of component  $i$  in the liquid phase  
 $y_i$  = mole fraction of component  $i$  in the vapor phase  
 $z$  = overall composition in mole fractions  
 $z_i$  = mole fraction of component  $i$  in the overall composition  
 $\beta_I$  = mole fraction of phase I  
 $\beta_{II}$  = mole fraction of phase II  
 $\beta_{III}$  = mole fraction of phase III  
 $\beta_i$  = mole fraction of phase  $i$   
 $\beta_j$  = mole fraction of phase  $j$   
 $2\Phi$  = two-phase region  
 $3\Phi$  = three-phase region

---

## References

1. Lake, L.W.: *Enhanced Oil Recovery*, Prentice Hall Publishers, New York City (1989).
2. Whitson, H.C. and Brulé, R.M.: *Phase Behavior*, Monograph Series, SPE, Richardson, Texas (2000) **20**.
3. *Engineering Data Book*, ninth edition, Gas Processors Suppliers Assn., Tulsa, Oklahoma (1972).
4. Stalkup, F.I. Jr.: *Miscible Displacement*, Monograph Series, SPE, Richardson, Texas (1983) **8**.
5. Orr, F.M. Jr. and Jensen, C.M.: "Interpretation of Pressure-Composition Phase Diagrams for CO<sub>2</sub>-Crude Oil Systems," *SPEJ* (October 1984) 485.
6. Reamer, H.H., Fiskin, J.M., and Sage, B.H.: "Phase Equilibria in Hydrocarbon Systems," *Industrial and Engineering Chemistry* (December 1949) **41**, 2871.
7. Sage, B.H. and Lacey, W.N.: *Thermodynamic Properties of the Lighter Paraffin Hydrocarbons and Nitrogen*, Monograph on API Research Project 37, API, New York City (1950).
8. Peng, D.Y. and Robinson, D.B.: "A New Two-Constant Equation of State," *Industrial and Engineering Chemical Fundamentals* (1976) **15**, 59.
9. Pedersen, K.S., Fredenslund, A.A., and Thomassen P.: "Properties of Oils and Natural Gases," *Contributions in Petroleum Geology and Engineering*, Gulf Publishing Co., Houston (1989) 5.
10. Hunt, J.M.: *Petroleum Geochemistry and Geology*, W.H. Freeman and Co., San Francisco (1979).

11. Nelson, R.C. and Pope, G.A.: "Phase Relationships in Chemical Flooding," *SPEJ* (October 1978) 325.
12. Graue, D.J. and Zana, E.T.: "Study of a Possible CO<sub>2</sub> Flood in the Rangely Field, Colorado," *JPT* (July 1981) 1312.
13. Metcalfe, R.S. and Yarborough, L.: "The Effect of Phase Equilibria on the CO<sub>2</sub> Displacement Mechanism," *SPEJ* (August 1979) 242; *Trans., AIME*, **267**.
14. Olds, R.H. *et al.*: "Phase Equilibria in Hydrocarbon Systems," *Industrial and Engineering Chemistry* (March 1949) **41**, 475.
15. Reamer, H.H. and Sage, B.H.: "Phase Equilibria in Hydrocarbon Systems. Volumetric and Phase Behavior of the n-Decane-CO<sub>2</sub> System," *J. Chemical Engineering Data* (1963) **8**, No. 4, 508.
16. Larsen L.L. *et al.*: "Temperature Dependency of L<sub>1</sub>/L<sub>2</sub>/V Phase Behavior in CO<sub>2</sub>/Hydrocarbon Systems," *SPEE* (February 1989) 105.
17. Dumore, J.M., Hagoort, J., and Risseuw, A.S.: "An Analytical Method for One-Dimensional, Three-Component Condensing and Vaporizing Gas Drives," *SPEJ* (April 1984) 169.
18. Johns, R.T., and Orr, F.M. Jr.: "Miscible Gas Displacement of Multicomponent Oils," *SPEJ* (March 1996) 39.
19. Monroe, W.W. *et al.*: "Composition Paths in Four-Component Systems: Effects of Dissolved Methane in 1D CO<sub>2</sub> Flooding Performance," *SPEE* (August 1990) 423.
20. Zick, A.A.: "A Combined Condensing/Vaporizing Mechanism in the Displacement of Oil by Enriched Gases," paper SPE 15493 presented at the 1986 Annual Technical Conference and Exhibition, New Orleans, 5–8 October.
21. Johns, R.T., Dindoruk, B., and Orr, F.M. Jr.: "Analytical Theory of Combined Condensing/Vaporizing Gas Drives," *SPE Advanced Technology Series* (July 1993) 7.
22. Jessen, K., Michelsen, M.L., and Stenby, E.H.: "Global Approach for Calculation of Minimum Miscibility Pressures," *Fluid Phase Equilibria* (1998) **153**, 251.

### SI Metric Conversion Factors

°API	141.5/(131.5+°API)		= g/cm <sup>3</sup>
ft ×	3.048*	E – 01	= m
°F	(°F – 32)/1.8		= °C
psi ×	6.894 757	E + 00	= kPa

\*Conversion factor is exact.

## Chapter 9

# Asphaltenes and Waxes

Long X. Nghiem and Bruce F. Kohse, Computer Modelling Group

### 9.1 Introduction

Deposition of the high-molecular-weight components of petroleum fluids as solid precipitates in surface facilities, pipelines, downhole tubulars, and within the reservoir are well-recognized production problems. Depending on the reservoir fluid and the type of recovery process, the deposited solid may consist of asphaltenes, waxes, or a mixture of these materials. The deposits also can contain resins, crude oil, fines, scales, and water.<sup>1</sup>

This chapter discusses the experimental measurement and thermodynamic modeling of the phase behavior of solid waxes and asphaltenes in equilibrium with fluid hydrocarbon phases. Models for solid deposition in the reservoir and in pipelines also are presented. Although some of the laboratory techniques for determining solid precipitation are applicable to both waxes and asphaltenes, the characteristic behaviors of these materials can be very different; therefore, wax and asphaltene topics are treated separately.

**Sec. 9.1** presents some commonly observed behaviors of asphaltenic and waxy crudes. **Sec. 9.2** gives the chemical characteristics of asphaltenes and waxes. **Secs. 9.3** through **9.6** discuss asphaltene measurement, precipitation modeling, and deposition modeling and provide a brief review of remediation methods. **Secs. 9.7** through **9.10** present the same sequence of topics for waxes. See the chapters on phase behavior and phase diagrams in this section of the handbook for additional information on hydrocarbon phase behavior. Information on water/hydrocarbon systems is given in the chapters on water hydration and crude oil emulsions.

**9.1.1 Asphaltene-Precipitation Behavior.** Asphaltenes precipitation is caused by a number of factors including changes in pressure, temperature, and composition. The two most prevalent causes of asphaltene precipitation in the reservoir are decreasing pressure and mixing of oil with injected solvent in improved-oil-recovery (IOR) processes. Drilling, completion, acid stimulation, and hydraulic fracturing also can induce precipitation in the near-wellbore region. As oil flows up the wellbore, asphaltene can precipitate as a result of pressure and temperature changes. A summary of the different field and laboratory observations associated with asphaltene precipitation during primary depletion and IOR gas injection follows.

***Asphaltene Precipitation During Primary Depletion.*** In normal pressure depletion, reservoirs that experience asphaltene precipitation usually have the following characteristics<sup>2</sup>:

- The fluid in place is light to medium oil with small asphaltene content.

- The initial reservoir pressure is much larger than the saturation pressure. That is, the fluid is highly undersaturated.
- Maximum precipitation occurs around the saturation pressure.

Heavier crudes that contain a larger amount of asphaltene have very few asphaltene-precipitation problems because they can dissolve more asphaltene. Leontaritis and Mansoori<sup>3</sup> and Kokal and Sayegh<sup>4</sup> compiled field cases with asphaltene-precipitation problems during primary depletion. Extreme cases include the Venezuelan Boscan crude with 17 wt% asphaltene produced nearly without precipitation, whereas the Venezuelan Mata-Acema crude with 0.4 to 9.8 wt% asphaltene and the Algerian Hassi Messaoud crude with 0.062 wt% encountered serious precipitation problems during production.

**Asphaltene Precipitation During IOR Gas Injection.** The injection of hydrocarbon gases or CO<sub>2</sub> for IOR promotes asphaltene precipitation. Numerous field reports and laboratory studies on this phenomenon have been published.<sup>4-12</sup> Although it frequently manifests itself at the production wellbore at solvent breakthrough, precipitation can occur anywhere in the reservoir.

Asphaltene precipitation also may occur during solvent injection into heavy-oil reservoirs.<sup>13</sup> Butler and Mokrys<sup>14</sup> proposed an in-situ solvent-extraction process for heavy oils and tar sands called VAPEX. This process uses two horizontal wells (one injector and one producer). The injection of solvent (e.g., propane) creates a solvent chamber in which oil is mobilized and drained toward the producer. In addition to the mobilization process, the solvent may induce asphaltene precipitation, which provides an in-situ upgrading of the oil.

**Asphaltene Precipitation and Deposition.** Sec. 9.2.2 discusses the chemistry of asphaltenes and nature of the thermodynamic equilibrium of asphaltenes in petroleum fluids. Changes in pressure, temperature, and composition may alter the initial equilibrium state and cause asphaltene precipitation.

The region in which precipitation occurs is bounded by the asphaltene precipitation envelope (APE). Fig. 9.1 shows a typical pressure-composition APE and a pressure-temperature APE.<sup>15,16</sup> The APEs also are referred to as asphaltene deposition envelopes. In this chapter, precipitation refers to the formation of the asphaltene precipitate as a result of thermodynamic equilibrium and deposition refers to the settling of the precipitated asphaltene onto the rock surface in a porous medium. The onset conditions correspond to points on the APE. Within the APE, the amount of precipitated asphaltene increases as pressure decreases from the upper onset pressure to the saturation pressure of the oil. The precipitation reaches a maximum value at the saturation pressure and decreases as pressure decreases below the saturation pressure.

Inside the reservoir, after precipitation has occurred, the asphaltene precipitate can remain in suspension and flow within the oil phase or can deposit onto the rock surface. The main deposition mechanisms are adsorption and mechanical entrapment. The deposited asphaltene may plug the formation and alter rock wettability from water-wet to oil-wet.

**9.1.2 Wax-Precipitation Behavior.** Wax components can precipitate from petroleum fluids when the original equilibrium conditions of the reservoir are changed so that the solubility of the waxes is reduced; however, wax precipitation does not necessarily lead to deposition. Individual wax crystals tend to disperse in the fluid instead of depositing on a surface. If the number of wax crystals becomes large enough or if other nucleating materials such as asphaltenes, formation fines, clay, or corrosion products are present, the crystals may agglomerate into larger particles. These larger particles then may separate out of the fluid and form solid deposits.

Fig. 9.2 shows a typical wax-precipitation envelope on a pressure-temperature diagram. In contrast to the APE, the solid/liquid-phase boundary is nearly vertical for waxes, illustrating wax precipitation's strong dependence on temperature and weak dependence on pressure.

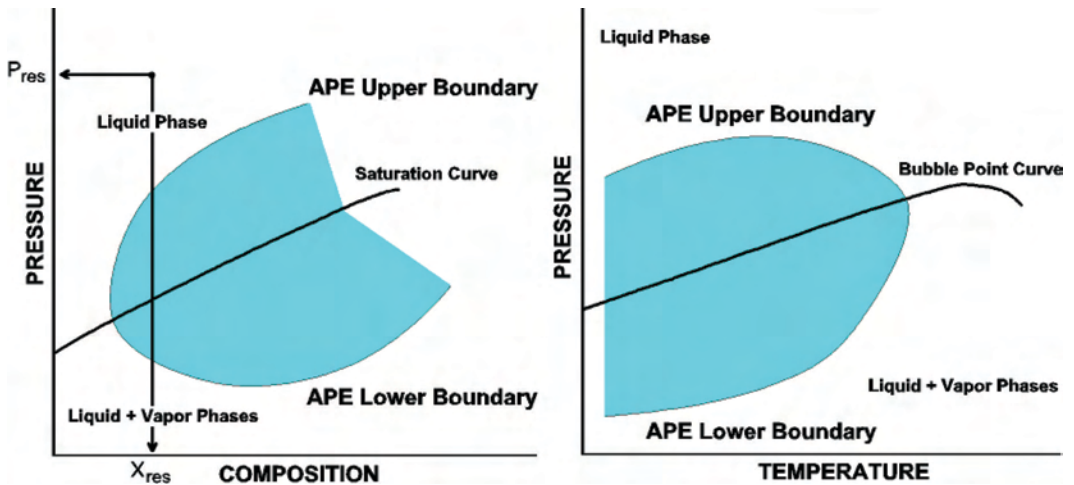


Fig. 9.1—Pressure-composition and pressure-temperature APEs<sup>15</sup> (after Leontaritis<sup>16</sup>).

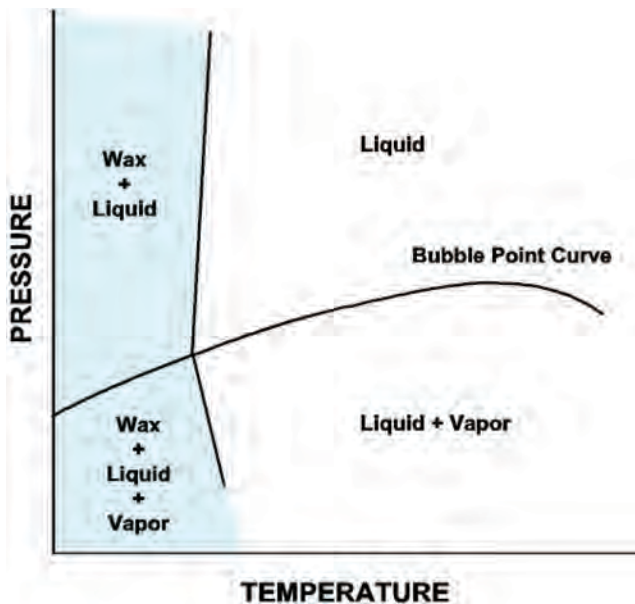


Fig. 9.2—Pressure-temperature wax precipitation envelopes (after Leontaritis<sup>16</sup>).

Temperature reduction is the most common cause of wax deposition because wax solubility in hydrocarbon fluids decreases as the temperature is lowered.<sup>1</sup> Reservoir fluid cooling occurs throughout the producing fluid system. Cooling can be caused by oil and gas expansion at the formation face, through casing perforations, or through other orifices or restrictions; by dissolved gas being liberated from solution; by radiation of heat from the fluid to the surrounding formation as it flows up the wellbore; by transfer of the fluid through low-temperature surface facilities; and by injection of water or other fluids at temperatures below the reservoir temperature.

Pressure changes usually have a very small effect on wax-precipitation temperatures and amounts; however, changes in the original equilibrium composition of the fluids can result in a loss of wax solubility. A fairly consistent trend is that the lightest components in a crude oil

act as good solvents for waxes. Liberation of solution gas from a crude oil as pressure decreases below the bubblepoint of the fluid has been shown to increase the cloud-point temperature of the oil.<sup>17</sup> This effect also has been observed in synthetic mixtures of methane, decane, and heavy *n*-alkanes with carbon numbers from 18 to 30<sup>18</sup> and for stock-tank oils mixed with methane and carbon dioxide.<sup>19</sup> This trend has been shown to be reversed in a study of two gas-condensate fluids in which the cloud-point temperature decreases as pressure is reduced below the vapor/liquid-phase boundary and may increase only at very low pressures.<sup>20</sup> The addition of intermediate paraffinic, naphthenic, and aromatic components with carbon numbers from 5 to 10 has been shown experimentally to decrease the cloud-point temperature for two crude oils.<sup>21</sup> Some model predictions contradict these results, indicating an increase in cloud-point temperature when pentane, hexane, or nonane were mixed with stock-tank oils.<sup>19</sup>

## 9.2 Characteristics of Asphaltenes and Waxes

**9.2.1 Chemical Classification of Petroleum Fluids.** Petroleum-reservoir fluids are complex multicomponent mixtures. The chemical constituents of petroleum may be classified broadly as belonging either to the  $C_6$  or the  $C_{6+}$  fraction. The light end, or  $C_6$  fraction, of petroleum fluids is composed of well-defined pure hydrocarbon components with carbon numbers up to 5 and the light gases  $N_2$ ,  $CO_2$  and  $H_2S$ . The hydrocarbons in the light end primarily are straight-chain normal alkanes (*n*-alkanes) and their branched isomers (*i*-alkanes). The heavy end, or  $C_{6+}$  fraction, consists of all the components with carbon numbers of 6 or greater.

**Classification of Petroleum Constituents.** A classification system and nomenclature commonly used in the petroleum industry describes components as belonging to the paraffinic (P), naphthenic (N), or aromatic (A) fractions.<sup>22,23</sup> These are often referred to jointly as PNA.

**Paraffins.** This class includes *n*-alkanes and *i*-alkanes that consist of chains of hydrocarbon segments ( $-CH_2-$ ,  $-CH_3$ ) connected by single bonds. Methane ( $CH_4$ ) is the simplest paraffin and the most common compound in petroleum-reservoir fluids. The majority of components present in solid-wax deposits are high-molecular-weight paraffins.

**Naphthenes.** This class includes the cycloalkanes, which are hydrocarbons similar to paraffins but contain one or more cyclic structures. The elements of the cyclic structures are joined by single bonds. Naphthenes make up a large part of microcrystalline waxes.

**Aromatics.** This class includes all compounds that contain one or more ring structures similar to benzene ( $C_6H_6$ ). The carbon atoms in the ring structure are connected by six identical bonds that are intermediate between single and double bonds, which are referred to as hybrid bonds, aromatic double bonds, or benzene bonds.

**Resins and Asphaltenes.** Resins and asphaltenes primarily are a subclass of the aromatics, although some resins may contain only naphthenic rings. They are large molecules consisting primarily of hydrogen and carbon, with one to three sulfur, oxygen, or nitrogen atoms per molecule. The basic structure is composed of rings, mainly aromatics, with three to ten or more rings per molecule.

**SARA Classification of Petroleum Constituents.** The components of the heavy fraction of a petroleum fluid can be separated into four groups: saturates, aromatics, resins, and asphaltenes (SARA).

- Saturates include all hydrocarbon components with saturated (single-bonded) carbon atoms. These are the *n*-alkanes, *i*-alkanes, and cycloalkanes (naphthenes).
- Aromatics include benzene and all the derivatives composed of one or more benzene rings.
- Resins are components with a highly polar end group and long alkane tails. The polar end group is composed of aromatic and naphthenic rings and often contains heteroatoms such as oxygen, sulfur, and nitrogen. Pure resins are heavy liquids or sticky solids.



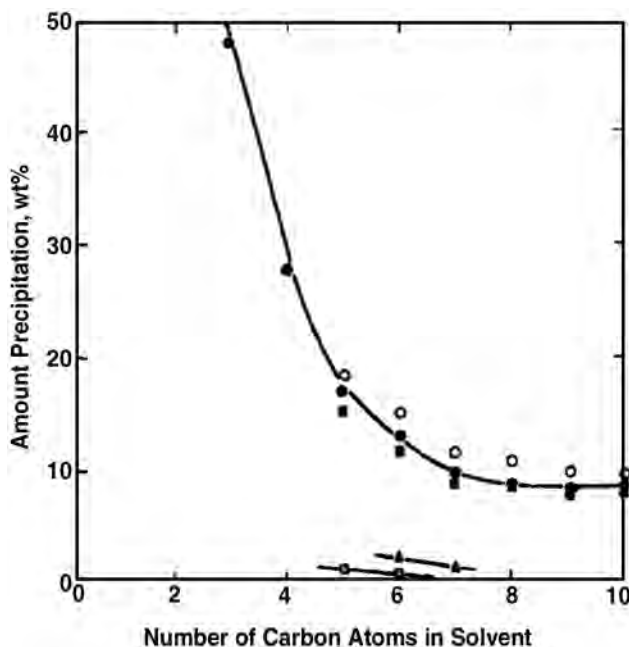


Fig. 9.3—Relation of amount precipitated to carbon-numbering nonaromatic solvents. (Reprinted from *Fuel*, Vol. 52, D.L. Mitchell and J.G. Speight, "The Solubility of Asphaltenes in Hydrocarbon Solvents," pages 149–152, Copyright 1973, with permission from Elsevier Science.)

- Asphaltenes are large highly polar components made up of condensed aromatic and naphthenic rings, which also contain heteroatoms. Pure asphaltenes are black, nonvolatile powders.

The experimental method used to determine the weight fractions of these groups is called SARA analysis.<sup>24</sup>

**9.2.2 Asphaltene Characteristics. Nature of Asphaltenes.** Asphaltenes are a solubility class that is soluble in light aromatics such as benzene and toluene but is insoluble in lighter paraffins.<sup>25,26</sup> They normally are classified by the particular paraffin used to precipitate them from crude (e.g., n-pentane or n-heptane). Fig. 9.3 from Mitchell and Speight<sup>25</sup> shows that different alkane solvents yield different amounts of precipitates. Fig. 9.4 from Speight *et al.*<sup>26</sup> shows dependence of the aromaticity (hydrogen/carbon atomic ratio) and molecular weight of asphaltene on the precipitating solvent. These figures also indicate that the amounts and natures of asphaltenes precipitated with n-heptane or heavier alkanes are very similar. Ref. 26 provides a summary of standard analytical methods for asphaltene separation with either n-pentane or n-heptane.

Although the exact nature of the original state of equilibrium of asphaltenes in petroleum fluids is still under investigation, one characteristic is the tendency of asphaltenes to form aggregates in hydrocarbon solutions. These aggregates are called micelles. The micelles and the hydrocarbon medium form a colloidal system. One commonly held view is that the colloids are stabilized by resins adsorbed on their surface,<sup>27,28</sup> and the dispersion of colloids in the fluid form a two-phase system. Fig. 9.5 from Leontaritis<sup>29</sup> schematically shows asphaltene-resin micelles that are suspended in the oil. Colloids also may be solvated by the surrounding medium, forming a true single-phase solution. Thermodynamic models (e.g., the solubility-parameter model of Hirschberg *et al.*)<sup>6</sup> inherently assume the single-phase view. The role of resins in the single-phase or two-phase solution models may be quite different.<sup>30</sup> Changes in pressure, temperature,

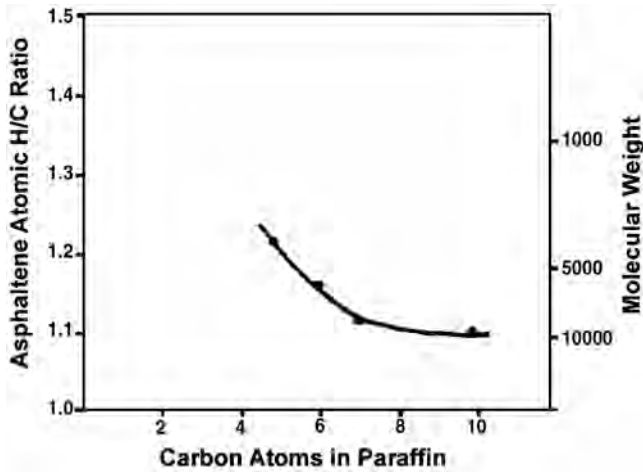


Fig. 9.4—Relationship of asphaltene aromaticity to carbon number of the paraffin. (Reprinted from *Fuel*, J.G. Speight, R.B. Long, and T.D. Trowbridge, "Factors Influencing the Separation of Asphaltenes From Heavy Petroleum Feedstocks," pages 616–620, Copyright 1984, with permission from Elsevier Science.)

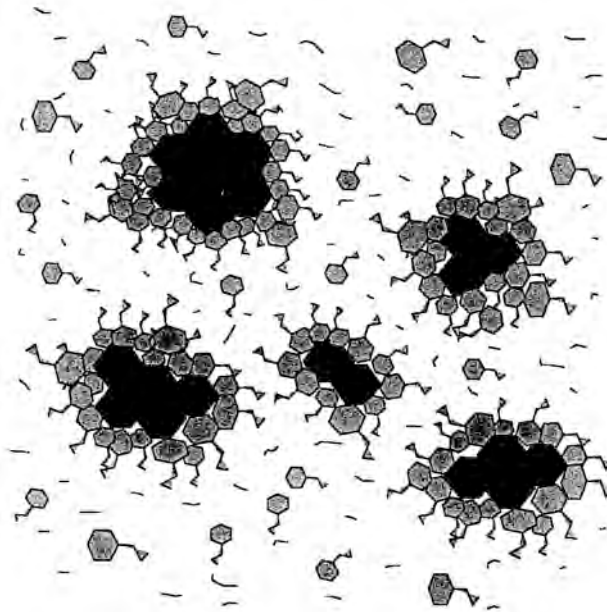


Fig. 9.5—Asphaltene-resin micelles.<sup>29</sup>

and composition may alter the solubility parameter of the oil and/or the asphaltene-resin association and cause precipitation.

The definition of asphaltenes as compounds that are soluble in aromatics such as toluene and insoluble in light alkanes are referred to as laboratory asphaltenes by Joshi *et al.*<sup>31</sup> Asphaltenes that precipitate in the field from a depressurization process are called field asphaltenes and contain different constituents. Laboratory and field precipitates contain combinations of asphaltenes and resins. Speight<sup>24</sup> referred to them as asphalts, but that distinction is not made here.

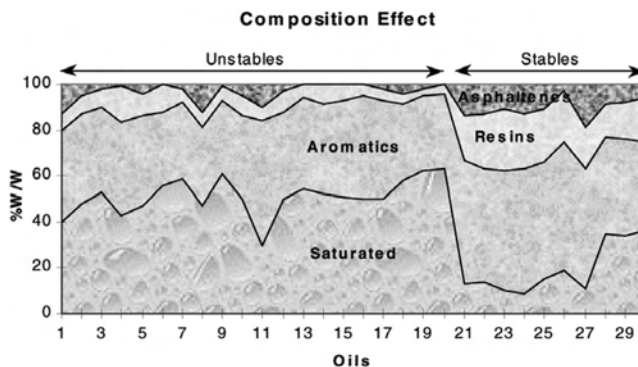


Fig. 9.6—SARA effect on the stability of several crude oils regarding asphaltene precipitation.<sup>32</sup>

**Stability of Asphaltenic Crudes.** SARA ratios play an important role in the solubility of asphaltenes. Avila *et al.*<sup>32</sup> performed SARA analyses on 30 Venezuelan oil samples and attempted to associate the SARA contents with asphaltene precipitation observed in the field. Fig. 9.6 shows the SARA contents of crude oils that experience asphaltene precipitation in the field and those that do not. Crude oils with a high content of saturates and low contents of aromatics and resins clearly are more prone to asphaltene precipitation.

**Correlation for Asphaltene Precipitation With Alkanes.** Asphaltene precipitation at laboratory and field conditions can be predicted with thermodynamic models. Sec. 9.4 discusses this topic in detail. For precipitation with alkanes at atmospheric conditions, a simple correlation from Rassamdana *et al.*<sup>33</sup> and Sahimi *et al.*<sup>34</sup> can be used.

Fig. 9.7 from Sahimi *et al.*<sup>34</sup> shows the experimental weight percents of precipitated asphaltene,  $W$  (g of precipitated asphaltene/g of crude oil  $\times 100\%$ ), as a function of the solvent to crude oil ratio,  $R$  ( $\text{cm}^3$  of solvent /g of crude oil), from precipitation experiments of an Iranian crude oil with  $n\text{-C}_5$ ,  $n\text{-C}_6$ ,  $n\text{-C}_7$ ,  $n\text{-C}_8$ , and  $n\text{-C}_{10}$  at  $26^\circ\text{C}$  and atmospheric pressure. As expected, the amount of precipitates decreases with increasing solvent carbon number. Rassamdana *et al.*<sup>33</sup> and Sahimi *et al.*<sup>34</sup> found that the experimental points in Fig. 9.7 could be collapsed onto a scaling curve of  $Y$  vs.  $X$  with

$$X = r / (M_a)^{1/4} \dots\dots\dots (9.1)$$

$$\text{and } Y = WR^2, \dots\dots\dots (9.2)$$

where  $M_a$  is the molecular weight of the alkane solvent. Fig. 9.8 shows the resulting scaling curve. This curve can be represented accurately by a cubic order polynomial:

$$Y = 1.18 - 14.9 X + 39.16 X^2 + 0.92 X^3 \dots\dots\dots (9.3)$$

The critical solvent ratio,  $R_c$ , where precipitation starts to occur obeys the correlation

$$R_c = 0.275(M_a)^{1/4} \dots\dots\dots (9.4)$$

The factor 0.275 corresponds to a temperature of  $26^\circ\text{C}$ . For other temperatures, the following correlation is proposed.

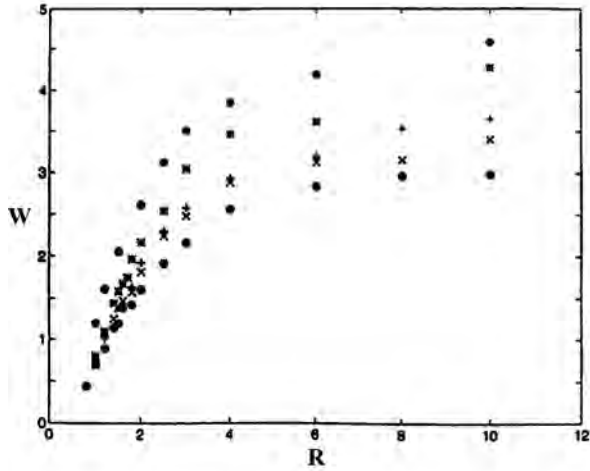


Fig. 9.7—Experimental data for the weight percent, *W*, of precipitated asphaltene as a function of the solvent to crude oil ratio, *R*, in cm<sup>3</sup>/g.<sup>34</sup> The results are, from top to bottom, for n-C<sub>5</sub>, n-C<sub>7</sub>, n-C<sub>8</sub> and n-C<sub>10</sub> as the precipitating agent.

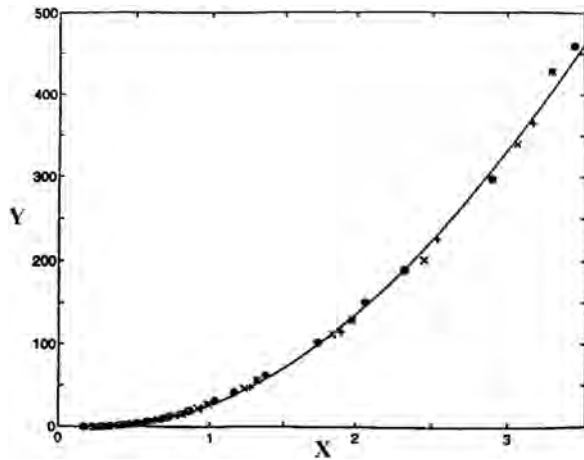


Fig. 9.8—Scaling curve for data in Fig. 9.7.<sup>34</sup>

$$R_c = T_c(M_a)^{1/4}, \dots\dots\dots (9.5)$$

where *T<sub>c</sub>* is a temperature-dependent parameter.

**9.2.3 Characteristics of Petroleum Waxes.** This section discusses the phase behavior and properties of wax-forming components, primarily normal alkanes, relevant to understanding and modeling wax-phase behavior.

**Types of Petroleum Waxes.** Petroleum waxes are complex mixtures of n-alkanes, i-alkanes, and cycloalkanes with carbon numbers ranging approximately from 18 to 65.<sup>35</sup> The minimum energy-chain structure of alkanes is a flat zig-zag of carbon atoms with the hydrogen atoms located in planes passing through the carbon atoms perpendicular to the chain axes. Fig. 9.9<sup>36</sup> shows this structure schematically for typical petroleum-wax components.

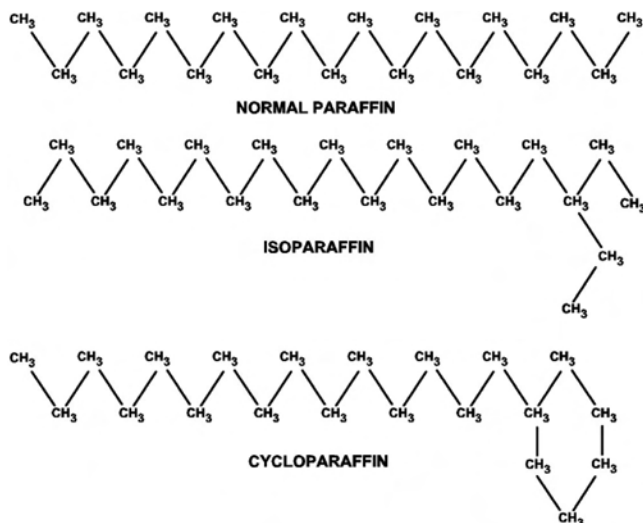


**Fig. 9.9—Example structure of wax-forming components.** (Reprinted from *Asphaltenes and Asphalts*, 2, C. Lira-Galeana and A. Hammami, "Wax Precipitation from Petroleum Fluids: A Review," pages 557–608, Copyright 2000, with permission from Elsevier Science.)

<b>TABLE 9.1—TYPICAL COMPOSITION AND PROPERTIES OF COMMERCIALY AVAILABLE PARAFFIN AND MICROCRYSTALLINE WAXES<sup>37</sup></b>		
	<u>Paraffin Waxes</u>	<u>Microcrystalline Waxes</u>
Normal paraffins, %	80 to 95	0 to 15
Branched paraffins, %	2 to 15	15 to 30
Cycloparaffins, %	2 to 8	65 to 75
Melting point range, °C	50 to 65	60 to 90
Average molecular weight range	350 to 430	500 to 800
Typical carbon number range	18 to 36	30 to 60
Crystallinity range, %	80 to 90	50 to 65

There are two general classes of petroleum waxes. Waxes composed primarily of normal alkanes crystallize in large flat plates (macrocrystalline structures) and are referred to as paraffin waxes. Waxes composed primarily of cycloalkanes and i-alkanes crystallize as small needle structures and are referred to as microcrystalline waxes.<sup>35</sup> Table 9.1 shows a comparison of the properties of paraffin and microcrystalline waxes as given by Gilby.<sup>37</sup> Musser and Kilpatrick<sup>38</sup> isolated waxes from sixteen different crude oils and found that paraffinic waxes had molecular weight ranges of 350 to 600, while microcrystalline waxes had large molecular weight ranges of 300 to 2,500. Of the 16 oils analyzed, five exhibited microcrystalline wax deposition, six precipitated paraffinic waxes, and the remaining five showed a mixture of paraffinic and microcrystalline waxes.

In addition to the possibility of precipitating mixtures of the two different types of waxes, the crystal structures in solid-wax deposits will be malformed to some degree because of the complex precipitation environment encountered in petroleum production. Crystal imperfections

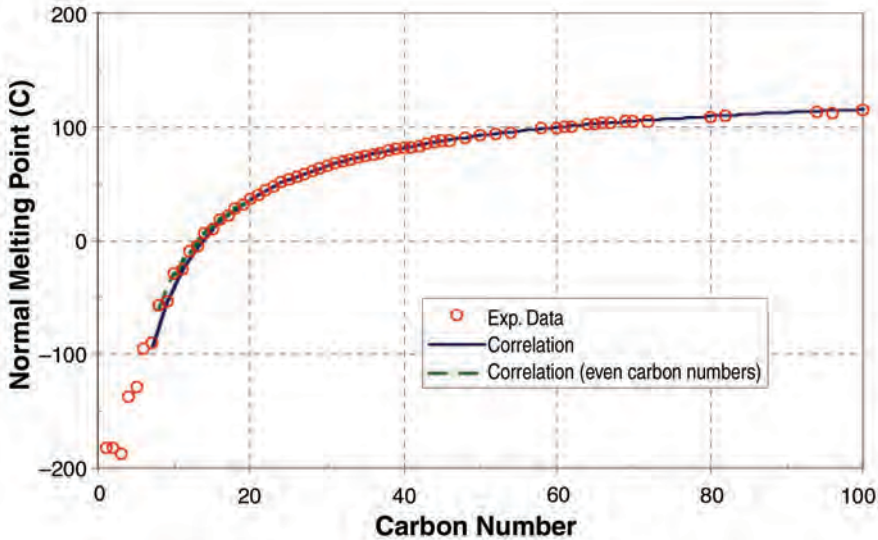


Fig. 9.10—Experimental<sup>42,43</sup> and correlated<sup>44</sup> normal melting points of n-alkanes.

may occur when the temperature of the solution is decreased rapidly or when heavy aromatic components of the oil are incorporated into the lattice structure. The presence of molecules that hinder the lattice formation result in a wax phase composed of many small, independent crystal lattices.<sup>39</sup>

**Precipitation of Petroleum Waxes.** Solid-wax formation consists of two distinct stages: nucleation and crystal growth. As the temperature of a liquid solution is lowered to the wax-appearance temperature (WAT), the wax molecules form clusters. Wax molecules continue to attach and detach from these clusters until they reach a critical size and become stable. These clusters are called nuclei and the process of cluster formation is called nucleation. Once the nuclei are formed and the temperature remains below the WAT, the crystal-growth process occurs as further molecules are laid down in a lamellar or plate-like structure.<sup>40</sup>

Nucleation is described as either homogeneous or heterogeneous. Homogeneous nucleation occurs in liquids that are not contaminated with other nucleating materials. In this case, the development of nucleation sites is time dependent. Heterogeneous nucleation occurs when there is a distribution of nucleating material throughout the liquid. If there is sufficient nucleating material, heterogeneous nucleation can be nearly instantaneous. Pure hydrocarbon mixtures in laboratories rarely undergo heterogeneous nucleation,<sup>39</sup> whereas crude oil in the reservoir and production tubing will most likely nucleate this way because of the presence of asphaltenes, formation fines, clay, and corrosion products.

**Solidification Behavior of Normal Alkanes.** Turner<sup>41</sup> reviewed the properties of normal alkanes found in petroleum waxes, including solid-phase transitions, crystal structures, and phase behavior of binary mixtures. Fig. 9.10 shows experimental data<sup>42,43</sup> and correlation predictions<sup>44</sup> for normal alkane-melting temperatures at atmospheric pressure as a function of carbon number. In addition to the solid/liquid-phase transition indicated in this figure, many normal alkanes undergo solid/solid-phase transitions within a few degrees below the melting point.<sup>35</sup>

Normal alkanes can assume four different crystal structures: hexagonal, orthorhombic, triclinic, and monoclinic. For normal alkanes with odd carbon numbers from 11 to 43 and even carbon numbers from 22 to 42, the crystal structure formed on cooling from a melt is hexagonal. This structure has a high degree of molecular-rotational freedom and is characteristically

plastic and translucent. All the other crystal structures are restricted rotationally, resulting in a hard deposit and opaque appearance. The even-carbon-number alkanes from 12 to 20 form a triclinic structure on cooling from the melt, whereas all alkanes with carbon numbers 43 or greater form an orthorhombic structure on cooling from the melt. This is also the stable low-temperature form of the alkanes with odd carbon numbers less than 43, which is achieved by further cooling from the hexagonal structure. The monoclinic structure is never attained directly from the melt but is assumed by the even-carbon-number alkanes on cooling from the hexagonal or orthorhombic structures.

**Solidification Behavior of Alkane Mixtures.** Binary mixtures of wax-forming n-alkanes are completely miscible in the liquid state. In general, these binary mixtures form continuous-solid solutions if both molecules are similar in form and dimension and exhibit the same crystal structure in their pure state. Practically, this means that single-phase-solid solutions form when the molecular length difference is less than 6%. For n-alkanes with carbon numbers 18 to 35, the critical length difference is 2 to 6 carbon atoms.<sup>41</sup> The behavior of binary mixtures depends on whether the constituents are both odd-numbered alkanes, both even-numbered alkanes, or a mixture of odd- and even-numbered alkanes because of the different pure component crystal structures.

The solid-phase behavior of binary mixtures also has been observed to be time and temperature dependent. Dorset<sup>45,46</sup> shows that some mixtures, such as C<sub>30</sub> with C<sub>36</sub>, form metastable continuous-solid solutions that separate into eutectics with complete fractionation of the constituents over a period of days. Other mixtures, such as C<sub>30</sub> with C<sub>40</sub>, show complete immiscibility immediately on cooling.

For binary mixtures that form continuous-solid solutions, the stable low-temperature configuration is an orthorhombic structure, which is slightly different from the pure component orthorhombic crystal. This occurs for systems in which one alkane is contaminated with even 1 or 2% neighboring alkanes.<sup>35</sup> This same structure has been observed for synthetic ternary and higher mixtures, as well as for diesel fuels.<sup>47</sup> The diesel fuels exhibited an amorphous (microcrystalline) solid phase in addition to the orthorhombic macrocrystalline phase. Pedersen *et al.*<sup>48</sup> and Hansen *et al.*<sup>49</sup> also noted the probable existence of solid/solid-phase transitions with variations in temperature in their studies on a number of North Sea crude oils.

In contrast with the phase separations observed in binary mixtures of alkanes with significant length differences, Dirand *et al.*<sup>50</sup> and Chevallier *et al.*<sup>51</sup> found that commercial paraffin waxes with continuous distributions of 20 to 33 consecutive n-alkanes formed single-phase orthorhombic-solid solutions at room temperature. The wax deposit from one crude oil also showed the same single-phase macrocrystalline structure; however, an amorphous solid was also present. Increasing the temperature of the commercial waxes to their melting points of 55 to 65°C showed the existence of several different two-phase solid domains for these mixtures.

**Significance of Experimental Solidification Behavior for Model Development.** As indicated in the previous discussion, solidification behavior of petroleum-mixture components can range from the relatively simple crystallization of pure n-alkanes into well-defined solid structures to the very complex precipitation of solids from live reservoir fluids into multiphase microcrystalline and imperfect macrocrystalline domains. Development of thermodynamic models for predicting the equilibrium-phase behavior of solid waxes depends on which phenomena are to be modeled and on the availability of experimental data for estimating parameters and testing models. The determination of the properties and phase behavior of solid waxes is an area of active research.

The simplest models are written for a single-component single-phase solid. Models of this type may be applied to pure-component-solidification cases or as an approximation in which a multicomponent wax is treated as one lumped component. More common is the solid-solution model in which a single-phase multicomponent-solid deposit is assumed. Some researchers

have extended the experimental evidence of immiscible pure solid phases for binary mixtures to the multicomponent case. Lira-Galeana *et al.*<sup>52</sup> proposed a multisolid wax model in which the solid deposit is assumed to consist of a number of immiscible solid phases, each of which is composed of a single pure component. Generally, the solid deposit is considered to be made up of a number of multicomponent phases, as in the work of Coutinho.<sup>53</sup>

The experimental work discussed generally supports the assumption of multiple solid phases, although Dirand *et al.*<sup>50</sup> and Chevallier *et al.*<sup>51</sup> have shown that commercial waxes with a large number of consecutive n-alkanes can form a single multicomponent solid solution at room temperature. As Sec. 9.8 discusses, the models currently available are able to operate in predictive mode for some well-defined systems, but reservoir-fluid modeling still relies heavily on the availability of experimental data.

### 9.3 Experimental Measurements of Asphaltene Precipitation

**9.3.1 Measurements of APE.** As previously discussed, the APE defines the region in which asphaltene precipitation occurs. Accurate measurements of the APE and the amounts of precipitate within the APE are required for design purposes and for tuning existing models. The upper pressure on the APE is denoted by  $p_{Au}$  and the lower pressure on the APE is denoted by  $p_{Al}$ . Several techniques are available for determining the onset of precipitation with various degrees of accuracy.

**Gravimetric Technique.** This technique<sup>5,54</sup> is conducted in a conventional pressure/volume/temperature (PVT) cell. For a pressure below the  $p_{Au}$ , precipitation occurs and larger particles segregate and settle at the bottom of the cell because of gravity. Asphaltene analysis (titration with n-pentane or n-heptane) of the oil shows a decrease in asphaltene content compared with the original oil. Pressure steps must be chosen carefully to capture the inflection point at  $p_{Au}$  and  $p_{Al}$ .

**Acoustic-Resonance Technique.** The acoustic-resonance technique has been used effectively to define  $p_{Au}$ .<sup>4,55</sup> The live oil is charged at a high pressure (e.g., 8,500 psia) into a resonator cell maintained at the reservoir temperature. The resonator pressure then is decreased at a very low rate (e.g., 50 psia/min) by changing the volume. The depressurization rate decreases with time to a typical rate of 5 psia/min toward the end of the experiment. Acoustic data exhibit sharp changes at  $p_{Au}$  and at the oil saturation pressure,  $p_s$ .

**Light-Scattering Technique.** Light-scattering techniques also have been successfully used to measure the APE.<sup>40,55-58</sup> For dark-colored oil, a near-infrared laser light system ( $800 \times 10^{-9}$  m to  $2200 \times 10^{-9}$  m wavelength) is required to detect asphaltene-precipitation conditions. The principle behind the measurements is based on the transmittance of a laser light through the test fluid in a high-pressure, high-temperature visual PVT cell undergoing pressure, temperature, and composition changes. A receiver captures the amount of light that passes through the oil sample. The power of transmitted light (PTL) is inversely proportional to the oil mass density, to the particle size of the precipitate, and to the number of particles per unit volume of fluid.<sup>58</sup> The PTL curve exhibits sharp jumps at  $p_{Au}$ ,  $p_s$ , and  $p_{Al}$ .

**Filtration Technique.** In this method, the cell contents during a depressurization test are mixed in a magnetic mixer, and small amounts of the well-mixed reservoir fluid are removed through a hydrophobic filter at various pressures.<sup>54</sup> The material retained on the filter is analyzed for SARA contents.

**Electrical-Conductance Technique.** This technique measures the change in the fluid conductivity with changes in concentration and mobility of charged components.<sup>56,59</sup> Asphaltenes have large dipole moments, and, therefore, the conductivity curve exhibits a change in the slope when precipitation occurs.



**Viscometric Technique.** The key point of this method is the detection of a marked change in the viscosity curve at the onset of precipitation<sup>12,60</sup> because the viscosity of oil with suspended solids is higher than that of the oil itself.

**Other Techniques.** Asphaltene precipitation has been detected through visual observations with a microscope.<sup>6</sup> Measurements of interfacial tension between oil and water<sup>61,62</sup> also can be used to detect the onset. A technique based on pressure-drop measurements across a capillary tube was discussed by Broseta *et al.*<sup>63</sup>

**Comparison of Different Methods.** Fig. 9.11 shows the results of Jamaluddin *et al.*'s<sup>54</sup> comprehensive comparison of measurements with the gravimetric, acoustic-resonance, light-scattering, and filtration techniques on the same oil. These methods, except for the acoustic-resonance technique, determine both the upper and lower APE pressure. The acoustic-resonance technique normally provides only the upper onset pressure. In addition to APE pressures, the gravimetric and filtration techniques also give the amount of precipitated asphaltene within the precipitation region. The gravimetric and filtration techniques are more time consuming than the acoustic-resonance and light-scattering techniques. Fotland *et al.*<sup>59</sup> showed that the electrical-conductance technique can determine both precipitation onset and amounts of precipitate that are consistent with the gravimetric technique. The advantage of the viscometric technique is in its applicability to heavy crude oil, which may give some difficulties to light-scattering techniques, and in the low-cost equipment. In many cases, two measurement techniques are applied to the same oil to enhance data interpretation. MacMillan *et al.*<sup>56</sup> recommended the combination of light-scattering and electrical-conductance techniques, while Jamaluddin *et al.*<sup>54</sup> suggested the simultaneous application of light-scattering and filtration techniques.

**9.3.2 Reversibility.** The reversibility of asphaltene precipitation is a subject of some controversy. Fotland<sup>64</sup> and Wang *et al.*<sup>65</sup> suggested that asphaltene precipitation is less likely to be reversible for crude oils subjected to conditions beyond those of the precipitation onset. Hirschberg *et al.*<sup>6</sup> speculated that asphaltene precipitation is reversible but that the dissolution process is very slow. Hammami *et al.*<sup>58</sup> reported experimental measurements that seem to support this conjecture. They observed that asphaltene is generally reversible but that the kinetics of the redissolution vary significantly depending on the physical state of the system. Fig. 9.12 from Hammami *et al.*<sup>58</sup> shows the laser-power signal (light-scattering technique) from a depressurizing and repressurizing experiment on a light oil that exhibits strong precipitation behavior. The laser-power signal increased linearly as the pressure decreased from 76 to 56 MPa. This increase results from the continuous decrease of oil density above the bubblepoint as the pressure is reduced. With further depletion between 56 and 52 MPa, a large drop (one order of magnitude) in the laser-power signal occurred. The onset of asphaltene precipitation was estimated to be 55.7 MPa and the laser-power signal dropped to a very low level at 45 MPa. The bubblepoint pressure for this oil is 33.5 MPa. On repressurization of this oil from 27 MPa (7 MPa below the bubblepoint), almost the entire laser-power signal was recovered, but the signal followed a slightly different curve. Fig. 9.12 shows that the repressurization laser-power curve lags the depressurization curve, which is an indication that the kinetics of redissolution is slower than the kinetics of precipitation. Fig. 9.12 also shows that the ultimate laser-power value reached from repressurization is higher than the predepletion value. Hammami *et al.*<sup>58</sup> suggested that a large fraction of the precipitated asphaltene (the suspended solid) could easily go back into solution while a smaller fraction exhibits partial irreversibility or slow dissolution rate. The oil at the end of the repressurization process is partially deasphalted and is slightly lighter than the original oil.

Joshi *et al.*<sup>31</sup> performed further experiments to study the reversibility process. Their results corroborate the observations of Hammami *et al.*<sup>58</sup> for depressurization and repressurization experiments at field conditions; however, they observed that the precipitation caused by the

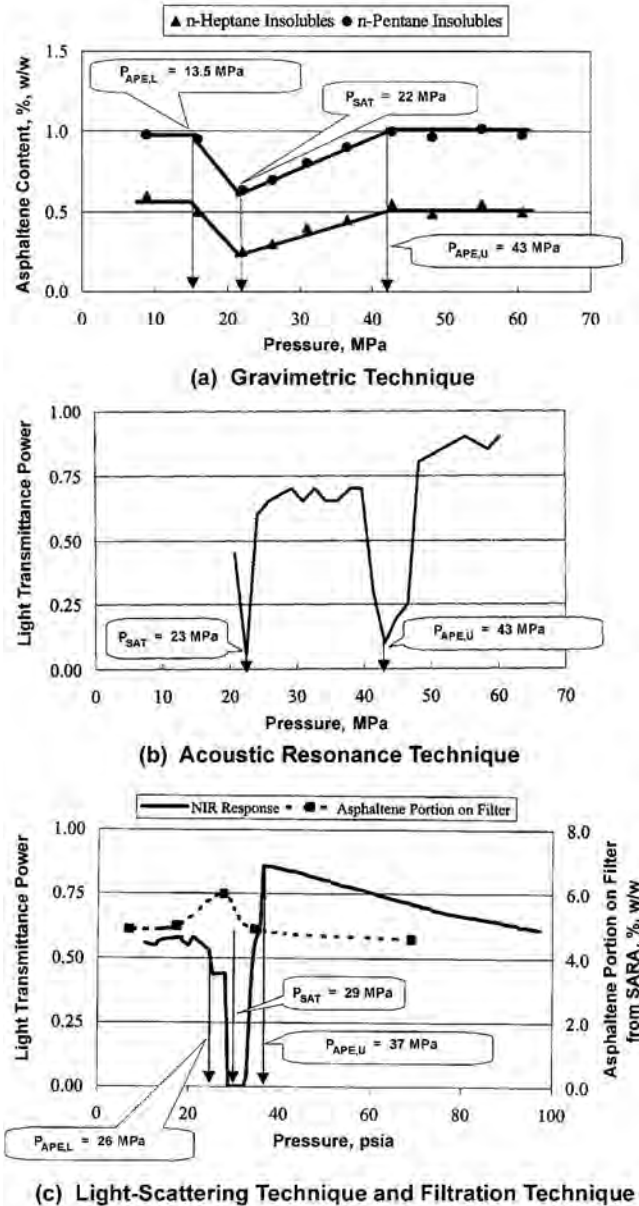


Fig. 9.11—APE pressure measurements with different methods (after Jamaluddin *et al.*<sup>54</sup>).

addition of alkane at atmospheric conditions is partially irreversible. They explained that asphaltene precipitation with pressure depletion at field conditions (field asphaltenes) results from the destabilization but not the destruction of asphaltene micelles. On the other hand, asphaltene precipitation caused by the addition of an alkane solvent in the laboratory under atmospheric conditions (laboratory asphaltenes) strips the asphaltene micelles of their resin components, and the restoration of reformed micelles is a very difficult process.

Similar experimental results on partial irreversibility were obtained by Rassamdana *et al.*<sup>33</sup> with an Iranian oil and different alkane solvents at atmospheric conditions. The laboratory asphaltenes from Joshi *et al.*<sup>31</sup> and Rassamdana *et al.*<sup>33</sup> were precipitated from light oils.

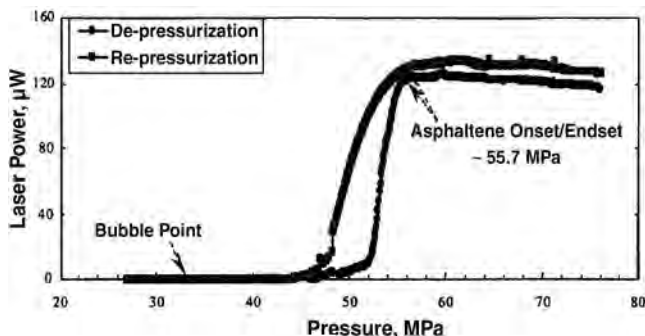


Fig. 9.12—Laser power in the depressurization and repressurization of a crude oil. [Reprinted with permission from Hammami, A. *et al.*: “Asphaltene Precipitation from Live Oils: An Experimental Investigation of the Onset Conditions and Reversibility,” *Energy & Fuels* (2000) V. 14, 14. Copyright 2000 American Chemical Society.]

Peramanu *et al.*<sup>66</sup> performed precipitation experiments with Athabasca and Cold Lake bitumens and n-heptane solvent and found the process completely reversible. It could be argued that in heavy oils and bitumens, larger amounts of resins and asphaltenes facilitate the reversibility of asphaltene precipitation with alkane solvents; thus, precipitation behaviors for light oils and heavy oils/bitumens are quite different and need to be examined separately.

Many of the references in Secs. 9.3.1 and 9.3.2 contain data on precipitation caused by pressure depletion. Additional data can be found in Hirschberg *et al.*<sup>6</sup> and Burke *et al.*<sup>5</sup> Asphaltene precipitation also occurs during rich-gas and CO<sub>2</sub>-flooding processes. Sec. 9.3.3 discusses the experimental results on these processes.

**9.3.3 Asphaltene Precipitation During Rich-Gas and CO<sub>2</sub> Flooding.** Hirschberg *et al.*<sup>6</sup> presented static precipitation data of a recombined crude oil with the separator gas, a lean gas, and a rich gas. The results show that precipitation is more pronounced with rich gas and that the injection of separator gas could induce asphaltene precipitation at reservoir conditions. Burke *et al.*<sup>5</sup> reported comprehensive static precipitation data for six recombined reservoir oils and different hydrocarbon gases. Their results indicate that precipitation depends on the composition of the crude oil, the added solvent, and the concentration of asphaltene in the crude. They also observed that for oil/solvent mixtures that exhibit a critical point on the *p*-*x* diagram, maximum precipitation occurred at the critical point.

Monger and Fu<sup>67</sup> and Monger and Trujillo<sup>7</sup> provided extensive data on asphaltene precipitation in CO<sub>2</sub> flooding. In Monger and Trujillo,<sup>7</sup> 17 stock-tank oils with gravity ranging from 19.5 to 46.5°API were used in a variable-volume circulating cell that could reproduce multiple-contact experiments. The temperature was set to 114°F (319 K) and run pressures were set above the minimum miscibility pressures. Fig. 9.13 shows the amounts of precipitation induced by CO<sub>2</sub> in the variable-volume circulating cell vs. the n-C<sub>5</sub> asphaltene content of the stock-tank oil. This figure shows that the CO<sub>2</sub>-induced precipitate is not the same as the n-pentane precipitate from the stock-tank oil. For Samples 1, 2, and 8, the extent of precipitation is substantially less than the asphaltene content. For Samples 3 and 9, the extent of precipitation exceeds the asphaltene content. They concluded that the precipitation of asphaltene by CO<sub>2</sub> was neither complete nor exclusive. Some asphaltenes can remain suspended, and other heavy organic compounds can precipitate. It also was observed that precipitation usually occurs in the development of miscibility. Srivastava *et al.*<sup>10,11</sup> studied asphaltene precipitation for Saskatchewan Weyburn’s oil with CO<sub>2</sub> and found that precipitation started to occur at 42 mol% CO<sub>2</sub> concentration in a static test. After that, there was a linear increase in asphaltene precipitate with CO<sub>2</sub>.

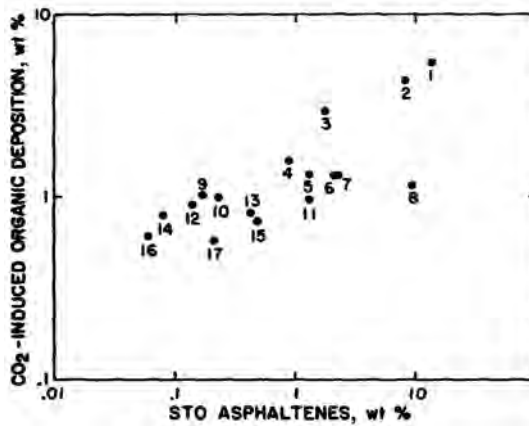


Fig. 9.13—Relationship between CO<sub>2</sub>-induced solid precipitation and n-C<sub>5</sub> asphaltene content in stock-tank oil.<sup>7</sup>

It has been reported that asphaltene precipitation from static tests may be quite different from dynamic tests. Parra-Ramirez *et al.*<sup>68</sup> performed static and multiple-contact precipitation experiments with a crude oil from the Rangely field and CO<sub>2</sub>. They observed that live oils yielded significantly higher amounts of precipitates than the corresponding dead oil and that multiple-contact experiments gave rise to more precipitation than single-contact experiments.

This discussion shows that field asphaltene precipitates resulting from a rich-gas or CO<sub>2</sub>-injection process are different from laboratory asphaltenes induced by the addition of alkane. This field asphaltene is also different from the field asphaltene resulting from pressure depletion, and its nature also varies with the composition of the injection fluid.

## 9.4 Thermodynamic Models for Asphaltene Precipitation

**9.4.1 Thermodynamic Equilibrium.** Thermodynamic models for predicting asphaltene-precipitation behavior fall into two general categories: activity models and equation-of-state (EOS) models. With the precipitated asphaltene treated as a single-component or multicomponent solid, the condition for thermodynamic equilibrium between the oil (liquid) and solid phase is the equality of component chemical potentials in the oil and solid phases. That is,

$$\mu_{iO} = \mu_{iS}, \quad i = 1, \dots, n_c, \dots \dots \dots (9.6)$$

where  $\mu_{iO}$  and  $\mu_{iS}$  are the chemical potential of component  $i$  in the oil and solid phases, respectively, and  $n_c$  is the number of components. The application of activity coefficient models or EOS models gives different expressions for the chemical potential. In addition, not all components in the oil phase undergo precipitation; therefore, Eq. 9.6 applies only to those components that precipitate.

**9.4.2 Activity Models. Activity Coefficients.** Because asphaltenes are a solubility class that can be precipitated from petroleum by the addition of solvent, activity-coefficient models have been applied to model the phase-equilibrium phenomena. The introduction of activity coefficients in Eq. 9.6 yields

$$y_{io} \gamma_{io} f_{io}^* \exp\left(\int_0^p \frac{v_{io}}{RT} dp\right) = y_{is} \gamma_{is} f_{is}^* \exp\left(\int_0^p \frac{v_{is}}{RT} dp\right), \dots\dots\dots (9.7)$$

where  $f_{ik}^*$  = standard state fugacity of component  $i$  in phase  $k$  ( $k = o, s$ ),  $v_{ik}$  = partial molar volume of component  $i$  in phase  $k$  ( $k = o, s$ ),  $y_{ik}$  = mole fraction of component  $i$  in phase  $k$  ( $k = o, s$ ), and  $\gamma_{ik}$  = activity coefficient of component  $i$  in phase  $k$  ( $k = o, s$ ).

Several approaches that use the activity-coefficient model assume the oil and asphaltene as two pseudocomponents: one component representing the deasphalted oil and the other the asphaltenes. Andersen and Speight<sup>69</sup> provided a review of activity models in this category. Other approaches represent the precipitate as a multicomponent solid. Chung,<sup>70</sup> Yarranton and Masliyah,<sup>71</sup> and Zhou *et al.*<sup>72</sup> gave detailed descriptions of these models.

**Flory-Huggins Model.** The solubility model used most in the literature is the Flory-Huggins solubility model introduced by Hirschberg *et al.*<sup>6</sup> Vapor/liquid equilibrium calculations with the Soave-Redlich-Kwong EOS<sup>73</sup> are performed to split the petroleum mixture into a liquid phase and a vapor phase. The liquid phase then is divided into two components: a component that corresponds to the asphaltene and a component that represents the remaining oil (deasphalted oil). When solvent is added into the oil, the second component represents the mixture of deasphalted oil and solvent. These two components are for modeling purposes and do not correspond to any EOS components used in the vapor/liquid calculations. It also is assumed that asphaltene precipitation does not affect vapor/liquid equilibrium.

Application of the Flory-Huggins solution theory gives the following expression for the chemical potential of the asphaltene component in the oil phase.

$$\frac{\mu_{am} - \mu_a^*}{RT} = 1 - \frac{v_a}{v_m} + \ln \Phi_a + \frac{v_a}{RT} (\delta_m - \delta_a)^2 \dots\dots\dots (9.8)$$

$$\text{with } \delta_m = \sum_{i=a,o} y_i \delta_i, \dots\dots\dots (9.9)$$

where subscripts  $a, o$ , and  $m$  are used to denote the asphaltene component, the deasphalted oil, and the oil phase mixture, respectively, and where  $v_a$  = molar volume of pure asphaltene,  $v_m$  = molar volume of mixture,  $\delta_i$  = solubility parameter of component  $i$ ,  $\delta_m$  = solubility parameter of mixture,  $\Phi_a$  = volume fraction of asphaltene in the mixture,  $\mu_{am}$  = chemical potential of asphaltene in the mixture, and  $\mu_a^*$  = reference chemical potential of asphaltene component.

Because the precipitated asphaltene is pure asphaltene,  $\mu_s = \mu_a^*$ . From the equality of chemical potential  $\mu_{am} = \mu_s$ , Eq. 9.8 gives

$$\ln \Phi_a = \frac{v_a}{v_m} - \frac{v_a}{RT} (\delta_m - \delta_a)^2 - 1. \dots\dots\dots (9.10)$$

The molar volume,  $v_m$ , of the oil mixture is calculated from the composition of the liquid phase obtained from vapor/liquid calculations that use the Soave-Redlich-Kwong EOS. The solubility parameter,  $\delta_m$ , is calculated from

$$\delta_m = \sqrt{\Delta U_v / v_m}, \dots\dots\dots (9.11)$$

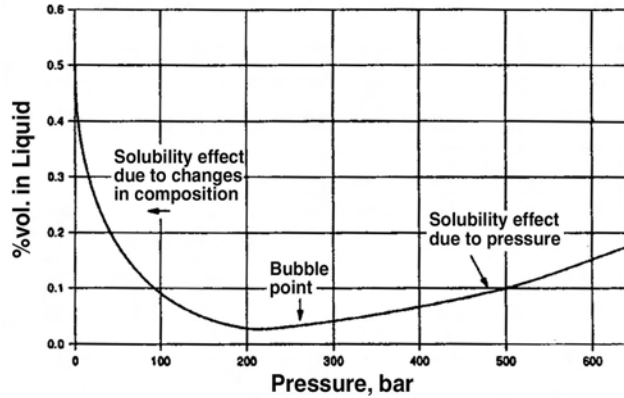


Fig. 9.14—Asphaltene solubility for a light crude oil.<sup>2</sup>

where  $\Delta U_v$  is the molar internal energy of vaporization at the system temperature, which also can be calculated from the Soave-Redlich-Kwong EOS. The remaining parameters are the molar volume of asphaltene,  $v_a$ , and the solubility parameter of asphaltene,  $\delta_a$ , which are essential to the performance of this model. The molar volume of asphaltene can only be speculated on. Hirschberg *et al.*<sup>6</sup> used values of  $v_a$  in the range of 1 to 4 m<sup>3</sup>/kmol. The solubility parameter of asphaltene can be estimated by measuring the solubility of asphaltene in different solvents of increasing solubility parameters. The asphaltene is assumed to have the solubility parameter of the best solvent. Hirschberg *et al.*<sup>6</sup> suggests that the solubility parameter of asphaltene is close to that of naphthalene. Eq. 9.10 gives the amount (volume fraction) of asphaltene soluble in the oil mixture. The amount of precipitation is determined by the difference between the total amount of asphaltenes present in the initial oil and the solubility of asphaltene under given conditions.

The solubility parameter can be correlated as a linear equation with respect to temperature as

$$\delta_a = a + bT, \dots\dots\dots (9.12)$$

where  $a$  and  $b$  are constants. Parameter  $b$  is negative as the solubility parameter decreases with increasing temperature. Buckley *et al.*<sup>74</sup> and Wang and Buckley<sup>75</sup> showed that the measurements of the refractive index of crude oils can be used to determine the solubility parameters required for the Flory-Huggins model.

The Hirschberg *et al.*<sup>6</sup> approach also has been used with some degree of success by Burke *et al.*,<sup>5</sup> Kokal and Sayegh,<sup>4</sup> Novosad and Costain,<sup>8</sup> Nor-Azian and Adewumi,<sup>76</sup> and Rassamdana *et al.*<sup>33</sup>; de Boer *et al.* used this model to screen crude oils for their tendency to precipitate asphaltene. They compared properties of some crudes in which asphaltene problems were encountered and properties of crudes that operated trouble free. They found that asphaltene problems were encountered with light crudes with high C<sub>1</sub> to C<sub>3</sub> contents, high bubblepoint pressures, large differences between reservoir pressure and bubblepoint pressure, and high compressibility. With an asphaltene molar volume of 1 m<sup>3</sup>/kmol, de Boer *et al.*<sup>2</sup> showed that the solubility of asphaltene in a light crude oil with Eq. 9.10 follows the curve shown in Fig. 9.14. Above the bubblepoint, the decrease in asphaltene solubility is caused by pressure effects. Below the bubblepoint, the increase in asphaltene solubility is caused by the variation in the oil composition. Clearly, a minimum asphaltene solubility occurs around the bubblepoint.

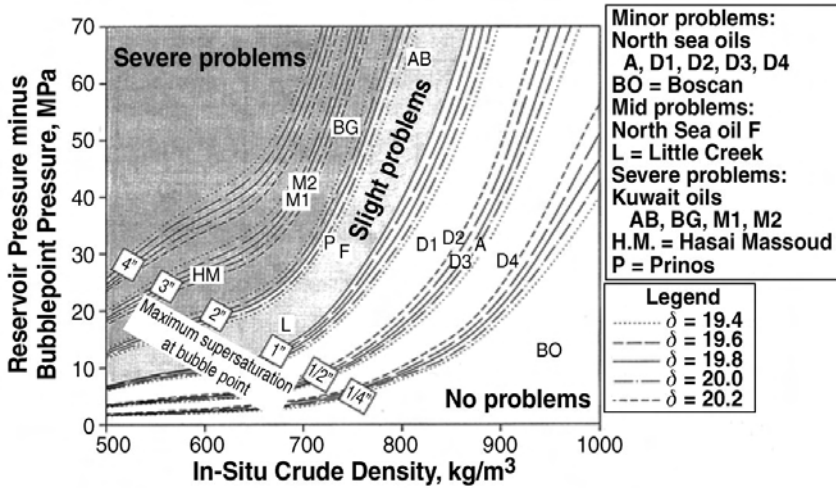


Fig. 9.15—Maximum supersaturation of asphaltene at saturation pressure.<sup>2</sup>

de Boer *et al.*<sup>2</sup> calculated the solubility of asphaltene with Eq. 9.10 for different values of in-situ crude oil densities and asphaltene-solubility parameters. They also introduced a maximum supersaturation at bubblepoint defined as

$$\frac{\Delta\Phi_a}{\Phi_a} = \int_{p_b}^{p_r} \left( \frac{1}{\Phi_a} \frac{\partial \Phi_a}{\partial p} \right)_T dp \cong \left( \frac{1}{\Phi_a} \frac{\partial \Phi_a}{\partial p} \right)_{T, p_b} (p_r - p_b), \dots\dots\dots (9.13)$$

where  $p_r$  and  $p_b$  are, respectively, the reservoir pressure and the bubblepoint pressure at the reservoir temperature. Fig. 9.15 shows the maximum supersaturation at the bubblepoint as a function of the difference between reservoir and bubblepoint pressure, the in-situ oil density, and the asphaltene-solubility parameter. The influence of the asphaltene-solubility parameter is very small. Supersaturations are larger for lighter crudes. The boundary between problem and nonproblem areas lies at a maximum supersaturation of approximately 1. Although these results were derived with North Sea and Kuwait crudes, Hammami *et al.*<sup>58</sup> showed that they also are applicable to crudes from the Gulf of Mexico.

**Extension of Flory-Huggins Model.** The Flory-Huggins model initially was developed for polymer solutions. The Hirschberg *et al.*<sup>6</sup> approach is based on the representation of asphaltene as a homogeneous polymer. Novosad and Constain<sup>8</sup> used an extension of the model that includes asphaltene polymerization and asphaltene-resin association in the solid phase. Kawanaka *et al.*<sup>77</sup> proposed an improvement whereby the precipitated asphaltene is treated as a heterogeneous polymer (i.e., a mixture of polymers of different molecular weights). The Scott-Magat theory was used to obtain a solubility model for a given molecular-weight distribution for asphaltene. Cimino *et al.*<sup>57</sup> also used the Flory-Huggins model with two components (solvent and asphaltene) but considered the solid phase to be a mixture of solvent and asphaltene instead of pure asphaltene as in Hirschberg *et al.*'s approach. Yang *et al.*<sup>78</sup> proposed a multicomponent Flory-Huggins model in which components are the same as the EOS components used in the oil/gas flash calculations.

**Multicomponent Activity Coefficient Models.** These models are derived from methods for modeling wax precipitation.<sup>39,79,80</sup> Multicomponent solid/liquid  $K$  values are derived from Eq.

9.7 and then used with an EOS in a three-phase oil/gas/solid flash calculation. The solid/liquid  $K$  values are defined as

$$K_{is} = \frac{y_{is}}{y_{io}} \quad \text{..... (9.14)}$$

Eq. 9.7 gives

$$K_{is} = \frac{\gamma_{io} f_{io}^*}{\gamma_{is} f_{is}^*} \exp\left(\int_0^p \frac{\Delta v_i}{RT} dp\right) \quad \text{..... (9.15)}$$

$$\text{with } \Delta v_i = v_{io} - v_{is} \quad \text{..... (9.16)}$$

Eq. 9.16 is equivalent to<sup>79,80</sup>:

$$K_{is} = \frac{\gamma_{io}}{\gamma_{is}} \exp\left[\frac{\Delta H_{if}}{RT} \left(1 - \frac{T}{T_{if}}\right) - \frac{\Delta C_{pi}}{R} \left(1 - \frac{T_{if}}{T} + \ln\left(\frac{T_{if}}{T}\right)\right) + \int_0^p \frac{\Delta v_i}{RT} dp\right], \quad \text{..... (9.17)}$$

where  $T_{if}$  = fusion temperature of component  $i$ ,  $\Delta C_{pi} = C_{po,i} - C_{ps,i}$ , heat capacity change of fusion, and  $\Delta H_{if}$  = heat of fusion of component  $i$ .  $\Delta C_{pi}$  is assumed to be independent of temperature in Eq. 9.17.

Starting with Eq. 9.17, methods were derived through the use of different models for activity coefficients. The earliest approach is from Won<sup>79</sup> in the modeling of wax precipitation. Won<sup>79</sup> suggested that the term involving  $\Delta C_{pi}$  and the integral involving  $\Delta v_i$  are negligible and used regular solution theory to calculate the activity coefficients in Eq. 9.17 as follows.

$$\gamma_{io} = \exp\left[\frac{v_{io}(\delta_o - \delta_{io})}{RT}\right]; \quad \gamma_{is} = \exp\left[\frac{v_{is}(\delta_s - \delta_{is})}{RT}\right], \quad \text{..... (9.18)}$$

$$\delta_o = \sum_{i=1}^{n_c} \Phi_{io} \delta_{io}; \quad \delta_s = \sum_{i=1}^{n_c} \Phi_{is} \delta_{is}; \quad \text{and..... (9.19)}$$

$$\Phi_{io} = \frac{y_{io} v_{io}}{\sum_{i=1}^{n_c} y_{jo} v_{jo}}; \quad \Phi_{is} = \frac{y_{is} v_{is}}{\sum_{j=1}^{n_c} y_{js} v_{js}}, \quad \text{..... (9.20)}$$

where  $\delta_{ik}$  is the solubility parameter of component  $i$  in phase  $k$  ( $k = o, s$ ),  $v_{ik}$  is the molar volume of component  $i$  in phase  $k$ , and  $\Phi_{ik}$  is the volume fraction of component  $i$  in phase  $k$ . Won gave solubility parameter values,  $\delta_{io}$  and  $\delta_{is}$ , for normal paraffins up to  $C_{40}$ . Correlations also are provided to calculate  $\Delta H_{if}$ ,  $v_{io}$ , and  $v_{is}$ . Although Won's model was developed for wax precipitation, Thomas *et al.*<sup>9</sup> have applied it with some success in predicting asphaltene precipitation. However, they have developed their own correlations for solubility parameters. MacMillan *et al.*<sup>56</sup> also used Won's model but kept all the terms in Eq. 9.17 instead of neglecting the



terms involving  $\Delta C_{pi}$  and  $\Delta v_i$  as Won did. They also included additional multiplication factors to the different terms in Eq. 9.17 to facilitate phase-behavior matching.

Hansen *et al.*<sup>38</sup> and Yarranton and Masliyah<sup>71</sup> used the Flory-Huggins model to calculate the activity coefficients in Eq. 9.17. Hansen *et al.*<sup>38</sup> applied their method to the modeling of wax precipitation, while Yarranton and Masliyah<sup>71</sup> modeled precipitation of Athabasca asphaltenes. Yarranton and Masliyah<sup>71</sup> proposed an approach for calculating the molar volumes and solubility parameters from experimental measurements of molar mass and density. Asphaltene density, molar volume, and solubility parameter are correlated with molar mass. Zhou *et al.*<sup>72</sup> used the Flory-Huggins polymer-solution theory with a modification to account for the colloidal suspension effect of asphaltenes and resins.

**9.4.3 EOS Models.** These approaches model the oil, gas, and precipitate by an EOS, which is used to calculate the component fugacities in different phases. Cubic EOSs have been used to model petroleum-reservoir fluids that exhibit vapor/liquid 1/liquid 2 behavior (see Fussell,<sup>81</sup> Nghiem and Li,<sup>82</sup> or Godbole *et al.*<sup>83</sup>). Godbole *et al.*<sup>83</sup> observed that the apparent second liquid phase could be approximated as a mixture of aggregated asphaltenes (solid phase) entrained in a portion of the other liquid phase in the modeling of mixtures of crude oil from the North Slope of Alaska and enriched gas. Under certain conditions, a phase-behavior program that includes a three-phase calculation with an EOS could be used to model some aspects of asphaltene precipitation; however, the prevailing approach consists of the use of a cubic EOS (e.g., Soave-Redlich-Kwong EOS<sup>73</sup> or Peng-Robinson EOS<sup>84</sup>) for the oil and gas phases and a solid model for the precipitate.

The simplest model for precipitated asphaltene is the single-component solid model. The precipitated asphaltene is represented as a pure solid, while the oil and gas phases are modeled with a cubic EOS. The fugacity of the pure solid is given by

$$\ln f_s = \ln f_s^* + \frac{v_s(p - p^*)}{RT}, \dots\dots\dots (9.21)$$

where  $f_s$  = solid fugacity,  $f_s^*$  = reference solid fugacity,  $p$  = pressure,  $p^*$  = reference pressure,  $R$  = gas constant,  $v_s$  = solid molar volume, and  $T$  = temperature. The following fugacity-equality equations are solved to obtain oil/gas/solid equilibrium.

$$f_{io} = f_{ig}, \quad i = 1, \dots, n_c \dots\dots\dots (9.22a)$$

$$\text{and } f_{ao} = f_s \dots\dots\dots (9.22b)$$

The oil and gas fugacities,  $f_{io}$  and  $f_{ig}$ , for component  $i$  are calculated from an EOS. In Eq. 9.22b, subscript  $a$  denotes the asphaltene component in solution. Normally, this asphaltene component is the heaviest and last component of the oil (i.e.,  $a = n_c$ ). The following simple stability test can be used to determine whether there is asphaltene precipitation: if  $f_{ao} \geq f_s$ , asphaltene precipitation occurs, and if  $f_{ao} < f_s$ , there is no precipitation.

Earlier applications of the single-component solid model for asphaltene precipitation were not successful.<sup>9</sup> Nghiem *et al.*<sup>85</sup> introduced a method for representing the asphaltene component in the oil that improves the capabilities of the single-component solid model to predict asphaltene precipitation. The method was subsequently refined by Nghiem *et al.*<sup>86-90</sup> The key to the approach is the split of the heaviest fraction of the oil into two pseudocomponents: one that does not precipitate (nonprecipitating component) and one that can precipitate (precipitating component). These two pseudocomponents have identical critical temperatures, critical pres-

**TABLE 9.2—MODELED FLUID COMPOSITION FOR A NORTH SEA RESERVOIR FLUID<sup>87</sup>**

No.	Component	Dead Oil Composition (mol%)	Separator Gas Composition (mol%)	MW
1	N <sub>2</sub> & C <sub>1</sub>	8.365	70.216	16.614
2	C <sub>2</sub> -C <sub>5</sub>	25.273	28.319	41.425
3	C <sub>6</sub> -C <sub>9</sub>	27.014	1.465	94.626
4	C <sub>10</sub> -C <sub>15</sub>	24.625	0.000	167.200
5	C <sub>21</sub> -C <sub>31</sub>	9.698	0.000	354.646
6	C <sub>32A+</sub>	3.654	0.000	591.682
7	C <sub>32B+</sub>	1.371	0.000	591.682
	Total	100.000	100.000	

tures, acentric factors, and molecular weights. The differences are in the interaction coefficients. The interaction coefficients between the precipitating components and the light components are larger than those between the nonprecipitating component and the light components. The parameters of the model are the reference fugacity and the solid molar volume. The reference fugacity could be estimated from a data point on the APE, and a value for solid molar volume slightly larger than the EOS value for the pure component  $a$  is adequate.<sup>85</sup>

The following application of the model to a North Sea fluid from Nghiem *et al.*<sup>87</sup> illustrates the procedure. **Table 9.2** shows the pseudocomponent representation of the reservoir fluid with the separator gas and separator oil compositions. The reservoir oil corresponds to a combination of 65.3 mol% separator oil and 34.7 mol% separator gas. The crucial step in the modeling of asphaltene is the split of the heaviest component in the oil (e.g., C<sub>32+</sub>) into a nonprecipitating component (C<sub>32A+</sub>) and a precipitating component (C<sub>32B+</sub>). These two components have identical critical properties and acentric factors but different interaction coefficients with the light components. The precipitating component has larger interaction coefficients with the light components. With larger interaction coefficients, the precipitating component becomes more “incompatible” with the light components and tends to precipitate as the amount of light component in solution increases. Although C<sub>32B+</sub> is called the precipitating component, the amount that precipitates is governed by Eq. 9.21. Normally, only a portion of the total amount of C<sub>32B+</sub> will precipitate during a calculation. Hirschberg *et al.*<sup>6</sup> reports that the asphalt precipitate from a tank oil consists mainly (90%) of C<sub>30</sub> to C<sub>60</sub> compounds. For the purpose of modeling asphaltene precipitation, a heaviest component in the vicinity of C<sub>30+</sub> is adequate. For this example, C<sub>32+</sub> is used.

The Peng-Robinson EOS was used to model the oil and gas phases. The critical properties and acentric factors of the pseudocomponents in **Table 9.2** are calculated as described in Li *et al.*<sup>91</sup> The interaction coefficients are calculated from

$$d_{ij} = 1 - \left( \frac{2 \cdot v_{ci}^{1/6} \cdot v_{cj}^{1/6}}{v_{ci}^{1/3} + v_{cj}^{1/3}} \right)^e, \dots\dots\dots (9.23)$$

where  $d_{ij}$  = the interaction coefficient between component  $i$  and  $j$ ,  $v_{ci}$  = the critical volume of component  $i$ , and  $e$  = an adjustable parameter. A value of  $e(C_{32A+}) = 0.84$  and a value of  $e(C_{32B+}) = 1.57$  were found to provide a good match of the saturation and onset pressure. The reference solid fugacity was obtained by calculating the fugacity of oil at one point on the

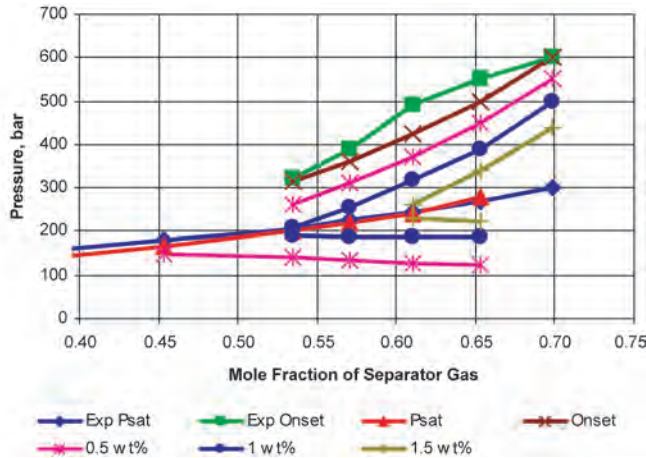


Fig. 9.16—PX asphaltene precipitation and saturation curves for a North Sea fluid at 90°C.<sup>87</sup>

APE (recombined oil with 69.9 mol% separator gas and 30 000 kPa) with the Peng-Robinson EOS and equating it to  $f_s^*$ . The molar volume of the asphaltene precipitate was assumed equal to 0.9 m<sup>3</sup>/kmol.

Fig. 9.16 shows a good match of the experimental and calculated APE and saturation pressure curves at the reservoir temperature of 90°C. The model was able to predict precipitation conditions that are far from the reference conditions used to determine  $f_s^*$ . Fig. 9.16 shows the amounts of precipitation calculated as constant weight percent of precipitate (similar to “quality lines” in oil/gas phase diagrams). As pressure decreases below the APE, the amount of precipitation increases and reaches a maximum at the saturation pressure. Below the saturation pressure, the amount of precipitation decreases with decreasing pressure. The results are consistent with the laboratory observations described in Sec. 9.3.

For nonisothermal conditions, Eq. 9.24 can be used to calculate the solid fugacity at ( $p, T$ ) from the solid fugacity at a reference condition ( $p^*, T^*$ ).<sup>88,92</sup>

$$\begin{aligned} \ln f_s(p, T) - \ln f_s(p^*, T^*) &= \ln f_\ell(p, T) - \ln f_\ell(p^*, T^*) \\ &- \frac{\Delta H_f}{R} \left( \frac{1}{T} - \frac{1}{T^*} \right) - \frac{\Delta C_p}{R} \left[ \ln \left( \frac{T}{T^*} \right) - T_f \left( \frac{1}{T} - \frac{1}{T^*} \right) \right] \\ &+ \frac{1}{RT} \int_{p_f}^p (v_s - v_\ell)_T dp - \frac{1}{RT^*} \int_{p_f}^{p^*} (v_s - v_\ell)_{T^*} dp, \dots\dots\dots (9.24) \end{aligned}$$

where  $f_\ell$  = fugacity of the asphaltene component in the pure liquid state,  $T_f$  = melting point temperature,  $v_\ell$  = molar volume of liquid,  $\Delta C_p$  = heat capacity of fusion, and  $\Delta H_f$  = enthalpy of fusion.

Kohse *et al.*<sup>92</sup> used Eq. 9.24 to model the precipitation behavior of a crude oil with changes in pressure and temperature. Fig. 9.17 shows good agreements between the experimental and calculated APE and saturation-pressure curves. The measured data point of 1.6 wt% of precipitate also is close to the predictions.

The previous two examples illustrate the application of the single-component solid model to the modeling of precipitation behavior of crudes with changes in pressure, temperature, and composition. From a mechanistic point of view, the nonprecipitating component can be related

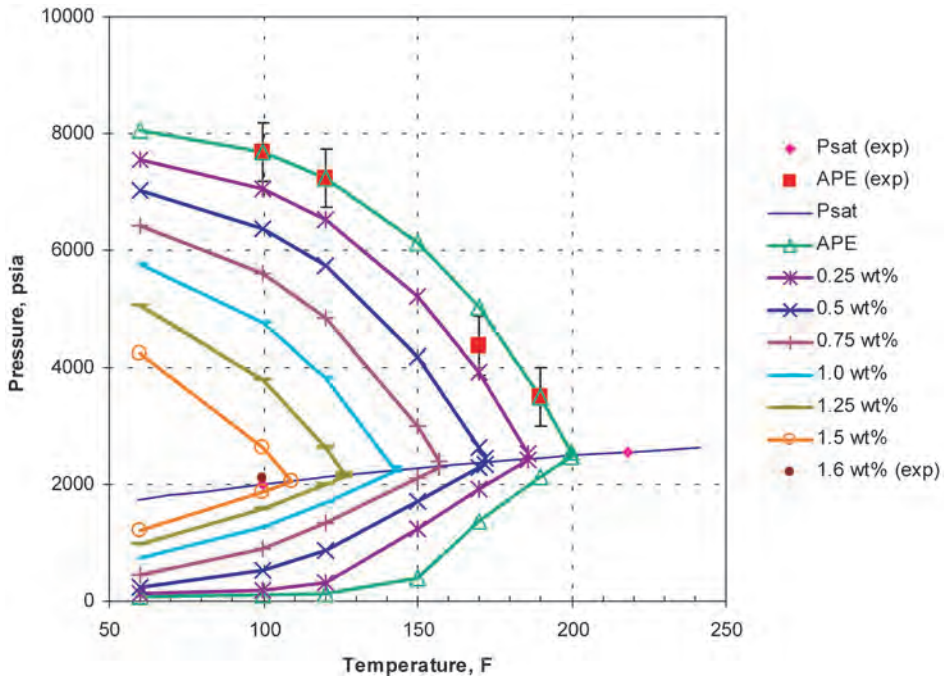
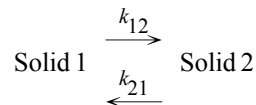


Fig. 9.17—PT asphaltene and saturation curves for a South American fluid.<sup>92</sup>

to resins, asphaltene/resin micelles that do not dissociate, and heavy paraffins. The precipitating component corresponds to both the asphaltenes that dissociate and the asphaltene/resin micelles that precipitate unaltered. Because of identical critical properties and acentric factors, the non-precipitating and precipitating components behave as a single component in solution. The larger interaction coefficients between the precipitating and the solvent components cause the precipitation of the former with the addition of solvent. The amount of precipitation depends on the solution of Eqs. 9.22a and 9.22b. Normally, only a portion of the precipitating component actually precipitates.

Solid precipitation with the previous model is reversible. Nghiem *et al.*<sup>90</sup> proposed an enhancement to the approach to obtain partial irreversibility. A second solid (Solid 2) is introduced that is obtained from the reversible solid (Solid 1) through a chemical reaction:



If the forward reaction rate  $k_{12}$  is much larger than the backward reaction rate  $k_{21}$ , Solid 2 behaves as a partially irreversible solid.

**9.4.4 Thermodynamic-Colloidal Model.** Leontaritis and Mansoori<sup>28</sup> proposed a more mechanistic approach based on the assumption that asphaltenes exist in the oil as solid particles in colloidal suspension stabilized by resins adsorbed on their surface. This thermodynamic-colloidal model assumes thermodynamic equilibrium between the resins in the oil phase and the resins adsorbed on the surface of colloidal asphaltene (asphaltene micelle). The corresponding equilibrium equation is

$$\mu_{r,o} = \mu_{r,m} \dots \dots \dots (9.25)$$

Assuming that resins behave as monodisperse polymers and applying the Flory-Huggins polymer-solution theory gives the volume fraction of dissolved resins as

$$\ln \Phi_r = \frac{v_r}{v_m} - \frac{v_r}{RT} (\delta_m - \delta_r)^2 - 1, \dots \dots \dots (9.26)$$

which is analogous to Eq. 9.10 for the asphaltene component in Hirschberg *et al.*'s approach. In Hirschberg *et al.*'s approach, the asphaltene component contains both resins and asphaltene, whereas Eq. 9.26 applies to the resins only. As in Hirschberg *et al.*'s approach, EOS flash calculations with a multicomponent system are performed to obtain an oil/gas split and oil properties from which  $\Phi_r$  is calculated. This value of  $\Phi_r$  is compared with a critical resin concentration,  $\Phi_{cr}$ , which is given as a function of pressure, temperature, molar volume, and solubility parameters.  $\Phi_{cr}$  is the key parameter of the model. If  $\Phi_r > \Phi_{cr}$ , the system is stable and no precipitation occurs. If  $\Phi_r \leq \Phi_{cr}$ , asphaltene precipitation occurs. The amount of precipitated asphaltene can be made a function of the asphaltene particle sizes.

**9.4.5 Thermodynamic-Micellization Model.** Pan and Firoozabadi<sup>93,94</sup> proposed the most mechanistic approach to model asphaltene precipitation by calculating the Gibbs free energy of formation of the asphaltene micelle and including it in the phase-equilibrium calculations. Details of the approach can be found in Firoozabadi.<sup>95</sup> Fig. 9.18 portrays schematically the system to be modeled. The species in the liquid phase ( $L_1$ ) are monomeric asphaltenes, monomeric resins, micelles, and asphalt-free oil species. The micelle consists of a core of  $n_1$  asphaltene molecules surrounded by a shell containing  $n_2$  resins molecules. The precipitate phase is considered as a liquid mixture ( $L_2$ ) of asphaltene and resin molecules. An expression for Gibbs free energy of formation of the micelle,  $\Delta G_m^0$ , which includes  $n_1$ ,  $n_2$ , and the shell thickness,  $D$ , was proposed. The Gibbs free energy of the liquid phase,  $L_1$ , then is derived with an EOS for the asphalt-free oil species, activity models for the monomeric asphaltenes and resins, and the Gibbs free energy of formation of the micelle,  $\Delta G_m^0$ . Similarly, the Gibbs free energy of the precipitated phase,  $L_2$ , which is a binary mixture of monomeric asphaltenes and resins, also is derived with the use of an EOS. The total Gibbs free energy of the system,

$$G = G_{L_1} + G_{L_2}, \dots \dots \dots (9.27)$$

then is minimized with respect to  $n_1$  = number of asphaltene molecules in the micellar core,  $n_2$  = number of resin molecules in the micellar cell,  $D$  = shell thickness of the micelle,  $N_{a, L_1}$  = number of asphaltene monomers in liquid phase  $L_1$ ),  $N_{r, L_1}$  = number of resin monomers in phase  $L_1$ ,  $N_{m, L_1}$  = number of micelles in phase  $L_1$ ,  $N_{a, L_2}$  = number of asphaltene monomers in precipitated phase  $L_2$ , and  $N_{r, L_2}$  = number of resin monomers in phase  $L_2$ . The minimization requires a robust numerical procedure.

The model was applied to predict precipitation from a tank oil with propane,<sup>6</sup> Weyburn oil with CO<sub>2</sub>,<sup>10</sup> and a North Sea oil with separator gas. Fig. 9.19 shows the predictions of Weyburn oil with CO<sub>2</sub> obtained with the thermodynamic-micellization model. For comparison, the match obtained with the pure solid model<sup>187</sup> also is shown.

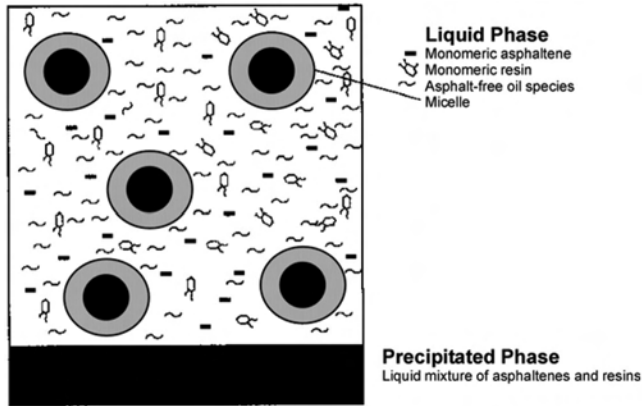


Fig. 9.18—Schematic representation of crude oil with asphaltene micelles.<sup>94</sup>

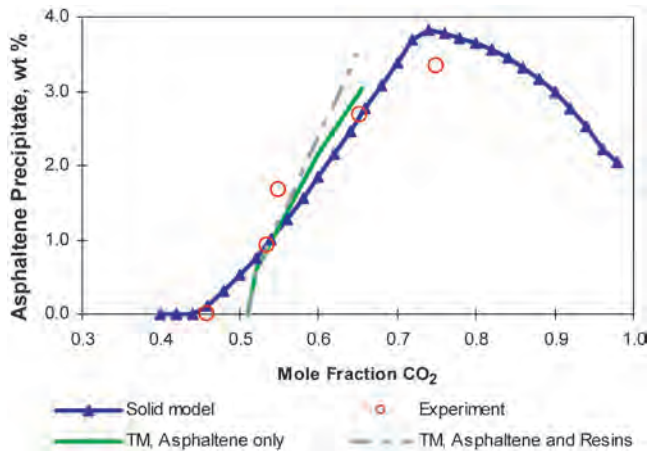


Fig. 9.19—Experimental and calculated precipitation with thermodynamics-micellization model<sup>94</sup> and solid model<sup>87</sup> of Weyburn reservoir fluid and CO<sub>2</sub> mixtures at 160 bar and 332 K. Experimental data from Srivastava *et al.*<sup>10</sup>

## 9.5 Asphaltene Deposition and Plugging

**9.5.1 Outline.** The measurements and modeling of the phase behavior aspect of asphaltene precipitation were described in the previous sections. After precipitation, asphaltene can remain as a suspended solid in the oil or deposit onto the rock. Here, the term precipitation corresponds to the formation of a solid phase from thermodynamic equilibrium and deposition means the settling of solid particles onto the rock surface. Deposition will induce alteration of wettability (from water-wet to oil-wet) of the rock and plugging of the formation. These aspects have been known for a long time and are the subject of many recent investigations. This section reviews the investigations and laboratory observations of these aspects.

**9.5.2 Experiments.** Measurements of the deposition and plugging effects were performed by Piro *et al.*<sup>96</sup> in sand packs and by Turta *et al.*,<sup>12</sup> Minssieux,<sup>97</sup> and Ali and Islam<sup>98</sup> in cores to study asphaltene deposition and the subsequent effect of permeability reduction. Yeh *et al.*,<sup>99</sup> Kamath *et al.*,<sup>100</sup> and Yan *et al.*<sup>101</sup> performed core displacements to investigate the effect of

wettability alteration caused by deposition and its subsequent effect on the recovery. The following sections discuss the results from these experiments with techniques for modeling the observed phenomena.

**9.5.3 Deposition and Plugging.** Asphaltene deposition in porous media exhibits similarities with the deposition of fines. The main phenomena are adsorption, surface deposition, and plugging deposition.

Piro *et al.*<sup>96</sup> used asphaltene precipitates collected from a field in northern Italy or induced by diluting two crude oils with n-heptane. The diluted mixture of crude oil with a given concentration of precipitate was injected into sand packs, and the concentration of asphaltene precipitate at the outlet was measured. The deposited amounts were calculated by difference.

Minssieux<sup>97</sup> performed comprehensive core experiments for three crude oils from different parts of the world (France, North Africa, and North America) and four types of cores (three sandstone cores with different permeabilities and clay contents and a core from the Algerian Hassi Messaoud field, which suffers strong asphaltene-precipitation problems). Asphaltene precipitates were obtained by diluting crude oils with n-heptane. Pressure drops across the core were measured to determine the permeability reduction caused by asphaltene deposition. The amounts of deposited asphaltene along the core were estimated with a pyrolysis technique.

Ali and Islam<sup>98</sup> performed core tests with crude oils from the United Arab Emirates. Crude oil with 3 wt% of asphaltene precipitate (induced by n-heptane) was injected into carbonate cores at four different rates. The pressure drops across the core were measured to determine the permeability reduction.

Turta *et al.*<sup>12</sup> performed high-pressure core-displacement experiments with propane. Crude oils from west-central and northwestern Alberta were used. Asphaltene precipitation occurred within the core when propane mixed with the oil in the displacement process. Permeability reduction was inferred by measuring pressure drops across the core.

**Adsorption.** The first step in the deposition is the adsorption of asphaltene onto the rock surface. The adsorption of asphaltene onto different rocks has been measured extensively in static experiments that showed that the asphaltene adsorption onto different rocks can be modeled with Langmuir isotherms.<sup>102–104</sup> Fig. 9.20 from Dubey and Waxman<sup>103</sup> shows typical Langmuir isotherms for asphaltene adsorption on different rocks. The Langmuir isotherm equation is

$$w_{sa} = \frac{(w_{sa})_{\max} K_a C_{sf}}{K_a C_{sf} + 1}, \dots\dots\dots (9.28)$$

where  $C_{sf}$  = concentration of suspended solid in the oil phase,  $w_{sa}$  = mass of adsorbed asphaltene per mass of rock,  $(w_{sa})_{\max}$  = maximum adsorbed mass fraction (the plateau in Fig. 9.20), and  $K_a$  = ratio of rate constants of the adsorption/desorption reactions. Adsorption is higher for rock containing a higher content of shales. Because adsorption is a surface phenomenon, its main effect is the alteration of the rock wettability from water-wet to oil-wet.

**General Deposition Process.** In addition to adsorption, Minssieux<sup>97</sup> showed that deposition occurs because of mechanical entrapment similar to the deposition of fines in porous media. Pressure drops across the core were measured for several experiments to assess the deposition and plugging effects caused by asphaltene. Minssieux reported that the most noticeable plugging occurred in sandstones containing clays and in tight sandstones. Fig. 9.21 shows the reduction of oil permeability as a function of pore volume injected for sandstones with and without clay. Fig. 9.22 shows the permeability reduction for tight sandstone. Minssieux also used the pore-blocking model of Wojtanowicz *et al.*<sup>105</sup> to analyze the experimental results.

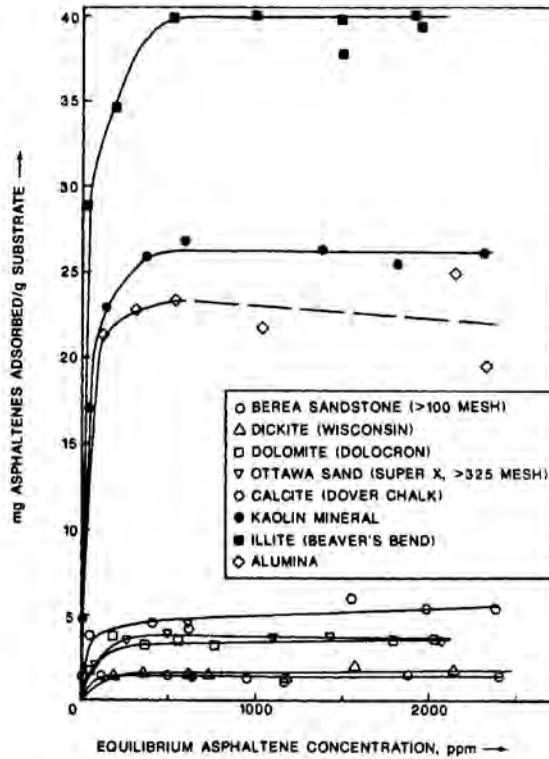


Fig. 9.20—Langmuir isotherms for asphaltene adsorption.<sup>103</sup>

Ali and Islam<sup>98</sup> combined a model for adsorption with the model of Gruesbeck and Collins<sup>106</sup> for the entrainment and deposition of fines in porous media to analyze their experimental results. Gruesbeck and Collins assumed that the porous medium could be divided into two parallel pathways: small pore sizes, in which plug-type deposits occur and can eventually be plugged completely, and larger pore sizes, in which surface nonplugging deposits occur. Particles could be mobilized from the surface deposits if the fluid velocity exceeds a critical value. Fig. 9.23 illustrates this concept.

For nonpluggable pathways,

$$\frac{\partial \sigma_{np}}{\partial t} = \begin{cases} \beta C_a - \alpha(u_{np} - u_c)\sigma_{np} & \text{if } u_{np} > u_c \\ \beta C_a & \text{if } u_{np} \leq u_c \end{cases}, \dots\dots\dots (9.29)$$

whereas for pluggable pathways,

$$\frac{\partial \sigma_p}{\partial t} = (\gamma + \chi\sigma_p)u_p C_a, \dots\dots\dots (9.30)$$

where  $C_a$  = concentration of precipitated asphaltene in weight percent,  $u_c$  = critical speed required to mobilize surface deposit asphaltene,  $u_{np}$  = fluid velocity in nonpluggable pathways,  $\sigma_{np}$  = volume fraction of deposited asphaltene in nonpluggable pathway,  $\sigma_p$  = volume fraction of deposited asphaltene in pluggable pathway, and  $\alpha, \beta, \chi,$  and  $\gamma$  = model parameters.



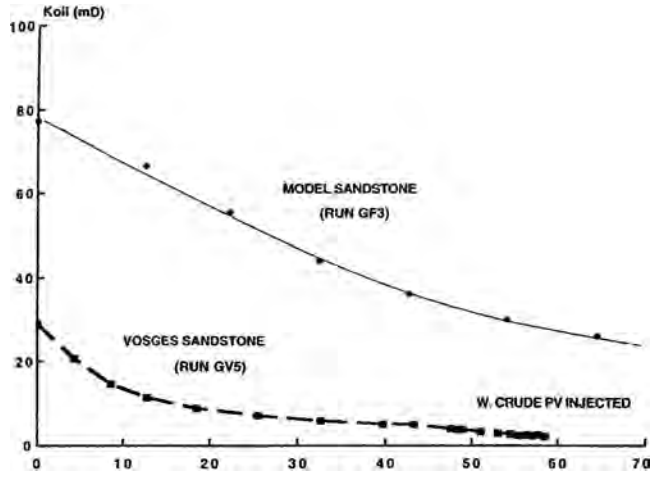


Fig. 9.21—Clay influence on plugging evolution.<sup>97</sup>

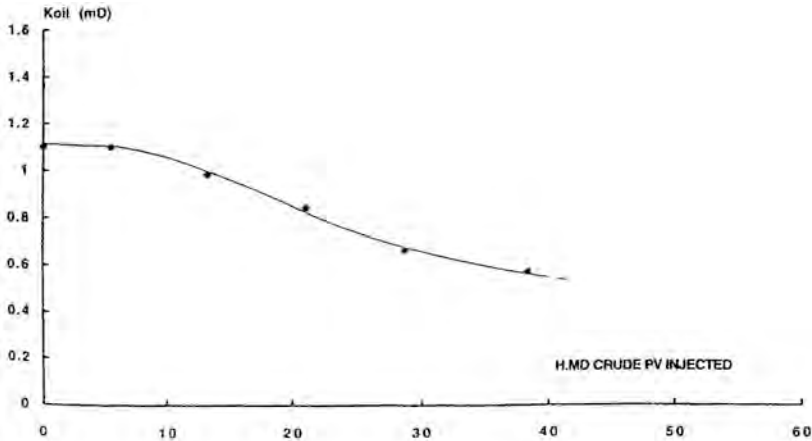


Fig. 9.22—Plugging evolution in a tight sandstone.<sup>97</sup>

Gruesbeck and Collins gave empirical correlations for calculating  $u_p$  and  $u_{np}$  from  $u$ , as well as the permeabilities of pluggable and nonpluggable pathways as functions of the volumes of deposited asphaltene. Eq. 9.29 implies that the deposited asphaltene in nonpluggable pathways is mobilized if the velocity,  $u_{np}$ , is greater than the critical velocity,  $u_c$ . Ali and Islam<sup>98</sup> developed a 1D, single-phase flow simulator with the Gruesbeck and Collins deposition model. They identified three regimes for asphaltene deposition and plugging depending on the flow rate: monotonous steady state, quasisteady state, and continuous plugging. Fig. 9.24 shows the experimental results and the match obtained with the model described in Eqs. 9.29 and 9.30. At low flow rates (monotonous steady-state regime), the permeability reduction took place in a monotonous fashion. At intermediate flow rates (quasisteady-state regime), initial reduction in permeability was observed until a minimum was reached. After reaching this minimal value, the trend was reversed with an increase in permeability. Ali and Islam attributed this increase to the mobilization of asphaltene deposited in nonpluggable pathways. At higher flow rates

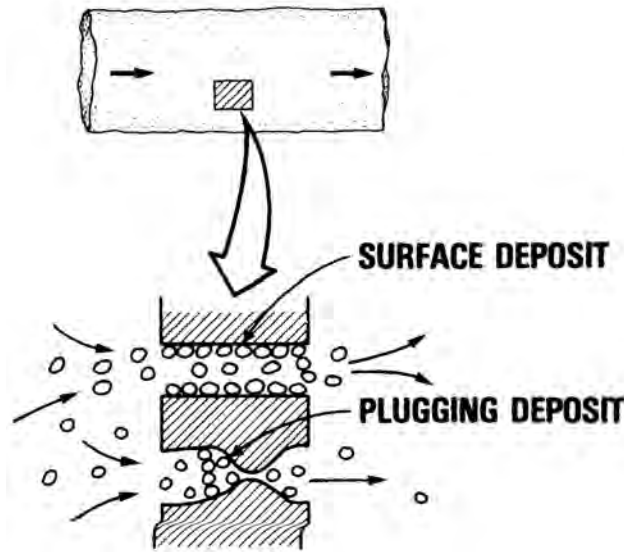


Fig. 9.23—Parallel pathway model for deposition.<sup>105</sup>

(continuous-plugging regime), the permeability reduction began late in the injection process but was very rapid once begun.

Wang and Civan<sup>107,108</sup> modified the Gruesbeck and Collins model to obtain

$$\frac{\partial E_a}{\partial t} = \beta C_a \Phi - \alpha E_a (v_o - v_c) + \gamma(1 + \eta) u_o, \dots\dots\dots (9.31)$$

where  $E_a$  = volume of deposited asphaltene per bulk volume of rock,  $v_c$  = critical interstitial velocity for surface deposition,  $v_o$  = interstitial oil velocity ( $= u_o/\Phi$ ), and  $\alpha, \beta, \gamma, \eta$  are model parameters. The separation of pathways into pluggable and nonpluggable has been eliminated. The last term in Eq. 9.31 represents the plugging deposit and is set to zero if the average pore throat diameter is greater than a critical pore throat diameter (i.e., there is no plugging deposit if the pore throat is large).

The porosity occupied by the fluid is

$$\Phi = \Phi_0 - E_a, \dots\dots\dots (9.32)$$

where  $\Phi_0$  is the initial porosity. The reduction in permeability is calculated from

$$k = f_p k_0 \left( \frac{\Phi}{\Phi_0} \right)^3, \dots\dots\dots (9.33)$$

where  $k_0$  is the initial permeability and  $f_p$  is the porous medium particle transport efficiency factor.<sup>107</sup> Wang and Civan<sup>107</sup> developed a 1D, three-phase, four-pseudocomponent simulator that incorporates the previous deposition and plugging model. They showed that their model could match some of the core deposition experiments by Minssieux<sup>97</sup> and Ali and Islam.<sup>98</sup>

Kocabas and Islam<sup>109</sup> extended the model of Ali and Islam to the analysis of deposition and plugging in the near-wellbore region. Leontaritis<sup>110</sup> also developed a single-phase radial

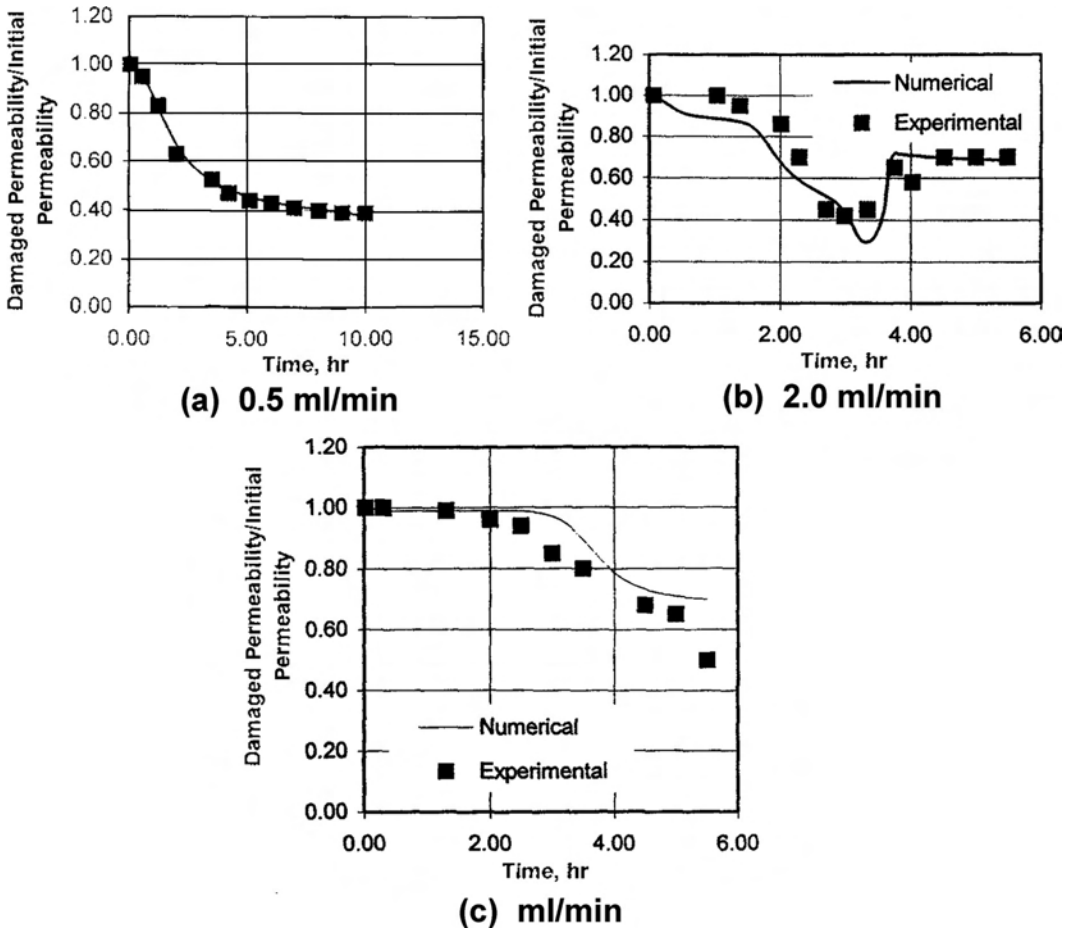


Fig. 9.24—Effect of flow rates on permeability reduction.<sup>98</sup>

model to analyze the near-well pressure behavior when asphaltene deposition and plugging occur. Ring *et al.*<sup>111</sup> described a three-component, thermal reservoir simulator for the deposition of waxes in which only surface deposition is considered. Nghiem *et al.*<sup>87,88</sup> have incorporated in a 3D compositional simulator both a thermodynamic single-component solid model for asphaltene precipitation and a deposition model based on adsorption and plugging deposit. A resistance factor approach was used to model permeability reduction caused by asphaltene deposition. Qin *et al.*<sup>112</sup> proposed a method for compositional simulation based on similar approaches.

**9.5.4 Wettability Alteration.** The alteration of formation wettability caused by asphaltene deposition has been the subject of numerous investigations. Asphaltene adsorption onto the rock surface is the main factor for wettability alteration from water-wet to oil-wet. Collins and Melrose,<sup>102</sup> Kamath *et al.*,<sup>100</sup> Clementz,<sup>113</sup> Crocker and Marchin,<sup>114</sup> and Buckley *et al.*<sup>115,116</sup> described the change of formation wettability from water-wet to mixed-wet or oil-wet on adsorption of asphaltene onto the rock surface. Clementz<sup>113</sup> discussed the permanent alteration of core properties after asphaltene adsorption. Collins and Melrose<sup>102</sup> showed that asphaltene adsorption is reduced but not eliminated by the presence of water films on water-wet rock. Crocker and Marchin<sup>114</sup> and Buckley *et al.*<sup>115,116</sup> studied asphaltene adsorption for different oil compositions and the corresponding degree of wettability alteration. Yan *et al.*<sup>101</sup> performed injection of

asphaltenes (obtained for diluting crude oils from Wyoming and Prudhoe Bay with n-hexane) into Berea core. After the displacements, imbibition tests were performed to determine changes in core wettability. They showed that the amount of adsorbed asphaltene is dependent on the ions present in the brines (in this case  $\text{Na}^+$ ,  $\text{Ca}^{2+}$ , and  $\text{Al}^{3+}$ ) and that adsorption increases with an increase in ion valency. The highest adsorption occurred with  $\text{Al}^{3+}$  in the brine. Significant changes in wettability of the sandstone core were observed after asphaltene adsorption.

Morrow<sup>117</sup> reviewed the effect of wettability on oil recovery. Wettability has been shown to affect relative permeabilities, irreducible water saturation, residual oil saturation, capillary pressures, dispersion, and electrical properties. The alteration of relative permeabilities and endpoints has the strongest influence on displacement processes. Morrow<sup>117</sup> reviewed results for core waterfloods showing that the shift toward a less water-wet condition can range from being highly adverse to highly beneficial to oil recovery. Huang and Holm,<sup>118</sup> Lin and Huang,<sup>119</sup> and Yeh *et al.*<sup>99</sup> presented results on the implication of wettability changes on water-alternating-gas (WAG) processes. Typical results for  $\text{CO}_2$  WAG processes<sup>118</sup> indicate that the amount of oil trapped in water-wet cores (45%) was much higher than that trapped in either mixed-wet (15 to 20%) or oil-wet cores (5%).

Yeh *et al.*<sup>99</sup> performed experiments in a capillary-tube visual cell showing the change in wettability on asphaltene precipitation by mixing a west Texas oil with  $\text{CO}_2$  and a Canadian Mitsue crude oil with hydrocarbon gas at reservoir conditions. They also carried out WAG coreflood experiments under reservoir conditions in which asphaltene precipitation occurred. The residual oil saturation after each flood was measured and compared with the value obtained in displacements with refined oils in which there were essentially no changes in wettability. For some experiments, they observed substantial reduction in residual oil saturations when wettability was altered. A wettability change from water-wet to oil-wet conditions increases the contact between oil and solvent and is responsible for a decrease in residual oil saturation.

Kamath *et al.*<sup>100</sup> performed injection of a precipitating solvent (n-pentane or n-heptane) in cores saturated with crude oil. The plugging caused by asphaltene was assessed by measuring pressure drops across the cores. After the injection of solvent, water was injected and recovery and relative permeabilities were measured to study the effect of deposition on displacement efficiency. Three cores were used. Core 1 is a Berea sandstone core with permeability of 236 md and porosity of 27.9%. Cores 2 and 3 are unconsolidated sandpack cores with permeability of 2380 and 1520 md and porosity of 32.7 and 31.3%, respectively. **Fig. 9.25** shows the reduction in permeability with respect to the degree of asphaltene deposition. As expected, permeability reduction was highest for the least permeable core (Core 1) and smallest for the most permeable core (Core 2). **Fig. 9.26** shows cumulative fractional recovery for Core 1 vs. pore volume of water injected for various degrees of asphaltene deposition. The results show an improved displacement efficiency with an increase in the deposited amounts. Similar results were obtained for Cores 2 and 3. Kamath *et al.*<sup>100</sup> concluded from their experiments that although deposition causes permeability reduction, it may improve the sweep efficiency through the alteration of relative permeability curves and flow-diverting effects. Shedid<sup>120</sup> performed similar displacement experiments on low-permeability carbonate cores instead of sandstone cores and observed substantial permeability damage with deposition.

The wettability alteration caused by asphaltene deposition is a complex process that is still a subject of many investigations. The degree of wettability change may not be uniform, as discussed in Al-Maamari and Buckley.<sup>121</sup> The subsequent effect of wettability on relative permeabilities and oil recovery is also a complex subject. There are still unexplored areas, and the whole process is not completely understood at this time. Although the change from water-wet to oil-wet conditions caused by asphaltene precipitation may favor sweep efficiency of waterflood or WAG processes inside the reservoir, the plugging effect near the wellbore remains

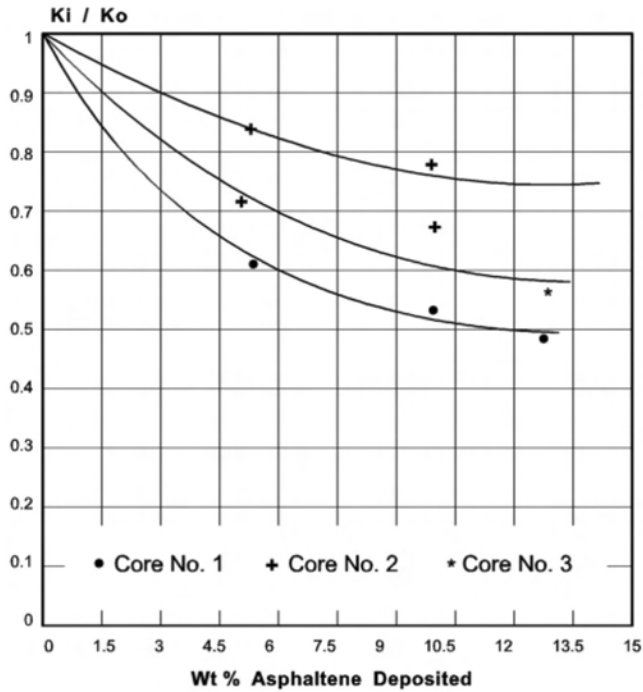


Fig. 9.25—Permeability reduction for different cores.<sup>100</sup>

detrimental to oil production. Inside the reservoir, fluids can find their way around regions of deposition, but, around the wellbore, plugging will prevent flow of oil from converging to the wellbore. Remedial actions then are required to increase production.

### 9.6 Remedial Treatment for Asphaltene Precipitation

Asphaltene precipitation and its subsequent deposition in the wellbore and near-well region are detrimental to oil production. The most effective preventive method is to operate at conditions outside the APE. This is not always possible because of the large drawdown in the vicinity of the wellbore, which lowers the reservoir pressure below the onset pressure. For precipitation in the wellbore, mechanical methods, such as rod and wireline scrapers, can be used to remove asphaltene deposits. Although these methods provide good cleaning and minimal formation damage, their application is limited to the wellbore and does not resolve the problem associated with near-wellbore formation plugging.

Because the solubility of asphaltene increases with an increase in aromatic contents, solvents such as xylene and toluene commonly are used to dissolve asphaltene deposits in both the wellbore and formation. Stricter regulations governing disposals, volatile-emission limits, and flammability concerns have made the use of xylene and toluene less attractive, and alternate solvents have been investigated.<sup>122</sup> Cosolvents for asphaltene removal also have been studied.<sup>123</sup> Cosolvents are xylene-enriched materials with water-wetting properties that use moderate-length carbon-chain alcohols. Production restoration is comparable to that obtained with xylene, but the treatment lasts longer (average of 6 to 8 months). Polymeric dispersants also have been used as alternatives to aromatic solvents.<sup>124</sup> These dispersants inhibit the deposition of asphaltene by breaking the precipitate into smaller particle sizes, which can remain in suspension in the oil phase. Solubility-parameter models have been used to evaluate and screen solvents and inhibitors.<sup>122,124</sup> Jamaluddin *et al.*<sup>125</sup> performed experiments that showed that deas-

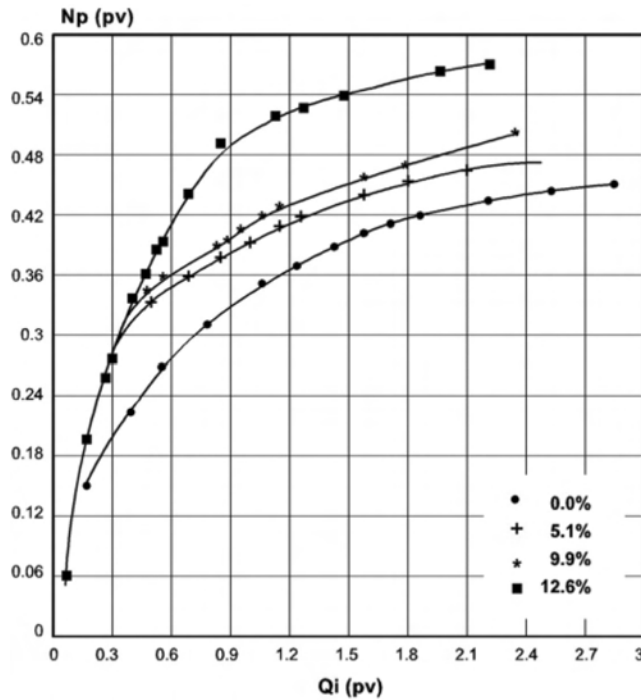


Fig. 9.26—Cumulative fractional-oil recovery vs. PV water injected for various degrees of asphaltene deposition.<sup>100</sup>

phaltned oil is a strong solvent for asphaltene because of its native resin and aromatic contents; however, the cost of producing large amounts of deasphalted oil to be used as solvent is not viable economically.

### 9.7 Experimental Analysis of Wax Characteristics of Petroleum Fluids

There are a number of experimental measurements performed on petroleum fluids to define their tendency to precipitate wax. Measurements of the temperature at which wax precipitation occurs and the amount of wax precipitated are done with stabilized (stock tank) oils and live reservoir fluids. Compositional analysis of the fluids is performed to determine the concentrations of chemical species that can precipitate as waxes. This section describes these types of analyses.

**9.7.1 Compositional Analysis of Petroleum Fluids.** As discussed in Sec. 9.2, petroleum constituents may be broadly classified as belonging to the  $C_6$ - or the  $C_{6+}$  fraction. The heavy end may be further classified with SARA analysis. Various chromatography methods allow the determination of the mass fractions of single carbon number (SCN) fractions of a fluid. One SCN is composed of all the components with boiling points between consecutive n-alkane boiling points. For example, the  $C_7$  SCN is composed of all the components with boiling points between the boiling point of n- $C_7$  and n- $C_8$ . These analyses routinely extend up to carbon number 30 and may be done up to a carbon number of 45 or more.

Detailed PNA analyses also can be performed. Depending on the details of the analysis, the aromatic fraction may or may not include the resins and asphaltenes. It is also possible to determine the amounts of individual n-alkanes. These types of analyses, although expensive, are especially valuable for wax-precipitation modeling because they very accurately define the components of a fluid that will precipitate as wax.

**9.7.2 Measurement of Wax-Precipitation Data.** There are a few basic measurements that characterize a fluid's tendency to precipitate wax. Lira-Galeana and Hammami<sup>36</sup> reviewed the experimental techniques used to obtain these measurements.

**Wax-Appearance Temperature or Cloud Point.** When a liquid solution or melt is lowered to the WAT, the wax molecules form clusters of aligned chains. Once these nuclei reach a critical size, they become stable and further attachment of molecules leads to growth of the crystal. Formation of these nuclei causes the fluid to take on a cloudy appearance, hence the name cloud point. This also is referred to as the wax-crystallization temperature or wax-appearance point. Determination of a WAT significantly higher than the temperatures expected to be encountered during production indicates the potential for wax-deposition problems.

The WAT depends on which technique is used for the analysis. For example, a microscopy method allows for observation of much smaller wax crystals than a visual technique with the unaided eye. The following techniques are used to determine the WAT.

- American Soc. for Testing and Materials (ASTM) visual methods. Oil in a glass jar is submerged in a cooling bath. As the temperature of the bath is lowered, the temperature at which the fluid's cloudiness is first observed is determined to be the cloud point.

- Cold finger. A temperature-controlled rod is inserted in a gently heated oil sample. The WAT is determined as the temperature at which wax begins to adhere to the rod.

- Viscometry methods. Viscometric techniques rely on detection of changes in rheological properties of an oil as wax precipitates. A break in the curve of viscosity plotted vs. temperature is taken as the WAT.

- Differential-scanning calorimetry. This method detects the latent heat of fusion released on crystallization. Although there can be some uncertainty in interpretation of the results, differential-scanning calorimetry has been widely used for WAT determination and also can provide data on the heat capacities and heats of fusion or transition associated with liquid/solid and solid/solid phase transitions.

- Cross-polarized microscopy. In this technique, a microscope with a temperature-controlled "hot stage" is used to view an oil sample that is being cooled at a constant rate. The use of a polarized light source and polarized objectives on the microscope allow the wax crystals to show up as bright spots on a black background. This technique usually provides the highest WAT value for dead oils.

- Light transmittance. The experimental apparatus for this method consists of a PVT cell with a light source and a light power receiver mounted on opposite sides of the cell. When wax crystals appear in the fluid, the amount of light transmitted is reduced dramatically, and the WAT can be seen as a sharp drop in a plot of light power received vs. temperature. This method can be used at high pressure and, therefore, can be applied to live reservoir fluids as well as stock-tank oils.

- Ultrasonics. Similar to the light-transmittance technique, an ultrasonic signal is sent through the fluid sample and received at a transducer. The velocity of the ultrasonic wave depends on the density of the medium; thus, the transit time for the wave will change at the WAT.

**Wax-Dissolution Temperature.** The wax-dissolution temperature is defined as the temperature at which all precipitated wax has been dissolved on heating the oil. The experimental techniques most often used for determining wax-dissolution temperature are differential-scanning calorimetry and cross-polar microscopy.

**Pour-Point Temperature.** The pour-point temperature is the lowest temperature at which the oil is mobile. This is usually identified as the stock-tank-oil gelation temperature. The ASTM pour-point test, similar to the ASTM cloud point tests, involves placing a sample of the fluid in a jar and cooling it in a temperature-controlled bath. At each 3°C temperature step, the sample is tested by tipping the jar to determine if the oil is still mobile.

**Quantification of Wax Precipitation.** None of the tests used to determine the WAT provide data on the amount of solid precipitated at a temperature below the WAT. Experimental techniques to determine the amount of precipitated wax are described next.

**Bulk-Filtration Apparatus.** In this simple experiment, oil in a cylinder is equilibrated at the desired conditions of pressure, temperature, and, possibly, solvent concentration. The entire contents of the cylinder, including oil and any solids that may have precipitated, are ejected through a filter. The solids collected in the filter then may be analyzed for amount and chemical composition. This technique is time consuming and expensive but has the advantage of providing samples of the precipitated solid for analysis.

**Pulsed Nuclear Magnetic Resonance (NMR).** Pedersen *et al.*<sup>48</sup> used an NMR apparatus to determine the amount of precipitated solids as a function of temperature for 17 crude oils. The experimental NMR signals for each oil were compared with calibrated samples of polyethylene in wax-free oil. Although this technique does not allow for chemical analysis of the deposited solids, results are obtained much more quickly than with the bulk-filtration apparatus.

## 9.8 Thermodynamic Models for Wax Precipitation

The thermodynamic basis of solid/liquid equilibrium of components in a melt or dissolved in a solution is well established and is described in many standard texts (e.g., Prausnitz *et al.*<sup>126</sup>). The basic principles continue to be applied to more complex systems as researchers attempt to develop more accurate models of solid-wax precipitation. Lira-Galeana and Hammami<sup>36</sup> reviewed experimental techniques and thermodynamic models for studying wax precipitation in petroleum fluids.

The predictive capability of the thermodynamic models is affected both by the form and assumptions of the models themselves and the characterization procedures used to quantify the number and properties of wax-forming components present in a fluid. This section presents a general form of the thermodynamic relation used to define the  $K$  values for solid and liquid phases in equilibrium, and the effect of different simplifying assumptions and thermodynamic descriptions of the phases involved on the model results are examined.

**9.8.1 Thermodynamics of Solid/Liquid Equilibrium. Thermodynamic Equilibrium.** Thermodynamic models for predicting wax precipitation may be derived assuming single-component or multicomponent, single-phase or multiphase solid deposits. Regardless of which set of assumptions is chosen, the condition of thermodynamic equilibrium between phases is expressed as the equality of chemical potential for each component in all phases. For one solid phase in equilibrium with an oil, this condition is given by

$$\mu_{iO} = \mu_{iS}, \quad i = 1, \dots, n_c, \dots \quad (9.34)$$

where  $\mu_{iO}$  and  $\mu_{iS}$  are the chemical potentials of component  $i$  in the oil and solid phases, respectively, and  $n_c$  is the number of components. With the fundamental relation between chemical potential and fugacity of component  $i$  ( $n_c$ ),

$$(d\mu_i = RT d \ln f_i)_T, \dots \quad (9.35)$$

the equilibrium relation also may be expressed in terms of fugacities:

$$f_{iO} = f_{iS}, \quad i = 1, \dots, n_c, \dots \quad (9.36)$$

where  $f_{iO}$  and  $f_{iS}$  are the fugacities of component  $i$  in the oil and solid phases, respectively.



**Calculation of Pure Solid Component Fugacity.** EOSs are not available to describe the volumetric behavior of the solid phase as a general function of temperature and pressure; therefore, thermodynamic solid-precipitation models are derived by relating the chemical potential of a pure solid to the chemical potential of the pure liquid at the same pressure and temperature in terms of experimentally known melting properties. Derivation of this expression is discussed in standard thermodynamics texts such as Prausnitz *et al.*<sup>126</sup> The most general form of this relationship, including multiple solid-phase transitions, is<sup>127,128</sup>

$$\begin{aligned} \frac{\mu_{pi, o} - \mu_{pi, s}}{RT} = & \frac{\Delta H_{if}}{RT} \left(1 - \frac{T}{T_{if}}\right) + \sum_{j=1}^{n_{tr}} \frac{\Delta H_{ij, tr}}{RT} \left(1 - \frac{T}{T_{ij, tr}}\right) \\ & + \frac{1}{R} \int_T^{T_{if}} \frac{\Delta C_{pi}}{T} dT - \frac{1}{RT} \int_T^{T_{if}} \Delta C_{pi} dT + \sum_{j=1}^{n_{tr}} \left[ \frac{1}{R} \int_T^{T_{ij, tr}} \frac{\Delta C_{pij, tr}}{T} dT - \frac{1}{RT} \int_T^{T_{ij, tr}} \Delta C_{pij, tr} dT \right] \\ & + \frac{1}{RT} \int_{P_{if}}^P \Delta v_i dP, \dots\dots\dots (9.37) \end{aligned}$$

where

- $\mu_{pi,k}$  = chemical potential of pure component  $i$  in phase  $k$  ( $k = o, s$ ),
- $\Delta H_{if}$  = enthalpy of fusion of component  $i$ ,
- $T_{if}$  = temperature of fusion (melting temperature) of component  $i$ ,
- $n_{tr}$  = number of solid state transitions,
- $\Delta H_{ij,tr}$  = enthalpy of the  $j$ th solid state transition of component  $i$ ,
- $T_{ij,tr}$  =  $j$ th solid state transition temperature of component  $i$ ,
- $\Delta C_{pi} = (C_{p_{o,i}} - C_{p_{s,i}})$ , heat capacity of fusion of component  $i$ ,
- $P_{if}$  = pressure of fusion (corresponding to  $T_{if}$ ) of component  $i$ ,
- $\Delta C_{pij,tr}$  = heat capacity of  $j$ th solid state transition of component  $i$ , and
- $\Delta v_i = (v_{o,i} - v_{s,i})$ , change of molar volume caused by fusion of component  $i$ .

In the majority of wax-precipitation models, multiple-solid-state transitions are not considered, or the effects are lumped into the enthalpy of fusion and heat capacity of fusion terms. Removing these terms and applying the relation between chemical potential and fugacity given in Eq. 9.35, Eq. 9.37 can be written in terms of fugacities as

$$\ln \left( \frac{f_{is}}{f_{io}} \frac{f_{io}^0}{f_{is}^0} \right) = \frac{\Delta H_{if}}{RT} \left(1 - \frac{T}{T_{if}}\right) + \frac{1}{R} \int_T^{T_{if}} \frac{\Delta C_{pi}}{T} dT - \frac{1}{RT} \int_T^{T_{if}} \Delta C_{pi} dT + \frac{1}{RT} \int_{P_{if}}^P \Delta v_i dP, \dots\dots\dots (9.38)$$

where  $f_{ik}^0$  is the fugacity of pure component  $i$  in phase state  $k$  ( $k = o, s$ ).

**K-Value Equations.** Eq. 9.38 may be used directly to determine pure-solid-component fugacities, or it may be combined with activity- or fugacity-coefficient models to derive expressions for solid/liquid  $K$  values. This section gives the fundamental forms of these  $K$ -value equations. These equations then are used with various assumptions to perform solid/liquid or solid/liquid/vapor equilibrium calculations.

**Activity-Coefficient Models.** Activity coefficients can be defined in terms of fugacities as<sup>95</sup>

$$\gamma_i = \frac{f_i(p, T, \mathbf{x})}{x_i f_i^0(p, T)}, \dots\dots\dots (9.39)$$

where  $\gamma_i$  = activity coefficient of component  $i$  in a mixture,  $f_i$  = fugacity of component  $i$  in the mixture,  $x_i$  = mole fraction of component  $i$  in the mixture, and  $f_i^0$  = standard state fugacity of component  $i$ . The standard state fugacity is the fugacity of component  $i$  in the same state and at the same temperature as the mixture and at an arbitrarily chosen pressure and composition. If the activity coefficients are defined with reference to an ideal solution in the sense of Raoult's law, then the pressure is chosen as the system pressure and the composition is chosen as pure component  $i$ . The development of the equations presented here uses this definition.

An expression for solid/liquid  $K$  values in terms of activity coefficients can be derived with the use of the definition of Eq. 9.39 as

$$K_{is} = \frac{x_{is}}{x_{io}} = \frac{\gamma_{io} f_{io}^0}{\gamma_{is} f_{is}^0}, \dots\dots\dots (9.40)$$

where  $K_{is}$  = solid/liquid  $K$  value for component  $i$ ,  $x_{ik}$  = mole fraction of component  $i$  in phase  $k$  ( $k = o, s$ ),  $\gamma_{ik}$  = activity coefficient of component  $i$  in phase  $k$  ( $k = o, s$ ), and  $f_{ik}^0$  = fugacity of pure component  $i$  in phase  $k$  ( $k = o, s$ ). For use with activity-coefficient models, the condition of equilibrium between the solid and liquid phases given in Eq. 9.36 can be substituted into Eq. 9.38 to yield the following relation in terms of pure component fugacities.

$$\frac{f_{io}^0}{f_{is}^0} = \exp \left[ \frac{\Delta H_{if}}{RT} \left( 1 - \frac{T}{T_{if}} \right) + \frac{1}{R} \int_T^{T_{if}} \frac{\Delta C_{pi}}{T} dT - \frac{1}{RT} \int_T^{T_{if}} \Delta C_{pi} dT + \frac{1}{RT} \int_{p_{if}}^p \Delta v_i dp \right] \dots\dots\dots (9.41)$$

Substituting Eq. 9.41 into Eq. 9.40 then gives the general relationship for solid/liquid  $K$  values in terms of activity coefficients and melting properties:

$$K_{is} = \frac{x_{is}}{x_{io}} = \frac{\gamma_{io}}{\gamma_{is}} \exp \left[ \frac{\Delta H_{if}}{RT} \left( 1 - \frac{T}{T_{if}} \right) + \frac{1}{R} \int_T^{T_{if}} \frac{\Delta C_{pi}}{T} dT - \frac{1}{RT} \int_T^{T_{if}} \Delta C_{pi} dT + \frac{1}{RT} \int_{p_{if}}^p \Delta v_i dp \right] \dots\dots (9.42)$$

*Fugacity-Coefficient Models.* For use with EOSs, it is convenient to write the solid/liquid  $K$ -value equation in terms of the wax-melting properties and fugacity coefficients, as opposed to activity coefficients. Fugacity coefficients are defined as

$$\Phi_{ik}^0 = \frac{f_{ik}^0}{P} \dots\dots\dots (9.43)$$

$$\text{and } \Phi_{ik} = \frac{f_{ik}}{x_{ik} P}, \dots\dots\dots (9.44)$$

where  $\Phi_{ik}^0$  = fugacity coefficient of pure component  $i$  in phase state  $k$  and  $\Phi_{ik}$  = fugacity coefficient of component  $i$  in phase  $k$ . Substituting the fugacity-coefficient definitions, Eq. 9.38 can be rearranged to give the solid/liquid  $K$ -value expression

$$K_{is} = \frac{x_{is}}{x_{io}} = \frac{\Phi_{io}}{\Phi_{io}^0} \frac{\Phi_{is}^0}{\Phi_{is}} \exp \left[ \frac{\Delta H_{if}}{RT} \left( 1 - \frac{T}{T_{if}} \right) + \frac{1}{R} \int_T^{T_{if}} \frac{\Delta C_{pi}}{T} dT - \frac{1}{RT} \int_T^{T_{if}} \Delta C_{pi} dT + \frac{1}{RT} \int_{p_{if}}^p \Delta v_i dp \right] \quad (9.45)$$

*Mixed-Activity and Fugacity-Coefficient Models.* The use of the fugacity coefficient as defined in Eq. 9.44 for the liquid phase and the activity coefficient as defined in Eq. 9.39 for the solid phase leads to the following equation for the solid/liquid  $K$  values when the equality of fugacity condition is applied.

$$K_{is} = \frac{\Phi_{io} P}{\gamma_{is} f_{is}^0} \quad (9.46)$$

This formula is convenient when the fluid-phase fugacities are determined with an EOS and the solid-phase activity coefficient is determined with another model.

**9.8.2 Pure Ideal Solid Model.** In Eq. 9.42, the last term in the exponential accounting for the difference in molar volume between the solid and liquid as a function of pressure is usually the smallest and is most often neglected. The heat-capacity term is of larger magnitude but also is assumed negligible in many applications. If the nonidealities of the oil and solid phases also are considered to be small (i.e.,  $\gamma_{io}/\gamma_{is} = 1$ ) and the solid phase is assumed to be a pure component, the equation of ideal solubility results in

$$x_{io} = \exp \left[ \frac{\Delta H_{if}}{R} \left( \frac{1}{T_{if}} - \frac{1}{T} \right) \right] \quad (9.47)$$

This equation may be regarded as being based on the Clausius-Clapeyron or van't Hoff equations.<sup>129</sup>

Reddy<sup>130</sup> reported one application of the ideal solubility equation. Eq. 9.47 was used to determine the cloud points and amounts of precipitated wax for synthetic fuels and diesels. In this case, only n-paraffins were assumed to precipitate. For the synthetic fuels, measured quantities of n-paraffins were combined with a solvent. For the diesel fuels, the amounts of n-paraffins up to C<sub>27</sub> were determined experimentally. The ideal solubility equation was used to convert the amounts of all n-paraffins in a system to an equivalent amount of reference paraffin. The solubility behavior of the reference component, n-eicosane, was determined experimentally. The mixtures then were treated as binary solute/solvent systems for computation. The predicted amount of wax precipitated at one temperature below the cloud point is compared with the experimental values in Fig. 9.27. These results illustrate the ability of the ideal solubility equation to correlate correctly experimentally observed trends, provided the distribution of wax-forming components is well defined.

The ideal solubility equation also was used by Weingarten and Euchner<sup>131</sup> for predicting wax precipitation from live reservoir fluids. Experimental determination of wax-crystallization temperatures (cloud points) for two reservoir fluids was performed at 10 different bubblepoint pressures during differential-liberation experiments. Constants relating the enthalpy of fusion

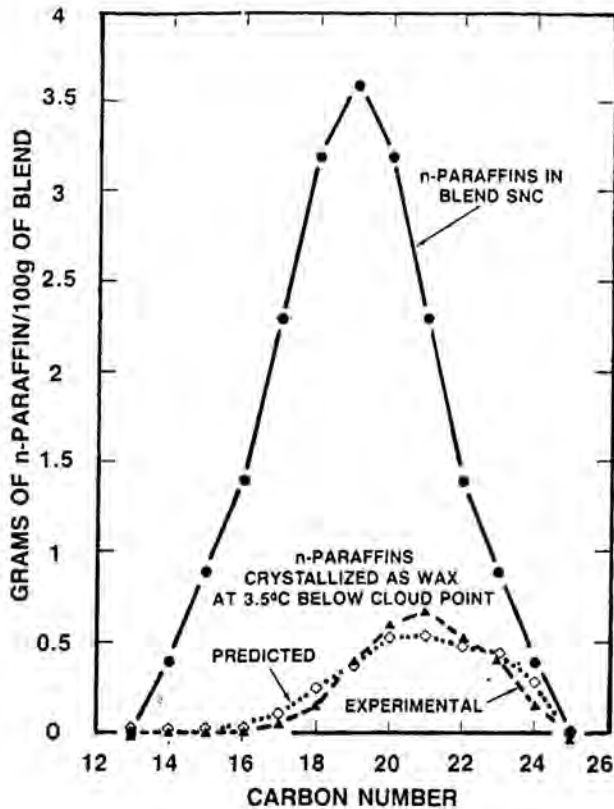


Fig. 9.27—Ideal solubility model predictions compared with measured values for composition of wax formed in a synthetic fuel blend. (Reprinted from *Fuel*, Vol. 65, S.R. Reddy, "A Thermodynamic Model for Predicting *n*-Paraffin Crystallization in Diesel Fuels," pages 1647–1652, Copyright 1986, with permission from Elsevier Science).

and temperature of fusion were determined by linear regression to the experimental data. Fig. 9.28 shows a comparison of the crystallization temperature predicted by the model to the experimental values. In this implementation, no characterization of the feed is necessary. The precipitated wax is treated as a single component. The model is able to only approximately reproduce an important trend in the data as a function of pressure: at high pressures, at which only small amounts of the lightest gases are being liberated, the crystallization temperature increases slowly with decreasing pressure; at lower pressures, at which more gas and heavier gas components are liberated, the crystallization temperature increases more rapidly with decreasing pressure.

**9.8.3 Solid-Solution Models.** Wax models describing the precipitated solid as a single-phase multicomponent solution have been used in a large number of studies. The solid phase has most often been modeled as an ideal or regular solution. The fluid phases are modeled with the regular solution theory, Flory-Huggins theory, or EOSs. This section describes some of the variations of the solid-solution model.

**Regular Solid-Solution Models.** Regular solution theory, as developed by Scatchard and Hildebrand, refers to mixtures with zero-excess entropy provided that there is no volume change of mixing. The Scatchard-Hildebrand equation for activity coefficients is<sup>126</sup>

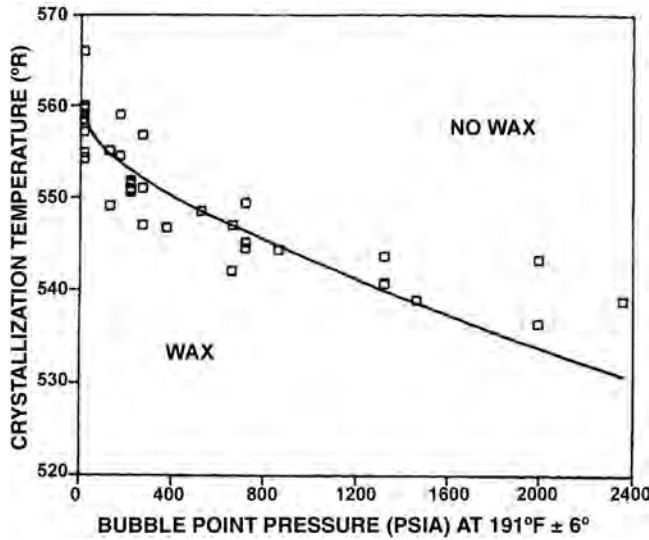


Fig. 9.28—Crystallization temperatures fitted to ideal solution theory.<sup>131</sup>

$$\ln \gamma_{ik} = \frac{v_{ik}(\delta_{ik} - \bar{\delta}_k)^2}{RT}, \dots\dots\dots (9.48)$$

where  $\delta_{ik}$  = solubility parameter for pure component  $i$  in phase  $k$  and  $\bar{\delta}_k$  = volume fraction average solubility parameter for phase  $k$ . The volume fraction average solubility parameter for a phase is given by

$$\bar{\delta}_k = \sum_{i=1}^{n_c} \Phi_{ik} \delta_{ik}; \quad \Phi_{ik} = \frac{x_{ik} v_{ik}}{\sum_{j=1}^{n_c} x_{jk} v_{jk}} \dots\dots\dots (9.49)$$

At conditions far removed from the critical point, the solubility parameter for a component in the oil phase may be expressed in terms of the enthalpy of vaporization and the molar volume of the component.

$$\delta_{io} = \left( \frac{\Delta H_{iv} - RT}{v_{io}} \right)^{1/2} \dots\dots\dots (9.50)$$

*Equation of State for Liquid and Vapor Phases.* Won<sup>79</sup> proposed a modified regular solution theory in which the solubility parameter for a component in the solid phase is given by

$$\delta_{is} = \left( \frac{\Delta H_{iv} + \Delta H_{if} - RT}{v_{is}} \right)^{1/2} \dots\dots\dots (9.51)$$

With Eq. 9.48 and assuming that  $v_{is} = v_{io}$ , the activity-coefficient ratio can be described by

$$\frac{\gamma_{io}}{\gamma_{is}} = \exp \left[ \frac{v_{io}}{RT} \left( (\delta_{io} - \bar{\delta}_o)^2 - (\delta_{is} - \bar{\delta}_s)^2 \right) \right] \dots \dots \dots (9.52)$$

Substituting Eq. 9.52 into Eq. 9.42 and assuming the pressure and heat-capacity terms are negligible gives the final equation used by Won<sup>79</sup> for the solid/liquid  $K$  values as

$$K_{is} = \frac{x_{is}}{x_{io}} = \exp \left[ \frac{\Delta H_{if}}{RT} \left( 1 - \frac{T}{T_{if}} \right) + \frac{v_{io}}{RT} \left( (\delta_{io} - \bar{\delta}_o)^2 - (\delta_{is} - \bar{\delta}_s)^2 \right) \right] \dots \dots \dots (9.53)$$

Won also presented correlations for the heat of fusion, temperature of fusion, and molar volume as functions of molecular weight and tabulates values of the solubility parameters for the liquid and solid phases. The correlations are applicable to normal paraffins. The heat of fusion is given by

$$\Delta H_{if} = 0.1426 M_i T_{if}, \dots \dots \dots (9.54)$$

where  $M_i$  is the molecular weight of component  $i$ . The heat of fusion from Eq. 9.54 is approximately equal to the sum of the heat of fusion and one-half the heat of transition for molecules heavier than  $C_{22}$  and approximately equal to the heat of fusion for odd carbon number molecules lighter than  $C_{22}$ . The temperature of fusion is given by

$$T_{if} = 374.5 + 0.02617 M_i - 20172 / M_i, \dots \dots \dots (9.55)$$

and the molar volume is given by

$$v_{io} = M_i / \left( 0.8155 + 0.6272 \times 10^{-4} M_i - 13.06 / M_i \right) \dots \dots \dots (9.56)$$

In Won's<sup>79</sup> model, solid/liquid/vapor equilibrium is determined. Liquid/vapor  $K$  values are calculated with the Soave-Redlich-Kwong EOS.<sup>73</sup> These  $K$  values are used with the solid/liquid  $K$  values in a three-phase flash algorithm to determine the solid/liquid/vapor-phase split as a function of temperature and pressure. There is an inconsistency in this technique in that the liquid properties are calculated from an activity-coefficient model for the solid/liquid  $K$  values and from an EOS for the vapor/liquid  $K$  values. Despite this inconsistency, Won's technique has some important advantages over the ideal solubility models presented previously. These advantages include accounting for nonidealities in the solid and liquid phases and accounting for the simultaneous effects of pressure, temperature, and vaporization or solution of gas in the liquid on solid precipitation.

Won<sup>79</sup> applied this method to a hydrocarbon gas defined as a mixture of SCN fractions from  $C_1$  to  $C_{40}$ . These SCN fractions are assumed to have paraffinic properties as given by Eqs. 9.54 through 9.56. The feed composition is determined by extrapolating the measured mole fractions of  $C_{15}$  through  $C_{19}$ . Fig. 9.29 shows the effect of temperature on the molar-phase splits for this feed gas. The cloud-point temperature can be seen as the highest temperature at which the solid phase exists, just below 310°K. The amount of solid increases rapidly as the temperature is decreased below this point. Fig. 9.30 shows the effect of pressure on the phase equilibrium.

*Regular Solution Theory Model for Liquid Phase.* Pedersen *et al.*<sup>80</sup> use the general form of the solid/liquid  $K$ -value relation as given in Eq. 9.42, including the heat-capacity term but neglecting the pressure term. This results in the following equation for the  $K$  values:

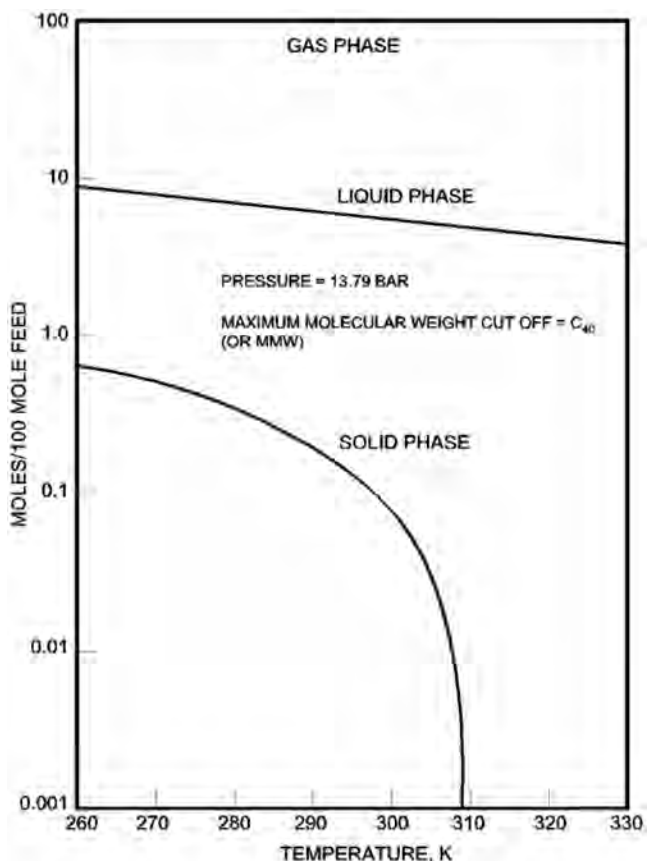


Fig. 9.29—Effect of temperature on the phase equilibria of a gas condensate predicted with the activity-coefficient model with regular-solution theory. (Reprinted from *Fluid Phase Equilibria*, Vol. 30, K.W. Won, “Thermodynamics for Solid-Liquid-Vapor Equilibria: Wax Phase Formation From Heavy Hydrocarbon Mixtures,” pages 265–279, Copyright 1986, with permission from Elsevier Science.)

$$K_{is} = \frac{x_{is}}{x_{io}} = \frac{\gamma_{io}}{\gamma_{is}} \exp \left[ \frac{\Delta H_{if}}{RT} \left( 1 - \frac{T}{T_{if}} \right) + \frac{1}{R} \int_T^{T_{if}} \frac{\Delta C_{pi}}{T} dT - \frac{1}{RT} \int_T^{T_{if}} \Delta C_{pi} dT \right] \dots \dots \dots (9.57)$$

The activity-coefficient ratio is calculated with the regular solution theory (Eq. 9.52), as in Won’s<sup>79</sup> model. Correlations are given for the solubility parameters of paraffins in the oil and solid phases as

$$\delta_{io} = 7.41 + a_1 (\ln C_i - \ln 7) \dots \dots \dots (9.58)$$

$$\text{and } \delta_{is} = 8.50 + a_2 (\ln C_i - \ln 7), \dots \dots \dots (9.59)$$

where  $C_i$  is the carbon number of component  $i$ . Won’s correlation for the enthalpy of formation (Eq. 9.55) is modified as

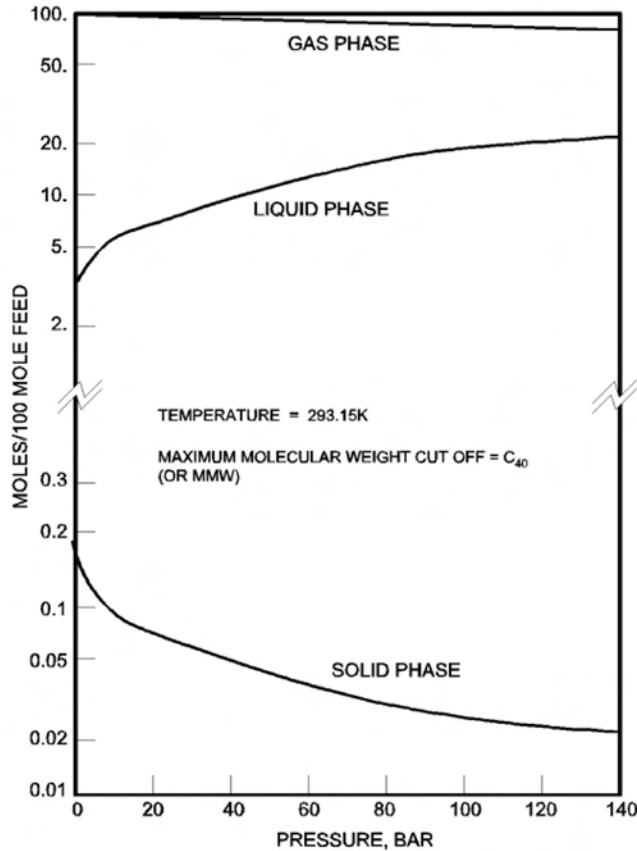


Fig. 9.30—Effect of pressure on the phase equilibria of a gas condensate predicted with the activity-coefficient model with regular-solution theory. (Reprinted from *Fluid Phase Equilibria*, Vol. 30, K.W. Won, “Thermodynamics for Solid-Liquid-Vapor Equilibria: Wax Phase Formation From Heavy Hydrocarbon Mixtures,” pages 265–279, Copyright 1986, with permission from Elsevier Science.)

$$\Delta H_{if} = a_3(0.1426 M_i T_{if}), \dots\dots\dots (9.60)$$

and the model is completed by defining a relation for the heat-capacity difference as

$$\Delta C_{pi} = a_4 M_i + a_5 M_i T \dots\dots\dots (9.61)$$

Constants  $a_1$  through  $a_5$  were determined by a least-squares fit to the data of Pedersen *et al.*<sup>48</sup> as  $a_1 = 0.5914 \text{ (cal/cm}^3\text{)}^{0.5}$ ,  $a_2 = 5.763 \text{ (cal/cm}^3\text{)}^{0.5}$ ,  $a_3 = 0.5148$ ,  $a_4 = 0.3033 \text{ cal/(g}\cdot\text{K)}$ , and  $a_5 = 0.635 \times 10^{-4} \text{ cal/(g}\cdot\text{K}^2\text{)}$ .

The oils were characterized on the basis of experimentally determined SCN fraction distributions. The fractions are subdivided into a paraffinic part and a naphthenic plus aromatic (NA) part. The NA fractions are given solubility parameters 20% higher than those obtained from Eqs. 9.8 and 9.59, while the enthalpy of formation for the NA fractions is set to 50% of the value calculated from Eq. 9.60.

Pedersen *et al.*<sup>80</sup> compared experimental wax precipitation as a function of temperature with model predictions for 16 crude oils. Only liquid/solid equilibrium was calculated. Fig. 9.31 shows typical predictions illustrating the effect of various model assumptions. The squares indi-



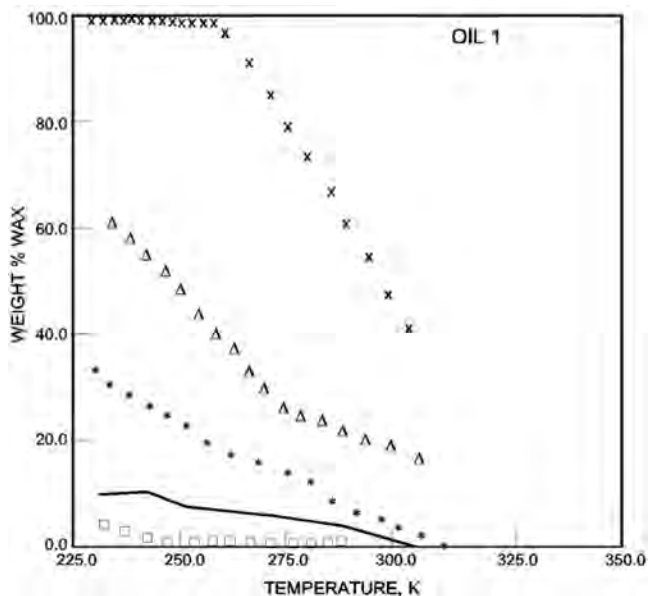


Fig. 9.31—Effect of parameters on the activity-coefficient model for prediction of wax-precipitation amounts as a function of temperature. [Reprinted with permission from K.S. Pedersen, P. Skovborg, and H.P. Rønningsen: “Wax Precipitation from North Sea Crude Oils. 4. Thermodynamic Modeling,” *Energy & Fuels* (1991) V. 5, 924. Copyright 1991 American Chemical Society.]

cate the experimental results, while the solid line indicates the full model predictions as given by Eqs. 9.57 through 9.61. The asterisks show the calculation results obtained when the heat-capacity difference is neglected. The triangles show the results of the use of pure component enthalpies of fusion of n-alkanes instead of those obtained with Eq. 9.60, and the crosses show the results of the use of the liquid- and solid-solubility parameters of Won, as opposed to those given by Eqs. 9.58 and 9.59.

*Internally Consistent Model With EOS for Fluid Phases.* Mei *et al.*<sup>132</sup> applied the mixed activity/fugacity coefficient model given in Eq. 9.46 with a three-phase flash algorithm, in conjunction with liquid/vapor *K* values obtained from the Peng-Robinson EOS. As opposed to Won’s model,<sup>79</sup> this form maintains internal consistency with the use of the EOS for all fluid phase calculations and uses regular-solution theory only for the solid solution. The fugacity of the pure solid is calculated with Eq. 9.41, neglecting the pressure effect. Solid-solubility parameters required for regular-solution theory are calculated with a correlation given by Thomas *et al.*<sup>9</sup> Won’s correlations<sup>79</sup> for enthalpy of fusion, temperature of fusion, and molar volume are used with additional adjustable coefficients. A heat capacity of fusion correlation of the form given by Pedersen<sup>133</sup> completes the model.

Fluids used in the study were characterized on the basis of experimental SCN analysis to C<sub>40</sub>. No further subdivision of the components into P, N, and A subfractions was performed. A good match to experimental cloud points and wax precipitation amounts as a function of temperature was attained through the adjustment of five correlation coefficients.

*Ideal Solid-Solution Models.* Applying the assumptions that the solid phase may be considered an ideal solution, the heat capacity terms are negligible, and the pressure terms are negligible, the *K*-value expression from Eq. 9.42 can be written as

$$K_{is} = \frac{x_{is}}{x_{io}} = \gamma_{io} \exp \left[ \frac{\Delta H_{if}}{RT} \left( 1 - \frac{T}{T_{if}} \right) \right] \dots \dots \dots (9.62)$$

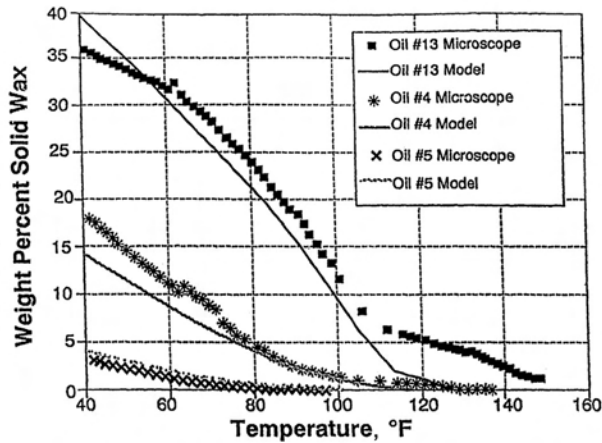


Fig. 9.32—Comparison of multicomponent ideal solubility model predictions and experimental wax-precipitation amounts as a function of temperature.<sup>135</sup>

*Flory-Huggins Model for the Liquid Phase.* Flory and Huggins derived expressions for the thermodynamic properties of polymer solutions. A key parameter in determining the properties of these mixtures was found to be the large difference in molecular size between the polymer and the solvent species. The same situation is found in petroleum fluids, in which the large molecules of the heavy end are in solution with much smaller hydrocarbons. Flory-Huggins theory has been applied to asphaltene-precipitation modeling as discussed in Sec. 9.4.

Hansen *et al.*<sup>39</sup> used the generalized polymer-solution theory given by Flory<sup>134</sup> to derive an expression for the activity coefficient of a component in the liquid phase. Eq. 9.62 then was applied to liquid/solid equilibrium calculations. Characterization of the oils is done on the basis of experimental determination of the SCN fraction distribution to at least C<sub>20+</sub>. Each of the SCN fractions then is divided into two subfractions: the aromatic part and the combined paraffinic and naphthenic part. Flory interaction parameters are calculated between the subfractions with a group-contribution method. Although good results were obtained, the resulting expression is complicated and the model has not been used by other researchers.

*Ideal Solution Model for the Liquid Phase.* Erickson *et al.*<sup>135</sup> used Eq. 9.62 with the additional assumption that the liquid phase is also an ideal solution. These authors note that the heat of fusion and melting-temperature terms are of much greater importance than the activity-coefficient terms for prediction of liquid/solid equilibria of stabilized liquids, justifying the use of the ideal solubility equation. Won's correlation<sup>79</sup> for melting temperature as given in Eq. 9.55 is used for n-alkanes. A modification of this expression is used for all other species in the fluid. A single constant multiplying Won's enthalpy of fusion correlation is used as an adjustable parameter to enable a better fit of the experimental data.

Erickson *et al.*<sup>135</sup> applied the model to stabilized oils with detailed experimental compositional analysis, which allows a direct determination of the amount of n-alkanes in each SCN fraction up to carbon numbers of 35 or 40. Extrapolation to C<sub>50</sub> or higher is then performed. They also apply a "staged" equilibrium flash, which assumes that once a solid forms, it does not remix with additional solid that precipitates at lower temperatures. Fig. 9.32 compares model results with experimental data.

*EOS Models for Liquid and Vapor Phases.* Brown *et al.*<sup>17</sup> used a simplification of the fugacity coefficient form of the solid/liquid *K*-value expression (Eq. 9.45) to study the effects of pressure and light components on wax formation. The assumptions used are that the heat capac-

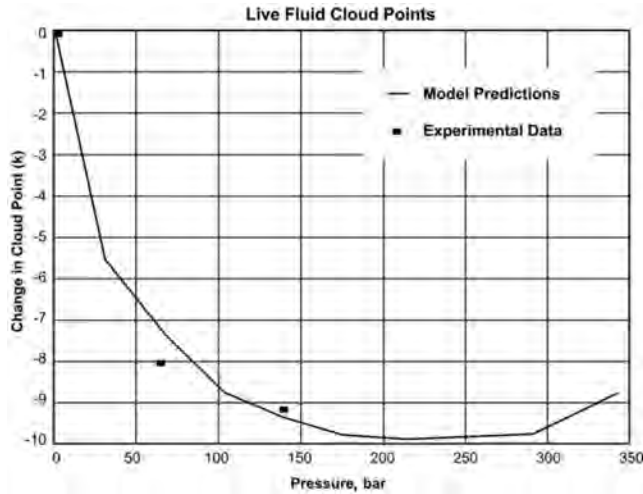


Fig. 9.33—Ideal solubility model with SPHCT EOS; effect of pressure on cloud-point temperatures for a live oil.<sup>17</sup>

ity difference is negligible, the solid phase can be considered an ideal solution,  $\Delta v_i$  is constant, and  $p_{if}$  is small compared with  $p$ . Applying these conditions leads to the final  $K$ -value expression:

$$K_{is} = \frac{x_{is}}{x_{io}} = \frac{\Phi_{io}}{\Phi_{io}^0} \exp \left[ \frac{\Delta H_{if}}{RT} \left( 1 - \frac{T}{T_{if}} \right) + \frac{p\Delta v_i}{RT} \right] \dots\dots\dots (9.63)$$

The melting temperature and heat of fusion terms are calculated with the correlations given by Erickson *et al.*,<sup>135</sup> and the molar-volume difference is correlated as function of molecular weight. Brown *et al.* used the simplified perturbed-hard-chain theory EOS to calculate the fugacity coefficients. A correlation was developed for binary-interaction parameters of the paraffin components. The fluid-characterization method is the same as that described for the model of Erickson *et al.*<sup>135</sup>

Model predictions are compared with experimental data in Fig. 9.33 for a live fluid with a bubblepoint of 285 bar. The model predictions show that increasing the pressure from atmospheric (dead) oil causes a decrease in the cloud-point temperature as light ends dissolve in the oil phase. The light ends increase the solubility of heavy-wax components in the oil. A minimum in the cloud point is achieved at the bubblepoint of the oil. Further pressure increase in the single-phase region causes an increase in the cloud-point temperature.

Pedersen<sup>133</sup> used the fugacity-coefficient model of Eq. 9.63 with the additional simplification that the pressure effects were neglected, resulting in the following expression for the solid/liquid  $K$  values:

$$K_{is} = \frac{x_{is}}{x_{io}} = \frac{\Phi_{io}}{\Phi_{io}^0} \exp \left[ \frac{\Delta H_{if}}{RT} \left( 1 - \frac{T}{T_{if}} \right) \right] \dots\dots\dots (9.64)$$

The Soave-Redlich-Kwong EOS is used to determine the fugacity coefficients for liquid and vapor phases. The characterization of the fluid is performed on the basis of a standard extended compositional analysis in which the mole fraction, molecular weight, and density of each SCN fraction is given. Pedersen<sup>133</sup> developed an empirical expression to calculate the

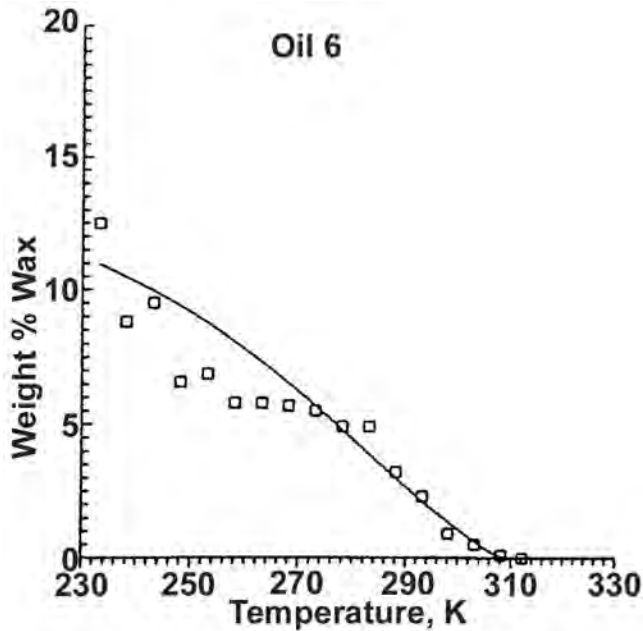


Fig. 9.34—EOS fluid/ideal solid model: comparison of predicted and experimental wax precipitation amounts as a function of temperature.<sup>133</sup>

mole fraction of the potentially wax-forming part of any SCN fraction. This approach is in contrast to the characterization procedure of Erickson *et al.*,<sup>135</sup> in which all the subfractions of a SCN fraction may potentially enter the wax phase, but the parameters of the nonnormal alkane fractions are defined such that they will enter the solid phase in lesser amounts.

Three adjustable parameters are used in the expression to determine the mole fraction of the wax-forming part of each SCN fraction. Fig. 9.34 shows example results for the model comparing the predicted and experimental amount of wax precipitated as a function of temperature.

**9.8.4 Multiple-Pure-Solid-Phase (Multisolid) Models.** All the models discussed up to this point treat the deposited wax as a single phase, consisting of either a pure component or a mixture of components as a solid solution. As discussed in Sec. 9.2, experimental work on binary-alkane mixtures shows that the components can separate into two immiscible solid phases, where each phase is essentially a pure component. Solid-phase transitions also are observed in crude oils.

Lira-Galeana *et al.*<sup>52</sup> developed a thermodynamic model for wax precipitation based on the concept that the precipitated wax is made up of several solid phases, at which each phase consists of a single component or pseudocomponent. From stability considerations, a component may exist as a pure solid if the following inequality is satisfied:

$$f_{io} - f_{is}^0 \geq 0 \dots\dots\dots (9.65)$$

The number of solid-forming components and the number of solid phases,  $n_s$ , is determined from Eq. 9.65. Once the number of solid phases is known, the phase-equilibrium relationships for vapor, liquid, and solid are given by

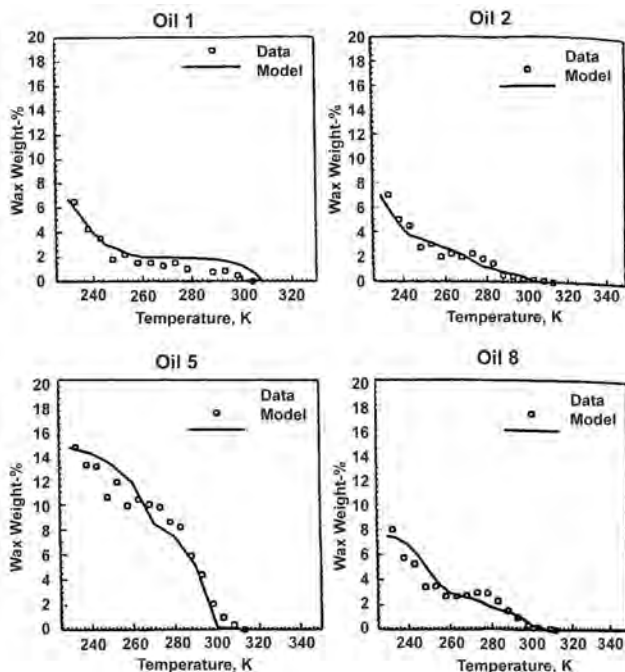


Fig. 9.35—Multisolid-wax model: comparison of predicted and experimental wax-precipitation amounts as a function of temperature. [After Lira-Galeana, C., Firoozabadi, A., and Prausnitz, J.M.: “Thermodynamics of Wax Precipitation in Petroleum Mixtures,” *AIChE J.* (1996) V. 42, 239. Reproduced with permission of the American Institute of Chemical Engineers. Copyright © 1996 AIChE. All rights reserved.]

$$f_{ig} = f_{io}; \quad i = 1, \dots, n_c - n_s \dots \dots \dots (9.66)$$

$$\text{and } f_{ig} = f_{io} = f_{is}^0; \quad i = n_c - n_s + 1, \dots, n_c \dots \dots \dots (9.67)$$

Eq. 9.41 is used, neglecting pressure effects, to obtain the pure-solid fugacity. The pure-liquid fugacity is obtained from the Peng-Robinson EOS,<sup>84</sup> as are the component fugacities in the liquid and vapor phases.

In the original multisolid-wax model presented by Lira-Galeana *et al.*,<sup>52</sup> the fluids are characterized by splitting the C<sub>7+</sub> fraction into 7 to 12 pseudocomponents. No further subdivision of the pseudocomponents into P, N, or A fractions is performed. Instead, melting temperature and enthalpy of fusion correlations are developed to define properties that represent an average of the three subgroups. These correlations weight the aromatic properties more heavily for heavier molecular-weight pseudocomponents. The heat capacity of fusion is given by the correlation of Pedersen *et al.*,<sup>48</sup> as shown in Eq. 9.61. Fig. 9.35 shows experimental data and predicted results of the model.

Pan *et al.*<sup>19</sup> also have used the multisolid-wax model but with a different fluid-characterization procedure. The characterization is based on experimental SCN analysis. Every five consecutive carbon number fractions are lumped together. The relative amounts of the P, N, and A subfractions are determined experimentally or with correlations. Melting temperature and enthalpy of fusion properties are assigned to the paraffinic subfractions with Won’s correlations.<sup>79</sup> For naphthenes and aromatics, the correlations of Lira-Galeana *et al.*<sup>52</sup> were used, with the exception of the enthalpy of fusion for aromatics, which was fit with a new correlation independent of the molecular weight. For the heat capacity of fusion, the correlation of Pedersen

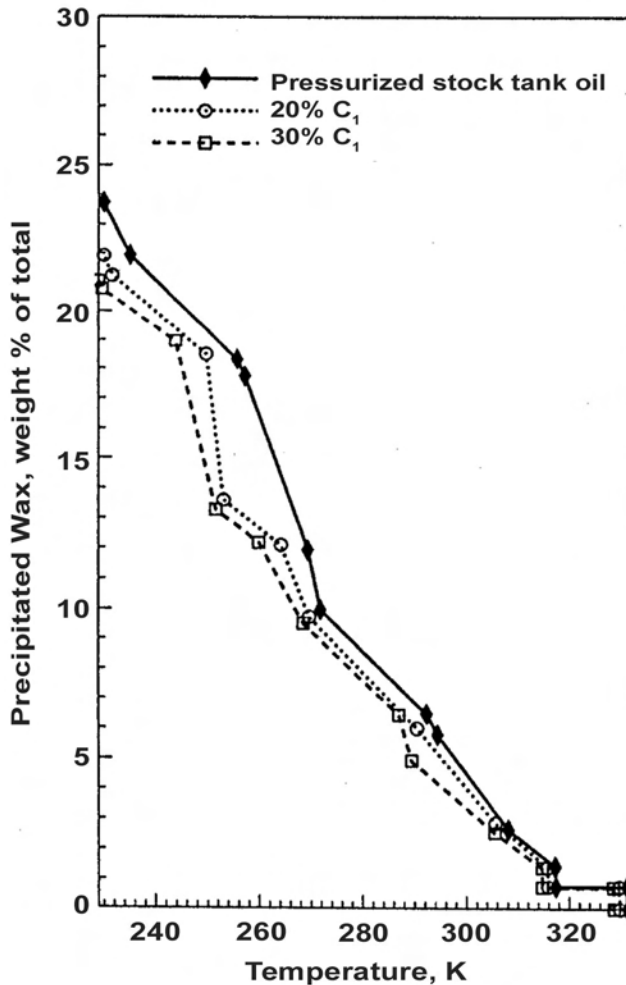


Fig. 9.36—Multisolid-wax model with PNA characterization: effect of  $C_1$  on amount of precipitated wax.<sup>19</sup>

*et al.*<sup>48</sup> was used for all components. Results of the model for a synthetic oil at 110 bar are shown in Fig. 9.36, illustrating the reduction in cloud point and also the reduction in amount of wax precipitated with the addition of methane to the system.

**Multisolid-Wax Model Including Enthalpies of Transition.** Nichita *et al.*<sup>128</sup> used Eq. 9.37 to derive an expression for the ratio between the pure-solid and pure-liquid fugacities including the effect of multiple solid-state transitions. Assumptions used in the derivation are that the heat capacity of fusion is constant, the heat capacities of transition are negligible, the solid/liquid molar-volume difference is constant, and the terms for the enthalpies of transition are all evaluated at the temperature of the first transition. The authors state that this treatment of the enthalpies of transition may lead to relative differences in results of up to 10% compared with lumping the enthalpies of transition in with the enthalpy of fusion. Applying these considerations results in

$$\ln \frac{f_{io}^0}{f_{is}^0} = \frac{\Delta H_{if}}{RT} \left( 1 - \frac{T}{T_{if}} \right) + \frac{1}{RT} \left( 1 - \frac{T}{T_{i1, tr}} \right) \sum_{j=1}^{n_s} \Delta H_{ij, tr}$$

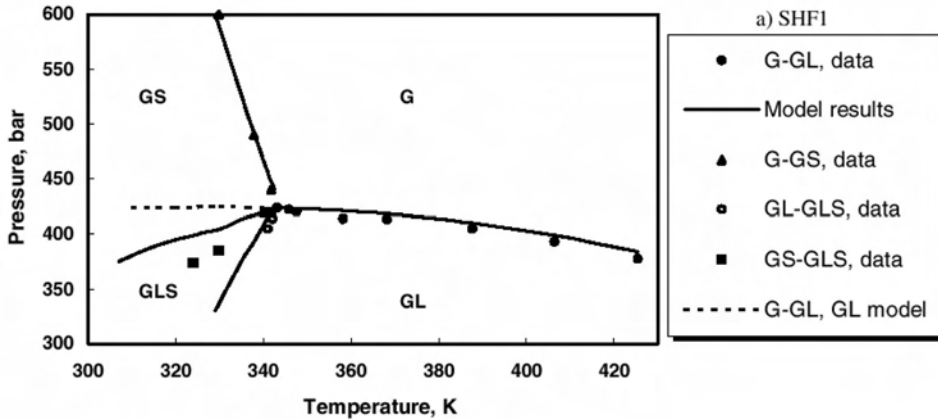


Fig. 9.37—Multisolid-wax model with multiple-phase transitions: phase diagram for a synthetic gas mixture with phenanthrene.<sup>128</sup>

$$+ \frac{\Delta C_{Pi}}{R} \left[ \ln \left( \frac{T_{if}}{T} \right) - \frac{T_{if}}{T} + 1 \right] + \frac{\Delta v_i (P - P_{if})}{RT} \dots \dots \dots (9.68)$$

Ungerer *et al.*<sup>136</sup> derived a similar expression with multiple enthalpies of transition; however, the enthalpy terms are evaluated at the fusion temperature rather than the first transition temperature. The model is applied with a single pure-component-solid phase. Nichita *et al.*<sup>128</sup> used Eq. 9.68 with the modified multisolid-wax model presented in Pan *et al.*,<sup>19</sup> including the correlations for all component properties except enthalpies of fusion and enthalpies of transition; new correlations are presented for these properties. The model of Nichita *et al.*<sup>128</sup> is used with the Peng-Robinson EOS to calculate a pressure-temperature phase diagram, shown in Fig. 9.37, for a synthetic fluid with phenanthrene as the precipitating component. The binary-interaction parameter between methane and phenanthrene was adjusted to match the vapor/liquid dewpoint.

**9.8.5 Excess Gibbs Energy Models.** Activity coefficients are related to the partial molar excess Gibbs energy for a component *i*,  $\bar{G}_i^E$ , and the total excess Gibbs energy for a phase,  $G^E$ , by

$$\ln \gamma_i = \frac{\bar{G}_i^E}{RT} \dots \dots \dots (9.69)$$

$$\text{and } \sum_{i=1}^{n_c} x_i \ln \gamma_i = \frac{G^E}{RT} \dots \dots \dots (9.70)$$

Excess-free-energy models thus can be used with the solid/liquid *K*-value equation expressed in terms of activity coefficients for wax-precipitation modeling.

Coutinho and coworkers published a number of studies on modeling paraffin-wax formation from synthetic and real petroleum fluids.<sup>53,137-139</sup> In these works, an equation is used for the pure-component solid to liquid-fugacity ratio similar to that given in Eq. 9.68, with the additional assumption that only a single enthalpy of transition term is used and the pressure effect is

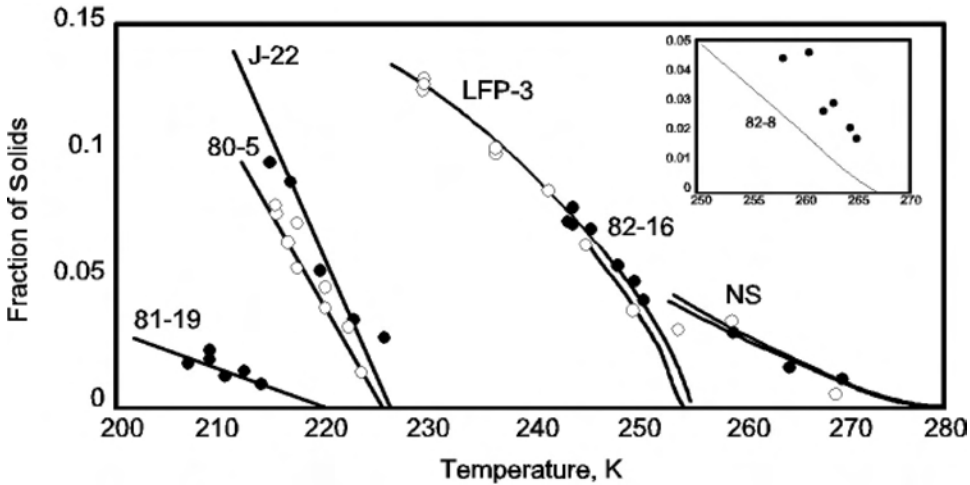


Fig. 9.38—Amount of solids precipitated as a function of temperature for jet and diesel fuels predicted with the excess  $G^E$  model. [Reprinted with permission from J.A.P. Coutinho, “A Thermodynamic Model for Predicting Wax Formation in Jet and Diesel Fuels,” *Energy & Fuels* (2000) V. 14, 625. Copyright 2000 American Chemical Society.]

neglected. This results in the following solid/liquid  $K$ -value expression in terms of activity coefficients:

$$K_{is} = \frac{x_{is}}{x_{io}} = \frac{\gamma_{io}}{\gamma_{is}} \exp \left[ \frac{\Delta H_{if}}{RT} \left( 1 - \frac{T}{T_{if}} \right) + \frac{\Delta H_{i1, tr}}{RT} \left( 1 - \frac{T}{T_{i1, tr}} \right) + \frac{\Delta C_{pi}}{R} \left[ \ln \left( \frac{T_{if}}{T} \right) - \frac{T_{if}}{T} + 1 \right] \right] \dots \dots \dots (9.71)$$

The liquid-phase activity coefficient is given by

$$\ln \gamma_{io} = \ln \gamma_{io}^{cfv} + \ln \gamma_{io}^r \dots \dots \dots (9.72)$$

where the combinatorial free-volume contribution,  $\ln \gamma_{io}^{cfv}$ , is obtained from a Flory free-volume model, and the residual contribution,  $\ln \gamma_{io}^r$ , is obtained from the UNIFAC model, which is based on the universal quasichemical (UNIQUAC) equation. Coutinho *et al.*<sup>137</sup> contains more detail and references on these models.

Excess Gibbs energy models are used for the solid phase. A modified Wilson’s equation with one adjustable parameter was used initially.<sup>138</sup> Then, a predictive version of the UNIQUAC equation was developed,<sup>53</sup> which incorporates multiple-mixed-solid phases and is used to predict wax formation in jet and diesel fuels.<sup>139</sup> An analysis of the amounts of the individual n-alkanes is required for the fluid characterization. The N and A subfractions of a SCN fraction can be treated separately or lumped as a single pseudocomponent. Fig. 9.38 presents model results for the amount of wax precipitated as a function of temperature compared with experimental data for a number of fuels. Fig. 9.39 shows the change in composition of the solid phase as a function of temperature. The accuracy of the model is very good.

Pauly *et al.*<sup>140</sup> presented further development of the excess Gibbs energy model. In this model, the modified Wilson equation, as given by Coutinho and Stenby,<sup>138</sup> is used for the activ-



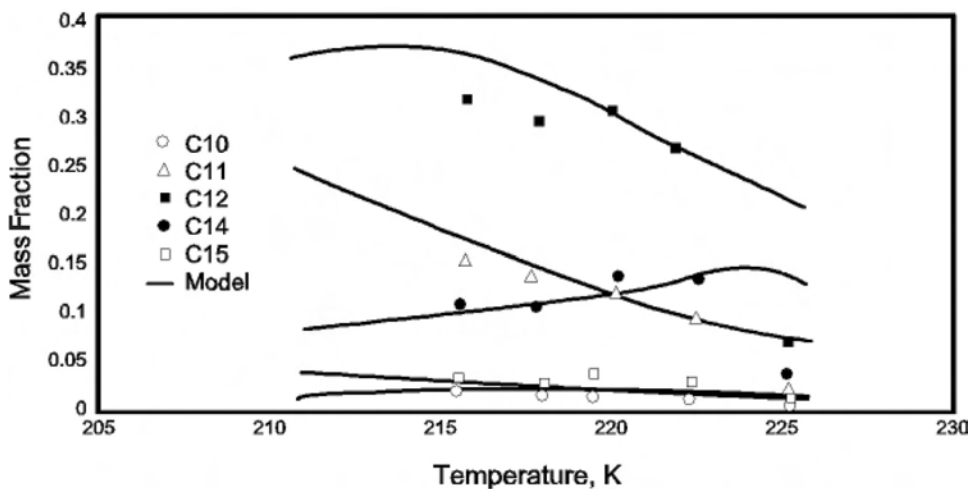


Fig. 9.39—Composition of the precipitated solid phase as a function of temperature for a diesel fuel predicted with the excess  $G^E$  model. Reprinted with permission from J.A.P. Coutinho, “A Thermodynamic Model for Predicting Wax Formation in Jet and Diesel Fuels,” *Energy & Fuels* (2000) V. 14, 625. Copyright 2000 American Chemical Society.

ity coefficients in the solid phase at atmospheric pressure. The Poynting factor is used to determine the high-pressure solid fugacity from the fugacity determined at atmospheric pressure. The liquid phase is modeled with an EOS/ $G^E$  model. This combination of fluid and solid treatments yields good results for prediction of solid/liquid and solid/liquid/vapor phase boundaries up to 200 Mpa for binary and multicomponent systems of n-alkanes. The quality of the predictions is a result of the treatment of the pressure effect on the solid phase and the EOS/ $G^E$  model, which guarantees continuity between fugacities of the fluid and solid phases.

**9.8.6 Comparison of Models.** Pauly *et al.*<sup>139</sup> compared the models of Won,<sup>79</sup> Pedersen *et al.*,<sup>80</sup> Hansen *et al.*,<sup>39</sup> Coutinho and Stenby,<sup>138</sup> Ungerer *et al.*,<sup>136</sup> and the ideal solution model. The models are tested on systems composed of n-decane and a heavy fraction of normal alkanes from C<sub>18</sub> to C<sub>30</sub>. Fig. 9.40 compares the total amount of solid precipitate as a function of temperature for the models with experimental data. The solid-solution models overpredict the cloud-point temperature and the amount of solid precipitated, while the multisolid model gives better results for the cloud point but underpredicts the amount of wax precipitated, at least for the higher temperature region. Coutinho and Stenby’s model<sup>138</sup> gives a very good match of the data.

Nichita *et al.*<sup>128</sup> also compared their modification of the multisolid-wax model with a solid-solution model. The solid phase is assumed to be ideal, and the liquid phase is described by the EOS. Results for the two models are compared in Fig. 9.41 for three synthetic mixtures of n-decane with n-alkanes from C<sub>18</sub> to C<sub>30</sub>. As in the comparison performed by Pauly *et al.*,<sup>141</sup> the solid-solution model overpredicts the cloud-point temperature and the amount of wax precipitated, while the multisolid-wax model gives good estimates of the cloud-point temperature yet underpredicts the amount of wax precipitated.

## 9.9 Wax-Deposition Models

A number of thermodynamic models were described in the previous section to calculate the amount of solid wax precipitated as a function of pressure, temperature, and fluid composition. As discussed in Sec. 9.1, wax precipitation does not necessarily lead to solid deposition. Ther-

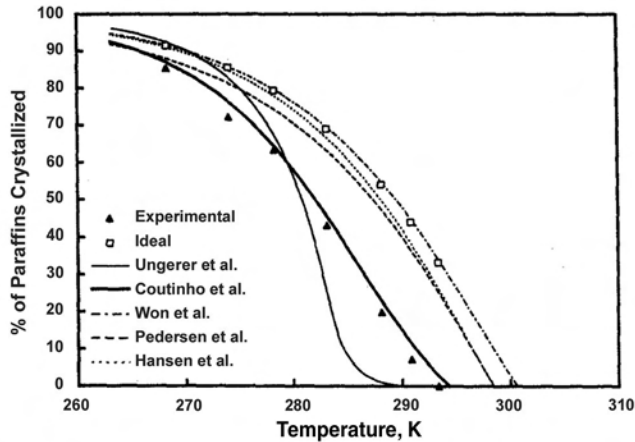


Fig. 9.40—Amount of solids precipitated as a function of temperature for a mixture of n-alkanes predicted with various models. (Reprinted from *Fluid Phase Equilibria*, Vol. 149, J. Pauly, C. Dauphin, and J.L. Dardou, "Liquid-Solid Equilibria in a Decane + Multi-Paraffins System," pages 191–207, Copyright 1998, with permission from Elsevier Science.)

hydrodynamic models for solid/liquid  $K$  values have been coupled with models for wax deposition in pipelines. The form of these models is discussed briefly in this section. For deposition to occur in pipelines, the following conditions must be fulfilled.<sup>142</sup>

- The pipeline wall temperature must be below the WAT for the fluid.
- A negative radial temperature gradient must be present in the flow. That is, the wall temperature must be lower than the centerline temperature. A zero gradient implies that no deposition will occur.
- Wall friction must be large enough so that wax crystals can stick to the wall.

Burger *et al.*<sup>143</sup> investigated the significant physical processes leading to wax deposition in pipelines. These processes are molecular diffusion, Brownian diffusion, shear dispersion, and gravity settling. Brownian movement of small solid-wax crystals will result in diffusion-like transport of these particles when a concentration gradient exists. This effect is normally neglected in pipeline-deposition models. Gravity settling can occur because precipitated wax crystals are denser than the surrounding liquid. Again, this effect is usually neglected in flow models. Molecular diffusion and shear dispersion are described next,<sup>144</sup> assuming that the three deposition conditions have been satisfied.

**9.9.1 Molecular Diffusion.** Flow in pipes will be laminar or will have a laminar sublayer adjacent to the pipe wall. There will be a temperature gradient across this sublayer with the lower temperature at the pipe wall. When the temperature is below the WAT, the flowing oil will contain precipitated solid wax, which is in equilibrium with the liquid. Because the temperature is colder toward the wall, more of the wax components will exist in the solid phase at equilibrium. This results in a concentration gradient in the liquid phase with a lower concentration of wax-forming components at the pipe wall. Wax molecules will be transported toward the wall by molecular diffusion. Once these molecules reach the solid/liquid interface, they are available to be added to the solid deposit by the mechanisms of crystal growth. The equation describing the rate of mass transport caused by molecular diffusion is

$$\frac{dm_i}{dt} = -\rho_{oil} D_i A \frac{dw_i}{dT} \frac{dT}{dr}, \dots \dots \dots (9.73)$$

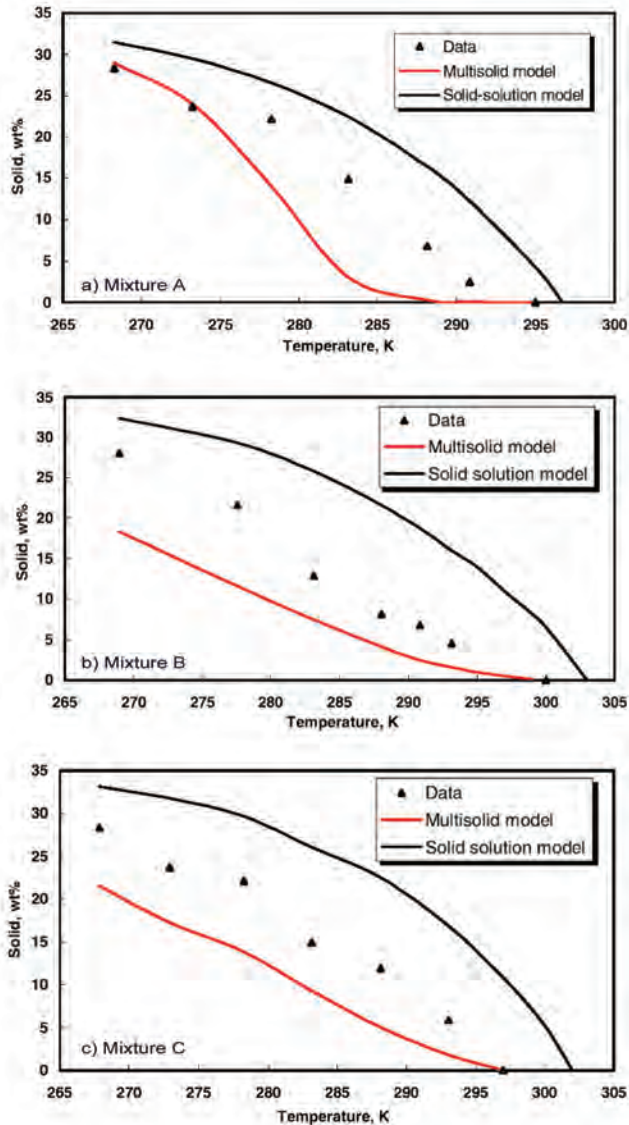


Fig. 9.41—Comparison of multisolid- and solid-solution wax-precipitation models.<sup>128</sup>

where  $m_i$  = mass of component  $i$ ,  $t$  = time,  $\rho_{oil}$  = mass density of oil,  $D_i$  = effective diffusion coefficient for component  $i$ ,  $A$  = deposition area,  $w_i$  = weight fraction of component  $i$ , and  $r$  = radial distance.

Because the radial-concentration gradient is not readily available, the chain rule is used in Eq. 9.73 to express this as the product of the mass-concentration (weight fraction) gradient with respect to temperature and the temperature gradient. The mass-concentration gradient is derived from the solubility limit as a function of temperature obtained from a thermodynamic model.

**9.9.2 Shear Dispersion.** When suspended solid particles are being transported in a fluid in the laminar-flow regime, they tend to travel with the mean speed and direction of the fluid. Particles have higher velocities at greater distances from the pipe wall, and the particles also rotate

as they flow. These rotating particles will exert drag forces, causing displacement of the flow paths of any neighboring particles. When the particle concentration is high, these interactions result in net transport of particles toward the low-velocity region at the pipe wall.

Considering all the wax-forming components together as a single wax pseudocomponent, the rate of mass transport of wax caused by shear dispersion takes the form

$$\frac{dm_w}{dt} = k^* C_w \gamma A, \dots\dots\dots (9.74)$$

where  $m_w$  = mass of wax,  $k^*$  = empirical constant,  $C_w$  = concentration of precipitated wax at the wall, and  $\gamma$  = shear rate. The form of this equation shows that the deposition rate increases linearly with increasing shear rate.

Weingarten and Euchner<sup>131</sup> reported results of diffusion and shear-deposition experiments and modeling with Eqs. 9.73 and 9.74. They note that shear rate also has an important effect that is not related to shear transport. Pieces of deposited wax can be dislodged from the pipe wall in a process called sloughing. Sloughing will be dependent on the shear rate, the nature of the deposit, and the nature of the wall surface. Sloughing occurs when the wall shear rate exceeds the shear strength of the deposit and may occur both in the laminar and turbulent flow regimes.

Keating and Wattenbarger<sup>145</sup> also have used the diffusion and shear-deposition equations in conjunction with a wellbore simulator to model wax deposition and removal in wellbores. Wax removal is caused by equilibrium conditions, not explicit modeling of the sloughing process. A study isolating and comparing the relative effects of molecular diffusion and shear dispersion on wax deposition concludes that molecular diffusion is the dominant effect.<sup>146</sup> Majeed *et al.*<sup>147</sup> obtained good results modeling wax deposition in pipelines considering only the diffusive transport.

A detailed compositional wax-deposition model for pipelines has been derived by combining the differential equations of mass and energy conservation and the laws of diffusion with a thermodynamic model for solid/liquid  $K$  values of the form given in Eq. 9.54.<sup>142</sup> These mass and heat-transfer relations also have been applied with the multisolid-wax model by Ramirez-Jaramillo *et al.*<sup>148</sup>

## 9.10 Prevention and Remediation of Wax Precipitation

Crystallization of waxes in crude oils leads to non-Newtonian flow characteristics, including very high yield stresses that are dependent on time and the shear and temperature histories of the fluid. This crystallization may cause three problems: high viscosity, which leads to pressure losses; high-yield stress for restarting flow; and deposition of wax crystals on surfaces.<sup>149</sup>

Wax-precipitation-induced viscosity increases and wax deposition on pipes are the primary causes of high flowline pressure drops. In turn, these pressure losses lead to low flow rates that make conditions for wax deposition more favorable. In extreme cases, pumping pressure can exceed the limits of the system and stop flow entirely. A related problem is the high-yield stress for restarting flow. When oil is allowed to stand in a pipeline at temperatures below its pour point, a certain pressure is required to break the gel and resume flow. Again, this pressure may be higher than the pressure limits of the pumps and pipelines.<sup>149</sup>

Wax can deposit on surfaces in the production system and in the formation. Wax deposition can be prevented or removed by a number of different methods. These methods fall into three main categories: thermal, chemical, and mechanical.

**9.10.1 Thermal.** Because precipitation is highly temperature dependent, thermal methods can be highly effective both for preventing and removing wax-precipitation problems. Prevention

methods include steam- and electrical-heat tracing of flowlines, in conjunction with thermal insulation. Thermal methods for removing wax deposition include hot oiling and hot watering. Hot-water treatments cannot provide the solvency effects that hot oiling can, so surfactants are often added to aid in dispersion of wax in the water phase. Surfactants are discussed under chemical methods.

Hot oiling is one of the most popular methods of deposited wax removal. Wax is melted and dissolved by hot oil, which allows it to be circulated from the well and the surface-producing system. Hot oil is normally pumped down the casing and up the tubing; however, in flowing wells, the oil may be circulated down the tubing and up the casing. There is evidence that hot oiling can cause permeability damage if melted wax enters the formation.<sup>1</sup>

Higher molecular-weight waxes tend to deposit at the high-temperature bottom end of the well. Lower molecular-weight fractions deposit as the temperature decreases up the wellbore. The upper parts of the well receive the most heat during hot oiling. As the oil proceeds down the well, its temperature decreases and the carrying capacity for wax is diminished. Thus, sufficient oil must be used to dissolve and melt the wax at the necessary depths.<sup>150</sup>

**9.10.2 Chemical.** The types of chemicals available for paraffin treatment include solvents, crystal modifiers, dispersants, and surfactants.

Solvents can be used to treat deposition in production strings and also may be applied to remediate formation damage.<sup>151</sup> Although chlorinated hydrocarbons are excellent solvents for waxes, they generally are not used because of safety and processing difficulties they create in the produced fluid. Hydrocarbon fluids consisting primarily of normal alkanes such as condensate and diesel oil can be used, provided the deposits have low asphaltene content. Aromatic solvents such as toluene and xylene are good solvents for both waxes and asphaltenes.

Crystal modifiers act at the molecular level to reduce the tendency of wax molecules to network and form lattice structures within the oil. Operating at the molecular level makes them effective in concentrations of parts per million, as opposed to hot oil and solvents, which must be applied in large volumes. Crystal modifiers have relatively high molecular weights to allow them to interact with high-molecular-weight waxes. Because they have high melting points, their use is limited in cold climates.<sup>150</sup>

Dispersants are chemicals that break deposited wax into particles small enough to be reabsorbed into the oil stream. These chemicals are used in low concentrations in aqueous solutions, making them relatively safe and inexpensive.

Surfactants may be used as deposition inhibitors or can act as solubilizing agents for nucleating agents in an oil. Surfactants are not used as generally as the other chemical types.

**9.10.3 Mechanical.** Scrapers and cutters are used extensively to remove wax deposits from tubing because they can be economical and result in minimal formation damage.<sup>1</sup> Scrapers may be attached to wireline units, or they may be attached to sucker rods to remove wax as the well is pumped. Deposits in surface pipelines can be removed by forcing soluble or insoluble plugs through the lines. Soluble plugs may be composed of naphthalene or microcrystalline wax. Insoluble plugs are made of plastic or hard rubber.

Another method of mechanical intervention to prevent deposition is the use of plastic or coated pipe. Low-friction surfaces make it more difficult for wax crystals to adhere to the pipe walls. Deposition will still occur if conditions are highly favorable for wax precipitation, and deposits will grow at the same rate as for other pipes once an initial layer of material has been laid down; therefore, the pipe and coating system must be capable of withstanding one of the other methods of wax removal.

## Nomenclature

- $a$  = constant  
 $a_{1-5}$  = constants  
 $A$  = deposition area, L<sup>2</sup>  
 $b$  = constant  
 $C_i$  = carbon number of component  $i$   
 $C_a$  = concentration of precipitated asphaltene in wt %, m/m  
 $C_{sf}$  = concentration of suspended solid in the oil phase [ppm (μg/g)]  
 $C_w$  = concentration of precipitated wax at the wall, m/m  
 $d_{ij}$  = interaction coefficient between component  $i$  and  $j$   
 $D$  = shell thickness of the micelle, L  
 $D_i$  = effective diffusion coefficient for component  $i$ , L<sup>2</sup>/t  
 $e$  = adjustable parameter in Eq. 9.23  
 $E_a$  = volume of deposited asphaltene per bulk volume of rock, L<sup>3</sup>/L<sup>3</sup>  
 $f_{ao}$  = fugacity of asphaltene component in oil phase, m/Lt<sup>2</sup>  
 $f_i$  = fugacity of component  $i$ , m/Lt<sup>2</sup>  
 $f_i^0$  = standard state fugacity of component  $i$ , m/Lt<sup>2</sup>  
 $f_{ig}$  = fugacity of component  $i$  in the oil phase, m/Lt<sup>2</sup>  
 $f_{ik}$  = fugacity of component  $i$  in phase  $k$  ( $k = o, s$ ), m/Lt<sup>2</sup>  
 $f_{ik}^0$  = fugacity of pure component  $i$  in phase state  $k$  ( $k = o, s$ ), m/Lt<sup>2</sup>  
 $f_{ik}^*$  = standard state fugacity of component  $i$  in phase  $k$  ( $k = o, s$ ), m/Lt<sup>2</sup>  
 $f_{io}$  = fugacity of component  $i$  in the oil phase, m/Lt<sup>2</sup>  
 $f_{io}^0$  = fugacity of pure component  $i$  in oil phase, m/Lt<sup>2</sup>  
 $f_{io}^*$  = standard state fugacity of component  $i$  in oil phase, m/Lt<sup>2</sup>  
 $f_{is}$  = fugacity of component  $i$  in the solid phase, m/Lt<sup>2</sup>  
 $f_{is}^0$  = fugacity of pure component  $i$  in solid phase, m/Lt<sup>2</sup>  
 $f_{is}^*$  = standard state fugacity of component  $i$  in solid phase, m/Lt<sup>2</sup>  
 $f_\ell$  = fugacity of the asphaltene component in the pure liquid state, m/Lt<sup>2</sup>  
 $f_p$  = porous medium particle transport efficiency factor  
 $f_s$  = solid fugacity, m/Lt<sup>2</sup>  
 $f_s^*$  = reference solid fugacity, m/Lt<sup>2</sup>  
 $G$  = total Gibbs free energy of the system, m/L<sup>2</sup>t<sup>2</sup>  
 $G^E$  = total excess Gibbs energy for a phase, m/L<sup>2</sup>t<sup>2</sup>  
 $\overline{G}_i^E$  = partial molar excess Gibbs energy for a component  $i$ , m/L<sup>2</sup>t<sup>2</sup>  
 $k$  = permeability, L<sup>2</sup>  
 $k^*$  = empirical constant for mass transport of wax caused by shear dispersion  
 $k_0$  = initial permeability, L<sup>2</sup>  
 $K_a$  = ratio of rate constants of the adsorption/desorption reactions  
 $K_{is}$  = solid/liquid  $K$  value for component  $i$   
 $m_i$  = mass of component  $i$ , m  
 $m_w$  = mass of wax, m  
 $M_a$  = molecular weight of alkane solvent, m  
 $M_i$  = molecular weight of component  $i$ , m  
 $n_c$  = number of components  
 $n_s$  = number of solid phases

- $n_{tr}$  = number of solid state transitions  
 $n_1$  = number of asphaltene molecules in the micellar core  
 $n_2$  = number of resin molecules in the micellar cell  
 $N_{a, L_1}$  = number of asphaltene monomers in phase  $L_1$   
 $N_{a, L_2}$  = number of asphaltene monomers in phase  $L_2$   
 $N_{m, L_1}$  = number of micelles in phase  $L_1$   
 $N_{r, L_1}$  = number of resin monomers in phase  $L_1$   
 $N_{r, L_2}$  = number of resin monomers in phase  $L_2$   
 $p$  = pressure, m/Lt<sup>2</sup>  
 $p^*$  = reference pressure, m/Lt<sup>2</sup>  
 $p_{Al}$  = lower pressure on the APE, m/Lt<sup>2</sup>  
 $p_{Au}$  = upper pressure on the APE, m/Lt<sup>2</sup>  
 $p_b$  = bubblepoint pressure, m/Lt<sup>2</sup>  
 $p_r$  = reservoir pressure, m/Lt<sup>2</sup>  
 $p_s$  = oil saturation pressure, m/Lt<sup>2</sup>  
 $P_{if}$  = pressure of fusion (corresponding to  $T_{if}$ ) of component  $i$ , m/Lt<sup>2</sup>  
 $r$  = radial distance, L  
 $R$  = gas constant  
 $\mathbf{R}$  = solvent to crude oil ratio  
 $R_c$  = critical solvent ratio  
 $t$  = time, t  
 $T$  = temperature, T  
 $T^*$  = reference temperature, T  
 $T_c$  = temperature-dependent parameter  
 $T_f$  = melting point temperature, T  
 $T_{if}$  = temperature of fusion (melting temperature) of component  $i$ , T  
 $T_{ij, tr}$  =  $j$ th solid state transition temperature of component  $i$ , T  
 $T_{il, tr}$  =  $l$ th solid state transition temperature of component  $i$ , T  
 $u_c$  = critical speed required to mobilize surface deposit asphaltene, L/t  
 $u_{np}$  = fluid velocity in nonpluggable pathways, L/t  
 $u_o$  = oil velocity, L/t  
 $v_a$  = molar volume of pure asphaltene, L<sup>3</sup>/n  
 $v_c$  = critical interstitial velocity for surface deposition, L/t  
 $v_{ci}$  = critical volume of component  $i$ , L<sup>3</sup>/n  
 $v_{cj}$  = critical volume of component  $j$ , L<sup>3</sup>/n  
 $v_{ik}$  = partial molar volume of component  $i$  in phase  $k$  ( $k = o, s$ ), L<sup>3</sup>/n  
 $v_{io}$  = partial molar volume of component  $i$  in oil phase, L<sup>3</sup>/n  
 $v_{is}$  = partial molar volume of component  $i$  in solid phase, L<sup>3</sup>/n  
 $v_{jk}$  = partial molar volume of component  $j$  in phase  $k$  ( $k = o, s$ ), L<sup>3</sup>/n  
 $v_{jo}$  = partial molar volume of component  $j$  in oil phase, L<sup>3</sup>/n  
 $v_{js}$  = partial molar volume of component  $j$  in solid phase, L<sup>3</sup>/n  
 $v_{\varnothing}$  = molar volume of liquid, L<sup>3</sup>/n  
 $v_m$  = molar volume of mixture, L<sup>3</sup>/n  
 $v_o$  = interstitial oil velocity ( $= u_o / \Phi$ ), L/t  
 $v_r$  = molar volume of resins, L<sup>3</sup>/n

- $v_s$  = solid molar volume,  $L^3/n$   
 $w_i$  = weight fraction of component  $i$ ,  $m/m$   
 $w_{sa}$  = mass of adsorbed asphaltene per mass of rock,  $m/m$   
 $(w_{sa})_{\max}$  = maximum adsorbed mass fraction (the plateau in Fig. 9.20),  $m/m$   
 $W$  = weight percent of precipitated asphaltene,  $m/m$   
 $x$  = mole fraction,  $n/n$   
 $x_i$  = mole fraction of component  $i$ ,  $n/n$   
 $x_{ik}$  = mole fraction of component  $i$  in phase  $k$  ( $k = o, s$ ),  $n/n$   
 $x_{io}$  = mole fraction of component  $i$  in oil phase,  $n/n$   
 $x_{is}$  = mole fraction of component  $i$  in solid phase,  $n/n$   
 $x_{jk}$  = mole fraction of component  $j$  in phase  $k$  ( $k = o, s$ ),  $n/n$   
 $X$  = defined in Eq. 9.1  
 $y_i$  = mole fraction of component  $i$ ,  $n/n$   
 $y_{ik}$  = mole fraction of component  $i$  in phase  $k$  ( $k = o, s$ ),  $n/n$   
 $y_{io}$  = mole fraction of component  $i$  in oil phase,  $n/n$   
 $y_{is}$  = mole fraction of component  $i$  in solid phase,  $n/n$   
 $y_{jo}$  = mole fraction of component  $j$  in oil phase,  $n/n$   
 $y_{js}$  = mole fraction of component  $j$  in solid phase,  $n/n$   
 $Y$  = defined in Eq. 9.2  
 $\alpha$  = asphaltene-deposition model parameters (Eqs. 9.29 and 9.31)  
 $\beta$  = asphaltene-deposition model parameters (Eqs. 9.29 and 9.31)  
 $\gamma$  = shear rate,  $L/t$   
 $\gamma$  = asphaltene-deposition model parameters (Eqs. 9.30 and 9.31)  
 $\gamma_i$  = activity coefficient of component  $i$  in a mixture  
 $\gamma_{ik}$  = activity coefficient of component  $i$  in phase  $k$  ( $k = o, s$ )  
 $\gamma_{io}$  = activity coefficient of component  $i$  in oil phase  
 $\gamma_{io}^{fv}$  = combinatorial free volume contribution  
 $\gamma_{io}^r$  = residual contribution  
 $\gamma_{is}$  = activity coefficient of component  $i$  in solid phase  
 $\delta_a$  = solubility parameter of asphaltene  
 $\delta_i$  = solubility parameter for component  $i$   
 $\delta_{ik}$  = solubility parameter for pure component  $i$  in phase  $k$  ( $k = o, s$ )  
 $\bar{\delta}_k$  = volume fraction average solubility parameter for phase  $k$   
 $\delta_m$  = solubility parameter of mixture  
 $\delta_o$  = solubility parameter of oil phase  
 $\bar{\delta}_o$  = volume fraction average solubility parameter of oil phase  
 $\delta_s$  = solubility parameter of solid phase  
 $\bar{\delta}_s$  = volume fraction average solubility parameter of solid phase  
 $\Delta C_p$  = heat capacity of fusion,  $mL^2/nt^2T$   
 $\Delta C_{pi}$  = heat capacity of fusion of component  $i$ ,  $mL^2/nt^2T$   
 $\Delta C_{pij, tr}$  = heat capacity of  $j$ th solid state transition of component  $i$ ,  $mL^2/nt^2T$   
 $\Delta G_m^0$  = expression for Gibbs free energy of formation of the micelle,  $mL^2/nt^2$   
 $\Delta H_f$  = enthalpy of fusion,  $mL^2/nt^2$   
 $\Delta H_{if}$  = enthalpy of fusion of component  $i$ ,  $mL^2/nt^2$



- $\Delta H_{ij,tr}$  = enthalpy of the  $j$ th solid state transition of component  $i$ ,  $\text{mL}^2/\text{nt}^2$   
 $\Delta H_{il,tr}$  = enthalpy of the  $l$ th solid state transition of component  $i$ ,  $\text{mL}^2/\text{nt}^2$   
 $\Delta H_{iv}$  = enthalpy of vaporization of component  $i$ ,  $\text{mL}^2/\text{nt}^2$   
 $\Delta U_v$  = molar internal energy of vaporization at the system temperature,  $\text{mL}^2/\text{nt}^2$   
 $\Delta v_i$  = change of molar volume caused by fusion of component  $i$ ,  $\text{L}^3$   
 $\eta$  = asphaltene deposition model parameters (Eq. 9.31)  
 $\mu_a^*$  = reference chemical potential of asphaltene component  
 $\mu_{am}$  = chemical potential of asphaltene in the mixture  
 $\mu_c$  = critical speed required to mobilize surface deposit asphaltene  
 $\mu_i$  = chemical potential of component  $i$ ,  $\text{m/L}^2\text{t}^2$   
 $\mu_{ik}$  = chemical potential of component  $i$  in phase  $k$ ,  $\text{m/L}^2\text{t}^2$   
 $\mu_{io}$  = chemical potential of component  $i$  in the oil phase,  $\text{m/L}^2\text{t}^2$   
 $\mu_{is}$  = chemical potential of component  $i$  in the solid phase,  $\text{m/L}^2\text{t}^2$   
 $\mu_{pi,k}$  = chemical potential of pure component  $i$  in phase  $k$  ( $k = o, s$ ),  $\text{m/L}^2\text{t}^2$   
 $\mu_{pi,o}$  = chemical potential of pure component  $i$  in oil phase,  $\text{m/L}^2\text{t}^2$   
 $\mu_{pi,s}$  = chemical potential of pure component  $i$  in solid phase,  $\text{m/L}^2\text{t}^2$   
 $\mu_{r,m}$  = chemical potential of resins on the surface of the asphaltene micelle,  $\text{m/L}^2\text{t}^2$   
 $\mu_{r,o}$  = chemical potential of resins in the oil phase,  $\text{m/L}^2\text{t}^2$   
 $\mu_s$  = chemical potential of the solid,  $\text{m/L}^2\text{t}^2$   
 $\rho_o$  = mass density of oil,  $\text{m/L}^3$   
 $\sigma_{np}$  = volume fraction of deposited asphaltene in nonpluggable pathway  
 $\sigma_p$  = volume fraction of deposited asphaltene in pluggable pathway  
 $\Phi$  = porosity  
 $\Phi_0$  = initial porosity  
 $\Phi_{ik}$  = fugacity coefficient of component  $i$  in phase  $k$   
 $\Phi_{ik}^0$  = fugacity coefficient of pure component  $i$  in phase state  $k$  ( $k = o, s$ )  
 $\Phi_{io}$  = fugacity coefficient of component  $i$  in oil phase  
 $\Phi_a$  = volume fraction of asphaltene in the mixture  
 $\Phi_{cr}$  = critical volume fraction of resins in the mixture  
 $\Phi_{ik}$  = volume fraction of component  $i$  in phase state  $k$  ( $k = o, s$ )  
 $\Phi_r$  = volume fraction of resins in the mixture  
 $\chi$  = asphaltene deposition model parameters (Eq. 9.30)

### Subscripts

- $L_1$  = Gibbs free energy of the liquid phase  
 $L_2$  = Gibbs free energy of the precipitated phase

---

### References

- Allen, T.O. and Roberts, A.P.: *Production Operations*, Vol. 2, second edition, Oil and Gas Consultants Intl., Tulsa, Oklahoma (1982).
- de Boer, R.B. *et al.*: "Screening of Crude Oils for Asphalt Precipitation: Theory, Practice, and the Selection of Inhibitors," *SPEPF* (February 1995) 55.
- Leontaritis, K.J. and Mansoori, G.A.: "Asphaltene Deposition: A Survey of Field Experiences and Research Approaches," *J. of Petroleum Science and Engineering* (1988) **1**, 229.
- Kokal, S.L. and Sayegh, S.G.: "Asphaltenes: The Cholesterol of Petroleum," paper SPE 29787 presented at the 1995 SPE Middle East Oil Show, Bahrain, 11–14 March.

5. Burke, N.E., Hobbs, R.E., and Kashou, S.F.: "Measurement and Modeling of Asphaltene Precipitation," *JPT* (November 1990) 1440.
6. Hirschberg, A. *et al.*: "Influence of Temperature and Pressure on Asphaltene Flocculation," *SPEJ* (June 1984) 283.
7. Monger, T.G. and Trujillo, D.E.: "Organic Deposition During CO<sub>2</sub> and Rich-Gas Flooding," *SPEERE* (February 1991) 17.
8. Novosad, Z. and Costain, T.G.: "Experimental and Modeling Studies of Asphaltene Equilibria for a Reservoir Under CO<sub>2</sub> Injection," paper SPE 20530 presented at the 1990 SPE Annual Technical Conference and Exhibition, New Orleans, 23–26 September.
9. Thomas, F.B. *et al.*: "Experimental and Theoretical Studies of Solids Precipitation From Reservoir Fluid," *J. Cdn. Pet. Tech.* (January 1992) 22.
10. Srivastava, R.K. *et al.*: "Quantification of Asphaltene Flocculation During Miscible CO<sub>2</sub> Flooding in the Weyburn Reservoir," *J. Cdn. Pet. Tech.* (October 1995) 31.
11. Srivastava, R.K., Huang, S.S., and Dong, M.: "Asphaltene Deposition During CO<sub>2</sub> Flooding," *SPEPF* (November 1999) 235.
12. Turta, A.T. *et al.*: "Permeability Impairment Due to Asphaltenes During Gas Miscible Flooding and Mitigation," paper SPE 37287 presented at the 1997 SPE International Symposium on Oilfield Chemistry, Houston, 18–21 February.
13. Kokal, S.L. *et al.*: "Measurement and Correlation of Asphaltene Precipitation From Heavy Oils by Gas Injection," *J. Cdn. Pet. Tech.* (April 1992) 24.
14. Butler, R.M. and Mokrys, I.J.: "Recovery of Heavy Oils Using Vapourized Hydrocarbon Solvents: Further Development of the Vapex Process," *J. Cdn. Pet. Tech.* (June 1993) 56.
15. Leontaritis, K.J., Amaefule, J.O., and Charles, R.E.: "A Systematic Approach for the Prevention and Treatment of Formation Damage Caused by Asphaltene Deposition," *SPEPF* (August 1994) 157.
16. Leontaritis, K.J.: "The Asphaltene and Wax Deposition Envelopes," *Fuel Science and Technology Intl.* (1996) **14**, 13.
17. Brown, T.S., Niesen, V.G., and Erickson, D.D.: "The Effects of Light Ends and High Pressure on Paraffin Formation," paper SPE 28505 presented at the 1994 SPE Annual Technical Conference and Exhibition, New Orleans, 25–28 September.
18. Daridon, J.L., Xans, P., and Montel, F.: "Phase Boundary Measurement on a Methane + Decane + Multi-Paraffins System," *Fluid Phase Equilibria* (1996) **117**, 241.
19. Pan, H., Firoozabadi, A., and Fotland, P.: "Pressure and Composition Effect on Wax Precipitation: Experimental Data and Model Results," paper SPE 36740 presented at the 1996 SPE Annual Technical Conference and Exhibition, Denver, 6–9 October.
20. Daridon, J.L. *et al.*: "Solid-Liquid-Vapor Phase Boundary of a North Sea Waxy Crude: Measurement and Modeling," *Energy and Fuels* (2001) **15**, 730.
21. Ruffier Meray, V. *et al.*: "Influence of Light Ends on the Onset Crystallization Temperature of Waxy Crudes Within the Frame of Multiphase Transport," paper SPE 26549 presented at the 1993 SPE Annual Technical Conference and Exhibition, Houston, 3–6 October.
22. McCain, W.D. Jr.: *The Properties of Petroleum Fluids*, second edition, PennWell Books, Tulsa, Oklahoma (1990).
23. Pedersen, K.S., Fredenslund, A., and Thomassen, P: *Properties of Oils and Natural Gases*, Gulf Publishing Co., Houston (1989).
24. Speight, J.G.: *The Chemistry and Technology of Petroleum*, Marcel Dekker, New York City (1991).
25. Mitchell, D.L. and Speight, J.G.: "The Solubility of Asphaltenes in Hydrocarbon Solvents," *Fuel* (April 1973) 149.
26. Speight, J.G., Long, R.B., and Trowbridge, T.D.: "Factors Influencing the Separation of Asphaltenes From Heavy Petroleum Feedstocks," *Fuel* (May 1984) 616.
27. Pfeiffer, J.P. and Saal, R.N.J.: "Asphaltic Bitumen as Colloid System," *J. of Physical Chemistry* (1940) **44**, 139.
28. Leontaritis, K.J. and Mansoori, G.A.: "Asphaltene Flocculation During Oil Production and Processing: A Thermodynamic Colloidal Model," paper SPE 16258 presented at the 1987 SPE International Symposium on Oilfield Chemistry, San Antonio, Texas, 4–6 February.

29. Leontaritis, K.J.: "Asphaltene Deposition: A Comprehensive Description of Problem Manifestations and Modeling Approaches," paper SPE 18892 presented at the 1989 SPE Production Operations Symposium, Oklahoma City, Oklahoma, 13–14 March.
30. Cimino, R. *et al.*: "Solubility and Phase Behavior of Asphaltenes in Hydrocarbon Media," *Asphaltenes: Fundamentals and Applications*, E.Y. Sheu and O.C. Mullins (eds.), Plenum Press, New York City (1995).
31. Joshi, N.B. *et al.*: "Asphaltene Precipitation from Live Crude Oil," *Energy & Fuels* (2001) **15**, 979.
32. Avila, C. *et al.*: "A Field Methodology to Estimate the Zone of Maximum Probability of Asphaltene Precipitation Occurrence," paper SPE 69531 presented at the 2001 SPE Latin American and Caribbean Petroleum Engineering Conference, Buenos Aires, 25–28 March.
33. Rassamdana, H. *et al.*: "Asphaltene Flocculation and Deposition: I. The Onset of Precipitation," *AIChE J.* (January 1996) 10.
34. Sahimi, M., Rassamdana, H., and Dabir, B.: "Asphalt Formation and Precipitation: Experimental Studies and Theoretical Modelling," *SPEJ* (June 1997) 157.
35. Srivastava, S.P. *et al.*: "Phase-Transition Studies in *n*-Alkanes and Petroleum-Related Waxes—A Review," *J. of Physical Chemistry Solids* (1993) **54**, 639.
36. Lira-Galeana, C. and Hammami, A.: "Wax Precipitation from Petroleum Fluids: A Review," *Asphaltenes and Asphalts*, 2, T.F. Yen and G.V. Chilingarian (eds.), Developments in Petroleum Science Series, Elsevier Science (2000) 557–608.
37. Gilby, G.W.: "The Use of Ethylene-Vinyl Acetate Copolymers as Flow Improvers and Wax Deposition Inhibitors in Waxy Crude Oil," *Chemicals in the Oil Industry* (1983) 108.
38. Musser, B.J., and Kilpatrick, P.K.: "Molecular Characterization of Wax Isolated from a Variety of Crude Oils," *Energy & Fuels* (1998) **12**, 715.
39. Hansen, J.H. *et al.*: "A Thermodynamic Model for Predicting Wax Formation in Crude Oils," *AIChE J.* (December 1988) 1937.
40. Hammami, A. and Raines, M.A.: "Paraffin Deposition From Crude Oils: Comparison of Laboratory Results With Field Data," *SPEJ* (March 1999) 9.
41. Turner, W.R.: "Normal Alkanes," *Industrial and Engineering Chemistry Product Research and Development* (1971) **10**, 238.
42. "TRC Thermodynamic Tables—Hydrocarbons," Thermodynamics Research Center, College Station, Texas (1997).
43. *Polymer Handbook*, J. Brandrup and E.H. Immergut (eds.), third edition, John Wiley and Sons Inc. (1989).
44. Marano, J.J. and Holder, G.D.: "General Equation for Correlating the Thermophysical Properties of *n*-Paraffins, *n*-Olefins, and Other Homologous Series. 2. Asymptotic Behavior Correlations for PVT Properties," *Industrial Engineering Chemistry Research* (1997) **36**, 1895.
45. Dorset, D.L.: "Crystal Structure of Lamellar Paraffin Eutectics," *Macromolecules* (1986) **19**, 2965.
46. Dorset, D.L.: "Chain Length and Cosolubility of *n*-Paraffins in the Solid State," *Macromolecules* (1990) **23**, 623.
47. Craig, S.R. *et al.*: "Investigation into the Structure of Binary-, Tertiary- and Quaternary-Mixtures of *n*-Alkanes and Real Diesel Waxes Using High-Resolution Synchrotron X-Ray Powder Diffraction," *J. of Material Chemistry* (1998) **8**, 859.
48. Pedersen, W.B. *et al.*: "Wax Precipitation from North Sea Crude Oils. 2. Solid-Phase Content as Function of Temperature Determined by Pulsed NMR," *Energy and Fuels* (1991) **5**, 908.
49. Hansen, A.B. *et al.*: "Wax Precipitation from North Sea Crude Oils. 3. Precipitation and Dissolution of Wax Studied by Differential Scanning Calorimetry," *Energy and Fuels* (1991) **5**, 914.
50. Dirand, M. *et al.*: "Multicomponent Paraffin Waxes and Petroleum Solid Deposits: Structural and Thermodynamic State," *Fuel* (1998) **77**, 1253.
51. Chevallier, V. *et al.*: "Mixtures of Numerous Different *n*-Alkanes: 2. Studies by X-Ray Diffraction and Differential Thermal Analyses with Increasing Temperature," *Polymer* (1999) **40**, 2129.
52. Lira-Galeana, C., Firoozabadi, A., and Prausnitz, J.M.: "Thermodynamics of Wax Precipitation in Petroleum Mixtures," *AIChE J.* (1996) **42**, 239.

53. Coutinho, J.A.P.: "Predictive UNIQUAC: A New Model for the Description of Multiphase Solid-Liquid Equilibria in Complex Hydrocarbon Mixtures," *Industrial Engineering Chemistry Research* (1998) **37**, 4870.
54. Jamaluddin, A.K.M. *et al.*: "Laboratory Techniques to Define the Asphaltene Precipitation Envelope," paper 2000-68 presented at the 2000 Petroleum Society's Canadian Intl. Petroleum Conference, Calgary, 4–8 June.
55. Sivaraman, A., Thomas, F.B., and Bennion, D.B.: "Advanced Acoustic Approach for Reservoir Solids Problems/Effects of Inhibitors on Solids Onset and EOS Modeling," paper 99-64 presented at the 1999 CSPG and Petroleum Society Joint Convention, Calgary, 14–18 June.
56. MacMillan, D.J. *et al.*: "A Unified Approach to Asphaltene Precipitation: Laboratory Measurement and Modeling," *JPT* (September 1995) 788.
57. Cimino, R. *et al.*: "Thermodynamic Modeling for Prediction of Asphaltene Deposition in Live Oils," paper SPE 28993 presented at the 1995 SPE International Symposium on Oilfield Chemistry, San Antonio, Texas, 14–17 February.
58. Hammami, A. *et al.*: "Asphaltene Precipitation from Live Oils: An Experimental Investigation of the Onset Conditions and Reversibility," *Energy & Fuels* (2000) **14**, 14.
59. Fotland, P., Anfinsen, H., and Fadnes, F.H.: "Detection of Asphaltene Precipitation and Amounts Precipitated by Measurement of Electrical Conductivity," *Fluid Phase Equilibria* (1993) **82**, 157.
60. Escobedo, J. and Mansoori, G.A.: "Viscometric Determination of the Onset of Asphaltene Flocculation: A Novel Method," *SPEPF* (May 1995) 115.
61. Vuong, L.T.: "Asphaltene Deposition and Its Role in Enhanced Oil Recovery (EOR) Miscible Gas Flooding Processes," MS thesis, U. of Illinois, Chicago (1985).
62. Kim, S.T., Boudh-Hir, M.-E., and Mansoori, G.A.: "The Role of Asphaltene in Wettability Reversal," paper SPE 20700 presented at the 1990 SPE Annual Technical Conference and Exhibition, New Orleans, 23–26 September.
63. Broseta, D. *et al.*: "Detection of Asphaltene Deposition by Capillary Flow Measurement," paper SPE 59294 presented at the 2000 SPE/DOE Improved Oil Recovery Symposium, Tulsa, 3–5 April.
64. Fotland, P.: "Precipitation of Asphaltenes at High Pressures: Experimental Technique and Results," *Fuel Science Tech. Intl.* (1996) **14**, 313.
65. Wang, J.X., Brower, K.R., and Buckley, J.S.: "Observation of Asphaltene Destabilization at Elevated Temperature and Pressure," *SPEJ* (December 2000) 420.
66. Peramanu, S. *et al.*: "Investigation of the Reversibility of Asphaltene Precipitation," *Energy and Fuels* (2001) **15**, 910.
67. Monger, T.G. and Fu, J.C.: "The Nature of CO<sub>2</sub>-Induced Organic Deposition," paper SPE 16713 presented at the 1987 SPE Annual Technical Conference and Exhibition, Dallas, 27–30 September.
68. Parra-Ramirez, M., Peterson, B., and Deo, M.D.: "Comparison of First and Multiple Contact Carbon Dioxide Induced Asphaltene Precipitation," paper SPE 65019 presented at the 2001 SPE International Symposium on Oilfield Chemistry, Houston, 13–16 February.
69. Andersen, S.I. and Speight, J.G.: "Thermodynamic Models for Asphaltene Solubility and Precipitation," *J. of Petroleum Science and Engineering* (1999) **22**, 53.
70. Chung, T.-H.: "Thermodynamic Modeling for Organic Solid Precipitation," paper SPE 24851 presented at the 1992 SPE Annual Technical Conference and Exhibition, Washington, DC, 4–7 October.
71. Yarranton, H.W. and Masliyah, J.H.: "Molar Mass Distribution and Solubility Modeling of Asphaltenes," *AIChE J.* (December 1996) **42**, 3533.
72. Zhou, X., Thomas, F.B., and Moore, R.G.: "Modelling of Solid Precipitation from Reservoir Fluid," *JCPT* (December 1996) 37.
73. Soave, G.: "Equilibrium Constants from a Modified Redlich-Kwong Equation of State," *Chemical Engineering Science* (1972) **27**, 1197.
74. Buckley, J.S. *et al.*: "Asphaltene Precipitation and Solvent Properties of Crude Oils," *Petroleum Science and Technology* (1998) **16**, 251.
75. Wang, J.X. and Buckley, J.S.: "An Experimental Approach to Prediction of Asphaltene Flocculation," paper SPE 64994 presented at the 2001 SPE International Symposium on Oilfield Chemistry, Houston, 13–16 February.

76. Nor-Azian, N. and Adewumi, M.A.: "Development of Asphaltene Phase Equilibria Predictive Model," paper SPE 26905 presented at the 1993 SPE Eastern Regional Meeting, Pittsburgh, Pennsylvania, 2–4 November.
77. Kawanaka, S., Park, S.J., and Mansoori, G.A.: "Organic Deposition From Reservoir Fluids: A Thermodynamic Predictive Technique," *SPE* (May 1991) 185.
78. Yang, Z. *et al.*: "Experimental and Modeling Studies on the Asphaltene Precipitation in Degassed and Gas-Injected Reservoir Oils," *Fluid Phase Equilibria* (1999) **157**, 143.
79. Won, K.W.: "Thermodynamics for Solid-Liquid-Vapor Equilibria: Wax Phase Formation From Heavy Hydrocarbon Mixtures," *Fluid Phase Equilibria* (1986) **30**, 265.
80. Pedersen, K.S., Skovborg, P., and Rønningsen, H.P.: "Wax Precipitation from North Sea Crude Oils. 4. Thermodynamic Modeling," *Energy & Fuels* (1991) **5**, 924.
81. Fussell, L.T.: "A Technique for Calculating Multiphase Equilibria," *SPEJ* (August 1979) 203.
82. Nghiem, L.X. and Li, Y.-K., "Computation of Multiphase Equilibrium Phenomena With an Equation-of-State," *Fluid Phase Equilibria* (1984) **17**, 77.
83. Godbole, S.P., Thele, K.J., and Reinbold, E.W.: "EOS Modeling and Experimental Observations of Three-Hydrocarbon-Phase Equilibria," *SPE* (May 1995) 101.
84. Peng, D.-Y. and Robinson, D.B.: "A New Two-Constant Equation of State," *Industrial Engineering Chemistry Fundamentals* (1976) **15**, 59.
85. Nghiem, L.X. *et al.*: "Efficient Modeling of Asphaltene Precipitation," paper SPE 26642 presented at the 1993 SPE Annual Technical Conference and Exhibition, Houston, 3–6 October.
86. Nghiem, L.X. and Coombe, D.A.: "Modeling Asphaltene Precipitation During Primary Depletion," *SPEJ* (June 1997) 170.
87. Nghiem, L.X., Coombe, D.A., and Farouq Ali, S.M.: "Compositional Simulation of Asphaltene Deposition and Plugging," paper SPE 54378 presented at the 1999 SPE Asia Pacific Oil and Gas Conference and Exhibition, Jakarta, 20–22 April.
88. Nghiem, L.X. *et al.*: "Asphaltene Precipitation: Phase Behaviour Modelling and Compositional Simulation," paper SPE 59432 presented at the 2000 SPE Asia Pacific Conference on Integrated Modelling for Asset Management, Yokohama, Japan, 25–26 April.
89. Nghiem, L.X., Sammon, P.H., and Kohse, B.F.: "Modeling Asphaltene Precipitation and Dispersive Mixing in the Vapex Process," paper SPE 66361 presented at the 2001 SPE Reservoir Simulation Symposium, Houston, 11–14 February.
90. Nghiem, L.X., Kohse, B.F., and Sammon, P.S.: "Compositional Simulation of the Vapex Process," *J. Cdn. Pet. Tech.* (August 2001) 54.
91. Li, Y.-K., Nghiem, L.X., and Siu, A.: "Phase Behaviour Computations for Reservoir Fluids: Effect of Pseudo Components on Phase Diagrams and Simulation Results," *J. Cdn. Pet. Tech.* (November–December 1985) 29.
92. Kohse, B.F. *et al.*: "Modelling Phase Behaviour Including the Effect of Pressure and Temperature on Asphaltene Precipitation," paper SPE 64465 presented at the 2000 SPE Asia Pacific Oil and Gas Conference and Exhibition, Brisbane, Australia, 16–18 October.
93. Pan, H. and Firoozabadi, A.: "Thermodynamic Micellization Model for Asphaltene Precipitation from Reservoir Crudes at High Pressures and Temperatures," paper SPE 38857 presented at the 1997 SPE Annual Technical Conference and Exhibition, San Antonio, Texas, 5–8 October.
94. Pan, H. and Firoozabadi, A.: "Thermodynamic Micellization Model for Asphaltene Aggregation and Precipitation in Petroleum Fluids," *SPEPF* (May 1998) 118.
95. Firoozabadi, A.: *Thermodynamic of Hydrocarbon Reservoirs*, McGraw-Hill Book Co. Inc., New York City (1999).
96. Piro, G. *et al.*: "Asphaltene Adsorption Onto Formation Rock: An Approach to Asphaltene Formation Damage Prevention," *SPEPF* (August 1996) 156.
97. Minssieux, L.: "Core Damage From Crude Asphaltene Deposition," paper SPE 37250 presented at the 1997 SPE International Symposium on Oilfield Chemistry, Houston, 18–21 February.
98. Ali, M.A. and Islam, M.R.: "The Effect of Asphaltene Precipitation on Carbonate-Rock Permeability: An Experimental and Numerical Approach," *SPEPF* (August 1998) 178.
99. Yeh, S.W., Ehrlich, R., and Emanuel, A.S.: "Miscible-Gasflood-Induced Wettability Alteration: Experimental Observations and Oil Recovery Implications," *SPEFE* (June 1992) 167.

100. Kamath, V.A., Yang, J., and Sharma, G.D.: "Effect of Asphaltene Deposition on Dynamic Displacements of Oil by Water," paper SPE 26046 presented at the 1993 SPE Western Regional Meeting, Anchorage, 26–28 May.
101. Yan, J., Plancher, H., and Morrow, N.R.: "Wettability Changes Induced by Adsorption of Asphaltenes," *SPEPF* (November 1997) 259.
102. Collins, S.H. and Melrose, J.C.: "Adsorption of Asphaltenes and Water on Reservoir Rock Minerals," paper SPE 11800 presented at the 1983 SPE International Symposium on Oilfield and Geothermal Chemistry, Denver, 1–3 June.
103. Dubey, S.T. and Waxman, M.H.: "Asphaltene Adsorption and Deposition From Mineral Surfaces," *SPERE* (August 1991) 389.
104. González, G. and Travalloni-Louvisse, A.M.: "Adsorption of Asphaltenes and Its Effect on Oil Production," *SPEPF* (May 1993) 91.
105. Wojtanowicz, A.K., Krilov, Z., and Langlinais, J.P.: "Study on the Effect of Pore Blocking Mechanisms on Formation Damage," paper SPE 16233 presented at the 1987 SPE Production Operations Symposium, Oklahoma City, Oklahoma, 8–10 March.
106. Gruesbeck, C. and Collins, R.E.: "Entrainment and Deposition of Fine Particles in Porous Media," *SPEJ* (December 1982) 847.
107. Wang, S. and Civan, F.: "Productivity Decline of Vertical and Horizontal Wells by Asphaltene Deposition in Petroleum Reservoirs," paper SPE 64991 presented at the 2001 SPE International Symposium on Oilfield Chemistry, Houston, 13–16 February.
108. Chang, F.F. and Civan, F.: "Practical Model for Chemically Induced Formation Damage," *J. of Petroleum Science and Engineering* (1997) **17**, 123.
109. Kocabas, I. and Islam, M.R.: "A Wellbore Model for Predicting Asphaltene Plugging," paper SPE 49199 presented at the 1998 SPE Annual Technical Conference and Exhibition, New Orleans, 27–30 September.
110. Leontaritis, K.J.: "Asphaltene Near-Wellbore Formation Damage Modeling," paper SPE 39446 presented at the 1998 SPE International Symposium on Formation Damage Control, Lafayette, Louisiana, 18–19 February.
111. Ring, J.N. *et al.*: "Simulation of Paraffin Deposition in Reservoirs," *SPEPF* (February 1994) 36.
112. Qin, X. *et al.*: "Modeling Asphaltene Precipitation in Reservoir Simulation," *Industrial Engineering Chemistry Research* (2000) **39**, 2644.
113. Clementz, D.M.: "Alteration of Rock Properties by Adsorption of Petroleum Heavy Ends: Implications for Enhanced Oil Recovery," paper SPE 10683 presented at the 1982 SPE/DOE Third Joint Symposium on Enhanced Oil Recovery, Tulsa, Oklahoma, 4–7 April.
114. Crocker, M.E. and Marchin, L.M.: "Wettability and Adsorption Characteristics of Crude-Oil Asphaltene and Polar Fractions," *JPT* (April 1988) 470.
115. Buckley, J.S. *et al.*: "Asphaltenes and Crude Oil Wetting—The Effect of Oil Composition," *SPEJ* (June 1997) 107.
116. Buckley, J.S., Liu, Y., and Monsterleet, S.: "Mechanisms of Wetting Alteration by Crude Oils," *SPEJ* (March 1998) 54.
117. Morrow, N.R.: "Wettability and Its Effect on Oil Recovery," *JPT* (December 1990) 1476.
118. Huang, E.T.S. and Holm, L.W.: "Effect of WAG Injection and Rock Wettability on Oil Recovery During CO<sub>2</sub> Flooding," *SPERE* (February 1988) 119.
119. Lin, E.C. and Huang, E.T.S.: "The Effect of Rock Wettability on Water Blocking During Miscible Displacement," *SPERE* (May 1990) 205.
120. Shedid, S.A.: "Influences of Asphaltene Deposition on Rock/Fluid Properties of Low Permeability Carbonate Reservoirs," paper SPE 68229 presented at the 2001 SPE Middle East Oil Show, Bahrain, 17–20 March.
121. Al-Maamari, R.S.H. and Buckley, J.S.: "Asphaltene Precipitation and Alteration of Wetting: Can Wettability Change During Oil Production?" paper SPE 59292 presented at the 2000 SPE/DOE Improved Oil Recovery Symposium, Tulsa, 3–5 April.
122. Samuelson, M.L.: "Alternatives to Aromatics for Solvency of Organic Deposits," paper SPE 23816 presented at the 1992 SPE International Symposium on Formation Damage Control, Lafayette, Louisiana, 26–27 February.

123. Trbovich, M.G. and King, G.E.: "Asphaltene Deposit Removal: Long-Lasting Treatment With a Cosolvent," paper SPE 21038 presented at the 1991 SPE International Symposium on Oilfield Chemistry, Anaheim, California, 20–22 February.
124. Bouts, M.N. *et al.*: "An Evaluation of New Asphaltene Inhibitors: Laboratory Study and Field Testing," *JPT* (September 1995) 782.
125. Jamaluddin, A.K.M. *et al.*: "Deasphalted Oil: A Natural Asphaltene Solvent," *SPEPF* (August 1996) 161.
126. Prausnitz, J.M., Lichtenthaler, R.N., and de Azevedo, E.G.: *Molecular Thermodynamics of Fluid-Phase Equilibria*, third edition, Prentice Hall, New Jersey (1999).
127. Choi, P.B. and McLaughlin, E.: "Effect of a Phase Transition on the Solubility of a Solid," *AIChE J.* (January 1983) 150.
128. Nichita, D.V., Goual, L., and Firoozabadi, A.: "Wax Precipitation in Gas Condensate Mixtures," paper SPE 56488 presented at the 1999 SPE Annual Technical Conference and Exhibition, Houston, 3–6 October.
129. Walas, S.M.: *Phase Equilibria in Chemical Engineering*, Butterworth Publishers, Boston, Massachusetts (1985).
130. Reddy, S.R.: "A Thermodynamic Model for Predicting *n*-Paraffin Crystallization in Diesel Fuels," *Fuel* (December 1986) 1647.
131. Weingarten, J.S. and Euchner, J.A.: "Methods for Predicting Wax Precipitation and Deposition," *SPEPE* (February 1988) 121.
132. Mei, H. *et al.*: "A Thermodynamic Modeling Method for Organic Solid Precipitation," paper SPE 56675 presented at the 1999 SPE Annual Technical Conference and Exhibition, Houston, 3–6 October.
133. Pedersen, K.S.: "Prediction of Cloud Point Temperatures and Amount of Wax Precipitation," *SPEPF* (February 1995) 46.
134. Flory, P.J.: *Principles of Polymer Chemistry*, Cornell U. Press (1953).
135. Erickson, D.D., Niesen, V.G., and Brown, T.S.: "Thermodynamic Measurement and Prediction of Paraffin Precipitation in Crude Oil," paper SPE 26604 presented at the 1993 Annual Technical Conference and Exhibition, Houston, 3–6 October.
136. Ungerer, P. *et al.*: "High Pressure-High Temperature Reservoir Fluids: Investigation of Synthetic Condensate Gases Containing a Solid Hydrocarbon," *Fluid Phase Equilibria* (1995) **111**, 287.
137. Coutinho, J.A.P., Andersen, S.I., and Stenby, E.H.: "Evaluation of Activity Coefficient Models in Prediction of Alkane Solid-Liquid Equilibria," *Fluid Phase Equilibria* (1995) **103**, 23.
138. Coutinho, J.A.P. and Stenby, E.H.: "Predictive Local Composition Models for Solid/Liquid Equilibrium in *n*-Alkane Systems: Wilson Equation for Multicomponent Systems," *Industrial Engineering Chemistry Research* (1996) **35**, 918.
139. Coutinho, J.A.P.: "A Thermodynamic Model for Predicting Wax Formation in Jet and Diesel Fuels," *Energy & Fuels* (2000) **14**, 625.
140. Pauly, J. *et al.*: "Prediction of Solid-Fluid Phase Diagrams of Light Gases—Heavy Paraffin Systems up to 200 MPa Using an Equation of State—GE Model," *Fluid Phase Equilibria* (2000) **167**, 145.
141. Pauly, J., Dauphin, C., and Daridon, J.L.: "Liquid-Solid Equilibria in a Decane + Multi-Paraffins System," *Fluid Phase Equilibria* (1998) **149**, 191.
142. Svendsen, J.A.: "Mathematical Modeling of Wax Deposition in Oil Pipeline Systems," *AIChE J.* (August 1993) 1377.
143. Burger, E.D., Perkins, T.K., and Striegler, J.H.: "Studies of Wax Deposition in the Trans Alaska Pipeline," *JPT* (June 1981) 1075.
144. Kok, M.V. and Saracoglu, O.: "Mathematical Modelling of Wax Deposition in Crude Oil Pipeline Systems," paper SPE 64514 presented at the 2000 SPE Asia Pacific Oil and Gas Conference and Exhibition, Brisbane, Australia, 16–18 October.
145. Keating, J.F. and Wattenbarger, R.A.: "The Simulation of Paraffin Deposition and Removal in Wellbores," paper SPE 27871 presented at the 1994 SPE Western Regional Meeting, Long Beach, California, 23–25 March.
146. Hamouda, A.A. and Davidsen, S.: "An Approach for Simulation of Paraffin Deposition in Pipelines as a Function of Flow Characteristics With a Reference to Teesside Oil Pipeline," paper

- SPE 28966 presented at the 1995 SPE International Symposium on Oilfield Chemistry, San Antonio, Texas, 14–17 February.
147. Majeed, A., Bringedal, B., and Overå, S. “Model Calculates Wax Deposition for N. Sea Oils,” *Oil & Gas J.* (18 June 1990) 63.
148. Ramirez-Jaramillo, E., Lira-Galeana, and Manero, O.: “Numerical Simulation of Wax Deposition in Oil Pipeline Systems,” *Petroleum Science and Technology* (2001) **19**, 143.
149. Misra, S., Baruah, S., and Singh, K.: “Paraffin Problems in Crude Oil Production and Transportation: A Review,” *SPEPF* (February 1995) 50.
150. Becker, J.R.: “Oilfield Paraffin Treatments: Hot Oil and Hot Water Compared to Crystal Modifiers,” paper SPE 63123 presented at the 2000 SPE Annual Technical Conference and Exhibition, Dallas, 1–4 October.
151. Fan, Y. and Llave, F.M.: “Chemical Removal of Formation Damage From Paraffin Deposition Part 1—Solubility and Dissolution Rate,” paper SPE 31128 presented at the 1996 SPE International Symposium on Formation Damage Control, Lafayette, Louisiana, 14–15 February.

### SI Metric Conversion Factors

°API	$141.5/(131.5+^{\circ}\text{API})$		= g/cm <sup>3</sup>
bar	× 1.0*	E + 05	= Pa
cal	× 4.184*	E + 03	= J
ft	× 3.048*	E - 01	= m
ft <sup>3</sup>	× 2.831 685	E - 02	= m <sup>3</sup>
°F	$(^{\circ}\text{F} - 32)/1.8$		= °C
°F	$(^{\circ}\text{F} + 459.67)/1.8$		= K
psi	× 6.894 757	E + 00	= kPa

\*Conversion factor is exact.



## Chapter 10

# Properties of Produced Water

David J. Blumer, ConocoPhillips

### 10.1 History of Produced Water in Oil and Gas Fields

Early U.S. settlements commonly were located near salt licks that supplied salt to the population. These salt springs were often contaminated with petroleum, and many of the early efforts to acquire salt by digging wells were rewarded by finding unwanted amounts of oil and gas associated with the saline waters. In the Appalachian Mountains, saline water springs commonly occur along the crests of anticlines.<sup>1</sup>

In 1855, it was found that petroleum distillation produced light oil that was, as an illuminant, similar to coal oil and better than whale oil.<sup>2</sup> This knowledge spurred the search for saline waters containing oil. With the methods of the salt producers, Colonel Edward Drake drilled a well on Oil Creek, near Titusville, Pennsylvania, in 1859. He struck oil at a depth of 70 ft, and this first oil well produced approximately 35 B/D.<sup>3</sup>

Early oil producers did not realize the significance of the oil and saline waters occurring together. In fact, it was not until 1938 that the existence of interstitial water in oil reservoirs was generally recognized.<sup>4</sup> Torrey<sup>5</sup> was convinced by 1928 that dispersed interstitial water existed in oil reservoirs, but his colleagues rejected his belief because most of the producing wells did not produce any water on completion. Occurrences of mixtures of oil and gas with water were recognized by Griswold and Munn,<sup>6</sup> but they believed that there was a definite separation of the oil and water, and that oil, gas, and water mixtures did not occur in the sand before a well tapped a reservoir.

It was not until 1928 that the first commercial laboratory for the analysis of rock cores was established, and the first core tested was from the Bradford third sand (Bradford field, McKean County, Pennsylvania). The percent saturation and percent porosity of this core were plotted vs. depth to construct a graphic representation of the oil and water saturation. The soluble mineral salts that were extracted from the core led Torrey to suspect that water was indigenous to the oil-productive sand.

Shortly thereafter, a test well was drilled near Custer City, Pennsylvania, that encountered greater than average oil saturation in the lower part of the Bradford sand. This high oil saturation resulted from the action of an unsuspected flood, the existence of which was not known when the location for the test well had been selected. The upper part of the sand was not cored. Toward the end of the cutting of the first core with a cable tool, core barrel oil began to come into the hole so fast that it was not necessary to add water for the cutting of the second

section of the sand. Therefore, the lower 3 ft of the Bradford sand was cut with oil in a hole free from water.

Two samples from this section were preserved in sealed containers for saturation tests, and both of them, when analyzed, had a water content of approximately 20% pore volume. This well made approximately 10 BOPD and no water after being stimulated with nitroglycerine. Thus, the evidence developed by the core analysis and the productivity test after completion provided a satisfactory indication of the existence of immobile water, indigenous to the Bradford-sand oil reservoir, which was held in its pore system and could not be produced by conventional pumping methods.<sup>5</sup>

Fettke<sup>7</sup> was the first to report the presence of water in oil-producing sand; however, he thought that the drilling process might have introduced it. Munn<sup>8</sup> recognized that moving underground water might be the primary cause of migration and accumulation of oil and gas. However, this theory had little experimental data to back it until Mills<sup>9</sup> conducted several laboratory experiments on the effect of moving water and gas on water/oil/sand and water/oil/gas/sand systems. Mills concluded that “the updip migration of oil and gas under the propulsive force of their buoyancy in water, as well as the migration of oil, either up or down dip, caused by hydraulic currents, are among the primary factors influencing both the accumulation and the recovery of oil and gas.” This theory was seriously questioned and completely rejected by many of his contemporaries.

Rich<sup>10</sup> assumed that “hydraulic currents, rather than buoyancy, are effective in causing accumulation of oil or its retention.” He did not believe that the hydraulic accumulation and flushing of oil required rapid movement of water, but rather that oil was an integral constituent of the rock fluids, and that it could be carried along with them whether the movement was very slow or relatively rapid.

The effect of water displacing oil during production was not recognized in the early days of the petroleum industry in Pennsylvania. Laws were passed, however, to prevent operators from injecting water into the oil reservoir sands through unplugged wells. In spite of these laws, some operators at Bradford secretly opened the well casing opposite shallow groundwater sands to start a waterflood in the oil sands. Effects of artificial waterfloods were noted in the Bradford field in 1907 and became evident approximately 5 years later in the nearby oil fields of New York.<sup>11</sup> Volumetric calculations of the oil-reservoir volume that were made for engineering studies of the waterflood operations proved that interstitial water was generally present in the oil sands. Garrison<sup>12</sup> and Schilthuis<sup>4</sup> reported on the distribution of oil and water in the pores of porous rocks. They described the relationship between water saturation and formation permeability, while discussing the origin and occurrence of “connate” water in porous rocks.

Lane and Gordon<sup>13</sup> first used the word “connate” to mean interstitial water deposited with the sediments. The processes of rock compaction and mineral diagenesis result in the expulsion of large amounts of water from sediments and movement out of the deposit through the more permeable rocks; therefore, it is highly unlikely that the water now in any pore is the same as when the particles that surround it were deposited. White<sup>14</sup> redefined connate water as “fossil” water because it has been out of contact with the atmosphere for an appreciable part of geologic time period. Thus, connate water is distinguished from “meteoric” water, which entered the rocks in geologically recent times, and from “juvenile” water, which came from deep in the earth’s crust and has never been in contact with the atmosphere.

Meanwhile, petroleum engineers and geologists had learned that waters associated with petroleum could be identified, with regard to the reservoir in which they occurred, by knowledge of their chemical characteristics.<sup>15</sup> Commonly, the waters from different strata differ considerably in their major dissolved chemical constituents, making the identification of water sourced from a particular stratum possible.<sup>16</sup> However, in some areas, the concentrations of dissolved constituents in waters from different strata do not differ significantly, and the identifi-

cation of such waters is difficult or impossible. [Sec. 10.4](#) describes new techniques to assist in this process, because several new analytical and statistical techniques for trace species apply nicely to this problem.

The enormous quantities of water produced from many fields originally surprised operators and, even today, water-handling costs continue to be significant to company management trying to reduce costs. The amount of water produced with the oil usually increases as the amount of oil produced decreases, even during primary production. At the end of the life of some reservoirs, 100 times (or more) as much water is processed as oil sold.

The history of oil production is replete with operators who decided that the water-handling costs were too high for an older field to be profitable, so they sold the property to another operator. The new operator finds ways of reducing the impacts of that water to produce the smaller oil stream profitably, until they become discouraged and sell to yet another operator, and so on. Very few mature reservoirs, especially those that have undergone secondary and tertiary recovery, have been completely abandoned because new technology and better engineering have made it economical to produce oil at extremely high water cuts or to reduce the water cut by controlling water production in the reservoir and wells. It is the challenge of producers to recover the most oil from the reservoir profitably, which means discovering methods to minimize the impacts of produced water for that particular field.

**10.1.1 Produced Water Is Important.** As mentioned previously, extraction of oil and gas from underground reservoirs often is accompanied by water or brine, which is referred to as produced water. As reservoirs mature, especially if secondary or tertiary recovery methods are used, the quantity of water climbs and often exceeds the volume of the hydrocarbons before the reservoir is exhausted. The cost of producing, handling, and disposing of the produced water often defines the economic lifetime of a field and the actual hydrocarbon reserves; therefore, understanding and predicting the aspects, behavior, and problems induced by the produced-water flow is important.

Because the produced water is not usually a revenue stream, the emphasis on water-flow prediction, technology development, and engineering application has not traditionally been a major focus of oil- and gas-production engineering. This is complicated by the multidisciplinary nature of produced-water issues, including chemistry; hydrodynamics; surface/interfacial science; materials science; corrosion; mechanical, chemical, and petroleum engineering; as well as environmental regulators. Compared with the advanced knowledge of water and brines, produced water is relatively poorly understood because of its unique aspects.

Produced water is chemically very complex. The process of producing and processing produced water causes changes in temperature and pressure. The addition of treating chemicals, along with the presence of coproduced gas, oil, and likely solids, changes the produced-water properties and behavior. Understanding how production perturbs the chemical state of the produced water is the key to predicting and controlling many problems. Also, the chemical composition is an excellent source of information about the particular reservoir and the reservoir depletion process.

Diagnosing the source of the increased water production from a well is important in deciding whether to pursue water-shutoff options. First, if the field is waterflooded, water must be produced to recover the oil in accordance with relative permeability; only water in excess of this should be a target for remedial treatments. If this is edge water, water shutoff can be difficult, even with polymer-gel technology. Polymer-gel water-shutoff treatments have proved successful in cases in which faults intersect the wellbore, causing a channel for water flow. If excess water production is bottomwater, the well can be plugged back. However, excess water production is often the result of intrusive water from a shallow sand or another aquifer gaining access to the well from a leaky casing or faulty completion. This source of intrusive water can be repaired, depending on the economics.<sup>17</sup>

Waters produced with petroleum are growing in importance from an environmental standpoint. In the past, these waters were considered waste and required disposal. Early on, less attention was paid to the fate of the produced water in the environment, because, after all, it was only water. It later became clear that possible contamination from produced-water disposal practices, especially on the surface, needs to be considered. The bulk of produced water from land-based operations is reinjected. Injection of these waters back into the petroleum reservoir serves three purposes: it produces additional petroleum through secondary recovery (waterflooding), it uses a potential pollutant, and, in some areas, it controls land subsidence.

Secondary and tertiary oil-recovery processes that use water injection result in the production of even more water with the oil. To inject these waters into reservoir rocks, suspended solids and oil must be removed to an appropriate degree to prevent plugging. Most offshore platforms dispose of their produced water directly into the ocean, but have to meet increasingly stringent regulations on the entrained and dissolved oil and other chemicals that are in the produced water. Some offshore operators are considering produced-water reinjection to avoid meeting these expensive ocean-disposal requirements.

**10.1.2 Where Does the Water Come From?** As discussed previously, in the original reservoir, the pores in the mineral matrix contain the natural fluids at chemical equilibrium. Because reservoir rock is largely of sedimentary origin, water was present at the time of rock genesis and, therefore, is trapped in the pores of the rock. Water may also move or migrate according to the hydraulic pressures induced by geological processes that also form the reservoirs.

In hydrocarbon reservoirs, some of the water is displaced by the hydrocarbon, but some water always remains. If the rock originated in a sea or ocean, then it will be saline. Rocks deposited in lakes, rivers, or estuaries have fresher water. Originally, the water was in chemical equilibrium with the mineral suite of the rock, but, on invasion of the oil and gas, a new equilibrium with those phases was achieved. Thus, there are both equilibria and chemical-reaction dynamics associated with the inorganic (mineral) phases and the oil and gas phases that are important to understand. Water is an excellent solvent; it will react to dissolve many of the phases it contacts.

## 10.2 Primary Production

When oil or gas is flowed or lifted from a reservoir, some water inevitably accompanies the other phases. This is a consequence of the relative permeability behavior of the rock, as discussed in the chapter on relative permeability in this section of the Handbook. In particular, if the water saturation is above the irreducible water saturation ( $S_{wr}$ ), then some water will move along with the oil and gas phases present as the fluids flow from the pores of the reservoir rock. This water is in chemical equilibrium with the rock and gas phases under the original temperature and pressure present in the reservoir. Because the pressure and temperature change as a consequence of producing the oil and gas, the chemical equilibrium of the water is perturbed. The perturbation can have severe detrimental effects. The operator must be interested in these effects to mitigate their economic and environmental impacts.

The chemical changes occurring during primary production are largely a result of cooling the water and reducing the pressure as it comes up the tubing into the surface production facilities. However, more-complex behavior can result if multiple zones or reservoirs are coproduced either within the same wellbore downhole or mixed on the surface. The mixing can lead to scale deposition, corrosion, and other effects. Artificial lift can also alter the stability of the water. In particular, gas lift and jet pumps are particular artificial-lift examples in which the chemical composition of the system may change because of the addition of foreign gas or water streams in the wellbore. Another impact of artificial lift is on the pressure profile of the system. Electrical submersible pumps can locally heat the water enough to enter a scaling

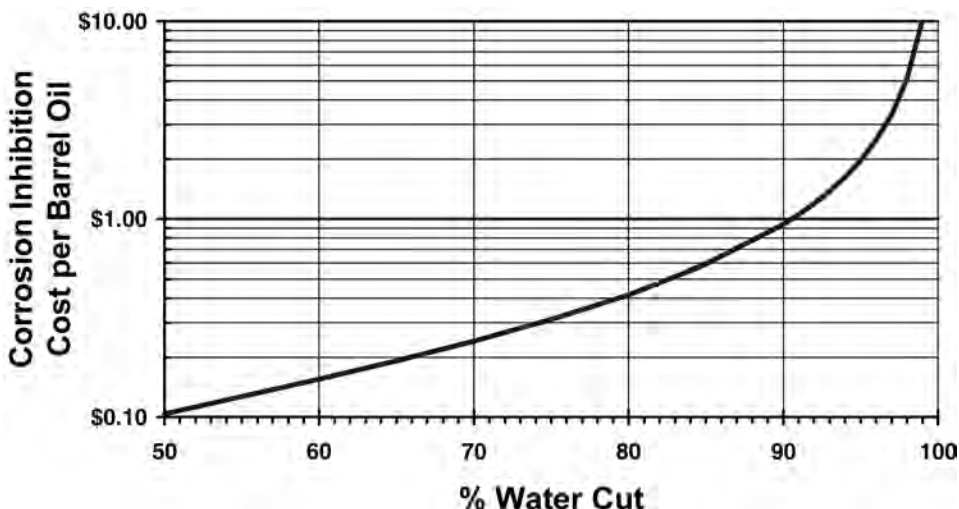


Fig. 10.1—Corrosion-inhibition cost on a per-barrel-oil basis determines the maximum producible economic water cut (assuming a constant inhibition cost of U.S. \$0.10/bbl water) and oil reserves. Increasing water cut eventually drives the cost of corrosion inhibitor above the value of the produced oil, unless inhibitor performance improves.

regime (particularly for calcium carbonate) in the area of the motor, deposit scale on it, and cause the motor to burn out.

During primary production, the water cut may increase as the reservoir is depleted. This is particularly important in reservoirs that have natural waterdrives so that a water aquifer is in both pressure and hydraulic communication with the hydrocarbon reservoir. Thus, as the hydrocarbon is produced, the water from the aquifer is drawn in to fill the void left behind, and the water saturation of the rock is increased. The pressure in the reservoir attempts to stay constant. Depending on the efficiency of the hydraulic connection to the aquifer, the pressure decline over time will be reduced, perhaps to zero in some cases. However, the proportion of water produced will rise until the cost of handling the water exceeds the value of the hydrocarbons produced. Oil and gas reserves of the typical reservoir are limited by this water-handling cost. Clearly, produced-water issues are central, although this may not be immediately apparent because only the hydrocarbons produce revenue.

### 10.3 Economics of Produced Water

Except in the case of gas production from coal seams, water production rates usually start slowly from the initial development of a property. Facility designers may deliberately forestall construction and installation of water-handling equipment at the beginning of a project to reduce upfront capital costs. The eventual appearance of water production requires the addition of the capital investment and operational expense to handle the growing water rates, which do not generate revenue to offset the cost. The natural tendency for companies is to minimize the immediate expense; as a result, companies often underdesign the equipment or fail to budget properly for operational expenses.

Fig. 10.1 demonstrates the impact of rising water cut on the total cost of producing a barrel of oil assuming a constant water-treatment cost of U.S. \$0.10 per barrel of water. Actual water costs can be lower or higher. This sobering fact vividly illustrates the importance of improving the technology of water treatment to lower the unit cost over time as reservoirs mature. Most secondary and tertiary oil reserves are produced at high water cuts.

Typically, the connate water (as the original water in the reservoir is called) is more saline than surface water. Many oil and gas reservoirs are in rocks originally lying at the bottom of oceans and were saturated with the seawater present at the time. Of course, the composition of these ancient seawaters may be significantly different than current seawater. Additionally, as the sediments were buried and the temperature and pressure increased, the chemical composition of the water and rock changed to maintain chemical equilibrium. These reactions took place over geologic time, so the aqueous phases of most oil reservoirs are in true chemical equilibrium with the mineral suite with which it is in contact. The converse is not necessarily true; many examples of meta-stable mineral suites are known in hydrocarbon reservoirs, probably because of mass-transfer limitations. Thus, one use of an examination of the water composition by geochemists is to provide insight into the burial history of the sediments in the reservoir. In particular, the isotope ratios of the elements are indicative of the origins of the waters and, in some cases, of the mechanisms by which the hydrocarbons were produced during geologic time.

Besides the commonly thought of species or components in the water such as salts and dissolved minerals, oilfield waters also contain organic species. Much less attention has been allocated to the organic chemical species in the produced water, yet they also have consequences. In particular, new environmental concerns about water and air pollution have required more focus on the dissolved organic species in the water. Some examples of these species include the volatile organic acids like formic, acetic, propionic, and butyric acids; naphthenic acids; and dissolved aromatic compounds like benzene, toluene, and xylenes. The latter species are particularly important for offshore overboard water-disposal operations, because they are often included in the measurements of the oil-in-water carryover, which are limited by law in many areas. The carryover of oil and other hydrocarbons in the produced water is one of the most important issues facing the surface engineer.

**10.3.1 How Do We Characterize Produced Water?** Because produced waters are chemically complex systems, compositional computer models are needed to predict their behavior accurately. This technology has advanced steadily since the mid-1970s. One of the first thermodynamics-based water-chemistry computer models was WATEQ, developed by Truesdale and Jones at USGS, along with its database of 522 dissolved species and 192 mineral phases. This computer code was converted to FORTRAN IV in 1974 and became known as WATEQF. It has become the standard against which all future chemistry models are measured. Several major efforts to improve and extend the range of applications of these chemistry models have resulted in sophisticated programs to model water flow and geochemical reactions in reservoirs, production of water to surface, and water-chemistry changes during processing in surface facilities. These changes can have extremely serious impacts through precipitation of scales and corrosion; therefore, the accuracy of these predictions affects the profitability and, sometimes, the viability of many oil and gas projects.

Along with the computer models is the improvement in analytical chemistry technology needed to characterize the individual water in a particular system and provide the fundamental chemical equilibrium and kinetics data that form the basis for the computer models. The analytical instruments now used include inductively coupled plasma spectroscopy (ICP), ion chromatography (IC), capillary electrophoresis (CE), ion selective electrodes, and automatic titrators. In certain special analyses, more advanced techniques are used such as mass spectroscopy, high performance liquid chromatography (HPLC), and various “hyphenated techniques” such as inductively coupled plasma-mass spectroscopy (ICP-MS), gas chromatography-mass spectroscopy, and HPLC-mass spectroscopy. In circumstances in which speciation of the inorganic constituents is particularly of interest, ion chromatography can be used along with ICP or ICP-MS detection. Laser light-scattering instruments are usually used for looking at suspended particles and entrained oil droplets and their size distribution.

One of the most significant produced-water developments during the last two decades has been in the environmental impact and regulatory area. It is no longer a technical issue regarding the composition and fate of the produced water from oil and gas extraction (and transportation and refining, also). In many cases, government regulations limit or change the options available and may define the degree of characterization through sampling and analysis imposed on the operator. In the United States, produced water is still an exempt effluent and need not meet the more stringent requirements of hazardous wastes; however, other regulations impose many other requirements that must be monitored, met, and documented continuously. These regulations, the priority of concerns, and their degree of enforcement differ worldwide. When operating in nondomestic areas, familiarization with these regulations is mandatory, preferably during the conceptual facility- and field-design stages of a new development. These regulations have changed worldwide toward more stringent requirements. When choosing a particular method to handle produced water, that method's viability for the long term must be considered.

#### 10.4 Scale Deposition and Corrosion

The two main detrimental effects encountered during handling produced water are deposition of insoluble scales and corrosion of metal surfaces, which leads to leaks and costly repairs.<sup>18,19</sup> In accordance with the importance of the topics of scale and corrosion, there is an enormous and quickly growing literature, which cannot be reviewed easily here. Scale deposition is predicted through the use of the computer chemistry models mentioned previously. The most common scales are calcium carbonate, calcium sulfate, barium sulfate, iron sulfide, and iron carbonate.

Inhibition of most of these scales is now successful through proper application of particular organic compounds, most of which act to poison the growth sites of the crystals while they are still submicron in size. Two common classes of these inhibitors are the organophosphonates, such as diethylenetriaminepentamethylene phosphonic acid, and low-molecular-weight polyacrylic acid polymers (commonly <1,000 molecular weight). Unfortunately, the computer programs are less useful in predicting precisely which scale inhibitor to select for a particular produced water; therefore, laboratory experiments are needed. These experiments are often done with synthetic waters made to reflect the composition of the actual produced water; however, because minor and trace species are sometimes ignored in formulating these synthetic test waters, the results of the laboratory tests can be incorrect in picking the most effective inhibitor,<sup>20</sup> which can result in ineffective inhibition or much higher treating costs.

Corrosion predictions for produced waters are much less certain than scale-precipitation predictions. The corrosion reactions are much more complex and involve many factors other than the thermodynamics of the obvious chemical reactions of oxidizing and dissolving the metal, such as mass transport, concentration cells, effect of fluid flow and velocity, scale deposition, and microbes. In cases in which H<sub>2</sub>S levels become high, improperly specified metallurgy or welding procedures can lead to catastrophic and rapid failure from sulfide stress cracking. Loss of life has resulted from this corrosion. Every effort must be taken to measure and predict the water and gas compositions properly, so that the metallurgy will accommodate those levels. If levels approaching 0.05 psia H<sub>2</sub>S are encountered, National Assn. of Corrosion Engineers (NACE) specifications should be followed carefully.

While there are several computer programs that attempt to predict corrosivity of a produced-water system, these are currently just reasonably good guides. Because of the complexity of real systems, an approach that begins with the water and gas composition inputs to these computer models and then is followed by laboratory testing, field testing, and, finally, an ongoing field-monitoring program is likely to result in successful corrosion control in that particular system. The level of effort applied should be proportional to the aggressiveness of the corrosion, the consequences of failure, and the length of time the system must operate.

Corrosion mitigation typically takes two forms: investment in corrosion-resistant alloys or a chemical corrosion-inhibition/monitoring program. Choosing the best option on a new project should involve a complete life-cycle cost analysis. Existing operations often have already determined that choice, so it is up to the engineers, production chemists, and operators to create the most cost-effective solutions to the corrosion challenges presented by that particular produced water. Like scale inhibitors, corrosion inhibitors must be chosen for each particular area by thorough laboratory and field testing to find the inhibitor with the best combination of cost and performance. Dosage adjustments based on field corrosion-monitoring results can ensure long facility life and few, if any, leaks. An inhibitor mitigation process that incorporates a feedback loop will optimize the dosages of the inhibitor until corrosion-damage/repair cost is minimized, while the amount of inhibitor pumped is no greater than necessary. A similar process can be applied to scale inhibitors and other treating chemicals with modifications with appropriate monitoring techniques.

**10.4.1 Sampling and Analyses of Produced Waters.** The composition of subsurface water commonly changes vertically and laterally in the same aquifer. Changes may be brought about by the intrusion of other waters and by discharge from and recharge to the aquifer. As a reservoir is produced, the compositions typically change with time; therefore, it is difficult, but important, to obtain a representative sample of a given subsurface body of water. Any one sample is a very small part of the total mass, which may vary widely in composition; therefore, it is generally necessary to obtain and analyze many samples. Also, the samples themselves may change with time as gases evolve from solution or may precipitate solids when coming to ambient conditions. The sampling sites should be selected to fit into a comprehensive network to cover an oil-productive basin, in which case the information is of value in both exploration and production.

Water compositions from particular wells change over time, so a periodic sampling program is needed. The sampling frequency needed is not universal. The best guideline is the particular field itself: the faster the composition changes, the more often the water needs sampling. Fields undergoing waterflood or tertiary recovery naturally show water-chemistry changes as the injected water mixes with the formation water. Reservoirs under primary production can show dilution from water moving from adjacent compacting clay beds into the petroleum reservoir as the pressure declines because of the removal of oil, gas, and brine. This can be a detector for possible subsidence of the reservoir and perhaps the surface. The composition of oilfield water can vary with the position within the geologic structure from which it is obtained. In some cases, the salinity will increase upstructure to a maximum at the point of oil/water contact.

## 10.5 Drillstem or Downhole Water Sampling

**10.5.1 Sample Methods.** Various techniques and devices are now available for the evaluation of newly drilled wells, but there remain some important factors that must be considered when obtaining these samples and evaluating the results. The primary problem stems from the contamination of the reservoir with the drilling, completion, and stimulation fluids used during the well-construction operation. The contamination is usually easily detected from the analytical results. If one realizes that high concentrations of particular species that were used in those wellbore fluids appear in the water-analysis results, then the sample was likely contaminated and the usefulness of the sample reduced accordingly. Naturally, one must always include these species in the analysis. Unfortunately, if a sample is contaminated there is seldom an opportunity to re-enter the hole and obtain a new sample, except at great cost.

One approach for a standard drillstem test (DST) is to sample the water after each stand of pipe is removed. Normally, the total-dissolved-solids (TDS) content will increase downward,



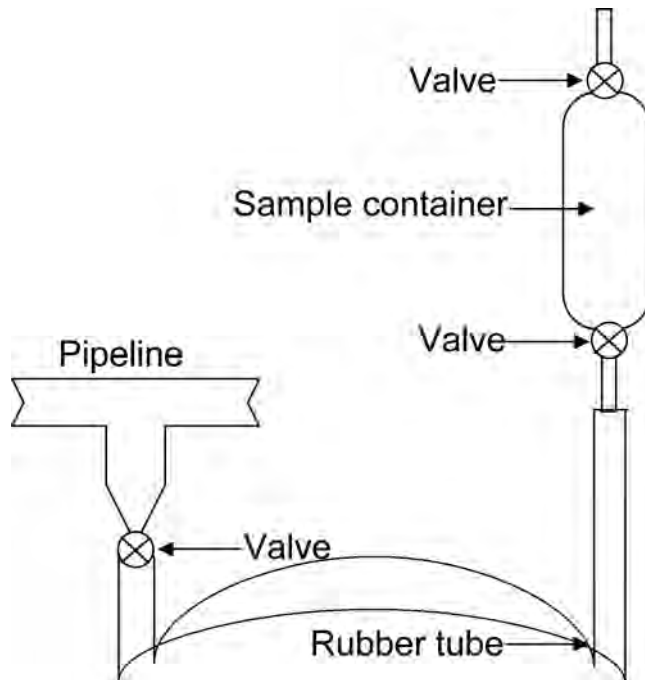


Fig. 10.2—Flowline sampler.

becoming constant when pure formation water is obtained. A test that flows water improves the chances of an uncontaminated sample; otherwise, the best chance is to sample just above the DST tool, because this was the last water to enter the tool. Newer downhole samplers sometimes allow multiple samples to be obtained; therefore, if one first pulls a large volume of water into the tool and then a second (or third) sample from the same interval, there is a chance of getting uncontaminated water in that sample.

For example, analyses of water obtained from a DST of Smackover limestone water in Rains County, Texas, demonstrates the errors caused by improper sampling of DST water. Analyses of top, middle, and bottom samples taken from a 50-ft zone of fluid recovery show an increase in salinity with depth in the drillpipe, indicating that the first water was contaminated by mud filtrate.<sup>20</sup> Thus, the bottom sample was the most representative of Smackover water.

**Sample Containing Dissolved Gas.** Knowledge of certain dissolved hydrocarbon gases is used in exploration.<sup>21,22</sup> Mapping anomalies of hydrocarbons in both surface water and subsurface aquifer water samples is an extraordinarily powerful geochemical tool.

**Sampling at the Flowline.** Another method of obtaining a sample for analysis of dissolved gases is to place a sampling device in a flowline, as Fig. 10.2 illustrates. The device is connected to the flowline, and water is allowed to flow into and through the container, which is held above the flowline, until 10 or more volumes of water have flowed through the container. The lower valve on the sample container is closed, and the container removed. If any bubbles are present in the sample, the sample is discarded, and a new one is obtained.

**Sampling at the Wellhead.** It is common practice to obtain a sample of formation water from a sampling valve at the wellhead. A plastic or rubber tube can be used to transfer the sample from the sample valve into the container (usually plastic). The source and sample container should be flushed to remove any foreign material before a sample is taken. After flushing the system, the end of the tube is inserted into the bottom of the container, and several volumes of fluid are displaced before the tube is removed slowly from the container and the

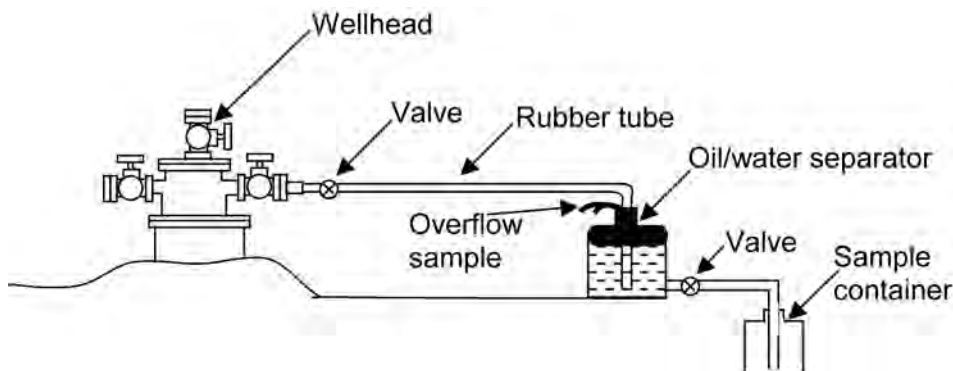


Fig. 10.3—Example of the method used to obtain a sample at the wellhead.

container is sealed. Fig. 10.3 illustrates a method of obtaining a sample at the wellhead. An extension of this method is to place the sample container in a larger container, insert the tube to the bottom of the sample container, allow the brine to overflow both containers, and withdraw the tube and cap the sample under the fluid.

At pumping wellheads, the brine will surge out in heads and be mixed with oil. In such situations, a larger container equipped with a valve at the bottom can be used as a surge tank, an oil/water separator, or both. To use this device, place the sample tube in the bottom of the large container, open the wellhead valve, rinse the large container with the well fluid, allow the large container to fill, and withdraw a sample through the valve at the bottom of the large container. This method obtains samples that are relatively oil free.

**Field-Filtered Sample.** For some studies, it is necessary to obtain a field-filtered sample. Fig. 10.4 shows a filtering system that has proved to be successful for various applications. This filtering system is simple and economical. It consists of a 50-mL disposable syringe, two check valves, and an inline-disk filter holder. The filter holder takes size 47-mm-diameter, 0.45- $\mu\text{m}$  pore-sized filters, with the option of a prefilter and depth prefilter. After the oilfield brine is separated from the oil, the brine is drawn from the separator into the syringe. With the syringe, it is forced through the filter into the collection bottle. The check valves allow the syringe to be used as a pump for filling the collection bottle. If the filter becomes clogged, it can be replaced in a few minutes. Approximately 2 minutes are required to collect 250 mL of sample. Usually three samples are taken, with one being acidified to pH 3 or less with concentrated HCl or HNO<sub>3</sub>, and another stabilized with biocide. The system can be cleaned easily or flushed with brine to prevent contamination.

**Sample for Stable-Isotope Analysis.** Stable isotopes have been used in several research studies to determine the origin of oilfield brines.<sup>23–25</sup> The most common isotopes studied are deuterium/hydrogen, <sup>2</sup>H/<sup>1</sup>H; oxygen, <sup>18</sup>O/<sup>16</sup>O; and stable carbon isotopes, <sup>13</sup>C/<sup>12</sup>C. Also, isotopically labeled compounds are sometimes used to trace injection waters or stimulation fluids. The isotopic analyses of the water, gas, and oil phases can be useful to geochemists in determining the sequence of fluid migrations in reservoirs during their genesis.

**Sample for Determining Unstable Properties or Species.** A mobile analyzer was designed to measure pH, Eh (redox potential), O<sub>2</sub>, resistivity, S<sup>2-</sup>, HCO<sub>3</sub><sup>-</sup>, CO<sub>3</sub><sup>2-</sup>, and CO<sub>2</sub> in oilfield water at the wellhead. Portable field kits for chemical analysis are available for these analyses, which provide reasonably accurate on-site results. When oilfield brine samples are collected in the field and transported to the laboratory for analysis, many of the unstable constituents change in concentration. The amount of change depends on the sampling method, sample storage, ambi-

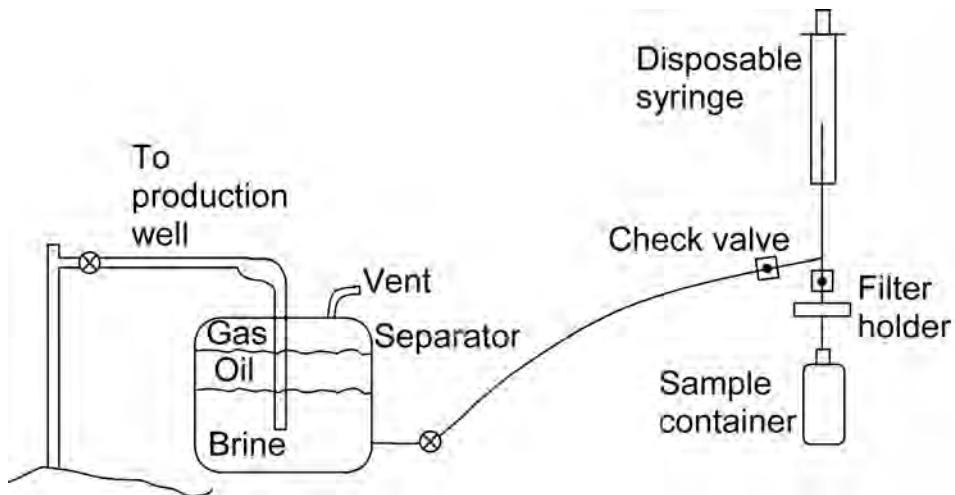


Fig. 10.4—Example of field-filtering equipment.

ent conditions, and the amounts of the constituents in the original sample. Therefore, an analysis of the brine at the wellhead is necessary to obtain reliable data.<sup>26</sup>

**Sample Containers.** The types of containers that are used include polyethylene, other plastics, hard rubber, metal cans, and borosilicate glass. Glass will adsorb various ions, such as iron and manganese, and may contribute boron or silica to the aqueous sample. Plastic and hard-rubber containers are not suitable if the sample is to be analyzed to determine its organic content, unless tested and shown otherwise. A metal container is used by some laboratories if the sample is to be analyzed for dissolved hydrocarbons such as benzene. Produced water often will corrode metal containers, unless they are lined. The corrosion will alter the chemical composition of the water by adding metal ions such as iron and manganese and by lowering the pH. The type of container selected depends on the planned use of the analytical data.

**10.5.2 Water Sampling and Analysis Specification.** This section defines a “standard water analysis” that specifies the complete suite of species and provides suggestions on sampling and analytical techniques. The analysis specifications have been used by the author for two decades and have been used by others, with adaptations for particular needs. The results of this extensive list of analyses are the required input for the various computer multicomponent simultaneous-equilibrium chemistry models that can predict correctly the changes in the water chemistry, scale precipitation, rock/water interactions, water sources and mixing, and corrosion.

While there is always temptation and pressure to limit the range of analyses performed on a sample, analytical technology has reduced dramatically the value of limiting the range of an analysis. Most instruments automatically measure many different species in a single run; therefore, it may cost the same to get one species as it does to get many, depending on the analytical technique. For instance, the commonly used ICP instruments typically measure 10 to 60 elements at a time (depending on the particular instrument) in a few minutes; therefore, adding or subtracting a species on the ICP changes the actual cost very little.

The analytical results should be stored in an electronic database for further analysis and comparison of samples from the same points over time. Certain evaluations can be performed on individual samples, such as scale-deposition predictions or monitoring for corrosion with dissolved manganese and iron. Other evaluations require successive samples, with consistent sample-collection and -analysis procedures, for the data to be meaningful. These results can be

Sample Number _____	Field _____	Farm/Lease/Platform _____
Well No. _____	Section _____	Township _____ Range _____
County _____	State _____	Country _____
Operator _____	Operator's Address _____	
Date/Time _____	Sample obtained by _____	Address _____
Representing _____	Sample obtained from _____ (flowline, separator, tank, etc.)	
Temperature _____	Pressure _____	Flow _____
Completion date of well _____	Name of productive zone from which sample is produced _____	
Sand _____	Shale _____	Lime _____ Other _____
Productive formation name _____	Names of formation well passes through _____	
Depths: Top of formation _____ Bottom of formation _____		
Top of producing zone _____ Bottom of producing zone _____		
Bottomhole pressure and date of pressure _____ Bottomhole temperature _____		
Date of last workover _____	Are any chemicals added to treat well _____	
If yes, what and concentration? _____		
Well production: Initial _____	Present _____	Casing service record _____
Oil, B/D _____	_____	
Water, B/D _____	_____	
Gas, ft <sup>3</sup> /D _____	_____	
Method of production (primary, secondary, or tertiary) _____		
Remarks (such as casing leaks, communication or other pay in same well, lease or field): _____		

Fig. 10.5—Description and label for each water sample.

mapped to follow the reservoir-area changes over time. They also can provide insight as to potential improvements in reservoir management of a waterflood, because the various ions provide natural tracer data for the injected water. The data are also useful for deciphering casing leaks, conductive (but unmapped) faults, and, in favorable cases, zonal splits of water production. If the data were not collected on each sample consistently or if the analysis suite was minimized to save money in the laboratory, these valuable evaluations are not possible.

**Tabulation of Sample Description.** Fig. 10.5 illustrates the information that should be obtained for each sample of oilfield water. As much information as possible should be recorded when taking the sample. The following measurements must be taken in the field at the sampling point coincident with taking the sample because these values change quickly once the sample is removed: temperature, pH, Eh (optional), dissolved O<sub>2</sub> (Chemet or meter), H<sub>2</sub>S, CO<sub>2</sub>, pressure, and bicarbonate (HCO<sub>3</sub><sup>-</sup>) alkalinity titration (recommended).

**Example 10.1 Problem.** Conduct laboratory analyses to generate the data needed to enter into the computer programs that will predict the stability of water, with respect to precipitation of scales as a function of temperature and pressure.

**Solution.** Obtain three bottles for each sample: one for cations/metals (Table 10.1), one for anions/etc. (Table 10.2), and one for organic acids (Table 10.3). The bottles should be polyethylene, Teflon, or polycarbonate. Not all polyethylenes are satisfactory because some contain relatively high amounts of metal contributed by catalysts in their manufacture. Fill a bottle with acid solution, let stand for a week, and then analyze the acid for metals to test the bottle's suitability. Glass should be avoided if the sample can freeze, because it is likely to break.

Cation Species	Analytical Technique	Sample Treatment
Na	ICP or DCP, AA	Acidified with 10 mL ultrapure HNO <sub>3</sub> in 1 L polyethylene, Teflon, or polycarbonate bottle
K	ICP or DCP, AA	
Li	ICP or DCP, AA	
Ca	ICP or DCP, AA	
Mg	ICP or DCP, AA	
Sr	ICP or DCP, AA	
Ba	ICP-MS, ICP or DCP	
Fe	ICP or DCP, AA	
Mn	ICP-MS, ICP	
Al	ICP-MS, ICP	
Cr	ICP-MS, ICP	
Si	ICP or DCP	
B	ICP or DCP, ICP-MS	
P	ICP-MS, ICP	

Anion* Species	Analytical Technique	Sample Treatment	
Cl <sup>-</sup>	Titration, IC, or EC	No additives, fill completely 1 L polyethylene, Teflon, or polycarbonate bottle	
Br <sup>-</sup>	CE or IC		
F <sup>-</sup>	Ion selective electrode		
I <sup>-</sup>	Ion selective electrode		
SO <sub>4</sub> <sup>=</sup>	IC or CE		
NO <sub>3</sub> <sup>-</sup>	IC or CE		
S <sup>=</sup>	Ion selective electrode		
NH <sub>4</sub> <sup>+</sup>	Ion selective electrode or IC		Cation that cannot be done on Bottle A
HCO <sub>3</sub> <sup>-</sup>	Titration or TOC analyzer		Should be done at sampling site
CO <sub>3</sub> <sup>=</sup>	Titration		Should be done at sampling site
Resistivity	Resistivity probe		
Conductivity	Conductivity cell		
pH (laboratory)	pH meter	Should be done at sampling site	
Eh (laboratory)	ORP (pH) meter	Should be done at sampling site	

Glass often is reactive with highly saline brines and strongly adsorbs some oils and other organics, including treating chemicals.

Filter a measured portion of the sample taken for the anion analysis through a 0.45- $\mu$ m filter to measure the total suspended solids. If a large amount of solids is collected, the filter paper should be saved for later X-ray powder diffraction, scanning electron microscopy/energy dispersive X-ray spectroscopy analysis (to identify the solids), and a laser particle-size analysis.

Tables 10.1 and 10.3 specify that the bottles for the cation and organic-acids analyses have additives: 10 mL of ultrapure nitric acid (HNO<sub>3</sub>) for the ICP analysis and 1 mL of glutaralde-

Organic Acids	Analytical Technique	Sample Treatment
Formic	IC or CE	1 mL Glutaraldehyde in 250 mL polyethylene, Teflon, or polycarbonate bottle
Acetic	IC or CE	
Propionic	IC or CE	
Butyric	IC or CE	

hyde for the organic acids. This stabilizes the samples so that precipitation of the metals does not ruin the results for the ICP analysis. In particular, the iron will precipitate as the sample sits and that precipitate removes many of the other species from solution. Also, the naturally present bacteria in the water will quickly eat the organic acids in the samples unless biocide is added to that sample. If no biocide, such as glutaraldehyde, has been added, no organic acids are detected; therefore, adding glutaraldehyde to a bottle used for the organic-acid analysis is highly recommended.

In addition to the water analysis, the gas in contact with the water is important. Taking a gas sample at the same time is recommended, although one taken at a different time can suffice for less critical applications. The main constituents of interest in the gas are the CO<sub>2</sub> and H<sub>2</sub>S. The H<sub>2</sub>S analysis usually is done at the sampling point. CO<sub>2</sub> and H<sub>2</sub>S are very important in predicting what will happen with the water.

In general, bacterial surveys are recommended, primarily with the serial dilution technique with one medium for sulfate-reducing bacteria (SRB) and another medium for general anaerobic bacteria. Many times, the exact medium composition (and sometimes the incubation temperature) has to be adjusted for a particular field to get that population to grow well. The bacteria have a lot of negative side effects, such as generating H<sub>2</sub>S, causing a safety and corrosion problem, and making the schmoos (organic/inorganic deposits) formation in the produced-water problem worse. Microbial-induced corrosion can be very severe, especially in deadlegs (stagnant areas in which water and solids are trapped), low-flow areas, and underdeposits.

**10.5.3 Physical Properties of Oilfield Waters.** This section discusses important physical properties of oilfield waters. As a rule, it is best to have reliable laboratory measurements of the physical properties of oilfield waters. If laboratory measurements are not available, correlations may have to be used. For example, McCain has published some of the most widely used correlations for the physical properties of oilfield waters.<sup>21,22</sup> In addition to defining physical properties of oilfield waters, we present correlations for calculating many of those properties.

## 10.6 Compressibility

The compressibility of formation water at pressures above the bubblepoint is defined as the change in water volume per unit water volume per psi change in pressure. This is expressed mathematically as

$$c_w = -\frac{1}{V} \left( \frac{\partial V}{\partial p} \right)_T, \dots\dots\dots (10.1a)$$

or

$$\bar{c}_w = -\frac{1}{\bar{V}} \left( \frac{V_2 - V_1}{p_2 - p_1} \right), \dots\dots\dots (10.1b)$$

or

$$\bar{c}_w = -\frac{1}{\bar{B}_w} \left( \frac{B_{w2} - B_{w1}}{p_2 - p_1} \right), \dots\dots\dots (10.1c)$$

where

- $\bar{c}_w$  = water compressibility at the given pressure and temperature, bbl/bbl-psi,
- $c_w$  = average water compressibility within the given pressure and temperature interval, bbl/bbl-psi,
- $V$  = water volume at the given pressure and temperature, bbl,
- $\bar{V}$  = average water volume within  $p$  and  $T$  intervals, bbl,
- $p_1$  and  $p_2$  = pressure at conditions 1 and 2 with  $p_1 > p_2$ , psi,
- $B_{w1}$  and  $B_{w2}$  = water formation volume factor (FVF)  $p_1$  and  $p_2$ , bbl/bbl, and
- $\bar{B}_w$  = average water FVF corresponding to  $V$ , bbl/bbl.

Water compressibility also depends on the salinity. In contrast to the literature, laboratory measurements by Osif<sup>23</sup> show that the effect of gas in solution on compressibility of water with NaCl concentrations up to 200 g/cm<sup>3</sup> is essentially negligible. Osif’s results show no effect at gas/water ratios (GWRs) of 13 scf/bbl. At GWRs of 35 scf/bbl, there is probably no effect, but certainly no more than a 5% increase in the compressibility of brine.

Laboratory measurements<sup>20</sup> of water compressibility resulted in linear plots of the reciprocal of compressibility vs. pressure. The plots of  $1/c_w$  vs.  $P$  have a slope of  $m_1$  and intercepts linear in salinity and temperature. Data points for the systems tested containing no gas in solution resulted in Eq. 10.2.

$$\frac{1}{c_w} = m_1 p + m_2 C + m_3 T + m_4, \dots\dots\dots (10.2)$$

where  $c_w$  = water compressibility, psi<sup>-1</sup>;  $p$  = pressure, psi;  $C$  = salinity, g/L of solution;  $T$  = temperature, °F;  $m_1 = 7.033$ ;  $m_2 = 541.5$ ;  $m_3 = -537$ ; and  $m_4 = 403.3 \times 10^3$ . Eq. 10.2 was fit for pressures between 1,000 and 20,000 psi, salinities of 0 to 200 g/L NaCl, and temperatures from 200 to 270°F. Compressibilities were independent of dissolved gas.

When conditions overlap, the agreement with the results reported by both Dorsey<sup>24</sup> and Dotson and Standing<sup>25</sup> is very good. Results from the Rowe and Chou<sup>26</sup> equation agree well up to 5,000 psi (their upper pressure limit) but result in larger deviations with increasing pressure. In almost all cases, the Rowe and Chou compressibilities are less than that of Eq. 10.2.

### 10.7 Density

The density of formation water is a function of pressure, temperature, and dissolved constituents. It is determined most accurately in the laboratory on a representative sample of formation water.<sup>27</sup> The formation-water density is defined as the mass of the formation water per unit volume of the formation water. Electronic densimeters can quickly determine the density with accuracy of +/-0.00001 g/cm<sup>3</sup> over a wide range of temperatures, although most oilfield data are reported at a 60°F reference temperature.

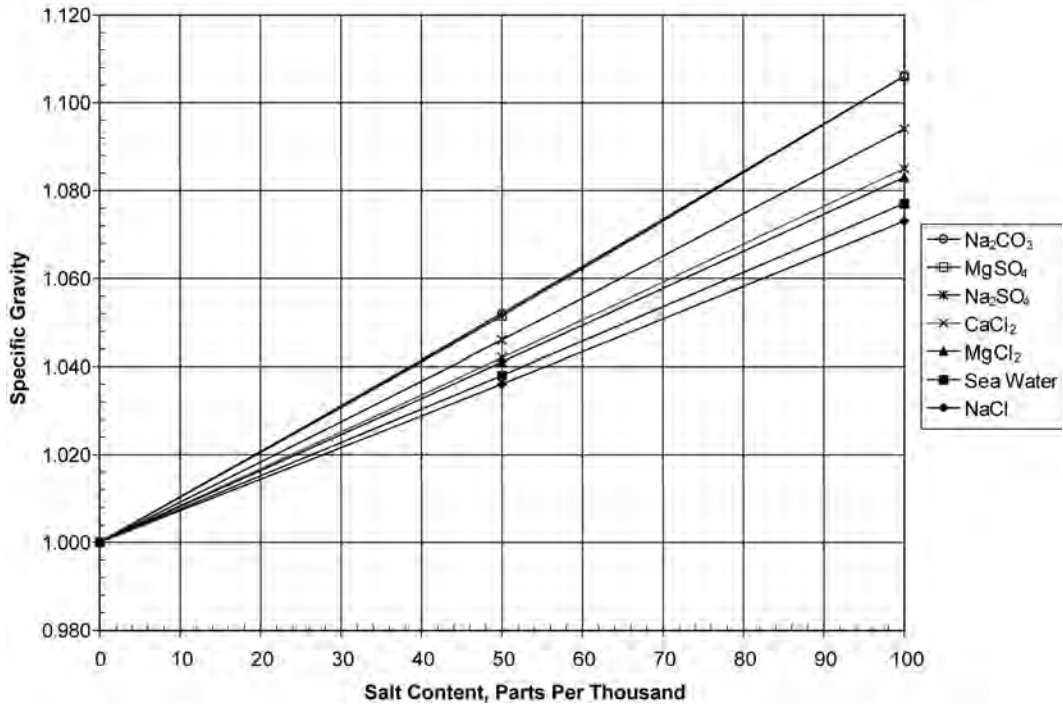


Fig. 10.6—Specific gravity of salt solutions at 60°F and 14.7 psia.

In the past, density in metric units ( $\text{g}/\text{cm}^3$ ) was considered equal to specific gravity; therefore, for most engineering calculations, density and specific gravity were interchangeable in most of the older designs.<sup>16</sup> However, process simulation software used in modern facility design uses the true density or specific gravity of the water to avoid significant cumulative errors, especially when working with low-gravity heavy oils or concentrated brines. Thus, water samples taken for providing input to these programs must have accurate densities determined experimentally. Alternatively, some modern multicomponent chemical equilibrium simulators accurately calculate the densities (and other physical properties) from the complete analysis of the waters within the temperature and pressure range of the thermodynamic database. Experimental verification of the computer predictions should be performed in cases in which any error could have significant impact.

When laboratory data or actual water samples are unavailable, the density of formation water at reservoir conditions can be estimated roughly (usually to within  $\pm 10\%$ ) from correlations (Figs. 10.6 through 10.8). The only field datum necessary is the density at standard conditions, which can be obtained from the salt content by use of Fig. 10.6. The salt content can be estimated from the formation resistivity, as measured from electric-log measurements. The density of formation water at reservoir conditions can be calculated in four steps.

- With the temperature and density at atmospheric pressure, obtain the equivalent weight percent NaCl from Fig. 10.7.
- Assuming the equivalent weight percent NaCl remains constant, extrapolate the weight percent to reservoir temperature and read the new density.
- Knowing the density at atmospheric pressure and reservoir temperature, use Fig. 10.8 to find the increase in specific gravity (density) when compressed to reservoir pressure. For oil reservoirs below the bubblepoint, the “saturated-with-gas” curves should be used; for water con-



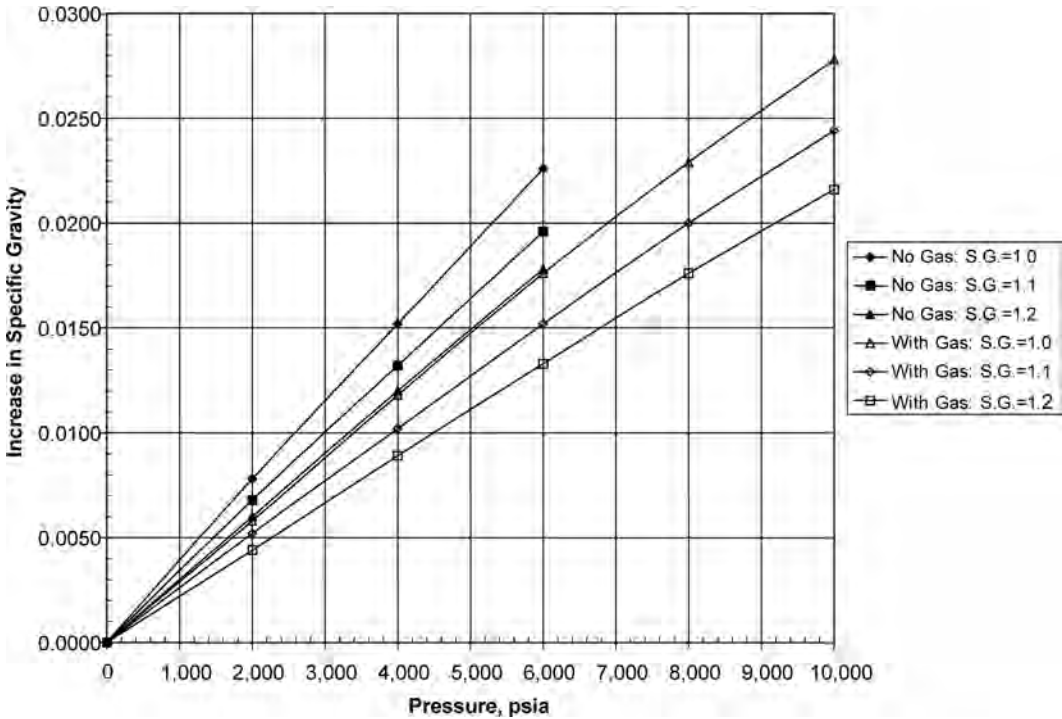


Fig. 10.7—Increase in specific gravity with pressure—salt water.

sidered to have no solution gas, the “no-gas-in-solution” curves should be used. These curves were computed from data given by Ashby and Hawkins.<sup>28</sup>

- The density of formation water (g/cm<sup>3</sup>) at reservoir conditions is the sum of the values read from Figs. 10.7 and 10.8. They can be added directly because the metric units are referred to the common density base of water (1 g/cm<sup>3</sup>). The metric units can be changed to customary units (lbm/ft<sup>3</sup>) by multiplying by 62.37.

Another approach to calculating water density is to first calculate the density of formation water at standard conditions with McCain’s correlation.<sup>21,22</sup>

$$\rho_w = 62.368 + 0.438603 \times S + 1.60074 \times 10^{-3} \times S^2, \dots\dots\dots (10.3)$$

where density is in lbm/ft<sup>3</sup>, and S is salinity in weight percent. Then, density at reservoir conditions is calculated by dividing the density in Eq. 10.3 by the brine FVF at the reservoir temperature and pressure of interest.

The specific gravity of formation water can be estimated, if the TDS is known, with

$$\gamma_w = 1 + C_{sd} \times 0.695 \times 10^{-6}, \dots\dots\dots (10.4)$$

where C<sub>sd</sub> = concentration of dissolved solids (also known as TDS), mg/L.

Rogers and Pitzer<sup>29</sup> provide precise but very detailed calculations. They tabulated a large number of values of compressibility, expansivity, and specific volume vs. molality, temperature, and pressure. A semiempirical equation of the same type was found to be effective in

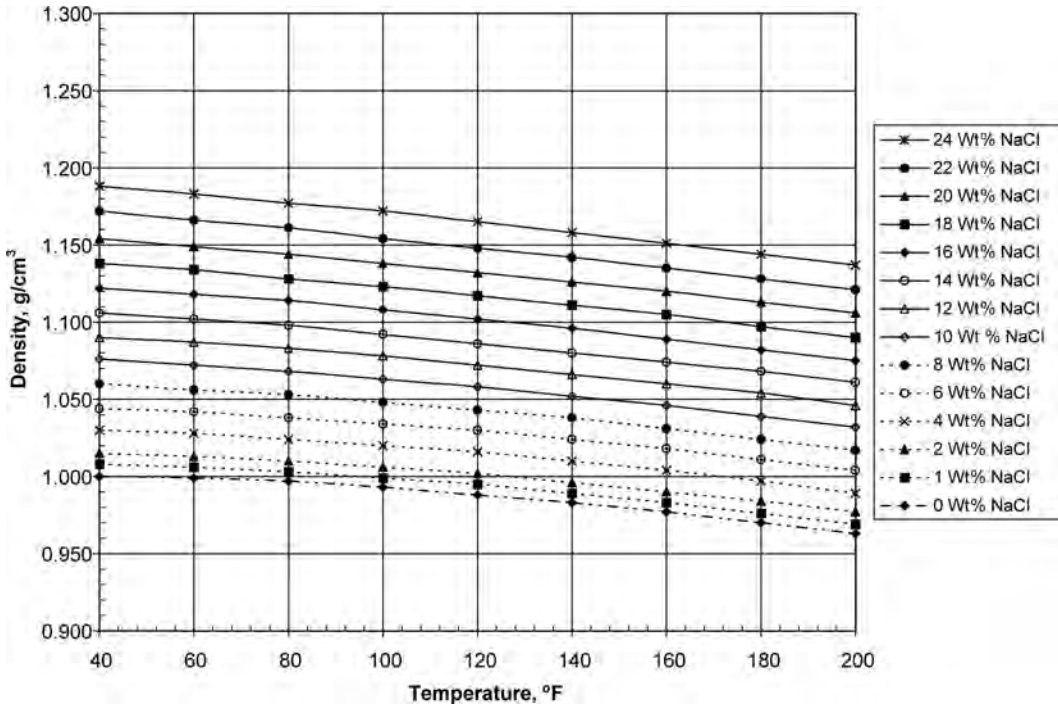


Fig. 10.8—Density of sodium chloride solutions at 14.7 psia vs. temperature.

describing thermal properties of NaCl (0.1 to 5 molality) and was used to reproduce the volumetric data from 0 to 300°C and 1 to 1,000 bars.

**10.8 Formation Volume Factor**

The water FVF,  $B_w$ , is defined as the volume at reservoir conditions occupied by 1 STB of formation water plus its dissolved gas. It represents the change in volume of the formation water as it moves from reservoir conditions to surface conditions. Three effects are involved: the liberation of gas from water as pressure is reduced, the expansion of water as pressure is reduced, and the shrinkage of water as temperature is reduced.

Fig. 10.9 is a typical plot of water FVF as a function of pressure. As the pressure is decreased to the bubblepoint,  $p_b$ , the FVF increases as the liquid expands. At pressures below the bubblepoint, gas is liberated, but, in most cases, the FVF still will increase because the shrinkage of the water resulting from gas liberation is insufficient to counterbalance the expansion of the liquid. This is the effect of the small solubility of natural gas in water.

The most accurate source of the FVF is laboratory data. It also can be calculated from density correlations if the effects of solution gas have been accounted for properly. Eq. 10.5 is used to estimate  $B_w$  if solution gas is included in the laboratory measurement or correlation of  $\rho_{rc}$ .

$$B_w = \frac{V_{rc}}{V_{sc}} \times \frac{\rho_{sc}}{\rho_{rc}}, \dots\dots\dots (10.5)$$

where

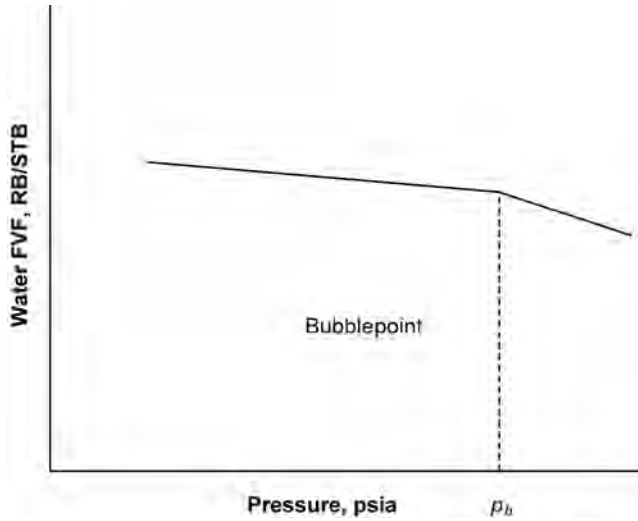


Fig. 10.9—Typical plot of water FVF vs. pressure.

$V_{rc}$  = volume occupied by a unit mass of water at reservoir conditions (weight of gas dissolved in water at reservoir or standard conditions is negligible),  $\text{ft}^3$ ,

$V_{sc}$  = volume occupied by a unit mass of water at standard conditions,  $\text{ft}^3$ ,

$\rho_{sc}$  = density of water at standard conditions,  $\text{lbm/ft}^3$ , and

$\rho_{rc}$  = density of water at reservoir conditions,  $\text{lbm/ft}^3$ .

The density correlations and the methods of estimating  $\rho_{sc}$  and  $\rho_{rc}$  were described previously. The FVF of water can be less than one if the increase in volume resulting from dissolved gas is not great enough to overcome the decrease in volume caused by increased pressure. The value of FVF is seldom higher than 1.06.

An alternative expression for the FVF of brine may be calculated from McCain:<sup>21,22</sup>

$$B_w = (1 + \Delta V_{wp})(1 + \Delta V_{wT}), \dots\dots\dots (10.6)$$

where

$$\Delta V_{wp} = -1.0001 \times 10^{-2} + 1.33391 \times 10^{-4}T + 5.50654 \times 10^{-7}T^2, \dots\dots\dots (10.7)$$

and

$$\begin{aligned} \Delta V_{wT} = & -1.95301 \times 10^{-9}pT - 1.72834 \times 10^{-13}p^2T \\ & - 3.58922 \times 10^{-7}p - 2.25341 \times 10^{-10}p^2, \dots\dots\dots (10.8) \end{aligned}$$

where  $p$  = pressure in psia, and  $T$  = temperature in °F. McCain reported that this correlation agrees with a limited set of published experimental data to within 2%. The correlation is considered valid for temperatures to 260°F, and pressures to 5,000 psia. An increase in dissolved solids causes a slight increase in  $\Delta V_{wT}$  and a slight decrease in  $\Delta V_{wp}$ , which offset each other to within 1%.

## 10.9 Resistivity

The resistivity of formation water is a measure of the resistance offered by the water to electrical current. It can be measured directly or calculated.<sup>16</sup> The direct-measurement method is essentially the electrical resistance through a 1-m<sup>2</sup> cross-sectional area of 1 m<sup>3</sup> of formation water. Formation-water resistivity,  $R_{wg}$ , is expressed in units of  $\Omega\cdot\text{m}$ . When resistivity of formation water is used in electric-log interpretation, the value is adjusted to formation temperature.

## 10.10 Surface (Interfacial) Tension

Surface tension is a measure of the attractive force acting at a boundary between two phases. If the phase boundary separates a liquid and a gas or a liquid and a solid, the attractive force at the boundary usually is called surface tension; however, the attractive force at the interface between two liquids is called interfacial tension (IFT). The lower the IFT, the smaller the droplet of the internal phase. At very low values of IFT, oil and water become miscible and behave as a single phase. IFT is an important factor in enhanced recovery. Also, the IFT determines the ease of separation of oil from water, because it determines the size of the oil or water droplets, depending on which phase is internal.

Most chemicals added during the course of drilling or production have a major effect on the IFT of the produced water and the hydrocarbons. Indeed, certain corrosion inhibitors added to the three-phase production stream can lower the produced-water IFT enough (<1 to 5 dyne/cm) to cause the droplet size of the entrained oil to be small enough that no injection-well plugging is observed, even at high oil carryover (percent levels) in the reinjected produced water.<sup>29</sup> In attempting to separate the oil from the three-phase production stream, the addition of emulsion breakers changes the IFT and promotes the agglomeration of small droplets into larger ones that separate quickly. Formulating, selecting, testing, and troubleshooting emulsion breakers is the focus of an enormous amount of the effort devoted to the impacts of producing water with hydrocarbons.

Surface tension is measured in the laboratory by a tensiometer, by the drop method, or by a variety of other methods. Descriptions of these methods are found in most physical chemistry texts. The laboratory measurements traditionally have been difficult and done only by specialized facilities. Computerized commercial pendant-drop and falling-drop tensiometers are now available for use by chemists in more general field R&D laboratories. IFT is a critical property of produced water, but is rarely measured because of the analytical difficulties. This new technology promises to improve the ability to troubleshoot problems by directly measuring IFT instead of trial-and-error testing.

## 10.11 Viscosity

The viscosity of formation water,  $\mu_w$ , is a function of pressure, temperature, and dissolved solids. In general, brine viscosity increases with increasing pressure, increasing salinity, and decreasing temperature.<sup>31</sup> Dissolved gas in the formation water at reservoir conditions generally results in a negligible effect on water viscosity. There is little information on the actual numerical effect of dissolved gas on water viscosity.

Gas-in-the-water phase behaves entirely differently than gas in hydrocarbons.\* In water, the presence of the gas actually causes the water molecules to interact with each other more strongly, thus increasing the rigidity and viscosity of the water. However, this effect is very small and has not been measured to date. In the physical chemistry literature, there is an enormous amount of indirect evidence to support this concept.

For the best estimation of the viscosity of water, refer to Kestin *et al.*<sup>32</sup> Their correlating equations involve 32 parameters for calculating the numerical effect of pressure, temperature,

\* Personal communication with J.C. Melrose, Mobil R&D Corp., Dallas (1985).

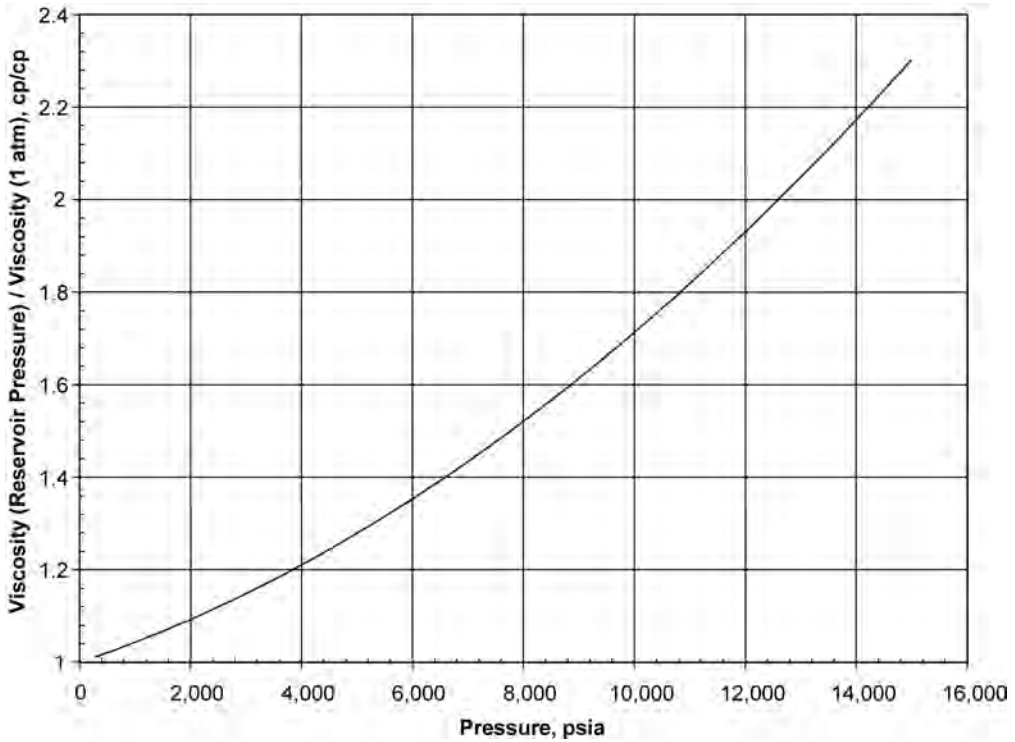


**Fig. 10.10—Effect of pressure on water viscosity. The ratio of water viscosity at reservoir pressure to water viscosity at 1 atm is shown.**

and concentration of aqueous NaCl solutions on the dynamic and kinematic viscosity of water. The 28 tables generated from the correlating equations cover a temperature range from 20 to 150°C, a pressure range from 0.1 to 35 mPa, and a concentration range from 0 to 6 molal.

**Figs. 10.10 through 10.12** may be used to approximate water viscosity. These figures are calculated from the following correlation presented by McCain<sup>20,21</sup> for water viscosity (in cp) at 1 atm:

$$\mu_{w1} = AT^{-B}, \dots\dots\dots (10.9)$$

where

$$A = 109.574 - 8.40564 \times S + 0.313314 \times S^2 + 8.72213 \times 10^{-3} \times S^3, \dots\dots\dots (10.10)$$

and

$$B = 1.12166 - 2.63951 \times 10^{-2} \times S + 6.79461 \times 10^{-4} \times S^2 + 5.47119 \times 10^{-5} \times S^3 - 1.55586 \times 10^{-6} \times S^4 \dots\dots\dots (10.11)$$

McCain reported that this correlation is within 5% of graphical correlations for temperatures between 100 and 400°F, and salinities to 26 wt%.

Water viscosity at reservoir pressure can be obtained from

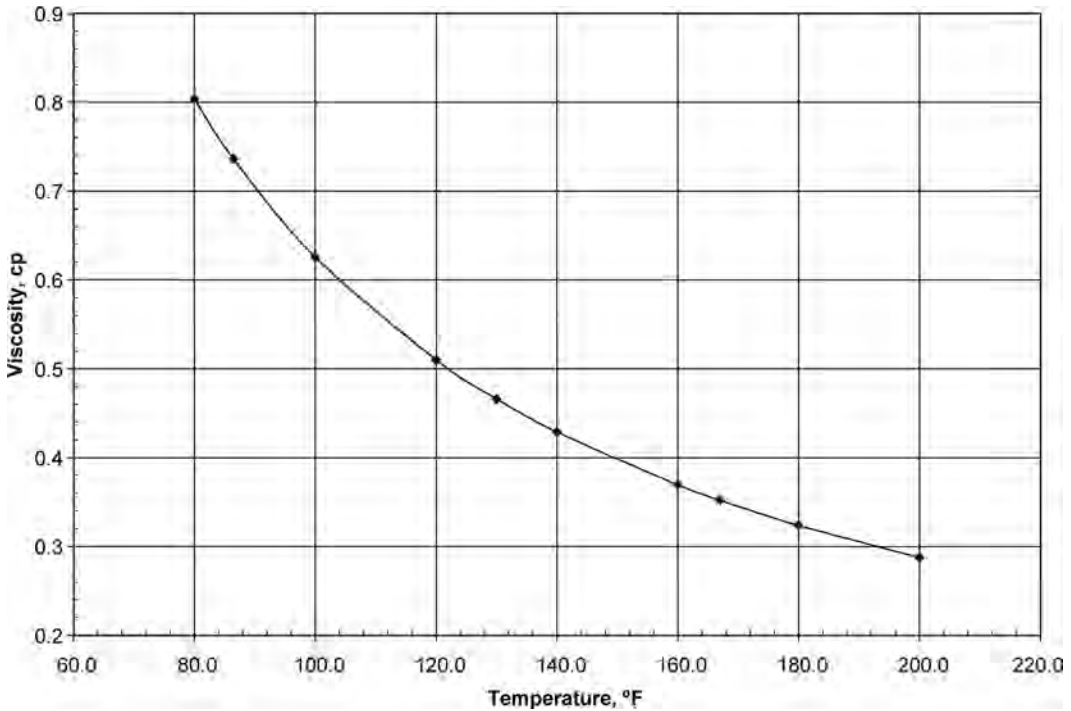


Fig. 10.11—Effect of temperature on water viscosity.

$$\frac{\mu_w}{\mu_{w1}} = 0.9994 + 4.0295 \times 10^{-5} \times p + 3.1062 \times 10^{-9} \times p^2 \dots \dots \dots (10.12)$$

McCain reported that Eq. 10.12 fits the data to within 4% for pressures below 10,000 psia and temperatures in the range from 86 to 167°F. The fit is within 7% for pressures between 10,000 and 15,000 psia.

Figs. 10.10 through 10.12 show the effects of pressure, temperature, and NaCl content on the viscosity of water. They may be used when the primary contaminant is sodium chloride. Alternatively, the viscosities are calculated and reported by computer chemistry models at the particular temperature, pressure, and gas compositions present in the facilities.<sup>33</sup>

Some engineers assume that reservoir-brine viscosity is equal to that of distilled water at atmospheric pressure and reservoir temperature. In this case, it is assumed that the viscosity of brine is essentially independent of pressure (a valid premise for the pressure ranges usually encountered). In some high-temperature/high-pressure reservoirs recently developed, this assumption breaks down. In those cases, experimental measurements under the relevant temperature/pressure conditions are recommended over attempting to extrapolate the distilled-water viscosities or even the computer models.

## 10.12 The pH

Water (H<sub>2</sub>O) reversibly dissociates into hydrogen ions and hydroxide ions, which is described by the equilibrium constant for this chemical reaction,  $K_{eq}(\text{H}_2\text{O})$  or simply  $K_w$ . The acidity or hydrogen ion activity of aqueous solutions controls many of its properties and is commonly expressed as the pH.

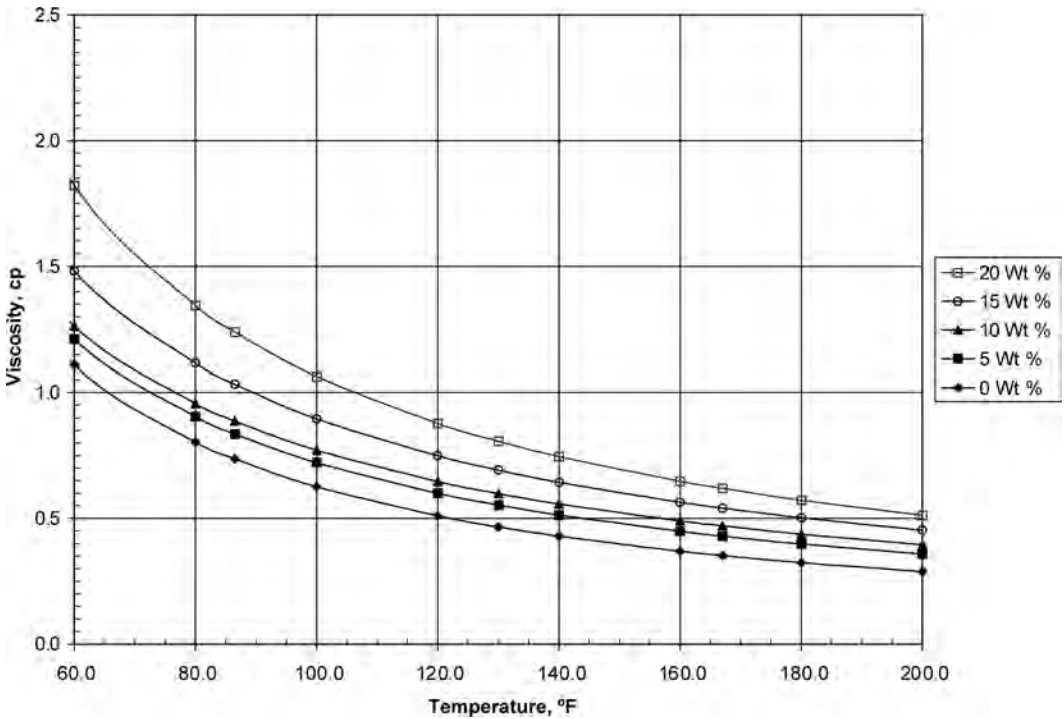
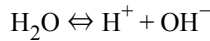


Fig. 10.12—Viscosity of sodium chloride solutions as a function of temperature and salinity (wt%) at 14.7 psia.



is the water dissociation reaction.

$$K_{eq} = 10^{-14} = a_{H^+} \times a_{OH^-} \dots\dots\dots (10.13)$$

and

$$pH = -\log_{10} a_{H^+}, \dots\dots\dots (10.14)$$

where  $a_{H^+}$  is known as the activity of hydrogen ion in solution. The hydrogen ion activity is related to the concentration of hydrogen ions  $[H^+]$  by means of the activity coefficient,  $\gamma_{H^+}$ , giving

$$a_{H^+} = \gamma_{H^+} \times [H^+]. \dots\dots\dots (10.15)$$

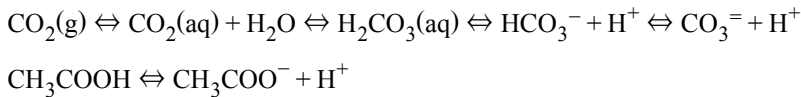
Solutions are known as neutral when the  $pH = 7$ , because at that point hydrogen ions and hydroxide ions are present in equal amounts,  $a_{H^+} = a_{OH^-} = 10^{-7}$  M. When hydrogen ions predominate, the  $pH$  falls below 7, and the solution is described as being acidic. In the opposite case in which hydroxide ions outnumber the hydrogen ions, the  $pH$  climbs above 7, and the solution is known as basic or alkaline. The  $pH$  is commonly accurately measured with an electrode and meter, while field determinations also may use  $pH$  paper strips or colorimetric methods.

When the water is very pure and contains little dissolved salts, the value of  $\gamma_{H^+}$  approaches 1.0. The activity and concentration of hydrogen ion are essentially the same, so that the pH definition simplifies to

$$\text{pH} = -\log_{10}[\text{H}^+]. \dots\dots\dots (10.16)$$

However, in what must seem to be nature's perversity, produced water from oil reservoirs usually contains large amounts of dissolved salts. The value of  $\gamma_{H^+}$  is  $< 1.0$  as a result, so the more simple form of the pH definition is not correct. Careful, direct pH measurement is the best approach for accurate pH determination, although some of the most sophisticated computer models give reasonable predictions at moderate conditions of brine concentration, temperature, and pressure.

The pH of oilfield waters usually is controlled by the  $\text{CO}_2$ /bicarbonate system. Because the solubility of  $\text{CO}_2$  is directly proportional to temperature and pressure, the pH measurement should be made in the field if a close-to-natural-conditions value is desired. The pH of the water is not very useful for water identification or correlation purposes, but it does indicate possible scale-forming or corrosion tendencies of a particular water. The pH also may indicate the presence of drilling-mud filtrate or well-treatment chemicals. Organic acids, such as acetic acid, also can control the pH. The following is a typical reaction.



The pH of concentrated brines usually is less than 7.0, and the pH will rise during laboratory storage, indicating that the pH of the water in the reservoir probably is appreciably lower than many published values. In pure water or brines with little buffering capacity, like seawater, the addition of gas containing  $\text{CO}_2$  at high pressure can depress the pH to less than 2.9, making the water very reactive. This water will dissolve and corrode steel with great rapidity or, if in the reservoir, will dissolve minerals either wholly or partly. This can lead to formation damage and dramatically reduce injection and production because the newly dissolved species reprecipitate as the pressure drops at the producer well.

Addition of the carbonate ion to sodium chloride solutions will raise the pH. If enough calcium is present, calcium carbonate precipitates. The reason the pH of most oilfield waters rises during storage in the laboratory is because of the formation of carbonate ions as a result of bicarbonate decomposition caused by evolution of dissolved  $\text{CO}_2$  gas. An important consideration of  $\text{CO}_2$  gas evolution/dissolution is that it is not anything close to instantaneous; a fact that has been underappreciated by many, with very expensive and confusing consequences.

In pure water, the  $\text{CO}_2$  equilibrium takes on the order of tens of minutes ( $\approx 20$  min.) to adjust to a change in  $\text{CO}_2$  pressure and for the pH to stabilize to a new level. However, with large amounts of bicarbonate in an oilfield water, the adjustment is even slower, while the buffering action of the bicarbonate itself will limit how much the pH will eventually change.

Organic acids play an extremely important role in the water chemistry.<sup>34</sup> Because the volatile fatty acids, such as formic, acetic, propionic, and butyric acids, are quite commonly found in the waters, they can control the water chemistry to a large degree, especially the  $\text{CO}_2$ /bicarbonate system. From a historical standpoint, this is important because analytical difficulties prohibited obtaining organic acid compositional data. Thus, much of the confusing behavior that workers observed in scale-deposition predictions based on the analysis of inorganic



species compared with the actual field results turns out to be explainable once the organic acids are considered.

Historically, the typical analytical procedure for bicarbonate, the alkalinity titration, also happens to titrate the organic acids because they have  $K_a$  values similar to that of bicarbonate. Thus, scale predictions that used those bicarbonate values are somewhat incorrect, with the degree of error depending on the amounts of organic acids that were included with the bicarbonate value. Oilfield waters sometimes will have an unusual odor, which often comes from rather high concentrations of these organic acids. The formic, acetic, propionic, and butyric acids will not precipitate scale under most conditions, but certainly do buffer the water system effectively. Also, they seem to slow down the approach to  $\text{CO}_2$  equilibrium as well, so that water samples containing several hundred ppm of organic acids will not change their pH significantly when stored for several days. This also means that the dissolved  $\text{CO}_2$  in the produced water remains high even after the pressure has been reduced in a separator. It still can remain corrosive, even though it would not normally be expected to be very corrosive. One procedure to correct the bicarbonate analysis for the volatile fatty organic acid concentration is to measure the organic acid content by an independent technique, such as IC or CE, calculate the equivalent amounts of the acids, and then subtract those equivalents from the apparent bicarbonate concentration as measured by the alkalinity titration.

Naphthenic acids can precipitate and form scales, in contrast to the volatile fatty acids. Calcium naphthenate scale deposits have been identified recently in several fields that produce high-acid-number crude oils; however, the concentration of naphthenic acids in water is limited by their higher molecular weights and high oil solubility.<sup>48</sup>

### 10.13 The Redox Potential

The redox potential (often abbreviated as Eh) may be referred to as oxidation potential, oxidation/reduction potential, or pE. It is expressed in volts or millivolts (mV), and, at equilibrium, it is related to the proportions of oxidized and reduced species present. Standard equations of chemical thermodynamics express the relationships.

The Nernst equation expresses the relationship between concentrations of oxidation-reduction couples. For example, a common redox couple involves the dissolved iron species Fe(II) and Fe(III), which can be described thermodynamically as

$$E = E_o - RT/nF \log (\text{Fe}^{+3})/(\text{Fe}^{+2}) = E_o - 0.0591T/n \log (\text{Fe}^{+3})/(\text{Fe}^{+2}) \dots \dots \dots (10.17)$$

and

$$\Delta G = -nFE, \dots \dots \dots (10.18)$$

where

$E$  = the voltage of the system vs. the standard hydrogen electrode,

$E_o$  = the voltage of the oxidation reaction at standard conditions (1 mole/liter, 298 K, 1 atmosphere pressure),

$n$  = the number of electrons transferred in the reaction,

$R$  = the ideal gas constant,

$T$  = temperature, °K, and

$F$  = Faraday's Constant.

Eh is usually measured with a platinum electrode against a different reference, such as Ag/AgCl or saturated calomel reference electrodes. Knowledge of the redox potential is useful in studies of how compounds such as uranium, iron, sulfur, and other minerals are transported in

aqueous systems. The solubility of some elements and compounds depends on the redox potential and the pH of their environment.

Some water associated with petroleum is interstitial (connate) water and has a negative Eh, which has been proved in various field studies. Knowledge of the Eh is useful in determining how to treat a water before it is reinjected into a subsurface formation. For example, the Eh of the water will oxidize if the water is open to the atmosphere, but, if it is kept in a closed system in an oil-production operation, the Eh should not change appreciably as it is brought to the surface and reinjected. In such a situation, the Eh value is useful in determining how much iron will stay in solution and not deposit in the wellbore.

Organisms that consume oxygen lower the Eh. In buried sediments, it is the aerobic bacteria that attract organic constituents that remove the free oxygen from the interstitial water. Sediments laid down in a shoreline environment will differ in degree of oxidation compared with those laid down in a deepwater environment. For example, the Eh of the shoreline sediments may range from  $-50$  to  $0$  mV, but the Eh of deepwater sediments may range from  $-150$  to  $-100$  mV.

Aerobic bacteria die when the free oxygen is totally consumed; anaerobic bacteria attack the sulfate ion, which is the second most important anion in the seawater. During this attack, the sulfate reduces to sulfide, the Eh drops to negative potentials (approximately  $-600$  mV), and  $H_2S$  is liberated. This process is known as reservoir souring and is a major concern to engineers working on fields undergoing waterflood with injected seawater or other sulfate-containing injectant. Most waterfloods have eventually gone sour. Hydrogen sulfide generation causes problems from a health and safety standpoint because it is so poisonous.  $H_2S$  also causes rapid, nearly instantaneous, failure of steel because of sulfide stress-corrosion cracking, unless the steel has been specified for "sour service." Besides the presence of sulfate ions, dissolved organic acids play a role in feeding the SRB. Predicting and mitigating reservoir souring is an active area of research. SRB and other bacteria often cause a different, much slower type of pitting corrosion on steel, known as microbially induced corrosion (MIC). MIC is commonly seen in low-flow piping areas, under deposits of solids or sludges, or in vessels and tanks.

#### 10.14 Dissolved Gases

Large quantities of dissolved gases are contained in oilfield brines. Most of these gases are hydrocarbons; however, other gases such as  $CO_2$ ,  $N_2$ , and  $H_2S$  often are present. The solubility of the gases in water generally decreases with increased water salinity and temperature and increases with pressure.

Hundreds of drillstem samples of brine from water-bearing subsurface formations in the U.S. Gulf Coast area were analyzed to determine the amounts and kinds of hydrocarbons.<sup>35</sup> The chief constituent of the dissolved gases usually was methane, with measurable amounts of ethane, propane, and butane. The concentration of the dissolved hydrocarbons generally increased with depth in a given formation and increased basinward with regional and local variations. In close proximity to some oilfields, the waters were enriched in dissolved hydrocarbons. Up to 14 scf dissolved gas/bbl water was observed in some locations.

#### 10.15 Organic Constituents

In addition to the simple hydrocarbons, many organic constituents in colloidal, ionic, and molecular form occur in oilfield brines.<sup>35</sup> Because the analytical problems are difficult and very time consuming, many organic constituents present in oilfield brines were not determined. In recent years, some of these organic constituents have been measured quantitatively, because better analytical techniques have been adapted to the difficult produced-water matrix.

Knowledge of the dissolved organic constituents is important because these constituents are related to the origin and/or migration of an oil accumulation, as well as to the disintegration or degradation of an accumulation.<sup>36</sup> The concentrations of organic constituents in oilfield brines

vary widely. In general, the more alkaline the water is, the more likely it will contain higher concentrations of organic constituents. The bulk of the organic matter consists of anions and salts of organic acids; however, other compounds also are present. Explorationists can use such data to look for anomalies in these constituents, while environmental scientists can use it to evaluate spills and effluents. The corrosion engineer needs to know how much of the inhibitor added at the well remains in the produced water so that its corrosion can be controlled. Organic-scale-inhibitor compounds are monitored routinely to verify that their concentration exceeds the minimum effective dose.

Knowledge of the concentrations of benzene, toluene, xylenes, and other components in oilfield brines is used in exploration. The solubilities of some of these compounds in water at ambient conditions and in saline waters at elevated temperatures and pressures have been determined.<sup>37,38</sup>

However, the actual concentrations of these and other organic constituents in subsurface oilfield brines are another matter. It has been shown experimentally that the solubilities of some organic compounds found in crude oil increase with temperature and pressure if pressure is maintained on the system. The increased solubilities become significant above 150°C. The solubilities decrease with increasing water salinity. Waters associated with paraffinic oils are likely to contain fatty acids, while those associated with asphaltic oils more likely contain naphthenic acids.

Quantitative recovery of organic constituents from oilfield brines is difficult. Temperature and pressure changes, bacterial actions, adsorption, and the high inorganic/organic-constituents ratio in most oilfield brines are some reasons why quantitative recovery is difficult. The effect of bacteria on the samples is particularly significant.<sup>39</sup> Unless samples are stabilized with an effective dose of biocide, significant or complete depletion of the organic acids is likely before the sample can be analyzed. Total loss of 300 ppm of acetic acid within 24 hours in an unstabilized produced-water sample was observed, while one containing 200 ppm of biocide suffered no loss of acetic acid.

**10.15.1 Interpretation of Chemical Analyses.** Oilfield waters include all waters or brines found in oil fields. Such waters have certain distinct chemical characteristics.<sup>40,41</sup> Approximately 70% of the world petroleum reserves are associated with waters containing more than 100 g/L of dissolved solids.<sup>42</sup> Water containing dissolved solids in excess of 100 g/L can be classified as brine. Waters associated with the other 30% of petroleum reserves contain less than 100 g/L of dissolved solids. Some of these waters are almost fresh; however, the presence of fresher waters usually is attributed to invasion after the petroleum accumulated in the reservoir trap.

Examples of some of the low-salinity waters can be found in the Rocky Mountain areas in Wyoming fields such as Enos Creek, South Sunshine, and Cottonwood Creek.<sup>43,44</sup> The Douleb oil field in Tunisia is another example. Extremely fresh water was discovered in the Cano Limon, Colombia, oil field with only 300 mg/L TDS, mostly sodium bicarbonate and sodium acetate. The chloride content was only approximately 20 mg/L.

The composition of dissolved solids found in oilfield waters depends on several factors. Some of these factors are the composition of the water in the depositional environment of the sedimentary rock, subsequent changes by rock/water interaction during sediment compaction, changes by rock/water interaction during water migration (if migration occurs), and changes by mixing with other waters, including infiltrating younger waters such as meteoric waters. The following are definitions of some types of water.

**Meteoric Water.** This is water that recently was involved in atmospheric circulation; furthermore, “the age of meteoric groundwater is slight when compared with the age of the enclosing rocks and is not more than a small part of a geologic period.”<sup>14</sup>

**Seawater.** The composition of seawater varies somewhat but, in general, will have a composition relative to the following (in mg/L): chloride—19,375, bromide—67, sulfate—2,712, potassium—387, sodium—10,760, magnesium—1,294, calcium—413, and strontium—8.

**Interstitial Water.** Interstitial water is the water contained in the small pores or spaces between the minute grains or units of rock. Interstitial waters are syngenetic (formed at the same time as the enclosing rocks) or epigenetic (originated by subsequent infiltration into rocks).

**Connate Water.** The term “connate” implies born, produced, or originated together (connascent); therefore, connate water probably should be considered interstitial water of syngenetic origin. Connate water of this definition is fossil water that has been out with the atmosphere for at least a large part of a geologic period. The implication that connate waters are “born with” the enclosing rocks is an undesirable restriction.<sup>14</sup>

**Diagenetic Water.** Diagenetic waters are those changed chemically and physically, before, during, and after sediment consolidation. Some of the reactions that occur in or to diagenetic waters include bacteria change, replacement (dolomitization), infiltration by permeation, and membrane filtration.

**Formation Water.** Formation water, as defined here, is water that occurs naturally in the rocks and is present in them immediately before drilling.

**Juvenile Water.** Juvenile water is water derived from primary magma.

**Condensate Water.** Water associated with gas is carried as vapor to the surface of the well, where it condenses and precipitates because of temperature and pressure changes. This water occurs more often in the winter, in colder climates, and in gas-producing wells. This water is easy to recognize because it contains a relatively small amount of dissolved solids, mostly derived from reactions with chemicals in or on the well casing or tubing or carried as a mist in high-rate-gas-flow wells.

Water analyses may be used to identify the water source. In the oil field, one of the prime uses of these analyses is to determine the source of extraneous water in an oil well so that casing can be set and can prevent such water from flooding the oil or gas horizons. In some wells, a leak may develop in the casing or cement, and water analyses are used to identify the water-bearing horizon so that the leaking area can be replaced. With the current emphasis on water pollution prevention, it is very important to locate the source of a brine so that remedial action can be taken.

Historically, comparisons of water-analysis data are tedious and time consuming; therefore, graphical methods were mainly used for positive, rapid identification. A number of systems were developed, all of which have some merit, with the most popular being the Stiff diagram (Fig. 10.13). The new computer chemistry models mentioned previously have largely displaced the manual graphics, but the visual comparisons are still useful in certain situations.

### 10.16 The Mixing-Line Technique

In situations in which two different waters are being mixed, it is desirable to measure the amounts of each in the mixed stream. Also, if that capability exists, it is desirable to look at each constituent to see if it undergoes any phenomenon other than simple mixing. Thus, this can be a powerful technique for detecting water/rock reactions that can lead to formation damage.<sup>45</sup>

The fundamental concept is that mixing two waters should result in the volume-weighted average of each constituent of the two original waters, unless some chemical or biological reaction occurred. This is essentially similar in appearance to a binary phase diagram, with the endpoints of the line defined by the concentrations of the constituent in each of the water streams being mixed. For the technique to be useful, at least one species needs to be found that can act as a tracer for one of the waters. The requirements for this species are that it does not participate in chemical or other reactions under the conditions of interest; it has a relatively

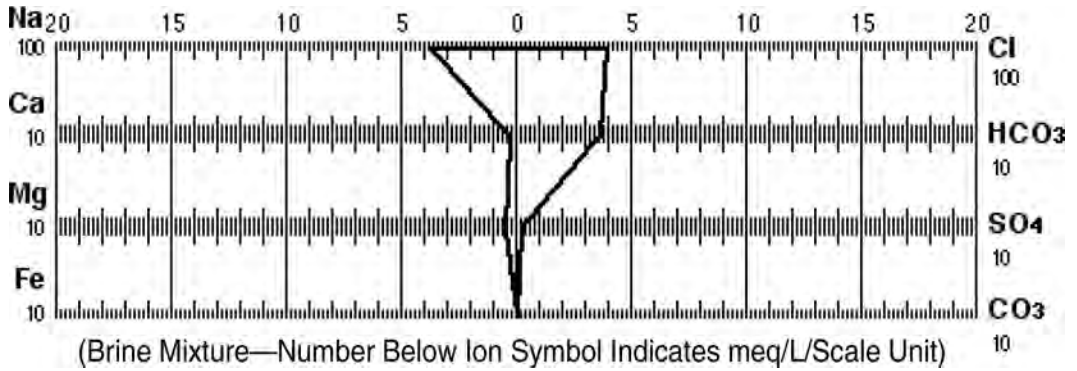


Fig. 10.13—Stiff diagram for a produced water composed of (in mg/L) Na—8727, Ca—69, Mg—60, Fe—1.0, Cl—13742, HCO<sub>3</sub>—2221, SO<sub>4</sub>—96, and CO<sub>3</sub>—0. The Stiff plot (in meq/L) gives Na—380, Ca—3.45, Mg—5.0, Fe—0.04, Cl—388, SO<sub>4</sub>—1.0, HCO<sub>3</sub>—36, and CO<sub>3</sub>—0.

large difference in concentration between the two waters; and its analysis is easy and cheap with excellent accuracy.

Candidate species include boron, iodide, bromide, and chloride. The boron species is one that has been valuable in this role for reservoirs in several areas, including the North Sea and the North Slope of Alaska. Seawater is used as the injection water, with a typical boron content of 4.5 mg/L. Boron typically does not undergo any precipitation, dissolution, ion exchange, adsorption, or microbiological reactions and is stable in samples. Boron analysis by ICP is cheap, fast, accurate, and has detection limits of better than 0.05 mg/L with ≈1% relative standard deviation. The formation waters have original boron concentrations ranging from 15 to 160 mg/L; thus, boron can serve as a tracer for the formation water.

$$X_{fm} = [B]_{pw} / ([B]_{fm} - [B]_{inj}), \dots\dots\dots (10.19)$$

$$W_f = 100 \times X_{fm}, \dots\dots\dots (10.20)$$

and

$$W_i = 100 - W_f, \dots\dots\dots (10.21)$$

where

- $X_{fm}$  = the fraction of formation water in the mixed produced water,
- $[B]_{pw}$  = the measured boron concentration in the produced water sample,
- $[B]_{fm}$  = the boron concentration in the original formation water,
- $[B]_{inj}$  = the boron concentration in the injection water,
- $W_i$  = the percentage of injection water in the mixed produced water, and
- $W_f$  = the percentage of original formation water in the mixed produced water.

With the use of this calculated index for the amount of formation (or injection) water, the concentrations of each of the species measured in the standard water analysis can be graphed. The pure formation and injection waters define the two endpoints of the mixing line. The analytical data for that species in each of the produced water samples are then plotted and compared with the theoretical mixing line.

### 10.17 Role of Suspended Solids in Produced Water

Solids are almost always present in an oil, gas, and water-producing stream. Unfortunately, the solids are usually ignored until the problems caused by the solids become so onerous that action is required. In some cases, the reservoir sands are known to be unconsolidated, and sand control is part of the project development. However, even if sand control is successful, fine solids will still be produced and end up in the produced-water system. If the volume of water handled is small, the solids issues may never be important. When a lot of water is present, problems such as pump wear, formation of deposits, injection-well plugging, filling vessels, corrosion, and oil carryover begin to appear. Water intended to be injected is often specified to meet certain levels of particulates with a maximum size.

The solids can be produced from the reservoir rock (e.g., clays, quartz) or from hydraulic fractures (proppant flowback), or it can precipitate from the produced water (e.g., iron sulfide). Particle sizes cover a wide range. In the hydraulic-fracture case, the proppant size may be 1 mm or larger, while iron sulfide precipitate can be  $< 0.1 \mu\text{m}$ .

Because the solids are denser than either the oil or the produced water, they tend to sink to the bottom of the pipes, vessels, or tanks. Systems with low flow rates usually build stagnant deposits of the solids. A rule of thumb that can be used is  $< 3 \text{ ft/sec}$  for lines that will build solids deposits. The solids often are coated with oil and become neutrally buoyant in the water or water/oil interface, so they remain suspended and can travel great distances. Treating chemicals such as corrosion or scale inhibitors or emulsion breakers are surface active, are strongly attracted to the surfaces of the solids, and act to attract oil, paraffins, asphaltenes, and bacteria, so that the once-dense particle is now much larger and less dense. They also are sticky and agglomerate easily, eventually forming what has been termed “schmoo.”<sup>46</sup> The resulting schmoo is an organic/inorganic scale that effectively coats the surfaces exposed to the produced water: piping, vessels, meters, tubing, and injector-well perforations. This heterogeneous coating has been observed in produced-water piping more than 1 to 3 in. thick around the full pipe circumference.

Schmoo deposits harbor bacteria implicated in corrosion of the produced-water system.<sup>47</sup> Also, schmoo can plug injector wells, primarily in the perforations and formation face, although occasionally large quantities slough off the tubing and fill the wellbore. Many times, the produced water in the injector-well tubing will build a thick enough layer of schmoo that wireline tools cannot be run. Oiled tubing-fill cleanouts are effective at removing the schmoo and restoring injectivity. Soaking the system with particular surfactant formulations has been effective in removing the schmoo deposits, preventing corrosion, and restoring injectivity.

#### Nomenclature

- $\alpha_{\text{H}^+}$  = activity of hydrogen ion in solution
- $\alpha_{\text{OH}^-}$  = activity of hydroxide ion in solution
- $B_{w1}, B_{w2}$  = water FVF at  $p_1$  and  $p_2$ , bbl/bbl
- $\bar{B}_w$  = water FVF
- $B_w$  = average water FVF corresponding to  $V$ , bbl/bbl
- $[B]_{fm}$  = the boron concentration in the original formation water
- $[B]_{inj}$  = the boron concentration in the injection water
- $[B]_{pw}$  = the measured boron concentration in the produced-water sample
- $c_w$  = water compressibility at the given pressure and temperature,  $\text{Lt}^2/\text{m}$ , bbl/bbl-psi
- $\bar{c}_w$  = average water compressibility within the given pressure and temperature interval,  $\text{Lt}^2/\text{m}$ , bbl/bbl-psi
- $C$  = salinity, g/L of solution
- $C_{sd}$  = concentration of dissolved solids (also known as TDS), mg/L

- $E$  = the voltage of the system vs. the standard hydrogen electrode  
 $E_o$  = the voltage of the oxidation reaction at standard conditions (1 mole/liter, 298 K, 1 atmosphere pressure)  
 $F$  = Faraday's Constant  
 $K_{eq}$  = equilibrium constant for water dissociation reaction  
 $K_w$  = equilibrium constant for water dissociation reaction  
 $m_1$  = 7.033  
 $m_2$  = 541.5  
 $m_3$  = -537  
 $m_4$  =  $403.3 \times 10^3$   
 $n$  = the number of electrons transferred in the reaction  
 $p$  = pressure, M/Lt<sup>2</sup>, psi  
 $p_1, p_2$  = pressure at conditions 1 and 2 with  $p_1 > p_2$ , M/Lt<sup>2</sup>, psi  
 $p_b$  = bubblepoint pressure, M/Lt<sup>2</sup>, psi  
 $R$  = the ideal gas constant  
 $R_{wg}$  = formation-water resistivity  
 $S$  = salinity in wt%  
 $S_{wr}$  = irreducible water saturation  
 $T$  = temperature, T, °F  
 $V$  = water volume at the given pressure and temperature, L<sup>3</sup>  
 $\bar{V}$  = average water volume within  $p$  and  $T$  intervals, L<sup>3</sup>  
 $V_{rc}$  = volume occupied by a unit mass of water at reservoir conditions (weight of gas dissolved in water at reservoir or standard conditions is negligible), L<sup>3</sup>, ft<sup>3</sup>  
 $V_{sc}$  = volume occupied by a unit mass of water at standard conditions, L<sup>3</sup>, ft<sup>3</sup>  
 $W_i$  = the percentage of injection water in the mixed produced water  
 $W_f$  = the percentage of original formation water in the mixed produced water  
 $X_{fm}$  = the fraction of formation water in the mixed produced water  
 $\gamma_H$  = activity coefficient  
 $\rho_{rc}$  = density of water at reservoir conditions, m/L<sup>3</sup>, lbm/ft<sup>3</sup>  
 $\rho_{sc}$  = density of water at standard conditions, m/L<sup>3</sup>, lbm/ft<sup>3</sup>  
 $\rho_w$  = density, m/L<sup>3</sup>, lbm/ft<sup>3</sup>

---

## References

1. Rogers, W.B. and Rogers, H.D.: "On the Connection of Thermal Springs in Virginia with Anticlinal Axes and Faults," *Am. Geol. Rep.* (1843) 323.
2. Howell, J.V.: "Historical Development of the Structural Theory of Accumulation of Oil and Gas," W.E. Wrather and F.H. Lahee (eds.), AAPG, Tulsa (1934) 1–23.
3. Dickey, P.A.: "The First Oil Well," *JPT* (January 1959) 14.
4. Schilthuis, R.J.: "Connate Water in Oil and Gas Sands," *Trans.*, AIME (1938) **127**, 199.
5. Torrey, P.D.: "The Discovery of Interstitial Water," *Prod. Monthly* (1966) **30**, 8–12.
6. Griswold, W.T. and Munn, M.J.: "Geology of Oil and Gas Fields in Steubenville, Burgettstown and Claysville Quadrangles, Ohio, West Virginia and Pennsylvania," *Bull.*, USGS (1907) **No. 318**, 196.
7. Fettke, C.R.: "Bradford Oil Field, Pennsylvania, and New York," *Bull.*, Pennsylvania Geologic Survey, fourth ser. (1938) **M21**, 1.

8. Munn, M.J.: "The Anticlinal and Hydraulic Theories of Oil and Gas Accumulation," *Econ. Geol.* (1920) **4**, 509–29.
9. Mills, F. van A.: "Experimental Studies of Subsurface Relationships in Oil and Gas Fields," *Econ Geol.* (1920) **15**, 398.
10. Rich, J.L.: "Further Notes on the Hydraulic Theory of Oil Migration and Accumulation," *Bull., AAPG* (1923) **7**, 213.
11. Torrey, P.D.: "A Review of Secondary Recovery of Oil in the United States," *Secondary Recovery of Oil in the United States*, API, New York City (1950) 3–29.
12. Garrison, A.D.: "Selective Wetting of Reservoir Rock and Its Relation to Oil Production" *Drill. & Prod. Prac.*, New York City (1935) 130–40.
13. Lane, A.C. and Gordon, W.C.: "Mine Waters and Their Field Assay." *Bull., Geologic Soc. of America* (1908) **19**, 501.
14. White, D.E.: "Magmatic, Connate, and Metamorphic Water," *Bull., Geologic Soc. of America* (1957) **68**, 1659.
15. Wallace, W.E.: "Water Production From Abnormally Pressured Gas Reservoirs in South Louisiana," *JPT* (August 1969) 969.
16. Collins, A.G.: *Geochemistry of Oilfield Waters*, Elsevier Scientific Publishing Co., New York City (1975).
17. Elworthy, R.T.: "A Field Method and Apparatus for the Determination by Means of Electrical Conductivity Measurements the Character of Waters Leaking into Oil and Gas Wells," C. Dept. Mines Summary Report No. 605 (1922) 58.
18. Cowan, J.C and Weintritt, D.J.: *Water Formed Scale Deposits*, Gulf Publishing Co., Houston (1976).
19. Patton, C.C.: *Applied Water Technology*, Campbell Petroleum Series (1986).
20. Kriel, B.G., Lacey, C.A., and Lane, R.H.: "The Performance of Scale Inhibitors in the Inhibition of Iron Carbonate Scale," paper SPE 27390 presented at the 1994 SPE International Symposium and Exhibition on Formation Damage Control, Lafayette, Louisiana, 7–10 February.
21. McCain, W.D. Jr.: *The Properties of Petroleum Fluids*, second edition, PennWell Books, Tulsa (1990).
22. McCain, W.D. Jr.: "Reservoir-Fluid Property Correlations—State of the Art," *SPEERE* (May 1991) 266.
23. Osif, T.L.: "The Effects of Salt, Gas, Temperature, and Pressure on the Compressibility of Water," *SPEERE* (February 1988) 175.
24. Dorsey, N. E.: *Properties of Ordinary Water Substances*, Monograph Series, American Chemical Soc. (1940) **208**, No. 81, 246.
25. Dotson, C.R. and Standing, M.B.: "Pressure, Volume, Temperature and Solubility Relations for Natural Gas-Water Mixtures," *Drill. & Prod. Prac.*, API (1944) 173.
26. Rowe, A.M. Jr. and Chou, J.C.S.: "Pressure-Volume-Temperature-Concentration Relations of Aqueous NaCl Solutions," *J. Chem. Eng. Data* (1970) **15**, 61.
27. "Saline and Brackish Waters, Sea Waters and Brines," *Annual Book of ASTM Standards*, American Soc. for Testing and Materials, Part 31—Water, Section VII, Philadelphia (1982).
28. Ashby, W.H. Jr. and Hawkins, M.F.: "The Solubility of Natural Gas in Oil-Field Brines," paper presented at the 1948 SPE Annual Meeting, Dallas, 4–6 October.
29. Rogers, P.S.Z. and Pitzer, K.S.: "Volumetric Properties of Aqueous Sodium Chloride Solutions," *J. Phys. Chem. Ref. Data* (1982) **11**, No 1, 15.
30. Martins, J.P. *et al.*: "Produced-Water Reinjection and Fracturing in Prudhoe Bay," *SPEERE* (August 1995) 176.
31. Amyx, J.W, Bass, C.M. Jr., and Whiting, R.L.: *Petroleum Reservoir Engineering*, McGraw-Hill Book Co. Inc., New York City (1960).
32. Kestin, J., Khalifa, H.E., and Corrcia, R.J.: "Tables of the Dynamic and Kinematic Viscosity of Aqueous NaCl Solutions in the Temperature Range 20-150°C and the Pressure Range 0 1-35 MPa," *J. Phys. Chem. Ref. Data* (1981) **10**, No. 1, 71.
33. Zemaitis, J.F. Jr. *et al.*: *Handbook of Aqueous Electrolyte Thermodynamics*, American Inst. of Chemical Engineers, New York (1986).
34. Carothers, W.W.: "Aliphatic Acid Anions and Stable Carbon Isotopes of Oil Field Waters in the San Joaquin Valley, California," MS thesis, San Jose State U., San Jose, California (1976).



35. Buckley, S.E., Hocott, C.R., and Taggan, M.S. Jr.: "Distribution of Dissolved Hydrocarbons in Subsurface Waters," *Habitat of Oil*, L.C. Weeks (ed.), AAPG, Tulsa (1958) 850–82.
36. Zarrella, W.M. *et. al.*: "Analysis and Significance of Hydrocarbons in Subsurface Brines," *Geochim. Cosmochim. Acta* (1967) **31**, 1155.
37. McAuliffe, C.D.: "Solubility in Water, Paraffin, Cycloparaffin, Olefin, Acetylene, Cyclo-olefin and Aromatic Hydrocarbons," *J. Phys. Chem.* (1966) **70**, 1267.
38. Prince, L.C.: "Aqueous Solubility of Petroleum as Applied to Its Origin and Primary Migration," *Bull.*, AAPG (1976) 213.
39. Postgate, J.R.: *The Sulfate Reducing Bacteria*, Cambridge U. Press, New York City (1979) 151.
40. Noad, D.F.: "Water Analysis Data, Interpretation and Application," *J. Can. Pet. Tech.* (1962) **1**, 82.
41. Ostroff, A.G.: "Introduction to Oilfield Water Technology," NACE, Houston (1979) 394.
42. Bright, J.: "Oilfield Water Analysis Data Bank," DOE/EC/10116-2, U.S. DOE, Washington, DC (1983).
43. Coffin, C.R. and DeFord, R.K.: "Waters of the Oil and Gas Bearing Formations of the Rocky Mountains," *Survey Po,v Memorial Volume*, AAPG (1934) 927.
44. Crawford, J.G.: "Waters of Producing Fields in the Rocky Mountain Region," *Trans.*, AIME (1948) **179**, 264.
45. Braden, J.C. and McLelland, W.G.: "Produced Water Chemistry Points to Damage Mechanisms Associated With Seawater Injection," paper SPE 26045 presented at the 1993 SPE Western Regional Meeting, Anchorage, 26–28 May.
46. Hsi, C.D. *et al.*: "Formation Injectivity Damage Due To Produced Water Reinjection," paper SPE 27395 presented at the 1994 SPE International Symposium on Formation Damage Control, Lafayette, Louisiana, 7–10 February.
47. Blumer, D.J., Bohon, W.M., and Chan, A.F.: "Novel Chemical Dispersant For Removal of Organic/Inorganic 'Schmoo' Scale In Produced Water Injection Systems," paper 98073 presented at the 1998 NACE Corrosion Annual Conference, Houston.
48. Baugh, T.D., Wolf, N.O., Mediaas, H., Vindstad, J.E., and Grande, K.: "Characterization of a Calcium Naphthenate Deposit—The ARN Acid Discovery," Petroleum Chemistry Division Preprints 2004, **49** (3), 274, Am. Chem. Society Annual Meeting (August 2004).

### SI Metric Conversion Factors

atm	× 1.013 250*	E + 05	= Pa
bar	× 1.0*	E + 05	= Pa
bb1	× 1.589 873	E – 01	= m <sup>3</sup>
cp	× 1.0*	E – 03	= Pa·s
dyne	× 1.0*	E – 02	= mN
ft	× 3.048*	E – 01	= m
ft <sup>3</sup>	× 2.831 685	E – 02	= m <sup>3</sup>
°F	(°F–32)/1.8		= °C
in.	× 2.54*	E + 00	= cm
in. <sup>3</sup>	× 1.638 706	E + 01	= cm <sup>3</sup>
lbm	× 4.535 924	E – 01	= kg
mL	× 1.0*	E + 00	= cm <sup>3</sup>
oz	× 2.957 353	E + 01	= cm <sup>3</sup>
psi	× 6.894 757	E + 00	= kPa

\*Conversion factor is exact.



## Chapter 11

# Phase Behavior of H<sub>2</sub>O + Hydrocarbon Systems

E.D. Sloan, SPE, Center for Hydrate Research, Colorado School of Mines

### 11.1 Introduction

The phase behavior of H<sub>2</sub>O + hydrocarbon mixtures differs significantly from the vapor/liquid equilibria of normal hydrocarbons in two ways: the aqueous and hydrocarbon components usually separate, with very low mutual solubility; and hydrates often form with water and hydrocarbons smaller than n-pentane. Water generally is avoided because it is incombustible, and hydrate solids usually are avoided because their presence creates flow assurance difficulties.

When hydrocarbon contacts water, the two components separate into two phases in which the mutual component solubility is less than 1.0 mol% at ambient conditions. This splitting of phases affects almost all treatments of H<sub>2</sub>O + hydrocarbon systems and is caused by the different molecular attractions within water and hydrocarbons. Hydrocarbon molecules have a weak, noncharged attraction for each other, while water attracts other water molecules through a strong, charged hydrogen bond.

Because hydrogen bonds are significantly stronger than those between hydrocarbon molecules, hydrocarbon solubility in water (and that of water in hydrocarbons) is very small. Hydrogen bonds are responsible for most of the unusual properties water displays. One example is water's very high heat of vaporization, which absorbs large amounts of heat and buffers many hydrocarbon reservoir temperatures. Another example is the very high normal boiling point water has relative to its molecular weight.

This chapter discusses H<sub>2</sub>O + hydrocarbon phase equilibria in macroscopic terms, such as temperature, pressure, concentration, and phase diagrams—more easily applied by the engineer—because a quantitative molecular prediction of H<sub>2</sub>O + hydrocarbon phase behavior is beyond the current state of the art. Quantitative predictions of macroscopic phase behavior are illustrated by example, along with a few results from hand calculations, though the many excellent commercial phase equilibria computer programs now available largely have eliminated the need for the hand calculations. This chapter also explains qualitative trends, to help the engineer to understand the implications of temperature, pressure, and composition changes. Such a qualitative understanding and a few hand calculation methods serve as an initial check on the quantitative predictions of computer programs.

This chapter is divided into three main sections. The first section covers phase definitions and the Gibbs<sup>1</sup> phase rule, which are used to define the problem. Only the two most common

concerns are treated in this section; for a rigorous discussion of H<sub>2</sub>O + hydrocarbon phase diagrams, see Harmens and Sloan.<sup>2</sup> The second section goes on to cover the simplest case—that of an H<sub>2</sub>O + hydrocarbon mixture when all phases are fluid, as vapor and/or liquid, and without hydrate formation. This H<sub>2</sub>O + hydrocarbon equilibrium without hydrates exists at high temperature or low pressure or when only large (greater in size than n-pentane) hydrocarbon components are present.

Because of the importance of hydrates in H<sub>2</sub>O + hydrocarbon equilibria, however, the largest and third section of this chapter deals with systems containing small hydrocarbon molecules (<9Å) that form hydrates with water. This is an important section—hydrates are the most common solid-phase problem in flow assurance. They are solid crystalline compounds that typically plug flow channels, valves, drillstrings, blowout preventers, etc.; therefore, hydrate-formation regions normally are avoided. A chapter on emerging technologies related to flow assurance and hydrates is in the Emerging and Peripheral Technologies section of this Handbook.

## 11.2 Phase Definitions and the Gibbs Phase Rule

Phases are homogeneous regions of matter—gas, liquid, or solid—that can be analyzed using common tools such as pressure gauges, thermocouples, and chromatographs. In this chapter, phases are distinct homogeneous regions larger than 100 μm. The shorthand used here for the various phases are:

- HC = hydrocarbon, typically with a very low (<1%) water concentration.
- I = pure ice.
- L = liquid that is either water (L<sub>w</sub>) or hydrocarbon (L<sub>HC</sub>).
- V = vapor that is always a single phase, never splitting.
- W = liquid water, usually of high (>99%) purity, except where indicated.
- H = hydrate or solid.

The order of phase listing is by decreasing water concentration. For example, the listing order L<sub>w</sub> > H > V > L<sub>HC</sub> means that hydrates (H) contain less water than the liquid water phase (L<sub>w</sub>), but more water than vapor (V), which in turn contains more water than liquid hydrocarbon (L<sub>HC</sub>).

The Gibbs<sup>1</sup> phase rule for nonreacting systems provides the most convenient method for determining how many intensive variables are important in phase equilibria. The Gibbs phase rule states:

$$F = C - P + 2, \dots\dots\dots (11.1)$$

where  $F$  = number of intensive variables (e.g., pressure, temperature, single phase composition) required to define the system (known as the degrees of freedom);  $C$  = number of components; and  $P$  = number of phases.

For example, when excess gas (*excess* so that its composition does not change) contacts water to form hydrates, there are three phases ( $P = 3$ , namely L<sub>w</sub> + H + V) and two components ( $C = 2$ , namely water and a gas of constant composition), so that  $F = 1$ ; only one intensive variable (either pressure, temperature, or one phase composition) is needed to define the system. If this system is uniquely specified at a given pressure, for example, the identical temperature, and same individual phase compositions always will occur for the initial components at that pressure, when three phases are present. This system definition assures the engineer of uniqueness, so that the identical equilibrium phase behavior will be achieved. If gas also condenses ( $P = 4$ , with the addition of L<sub>HC</sub>), however, or the gas quantity is small enough to change composition (such that  $C > 2$ ), then the  $F = 1$  restriction no longer holds.

As a second example, consider again the case of a constant composition hydrocarbon vapor in equilibrium with water, so that  $C = 2$ . With two phases (V + L<sub>w</sub>), by the Gibbs phase rule the degrees of freedom are two ( $F = 2$ ), so that for this example, both temperature and pres-

sure are needed to determine the water composition in the hydrocarbon at conditions under which the two phases coexist. In contrast to the single variable required for three-phase systems in the above paragraph, with this case of two phases and two components, the saturated water concentration in the hydrocarbon (or water dewpoint) is determined by two variables. The water content in a hydrocarbon vapor is correlated with temperature and pressure in [Sec. 11.3.1](#) below. Identical restrictions apply to the hydrocarbon content in the water phase, also considered briefly in [Sec. 11.3.1](#).

The same restriction of  $F = 2$  applies when a constant composition liquid hydrocarbon exists in equilibrium with liquid water. However, because both phases ( $L_W + L_{HC}$ ) are dense, very large pressure changes are required to influence the water content of the hydrocarbon. In general, when condensed phases coexist, temperature and concentrations have a much greater influence than does pressure. With liquid hydrocarbon and water, the temperature controls the mutual solubility (i.e., the concentration of the water in the hydrocarbon liquid, as well as the concentration of the hydrocarbon in the liquid water). The mutual solubility of water and liquid hydrocarbons is correlated with temperature in [Sec. 11.3.2](#) below.

The Gibbs phase rule is discussed further in Chap. 7 of the General Engineering section of this Handbook.

### 11.3 Equilibrium of H<sub>2</sub>O + Hydrocarbon Systems Without Hydrates

This section considers two equilibrium conditions. First, it investigates the point at which, at a given temperature and pressure, water becomes saturated in either hydrocarbon vapors or hydrocarbon liquids and forms a separate fluid phase. Second, it considers the point at which hydrocarbon becomes saturated in liquid water and forms a separate hydrocarbon phase. Thus, both water and hydrocarbon dewpoints are represented as the maximum solubility of each phase in the other.

The discussion in this section assumes that hydrates will not form; prevention of hydrate formation requires a high temperature, a low pressure, or that all hydrocarbons be larger than n-pentane (9Å). Prediction of hydrate formation is covered in [Sec. 11.4](#) of this chapter, whereas the discussion of nonhydrate-forming systems in this section provides a basis for understanding the subsequent equilibria of hydrocarbons and water.

**11.3.1 Water Solubility (Dewpoint) in a Hydrocarbon Gas.** The chart by McKetta and Wehe<sup>3</sup> ([Fig. 11.1](#)) acceptably correlates the water content of hydrocarbon gases as a function of temperature and pressure. Because  $F = 2$ , two intensive variables are needed to specify the system. At a given temperature and pressure, the user can determine the saturated water content of gases, the point at which a liquid water phase will precipitate. For this reason [Fig. 11.1](#) frequently is called the water dewpoint chart. Before using [Fig. 11.1](#), however, note that:

- Water content is given in H<sub>2</sub>O lbm/MMscf of gas at 60°F and 1 atm.
- Remarkably, the chart can be used for any hydrocarbon gas or gas mixture, regardless of gas composition. However, the water content should be multiplied by a slight correction factor for gas gravity (gas gravity = gas molecular weight divided by air molecular weight). Larger correction factors are required for sour (H<sub>2</sub>S + CO<sub>2</sub>) gases.
- To construct the chart, data from several investigators were measured at high (>50 lbm/MMscf) water contents and extrapolated (as ln water content vs. temperature) along isobaric lines of constant pressure to lower water content.
- While the semilogarithmic plot adequately correlates data for gases at higher water contents, the correlation cannot be extrapolated to lower water content (<20 lbm/MMscf) because the lines bend sharply downward at the hydrate formation temperature and pressure.
- Dashed lines in [Fig. 11.1](#) represent metastable equilibrium of water in the vapor, giving a metastable water content that is higher than the equilibrium water content of gas in equilibrium with hydrates, the stable condensed phase at lower temperatures.

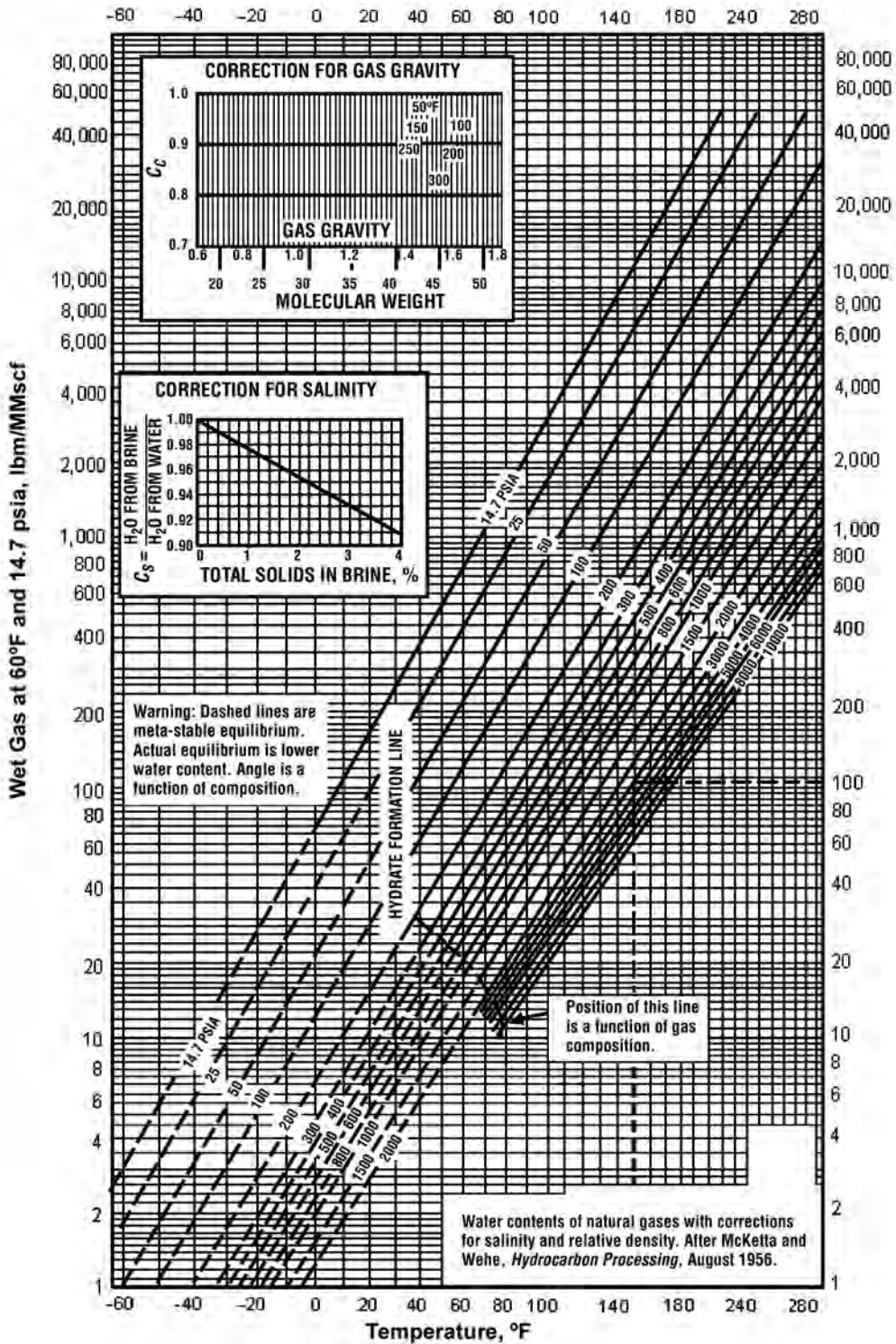


Fig. 11.1—Water content of hydrocarbon gases (from McKetta and Wehe<sup>3</sup>).  $C_s$  = correction factor for salinity,  $C_G$  = correction factor for gas gravity.

• Fig. 11.1 should not be used for low water concentrations; instead, use a computer program, as indicated in Sec. 11.4.2 below.

Despite its limitations, Fig. 11.1 is very useful and provides a check against high water content values calculated by commercial phase equilibria computer programs.

No similar measurements and charts are available for determining the hydrocarbon content in water vapor, with a separate liquid hydrocarbon phase. To approximate this at low pressures, an engineer may use the rule of thumb that hydrocarbon liquid will condense when the hydrocarbon partial pressure equals its vapor pressure. This calculation rarely is performed, however, because water's hydrogen bonds cause water vapor pressure to be lower than that of many hydrocarbons. At temperatures below 100°C, only alkanes with carbon numbers above seven (n-C<sub>8</sub>H<sub>18</sub><sup>+</sup>) have lower vapor pressures than water, because of water's strong hydrogen bonds.

For this reason, it is much more common for water to precipitate from a hydrocarbon vapor in gas/petroleum operations than it is for hydrocarbon to precipitate from a low-pressure water vapor. Therefore, Fig. 11.1 is most practical for determining water solubility in hydrocarbon vapor.

**11.3.2 Mutual Solubility of Liquid Water and Liquid Hydrocarbons.** Tsonopoulos<sup>4,5</sup> correlated mutual liquid solubility of liquid water and well-defined liquid hydrocarbons (normal alkanes, 1-alkenes, alkylcyclohexanes, and alkylbenzenes) for molecules that are too large (>9Å) to form hydrates. Solubilities in more general liquids (e.g., petroleum fractions) are not in the open literature and can be approximated using well-defined hydrocarbon fluid solubilities or their mixtures. The correlations for such fluids are given in four parts in this section:

- Solubility of hydrocarbons in liquid water at 298 K.
- Solubility of hydrocarbons in liquid water as a function of temperature.
- Solubility of water in liquid hydrocarbons at 298 K.
- Solubility of water in liquid hydrocarbons as a function of temperature.

Pressure does not significantly affect the mutual solubilities of liquids.

**Solubility of Hydrocarbon in Liquid Water at 298 K.** Because of dissimilarity in bonds between water and hydrocarbon, the mole fraction of well-defined hydrocarbon in water at 298 K always is very small, ranging from a high of  $5 \times 10^{-4}$  for alkylbenzenes with a carbon number of 6 ( $N_c = 6$ ), to a low of  $2 \times 10^{-9}$  for nonane, a normal alkane. Even with these low water concentrations, at the same carbon number, the hydrocarbon in water concentrations decrease in the order of alkylbenzenes > alkylcyclohexanes > linear 1-alkenes > normal alkanes, as shown in Fig. 11.2. For a given chemical type, larger molecules always are less soluble in water than are smaller molecules.

The correlation for the mole fraction of hydrocarbons in water ( $x_{\text{HC-W}}$ ) at 298 K is:

$$\ln x_{\text{HC-W}} = a + bN_c + \frac{c}{N_c}, \dots\dots\dots (11.2)$$

where  $N_c$  = the carbon number, and  $a$ ,  $b$ , and  $c$  = constants as given in Table 11.1. For normal alkanes, the correlation does not fit well after  $N_c = 11$ .

**Solubility of Hydrocarbon in Liquid Water as a Function of Temperature.** Liquid hydrocarbon solubility in water generally increases with temperature; however, there appears to be a minimum in solubility that ranges from 291 K for alkylbenzenes to 303 K for alkanes. As the temperature moves below these minimum values, the hydrocarbon concentration in water increases.

These solubilities change enough that the temperature effects for each compound must be treated individually. The hydrocarbon mole fraction for hydrocarbon liquids ( $x_{\text{HC-W}}$ ) in water, as a function of temperature ( $T$ ) in K, is well-described by the correlation:

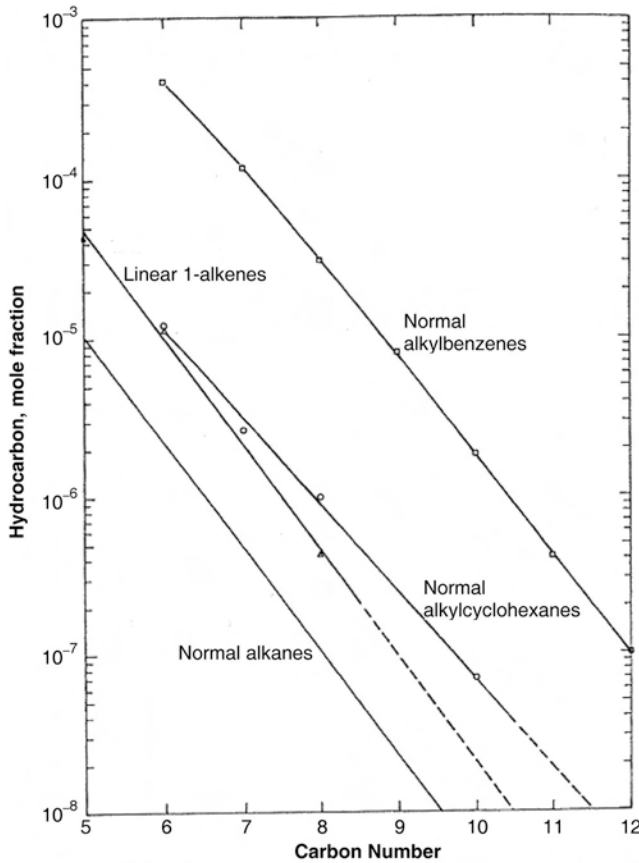


Fig. 11.2—Solubility of hydrocarbons in water at 298.15 K (from Tsonopoulos<sup>5</sup>).

TABLE 11.1—CONSTANTS AND RANGES OF APPLICATION IN EQ. 11.2 FOR SOLUBILITY OF HYDROCARBONS IN WATER AT 298 K				
Type	<i>a</i>	<i>b</i>	<i>c</i>	<i>N<sub>c</sub></i> Range
Normal alkanes	-3.9069	-1.51894	0	C5 to C11
Linear 1-alkenes	-2.24515	-1.54381	0	C5 to C8
Alkylbenzenes	4.25097	-1.59463	-14.89081	C6 to C12
Alkylcyclohexanes	-3.74419	-1.27431	0	C6 to C10

$$\ln x_{\text{HC-W}} = a + \frac{b}{T} + c \ln T, \dots\dots\dots (11.3)$$

where *a*, *b*, and *c* = constants for normal alkanes, as given in **Table 11.2**. For constants for individual 1-alkenes, alkylcyclohexanes, and alkylbenzenes, see Tsonopoulos.<sup>5</sup>

**Solubility of Water in Liquid Hydrocarbons at 298 K.** The solubility of water in hydrocarbon liquids at 298 K, like that of hydrocarbons in liquid water, is small, ranging from  $3.2 \times 10^{-4}$  for ethane to  $3 \times 10^{-3}$  for alkylbenzenes (*N<sub>c</sub>* = 6), as shown in **Fig. 11.3**. The solubility of water in liquid hydrocarbons decreases in the following order for the same *N<sub>c</sub>*: alkylbenzenes > linear 1-alkenes > normal alkanes > alkylcyclohexanes.



TABLE 11.2—CONSTANTS AND RANGES OF APPLICATION IN EQ. 11.3 FOR TEMPERATURE EFFECT ON SOLUBILITY OF NORMAL ALKANES IN WATER				
Compound	<i>a</i>	<i>b</i> , K	<i>c</i>	<i>T</i> Range, K
Pentane	-333.59719	14 537.472	47.97436	273 to 413
Hexane	-374.90804	16 327.128	53.89582	273 to 413
Heptane	-396.93979	17 232.298	56.95927	273 to 413
Octane	-415.7563	17 975.386	59.55451	273 to 413
Nonane	-433.434	18 767.82	61.940	273 to 413

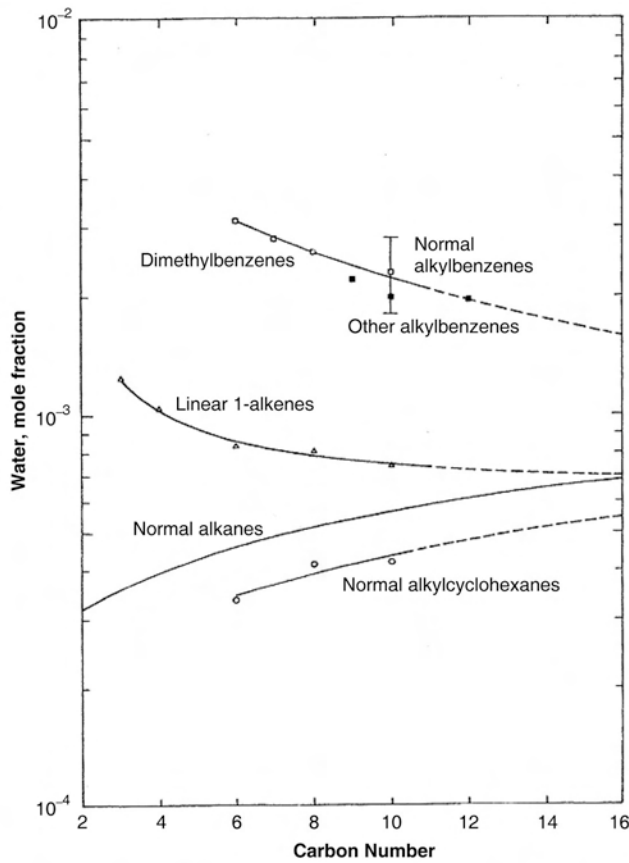


Fig. 11.3—Solubility of water in hydrocarbons at 298.15 K (from Tsonopoulos<sup>5</sup>).

The correlation for mole fraction of water in liquid hydrocarbons for well-defined fluids is:

$$\ln x_{W-HC} = \frac{a + bN_c}{c + N_c}, \dots\dots\dots (11.4)$$

where *a*, *b*, and *c* = constants as given in **Table 11.3**.

**TABLE 11.3—CONSTANTS AND RANGES OF APPLICATION IN EQ. 11.4 FOR SOLUBILITY OF WATER IN HYDROCARBONS AT 298 K**

Type	<i>a</i>	<i>b</i>	<i>c</i>	<i>N<sub>c</sub></i> Range
Normal alkanes	-79.6677	-6.6547	9.5470	C2 to C16
Linear 1-alkenes	4.6649	-7.3894	-0.3834	C3 to C16
Alkylbenzenes	-78.1518	-7.9107	15.7423	C6 to C16
Alkylcyclohexanes	-102.4415	-6.7228	11.9077	C6 to C16

**TABLE 11.4—CONSTANTS AND RANGES OF APPLICATION IN EQ. 11.5 FOR TEMPERATURE EFFECT ON SOLUBILITY OF WATER IN NORMAL ALKANES**

Compound	<i>a</i>	<i>b</i>	$\Delta H_1$	<i>T</i> Range
Pentane	6.951930	-4,381.365	36.4	273 to 343
Hexane	6.698073	-4,291.186	35.7	273 to 343
Heptane	6.761260	-4,290.700	35.7	273 to 343
Octane	6.839365	-4,290.165	35.7	273 to 539
Decane	6.476563	-4,179.296	34.7	273 to 343
Hexadecane	6.418156	-4,089.393	34.0	273 to 343

**Solubility of Water in Liquid Hydrocarbons as a Function of Temperature.** Unlike the three above solubility correlations, the solubility of water in hydrocarbons increases dramatically with temperature. At high temperatures (>500 K) the solubility of water in hydrocarbons can exceed 0.1 mole fraction, and may not be negligible, as with some of the above concentrations. These solubilities change so dramatically that the temperature solubility of each compound must be treated individually. The correlation of the mole fraction of water in liquid hydrocarbons as a function of temperature (K) is:

$$\ln x_{W-HC} = a + \frac{b}{T}, \dots\dots\dots (11.5)$$

where *a* and *b* = constants as given in **Table 11.4** for normal alkanes, as well as the heat of solution (*H*<sub>1</sub>) defined as the enthalpy of water in the hydrocarbon solution minus that of pure liquid water. Consult Tsonopoulos<sup>5</sup> for constants and ranges for individual 1-alkenes, alkylcyclohexanes, and alkylbenzenes.

#### 11.4 Equilibrium of an H<sub>2</sub>O + Hydrocarbon System With Hydrates

For systems containing both water and small (<9Å) hydrocarbons, hydrates are an important part of the phase diagram. This section addresses phase equilibria with hydrates, and is divided into two subsections: hydrate structures, stability, and measurements (**Sec. 11.4.1**); and phase equilibria and calculations involving hydrates (**Sec. 11.4.2**). A discussion of hydrates relative to such issues as safety, flowline blockage, gas storage, seafloor stability, and energy recovery is offered in the Emerging and Peripheral Technologies section of this Handbook.

**11.4.1 Hydrate Structures, Stability, and Measurements.** On a molecular scale, hydrates form when single, small guest molecules are engaged (enclathrated) by hydrogen-bonded water cages, which then combine as solid unit crystals in these nonstoichiometric hydrates. Hydrocarbon guest repulsions prop open different sizes of water cages, which combine to form the three well-defined unit crystal structures shown in **Fig. 11.4**. Cubic structure I (sI), with small (4.0

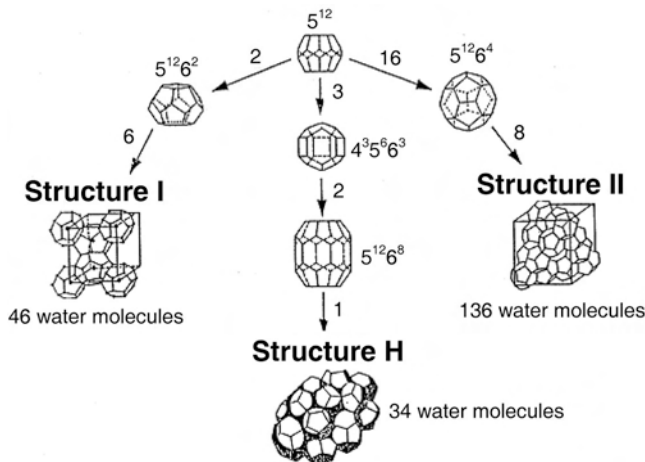


Fig. 11.4—Three hydrate unit crystals and constituent cavities (from Sloan<sup>6</sup>).

TABLE 11.5—GEOMETRY OF CAGES IN THREE HYDRATE CRYSTAL STRUCTURES IN FIG. 11.4

Hydrate Crystal Structure	I		II		H		
	Small	Large	Small	Large	Small	Medium	Large
Description	5 <sup>12</sup>	5 <sup>12</sup> 6 <sup>2</sup>	5 <sup>12</sup>	5 <sup>12</sup> 6 <sup>4</sup>	5 <sup>12</sup>	4 <sup>3</sup> 5 <sup>6</sup> 6 <sup>3</sup>	5 <sup>12</sup> 6 <sup>8</sup>
Cavities/unit cell	2	6	16	8	3	2	1
Average cavity radius, Å	3.95	4.33	3.91	4.73	3.91 <sup>a</sup>	4.06 <sup>a</sup>	5.71 <sup>a</sup>
Variation in radius, %	3.4	14.4	5.5	1.73	Not Available		
Coordination number <sup>c</sup>	20	24	20	28	20	20	36
Number of waters/unit cell	46		136		34		

<sup>a</sup>Estimates of structure H cavities from geometric models; <sup>b</sup>variation in distance of oxygen atoms from center of cage; <sup>c</sup>number of oxygens at the periphery of each cavity.

to 5.5 Å) guests, predominates in natural environments. Cubic structure II (sII) generally has larger (6.0 to 7.0 Å) guests and mostly occurs in man-made environments. Hexagonal structure H (sH) may occur in either environment, but only with mixtures of small (4.0 to 5.5 Å) and the very large (8.0 to 9.0 Å) molecules. The smallest hydrated molecules (Ar, Kr, O<sub>2</sub>, and N<sub>2</sub>), with diameters of less than 4.0 Å, form sII; still smaller molecules cannot be enclathrated except at extreme pressures.

These three common hydrate structures each have large and small cavities. In all three structures, the small cavity is similar and is called a 5<sup>12</sup> cavity because it contains 12 pentagonal faces composed of water molecules. In structure I, however, the large 5<sup>12</sup>6<sup>2</sup> cavity has 12 pentagonal faces and two hexagonal faces and is somewhat smaller than the large 5<sup>12</sup>6<sup>4</sup> cavity in structure II, which has four hexagonal faces and is large enough to contain molecules as large as n-butane. Structure H has the largest cavity—a 5<sup>12</sup>6<sup>8</sup> that can hold molecules as large as 9.0 Å—as well as three 5<sup>12</sup> cavities and two unusual 4<sup>3</sup>5<sup>6</sup>6<sup>3</sup> cavities with three square faces. Table 11.5 shows properties of these three common unit crystals.

Remarkably, when all hydrate cavities are filled, the three crystal types have similar component concentrations: 85 mol% water and 15 mol% guest(s). This makes hydrate formation most probable at the interface between the bulk guest and aqueous phases because hydrate component concentrations exceed the mutual water/hydrocarbon solubilities. The solid hydrate film at the interface acts as a barrier against further contact of the bulk fluid phases, and fluid surface renewal is required for continued hydrate formation. The gas concentration in hydrates is comparable to that of a highly compressed gas (e.g., methane at 273 K and 17 MPa).

In addition to the three crystal structures in Fig. 11.4 and Table 11.5, a fourth<sup>8</sup> and a fifth\* hydrate structure recently were found. These two new structures are omitted from this overview because hydrocarbons have yet to be found in them, but their discovery points to the probability that more hydrate structures exist. Accurate stability predictions rely on accurate knowledge of the phases present, but for now, an accurate answer to the question of how many hydrate structures exist is unavailable. Currently, one must manage with the rule of thumb that three structures are common with hydrocarbons.

Hydrate stability conditions, which depend on hydrate structure, usually are measured in terms of dissociation because there is much less metastability on dissociation than on formation, when the two disordered phases of gas and water must organize themselves to hydrate. Hydrate dissociation typically is detected at low pressures (<70 MPa) by visual crystal disappearance and at higher pressures by measuring the gas phase pressure increase (because of high gas concentration in the hydrate phase) or liquid phase temperature decrease or salinity decrease (because of the endothermic heat of dissociation or hydrate phase water intake).

Because there are several hydrate structures, however, measuring every phase *except* the hydrate phase can introduce large data errors. For example, recently it was proven<sup>9</sup> that mixtures of methane and ethane (each an sI former as a pure guest) form sII at methane gas concentrations ranging from 77 to 99.4% at deep-sea temperature (277 K). This finding means that more than 50% of the methane + ethane hydrate data measured since 1934 incorrectly assumed the sI hydrate structure for this most common hydrocarbon binary mixture.

Three experimental tools are used for nondestructive hydrate phase measurements: diffraction tools, such as X-ray or neutron,<sup>10</sup> Raman spectroscopy,<sup>11</sup> and nuclear magnetic resonance (NMR) spectroscopy.<sup>12</sup> Without hydrate phase measurement, one must assume the hydrate structure and properties are predicted acceptably by a mathematical model. This can lead to inaccuracies, as shown in the above case of the methane + ethane system.

**11.4.2 Phase Equilibria and Calculations Involving Hydrates.** There are four types of H<sub>2</sub>O + hydrocarbon equilibrium that include hydrates, as indicated in the pressure/temperature (P/T) diagrams. These equilibria types are:

- Gases, such as CH<sub>4</sub> or N<sub>2</sub>, that exist only as vapor for conditions of interest (Fig. 11.5a).
- Gas + single condensate + water systems (e.g., H<sub>2</sub>O + C<sub>2</sub>H<sub>6</sub>, C<sub>3</sub>H<sub>8</sub>, or i-C<sub>4</sub>H<sub>10</sub>) in which the hydrocarbon may be vapor or liquid (Fig. 11.5b).
- Systems with gas + mixed oil/condensate + water (Fig. 11.5c).
- Systems with inhibitors (Fig. 11.5d).

Pressure/temperature diagrams for each of the above system types are discussed in the next four sections of 11.4.2. The section following those presents hand calculation methods for estimating hydrate equilibria.

**Pressure/Temperature Diagram of a Gas Above Its Hydrocarbon Dewpoint.** Consider the P/T diagram in Fig. 11.5a, shown schematically for the methane + water system at conditions both above the solid hydrate/ice region (to the right of all lines) and below the solid region (to

\* Personal communication with J.A. Ripmeester, 17 March 2000.

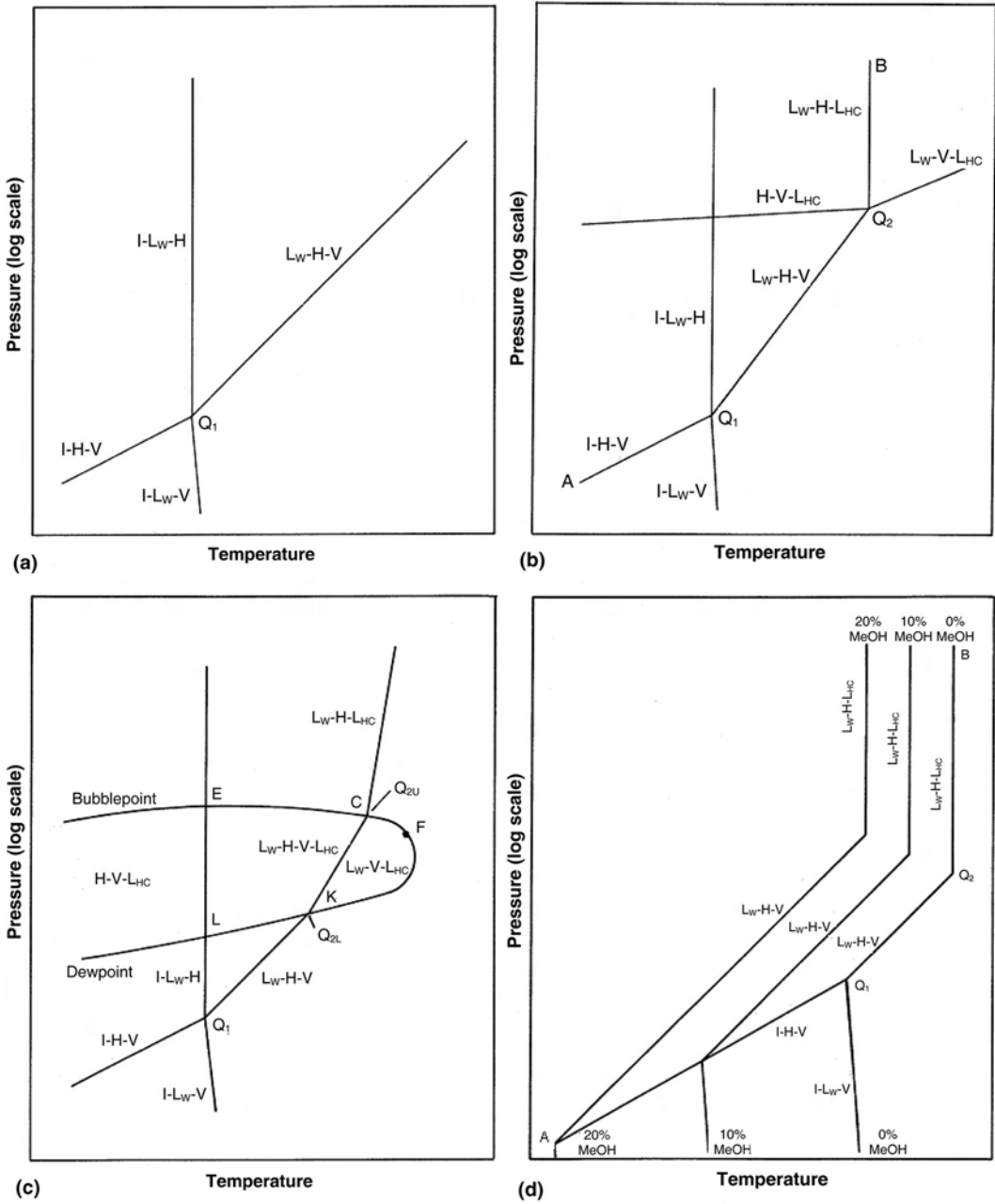


Fig. 11.5a—Pressure/temperature diagram for methane + water or nitrogen + water systems in the hydrate region (from Sloan<sup>7</sup>).

the left of all lines). Because methane is the major component of natural gas, this diagram provides phase behavior understanding for gas systems without a liquid hydrocarbon phase.

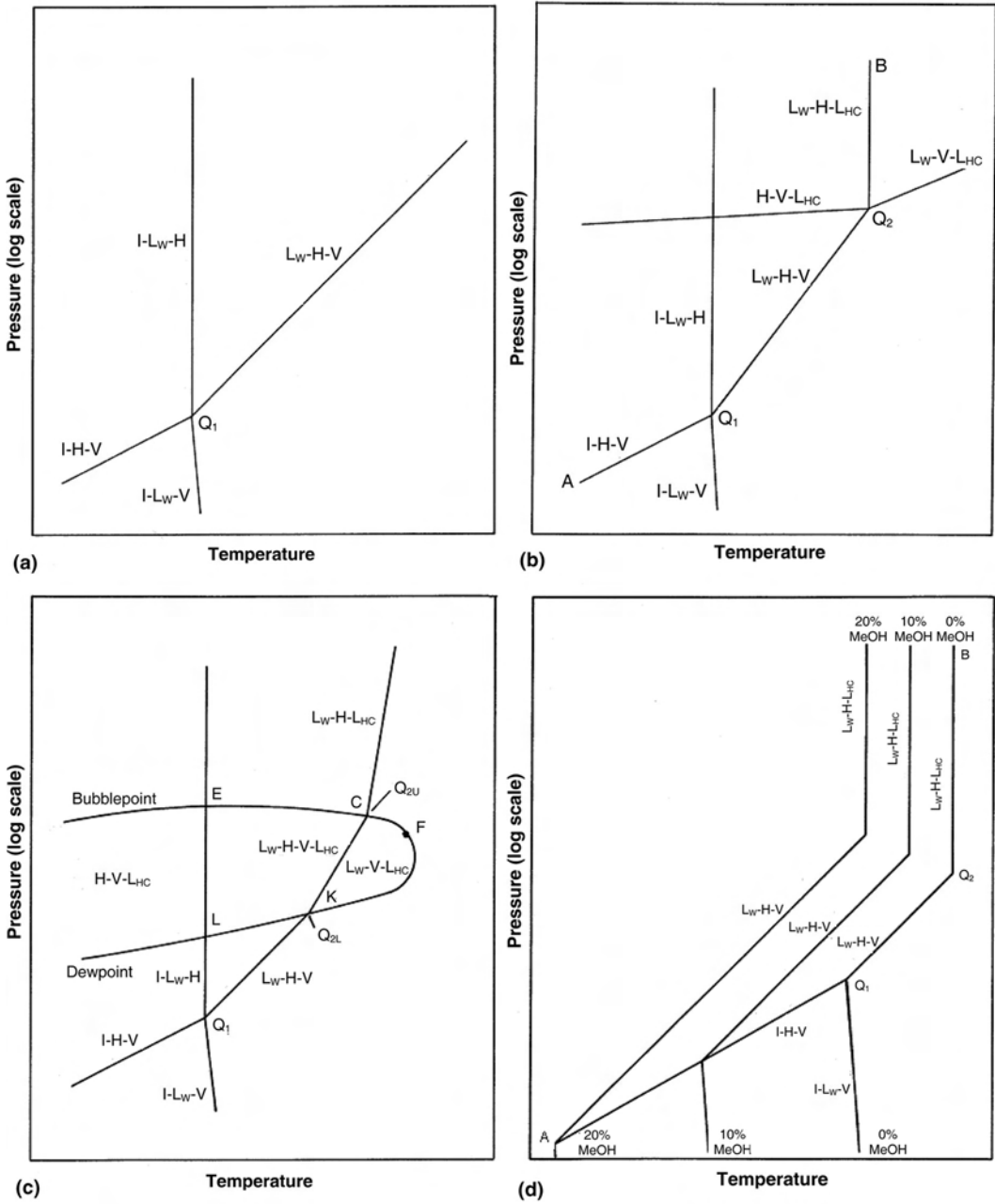


Fig. 11.5b—Pressure/temperature diagram of hydrocarbon single components with upper quadruple points (from Sloan<sup>7</sup>).

This diagram assumes that a flash calculation has been performed to ensure that a liquid hydrocarbon phase will not form. Furthermore, the vapor hydrocarbon phase should be large

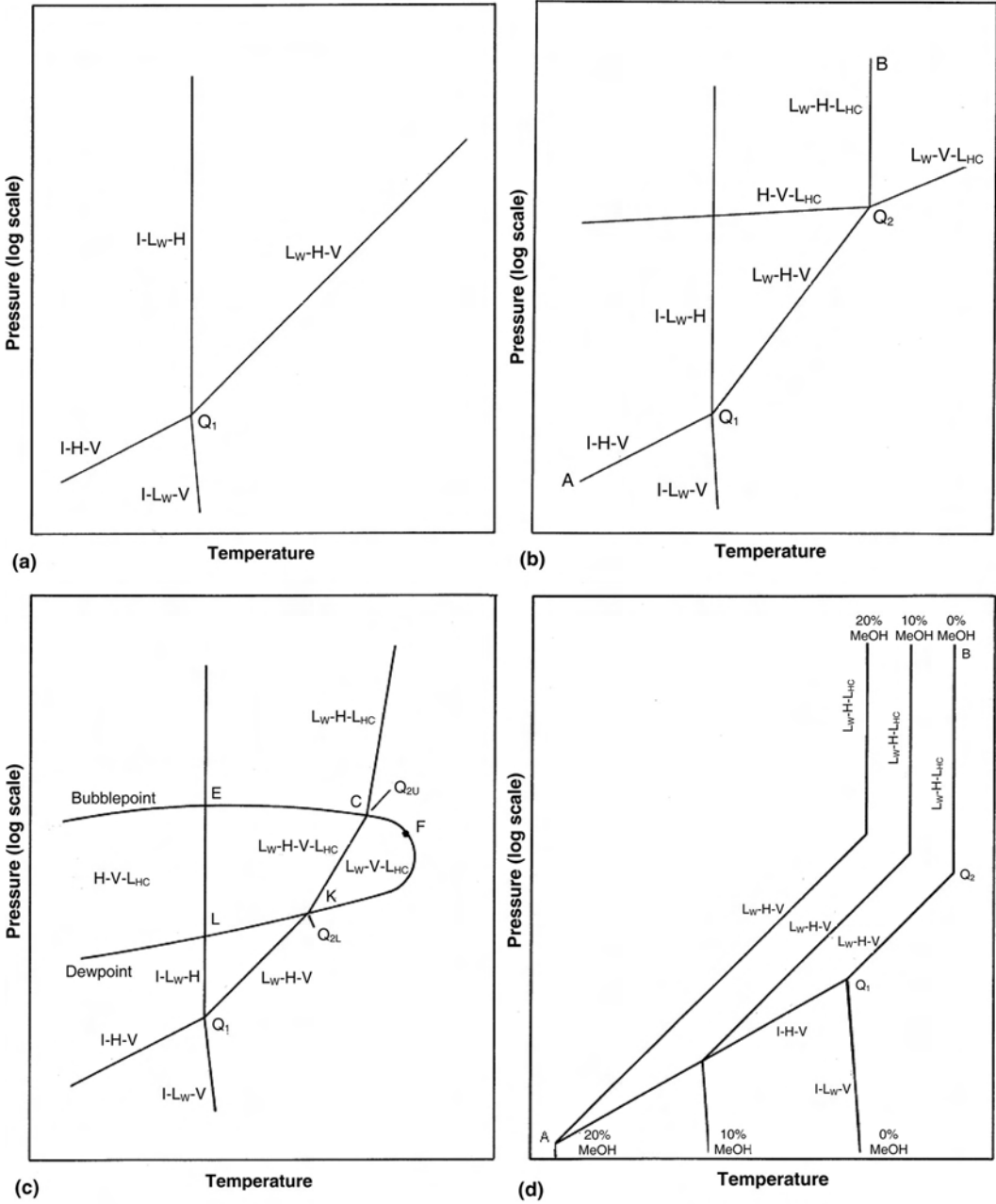


Fig. 11.5c—Pressure/temperature diagram for multicomponent natural gas + water systems (from Sloan<sup>7</sup>).

enough that it neither changes composition nor condenses, in which case the vapor composition is constant ( $C_v = 1$ ). If water forms a condensed phase, however, which it frequently does, then the system is below the water dewpoint, but above the hydrocarbon dewpoint.

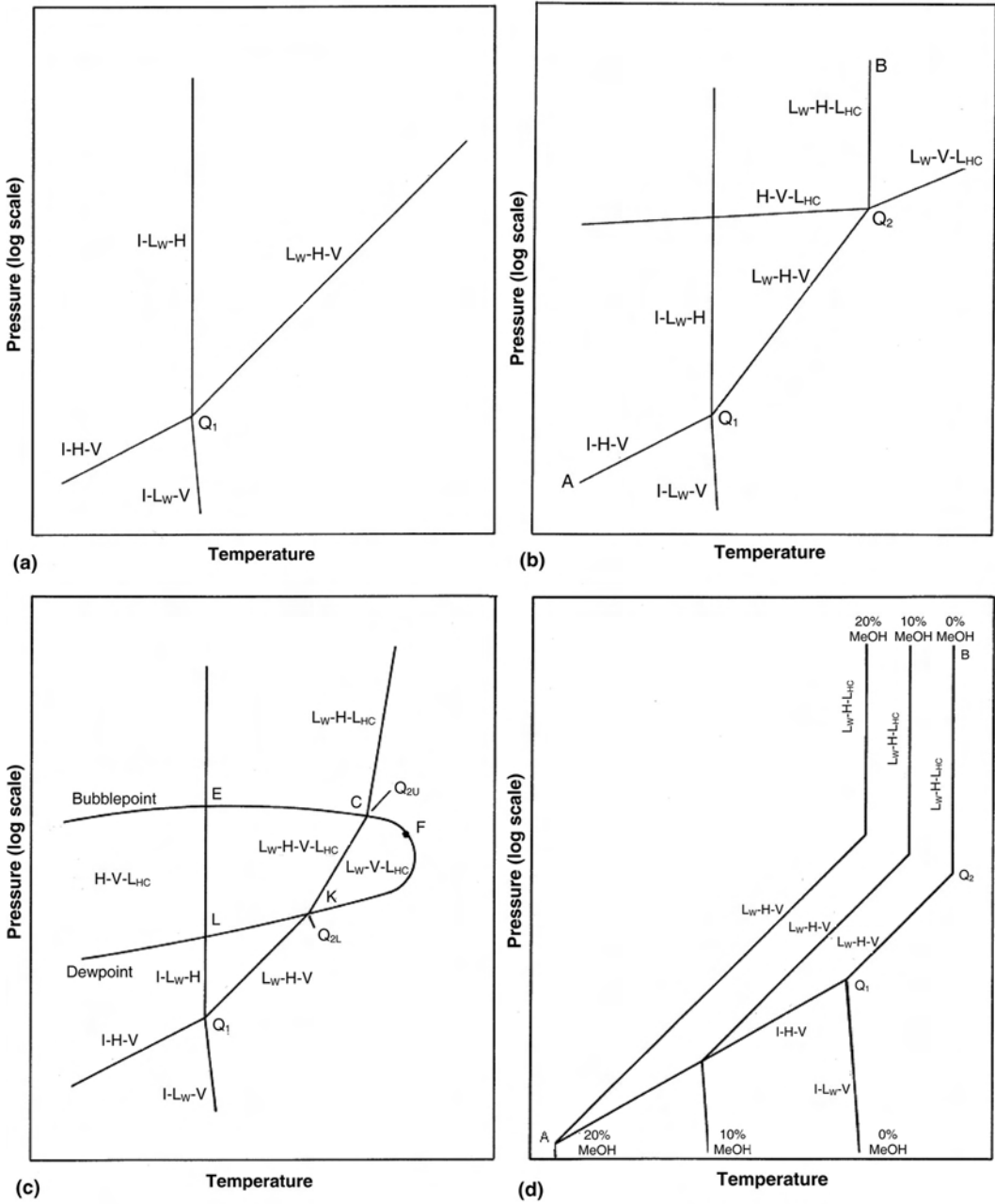


Fig. 11.5d—Pressure/temperature diagram for H<sub>2</sub>O + hydrocarbon systems with inhibitors (after Sloan<sup>7</sup>).

According to the Gibbs phase rule,<sup>1</sup> a two-component system such as methane + water is represented on a P/T diagram as an area (two phases), a line (three phases), or a point (four



**TABLE 11.6—HYDRATE FORMATION FOR THREE PHASE CONDITIONS OF SINGLE NATURAL GAS COMPONENTS**

Compound	Type	<i>T</i> Range, °C	<i>a</i>	<i>b</i>
Methane	LW-H-V	0 to 25	38.980	-8,533.80
Methane	I-H-V	-25 to 0	14.717	-1,886.79
Ethane	LW-H-V	0 to 14	44.273	-10,424.25
Ethane	I-H-V	-25 to 0	17.511	-3,104.54
Propane	LW-H-V	0 to 5	67.130	-16,921.84
Propane	I-H-V	-25 to 0	17.156	-3,269.65
Isobutane	LW-H-V	0 to 1.5	61.740	-15,571.43
Isobutane	I-H-V	-25 to 0	18.950	-3,887.32
Carbon dioxide	LW-H-V	0 to 11	44.580	-10,246.28
Carbon dioxide	I-H-V	-25 to 0	18.594	-3,161.41
Nitrogen	LW-H-V	0 to 25	37.808	-7,688.63
Nitrogen	I-H-V	-25 to 0	15.129	-1,504.28
Hydrogen sulfide	LW-H-V	0 to 25	34.828	-8,266.10
Hydrogen sulfide	I-H-V	-25 to 0	16.560	-3,270.41

(From Kamath<sup>23</sup>)

phases). To obtain nearly straight lines, semilogarithmic plots [ $\ln$  pressure ( $p$ ) vs. absolute temperature ( $T_a$ )] are used.

Consider the quadruple point ( $Q_1$ ) in Fig. 11.5a, where four phases (I-L<sub>W</sub>-H-V) coexist. The  $Q_1$  temperature is close to 273 K for all hydrate formers, yet the quadruple pressures vary widely (e.g., 0.0113 MPa for i-C<sub>4</sub>H<sub>10</sub>, 2.56 MPa for CH<sub>4</sub>, and 14.3 MPa for N<sub>2</sub>).  $Q_1$  is the starting point for four 3-phase lines:

- The L<sub>W</sub>-H-V line, which has P/T conditions at which water and vapor form hydrates, conditions of most interest in natural gas hydrate systems.
- The I-H-V line, which terminates at about 273 K and has a lower slope than the L<sub>W</sub>-H-V line. Industrially, the region below 273 K is avoided, if possible, because of flow assurance problems stemming from either ice or hydrate formation.
- The I-L<sub>W</sub>-H line, which rises vertically from  $Q_1$ , with very large pressure changes for small temperature changes, typical of incompressible phases.
- The I-L<sub>W</sub>-V line, which connects  $Q_1$  to the pure water triple point (I-L<sub>W</sub>-V) (273.16 K, 0.62 kPa) and denotes the transition between water and ice without hydrate formation. Because  $Q_1$  is close to 273 K for all natural gas systems, the I-L<sub>W</sub>-V line extends almost vertically below  $Q_1$  to 0.62 kPa.

Eq. 11.6 and Table 11.6 enable prediction of the most common regions of interest for simple natural gas components—the pressure and temperature conditions for both L<sub>W</sub>-H-V and I-H-V.

$$p = \exp\left(a + \frac{b}{T}\right), \dots\dots\dots (11.6)$$

where  $p$  = pressure, in kPa;  $a$  and  $b$  = constants; and  $T$  = temperature, in K, as shown in Table 11.6.

Component	Q <sub>1</sub>		Q <sub>2</sub>	
	T, K	p, MPa	T, K	p, MPa
Methane	272.9	2.563	— No Q <sub>2</sub> —	
Ethane	273.1	0.530	287.8	3.390
Propane	273.1	0.172	278.8	0.556
Isobutane	273.1	0.113	275.0	0.167
Carbon dioxide	273.1	1.256	283.0	4.499
Nitrogen	271.9	14.338	— No Q <sub>2</sub> —	
Hydrogen sulfide	272.8	0.093	302.7	2.239

When using Eq. 11.6, carefully note the temperature limits. It would be a mistake, for example, to extend the prediction of the L<sub>w</sub>-H-V region beyond the temperature of either Q<sub>1</sub> or Q<sub>2</sub> (given in Table 11.7), where L<sub>w</sub>-H-V cannot exist.

The pressures and temperatures in Fig. 11.5a are of interest in natural gas systems for the following reasons:

- The pressures and temperatures of the L<sub>w</sub>-H-V and the I-H-V lines mark the limits of hydrate formation. Hydrates cannot form to the right of either line, but will form to the left of both. Because both ice and hydrates cause flow problems, a gas pipeline rule of thumb is to keep the system temperature above the ice point and to the right of the L<sub>w</sub>-H-V line.

- The L<sub>w</sub>-H-V line has no upper pressure or temperature limit because the methane (or nitrogen) vapor/liquid critical points (191 and 126 K, respectively) are far below Q<sub>1</sub>. Such low critical temperatures prevent intersection of the vapor pressure line with the L<sub>w</sub>-H-V line above 273 K, and so prevent the forming of an upper quadruple point. Similarly, a gas at conditions above its dewpoint will not have an upper point where the liquid phase occurs, and the L<sub>w</sub>-H-V line will continue to much higher temperatures and pressures.

- No upper pressure limit to the I-L<sub>w</sub>-H line is known. Note that these phases all are nearly incompressible, so that only a small temperature change is required to cause a very large pressure change.

- The areas between the three-phase lines represent the two-phase region held in common with the bounding three-phase lines. For instance, the area between L<sub>w</sub>-H-V and I-H-V is the H-V region, in which hydrates are in equilibrium only with water-saturated hydrocarbon vapor. Similarly, the L<sub>w</sub>-H two-phase region exists between L<sub>w</sub>-H-V and I-L<sub>w</sub>-H lines, and the I-H two-phase region exists between the I-L<sub>w</sub>-H and I-H-V lines. The two-phase regions overlap, so that at some P/T conditions there are two 2-phase regions that differ in water composition. This seeming paradox is resolved by the fact that the three-phase lines all are not in the plane of the page, but rather have been compressed from 3D (P/T/composition) into 2D (P/T).

- The diagram schematic is the same for sI hydrate systems (CH<sub>4</sub> + H<sub>2</sub>O) and sII formers (N<sub>2</sub> + H<sub>2</sub>O), as well as for those of fixed natural gas mixture compositions without an L<sub>HC</sub> phase.

**Gas + Pure Condensate + Water Systems (e.g., H<sub>2</sub>O + C<sub>2</sub>H<sub>6</sub>, C<sub>3</sub>H<sub>8</sub>, or i-C<sub>4</sub>H<sub>10</sub>).** Fig. 11.5b is slightly more complex than Fig. 11.5a, for systems such as ethane + water, propane + water, isobutane + water, or water + either carbon dioxide or hydrogen sulfide, two common noncombustibles. If the hydrocarbon phases are maintained at the same, constant composition in both vapor and liquid phases, these systems can represent multicomponent gas and oil/condensate systems.

The systems differ from those in Fig. 11.5a in that they have an additional three-phase ( $L_W$ -V- $L_{HC}$ ) line at the upper right area of the diagram. This line is very close to the vapor pressure (V- $L_{HC}$ ) line of the pure hydrocarbon, because the presence of the nearly pure water phase adds a very low vapor pressure to the system. In this system, each liquid phase,  $L_{HC}$  and  $L_W$ , exerts its vapor pressure.

Fig. 11.5b shows that where the  $L_W$ -V- $L_{HC}$  line intersects the  $L_W$ -H-V line is a second quadruple point ( $Q_2$ ), with phases  $L_W$ -H-V- $L_{HC}$ . Table 11.7 shows measured upper quadruple points for simple natural gas components.  $Q_2$  is the origin for two additional 3-phase lines: a vertical  $L_W$ -H- $L_{HC}$  line that is very incompressible and an H-V- $L_{HC}$  line (of less concern).

For systems with an upper quadruple point, the hydrate region is bounded by line I-H-V at conditions below  $Q_1$ , by line  $L_W$ -H-V at conditions between  $Q_1$  and  $Q_2$ , and by line  $L_W$ -H- $L_{HC}$  at conditions above  $Q_2$ . Hydrates will form at temperatures and pressures to the left of the region enclosed by the three lines, whereas to the right of this region, hydrates are not possible. Upper quadruple point  $Q_2$  often is approximated as the maximum temperature of hydrate formation because line  $L_W$ -H- $L_{HC}$  is approximately vertical because of the incompressibility of those three phases.

To a good approximation, P/T conditions for  $L_W$ -H-V of the pure components in Table 11.7 lie on a straight line between  $Q_1$  and  $Q_2$ , on a semilogarithmic plot ( $\ln p$  vs.  $1/T_a$ ). As discussed below in the *Hand Calculations of Hydrate Formation Conditions* section, there is no simple way to expand the above pure lines into that for a mixture, though there are several ways to hand-calculate  $L_W$ -H-V conditions (P/T) for mixed hydrocarbon hydrate formers.

In Fig. 11.5b, the areas between the three-phase lines represent two-phase regions held in common with the three-phase lines. The P/T area bounded by three 3-phase lines ( $L_W$ -H-V,  $L_W$ -H- $L_{HC}$ , and I- $L_W$ -H) is the  $L_W$ -H region, in which hydrates are in equilibrium only with liquid water. Similarly, the H-V region is between the three 3-phase lines (H-V- $L_{HC}$ ,  $L_W$ -H-V, and I-H-V). Finally, the H- $L_{HC}$  two-phase region exists between  $L_W$ -H- $L_{HC}$  and H-V- $L_{HC}$  lines, and the I-H two-phase region exists between the I- $L_W$ -H and I-H-V lines.

Note that the last paragraph contains three 2-phase regions (H-V, H- $L_{HC}$ , and I-H) for hydrate equilibrium with phases that are not liquid water. It is a common misconception that hydrates cannot form without a liquid water phase, yet this clearly is possible according to these diagrams. Professor Kobayashi's laboratory at Rice U. has measured hydrate equilibria without a free-water phase for more than a quarter century,<sup>14</sup> so there is no thermodynamic prohibition to hydrate formation without a free-water phase. However, the kinetics of such hydrate formation are extremely slow, so that in man-made systems and time scales, it may not be practical to consider hydrate formation without a free-water phase.

**Pressure/Temperature Diagrams for Gas + Oil/Condensate Systems.** For natural gases without a liquid hydrocarbon, the P/T phase diagram is similar to that shown in Fig. 11.5a. The few changes would be that the  $L_W$ -H-V line would be for a fixed composition mixture of hydrocarbons rather than for pure methane; that  $Q_1$  would be at the intersection of the  $L_W$ -H-V line and 273 K, at a pressure lower than that for methane; and that the other three-phase lines (for I- $L_W$ -H and I-H-V) would have nearly the same slope at  $Q_1$ , but  $Q_1$  would be at a lower pressure than for methane. Otherwise, the same points in Sec. 11.4.1 apply.

For natural gases that contain oils or mixed condensates, however, the upper portion of the diagram is more like that in Fig. 11.5b. A straight line labeled  $L_W$ -H-V represents the hydrate formation region that is equivalent to the region between  $Q_1$  (I- $L_W$ -H-V) and  $Q_2$  ( $L_W$ -H-V- $L_{HC}$ ) in Fig. 11.5b.

A second significant change is that point  $Q_2$  becomes a quadruple line. When a liquid hydrocarbon mixture is present, the  $L_W$ -V- $L_{HC}$  line, to the right of  $Q_2$  in Fig. 11.5b, broadens to become an area, such as that labeled CFK in Fig. 11.5c. This area develops because a single hydrocarbon is no longer present, so that a combination of hydrocarbon and water vapor pres-

tures creates a broader phase-equilibria envelope. Consequently,  $Q_2$  evolves into a line KC between  $Q_{2L}$  and  $Q_{2U}$  for the multicomponent hydrocarbon system.

Line KC might not be straight in the four-phase region, though it is drawn as such here for illustration purposes. The lower point, K's location, is determined by the point at which the phase envelope ECFKL intersects the  $L_W$ -H-V line. To determine the upper point C, calculate the vapor/liquid equilibrium, assuming that the liquid phase (exiting the envelope at point C) is the vapor composition at point K. The resulting equilibrium (bubblepoint) vapor is plugged into a vapor/liquid water/hydrate calculation to find the upper intersection with the phase envelope ECFKL.

**Pressure/Temperature Diagrams for Systems With Inhibitors.** The presence of inhibitors causes a change in the P/T diagram, as illustrated in Fig. 11.5d. For simplicity, the diagram shows only the hydrate bounding region (to the left of line  $AQ_1Q_2B$ ) for an uninhibited pure component system with upper and lower quadruple points ( $Q_1$  and  $Q_2$ ). Line  $AQ_1Q_2B$  in Fig. 11.5d is equivalent to line  $AQ_1Q_2B$  in Fig. 11.5b, with three slopes that change at the quadruple points.

In Fig. 11.5d, the presence of an inhibitor [e.g., methanol (MeOH)] shifts the upper two-thirds of the line  $Q_1Q_2B$  to the left, approximately parallel to the uninhibited line on a semilogarithmic plot ( $\ln p$  vs.  $T_a$ ). With an inhibitor however, the transition temperature from water to ice ( $Q_1$ ) is decreased, so that the inhibited  $L_W$ -H-V line intersects the I-H-V at a lower point (labeled  $Q_1$  for 10 wt% methanol and  $Q_1$  for 20 wt% methanol). The three inhibited parallel lines represent  $L_W$ -H-V and  $L_W$ -H- $L_{HC}$  equilibria at 0, 10, and 20 wt% methanol concentrations in the free-water phase.

Each line in Fig. 11.5d bounds hydrate formation conditions listed with a methanol concentration in the free-water phase. To the left of each line, hydrates will form with a water phase of the given methanol composition; to the right of each line, hydrates will not form. For example, when the free-water phase has 10% methanol, hydrates will not form at P/T conditions to the right of the line marked 10% MeOH. Yet, if no methanol were present, the hydrates would form at pressures and temperatures between the two lines marked 10% and 0% MeOH. Similarly, more than 20% methanol would be required to prevent hydrate formation to the left of the line marked 20% MeOH.

For clarity, Fig. 11.5d has omitted the lines analogous to the three 3-phase lines in Fig. 11.5b (I- $L_W$ -H, which would intersect Fig. 11.5d's  $AQ_1Q_2B$  at  $Q_1$ , and  $L_W$ -V- $L_{HC}$  and H-V- $L_{HC}$ , which would intersect it at  $Q_2$ ). Such lines are less important for hydrate formation, but join the diagram at the appropriate, shifted quadruple points. For systems without an upper quadruple point (as in Fig. 11.5a) and systems with a liquid hydrocarbon region (as in Fig. 11.5c), the hydrate boundary region similarly is shifted to the left of (and is approximately parallel to) the uninhibited phase lines.

Other inhibitors, such as monoethylene glycol (MEG) and salts, shift the hydrate lines similarly to the left, but to a different degree. However, methanol is the most economical inhibitor on a weight basis. Note that all inhibited  $L_W$ -H-V lines are parallel to the pure water  $L_W$ -H-V line; that is, the hydrate temperature depression ( $\Delta T$ ) is constant, regardless of pressure. To estimate  $\Delta T$  for several inhibitors in the aqueous liquid, the natural gas industry uses the original Hammerschmidt<sup>15</sup> expression:

$$\Delta T = \frac{2,335W}{100M - MW}, \dots\dots\dots (11.7)$$

where  $\Delta T$  = hydrate temperature depression from the equilibrium temperature at a given pressure, °F);  $M$  = molecular weight of the inhibitor; and  $W$  = wt% of the inhibitor in the free-water phase.

With the above equation, the engineer can determine how much inhibitor should be added to the free-water phase to bring the L<sub>W</sub>-H-V line below the lowest operating temperature of the system. Before the Hammerschmidt equation can be used, however, one must determine the equilibrium temperature  $T_{eq}$  that is to be depressed by the inhibitor. The *Hand Calculations of Hydrate Formation Conditions* section below covers determination of  $T_{eq}$  and provides a method to estimate the total amount of inhibitor to inject, including not only the inhibitor amount in the aqueous liquid as calculated here by the Hammerschmidt equation, but also the amount in the vapor and liquid hydrocarbon.

**Hand Calculations of Hydrate Formation Conditions.** The most accurate predictions of hydrate formation conditions are made using commercial phase equilibria computer programs such as ASPEN, HYSYS, Multiflash, Process II, and PVTsim.\* These programs are of two types: those which enable the prediction of the pressure and temperature at which hydrates begin to form (incipient hydrate formation programs), and those which predict all phases and amounts at higher pressures and lower temperatures than the incipient hydrate formation point (flash programs, or Gibbs energy minimization programs).

Of these two program types, the flash/Gibbs type is gaining pre-eminence because its predictions are available in the phase diagram interior (where many systems operate), whereas the incipient type provides the P/T points of hydrate initiation. At present, state-of-the-art programs are transitioning to the flash/Gibbs free-energy type.

The basis for both program types is a hydrate equation-of-state (EOS). A clear, prescriptive method for constructing the hydrate flash program has recently been published.<sup>16</sup> The hydrate flash program usually is so complex as to require two or more man-years of single-minded effort to construct a robust version of the program. For this reason and because of readily available commercial programs, engineers usually elect to use those rather than construct another program. (For more details about the hydrate EOS, however, see Chap. 5 of Sloan.<sup>7</sup>)

When gathering critical prediction results for a design, however, it is important to check the program results by hand to determine whether the program has made an unusual prediction. This section offers some hand-calculation techniques for this type of evaluation.

*Which Hydrate Conditions Are Calculable by Hand?* Not all hydrate conditions are calculable by hand. The *Three-Phase L<sub>W</sub>-H-V Calculations, Estimating the Total Amount of MeOH or MEG to Inject to Inhibit Hydrates*, and *Hydrate Formation on Expansion Across a Valve or Restriction* sections below give hydrate formation hand calculations along the three-phase (L<sub>W</sub>-H-V) system and for three-phase (L<sub>W</sub>-H-V) hydrate formation on wet gas expansion, as through a valve.

The other three-phase regions (e.g., L<sub>W</sub>-H-L<sub>HC</sub> and I-H-V) are less important, and methods presented in *Three-Phase L<sub>W</sub>-H-V Calculations* are suitable for checking the accuracy of a computer program in the L<sub>W</sub>-H-V region as an indication of the quality of the other three-phase predictions. Four-phase (L<sub>W</sub>-H-V-L<sub>HC</sub>) hand calculation methods are not available, and one generally must rely on computer methods for this most common flow assurance hydrate concern. Recent work by Hopgood<sup>17</sup> shows that hydrate prediction programs commonly are in error by as much as 5°C for hydrate formation conditions in black oils; this is an area of current research.

For the two-phase regions of hydrate equilibria, such as those shown schematically in the *Gas + Pure Condensate + Water Systems (e.g., H<sub>2</sub>O + C<sub>2</sub>H<sub>6</sub>, C<sub>3</sub>H<sub>8</sub>, or i-C<sub>4</sub>H<sub>10</sub>)* section above (i.e., V-H, L<sub>HC</sub>-H, and I-H), the key question is that of water content: how much water can a vapor or liquid hydrocarbon phase hold before hydrates will precipitate? Just as knowing the V and L<sub>HC</sub> saturation conditions allows the engineer to avoid solid hydrate formation, determining the I-H region (below 273 K) lets the engineer avoid ice or hydrate formation, both of which

\* ASPEN and HYSYS are products of AspenTech. Multiflash is a product of Infochem Services Ltd, London. Process II is a product of Simsci-Esscor, Lake Forest, California. PVTsim is a product of CalSep, Houston.

cause flow problems. Unfortunately, however, for hydrate precipitation from a vapor or liquid hydrocarbon, there is no water content hand calculation analogous to either Fig. 11.1 (for V-L<sub>W</sub> water dewpoints) or Fig. 11.3 (for L<sub>HC</sub>-L<sub>W</sub> water dewpoints).

*Three-Phase L<sub>W</sub>-H-V Calculations.* There are several ways to do hand calculations for three-phase L<sub>W</sub>-H-V conditions:

- For pure hydrate guests (e.g., CH<sub>4</sub>, C<sub>2</sub>H<sub>6</sub>, C<sub>3</sub>H<sub>8</sub>, and i-C<sub>4</sub>H<sub>10</sub>), Eq. 11.6 can be used with the constants in Table 11.6, noting the range of application. A somewhat less accurate semilogarithmic interpolation can be performed between the two quadruple points listed for pure components in Table 11.7, as briefly discussed in *Gas + Pure Condensate + Water Systems* (e.g., H<sub>2</sub>O + C<sub>2</sub>H<sub>6</sub>, C<sub>3</sub>H<sub>8</sub>, or i-C<sub>4</sub>H<sub>10</sub>).

- For gas mixtures, a relatively low pressure is required for hydrate formation. For example, at a typical seafloor temperature of 277 K, hydrates will form in a natural gas system if free water is available and the pressure is greater than 1.2 MPa. Hydrate formation data at 277 K were averaged for 20 natural gases,<sup>7</sup> and the average formation pressure was 1.2 MPa. Of the 20 gases, the lowest formation pressure was 0.67 MPa for a gas with 7.0 mol% C<sub>3</sub>H<sub>8</sub>, while the highest value was 2.00 MPa for a gas with 1.8 mol% C<sub>3</sub>H<sub>8</sub>. At temperatures below 277 K, pressures below the 1.2 MPa average are required.

- Although it is not presented in this section, the Katz<sup>18</sup>  $K_{VH}$  value method can be used for hydrate formation condition estimation from gas mixtures. Hydrate  $K_{VH}$  values (defined as a component's mole fraction divided by that in the hydrate) for each gas component are used to determine a hydrate dewpoint for a gas of constant composition. As with the more common DePriester<sup>19</sup> vapor/liquid values ( $K_{VL}$ ), the hydrate  $K_{VH}$  values are functions of temperature and pressure. The  $K_{VH}$  method is not considered here for two reasons. First, at a given temperature and pressure, the method gives the same  $K_{VH}$  value, regardless of hydrate type, even though the  $K_{VH}$  value should be a strong function of crystal type. Second, the number of plots (>11) for the corrected method is unwieldy. See Sloan<sup>7</sup> for details and examples of the original  $K_{VH}$  method, including an extension to hydrate formation from water and liquid hydrocarbon (L<sub>W</sub>+L<sub>HC</sub>+H).

- A more compact, accessible method for hydrate formation from water and gas mixtures is the gas gravity method. Presented in detail below, the gas gravity method is suitable for calculation of L<sub>W</sub>-H-V equilibrium pressures and temperatures at the point of hydrate formation. Although the method is only up to 75% accurate in pressure, it gives a fast initial estimate and has the advantage of being extended easily to expansion calculations for hydrate formation from wet gases.

The gas gravity method is the simplest method for quantifying the hydrate formation temperature and pressure. Gas gravity is defined as the molecular weight of the gas divided by that of air. To use the chart shown in Fig. 11.6, calculate the gas gravity and specify the lowest temperature of the pipeline/process. The pressure at which hydrates will form then is read directly from the chart at that gas gravity and temperature.

To the left of every line, hydrates will form with a gas of that gravity. At pressures and temperatures to the right of every line, the system will be hydrate-free. The following example, modified from Katz's<sup>20</sup> original work, illustrates chart use.

---

**Example 11.1** A gas is composed of (mol%) 92.67% methane, 5.29% ethane, 1.38% propane, 0.182% i-butane, 0.338% n-butane, and 0.14% pentane. When free water is present with the gas, find:

- The pressure at which hydrates form at 283.2 K (50°F).
- The temperature at which hydrates form at 6.8 MPa (1,000 psia).

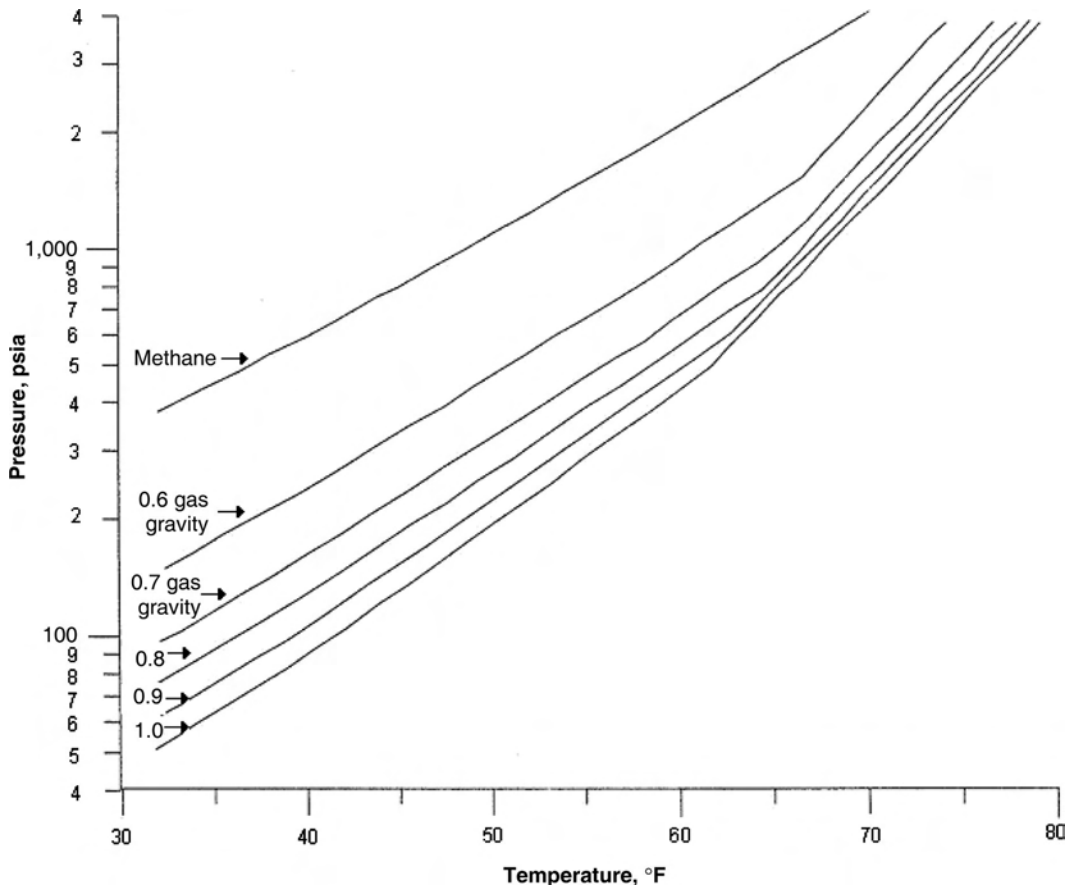


Fig. 11.6—Pressure/temperature curves for predicting hydrate formation (from Katz<sup>20</sup>).

• The highest gas gravity without hydrate formation, when the pressure is 4.76 MPa (700 psia) and the temperature is 289 K (60°F).

The gas gravity ( $\gamma_g$ ) is calculated as 0.603, using the average molecular weight calculated in [Table 11.8](#) and [Eq. 11.8](#):

$$\gamma_g = \frac{\overline{M}_g}{M_a} = \frac{17.470}{28.966} = 0.603, \dots\dots\dots (11.8)$$

where  $\overline{M}_g$  = the total molecular weight of the gas in the mixture and  $M_a$  = the molecular weight of air. Using this gas gravity number to read [Fig. 11.6](#) indicates that:

- At 50°F, the hydrate formation pressure is 450 psia at a gas gravity of 0.603.
- At 1,000 psia, the hydrate formation temperature is 61°F at a gas gravity of 0.603.
- At 700 psia and 60°F, gases with gravity below 0.69 are not expected to form hydrates.
- Caution: this method is only approximate for several reasons:

• [Fig. 11.6](#) was generated for gases containing only hydrocarbons and should be used with caution for gases with substantial amounts of CO<sub>2</sub>, H<sub>2</sub>S, or N<sub>2</sub>.

• The curves should not be extrapolated to temperatures below 273 K (32°F) or to pressures above 2.72 MPa (4,000 psia)—the data limits upon which the gas gravity plot is based.

TABLE 11.8—CALCULATION OF AVERAGE MOLECULAR WEIGHT FOR EX. 1

Component	Mole fraction in mixture, $z$	Molecular weight, $M$	Average $M$ of gas in mixture, $\bar{M}_g$ ( $z \times M$ )
Methane	0.9267	16.043	14.867
Ethane	0.0529	30.070	1.591
Propane	0.0138	44.097	0.609
i-butane	0.00182	58.124	0.106
n-butane	0.00338	58.124	0.196
Pentane	0.0014	72.151	0.101
	1.000		$\bar{M}_g = 17.470$

• For the hydrate equilibrium temperature ( $T_{eq}$ ) and pressure ( $p_{eq}$ ), the estimated inaccuracies<sup>21</sup> for 0.6 gravity gas are at a maximum of  $\pm 7^\circ\text{F}$  or  $\pm 500$  psia.

Over the 60 years since the generation of the chart in Fig. 11.6, the development of more accurate hydrate data and prediction methods have led to the gravity method being used as a first estimate or a check, rather than as a principle method, despite its ease of calculation. The introduction of the *Hand Calculations of Hydrate Formation Conditions* section above discusses the computer programs available, which are the current and most accurate method for prediction of hydrate conditions.

Most commonly now, perhaps, the gas gravity chart is used to check the conditions at which a flowline fluid will enter the hydrate formation region. Such a calculation requires a second multiphase fluid flow simulator, such as OLGA or Pipephase.\* A discussion of such simulators is beyond the scope of this chapter, however.

*Estimating the Total Amount of MeOH or MEG to Inject to Inhibit Hydrates.* The amount of injected MeOH or MEG needed to inhibit hydrate formation is the total of the amounts that reside in three phases: aqueous liquid, hydrocarbon vapor, and liquid hydrocarbon. The inhibitor in the hydrocarbon vapor and liquid hydrocarbon phases has no effect—hydrate inhibition occurs only in the aqueous phase—but this inefficiency is unavoidable.

The Hammerschmidt<sup>15</sup> equation (Eq. 11.7) provides the MeOH or MEG concentration in the aqueous phase. With that inhibitor concentration as a basis, the amount of inhibitor in the vapor or liquid hydrocarbon phases is estimated by:

$$K = \exp\left(a - \frac{b}{T}\right), \dots\dots\dots (11.9)$$

where  $K$  is a function of inhibitor used and the phase into which it partitions [e.g.,  $(K_V)_{\text{MeOH}}$  or  $(K_L)_{\text{MEG}}$ ];  $a$  and  $b$  = constants<sup>6</sup> for the two most common inhibitors, MeOH and MEG, as listed in Table 11.9; and  $T$  = temperature, in  $^\circ\text{R}$ .

With Eq. 11.9, one can calculate the total amount of hydrate inhibitor needed, as shown below in Ex. 2. Note that the fourth (missing) value of  $(K_V)_{\text{MEG}}$  in the above table is taken as zero because the amount of ethylene glycol lost to the vapor phase is too small to measure. Although these expressions for the inhibitor partitioning are the most current, inhibitor partition-

\* OLGA is a product of Scandpower AS, Oslo, Norway (2000). Pipephase is a product of Invensys, Inc., Lake Forest, California (2004).



**TABLE 11.9—INHIBITOR PARTITIONING COEFFICIENTS IN EQ. 11.9 FOR THE VAPOR AND LIQUID HYDROCARBON PHASES**

$K$	Inhibitor	Loss to	Definition	Partitioning in phases	$a$	$b$
$(K_V)_{\text{MeOH}}$	MeOH	Vapor	$y_{\text{MeOH}}/x_{\text{MeOH}}$	Vapor HC/aqueous liquid	5.706	5738
$(K_L)_{\text{MeOH}}$	MeOH	Liquid	$z_{\text{MeOH}}/x_{\text{MeOH}}$	Liquid HC/aqueous liquid	5.90	5404.5
$(K_L)_{\text{MEG}}$	MEG	Liquid	$z_{\text{MEG}}/x_{\text{MEG}}$	Liquid HC/aqueous liquid	4.20	7266.4

ing is an active research area, for which new equations and constants will be developed over the coming few years.

**Example 11.2** A pipeline with the gas composition below has inlet pipeline conditions of 195°F and 1,050 psia. The gas flowing through the pipeline is cooled to 38°F by the surrounding water. The gas also experiences a pressure drop to 950 psia. Gas exits the pipeline at a rate of 3.2 MMscf/D. The pipeline produces condensate at a rate of 25 B/D, with an average density of 300 lbm/bbl and an average molecular weight of 90 lbm/lbm mol. Produced free water enters the pipeline at a rate of 0.25 B/D.

Find the rate of methanol injection that will prevent hydrates in the pipeline for a natural gas composed of (mol%) 71.60% methane, 4.73% ethane 1.94% propane, 0.79% n-butane, 0.79% n-pentane, 14.19% carbon dioxide, and 5.96% nitrogen.

The basis for these calculations is 1.0 MMscf/D. Methanol will exist in three phases: water, gas, and condensate. The steps in the solution are:

1. Calculate hydrate formation conditions using the gas gravity chart (Fig. 11.6).
2. Calculate the wt% MeOH needed in the free-water phase.
3. Calculate the free (produced and condensed) H<sub>2</sub>O/MMscf of natural gas.
4. Calculate the methanol needed in the aqueous phase.
5. Calculate the methanol lost to the gas phase.
6. Calculate the methanol lost to the liquid hydrocarbon phase.
7. Sum the amounts in steps 4, 5, and 6 for the total methanol needed.

*Step 1—Calculate hydrate formation conditions using the gas gravity chart.* Start by calculating the gas gravity ( $\gamma_g$ ), using Eq. 11.8 and the data in Table 11.10:

$$\gamma_g = \frac{\bar{M}_g}{M_a} = \frac{22.708}{28.966} = 0.784.$$

At  $\gamma_g = 0.704$ , the gas gravity chart shows the hydrate temperature to be 65°F at 1,050 psia.

*Step 2—Calculate the wt% MeOH needed in the free-water phase.* Recall the Hammerschmidt<sup>15</sup> equation (Eq. 11.7):

$$\Delta T = \frac{2,335W}{100M - MW},$$

where  $\Delta T$  = the hydrate temperature depression from the equilibrium temperature at a given pressure (65°F – 38°F = 27°F);  $M$  = molecular weight of the inhibitor (methanol = 32.0); and  $W$  = wt% of the inhibitor in the free-water phase. Rearranging the Hammerschmidt equation to find  $W$ :

TABLE 11.10—CALCULATION OF AVERAGE MOLECULAR WEIGHT FOR EX. 2			
Component	Mole fraction in mixture, $z$	Molecular weight, $M$	Average $M$ of gas in mixture, $\bar{M}_g$ ( $z \times M$ )
Methane	0.7160	16.04	11.487
Ethane	0.0473	30.07	1.422
Propane	0.0194	44.09	0.855
n-butane	0.0079	58.12	0.459
n-pentane	0.0079	72.15	0.570
Nitrogen	0.0596	28.01	1.670
Carbon dioxide	0.1419	44.01	6.245
	1.000		$\bar{M}_g = 22.708$

$$W = \frac{100M\Delta T}{M\Delta T + 2,335} = \frac{(100)(32)(27)}{(32)(27) + 2,335} = 27,$$

yields that 27 wt% of methanol is needed in the free-water phase to provide hydrate inhibition at 1,050 psia and 38°F (highest pressure, lowest temperature) for this gas.

*Step 3—Calculate the mass of liquid water/MMscf of natural gas.*

a) *Calculate the mass of condensed H<sub>2</sub>O.* In the absence of a water analysis, use the water content chart (Fig. 11.1) to calculate the amount of water in the vapor/MMscf. By this chart, 1,050 psia and 195°F, the inlet gas water content is 600 lbm/MMscf. At 950 psia and 38°F, the exiting gas contains 9 lbm/MMscf of water. The difference between the original water and the water remaining in the gas is the mass of liquid water from condensation: 600 – 9 = 591 lbm/MMscf.

b) *Calculate the mass of produced H<sub>2</sub>O flowing into the line.* Convert the produced water of 0.25 B/D to lbm/MMscf:

$$0.25 \text{ B/D} \times 42 \text{ U.S. gal/bbl} \times 8.34 \text{ lbm/gal} \times 1 \text{ d}/3.2 \text{ MMscf} = 27.4 \text{ lbm/MMscf H}_2\text{O}.$$

c) *Calculate the total mass of water/MMscf of gas.* Sum the condensed and produced water:

$$591 + 27.4 = 618.4 \text{ lbm/MMscf}.$$

*Step 4—Calculate the rate of methanol needed in the aqueous phase.* With 27.0 wt% methanol required to inhibit the free-water phase, and the mass of water/MMscf calculated at 618.4 lbm in the free-water phase, the mass ( $m$ ) of MeOH/MMscf is

$$27.0 \text{ wt \% MeOH} = \frac{m \text{ lbm MeOH}}{m \text{ lbm MeOH} + 618.4 \text{ lbm H}_2\text{O}} \times 100 \%$$

Solving this equation yields  $m = 228.7$  lbm MeOH in the water phase.

The mole fraction MeOH in the free-water phase ( $x_{\text{MeOH-W}}$ ) is:

	MeOH
In water, lbm/MMscf	228.7
In gas, lbm/MMscf	42.9
In condensate, lbm/MMscf	1.0
Total, lbm/MMscf	272.6
Total, gal/MMscf	41.0

$$= \frac{x_{\text{MeOH-W}} \cdot 228.7 \text{ lbm MeOH} / (32 \text{ lbm} / \text{lbm mol MeOH})}{228.7 \text{ lbm MeOH} / (32 \text{ lbm} / \text{lbm mol MeOH}) + 618.4 \text{ lbm H}_2\text{O} / (18 \text{ lbm} / \text{lbm mol H}_2\text{O})}$$

The mole fraction MeOH in the free-water phase is  $x_{\text{MeOH-W}} = 0.172$ .

*Step 5—Calculate the MeOH lost to the gas phase.* The distribution constant of MeOH in the gas is calculated by Eq. 11.9 to be 38°F (497.7°R), relative to the methanol in the water:

$$(K_V)_{\text{MeOH}} = \exp[(5.706 - 5738 \times (1/497.7))] = 0.00296$$

The mole fraction of MeOH in the vapor ( $y_{\text{MeOH-V}}$ ) is:

$$y_{\text{MeOH-V}} = (K_V)_{\text{MeOH}} \times x_{\text{MeOH-W}} = 0.00296 \times 0.172 = 0.000509.$$

The daily gas rate is 8,432 lbm mol [=  $3.2 \times 10^6$  scf/(379.5 scf/lbm mol), where an scf is at 14.7 psia and 60°F], so that the MeOH lost to the gas is 4.29 lbm mol (=  $0.000509 \times 8,432$ ) or 137.3 lbm/D. Because the calculation basis is 1 MMscf/D, the amount of MeOH lost is 42.9 lbm/MMscf (= 137.3 lbm/3.2 MMscf).

*Step 6—Calculate the amount of MeOH lost to the condensate.*

$$(K_L)_{\text{MeOH}} = \exp[5.90 - 5404.5 \times (1/497.7^\circ\text{R})] = 0.00702$$

The mole fraction MeOH in condensate ( $x_{\text{MeOH-HC}}$ ) is:

$$x_{\text{MeOH-HC}} = (K_L)_{\text{MeOH}} \times x_{\text{MeOH-W}} = 0.00702 \times 0.172 = 0.001207.$$

The condensate rate is 26.0 lbm mol/MMscf (= 25 B/D  $\times$  300 lbm/bbl  $\times$  1 lbm mol/90 lbm  $\times$  1 d/3.2 MMscf), so that the amount of MeOH in condensate is 0.0314 lbm mol/MMscf [=  $0.001207 \times 26/(1 - 0.001207)$ ], or 1.0 lbm/MMscf).

*Step 7—Sum the total amount of MeOH/MMscf.* The amounts of MeOH in Ex. 2 are shown in Table 11.11.

This example illustrates the fact that a significant amount of MeOH partitions into the vapor and liquid hydrocarbon phases. The calculation could be done equally well for MEG,

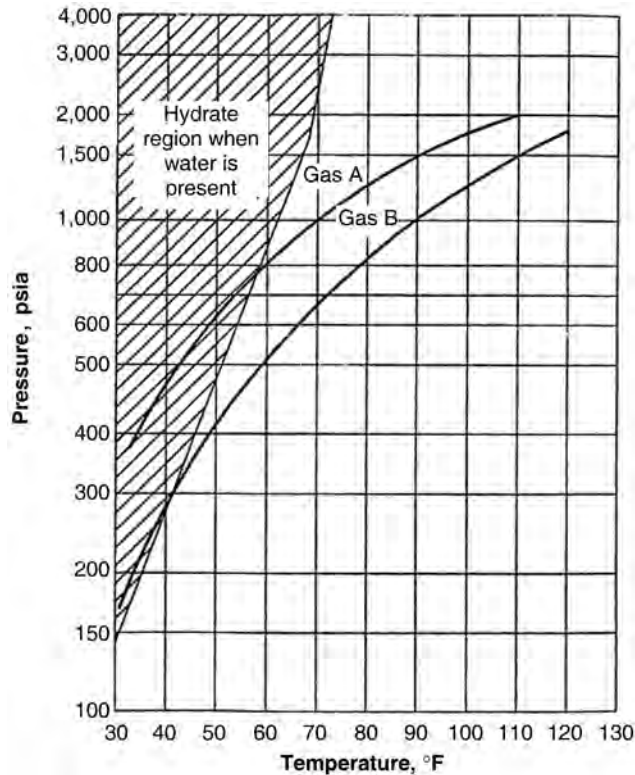


Fig. 11.7—Intersection of free expansion curves with hydrate-formation region for 0.6-gravity gases (from Katz<sup>20</sup>).

substituting appropriate constants in Eq. 11.9. See Sloan<sup>6</sup> for further examples of MeOH and MEG partitioning.

*Hydrate Formation on Expansion Across a Valve or Restriction.* When water-wet gas expands rapidly through a valve, orifice, or other restriction, hydrates form because of rapid gas cooling by Joule-Thomson (constant enthalpy) expansion. Hydrate formation with rapid expansion from a wet line is common in fuel gas or instrument gas lines. In well-testing, startup, and gas lift operations, hydrates can form with high pressure drops, even with a high initial temperature, if the pressure drop is very large. This section provides an initial hand calculation method for situations when hydrates will form upon rapid expansion. Sloan<sup>6</sup> (pp. 21ff) contains a more accurate computer calculation method and discussion.

If a gas expands rapidly through a valve or restriction, the fluids will cool much faster than with heat transfer, possibly causing the system to enter the hydrate formation regime at the valve/restriction discharge. Two rapid expansion curves for the same 0.6-gravity gas are shown in Fig. 11.7. Intersections of the gas expansion curves with the hydrate formation line limits the expansion discharge pressures from two different high initial P/T conditions, labeled Gas A and Gas B.

In Fig. 11.7, the curves determine the restriction downstream pressure at which hydrate blockages will form for a given upstream pressure and temperature. Gas A expands from 13.6 MPa (2,000 psia) and 316 K (110°F) until it strikes the hydrate formation curve at 0.53 MPa (780 psia) and 287 K (57°F), so 0.53 MPa (780 psia) represents the limit to hydrate-free expansion.

sion. Gas B expands from 12.2 MPa (1,800 psia) and 322 K (120°F) to intersect the hydrate formation curve at a limiting pressure of 1.97 MPa (290 psia) and 279 K (42°F). In expansion processes, the upstream temperature and pressure are known, but the discharge temperature usually is unknown, and a downstream vessel normally sets the discharge pressure.

Cooling curves such as the two in Fig. 11.7 were determined for constant enthalpy (Joule-Thomson) expansions, obtained from the First Law of Thermodynamics for a system flowing at steady state, ignoring kinetic and potential energy changes:

$$\Delta H_2 = Q - W_s, \dots\dots\dots (11.10)$$

where  $\Delta H_2$  = the enthalpy difference across the restriction (downstream to upstream),  $Q$  = the heat added, and  $W_s$  = shaft work obtained at the restriction. Normal flow restrictions (e.g., valves and orifices) have no shaft work, and because rapid flow approximates adiabatic operation, both  $W_s$  and  $Q$  are zero. The result is constant enthalpy ( $\Delta H_2 = 0$ ) operation on expansion.

Katz<sup>20</sup> generated charts to determine the hydrate-free limit to gas expansion, combining the gas gravity chart (Fig. 11.6) and the gas enthalpy/entropy charts by Brown<sup>22</sup> to determine Fig. 11.7's hydrate formation line and cooling lines labeled Gas A and Gas B, respectively. Interestingly, Brown's charts also could be used with Fig. 11.6 to determine the limits to wet gas expansion across an isentropic device such as a nozzle or turboexpander; however, that has not been done.

Cautioning that the charts apply to gases of limited compositions, Katz<sup>20</sup> provided constant enthalpy expansion charts for gases of 0.6, 0.7, and 0.8 gravities, shown in Figs. 11.8, 11.9, and 11.10, respectively. The abscissa (x-axis) in each figure represents the lowest downstream pressure without hydrate formation, given the upstream pressure on the ordinate (y-axis) and the upstream temperature (a parameter on each line).

Note that maxima in Figs. 11.8 through 11.10 occur at the upstream pressure of 40.8 MPa (6,000 psia), the Joule-Thomson inversion pressure. At pressures above 6,000 psia, these gases will cool on expansion.

The following three examples of chart use are from Katz's<sup>20</sup> original work.

**Example 11.3a** To what pressure can a 0.6-gravity gas at 13.6 MPa (2,000 psia) and 311 K (100°F) be expanded without danger of hydrate formation?

According to Fig. 11.8, the maximum pressure of gas expansion is 7.14 MPa (1,050 psia).

**Example 11.3b** How far can a 0.6-gravity gas at 13.6 MPa (2,000 psia) and 333 K (140°F) be expanded without hydrate formation?

Fig. 11.8 shows that there is no intersection with the 333 K (140°F) isotherm. Hydrates will not form upon expansion to atmospheric pressure.

**Example 11.3c** A 0.6-gravity gas is to be expanded from 10.2 MPa (1,500 psia) to 3.4 MPa (500 psia). What is the minimum initial temperature that will permit the expansion without danger of hydrates?

Fig. 11.8 shows that 310 K (99°F) is the minimum initial temperature to avoid hydrates.

Figs. 11.8 through 11.10 incorporate the inaccuracies of the gas gravity charts from which they were derived. As indicated in the *Three-Phase L<sub>w</sub>-H-V Calculations* section above, the 0.6-gravity chart (used for both hydrate formation and gas expansion) may have inaccuracies of

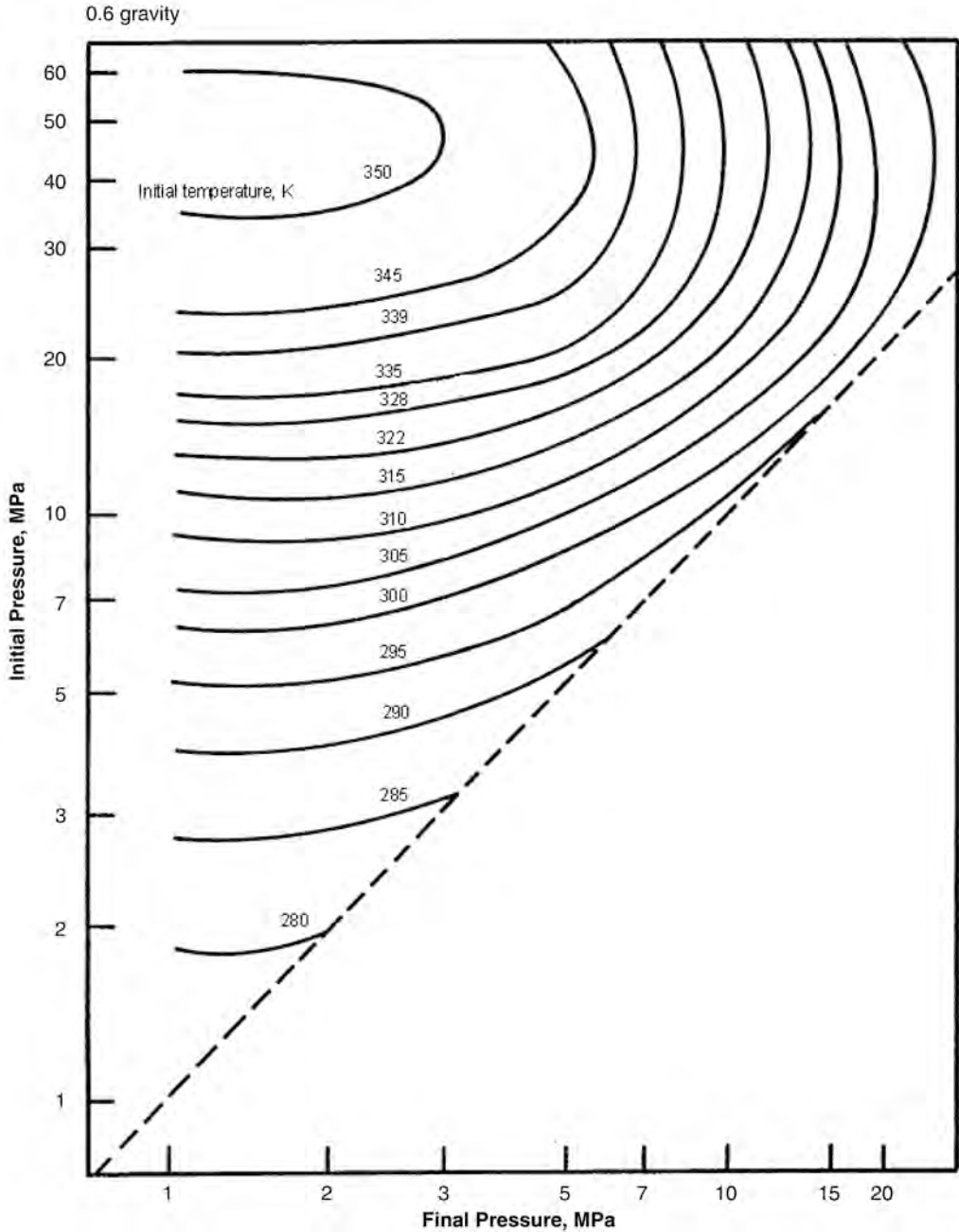


Fig. 11.8—Permissible expansion of a 0.6-gravity natural gas without hydrate formation (from Katz<sup>20</sup>).

$\pm 3.4$  MPa (500 psia). Accuracy limits for these expansion curves have been tested by Loh *et al.*,<sup>23</sup> who found, for example, that the allowable 0.6-gravity gas expansion from 23.8 MPa (3,500 psia) and 338 K (150°F) should be 2.8 MPa (410 psia), rather than the value of 4.76 MPa (700 psia) given by Fig. 11.8.

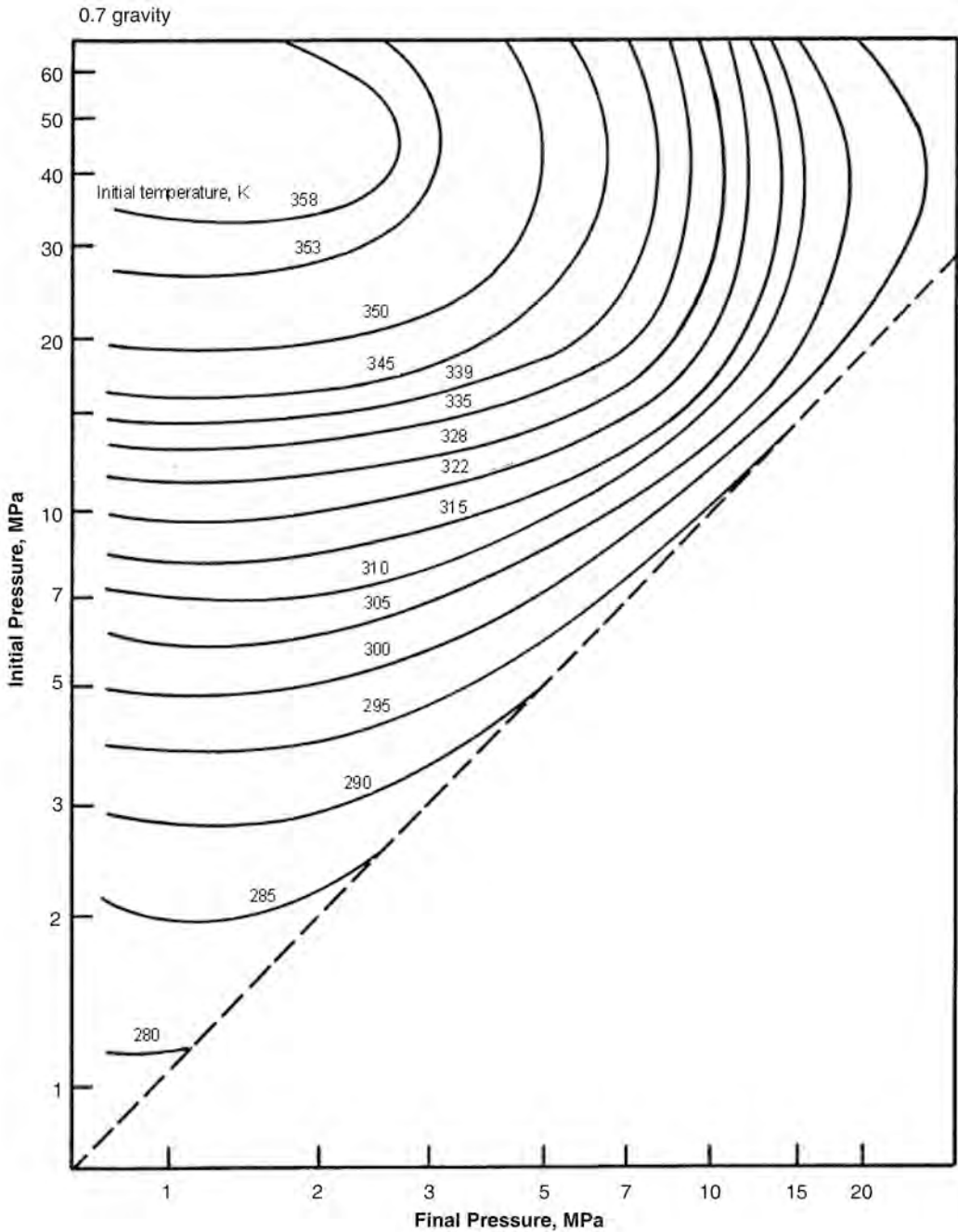


Fig. 11.9—Permissible expansion of a 0.7-gravity natural gas without hydrate formation (from Katz<sup>20</sup>).

### 11.5 Conclusions

The fundamental reason an engineer should consider the equilibria is the possible existence of a water phase, in which hydrates can form, causing multiphase flow, flow blockage, and other engineering challenges. Flowline blockages can cause losses of millions of dollars of income while blockage remediation is occurring. The most accurate prediction methods allow avoid-

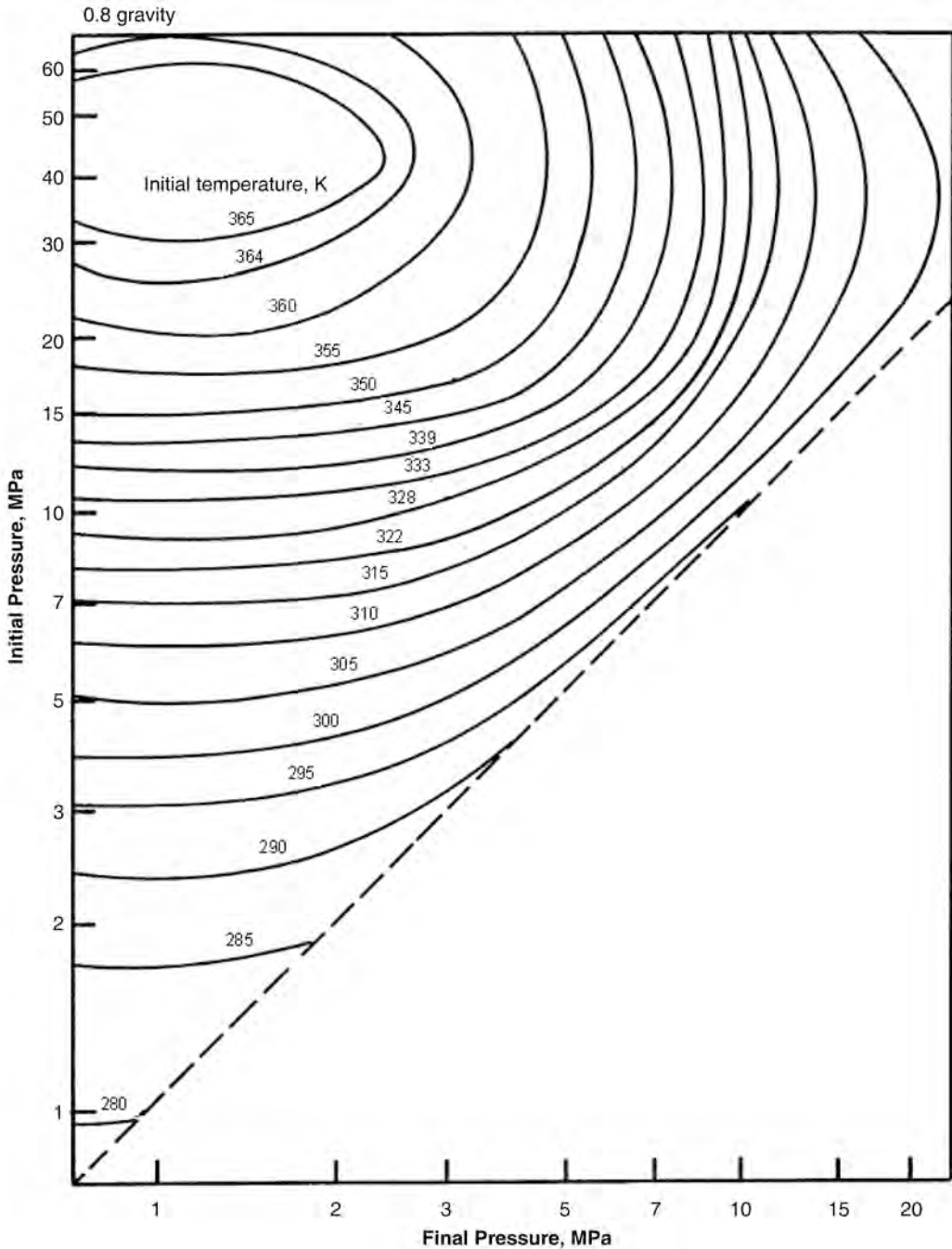


Fig. 11.10—Permissible expansion of a 0.8-gravity natural gas without hydrate formation (from Katz<sup>20</sup>).

ance of flowline blockages. With this review of the topic of  $H_2O +$  hydrocarbon equilibria and the hand-calculation methods provided in this chapter, the engineer should be able to determine whether the computer calculation is within the accuracy bounds of the hand-calculation methods and, if not, whether the circumstances require a more accurate computer calculation. For a more complete exposition of the hydrate calculation methods, see Makogon<sup>24</sup> and Sloan.<sup>6,7</sup>



**Nomenclature**

- $a$  = constant  
 $b$  = constant  
 $c$  = constant  
 $C$  = in the Gibbs phase rule, the number of components in a nonreacting system  
 $C_G$  = correction factor for gas gravity  
 $C_S$  = correction factor for salinity  
 $C_v$  = vapor composition  
 $F$  = in the Gibbs phase rule, the number of intensive variables required to define a nonreacting system (degrees of freedom)  
 $H_1$  = the enthalpy of water in the hydrocarbon solution minus that of pure liquid water, Btu/lbm  
 $H_2$  = enthalpy difference across a valve or restriction, Btu/lbm  
 $K$  = amount of inhibitor in the vapor or liquid hydrocarbon phases  
 $(K_L)_{\text{MEG}}$  = liquid distribution coefficient,  $x_{\text{HC}}/x_{\text{H}_2\text{O}}$ , of MEG, dimensionless  
 $(K_L)_{\text{MeOH}}$  = liquid distribution coefficient,  $x_{\text{HC}}/x_{\text{H}_2\text{O}}$ , of MEOH, dimensionless  
 $K_{\text{VH}}$  = a Katz's value term, defined as a component's mole fraction divided by that in the hydrate  
 $K_{\text{VL}}$  = DePriester's vapor/liquid value, defined as a component's mole fraction divided by that in the liquid  
 $(K_V)_{\text{MEG}}$  = vapor distribution coefficient,  $y_{\text{HC}}/y_{\text{H}_2\text{O}}$ , of MEG, dimensionless  
 $(K_V)_{\text{MeOH}}$  = vapor distribution coefficient,  $y_{\text{HC}}/y_{\text{H}_2\text{O}}$ , of MEG, dimensionless  
 $m$  = mass, lbm  
 $M$  = molecular weight  
 $M_a$  = the molecular weight of air  
 $\overline{M}_g$  = the average molecular weight of a gas in a mixture  
 $N_c$  = carbon number  
 $p$  = pressure, psia  
 $p_{\text{eq}}$  = pressure, hydrate equilibrium, psia  
 $P$  = in the Gibbs phase rule, the number of phases in a nonreacting system  
 $Q$  = heat added to a system flowing at steady state, Btu/hr  
 $T$  = temperature, °F  
 $T_a$  = temperature, absolute, °F  
 $T_{\text{eq}}$  = temperature, hydrate equilibrium, °F  
 $W$  = wt% of the inhibitor in the free-water phase  
 $W_s$  = shaft work  
 $x_{\text{HC-W}}$  = mole fraction for hydrocarbon in liquid water  
 $x_{\text{MeOH-HC}}$  = mole fraction MeOH in condensate  
 $x_{\text{MeOH-W}}$  = mole fraction MeOH in the free-water phase  
 $x_{\text{W-HC}}$  = mole fraction for water in liquid hydrocarbon  
 $y_{\text{MeOH-V}}$  = mole fraction of MeOH in vapor  
 $z$  = mole fraction of a component in mixture  
 $\gamma_g$  = gas gravity  
 $\Delta T$  = hydrate temperature depression below the equilibrium temperature at a given pressure, °F

---

## References

1. Gibbs, J.W.: *The Collected Works of J. Willard Gibbs*, Vol. VI, Longmans, Green & Co., New York (1931).
2. Harmens, A. and Sloan, E.D.: "The Phase Behavior of the Propane-Water System: A Review," *Canadian J. of Chemical Engineering*, **68** (February 1990) 151.
3. McKetta, J.J. and Wehe, A.H.: "Use This Chart for Water Content of Natural Gases," *Petroleum Refiner* (1958) **37**, No. 8, 153.
4. Tsonopoulos, C.: "Thermodynamic analysis of the mutual solubilities of normal alkanes and water," *Fluid Phase Equilibria* (1999) **156**, No. 1–2, 21.
5. Tsonopoulos, C.: "Thermodynamic analysis of the mutual solubilities of hydrocarbons and water," *Fluid Phase Equilibria* (2001) **186**, No. 1–2, 185.
6. Sloan, E.D. Jr.: *Hydrate Engineering*, Monograph Series, SPE, Richardson, Texas (2000) **21**, 89.
7. Sloan, E.D. Jr.: *Clathrate Hydrates of Natural Gases* (second edition), Marcel Dekker Inc., New York (1998) 704.
8. Udachin, K.A., and Ripmeester, J.A.: "A Complex Clathrate Hydrate Structure Showing Bimodal Guest Hydration," *Nature*, **397** (February 1999) 420.
9. Subramanian, S. *et al.*: "Evidence of Structure II Hydrate Formation from Methane+Ethane Mixtures," *Chemical Engineering Science* (2000) **55**, No. 11, 1981.
10. Tse, J.S.: "Dynamical Properties and Stability of Clathrate Hydrate," *First International Hydrate Conference*, Happel, Hnatow, and Sloan (eds.), New York Academy of Science, New York (1994) **712**, 187.
11. Subramanian, S. and Sloan, E.D.: "Molecular Measurements of Clathrate Hydrate Formation," *Fluid Phase Equilibria* **158–160** (June 1999) 813.
12. Ripmeester, J.A. and Ratcliffe, C.: "On the Contribution of NMR Spectroscopy to Clathrate Science," *Journal of Structural Chemistry* (1999) **40**, 654.
13. Kamath, V.A.: "Study of Heat Transfer Characteristics During Dissociation of Gas Hydrates in Porous Media," PhD dissertation, U. Pittsburgh, University Microfilms, Ann Arbor, Michigan (1984), No. 8417404, 6.
14. Sloan, E.D., Khoury, F.M., and Kobayashi, R.: "Water Content of Methane Gas in Equilibrium with Hydrates," *Industrial Engineering Chemistry Fundamentals* (1976) **15**, No. 4, 318.
15. Hammerschmidt, E.G.: "Gas Hydrate Formation in Natural Gas Pipelines," *Oil & Gas J.* (1939) **37**, No. 50, 66.
16. Ballard, A.L. and Sloan, E.D.: "The Next Generation of Hydrate Prediction: An Overview," *Journal of Supramolecular Chemistry* (2002) **2**, No. 4–5, 385.
17. Hopgood, D.: "Why Improve Hydrate Predictions for Deepwater Black Oil?" paper OTC 13037 presented at the 2001 Offshore Tech. Conference, Houston, 30 April–3 May.
18. Katz, D.L. *et al.*: *Handbook of Natural Gas Engineering*, McGraw-Hill Book Co. Inc., New York (1959).
19. DePriester, C.L.: "Light-hydrocarbon vapor-liquid distribution coefficients: Pressure-temperature-composition charts and pressure-temperature nomographs," *Chemical Engineering Progress Symposium Series*, **49**(7) (1953) 45.
20. Katz, D.L.: "Prediction of Conditions for Hydrate Formation in Natural Gases," *Trans., AIME* (1945) **160**, 140.
21. Sloan, E.D.: "The CSM Hydrate Prediction Program," *Proc.*, 64<sup>th</sup> Annual Convention of the Gas Producers Assn. (1985) **64**, 125.
22. Brown, G.G.: "A Series of Enthalpy-Entropy Charts for Natural Gases," *Trans., AIME* (1945) **160**, 65.
23. Loh, J., Maddox, R.N., and Erbar, J.H.: "New Hydrate Formation Data Reveal Differences," *Oil & Gas J.* (1983) **81**, No. 20, 96.
24. Makogon, Y.F.: *Hydrates of Hydrocarbons*, PennWell Publishing, Tulsa (1997) 482.

**SI Metric Conversion Factors**

Å × 1.0*	E - 01 = nm
atm × 1.013 250	E + 05 = Pa
bbl × 1.589 873	E - 01 = m <sup>3</sup>
Btu × 1.055 056	E + 00 = kJ
°C °C + 273	= K
°F °F + 459.67/1.8	= K
°F (°F - 32) / 1.8	= °C
ft <sup>3</sup> × 2.831 685	E - 02 = m <sup>3</sup>
lbm × 4.535 924	E - 01 = kg
psia × 6.894 757	E + 00 = kPa
°R × 5/9	= K
U.S. gal × 3.785 412	E - 03 = m <sup>3</sup>

\*Conversion factor is exact.



# Chapter 12

## Crude Oil Emulsions

Sunil L. Kokal, Saudi Aramco

### 12.1 Introduction

Crude oil is seldom produced alone because it generally is commingled with water. The water creates several problems and usually increases the unit cost of oil production. The produced water must be separated from the oil, treated, and disposed of properly. All these steps increase costs. Furthermore, sellable crude oil must comply with certain product specifications, including the amount of basic sediment and water (BS&W) and salt, which means that the produced water must be separated from the oil to meet crude specifications.

Produced water may be produced as “free” water (i.e., water that will settle out fairly rapidly), and it may be produced in the form of an emulsion. A regular oilfield emulsion is a dispersion of water droplets in oil. Emulsions can be difficult to treat and may cause several operational problems in wet-crude handling facilities and gas/oil separating plants. Emulsions can create high-pressure drops in flow lines, lead to an increase in demulsifier use, and sometimes cause trips or upsets in wet-crude handling facilities. The problem is usually at its worst during the winter because of lower surface temperatures. These emulsions must be treated to remove the dispersed water and associated inorganic salts to meet crude specifications for transportation, storage, and export and to reduce corrosion and catalyst poisoning in downstream processing facilities.

Emulsions occur in almost all phases of oil production and processing: inside reservoirs, wellbores, and wellheads; at wet-crude handling facilities and gas/oil separation plants; and during transportation through pipelines, crude storage, and petroleum processing. The chapter on emulsion treating in the Facilities section of this handbook deals with the hardware of emulsion-treating equipment. This chapter is limited to the produced oilfield emulsions at the wellhead and in the wet-crude handling facilities. The primary focus is on the fundamentals and the application of available technologies in resolving emulsions. The chapter looks at the characteristics, occurrence, formation, stability, handling, and breaking of produced oilfield emulsions. There are several good general references available for more detailed and diversified discussions on crude oil emulsions. A comprehensive presentation and further basic information can be found in an encyclopedia of emulsion technology,<sup>1-3</sup> Becher’s classic book<sup>4</sup> on the subject, and recent books on petroleum emulsions.<sup>5,6</sup>

This chapter covers four aspects of produced oilfield emulsions. [CD edition includes [video](#).]

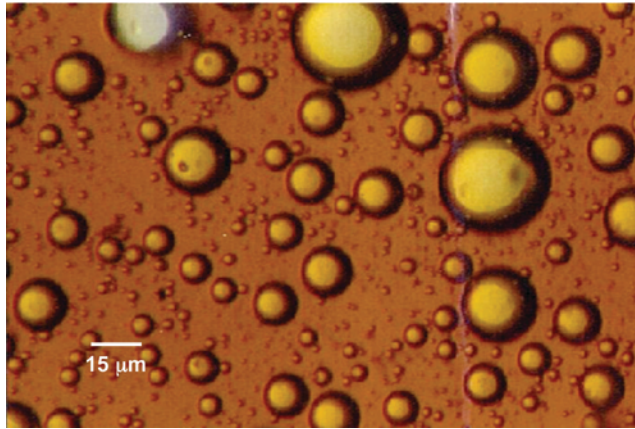


Fig. 12.1—Photomicrograph of a water-in-oil emulsion.

- **Sec. 12.1** provides a brief introduction to the occurrence, types, and characteristics of emulsions. It deals with the fundamental nature of emulsions including their definitions, how they form, and their physical properties. It also includes a subsection on viscosities of emulsions.
- **Sec. 12.2** discusses the stability of emulsions including the formation of films or “skins” on the droplets. Factors that affect emulsion stability include heavy polar material in the oil (asphaltenes, waxes), very fine solids, temperature, droplet size, pH, and brine composition. This section also discusses how to measure emulsion stability.
- **Sec. 12.3** visits the mechanisms of demulsification. The factors that destabilize emulsions include temperature, shear, removal of solids, and control of emulsifying agents. This section also discusses the practical aspects of demulsification and highlights methods of emulsion breaking including thermal, mechanical, electrical, and chemical.
- **Sec. 12.4** discusses field applications and special topics that should be useful for the practicing engineer dealing with emulsions, either regularly or on a limited basis. A method to sample oilfield emulsions is included. A field emulsion treatment program is discussed and, more importantly, methods to prevent emulsion problems are highlighted. Finally, the practical aspects of demulsifier selection and optimization are included.

**12.1.1 Definition.** An emulsion is a dispersion (droplets) of one liquid in another immiscible liquid. The phase that is present in the form of droplets is the dispersed or internal phase, and the phase in which the droplets are suspended is called the continuous or external phase. For produced oilfield emulsions, one of the liquids is aqueous and the other is crude oil. The amount of water that emulsifies with crude oil varies widely from facility to facility. It can be less than 1% and sometimes greater than 80%.

**12.1.2 Types of Emulsions.** Produced oilfield emulsions can be classified into three broad groups: water-in-oil, oil-in-water, and multiple or complex emulsions. Water-in-oil emulsions consist of water droplets in a continuous oil phase, and oil-in-water emulsions consist of oil droplets in a water-continuous phase. **Figs. 12.1 and 12.2** show the two basic (water-in-oil and oil-in-water) types of emulsions. In the oil industry, water-in-oil emulsions are more common (most produced oilfield emulsions are of this kind); therefore, the oil-in-water emulsions are sometimes referred to as “reverse” emulsions.

Multiple emulsions are more complex and consist of tiny droplets suspended in bigger droplets that are suspended in a continuous phase. For example, a water-in-oil-in-water emul-

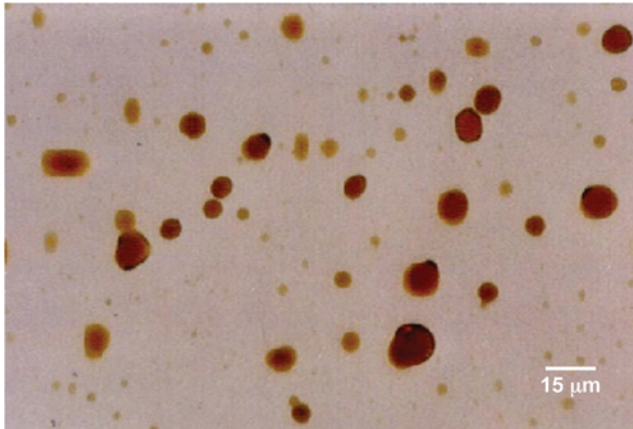


**Fig. 12.2—Photomicrograph of an oil-in-water emulsion.**

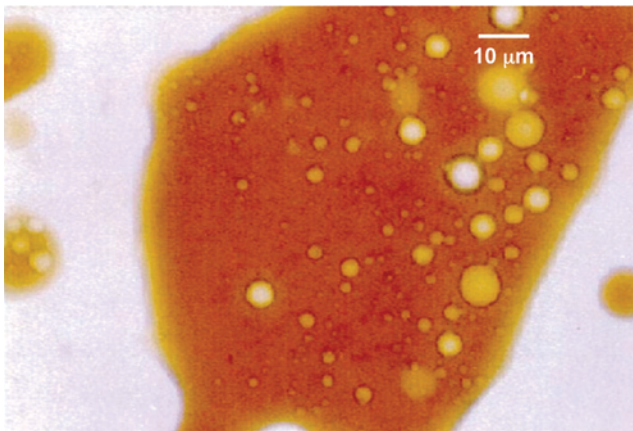


**Fig. 12.3—Photomicrograph of a water-in-oil-in-water emulsion.**

sion consists of water droplets suspended in larger oil droplets that, in turn, are suspended in a continuous water phase. [Fig. 12.3](#) shows an example of a multiple emulsion.

Given the oil and water phases, the type of emulsion formed depends on several factors. As a rule of thumb, when the volume fraction of one phase is very small compared with the other, the phase that has the smaller fraction is the dispersed phase and the other is the continuous phase. When the volume-phase ratio is close to 1 (a 50:50 ratio), then other factors determine the type of emulsion formed.

Emulsions are also classified by the size of the droplets in the continuous phase. When the dispersed droplets are larger than 0.1 μm, the emulsion is a macroemulsion.<sup>5,7</sup> Emulsions of this kind are normally thermodynamically unstable (i.e., the two phases will separate over time because of a tendency for the emulsion to reduce its interfacial energy by coalescence and separation). However, droplet coalescence can be reduced or even eliminated through a stabilization mechanism. Most oilfield emulsions belong in this category. In contrast to macroemulsions, there is a second class of emulsions known as microemulsions. These emulsions form spontaneously when two immiscible phases are brought together because of their extremely low interfacial energy. Microemulsions have very small droplet sizes, less than 10 nm, and are

considered thermodynamically stable. Microemulsions are fundamentally different from macroemulsions in their formation and stability.

**12.1.3 Formation of Emulsions.** Crude oil emulsions form when oil and water (brine) come into contact with each other, when there is sufficient mixing, and when an emulsifying agent or emulsifier is present. The amount of mixing and the presence of emulsifier are critical for the formation of an emulsion. During crude oil production, there are several sources of mixing, often referred to as the amount of shear, including flow through reservoir rock; bottomhole perforations/pump; flow through tubing, flow lines, and production headers; valves, fittings, and chokes; surface equipment; and gas bubbles released because of phase change. The amount of mixing depends on several factors and is difficult to avoid. In general, the greater the mixing, the smaller the droplets of water dispersed in the oil and the tighter the emulsion. Emulsion studies have shown that the water droplets can vary in size from less than 1  $\mu\text{m}$  to more than 1000  $\mu\text{m}$ .

The second factor important in emulsion formation is the presence of an emulsifier. The presence, amount, and nature of the emulsifier determines, to a large extent, the type and “tightness” of an emulsion. The natural emulsifiers in a crude are resident in the heavy fraction. Because there are different types of crudes and because these crudes have different amounts of heavy components, the emulsifying tendencies vary widely. Crude with a small amount of emulsifier forms a less stable emulsion and separates relatively easily. Other crudes contain the right type and amount of emulsifier, which lead to very stable or tight emulsions.

**12.1.4 Emulsifying Agents.** Produced oilfield water-in-oil emulsions contain oil, water, and an emulsifying agent. Emulsifiers stabilize emulsions and include surface-active agents and finely divided solids.

**Surface-Active Agents.** Surface-active agents (surfactants) are compounds that are partly soluble in both water and oil. They have a hydrophobic part that has an affinity for oil and a hydrophilic part that has an affinity for water. Because of this molecular structure, surfactants tend to concentrate at the oil/water interface, where they form interfacial films. This generally leads to a lowering of the interfacial tension (IFT) and promotes dispersion and emulsification of the droplets. Naturally occurring emulsifiers in the crude oil include higher boiling fractions, such as asphaltenes and resins, organic acids, and bases. These compounds have been shown to be the main constituents of interfacial films that form around water droplets in many oilfield emulsions. The stabilizing effects of asphaltenes are discussed in [Sec. 12.2.2](#). Other surfactants that may be present are from the chemicals injected into the formation or wellbores (e.g., drilling fluids, stimulation chemicals, corrosion inhibitors, scale inhibitors, wax, and asphaltene-control agents).

**Finely Divided Solids.** Fine solids can act as mechanical stabilizers. These particles, which must be much smaller than emulsion droplets (usually submicron), collect at the oil/water interface and are wetted by both oil and water. The effectiveness of these solids in stabilizing emulsions depends on factors such as particle size, interparticle interactions, and the wettability of the particles.<sup>8</sup> Finely divided solids found in oil production include clay particles, sand, asphaltenes and waxes, corrosion products, mineral scales, and drilling muds. [Fig. 12.4](#) shows the photomicrograph of an emulsion showing the presence of solids.

**12.1.5 Characteristics and Physical Properties.** Oilfield emulsions are characterized by several properties including appearance and color, BS&W, droplet size, and bulk and interfacial viscosities.

**Appearance and Color.** Color and appearance is an easy way to characterize an emulsion. The characterization becomes somewhat easy if the emulsion is transferred into a conical glass centrifuge tube. The color of the emulsion can vary widely depending on the oil/water content



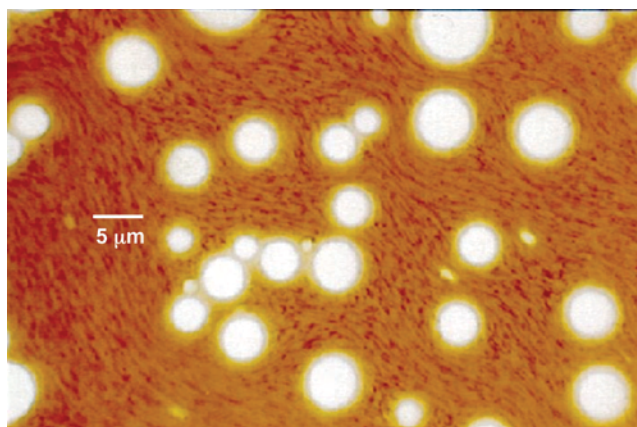


Fig. 12.4—Photomicrograph of an emulsion showing the presence of solids.

and the characteristics of the oil and water. The common colors of emulsions are dark reddish brown, gray, or blackish brown; however, any color can occur depending on the type of oil and water at a particular facility. Emulsion brightness is sometimes used to characterize an emulsion. An emulsion generally looks murky and opaque because of light scattering at the oil/water interface. When an emulsion has small diameter droplets (large surface area), it has a light color. When an emulsion has large diameter droplets (low total interfacial surface area), it generally looks dark and less bright. Understanding the characteristics of an emulsion by visual observation is an art that improves with experience.

**Basic Sediment and Water.** BS&W is the solids and aqueous portion of an emulsion. It is also referred to as BSW, bottom settlings and water, or bottom solids and water. Several methods are available to determine the amount of water and solids in emulsions. Standard methods have been proposed by several organizations including the Institute of Petroleum, American Petroleum Institute, and the American Society for Testing Materials.<sup>5</sup> The most common technique for the determination of oil, water, and solids consists of adding a slight overdose of a demulsifier to an emulsion, centrifuging it, and allowing it to stand. The amount of solids and water separated is measured directly from specially designed centrifuge tubes. When only the water content is desired, Karl-Fischer titration can also be used. It is very accurate at low contents of water (<2%) but can also be used for determining higher content (>10%). Other, less common methods are based on electrical properties (conductance and dielectric constants), gamma-ray attenuation, and microwave-based meters.<sup>5</sup>

**Droplet Size and Droplet-Size Distribution.** Produced oilfield emulsions generally have droplet diameters that exceed 0.1 μm and may be larger than 100 μm. Emulsions normally have a droplet size range that can be represented by a distribution function. Fig. 12.5 shows the drop-size distributions of typical petroleum emulsions. The droplet-size distribution in an emulsion depends on several factors including the IFT, shear, nature and amount of emulsifying agents, presence of solids, and bulk properties of oil and water. Droplet-size distribution in an emulsion determines, to a certain extent, the stability of the emulsion and should be taken into consideration in the selection of optimum treatment protocols. As a rule of thumb, the smaller the average size of the dispersed water droplets, the tighter the emulsion and, therefore, the longer the residence time required in a separator, which implies larger separating plant equipment sizes. The photomicrographs in Figs. 12.1 through 12.4 show the droplet-size distribution for several emulsions.

The droplet-size distribution for oilfield emulsions is determined by the following methods.<sup>5</sup>

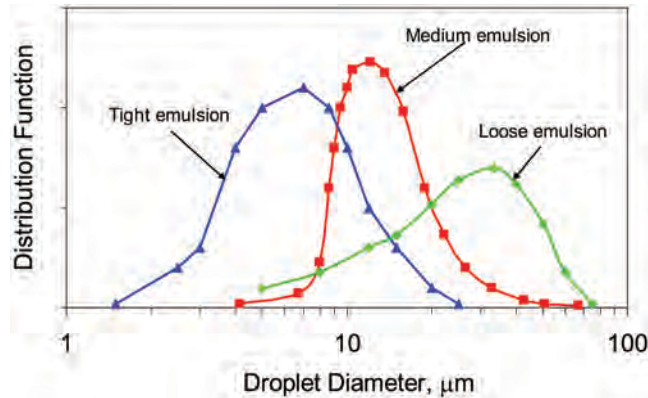


Fig. 12.5—Droplet-size distribution of petroleum emulsions.

- Microscopy and image analysis. For example, the emulsion photomicrographs in Figs. 12.1 through 12.4 can be digitized and the number of different-sized particles measured with image analysis software.
- By the use of electrical properties such as conductivity and dielectric constants.
- By the use of scattering techniques such as light scattering, neutron scattering, and X-ray scattering. These techniques cover droplet sizes from 0.4 nm to more than 100  $\mu\text{m}$ .
- Physical separation including chromatographic techniques, sedimentation techniques, and field-flow fractionation.

**Rheology. Viscosity of Emulsions.** Emulsion viscosity can be substantially greater than the viscosity of either the oil or the water because emulsions show non-Newtonian behavior. This behavior is a result of droplet crowding or structural viscosity. A fluid is considered non-Newtonian when its viscosity is a function of shear rate. At a certain volume fraction of the water phase (water cut), oilfield emulsions behave as shear-thinning or pseudoplastic fluids (i.e., as shear rate increases, viscosity decreases). Fig. 12.6 shows the viscosities of tight emulsions at 125°F at different water cuts. The constant values of viscosity for all shear rates, or a slope of zero, indicate that the emulsions exhibit Newtonian behavior up to a water content of 40%. At water cuts greater than 40%, the slope of the curves deviate from zero, which indicate non-Newtonian behavior. The non-Newtonian behavior is pseudoplastic or shear-thinning behavior. The very high viscosities achieved as the water cut increase up to 80% (compared with viscosities of oil approximately 20 cp and water <1 cp). At approximately 80% water cut, an interesting phenomenon is observed. Up to a water cut of 80%, the emulsion is a water-in-oil emulsion; at 80%, the emulsion “inverts” to an oil-in-water emulsion, and the water, which was the dispersed phase, now becomes the continuous phase. In this particular case, multiple emulsions (water-in-oil-in-water) were observed up to very high water concentrations (>95%).

Temperature also has a significant effect on emulsion viscosity. Fig. 12.7 shows an example of the effect of temperature on emulsion viscosity. Emulsion viscosity decreases with increasing temperature (the data have been plotted on a semilog scale). The viscosity of emulsions depend on several factors: viscosities of oil and water, volume fraction of water dispersed, droplet-size distribution, temperature, shear rate, and amount of solids present.

Figs. 12.6 and 12.7 show that the viscosity of the emulsion can be substantially higher than the viscosity of the oil or water at a given temperature. The ratio of the viscosity of an emulsion to the viscosity of the virgin crude oil at the same temperature can be approximated by the following equation.

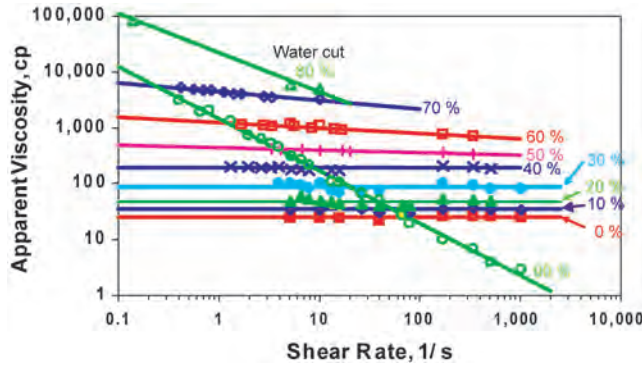


Fig. 12.6—Viscosities of very tight emulsions at 125°F.

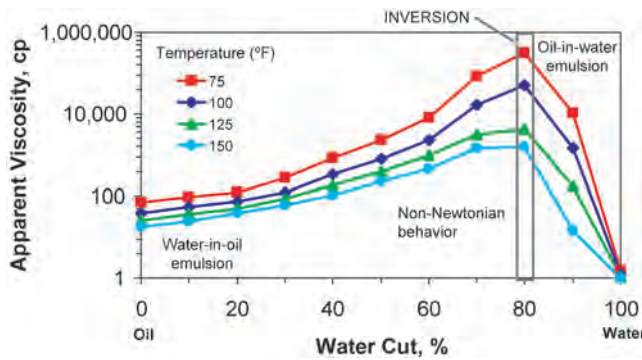


Fig. 12.7—Viscosities of very tight emulsions at a shear rate of 0.1 (1/s).

$$\frac{\mu_e}{\mu_o} = e^{5\Phi(1 - 3\Phi + a\Phi^2)}, \dots\dots\dots (12.1)$$

where  $a$  is the factor for the type of emulsion,  $\mu_e$  is the viscosity of emulsion,  $\mu_o$  is the viscosity of clean oil at same temperature, and  $\Phi$  is water cut or fraction of water. The value of  $a$  varies depending on the type of emulsion: 7.3 for very tight emulsion, 5.5 for tight emulsion, 4.5 for medium emulsion, 3.8 for loose emulsion, and 3.0 for very loose emulsion.

Fig. 12.8 shows viscosities calculated with Eq. 12.1. Emulsion viscosity depends on several factors, and Eq. 12.1 provides an estimate only. For more precise values, experimental data must be used. Emulsion viscosity is measured by standard viscometers, such as capillary tube and rotational viscometers (concentric cylinder, cone and plate, and parallel plate). It is important that temperature is constant and quoted with the viscosity data. Special procedures must be adopted for measuring the rheology of emulsions.<sup>5</sup>

*Interfacial Viscosity.* The previous discussion on viscosity was limited to bulk emulsion viscosity. A closely related and very important property, especially for demulsification, is the interfacial viscosity, or the viscosity of the fluid at the oil/water interface. As mentioned previously, water-in-oil emulsions form rigid interfacial films encapsulating the water droplets. These interfacial films stabilize an emulsion by lowering IFT and increasing interfacial viscosity. These films retard the rate of oil-film drainage (see Sec. 12.2.2) during the coalescence of water droplets, thereby greatly reducing the rate of emulsion breakdown. The oil-drainage rate

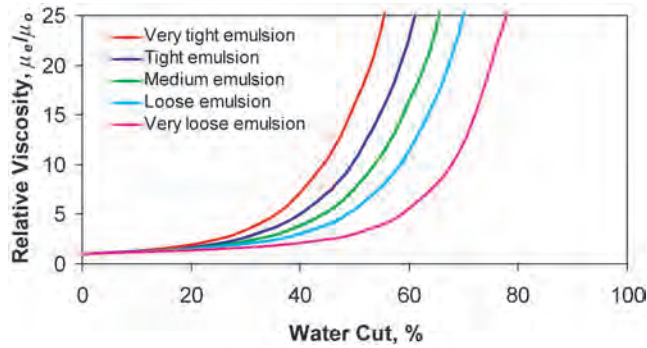


Fig. 12.8—Relative viscosities of emulsions.

depends on the interfacial shear viscosity. High interfacial viscosities significantly slow the liquid drainage rate and thus have a stabilizing effect on the emulsion. Emulsion interfacial viscosity plays a very important role in demulsification and is discussed in [Sec. 12.2.1](#). [Refs. 9](#) through [11](#) provide a detailed discussion of measurement techniques and application to emulsion stability.

## 12.2 Stability of Emulsions

From a purely thermodynamic point of view, an emulsion is an unstable system because there is a natural tendency for a liquid/liquid system to separate and reduce its interfacial area and, hence, its interfacial energy. However, most emulsions demonstrate kinetic stability (i.e., they are stable over a period of time). Produced oilfield emulsions are classified on the basis of their degree of kinetic stability. Loose emulsions separate in a few minutes, and the separated water is free water. Medium emulsions separate in tens of minutes. Tight emulsions separate (sometimes only partially) in hours or even days.

Water-in-oil emulsions are considered to be special liquid-in-liquid colloidal dispersions. Their kinetic stability is a consequence of small droplet size and the presence of an interfacial film around water droplets and is caused by stabilizing agents (or emulsifiers). These stabilizers suppress the mechanisms involved (sedimentation, aggregation or flocculation, coalescence, and phase inversion) that would otherwise break down an emulsion. Sedimentation is the falling of water droplets from an emulsion because of the density difference between the oil and water. Aggregation or flocculation is the grouping together of water droplets in an emulsion without a change in surface area. Coalescence is the fusion of droplets to form larger drops with reduced total surface area. [Sec. 12.3](#) discusses the mechanisms of emulsion breakup.

**12.2.1 Surface Films and Stability to Coalescence.** As mentioned previously, produced oilfield emulsions are stabilized by films that form around the water droplets at the oil/water interface. These films are believed to result from the adsorption of high-molecular-weight polar molecules that are interfacially active (surfactant-like behavior). These films enhance the stability of an emulsion by increasing the interfacial viscosity. Highly viscous interfacial films retard the rate of oil-film drainage during the coalescence of the water droplets by providing a mechanical barrier to coalescence, which can lead to a reduction in the rate of emulsion breakdown. [Figs. 12.9 and 12.10](#) show the persistent film in a water-in-oil emulsion. The presence of fine solids can also strengthen the interfacial film and further stabilize emulsions.

The properties of interfacial films depend on the type of crude oil (asphaltic, paraffinic, etc.), composition and pH of the water, temperature, the extent to which the adsorbed film is compressed, contact or aging time, and the concentration of polar molecules in the crude

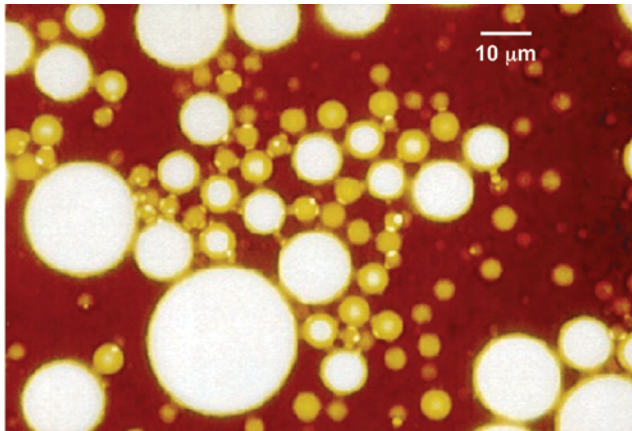


Fig. 12.9—Photomicrograph of an emulsion showing interfacial films.

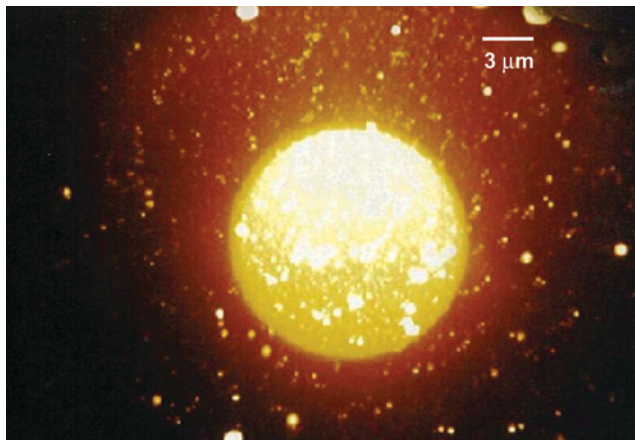


Fig. 12.10—Photomicrograph of an emulsion showing interfacial films (magnified).

oil.<sup>5,12-14</sup> A good correlation exists between the presence of incompressible interfacial film and emulsion stability. These films are classified into two categories on the basis of their mobilities.<sup>12,13</sup> Rigid or solid films are like an insoluble, solid skin on water droplets characterized by very high interfacial viscosity. There is considerable evidence that very fine solids stabilize these films. They provide a structural barrier to droplet coalescence and increase emulsion stability. These films also have viscoelastic properties. Mobile or liquid films are characterized by low interfacial viscosities. Liquid films are formed, for example, when a demulsifier is added to an emulsion. They are inherently less stable than rigid or solid films, and coalescence of water droplets is enhanced.

Emulsion stability has been correlated with the mobility of interfacial films.<sup>10,13</sup> Surfactants that modify the rigidity of the film can affect demulsification considerably. [Sec. 12.3](#) discusses this topic further.

**12.2.2 Factors Affecting Stability.** It is evident from the previous discussion that interfacial films are primarily responsible for emulsion stability. In this section we discuss the factors that affect interfacial films and, therefore, the emulsion stability. Important factors are heavy polar fractions in the crude oil; solids, including organic (asphaltenes, waxes) and inorganic (clays,

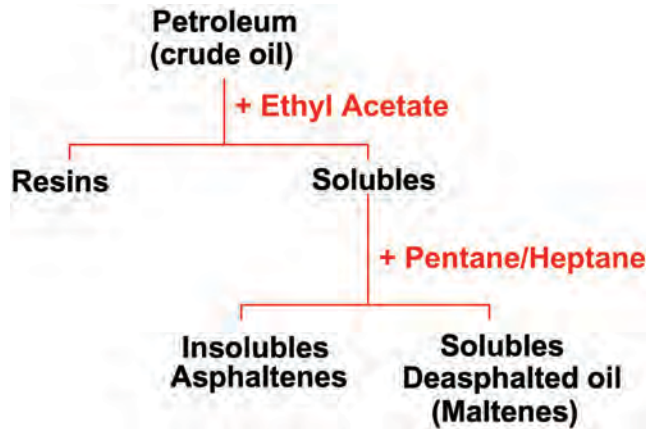


Fig. 12.11—Definition chart of petroleum asphaltenes.

scales, corrosion products, etc.) materials; temperature; droplet size and droplet-size distribution; pH of the brine; and brine composition.<sup>12–16</sup>

**Heavy Polar Fraction in Crude Oil.** Naturally occurring emulsifiers are concentrated in the higher-boiling polar fraction of the crude oil.<sup>12–18</sup> These include asphaltenes, resins, and oil-soluble organic acids (e.g., naphthenic, carboxylic) and bases. These compounds are the main constituents of the interfacial films surrounding the water droplets that give emulsions their stability.

**Asphaltenes.** Fig. 12.11 shows that asphaltenes are complex polyaromatic molecules defined to be soluble in benzene/ethyl acetate and insoluble in low-molecular-weight n-alkanes.<sup>19,20</sup> They are dark brown to black friable solids with no definite melting point. Asphaltenes are considered to consist of condensed aromatic sheets with alkyl and alicyclic side chains and heteroatoms (nitrogen, oxygen, sulfur, and trace metals like vanadium and nickel) scattered throughout. Fig. 12.12 shows the hypothetical structure of a petroleum asphaltene, and Fig. 12.13 shows a 3D representation. Asphaltene molecules can have carbon numbers from 30 and over and molecular weights from 500 to more than 10,000. They are characterized by a fairly constant hydrogen/carbon ratio of 1.15 with a specific gravity near one.

The nature of asphaltenes in the crude oil is still a subject of debate (see the chapter on asphaltenes in this section of the Handbook). The asphaltenes are believed to exist in the oil as a colloidal suspension and to be stabilized by resins adsorbed on their surface.<sup>21</sup> In this regard, the resins act as peptizing agents for asphaltenes and together form clusters called micelles (Fig. 12.14). These micelles or colloids contain most of the polar material found in the crude oil and possess surface-active properties (interfacially active material). The surface-active properties are the result of the sulfur, nitrogen, oxygen, and metal containing entities in asphaltene molecules that form polar groups such as aldehydes, carbonyl, carboxylic, amine, and amides.

It is this surface-active behavior of asphaltenes that makes them good emulsifiers. Surfactants are compounds that have a polar part with an affinity to water and a nonpolar part with an affinity to oil (Fig. 12.15). This dual affinity is satisfied when they are positioned (or adsorbed) at the oil/water interface with the polar part immersed in water and the nonpolar part in oil. This orientation results in a decrease in the thermodynamic free energy of the system. The accumulation of high-molecular-weight substances at the interface results in the formation of the rigid film. Fig. 12.16 shows an asphaltene-stabilized water droplet. When such a film forms, it acts as a barrier to drop coalescence. For two drops to coalesce, the film must be drained and ruptured. The presence of the asphaltenes can naturally retard the drainage of this film. The primary mechanism involved in this retardation is the steric repulsion or hindrance

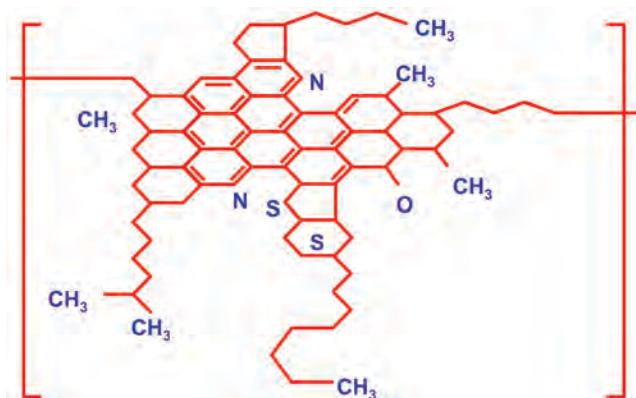


Fig. 12.12—Hypothetical structure of a petroleum asphaltene. [Reprinted with permission from J.G. Speight and S.E. Moschopedis: “On the Molecular Nature of Asphaltenes,” *Advances in Chemistry Series*, J.W. Bunger and N.C. Li (eds.), American Chemical Society (1981) 195, 1–15. Copyright 1981 American Chemical Society.]

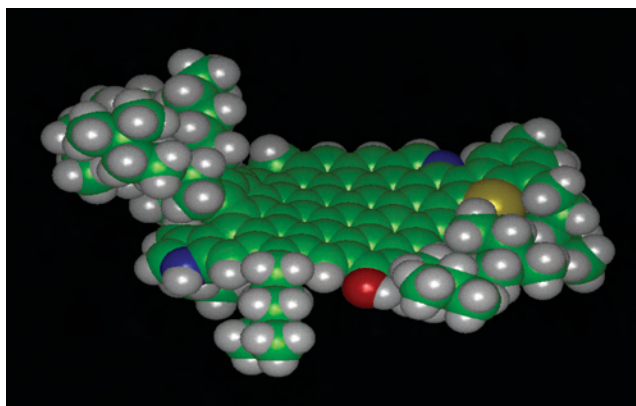


Fig. 12.13—3D representation of a Venezuelan asphaltene molecule (courtesy of J. Murgich and A. Mansoori).

caused by the high-molecular-weight materials in the film.<sup>8,22</sup> Fig. 12.17 shows the steric repulsion produced by the interaction between the nonpolar or hydrophobic groups of the surfactant molecules. With asphaltenic-surfactant molecules, the side chains can extend considerably into the oil phase and steric repulsion can maintain the interface at a distance sufficient to inhibit coalescence. The molecules at the oil/water interface result in an increase in both the interfacial viscosity and the apparent viscosity of the oil in the film between the droplets. Both of these effects oppose film drainage and inhibit coalescence.<sup>22</sup>

The state of asphaltenes in the crude oil has an effect on its emulsion-stability properties. While asphaltenes stabilize emulsions when they are present in a colloidal state (not yet flocculated), there is strong evidence that their emulsion-stabilizing properties are enhanced significantly when they are precipitated from the crude oil and are present in the solid phase. The effect of polar fractions (primarily asphaltenes) on the film properties was investigated by Stassner.<sup>13</sup> In a series of tests, it was demonstrated that the removal of asphaltenes (deasphalting) from the crude oil resulted in a very loose emulsion characterized by mobile films. Adding the precipitated asphaltenes back to the deasphalted oil in increasing quantities resulted in the for-

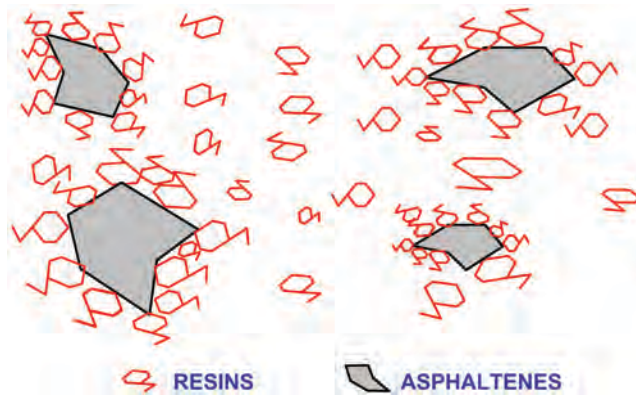


Fig. 12.14—Asphaltene-resin micelle.

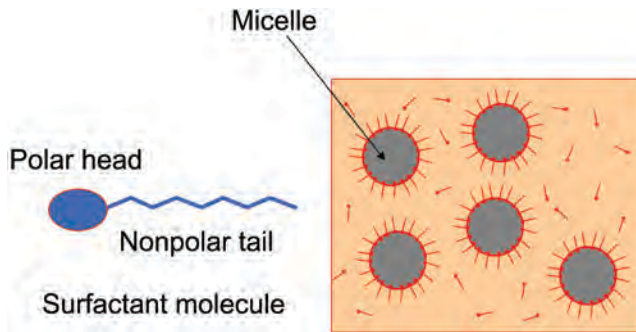


Fig. 12.15—Schematic of a surfactant molecule and formation of micelles.

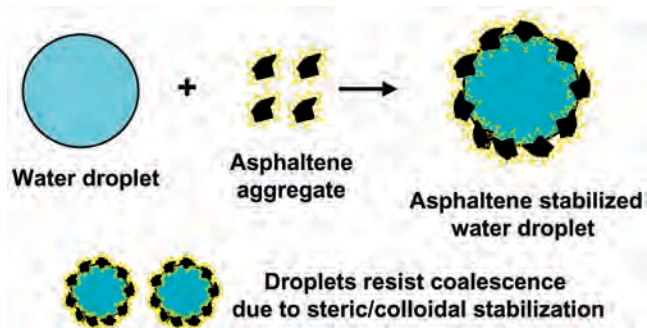


Fig. 12.16—Mechanism of emulsion stabilization by asphaltenes.

mation of rigid or solid films and increasingly stable emulsions. **Fig. 12.18** shows the effect of asphaltenes (when added to deasphalted oil) on emulsion stability. Another study<sup>18</sup> examined the effect of asphaltenes on emulsion stabilization and showed that the extent of emulsification was related to the aromatic/aliphatic ratio of the crude oil. This was further substantiated by Bobra.<sup>15</sup> Both studies<sup>15,18</sup> reported that two factors control emulsion stability: the amount of asphaltenes and the aromatic/alkane ratio in the crude oil. Emulsification tendencies reduce



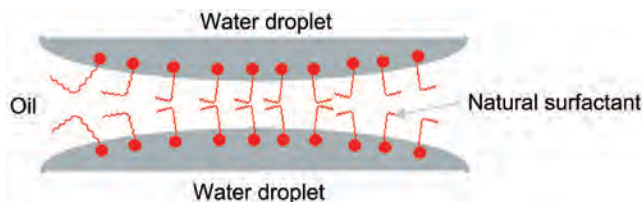


Fig. 12.17—Steric repulsion between two water droplets, which retards film drainage and coalescence.

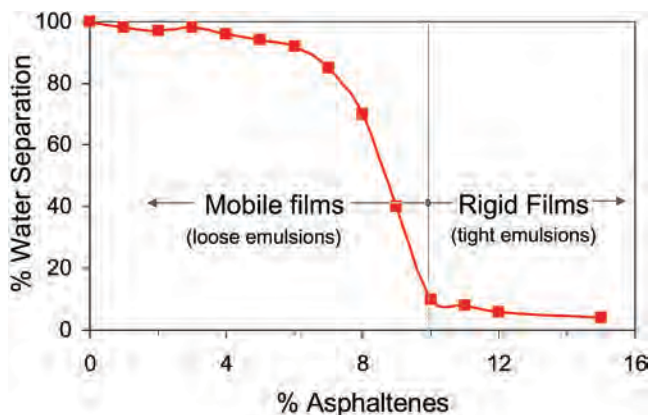


Fig. 12.18—Effect of asphaltenes, added to deasphalted oil, on emulsion stability.

with increasing aromatic content of the crude oil. Asphaltenes, apart from stabilizing emulsions themselves, alter the wettability of other solids present and make them act as emulsifying agents for water-in-oil emulsions.<sup>16,17,23–25</sup>

*Resins.* Resins are complex high-molecular-weight compounds that are not soluble in ethyl-acetate but are soluble in n-heptane (Fig. 12.11). They are heterocompounds, like asphaltenes, that contain oxygen, nitrogen, and sulfur atoms. Molecular weights of resins range from 500 to 2,000. As Fig. 12.14 shows, resins have a strong tendency to associate with asphaltenes, and together they form a micelle. As Figs. 12.16 and 12.17 illustrate, the asphaltene-resin micelle plays a key role in stabilizing emulsions. It appears that the asphaltene-resin ratio in the crude oil is responsible for the type of film formed (solid or mobile) and, therefore, is directly linked to the stability of the emulsion.<sup>13,15</sup>

*Waxes.* Waxes are high-molecular-weight alkanes naturally present in the crude oil that crystallize when the oil is cooled below its “cloud point.” They are insoluble in acetone and dichloromethane at 30°C. There are two types of petroleum waxes: paraffin and microcrystalline. Paraffin waxes are high-molecular-weight normal alkanes, and microcrystalline waxes are high-molecular-weight iso-alkanes that have melting points greater than 50°C.

Waxes by themselves are soluble in oil and, in the absence of asphaltenes, do not form stable emulsions in model oils.<sup>15</sup> However, the addition of a nominal amount of asphaltenes (an amount insufficient by itself to produce emulsions) to oils containing wax can lead to the formation of stable emulsions. Therefore, waxes can interact synergistically with asphaltenes to stabilize emulsions. The physical state of the wax in the crude oil also plays an important role in emulsion stabilization. Waxes are more apt to form a stable emulsion when they are present as fine solids in the emulsion; thus, waxy emulsions are more likely at lower temperatures. Waxes, being oil-wet, have a tendency to stabilize water-in-oil emulsions. Crudes that have a

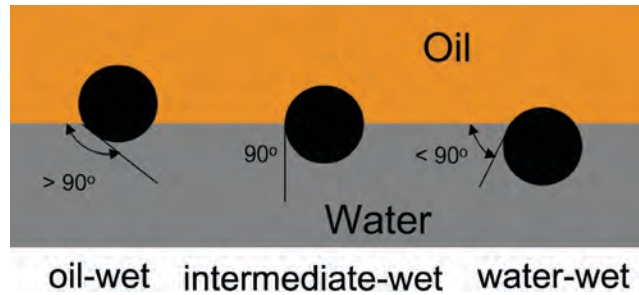


Fig. 12.19—Wetting behavior of solids at the oil/water interface.

high cloud point generally have a greater tendency to form stable and tight emulsions than crudes with low cloud points. Similarly, lower temperatures generally enhance the emulsion-forming tendencies of crude oils.

**Solids.** Fine solid particles present in the crude oil are capable of effectively stabilizing emulsions. The effectiveness of these solids in stabilizing emulsions depends on factors such as the solid particle size, interparticle interactions, and the wettability of the solids.<sup>8,26,27</sup> Solid particles stabilize emulsions by diffusing to the oil/water interface, where they form rigid films that can sterically inhibit the coalescence of emulsion droplets. Furthermore, solid particles at the interface may be electrically charged, which may also enhance the stability of the emulsion. Particles must be much smaller than the size of the emulsion droplets to act as emulsion stabilizers. Typically these solid particles are submicron to a few microns in diameter.<sup>8</sup>

The wettability of the particles plays an important role in emulsion stabilization. Wettability is the degree to which a solid is wetted by oil or water when both are present. Fig. 12.19 shows the three cases of wettability in terms of the contact angle. When the contact angle,  $\delta$ , is less than  $90^\circ$ , the solid is preferentially oil-wet. Similarly, when the contact angle is greater than  $90^\circ$ , the solid is preferentially water-wet. Contact angles close to  $90^\circ$  result in an intermediately wetted solid that generally leads to the tightest emulsions. If the solid remains entirely in the oil or water phase, it will not be an emulsion stabilizer. For the solid to act as an emulsion stabilizer, it must be present at the interface and must be wetted by both the oil and water phases. In general, oil-wet solids stabilize a water-in-oil emulsion. Oil-wet particles preferentially partition into the oil phase and prevent the coalescence of water droplets by steric hindrance. Similarly, water-wet solids stabilize a water-continuous or an oil-in-water emulsion. Examples of oil-wet solids are asphaltenes and waxes. Examples of water-wet solids are inorganic scales ( $\text{CaCO}_3$ ,  $\text{CaSO}_4$ ), clays, sand, and corrosion products. Water-wet particles can be made oil-wet with a coating of heavy organic polar compounds.<sup>23,24</sup>

When solids are wetted by the oil and water (intermediate wettability), they agglomerate at the interface and retard coalescence. These particles must be repositioned into either the oil or water for coalescence to take place. This process requires energy and provides a barrier to coalescence.

The role of colloidal solid particles in emulsion stability and the mechanisms involved are summarized in the following points.<sup>8</sup>

- The particles must be present at the oil/water interface before any stabilization can take place. The ability of the particles to diffuse to the interface and adsorb at the interface depends on its size, wettability, and the state of dispersion of the solids (whether flocculated or not).
- The ability of the solids to form a rigid, protective film encapsulating the water droplets is important for stabilizing these emulsions.
- Water-wet particles tend to stabilize oil-in-water emulsions, and oil-wet particles stabilize water-in-oil emulsions.

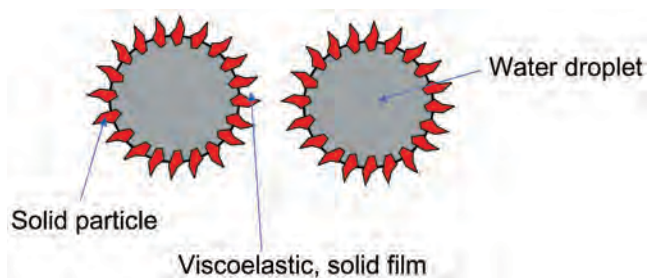


Fig. 12.20—Droplet stabilization by solids.

- Some degree of particle interaction is necessary for effective stabilization.

The effectiveness of colloidal particles in stabilizing emulsions depends largely on the formation of a densely packed layer of solid particles (film) at the oil/water interface (Fig. 12.20). This film provides steric hindrance to the coalescence of water droplets. The presence of solids at the interface also changes the rheological properties of the interface that exhibits viscoelastic behavior. This affects the rate of film drainage between droplets and also affects the displacement of particles at the interface. It has also been demonstrated<sup>15</sup> that for asphaltenes and waxes to be effective emulsifiers, they must be present in the form of finely divided submicron particles.

**Temperature.** Temperature can affect emulsion stability significantly. Temperature affects the physical properties of oil, water, interfacial films, and surfactant solubilities in the oil and water phases. These, in turn, affect the stability of the emulsion. Perhaps the most important effect of temperature is on the viscosity of emulsions because viscosity decreases with increasing temperatures (Fig. 12.7). This decrease is mainly because of a decrease in the oil viscosity. When waxes are present (the temperature of the crude is below its cloud point) and are the source of emulsion problems, application of heat can eliminate the problem completely by re-dissolving the waxes into the crude oil. Temperature increases the thermal energy of the droplets and, therefore, increases the frequency of drop collisions. It also reduces the interfacial viscosity, which results in a faster film-drainage rate and faster drop coalescence.

The effect of temperature on crude oil/water interfacial films was studied in some detail by Jones *et al.*,<sup>12</sup> who showed that an increase in temperature led to a gradual destabilization of the crude oil/water interfacial films. However, even at higher temperatures, a kinetic barrier to drop coalescence still exists. Temperature influences the rate of buildup of interfacial films by changing the adsorption rate and characteristics of the interface. It also influences the film compressibility by changing the solubility of the crude oil surfactants in the bulk phase.

Slow degassing (removal of light ends from the crude oil) and aging lead to significant changes in the interfacial film behavior at high temperatures. The films generated by this process remain incompressible and nonrelaxing (solid films) at high temperatures at which emulsion resolution is not affected by heating.

**Drop Size.** As mentioned earlier, emulsion droplet sizes can range from less than a micron to more than 50 microns. Fig. 12.5 shows the typical droplet-size distributions for water-in-crude oil emulsion. Droplet-size distribution is normally represented by a histogram or by a distribution function.

Emulsions that have smaller size droplets will generally be more stable. For water separation, drops must coalesce—and the smaller the drops, the greater the time to separate. The droplet-size distribution affects emulsion viscosity because it is higher when droplets are smaller. Emulsion viscosity is also higher when the droplet-size distribution is narrow (i.e., droplet size is fairly constant).

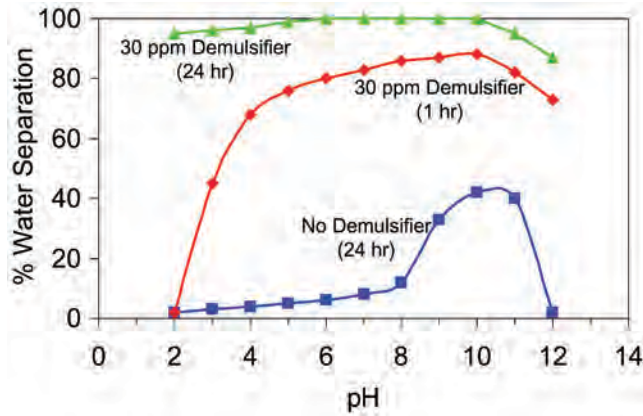


Fig. 12.21—Effect of pH and demulsifier concentration on emulsion stability.<sup>13</sup>

**pH.** The pH of water has a strong influence on emulsion stability.<sup>12–14</sup> The stabilizing, rigid emulsion film contains organic acids and bases, asphaltenes with ionizable groups, and solids. Adding inorganic acids and bases strongly influences their ionization in the interfacial films and radically changes the physical properties of the films. The pH of water affects the rigidity of the interfacial films. It was reported<sup>13</sup> that interfacial films formed by asphaltenes are strongest in acids (low pH) and become progressively weaker as the pH is increased. In alkaline medium, the films become very weak or are converted to mobile films. The films formed by resins are strongest in base and weakest in acid medium. Solids in the emulsions can be made oil-wet by asphaltenes, an effect that is stronger in an acidic than in a basic medium. These partially oil-wet solids tend to stabilize water-in-oil emulsions.

pH also influences the type of emulsion formed. Acid or low pH generally produces water-in-oil emulsions (corresponding to oil-wetting solid films), whereas basic or high pH produces oil-in-water emulsions (corresponding to water-wetting mobile soap films). Fig. 12.21 shows the effect of pH on emulsion stability for a Venezuelan crude.<sup>13</sup> Optimum pH for demulsification is approximately 10 in the absence of a demulsifier.

Brine composition also has an important effect (in relation to pH) on emulsion stability. Fig. 12.22 shows the effect of a bicarbonate brine and distilled water on emulsion stability as a function of pH.<sup>13</sup> Optimal pH for water separation changes from approximately 10 for distilled water to between 6 and 7 for the brine solution because of an ionization effect (association/interaction of ions present in the brine with the asphaltenes). The study suggests that for most crude oil/brine systems an optimum pH range exists for which the interfacial film exhibits minimum emulsion-stabilizing or maximum emulsion-breaking properties. The optimum pH for maximum emulsion stability depends on both the crude oil and brine compositions. The latter seems to be more important.

Frequently, severe emulsion upsets occur in surface-treating facilities following acid stimulation.<sup>28–30</sup> It has also been linked to formation damage. Following acid treatment, wells can be very slow to clean up, often resulting in partial or complete plugging of the well. This plugging and formation damage generally occurs because of solid precipitates or sludges forming on contact of the crude oil with the acid. These precipitates are mainly asphaltenes, resins, and other high-molecular-weight hydrocarbons. These materials are apparently precipitated from the crude oil by the reduction in pH<sup>30</sup> and are among the tightest emulsions produced. Proper design of the acid treatment is necessary to avoid well productivity decline and emulsion upsets caused by acidization.<sup>29</sup>

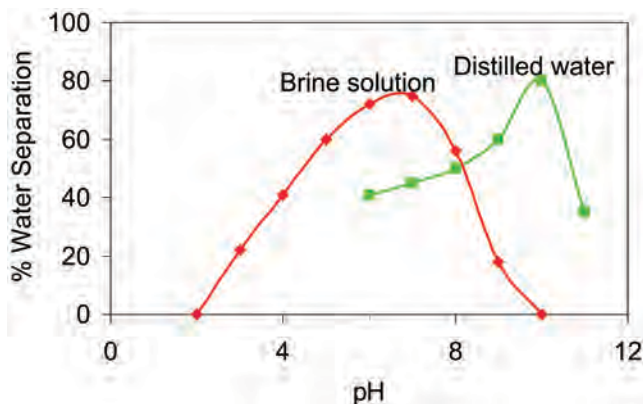


Fig. 12.22—Effect of brine and pH on emulsion stability.<sup>13</sup>

**Brine Composition.** Specific ions present in the brine can also influence interfacial film behavior. The effect of brine composition on interfacial film and emulsion stability has been reported.<sup>12–14</sup> Waters from petroleum formations generally contain many ions. Sodium and chloride ions are usually present in high concentrations, while other ions are present in wide-ranging quantities. At the interface, these ions may react chemically with the hydrophilic groups to form insoluble salts. In the studies cited, an insufficient number and variety of crude oil/brine systems were tested to draw any concrete conclusions regarding the effect of brine and its composition on interfacial film and emulsion-stabilizing properties. However, the following general trends are noted.

- Brine composition (alkalinity in particular because of a buffering effect) is intimately tied to the pH in determining the stabilizing properties of the interfacial films.<sup>13</sup>
- Brines with high  $\text{Ca}^{++}$  ions and a high  $\text{Ca}^{++}/\text{Mg}^{++}$  ratio form nonrelaxing, rigid films around the water droplets, resulting in stable emulsions.<sup>12</sup>
- Higher concentration of divalent ions and high pH result in reduced emulsion stability.

Many species of polar molecules are present at the interface, and each species responds differently. Synergistic effects may occur when several different cations are present at the same time.

**12.2.3 Stability Measurement.** From a practical point of view, measurement of stability is one of the most important tests that can be performed on an emulsion. It determines the ease with which the oil and water separates in an emulsion. There are numerous methods available for determining emulsion stability,<sup>5</sup> and the most common is the simple bottle test.

The bottle test involves diluting the emulsion with a solvent, mixing in a demulsifier, shaking to disperse the demulsifier, and observing the phase separation as a function of time. The tests are normally done at elevated temperature and may involve centrifugation to speed up the separation. While different methods and procedures are followed by various laboratories, there is a standard ASTM method (ASTM 4007) for determining the bottom sediments and water in an emulsion. The stability of the emulsion is generally related to the ease of water separation with time and demulsifier dosage. For example, at a given demulsifier concentration, emulsions can be rated on their stability by the amount of water separated in a given period of time. Alternatively, for a fixed length of time and a given demulsifier concentration, different demulsifiers can be graded in terms of their demulsification qualities. The bottle test is used regularly as a screening test for potential demulsifiers.

While a standard method is available for determining BS&W, no standard method is available in the literature for determining the stability of the emulsion with the bottle test. Recently, a method was proposed<sup>31</sup> for measuring the stability of an emulsion quantitatively. The concept

of an emulsion separation index was proposed to measure the tightness of an emulsion. The fraction of the total water separated in a regular bottle test at different demulsifier dosages is averaged to determine a separation index for the emulsion. The separation index measures from zero (no separation) to 100% (full separation). The separation index thus provides a measure of emulsion tightness (or stability): the lower the index, the greater the tightness or stability. The index must be quoted at the temperature of the test and for a given demulsifier. The index is very useful for comparing the stability of emulsions from different sources (for example, different wells or wet-crude handling facilities). Appendix A briefly describes the procedure, and Ref. 31 provides additional details.

Other techniques also have been used for the measurement of emulsion stability. A technique based on light scattering in crude-oil emulsions was used to measure the coalescence of water droplets (and, hence, emulsion stability).<sup>32</sup> The method can be used to monitor the coalescence action of demulsifiers. Another technique<sup>33</sup> suggests the measurement of dielectric constant of oilfield emulsions as a measure of their stability. The dielectric constant, which can be measured readily, can be used to characterize emulsions. A change in dielectric constant with time or demulsifier dosage can be used as a measure of the emulsion stability. This technique may be used for screening, ranking, and selecting demulsifiers for emulsion resolution. Recently, electroacoustical techniques<sup>5,34</sup> have shown promise for electrokinetic measurement of colloidal phenomena in emulsions and the rate of flocculation and coalescence of water droplets in water-in-oil emulsions. The technique, based on the ultrasound vibration potential, which involves the application of a sonic pulse and the detection of an electric field, was used successfully in monitoring coagulation in a water-in-oil emulsion.<sup>5</sup> Another technique developed recently used critical electric field measurements for emulsion stability.<sup>35</sup>

### 12.3 Demulsification

Demulsification is the breaking of a crude oil emulsion into oil and water phases. From a process point of view, the oil producer is interested in three aspects of demulsification: the rate or the speed at which this separation takes place, the amount of water left in the crude oil after separation, and the quality of separated water for disposal. A fast rate of separation, a low value of residual water in the crude oil, and a low value of oil in the disposal water are obviously desirable. Produced oil generally has to meet company and pipeline specifications. For example, the oil shipped from wet-crude handling facilities must not contain more than 0.2% BS&W and 10 pounds of salt per thousand barrels of crude oil. This standard depends on company and pipeline specifications. The salt is insoluble in oil and associated with residual water in the treated crude. Low BS&W and salt content is required to reduce corrosion and deposition of salts. The primary concern in refineries is to remove inorganic salts from the crude oil before they cause corrosion or other detrimental effects in refinery equipment. The salts are removed by washing or desalting the crude oil with relatively fresh water.

**12.3.1 Destabilizing Emulsions.** As mentioned previously, produced oilfield emulsions possess some kinetic stability. This stability arises from the formation of interfacial films that encapsulate the water droplets. To separate this emulsion into oil and water, the interfacial film must be destroyed and the droplets made to coalesce. Therefore, destabilizing or breaking emulsions is linked directly to the removal of this interfacial film. The factors that affect the interfacial film and, consequently, the stability of the emulsions were discussed earlier. The factors that enhance or speed up emulsion breaking are discussed here.

**Temperature.** Application of heat promotes oil/water separation and accelerates the treating process. An increase in temperature has the following effects.

- Reduces the viscosity of the oil.
- Increases the mobility of the water droplets.
- Increases the settling rate of water droplets.

- Increases droplet collisions and favors coalescence.
- Weakens or ruptures the film on water droplets because of water expansion and enhances film drainage and coalescence.
- Increases the difference in densities of the fluids that further enhances water-settling time and separation.

All these factors favor emulsion destabilization and oil/water separation; however, heat by itself is not a cure-all and even has some disadvantages (e.g., loss of light ends from the crude oil). An economic analysis should be performed that takes into consideration factors such as heating costs, reduced treating time, and residual water in the crude. An increase in temperature also can be achieved by burying crude-oil pipelines or by insulating them. These factors should be evaluated carefully during development, especially at facilities where emulsion problems are anticipated.

**Agitation or Shear.** Generally, reducing agitation or shear reduces emulsion stability. Very high shear is detrimental and should be avoided. High shear causes violent mixing of oil and water and leads to smaller droplet sizes. Smaller droplets are relatively more stable than larger droplets; therefore, measures that increase shearing of the crude oil (for example, mechanical chokes, valves, flow obstructions, and pressure drops) should be avoided or minimized where possible. However, a certain amount of shear is required for mixing the chemical demulsifier into the bulk of the emulsion.

**Residence or Retention Time.** The period of time that the emulsion is held at the treating temperature is the residence, retention, or treating time. This typically is between 10 to 30 minutes for normal crude oil production; however, it may need to be much longer to treat tight emulsions effectively. An increase in residence time increases the separation efficiency and reduces the residual amount of water in the crude. Increasing residence time, however, comes at the expense of high separator-equipment costs.

**Solids Removal.** Solids have a strong tendency to stabilize emulsions, especially if they are present as fines or when they are wetted by both oil and water. Removing the solids or their source is sometimes all that is required for eliminating or reducing the emulsion problem. Oil-wet solids stabilize water-in-oil emulsions. Water-wet solids can also be made oil-wet with a coating of heavy polar materials and can participate effectively in the stabilization of water-in-oil emulsions.<sup>23,24</sup> The presence of solid asphaltenes and waxes has a definite detrimental effect on the emulsion problem, and every effort should be made to eliminate their presence in the crude oil. The solids can be removed by dispersing them into the oil or can be water-wetted and removed with the water.

**Control of Emulsifying Agents.** Because emulsifying agents are necessary in the stabilization of emulsions, controlling them allows for their destabilization and resolution. Some of the ways to control emulsifiers include the following processes.

- Careful selection of chemicals that are injected during oil production. The chemicals include, for example, acids and additives during acidization, corrosion inhibitors for corrosion protection, surfactants and dispersants for organic- and inorganic-deposition control, and polymers and blocking agents for water-production control. Laboratory compatibility testing of these chemicals should be conducted before field injection to avoid tight emulsions.

- Avoiding incompatible crude-oil blends. A crude-oil blend is incompatible if it results in the precipitation of solids (organic and inorganic). This occurs, for example, when an asphaltic crude oil is mixed with a paraffinic crude oil, resulting in the precipitation of asphaltenes. Again, laboratory testing can identify incompatible crudes.

- Use of dispersants for controlling the precipitation of asphaltenes and the use of pour-point depressants for controlling waxes. Alternatively, emulsion stability can be controlled by raising the temperature of the crude above its cloud point.

- Neutralizing the effect of stabilizing film encapsulating the water droplets by demulsifiers. These chemicals promote coalescence of water droplets and accelerate water separation.

**Retrofitting.** Additional water separation can be achieved by retrofitting the existing equipment. Invariably, emulsion problems increase after the separation equipment has been installed because of field aging, increased watercuts, improper design, or several other reasons. Additional equipment (for example, free-water knockout drums and heater treaters) can be installed to assist in the breaking of oilfield emulsions. Internals can also be installed or retrofitted in production-separation traps. The most common retrofitting is the installation of a coalescer section that assists in coalescing water droplets. There are several options available, and re-engineering is generally required on a case-by-case basis. The chapter on emulsion treating in the Facilities section of this Handbook provides further information.

**12.3.2 Mechanisms Involved in Demulsification.** Demulsification, the separation of an emulsion into its component phases, is a two-step process. The first step is flocculation (aggregation, agglomeration, or coagulation). The second step is coalescence. Either of these steps can be the rate-determining step in emulsion breaking.

**Flocculation or Aggregation.** The first step in demulsification is the flocculation of water droplets. During flocculation, the droplets clump together, forming aggregates or “flocs.” The droplets are close to each other, even touching at certain points, but do not lose their identity (i.e., they may not coalesce). Coalescence at this stage only takes place if the emulsifier film surrounding the water droplets is very weak. The rate of flocculation depends on the following factors.<sup>15</sup>

- Water content in the emulsion. The rate of flocculation is higher when the water cut is higher.

- Temperature of the emulsion is high. Temperature increases the thermal energy of the droplets and increases their collision probability, thus leading to flocculation.

- Viscosity of the oil is low, which reduces the settling time and increases the flocculation rate.

- Density difference between oil and water is high, which increases the sedimentation rate.

- An electrostatic field is applied. This increases the movement of droplets toward the electrodes, where they aggregate.

**Coalescence.** Coalescence is the second step in demulsification. During coalescence, water droplets fuse or coalesce together to form a larger drop. This is an irreversible process that leads to a decrease in the number of water droplets and eventually to complete demulsification. Coalescence is enhanced by the following factors.<sup>5,15</sup>

- High rate of flocculation increases the collision frequency between droplets.

- The absence of mechanically strong films that stabilize emulsions.

- High interfacial tension. The system tries to reduce its interfacial free energy by coalescing.

- High water cut increases the frequency of collisions between droplets.

- Low interfacial viscosity enhances film drainage and drop coalescence.

- Chemical demulsifiers convert solid films to mobile soap films that are weak and can be ruptured easily, which promotes coalescence.

- High temperatures reduce the oil and interfacial viscosities and increase the droplet collision frequency.

**Sedimentation or Creaming.** Sedimentation is the process in which water droplets settle down in an emulsion because of their higher density. Its inverse process, creaming, is the rising of oil droplets in the water phase. Sedimentation and creaming are driven by the density difference between oil and water and may not result in the breaking of an emulsion. Unresolved emulsion droplets accumulate at the oil/water interface in surface equipment and form



an emulsion pad or rag layer. A pad in surface equipment causes several problems including the following.

- Occupies space in the separation tank and effectively reduces the retention or separation time.
- Increases the BS&W of the treated oil.
- Increases the residual oil in the treated water.
- Increases arcing incidences or equipment upset frequency.
- Creates a barrier for water droplets and solids migrating down into the bulk water layer.

Emulsion pads are caused or exacerbated by ineffective demulsifier (unable to resolve the emulsion); insufficient demulsifier (insufficient quantities to break the emulsion effectively); other chemicals that nullify the effect of the demulsifier; low temperatures; and the presence of accumulating solids. Because emulsion pads cause several operational problems, their cause should be determined and appropriate actions taken to eliminate them.

**12.3.3 Methods of Emulsion Breaking or Demulsification.** In the oil industry, crude-oil emulsions must be separated almost completely before the oil can be transported and processed further. Emulsion separation into oil and water requires the destabilization of emulsifying films around water droplets. This process is accomplished by any, or a combination, of the following methods:

- Adding chemical demulsifiers.
- Increasing the temperature of the emulsion.
- Applying electrostatic fields that promote coalescence.
- Reducing the flow velocity that allows gravitational separation of oil, water, and gas. This is generally accomplished in large-volume separators and desalters.

Demulsification methods are application specific because of the wide variety of crude oils, brines, separation equipment, chemical demulsifiers, and product specifications. Furthermore, emulsions and conditions change over time, which adds to the complexity of the treatment. The most common method of emulsion treatment is the application of heat and an appropriate chemical demulsifier to promote destabilization, followed by a settling time with electrostatic grids to promote gravitational separation.

**Thermal Methods.** Heating reduces the oil viscosity and increases the water-settling rates. Increased temperatures also result in the destabilization of the rigid films because of reduced interfacial viscosity. Furthermore, the coalescence frequency of water droplets is increased because of the higher thermal energy of the droplets. In other words, heat accelerates emulsion breaking; however, it very rarely resolves the emulsion problem alone. Increasing the temperature has some negative effects. First, it costs money to heat the emulsion stream. Second, heating can result in the loss of light ends from the crude oil, reducing its API gravity and the treated oil volume. Finally, increasing the temperature leads to an increased tendency toward some forms of scale deposition and an increased potential for corrosion in treating vessels.

The application of heat for emulsion breaking should be based on an overall economic analysis of the treatment facility. The cost-effectiveness of adding heat should be balanced against longer treatment time (larger separator), loss of light ends and a resultant lower oil-product price, chemical costs, and the costs of electrostatic grid installation or retrofitting.

**Mechanical Methods.** There is a wide variety of mechanical equipment available for breaking oilfield emulsions including free-water knockout drums, two- and three-phase separators (low- and high-pressure traps), desalters, settling tanks, etc. See the chapter on emulsion treating in the Facilities section of this Handbook for a detailed description of emulsion-treating equipment.

**Free-Water Knockout Drums.** Free-water knockout drums separate the free water from the crude oil/water mixture. Some of the associated gases may be separated in these drums. Free-

water knockout drums are supplementary equipment that aid in the treatment of produced crude oil emulsions.

*Production Traps or Three-Phase Separators.* Three-phase separators or production traps are used to separate the produced fluids into oil, water, and gas. These separators can be either horizontal or vertical in configuration. Each separator is sized with a set retention time to provide adequate separation at a given throughput rate. The separator may include a heater section, wash water, a filter section, a coalescing or stabilizing section, and electrostatic grids. **Fig. 12.23** shows a typical three-phase separator.<sup>36</sup> There is a large variety of separators in use today. For example, a separator may have a large heater section or may have no coalescer packing. Selecting the right separator for any given set of conditions is a complex engineering task that depends on several factors.

Oil/water separation is usually based on a gravitational separation. Because water has a higher density than oil, water droplets have a tendency to settle down. Stokes' Law approximates the settling rate of water droplets.

$$v = \frac{2gr^2(\rho_w - \rho_o)}{9\mu}, \dots\dots\dots (12.2)$$

where  $v$  is the settling velocity of the water droplets,  $g$  is the acceleration caused by of gravity,  $r$  is the radius of the droplets,  $(\rho_w - \rho_o)$  is the density difference between the water and oil, and  $\mu$  is the oil viscosity. Stokes' Law suggests that the settling velocity is increased by increasing the density difference between water and oil, reducing the viscosity, and increasing the drop size. However, Stokes' Law should be applied to emulsions with caution. Increasing the coalescence rate increases the droplet size and has the strongest effect on the settling velocity. While it is true that larger diameter droplets settle faster, emulsifiers prevent droplet coalescence in an actual treating system. Another important consideration is that Stokes' Law applies only to a static system with nondeforming droplets. Both these assumptions are not true in complex emulsion-treating equipment. It is a dynamic system, and where the motion is vigorous, re-emulsification is possible. Stokes' Law also applies only to isolated particles or, in this application, to dilute emulsions.

A degree of flexibility in the separator design, with options to modify, is the best strategy when designing emulsion-treatment separators. Operating conditions (such as pressures, temperatures, water cuts, and oil/brine compositions) change during the life of the field, and the equipment should be able to handle these changes or be modified to account for them.

One way to improve the efficiency of separators is to install coalescer packs. These packs increase the travel of the fluid through the separator. The wiping or rolling action of the emulsion as it passes through the packing or baffles causes the water droplets to coalesce. Spreaders also can be installed to increase the collision frequency between droplets.

*Desalters.* The oil from the separator is generally "off-spec" (i.e., it still contains unacceptably high levels of water and solids). It must be further treated to meet crude specifications. For the refinery, the salt level must be further reduced. Refinery crude should contain no more than a specified amount of inorganic solids (salts). This is generally expressed in pounds per thousand barrels. The industry standard is 1 pound per thousand barrels. The removal of the salts, along with the remaining water, is the process of desalting.

Desalters are normally designed as either one-stage or multistage desalters. **Fig. 12.24** shows a schematic of a one-stage desalter. Generally, desalters use a combination of chemical addition, electrostatic treating, and settling time. The retention time is based on a certain oil specification for a given product rate. Also, fresh water (wash water) is added with the chemi-

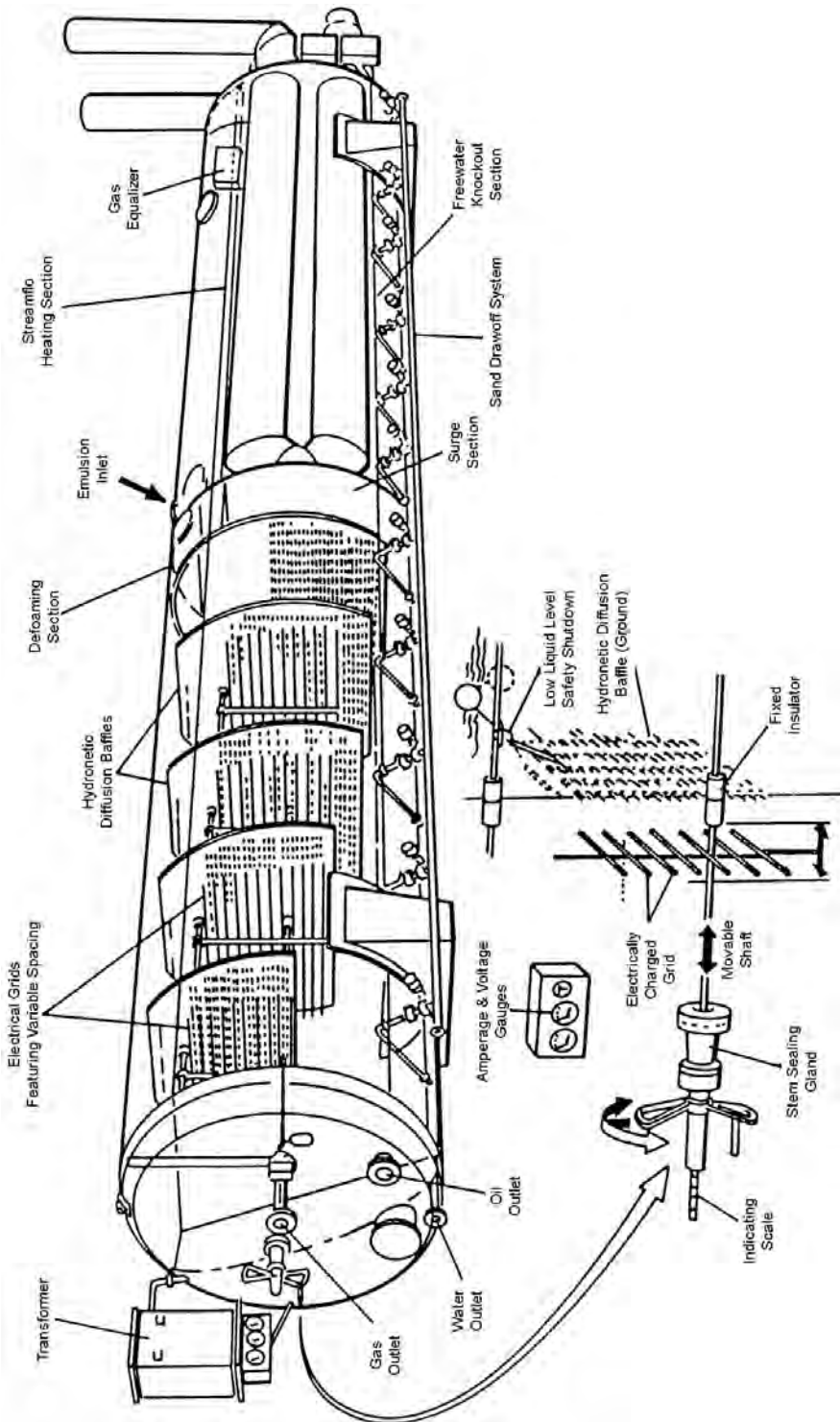


Fig. 12.23—Three-phase emulsion separator.<sup>36</sup>

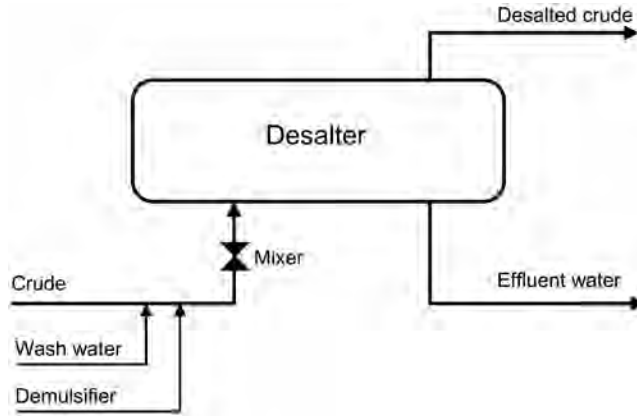


Fig. 12.24—One-stage desalter.

calls to reduce the concentrations of dissolved salt (by diluting) in the treated water and, hence, the outgoing crude.

Desalter performance is generally optimized by a careful manipulation of system parameters. Operational data are obtained by altering the system parameters and monitoring their effect on the quality of oil (or water/salt removal). Optimum set points can be obtained for operating temperatures, interface level, treating chemicals, wash-water rates and injection points, and mix valves settings.

**Electrical Methods.** Electrostatic grids are sometimes used for emulsion treatment. High-voltage electricity (electrostatic grids) is often an effective means of breaking emulsions. It is generally theorized that water droplets have an associated net charge, and when an electric field is applied, the droplets move about rapidly and collide with each other and coalesce. The electric field also disturbs the interfacial film by rearranging the polar molecules, thereby weakening the rigid film and enhancing coalescence. Fig. 12.23 shows a cross section of a typical electrostatic treater<sup>36</sup> (a three-phase separator, in this case). The electrical system consists of a transformer and electrodes that provide high-voltage alternating current. The electrodes are placed to provide an electric field that is perpendicular to the direction of flow. The distance between the electrodes is often adjustable so that the voltage can be varied to meet the requirement of the emulsion being treated.

Electrostatic dehydration generally is used with chemical and heat addition. Invariably, the use of electrostatic dehydration results in reduced heat requirements. Lower temperatures result in fuel economy, reduced problems with scale and corrosion formation, and reduced light-end loss. Electrostatic grids can also lead to a reduction in the use of emulsion-breaking chemicals. The one limitation of electrostatic dehydration is shorting/arcing, which generally happens when excess water is present. Recent designs in electrostatic grids have eliminated shorting/arcing.

**Chemical Methods.** The most common method of emulsion treatment is adding demulsifiers. These chemicals are designed to neutralize the stabilizing effect of emulsifying agents. Demulsifiers are surface-active compounds that, when added to the emulsion, migrate to the oil/water interface, rupture or weaken the rigid film, and enhance water droplet coalescence. Optimum emulsion breaking with a demulsifier requires a properly selected chemical for the given emulsion; adequate quantity of this chemical; adequate mixing of the chemical in the emulsion; and sufficient retention time in separators to settle water droplets. It may also require the addition of heat, electric grids, and coalescers to facilitate or completely resolve the emulsion.

**Chemical Selection.**<sup>31,37-40</sup> Selection of the right demulsifier is crucial to emulsion breaking. The selection process for chemicals is still viewed as an art rather than a science. However,

with the increasing understanding of emulsion mechanisms, the availability of new and improved chemicals, and new technology, research, and development efforts, selection of the right chemical is becoming more scientific. Many of the failures of the past have been eliminated.

Demulsifier chemicals contain the following components: solvents, surface-active ingredients, and flocculants. Solvents, such as benzene, toluene, xylene, short-chain alcohols, and heavy aromatic naphtha, are generally carriers for the active ingredients of the demulsifier. Some solvents change the solubility conditions of the natural emulsifiers (e.g., asphaltenes) that are accumulated at the oil/brine interface. These solvents dissolve the indigenous surface-active agents back into the bulk phase, affecting the properties of the interfacial film that can facilitate coalescence and water separation.

Surface-active ingredients are chemicals that have surface-active properties characterized by hydrophilic-lipophilic balance (HLB) values. For a definition and description of HLB, see [Ref. 5](#). The HLB scale varies from 0 to 20. A low HLB value refers to a hydrophilic or water-soluble surfactant. In general, natural emulsifiers that stabilize a water-in-oil emulsion exhibit an HLB value in the range of 3 to 8.<sup>5</sup> Thus, demulsifiers with a high HLB value will destabilize these emulsions. The demulsifiers act by total or partial displacement of the indigenous stabilizing interfacial film components (polar materials) around the water droplets. This displacement also brings about a change in properties such as interfacial viscosity or elasticity of the protecting film, thus enhancing destabilization. In some cases, demulsifiers act as a wetting agent and change the wettability of the stabilizing particles, leading to a breakup of the emulsion film.

Flocculants are chemicals that flocculate the water droplets and facilitate coalescence. A detailed process for selecting the appropriate demulsifier chemicals, described in [Ref. 5](#), includes the following steps.

- Characterization of the crude oil and contaminants includes the API gravity of the crude oil, type and composition of oil and brine, inorganic solids, amount and type of salts, contaminant type and amounts.
- Evaluation of operational data includes production rates, treating-vessel capabilities (residence time, electrostatic grids, temperature limitations, etc.), operating pressures and temperatures, chemical dosage equipment and injection points, sampling locations, maintenance frequency, and wash-water rates.
- Evaluation of emulsion-breaking performance: past experience and operating data including oil, water, and solids content during different tests; composition and quality of interface fluids; operating costs; and amounts of water generated and its disposal.

Testing procedures are available to select appropriate chemicals.<sup>31</sup> These tests include bottle tests, dynamic simulators, and actual plant tests. All test procedures have limitations. Hundreds of commercial demulsifier products are available that may be tested. Changing conditions at separation facilities result in a very slow selection process, especially at large facilities; therefore, it is important at such facilities to maintain a record of operational data and testing procedures as an ongoing activity.

*Mixing/Agitation.* For the demulsifier to work effectively, it must make intimate contact with the emulsion and reach the oil/water interface. Adequate mixing or agitation must be provided to thoroughly mix the chemical into the emulsion. This agitation promotes droplet coalescence; therefore, the point at which the demulsifier is added is critical. Once the emulsion has broken, agitation should be kept to a minimum to prevent re-emulsification. There should be sufficient agitation in the flow stream to allow the chemical to mix thoroughly, followed by a period of gentle flow inside the separator to promote gravity separation.

*Dosage.* The amount of chemical added is also important. Too little demulsifier will leave the emulsion unresolved. Conversely, a large dose of demulsifier (an overtreat condition) may be detrimental. Because demulsifiers are surface-active agents like the emulsifiers, excess demul-

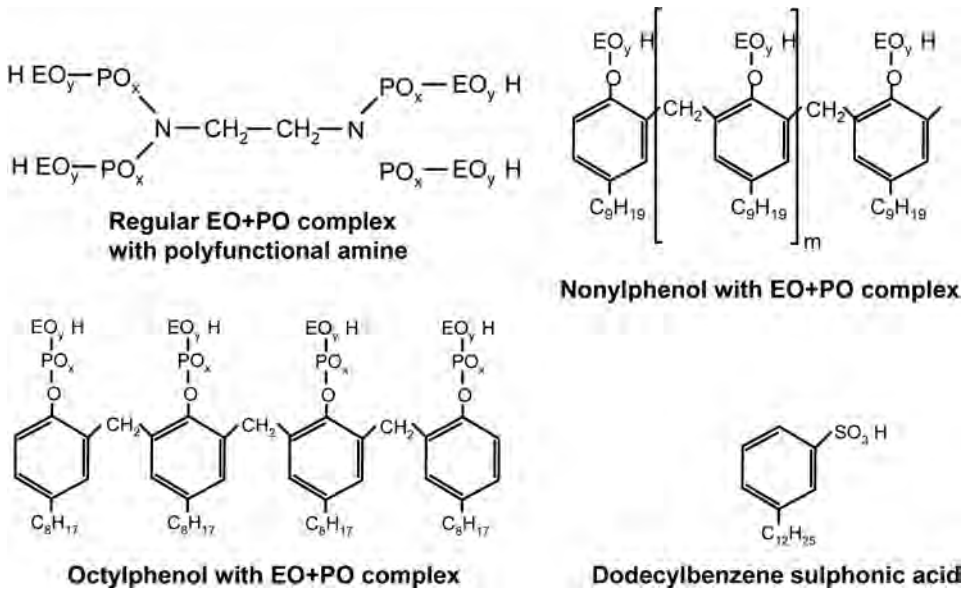


Fig. 12.25—Typical demulsifier molecular formulas.

sifier may produce very stable emulsions. The demulsifier simply replaces the natural emulsifiers at the interface.

It is difficult to prescribe standard or typical dosage rates for treating emulsions because of the wide variety of demulsifier chemicals available, the different types of crude being handled, the choice of separation equipment, and the variations in product qualities. Furthermore, some of the chemicals come in different concentrations (active ingredient in a carrier solvent). The amount or dosage of demulsifier required is very site-specific and depends on several factors, some of which are discussed in this chapter. On the basis of an evaluation of the literature, the demulsifier rates quoted vary from less than 10 to more than 100 ppm (based on total production rates). These numbers are provided for primary or secondary oil-recovery emulsions. During tertiary oil recovery (especially during surfactant or micellar flooding), demulsifier rates typically can be in the hundreds of ppm and even higher in extreme cases.

*Factors Affecting Demulsifier Efficiency.* Several factors affect demulsifier performance including temperature, pH, type of crude oil, brine composition, and droplet size and distribution. As described previously, an increase in temperature results in a decrease in emulsion stability, and, hence, a lower dosage of demulsifier is required. pH also affects demulsifier performance. Generally, basic pH promotes oil-in-water emulsions and acidic pH produces water-in-oil emulsions. High pH, therefore, helps in destabilizing water-in-oil emulsions. It has also been reported that basic pH reduces demulsifier dosage<sup>13</sup> requirements (see Fig. 12.21).

Demulsifiers that work for a given emulsion may be completely ineffective for another. Demulsifiers are typically formulated with polymeric chains of ethylene oxides and polypropylene oxides of alcohol, ethoxylated phenols, ethoxylated alcohols and amines, ethoxylated resins, ethoxylated nonylphenols, polyhydric alcohols, and sulphonic acid salts. Fig. 12.25 shows typical demulsifier molecular formulas. Commercial demulsifiers may contain one or more types of active ingredient. There is a wide variation within the active ingredient type as well. For example, the molecular weight and structure of the ethylene or propylene oxides can be changed to effect a complete range of solubilities, HLBs, charge neutralization tendencies, solids-wetting characteristics, and costs.

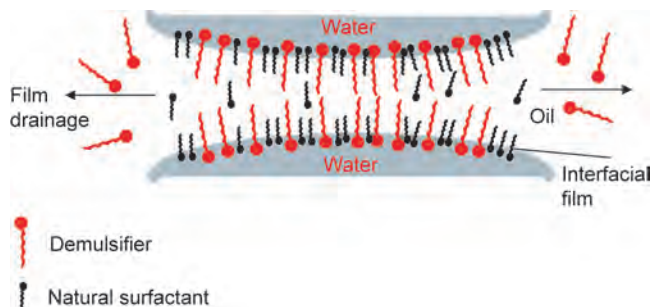


**Fig. 12.26—Film drainage in the presence of a demulsifier.**  
**The demulsifier displaces the indigenous surfactants in the interfacial film.**

*Mechanisms Involved in Chemical Demulsification.* Chemical demulsification is very complex. There are several hypotheses and theories regarding the physicochemical mechanism for the action of a chemical demulsifier.<sup>22</sup> The only clear generalization regarding demulsifiers is that they have a high molecular weight (about the same as natural surfactants) and, when used as emulsifying agents, they tend to establish an emulsion opposite in type to that stabilized by natural surfactants. There are thousands of products that have been patented as crude oil demulsifiers. A detailed knowledge of the functionality of demulsifiers and their effectiveness in breaking emulsions is still lacking; however, there are a few general rules for chemical demulsifiers and their ability in breaking emulsions.<sup>41</sup>

Several studies have been conducted on certain aspects of the chemical demulsification process.<sup>7,12,16,22,37–47</sup> It has been suggested<sup>39</sup> that demulsifiers displace the natural stabilizers present in the interfacial film around the water droplets. This displacement is brought about by the adsorption of the demulsifier at the interface and influences the coalescence of water droplets through enhanced film drainage.

**Fig. 12.26** shows the film drainage process schematically. When two droplets approach each other, the thickness of the interfacial film decreases as the liquid flows out of the film. This sets up an IFT gradient with high IFT inside the film and low IFT outside the film. The interfacial viscosity is very high because of the adsorbed natural surfactants (asphaltenes). Demulsifier molecules have a higher surface activity than natural surfactants and, therefore, replace them at the interface. When demulsifier molecules are adsorbed in the spaces left by the natural surfactants, the IFT gradient is reversed, film drainage is enhanced, and the interfacial viscosity is reduced.<sup>44,45</sup> This causes the film to become very thin and collapse, resulting in droplet coalescence. The efficiency of the demulsifier thus depends on its adsorption at the droplet surface. There is competition for adsorption when other surface-active species are present.<sup>39</sup> The indigenous surfactants, like asphaltenes, present in the crude oil are only weakly adsorbed and are readily displaced by the demulsifier.

Because of the large variety of components in the crude oil, it is not surprising that the effectiveness of a given demulsifier is sensitive to the crude oil type. In addition, the adsorption and displacement processes and, hence, the demulsifier effectiveness also depend on pH, salt content, and temperature. The best demulsifiers are those that readily displace preformed rigid films and leave mobile films (films that exhibit little resistance to coalescence) in their place.

Besides displacing the natural surfactants at the interface (breaking the rigid film), many chemical additives reduce or inhibit the rate of buildup of interfacial films. The best demulsifiers should possess both types of film modifying behavior: displacement of components in rigid interfacial films and inhibition of the formation of the rigid films.

The demulsifier effectiveness also depends on its dosage. An increase in demulsification rate is generally observed with increasing demulsifier concentration up to a critical concentration (the critical aggregation concentration). This is attributed to a monolayer adsorption of the demulsifier at the interface (simultaneously displacing the indigenous crude oil surfactant film). Higher concentrations beyond this critical concentration (overdosing) result in two different types of behavior.<sup>39,42</sup> Type I behavior is the leveling of the demulsification rate with increased demulsifier concentration. This type of behavior is attributed to the formation of a liquid crystalline phase. Type II behavior is a reduction in demulsification rate with increased demulsifier concentration. This type of behavior is attributed to steric stabilization of grown water droplets and is detrimental to demulsification because it retards the separation rate during overdosing. The type of behavior observed depends on the concentration and type of demulsifier. Some demulsifiers form aggregates in water or oil to give a viscous phase, while others may stabilize the emulsion sterically.

The solubility of the demulsifier in oil and water, or its partitioning, is also very crucial in determining the effectiveness of the demulsifier. The partitioning of the surfactant is measured either by the partition coefficient or by its HLB value. Several studies<sup>33,38,41,44,45</sup> have tried to link the demulsifier effectiveness to its partition coefficient. For the demulsifier to be fairly active, it must be an amphiphile with a partition coefficient of unity<sup>44,45</sup> (i.e., the demulsifier should partition equally between the oil and water phases). The surface adsorption rate is faster when the demulsifier has a partition coefficient of close to one. Because of this criterion and the fact that demulsifiers are added to the continuous oil phase, demulsifiers that are soluble in water only (low partition coefficient or low HLB) are not very effective in breaking water-in-oil emulsions. Oil solubility is important because oil forms the continuous phase, permits a thorough distribution of the demulsifier in the emulsion, and affects its diffusion to the oil/water interface. When this demulsifier reaches the interface, it must partition into the water phase (droplets) to displace the natural stabilizers at the interface effectively. This results in a reduction of interfacial viscosity and a change in the IFT gradient, both of which enhance film thinning and water droplets coalescence.

To ensure good overall performance, a demulsifier should meet the following criteria.<sup>44</sup>

- Dissolve in the continuous oil phase.
- Have a concentration large enough to diffuse to the oil/water interface. However, it should not be higher than the critical aggregate concentration.
- Partition into the water phase (partition coefficient close to unity).
- Possess a high rate of adsorption at the interface.
- Have an interfacial activity high enough to suppress the IFT gradient, thus accelerating the rate of film drainage and promoting coalescence.

## 12.4 Special Topics in Crude Oil Emulsions

**12.4.1 Emulsion Sampling.** Samples of the emulsion may be required for several reasons including crude specification verification, performance evaluation of the emulsion-treating system, or simply for laboratory testing. Invariably, the emulsion to be sampled is under pressure, and special procedures must be used to obtain representative samples. For crude specification testing, it is not important to maintain the integrity of the water droplets; however, the sample location point may be critical. In general, samples should not be withdrawn from the bottom of the pipe or vessel. Free water may be present and accumulate at the bottom of the pipe or vessel, affecting the BS&W reading. Neither should the sample be withdrawn from the top of the vessel because it primarily will be oil. The best position in the pipe to take an emulsion sample is on the side, preferably with a quill. Turbulence and high fluid velocity in the pipe may also ensure that the sample is homogenous and representative.



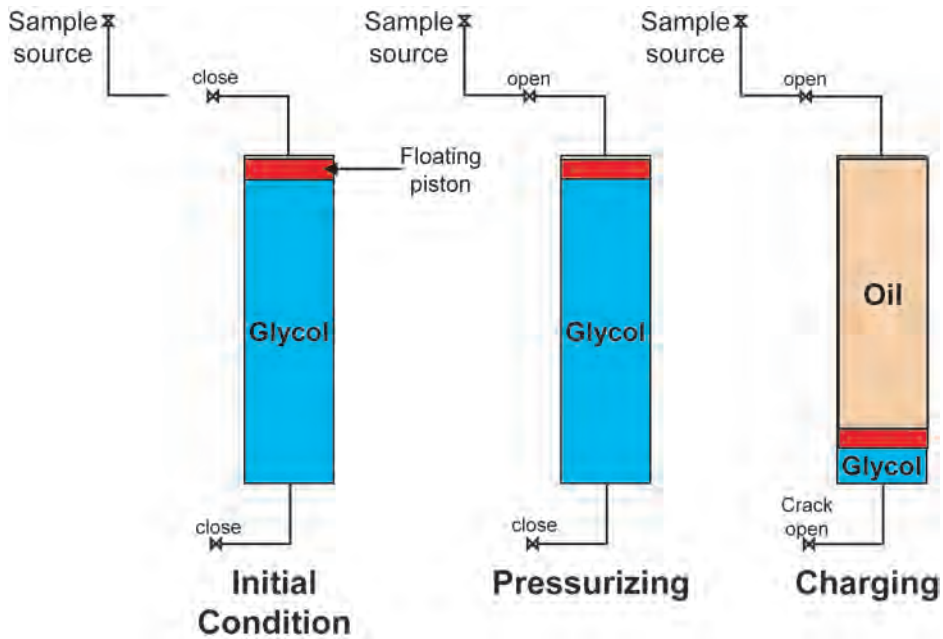


Fig. 12.27—Sampling of a high-pressure emulsion.

Every effort should be made to obtain a sample that closely represents the liquid from which it is taken. This is especially true of liquids under pressure. Emulsification should not occur during the sampling itself. For example, samples obtained at the wellhead or production headers may show a high percentage of emulsion, whereas the actual oil and water inside the piping may or may not be in the form of an emulsion. This indicates that the emulsification was a consequence of the sampling because the sample was depressurized into the sample container.

A special procedure is used to obtain representative samples from pressurized sources without further emulsification of the liquids. Fig. 12.27 shows a floating piston cylinder used in the procedure. The cylinder is first evacuated and filled with a pressurizing fluid (for example, glycol or a synthetic oil) on one side of the floating piston. The top of the cylinder (evacuated side) is then connected to the sampling location from which the sample is to be taken. The bottom valve on the cylinder is closed and the top valve slowly opened to pressurize the fluid in the cylinder. This is usually a small amount because of the low compressibility of the liquid in the cylinder. Once the top valve is completely open, the bottom valve is opened very slowly to drain the pressurizing liquid while allowing the sample liquid to be taken in from the top into the cylinder. The procedure should be performed slowly to obtain the sample without a pressure drop between the cylinder and the sampling location. Another variation of the method is to charge the sample into a simple cylinder, without a floating piston, filled with water or mercury. Once the sample is captured, the cylinder can be depressurized extremely slowly with little effect on the sample. In situations in which this procedure is not possible, the best sampling method is to bleed the sample line very slowly into the sample container. The idea is to minimize shear and reduce emulsification that may be caused by the sampling procedures.

**12.4.2 Field Emulsion-Treatment Program.** There is a lack of specific case studies on emulsion treatment in the open literature for the following reasons.

- An emulsion treatment program is very site-specific. Each producing system is unique and is reviewed individually for solutions.

- Traditionally, demulsifier selection has been conducted by the chemical service companies, who have been reluctant to part with the information. This has also been, in part, because of the lack of understanding of emulsion treatment.

- Chemical selection has been viewed as a “black art”<sup>5</sup> that has produced as many failures as successes.

- The scope of emulsion treatment is very broad, and it is usually difficult to address the complexities in generalized studies. Parts of the specifics have been reported extensively.

- Most of the operating oil companies have some sort of optimization programs for emulsion treatment. In general, this includes addition of chemicals, heat, and retrofitting.

The design of emulsion-treating equipment and procedures for a given field or application requires experience and engineering judgment. The engineer must rely on laboratory data, data from nearby wells or fields, and experience. There is no standard solution available for striking a balance between, for example, the amount of chemical and heat to resolve emulsions. The greater the treatment temperature, the lower the amount of demulsifier needed. In general, economic analysis dictates the type and size of equipment used and the balance between the amount of chemical used and heating requirements. In some cases, crude oil specifications may decide the system to be used for emulsion treatment. Other factors include internal packing and the size of the equipment. The savings in equipment cost must be balanced against the increased capital and operating costs of the packing or coalescing grids.

Laboratory bottle tests can provide an estimate of treating temperatures and retention times that can be used for design and operation; however, these tests are done under static conditions, and field usage is dynamic. Demulsifier dosages, for example, generally are much greater in the static bottle tests than during field conditions. However, laboratory testing is excellent for screening different emulsion samples for relative tightness, evaluating prospective demulsifiers, and evaluating the effects of different variables on emulsion resolution.

General guidelines for an emulsion-treatment program in the field include the following points.

- Each producing stream is unique and must be evaluated individually to determine the best separation strategy. Laboratory tests should be conducted with actual samples to determine the tightness of the emulsions; however, data from nearby wells and fields can be used as estimates.

- During the early design of the separation facility, planning for future emulsion treatment should begin. For example, if water cuts are anticipated to increase, appropriate measures should be taken in the design phase of the equipment or handling facilities for increased water handling.

- Operational experience and laboratory work are needed to substantiate emulsion concerns and identify solutions. Pilot and plant tests should determine the actual treatment requirements. As noted previously, bottle tests have limitations in determining dosage but are good for screening and trend analysis.

- Treatment capacities can be increased for existing separator trains by re-engineering and retrofitting. For example, internal packing can be installed in the separator for improving emulsion resolution. See the chapter on emulsion treating in the Facilities section of this Handbook for additional details.

- For existing systems, demulsifier and other relevant operational data (production rates, water cuts, temperatures, and costs) should be recorded over time. These data can be useful for analyzing demulsifier dosages (for example, during summer and winter) and unit demulsifier costs and can pinpoint certain activities that may be responsible for emulsion upsets and underlying problems. These data are also very useful for optimization of emulsion-treatment programs.

- The emulsion-treatment program should be reviewed periodically because conditions change. The frequency of evaluation depends on many factors including the relative cost of the demulsifier usage, heating costs, capacity limitations, and manpower requirements.

**12.4.3 Emulsion Prevention.** Emulsions are always a drain on the operating budget. It is almost impossible to eliminate emulsions during crude production; however, emulsion problems can be reduced and optimized by following good operating practices. The following points should be included in operating practices.

- Solids management. Fine solids stabilize emulsions, and efforts should be made to reduce solid contaminants during production. These solids include asphaltenes, which can be controlled by effective asphaltene management, dispersants, etc.; scales, which should be reduced by scale inhibitors; and waxes, which should be controlled with pour-point depressants or heating.

- Reduction of corrosion products. These products can be reduced with effective corrosion inhibitors.

- Acidization. Stimulation with acids can cause very tight emulsions; consequently, acid jobs should be designed with care, and their field performance should be reviewed. To avoid emulsion upsets, the acid job design should incorporate effective demulsifiers at relatively high concentrations, use mutual solvents, and minimize fines and precipitates during acidization.

- Mixing or turbulence. Chokes and other devices such as pumps should be controlled to optimize shear and mixing. While a moderate amount of mixing is necessary and beneficial, severe mixing leads to tight emulsions or even re-emulsification after water separation. Another place to control mixing is in gas lift operations by injecting the optimum amount of gas.

- Compatibility of chemicals. Increasingly, more chemicals are being used for improved oil recovery and crude processing. The chemical may be the source of the emulsion problem. Compatibility studies should be performed with the chemicals that are used during crude oil production (from the reservoir to the separation facilities), and their emulsion-forming tendencies should be evaluated.

**12.4.4 Demulsifier Selection and Optimization.** For an existing facility, important questions include, “Are we using the best demulsifier?” and, “Is my demulsifier usage optimized?” Demulsifier selection is still considered an art that improves with experience; however, there are methods now available to eliminate some of the uncertainties involved in demulsifier screening and selection. The properties of a good demulsifier were addressed previously. How to select the best demulsifier and to optimize its usage is addressed here.

Demulsifier selection should be made with the emulsion-treatment system in mind. Some of the questions to be asked include the following.

- What is the retention time of the emulsion in the equipment?
- What type of emulsion is to be treated?
- What is the water cut?
- Is the system heated, or can it be heated if necessary?
- What is the range of operating temperatures during the summer and winter months?
- Is the feed constant or changing in composition?

As field conditions change, demulsifier requirements also change. Lower temperatures in the winter can induce wax-related and other problems. Well treatments can upset the treatment plant. For example, acidizing a well can result in asphaltenic sludges that may form tight and stable emulsions. Similarly, well workovers and chemical treatments can lead to emulsion-related problems at the treatment facility. The consequences of well treatments and other activities should be anticipated, and the operator should be ready to increase the demulsifier dosage, if necessary. It cannot be expected that the same demulsifier or the same demulsifier dosage will be capable of resolving emulsions when conditions change.

To select a demulsifier for a given system, one generally starts with the bottle tests. Representative emulsion samples are taken and transferred into several centrifuge tubes. Several demulsifiers, usually from different demulsifier vendors, are added to the centrifuge tubes in various amounts, and water-dropout data are collected and analyzed to determine the best demulsifier. Before the tests, the demulsifier vendors can be invited to provide one or two of their

demulsifiers. Most vendors would want to test their chemicals with emulsions from the field before submitting their best candidates. A quantitative method for demulsifier testing was developed recently,<sup>31</sup> and the calculation procedures are described in the Appendix. For selecting the best demulsifier, several sets of tests may be necessary at different concentrations, temperatures, water cuts, etc. The demulsifier dosages obtained in the lab are generally greater than what will be needed in the field. It is highly recommended that the bottle test be conducted with fresh emulsions (i.e., within a few minutes of sampling), because sample aging has a significant effect on demulsifier dosages. During the bottle tests, other factors should be noted: color and appearance of the emulsion, clarity of the water, sediments in the water, presence of a rag layer, and loose solids hanging at the interface. These factors can provide information that may be important during demulsifier selection.

After the bottle tests, two or three promising demulsifiers are selected for field testing. During the field trials, the screened chemicals should be tested at various concentrations, operating temperatures, and settling times and tested for clarity of separated water and, most importantly, the amount of water and salt remaining in the produced crude. It is also a good idea to test the chemicals over a period of time (minimum of 1 to 2 days and longer, if possible) to evaluate the performance and compare it with the incumbent chemical performance. The best demulsifier is the one that produces the fastest, cleanest separation at the lowest possible cost per unit barrel of crude.

The demulsifier concentrations generally range from less than 5 ppm (approximately 1 gal/5,000 bbl) to more than 200 ppm (approximately 8 gal/1,000 bbl). The most common range is between 10 and 50 ppm. Whatever the demulsifier dosage and range, it may be possible to reduce and optimize the demulsifier usage by evaluating various components in the treatment program.

**Proper Demulsifier Mixing.** For the demulsifier to be effective, it must mix intimately with the emulsion and migrate to the film surrounding the water droplets. If the mixing is poor, the demulsifier will be ineffective. Ideally, the demulsifier should be injected in a continuous stream through inline mixers that are sufficiently upstream so that the demulsifier has time to mix thoroughly with the emulsion. Demulsifier slugging should be avoided because it creates localized high concentration regions (an overtreat condition) and promotes re-emulsification. One way to enhance the mixing is to dilute the demulsifier with sufficient quantities of a diluent, generally a solvent, and inject the diluted demulsifier/solvent mixture into the emulsion. The larger quantity of the mixture makes it possible for the chemical to be mixed more uniformly with the emulsion.

Similarly, turbulence enhances the diffusion and dispersion of demulsifier into the emulsion and increases the probability of collisions between water droplets. This turbulence must persist long enough to allow the chemical to reach the interface between the oil and water, but the intensity should not be so severe that it causes further tightening of the emulsion. This level of turbulence is usually provided by normal flow through the emulsion-treating unit that occurs in the pipes, manifolds, valves, and separators. When the flow rates are too low for proper mixing, special care must be taken for mixing the chemical. Special mixers, such as mixing valves, injection quills, kinetic mixers, and vortex mixers, may be installed to ensure proper demulsifier mixing.

The point at which the demulsifier is injected is also important. In general, the further upstream the demulsifier is injected, the better. However, if there is considerable turbulence and shear between the point where the demulsifier is injected and the point where water is removed, it may be worthwhile to reconsider that decision. Another problem with very far upstream injection is the separation of water in the pipes, which can lead to other problems, such as corrosion. In many instances, demulsifier is injected at multiple points to optimize its

overall usage; however, this is an option for high-volume treatment facilities and, here again, the demulsifier-split ratio (between different points) should be optimized by trial and error.

Another problem sometimes ignored is the settling characteristics of the demulsifier. The active ingredients in some demulsifiers tend to settle at the bottom of demulsifier tanks because of insolubility, incomplete mixing, and density differences. If this happens, the surface-active ingredient injection into the treatment facility is erratic. During the first few days of the tank charge and injection, the demulsifier may work satisfactorily; however, subsequent performance may deteriorate as the active ingredients are exhausted and only the carrier solvent is injected. If this cycle is observed, the culprit is the settling of the active ingredients of the demulsifier in the tank. Steps to eliminate settling include installing a mixer in the demulsifier tank or replacing the demulsifier.

**Demulsifier Overdosing.** Overdosing of the chemical can result in enhanced stability of the emulsion, leading to rag layers or pads inside the separators. This is a severe problem because it worsens with increased demulsifier costs. It can be difficult to determine that there is demulsifier overdosing at a treatment facility. One way to reduce overdosing is to conduct field-optimization tests periodically to determine optimum demulsifier rates. These tests are done by going through a series of demulsifier rates at the treatment facility and monitoring the product crude and water characteristics. These trials provide the best demulsifier rates for the facility. A better way to optimize demulsifier rates is by installing automated or semiautomated demulsifier control systems. The control systems receive input from sensors in the treatment facility and take action to increase or decrease the demulsifier rates. The sensors monitor grid voltages in the dehydrator and desalter, emulsion layer inside the separator (monitoring through interface levels), crude and water quality, and operating temperature. The controller can also inject additional demulsifier into the separator inlet during upset conditions to minimize their impact. An automatic controller should always be searching for the minimum demulsifier usage.

**Understanding the Causes of Emulsions.** For larger facilities it may be worthwhile to understand the causes of tight emulsions. Some of the factors that stabilize emulsions, such as fine solids, asphaltenes and waxes, temperature, size of water droplets, pH, brine composition, etc., were highlighted earlier. Some of the factors, such as brine composition and water cuts, cannot be controlled; however, other factors can be controlled. The temperature can be increased by heating the crude or burying/insulating the flowlines. Water droplet sizes can be increased by reducing mixing or shearing. Organic precipitates can be eliminated with dispersants and specialty chemicals. The first task is to diagnose the causes. Understanding the causes leads to better decisions for controlling the demulsifier usage. Several investigative case studies have been reported for understanding the causes of tight emulsions<sup>16,31,48</sup> and optimizing demulsifier usage.

**Evaluating the Process.** A thorough evaluation of the emulsion-treatment facility may be worthwhile for optimizing costs. Some of the factors to explore include the extent of agitation, wash-water rates, electrostatic grid voltages, retention times, and separator internals.

**Agitation.** Some agitation is necessary to mix the demulsifier into the bulk of the emulsion. Agitation is also necessary for the water droplets to collide, increasing the probability of their coalescence. However, every effort should be taken to prevent excessive agitation because this may lead to further emulsification. In other words, a moderate level of agitation is required, and excessive turbulence should be avoided. Demulsification can be assisted by the use of plate packing or baffles inside the separators. These baffle plates distribute the emulsion evenly and cause gentle agitation, which assists in the coalescing of droplets. The surface of the plates also helps in drop coalescence.

**Retention Time.** The gentle agitation necessary after the mixing of the demulsifier should be followed by a period of quiescent settlement to enhance coalescence, generally by gravity

**TABLE 12.1—DEMULSIFIER OPERATIONAL DATA FOR A WET-CRUDE HANDLING FACILITY**

Month	Oil Rate (1,000 BOPD)	Water Rate (1,000 BWPD)	Total Rate (1,000 B/D)	T (°F)	Water Cut (%)	Demulsifier Rate (gal/D)	Demulsifier Concentration (ppm)	Demulsifier Cost (\$/thousand bbl)
January	133.0	17.0	150.0	75.8	11.3	114.4	18.2	4.12
February	135.6	18.8	154.4	74.4	12.2	115.0	17.7	4.02
March	145.4	20.4	165.8	79.2	12.3	96.2	13.8	3.13
April	107.2	18.8	126.0	83.0	14.9	69.2	13.1	2.97
May	128.6	20.8	149.4	93.5	13.9	73.6	11.7	2.66
June	138.4	22.0	160.4	94.8	13.7	79.2	11.8	2.67
July	138.8	18.6	157.4	94.8	11.8	76.3	11.5	2.62
August	122.6	19.2	141.8	96.2	13.5	68.6	11.5	2.61
September	137.8	20.0	157.8	97.4	12.7	85.6	12.9	2.93
October	112.2	18.2	130.4	91.4	14.0	81.9	15.0	3.39
November	133.0	21.0	154.0	84.9	13.6	94.6	14.6	3.32
December	138.2	18.6	156.8	79.8	11.9	115.0	17.5	3.96

settling. This relates to the retention time of the fluid in the separator and the dimensions of the vessel.

**Electrostatic Coalescing.** Drop coalescence can be assisted by the application of a high-voltage electric field to the emulsion. This is particularly beneficial for polishing the oil and reducing the oil's water content to very low levels (less than 0.5%). Electrostatic coalescing works by charging the water droplets and increasing the frequency of their collision, which improves their chance of coalescence.

**Maintaining a Database on Usage and Costs.** Experience and demulsifier data are important because they can be used to optimize usage. Typical data to maintain in a database include oil and water rates, temperatures, demulsifier rates, demulsifier costs, and comments regarding any changes that were made in the treatment facilities. **Table 12.1** provides typical data for an operating wet-crude handling facility. Such data can be analyzed to diagnose demulsifier-usage problems. They can also be used as a base to compare the results for new and experimental demulsifiers. Furthermore, they provide a quick, easy reference for understanding the seasonal variation in consumption, causes of upsets, or increased demulsifier usage.

### Nomenclature

- $a$  = factor for the type of emulsion
- $e$  = exponential function
- $g$  = acceleration caused by of gravity,  $L/t^2$ ,  $m/s^2$
- $I$  = emulsion separation index, %
- $n$  = number of experiments
- $r$  = radius of the droplets, L, m
- $T$  = temperature, T, °F
- $v$  = settling velocity of the water droplets, L/t, m/s
- $W$  = water separation at a given demulsifier concentration/time as a percentage of BS&W
- $\delta$  = contact angle, degrees
- $\mu$  = viscosity, m/Lt, cp
- $\mu_e$  = viscosity of emulsion, m/Lt, cp
- $\mu_o$  = viscosity of clean oil at same temperature, m/Lt, cp

$\rho_w$  = density of water, m/L<sup>3</sup>, lbm/ft<sup>3</sup>

$\rho_o$  = density of oil, m/L<sup>3</sup>, lbm/ft<sup>3</sup>

$\Phi$  = water cut or fraction of water

## Acknowledgments

This chapter is based on a literature review conducted at Saudi Aramco as part of a Ghawar Emulsion Study Team with contributions from Mohammad Abdulmoghini, Bob Hintermeier, and Edward Chen. Review of the chapter by Henry Halpern and Martin Wingrove of Saudi Aramco is also acknowledged.

## References

1. *Encyclopedia of Emulsion Technology*, Becher, P. (ed.), Vol. 1, Dekker, New York (1983).
2. *Encyclopedia of Emulsion Technology*, Becher, P. (ed.), Vol. 2, Dekker, New York (1985).
3. *Encyclopedia of Emulsion Technology*, Becher, P. (ed.), Vol. 3, Dekker, New York (1988).
4. Becher, P.: *Emulsions: Theory and Practice*, second edition, Advances in Chemistry Series No. 162, American Chemical Soc., Washington, DC (1966).
5. *Emulsions: Fundamentals and Applications in the Petroleum Industry*, L.L. Schramm (ed.), Advances in Chemistry Series No. 231, Washington, DC (1992).
6. Manning, F.S. and Thompson, R.E.: "Water-in-Crude-Oil Emulsions," *Oilfield Processing* (1994) **2**.
7. Schubert, H. and Armbroster, H.: "Principles of Formation and Stability of Emulsions," *Intl. Chem. Eng.* (1992) **32**, No. 1, 14.
8. Tambe, D.E. and Sharma, M.M.: "Factors Controlling the Stability of Colloid-Stabilized Emulsions," *J. of Colloid Interface Science* (1993) **157**, 244.
9. *Thin Liquid Films*, I.B. Ivanov (ed.), Surfactant Science Series, Dekker, New York (1988).
10. Mohammad, R.A. *et al.*: "The Effect of Demulsifiers on the Interfacial Rheology and Emulsion Stability of Water-in-Crude Oil Emulsions," *Colloids and Surfaces A: Physicochemical and Engineering Aspects* (1994) **91**, 129.
11. Chen, G. and Towner, J.W.: "Study of Dynamic Interfacial Tension for Demulsification of Crude Oil Emulsions," paper SPE 65012 presented at the 2001 SPE International Symposium on Oilfield Chemistry, Houston, 13–16 February.
12. Jones, T.J., Neustadter, E.L., and Wittingham, K.P.: "Water-in-Crude Oil Emulsion Stability and Emulsion Destabilization by Chemical Demulsifiers," *J. Cdn. Pet. Tech.* (April–June 1978) 100.
13. Strassner, J.E.: "Effect of pH on Interfacial Films and Stability of Crude Oil-Water Emulsions," *JPT* (March 1968) 303.
14. Kimbler, O.K., Reed, R.L., and Silberberg, I.H.: "Physical Characteristics of Natural Films Formed at the Crude Oil-Water Interfaces," *JPT* (June 1966) 153.
15. Bobra, M.: "A Study of the Formation of Water-in-Oil Emulsions," *Proc.*, 1990 Arctic and Marine Oil Spill Program Technical Seminar, Edmonton, Canada (1990).
16. Kokal, S.L. and Al-Juraid, J.I.: "Quantification of Various Factors Affecting Emulsion Stability: Water Cut, Temperature, Shear, Asphaltene Content, Demulsifier Dosage and Mixing Different Crudes," paper SPE 56641 presented at the 1999 SPE Annual Technical Conference and Exhibition, Houston, 3–6 October.
17. Svetgoff, J.A.: "Demulsification Key to Production Efficiency," *Petroleum Engineer Intl.* (1989) **61**, No. 8, 28.
18. Eley, D.D., Hey, M.J., and Symonds, J.D.: "Emulsions of Water in Asphaltene Containing Oils," *Colloids & Surfaces* (1998) **32**, 87.
19. Kokal, S.L. and Sayegh, S.G.: "Asphaltenes: The Cholesterol of Petroleum," paper SPE 29787 presented at the 1995 Middle East Oil Show, Bahrain, 11–14 March.
20. Michell, D.L. and Speight, J.G.: "The Solubility of Asphaltenes in Hydrocarbon Solvents," *Fuel* (1973) **53**, 149.

21. Leontaritis, K.J. and Mansoori, G.A.: "Asphaltene Deposition: A Comprehensive Description of Problem Manifestations and Modeling Approaches," paper SPE 18892 presented at the 1998 SPE Production and Operations Symposium, Oklahoma City, Oklahoma, 13–14 March.
22. Salager, J.L.: "The Fundamental Basis for the Action of a Chemical Dehydrant: Influence of Physical and Chemical Formulation on the Stability of an Emulsion," *Intl. Chemical Engineering* (1990) **30**, No. 1, 103.
23. Menon, V.B. and Wasan, D.T.: "Particle-Fluid Interactions With Applications to Solid-Stabilized Emulsions Part III. Asphaltene Adsorption in the Presence of Quinaldine and 1,2-Dimethylindole," *Colloids & Surfaces* (1987) **23**, 353.
24. Kokal, S. and Al-Juraid, J.I.: "Reducing Emulsion Problems by Controlling Asphaltene Solubility and Precipitation," paper SPE 48995 presented at the 1998 SPE Annual Technical Conference and Exhibition, New Orleans, 27–30 September.
25. Davies, G.A., Nilsen, F.P., and Gramme, P.E.: "The Formation of Stable Dispersions of Crude Oil and Produced Water: The Influence of Oil Type, Wax, and Asphaltene Content," paper SPE 36587 presented at the 1996 Annual Technical Conference and Exhibition, Denver, 6–9 October.
26. Levine, S. and Sanford, E.: "Stabilization of Emulsion Droplets by Fine Powders," *Canadian J. Chemical Engineering* (1985) **62**, 258.
27. Menon, V.B., Nikolov, A.D., and Wasan, D.T.: "Interfacial Effects of Solids-Stabilized Emulsions: Measurements of Film Tension and Particle Interaction Energy," *J. of Colloid and Interface Science* (July 1988) **124**, No. 1, 317.
28. Coppel, C.P.: "Factors Causing Emulsion Upsets in Surface Facilities Following Acid Stimulation," *JPT* (September 1975) 1060.
29. Ali, S.A., Durham, D.K., and Elphingstone, E.A.: "Test Identifies Acidizing Fluid/Crude Compatibility Problems," *Oil & Gas J.* (March 1994) 47.
30. Moore, E.W., Crowe, L.W., and Hendrickson, A.R.: "Formation, Effects, and Prevention of Asphaltene Sludges During Stimulation Treatments," *JPT* (September 1965) 1023.
31. Kokal, S.L. and Wingrove, M.D.: "Emulsion Separation Index: From Laboratory to Field Case Studies," paper SPE 63165 presented at the 2000 SPE Annual Technical Conference and Exhibition, Dallas, 1–4 October.
32. Miller, D.J. and Bohm, R.: "Optical Studies of Coalescence in Crude Oil Emulsions," *J. of Petroleum Science and Engineering* (1993) **9**, 1.
33. Ajienka, J.A., Ogbe, N.O., and Ezeamiekwe, B.C.: "Measurement of Dielectric Constant of Oilfield Emulsions and its Application to Emulsion Resolution," *J. of Petroleum Science and Engineering* (1993) **9**, 331.
34. Isaacs, E.E. *et al.*: "Electroacoustic Method for Monitoring the Coalescence of Water-In-Oil Emulsions," *Colloids & Surfaces* (1990) **46**, No. 2, 177.
35. Aske, N., Kallevik, H., and Sjoblom, J.: "Water-in-Crude Oil Emulsion Stability Studied by Critical Electric Field Measurements. Correlation to Physicochemical Parameters and Near-Infrared Spectroscopy," *J. of Petroleum Science and Engineering* (2002) **36**, No. 1, 1.
36. *Petroleum Engineering Handbook*, H.B. Bradley (ed.), SPE, Richardson, Texas (1987) 19–26.
37. Marquez-Silva, R.L. *et al.*: "Chemical Dehydration: Correlations Between Crude Oil, Associated Water and Demulsifier Characteristics in Real Systems," paper SPE 37271 presented at the 1997 SPE International Symposium on Oilfield Chemistry, Houston, 18–21 February.
38. Berger, P.D., Hsu, C., and Arendell, J.P.: "Designing and Selecting Demulsifiers for Optimum Field Performance Based on Production Fluid Characteristics," *SPEPE* (1988) 522.
39. Aveyard, R. *et al.*: "The Resolution of Water-in-Crude Oil Emulsions by the Addition of Low Molar Mass Demulsifiers," *J. of Colloid Interface Science* (1990) **139**, 128.
40. Yang, M., Stewart, A.C., and Davies, G.A.: "Interactions Between Chemical Additives and Their Effect on Emulsion Separation," paper SPE 36617 presented at the 1996 SPE Annual Technical Conference and Exhibition, Denver, 6–9 October.
41. Sjoblom, J. *et al.*: "Water-in-Crude Oil Emulsions from the Norwegian Continental Shelf: Part II Chemical Destabilization and Interfacial Tensions," *Colloids & Polymer Science* (1990) **268**, No. 4, 389.
42. Mohammad, R.A. *et al.*: "Dewatering Crude Oil Emulsions. 3 Emulsion Resolution by Chemical Means," *Colloids & Surfaces: Physicochemical and Engineering Aspects* (1994) **83**, 261.



43. Sjoblom, J. *et al.*: “Water-in-Crude Oil Emulsions: Formation, Characterization and Destabilization,” *Progress in Colloid and Polymer Science* (1990) **82**, 131.
44. Krawczyk, M.A., Wasan, D.J., and Shetty, C.S.: “Chemical Demulsification of Petroleum Emulsion Using Oil Soluble Demulsifier,” *Industrial and Engineering Chemistry Research* (1991) **30**, No. 2, 367.
45. Bhardwaj, A. and Hartland, S.: “Dynamics of Emulsification and Demulsification of Water-in-Crude Oil Emulsions,” *Industrial and Engineering Chemistry Research* (1994) **33**, 1271.
46. Manek, M.B.: “Asphaltene Dispersants as Demulsification Aids,” paper SPE 28972 presented at the 1995 SPE International Symposium on Oilfield Chemistry, San Antonio, Texas, 14–17 February.
47. Singh, B.P.: “Performance of Demulsifiers: Prediction Based on Film Pressure Area Isotherm and Solvent Properties,” *Energy Sources* (1994) **16**, 377.
48. Kokal, S.L. *et al.*: “Very Thick Crude Emulsions: A Field Case Study of a Unique Crude Production Problem,” paper SPE 71467 presented at the 2001 SPE Annual Technical Conference and Exhibition, New Orleans, 30 September–3 October.

### Appendix A—Emulsion Separation Index (ESI) Test

The emulsion bottle test is a quantitative method for demulsifier testing and involves the following procedure.

- The crude oil emulsion sample is tested as soon as possible after it is received in the lab. The pressurized method for sampling the emulsion is recommended. The samples are remixed with a standard bottle shaker for approximately a minute. The same amount of shaking should be used in all tests.
- The mixed emulsion sample is added to 100-ml standard centrifuge tubes.
- The centrifuge tubes are placed in a water bath for a minimum of 30 minutes to reach the desired temperature.
- The required dosage of the chemical is added to the centrifuge tubes. The amount of chemical is based on the total amount of emulsion (oil and water).
- The tubes are shaken by hand a given number of times (approximately 20 shakes) and placed in the water bath at the desired temperature.
- The amount of water separated is measured with time (5, 10, 15, and 20 minutes).
- After 20 minutes, the tubes are centrifuged for another 20 minutes at the desired temperature, and the final amounts of water and emulsion or rag layer are measured.
- Generally, these experiments should be done in sets to investigate the effect of certain variables. All efforts should be made to keep all the variables constant except the one under investigation.

The ESI is then calculated from the measured oil/water separation data.

$$I = \frac{\sum W}{\sum n}, \dots\dots\dots (A-1)$$

where  $I$  = emulsion separation index,  $W$  = water separation at a given demulsifier concentration/time as a percentage of BS&W, and  $n$  = number of experiments.

#### 12.A1 Notes

- Direct comparison of demulsifier dosage obtained in the laboratory with field observations should always be made with caution because the laboratory experiments are made under static conditions, and field usage observations are made under dynamic conditions. Furthermore, ESI tests are done on dead crude, while field usage tests are on live (gas dissolved) crudes. However, laboratory testing is excellent for screening wellhead samples for relative emulsion tightness; evaluating prospective demulsifiers; and evaluating the effects of different variables on

Demulsifier	Volume Separated With Time				After Centrifuge	BS&W (%)
	5 min.	10 min.	15 min.	20 min.		
P	0.0	0.0	1.3	3.2	26	26
C	0.0	3.8	12.5	18.0	26	26
A	11.0	14.5	17.5	19.0	24	24
AB	11.5	20.5	23.0	23.5	25	25

Demulsifier	Water Separation Percentage				After Centrifuge	ESI (%)
	5 min.	10 min.	15 min.	20 min.		
P	0	0.00	5.00	12.31	100	23.46
C	0	14.62	48.08	69.23	100	46.38
A	45.83	60.42	72.92	79.17	100	71.67
AB	46.00	82.00	92.00	94.00	100	82.80

emulsion resolution because all the conditions are kept constant except the variable under investigation.

- Although ESI quantifies the bottle tests, it has a qualitative edge and has a range of reproducibilities because of several possible errors. These possible errors include sampling error, operator error, inability to read the level of water separated properly because the oil has a tendency to stick to the glass, and temperature error.
- There is a definite effect of aging. The longer an emulsion (oil/water mixture) stays in the lab before testing, the higher the demulsifier dosage required to break it; therefore, for best results, ESI tests should be done on fresh emulsion samples.

**Example 12.A.1** Given the data in [Tables A-1](#) and [A-2](#), calculate the ESI for Demulsifier C.

*Solution.* Eq. A-1 can be used to give

$$I = \frac{(0 + 3.8 + 12.5 + 18 + 26)}{26 \times 5} \times 100 = 46.38.$$

### SI Metric Conversion Factors

cp	× 1.0*	E-03	=Pa·s
ft <sup>3</sup>	× 2.831 685	E-02	=m <sup>3</sup>
°F	(°F-32)/1.8		=°C
lbm	× 4.535 924	E-01	=kg

\*Conversion factor is exact.

## Chapter 13

### Rock Properties

**M. Batzle**, Colorado School of Mines, **D.-H. Han**, U. of Houston, and **R. Hofmann**, Colorado School of Mines

#### 13.1 Introduction

Rock and fluid properties provide the common denominator around which we build the models, interpretations, and predictions of petroleum engineering, as well as geology and geophysics. We consider here the properties of sedimentary rocks, particularly those that make up hydrocarbon reservoirs. Usually, these consist of sandstones, limestones, and dolomites. We must be more inclusive, and consider rocks such as shales, evaporates, and diatomites because these provide the seals, bounding materials, or source rocks to our reservoirs. It is important to note that shales and claystones make up the most abundant rock type in the typical sedimentary column. Features such as seismic signature depend as much on the enclosing shale as on the reservoir sands.

In this chapter, we will tabulate important mineral and rock properties, and provide many of the mathematical models used to describe and predict properties. Much of this summary is drawn upon the extensive work and compilations already available. As examples, Clark<sup>1</sup> provides an extensive list of mineral and rock properties; Birch<sup>2</sup> presents tables of compressional velocities, and Gregory<sup>3</sup> gives a detailed overview of the use of rock property information in seismic interpretation. Castagna *et al.*<sup>4</sup> focused on rock properties for use in amplitude versus offset analyses. Useful handbooks on this topic include Carmichael<sup>5</sup> and Lama and Vutukuri.<sup>6,7</sup> Probably the best reference covering a wide range of rock property formulas and models is Mavko *et al.*<sup>8</sup> These references can be consulted for details not presented here.

**13.1.1 Knowledge of Rock Properties Is Largely Empirical.** Many theoretical models have been developed to predict or correlate specific physical properties of porous rock. Most theoretical models are built on simplified physical concepts: what are the properties of an ideal porous media. However, in comparison with real rocks, these models are always oversimplified (they must be, to be solvable). Most of these models are capable of “forward modeling” or predicting rock properties with one or more arbitrary parameters. However, as is typical in Earth science, our models cannot be inverted from measurements to predict uniquely real rock and pore-fluid properties. Many efforts have been made and will continue to be made to build porous rock models, but progress is very limited. Some of the most fundamental questions are still unanswered.

<b>TABLE 13.1—RELATIVE MERITS AND PROBLEMS ASSOCIATED WITH SEVERAL ROCK AND FLUID MEASUREMENT TECHNIQUES</b>	
<u>In-Situ Measurements (e.g., Logs, Crosswell, VSP, and Seismic Data)</u>	
<u>Advantages</u>	
	In-situ stress conditions
	In-situ temperature
	In-situ pore fluids
	Undisturbed fabric
	Wider coverage
<u>Disadvantages</u>	
	Numerous unknown parameters
	Fluids, stress, lithology, homogeneity, anisotropy, etc.
	Unknown geometry
	Disturbed zones
	Low resolution or restricted zone of measurement
<u>Laboratory (Core) Measurements</u>	
<u>Advantages</u>	
	Controlled conditions
	Determined pore fluids
	Characterized fabric
	Multiple measurements
	Varied experimental scenarios
<u>Disadvantages</u>	
	Disturbed samples
	Stress-relief, pore fluid loss, fabric disturbance
	Poorly reproduced in-situ conditions
	Incomplete characterization
	Expense and time

To establish the basic relationships between physical properties and rock parameters, laboratory investigations are made. Laboratory measurements of rock samples can provide controlled conditions and high data quality (“hard data”). These relationships can be extended to a larger scale, or can even be made scaleless. Typically, models and relations based on laboratory data are then applied to in-situ measurements to derive the parameters we actually need (say, permeability) from information we can actually collect (say, density and gamma ray radiation). The relative merits and problems associated with several rock and fluid measurement techniques are presented in [Table 13.1](#).

Although many empirical relationships already have been established, when facing a frontier basin, new development areas, or untested portions of known formations, valid prediction of rock properties usually requires core data (including “sidewall” plugs). For many applications, standard trend data may not be adequate. A broad investigation is needed.

**13.1.2 A Philosophy for Rock Properties.** Many of the factors affecting rock properties are incompletely ascertained. For example, acoustic velocities can be affected by numerous parame-

ters, many of which cannot be measured. In addressing a rock physics problem, the following aspects should be remembered:

- There may be no exact solution.
- Rock properties are controlled by rock parameters, and these physical correlations can be examined and recognized (although perhaps not understood).
- Often nature gives us a break. At certain conditions, relationships between the rock properties and rock parameters can be simplified (such as Archie's Law).
- We usually must settle on imperfect solutions with some uncertainty. Statistical trends or high and low bounds might be used to handle the uncertainty.
- Every measurement is, to some degree, wrong. The question is: Can we tolerate the errors and understand how they propagate through our analyses?

We will begin this chapter with a suite of definitions and examples, then move on to data and models of individual properties. By necessity, we will be restricted in the material we can cover in a single chapter. As a result, we will not go into many details of rock fabrics and petrography. Also, with a few exceptions, the information provided here assumes that rocks are homogeneous and isotropic.

### 13.2 Rocks: Minerals Plus Pores

Rocks are defined for our purposes as aggregates or mixtures of minerals plus pores. The three general rock types are classified as igneous, metamorphic, and sedimentary. Although hydrocarbon reservoirs have been found in all three rock types, we will consider here primarily sedimentary rocks, by far the most common rocks associated with hydrocarbons.

Minerals are defined as naturally occurring solids: They have a definite structure, composition, and suite of properties that are either fixed or vary systematically within a definite range. Although there are dozens of elements and hundreds of described minerals available in the Earth's crust, the actual number that we must concern ourselves with for reservoir engineering purposes is remarkably small. Classification can be broken into silicates, carbonates, sulfates, sulfides, and oxides. In addition, "solid" organic mixtures such as coal or bitumen can be abundant. Common sedimentary silicates include quartz, feldspars, micas, zeolites, and clays. Carbonates usually consist of calcite and dolomite, although siderite may be present. Gypsum and anhydrite are the most common sulfates, with pyrite the typical sulfide. Oxides are usually materials such as magnetite and hematite. For most of our purposes, we can further restrict our attention to the subset of quartz, feldspars, clays, calcite, dolomite, and anhydrite. A working knowledge of six or so minerals fulfills most engineering needs.

Clays represent an entire family of minerals with widely differing properties. This situation is compounded by the fact that clays are among the most abundant minerals in the sedimentary section. Clays are also problematic because their properties can vary with the in-situ pressure, temperature, and chemical environment. These issues have led to an unfortunate bias against clays when measuring or describing rocks. A "clean" sand, for example, is one that has little or no clay. "Dirty" sandstones or limestones have significant amounts of clay. Clays and their influence on rock properties remain poorly understood and continue to be an area requiring intensive research.

The properties of primary engineering interest are often controlled more by the rock fabric than by the bulk composition. The "holes" are usually more important than the mineral frame. With the following few examples, we will see many of the most common sedimentary rock forms and textures. Numerous attempts have been made to extract rock properties from images of the rock and pore space.<sup>9-11</sup> These techniques often work well, but depend on the observation scale, representative nature of the image, and internal heterogeneity.

A thin section of clean sandstone is shown in **Fig. 13.1**. Under plane-polarized light, quartz grains appear white and pores are stained blue. This is a high-porosity, friable sample that has not undergone substantial consolidation. Silica cement can be seen coating the individual grains

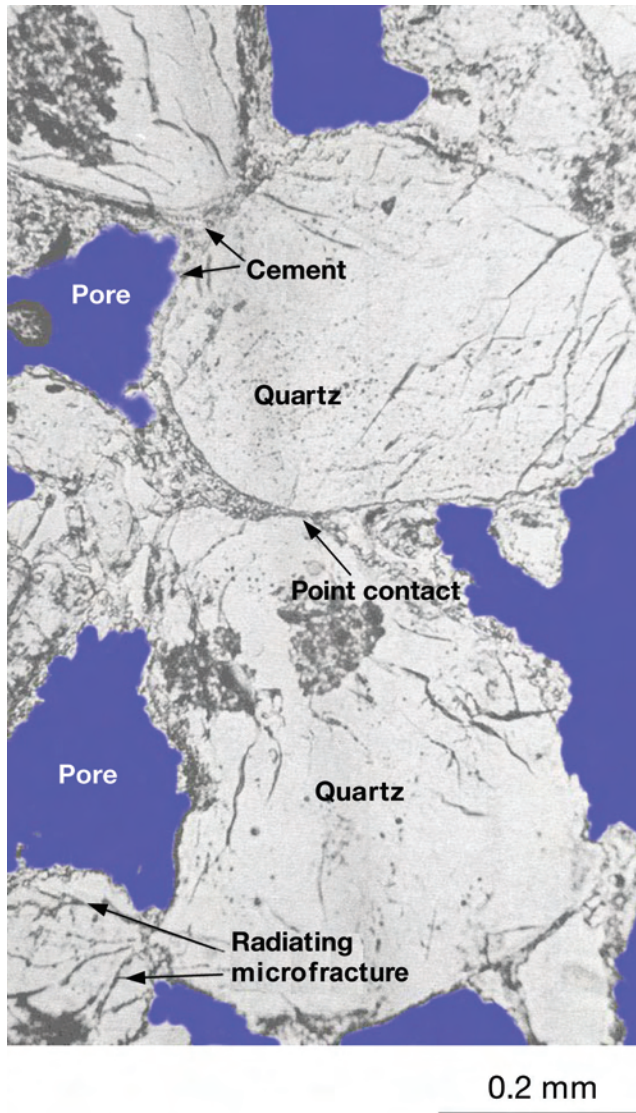


**Fig. 13.1—Common sandstone textures include point contacts, cements, and microfractures. These microstructures determine the properties of the rock on a whole.**

and bonding the largely unchanged, rounded quartz grains. Grain-to-grain stress is indicated by the fractures radiating from points of grain contact. Although these fractures have a relatively small volume, they have a disproportionately large influence on the mechanical properties, particularly the pressure dependence. With continued diagenesis, quartz grains typically would become intergrown, and large amounts of cement would develop, reducing the pore volume.

A Scanning Electron Microscope (SEM) image of another sandstone is seen in [Fig. 13.2](#). A higher degree of compaction is indicated here by the intergrown, sutured contacts of the quartz grains (gray areas). A grain undergoing alteration (a) as well as some of the matrix quartz (b) contain isolated, ineffective porosity. Fractures are again present, particularly near point of grain contact. Many of these fractures, however, may be caused by stress relief as the sample was cored, or by the cutting and polishing. The most obvious features are the contorted and rotated mica grains (d). These micas were crushed due to compaction, and now host numerous

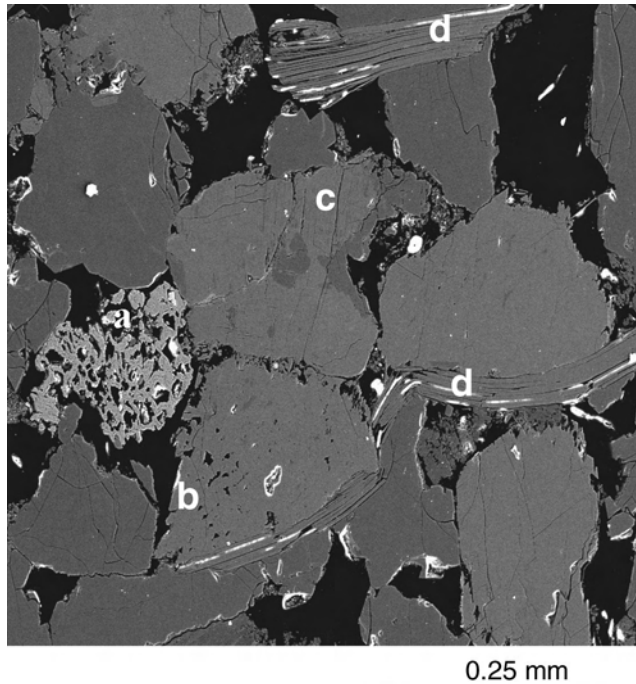


**Fig. 13.2—Scanning electron microscope (SEM) image of sandstone AT49 showing numerous compaction features. Some grains are either altering (a) or have internal, ineffective porosity (b). Fractures (c) cut numerous grains. Mica plates (d) are rotated and crushed, forming parallel sets of microfractures.**

sets of parallel fractures. Some diagenetic clays are also beginning to grow in the pore spaces and act as a cement.

A cementation “front” is visible in [Fig. 13.3](#). Cements come in a wide variety of forms. Open pores are black in the SEM image. In this case, the lighter gray calcite has filled the pores in the lower portion of the image. Unlike the dispersed silica and clay cements seen in the previous figures, the calcite is deposited with an abrupt front. This kind of texture is common for carbonate cements in sands and is probably caused by the availability of crystal nucleation sites available to a slightly supersaturated pore fluid. We would obviously expect vastly different properties of the uncemented vs. cemented portions separated by only a few grain diameters. This rock is an example of the extreme heterogeneity that can frequently occur even within the same small geologic unit of the same formation.

Carbonates can have extremely complex textures resulting from the mixture of fossils and matrix building the rock. In [Fig. 13.4](#), an optical image demonstrates the multitude of forms that can be present. Shell fragments appear as crescent shapes in cross section. Much of the material between fragments can be filled with carbonate mud, reducing the porosity substantially. In this sample, bulk porosity is dominated by the larger disconnected vugs. Such vugs can occur as parts of fossils or as a result of chemical dissolution after deposition. Here, a coating of crystals has grown on the vug surfaces. Because of the wide range of sizes, shapes, and compositions that can occur in carbonate rocks, they are often difficult to characterize with core or even log sampling.

Dolomites are usually formed by recrystallization of original aragonite or calcite crystals in sediments. Magnesium in the pore fluids replace some of the calcium, forming a Mg-Ca carbonate structure. Because of the greater density of dolomite, this transformation can include a porosity increase. Sometimes, the replacement can be subtle, and original sedimentary struc-

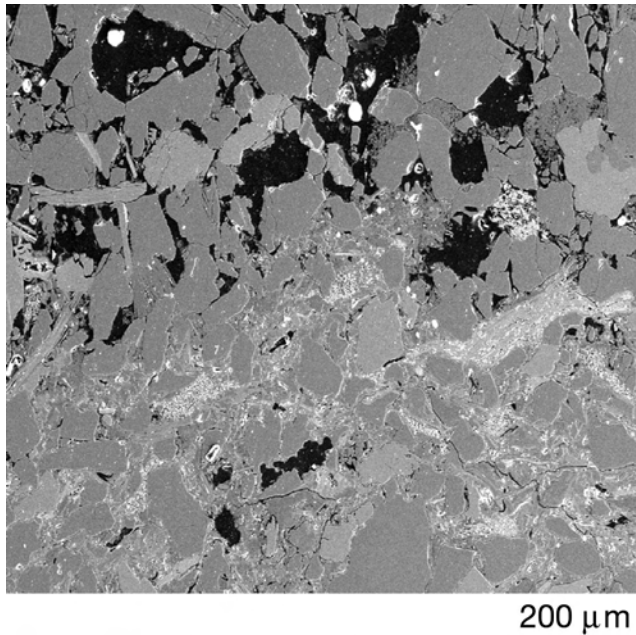


**Fig. 13.3—SEM image of sandstone AT41 showing a progressing calcite cementation front.**

tures and fossil forms can be preserved. Often, however, the recrystallization largely destroys the original rock fabric and rhombohedral dolomite crystals appear, as at (a) in [Fig. 13.5](#). The other intergrown dolomite crystals form porosity that is polygonal. In this sample, many of the pores are coated (b) with pyrobitumin, a complex organic material similar to coal. This pyrobitumen is sometimes incased within dolomite crystals. In this case, it will lower the apparent grain density and strength of the rock.

As mentioned, clays are among the most abundant minerals. These minerals can influence or control physical properties to a major degree. In addition, many clays are sensitive to the environment and will change properties and forms under different conditions. An example of such “sensitive” clay fabrics is shown in [Fig. 13.6](#). Note that the scale is much finer here than in previous figures. In [Fig. 13.6a](#), chlorite originally coats the quartz grains. On top of the chlorite, a smectite coating was developed. This core sample was allowed to dry, and the smectite collapsed, forming long slender columns in the pore space. Resaturating the rock with distilled water allowed the smectite coating to expand and fill the pore space ([Fig. 13.6b](#)). The closed pores will obviously have different fluid-flow characteristics. In this case, we cannot assume the mineral in is a passive, inert solid. This rock will change properties according to pore fluid chemistry.

The most common sedimentary rock types are shales and silts. In [Fig. 13.7](#), white quartz grains float in the surrounding clay matrix. Black organic material in thin layers indicates the horizontal bedding. As a result, this rock has properties that vary strongly with direction and are thus anisotropic. This material could serve as both a source rock and reservoir seal. This sample demonstrates how a mudstone or shale could have a complex composition. Although clays typically make up a large portion of fine-grained rocks, terms such as “clay” and “shale” are not synonymous.

Most sedimentary rocks have porosities under 0.50 (fractional). This is easy to understand, particularly with coarser clastic sediments, in which open grain packings that can support a matrix framework have maximum porosities around 0.45. Exceptions to this and other general-



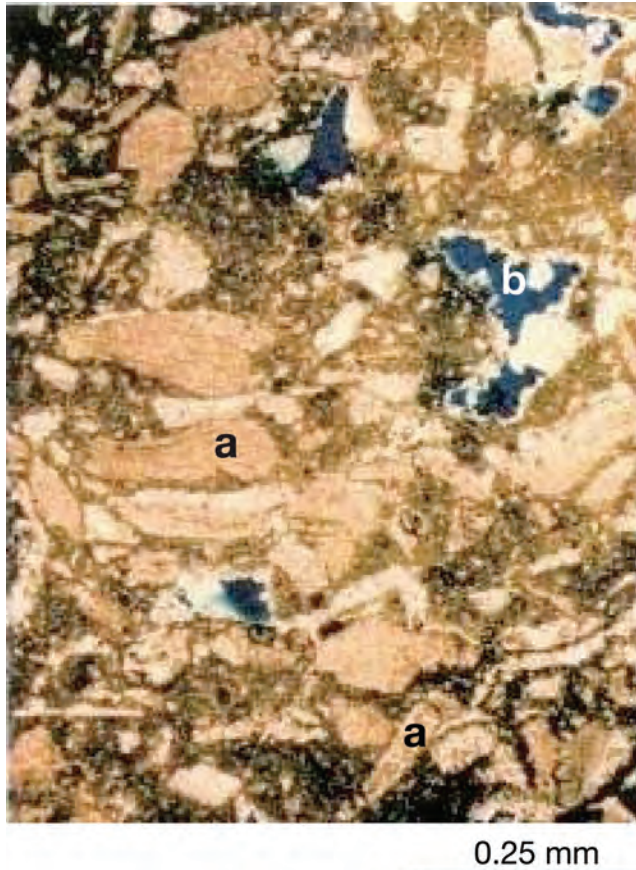


**Fig. 13.4—Thin-section image of carbonate textures; in this limestone, numerous curved shell fragments [e.g., at (a)] are packed together and bound by a fine-grained lime mud. Calcite crystals (b) are growing into the pore spaces.**

izations can occur, and an example is shown in [Fig. 13.8](#). This globigerina “ooze” is composed largely of the small shells or tests of organisms. The matrix mud fills the region between tests, but interiors remain empty. In addition, the tests themselves are porous. As a result, porosities can be as high as 0.8. Despite these huge porosities, because of the isolated nature of the pores, permeability can be in the microdarcy range. A similar situation often occurs in shallow clay-rich sediments where the open clay plate structure results in initial very high porosities. In the remainder of this chapter, however, these types of sediments will be considered exceptional and will not be included in our analyses.

The rock images shown in these several figures are meant to convey a feel for the types of textures common in sedimentary rocks, and that influence physical properties. We will refer back to these images later in the chapter. These few images can in no way be considered a complete description of rock textures. For a more thorough treatment, the reader should consult one of the standard petrography texts or pertinent papers.<sup>12–14</sup>

### 13.3 Density and Porosity

**13.3.1 Basics and Definitions.** Density is defined as the mass per volume of a substance.

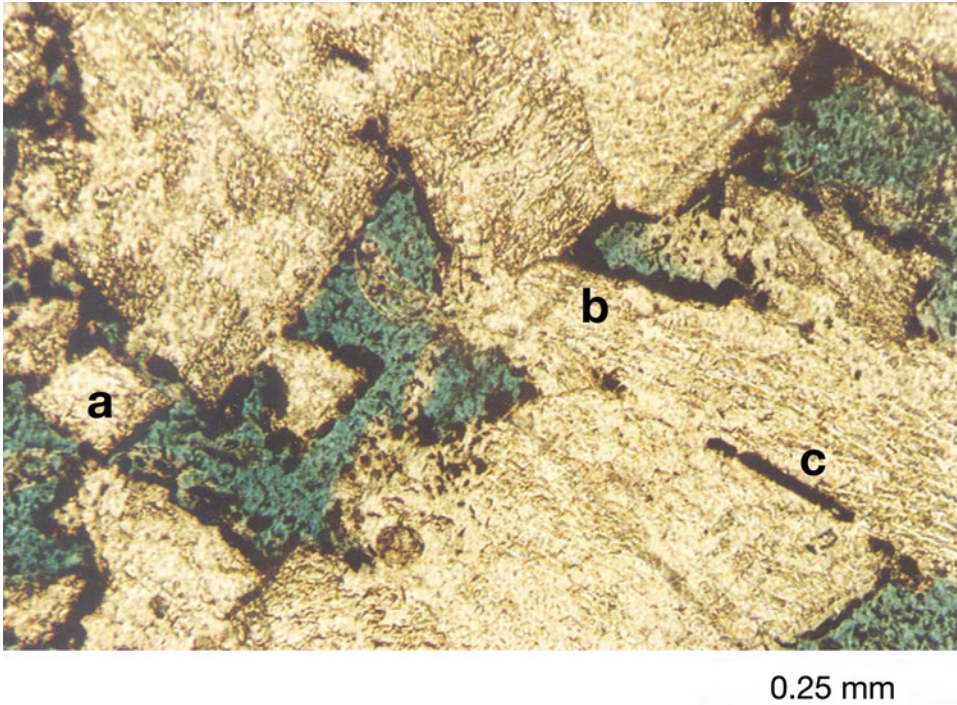


**Fig. 13.5—Thin-section image of a dolomite. Dolomite rhombohedra (a) are common. Within the pore space and between grains are black layers of phytobitumen (b and c).**

$$\text{Density} = \frac{\text{Mass}}{\text{Volume}} = \rho, \dots\dots\dots (13.1)$$

typically with units of g/cm<sup>3</sup> or kg/m<sup>3</sup>. Other units that might be encountered are lbm/gallon or lbm/ft<sup>3</sup> (see [Table 13.2](#)).

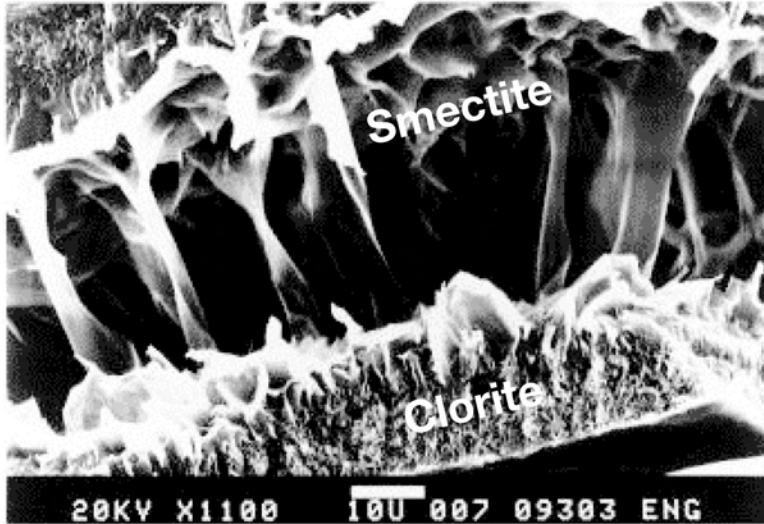
For simple, completely homogeneous (single-phase) material, this definition of density is straightforward. However, Earth materials involved in petroleum engineering are mixtures of several phases, both solids (minerals) and fluids. Rocks, in particular, are porous, and porosity is intimately related to density. For rocks, porosity ( $\Phi$ ) is defined as the nonsolid or pore-volume fraction.

$$\text{Porosity} = \frac{\text{Pore Volume}}{\text{Total Volume}} = \Phi, \dots\dots\dots (13.2)$$

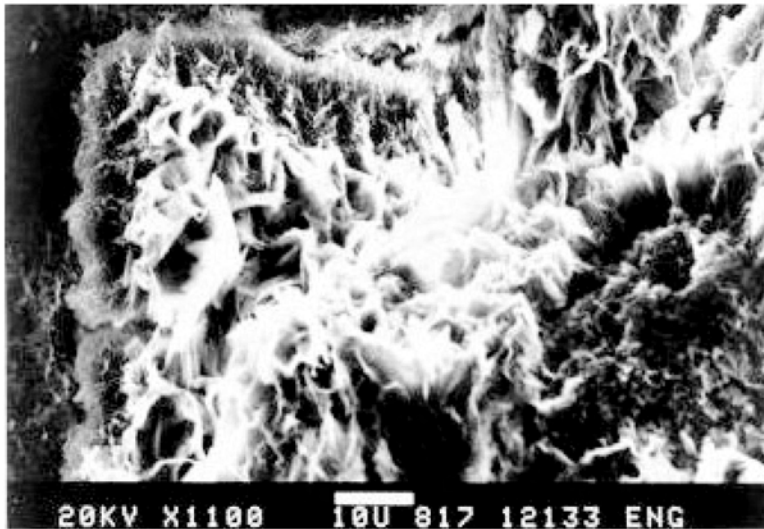
Porosity is a volume ratio and thus dimensionless, and is usually reported as a fraction or percent. To avoid confusion, particularly when variable or changing porosities are involved, it is often reported in porosity units (1 PU = 1%).

Several volume definitions are required to describe porosity:

- Total volume of rock =  $V_T$  or  $V_{rx}$
- Volume of mineral phase =  $V_g$  or  $V_m$
- Volume of pores or openings =  $V_{por}$



a. Collapsed (dry)



b. Expanded (wet)

20 μm

Fig. 13.6—SEM images of a smectite-rich sandstone. When dry (a), the smectites have collapsed. After saturation with distilled water, the smectites have expanded (b) to plug the pore space.

Volume of interconnected pores	= $V_{p-con}$	
Volume of isolated pores	= $V_{p-iso}$	
Volume of cracks or fractures	= $V_{fx}$ or $V_{cx}$	
Volume of fluid Phase 1, 2	= $V_{f1}, V_{f2},$ etc.	..... (13.3)

From these we can define the various kinds of porosity encountered:

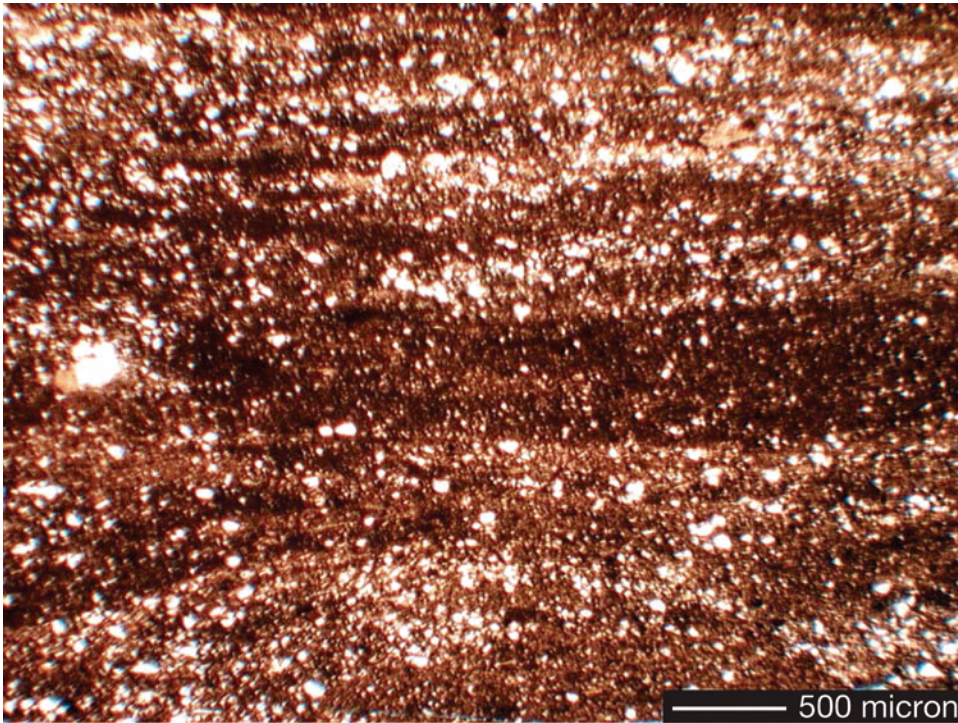


Fig. 13.7—Thin-section image of an organic-rich siltstone. Quartz grains (white) are surrounded by silt and clay (brown). Thin organic layers (black) are aligned to give the rock a strong anisotropy.

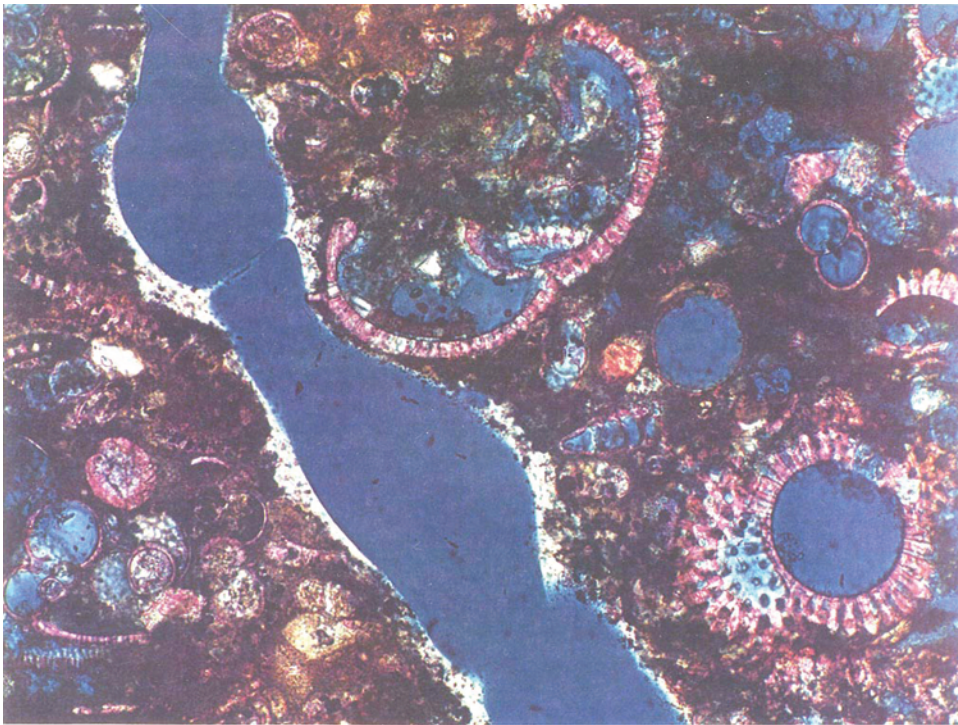
Total porosity	$\Phi$	$= V_{\text{por}} / V_T$	
Effective porosity	$\Phi_{p-e}$	$= V_{p-\text{con}} / V_T$	
Ineffective porosity	$\Phi_{p-\text{iso}}$	$= V_{p-\text{iso}} / V_T$	
Crack or fracture porosity	$\Phi_{fx}$	$= V_{fx} / V_T$	..... (13.4)

Fig. 13.9 shows the appearance of these types of porosity in a sandstone.

Similarly, the definitions of the standard densities associated with rocks then follows:

Grain density	$\rho_g$	$= M_s / V_g$	
Dry density	$\rho_d$	$= M_d / V_T$	
Saturated density	$\rho_{\text{sat}}$	$= M_{\text{sat}} / V_T$	
Buoyant density	$\rho_b$	$= M_b / V_T$	
Fluid density	$\rho_{fl}$	$= M_s / V_T$ ,	..... (13.5)

where  $M_s$ ,  $M_d$ ,  $M_{\text{sat}}$ ,  $M_b$ , and  $M_{fl}$  are the mass of the solid, dry rock, saturated rock, buoyant rock, and fluid, respectively.



0.5 mm

**Fig. 13.8—Thin-section image of fossil-rich globigerina ooze. Because of the porosity of the individual fossil tests, the total rock porosity reaches 80%. Much of this is microporosity. Despite the high porosity and soft nature of this rock, a fracture has formed across the sample.**

**TABLE 13.2—DENSITY CONVERSIONS**

	<u>g/cm<sup>3</sup></u>	<u>kg/m<sup>3</sup></u>	<u>lbm/gal</u>	<u>lbm/ft<sup>3</sup></u>
1 g/cm <sup>3</sup> =	1	1000	8.347	62.43
1 kg/m <sup>3</sup> =	0.001	1	0.008347	0.06243
1 lbm/gal =	0.1198	119.8	1	7.479
1 lbm/ft <sup>3</sup> =	0.016018	16.02	0.1337	1

**13.3.2 Relationships.** The density of a composite such as rocks (or drilling muds) can be calculated from the densities and volume fraction of each component. For a two-component system,

$$\rho_{\text{mix}} = A\rho_A + B\rho_B = A\rho_A + (1 - A)\rho_B, \dots\dots\dots (13.6)$$

where  $\rho_{\text{mix}}$  is the density of the mixture;  $\rho_A$  is the density of Component A;  $\rho_B$  is the density of B; A and B are the volume fractions of A and B respectively (and so B = 1-A).

Expanding this into a general system with *n* components,

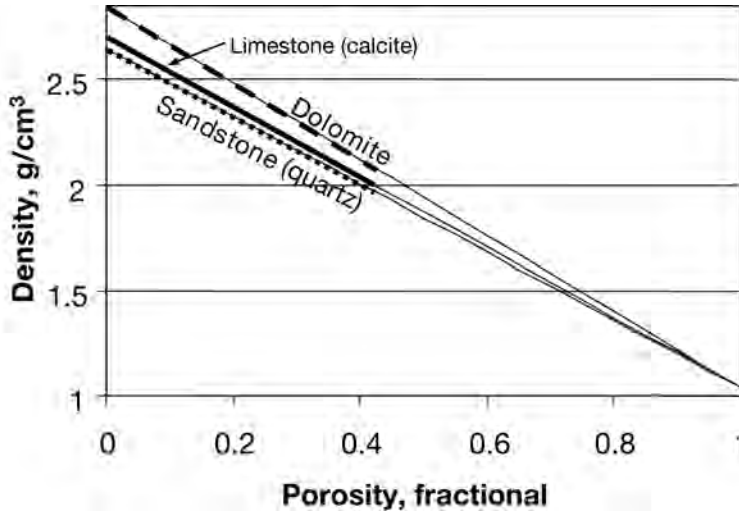


Fig. 13.9—Calculated density vs. porosity for sandstone, limestone, and dolomite.

$$\rho_{\text{mix}} = A_1\rho_{A1} + A_2\rho_{A2} + A_3\rho_{A3} + \dots + (1 - A_1 - A_2 - A_3 \dots - A_{n-1})\rho_n \dots (13.7)$$

For example, exploiting Eqs. 13.4, 13.5, and 13.6 for a rock made up of two minerals,  $m_1$  and  $m_2$ , and two fluids,  $f_1$  and  $f_2$ , we find

$$\begin{aligned} \rho_g &= A_{m1}\rho_{m1} + (1 - A_{m1})\rho_{m2} \\ \rho_f &= A_{f1}\rho_{f1} + (1 - A_{f1})\rho_{f2} \dots (13.8) \end{aligned}$$

and

$$\rho_{rx} = \Phi\rho_f + (1 - \Phi)\rho_g \dots (13.9)$$

Eq. 13.8 is a fundamental relation used throughout the Earth sciences to calculate rock density. Given a porosity and specific fluid, density can be easily calculated if the mineral or grain density is known. Grain densities for common rock-forming minerals are shown in Table 13.3. The result of applying Eq. 13.9 is shown in Fig. 13.9.

Note in Table 13.3 that there are several densities reported for the same mineral group, such as feldspar or clay. The density will change systematically as composition varies. For example, in the plagioclase series, the density increases as sodium (albite,  $\rho = 2.61 \text{ g/cm}^3$ ) is replaced by calcium (anorthite,  $\rho = 2.75 \text{ g/cm}^3$ ). The most problematic minerals are clays, particularly expanding clays (montmorillonite or smectite) capable of containing large and variable amounts of water. In this case, densities can vary 40% or more. This is a particular problem, because clays are among the most common minerals in sedimentary rocks.

Reservoir rocks often contain significant amounts of semisolid organic material such as bitumen. These will typically have light densities similar in magnitude to those of coals.

Pore-fluid densities are covered in detail in the fluid property section (13.4).

**13.3.3 In-Situ Density and Porosity.** In general, density increases and porosity decreases monotonically with depth. This is expected, because differential pressures usually increase with

TABLE 13.3—GRAIN DENSITIES FOR COMMON ROCK-FORMING MINERALS

Mineral Name	Grain Density (g/cm <sup>3</sup> )	Mineral Name	Grain Density (g/cm <sup>3</sup> )
Albite (Na Feldspar)	2.61	Hornblende	3.12
Almandine	4.08	Kaolinite (Clay 3)	2.59
Anhydrite	2.96	Illite (Clay 4)	2.66
Anorthite (Ca Feldspar)	2.75	Magnesite	2.97
Apatite	3.23	Magnetite	5.18
Aragonite	2.99	Matrolite	2.25
Augite A	3.32	Montmorillonite (Clay 5)	2.1–2.6
Augite B	3.42	Muscovite (Mica 3)	2.78
Barite A	4.50	Olivine A	3.31
Biotite A (Mica 1)	3.00	Olivine C	3.13
Biotite B (Mica 2)	3.05	Orthoclase (K feldspar)	2.57
Calcite	2.71	Phlogophite (Mica 4)	2.82
Chlorite (Clay 1)	2.80	Plagioclase A	2.64
Clinoperthite A	2.54	Plagioclase F	2.69
Clinoperthite G	2.57	Pyrite	5.02
Coal	1.2–1.8	Quartz	2.65
Diopside	3.31	Rhodochrosite	3.57
Dolomite A	2.85	Rutile	4.2
Dolomite B	2.87	Siderite	3.75
Epidote	3.40	Sillikanite	3.19
Fluorite	3.18	Smectite (Clay 5)	2.1–2.6
Forsterite	3.22	Sphalerite	4.00
Galena	7.50	Staurolite	3.78
Garnet A	3.60	Sulfur	2.07
Garnet I	4.25	Sylvite	1.99
Glaconite (Clay 2)	2.30	Topaz	3.50
Gypsum	2.31	Tourmaline	3.23
Halite	2.16	Zircon	4.70
Hematite	5.26		
From Refs. 15–17			

depth. As pressure increases, grains will shift and rotate to reach a more dense packing. More force will be imposed on the grain contacts. Crushing and fracturing is a common result. In addition, diagenetic processes such as cementation work to fill the pore space. Material may be dissolved at point contacts or along stylolites and then transported to fill pores. Some of the textures resulting from these processes were seen in the photomicrographs of the previous section. In **Fig. 13.10**, generalized densities as a function of depth for shales are plotted. The shapes and overall behaviors for these curves are similar, even though they come from a wide variety of locations with different geologic histories. These kinds of curves are often fit with exponential functions in depth to define the local compaction trend.

Differential or effective pressures do not always increase with increasing depth. Abnormally high pore fluid pressures (“overpressure”) can occur because of rapid compaction, low permeability, mineral dewatering, or migration of high-pressure fluids. The high pore pressure results in an abnormally low differential of effective pressure. This can retard or even reverse the nor-

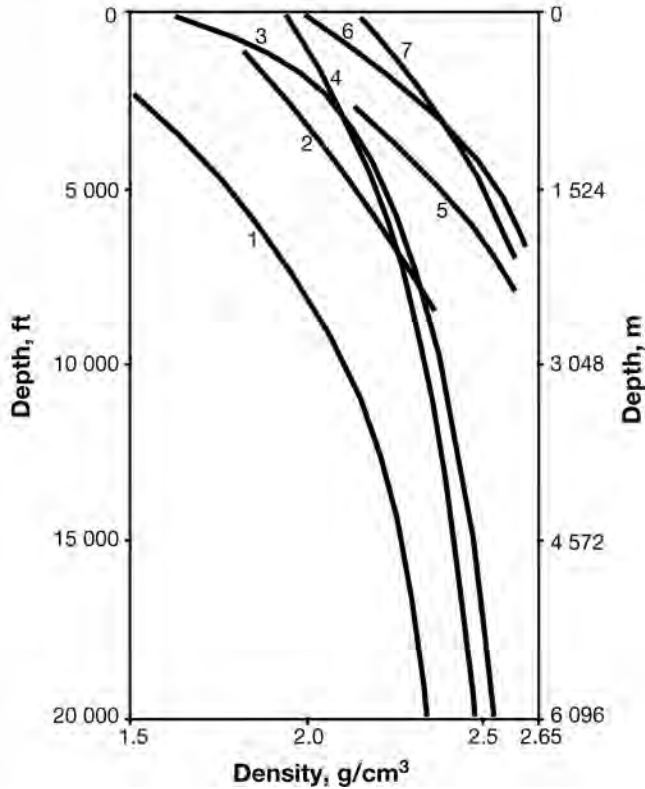


Fig. 13.10—Shale density as a function of depth from several sedimentary basins (after Castagna *et al.*<sup>18</sup> and Rieke and Chillingarian<sup>19</sup>). 1 = Gas saturated clastics: probable minimum density (McCulloh<sup>20</sup>), 2 = Po river valley mudstone (Storer<sup>21</sup>), 3 = average coastal Gulf of Mexico shales from geophysical measurements (Dickinson<sup>22</sup>), 4 = average coastal Gulf of Mexico shales from density logs (Eaton<sup>23</sup>), 5 = Maracaibo basin well (Dallmus<sup>24</sup>), 6 = Hungary calculated wet densities (Skeels<sup>25</sup>), 7 = Pennsylvanian and Permian dry shales (Dallmus<sup>24</sup>), 8 = Eastern Venezuela (Dallmus<sup>24</sup>).

mal compaction trends. Such a situation is seen in Fig. 13.11. Porosities for both shales and sands show the expected porosity loss with increasing depth in the shallow portions. However, at about 3500 m, pore pressure rises and porosity actually increases with depth. This demonstrates why local calibration is needed. This behavior is also our first indication of the pressure dependence of rock properties, a topic covered in more detail in Section 13.5.

**13.3.4 Measurement Techniques. Laboratory.** Numerous methods can be used in the laboratory to determine porosity and density. The most common are by saturation weight and Boyle's law. For rocks without sensitive minerals such as smectites, the porosity and dry, grain, and saturated densities can be derived from the saturated mass, dry mass, and volume (or buoyant weight). These measurements allow calculation of saturated, dry, and grain density as well as porosity and mineral and pore volume by employing Eqs. 13.3 through 13.5.

The Boyle's law technique measures the relative changes in gas pressures inside a chamber with and without a rock specimen. The internal (connected) pore volume is calculated from these variations in pressure, from which porosities and densities are extracted.

**Logging.** Several logging techniques are available to measure density or porosity.<sup>27,28</sup> These indirect techniques can have substantial errors depending on borehole conditions, but they do



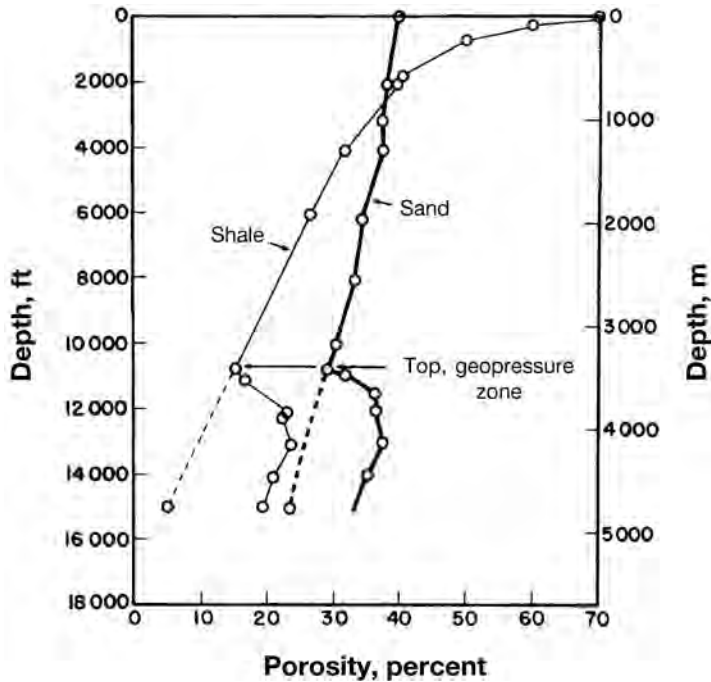


Fig. 13.11—Shale and sandstone porosity with depth. Porosity decreases until high pore pressures (= geopressure) reduce the effective pressure and cause an increase in porosity (from Stuart<sup>26</sup>).

provide a measure of the in-situ properties. Gamma ray logs bombard the formation with radiation from an active source. Radiation is scattered back to the logging tool, depending on the electron density of the material. Formation density is extracted from the amplitude of these back-scattered gamma rays. The neutron log estimates porosity by particle interaction with hydrogen atoms. Neutrons lose energy when colliding with hydrogen atoms, thus giving a measure of the hydrogen content. Because most of the hydrogen in rocks resides in the pore space (water or oil), this is then related to the liquid-filled porosity. Note that the neutron log will include bound water within clays as porosity. In addition, when relatively hydrogen-poor gas is the pore fluid, the neutron log will underestimate porosity. In a similar fashion, the nuclear magnetic resonance (NMR) log will resolve the hydrogen content. This tool, however, has the ability to differentiate between free bulk water and bound water. Sonic logs are also used for porosity measurements, particularly when anomalous minerals (such as siderite) or borehole conditions render other tools less accurate. The technique involves inverting velocity to porosity using one of the relationships provided in the velocity section below. Gravimetry has also been used down-hole to measure variations in density. Although this tool is insensitive to fine-scale changes, it permits density measurement far out into the formation.

**Seismic.** On a coarse scale, densities can sometimes be extracted from seismic data. This method requires separating the density component of impedance. This normally requires an analysis of the seismic data as a function of offset or reflection angle. This technique will probably see more use as seismic data improves and is further incorporated into reservoir description.

### 13.4 Fluid Properties

Hydrocarbons occur in a variety of conditions, in different phases, and with widely varying properties. In this section, we will cover the important geophysical properties of pore fluids. For more general information on the engineering properties of fluids, see the appropriate sec-

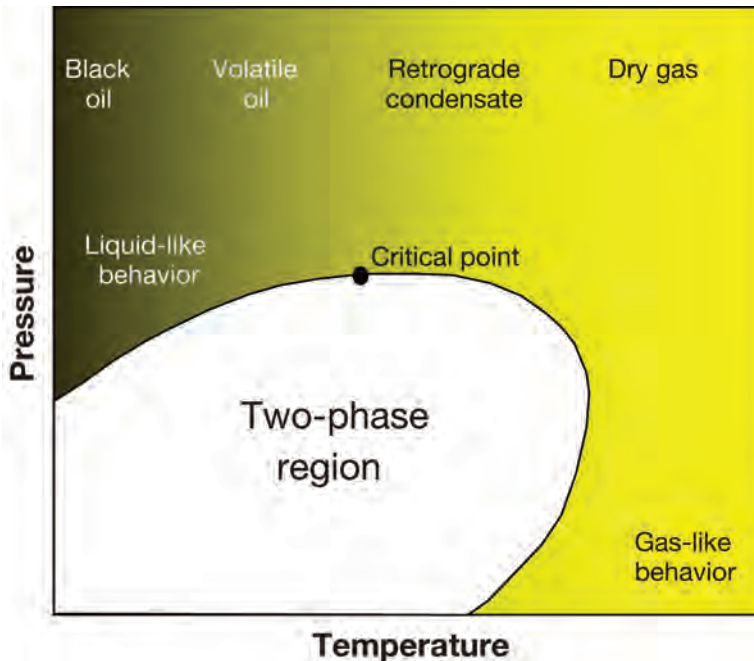


Fig. 13.12—General fluid phase behavior for hydrocarbon mixtures. Above the critical point, there is a continuum of compositions and properties from heavy oil to light gas.

tion in the *Handbook*. Fig. 13.12 shows schematically the relation among the different mixtures. For a single, constant composition mixture, as we vary temperature and pressure over a wide range, we would encounter the boundary between the single and multiphase regions. In contrast, if we restrict the temperatures and pressures to those typical of reservoirs, we could again move in this phase “space” by changing compositions. Velocities and densities will be high (close to water) for heavy “black” oils to the left of the figure and decrease dramatically as we move right toward lighter compounds. In many cases, the hydrocarbons are greater than critical pressure and temperature conditions (greater than critical point). Properties then can vary continuously from liquid-like, for oils with gas in solution, to gas-like, for mixtures of light molecular weight. With changing pressure and temperature conditions, phase boundaries can be crossed, resulting in abrupt changes in fluid properties. Additional components are often injected during production, further complicating the distribution of compositions and properties.

**13.4.1 Gas.** The gas phase is the easiest to characterize. The compounds are usually relatively simple, and the thermodynamic properties have been thoroughly examined. Hydrocarbon gases usually consist of the light hydrocarbons of methane, butane, and propane. Additional gases, such as water vapor and heavier hydrocarbons, will occur in the gas depending on the pressure, temperature, and history of the deposit. The specific weight of these gases, as compared to air at standard temperature and pressure, will vary from about 0.6 for nearly pure methane to over 1.5 for gases with heavier components. Fortunately, when a rough idea of the gas weight is known, a fairly accurate estimate can be made of the gas properties at pressure and temperatures. Thomas *et al.*<sup>29</sup> did a complete analysis of the acoustic properties of natural gases, and we will follow a similar analysis here.

The important seismic characteristics of a fluid (the bulk modulus, density, and sonic velocity) are all related to primary thermodynamic properties. Therefore, for gases, we are obliged to start with the ideal gas law.

$$PV = nRT_a, \dots\dots\dots (13.10)$$

where  $P$  is pressure,  $V$  is volume,  $n$  is the number of moles of the gas,  $R$  is the gas constant, and  $T_a$  the absolute temperature. This leads to a density  $\rho$ , of

$$\rho = \frac{nM}{V} = \frac{MP}{RT}, \dots\dots\dots (13.11)$$

where  $M$  is the molecular weight. The isothermal compressibility  $\beta_T$  is

$$\beta_T = -\frac{1}{V} \left[ \frac{\partial V}{\partial P} \right]_T \dots\dots\dots (13.12)$$

for compressibility defined as a positive number.

If we calculate the “isothermal” velocity  $V_T$ , we find

$$V_T^2 = \frac{1}{\beta_T \rho} = \frac{RT}{M} \dots\dots\dots (13.13)$$

for an ideal gas. The acoustic velocity is controlled by the stiffness of the material and its density (see the derivation in Section 13.5.5). Therefore, velocity would increase with temperature and be independent of pressure.

Two mitigating factors bring the relationship closer to reality. First, because there are rapid temperature changes associated with the passage of an acoustic wave, we must use the adiabatic compressibility,  $\beta_S$ , rather than the isothermal compressibility  $\gamma \beta_S = \beta_T$ .

Here,  $\gamma$  is the ratio of heat capacity at constant pressure to the heat capacity at constant volume. In most solid materials, the difference between the isothermal and adiabatic compressibilities is negligible. However, in fluid phases, particularly gases, the isothermal compressibility can be twice the adiabatic value.

The second, more obvious factor stems from the inadequacies of the ideal gas law (Eq. 13.10). The gas law can be corrected by adding a compressibility factor ( $Z$ ). The relationships are thus modified:

$$PV = ZnRT_a, \dots\dots\dots (13.14)$$

$$\rho = MP / ZnRT_a, \dots\dots\dots (13.15)$$

and

$$\beta_S = \beta_T / \gamma = M / (\gamma \rho ZRT_a). \dots\dots\dots (13.16)$$

The heat capacity ratio can itself be derived if the equations of state of the material are known. The seismic characteristics of the gas can, therefore, be described if we have an adequate description of  $Z$  with pressure, temperature, and composition.

Thomas *et al.*<sup>29</sup> made use of the Benedict-Webb-Rubin (BWR) equation to define the gas behavior. The BWR equation of state is a rational equation, with numerous constants based on the behavior of natural gas mixtures. These gas mixtures range in gravity  $G$  (relative to air) from about 0.5 to 1.8. The results of the density calculations are shown in Fig. 13.13. As

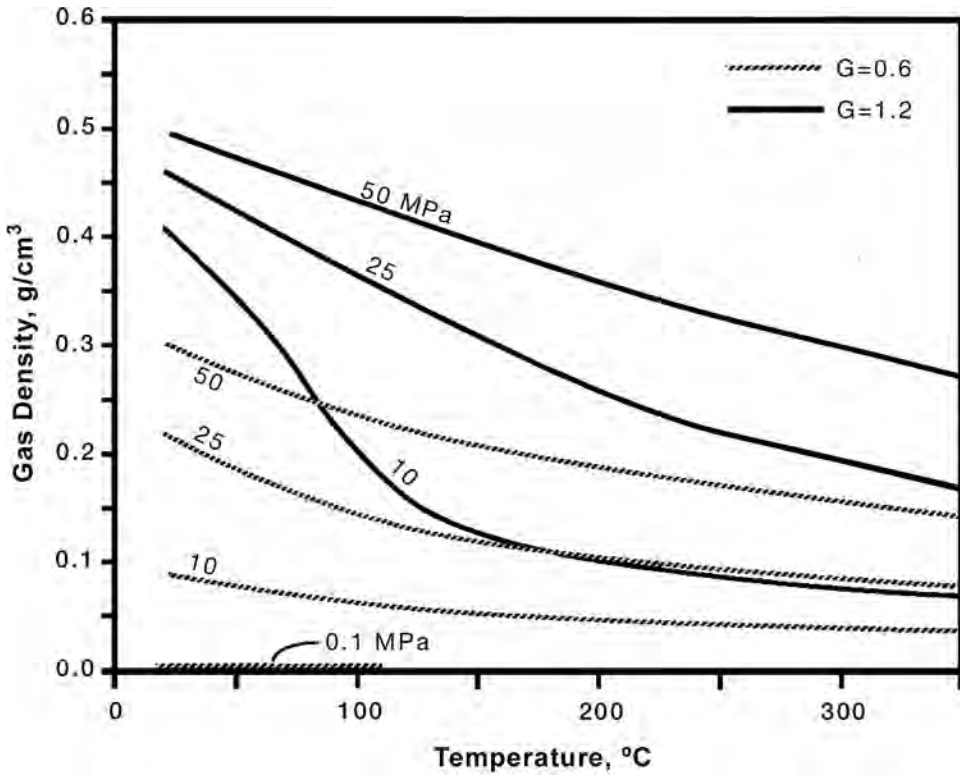


Fig. 13.13—Hydrocarbon gas densities as a function of pressure and temperature for gas gravities of  $G = 0.6$  and  $G = 1.2$  (from Batzle and Wang<sup>30</sup>).

would be expected, the gas densities increase with pressure and decrease with temperature. However, the densities also strongly depend on the gas gravity, which is composition-dependent.

The adiabatic gas modulus  $K$  (the inverse of  $\beta$ ) also strongly depends on the composition as well as the pressure and temperature conditions. Fig. 13.14 shows the calculated modulus from the Thomas relationships. Again, the modulus increases with pressure and decreases with temperature, but the relationship is not as linear. The impact of variable composition (gravity) is again obvious.

**13.4.2 Oil.** Crude oils can be mixtures of extremely complex organic compounds. Natural oils range from the lightest condensate liquids of low carbon number to very heavy tars. At the heavy extreme are bitumen and kerogen, which may be denser than water and act essentially like solids. At the light extreme are condensates that may become gas with decreasing pressure. Oils can absorb large quantities of hydrocarbon gases under pressure, thus significantly decreasing the moduli. Under room conditions, the densities can vary from 0.5 to greater than 1 gm/cc with most produced oils in the 0.7 to 0.8 gm/cc range. The American Petroleum Institute (API) number is defined as

$$API = 141.4 / \rho - 131.5 \dots\dots\dots (13.17)$$

This results in API numbers of about 5 for very heavy oils to near 100 for light condensates. The extreme variations in composition and ability to absorb gases produce greater variations in the seismic properties of oils.

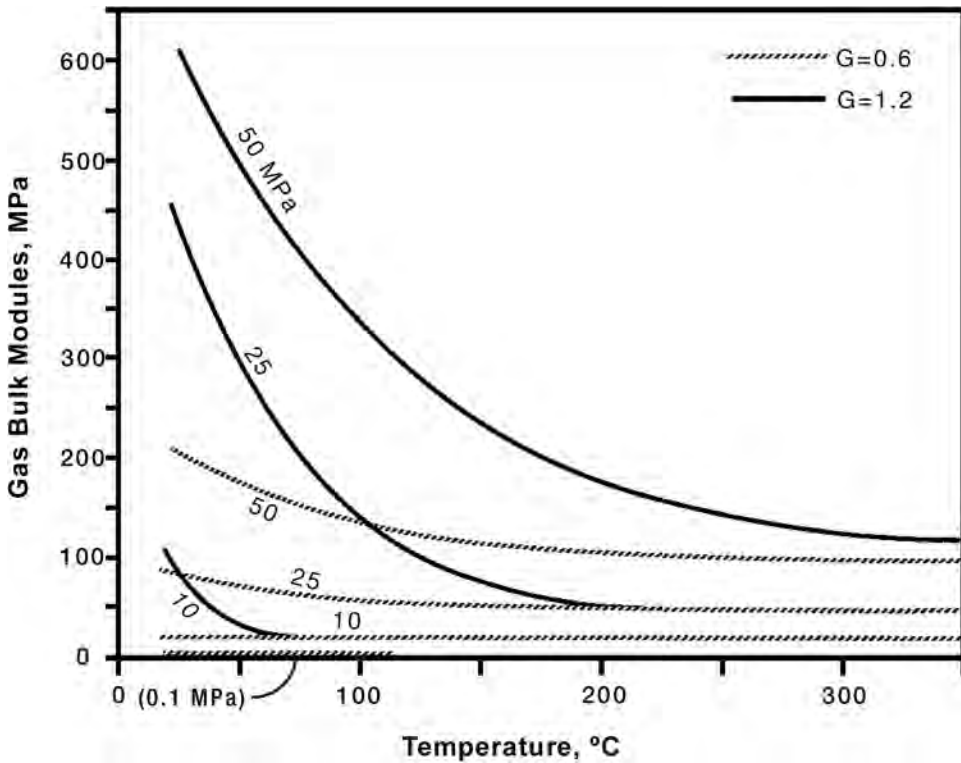


Fig. 13.14—Hydrocarbon gas modulus as a function of pressure and temperature for gas gravities of 0.6 and 1.2 (from Batzle and Wang<sup>30</sup>).

If we had a general equation of state for oils, we could calculate the moduli and densities as we did for the gases. Such equations abound in the petroleum engineering literature. Unfortunately, the equations are almost always strongly dependent on the exact composition of a given oil. For the purposes of this *Handbook*, we will develop only very general relations. Often, in petrophysical analysis we only have a rough idea of what the oils may be like. In some reservoirs, individual yet adjacent zones will have quite distinct oil types. We will, therefore, proceed along empirical lines based on the density of the oil.

The acoustic properties of numerous organic fluids have been studied as a function of pressure or temperature (see, for example, Rao and Rao<sup>31</sup>). Generally, the velocities, densities, and moduli are quite linear with pressure and temperature away from phase boundaries. In organic fluids typical of crude oils, the moduli decrease with increasing temperature and increase with increasing pressure. Wang and Nur<sup>32</sup> did an extensive study of several light alkanes, alkenes, and cycloparaffins and found simple relationships among the density, moduli, temperature, and carbon number or molecular weight. For velocity they found

$$V_T = V_o - b\Delta T, \dots\dots\dots (13.18)$$

where  $V_o$  is the initial velocity,  $V_T$  is the velocity at temperature  $T$ ,  $\Delta T$  is the temperature change, and  $b$  is a constant for each compound of molecular weight  $M$ :

$$b = 0.306 - 7.6/M. \dots\dots\dots (13.19)$$

Similarly, the velocities are related in molecular weight by

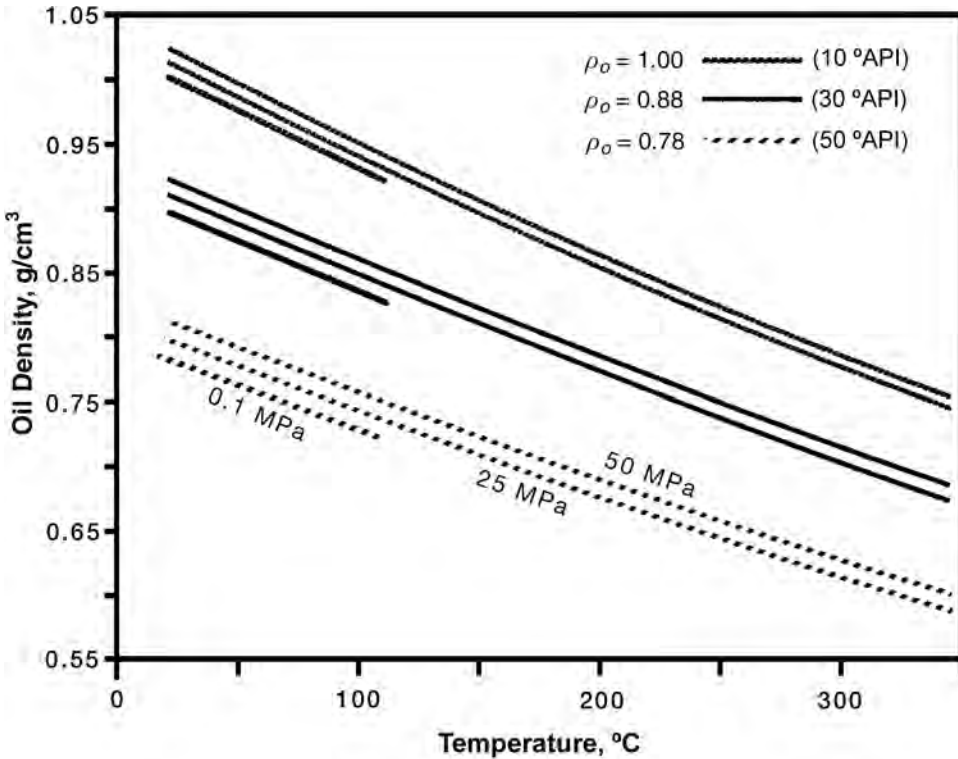


Fig. 13.15—Oil density as a function of pressure and temperature for three weights of oil: API = 10, 30, and 50 (from Batzle and Wang<sup>30</sup>).

$$V_{TM} = V_{TOMO} - b\Delta T - a_m[1/M - 1/M_o], \dots\dots\dots (13.20)$$

where  $V_{TM}$  is the velocity of oil of weight  $M$ , and  $V_{TOMO}$  is the velocity of a reference oil of weight  $M_o$  at temperature  $T_o$ . The variable  $a_m$  is a positive function of temperature. We can see from the rightmost term in Eq. 13.20 that the velocity of the fluid will increase with increasing molecular weight. When compounds are mixed, Wang and Nur<sup>32</sup> found that the resulting velocity is a simple fractional average of the end components. This is roughly equivalent to a fractional average of the bulk moduli of the end components. Pure simple hydrocarbons, therefore, behave in a simple predictable way. We must extend this analysis to include crude oils, which are generally much heavier and have more complex compositions. The influence of pressure must also be determined. In the petroleum engineering literature, broad empirical relationships are available. By empirically fitting equations to these data, we can get density as functions of initial density (or API number), temperature, and pressure

$$\rho = F(\rho_o, T, P). \dots\dots\dots (13.21)$$

These densities are shown in Fig. 13.15.

By differentiating Eq. 13.21, we obtain the isothermal compressibility  $\beta_T$ ,

$$\beta_T = \frac{1}{\rho} \left[ \frac{\partial \rho}{\partial P} \right]_T \dots\dots\dots (13.22)$$

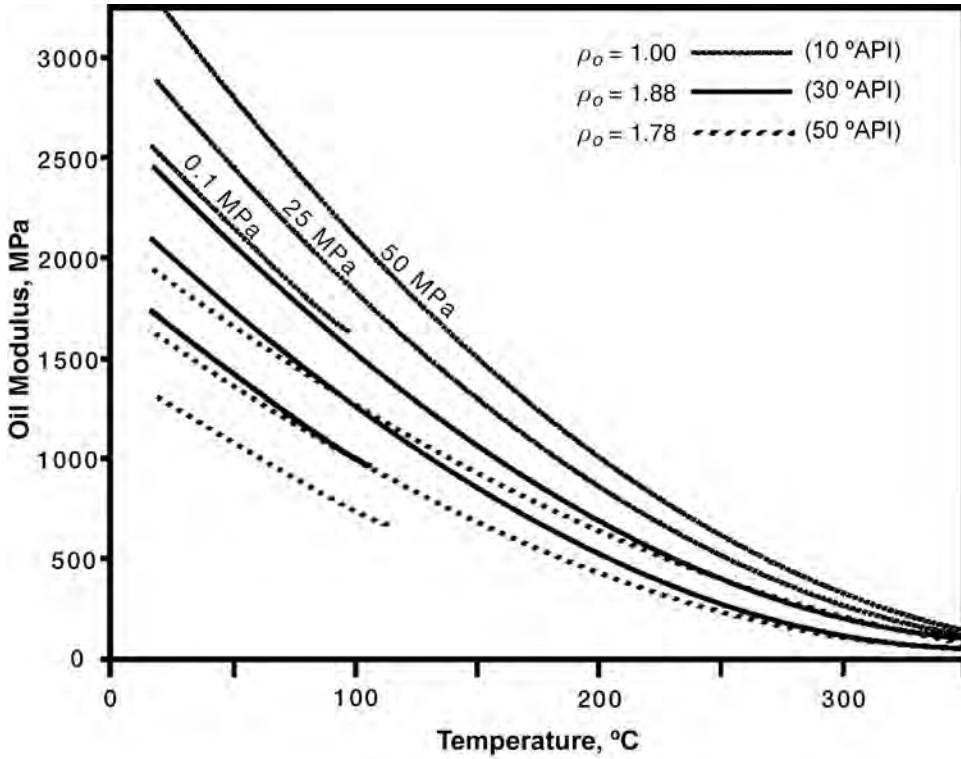


Fig. 13.16—Oil modulus as a function of pressure and temperature for three weights of oil: API = 10, 30, and 50 (from Batzle and Wang<sup>30</sup>).

If we assume a reasonable and constant heat capacity ratio  $\gamma$  of 1.15, we obtain the adiabatic bulk moduli  $K$ .

$$K_S = \frac{\gamma}{\rho\beta_T} = \frac{\gamma p}{\left[\frac{\partial \rho}{\partial P}\right]_T} \dots\dots\dots (13.23)$$

The ultrasonic velocities of a variety of crude oils measured recently are reported in Wang *et al.*<sup>33</sup> A general relationship of oil velocity was derived.

$$V = 15,454(77.1 + \text{API})^{-1/2} - 1.14T + 0.462P - (1.146 \times 10^{-3} - 4.13 \times 10^{-4}\text{API}^{1/2})TP, \dots\dots\dots (13.24)$$

where  $V$  is in m/s,  $T$  in °C,  $P$  in bars, and API is the API degree of the oil, or

$$V = 215 + 50700(77.1 + \text{API})^{-1/2} - 6.72T + (.1096 - 0.00166 \text{API}^{1/2})P - (1.44 \times 10^{-4} - 5.18 \times 10^{-5} \text{API}^{1/2})TP, \dots\dots\dots (13.25)$$

for  $V$  in ft/s,  $T$  in °F, and  $P$  in psi.

Using these velocities and the densities as shown in Fig. 13.15, we find the moduli shown in Fig. 13.16.

Very large amounts of gas or light hydrocarbons can go into solution in crude oils. In fact, the lighter crudes are condensates from the gas phase. We would expect the “live” or gas-saturated oils to have significantly different properties than the “dead” or gas-free oils commonly available and measured. The amount of gas that can be dissolved is a function of pressure, temperature, and the composition of both the gas and the oil.<sup>34</sup>

$$R = 0.1266G[P \exp (.02878API - 0.00378T)]^{1.205}, \dots\dots\dots (13.26)$$

where  $R$  is the gas-oil ratio in liters/liter (1 liter/liter = 5.615 cu ft/bbl) at atmospheric pressure and at 15.5°C and  $G$  is the gas gravity. Eq. 13.26 indicates that much larger amounts of gas can go into the light (high API number) oils. In fact, heavy oils may precipitate heavy compounds if much gas goes into solution.

The effect of this gas in solution on the oil acoustic properties has not been well documented. Sergeev<sup>35</sup> noted that gas in solution will reduce both oil and brine velocities. He calculated that this mix would change some reservoir reflection coefficients by more than a factor of two. A rough estimate of this dissolved gas effect can be made by assuming that the relationship in Eq. 13.26 remains valid and by adjusting the oil density to include the gas component. We are assuming here that the gas is a liquid component with its own volume and density and that the result is an ideal liquid mixture. The simple additive relations found in Wang and Nur<sup>32</sup> support this concept. The estimated density becomes

$$\rho_G = \rho_O(0.972 + 0.000147F^{1.175}), \dots\dots\dots (13.27)$$

where  $\rho_O$  is the dead oil density and  $\rho_G$  is the gas saturated live oil density. The factor  $F$  is derived from the gas/oil ratio

$$F = R[G/\rho_O]^{1/2} + 75. \dots\dots\dots (13.28)$$

Fig. 13.17 shows the live and dead oil velocities measured in Wang *et al.*<sup>33</sup> along with the estimates using Eqs. 13.25, 13.27, and 13.28.

**13.4.3 Brines.** The great bulk of the pore fluids consists of brines. Their composition can range from almost pure water to saturated saline solutions. Gulf of Mexico area brines often have rapid increases in concentration with increasing depth. In other areas, the concentrations are often lower but can vary drastically between adjacent fields.

The thermodynamic properties of aqueous solutions have been studied in detail. Keenan *et al.*<sup>36</sup> give a relation for pure water that can be iteratively solved to give densities at pressure and temperature. Helgeson and Kirkham<sup>37</sup> use this and other data to calculate a wide variety of water properties over an extensive temperature and pressure range. One obvious effect of salinity is to increase the density of the fluid. Rowe and Chou<sup>38</sup> presented a polynomial to calculate both specific volume and compressibility of various salt solutions at pressure over a limited temperature range. Extensive additional data on sodium chloride solutions is provided in Zarembo and Fedorov<sup>39</sup> and Potter and Brown.<sup>40</sup> Using all these data, a simple polynomial can be constructed that will adequately calculate the density of sodium chloride solutions:

$$\rho_w = \sum_{i=0}^4 \sum_{j=0}^2 a_{ij} T^i P^j, \dots\dots\dots (13.29a)$$

and



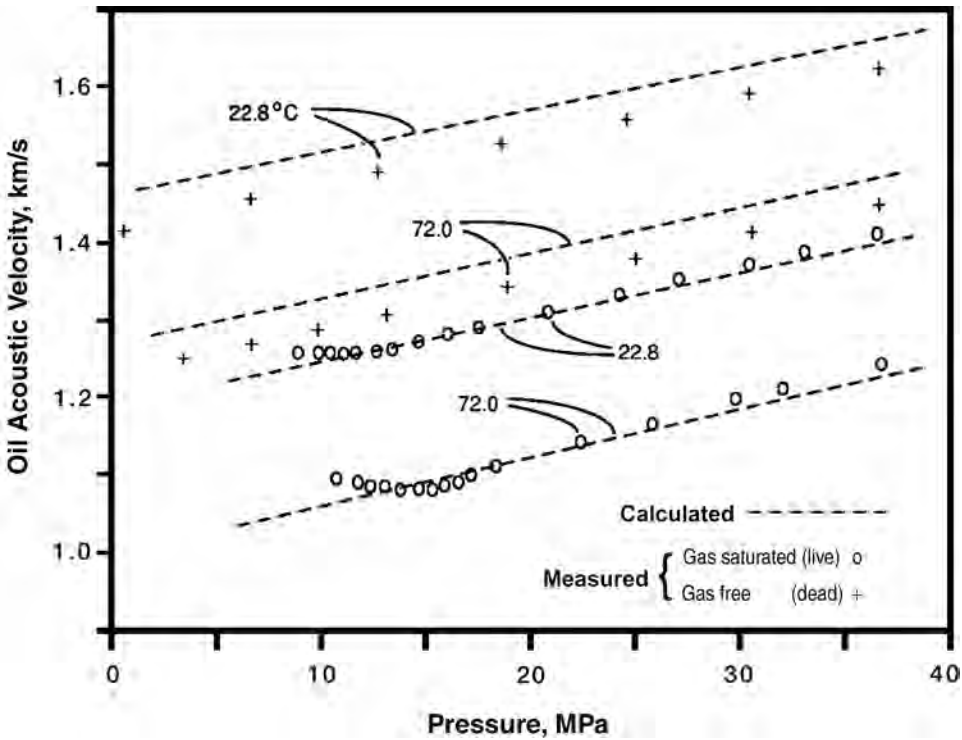


Fig. 13.17—Acoustic velocity of a 23 API oil both “dead” or gas-free and “live” with 85 L/L gas in solution. Dissolved lowers both the effective density and velocity of the live oil mixture.

$$\rho_B = \sum_{i=0}^4 \sum_{j=0}^2 \sum_{k=1}^2 b_{ijk} T^i P^j x^k. \dots\dots\dots (13.29b)$$

Here,  $T$  and  $P$  are in °C and bars, respectively;  $x$  is the weight fraction of sodium chloride; and  $\rho_B$  is the density of the brine in gm/cm<sup>3</sup>. The calculated brine densities, along with selected data from Zaremba and Federov,<sup>39</sup> are plotted in Fig. 13.18. The accuracy of this relationship is limited largely to the extent that other mineral salts, particularly divalent ions, are in solution.

A vast amount of acoustic data is available for brines, but generally for pressure, temperature, and salinity expected under oceanic conditions. Wilson<sup>41</sup> provides a relationship for the velocity  $V_w$  of pure water to 100°C and about 1000 bars

$$\rho_w = \sum_{i=0}^4 \sum_{j=0}^3 w_{ij} T^i P^j, \dots\dots\dots (13.30)$$

Millero *et al.*<sup>42</sup> and Chen *et al.*<sup>43</sup> give additional factors to be added to the velocity of water to calculate the effects of salinity. Their corrections, unfortunately, are limited to 55°C and 1 molar ionic strength (55,000 ppm). We can extend their results by using the data of Wyllie *et al.*<sup>44</sup> to 100°C and 150,000 ppm NaCl. Still, this leaves the high-temperature and -pressure region with no data. Here we can use the isothermal modulus calculated from Eq. 13.29 to estimate the adiabatic moduli. We can also use the velocity function provided in Chen *et al.*<sup>43</sup> but with the constants modified to fit the additional data. The heat capacity ratio for the brine can be

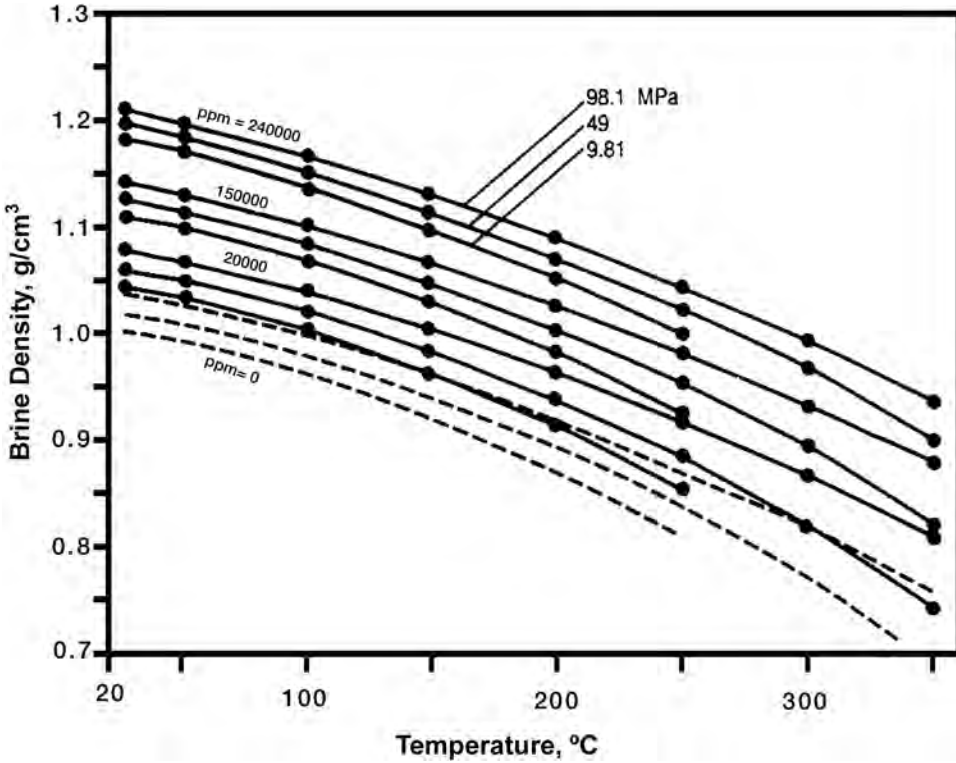


Fig. 13.18—Brine density as a function of temperature pressure and salinity (ppm = parts per million NaCl). Solid circles are from Zarembo and Fedorov.<sup>39</sup>

estimated from the PVT relationship in Eq. 13.29 and estimates of the isobaric heat capacity from Helgeson and Kirkham<sup>37</sup>:

$$B = m \sum_{i=0}^4 \sum_{j=0}^3 c_{ij} T^i P^j + m^{1.5} \sum_{i=0}^2 \sum_{j=0}^2 d_{ij} T^i P^j + m^2 \sum_{i=1}^2 e_i P^i \dots\dots\dots (13.31)$$

and

$$V_B = V_W + B \dots\dots\dots (13.32)$$

In this equation, *m* is the molal salt concentration and *c<sub>ij</sub>*, *d<sub>ij</sub>*, and *e<sub>i</sub>* are constants. Using the calculated density and velocity of brine produces the modulus, and this is shown in Fig. 13.19.

**13.5 Elasticity, Stress-Strain, and Elastic Waves**

We will begin this section with an introduction to stress-strain relations. These form the foundation for several rock properties, such as elastic moduli (incompressibility), effective media theory, elastic wave velocity, and rock strength.

**13.5.1 Stress and Pressure—Definitions.** Stress is the force per unit area.

$$\text{Stress} = \frac{\text{Force}}{\text{Area}} = \sigma_{ij} \dots\dots\dots (13.33)$$

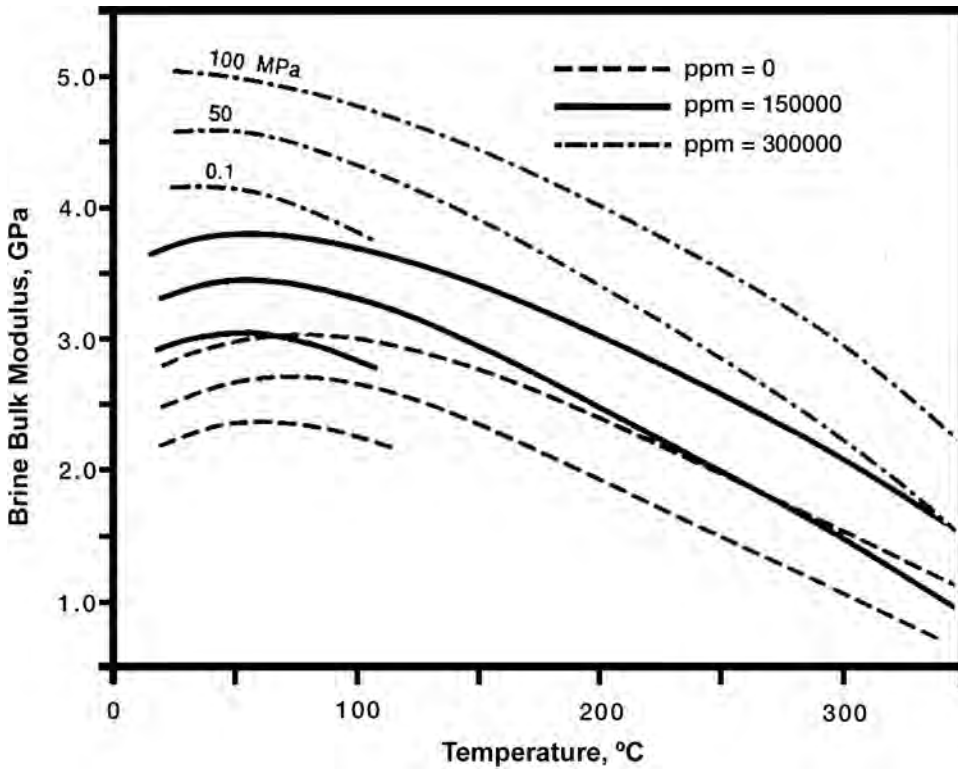


Fig. 13.19—Brine modulus as a function of temperature, pressure, and salinity (ppm = parts per million NaCl). Water and brines are peculiar fluids in that they have a modulus (and velocity) maximum around 70°C.

The metric units of stress or pressure are  $\text{N/m}^2$  or Pascals (Pa). Other units that are commonly used are bars, megapascals (MPa), and  $\text{lbm/in.}^2$  (psi) (see Table 13.4). These stresses can take various forms such as a homogeneous pressure  $P$ , normal stress  $\sigma_n$ , or stress applied at a general angle  $\sigma_g$  (Fig. 13.20). This general stress can be decomposed into normal and tangential components. We usually refer to balanced stresses because, under quasistatic conditions, they produce no net acceleration. Stress is a second-order tensor denoted by  $\sigma_{ij}$ , where the first index denotes the surface and the second the direction of the applied force (see Fig. 13.21). In Earth sciences and engineering, compressive stresses are usually considered positive, whereas most material sciences consider tensional stress positive. More details on the influence of stresses and the stress tensor can be found in Jaeger and Cook<sup>46</sup> and Nye.<sup>47</sup>

Several standard stress conditions are either assumed for the Earth for analysis or modeling, or applied in the laboratory:

Hydrostatic stress: all confining stresses are equal

Uniaxial stress: one stress applied along a single axis (other stresses are zero or held constant during an experiment)

Biaxial stress: two nonequal stresses applied (third direction is equal to one of the others)

Triaxial stress: (1) Common usage—separate vertical and two equal horizontal stresses (e.g., biaxial); (2) better—three independent principal stresses.

Anisotropic stresses are usually responsible for rock deformation and failure (see Section 13.7). In much of this section, however, we will concern ourselves primarily with mean stress ( $\sigma_m$ ) or pressure ( $P$ ).

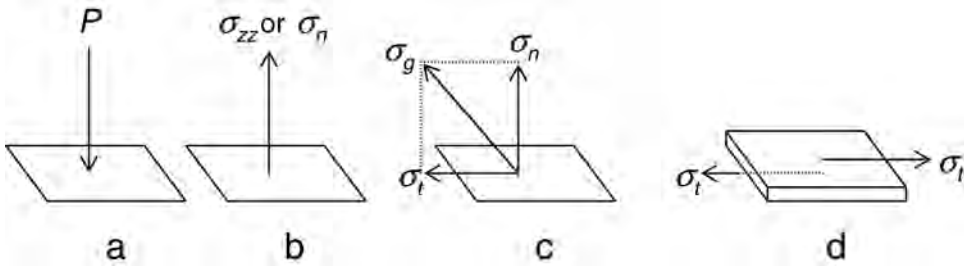


Fig. 13.20—Types of stresses: (a) pressure, (b) tensile, (c) general with normal and tangential components, and (d) shearing stress (modified from Hubbert<sup>45</sup>).

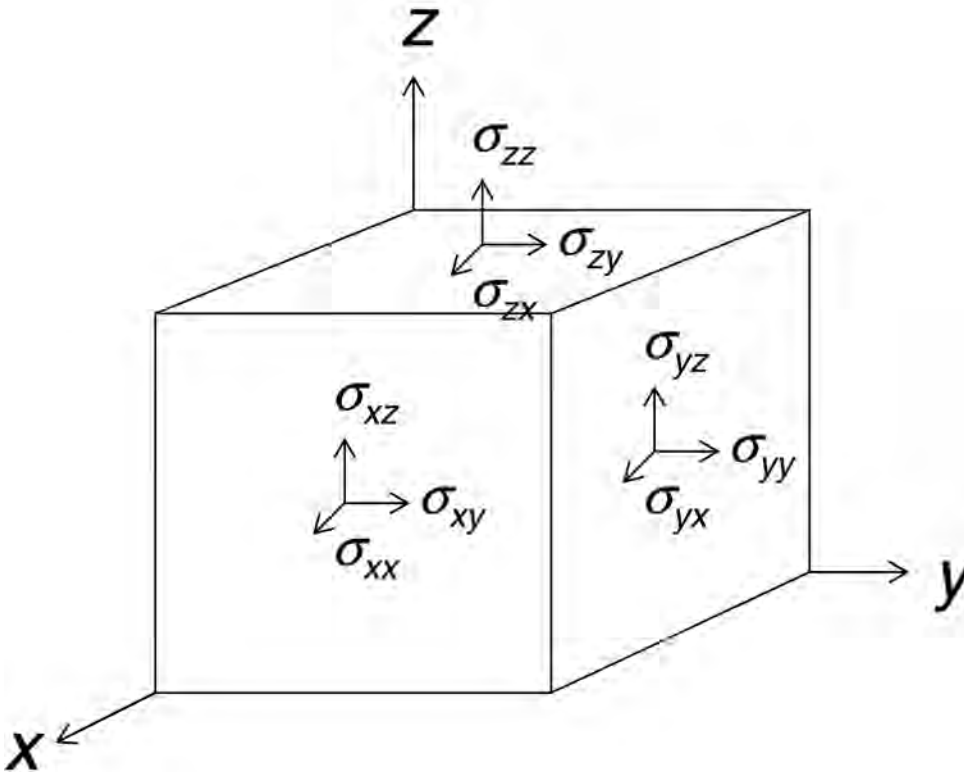


Fig. 13.21—Stresses acting on the elemental cube. The stresses must be balanced so that there is no acceleration of the body.

$$\sigma_m = \frac{\sigma_{11} + \sigma_{22} + \sigma_{33}}{3} \dots\dots\dots (13.34)$$

It is important to distinguish among the various kinds of pressure, because the combination often determines any specific rock property and influences the response to any production procedure.

TABLE 13.4—PRESSURE CONVERSIONS			
Pa	MPa	Bar	psi
1 Pa = 1	0.000001	0.00001	0.000145
1 MPa = 1000000	1	10.0	145.0
1 bar = 100000	0.1	1	14.5
1 psi = 6900	0.00690	0.0690	1

- Confining pressure =  $P_c$  = Overburden pressure on rock frame
- Pore pressure =  $P_p$  = Fluid pressure inside pore space
- Differential (or net) pressure =  $P_d$  = Difference between  $P_c$  and  $P_p$
- Effective pressure =  $P_e$  = Combination of  $P_c$  and  $P_p$  controlling a property

Increasing confining pressure ( $P_c$ ) alone will result in a decrease of rock volume, or compaction. In contrast, increasing the pore pressure ( $P_p$ ) tends to increase rock volume.  $P_p$  counteracts the effects of  $P_c$ . Thus, rock properties are controlled largely by the difference between  $P_c$  and  $P_p$ , or the differential pressure  $P_d$ . A more exact form will account for the interaction of the fluid pressure with the pore space and minerals and result in an effective stress ( $P_e$ ) law

$$P_e = P_c - nP_p, \dots\dots\dots (13.35)$$

where  $n$  is a term that can be derived theoretically or defined experimentally for each property.

**13.5.2 Deformation, Strain, and Modulus.** Application of a single (vertical) stress is one typical experiment run to measure material mechanical properties (Fig. 13.22). If this stress continues to increase, eventually the material will fail when the uniaxial compressive strength is reached (see Section 13.7). For the rest of this chapter, however, we will deal only with small deformations and stresses such that the rock remains in the elastic region. Under this restriction, several important material properties can be defined. For an isotropic, homogeneous material, there is a vertical deformation ( $\Delta L$ ) associated with the vertical stress. Normalizing this deformation by the original length of the sample,  $L$ , gives the vertical strain

$$\epsilon_{zz} = \frac{\Delta L}{L} \dots\dots\dots (13.36)$$

By definition, Young’s modulus,  $E$ , is the ratio of the applied stress ( $\sigma_{zz}$ ) to this strain

$$E = \frac{\sigma_{zz}}{\epsilon_{zz}} \dots\dots\dots (13.37)$$

Because strain is dimensionless,  $E$  is in units of stress.

This same stress will generally result in a lateral or horizontal deformation,  $\Delta W$ . The lateral strain can then be defined

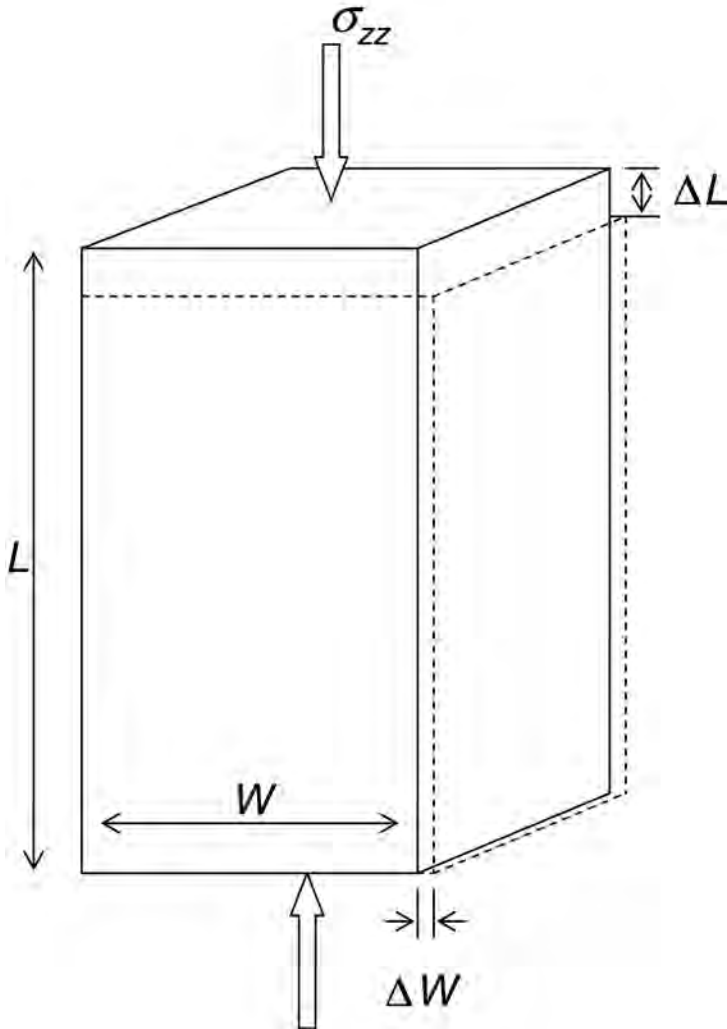


Fig. 13.22—Deformation of a material under vertical uniaxial stress ( $\sigma_{zz}$ ) giving rise to vertical ( $\Delta L$ ) and horizontal ( $\Delta W$ ) deformation.

$$\epsilon_{y,y} = \frac{\Delta W}{W} \dots\dots\dots (13.38)$$

One important parameter relating the vertical and horizontal strains is Poisson’s ratio

$$\nu = - \frac{\epsilon_{zz}}{\epsilon_{y,y}} \dots\dots\dots (13.39)$$

The minus sign is attached because the signs of the deformations are opposite for the horizontal vs. vertical strains in this simple case.

If instead we applied a pressure, we would get a volumetric strain  $\epsilon_v$ :

$$\varepsilon_V = \frac{\Delta V}{V} \dots\dots\dots (13.40)$$

The bulk modulus of a material is then defined as the ratio of applied pressure to volumetric strain

$$K = -\frac{P}{\varepsilon_V} \dots\dots\dots (13.41)$$

Bulk modulus is equivalent to the inverse of compressibility,  $\beta$ .

In a similar way, shear modulus,  $\mu$  (often “G” in many publications), can be defined as the ratio of shear stress to shear strain:

$$\mu = \frac{\sigma_{\text{shear}}}{\varepsilon_{\text{shear}}} \dots\dots\dots (13.42)$$

These various equations are special cases of Hooke’s Law, which can be written for the general case

$$\sigma_{ij} = C_{ijkl} \varepsilon_{kl} \dots\dots\dots (13.43)$$

Stress and strain are both tensors with 9 components.  $C_{ijkl}$  would then be a tensor with 81 components. However, because of symmetry considerations, only a maximum of 21 can be independent (a thorough treatment of the tensor relations is provided in Nye<sup>47</sup>). For isotropic materials, this reduces to

$$\sigma_{ij} = \lambda \delta_{ij} + 2\mu \varepsilon_{ij}, \dots\dots\dots (13.44)$$

where  $\lambda$  is Lamé’s constant. In fact, for isotropic materials, there are only two independent elastic parameters. Any isotropic elastic constant can be written in terms of two others. For example,  $\lambda$  can be defined as

$$\lambda = K - \frac{2\mu}{3} \dots\dots\dots (13.45)$$

The possible combinations among various isotropic elastic constants are shown in **Table 13.5**. This becomes important in applications, because restricting one term, say  $\nu$ , fixes the ratio of other moduli such as  $\mu$  and  $K$ .

**13.5.3 Effective Media, Bounds.** Rocks are usually not homogeneous, but are made up of multiple components such as mineral grains and pore space. On a larger scale, the bulk properties of rocks will be some weighted combination of the small-scale components. This averaging or upscaling step is needed if we wish to understand the behavior of our laboratory data or extract useful parameters from field data such as logs or seismic measurements.

The simplest bounds are provided by the constant strain and constant stress limits. This method is equivalent to the series vs. parallel effective resistance of a resistor network. In the case that strains of the two materials making up our material are equal, as with the parallel plates in **Fig. 13.23a**, we get the upper s(Voigt) limit. The response is controlled by the stiffer component.

TABLE 13.5—MODULUS RELATIONS FOR ISOTROPIC SOLIDS

Given	$E, K$	$E, \mu$	$E, \nu$	$E, \lambda$	$K, \mu$	$K, \nu$	$K, \lambda$	$\mu, \nu$	$\mu, \lambda$	$\lambda, \nu$
$E$	—	—	—	—	$\frac{9K\mu}{3K + \mu}$	$3K(1 - 2\nu)$	$\frac{9K(K - \lambda)}{3K - \lambda}$	$2\mu(1 + \nu)$	$\frac{\mu(3\lambda + 2\mu)}{\lambda + \mu}$	$\frac{\lambda(1 + \nu)(1 - 2\nu)}{\nu}$
$K$	—	$\frac{E\mu}{3(3\mu - E)}$	$\frac{E}{3(1 - 2\nu)}$	$\frac{E + 3\lambda + [(E + \lambda)^2 + 8\lambda^2]^{1/2}}{6}$	—	—	—	$\frac{2\mu(1 + \nu)}{3(1 - 2\nu)}$	$\lambda + \frac{2}{3}\mu$	$\frac{\lambda(1 + \nu)}{3\nu}$
$\mu$	$\frac{3EK}{9K - E}$	—	$\frac{E}{2(1 + \nu)}$	$\frac{E - 3\lambda + [(E + \lambda)^2 + 8\lambda^2]^{1/2}}{4}$	—	$\frac{3K(1 - 2\nu)}{2(1 + \nu)}$	$\frac{3}{2}(K - 2\lambda)$	—	—	$\frac{\lambda(1 - 2\nu)}{2\nu}$
$\nu$	$\frac{1}{2} - \frac{E}{6K}$	$\frac{E}{2\mu} - 1$	—	$\frac{[(E + \lambda)^2 + 8\lambda^2]^{1/2} - E - \lambda}{4\lambda}$	$\frac{3K - 2\mu}{2(3K + \mu)}$	—	$\frac{\lambda}{3K - \lambda}$	—	$\frac{\lambda}{2(\lambda + \mu)}$	—
$\lambda$	$\frac{3K(3K - E)}{9K - E}$	$\frac{\mu(E - 2\mu)}{3\mu - E}$	$\frac{\nu E}{(1 + \nu)(1 - 2\nu)}$	—	$K - \frac{2}{3}\mu$	$\frac{3K\nu}{1 + \nu}$	—	$\frac{2\mu\nu}{1 - 2\nu}$	—	—

$E$  = Young's modulus

$K$  = Bulk modulus

$\mu$  = Shear modulus

$\nu$  = Poisson's ratio

$\lambda$  = Lamé's parameter



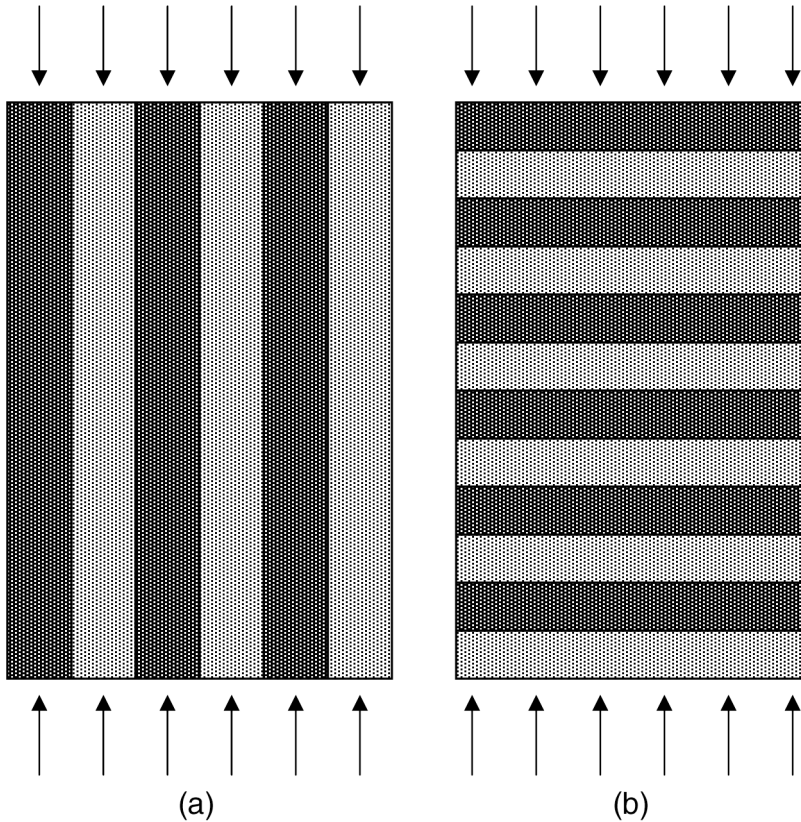


**Fig. 13.23—Constraints leading to bounds on the elastic properties of a composite material. For rocks, one component is usually considered the mineral matrix, the other component the pore space: (a) constant strain condition, Voigt bound; (b) constant stress condition, Reuss bound.**

$$M_V = A M_A + (1 - A) M_B, \dots\dots\dots (13.46)$$

where  $M_V$  is the effective Voigt modulus,  $M_A$  and  $M_B$  are the component moduli, and  $A$  is the volume fraction of component  $A$ . In contrast, with the constant-stress case (Fig. 13.23b), the soft component dominates the deformation and we get the lower (Reuss) limit.

$$1 / M_R = A / M_A + (1 - A) / M_B, \dots\dots\dots (13.47)$$

where  $M_R$  is the lower Reuss effective modulus. The average value between these two limits is often used in property estimation and is termed the Voigt-Reuss-Hill relation

$$M_{VRH} = (M_V + M_R) / 2. \dots\dots\dots (13.48)$$

Note that in the case for minerals plus pores,  $M_{\text{pore}} = 0$  and  $M_V$  decreases linearly with porosity.  $M_R$  equals zero for all porosities.

An alternative approach, known as the Hasin-Shtrikman technique,<sup>48</sup> is to fill space with concentric spheres. Material 1 is in the interior, and Material 2 forms a surrounding shell. Spheres such as these but of varying size are packed together to fill the entire medium (Fig.

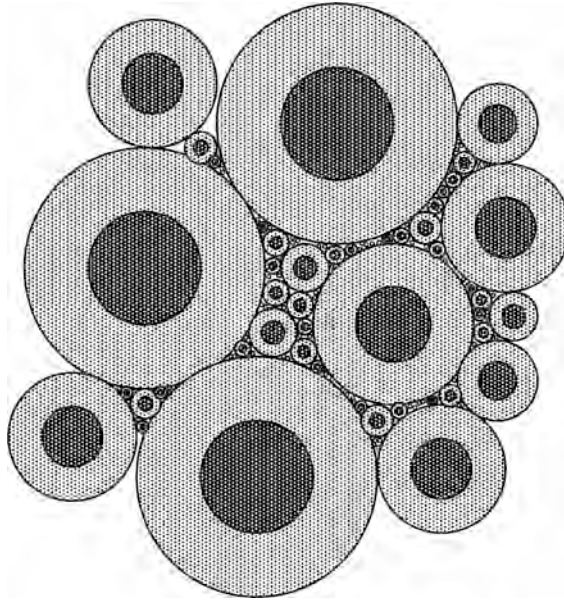


Fig. 13.24—Schematic view of the composite material modeled by Hashin-Shtrikman method.

13.24). The resulting upper and lower bounds (“+” vs. “-” respectively) for bulk and shear modulus are given by

$$K_{HS \pm} = K_1 + \frac{f_2}{(K_2 - K_1)^{-1} + f_1(K_1 + \frac{4}{3}\mu_1)^{-1}}, \dots\dots\dots (13.49)$$

and

$$\mu_{HS \pm} = \mu_1 + \frac{f_2}{(\mu_2 - \mu_1)^{-1} + \frac{2f_1(K_1 + 2\mu)}{5\mu_1(K_1 + \frac{4}{3}\mu)}}, \dots\dots\dots (13.50)$$

where  $K_i$ ,  $\mu_i$ , and  $f_i$  refer to the bulk and shear moduli and volume fraction of component  $i$ , respectively. The upper and lower bounds are derived by exchanging the stiff and soft components as “1” or “2.”

The results of using Eqs. 13.46 through 13.50 are shown in Fig. 13.25. Using quartz as the first component and porosity as the second, the composite bulk modulus is plotted in Fig. 13.25a as a function of porosity. In one case, the pores are empty (black), in the other, water fills the pores and is the second component (blue). Because we used quartz as the solid component (Table 13.6), these bounds should contain all possible values for sandstones (remember: for isotropic and homogeneous sandstones). If, on the other hand, our rock was made up of only quartz and calcite, we get bounds that appear in Fig. 13.25b. Note that the bounds have collapsed and produce only a narrow spread. This is a result of the two end components both being stiff and closer together. In cases such as these, a simple linear average can work well.

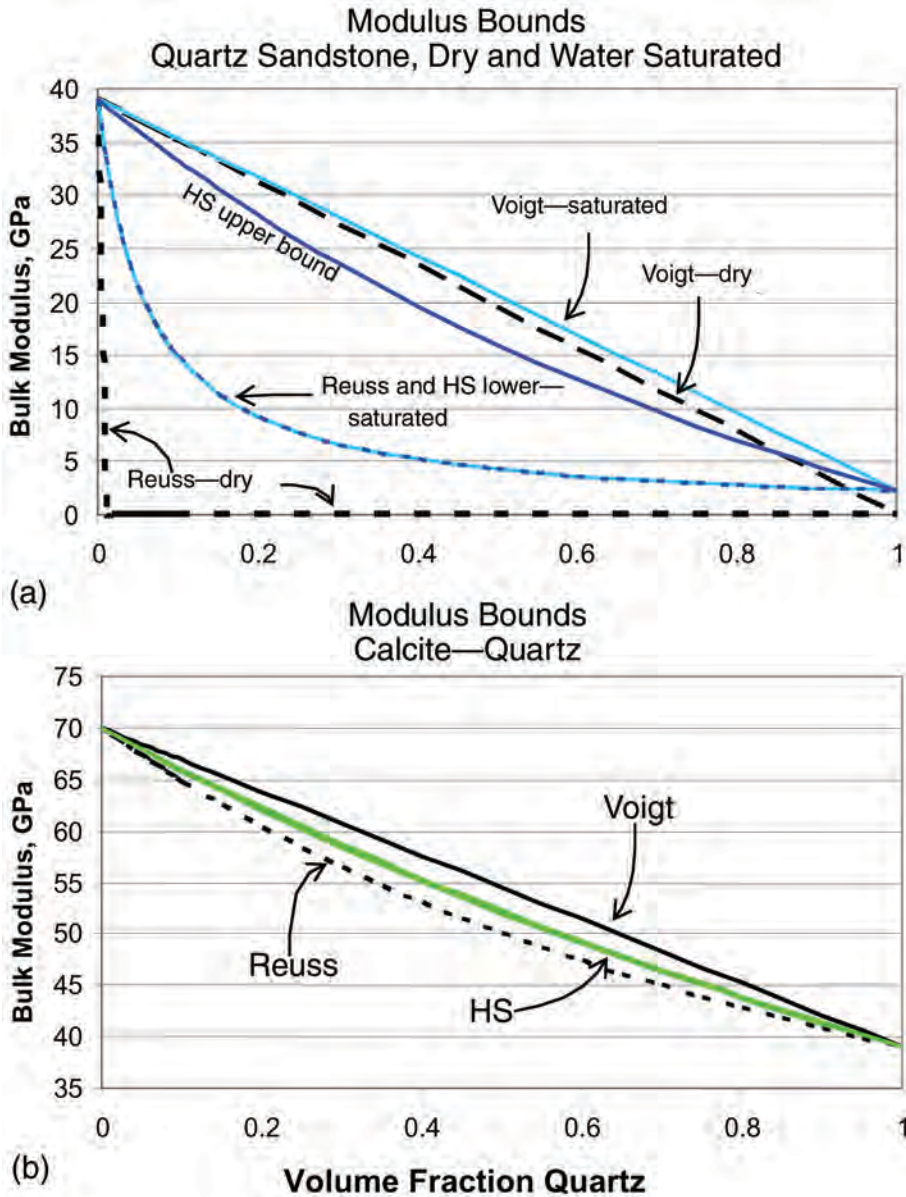


Fig. 13.25—(a) General bounds of a porous material made of quartz, both dry and saturated with water (HS = Hasin-Shtrikman). With extreme differences in material properties, the bounds can be very wide. (b) Example of bounds for a quartz-calcite mixture. Because the properties are comparable between the two minerals, the bounds act much more like simple linear averages.

**13.5.4 Mineral Properties.** There are numerous ways to measure mineral moduli. The most obvious is by deforming single crystals. Alternatively, elastic velocities can be measured and moduli extracted for zero porosity aggregates. Tables 13.6a and 13.6b present lists of “isotropic” densities, mineral bulk and shear moduli, and elastic velocities. In reality, minerals are anisotropic, and the values listed in the table are averages derived from the effective media formulas presented above to represent polygrained isotropic composites. The highest-velocity, highest-moduli are for such minerals as almandine and rutile. Velocities can reach 9 km/s for

$V_p$ , and moduli can be in the hundreds of GPa. Clays are a particular problem. As noted before, they are among the most abundant minerals on the surface of the Earth, and are common in most sedimentary rocks. Their small size, variable composition, and chemical activity make them difficult to characterize from a mechanical point of view. The results of Katahara,<sup>49</sup> Wang *et al.*,<sup>50</sup> and Prasad *et al.*<sup>51</sup> are given in Table 13.6b.

Mineral properties can also be extracted from the numerous empirical trends developed for rocks, as we will see below.

**13.5.5 Elastic Wave Velocities.** So far, we have considered only the static elastic deformation of materials. By adding the dynamic behavior, we arrive at how elastic waves propagate through materials. If a body is changing its speed as well as deforming, there will be an unbalanced force because of the acceleration described through Newton’s Second Law:

$$\sum_{i=1}^3 \frac{\partial}{\partial x_i} \sigma_{ij} = \rho a_j = \rho \frac{\partial^2 u_j}{\partial t^2}, \dots\dots\dots (13.51)$$

where  $\rho$  is density,  $a$  is acceleration,  $u$  is displacement, and  $t$  is time. Combining this with Hook’s Law (Eq. 13.43) gives the general wave equation. For a plane wave in the  $xx$  direction, this can be written as

$$\frac{\partial \sigma_{xx}}{\partial x} + \frac{\partial \sigma_{xy}}{\partial y} + \frac{\partial \sigma_{xz}}{\partial z} = \rho \frac{\partial^2 u_x}{\partial t^2} \dots\dots\dots (13.52)$$

However, if the material is being deformed, we will have strains associated with the change of displacement with position. In turn, these strains can be related to the stresses through the appropriate modulus,  $M$  (for example, Eq. 13.37):

$$\frac{\partial u_i}{\partial x_j} = \epsilon_{ij} = \frac{\sigma_{ij}}{M} \dots\dots\dots (13.53)$$

For constant elastic components, this simplifies to

$$\left( \frac{\lambda + 2\mu}{\rho} \right) \frac{\partial^2 u_x}{\partial x^2} = \frac{\partial^2 u_x}{\partial t^2} \dots\dots\dots (13.54)$$

The solution to this equation gives the compressional velocity

$$V_p = \sqrt{\frac{\lambda + 2\mu}{\rho}} = \sqrt{\frac{K + \frac{4}{3}\mu}{\rho}} \dots\dots\dots (13.55)$$

Similarly, for shear motion

$$\frac{\mu}{\rho} \frac{\partial^2 u_x}{\partial y^2} = \frac{\partial^2 u_x}{\partial t^2}, \dots\dots\dots (13.56)$$

and we get the shear velocity:

**TABLE 13.6A—MINERAL DYNAMIC ELASTIC PROPERTIES (ZERO POROSITY, ISOTROPIC GRAINPACK EQUIVALENT)**

Mineral	Density (gm/cc)	Moduli		Velocity	
		Shear (GPa)	Bulk (GPa)	Compress. (m/s)	Shear (m/s)
Albite	2.61	30.17	55.94	6070	3400
Almandine	4.08	95.14	176.38	8621	4829
Anorthite	2.75	40.76	91.80	7290	3850
Apatite	3.23	57.38	84.62	7063	4215
Aragonite	2.99	35.59	74.83	6395	3450
Augite A	3.32	58.01	95.72	7220	4180
Augite B	3.42	57.21	106.97	7320	4090
Barite A	4.5	21.11	58.85	4397	2166
Barite B	4.5	20.49	53.19	4230	2134
Barite C	4.5	21.39	52.35	4239	2180
Biotite A	3	12.44	55.07	4887	2036
Biotite B	3.05	25.12	50.89	5260	2870
Calcite 6	2.71	28.41	65.35	6172	3238
Calcite A	2.71	27.72	64.51	6119	3198
Calcite C	2.71	28.69	81.94	6660	3254
Calcite D	2.71	25.77	71.63	6254	3084
Calcite E	2.71	30.59	74.76	6530	3360
Clinoperthite A	2.54	23.78	46.81	5560	3060
Clinoperthite B	2.54	23.47	46.10	5520	3040
Clinoperthite C	2.56	27.04	53.36	5910	3250
Clinoperthite D	2.57	24.86	50.36	5700	3110
Clinoperthite E	2.57	24.86	51.53	5740	3110
Clinoperthite F	2.57	26.15	53.08	5850	3190
Clinoperthite G	2.57	23.91	54.58	5800	3050
Diopside	3.31	63.50	111.58	7700	4380
Dolomite A	2.85	35.92	91.76	7000	3550
Dolomite B	2.87	49.67	74.41	7000	4160
Dolomite C	2.87	52.08	73.20	7050	4260
Dolomite D	2.85	43.13	82.15	7000	3890
Epiote	3.4	61.12	106.20	7430	4240
Fluorite A	3.18	40.85	84.82	6618	3584
Fluorite B	3.18	42.74	85.90	6703	3666
Fluorite C	3.18	41.17	88.20	6708	3598
Fluorite D	3.18	39.96	89.64	6704	3545
Fluorite E	3.18	42.60	84.25	6660	3660
Forsterite 8	3.22	81.15	128.30	8570	5020
Forsterite A	3.22	81.47	128.98	8590	5030
Galena A	7.5	27.79	55.56	3514	1925
Galena B	7.5	30.82	61.48	3698	2027
Garnet A	3.6	92.54	150.36	8720	5070

**TABLE 13.6A—MINERAL DYNAMIC ELASTIC PROPERTIES (ZERO POROSITY, ISOTROPIC GRAINPACK EQUIVALENT) (Continued)**

Mineral	Density (gm/cc)	Moduli		Velocity	
		Shear (GPa)	Bulk (GPa)	Compress. (m/s)	Shear (m/s)
Garnet B	3.67	86.68	152.71	8550	4860
Garnet C	4.01	88.96	149.06	8170	4710
Garnet D	4.06	95.50	162.56	8450	4850
Garnet E	4.06	83.68	150.87	8040	4540
Garnet F	4.16	90.73	160.12	8220	4670
Garnet G	4.16	94.26	177.01	8530	4760
Garnet H	4.18	95.11	176.62	8520	4770
Garnet I	4.25	96.70	175.97	8470	4770
Garnet J	4.25	96.29	177.23	8480	4760
Halite A	2.16	14.49	24.62	4510	2590
Halite B	2.16	14.60	24.47	4510	2600
Halite C	2.16	14.60	24.08	4490	2600
Hematite A I	5.26	91.90	97.65	6470	4180
Hematite B	5.25	90.85	206.52	7900	4160
Hornblende A	3.12	43.18	87.13	6810	3720
Magnesite	2.97	62.57	112.40	8120	4590
Magnetite A	5.18	91.38	160.30	7380	4200
Magnetite B	5.18	90.94	161.64	7390	4190
Matrolite	2.25	84.00	51.72	8530	6110
Muscovite A	2.78	22.26	42.91	5110	2830
Muscovite B	2.79	30.94	52.28	5790	3330
Nornblende B	3.15	45.73	95.15	7040	3810
Olivine A	3.31	79.15	129.14	8420	4890
Olivine B	3.32	80.69	131.16	8480	4930
Olivine C	3.13	60.87	152.49	8640	4410
Phlogo A	2.8	23.22	55.28	5550	2880
Phlogo B	2.82	25.21	49.84	5440	2990
Plagioclase A	2.64	27.54	65.41	6220	3230
Plagioclase B	2.64	29.45	62.87	6220	3340
Plagioclase C	2.64	31.24	63.13	6300	3440
Plagioclase D	2.68	33.40	71.16	6570	3530
Plagioclase E	2.68	33.77	75.27	6700	3550
Plagioclase F	2.69	37.83	67.45	6620	3750
Pyrite B	5.02	129.04	147.63	7980	5070
Pyrite D	5.02	123.50	136.07	7740	4960
Pyrite E	5.02	123.00	143.77	7830	4950
Pyrite F	5.02	127.52	147.26	7950	5040
Pyrite G	5.02	132.63	110.08	7560	5140
Quartz A	2.65	41.77	35.94	5880	3970
Quartz B	2.65	41.77	39.08	5980	3970

**TABLE 13.6A—MINERAL DYNAMIC ELASTIC PROPERTIES (ZERO POROSITY, ISOTROPIC GRAINPACK EQUIVALENT) (Continued)**

Mineral	Density (gm/cc)	Moduli		Velocity	
		Shear (GPa)	Bulk (GPa)	Compress. (m/s)	Shear (m/s)
Quartz C	2.65	41.14	37.40	5900	3940
Quartz D	2.65	41.14	37.40	5900	3940
Quartz E	2.65	44.33	37.89	6050	4090
Rhodochrosite	3.57	41.27	120.41	7010	3400
Rutile A	4.2	97.17	268.07	9730	4810
Rutile B	4.2	67.54	256.23	9080	4010
Rutile C	4.26	112.55	215.23	9260	5140
Siderite	3.75	48.06	116.01	6930	3580
Sillikanite	3.19	82.32	184.23	9600	5080
Sphalerite A	4	28.52	69.31	5180	2670
Sphalerite B	4	27.04	80.59	5400	2600
Sphalerite C	4	24.60	77.45	5250	2480
Staurolite	3.78	45.25	124.88	7000	3460
Sulfur	2.07	8.20	17.83	3550	1730
Sylvite A	1.99	8.44	18.39	3860	2060
Sylvite B	1.99	8.36	18.04	3830	2050
Sylvite C	1.99	8.44	17.78	3820	2060
Sylvite D	1.99	8.44	16.43	3730	2060
Topaz	3.5	113.72	166.26	9530	5700
Tourmaline A	3.23	82.05	87.12	7800	5040
Tourmaline B	3.23	82.37	97.41	8010	5050
Tourmaline C	3.23	72.26	102.69	7850	4730
Tourmaline D	3.23	82.70	110.65	8270	5060
Zircon	4.7	378.17	-198.88	8060	8970

$$V_s = \sqrt{\frac{\mu}{\rho}} \dots\dots\dots (13.57)$$

**13.5.6 Porosity Dependence.** The bounding relations we examined above can be applied directly to rock acoustic velocities. Some dolomites with vuggy pores may approach the Voigt bound. Highly fractured rocks may approach the Reuss bound. However, there is often a great difference between these idealized bounds and real rocks. For sandstones, we would expect to begin with quartz velocity at zero porosity and have decreasing velocity with increasing porosity. By combining Eqs. 13.46 and 13.47 for moduli in Eq. 13.55, we can plot expected velocity bounds, as in Fig. 13.26a. Observed distributions for sandstones are also plotted, and we see a systematic discrepancy with the upper (Voigt) bound. At high porosities, grains separate, and the mixture acts as a suspension. The majority of rocks have an upper limit to their porosity

**TABLE 13.6B—CLAY DYNAMIC ELASTIC PROPERTIES (ZERO POROSITY, ISOTROPIC GRAINPACK EQUIVALENT)**

	$V_p$ (km/s)	$V_s$ (km/s)			
<u>Katahara</u>					
Illite	5.80	3.35			
Chlorite	5.90	3.30			
Kaolinite	6.20	3.60			
Tosaya	3.40	1.70			
Castagna <i>et al.</i>	3.75	1.80			
Han <i>et al.</i>	3.40	1.75			
Eastwood and Castagna	4.35	2.60			
			Density	$\mu$	$K$
<u>Wang <i>et al.</i></u>			(gm/cc)	(GPa)	(Gpa)
Mont. (Saz-1)	5.142	2.738	2.268	17.00	37.30
Mont. (S Wy-2)	4.894	2.788	2.598	20.19	35.31
Mont. (STX-1)	5.936	3.250	2.338	24.70	49.46
Mont. (S Wy-1)	4.448	2.504	2.600	16.30	29.71
Mont. (Shca-1)	6.202	3.182	2.667	27.00	66.59
Kaolinite (Kga-2)	5.650	3.130	2.439	23.89	46.01
Kaolinite (Kga-1b)	5.511	2.853	2.444	19.89	47.71
Illite (IMT-2)	5.971	3.082	2.706	25.70	62.21
Illite (ISMT-2)	4.832	2.644	2.546	17.80	35.72
Chlorite (CCa-2)	9.088	4.284	2.839	52.10	165.02
Chlorite (Ch-1)	9.457	5.604	2.681	84.20	127.54
Smectite (S Wa-1)	2.780	1.698	2.394	6.90	9.30
Attapulgit (PFI-1)	7.490	4.278	2.220	40.63	70.38
Saponite (SapCA2)	3.838	2.205	2.509	12.20	20.70
Saponite (SepSp-1)	8.653	5.291	2.354	65.90	88.41
Mont. (SYn-1)	6.632	4.008	2.459	39.50	55.50

usually termed “critical porosity,”  $\Phi_c$  (Yin *et al.*<sup>53</sup> and Nur *et al.*<sup>54</sup>). At this high porosity limit, we reach the threshold of grain contacts and grain support (Han *et al.*<sup>55</sup>).

Brine-saturated sandstone velocities can be separated into classes based on their velocity-porosity relations (Fig. 13.26b). Very clean sandstones (Class I) decrease in a simple linear trend from the 6 km/s velocity of quartz as porosity increases. Most consolidated rocks (Class II) have somewhat lower velocities, still decreasing with increasing porosity. Poorly cemented sands (Class III) approach the lower Reuss bound for velocity. Pure suspensions are dominated by the modulus of water (Class IV) and are almost independent of the porosity. However, such suspensions are rare. Another important class is dominated by fractures (Class V). As we shall



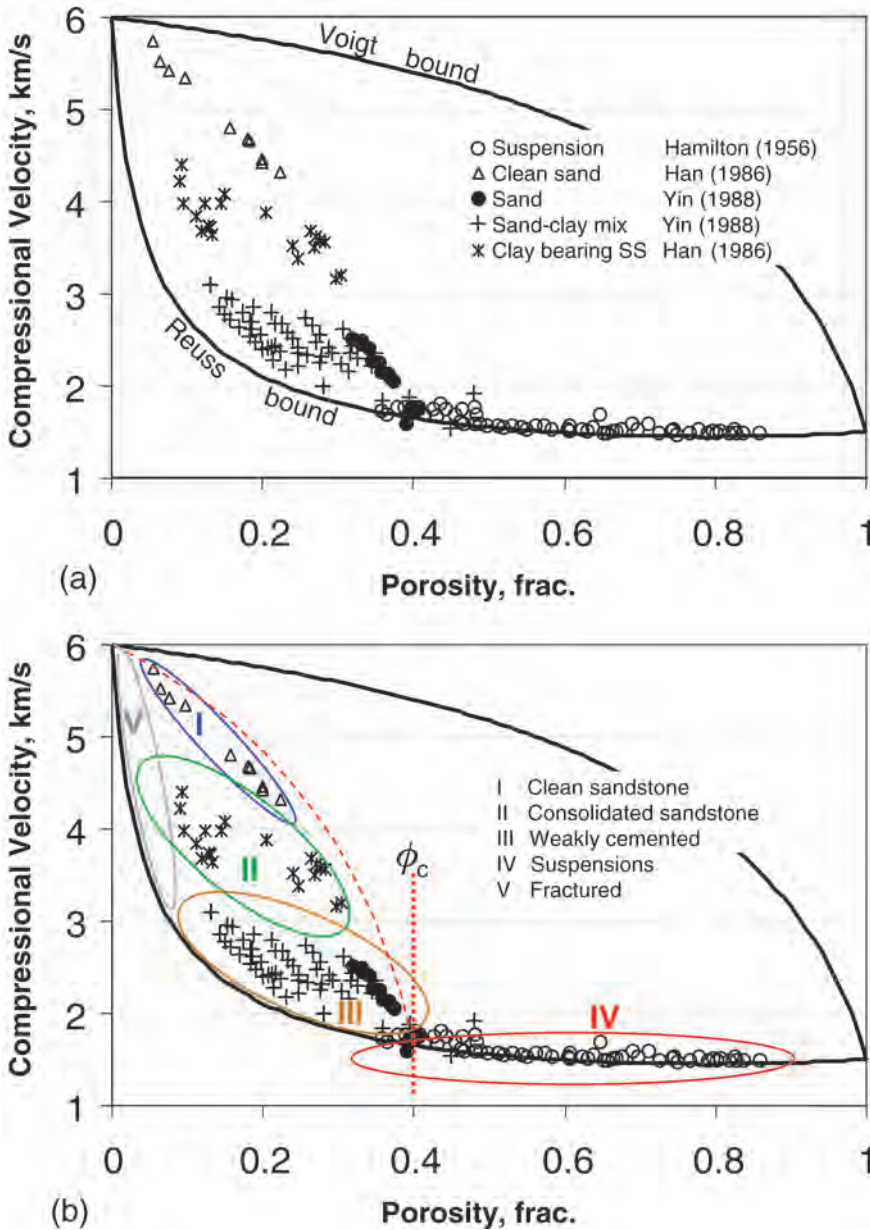


Fig. 13.26—(a) Compressional velocity vs. porosity in sandstones: laboratory data with elastic bounds (modified from Marion<sup>52</sup>). (b) Sandstone velocities divided into classes.

see later, fractures have a far greater effect on velocity than might be expected for their low porosity, and may approach the Reuss bound.

**13.5.7 Measured Velocity-Porosity Relations.** Numerous systematic investigations into the relationship of velocity, porosity, and lithology (usually clay content) have been conducted. The results of Vernik and Nur<sup>56</sup> for brine-saturated sandstones are shown in Fig. 13.27 for compressional and shear velocities, respectively. Very clean sands (clean arenites) show the

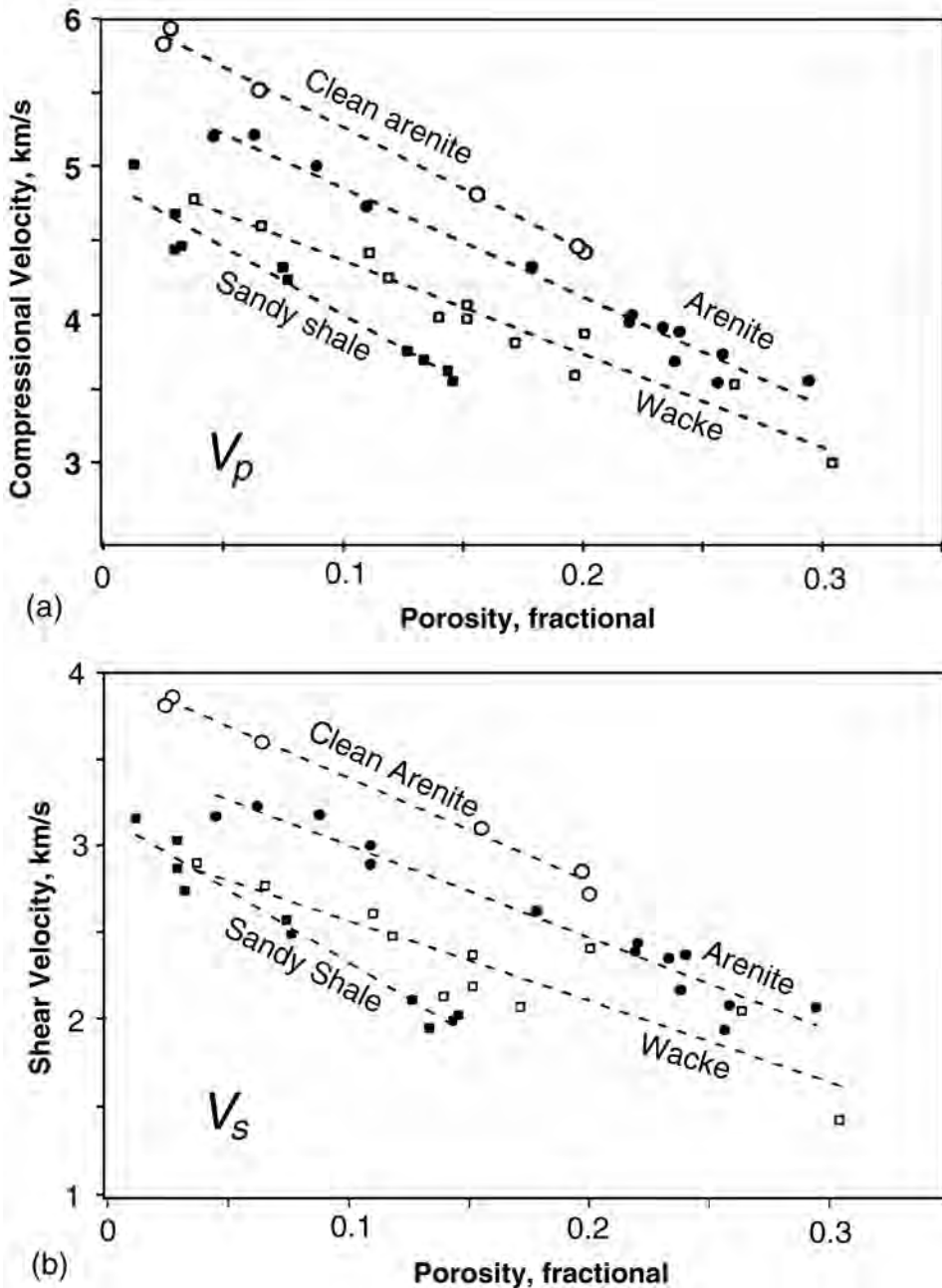


Fig. 13.27—(a) Brine-saturated sandstone compressional velocities as a function of porosity. Sandstones are segregated into lithologic type, and show decreasing velocity as rocks depart from pure quartz content (after Vernik and Nur<sup>56</sup>). (b) Brine-saturated sandstone shear velocities as a function of porosity. Behavior is similar to the  $V_p$  trends seen in (a) above (after Vernik and Nur<sup>56</sup>).

linear decrease from quartz velocity. However, even small amounts of clays will substantially lower the trend. Increasing clay content will then continue to lower velocities.

Numerous examples of general porosity/velocity/clay content relations for sandstones are given in [Table 13.7 a and b](#) (symbol definitions for these relations are in [Table 13.7c](#)). These

TABLE 13.7A—VELOCITY-POROSITY-CLAY RELATIONS FOR SANDSTONES	
Wyllie, Gregory, and Gardner	
$\frac{1}{V_p} = \frac{\phi}{V_f} + \frac{1-\phi}{V_M}$	
Hunt, Raymer, and Gardner	
$V_p = (1-\phi)^2 V_M + \phi V_f$	$0 < \phi < 0.37$
$\frac{1}{V_p} = \frac{0.47-\phi}{0.10} \frac{1}{V_p(\phi=0.37)} + \frac{\phi-0.37}{0.10} \frac{1}{V_p(\phi=0.47)}$	
$\frac{1}{V_p^2} = \frac{\rho\phi}{\rho_f V_f^2} + \frac{\rho(1-\phi)}{\rho_M V_M^2}$	$\phi > 0.47$
Tosaya	
$V_p = (1-\phi)^2 V_M + \phi V_f$	$V_s = 3.7 - 6.3\phi - 2.1C$
Dominico	
$\frac{1}{V_p} = 0.163 + 0.365\phi$	$\frac{1}{V_s} = 0.224 + 0.889\phi$
Castagna, Batzle, and Eastwood	
$V_p = 5.81 - 9.42\phi - 2.21C$	$V_s = 3.89 - 7.07\phi - 2.04C$
Han, Nur, and Morgan	
$V_p = 5.59 - 6.93\phi - 2.18C$	$V_s = 3.52 - 7.07\phi - 1.89C$
Eberhart-Phillips, Han, and Zoback	
$V_p = 5.77 - 6.94\phi - 1.73C^{1/2} + 0.446P$	$V_s = 3.70 - 4.94\phi - 1.57C^{1/2} + 0.361P$
where $P = P_e - e^{-16.7P_e}$	

types of relations have proved very useful in giving velocities under general conditions, providing the overall effects of clay, and establishing the relation of compressional to shear velocity ( $V_p/V_s$  ratios).  $V_p-V_s$  relations are extremely important, because shear logs are relatively rare, yet shear velocities are critical in determining seismic direct hydrocarbon indicators such as reflection Amplitude-Versus-Offset (AVO) trends (Castagna *et al.*<sup>18</sup>).

Measured data for carbonates are less abundant. A systematic investigation of samples from several wells was reported by Rafavich *et al.*<sup>57</sup> A plot of their results for carbonate  $V_p$  as functions of porosity and composition is shown in Fig. 13.28. They collected detailed information on fabric and texture as well as porosity and mineralogy. Performing regressions on their extensive data set produced the relations given in Table 13.8a. The coefficients associated with these equations are given in Table 13.8b. Note that the relations are dependent on the effective pressure.

A similar set of measurements by Wang *et al.*<sup>58</sup> are shown in Fig. 13.29. For carbonates, the data can be quite scattered, but can still show the general velocity decrease with increasing

TABLE 13.7B—COMPRESSIONAL SHEAR VELOCITY RELATIONS ( $V_p : V_s$ )	
<b>Pickett</b>	
$V_s = 0.866 V_p - 1.16$	Sandstone
$V_s = 0.526 V_p$	Limestone
$V_s = 0.555 V_p$	Dolomite
<b>Castagna, Batzle, and Eastwood</b>	
$V_s = 0.862 V_p - 1.17$	Mudrock line
$V_s = 0.667 V_p$	Dry
<b>Krief <i>et al.</i></b>	
$V_s^2 = 0.45 V_p^2 - 1.59 + \frac{1.32}{V_p^2}$	
<b>Greenberg and Castagna</b>	
$V_s = -0.02180 V_p^2 - 0.9629 V_p - 1.0828$	Sandstone
$V_s = -0.02280 V_p^2 - 0.9139 V_p - 1.1347$	Shale
$V_s = -0.00271 V_p^2 - 0.4727 V_p - 0.2138$	Limestone
$V_s = -0.00984 V_p^2 - 0.6036 V_p - 0.0217$	Dolomite
<b>Freund</b>	
$V_s = 0.763 V_p - 0.603$	

TABLE 13.7C—NOMENCLATURE FOR TABLES 13.7A AND B	
Where: $V_p$ = rock compressional velocity (km/s)	$C$ = clay content (fractional)
$V_s$ = rock shear velocity (km/s)	$f$ = porosity (fractional)
$V_f$ = pore fluid velocity (km/s)	$r$ = rock density (g/cc)
$V_M$ = solid mineral compressional velocity	$r_f$ = fluid density (g/cc)
$P_e$ = effective pressure (MPa)	$r_m$ = mineral density (g/cc)

porosity. These results were summarized in a set of relations (**Table 13.9**) again showing pressure dependence. Their data, however, includes measurements made with samples not only brine-saturated, but hydrocarbon-saturated and after simulated reservoir floods. They demonstrate that the overall velocity and impedance changes were strongly dependent on the imposed sequence of flooding. The ability to observe a particular reservoir process will be more complicated than simply completely substituting fluids into the rocks.

**13.5.8 Pressure.** Rock moduli (compressibility) and elastic velocities are strongly influenced by pressure. With increasing effective pressure, compliant pores within a rock will deform, contract, or close. The rock becomes stiffer, and, as a result, velocities increase. Two examples are shown in **Fig. 13.30**. The typical behavior is rapid increase in velocity, with increasing pressure at low pressures, followed by a flattening of the curve at higher pressures. Presumably, compliant pores and cracks are closed at higher pressure, and velocities asymptotically approach a relatively constant velocity. This specific behavior at high pressures leads to the simple velocity-porosity transforms and probably is responsible for our ability to use sonic tools as in-situ porosity indicators with little regard to local pressures.

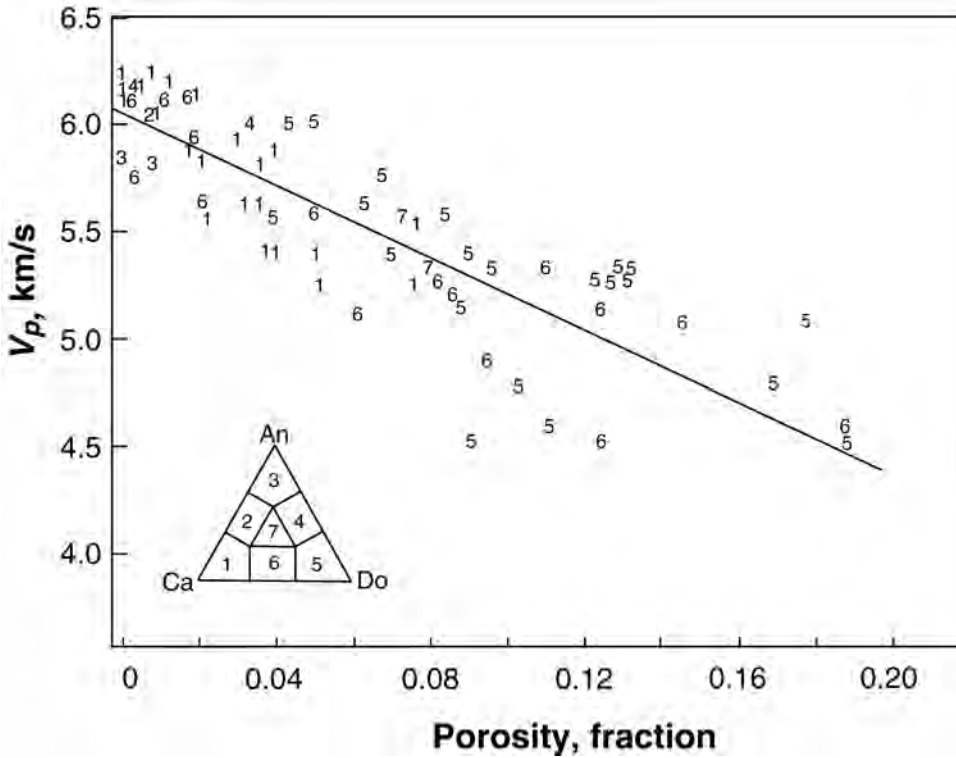


Fig. 13.28—Carbonate compressional velocity as functions of porosity and mineralogy. The compositions are plotted by number according to the Anhydrite-Calcite-Dolomite triangular diagram in the lower-left portion of the figure (from Rafavich *et al.*<sup>57</sup>).

The stress dependence of granular material has been examined extensively. For example, Gassmann<sup>60</sup> and Duffy and Mindlin<sup>61</sup> modeled various packings of spheres. In general, they found that

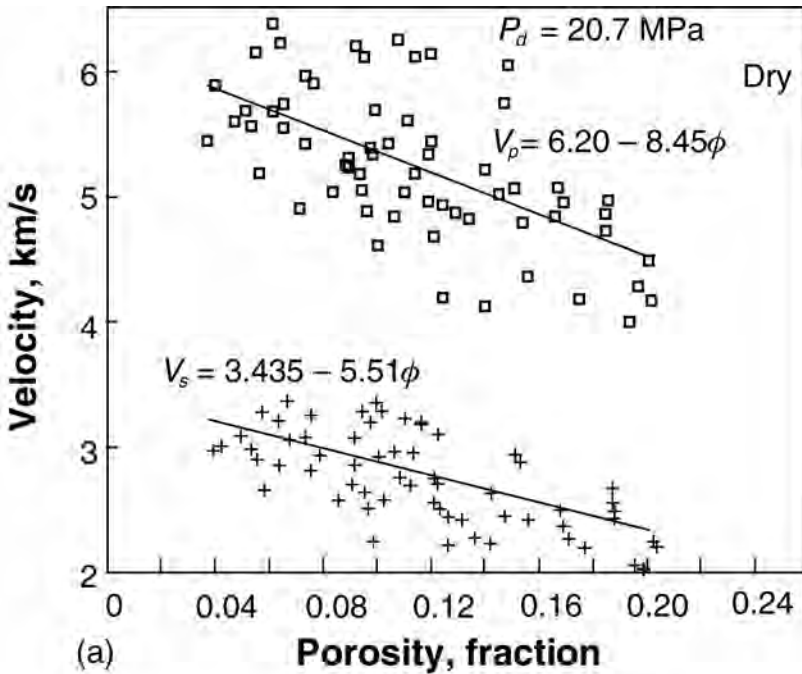
$$V_p^2 = f(P_e^{1/3}), \dots\dots\dots (13.58)$$

where  $f$  is approximately linear. This type of relation is particularly useful for poorly consolidated sands.

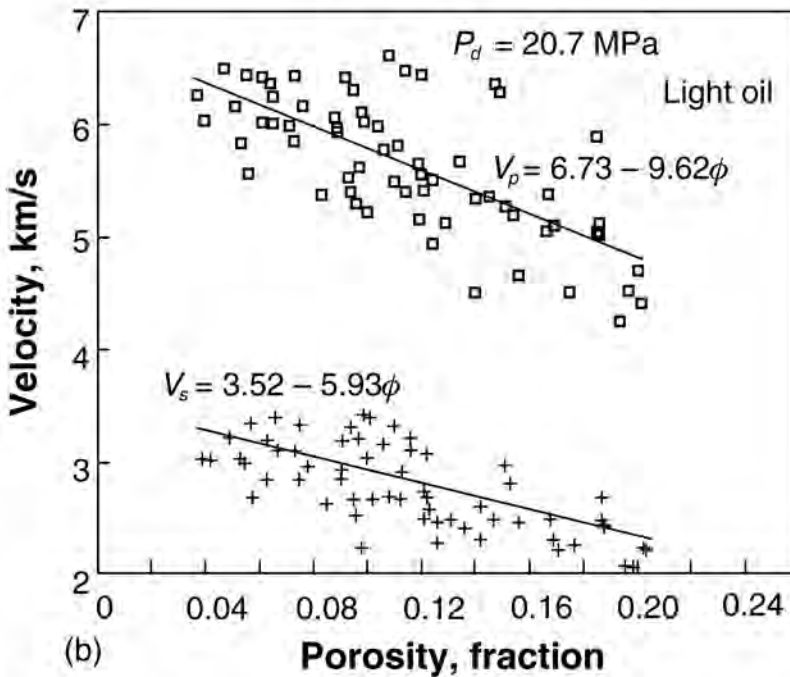
Although the absolute pressure dependences shown in Fig. 13.30a vs 13.30b are in significant contrast, for most sandstones, relative changes are more consistent. By normalizing the velocities to those at high pressure (40 MPa), we get a much more consistent behavior (Fig. 13.31).

$$\frac{V_p}{V_p(40)_s} = 1.0 - 0.38 \exp\left(\frac{-P_e}{12}\right) \dots\dots\dots (13.59)$$

Examining a similar set of data allowed Eberhart-Phillips *et al.*<sup>62</sup> to develop a pair of relations for both  $V_p$  and  $V_s$  (see also Table 13.7)



(a)



(b)

Fig. 13.29—(a) Dry carbonate velocities. Although there is considerable scatter, perhaps because of the heterogeneous nature of the porosity, a systematic decrease in both compressional and shear velocities with increasing porosity is obvious (from Wang *et al.*<sup>58</sup>). (b) Carbonate velocities when saturated with a light refined oil. Compressional velocities are higher and shear velocities slightly lower. The porosity dependence is similar to the dry case (from Wang *et al.*<sup>58</sup>).

$$V_p = 5.77 - 6.94\phi - 1.73C^{\frac{1}{2}} + 0.446[P_e - \exp(-16.7P_e)], \dots\dots\dots (13.60a)$$

**TABLE 13.8A—RAFAVICH *ET AL.*,<sup>57</sup> CARBONATE  $V_p$  AND  $V_s$  RELATIONS**

$$V_{pb} = A_0 + A_1\rho_b - A_2\phi - A_3ANC - A_5CAX - A_6SKG + A_7(GTO + CAM) - A_8(XTO + DOX + DOC - CAC)$$

$$V_{pa} = A_0 + A_1\rho_a - A_2\phi - A_3ANC - A_5CAX - A_6SKG + A_7(GTO + CAM) - A_8(XTO + DOX + DOC - CAC)$$

$$V_{sb} = A_0 + A_1\rho_b - A_2\phi - A_3ANC - A_5CAX - A_6SKG + A_7(GTO + CAM) - A_8(XTO + DOX + DOC - CAC)$$

$$V_{sa} = A_0 + A_1\rho_a - A_2\phi - A_3ANC - A_5CAX - A_6SKG + A_7(GTO + CAM) - A_8(XTO + DOX + DOC - CAC)$$

Where:

$\rho_b$	Brine-saturated density
$\rho_a$	Air-saturated density
$\phi$	Porosity
QUC	Total quartz (%)
ANC	Total anhydrite (%)
CAX	Crystalline calcite (%)
SKG	Skeletal grains
GTO	Total grains (%)
CAM	Calcite mud (%)
XTO	Total crystals (%)
DOX	Dolomite crystals (%)
DOC	Total dolomite (%)
CAC	Total calcite (%)

$$V_s = 3.70 - 4.94\phi - 1.57C^{1/2} + 0.361[P_e - \exp(-16.7P_e)] \dots\dots\dots (13.60b)$$

where  $P_e$  is the effective pressure. For carbonates, the explicit pressure dependence given in [Tables 13.8a](#) and [13.9](#) allow the pressure dependence to be evaluated. The pressure dependence for carbonate  $V_p$  from Rafavich *et al.*<sup>57</sup> is shown in [Fig. 13.32](#). Note that pressure sensitivity increases with increasing porosity. These types of relations permit velocity changes associated with pressure changes in the reservoir to be modeled.

It is important to note that all these relations involve either differential pressure ( $P_d$ ) or effective pressure ( $P_e$ ). Pore pressure ( $P_p$ ) counters the influence of confining pressure ( $P_c$ ), so the difference between these two controls rock properties. This has been expressed simply in the Terzaghi<sup>63</sup> relation for the pressure dependence of a given porous material property  $S$ ,

$$S' = S(P_c - P_p) \dots\dots\dots (13.61)$$

This kind of behavior has been seen in numerous cases, as in [Fig. 13.33](#). This is one reason why properties such as density, resistivity, and velocity can decrease with increasing depth when “overpressure” or when increased pore pressure is encountered. Changes in reservoir pore pressure will have a similar influence. More precisely, it is the effective pressure ([Eq. 13.35](#)) that controls properties rather than just the differential. However, the magnitude of effective pressure is often found to be close to the simpler differential pressure.

TABLE 13.8B—RAFAVICH ET AL.<sup>57</sup> COEFFICIENTS

Differential Pressure (Mpa)	$A_0$	$A_1$	$A_2$	$A_3$	$A_4$	$A_5$	$A_6$	$A_7$	$A_8$
	$V_p$ (Brine Saturated)								
3.45	-1082.1	2575.6	60.96	27.43	3.96	3.35	3.05	1.52	1.52
13.79	-228.6	2270.8	54.86	24.38	4.57	0.00	0.00	1.22	0.91
27.59	289.6	2118.4	48.77	24.38	4.88	0.00	0.00	0.91	0.61
41.38	472.4	2072.7	48.77	24.38	5.49	0.00	0.00	0.61	0.61
55.17	655.3	2011.7	45.72	24.38	5.79	0.00	0.00	0.30	0.30
68.97	685.8	1996.5	45.72	24.38	6.10	0.00	0.00	0.00	0.00
$V_p$ (Air Saturated)									
3.45	1920.3	1402.1	42.67	42.67	0.00	10.06	9.14	1.52	1.22
13.79	2484.2	1204.0	36.58	36.58	0.00	6.10	5.49	1.22	0.91
27.59	2636.6	1188.7	36.58	36.58	0.00	4.27	3.66	0.61	0.61
41.38	2682.3	1188.7	36.58	33.53	0.00	2.74	2.74	0.61	0.30
55.17	2636.6	1234.5	39.62	33.53	3.05	2.44	2.13	0.00	0.00
68.97	2545.1	1264.9	39.62	33.53	3.35	0.00	0.00	0.00	0.00
$V_s$ (Brine Saturated)									
3.45	-228.6	1234.5	30.48	0.00	0.00	3.35	3.05	0.61	0.61
13.79	320.0	1066.8	24.38	0.00	0.00	2.13	2.13	0.30	0.30
27.59	624.8	990.6	24.38	10.36	2.13	1.83	1.52	0.00	0.00
41.38	762.0	944.9	21.34	10.36	2.13	1.52	1.22	0.00	0.00
55.17	868.7	914.4	21.34	10.36	2.44	1.22	1.22	0.00	0.00
68.97	883.9	899.2	21.34	10.06	2.44	0.00	0.00	0.00	0.00
$V_s$ (Air Saturated)									
3.45	1493.5	655.3	21.34	0.00	0.00	4.57	4.27	0.00	0.00
13.79	1691.7	594.4	18.29	0.00	0.00	3.05	2.74	0.00	0.00
27.59	1844.1	563.9	18.29	9.75	1.83	2.13	2.13	0.00	0.00
41.38	1874.5	548.6	18.29	9.45	1.83	1.83	1.52	-0.30	-0.30
55.17	1874.5	563.9	18.29	8.53	2.13	1.52	1.52	-0.30	-0.30
68.97	1874.5	579.1	18.29	8.84	2.44	1.52	1.22	-0.30	-0.30

**13.5.9 In-Situ Stresses.** The in-situ “lithostatic” stresses are usually unequal. Such different stresses are required or faults, folds, and other structural features would never be developed. In contrast, most laboratory data are collected under equal stress or “hydrostatic” conditions. Differential or triaxial measurements are comparatively rare (e.g., Gregory,<sup>65</sup> Nur and Simmons,<sup>66</sup> Yin,<sup>67</sup> and Scott *et al.*<sup>68</sup>).

In a simple compacting basin with neither lateral deformation nor tectonic stresses, the vertical stress will be largest. Lateral stresses will be developed in a basin as sediments are buried and compacted but are constrained horizontally. Both uniform hydrostatic and unequal lithostatic stress conditions are shown in Fig. 13.34.

A simple estimate of the horizontal stress,  $\sigma_h$ , can be made from the axial stress,  $\sigma_v$ , by

$$\sigma_h = \sigma_v \nu / (1 - \nu), \dots\dots\dots (13.62)$$



TABLE 13.8B—RAFAVICH ET AL.<sup>57</sup> COEFFICIENTS (Continued)

Differential Pressure (Mpa)	A <sub>0</sub>	A <sub>1</sub>	A <sub>2</sub>	A <sub>3</sub>	A <sub>4</sub>	A <sub>5</sub>	A <sub>6</sub>	A <sub>7</sub>	A <sub>8</sub>
V <sub>p</sub> (Brine Saturated)									
500	-3550	8450	200	90	13	11	10	5	5
2000	-750	7450	180	80	15	0	0	4	3
4000	950	6950	160	80	16	0	0	3	2
6000	1550	6800	160	80	18	0	0	2	2
8000	2150	6600	150	80	19	0	0	1	1
10000	2250	6550	150	80	20	0	0	0	0
V <sub>p</sub> (Air Saturated)									
500	6300	4600	140	140	0	33	30	5	4
2000	8150	3950	120	120	0	20	18	4	3
4000	8650	3900	120	120	0	14	12	2	2
6000	8800	3900	120	110	0	9	9	2	1
8000	8650	4050	130	110	10	8	7	0	0
10000	8350	4150	130	110	11	0	0	0	0
V <sub>s</sub> (Brine Saturated)									
500	-750	4050	100	0	0	11	10	2	2
2000	1050	3500	80	0	0	7	7	1	1
4000	2050	3250	80	34	7	6	5	0	0
6000	2500	3100	70	34	7	5	4	0	0
8000	2850	3000	70	34	8	4	4	0	0
10000	2900	2950	70	33	8	0	0	0	0
V <sub>s</sub> (Air Saturated)									
500	4900	2150	70	0	0	15	14	0	0
2000	5550	1950	60	0	0	10	9	0	0
4000	6050	1850	60	32	6	7	7	0	0
6000	6150	1800	60	31	6	6	5	-1	-1
8000	6150	1850	60	28	7	5	5	-1	-1
10000	6150	1900	60	29	8	5	4	-1	-1

where  $\nu$  is Poisson’s ratio. Calculated stresses typical for sands ( $\nu = 0.1$ ) and more clay-rich rocks ( $\nu = 0.25$ ) are also shown in Fig. 13.34. This basic relation (Eq. 13.62) is an oversimplification of actual conditions, but it does provide a useful conceptual model, and lateral stresses indeed are found to be lower in sandstones than in shaly sections in most places.

From a matrix of velocities measured over axial and lateral stress conditions, velocity surfaces could be calculated for a given rock sample. Data such as those shown in Fig. 13.35 were fitted to a form based on that of Eq. 13.58:

$$V^2 = a\sigma_e^{\frac{1}{2}} + b, \dots\dots\dots (13.63)$$

where  $\sigma_e$  is the effective stress. Fits are usually very good even for consolidated rocks with regression factors of around 0.98.

**TABLE 13.9—CARBONATE COMPRESSIONAL AND SHEAR VELOCITY RELATIONS (WANG ET AL.<sup>56</sup>)**

	$P_{\text{effective}}=6.9 \text{ Mpa (1000 psi)}$		$P_{\text{effective}}=20.7 \text{ Mpa (3000 psi)}$		$P_{\text{effective}}=34.5 \text{ Mpa (5000 psi)}$	
	$V_p$ (m/s)	$V_s$ (m/s)	$V_p$ (m/s)	$V_s$ (m/s)	$V_p$ (m/s)	$V_s$ (m/s)
Gas saturated	5672–8006 $\phi$	3260–5533 $\phi$	6199–8448 $\phi$	3435–5512 $\phi$	6446–8440 $\phi$	3351–5440 $\phi$
Oil saturated	6648–10515 $\phi$	3392–5959 $\phi$	6734–9616 $\phi$	3519–5926 $\phi$	6806–9332 $\phi$	3579–5815 $\phi$
Pentane flooded	6513–13316 $\phi$	3363–6819 $\phi$	6606–11407 $\phi$	3453–6171 $\phi$	6683–10669 $\phi$	3498–5809 $\phi$
Solvent flooded	6038–11688 $\phi$	3257–6103 $\phi$	6439–11305 $\phi$	3445–6208 $\phi$	6512–9825 $\phi$	3477–5535 $\phi$
Waterflooded	6586–11339 $\phi$	3379–6600 $\phi$	6690–10342 $\phi$	3471–6090 $\phi$	6764–10043 $\phi$	3529–5890 $\phi$

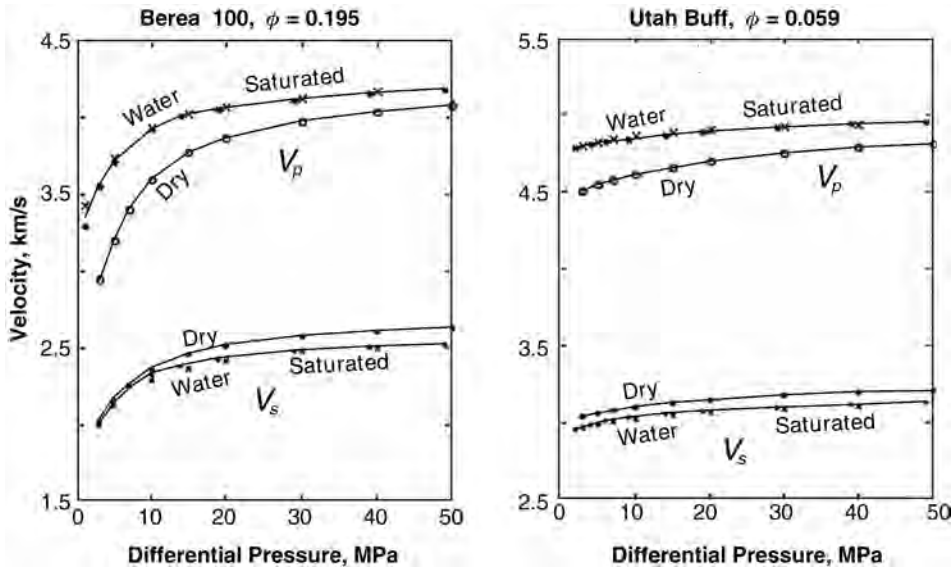


**Fig. 13.30—Examples of dry and water-saturated sandstone velocities as a function of hydrostatic differential pressure. As pressure increases, compliant pores close, making the rock stiffer with higher velocity and lower pore fluid sensitivity.**

Velocities can vary substantially over the stress field shown in Fig. 13.34, not only among samples but also between compressional and shear waves. Fig. 13.36 shows the  $V_p$  and  $V_s$  surfaces for Woodbine sandstone. Figures such as 13.36 demonstrate that the  $V_p$ ,  $V_s$ , and  $V_p/V_s$  ratio will all be strongly dependent on the exact stress tensor at depth. Laboratory measurements under hydrostatic conditions are at best a first-order approximation.

**13.5.10 Temperature.** For consolidated rocks (Classes I, II, and V, Fig. 13.26b), the elastic mineral frame properties are usually only weakly dependent on temperature. This is true for most reservoir operations with the exception of some thermal recovery procedures. In the case of poorly consolidated sands containing heavy oils, velocities show that a strong temperature dependence is observed (Fig. 13.37). Several factors can combine to produce such large effects. First, in heavy-oil sands, the material may actually be a suspension of minerals in tar (Fig. 13.26b, Class IV). The framework is basically a fluid, not solid. In addition, during many measurements, pore pressure cannot reach equilibrium. The large coefficient of thermal expansion of oils combined with the high viscosity often results in high pore pressures within the

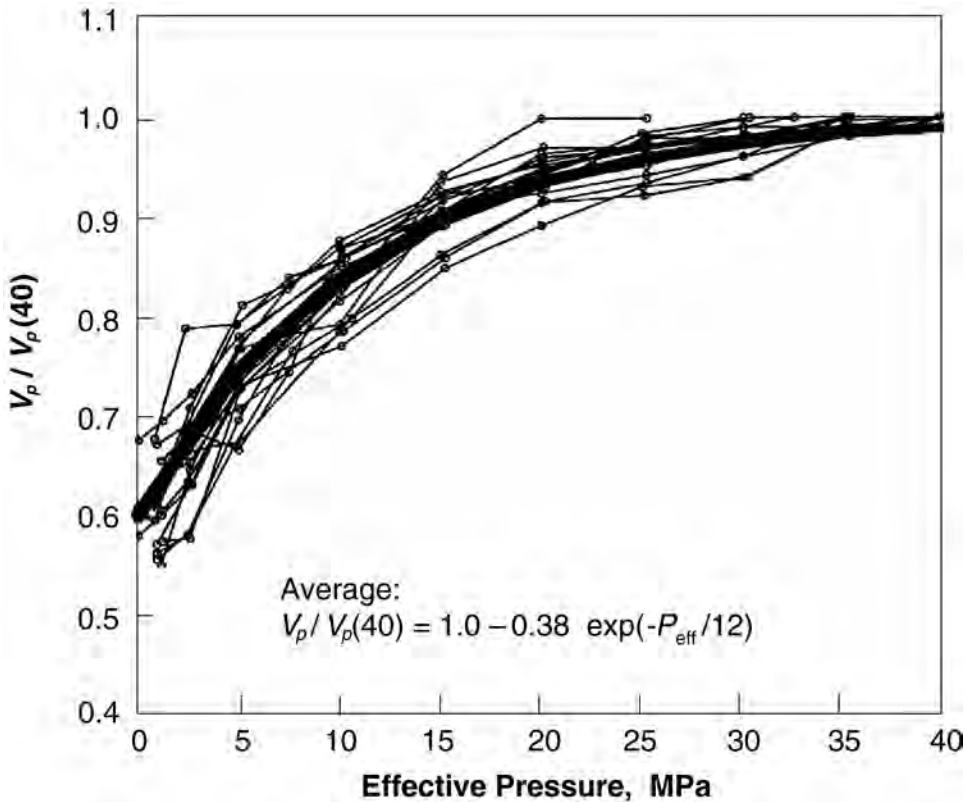


Fig. 13.31—Compressional velocities normalized by the velocity at 40 MPa. For many sandstones, the average trend can be used.

rock samples. Thus, effective pressures can drop substantially (Eq. 13.61). Care needs to be taken during such measurements that equilibrium pressures are reached.

The primary influence of temperature is through the pore fluid properties (refer to the Fluid Properties section). Fig. 13.38 demonstrates this general temperature dependence. For dry (gas-saturated) rock, or rock saturated with brine, almost no change in velocity is observed, even for changes of almost 150°C. At elevated pore pressures, both gas and brine have only weak temperature dependence. Mineral properties are almost unchanged. However, when the rocks are even partially saturated with oil, dramatic temperature dependence is observed. Such changes can be understood by first calculating fluid properties with temperature, then using a Gassmann substitution to calculate the bulk rock properties. Note that for heavy viscous oils, velocity dispersion (velocity dependence on frequency) can be significant, and measured ultrasonic data may not agree with seismic results.

Fluid phase changes may also occur as temperature is raised. These phase changes can have a strong influence, particularly for high-porosity rocks at low pressures. The effect can be seen in Fig. 13.38b, where exsolving a gas phase could reduce the velocity from nearly 3.2 km/s to around 2.1 km/s. In several thermal recovery monitoring projects, the strongest seismic expression was a result of gas coming out of solution to form a separate phase, rather than the thermal effects themselves.

**13.5.11 Gassmann Fluid Substitution.** To extract fluid types or saturations from seismic, cross-well, or borehole sonic data, we need a procedure to model fluid effects on rock velocity and

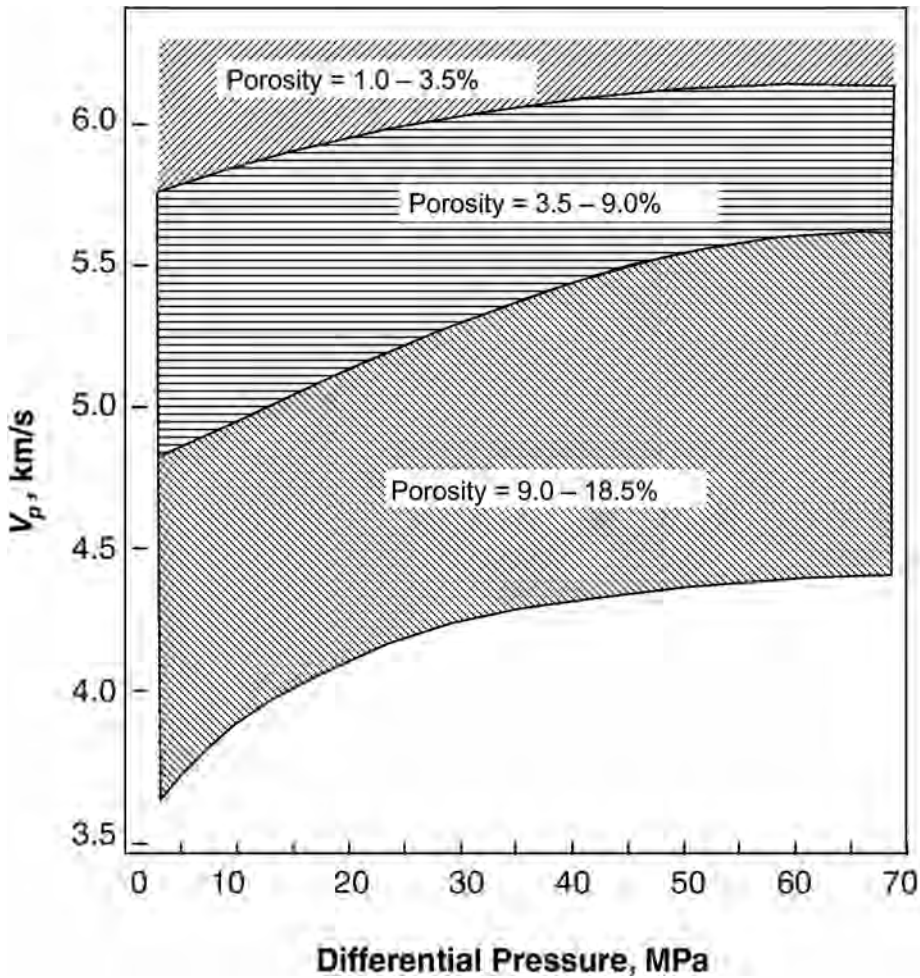


Fig. 13.32—Generalized compressional velocities dependence on pressure seen in carbonates by Rafavich *et al.*<sup>57</sup> Pressure dependence is a function of porosity.

density. Numerous techniques have been developed. Gassmann's equations are by far the most widely used relations to calculate seismic velocity changes because of different fluid saturations in reservoirs. Gassmann's formulation is straightforward, and the simple input parameters typically can be directly measured from logs or assumed based on rock type. This is a prime reason for its importance in geophysical techniques such as time-lapse reservoir monitoring and direct hydrocarbon indicators (DHI) such as amplitude "bright spots," and amplitude vs. offset (AVO). Because of the dominance of this technique, we will describe it at length.

Despite the popularity of Gassmann's equations and their incorporation within most software packages for seismic reservoir interpretation, important aspects of these equations are usually not observed. Many of the basic assumptions are invalid for common reservoir rocks and fluids. Many efforts have been made to understand the operation and application of Gassmann's equations (Han,<sup>70</sup> Mavko and Mukerji,<sup>71</sup> Mavko *et al.*,<sup>8</sup> Sengupta and Mavko,<sup>72</sup> and Nolen-Hoeksema<sup>73</sup>). Most of these works have attempted to isolate individual parameter effects. We will extend this analysis to incorporate mechanical bounds for porous media (see previous) and the magnitude of the fluid effect.

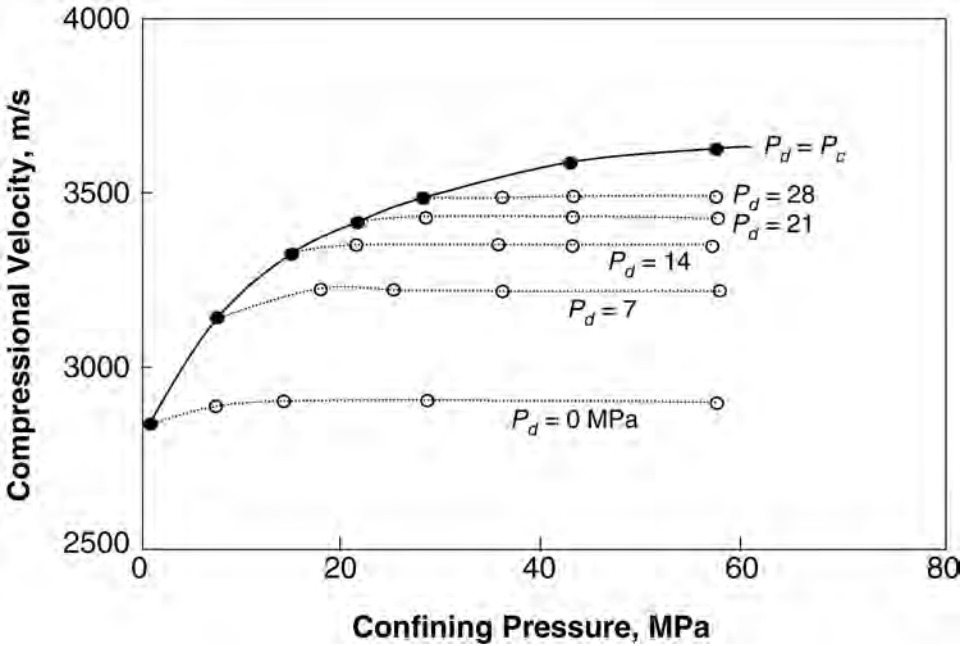


Fig. 13.33—Compressional velocities through a water-saturated, oil-wet sandstone sample at various confining and pore pressures. When confining and pore pressures are varied together to give constant differential pressure, the velocity stays almost constant (after Wyllie *et al.*<sup>64</sup>).

Compressional (P-wave) and shear (S-wave) velocities along with densities directly control the seismic response of reservoirs at any single location. Fig. 13.39a shows measured dry and water saturated P- and S-wave velocities of sandstones as a function of differential pressure. P-wave velocity increases, while S-wave velocity decreases slightly with water saturation. However, both P- and S-wave velocities are generally not the best indicators for any fluid saturation effect. This is a function of coupling between P- and S-wave through the shear modulus and bulk density. In contrast, if we plot bulk and shear modulus as functions of pressure (Fig. 13.39b), the water-saturation effect shows the following:

1. Bulk modulus increases about 50%.
2. Shear modulus remains almost constant.

Bulk modulus is more strongly sensitive to water saturation. The bulk volume deformation produced by a passing seismic wave results in a pore volume change, and causes a pressure increase of pore fluid (water). This has the effect of stiffening the rock and increasing the bulk modulus. Shear deformation usually does not produce pore volume change, and differing pore fluids often do not affect shear modulus.

Gassmann’s equations provide a simple model to estimate fluid saturation effect on bulk modulus. Eqs. 13.64a through 13.65 are convenient forms for Gassmann’s relations that show the physical meaning:

$$K_s = K_d + \Delta K_d, \dots\dots\dots (13.64a)$$

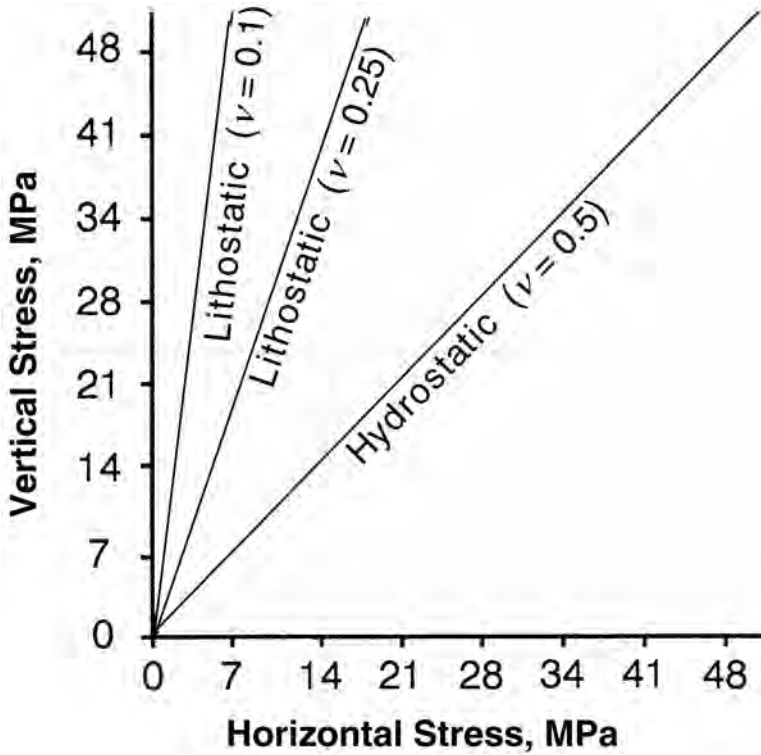


Fig. 13.34—Typical stress conditions that might be found in a compacting basin with no lateral deformation and no applied tectonic stresses.

$$\Delta K_d = \frac{K_0 \left(1 - \frac{K_d}{K_0}\right)^2}{1 - \Phi - \frac{K_d}{K_0} + \Phi \frac{K_0}{K_f}}, \dots\dots\dots (13.64b)$$

and

$$\mu_s = \mu_d, \dots\dots\dots (13.65)$$

where  $K_0$ ,  $K_f$ ,  $K_d$ , and  $K_s$ , are the bulk moduli of the mineral, fluid, dry rock, and saturated rock frame, respectively;  $\Phi$  is porosity; and  $\mu_s$  and  $\mu_d$  are the saturated and dry rock shear moduli.  $\Delta K_d$  is an increment of bulk modulus caused by fluid saturation. These equations indicate that fluid in pores will affect bulk modulus but not shear modulus, consistent with the earlier discussion. As pointed out by Berryman,<sup>74</sup> a shear modulus independent of fluid saturation is a direct result of the assumptions used to derive Gassmann’s equation.

Numerous assumptions are involved in the derivation of Gassmann’s equation:

1. The porous material is isotropic, elastic, monomineralic, and homogeneous.
2. The pore space is well connected and in pressure equilibrium (zero frequency limit).
3. The medium is a closed system with no pore fluid movement across boundaries.
4. There is no chemical interaction between fluids and rock frame (shear modulus remains constant).

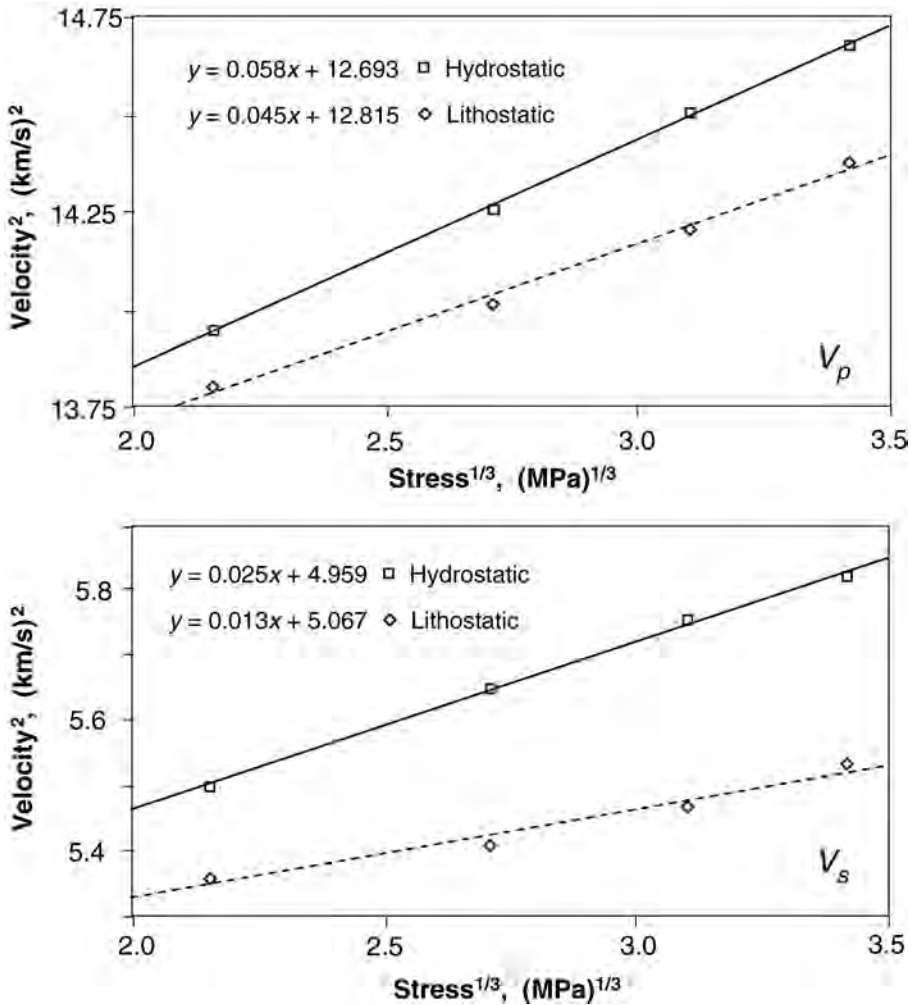


Fig. 13.35—Chocolate Sandstone (porosity = 0.225) compressional and shear velocities, both under hydrostatic and more realistic lithostatic stress conditions. In both cases, the velocities are fit well by the form  $V^2 = aP_e^{1/3} + b$ .

Many of these assumptions may not be valid for hydrocarbon reservoirs, and they depend on rock and fluid properties and in-situ conditions. For example, most rocks are anisotropic to some degree. The work of Brown and Korringa<sup>75</sup> provides an explicit form for an anisotropic fluid substitution. In seismic applications, it is normally assumed that Gassmann’s equation works best for seismic data at frequencies less than 100 Hz (Mavko *et al.*<sup>8</sup>). Recently published laboratory data (Batzle *et al.*<sup>76</sup>) show that acoustic waves may be dispersive in rocks within the typical seismic band, invalidating assumption 2. In such cases, seismic frequencies may still be too high for application of Gassmann’s equation. Pore pressures may not have enough time to reach equilibrium. The rock remains unrelaxed or only partially relaxed.

The primary measure of the sensitivity of rock to fluids is its normalized modulus  $K_n$ : the ratio of dry bulk modulus to that of the mineral.

$$K_n = K_d / K_0 \dots\dots\dots (13.66)$$

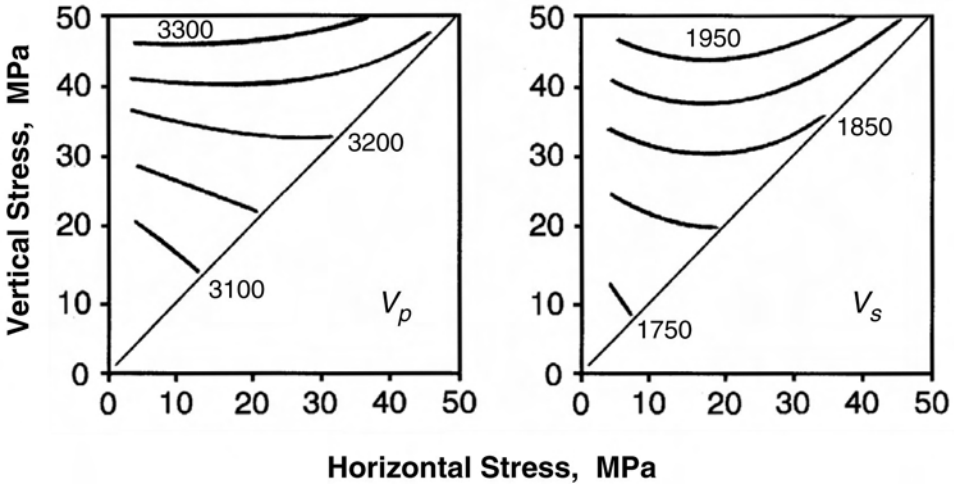


Fig. 13.36—Iso-velocity contours for the Woodbine sandstone related to the anisotropic stress condition described in Fig. 13.34. Propagation is vertical for both  $V_p$  and  $V_s$ . Both absolute velocities and velocity ratios will be affected by anisotropic stresses.

This function can be complicated and depends on rock texture (porosity, clay content, pore geometry, grain size, grain contact, cementation, mineral composition, and so on) and reservoir conditions (pressure and temperature). This  $K_n$  can be determined empirically or theoretically. For relatively clean sandstone at high differential pressure (>20 MPa), the complex dependence of  $K_n(x, y, z, \dots)$  can be simplified as a function of porosity.

$$K_n(x, y, z, \dots) \cong K_n(\Phi) \dots \dots \dots (13.67)$$

From Eq. 13.66, bulk modulus increment is then equal to

$$\Delta K_d = \frac{K_0 [1 - K_n(\Phi)]^2}{1 - \Phi - K_n(\Phi) + \Phi K_0 / K_f} \dots \dots \dots (13.68)$$

Here  $[1 - K_n(\Phi)]$  is also the Biot parameter  $\alpha_b$  (Biot<sup>77</sup>). Furthermore, because usually  $K_0 \gg K_f$ , it is reasonable to assume

$$0 \leq 1 - \Phi - K_n(\Phi) \ll \Phi \times K_0 / K_f \dots \dots \dots (13.69)$$

for sedimentary rocks with high porosity (>15%). Therefore,

$$\Delta K_d \approx G(\Phi) \times K_f, \dots \dots \dots (13.70)$$

where  $G(\Phi)$  is the saturation gain function defined as

$$G(\Phi) = \frac{[1 - K_n(\Phi)]^2}{\Phi} \dots \dots \dots (13.71)$$



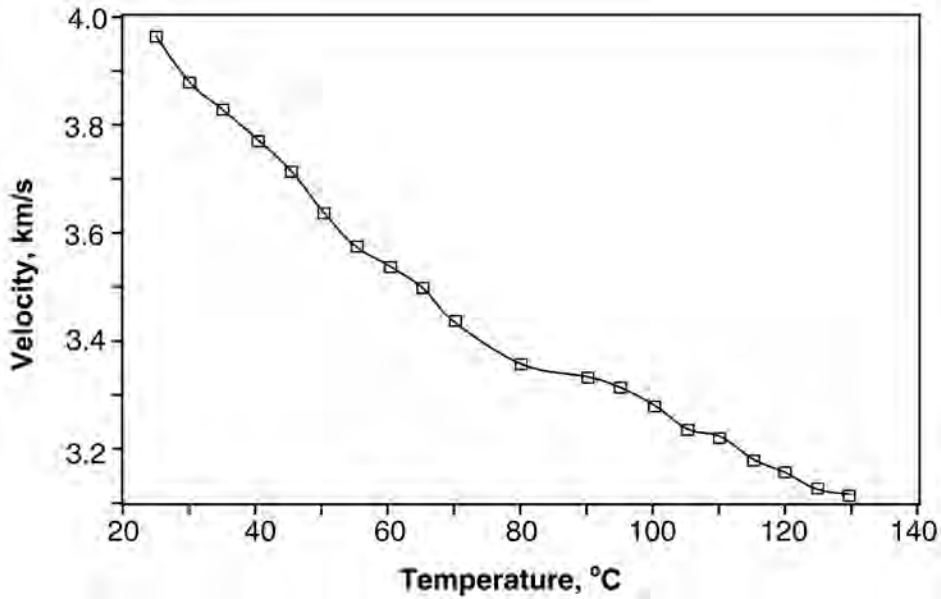


**Fig. 13.37—Compressional velocity as a function of temperature for a sandstone sample testing the effects of thermal flooding. The large drop in velocity is a combined effect of grain separation, pore pressure, and fluid modulus changes.**

Thus, fluid saturation effects on the bulk modulus are proportional to the gain function  $G(\Phi)$  and the fluid modulus  $K_f$ . The  $G(\Phi)$  in turn depends directly on dry rock properties: the normalized modulus and porosity. In general,  $G(\Phi)$  is independent of fluid properties (ignoring interactions between rock frame and pore fluid). We must know both gain function of dry rock frame and pore fluid modulus to evaluate the fluid saturation effect on seismic properties. Note that the normalized modulus must be a smooth function of porosity or  $G(\Phi)$  can be unstable, particularly at small porosities.

At high differential pressure (>20 MPa), the  $K_s$  of water-saturated sands calculated using simplified form is 3% overestimated for porous rock (porosity > 15%). Those errors will decrease significantly with low fluid modulus (gas and light oil saturation). For low-porosity sands with high clay content, the simplified Gassmann’s equation overestimates water saturation effects substantially.

In Eq. 13.64b, there are five parameters, and usually the only applied constraint is that the parameters are physically meaningful (>0). Incompatible or mismatched data might generate wrong or even unphysical results such as a negative modulus. In reality, only  $K_0$  and  $K_f$  are completely independent.  $K_s$ ,  $K_d$ , and porosity  $\Phi$  are actually closely correlated. Bounds on  $K_d$  as a function of porosity, for example, constrain the bounds of  $K_s$ .

Assuming porous media is a Voigt material, which is a high bound for  $K_d$  (Fig. 13.40),

$$K_d = K_0(1 - \Phi) \dots\dots\dots (13.72)$$

Putting this equation (13.72) into Gassmann’s Equation (13.64) gives

$$\Delta K_{dmin} = \Phi \times K_f \dots\dots\dots (13.73)$$

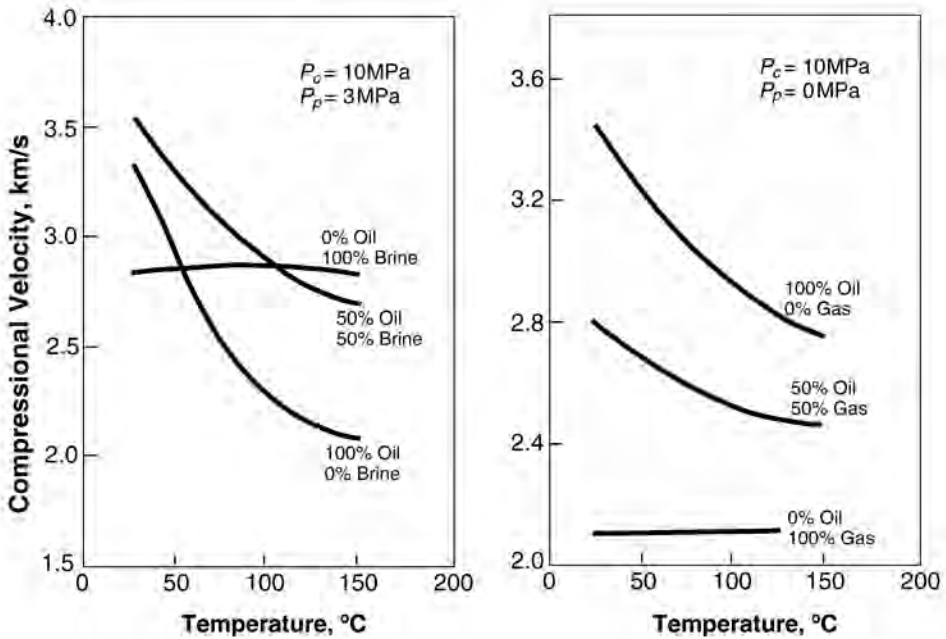


Fig. 13.38—Compressional velocity as a function of temperature for Venezuelan (a) and Kern River California (b) oil sand samples. When either dry (gas-saturated) or brine-saturated, there is little temperature dependence. With increasing oil saturation, temperature dependence becomes strong. The effects of fluid phase changes can be seen by the drop in velocity in (b) with increasing gas saturation (from Tosaya<sup>69</sup>).

and

$$K_s = K_d + \Delta K_{dmin} = K_0(1 - \Phi) + \Phi \times K_f \dots\dots\dots (13.74)$$

Because this Voigt bound is the stiffest upper limit, the fluid saturation effect on bulk modulus here ( $\Delta K_{dmin}$ ) will be a minimum (see Fig. 13.40).

As we have seen, the low modulus bound for porous media is the Reuss bound.

$$\frac{1}{K_R} = \frac{(1 - \Phi)}{K_0} + \frac{\Phi}{K_f} \dots\dots\dots (13.75)$$

$$K_R = \frac{K_0 \times K_f}{(1 - \Phi) \times K_f + \Phi \times K_0} \dots\dots\dots (13.76)$$

For completely empty (dry) rocks, the fluid modulus  $K_f$  is equal to zero, and both the Reuss bound and the normalized modulus ( $K_{nR}$ ) for a dry rock in this limit equals zero (for nonzero porosity).

$$K_{nR}(\Phi) = K_d / K_0 = 0 \dots\dots\dots (13.77)$$

Substituting Eq. 13.77 into Gassmann’s Equation (13.64), we find the fluid saturation effect on bulk modulus when the frame is at this lower bound.

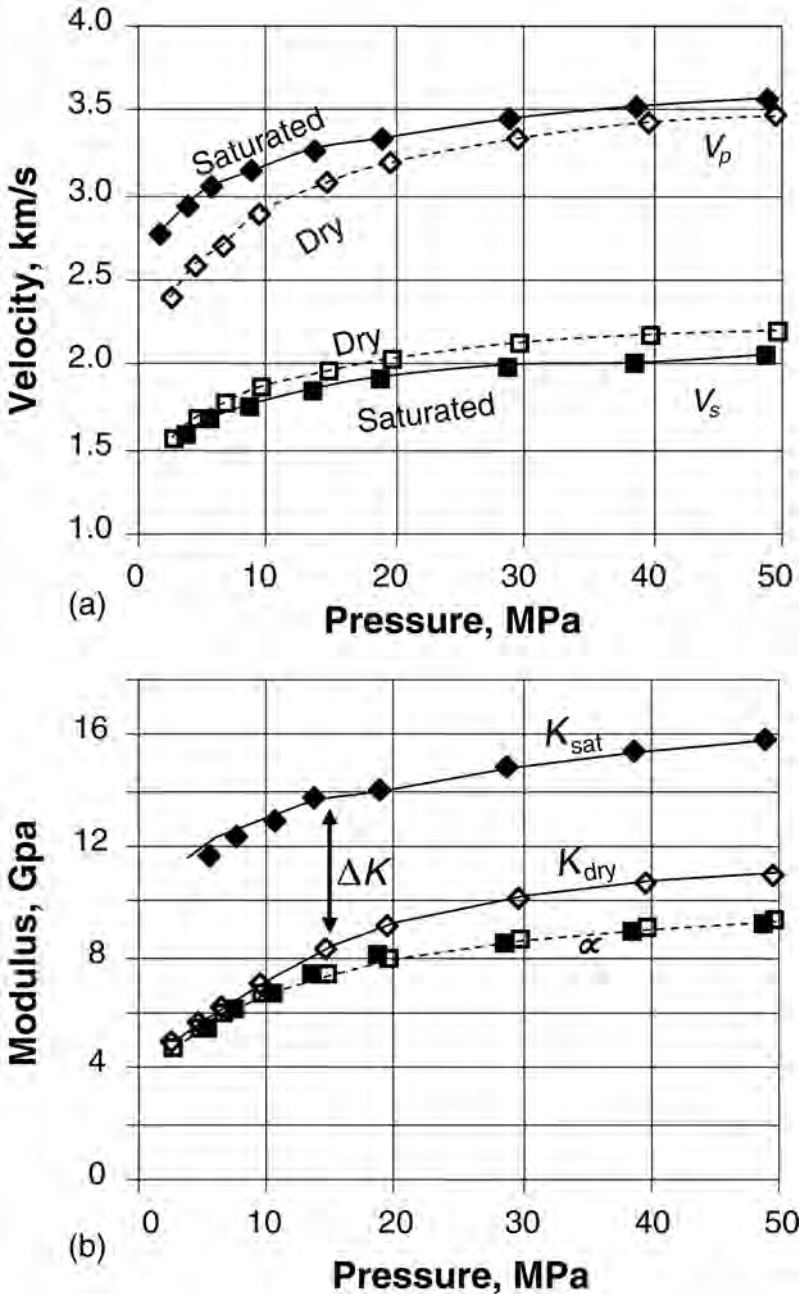


Fig. 13.39—(a) Compressional and shear velocity as a function of pressure for a dry and brine-saturated sandstone; (b) the same sandstone, but plotted in terms of bulk and shear moduli. The change in bulk modulus upon saturation is more dramatic than velocities.

$$\Delta K_{dmax} = \frac{K_0}{1 - \phi + \phi \times K_0 / K_f} = K_R \dots\dots\dots (13.78)$$

For this case, the modulus increment  $\Delta K$  from dry to fluid saturation is equal to the Reuss bound.

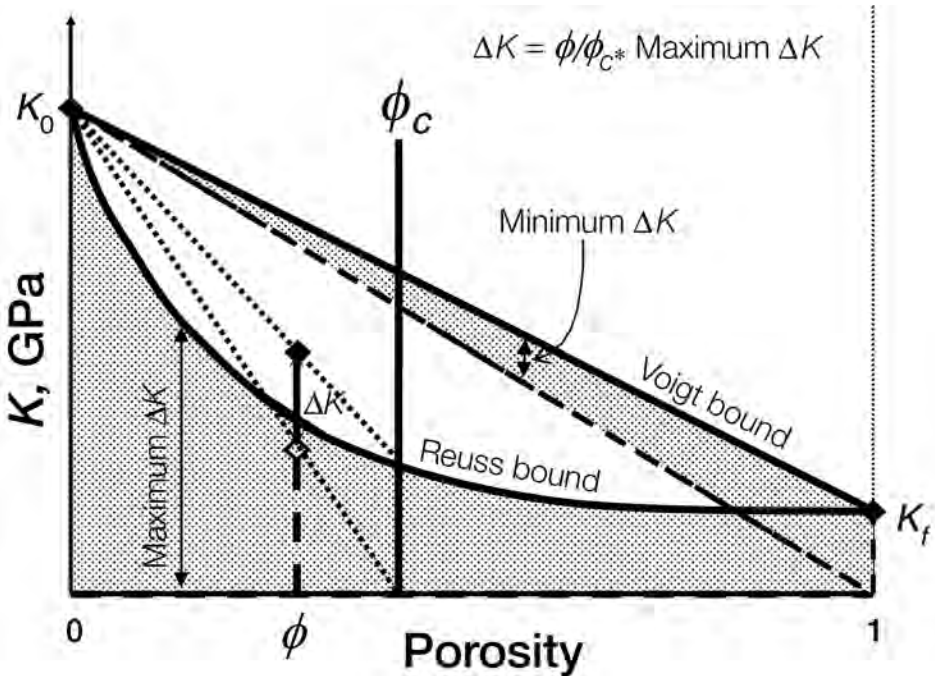


Fig. 13.40—Elastic bounds on bulk modulus for sandstone. Stippled regions represent the extremes in changes in modulus upon water saturation.

$$K_s = K_d + \Delta K_{dmax} = K_R \dots \dots \dots (13.79)$$

Again, Gassmann’s equation is consistent with the dry and fluid-saturated Reuss bounds. Physically, for rocks with the weakest frame, fluids have a maximum effect.

Critical porosity,  $\Phi_c$ , can be used to give tighter constraints for dry- and fluid-saturated bulk modulus for sands. A new triangle is formed which provides a linear formulation and a graphic procedure for Gassmann’s calculation: the fluid saturation effect on bulk modulus proportional to normalized porosity and the maximum fluid saturation effect on bulk modulus (Reuss bound) at the critical porosity (Fig. 13.40).

$$\Delta K_d = \Phi / \Phi_c \times K_{Rc} \dots \dots \dots (13.80)$$

This is consistent with the results of Mavko and Mukerji.<sup>71</sup>

For typical sandstones, the critical porosity  $\Phi_c$  is around 40%. Thus, we also can generate a simplified numerical formula of the normalized modulus  $K_n$  for modified Voigt model:

$$K_n(\Phi) = 1 - \Phi / \Phi_c = 1 - 2.5 \times \Phi \dots \dots \dots (13.81)$$

Using this in Gassmann’s Equation (13.64) yields fluid saturation effect

$$\Delta K_d = \frac{6.25 \times \Phi \times K_0}{1.5 + K_0 / K_f} < 6.25 \times \Phi \times K_f \dots \dots \dots (13.82)$$

Extending our empirical approach to first order, both P- and S-wave velocity can correlate linearly with porosity at high differential pressure. From [Table 13.7](#), for dry clean sands,

$$V_p = 5.97 - 7.85 \Phi, \dots\dots\dots (13.83)$$

$$V_s = 4.03 - 5.85 \Phi, \dots\dots\dots (13.84)$$

where we assume the density of these sands is equal to

$$\rho_d = 2.65 (1 - \Phi). \dots\dots\dots (13.85)$$

Since the modulus is the product of the density and square of velocity, we get an equation that is cubic in terms of porosity. The bulk modulus can be derived as

$$K_d = (1 - A \Phi + B \Phi^2 - C \Phi^3) * K_0, \dots\dots\dots (13.86)$$

where  $A = 3.206$ ,  $B = 3.349$ , and  $C = 1.143$ . [Eq. 13.86](#) can be further simplified if porosity  $\Phi$  is not too large (< 30%):

$$K_d = (1 - D * \Phi)^2 * K_0, \dots\dots\dots (13.87)$$

where  $D$  for clean sandstone is equal to 1.52. This includes an empirical expression of the normalized modulus as a direct dependence on porosity and “ $D$ ” parameter. [Table 13.10](#) and [Fig. 13.41](#) show empirical relations generated from dry velocity data of relatively clean rocks. The parameter  $D$  is related to rock texture and should be calibrated for local reservoir conditions. In general, it has a narrow range from 1.45 to slightly more than 2.0, primarily depending on rock consolidation.

By inserting this  $D$  function into [Eq. 13.71](#), we find

$$G(\Phi) = D^2 \times \Phi \times (2 - D \times \Phi)^2. \dots\dots\dots (13.88)$$

**13.5.12 Solid Mineral Bulk Modulus.** The mineral modulus (solid grain bulk modulus)  $K_0$  is an independent parameter, and the rock texture controls  $K_d$ . However, as mentioned previously, the normalized modulus  $K_n$  controls the fluid saturation effect rather than  $K_d$  or  $K_s$  individually. The mineral modulus  $K_0$  is equally as important as  $K_d$ . However, in most applications of the Gassmann’s equation, only  $K_d$  is measured. Properties of the mineral modulus  $K_0$  are often poorly understood and oversimplified.  $K_0$  is the modulus of the solid material that includes grains, cements, and pore fillings ([Figs. 13.1](#) through [13.8](#)). If clays or other minerals are present with complicated distributions and structures,  $K_0$  can vary over a wide range. Unfortunately, few measurements of  $K_0$  have been made on sedimentary rocks (Coyner<sup>78</sup>), and the moduli of clays are a particular problem (Wang *et al.*<sup>50</sup> and Katahara<sup>49</sup>; see [Table 13.6b](#)). These data show that at a high pressure,  $K_0$  for sandstone samples range from 33 to 39 MPa.  $K_0$  is not a constant and can increase more than 10% with increasing effective pressure. [Fig. 13.42](#) shows the influence of  $K_0$  on Gassmann’s calculation. This case uses a dry bulk modulus calculated with the mineral modulus of 40 GPa,  $D = 2$ , and a water modulus of 2.8 GPa. The water saturation effect was calculated for three mineral moduli of 65, 40, and 32 GPa. Results show that for the same  $K_d$  and  $K_f$ , bulk modulus increment  $\Delta K$  because of fluid saturation in-

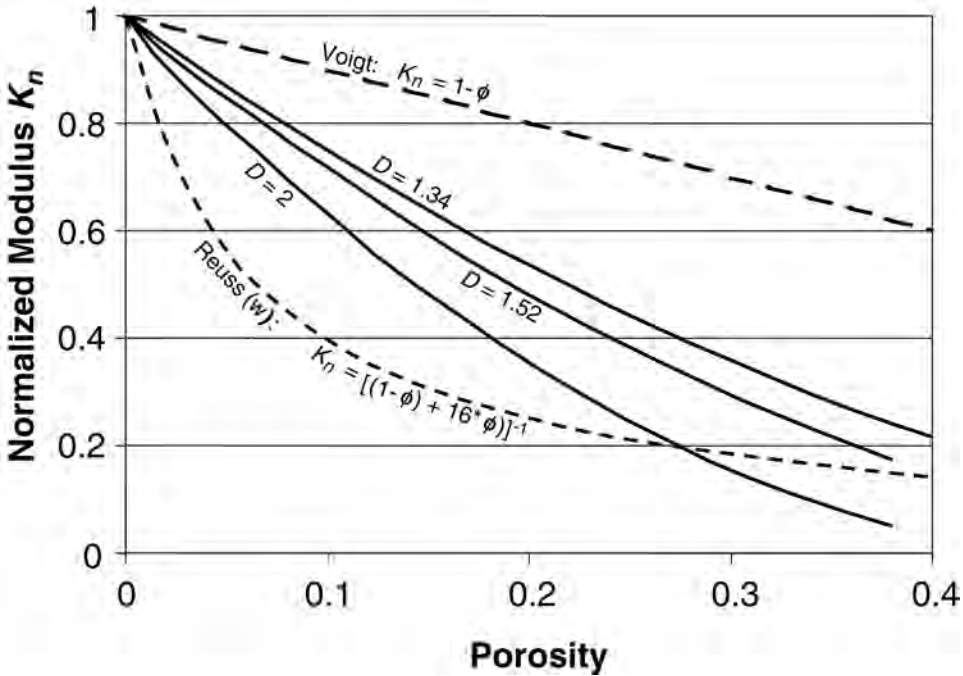


Fig. 13.41—Elastic bounds (Voigt and Reuss) and approximations to the normalized dry modulus ( $K_n = K_d/K_0$ ) for sandstone using the  $D$  factor.

creases with increasing mineral modulus  $K_0$ . Errors caused by uncertainty of  $K_0$  decrease with increasing porosity and fluid modulus  $K_f$ .

Because of lack of measurements on bulk mineral modulus, we often must use measured velocity/porosity/clay-content relationships for shaly sandstone to estimate the mineral modulus. Assuming zero porosity and grain bulk modulus of 2.65 gm/cc, we can derive mineral bulk and shear modulus from measured P- and S-wave velocity. The results are shown in [Table 13.11](#).

1. For relatively clean sandstone (with few percent clay content), mineral bulk modulus is 39 GPa, which is stable for differential pressures higher than 20 MPa. Mineral shear modulus is around 33 GPa, which is significantly less than 44 GPa for a pure quartz aggregate. Shear modulus is more sensitive to differential pressure and clay content.

2. For shaly sandstone, mineral bulk modulus decreases 1.7 GPa per 10% increment of clay content.

Such derived mineral bulk moduli can be used for Gassmann’s calculation if there are no directly measured data or reliable models for calculation.

With a change of fluid saturation from Fluid 1 to Fluid 2, the bulk modulus increment ( $\Delta K$ ) is equal to

$$\Delta K_{21} \approx G(\Phi) \times (K_{f2} - K_{f1}), \dots\dots\dots (13.89)$$

where  $K_{f1}$  and  $K_{f2}$  are the moduli of Fluids 1 and 2, respectively, and  $\Delta K_{21}$  represents the change in the saturation increment that results from substituting Fluid 2 for Fluid 1. [Eq. 13.89](#) uses the fact that the gain function  $G(\Phi)$  of the dry rock frame remains constant as fluid modu-

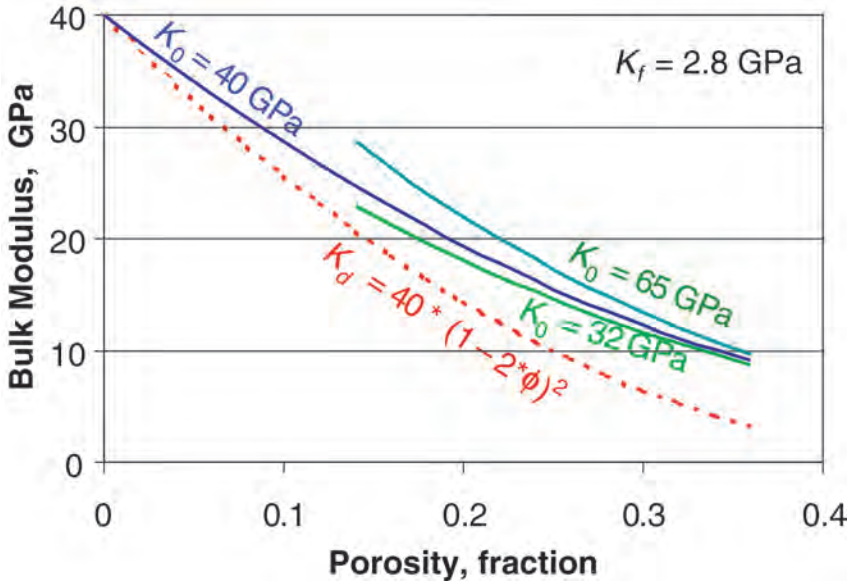


Fig. 13.42—Effect of varying mineral modulus ( $K_0$ ) on the calculated saturated bulk modulus ( $K_s$ ) for water-saturated sandstone.

TABLE 13.10—EMPIRICAL D FUNCTION VS. POROSITY		
Rock Type	V—Emp. Relation	$K_d = (1-D\phi)^2 K_0$
		D
Dry shaly sandstone	$V_p = 5.41-6.35 * \phi$ $V_s = 3.57-4.57 * \phi$	1.450
Dry clean sandstone	$V_p = 5.97-7.85 * \phi$ $V_s = 4.03-5.85 * \phi$	1.523
Silicate clastic (Castagna <i>et al.</i> <sup>4</sup> )	$V_p = 5.81-9.42 * \phi$ $V_s = 3.89-7.07 * \phi$	1.584
Dry vuggy limestone	$V_p = 6.47-5.84 * \phi$ $V_s = 3.39-3.03 * \phi$	1.340
Dry limestone	$V_p = 6.19-9.80 * \phi$ $V_s = 3.20-4.90 * \phi$	1.970
Dry dolomite	$V_p = 6.78-9.80 * \phi$ $V_s = 3.72-5.20 * \phi$	1.705

lus changed (this may not be true for real rocks). The fluid substitution effect on bulk modulus is simply proportional to the difference of fluid bulk modulus.

If we know the gain function for a rock formation, we can estimate the fluid substitution effect without knowing shear modulus.

$$\rho_2 V_{p2}^2 = \rho_1 V_{p1}^2 + G(\Phi) \times (K_{f2} - K_{f1}), \dots\dots\dots (13.90)$$

TABLE 13.11—MINERAL MODULUS DERIVED FROM EMPIRICAL VELOCITIES SHALY RELATION OF SANDSTONES						
Grain Bulk and Shear Moduli for Shaly Sands						
Pd (bars)	Clay = 0%		Clay = 10%		C = 0.2	
	$K_0$ (GPa)	$\mu_0$ (GPa)	$K_0$ (GPa)	$\mu_0$ (GPa)	$K_0$ (GPa)	$\mu_0$ (GPa)
400	39.03	32.83	37.27	29.40	35.51	26.16
300	39.08	31.91	37.26	28.56	35.44	25.40
200	39.27	30.45	37.30	27.29	35.35	24.30
100	38.74	26.46	36.72	25.73	34.72	22.94

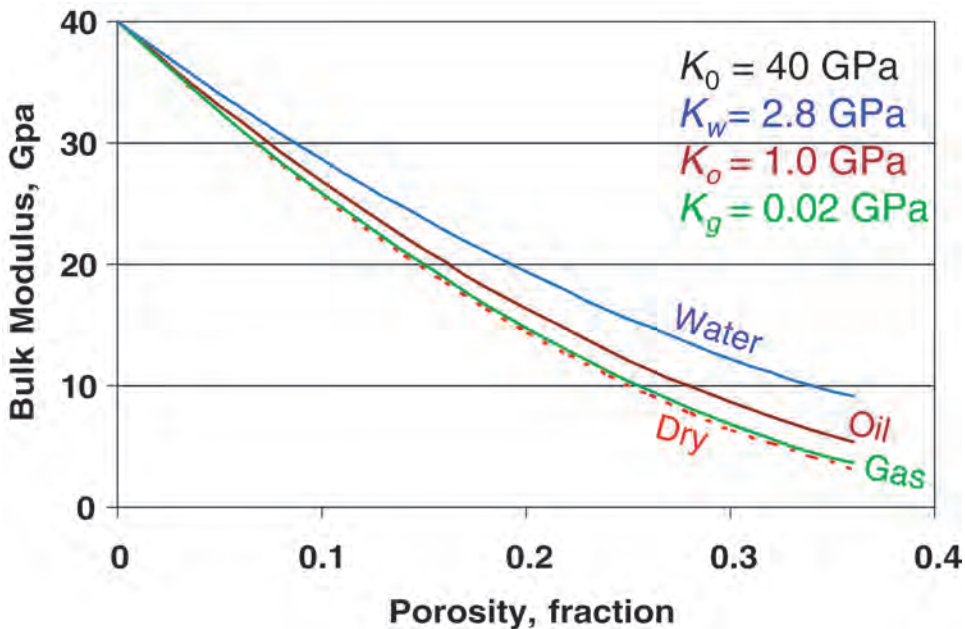


Fig. 13.43—Effect of varying fluid modulus ( $K_0$ ) on the calculated saturated bulk modulus ( $K_s$ ) for sandstones.

where  $\rho_1$ ,  $\rho_2$ ,  $V_{p1}$ , and  $V_{p2}$  are the density and velocity of rock with Fluid 1 and 2 saturation. Both Eqs. 13.89 and 13.90 are direct results from simplified Gassmann's equation (Eq. 13.64). In Fig. 13.43, we show the typical fluid modulus effect on the saturated bulk modulus  $K_s$ . Even at a modest porosity of 15%, changes can be substantial. At in-situ conditions, pore fluids are often multiphase mixtures. Dynamic fluid modulus may also depend on fluid mobility, fluid distribution, rock compressibility, and seismic wavelength.

**13.5.13 Cracked Rock.** For some cracked rocks, different methods of calculating velocities and the effects of pore fluids are preferable. Numerous theories have been developed to describe the effects of crack-like pores. Most view cracks as ellipsoids with their aspect ratio,  $\alpha$ , defined as the ratio of the semiminor to semimajor axes. Eshelby<sup>79</sup> examined the elastic deformation of such elliptical inclusions, and these results were then applied to the compressibility of rocks by Walsh.<sup>80</sup> In concept, long, narrow cracks are compliant and can be very effective at reducing the rock moduli at low crack porosities. The primary controlling factor for these



elliptical fractures is the aspect ratio,  $\alpha$ , defined as the ratio of the ellipse semiminor ( $a$ ) to semimajor ( $b$ ) axes:

$$\alpha = a / b \dots\dots\dots (13.91)$$

The smaller the value of  $\alpha$ , the softer the crack and cracked rock, resulting in lower velocities and stronger pressure dependence.

Numerous assumptions are made in the derivation and application of cracked media models, such as the following:

1. The porous material is isotropic, elastic, monomineralic, and homogeneous.
2. The fracture population is dilute, and few, or only first-order, mechanical interactions occur among fractures.
3. Fractures can be described by simple shapes.
4. The pore-fluid system is closed, and there is no chemical interaction between fluids and rock frame (however, shear modulus need not remain constant).

Some of these assumptions may be dropped, depending on the model involved. For example, Hudson<sup>81</sup> specifically includes the effect of anisotropic crack distributions.

One particularly useful result was derived by Kuster and Toksoz.<sup>82</sup> Using scattering theory, they derived the general relation of bulk and shear moduli of the cracked rock ( $K^*$ ,  $\mu^*$ ) to the crack porosity ( $c$ ), aspect ratio ( $\alpha_m$ ), mineral ( $K_0$ ,  $\mu_0$ ), and inclusion or crack moduli ( $K'$ ,  $\mu'$ ) (Cheng and Toksoz<sup>83</sup>).

$$\frac{K^* - K_0}{3K^* + 4\mu_0} = \frac{K' - K_0}{3(3K_0 + 4\mu_0)} \sum_{m=1}^M c(\alpha_m) T_1(\alpha_m), \dots\dots\dots (13.92)$$

$$\frac{\mu^* - \mu_0}{6\mu^*(K_0 + 2\mu_0) + \mu_0(9K_0 + 8\mu_0)} = \frac{\mu' - \mu_0}{25\mu_0(3K_0 + 4\mu_0)} \sum_{m=1}^M c(\alpha_m) \left[ T_2(\alpha_m) - \frac{1}{3} T_1(\alpha_m) \right] \dots\dots\dots (13.93)$$

Here,  $T_1$  and  $T_2$  are scalar functions of  $K_0$ ,  $\mu_0$ ,  $K'$ , and  $\mu'$ , and correspond to  $T_{ijj}$  and  $T_{ijj}$  in Kuster and Toksoz.<sup>82</sup> This formulation allows the effects of several populations (several values of  $m$ ) of cracks to be summed. The general limitation is that the porosity for any particular aspect ratio cannot exceed the value of the aspect ratio itself.

The results of the Kuster-Toksoz model are shown in **Fig. 13.44**. Numerous important features should be noted. Velocities drop rapidly for long, narrow cracks (small  $\alpha$ ), with even small crack porosities. For such soft cracks, the increase in velocity is dramatic. At a shape close to spherical ( $\alpha$  above about 0.5), the pores are stiff, and the change in density dominates. Thus, with  $\alpha$ s close to unity, going from dry to water-saturated actually decreases the velocity. Notice also that for small aspect ratios, the shear velocity increases with water saturation. This requires a changing shear modulus with saturation, in direct violation of a primary assumption of Gassmann's relations. This changing shear modulus is one reason why Gassmann's relations may not work well in fractured rocks. An example of a rock modeled by both Gassmann's and Kuster-Toksoz techniques is shown in **Fig. 13.45**. For this limestone, Gassmann's relations substantially under estimate the effect of liquid saturation. The Kuster-Toksoz prediction for oil saturation is close to the experimental observed values. However, the success of this model is not quite as spectacular as it seems, because an arbitrary population of fractures and aspect

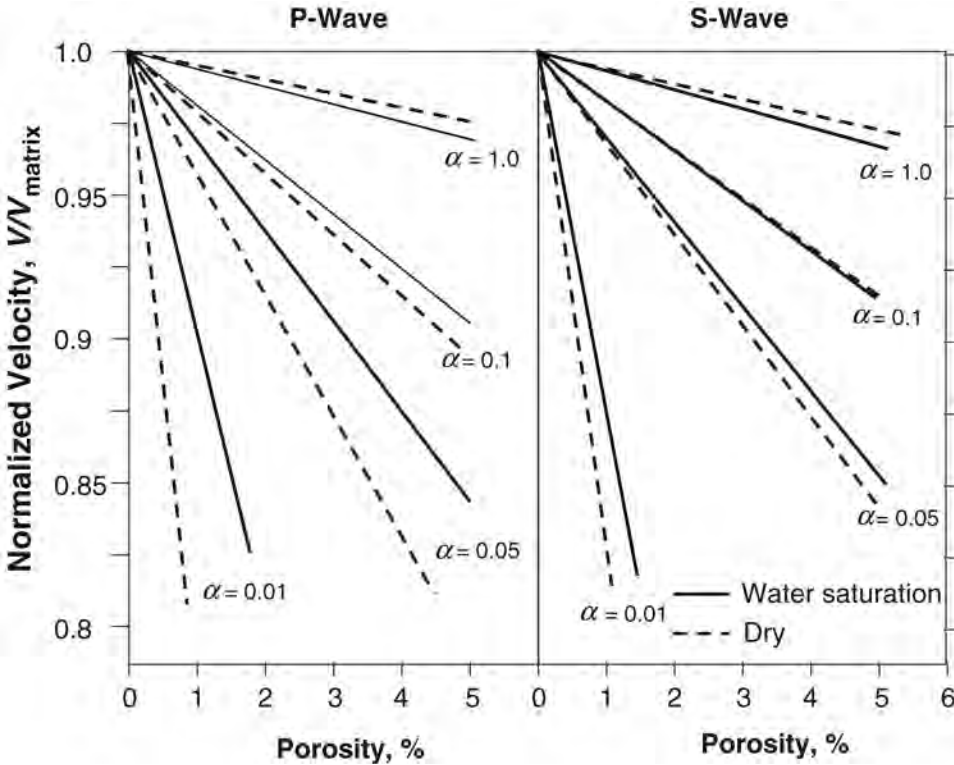


Fig. 13.44—Normalized compressional and shear velocities for cracked rocks ( $V_{rock} / V_{mineral}$ ) both dry and saturated using the Kunster-Toksoz<sup>82</sup> method (from Cheng and Toksoz<sup>83</sup>). Velocities are controlled by the crack aspect ratio ( $a = axis_{minor} / axis_{major}$ ) and crack porosity.

ratios ( $\alpha_m$ s) can be included to force such a good fit. The actual population of cracks in rocks remains unknown.

The expressions in Eqs. 13.92 and 13.93 are complicated and difficult to apply. The linear relation of normalized velocities to crack aspect ratio and porosity suggests that a simplified form can be derived to give a first-order approximation.

$$\frac{V_{rock}}{V_{mineral}} = 1 - [a - b \ln(\alpha)^c] \Phi_{crack} \dots\dots\dots (13.94)$$

**13.5.14 Anisotropy.** To this point, we have usually considered rocks to be isotropic. In reality, most rocks are anisotropic to some degree. Some dominant lithologies, such as shales, are by definition anisotropic (otherwise, they are mudstones). In addition, many ubiquitous sedimentary features such as bedding will lead to anisotropy on a larger scale. In-situ stresses are anisotropic (Fig. 13.34), resulting in an anisotropy in rock properties. Anisotropy in transport properties such as permeability is a common concern in describing reservoir flow. Fractured reservoirs typically have a preferred fracture and flow direction, and these directions often can be ascertained from oriented borehole or surface seismic data.

An interesting aspect of anisotropy is the phenomenon of shear-wave splitting. Elastic anisotropy means that the stiffness or effective moduli in one direction will be different from that in another. For shear waves, their particle motion will be approximately normal to the direction of propagation. The velocity will depend on the orientation of the particle motion.

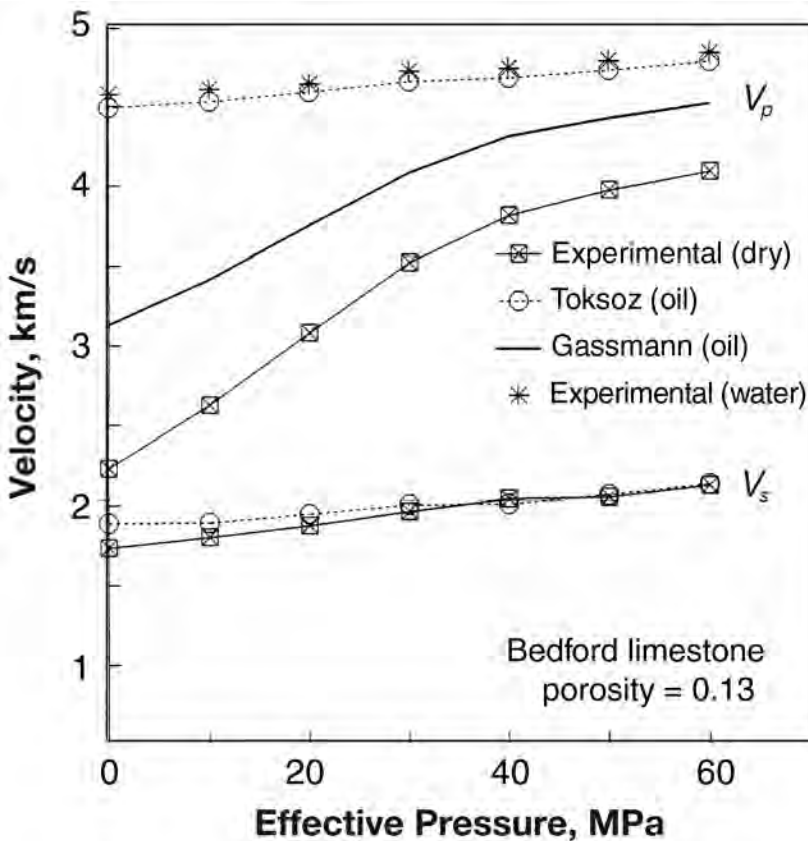


Fig. 13.45—Measured and modeled velocities on the Bedford Limestone (Wang *et al.*<sup>58</sup>).

The shear wave will then “split” into two shear waves with orthogonal particle motion, each traveling with the velocity determined by the stiffness in that direction. An example of this is shown in Fig. 13.46 from Sondergeld and Rai.<sup>84</sup> The recorded waveform can be seen as two distinct shear waves traveling at their own velocities. Note that when these distinct waves are examined in isolation, their velocity is independent of direction. A single input wave has been split into two waves. This is similar to the image splitting in optics when light travels through an anisotropic medium. On the other hand, because compressional waves have particle motion only along the direction of propagation, they have no splitting.

Although the split shear waves may travel each with a constant velocity, the amplitude within each will be strongly dependent on angle. The energy of the initial single shear wave is partitioned as vector components in each of the principal directions. This amplitude dependence on angle is shown in Fig. 13.47, also from Sondergeld and Rai.<sup>84</sup> Figs. 13.46 and 13.47 demonstrate that measurement of seismic shear waves at the surface will be useful in delineating in-situ anisotropy directions. This anisotropy can then be related to factors such as oriented fractures and in-situ stress directions.

A typical homogeneous but bedded sedimentary unit would have a horizontal plane of symmetry as well as a vertical symmetry axis of rotation. This situation is commonly referred to as Vertical Transverse Isotropy (VTI), although the term “Polar Anisotropy” has also been suggested (Thomsen<sup>85</sup>). For “weak” anisotropy (Thomsen<sup>86</sup>), the dependence of velocities as a function of angle ( $\theta$ ) from the symmetry axis can be written as

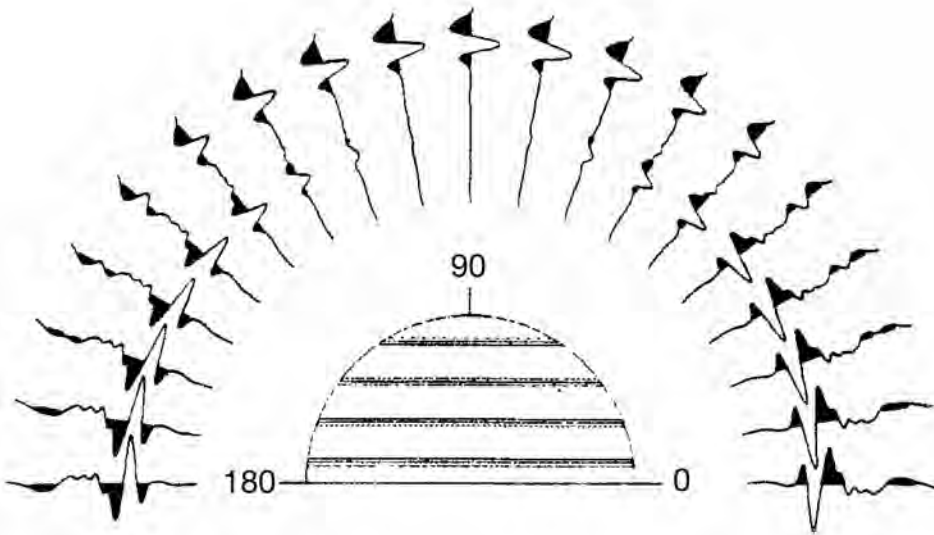


Fig. 13.46—Transmitter and receiver are rotated simultaneously through an azimuth aperture of 180°. When particle motion is either parallel or perpendicular to the shale fabric, only one arriving wave is seen. At other angles, both slow and fast waves are present (after Sondergeld and Rai<sup>84</sup>).

$$V_p(\theta) \approx V_{P0} [1 + \delta \sin^2 \theta \cos^2 \theta + \varepsilon \sin^4 \theta], \dots\dots\dots (13.95)$$

$$V_{S-}(\theta) \approx V_{S0} \left[ 1 + \frac{V_{P0}^2}{V_{S0}^2} (\varepsilon - \delta) \sin^2 \theta \cos^2 \theta \right], \dots\dots\dots (13.96)$$

$$V_{S\parallel}(\theta) \approx V_{S0} [1 + \gamma \sin^2 \theta], \dots\dots\dots (13.97)$$

where  $V_p(\theta)$  is the compressional velocity and  $V_{S-}(\theta)$  and  $V_{S\parallel}(\theta)$  are the shear velocities with particle polarizations perpendicular and parallel to the symmetry plane (e.g., bedding), respectively.

The Thomsen<sup>86</sup> anisotropic parameter  $\varepsilon$  can be defined as

$$\varepsilon \approx \frac{V_{P90} - V_{P0}}{V_{P0}}, \dots\dots\dots (13.98)$$

where  $V_{P0}$  is the compressional velocity parallel to the axis of symmetry, and  $V_{P90}$  is the velocity perpendicular to this axis. The parameter  $\gamma$  can be defined as

$$\gamma \approx \frac{V_{S\parallel 90} - V_{S0}}{V_{S0}}, \dots\dots\dots (13.99)$$

where  $V_{S0}$  is the shear velocity parallel to axis of symmetry, and  $V_{S\parallel 90}$  is the velocity perpendicular to this axis.

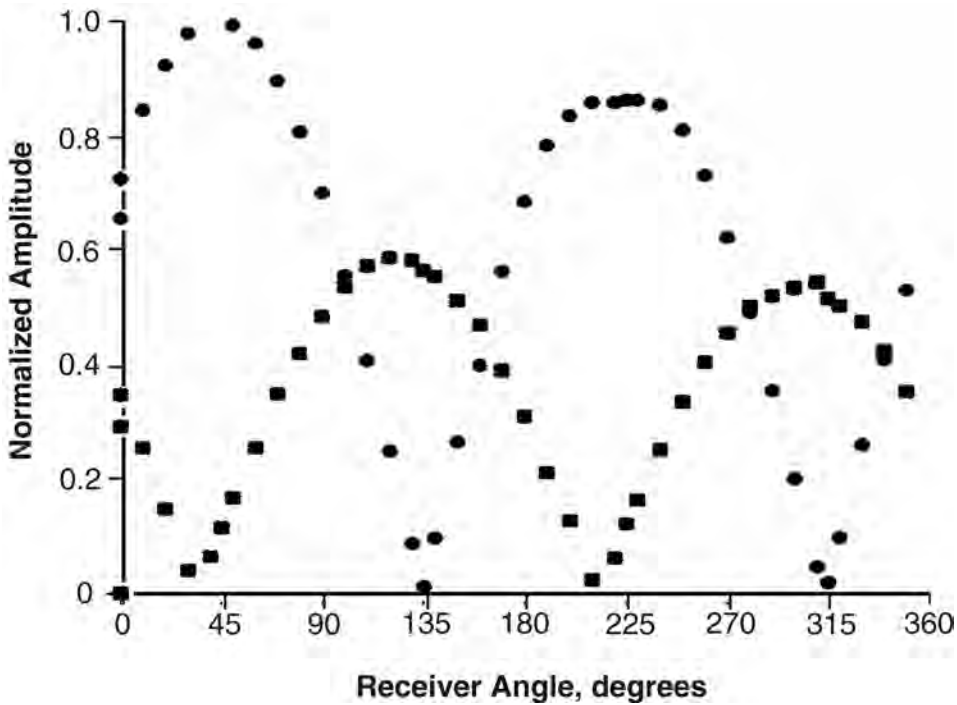


Fig. 13.47—Measured phase amplitudes for fast (circles) and slow (squares) shear-wave arrivals. Change in maximum amplitude for the two fast wave cycles is caused by variations in acoustic coupling (after Sondergeld and Rai<sup>84</sup>).

The anisotropic parameter  $\delta$  is more difficult to characterize, and is the primary component modifying the compressional moveout velocity from the isotropic case. To describe it, we must refer back to stiffness defined in the generalized Hooke’s law given in Eq. 13.43.

$$\delta_{\text{weak}} \equiv \frac{C_{1133} - C_{3333} + 2C_{2323}}{C_{3333}} \dots\dots\dots (13.100)$$

The advantage of these formulations is that they can be extracted from observed shear-wave splitting or extracted from normal moveout (NMO) corrections during seismic processing. Thus, they provide a valuable tool to describe the anisotropic character of reservoirs from remote measurements.

**13.5.15 Attenuation and Velocity Dispersion.** As seismic acoustic waves pass through rock, some of their energy will be lost to heat. For tight, hard rocks, this loss can be negligible. However, for most sedimentary rocks, this loss will be significant, particularly on seismic scales. In reality, all rocks are anelastic to some degree. We must rewrite our wave equation to include this energy or amplitude loss with depth,  $z$ .

$$A(z, t) = A_0 e^{i(k^* z - \omega t)}, \dots\dots\dots (13.101)$$

where  $A(z,t)$  is the amplitude at some point of depth and time,  $A_0$  is the initial amplitude, and  $k^*$  is the complex wave number ( $k^* = k + i\alpha_1$ ). Note that here  $\alpha_1$  is a loss parameter, and not an aspect ratio. Therefore, we can rewrite Eq. 13.101 as

$$A(z, t) = A_0 e^{-\alpha_l z} e^{i(kz - \omega t)} \dots\dots\dots (13.102)$$

Another common measure is the loss decrement  $\delta$ :

$$\delta = \alpha_l \lambda = \ln \left[ A(z_1) / A(z_2) \right], \dots\dots\dots (13.103)$$

where the wavelength  $\lambda$  depends on the velocity  $V$  and frequency  $f$ :  $\lambda = V/f$ . However, the most common measure of attenuation is  $1/Q$ .

$$1/Q = \delta / \pi \dots\dots\dots (13.104)$$

One of the most straightforward descriptions of the relation of velocity to attenuation was developed by Cole and Cole<sup>87</sup> and applied to attenuation measurements by Spencer.<sup>88</sup> The Cole-Cole relationships involve both a peak frequency or characteristic relaxation time,  $\tau$ , for the attenuation mechanism, and a spread factor,  $b$ , which determines the distribution of relaxation times. The real and imaginary components,  $B'$  and  $B''$ , of a general modulus,  $B = B' + iB''$ , are

$$B' = B_0 + \frac{1}{2}(B_\infty - B_0) \left\{ 1 + \frac{\sinh(1-b)y}{\cosh(1-b)y + \sin(\pi b/2)} \right\}, \dots\dots\dots (13.105)$$

$$B'' = \frac{\frac{1}{2}(B_\infty - B_0) \cos(\pi b/2)}{\cosh(1-b)y + \sin(\pi b/2)}, \dots\dots\dots (13.106)$$

where  $y = \ln(\omega\tau)$ ,  $B_0$  and  $B_\infty$  are the zero and infinite frequency moduli.

This would lead to a general attenuation of

$$\frac{1}{Q} = \frac{B''}{B'} \dots\dots\dots (13.107)$$

These relations connecting velocity and attenuation are plotted in **Fig. 13.48**. This figure represents losses and velocity dispersion (frequency dependence) caused by a single relaxation mechanism. At high frequencies, the material is unrelaxed and stiffer, and it has a higher velocity. At low frequencies, the material has time to relax, and velocities are lower.

Fluid mobility also influences rock inelastic properties. Most of the observed losses are caused by relative motion of fluid in the pore space. For a constant pore fluid type, permeability will control the motion and dissipation, thus making attenuation a permeability indicator. For variations in viscosities, mobility also will be dependent on frequency, and attenuation and dispersion may indicate fluid type.

Many models have been proposed, such as those of Biot,<sup>89</sup> O'Connell and Budiansky,<sup>90</sup> Walsh,<sup>91</sup> and Dvorkic and Nur.<sup>92</sup> Unfortunately, the different mechanisms proposed often give contradictory results.

Wave attenuation and dispersion in vacuum dry rock is relatively negligible.<sup>93</sup> Porous rocks containing fluids show a strong frequency-dependent attenuation. Variations in fluid properties such as modulus, viscosity, and polarity have a strong influence on  $1/Q$  (Clark,<sup>93</sup> Winkler *et al.*,<sup>94</sup> Murphy,<sup>95</sup> Tittmann *et al.*,<sup>96</sup> Jones,<sup>97</sup> and Tutuncu *et al.*<sup>98</sup>). These results indicate that the dominant  $1/Q$  mechanism is the interaction and motion of fluid in the rock frame rather

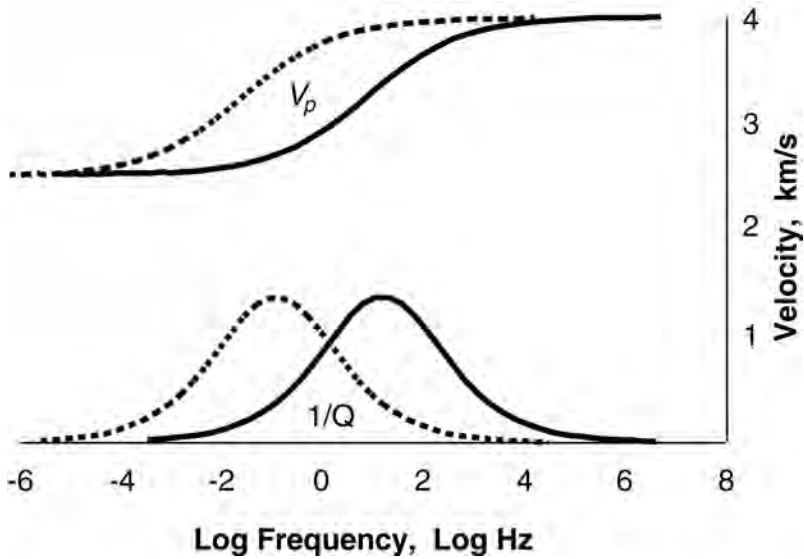


Fig. 13.48—Generalized rock velocity ( $V_p$ ) and attenuation ( $1/Q$ ) relations as a function of frequency. Changes in the relaxation mechanism (e.g., by changing fluid mobility) will shift the frequency response.

than intrinsic losses either in the frame or the fluids themselves. Squirt flow is believed to be the primary loss mechanism in consolidated rocks, although the inertial Biot mechanism may be important in highly permeable rocks (Vo-Thant,<sup>104</sup> Yamamoto *et al.*<sup>100</sup>).

Fluid motion and pressure control velocity changes and seismic sensitivity to pore fluid types. One obvious factor is viscosity. The two most commonly used theoretical concepts are the inertial coupling of Biot<sup>89</sup> and the squirt-flow mechanism (see, for example, O’Connell and Budiansky,<sup>90</sup> or Dvoricik and Nur<sup>92</sup>). Biot gives a characteristic frequency,  $\omega_c$  (roughly, the boundary between high and low frequency range) with the viscosity dependence,  $\eta$ , in the numerator:

$$\omega_c = \eta \Phi \Big|_{k\rho} \dots\dots\dots (13.108)$$

Here,  $\Phi$  is porosity,  $k$  is permeability, and  $\rho$  is fluid density. However, squirt-flow mechanisms lead to viscosity dependence in the denominator:

$$\omega_c = K\alpha^3 \Big|_{\eta} \dots\dots\dots (13.109)$$

Here,  $K$  is frame modulus, and  $\alpha$  is crack aspect ratio. These contrasting dependencies indicate that viscosity can be an obvious test to ascertain which theory is applicable.

Compressional ( $V_p$ ) and shear ( $V_s$ ) velocities for a sample of the Upper Fox Hills Sandstone (Heather well) are shown in Fig. 13.49. Several features should be noted. For the dry sample (open symbols),  $V_p$  and  $V_s$  show little frequency or temperature influence. This confirms that the primary dispersive and temperature effects are dependent on pore fluids. When saturated with glycerine, strong temperature and frequency dependence is obvious. Shear velocity is not independent of the fluid, but increases with increasing fluid viscosity, indicating a viscous contribution to the shear modulus.  $V_p$  increases with viscosity also. More importantly, the disper-

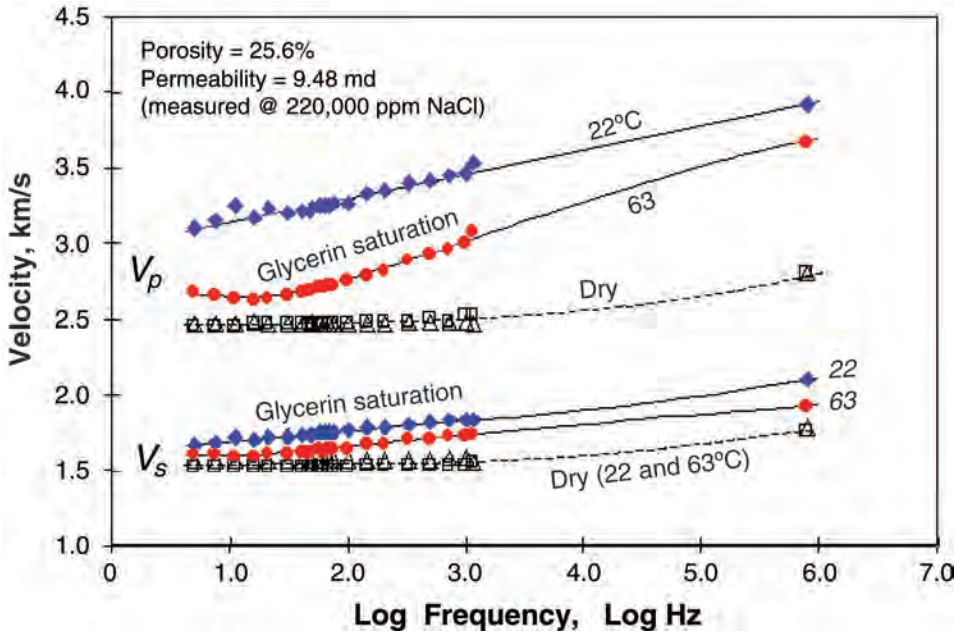


Fig. 13.49—Compressional ( $V_p$ ) and shear ( $V_s$ ) velocities as a function of frequency for Fox Hills sandstone both dry and saturated with glycerine. Dry velocities show almost no temperature dependence. After saturation with glycerine, dispersion occurs both in  $V_p$  and  $V_s$ . This dispersion is shifted to lower frequencies at lower temperatures because of the increased glycerine viscosity.

sion curve shows a systematic shift to lower frequencies with increasing velocities, consistent with squirt flow.

Attenuation ( $1/Q$ ) and velocity dispersion are strongly dependent on pore phase and compressibility, particularly as controlled by partial gas saturation. Attenuation could become a valuable direct hydrocarbon indicator (e.g., Tanner and Sheriff<sup>101</sup>). More recently, Klimentos<sup>102</sup> used the ratio of compressional to shear attenuations as a hydrocarbon indicator in well logs. Unfortunately, application of these properties is not frequent because of incomplete understanding of the phenomena and lack of appropriate tools to extract the information. Laboratory measurements at frequencies and amplitudes encompassing the seismic range have confirmed the strong dependence on partial gas saturation (Fig. 13.50a). However, attenuation is decreased by confining pressure, dropping rapidly as pressure increases (Fig. 13.50b). Attenuation peaks will also depend on specific rock characteristics. Absorption peaks seen in one frequency band may not be apparent in others.

With the improving quality of seismic data, maps of the estimated attenuation are becoming a common displayed attribute. The relative values of  $1/Q$  measured through time-lapse reservoir monitoring are becoming robust. As indicated in Fig. 13.50a,  $1/Q$  will be sensitive to many of the common recovery processes.

## 13.6 Rock Failure Relationships

**13.6.1 Introduction.** In this section, we will go through the various relationships describing mechanical failure in rocks. This is important because under reservoir pressure and stress conditions, production can induce rock failure, sometime with catastrophic effects. By applying strength criteria, within reservoir simulators we can predict when problems might occur. In Section 13.5, we examined the elastic behavior, which was largely reversible. Here we deal



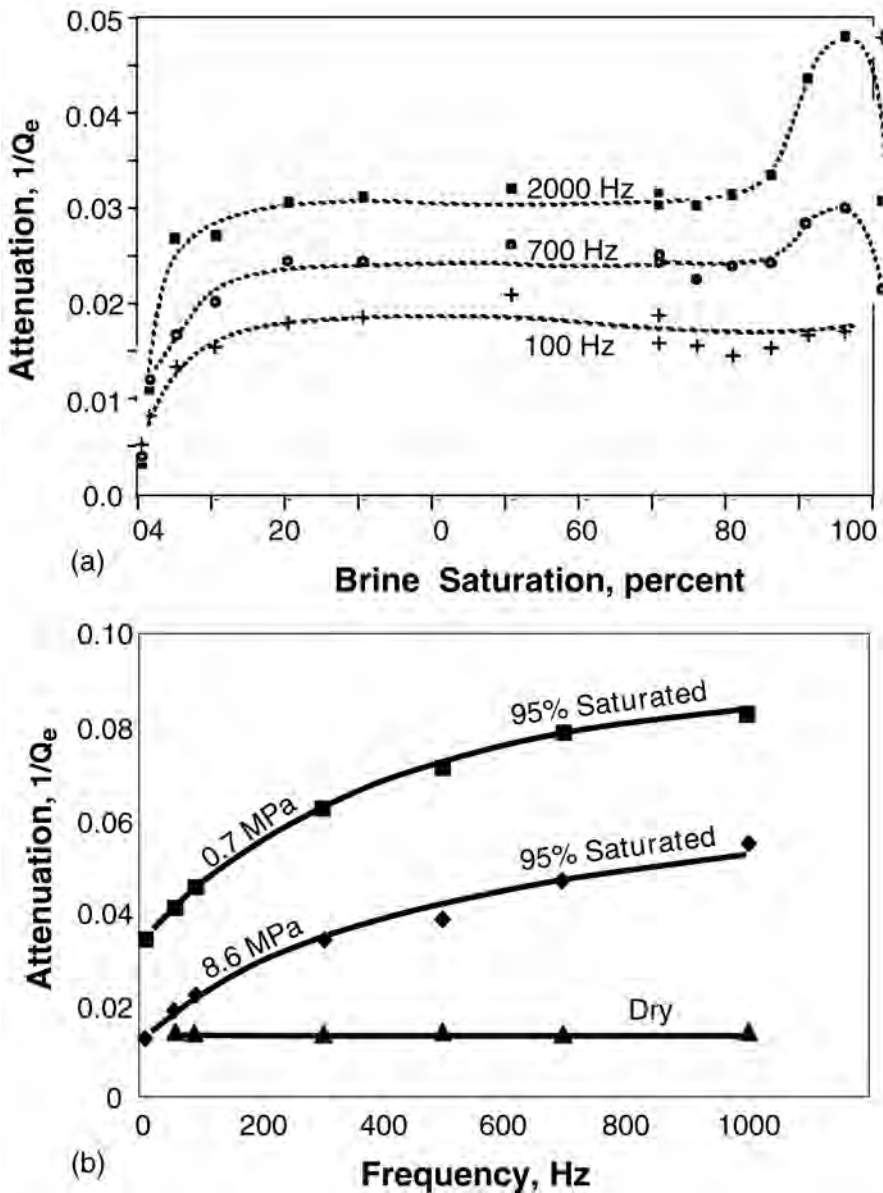


Fig. 13.50—Extensional (or Young’s modulus) attenuation ( $1/Q_e$ ) as a function of water saturation (a) and frequency (b) for Berea sandstone. With increasing saturation,  $1/Q_e$  increases and reaches a peak at approximately 95% saturation (a). Attenuation decreases with increasing pressure, as shown in (b).

with permanent deformation. By rock failure, we mean the formation of faults and fracture planes, crushing, and relative motion of individual mineral grains and cements. Failure can involve formation of discrete fracture zones and the more “ductile” or homogeneous deformation. The later deformation is caused by a broad distribution of fracture zones or general grain crushing during compaction. We will not consider deformation caused by plastic strains of the mineral components, as is common in salt and in calcite at higher temperatures. In our analysis, several assumptions are made: The material is isotropic and homogeneous; stresses are applied uniformly; textural characteristics such as grain size and sorting have no influence; tem-

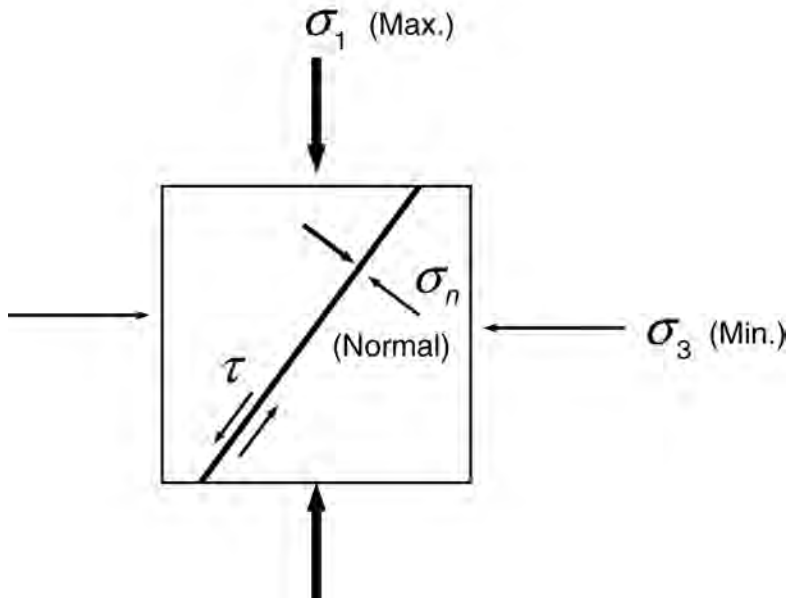


Fig. 13.51—Schematic diagram defining stress orientations along and across a plane.

perature and strain rate are ignored; and the intermediate stresses are presumed to play no role. Each of these assumptions can be violated, and some have been demonstrated to have major influences on rock strength.

**13.6.2 Coulomb-Navier Failure.** To begin with, a brief review of the standard Mohr failure criteria will be examined to introduce concepts and define terms, as well as to establish the basic mathematics behind the strength relationships. Units of stress and strength are the same as pressure and were covered previously. More detailed descriptions can be found in standard textbooks (i.e., Jaeger<sup>103</sup>). Mohr circles and a linear failure envelope are the most common methods used to plot stresses and indicate strength limits. This technique predicts failure when stresses surpass both the intrinsic strength of a rock and internal friction. The primary terms and characteristics are shown in Fig. 13.51. Normal stresses across any plane are plotted on the horizontal axis, and shear stresses are plotted on the vertical axis. Compressive stresses are defined as positive (as opposed to the mechanical engineering convention of tensional stresses being positive). For the hydrostatic case, all stresses are equal; this stress state is represented by a point on the horizontal axis. When stresses differ, the maximum principal stress,  $\sigma_1$ , and minimum stress,  $\sigma_3$ , are plotted on the horizontal axis and the possible shear stresses along any plane fall on a hemisphere connecting  $\sigma_1$  and  $\sigma_3$  (Fig. 13.52). The mean stress,  $\sigma_m$ , and radius of this circle,  $r$ , are simple sums and differences of the principal stresses.

$$\sigma_m = \frac{1}{2}(\sigma_1 + \sigma_3), \dots\dots\dots (13.110)$$

$$r = \frac{1}{2}(\sigma_1 - \sigma_3). \dots\dots\dots (13.111)$$

The normal stress across any plane,  $\sigma_n$ , and the shear stress along the plane,  $\tau$ , are functions of the principal stresses and the plane orientation.

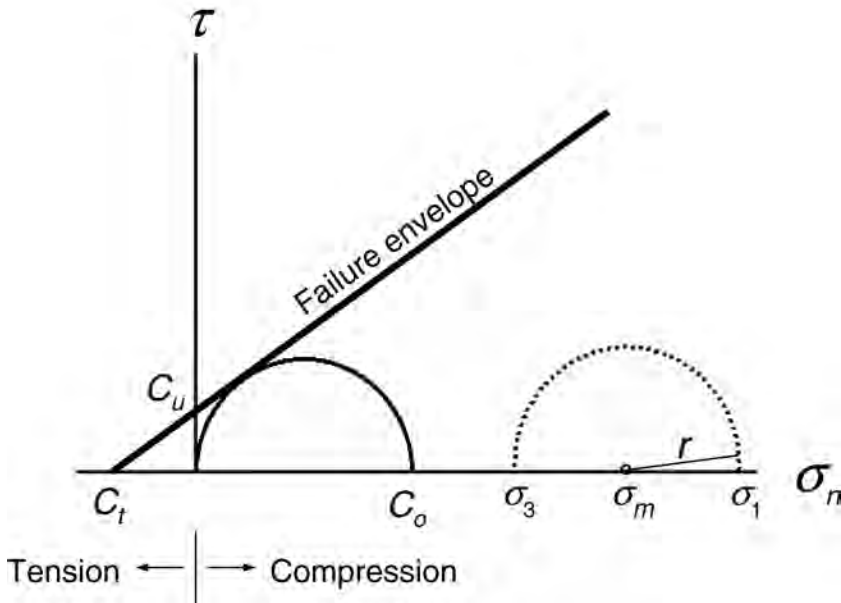


Fig. 13.52—Generalized rock failure with a linear envelope.

$$\sigma_n = \frac{1}{2}(\sigma_1 + \sigma_3) + \frac{1}{2}(\sigma_1 - \sigma_3) \cos 2\theta, \dots\dots\dots (13.112)$$

$$= \sigma_m + r \cos 2\theta, \dots\dots\dots (13.113)$$

$$\tau = \frac{1}{2}(\sigma_1 - \sigma_3) \sin 2\theta, \dots\dots\dots (13.114)$$

$$= r \sin 2\theta, \dots\dots\dots (13.115)$$

where  $\theta$  is the angle between the plane and the  $\sigma_3$  direction.

From Eqs. 13.114 and 13.115, the maximum shear occurs along a plane oriented at  $\theta = \frac{\pi}{4}$  (45°). However, because of friction, rocks do not fail along this plane. Instead, failure occurs along some rotated plane where friction is lower, yet shear stress is still high. This failure point (or plane) is shown in Fig. 13.51 as the nearly diagonal line. Fig. 13.51 also shows the associated normal and shear stresses. If numerous failure tests are made and plotted, an envelope is defined as in Fig. 13.52. In this case, friction is assumed to be a simple linear function of normal stress, and the resulting envelope is also linear. The slope of this envelope is  $\alpha$ , and we define  $\mu$  as the angle of internal friction

$$\mu = \tan^{-1} \alpha. \dots\dots\dots (13.116)$$

Within this framework, we can define several important properties of the rock as shown in Fig. 13.52:

- $C_0$  = Uniaxial or unconfined compressive strength ( $\sigma_3 = 0$ )
- $C_u$  = Cohesive strength or the intercept of the envelope with  $\sigma_n = 0$ .
- $C_t$  = Tensional strength.

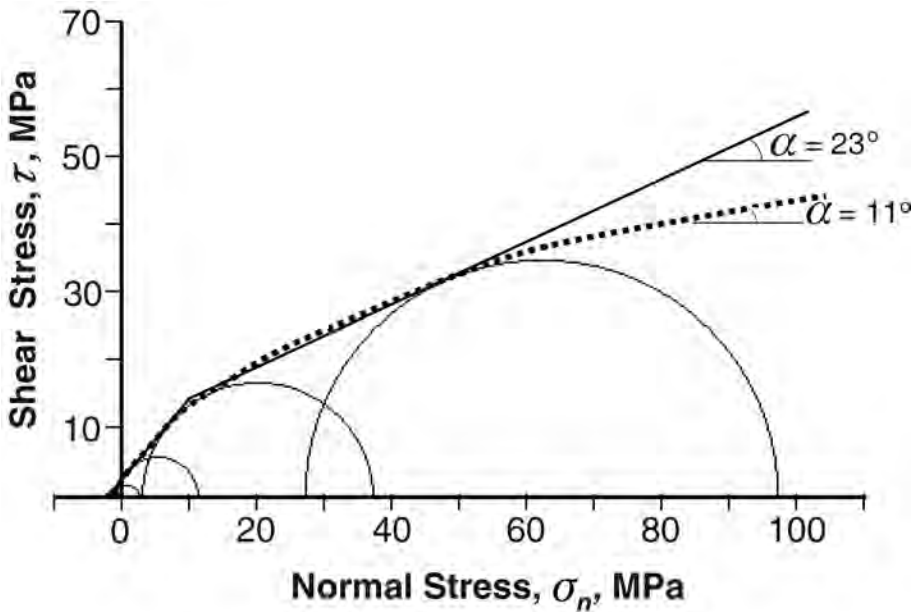


Fig. 13.53—Measured failure strengths for the B-d #1 sandstone with straight-line segments and curved envelope fits to failure.

The failure envelope is then defined by the line

$$\tau = C_u + \alpha \sigma_n \dots\dots\dots (13.117)$$

If the rock has already been broken, or a fracture already exists, then both  $C_u$  and  $C_t$  will be close to zero.

Several useful equations can be derived from the geometric relationships shown so far. From the equation for a circle,

$$\tau^2 = r^2 - (\sigma_n^*)^2 = r^2 - (\sigma_m - \sigma_n)^2 \dots\dots\dots (13.118)$$

At the intersection of the envelope and the circle, we must have

$$C_u + \alpha \sigma_n = \tau = [r^2 - (\sigma_m - \sigma_n)^2]^{\frac{1}{2}}, \dots\dots\dots (13.119)$$

which leads to

$$(1 + \alpha^2)\sigma_n^2 + 2(C_u\alpha - \sigma_m)\sigma_n + C_u^2 + \sigma_m^2 - r^2 = 0 \dots\dots\dots (13.120)$$

Using the general solution to a second-order polynomial gives

$$\sigma_n = \frac{-2(C_u\alpha - \sigma_m) \pm [4(C_u\alpha - \sigma_m)^2 - 4(1 + \alpha^2)(C_u^2 + \sigma_m^2 - r^2)]^{\frac{1}{2}}}{2(1 + \alpha^2)} \dots\dots\dots (13.121)$$

Because we want only a point where the circle touches the envelope, the square root term must vanish.

$$[4(C_u\alpha - \sigma_m)^2 - 4(1 + \alpha^2)(C_u + \sigma_m^2 - r^2)]^{1/2} = 0. \dots\dots\dots (13.122)$$

After some algebraic manipulation, we find

$$C_u = -\alpha\sigma_m + r(1 + \alpha^2)^{1/2}, \dots\dots\dots (13.123)$$

and

$$\alpha = \frac{[C_u\sigma_m - r(C_u^2 + \sigma_m^2 - r^2)]^{1/2}}{r^2 - \sigma_m^2} \dots\dots\dots (13.124)$$

Substitution of  $C_u$  (defined in Eq. 13.123) into Eq. 13.121 gives an expression for normal stress.

$$\sigma_n = \sigma_m - \alpha r(1 + \alpha^2)^{-1/2} \dots\dots\dots (13.125)$$

If the envelope could be continued into the tensional region, the tensional strength could easily be obtained:

$$C_t = \frac{C_u}{\alpha} \dots\dots\dots (13.126)$$

Under tension, the stresses are negative, although the tensional strength is a positive number. Thus, if rocks could fail according to a constant internal friction, we would have a simple way to relate the stresses involved and need only a couple of material constants, such as  $C_u$  and  $\alpha$ .

**13.6.3 Mohr Failure, Curved Envelopes, and Hoek-Brown Relationships.** We are immediately faced with two problems when we try to apply Coulomb-Navier failure criteria: (1) Rocks do not generally have a linear failure envelope, and (2) material properties controlling failure must be obtained either through logs or assumed behavior. Fig. 13.53 shows the type of envelope commonly seen. In fact, we know that the slope must change as stresses are increased because rocks begin yielding and act more plastically. Fig. 13.54 shows the generalized behavior expected. At normal stresses above the brittle-ductile transition, failure can no longer be maintained on a single plane, but is distributed more homogeneously throughout the sample. We must develop different failure criteria, one that produced an appropriately curved envelope, and we expect it to have a strong porosity dependence (Fig. 13.55).

Numerous failure criteria have been proposed that are primarily empirically based. Table 13.12 shows some of the criteria proposed both for general purposes and for specific rock types or conditions. Observed failure envelopes are smooth forms so simple exponential or power-law functions can usually be found that fit the data well. The relations of Bienlawski<sup>111</sup> and Hoek and Brown<sup>112</sup> are most common. Much of the recent work in rock mechanics has been directed toward ascertaining the constants of these relationships in terms of easily measurable rock properties. Note that these relationships apply primarily to the brittle failure regime and cannot be used for grain crushing or pore collapse (as we shall see later) or when substantial

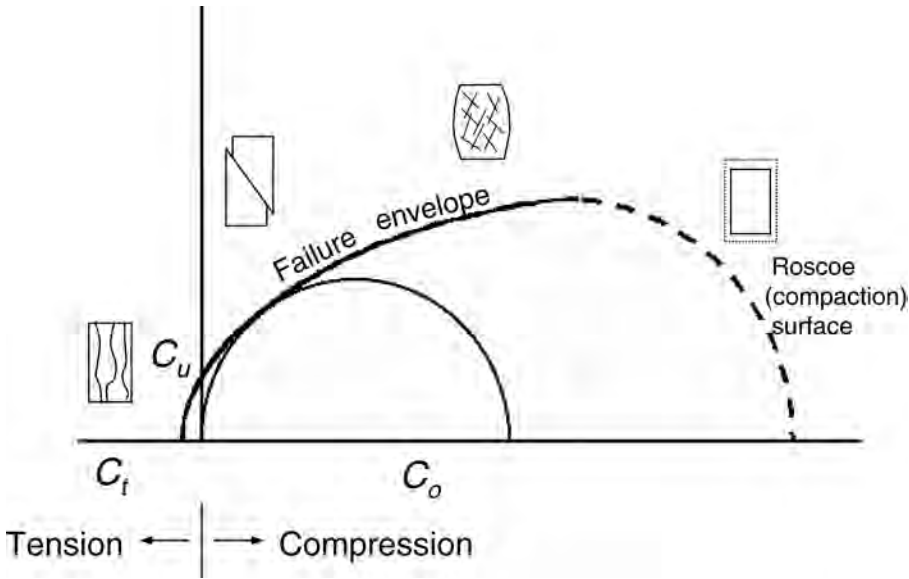


Fig. 13.54—Curved rock failure envelope with schematic failure styles at different mean pressure ranges.

ductile or plastic deformation is involved. We will examine these proposed forms to interrelate terms and reduce unknowns to variables that can be derived from logs.

Hoek and Brown<sup>112</sup> compiled extensive data on a variety of rock types and produced relationships that are simple and can be developed into forms amenable to well-log analysis. A primary feature of this failure criterion is a relation between the maximum and minimum stresses when both are normalized by the uniaxial compressive strength

$$\left(\frac{\sigma_1}{C_0} - \frac{\sigma_3}{C_0}\right)^2 = m \frac{\sigma_3}{C_0} + s. \dots\dots\dots (13.127)$$

This formulation was motivated by the systematic behavior seen in many tests as shown in Fig. 13.56. In Eq. 13.127, *m* and *s* are material constants dependent on the overall quality of the rock mass, and *m* is also dependent on the rock type (Table 13.13). Note that we could derive the value for *m* from a mineralogic analysis. In our analysis, we will presume that the local rock mass of interest is intact, and thus

$$s = 1. \dots\dots\dots (13.128)$$

For applications that are in sandstones, numeric results can often use

$$m = 15. \dots\dots\dots (13.129)$$

Eq. 13.127 can be rewritten to give one principal stress in terms of the other:

$$\sigma_1 = \sigma_3 + (mC_0\sigma_3 + C_0^2)^{1/2}, \dots\dots\dots (13.130)$$

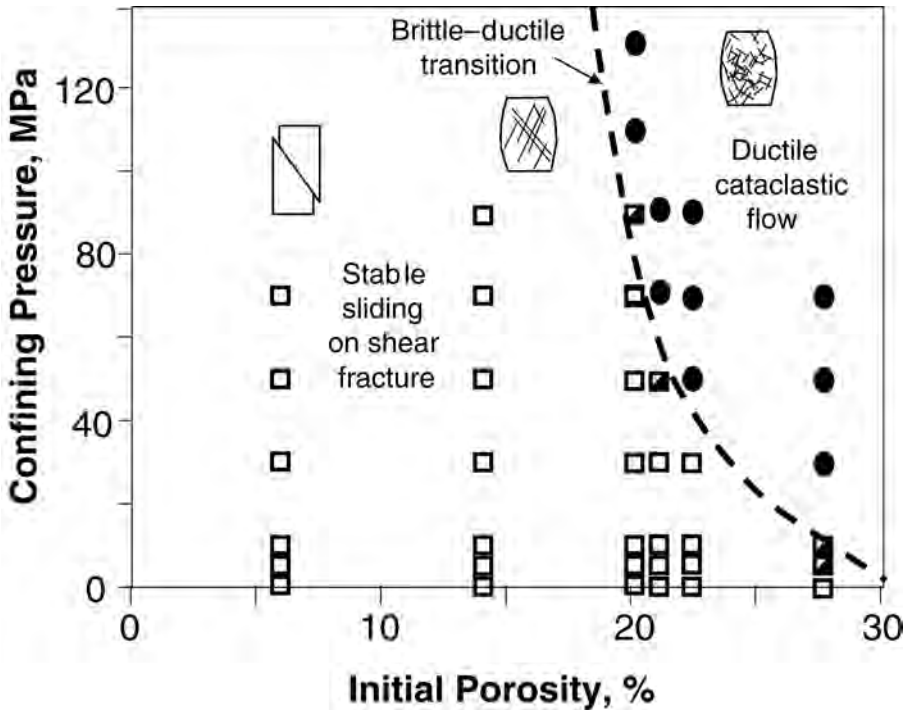


Fig. 13.55—Failure mechanisms as a function of porosity for sandstones (after Scott<sup>105</sup>).

$$\sigma_3 = \sigma_1 + \frac{1}{2} m C_0 \left[ 1 - \left( 1 + 4 \frac{\sigma_1}{m C_0} + \frac{4}{m^2} \right)^{\frac{1}{2}} \right] \dots\dots\dots (13.131)$$

Such normalized stress states were used to construct the curved envelope in Fig. 13.54.

The tensional strength, the stress at which an envelope would cross the horizontal axis, is found by equating  $\sigma_1$  to  $\sigma_3$  in Eq. 13.130 (note that  $C_t$  is defined as a positive number).

$$C_t = \frac{C_0}{m} \dots\dots\dots (13.132)$$

For sandstones, this results in  $\frac{C_0}{15}$ , or  $0.067 C_0$ . The 15 uniaxial tensional strength  $\sigma_\tau^*$  is slightly different and is defined as the value at which the maximum stress,  $\sigma_1$ , equals zero. From Eq. 13.130, we get

$$\sigma_\tau^* = \frac{1}{2} C_0 \left[ m - (m + 4)^{\frac{1}{2}} \right] \dots\dots\dots (13.133)$$

Other basic properties are not so simply derived.

We must produce from the stress relationships (Eqs. 13.127 or 13.130) an equation for a failure envelope that permits us to resolve the shear and normal stresses on a failure plane, its orientation, and an approximation of the internal friction, and simply predict regions of instability. The general envelope shapes seen in Figs. 13.54 and 13.56 suggest a form like that proposed by Murrell<sup>107</sup> and Bienlowski<sup>111</sup>:

TABLE 13.12—STRENGTH LAWS, SANDSTONES		
Plumb <i>et al.</i> <sup>104</sup>	$\sigma_1 = 275.5 - 5.8F + 10.8 P_0^{0.7}$	F = Percent fines
Scott <sup>105</sup>	$\sigma_1 = 38.95\phi^{-0.813}$	At 50 MPa P <sub>c</sub>
Dunn <i>et al.</i> <sup>106</sup>	$\sigma_1 = 50.1\phi^{-0.812}$	At 50 MPa P <sub>c</sub>
Murrell <sup>107</sup>	$\tau = a\sigma^n$	
Jizba <sup>108</sup>	$\tau = 37(0.36 - \phi)^{1.05} \bullet \sigma^{0.6}$	Sandstones 0 < C < 0.17
	$\tau = 63(1 - 1.15C) + \mu\sigma$	Shaly SS C' > 0.17 C' = clay content
Allison <sup>109</sup>	$\sigma_1 = a \bullet \exp(4.335 - 0.663\phi)$	Limestone and chalks
	$C_0 = 6.505E$	E = Young's modulus
Kazi <i>et al.</i> <sup>110</sup>	$\log C_0 = 0.608 + 0.314 \left(\frac{E}{P}\right)^{1/2}$	
Bienawski <sup>111</sup>	$\frac{\sigma_1}{C_0} - 1 = A \left(\frac{\sigma_1}{C_0}\right)^{0.75}$	Criterion I
	$\frac{\tau_m}{C_0} - 0.1 = A \left(\frac{\sigma_m}{C_0}\right)^{0.9}$	Criterion II
Hoek and Brown <sup>112</sup>	$\left(\frac{\sigma_1}{C_0}\right)^2 = m \left(\frac{\sigma_3}{C_0}\right) + s$	For intact sandstone: m ≅ 15, s ≅ 1

\* derived from their original data

$$\tau = A(\sigma_n + b)^n, \dots\dots\dots (13.134)$$

where A, b, and n are material constants. Because the envelope intersects the horizontal axis when the normal stress equals the tensional strength,

$$b = C_t \dots\dots\dots (13.135)$$

When the normal stress is zero, the envelope intersects the vertical axis at the cohesion value C<sub>u</sub>. From Eq. 13.134, this requires

$$A = C_u C_t^{-n} \dots\dots\dots (13.136)$$

Therefore, the general form for an envelope is

$$\tau = C_u C_t^{-n} (\sigma_n + C_t)^n \dots\dots\dots (13.137)$$



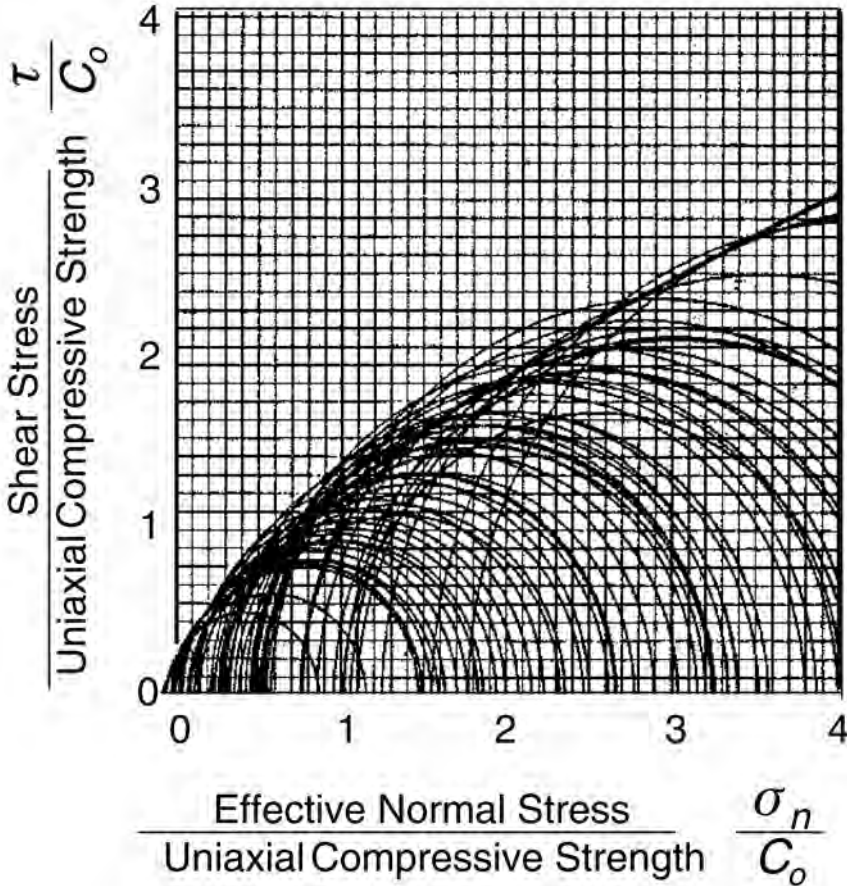


Fig. 13.56—Failure envelope for sandstones after Hoek and Brown.<sup>112</sup> Stresses are normalized by rock uniaxial compressive strength.

To derive the slope,  $\alpha$ , at any point, we note that the envelope is only slowly varying over a small stress range and could be locally approximated by a line. If we use a pseudocohe $sion$   $C_u^*$  defined by Eq. 13.123 for the stress condition,  $\sigma_m, r$  we can subtract the same  $C_u^*$  from a slightly different stress condition,  $\sigma_m, r'$ . Solving for  $\alpha$  gives

$$\alpha = \frac{(r - r')}{\left[ (\sigma_m - \sigma_m')^2 - (r - r')^2 \right]^{1/2}} \dots\dots\dots (13.138)$$

The Hoek-Brown stress criteria allow us to redefine the mean,  $\sigma_m$ , and differential,  $r$ , stresses

$$\sigma_m = \frac{1}{2}(\sigma_1 + \sigma_3) = \frac{1}{2} \left( 2\sigma_3 + [mC_0\sigma_3 + C_0^2]^{1/2} \right), \dots\dots\dots (13.139)$$

$$r = \frac{1}{2}(\sigma_1 - \sigma_3) = \frac{1}{2} (mC_0\sigma_3 + C_0^2)^{1/2} \dots\dots\dots (13.140)$$

**TABLE 13.13—HOEK AND BROWN<sup>112</sup> LITHOLOGIC AND QUALITY COEFFICIENTS**

Material	<i>m</i>			<i>s</i>
	Sandstone	Limestone and Dolomite	Siltstone and Shale	
Intact material	15.0	7.0	10.0	1.0
No joints				
No weathering				
High Quality	7.5	3.5	5.0	0.1
Few joints				
Little weathering				
Good Quality	1.5	0.7	1.0	0.004
Few joints				
Some weathering				
Medium Quality	0.3	0.14	0.2	0.0001
Joints 0.3 to 1 m				
Moderate weathering				
Poor Quality	0.08	0.04	0.05	0.00001
Joints every few cm				
Heavy weathering				
Cruddy	0.15	0.007	0.01	0.0
Numerous joints				
Heavy weathering				

By substituting these relations into Eq. 13.138 for two stresses  $\sigma_3$  and  $\sigma_3 + \delta \sigma_3$ , expanding the result and allowing the stress difference,  $\delta \sigma_3$ , to approach zero (what a pain!), we find

$$\alpha = \frac{mC_0}{2\left[4(mC_0\sigma_3 + C_0^2) + 2mC_0(mC_0\sigma_3 + C_0^2)^{\frac{1}{2}}\right]^{\frac{1}{2}}} \dots\dots\dots (13.141)$$

As we found previously (Eq. 13.125), the normal stress is then

$$\sigma_n = \sigma_m - \alpha r(1 + \alpha^2)^{\frac{1}{2}} \dots\dots\dots (13.142)$$

The cohesion is the shear stress value when  $\sigma_n$  equals zero. This will occur for  $\sigma_3$  somewhere between zero and  $-C_r$ . In other words,  $\sigma_n = 0$  for

$$\sigma_3 = -\beta \frac{C_0}{m}, \dots\dots\dots (13.143)$$

where  $\beta$  is a value around 0.5. We could substitute this term into Eqs. 13.141 and 13.142 and solve for  $\beta$ . However, this results in a rather complicated root to a third-order polynomial. Fortunately, by iteration, we can show that  $\beta$  is relatively constant at about 0.62 with little dependence on  $m$ . Using this value of  $\beta$  in Eq. 13.143 and substituting into the previous equations gives us our cohesion. For a sandstone with  $m = 15$ , we get

$$C_u = 0.154C_0 \dots\dots\dots (13.144)$$

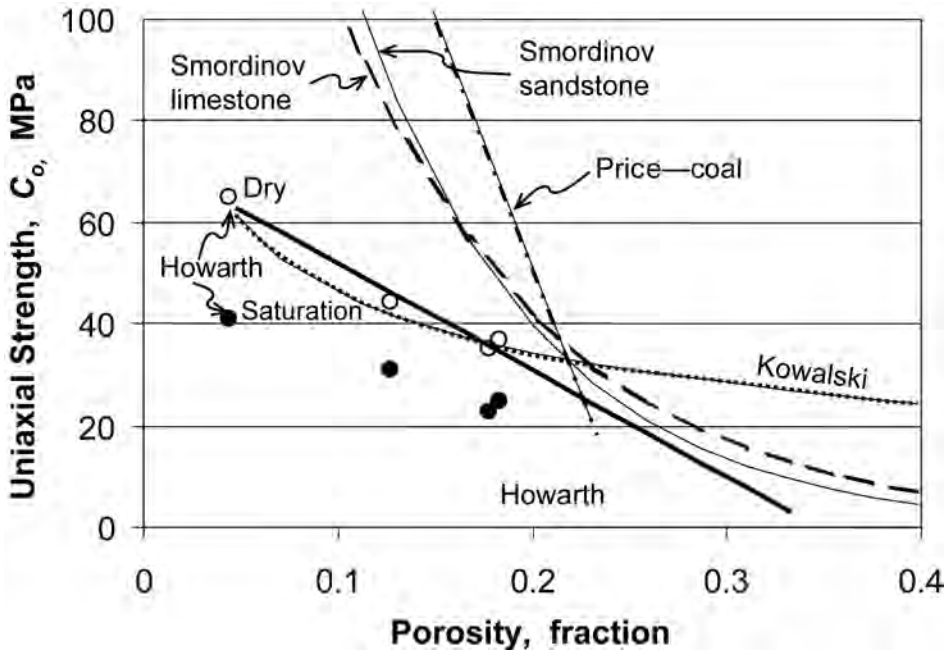


Fig. 13.57—Examples of reported uniaxial compressive strength ( $C_0$ ) relations for different rock types.

The definition of our curved envelope in Eq. 13.137 is not strictly compatible with the Hoek-Brown stress relations. However, we can get an estimate of the exponent,  $n$ , by using our tensile and cohesion strengths and some reasonable value of  $\sigma_n$  such as  $\sigma_n = C_0$ . From Fig. 13.54, we can see that  $\tau$  is approximately 1.1  $C_0$  at this point. From Eq. 13.137, with  $m$  equal to 15,

$$n = 0.71 \dots\dots\dots (13.145)$$

This value falls within the range of 0.65 to 0.75 suggested by Yudhbir *et al.*<sup>113</sup> Thus, from a presumed simple relation between  $\sigma_1$  and  $\sigma_3$ , almost all the necessary parameters can be derived.

**13.6.4 Uniaxial Compressive Strength.** We have seen how a general rock failure criterion can be reduced to a few parameters dependent on lithology ( $m$ ) and the uniaxial compressive strength ( $C_0$ ). Lithology is commonly derived during log analysis, so  $m$  may be estimated (Table 13.13). What is needed still is an initial measure of rock strength provided by  $C_0$ .  $C_0$  can be estimated from porosity or sonic velocities, but many factors such as grain size, clay content, or saturation have significant influences.

A large amount of  $C_0$  data is available and, although there is considerable scatter,  $C_0$  usually varies systematically with other rock characteristics. We will concentrate on porosity as the primary controlling factor because it is routinely available from logs and is a fundamental input into reservoir simulators.

Numerous relationships have been developed to estimate  $C_0$ , often in conjunction with general rock strength relationships. Table 13.14 lists many of the proposed relations for  $C_0$ , some of which are plotted for various rock types in Fig. 13.57 and for sandstones in Fig. 13.58. We expect  $C_0$  to decrease as porosity increases. At some transition porosity, rocks will lose all

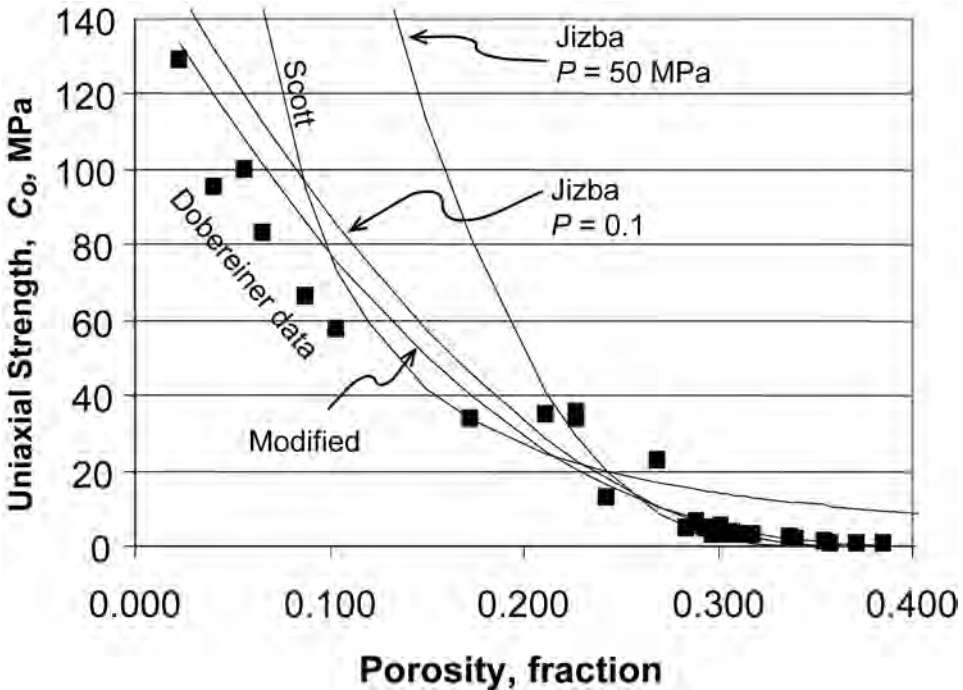


Fig. 13.58—Uniaxial compressive strength ( $C_0$ ) relations for sandstones.

initial strength and become merely a loose aggregate. No matter which relationship is chosen, variables such as cementation, alteration, texture, and so on can cause significant scatter.

If we accept the restrictive relationships for failure of Eq. 13.130 or 13.134, we can derive  $C_0$  from any such strength data:

$$C_0 = -25m + 25(m^2 - 2.4\Phi^{-1.63})^{1/2} \dots\dots\dots (13.146)$$

However, this equation predicts a finite strength even as porosity approaches 1.0. More realistic forms must be used so that strength vanishes at some porosity  $\Phi_c$ . This limiting porosity was shown as a crossover porosity from rock to a slurry by Raymer *et al.*<sup>119</sup> and was referred to as “critical porosity” elsewhere. Jizba<sup>108</sup> used such a concept to derive a general strength relationship for sandstones:

$$\tau = 37(0.36 - \Phi)^{1.05} \sigma_n^{0.6}, \dots\dots\dots (13.147)$$

where  $\tau$  and  $\sigma_n$  are the shear and normal stresses at failure.

The 0.36 within the parentheses is her presumed value for  $\Phi_c$ . Notice, however, that this form indicates that sandstones have no tensile or cohesive strength. We can obtain a better result by using Jizba’s relationship at elevated confining pressure (say, 50 MPa), where it is more valid, and recasting the trend in terms of Eq. 13.130, as we did for the Scott relation.<sup>105</sup> Dobereiner and DeFreitas<sup>121</sup> measured several weak sandstones, and their results suggest that critical porosity is approximately 0.42. Using this critical porosity, we derive a uniaxial compressive strength

TABLE 13.14—UNIAXIAL COMPRESSIVE STRENGTH, $C_0$		
Dowla <i>et al.</i> <sup>114*</sup>	$C_0 = 157.4 - 5.563\phi$	Berea SS $0.22 < \phi < 0.24$
Kowalski <sup>115</sup>	$C_0 = 21.18e - 0.358$	$e = \text{void ratio} = \frac{\phi}{1 - \phi}$
Griffith <sup>116</sup>	$C_0 = \frac{800}{\phi + 4}$	$C_0$ in psi
Howarth <sup>118</sup>	$C_0 = 73.0 - 2.1\phi$	Mixed rock types (in thousands of psi)
Price <sup>117</sup>	$C_0 = 36 - 1.43\phi$	Mixed rock types
Smordinov <i>et al.</i> <sup>118**</sup>	$C_0 = 3500 \exp(-0.108\phi)$	Quartzose rocks
	$C_0 = 2590 \exp(-0.09\phi)$	Carbonates
* derived from their original relationships		
** reported in Howarth <sup>118</sup>		

$$C_0 = -25m + 25 \{ m^2 + 2520(0.42 - \phi)^{2.8} \}^{1/2} \dots\dots\dots (13.148)$$

This  $C_0$  equation is plotted in Fig. 13.58 along with the modified Scott<sup>110</sup> and Jizba<sup>108</sup> equations and data of Dobreiner and DeFreitas.<sup>121</sup>

**13.6.5 Compaction Strength.** As was indicated in Fig. 13.55, at some elevated stress or confining pressure, the rock will begin to show ductile deformation. The grain structure begins to collapse, and the rock will compact and lose porosity. This compaction strength,  $C_c$ , is itself a function of porosity as well as mineralogy, diagenesis, and texture. In Figs. 13.59a and 13.59b, the behavior of two rocks under hydrostatic pressure is shown. The high-porosity (33%) sandstone (Fig. 13.59a) has a low “crush” strength of about 55 MPa. With a lower porosity of 19%, Berea sandstone has a much higher strength of 440 MPa (Fig. 13.59b). Notice that in both Figs. 13.59a and 59b, permanent deformation remains even after the stress is released. This hysteresis demonstrates the damage to the matrix structure caused by exceeding the crush strength.

In the cases in which studies are restricted to sandstones, an exponential dependence on porosity is usually observed (Fig. 13.59a). Scott<sup>110</sup> fit his and the Dunn *et al.*<sup>106</sup> data to the form

$$\sigma_f = 38.95\phi^{-0.815} [\text{at } \sigma_3 = 50 \text{ MPa}] \dots\dots\dots (13.149)$$

With a general relationship available for uniaxial compressive strength and the compaction limit, rock failure envelopes can be determined for sandstones at any porosity. Fig. 13.60 shows the complete envelopes for the porosity range 0.15 to 0.35.

**13.6.6 Clay Content.** Most sandstones are mixtures of mineral such as feldspars, calcite, dolomite, micas, clays, and of course quartz. Clays are a very common component and can make up anywhere from 0 to nearly 100% of a clastic rock. Usually, at some point greater than 40% clay, the rock is considered a shale or mudstone rather than a sandstone (refer to Section 13.7). The structure of clay minerals and their typical methods of bonding are signifi-

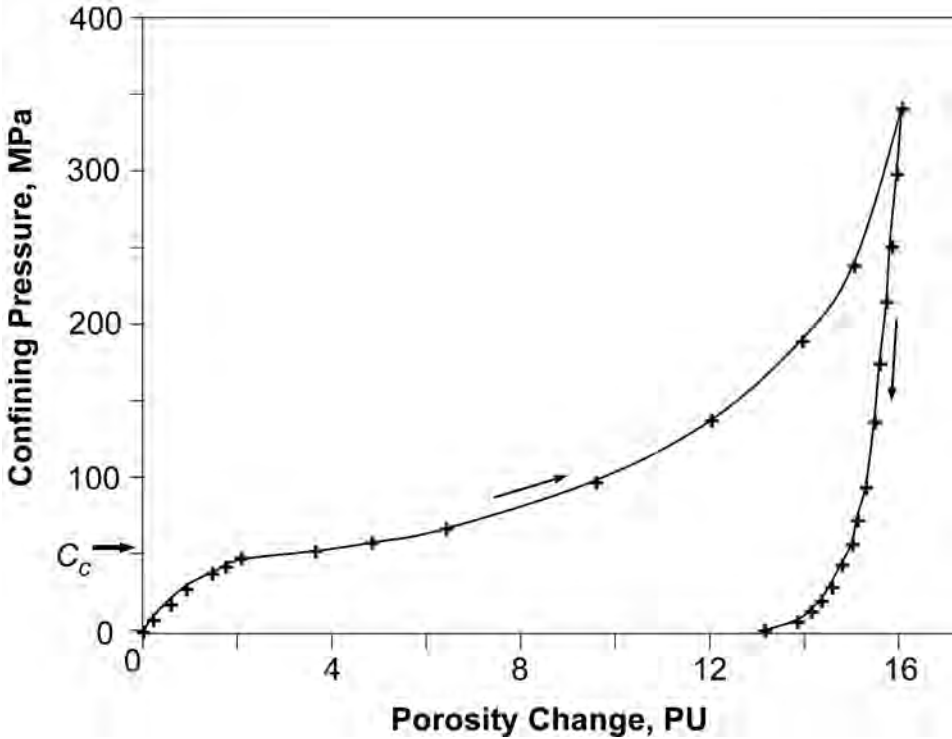


Fig. 13.59—(a) Hydrostatic compaction of a high-porosity Gulf of Mexico sandstone (T.E. Scott, personal communication); (b) hydrostatic compaction of Berea sandstone (T.E. Scott, personal communication).

cantly different from those of quartz, so we would expect clays to strongly influence mechanical properties. Such influences depend on the nature of the clay, the amount and location within the rock framework, and the state of hydration.

There have been few systematic studies of clay effects on the mechanical properties of rocks. Corbett *et al.*<sup>120</sup> demonstrated how the coefficient of internal friction and thus the strength of Austin chalk strongly depends on even a small clay fraction (Fig. 13.61). In particular, smectite content was found to have more influence in this case than other clays. This allows us to derive a general relationship between failure and clay content.

$$\sigma_f = 405 - 977\Phi - 3557C + (1.85 - 0.039\Phi)\sigma_3, \dots\dots\dots (13.150)$$

where *C* is the smectite fraction. Unfortunately, this equation was developed for dry samples.

Jizba<sup>114</sup> tested several dry clay-rich samples and proposed a general linear envelope form for shales and shaley sandstones.

$$\tau = 63(1 - 1.15C') = 0.7\sigma_n \dots\dots\dots (13.151)$$

More relevant data, however, comes from Steiger and Leung<sup>122</sup> with both dry and saturated shale measurements (Fig. 13.62). From these data, we derive an approximation for the wet shale uniaxial compressional strength.

$$C_0 = 88 - 110C \dots\dots\dots (13.152)$$

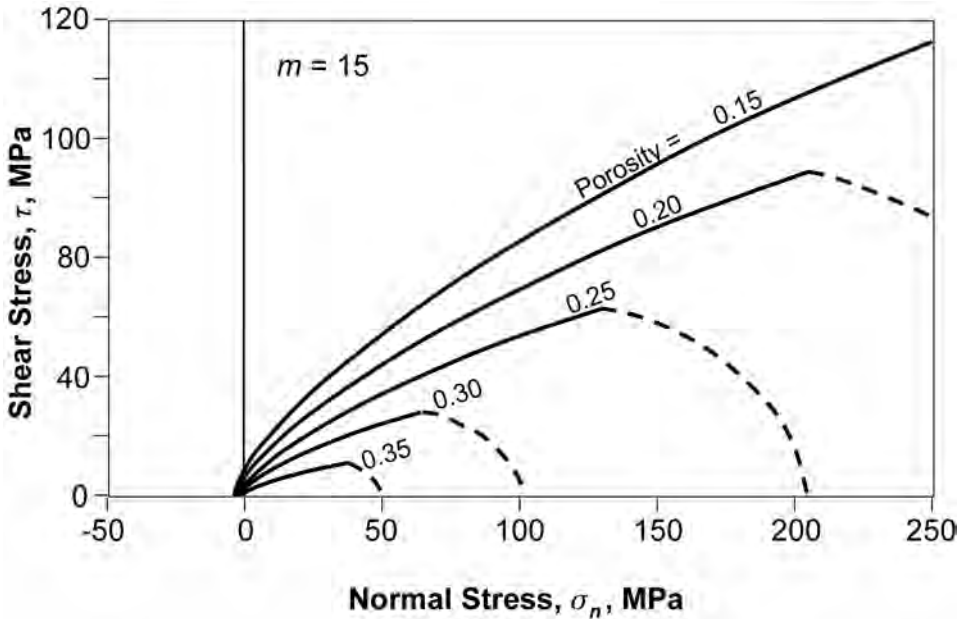


Fig. 13.60—Generalized failure envelope and Roscoe (crushing) surface at different porosities. Hoek-Brown parameter  $m = 15$  used.

This relation, as well as those for the Austin chalk, suggests a strong clay dependence. Jizba,<sup>108</sup> however, reported only a slight dependence of  $C_0$  on clay content in shaley sands.

It is likely that in many sands, clays reside as pore-filling materials and have only a secondary effect on mechanical properties. At this point, we expect clays to have a significant effect even in fairly pure sands (this will be seen also in sonic velocity measurements). Thus, a more general form for uniaxial compressive strength of sandstones would be

$$C_0 = -25m + 25 \{ m^2 + 2520(0.42 - \Phi)^{2.8} \}^{1/2} - aC, \dots\dots\dots (13.153)$$

where the coefficient  $a$  has a value of approximately 100. The influence of clays on the mechanical properties of rocks needs much further investigation.

**13.6.7 Pore Fluid Effects.** Fluids can alter rock mechanical properties of rocks through fluid pressure, chemical reactions with mineral surfaces, and by lubricating moving surfaces. The primary fluids encountered are brines and hydrocarbon oils and gases. Drilling, completion, and fracturing fluids can also be present, and their effects are typically studied to prevent formation damage. We will concentrate on the role of water and, in particular, how water saturation can influence rock strengths measured in the laboratory or derived from well logs.

**Effective Stress.** Pore fluid pressures will reduce the effective stress supported by the rock mineral frame. This effect has been well known since the publication of Terzaghi and Peck<sup>63</sup> and has been documented by numerous investigators. The most common form for the effective stress law is

$$\sigma_e = \sigma_a - nP_p, \dots\dots\dots (13.154)$$

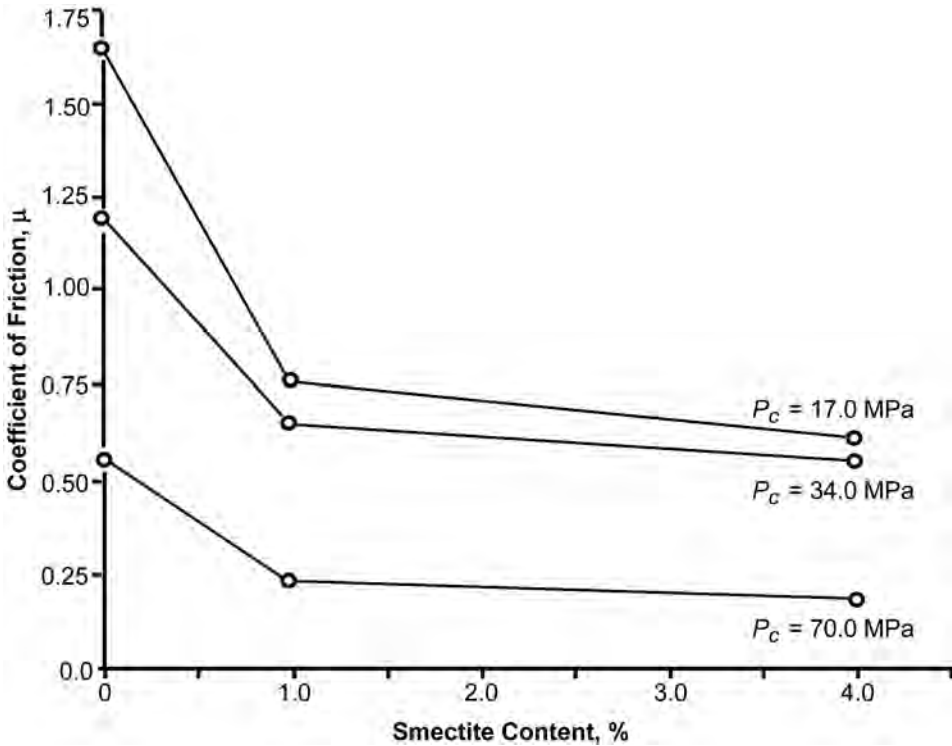


Fig. 13.61—Effect of smectite content on the coefficient of internal friction of Austin Chalk (from Corbett et al.<sup>120</sup>).

where  $\sigma_e$  is the effective stress,  $\sigma_a$  the applied stress on the rock surface,  $P_p$ , and the pore pressure. Note that this is the same as Eq. 13.35. The effective stress coefficient  $n$  is also called Biot’s poroelastic term.

$$n = 1 - \frac{K_d}{K_o}, \dots\dots\dots (13.155)$$

where  $K_d$  is the dry rock bulk modulus and  $K_o$  the mineral bulk modulus. Because the rock modulus is usually much lower than the mineral modulus,  $n$  is often close to unity. In many applications and when no other information is available,  $n$  is usually taken as one.

In our analyses, all of the stresses used to describe rock failure were actually effective stresses. Rock failure can be dramatically affected by pore pressure, as indicated in Fig. 13.63. An envelope is plotted for a sandstone with porosity of 25%. For applied principal stresses of 225 MPa for  $\sigma_1$ , 175 MPa for  $\sigma_3$ , and a  $P_p$  of 75 MPa, the effective Mohr circle plots well within the field of stability. The pore pressure has been subtracted from both applied stresses to give effective principal stresses of 150 and 100 MPa. If pore pressure is increased, the effective stresses decrease, and the Mohr circle is shifted left until eventually the envelope may be contacted and the rock fails by brittle fracture. On the other hand, if pore pressure decreases, the Mohr circle shifts right, and the rock may contract the Roscoe surface and fail by compaction or grain crushing. In any case, if pore pressures are known, their effects can be accounted for in a straightforward way.



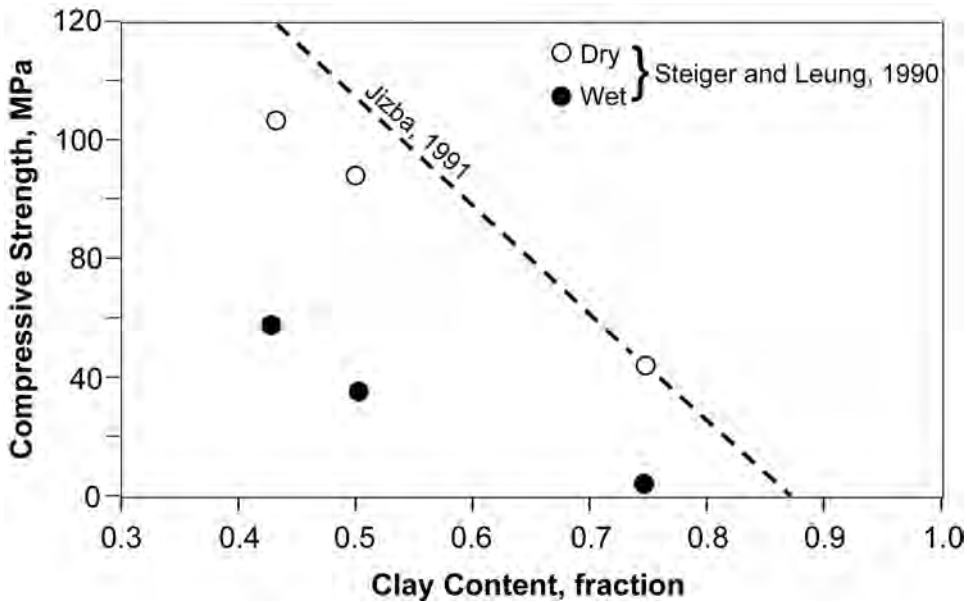


Fig. 13.62—Effect of increasing clay content on strength.

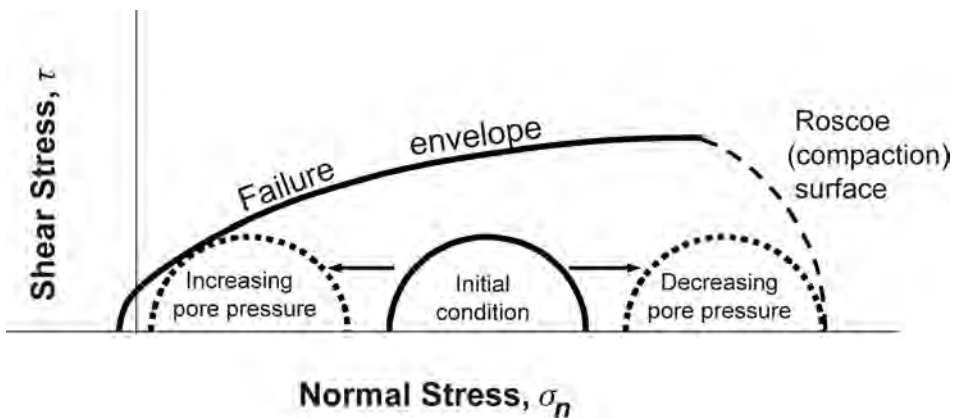


Fig. 13.63—Rock failure caused by either increasing or decreasing pore pressure. Increased pore pressure decreases effective stress, leading to fracture failure. Decreasing pore pressure increases effective stress, which can produce crushing.

Problems can arise experimentally because of the inability of pore pressure to reach equilibrium. If fluid can flow freely and constant pore pressure is maintained, then an experiment is termed “drained.” If deformation is too rapid, permeability low, fluid viscosity high, or boundaries are sealed, then fluid is trapped in the rock, and fluid pressure changes as a function of rock deformation. Brace and Martin<sup>123</sup> showed that strain rates must be very low in crystalline rocks of low permeability to maintain a uniform pore pressure and follow a macroscopically defined effective stress law such as Eq. 13.154. For most sandstones, permeability is sufficient to provide drained conditions. Problems usually occur in low-permeability rocks such as siltstone or shales. Considerable effort and time are usually needed to allow constant pore pressure, or merely to maintain pore pressure equilibrium (Steiger and Leung<sup>122</sup>). Tests are

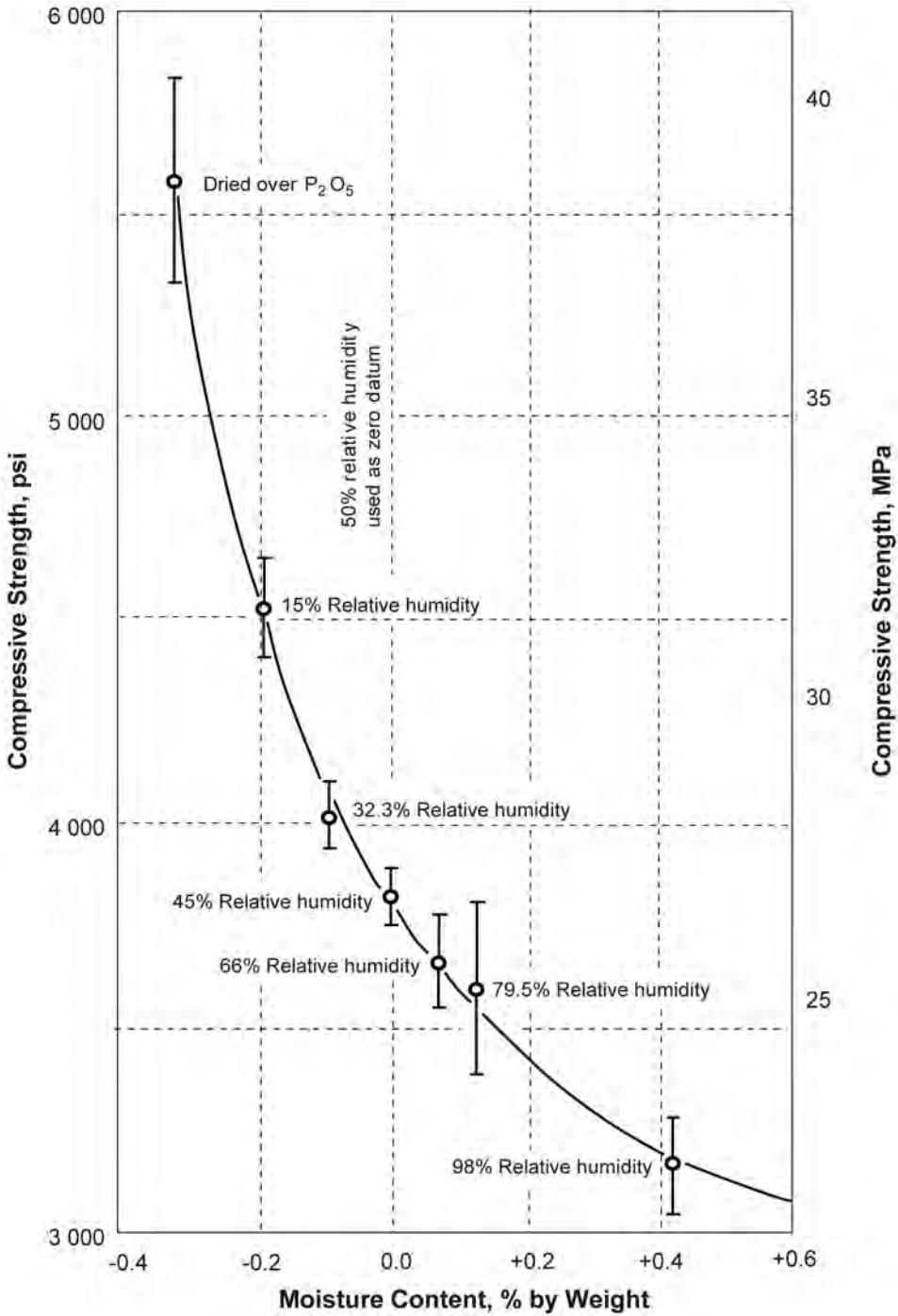


Fig. 13.64—Rock strength as a function of water content or humidity. Strength drops rapidly with the first few monolayers of water (from Colback and Wiid<sup>125</sup>).

made under undrained conditions, but the resulting changes in pore pressure must then be measured or otherwise calculated. These effects are mechanical problems that are often difficult to deal with, but the processes are basically well understood.

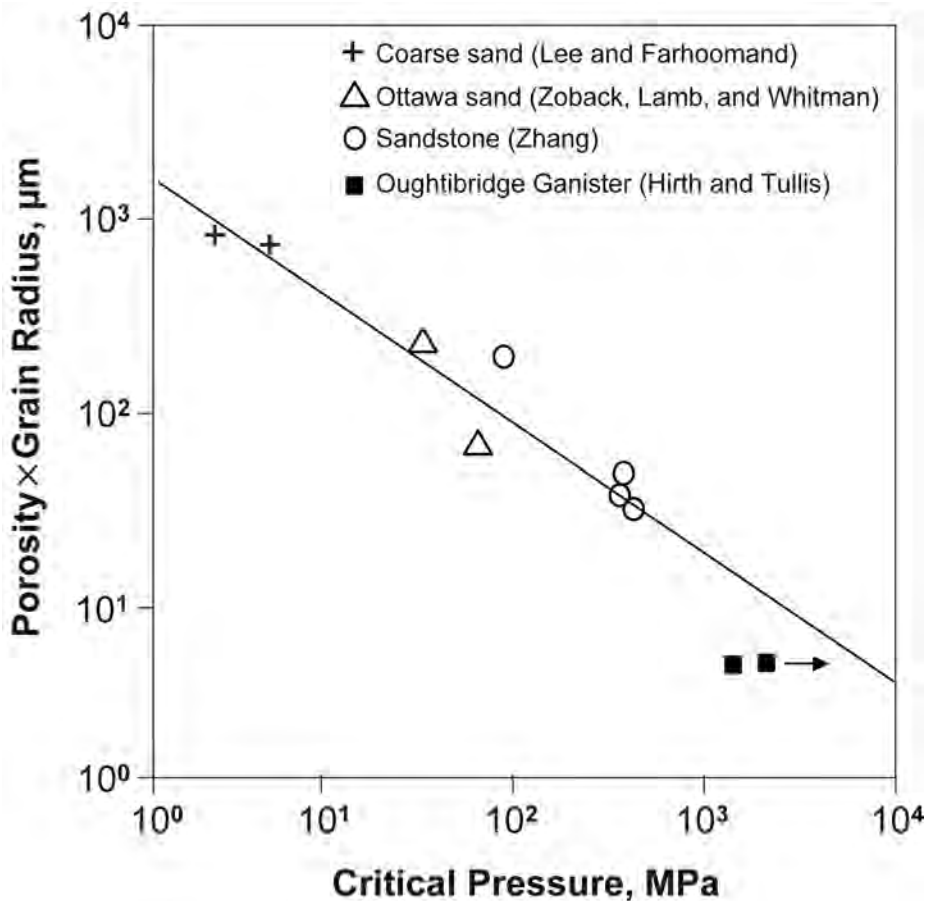


Fig. 13.65—Critical or crushing pressure as a function of the grain size-grain radius product (after Zhang<sup>131</sup>).

**Chemical Effects.** A more subtle problem involves chemical effects of pore fluids. Water is an active, polar compound, and numerous investigations (Griggs<sup>124</sup> and Kirby<sup>125</sup>) have shown that even small amounts of water or brine can have a substantial influence on rock mechanical properties. Colback and Wiid<sup>126</sup> demonstrated how even changes in the relative humidity or partial pressure of water in the pores can lower rock strength dramatically (Fig. 13.64). Colback and Wiid<sup>126</sup> and Dunning and Huff<sup>127</sup> saw a direct relationship between the loss in rock strength and the chemical activity of the pore fluid. Meredith and Atkinson,<sup>128</sup> Freeman,<sup>129</sup> and others have shown increased crack velocities and acoustic emissions at constant crack intensity factors when water is introduced. Ujtai *et al.*<sup>130</sup> saw substantial effects of water on all time-dependent tests for creep strain, fatigue, and slow crack growth. In general, uniaxial compressive strength is reduced by 20 to 25% in wet rocks. This implies that many laboratory measurements result in rock strengths that are systematically too high.

A strong influence of the chemical activity on rock mechanical properties is supported by other types of measurements. Seismic properties depend upon mineral grain stiffness and the stiffness of grain-to-grain contacts. In completely dry rocks (oven-dried under vacuum), there is almost no seismic attenuation, and rocks are stiff. Even small amounts of water, a few monolayers, can appreciably lower rock stiffness and seismic velocities.

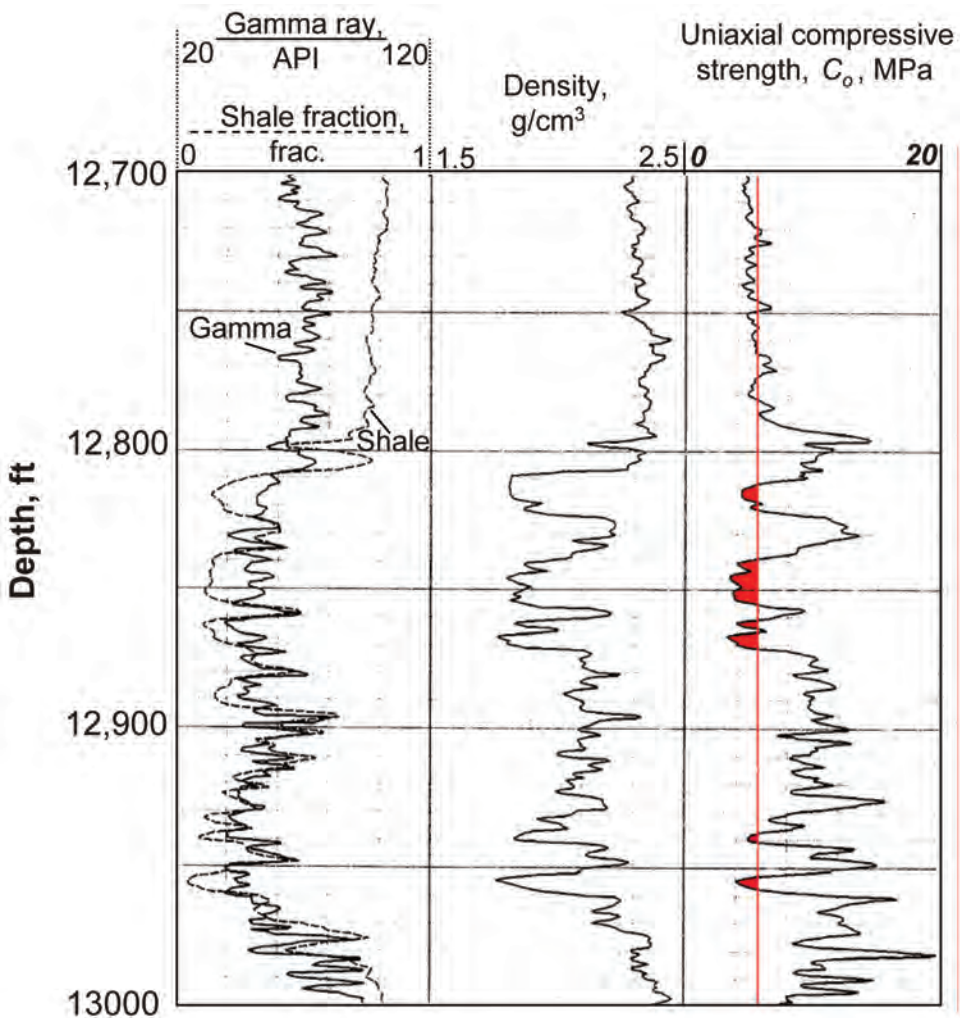


Fig. 13.66—Strength analysis applied to a Gulf of Mexico suite of logs. Sand/shale fraction is derived from gamma ray and SP logs (left track). Porosity is extracted from the density log (see previous sections). Uniaxial compressive strength is derived using Eq. 13.153. Weaker sands can be identified and failure predicted based on in-situ stresses around a borehole and a particular production scenario (red zones).

**Bulk Lubrication.** Common experience leads us to expect many geologic materials, such as soils, to be substantially weaker when wet. We have already seen this effect in chalk and shales. Surface bonding energies and water surface tension result in strong capillary forces that draw and hold water in pore spaces. Water penetrates and separates grains. Grain movement is facilitated by motion in mobile fluid layers. This is a highly scientific way of saying “slippery when wet.” Clay minerals in particular are well known for their ability to absorb large quantities of water. Swelling properties of clays and shales are often studied for drilling engineering purposes. Not only do clays have lower friction surfaces when wet, but water absorption and the resulting clay expansion can disaggregate the rock matrix. Loss of strength because of such mechanisms is more important in poorly consolidated or unconsolidated sediments. Dobereiner and DeFreitas<sup>121</sup> and Morgenstern *et al.*<sup>131</sup> report a 60% reduction in strength for muddy sediments upon saturation. At this point, we have not developed a systematic way of including a

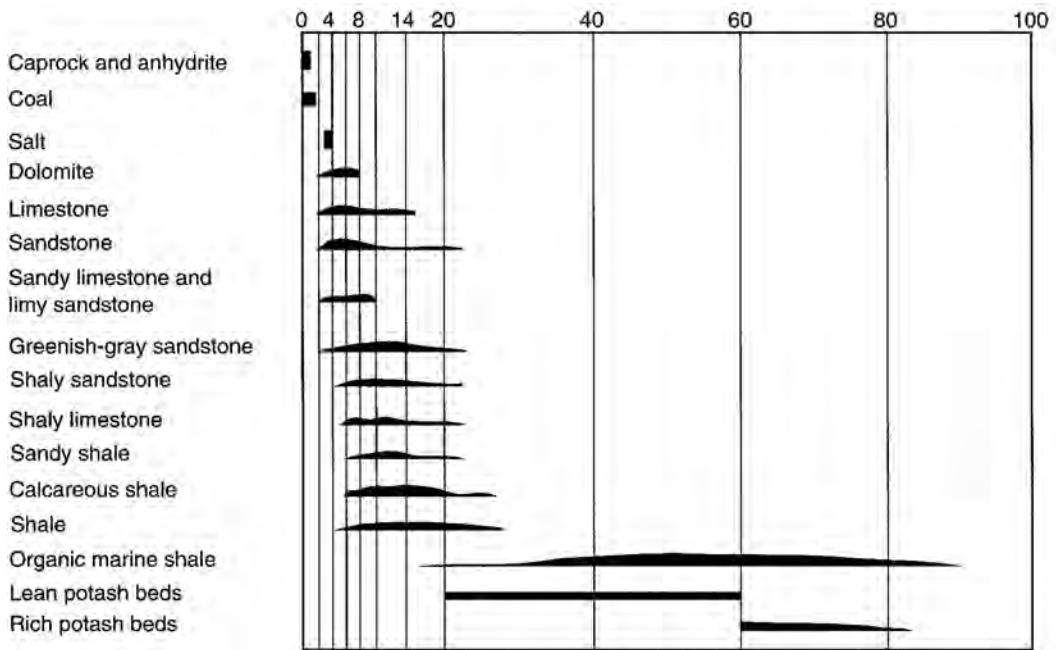


Fig. 13.67—Distribution of relative radioactivity level for various rock types (from Bigelow<sup>138</sup> after Russell<sup>137</sup>).

lubrication factor except as an implicit part of the clay corrections mentioned previously or as a measured reduction of the shear or Young’s modulus. We would expect the loss of intergrain friction to reduce the shear modulus significantly.

**13.6.8 Grain Size and Texture.** In granular rocks, grain size also influences strength. For constant porosity, mineralogy, and texture, a smaller grain size means greater strength. This tendency has been observed in several sandstones and can be understood in terms of grain contact models. Nelson<sup>132</sup> presents data on Navajo sandstone strength indicating a strong dependence on grain size. If a rock can be considered an aggregate of uniform spheres, smaller spheres will have more grain contacts per unit volume. Loads are distributed over more contracts, and each grain experiences lower stresses. Zhang<sup>133</sup> used Hertzian contact theory to calculate critical crushing strengths of quartz sands and found that porosity and grain radius combine to determine strength (Fig. 13.65). By fixing grain size, Zhang’s relationships could also provide crushing or compaction limits (Roscoe surfaces, Fig. 13.60) for sands at various porosities. For a grain size of 0.2 mm, we get a crushing strength,  $C_c$ , of

$$C_c = \frac{13.9}{\Phi} \dots\dots\dots (13.156)$$

However, factors such as cementation and grain angularity will strongly alter this simple relationship.

If grains become cemented, not only does porosity decrease, but the effective area of intergranular contracts increases. Even small amounts of cement will increase strength substantially. Angularity of grains and sorting will also influence strength. More angular grains result in sharper point contacts, stress concentrations, and lower strength.

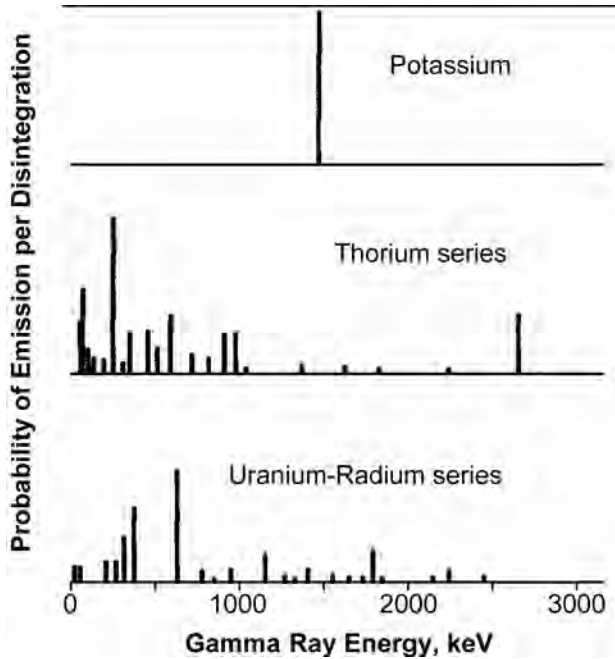


Fig. 13.68—Gamma-ray energy levels resulting from disintegration of unstable isotopes (adapted from Tittman *et al.*<sup>96</sup>).

In general, if grain size is known to be smaller or cementation greater (for a given porosity and composition), then increased strength can be estimated by reducing the Hoek-Brown coefficient  $m$ . A value of  $m = 0$  for siltstones and shales was suggested by Hoek and Brown.<sup>134</sup> Notice that this leads to minor contradiction because clays, with very fine grain size, weaken rocks. It is possible that many of Hoek and Brown’s “shales” were well indurated (slightly metamorphosed?), and grain size and increased cementation account for the increased strength (and reduced  $m$ ). In rocks with low levels of diagenesis, clays reduce strength and require an increased  $m$ .

**13.6.9 Rock Strength From Logs.** Several techniques have been proposed for deriving rock strength from well log parameters. Coates and Denoo<sup>135</sup> calculated stresses induced around a borehole and estimated failure from assumed linear envelopes with strength parameters derived from shear and compressional velocities. They relied on the work of Deere and Miller<sup>136</sup> to provide estimates of compressive strength from dynamic measurements. Simplified forms of these relations are:

$$C_0 = 1.839 E^{1058} \text{ for limestone} \dots\dots\dots (13.157a)$$

$$C_0 = 4.746 E^{0.9665} \text{ for sandstone} \dots\dots\dots (13.157b)$$

$$C_0 = 9.015 E^{0.901} \text{ for shale, } \dots\dots\dots (13.157c)$$

**TABLE 13.15—COMMON ROCK TYPES AND THEIR TYPICAL CONTENT OF POTASSIUM, URANIUM, AND THORIUM**

	Potassium (%)	Uranium (ppm)	Thorium (ppm)
<b>Rock and mineral carbonates</b>			
Range	0.0–2.0	0.1–9.0	0.1–7.0
Calcite, chalk, limestone, dolomite (pure)	<0.1	<1.0	<0.5
Dolomite (west Texas)	0.1–0.3	1.5–10	<2.0
<b>Limestone (clean)</b>			
Florida	<0.4	2.0	1.5
Cretaceous (Texas)	<0.3	1.5–15	<2.0
Hunton Lime (Oklahoma, Texas)	<0.2	<1.0	<1.5
<b>Sandstones, range</b>			
Beach sands (Gulf Coast)	<1.2	0.84	2.8
Allantic coast (Florida, North Carolina)	0.37	3.97	2.8
Allantic coast (New Jersey, Massachusetts)	0.3	0.8	2.07
<b>Shales typical range</b>			
	1.6–4.2	1.5–5.5	8–18
<b>Minerals</b>			
Allanite		30–700	500–5000
Apatite		5–150	20–150
Epidote		20–50	
Monzanite		500–5000	$(2.5–20) \times 10^4$
Sphene		100–700	100–600
Xenotime		$500–3.4 \times 10^4$	low
Zircon		300–3000	100–2500
<b>Clays</b>			
Bauxite		3–30	10–130
Glauconite		5.08–5.3	
Bentonite	<0.5	1–20	6–50
Montmorillonite	0.16	2–5	14–24
Kaolinite	0.42	1.5–3	6–19
Illite	4.5	1.5	
<b>Mica</b>			
Biotite	6.7–8.3		<0.01
Muscovite	7.9–3.8		<0.01
<b>Feldspars</b>			
Plagioclase	0.54		<0.01
Orthoclase	11.8–14.0		<0.01
Microcline	10.9		<0.01
Quartz (silica)	<0.15	<0.4	<0.2

Potassium, uranium, and thorium contents of typical rocks and minerals (after Bigelow<sup>1965</sup>).

where  $C_0$  is uniaxial compressive strength and  $E$  is dynamic Young's modulus (see Section 13.5). Alternatively, we can include an empirical dependence of the internal friction angle,  $\alpha$ , or the porosity,  $\Phi$ .

**TABLE 13.16—DISTRIBUTION OF POTASSIUM**

Material	Potassium Content by Weight (average)	Range
Sylvite	54	
Potash	44.9	
Langbeinite	20	
Microcline	16	
Kainite	15.1	
Carnallite	14.1	
Orthoclase	14	
Polyhalite	12.9	
Muscovite	9.8	
Biotite	8.7	
Illite	5.2	3.51–8.31
Arkose (sandstone)	4.6	4.4–5.1
Synite	4.53	
Glauconite	4.5	3.2–5.8
Granite	4.0	2.0–6.0
Norite	3.3	
Granodiorite	2.90	
Shale	2.7	1.6–9.0
General igneous rock	2.6	
Grayrock (sandstone)	1.5	1.2–2.1
Diorite	1.66	
Basalt	1.3	
Sandstone	1.1	5.1
Gabbro	0.87	
Diabase	0.75	
Kaolinite	0.63	0–1.49
Limestone	0.27	0–0.71
Montmorillonite	0.22	0–0.60
Orthoquartzite (sandstone)	0.08	0–0.12
Dolomite	0.07	0.03–0.1
Dunite	0.04	
Sea Water	0.035	

Additional reported potassium content and ranges for rocks and minerals (after Bigelow<sup>13b</sup>)

$$\alpha = 57.5 - 1.045 \Phi \dots\dots\dots (13.158)$$

Eqs. 13.159 and 13.160 provide a way to derive strengths assuming a linear envelope, and provided that compressional and shear velocity, lithology (e.g., gamma ray or SP), and density logs are available. If there is no shear log, one can be derived from the compressional velocity log and  $V_p$ - $V_s$  relationships previously shown in Table 13.7.

The strength-porosity trend shown in Eq. 13.146 and modulus-porosity trends in Section 13.5 imply a correlation between strength and shear modulus for sandstone:



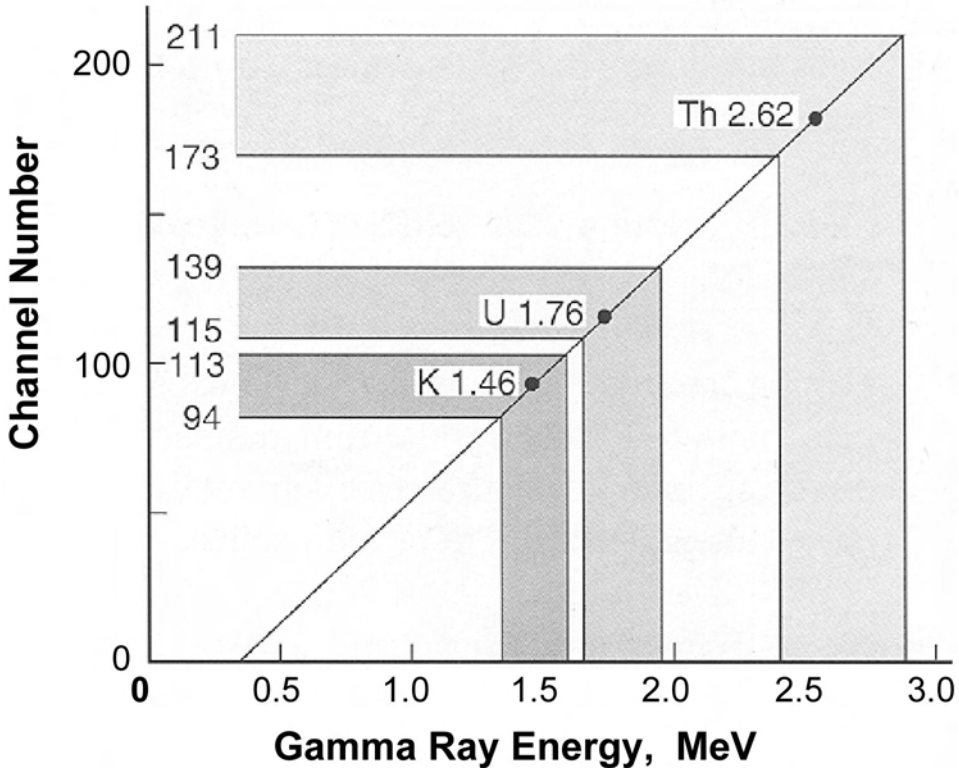


Fig. 13.69—Gamma-ray energy windows used for spectral gamma-ray logging (from Bigelow<sup>138</sup>).

$$C_0 = 0.09 G^2 (C_0 \text{ in MPa, } G \text{ in GPa} ) \dots\dots\dots (13.159)$$

This leads to a velocity transform if the bulk density is known:

$$C_0 = 0.09 V_S^4 \rho^2 [\text{velocity in km/s, } \rho \text{ in gm/cc}], \dots\dots\dots (13.160)$$

$$C_0 = 0.018 V_p^4 \rho^2 [\text{gas-saturated}] \dots\dots\dots (13.161)$$

If we presume a simple relationship between compressional velocity of brine-saturated sandstones and shear velocity as developed by Castagna *et al.*,<sup>4</sup> we get

$$C_0 = 0.0497 (V_p - 1.36)^4 \rho^2 [\text{brine-saturated}] \dots\dots\dots (13.162)$$

The shear modulus (or velocity) should be the most sensitive measure of strength, and shear properties are little affected by fluid saturations. Whenever possible, shear wave data should be collected and used in this analysis. If only compressional data is available, care must be used in translating the information into effective gas- or brine-saturated values (see Section 13.5.11). This is particularly true for partial oil saturations.

In our analysis,  $C_0$  was first determined from porosity. The influence of clay content was examined separately. The velocity-strength relationships above were derived from the porosity dependence, but clays are handled only indirectly through their effects on velocities. Strength

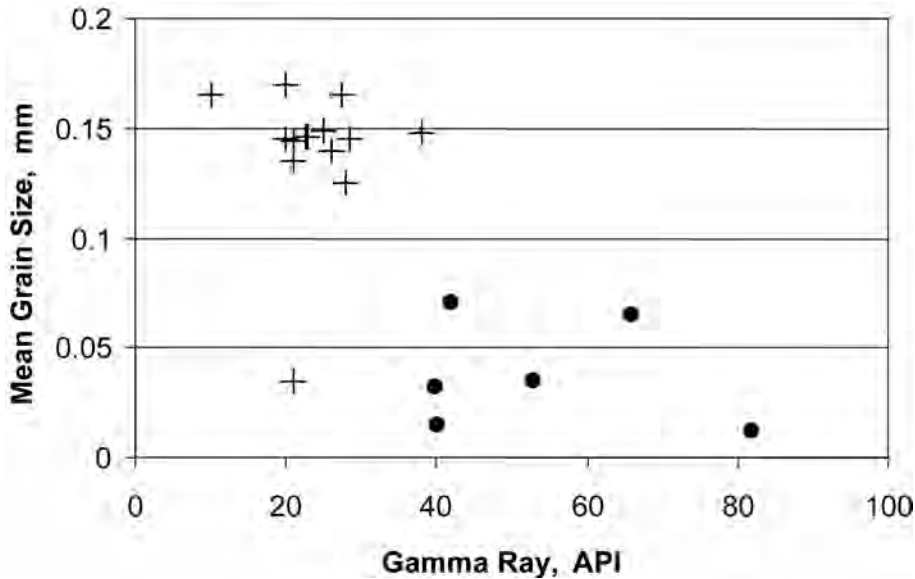


Fig. 13.70—Measured mean grain size vs. gamma-ray levels (calibrated to API value) for clastic samples. The rough correspondance of gamma ray value can be seen, but relationship is not simple (data from Georgi *et al.*<sup>141</sup>).

parameters can be calculated directly from porosity (Eq. 13.148), but clays must then be included, as in Eq. 13.153. Calculated strengths based directly on porosity and clay content are shown in Fig. 13.66. These types of logs can be very valuable in detecting weak zones and units susceptible to failure. If at all possible, these kinds of logs should be calibrated with strength measurements directly on core samples.

### 13.7 Gamma Ray Characteristics

**13.7.1 Introduction.** The radioactivity of rocks has been used for many years to help derive lithologies. Natural occurring radioactive materials (NORM) include the elements uranium, thorium, potassium, radium, and radon, along with the minerals that contain them. There is usually no fundamental connection between different rock types and measured gamma ray intensity, but there exists a strong general correlation between the radioactive isotope content and mineralogy. Observed distributions have been available for numerous decades. In Fig. 13.67, the distributions of radiation levels observed by Russell<sup>137</sup> are plotted for numerous rock types. Evaporites (NaCl salt, anhydrites) and coals typically have low levels. In other rocks, the general trend toward higher radioactivity with increased shale content is apparent. At the high radioactivity extreme are organic-rich shales and potash (KCl). These plotted values can include beta as well as gamma radioactivity (collected with a Geiger counter). Modern techniques concentrate on gamma ray detection.

The primary radioactive isotopes in rocks are potassium-40 and the isotope series associated with the disintegration of uranium and thorium. Fig. 13.68 shows the equilibrium distribution of energy levels associated with each of these groups. Potassium-40 ( $K^{40}$ ) produces a single gamma ray of energy of 1.46 MeV as it transforms into stable calcium. On the other hand, both thorium (Th) and uranium (U) break down to form a sequence of radioactive daughter products. Subsequent breakdown of these unstable isotopes produces a variety of energy levels. Standard gamma ray tools measure a very broad band of energy including all the prima-

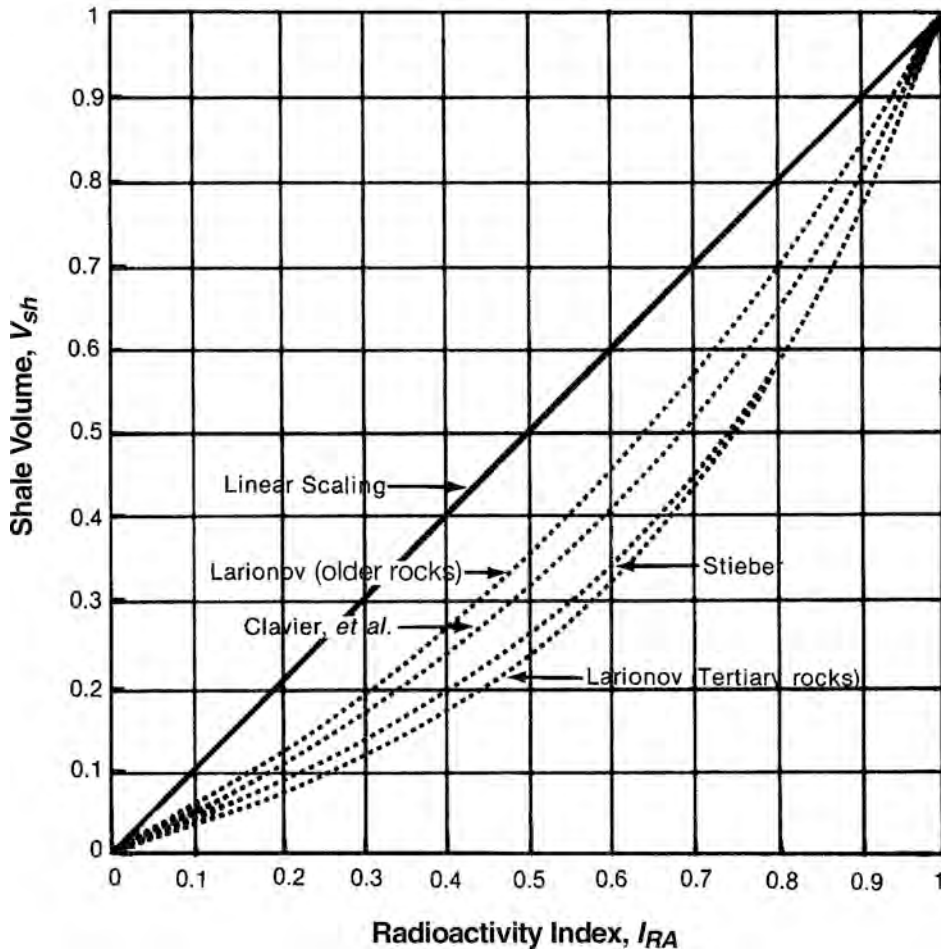


Fig. 13.71—Reported gamma-ray index to shale volume conversions (from Bigelow<sup>138</sup>).

ry peaks as well as lower-energy daughter peaks. As might be expected from Fig. 13.68, the total count can be dominated by the low-energy decay radiation.

The radionuclides, including radium, may become more mobile in formation waters found in oil fields. Typically, the greater the ionic strength (salinity), the higher the radium content. Produced waters can have slightly higher radioactivity than background. In addition, the radionuclides are often concentrated in the solid deposits (scale) formed in oilfield equipment. When enclosed in flow equipment (pipes, tanks, etc.) this elevated concentration is not important. However, health risks may occur when equipment is cleaned for reuse or old equipment is put to different application.

**Table 13.15** lists some of the common rock types and their typical content of potassium, uranium, and thorium. Potassium is an abundant element, so the radioactive  $K^{40}$  is widely distributed (**Table 13.16**). Potassium feldspars and micas are common components in igneous and metamorphic rocks. Immature sandstones can retain an abundance of these components. In addition, potassium is common in clays. Under extreme evaporitic conditions, KCl (sylvite) will be deposited and result in very high radioactivity levels. Uranium and thorium, on the other hand, are much less common. Both U and Th are found in clays (by absorption), volcanic ashes, and heavy minerals.

TABLE 13.17—OTHER PROPOSED GAMMA-RAY-SHALE VOLUME TRANSFORMS	
	$I_{GR} = \frac{R - R_{\text{clemsand}}}{R_{\text{shale}} - R}$
Stieber and related	
	$V_{Sh} = \frac{I_{GR}}{3.0 - 2.0I_{GR}}$
	$V_{Sh} = \frac{I_{GR}}{2.0 - I_{GR}}$
	$V_{Sh} = \frac{I_{GR}}{4.0 - 3.0I_{GR}}$
Larinov	
Older rocks	$V_{Sh} = 0.33(2^{2I_{GR}} - 1.0)$
Tertiary rocks	$V_{Sh} = 0.083(2^{3.7I_{GR}} - 1.0)$
Clavier	$V_{Sh} = 1.7 - [3.3 - (IGR + 0.7)^2]^{1/2}$

**13.7.2 Measurement.** Gamma ray logs are among the most common and useful tools in the oil and gas industry. Originally, measurements were reported in count rates, but all modern tools are calibrated to API units. Typical sedimentary response ranges from 0 to 200 in API units. Gamma ray log character is one of the primary methods used to correlate the stratigraphic section. For most engineering and geophysical applications, the gamma ray log is primarily used to extract lithologic, mineralogic, or fabric estimates.

The log response depends on the radiation, tool characteristics, and logging parameters. A 30-cm sodium iodide scintillation crystal with a photomultiplier tube is a common detector configuration. Thin, highly radioactive beds may be detected, but cannot be resolved below about 0.25 m. Radiation is damped primarily by formation material electron density and Compton scattering. This limits the depth of investigation to around 30 cm, although it will depend on the energy levels. Because the radioactive decay is a statistical process, slower logging rates produce better results. The low number of counts resulting from logging too fast cannot be increased by logging rate correction factors. Most tools are usually out of calibration if they are not centered in the borehole. Heavy barite mud can also lower the overall count rate, particularly for low-energy gamma rays.

Rather than merely measuring total gamma radiation, the energy levels can be detected separately. This allows the concentrations of K, U, and Th to be derived as independent parameters. Fig. 13.69 shows the energy windows used in a Baker-Atlas tool. This would allow, for example, the feldspars in immature sands to be separated from clays with adsorbed U or Th.

The most common use of gamma ray logs is to estimate the shale “volume” in rocks. It is important to remember that the tool measures radioactivity, and the correlation to shale content is empirical. Shales are presumed to be composed of clay minerals. Thus, the gamma ray level is assumed to be correlated with grain size. In reality, shales may be composed of 30% or more of quartz and other minerals. The clays within the shales may not be radioactive, and the adjacent sands may contain radioactive isotopes. However, radioactivity levels typically are re-

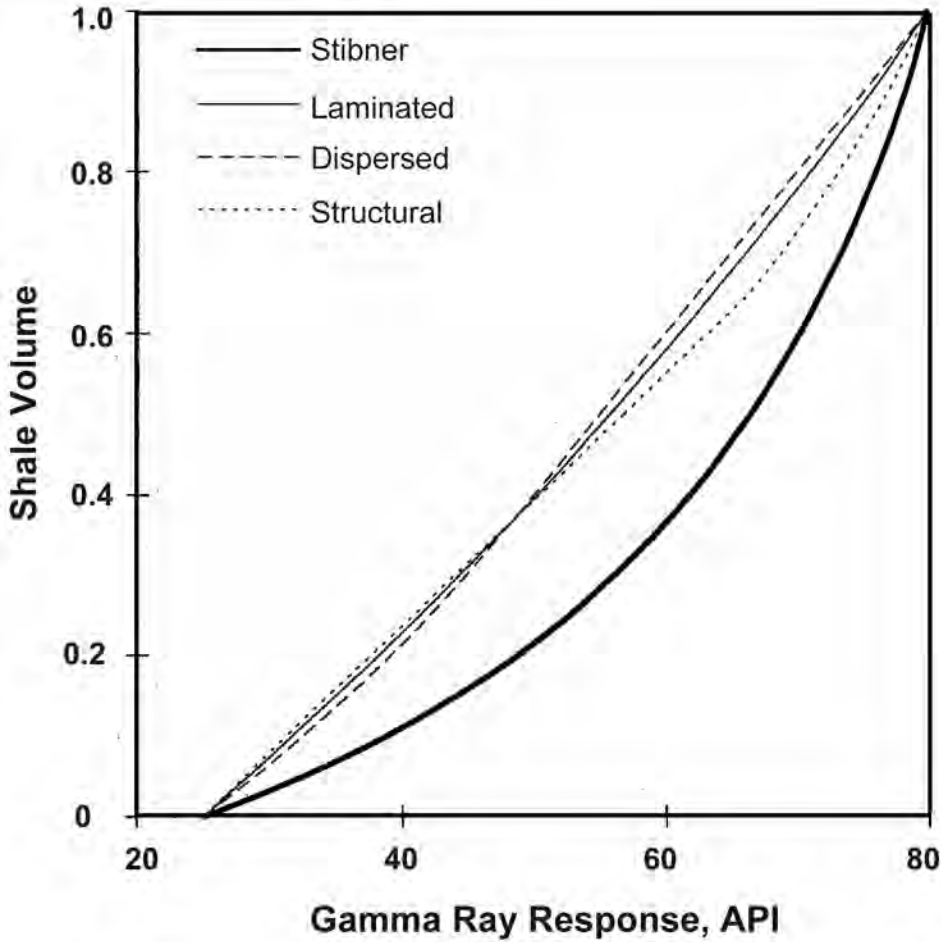


Fig. 13.72—Modeled gamma-ray response to different clay distributions within a shaley sand series (modified from Katahara<sup>140</sup>).

lated to grain size, as seen in Fig. 13.70. Here, core plugs were analyzed for median grain size and radioactivity level measured directly; crosses are fine-grained sands, while dots are silts and clay-rich rocks.

To extract the shale content in rocks, a linear or near-linear relation is used to convert a gamma ray index,  $I_{gr}$ , to shale volume  $V_{sh}$ . Because local sands can contain radioactive components, and the shales may vary with depth, local baseline levels are chosen near the zone of interest.

$$I_{gr} = \frac{R - R_{cleansand}}{R_{shale} - R}, \dots\dots\dots (13.163)$$

where  $R$  is the measured radiation level,  $R_{cleansand}$  is the baseline level through a reference sand, and  $R_{shale}$  is the baseline through a representative shale. Several relations have been developed to derive shale volume (Fig. 13.71). A linear relation simply sets the shale content equal to the gamma ray index.

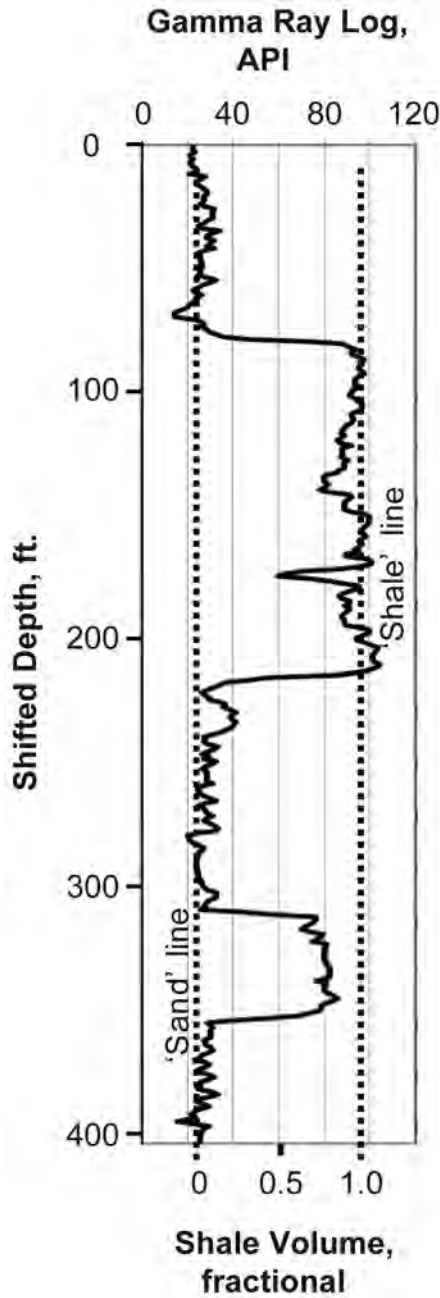


Fig. 13.73—Typical shale volume extraction from a Gulf of Mexico log. 100% “sand” and 100% “shale” lines are locally established; then, shale content is a linear interpolation between the two.

$$V_{sh} = I_{gr} \dots \dots \dots (13.164)$$

Other proposed relations shown in Fig. 13.71 are defined in Table 13.17. Several assumptions are made in these evaluations:

- Compositions of sand and shale components are constant.

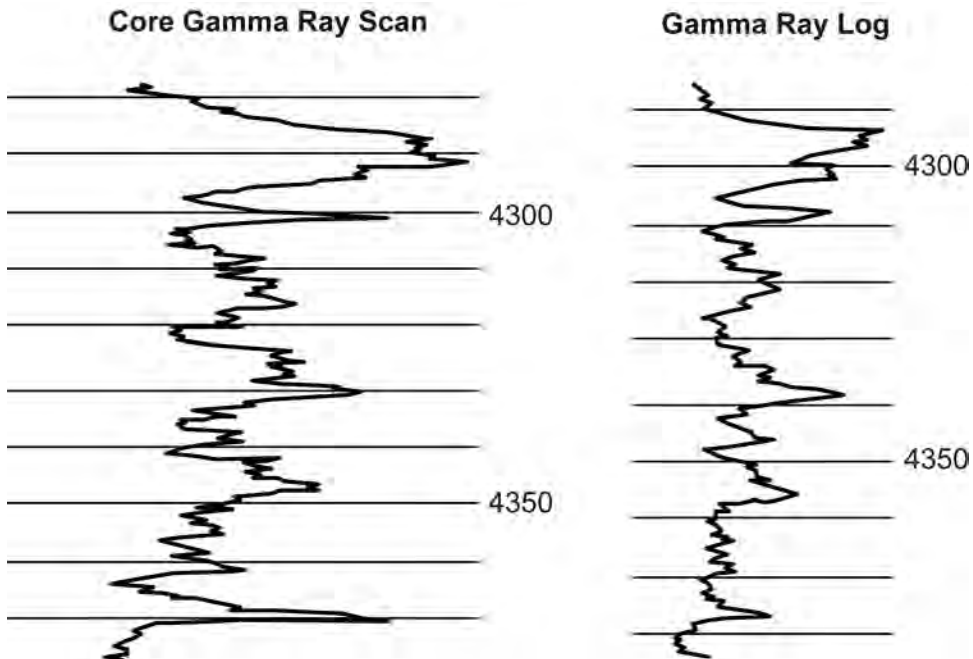


Fig. 13.74—A measured core gamma-ray profile vs. logged data in a carbonate section. Comparison of peaks shows the offset in measured depth (adapted from Core Labs data).

- Baselines are chosen on representative “shales” and “clean” sands (although these terms are very subjective).
- Simple mixture laws apply.
- Fabric is not important.

Many of these assumptions may be poor approximations.

A more likely presumption is that the radiation level is dependent on the mixture densities and not volumes (Wahl<sup>139</sup> and Katahara<sup>140</sup>). In this case, a fabric analysis can also be performed. Katahara<sup>139</sup> modeled the shale component of shaly sands as existing in three forms:

- Structural—an original depositional granular form.
- Dispersed—clay distributed through the rock and pore space.
- Laminated—thin layers of shale cutting the sand beds.

In Fig. 13.72, his results show a surprisingly simple form. The conclusion is that in most cases, the simple linear relation is appropriate.

As an example of this process, the shale content of a zone in a Gulf of Mexico well is estimated. In Fig. 13.73, a sand-shale sequence gives a gamma ray range of approximately 20 to 90 API units. A baseline of approximately 25 is chosen through the sand, and a baseline of approximately 98 is chosen for the shale. Using the relations in Eqs. 13.163 and 13.164 result in the shale volume estimates scaled at the bottom of the logged zone.

Gamma radiation levels can also be measured on core. This technique provides a profile of levels along the length of the core. The primary use is to correlate core depths to logged depths. An example is shown in Fig. 13.74. This procedure can be used to identify log features or positioning of the cored interval. Especially when core recovery is poor, this method is very useful in tying the core fragments to true depths. Core plugs can also be measured, although special equipment must be used to record the low levels of radiation associated with the small samples. In general, property correlations to the measured gamma ray levels are much better for cores than for the log because of the depth averaging in the log.<sup>141</sup>

## Nomenclature

- $a_{ij}$  = water density coefficients  
 $A$  = bulk modulus/porosity factor, Eq. 13.86  
 $A$  = strength material constant, Eq. 13.134  
 $A_0$  = initial wave amplitude  
 $A(z,t)$  = wave amplitude with distance and time  
 $A_{f1}, A_{f2}$  = fraction fluid component 1, 2, etc.  
 $A_{m1}, A_{m2}$  = fraction mineral component 1, 2, etc.  
 $A_1, A_2$  = fraction component 1, 2, etc.  
 $b$  = velocity/temperature constant, m/sC, Eq. 13.18  
 $b$  = strength envelope intercept, GPa or MPa, Eq. 13.134  
 $b_{ij}$  = brine density coefficients  
 $B$  = brine compressional velocity factor, m/s, Eq. 13.32b  
 $B$  = bulk modulus/porosity factor, Eq. 13.86  
 $B'$  = rock modulus, real component, GPa or MPa, Eq. 13.105  
 $B''$  = rock modulus, imaginary component, GPa or MPa  
 $B_0$  = rock modulus, zero frequency, GPa or MPa  
 $B_{\infty}$  = rock modulus, infinite frequency, GPa or MPa  
 $C$  = bulk modulus/porosity factor, Eq. 13.86  
 $C$  = clay content, Eq. 13.150  
 $C_{ijkl}$  = stiffness tensor components, GPa or MPa  
 $C_0$  = uniaxial or unconfined compressive strength, GPa or MPa  
 $C_t$  = tensional strength, GPa or MPa  
 $C_u$  = cohesive strength, GPa or MPa  
 $D$  = bulk modulus/porosity factor  
 $E$  = Young's modulus, GPa or MPa  
 $f$  = frequency,  $s^{-1}$ , Hz (cycles/s)  
 $F$  = volume factor  
 $G$  = shear modulus, GPa or MPa  
 $G(\Phi)$  = gain factor  
 $I_{gr}$  = gamma ray index  
 $k$  = permeability,  $m^2$ , Eq. 13.108  
 $k$  = wave number,  $m^{-1}$ , Eq. 13.102  
 $k^*$  = complex wave number,  $m^{-1}$   
 $K$  = bulk modulus, GPa or MPa  
 $K_d$  = dry bulk modulus, GPa or MPa  
 $K_{d \min}$  = minimum bulk modulus, GPa or MPa  
 $K_f$  = fluid bulk modulus, GPa or MPa  
 $K_{f1}, K_{f2}$  = bulk modulus of fluid 1, 2, etc., GPa or MPa  
 $K_{HS}$  = Hasin-Shtrikman bound bulk modulus, GPa or MPa  
 $K_n$  = normalized bulk modulus, numeric  
 $K_{nR}$  = normalized Reuss bound bulk modulus, numeric  
 $K_o$  = mineral bulk modulus, GPa or MPa  
 $K_R$  = Reuss bound bulk modulus, GPa or MPa  
 $K_s$  = saturated bulk modulus, GPa or MPa  
 $K_1, K_2$  = bulk modulus of component 1, 2, etc., GPa or MPa  
 $K^*$  = effective bulk modulus, GPa or MPa



- $K'$  = effective crack bulk modulus, GPa or MPa  
 $\Delta K_d$  = change in bulk modulus, GPa or MPa  
 $\Delta K_{d\max}$  = maximum change in bulk modulus, GPa or MPa  
 $\Delta K_{12}$  = change in bulk modulus, fluid 1 to fluid 2, GPa or MPa  
 $L$  = length, m  
 $\Delta L$  = change in length, m  
 $m$  = Hoek-Brown strength coefficient  
 $M$  = molecular weight, g/mole  
 $M_A, M_B$  = modulus of component  $a, b$ , etc., GPa or MPa  
 $M_O$  = reference oil molecular weight, g/mole  
 $M_R$  = Reuss bound modulus, GPa or MPa  
 $M_V$  = Voigt bound modulus, GPa or MPa  
 $M_{VRH}$  = Voigt-Reuss-Hill bound modulus, GPa or MPa  
 $n$  = number of moles, [Eq. 13.10](#)  
 $n$  = effective stress coefficient, [Eq. 13.35](#)  
 $n$  = strength envelope exponent, [Eq. 13.134](#)  
 $P$  = pressure, MPa  
 $P_c$  = confining pressure, MPa  
 $P_d$  = differential pressure, MPa  
 $P_e$  = effective pressure, MPa  
 $P_p$  = pore pressure, MPa  
 $Q$  = seismic quality factor, numeric  
 $r$  = radius of stress “circle,” GPa or MPa  
 $R$  = gas constant, (L MPa)/(K mole), [Eq. 13.10](#)  
 $R$  = gas/oil ratio, [Eq. 13.26](#)  
 $R$  = measured gamma radiation, API units  
 $R_{\text{cleansand}}$  = gamma radiation in a “clean” sand zone, API units  
 $R_{\text{shale}}$  = gamma radiation in a shale zone, API units  
 $s$  = Hoek-Brown strength coefficient  
 $S, S'$  = general rock property  
 $t$  = time, s  
 $T$  = temperature, °C  
 $T_a$  = absolute temperature, K  
 $T_1, T_2$  = Kunster-Toksoz coefficients  
 $\Delta T$  = change in temperature, K  
 $V_B$  = brine compressional velocity, m/s  
 $V_{fx}$  or  $V_{cx}$  = fracture or crack volume, m<sup>3</sup> or cm<sup>3</sup>  
 $V_{f1}, V_{f2}$  = fluid 1, 2, etc. volume, m<sup>3</sup> or cm<sup>3</sup>  
 $V_g$  or  $V_m$  = grain or mineral volume, m<sup>3</sup> or cm<sup>3</sup>  
 $V_{\text{mineral}}$  = mineral velocity, m/s  
 $V_o$  = reference compressional velocity, m/s  
 $V_p$  = compressional velocity, m/s  
 $V_{po}$  = vertical compressional velocity, m/s  
 $V_{por}$  = total pore volume, m<sup>3</sup> or cm<sup>3</sup>  
 $V_{p-con}$  = connected pore volume, m<sup>3</sup> or cm<sup>3</sup>  
 $V_{p-iso}$  = isolated pore volume, m<sup>3</sup> or cm<sup>3</sup>  
 $V_{\text{rock}}$  = rock velocity, m/s

- $V_S$  = shear velocity, m/s  
 $V_{sh}$  = shale volume, fractional  
 $V_{SO}$  = vertical shear velocity, m/s  
 $V_T$  = isothermal fluid compressional velocity, m/s  
 $V_T$  or  $V_{rx}$  = total rock volume, m<sup>3</sup> or cm<sup>3</sup>  
 $V_{TM}$  = oil weight m compressional velocity, m/s  
 $V_{TOMO}$  = oil weight m compressional velocity at  $t_o$ , m/s  
 $V_W$  = water compressional velocity, m/s  
 $w_{ij}$  = water compressional velocity coefficients  
 $x$  = weight fraction of NaCl, ppm, [Eq. 13.29b](#)  
 $x$  = directional component, m  
 $y$  = directional component, m  
 $z$  = directional component, m  
 $Z$  = compressibility factor  
 $\alpha$  = aspect ratio, [Eq. 13.91](#)  
 $\alpha$  = failure envelope slope, [Eq. 13.116](#)  
 $\alpha_m$  = aspect ratio of fracture population  $m$ , fractional  
 $\alpha_l$  = logarithmic decrement (loss), nepers/m  
 $\beta$  = strength factor, numeric  
 $\beta_S$  = adiabatic compressibility, MPa<sup>-1</sup>  
 $\beta_T$  = isothermal compressibility, MPa<sup>-1</sup>  
 $\gamma$  = heat capacity ratio, [Eq. 13.16](#)  
 $\gamma$  = Thomsen  $V_s$  anisotropy factor, [Eq. 13.95](#)  
 $\delta$  = Thomsen anisotropy factor, [Eq. 13.95](#)  
 $\delta$  = loss tangent, [Eq. 13.103](#)  
 $\varepsilon$  = Thomsen  $V_p$  anisotropy factor, numeric  
 $\varepsilon_{ij}$  = strain components, fractional  
 $\varepsilon_{kl}$  = strain components, fractional  
 $\varepsilon_{\text{shear}}$  = shear strain, fractional  
 $\varepsilon_V$  = volumetric strain, fractional  
 $\varepsilon_{yy}$  = horizontal strain, fractional  
 $\varepsilon_{zz}$  = vertical strain, fractional  
 $\eta$  = viscosity, Pa·s  
 $\theta$  = wave propagation angle to symmetry axis  
 $\lambda$  = Lamé's parameter, GPa or MPa, [Eq. 13.45](#)  
 $\lambda$  = wavelength, MPa<sup>-1</sup>, [Eq. 13.103](#)  
 $\mu$  = shear modulus, GPa or MPa, [Eq. 13.42](#)  
 $\mu$  = coefficient of internal friction, [Eq. 13.116](#)  
 $\mu_o$  = mineral shear modulus, GPa or MPa  
 $\mu_s$  = saturated shear modulus, GPa or MPa  
 $\mu_{sd}$  = dry shear modulus, GPa or MPa  
 $\mu^*$  = effective shear modulus, GPa or MPa  
 $\mu'$  = effective crack shear modulus, GPa or MPa  
 $\nu$  = Poisson's ratio, fractional  
 $\rho$  = density, kg/m<sup>3</sup> or g/cm<sup>3</sup>  
 $\rho_b$  = bulk density, kg/m<sup>3</sup> or g/cm<sup>3</sup>  
 $\rho_B$  = brine density, kg/m<sup>3</sup> or g/cm<sup>3</sup>

- $\rho_d$  = dry density, kg/m<sup>3</sup> or g/cm<sup>3</sup>  
 $\rho_f$  = fluid density, kg/m<sup>3</sup> or g/cm<sup>3</sup>  
 $\rho_g$  = grain or mineral density, kg/m<sup>3</sup> or g/cm<sup>3</sup>  
 $\rho_G$  = gas density, kg/m<sup>3</sup> or g/cm<sup>3</sup>  
 $\rho_O$  = oil density, kg/m<sup>3</sup> or g/cm<sup>3</sup>  
 $\rho_{\text{sat}}$  = saturated density, kg/m<sup>3</sup> or g/cm<sup>3</sup>  
 $\rho_W$  = water density, kg/m<sup>3</sup> or g/cm<sup>3</sup>  
 $\sigma_h$  = horizontal stress, GPa or MPa  
 $\sigma_{ij}$  = stress components, GPa or MPa  
 $\sigma_m$  = mean stress, GPa or MPa  
 $\sigma_n$  = normal stress, GPa or MPa  
 $\sigma_{\text{shear}}$  = shear stress components, GPa or MPa  
 $\sigma_v$  = axial (vertical) stress, GPa or MPa  
 $\sigma_{zz}$  = vertical stress component, GPa or MPa  
 $\sigma_1$  = stress in direction 1, GPa or MPa  
 $\sigma_3$  = stress in direction 3, GPa or MPa  
 $\tau$  = shear stress, GPa or MPa  
 $\tau$  = relaxation time, s<sup>-1</sup> (radians/s), Eq. 13.106  
 $\Phi$  = porosity  
 $\Phi_{fx}$  = fracture porosity  
 $\Phi_{p-e}$  = effective porosity  
 $\Phi_{p\text{-iso}}$  = isolated, ineffective porosity  
 $\omega$  = frequency (radian), s<sup>-1</sup> (radians/s)  
 $\omega_c$  = crossover frequency (radian), s<sup>-1</sup> (radians/s)

---

## References

1. Clark, S.P.: *Handbook of Physical Constants*, Geol. Soc. Am. Mem. 97, New York City (1966).
2. Birch, F.: "The velocity of compressional waves in rocks to 10 kilobars, Part 2," *J. Geophys. Res.* (1961) **66**, 2199.
3. Gregory, A.R.: "Aspects of rock physics from laboratory and log data that are important to seismic interpretation," *Seismic Stratigraphy—Application to Hydrocarbon Exploration*, AAPG, Memoir 26 (1977).
4. Castagna, J.P., Batzle, M.L., and Eastwood, R.L.: "Relationships between compressional-wave and shear-wave velocities in elastic silicate rocks," *Geophysics* (1985) **50**, 571.
5. Carmichael, R.S.: *Practical Handbook of Physical Properties of Rocks and Minerals*, CRC Press, Boca Raton, Florida (1989).
6. Lama, R.D. and Vutukuri, V.S.: "Static elastic constants of rocks," *Handbook on Mechanical Properties of Rocks—Testing Techniques and Results*, Vol. I, Trans Tech Pub. S.A., Aedermannsdorf, Switzerland (1978).
7. Lama, R.D. and Vutukuri, V.S.: "Dynamic elastic constants of rocks," *Handbook on Mechanical Properties of Rocks—Testing Techniques and Results*, Vol. II, Trans Tech Pub. S.A., Aedermannsdorf, Switzerland (1978).
8. Mavko, G., Mukerji, T., and Dvorkin, J.: *Rock Physics Handbook: Tools for Seismic Analysis in Porous Media*, Cambridge U. Press, Cambridge (1998).
9. Moore, C.H.: *Carbonate Reservoirs: Porosity Evolution and Diagenesis in a Stratigraphic Framework*, Elsevier, Amsterdam (2001).
10. Berryman, J.G. and Blair, S.C.: "Kozeny-Carman relations and image processing methods for estimating Darcy's constant," *J. Appl. Phy.* (1987) **62**, 2221.

11. Blair, S.C., Berg, P.A., and Berryman, J.G.: "Two-point correlation functions to characterize microgeometry and estimate permeability of synthetic and natural sandstones," Lawrence Livermore Natl. Lab. Pub. UCRL-LR-114182 (1993).
12. Keehm, Y., Mukerji, T., and Nur, A.: "Computational rock physics at the pore scale: Transport properties and diagenesis in realistic pore geometries," *The Leading Edge* (2001) **20**, 180.
13. Williams, H., Turner, F.J., and Gilbert, C.M.: *Petrography: An Introduction to the Study of Rocks in Thin Sections*, W.H. Freeman Co., San Francisco (1954).
14. Bloss, F.D.: *An Introduction to the Methods of Optical Crystallography*, Holt, Rinehart, and Winston, New York City (1961).
15. Berge, P.A., Berryman, J.G., and Bonner, B.P.: "Influence of microstructure on rock elastic properties," *Geophys. Res. Lett.* (1993) **20**, 2619.
16. Johnson, G.R. and Olhoeft, G.R.: "Density of rocks and minerals," *CRC Handbook of Physical Properties of Rocks*, R.S. Carmichael (ed.), Vol. II, CRC Press, Boca Raton, Florida (1984) 2–37.
17. Hurlbut, C.S.: *Dana's Manual of Mineralogy*, Wiley, New York City (1971).
18. Castagna, J.P., Batzle, M.L., and Kan, T.K.: "Rock physics—The link between rock properties and AVO response," *Offset-Dependent Reflectivity—Theory and Practice of AVO Analysis*, J.P. Castagna and M. Backus (eds.), Investigations in Geophysics, No. 8, SEG, Tulsa (1993) 135–171.
19. Rieke, H.H. and Chilingarian, G.V.: *Compaction of Argillaceous Sediments*, Elsevier, New York City (1974).
20. McCulloh, T.H.: "Mass properties of sedimentary rocks and gravimetric effects of petroleum and natural gas reservoirs," professional paper, U.S. Geological Survey (1967).
21. Storer, D.: "Compaction of the argillaceous sediments in the Padano Basin," in *The Gasiferous Deposits of Western Europe*, Vol. 2, Acad. Nazi. dei Lincei, Roma (1959) 519–536.
22. Dickinson, G.: "Geological aspects of abnormal reservoir pressures in Gulf Coast Louisiana," *Am. Assn. Petr. Geol.* (1953) **37**, 410.
23. Eaton, B.A.: "Fracture Gradient Prediction and its Application to Oilfield Operations," *JPT* (October 1969) 1353; *Trans., AIME*, **246**.
24. Dallmus, K.F.: "Mechanics of basin evolution and its relation to the habitat of oil in the basin," *Habitat of Oil*, L.G. Weeks (ed.), AAPG, Memoir 36, (1958) 2071–2174.
25. Skeels, C.: *Hydrological Processes* (25 October 2001) **15**, No. 15, 3073.
26. Stuart, C.A.: "Geopressures," Louisiana State U. 1970 Symposium on Abnormal Subsurface Pressure, Baton Rouge (1970).
27. Schlumberger, *Log Interpretation Charts*, Schlumberger Well Services, Houston (1985).
28. Hurst, A., Griffiths, C.M., and Worthington, P.F.: "Geologic Applications of wireline logs II," *Geological Soc. Spec. Pub.* 65, London (1992).
29. Thomas, L.K., Hankinson, R.W., and Phillips, K.A.: "Determination of Acoustic Velocities for Natural gas," *JPT* (July 1970) 889; *Trans., AIME*, **249**.
30. Batzle, M.L. and Wang, Z.J.: "Seismic properties of pore fluids," *Geophysics* (1992) **57**, 1396.
31. Rao, K.S. and Rao, B.R.: "Study of temperature variation of ultrasonic velocities in some organic liquids by modified fixed-path interferometer method," *J. Acoust. Soc. Am.* (1959) **31**, 439.
32. Wang, Z.J. and Nur, A.: "Effect of Temperature on Wave Velocities in Sands and Sandstones With Heavy Hydrocarbons," *SPERE* (February 1988) 158.
33. Wang, Z.J., Nur, A.M., and Batzle, M.L.: "Acoustic Velocities in Petroleum Oils," *JPT* (February 1990) 192.
34. Standing, M.B.: "Oil-system correlations," *Petroleum Production Handbook, Vol. 11, Part 19*, T.C. Frick, McGraw-Hill, New York City (1962).
35. Sergeev, L.A.: "Ultrasonic velocities in methane saturated oils and water for estimating sound reflectivity of an oil layer," 4th All-Union Acoust. Conf. Izd. Nauk SSSR, USSR (1948).
36. Keenan, J.H. et al.: *Steam Tables*, John Wiley and Sons, New York City (1969).
37. Helgeson, H.C. and Kirkham, D.H.: "Theoretical prediction of the thermodynamic behavior of aqueous electrolytes," *Am. J. Sci.* (1974) **274**, 1089.
38. Rowe, A.M. and Chou, J.C.S.: "Pressure-volume-temperature-concentration relation of aqueous NaCl solutions," *J. Chem. Eng. Data* (1970) **15**, 61.
39. Zarembo, V.I. and Fedorov, M.K.: "Density of sodium chloride solutions in the temperature range 25–350°C at pressures up to 1000 kg/cm," *J. Appl. Chem. USSR* (1975) **48**, 1949.

40. Potter, R.W. and Brown, D.L.: *U.S. Geol. Surv. Bull. 1421-C, The Volumetric Properties of Sodium Chloride Solutions From 0 to 500°C at Pressures up to 2,000 Bars Based on a Reversion of Available Data in the Literature* (1977).
41. Wilson, W.D.: "Speed of sound in distilled water as a function of temperature and pressure," *J. Acoust. Soc. Am.* (1959) **31**, 1067.
42. Millero, F.J., Ward, G.K., and Chetirkin, P.V.: "Relative sound velocities of sea salts at 25°C," *J. Acoust. Soc. Am.* (1977) **61**, 1492.
43. Chen, C.T., Chen, L.S., and Millero, F.J.: "Speed of sound in NaCl, MgCl<sub>2</sub>, Na<sub>2</sub>SO<sub>4</sub>, and MgSO<sub>4</sub> aqueous solutions as functions of concentration, temperature, and pressure," *J. Acoust. Soc. Am.* (1978) **63**, 1795.
44. Wyllie, M.R., Gregory, A.R., and Gardner, L.W.: "Elastic wave velocities in heterogeneous and porous media," *Geophysics* (1956) **21**, 41.
45. Hubbert, M.K.: "Theory of scale models applied to the study of geologic structures," *Bull. Geol. Soc. Am.* (1937) **48**, 1495.
46. Jaeger, J.C., and Cook, N.G.: *Fundamentals of Rock Mechanics*, Routledge, London (1979).
47. Nye, J.F.: *Physical Properties of Crystals*, Oxford U. Press, London (1972).
48. Hashin, Z. and Shtrikman, S.: "A variational approach to the elastic behavior of multiphase materials," *J. Mech. Phys. Solids* (1963) **11**, 127.
49. Katahara, K.: "Clay mineral elastic properties," paper RP, 1996 SEG Intl. Annual Meeting, Denver.
50. Wang, Z.-J., Wang, H., and Cates, M.E.: "Elastic properties of solid clays," expanded abstract, 1998 SEG Intl. Annual Meeting, New Orleans.
51. Prasad, M. *et al.*: "Measurement of Young's Modulus of Clay Minerals Using Atomic Force Acoustic Microscopy," *Geophys. Res. Lett.* (2002) **29**, No. 8, 13–1.
52. Marion, D.P.: "Acoustic, mechanical, and transport properties of sediments and granular materials," PhD dissertation, Stanford U., Palo Alto, California (1990).
53. Yin, H.-Z., Nur, A., and Mavko, G.: "Critical Porosity—a physical boundary in poroelasticity," *Proc.*, 1993 U.S. Rock Mechanics Symposium, Madison, Wisconsin, 27–30 June.
54. Nur, A. *et al.*: "Critical porosity: A key to relating physical properties to porosity in rocks," *The Leading Edge* (1998) **17**, 357.
55. Han, D.: "Effects of porosity and clay content on acoustic properties of sandstones and unconsolidated sediments," PhD dissertation, Stanford U., Palo Alto, California (1986).
56. Vernik, L. and Nur, A.: "Petrophysical classification of siliciclastics for lithology and porosity prediction from seismic velocities," *AAPG Bull.* (1992) **76**, 1295.
57. Rafavich, F. *et al.*: "The relationship between acoustic properties and the petrographic character of carbonate rocks," *Geophysics* (1984) **49**, 1622.
58. Wang, Z.J., Hirsche, W.K., and Sedgwick, G.: "Seismic velocities in carbonate rocks," *J. Cdn. Pet. Tech.* (1990) **30**, 112.
59. White, J.E., and Sengbush, R.L.: "Velocity measurements in near-surface formations," *Geophysics* (1953) **18**, 54.
60. Gassmann, F.: "Elastic waves through a packing of spheres," *Geophysics* (1951) **16**, 673.
61. Duffy, J. and Mindlin, R.D.: "Stress-strain relations and vibrations of a granular medium," (1957) **24**, 584–593.
62. Eberhart-Phillips, D., Han, D.H., and Zoback, M.D.: "Empirical relationships among seismic velocity, effective pressure, porosity, and clay content in sandstone," *Geophysics* (1989) **54**, 82.
63. Terzaghi, K. and Peck, R.B.: *Soil Mechanics in Engineering Practice*, Wiley, New York City (1948).
64. Wyllie, M.R., Gregory, A.R., and Gardner, L.W.: "An experimental investigation of factors affecting elastic wave velocities in porous media," *Geophysics* (1958) **23**, 459.
65. Gregory, A.R.: "Aspects of rock physics from laboratory and log data that are important to seismic interpretation" *Seismic Stratigraphy—Applications to Hydrocarbon Exploration, AAPG Memoir* (1977) **26**, 15.
66. Nur, A. and Simmons, G.: "The effect of viscosity of a fluid phase on velocity in low porosity rocks," *Earth and Planetary Sci. Lett.* (1969) **7**, 99.
67. Yin, H.-Z.: "Acoustic velocity and attenuation of rocks: isotropy, intrinsic anisotropy, and stress-induced anisotropy," PhD dissertation, Stanford U., Palo Alto, California (1992).

68. Scott, T.E. and Nielson, K.C.: "The effect of porosity on the brittle-ductile transition in sandstones" *J. Geophys. Res.* (1991) **96**, 405.
69. Tosaya, C.A.: "Acoustical properties of clay-bearing rocks," PhD dissertation, Stanford U., Palo Alto, California (1982).
70. Han, D.: "Fluid saturation effect on rock velocities in seismic frequencies," SEG Summer Workshop (1992).
71. Mavko, G. and Mukerji, T.: "Pore space compressibility and Gassmann's relation," *Geophysics* (1995) **60**, 1743.
72. Sengupta, M. and Mavko, G.: "Sensitivity analysis of seismic fluid detection," abstract, 1999 SEG Intl. Annual Meeting, Houston, 31 October–5 November.
73. Nolen-Hoeksema, R.C.: "Modulus-porosity relation, Gassmann's equations, and the low frequency elastic-wave response to fluids," *Geophysics* (2000) **65**, No. 5, 1355.
74. Berryman, J.G.: "Origin of Gassmann's Equations," *Geophysics* (1999) **64**, 1627.
75. Brown, R. and Korringa, J.: "On the dependence of the elastic properties of a porous rock on the compressibility of the pore fluid," *Geophysics* (1975) **40**, 608.
76. Batzle, M.L., Han, D., and Castagna, J.P.: "Fluids and frequency dependent seismic velocities of rocks," *The Leading Edge* (February 2001) 168.
77. Biot, M.A.: "General theory of three-dimensional consolidation," *J. Appl. Phys.* (1941) **12**, 155.
78. Coyner, K.B.: "Effects of stress, pore pressure, and pore fluids on bulk strain, velocity, and permeability in rocks," PhD dissertation, Massachusetts Inst. of Technology (1984).
79. Eshelby, J.D.: "The determination of the elastic field of an ellipsoidal inclusion, and related problems," *Proc. Royal Soc. London* (1957) **A241**, 376–396.
80. Walsh, J.B.: "The effect of cracks on the compressibility of rocks," *J. Geophys. Res.* (1965) **70**, 38.
81. Hudson, J.A.: "Overall elastic properties of isotropic materials with arbitrary distribution of circular cracks," *Geophys. J. Int.* (1990) **102**, 133.
82. Kuster, G.T. and Toksoz, N.M.: "Velocity and attenuation of seismic waves in two-phase media, 1. Theoretical formulations," *Geophysics* (1974) **39**, 607.
83. Cheng, C.H. and Toksoz, M.N.: "Inversion of seismic velocities for the pore aspect ratio spectrum of a rock," *J. Geophys. Res.* (1979) **84**, 7533.
84. Sondergeld, C.H. and Rai, C.S.: "Laboratory observations of shear-wave propagation in acoustic media," *The Leading Edge* (1986) **11**, 38.
85. Thomsen, L.: "Understanding seismic anisotropy in exploration and exploitation," lecture notes, SEG/EAGE Distinguished Instructor Short Course, No. 5, SEG, Tulsa (2002).
86. Thomsen, L.: "Weak elastic anisotropy," *Geophysics* (1986) **51**, 1954.
87. Cole, K.S. and Cole, R.H.: "Dispersion and absorption in dielectrics," *J. Chem. Phys.* (1941) **9**, 341.
88. Spencer, J.W.: "Stress relaxation at low frequencies in fluid saturated rocks: attenuation and modulus dispersion," *J. Geophys. Res.* (1981) **86B-3**, 1803.
89. Biot, M.A.: "Theory of propagation of elastic waves in a fluid saturated porous solid. II—Higher frequency range," *J. Acoust. Soc. Am.* (1956) **28**, 179.
90. O'Connell, R.J. and Budiansky, B.: "Viscoelastic properties of fluid-saturated cracked solids," *J. Geophys. Res.* (1977) **82**, 5719.
91. Walsh, J.B.: "Seismic wave attenuation in rock due to friction," *J. Geophys. Res.* (1966) **71**, 2591.
92. Dvorkin, J., and Nur, A.: "Dynamic poroelasticity: a unified model with the squirt and the Biot mechanisms," *Geophysics* (1993) **58**, 524-533.
93. Clark, V.A.: "Effects of volatiles on seismic attenuation and velocity in sedimentary rocks," PhD dissertation, Texas A&M U., College Station, Texas.
94. Winkler, K. and Nur, A.: "Pore fluid and seismic attenuation in rocks," *Geophys. Res. Lett.* (1979) **6**, 1.
95. Murphy, W.F.: "Effects of Microstructure and Pore Fluids on the Acoustic Properties of Granular Sedimentary Materials," PhD dissertation, Stanford U., Stanford, California (1982).
96. Tittmann, B.R. *et al.*: "Possible mechanisms for seismic attenuation in rocks containing small amounts of volatiles," *J. Geophys. Res.* (1980) **85**, 5199.
97. Jones, T.D.: "Pore fluids and frequency-dependent wave propagation in rocks," *Geophysics* (1986) **51**, 1939.

98. Tutuncu, A.T. *et al.*: “Nonlinear viscoelastic behavior of sedimentary rocks, Part I: Effect of frequency and strain amplitude,” *Geophysics* (1998) **63**, 184.
99. Vo-Thant, D.: “Effect of fluid viscosity on shear-wave attenuation in saturated sandstones,” *Geophysics* (1990) **55**, 712.
100. Yamamoto, T., Nye, T., and Kuru, M.: “Porosity, permeability, shear strength: Crosswell tomography below an iron boundary,” *Geophysics* (1994) **59**, 1530.
101. Tanner, M.T. and Sheriff, R.E.: “Application of amplitude, frequency, and other attributes to stratigraphic and hydrocarbon determination,” *Seismic Stratigraphy—Applications to Hydrocarbon Exploration*, C.E. Payton (ed.), *AAPG Memoir 26* (1977) 301–327.
102. Klimentos, T.: “Attenuation of P- and S-waves as a method of distinguishing gas and condensate from oil and water,” *Geophysics* (1995) **60**, 447.
103. Jaeger, J.C.: *Elasticity, Fracture, and Flow: With Engineering and Geologic Applications*, Methuen and Co., London (1969).
104. Plumb, R.A., Herron, S.L., and Olsen, M.P.: “Influence of Composition and Texture on Compressive Strength Variations in the Travis Peak Formation,” paper SPE 24758 presented at the 1992 SPE Annual Technical Conference and Exhibition, Washington, DC, 4–7 October.
105. Scott, T.E.: “The effects of porosity on the mechanics of faulting in sandstones,” PhD dissertation, U. Texas at Dallas, Dallas (1989).
106. Dunn, D.E., LaFountain, L.J., and Jackson, R.E.: “Porosity dependence and mechanism of brittle fracture in sandstones,” *J. Geophys. Res.* (1973) **78**, 2403.
107. Murrell, S.A.F.: “The effect of triaxial stress systems on the strength of rocks at atmospheric temperatures,” *Geophys. J. R. Astr. Soc.* (1965) **10**, 231.
108. Jizba, D.L.: “Mechanical and acoustical properties of sandstones and shales,” PhD dissertation, Stanford U., Palo Alto, California (1991).
109. Allison, R.J.: “Non-destructive determination of Young’s modulus and its relationship with compressive strength, porosity, and density,” *Deformation of Sediments and Sedimentary Rocks*, M.E. Jones and R.M.F. Preston (eds.), Geological Society of London Special Publication 29, London (1987) 63–69.
110. Kazi, A., Sen, Z., and Sadagah, B.-E.H.: “Relationship between sonic pulse velocity and uniaxial compressive strength of rocks,” *Proc.*, 1983 U.S. Symposium on Rock Mechanics, College Station, Texas, June.
111. Bienawski, Z.T.: “Estimating the strength of rock materials,” *J. South African Inst. Min. Metall.* (1974) **74**, 312.
112. Hoek, E., and Brown, E.T.: *Underground Excavations in Rock*, Inst. Mining and Metal., London (1980).
113. Yudhbir, Lemanza, W., and Prinzi, F.: “An empirical failure criterion for rock masses,” *Proc.*, 1983 Congress of the Intl. Society of Rock Mechanics, Melbourne, PBI–PB8.
114. Dowla, N. *et al.*: “Laboratory investigation of saturation effect on mechanical properties of rocks,” Paper EE presented at the 1990 SPWLA Annual Well Logging Symposium, Lafayette, Louisiana.
115. Kowalski, W.C.: “The interdependence between the strength and voids ratio of limestones and marls in connection with their water saturation and anisotropy,” *Proc.*, 1966 Congress of the Intl. Society of Rock Mechanics, Lisbon, 143.
116. Griffith, A.A.: “The theory of rupture,” *First Int. Cong. Appl. Mech.* Delft, The Netherlands, (1924) 54–63.
117. Price, N.J.: “The compressive strength of coal measure rocks,” *Colliery Engng.* (1960) **37**, 282.
118. Smordinov *et al.*, reported in Howarth, D.F.: “The effect of pre-existing microcavities on mechanical rock performance in sedimentary and crystalline rock,” *Int. J. Rock Mech. Min. Sci., Geomech. Abstr.* (1987) **24**, 223.
119. Raymer, L.L., Hunt, E.R., and Gardner, J.S.: “An improved sonic transit-time-porosity transform, Paper P presented at the 1980 SPWLA Annual Well Logging Symposium, Lafayette, Louisiana, 8–11 July.
120. Corbett, K., Friedman, M., and Spang, J.: “Fracture development and mechanical stratigraphy of Austin Chalk, Texas,” *AAPG Bull.* (1987) **71**, 17.
121. Dobreiner, L. and DeFreitas, M.H.: “Geotechnical properties of weak sandstones,” *Geotechnique* (1986) **36**, 79.

122. Steiger, R.P. and Leung, P.K.: "Predictions of wellbore stability in shale formations at great depth," *Rock at Great Depth*, Maury and Fourmaintraux (eds.), Balkema, Rotterdam, The Netherlands (1990) 1209.
123. Brace, W.F., and Martin, R.J.: HI, "A test of the law of effective stress for crystalline rocks of low porosity," *Int. J. Rock Mech. Min. Sci. Geomech. Abst.* (1968) 415–426.
124. Griggs, D.T.: "Hydrologic weakening of quartz and other silicates," *Geophys. J.R. Astr. Soc.* (1967) **14**, 19–31.
125. Kirby, S.H.: "Introduction and digest to the special issue on chemical effects of water on the deformation and strength of rocks," *J. Geophys. Res.* (1984) **89**, 3991.
126. Colback, P.S.B. and Wiid, B.L.: "The influence of moisture content on the compressive I strength of rocks," *Proc.*, 1964 Canadian Rock Mechanics Symposium (1964).
127. Dunning, J.D. and Huff, W.L.: "The effects of aqueous chemical environments on crack and hydraulic fracture propagation and morphologies," *J. Geophys. Res.* (1983) **88**, 6491.
128. Meredith, P.G. and Atkinson, B.K.: "Stress corrosion and acoustic emission during tensile crack propagation in Whin Sill Dolorite and other basic rocks," *Geophys. J. R. Astr. Soc.* (1983) **75**, 1.
129. Freeman, S.W.: "Effects of chemical environment on slow crack growth in glasses and ceramics, Part 1," *J. Geophys. Res.* (1984) **89**, 4072.
130. Ujtai *et al.*: "Effects of water on all time-dependent tests for creep strain, fatigue, and slow crack growth," (1987).
131. Morgenstern, N.R., Asce, M., and Eigenbrod, K.D.: "Classification of argillaceous soils and rocks," *J. Geotech. Eng. Dir. ASCE* (1974) **100**, No. OTIO, 1137.
132. Nelson, R.A.: *Geological Analysis of Naturally Fractured Reservoirs*, Gulf Pub. Co., Houston (1983).
133. Zhang, J.-X.: "Mechanical compaction and the brittle ductile transition in porous rocks: Geological implications for accretionary wedge seismicity," PhD dissertation, State U. of New York, Stony Brook, Stony Brook, New York (1991) 218.
134. Hoek, E. and Brown, E.T.: "The Hoek-Brown Failure Criterion—A 1988 Update," *Proc.*, 15<sup>th</sup> Can. Rock Mech. Symp., U. of Toronto, 31–38.
135. Coates, G.R., and Denoo, S.A.: "Mechanical properties program using borehole analysis and Mohr's circle," paper DD presented at the 1981 SPWLA Annual Well Logging Symposium, Galveston, Texas, 22–25 June.
136. Deere, D.U. and Miller, R.P.: "Engineering classification and index properties for intact rock," report, AFWL-TR-67-144, U.S. Air Force Weapons Lab, Kirtland AFB, New Mexico (1969).
137. Russell, W.L.: "The total gamma ray activity of sedimentary rocks as indicated by Geiger counter determinations," *Geophysics* (1944) **9**, 180.
138. Bigelow, E.L.: "Introduction to Wireline Logging," Western Atlas International Inc., Houston Houston (1995) 1–312.
139. Wahl, J.S.: "Gamma-ray logging," *Geophysics* (1983) **48**, 1536.
140. Katahara, K.W.: "Gamma-ray log response in shaly sands," *The Log Analyst* (July–August 1995) 50.
141. Georgi, D.T., Bergren, P.A., and Devier, C.A.: "Plug gamma ray: Key to formation evaluation," paper SCA-9732 presented at the 1997 SPWLA Annual Well Logging Symposium, Houston, 15–18 June.

---

## General References

- Aldrich, M.J.: "Pore pressure effects on Berea Sandstone subjected to experimental deformation," *Geo. Soc. Am. Bull.* (1969) **80**, 1577.
- Anderson, O.L. and Lieberman, R.C.: "Sound velocities in rocks and minerals," VESIAC state-of-the-art report no. 7885-4-X, U. of Michigan, Ann Arbor, Michigan (1966).
- Anderson, R.G. and Castagna, J.P.: "Analysis of sonic log compressional wave amplitudes using borehole compensation techniques," paper K presented at the 1984 SPWLA Annual Symposium, New Orleans, June.



- Atkinson, B.K.: "Subcritical crack growth in geologic materials," *J. Geophys. Res.* (1984) **89**, 4077.
- Ateksandrov, K.S. and Ryzhova, T.V.: "The elastic properties of crystals," *Sov. Phys. Crystall-gr.* (1961) **6**, 228.
- Backus, G.E.: "Long-wave elastic anisotropy produced by horizontal layering," *J. Geophys. Res.* (1962) **67**, 4427.
- Billings, M.P.: *Structural Geology*, Prentice-Hall, New York City (1972).
- Biot, M.A.: "Mechanics of deformation and acoustic propagation in porous media," *J. Appl. Phys.* (1962) **23**, 1482.
- Birch, F.: "Compressibility; elastic constants," *Handbook of Physical Constants*, S.P. Clark Jr. (ed.), GSA Memoir, 97 (1966) 97–174.
- Blatt, H., Middleton, G.V., and Murray, R.C.: *Origin of Sedimentary Rocks*, Prentice-Hall, New York City (1972).
- Boozer, G.D., Hiller, K.H., and Serdengecti, A.: "Effects of pore fluids on the deformation behavior of rocks subjected to triaxial compression," paper C presented at the 1962 ISRM Annual Symposium, Fairhurst, Minnesota.
- Boretti-Onyszkiewicz, W.: "Joints in the flysch sandstones on the ground of strength examinations," *Proc.*, 1966 Congress of the Intl. Society of Rock Mechanics, Lisbon.
- Brill, J.P. and Beggs, H.D.: *Two-Phase Flow in Pipes*, U. of Tulsa Press, Tulsa (1977).
- Brook, N.: "Estimating the triaxial strength of rocks," *Int. J. Rock Mech. Min. Sci. Geomech. Abstr.* (1979) **16**, 261.
- Brunauer, S., Kanthro, D.L., and Weise, C.H.: "The surface energies of amorphous silica and hydrous amorphous silica," *Can. J. Chem.* (1956) **34**, 1483.
- Bulau, J.R. *et al.*: "The role of aqueous fluids in the internal friction of rock," *J. Geophys. Res.* (1984) **89**, 4207.
- Campbell, F.A. and Oliver, T.A.: "Mineralogic and chemical composition of Freton and Duvernay Formations, Central Alberta," *Bull. Canadian Pet. Geol.* (1968) **16**, 40.
- Castagna, J.P.: "Shear-wave time-average equation for sandstones," paper presented at the 1985 SEG Annual Intl. Meeting, Washington, DC.
- Culberson, O.L. and McKetta, J.J. Jr.: "Phase Equilibria in Hydrocarbon-Water Systems. II. The Solubility of Methane in Water at Pressures to 10,000 PSIA," *Trans.*, AIME (1951) **192**, 223.
- Dandekar, D.P.: "Pressure dependence of the elastic constants of calcite," *Phys. Rev.* (1968) **172**, 873.
- D'Andrea, D.V., Fischer, R.L., and Fogelson, D.E.: "Prediction of compressive strength from other rock properties," U.S. Bureau of Mines Report, Invest. #6702 (1965) 1–23.
- Davey, F.J. and Cooper, A.K.: "Gravity studies of the Victoria Land Basin and Iselin Bank," *The Antarctic Continental Margin and Geophysics of the Western Ross Sea*, A.K. Cooper and F.J. Davey (eds.), CPCEMR Earth Science Series, Circum-Pacific Council for Energy and Mineral Resources, Houston (1987).
- DeVilbiss, J., Ito, H., and Nur, A.: "Measurement of compressional and shear wave velocities of water filled rocks during water-steam transition," *Geophysics* (1979) **44**, 407.
- Dickey, P.A.: "Patterns of chemical composition in deep subsurface waters," *Am. Assn. Petr. Geol.* (1966) **50**, 2472.
- Dodson, C.R. and Standing, M.B.: "Pressure-volume-temperature and solubility relations for natural-gas-water mixtures," *Drilling and Production Practices, 1944*, Am. Pet. Inst., New York City (1944) 173–179.
- Domenico, S.N.: "Effect of brine-gas mixture on velocity in an unconsolidated sand reservoir," *Geophysics* (1976) **41**, 887.

- Domenico, S.N.: "Elastic properties of unconsolidated porous sand reservoirs," *Geophysics* (1977) **42**, 1339.
- Domenico, S.N.: "Rock lithology and porosity determination from shear and compressional wave velocity," *Geophysics* (1984) **49**, 1188.
- Dvorkin, J., and Nur, A.: "Dynamic poroelasticity: A unified model with the squirt and the Biot mechanisms," *Geophysics* (1993) **58**, 524.
- Eastwood, R.L. and Castagna, J.P.: "Interpretation of V/V ratios from sonic logs," *Shear Wave Exploration*, S.H. Danbom and S.N. Domenico (eds.), Geophysical Developments No. 1, SEG, Tulsa (1986).
- Engelder, T. and Plumb, R.: "The relation between ultrasonic properties and strain relaxation," *Int. J. Rock Mech. Min. Sci. and Geomech. Abs.* (1984) **21**, 7.
- Fertl, W.H.: *Abnormal Formation Pressures*, Elsevier, New York City (1976).
- Freed, R.L.: "Shale Mineralogy of the No. 1 Pleasant Bayou Geothermal Test Well," progress report, *Proc.*, 1980 United States Gulf Coast Geopressured-Geothermal Energy Conference, Research and Development, Center for Energy Studies, U. of Texas at Austin, Austin, Texas.
- Freund, D.: "Ultrasonic compressional and shear velocities in dry clastic rocks as a function of porosity, clay content, and confining pressure," *Geophys. J. Int.* (1992) **108**, 125.
- Ganley, D.C. and Kanasewich, E.R.: "Measurement of absorption and dispersion from check shot surveys," *J. Geophys. Res.* (1980) **85**, 5219.
- Gardner, G.H.F., Gardner, L.W., and Gregory, A.R.: "Formation velocity and density—The diagnostic basis for stratigraphic traps," *Geophysics* (1974) **39**, 770.
- Gassmann, F.: "Über die elastizität poröser medien," *Vier, der Natur Gesellschaft* (1951) **96**, 1.
- Greenberg, M.L. and Castagna, J.P.: "Shear-wave velocity estimation in porous rocks: Theoretical formulation, preliminary verification, and applications," *Geophys. Prosp.* (1992) **40**, 195.
- Greenhaigh, S.A. and Emerson, D.W.: "Physical properties of Permian bituminous coals from the Sydney Basin, New South Wales," paper presented at the 1981 SEG Annual Intl. Meeting, Los Angeles, October.
- Gregory, A.R.: "Fluid saturation effects on dynamic elastic properties of sedimentary rocks," *Geophysics* (1976) **41**, 895.
- Gretener, P.E.: "Pore pressure: fundamentals, general ramifications, and implications for structural geology (revised)," *Education Course Notes Series*, No. 4, AAPG (1979).
- Gretener, P.E.: "Geothermics-using temperature in hydrocarbon exploration," *Education Course Notes Series*, No. 17, AAPG (1981).
- Griffith, A.A.: "The theory of rupture," *Proc.*, First Intl. Congress for Applied Mechanics, Delft, The Netherlands (1924) 54–63.
- Griggs, D.T.: "Hydrologic weakening of quartz and other silicates," *Geophys. J. R. Astron. Soc.* (1967) **14**, 19.
- Hadley, K.: "Comparison of calculated and observed crack densities and seismic velocities in Westerly Granite," *J. Geophys. Res.* (1976) **81**, 3484.
- Hamilton, E.L.: "Low sound velocities in high porosity sediments," *J. Acoust. Soc. Am.* (1956) **28**, 16.
- Hamilton, E.L.: "Compressional-wave attenuation in marine sediments," *Geophysics* (1972) **37**, 620.
- Hamilton, E.L.: "Variations of density and porosity with depth in deep-sea sediments," *J. Sed. Pet.* (1976) **46**, 280.
- Han, D.-H., Nur, A., and Morgan, D.: "Effects of porosity and clay content on wave velocities in sandstones," *Geophysics* (1986) **51**, 2093.
- Han, D. and M. Batzle: "Velocity, density and modulus of hydrocarbon fluids—Data measurement," expanded abstract, paper RPB 7.2., 2000 SEG Annual Intl. Meeting, Calgary, 6–11 August (2000a).

- Han, D. and M. Batzle: "Velocity, density and modulus of hydrocarbon fluids—Empirical modeling," expanded abstract, paper RPB 7.3., 2000 SEG Annual Intl. Meeting, Calgary, 6–11 August (2000b).
- Harrison, A.R. *et al.*: "Acquisition and Analysis of Sonic Waveforms From a Borehole Monopole and Dipole Source for the Determination of Compressional and Shear Speeds and Their Relation to Rock Mechanical Properties and Surface Seismic Data," paper SPE 20557 presented at the 1990 SPE Annual Technical Conference and Exhibition, New Orleans, 23–26 September.
- Hauge, P.S.: "Measurement of attenuation from vertical seismic profiles," *Geophysics* (1981) **46**, 1548.
- Hedburg, H.D.: "Gravitational compaction of clays and shales," *Am. J. Sci.* (1936) **31**, 241.
- Hill, R.: "The elastic behavior of a crystalline aggregate," *Proc. Phys. Soc. London, Ser. A* (1952) **65**, 349.
- Hinz, K., Dostmann, H., and Fritsch, J.: "The continental margin of Morocco: Seismic sequences, structural elements, and geological development," *Geology of the Northwest African Continental Margin*, U. von Rad *et al.* (eds.), Springer-Verlag, New York City (1982).
- Howarth, D.F.: "The effect of pre-existing microcavities on mechanical rock performance in sedimentary and crystalline rocks," *Int. J. Rock Mech. Min. Sci. Geomech. Abstr.* (1987) **24**, 223.
- Jachens, R.C. and Griscom, A.: "An isostatic residual gravity map of California—a residual map for interpretation of anomalies from intracrustal sources," *The Utility of Regional Gravity and Magnetic Anomaly Maps*, W.J. Hinze (ed.), SEG, Tulsa (1985).
- Johnston, D.H.: "Shale properties at temperature and pressure," *Oil and Gas J.* (1986) **13**, 60.
- Jones, T.D. and Nur, A.: "Velocity and attenuation in sandstone at elevated temperatures and pressures," *Geophys. Res. Lett.* (1983) **10**, 140.
- Kan, T.K., Batzle, M.L., and Gaiser, J.E.: "Attenuation measured from VSP, evidence of frequency dependent Q," paper presented at the 1983 SEG Annual Intl. Meeting, Las Vegas.
- Keller, G.R. *et al.*: "Regional gravity and magnetic study of west Texas," *The Utility of Regional Gravity and Magnetic Anomaly Maps*, W.J. Hinze (ed.), SEG, Tulsa (1985).
- Kowallis, B., Jones, L.E.A., and Wang, H.F.: "Velocity-porosity-clay content systematics of poorly consolidated sandstones," *J. Geophys. Res.* (1984) **89**, 10355.
- Krief, M. *et al.*: "A petrophysical interpretation using the velocities of P and S waves (full waveform sonic)," *The Log Analyst* (November–December 1990) 355.
- Krynine, P.D.: "The megascopic study of field classification of sedimentary rocks," *J. Geol.* (1948) **56**, 130.
- Lajtai, E.Z., Schmidtke, R.H., and Bielus, L.P.: "The effect of water on the time-dependent deformation and fracture of a granite," *Int. J. Rock Mech. Min. Sci. Geomech. Abstr.* (1987) **24**, 247.
- Martin, R.J.: "Time-dependent crack growth in quartz and its application to creep in rocks," *J. Geophys. Res.* (1972) **77**, 1406.
- Matthews, J.C. and Matthews, W.R.: "Program calculates frac gradients for many basins," *Oil and Gas J.* (1985).
- Mavko, G.M., and Nur, A.: "The effect of nonelliptical cracks on the compressibility of rocks," *J. Geoph. Res.* (1977) **84**, 4769.
- McDonal, F.J. *et al.*: "Attenuation of shear and compressional waves in Pierre Shale," *Geophysics* (1958) **23**, 421.
- McSkimin, H.J., Andreatch, P. Jr., and Thurston, R.N.: "Elastic moduli of quartz vs. hydrostatic pressure at 25° and 195.8°C," *J. Appl. Phys.* (1965) **36**, 1632.
- Milholland, P. *et al.*: "Geoacoustic modeling of deep-sea carbonate sediments," *J. Acoust. Soc. Am.* (1980) **68**, 1351.

- Murphy, S.A.F.: "The effect of triaxial stress systems on the strength of rocks at atmospheric temperatures," *I. R. Astr. Soc.* (1965) **10**, 231.
- Murphy, W.F., Schwartz, L.M., and Homby, B.: "Interpretation of  $V_p$  and  $V_s$  in sedimentary rocks," paper FF presented at the 1991 SPWLA Annual Well Logging Symposium, Midland, Texas, June.
- Murphy, W.F., Reischer, A., and Hsu, K.: "Modulus decomposition of compressional and shear velocities in sand bodies," *Geophysics* (1993) **58**, 227.
- Murphy, W.F. III.: "Effects of microstructure and pore fluids on acoustic properties of granular sedimentary materials," PhD dissertation, Stanford U., Palo Alto, California (1982).
- Nelson, R.A.: *Geological Analysis of Naturally Fractured Reservoirs*, Gulf Pub. Co., Houston (1983).
- O'Connell, R.J. and Budiansky, B.: "Seismic velocities in dry and saturated cracked solids," *J. Geophys. Res.* (1974) **79**, 5412.
- Parks, G.A.: "Surface and interfacial free energies of quartz," *J. Geophys. Res.* (1984) **89**, 3997.
- Peck, L.: "Stress corrosion cracking of quartzite," *Abstr. EOS* (1980) **61**, 361.
- Pettijohn, F.S.: *Sedimentary Rocks*, Harper and Row, New York City (1975).
- Pickett, G.R.: "Acoustic Character Logs and Their Applications in Formation Evaluation," *JPT* (June 1963) 659; *Trans.*, AIME, **228**.
- Robinson, B.E.: "Lithofacies and fracture potential of the upper Cretaceous Austin Chalk, Eagleford Shale, and Buda limestone along the Austin Chalk-Buda limestone production trend of south Texas," ARCO Tech. Serv. Memo 91-0035 (1991).
- Ruiz, M.D.: "Some technological characteristics of twenty-six Brazilian rock types," *Proc.*, 1966 Congress of the Intl. Society of Rock Mechanics, Lisbon, 115.
- Russell, W.L.: *Principles of Petroleum Geology*, McGraw-Hill, New York City (1951).
- Shaw, D.B. and Weaver, C.E.: "The mineralogical composition of shales," *J. Sed. Petrology* (1965) **35**, 213.
- Simmons, G.: "Ultrasonics in geology," *IEEE* (1965) **53**, 1337.
- Simmons, G. and Brace, W.F.: "Comparison of static and dynamic measurements of compressibility of rocks," *J. Geophys. Res.* (1965) **70**, 5649.
- Stoll, R.D. and Houtz, R.E.: "Attenuation measurements from sonobuoys," *J. Acoust. Soc. Am.* (1983) **73**, 163.
- Sultanov, R.G., Skripka, V.G., and Namiot, A.Y.: "Solubility of methane in water at high temperatures and pressures," *Gazovaia Promyshienmost* (May 1972) 6.
- Thomas, E.C. and Stieber, S.J.: "The distribution of shale in sandstones and its effect upon density," paper T presented at the 1975 SPWLA Annual Well Logging Symposium, New Orleans.
- Timur, A.: "Temperature dependence of compressional and shear wave velocities in rocks," *Geophysics* (1977) **42**, 950.
- Toksoz, M.N. and Johnston, D.H.: *Seismic Wave Attenuation*, SEG, Tulsa (1981).
- Tullos, F.N., and Reid, A.C.: "Seismic attenuation of Gulf Coast sediments," *Geophysics* (1969) **34**, 516.
- Van Voorhis, J.J., Craig, R.G., and Barbell, F.E.: "Free energy of immersion of compressed powders with different liquids. 11. Silica powder," *J. Chem.* (1957) **61**, 1513.
- Volarovich, M.P., Bayuk, E.I., and D'Yaur, J.J.: "Change in the velocity of longitudinal waves during deformation of samples," *Izvestiya, Earth Physics* (1985) **21**, 302.
- Watt, J.P., Davies, G.F., and O'Connell, R.J.: "The elastic properties of composite materials," *Rev. Geophys. and Space Physics* (1976) **14**, 541.
- White, J.E.: *Underground Sound: Application of Seismic Waves*, Elsevier, New York City (1983).
- Wilkins, R., Simmons, G., and Caruso, L.: "The ratio  $VP/V_s$  as a discriminant of composition for siliceous limestones," *Geophysics* (1984) **49**, 1850.

Winkler, K.E., Nur, A., and Gladwin, K.: "Friction and seismic attenuation in rocks," *Nature* (1979) **277**, 528.

Winkler, K.W.: "Estimates of velocity dispersion between seismic and ultrasonic frequencies," *Geophysics* (1986) **51**, 183.

Wood, A.B.: *A Textbook of Sound*, MacMillan, New York City (1941).

Yin, C.S.: "Wave attenuation in partially saturated porous solids," PhD dissertation, Stanford U., Palo Alto, California (1992).

### SI Metric Conversion Factors

°API	$141.5/(131.5 + \text{°API})$		= g/cm <sup>3</sup>
bbbl	× 1.589 873	E-01	= m <sup>3</sup>
ft	× 3.048*	E-01	= m
ft <sup>3</sup>	× 2.831 685	E-02	= m <sup>3</sup>
°F	$(\text{°F}-32)/1.8$		= °C
psi	× 6.894 757	E + 00	= kPa

\*Conversion factor is exact.



# Chapter 14

## Single-Phase Permeability

Philip H. Nelson, U.S. Geological Survey and Michael L. Batzle, Colorado School of Mines

### 14.1 Introduction

The capacity to flow fluids is one of the most important properties of reservoir rocks. As a result, extensive research has been applied to describe and understand the permeability of rocks to fluid flow. In this chapter, only single-phase or absolute permeability will be considered. Multiphase relative permeabilities must be derived using relations described in the chapter on relative permeability and capillary pressure.

Permeability ( $k$ ) is a rock property relating the flow per unit area to the hydraulic gradient by Darcy's law,

$$q / A = -(k / \mu) \text{grad}(p - \rho g z), \dots \dots \dots (14.1)$$

where  $p$  is pressure,  $\rho$  is fluid density,  $g$  is gravitational acceleration,  $z$  is elevation, and  $\mu$  is the dynamic viscosity. The ratio  $q/A$  has the units of velocity and is sometimes referred to as the "Darcy velocity" to distinguish it from the localized velocity of flow within pore channels. The natural unit of  $k$  is length squared; however, petroleum usage casts Eq. 14.1 in mixed units, so that the unit of  $k$  is the darcy, which is defined as the permeability of a porous medium filled with a single-phase fluid of 1-cp viscosity flowing at a rate of 1 cm<sup>3</sup>/s per cross-sectional area of 1 cm<sup>2</sup> under a gradient of 1 atm pressure per 1 cm.<sup>1</sup> Reservoir rocks are usually characterized in millidarcies (md), a unit that is 1/1000 of a darcy. Conversion factors are 1 darcy = 0.9869×10<sup>-12</sup> m<sup>2</sup> or 1 md = 0.9869×10<sup>-11</sup> cm<sup>2</sup>. Bass<sup>2</sup> noted that Darcy's law holds only for viscous flow and that the medium must be 100% saturated with the flowing fluid when the determination of permeability is made. Furthermore, the medium and the fluid must not react by chemical reaction, absorption, or adsorption; otherwise, the permeability changes as the fluid flows through the sample. Darcy's law (Eq. 14.1) has many practical applications, including determination of permeability in the laboratory and wellbore.

In hydrological applications, the fluid is assumed to be water at near-surface conditions. The viscosity of water is factored into the transport term, which is called hydraulic conductivity ( $K$ ) and has the units of velocity. Darcy's law is then written as

$$q/A = -K \text{ grad}(p/\rho g - z) \dots \dots \dots (14.2)$$

This version of Darcy's law is not useful to the petroleum engineer, but it is sometimes handy to be able to convert from hydraulic conductivity units to permeability. To obtain  $k$  in darcies, multiply  $K$  in m/s by  $1.04 \times 10^5$ .

Permeability is a property of pore space geometry; specifically, it has been found to be proportional to  $(R\Phi)^2$ , where  $R$  is a pore throat dimension and  $\Phi$  is porosity. However, a measure of  $R$  is not available unless capillary pressure determinations have been made, in which case permeability has also been determined in the laboratory. Because permeability can be measured only on a restricted set of samples or from a limited number of well tests, it must often be derived from other properties or measurements. Porosity and permeability are routinely measured on core plugs; for this reason, the systematics of permeability and porosity are reviewed in this chapter.

The topics of fluid sensitivity and stress also deserve consideration. Many rocks contain clays or other minerals that are sensitive to the pore fluid. If an incompatible pore fluid is introduced during a production process, these minerals can change form, swell, or migrate. Permeability can then decrease by orders of magnitude. As effective pressure is increased, pore space decreases and permeability is lowered. The change in permeability with pressure is greater at low effective pressures. This pressure dependence is also strong in poorly consolidated rocks or rocks where flow is dominated by fractures. As rocks become consolidated or well cemented, the pressure dependence may become negligible.

Finally, the problem of quantitatively predicting permeability from porosity and other measurements that can be made with well logs is examined. To predict permeability, one needs a physical model and a method of zoning or clustering the data. Models used to predict permeability from porosity and other measurable rock parameters fall into classes based on grain size, mineralogy, surface area, or pore dimension parameters. Zonation techniques include database, statistical, clustering, and neural network approaches. Ultimately, the choices of model and zonation method depend on the problem at hand, the data available, and the resources devoted to the task.

## 14.2 Petrologic Controls

Permeability values of rocks range over many factors of 10; therefore, permeability is plotted on a logarithmic scale. Values commonly encountered in petroleum reservoirs range from a fraction of a millidarcy to several darcies. The  $\log_{10}(k)$ - $\Phi$  plot of Fig. 14.1 shows four data sets from sands and sandstones, illustrating the reduction in permeability and porosity that occurs as pore dimensions are reduced with compaction and alteration of minerals (diagenesis). In these examples,  $k$  of newly deposited beach sands exceeds 30 darcies,  $k$  of partially consolidated sandstones ranges from 300 to 2,000 md,  $k$  of consolidated sandstones ranges from 0.01 to 100 md, and  $k$  of tight gas sandstones is  $<0.01$  md. Porosity is reduced from a maximum of 52% in newly deposited sandstones to as low as 1% in consolidated sandstones. In this section, some of the causes of variability in  $\log_{10}(k)$ - $\Phi$  space are examined.

The permeability and porosity of a rock are the result of both depositional and diagenetic factors (Fig. 14.2) that combine to produce a unique set of pore space geometries as the rock is formed. Consequently, the heavy line in Fig. 14.2 represents only one of many possible evolutionary paths in  $\log(k)$ - $\Phi$  space. First, consider the depositional factors. Better sorting increases both  $k$  and  $\Phi$ . Gravel and coarse grain size produce anomalously high  $k$  even though decreasing  $\Phi$ . Very fine grains of silt and detrital clay produce low permeability at high porosity. High quartz content can produce efficient systems having good permeability even at low porosity, whereas sandstones with feldspar or lithic grains may develop significant noneffective porosity content. Diagenetic effects, starting with compaction and followed by cementation and



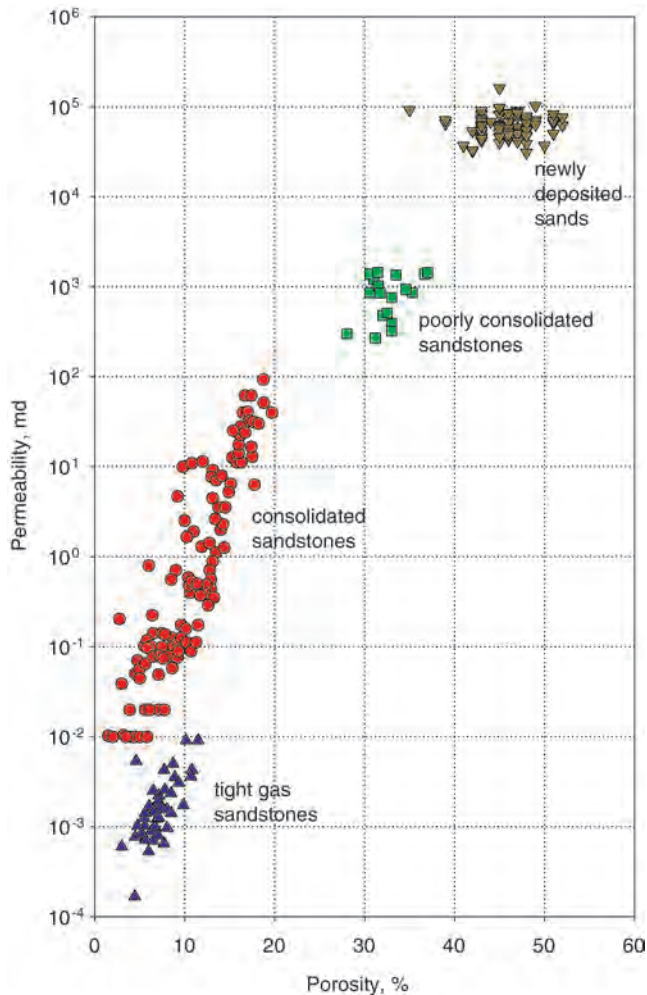


**Fig. 14.1—Permeability/porosity plot showing newly deposited beach sands and three sample suites from wells in oil and gas fields. Permeability scale ranges from 1,000 darcies to 0.1  $\mu$ d.**

alteration of depositional minerals to clays, tend to decrease  $\log(k)$  proportionately as  $\Phi$  is decreased. Several examples are presented to illustrate these controls.

In newly deposited sands and poorly consolidated sandstones, grain size correlates well with pore size and hence is a primary control on permeability. Grain size ranges for sandstones are defined by factors of two (Fig. 14.3). For example, a sand with grain diameters between 250 and 500  $\mu$ m is classed as a medium-grained sand. The sedimentological phi scale provides a convenient label to the size classes, and  $D=2^{-\text{phi}}$  is the grain diameter in mm (for example,  $2^{-3}=0.125$  mm=125  $\mu$ m). Also shown in Fig. 14.3 are size ranges for various types of carbonates. Note that grain diameters can be as large as 2,000  $\mu$ m in very coarse-grained sands and as small as 1  $\mu$ m in chalks.

**14.2.1 Unconsolidated Sandpacks.** One laboratory study deserves examination because it illustrates the relationships among grain size, sorting,  $k$ , and  $\Phi$ . Using sand from two Texas rivers, Beard and Weyl<sup>3</sup> sieved 48 sand samples into 8 size classes and 6 sorting classes. Each data point shown in Fig. 14.4 represents the permeability and porosity of a sample with a unique

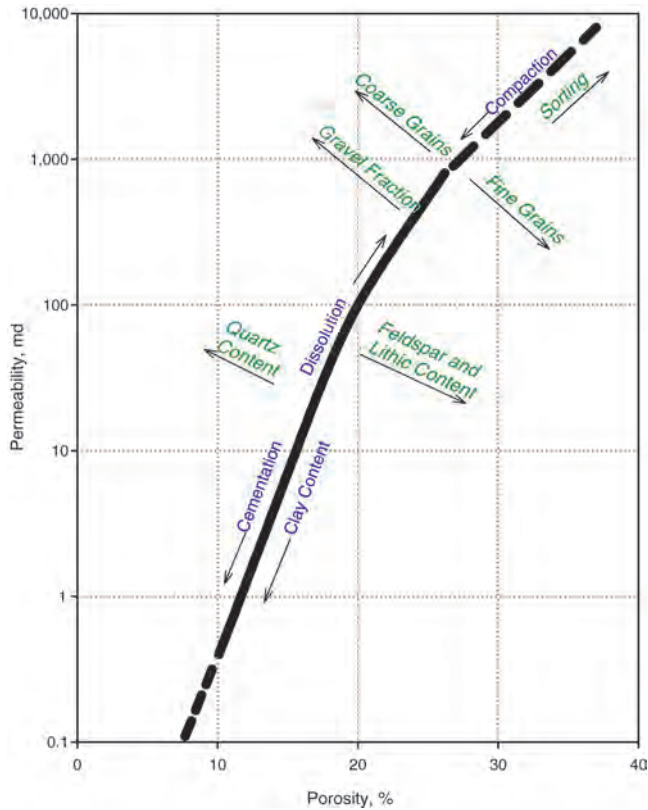


**Fig. 14.2—Sketch of the impact of primary depositional features (such as quartz content and sorting, in italics) and diagenetic processes (such as compaction and cementation) on permeability/porosity trends in sandstones.**

grain size and sorting. Median grain size ranges from 0.840 mm for the coarse sample to 0.074 mm for the very fine sample. The authors present photomicrographs of thin-section comparators for each of the 48 samples to document the wide range of size and sorting represented by the sample suite. The maximum permeability value for a well-compacted, unconsolidated sand-pack is about 500 darcies. Porosity ranges from 23.4% to 43.5%. Note the general increase in permeability as grain size increases from very fine to coarse and the increase in both porosity and permeability as sorting progresses from very poor to well sorted.

Consider the extremely well-sorted samples represented by the open-circle data points along the right-hand edge of Fig. 14.4. For these extremely well-sorted samples, porosity is independent of grain size, as it should be for a packing of uniform spheres. However, for those samples that are not well sorted, an increase in coarse grain content results in somewhat decreased  $\Phi$  even as  $k$  increases. This pattern is preserved in some consolidated samples. The extremely well-sorted samples of Fig. 14.4 also show that  $\log(k)$  increases in equal increments as grain size increases. The samples were sized so that the mean grain diameter of each adjacent size interval increases by the square root of 2. Permeability increases by a factor of 2 for each increment of grain size. Thus, Beard and Weyl's data show that permeability is proportional to the square of grain size. Because theoretical models show that flow is proportional to the square of the radius of a pore opening, it can be said that Beard and Weyl's data demonstrate that pore size is proportional to grain size in sandpicks.

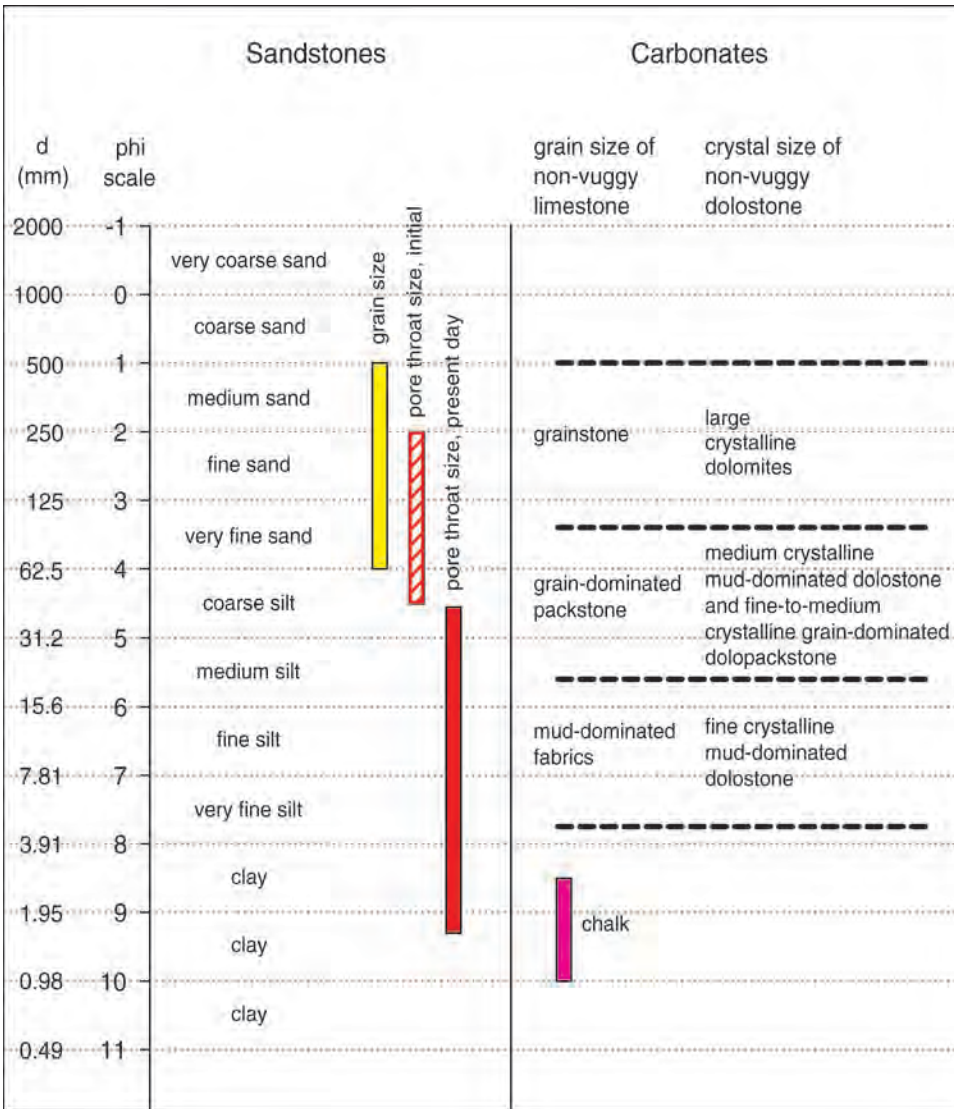
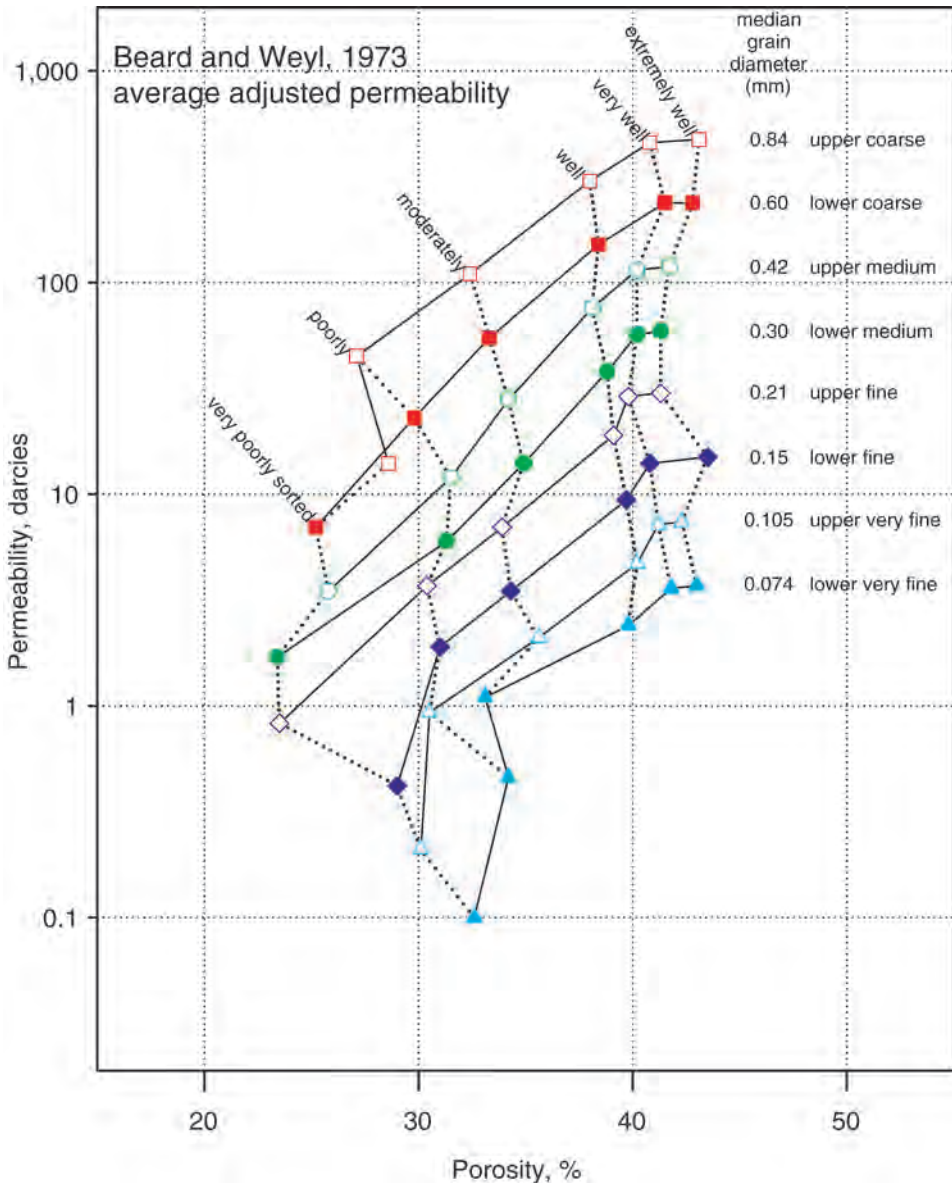


Fig. 14.3—Grain size categories in sandstone, limestone, and dolostone. Sedimentological scale (phi scale) is logarithmic in powers of two. Grain diameter (*d*) (crystal size in case of dolostones) is given in micrometers. Limestone and dolostone classes are from Lucia<sup>13,59</sup>; chalk data are from Mortensen *et al.*<sup>12</sup> See Discussion for explanation of vertical bars showing grain and pore throat sizes in a consolidated sandstone.

**14.2.2 Clays and Shales.** The permeability of shales and mudstones determines the effectiveness of seals for many hydrocarbon reservoirs, but measurements are few. Neuzil<sup>4</sup> compiled data sets from 12 laboratory studies and 7 field studies that provided ranges of permeability and porosity data in bottom muds, clay, unconsolidated sediment, glacial till, clayey siltstone and sandstone, claystone, mudstone, and argillite. Permeability is as high as 1 md in unconsolidated sediment with 70% porosity and as low as 0.01 nanodarcy (nd) in argillite with 5% porosity. With few exceptions, permeability ranges over 3 factors of 10 at a given porosity and decreases progressively as porosity decreases. For example, at a porosity of 20%, permeability ranges from 0.1  $\mu$ d to 0.1 nd, a range well below the lower limit of *k* plotted in Fig. 14.1.



**Fig. 14.4—Permeability/porosity data from unconsolidated artificial sandpacks by Beard and Weyl.<sup>3</sup> Symbols linked with solid lines denote size ranges; dotted lines distinguish sorting classes.**

Although it was expected that permeability would be scale dependent in clays and shales (regional permeability would be greater than laboratory sample permeability because of fractures), it was found that permeability ranges from the field studies are roughly the same as the laboratory studies, thereby indicating a lack of scale dependence.

**14.2.3 Sandstones.** Thomson<sup>5</sup> describes continental sandstones from the Lower Cretaceous Hosston formation in Mississippi (Fig. 14.5): “Secondary quartz cement and compaction through pressure solution of grains are the principal causes of porosity reduction. The early introduction of large amounts of dolomite has inhibited compaction of framework grains. Kaolinite ranges from 5% to 15% of total rock volume. All samples contain a little illite. The

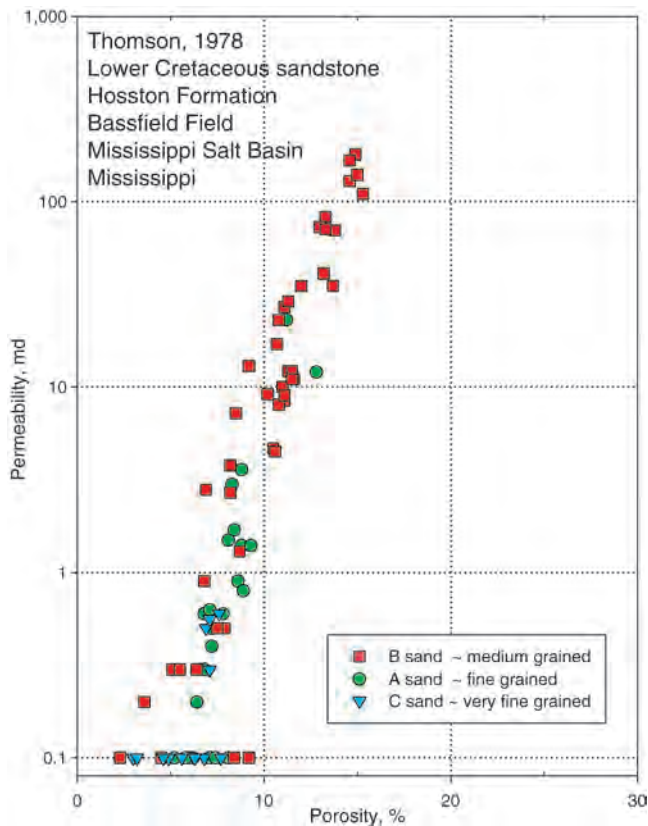


Fig. 14.5—Permeability/porosity data from the Lower Cretaceous Hosston Sandstone from Thomson.<sup>5</sup>

permeability/porosity plots indicate a progressive and uniform loss of permeability as porosity is reduced, suggesting that the sandstones underwent a simple diagenetic history, uncomplicated by such late processes as leaching, development of authigenic clay minerals, and so forth.” Thomson also suggests that the introduction of hydrocarbons caused a cessation in diagenesis in the lower part of the reservoir. The effect of grain size remains apparent in the data of Fig. 14.5, although diagenetic effects have blurred the separations seen in Fig. 14.4, so some of the medium-grained samples have  $k$  as low as in the very fine-grained samples.

Permeability in Oligocene-Miocene sandstones ranges from  $<1.0$  to  $>1,000$  md (Fig. 14.6). Bloch<sup>6</sup> reports that the sandstones were deposited in a variety of environments and that lithology ranges from lithic arkoses to feldspathic litharenites, meaning that 25% or more of the primary grain composition is either lithic fragments or feldspar grains. Up to 30% of porosity is secondary porosity, formed by dissolution of potassium feldspar. Because permeability is  $>1$  darcy at porosity values  $<20\%$ , the secondary porosity is probably well connected and contributing to flow. Although the samples with coarsest grain sizes tend to have the highest permeability values, the symbols depicting different grain sizes are intermixed, another indication that secondary porosity is contributing to flow.

Bos<sup>7</sup> describes results from an exploration well that encountered (1) clean sandstone, (2) sandstone with pores filled with kaolinite, (3) laminated sandstone, part clean and part filled with kaolinite (indicated as “laminated” in Fig. 14.7), and (4) shale. Scanning electron microscope photographs document the extent to which kaolinite fills the pores, thereby reducing  $k$  as shown in Fig. 14.7. Here again we see a linear relationship between  $\log(k)$  and  $\Phi$ , with pore-infilling clays reducing both  $k$  and  $\Phi$  in a fairly systematic fashion.

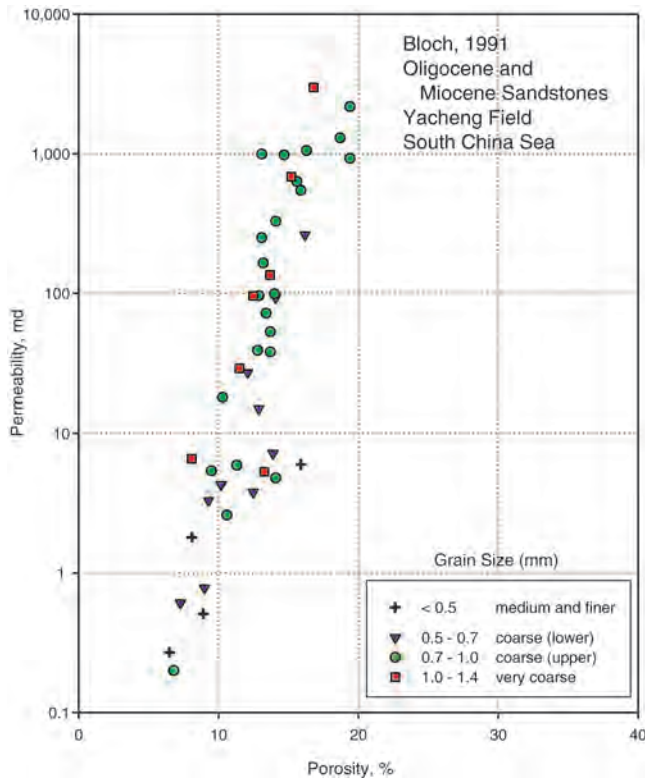


Fig. 14.6—Permeability/porosity data from Oligocene and Miocene sandstones from Bloch.<sup>6</sup>

Wilson<sup>8</sup> contends that many clay coatings, particularly on eolian sandstones, formed on the framework grains before deposition. Their presence actually preserves porosity because quartz overgrowths cannot readily form. According to Wilson, many of the largest petroleum reservoirs (North Sea, North Slope of Alaska) have retained good porosity because of detrital clay coatings. Samples in which kaolinite and illite occur as clay coatings fall within the boundaries of the three upper fields in Fig. 14.8. However, fibrous illite can form within the pore space in the Rotliegend sandstones (lower two fields in Fig. 14.8), reducing the permeability one to two orders of magnitude compared with rocks in which clay occurs as grain coatings. Under the scanning electron microscope, the appearance of numerous fine strands of illite within pores makes it obvious why permeability is so impaired.<sup>9</sup> Special core preparation techniques are required to preserve clay textures so that laboratory measurements reflect the in-situ permeability values.<sup>10</sup>

**14.2.4 Carbonates.** Samples from an oil-productive dolomite facies in the Williston basin of North Dakota were characterized in terms of the size of dolomite grains.<sup>11</sup> Originally deposited as a carbonate mud, after burial this facies was altered to a sucrosic dolomite or calcareous dolomite with good intercrystalline porosity. At any given porosity, samples with the larger dolomite crystal sizes have the highest permeability (Fig. 14.9). At a given crystal size, an important control on porosity is the amount of calcite, which is believed to be recrystallized lime mud. Vuggy porosity is 5% or less. Different productive zones in the same field may have different dolomite textures,<sup>11</sup> suggesting that original sediment texture and chemistry were the main factors determining the distribution of crystal sizes.

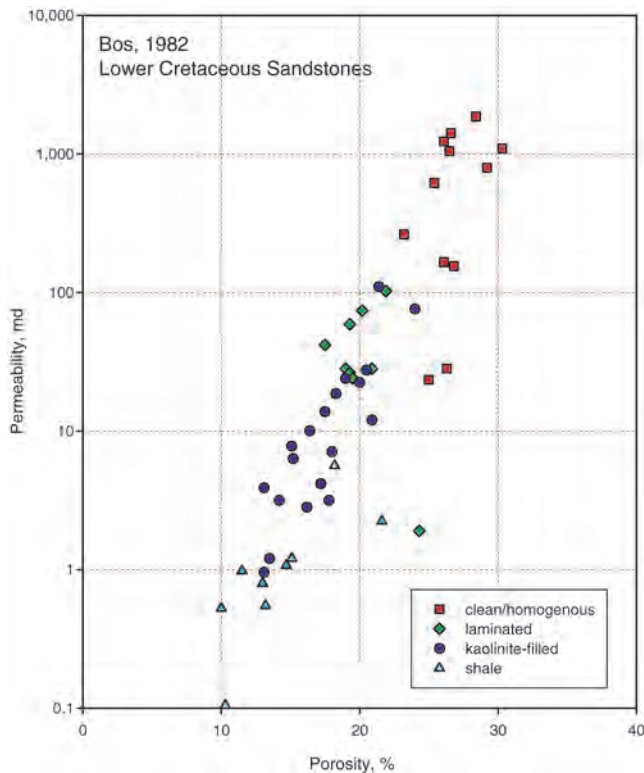
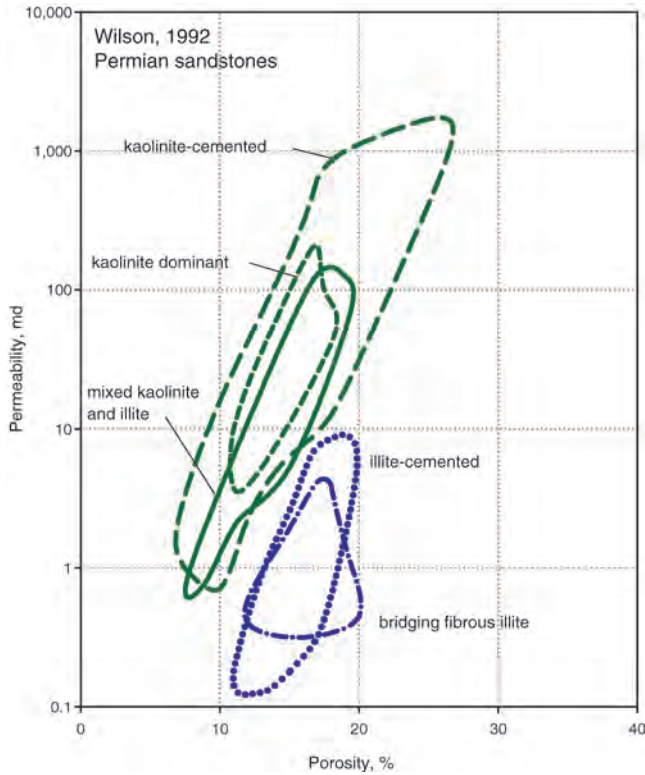


Fig. 14.7—Permeability/porosity data from a Lower Cretaceous sandstone from the North Sea from Bos.<sup>7</sup>

In the North Sea, oil is produced from Cretaceous and Tertiary chalks, even though permeability is <10 md (Fig. 14.10). From measurements of specific surface area, the equivalent grain diameter is computed to range from 1.0 to 2.7  $\mu\text{m}$ . As indicated in Fig. 14.10, the separation between the two chalks is attributed to specific surface area, which is higher in the lower-permeability Danian samples than in the Maastrichtian samples. The addition of pore space produces modest gains in permeability (low slopes for the two data sets in Fig. 14.10), from which one can infer that a significant fraction of the pore space is poorly connected or of very small size. Mortensen *et al.*<sup>12</sup> conclude that the intrafossil porosity behaves the same, in terms of flow, as interparticle porosity.

Lucia<sup>13</sup> found a size effect in limestones and dolostones, as evidenced by dolostone data shown in Fig. 14.11. To obtain petrophysically viable groupings, Lucia grouped all dolomitized grainstones with mud-dominated samples having large dolomite crystals and grouped dolomitized packstones with mud-dominated samples having medium-sized dolomite crystals (key in Fig. 14.11). He suggests that the plot can be used to estimate permeability of a nonvuggy carbonate rock if the porosity and particle size are known. He points out that the effect of vugs is to increase porosity but not alter permeability much. In Fig. 14.11 we can see the quasilinear log ( $k$ )- $\Phi$  relationship and the decline in slope (and  $k$ ) with decreasing grain size. It appears that the fundamental controls observed in the sandstones are also present in these selected carbonates, if care is exercised in categorizing the carbonates in terms of grain or crystal size.

**14.2.5 Summary: Empirical Trends.** Figs. 14.5 through 14.11 exhibit a linear or piecewise-linear relationship between  $\log(k)$  and  $\Phi$  as determined in many consolidated sandstones and in



**Fig. 14.8—Permeability/porosity data fields from wells penetrating the Permian (Rotliegend) sandstones of the southern North Sea, measured at ambient conditions, from Wilson.<sup>8</sup>**

carbonates if care is taken to isolate rock types. Such linear trends are often seen in samples from an individual rock unit or formation. These trends have the general form of

$$\log(k) = a + b\Phi \dots\dots\dots (14.3)$$

Eq. 14.3 is strictly an empirical relationship between  $\log(k)$  and  $\Phi$ . It is useful when data from an area of interest are available because  $\log(k)$  can be predicted simply from  $\Phi$ . However it masks the dependence of  $\log(k)$  on pore throat size and thereby obscures the physics of flow in porous media, as is shown in a subsequent section.

**14.3 Corrections to Core Measurements**

Before selecting a method of determining permeability in a specific reservoir, one must first be assured that the core measurements are appropriate for reservoir conditions. Sample collection, selection, and preparation are important steps in ensuring that the data set represents the geology at in-situ conditions; some precautions are discussed in the chapter on relative permeability and capillary pressure. Adjustments may be necessary for the type of test fluid and for pressure effects.

**14.3.1 Klinkenberg Effect.** The permeability of a sample to a gas varies with the molecular weight of the gas and the applied pressure, as a consequence of gas slippage at the pore wall. Klinkenberg<sup>14</sup> determined that liquid permeability ( $k_L$ ) is related to gas permeability ( $k_g$ ) by  $k_L = k_g / (1 + b/p)$ , where  $p$  is the mean flowing pressure and  $b$  is a constant for a particular gas in



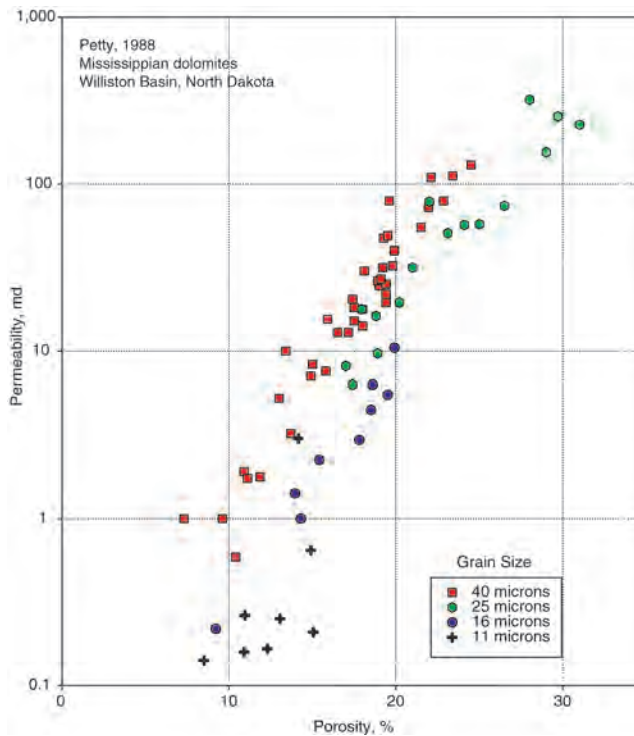


**Fig. 14.9—Permeability/porosity data from a sucrosic dolomite in the Williston basin of North Dakota, from Petty.<sup>11</sup>**

a given rock type. The correction parameter  $b$  is determined by conducting the test at several flowing pressures and extrapolating to infinite pressure. Alternatively, one can use an empirical correlation established by Jones<sup>15</sup> to estimate  $b$ . The correlation, with  $R^2$  of 0.90, is based on measurements on 384 samples (mostly sandstones) with permeabilities ranging from 0.01 to 2500 md. For helium,  $b_{\text{helium}} = 44.6(k/\Phi)^{-0.447}$  and for air,  $b_{\text{air}} = 0.35b_{\text{helium}}$ . The units of  $b$  are psi for permeability in units of md and porosity expressed as a fraction. Another empirical correlation was established by Jones and Owens<sup>16</sup> for tight gas sandstones with permeabilities ranging from 0.0001 to 10 md:  $b = 0.86k^{-0.33}$ , where  $b$  is in atm and  $k$  is in md. The Klinkenberg correction is quite important for low-permeability rocks and less important or unimportant for high-permeability rocks. The value of  $k_L$  obtained after applying the correction represents the permeability to a gas at infinite pressure or to a liquid that does not react with the component minerals of the rock.

**14.3.2 Pore Fluid Sensitivity.** The clays or other materials coating grain surfaces can be sensitive to pore fluid. This complicates the problem of describing permeability because flow properties depend not only on the lithology but also on pore fluid chemistry. This kind of reaction was seen in Fig. 13.6. Measured permeabilities on this sample as a function of salinity are shown in Fig. 14.12. Samples were obtained after drying and storage, and as a result, clays had collapsed (Fig. 13.6a). This collapsed state did not significantly change when the rock was saturated with very-high-salinity brine. As the pore fluid decreased in salinity, at a point near 30,000 ppm salt content, the clays expanded and effectively plugged the pore space. This result demonstrates the need to take special precautions in preserving and drying the core, as mentioned previously.

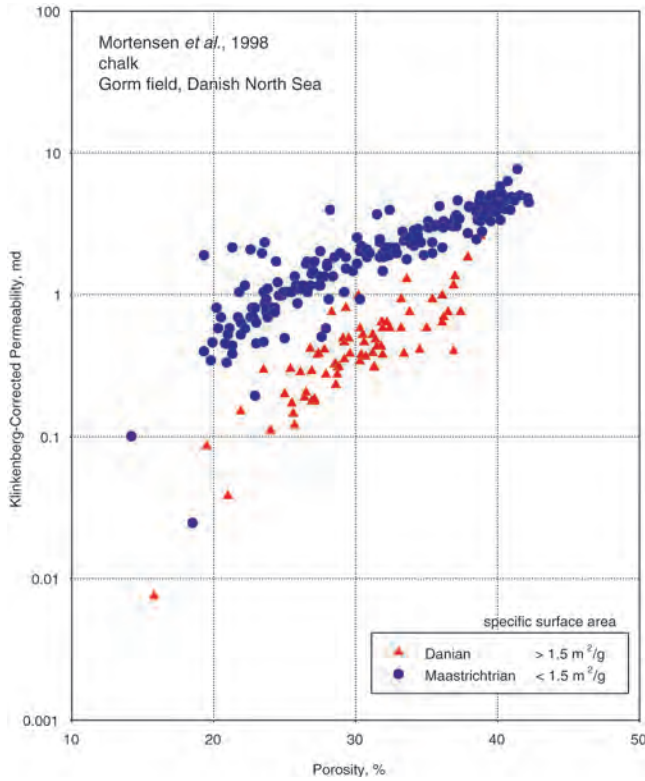


**Fig. 14.10—Permeability/porosity data from two chalk reservoirs of Cretaceous (Maastrichtian) and Paleocene (Danian) age, from Mortensen *et al.*<sup>12</sup>**

In low-permeability sandstones, permeability to water ( $k_w$ ) is systematically less than the Klinkenberg-corrected permeability ( $k_L$ ). A correction equation<sup>16</sup> based on >100 samples with a permeability range of  $0.0001 < k_L < 1$  md is  $k_w = k_L^{1.32}$ . The correction is only approximate, as scatter on a graph of  $k_w$  vs.  $k_L$  is high at  $k_L < 0.01$  md. Surprisingly, the sensitivity to brine concentration in low-permeability sandstones is reported to be less than that in high-permeability sandstones.<sup>16</sup>

**14.3.3 Pressure Dependence.** Permeabilities discussed so far were measured at constant effective pressure. However, as increasing pressure closes fractures and compresses the pore space, permeability will decrease. The magnitude of the change depends on the rock fabric. Weak, unconsolidated rocks will collapse easily, and the drop in permeability can be dramatic. As the rock becomes better consolidated, this pressure dependence decreases. On the other hand, even for tight rocks, as fractures are introduced and begin to dominate the fluid flow, this general trend is reversed and pressure dependence increases.

The pressure dependence can often be fit well with an empirical power law and negative exponential relation,

$$k(p_e) = k_o \exp(-bp_e^{1/2}), \dots\dots\dots (14.4)$$

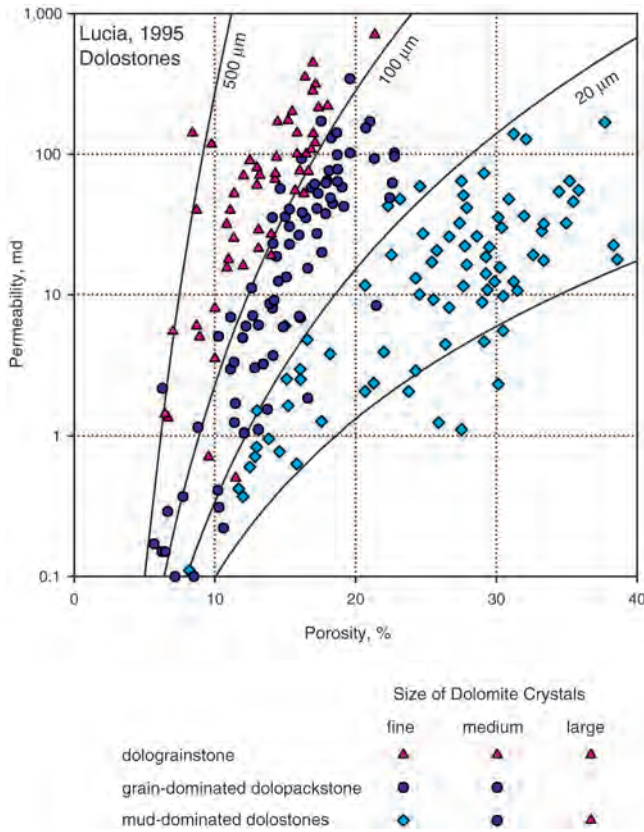


Fig. 14.11—Permeability/porosity data and classifications for selected nonvuggy dolostones from Lucia.<sup>13</sup>

where  $k(p_e)$  is the permeability measured at effective pressure  $p_e$ ,  $k_o$  is the permeability at zero pressure, and  $b$  is a parameter adjusted to fit each rock. This general relation for normalized permeability is shown in Fig. 14.13. A larger  $b$  factor yields a stronger pressure dependence.

In Fig. 14.14, sample D1452-281 seen previously in Fig. 13.1 is a clean sandstone with a high porosity of 35%. The pressure dependence is strong, as can be seen in Fig. 14.14. A  $b$  factor of 0.13 fits the general trend of the data (when pressure is expressed in MPa). In more compacted or cemented samples, such as in Fig. 14.15, with a lower porosity of 18%, the permeability decrease can be fit well with  $b=0.07$ . In general, as cementation increases, the pressure sensitivity declines, and the value of  $b$  approaches zero. On the other hand, in low-porosity, brittle rocks, flow often becomes fracture dominated. Because fractures are compliant and close easily with pressure, the pressure dependence of permeability again becomes high. In Fig. 14.16, permeability of a very-low-porosity (0.18%) crystalline rock is plotted on a logarithmic scale. Even though the absolute value of permeability is low to begin with,  $k$  drops to 1% of its unconfined value at 100 MPa, and the decline curve can be fit with a  $b$  factor of 0.6.

A more elaborate equation relating Klinkenberg-corrected permeability  $k$  to effective confining pressure  $p$  is<sup>17</sup>

$$\ln[k(1 + C)] = \ln k_o - a[1 - \exp(-p/P^*)],$$

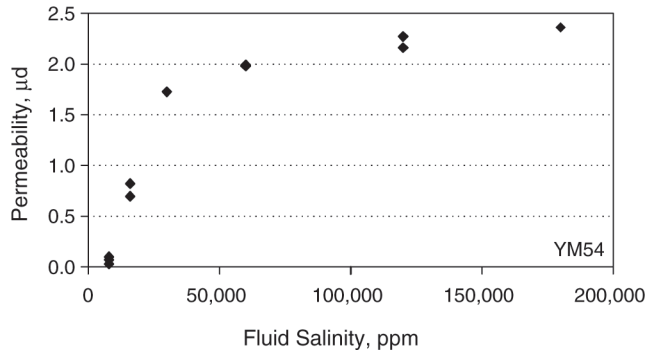


**Fig. 14.12—Permeability of a clay-rich sandstone sample containing fluid-sensitive smectitic clays decreases dramatically as pore fluid salinity decreases.**

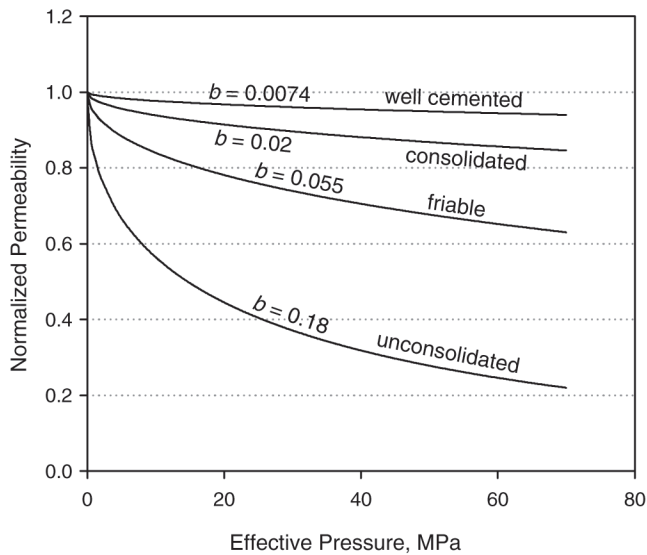


**Fig. 14.13—General pressure dependence of permeability of the form  $k(P_e) = k_o \exp(-bP_e^{1/2})$  in four sandstone samples that have undergone various levels of compaction and cementation.**

where  $k_o$ , the permeability at zero confining pressure, slope  $a$ , pressure coefficient  $P^*$ , and coefficient  $C$  are determined from experimental data. However, if constant values of  $C=3 \times 10^{-6}$  psi<sup>-1</sup> and  $P^*=3,000$  psi are used, errors are about 5%, and the two remaining coefficients,  $k_o$  and  $a$ , can be determined if  $k$  is determined at only two values of  $p$ . Jones<sup>17</sup> recommends the use of 1,500 and 5,000 psi, although very poorly consolidated samples may require that the higher value of  $p$  be reduced so as not to exceed the yield strength of the sample.

In practice, one may be required to correct values of  $k$  measured with air at ambient conditions to  $k$  for brine at reservoir conditions. The correction should be based on samples and conditions for the problem at hand. As a guide, Swanson<sup>18</sup> established a correction of  $k_{\text{brine}} = 0.292 k_{\text{air}}^{1.186}$  for a collection of 24 sandstone and 32 limestone samples ( $0.002 < k_{\text{brine}} < 400$  md), where  $k_{\text{brine}}$  was measured at 1,000-psi effective stress. Swanson's empirical equation appears to incorporate all three factors discussed above: the gas slippage effect, presence of brine as opposed to an inert fluid, and effect of stress.

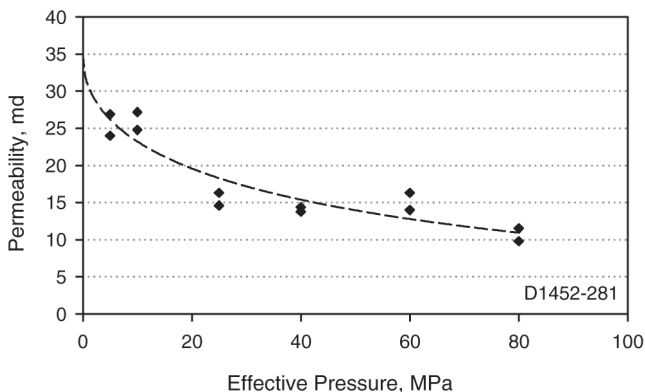


Fig. 14.14—Dependence of permeability on effective pressure in a high-porosity (35%) sample.

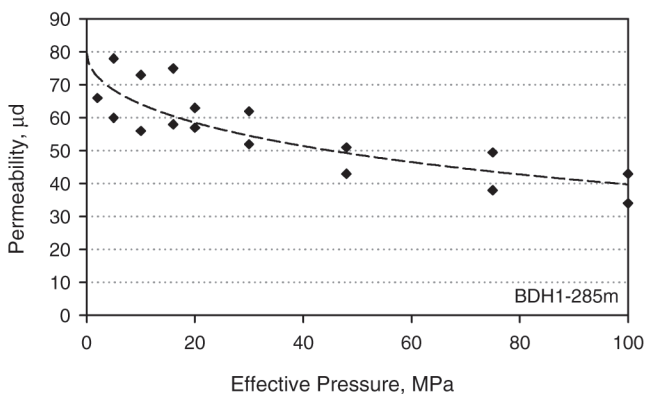


Fig. 14.15—Dependence of permeability on effective pressure in a medium-porosity (18%) sample.

### 14.4 Petrophysical Models

**14.4.1 Kozeny-Carman Equation.** The problem of predicting permeability is one of selecting a model expressing  $k$  in terms of other, measurable rock properties. Historically, the first approaches were based on a tube-like model of rock pore space known as the Kozeny-Carman relationship.<sup>19–22</sup> The derivation of this “equivalent channel model” has been reworked by Paterson<sup>23</sup> and Walsh and Brace.<sup>24</sup> The model assumes that flow through a porous medium can be represented by flow through a bundle of tubes of different radii. Within each tube, the flow rate is low enough that flow is laminar rather than turbulent. A tube is assigned a shape factor  $f$ , a dimensionless number between 1.7 and 3, and length  $L_a$  that is greater than the sample length  $L$ . The assumption is that each flow path forms a twisted, tortuous, yet independent route from one end of the rock to the other. The tortuosity is defined as  $\tau=(L_a/L)^2$ . From considerations of flow through tubes, the resulting equation is

$$k = \Phi r_h^2 / f \tau = \Phi / f \tau \Sigma_p^2, \dots\dots\dots (14.5a)$$

where the hydraulic radius,  $r_h$ , is defined as the reciprocal of  $\Sigma_p$ , the ratio of pore surface area to pore volume. The pore surface area normalized by a volume is often called the specific

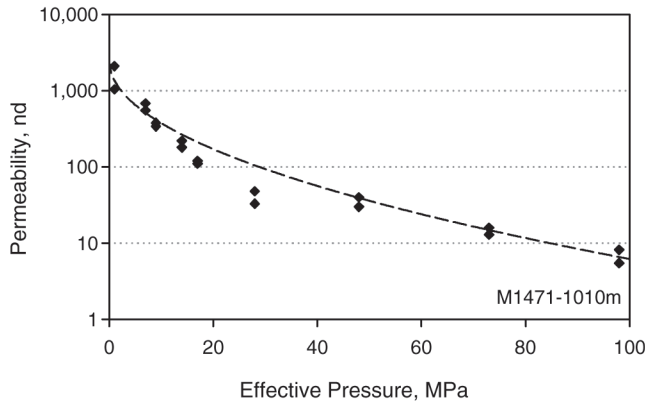


**Fig. 14.16—Permeability of a crystalline sample (porosity equals 0.18%) showing dependence on pressure. Note logarithmic scale for permeability.**

surface area. The form of Eq. 14.5a depends on which volume is used to normalize the pore surface area. If specific surface area is instead expressed as  $\Sigma_p$ , the ratio of pore surface area to rock volume, then Eq. 14.5a becomes

$$k = \Phi^3 / f \tau \Sigma_p^2 \dots \dots \dots (14.5b)$$

If specific surface area is defined as the ratio of pore surface area to grain volume,  $\Sigma_g$ , the expression is

$$k = \Phi^3 / f \tau \Sigma_g^2 (1 - \Phi)^2 \dots \dots \dots (14.5c)$$

Thus, the functional dependence of  $k$  on  $\Phi$ , which differs among Eqs. 14.5a, 14.5b, and 14.5c, depends on the definition of specific surface area.

Paterson<sup>23</sup> and Walsh and Brace<sup>24</sup> establish a relationship between electrical properties and tortuosity, determining that formation factor  $F = (L_a/L)^2 / \Phi = \tau / \Phi$ . They note that this expression differs from earlier incorrect formulations. With it, tortuosity can be eliminated from Eq. 14.5a to obtain

$$k = r_h^2 / f F = 1 / f F \Sigma_p^2 \dots \dots \dots (14.5d)$$

Different approaches to porous media theory apply the concept of tortuosity in different ways.<sup>25</sup> For purposes of this chapter, tortuosity is represented by electrical formation factor, as in Eq. 14.5d, or by porosity raised to an exponent.

As shown in the following sections, many models that relate  $k$  to a pore dimension  $r$  are derived, either in spirit or in rigor, from the Kozeny-Carman relationship, which recognizes explicitly the dependence of  $k$  on  $r^2$ .

**14.4.2 Models Based On Grain Size. Krumbein and Monk’s Equation.** Using experimental procedures that were later adopted by Beard and Weyl,<sup>3</sup> Krumbein and Monk<sup>26</sup> measured permeability in sandpacks of constant 40% porosity for specified size and sorting ranges. Analysis of their data, coupled with dimensional analysis of the definition of permeability, led to

$$k = 760d_g^2 \exp(-1.31\sigma_D), \dots\dots\dots (14.6)$$

where  $k$  is given in darcies,  $d_g$  is the geometric mean grain diameter (in mm), and  $\sigma_D$  is the standard deviation of grain diameter in phi units, where  $\text{phi} = -\log_2(d)$  and  $d$  is expressed in millimeters. Although the Krumbein and Monk equation is based on sandpacks of 40% porosity and does not include porosity as a parameter, Beard and Weyl showed that Eq. 14.6 fits their own data fairly well even though porosity of the Beard and Weyl samples ranges from 23% to 43%. In fact, because of difficulties in obtaining homogeneous sandpacks, Beard and Weyl chose to use computed  $k$  values from Eq. 14.6 rather than their measured data in tabulating values for fine and very fine samples with poor or very poor sorting. If Eq. 14.6 can predict  $k$  for a varying  $\Phi$  in unconsolidated sandpacks, then the exponential dependence on sorting must be adequate to describe all the effects associated with porosity reduction. In other words, both  $k$  and  $\Phi$  reduction pictured in Fig. 14.2 are due primarily to a decline in degree of sorting.

The laboratory studies of Krumbein and Monk<sup>26</sup> and Beard and Weyl<sup>3</sup> dealt with sieved sands from a common source, so such grain properties as angularity, sphericity, and surface texture did not vary much. Moreover, sorting was purposely controlled to be log normal. In situations where these ideal conditions are not met, other techniques must be invoked to predict permeability in unconsolidated sands. A disproportionate amount of fines can drastically reduce  $k$  in unconsolidated sands. Morrow *et al.*,<sup>27</sup> using statistical techniques on data from Gulf Coast sands, found that permeability correlated best with the logarithm of grain size times sorting if the fines fraction, taken to be <44  $\mu\text{m}$ , was accounted for.

**Berg’s Model.** An interesting model linking petrological variables—grain size, shape, and sorting—to permeability is that of Berg.<sup>28</sup> Berg considers “rectilinear pores,” defined as those pores that penetrate the solid without change in shape or direction, in various packings of spheres. Simple expressions for  $k$  are derived from each packing, which form a linear trend when  $\log(k)$  is plotted against  $\log(\Phi)$ . From these geometrical considerations comes an expression relating  $k$  to  $\Phi$  raised to a power and to the square of the grain diameter,

$$k = 5.1 \times 10^{-6} \Phi^{5.1} d^2 e^{-1.385p}, \dots\dots\dots (14.7a)$$

where  $k$  is given in darcies,  $d$  (in mm) is the median grain diameter,  $\Phi$  is porosity in percent, and  $p$ , a sorting term, is explained below. If permeability is expressed in millidarcies,  $d$  in micrometers, and  $\Phi$  as fractional porosity, this expression becomes

$$k = 80.8 \Phi^{5.1} d^2 e^{-1.385p} \dots\dots\dots (14.7b)$$

To account for a range of grain sizes, Berg considered two mixtures of spheres and assumed that  $k$  will be controlled primarily by the smaller grains. This introduces a sorting term  $p = P_{90} - P_{10}$ , called the percentile deviation, to account for the spread in grain size. The  $p$  term is expressed in phi units, where  $\text{phi} = -\log_2 d$  (in mm). For a sample with a median grain diameter of 0.177 mm, a value of 1.0 for  $p$  implies that 10% of the grains are >0.25 mm and 10% are <0.125 mm.

Berg’s expression (Eq. 14.7b) is illustrated in Fig. 14.17 for  $p=1$  and varying  $d$ . Permeability increases rapidly with increasing porosity, depending on  $\Phi$  to the fifth power, and the curves migrate downward and to the right with decreasing grain size. Nelson<sup>29</sup> finds that Fig. 14.17 is remarkably concordant with several published data sets. Berg’s model appears to be a usable means of estimating permeability in unconsolidated sands and in relatively clean consolidated quartzose rocks. This is true even though Berg did not expect his model to be applicable for porosity values <30%.

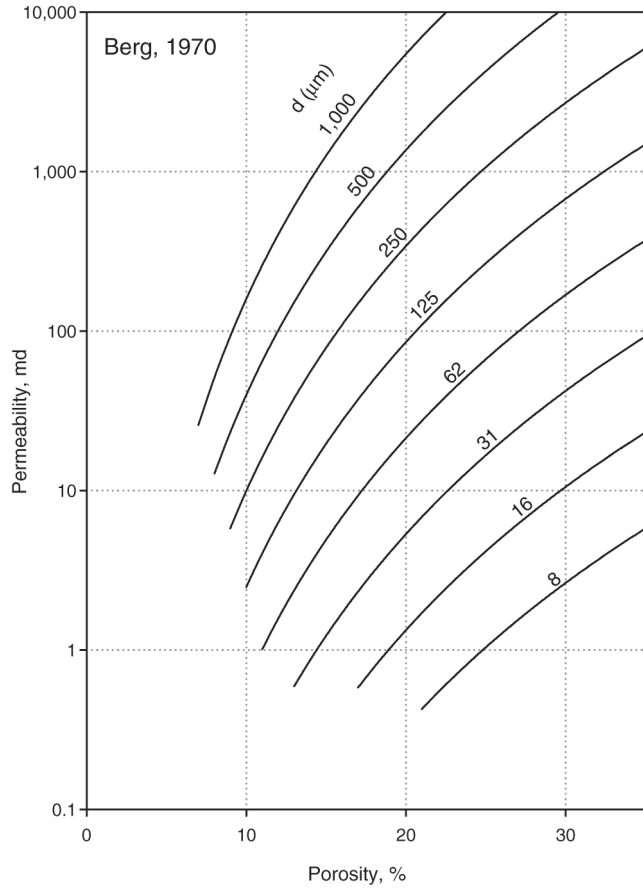


**Fig. 14.17—Theoretical model by Berg<sup>28</sup> relating permeability to porosity with varying median grain size (*d*).**

**Van Baaren’s Model.** Proceeding along more empirical lines, Van Baaren<sup>30</sup> obtains a result nearly identical to that of Berg. Van Baaren begins with the Kozeny-Carman expression of Eq. 14.5b and makes a series of substitutions (see summary by Nelson<sup>29</sup>) that result in

$$k = 10d_d^2\Phi^{3.64+m}C^{-3.64}, \dots\dots\dots (14.8a)$$

where  $d_d$  (in  $\mu\text{m}$ ) is the dominant grain size from petrological observation,  $m$  is the cementation exponent, and  $C$  is a sorting index that ranges from 0.7 for very well sorted to 1.0 for poorly sorted sandstones. Consequently, Eq. 14.8a can be used to estimate  $k$  from petrological observations on dominant grain diameter  $d_d$  and degree of sorting, along with a porosity estimate obtained from either core or logs.

Assuming that the dominant grain size  $d_d$  is equivalent to Berg’s median grain diameter  $d$ , then Eq. 14.8a is very similar in form to Eq. 14.7a. For example, a sorting parameter  $p=1$  in Berg’s Eq. 14.7b results in

$$k = 20.2d^2\Phi^{5.1}, \dots\dots\dots (14.7c)$$



where  $k$  is given in millidarcies, whereas for a well-sorted sandstone,  $C=0.84$  and Eq. 14.8a becomes

$$k = 18.8d_d^2\Phi^{3.64+m} \dots\dots\dots (14.8b)$$

Van Baaren's Eq. 14.8b is so close to Berg's Eq. 14.7c that a separate  $\log(k)$ - $\Phi$  plot is not warranted here. Van Baaren's expression is probably easier to use because the parameters are directly related to practical petrological variables. Both models display a porosity exponent  $>5$ , and both are compatible with the data of Beard and Weyl on unconsolidated sands in that  $k$  increases with the square of grain size.

**14.4.3 Models With Mineralogical Factors.** Several models have been devised to accommodate the influence of mineralogical textures on  $k$ . The first two described below are based on the Kozeny-Carman equation; the third uses a network topology that is independent of the Kozeny-Carman equation.

Herron<sup>31</sup> uses Eq. 14.5c as a starting point for a model using mineralogical abundances in place of specific surface area. He obtains

$$k = A_f[\Phi^3/(1-\Phi)^2]\exp(\Sigma B_i M_i), \dots\dots\dots (14.9)$$

where  $M_i$  is the weight fraction of each mineral component in the solid rock and  $B_i$  is a constant for each mineral, so that quartz produces high  $k$  and clay minerals produce low  $k$ . Mineral abundances are obtained by performing an element-to-mineral transform on data from a logging tool that measures chemical elemental concentrations by means of neutron-induced gamma ray spectroscopy. The coefficient  $A_f$  is a textural maturity indicator; it can be used to reflect the amount of feldspar alteration to clay minerals. Nelson<sup>29</sup> gives further details on the model.

Panda and Lake<sup>32</sup> extended the Kozeny-Carman expression to include the effect of grain-size sorting. They assume a sandpack of spherical grains having a log-normal distribution of grain diameters  $d$ , characterized by mean diameter, standard deviation, and skewness. Their expression is based on Eq. 14.5c, substituting  $\Sigma_g=6/D$  and incorporating an additional term including standard deviation and skewness. With the additional term accounting for sorting, their extended model agrees well with Beard and Weyl's data for sandpacks but overpredicts  $k$  in consolidated sandstones. To make the model applicable to consolidated sandstones, three types of cement filling the pore space were considered<sup>33</sup>: pore-bridging, pore-lining, and pore-filling cement. Their resulting equation for  $k$  includes the sum of surface areas contributed by each of the cement geometries and a tortuosity factor that is a function of cement type, as well as statistical terms describing the log-normal distribution of grain diameters  $d$ .

Bryant *et al.*<sup>34</sup> and Cade *et al.*<sup>35</sup> performed numerical modeling on a pack of (initially) equally sized spheres in a geometry based on a laboratory random pack. Permeability is computed directly by considering flow across the faces of individual linked tetrahedra; thus, the method is independent of the Kozeny-Carman equation. Their method simulates a quartz system in which all surfaces participate in compaction and cementation processes, causing  $k$  and  $\Phi$  to decrease along a characteristic curve in  $\log(k)$ - $\Phi$  space. At some point in this process, clay minerals are introduced in grain-rimming or pore-filling geometries, and  $k$  decreases more sharply with a continuing decrease in  $\Phi$ . The resulting computed curve in  $\log(k)$ - $\Phi$  space tracks the effects of progressive diagenesis of a single pack as burial progresses.

**14.4.4 Models Based on Surface Area and Water Saturation.** Two ideas inherent in Eq. 14.5 are important for later developments: the dependence of  $k$  on a power of porosity and on the

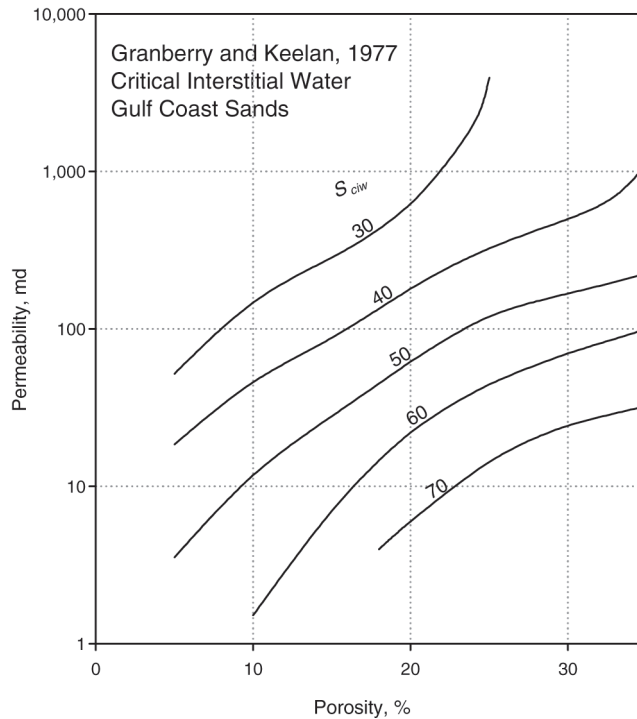


**Fig. 14.18—Empirical chart relating permeability to porosity with critical interstitial water  $S_{ciw}$  as a parameter, after Granberry and Keelan.<sup>36</sup>**

inverse square of surface area. Eq. 14.5 has been used as a starting point for predicting permeability from well log data by assuming that residual water saturation is proportional to specific surface area,  $\Sigma$ .

**Granberry and Keelan's Chart.** Granberry and Keelan<sup>36</sup> published a set of curves relating permeability, porosity, and “critical water” saturation ( $S_{ciw}$ ) for Gulf Coast Tertiary sands that frequently are poorly consolidated. Their chart, originally presented with  $S_{ciw}$  as a function of permeability with porosity as a parameter, is transposed into  $\log(k)$ - $\Phi$  coordinates in Fig. 14.18. The  $S_{ciw}$  parameter is taken from the “knee” of a capillary pressure curve and is greater than irreducible water saturation,  $S_{wi}$ . It is said that if the water saturation in the formation is less than this critical value, the well will produce water free. Because  $S_{ciw}$  is taken from the capillary pressure curve, it is a function of the size of interconnected pores. Fig. 14.18 cannot be used to estimate permeability from porosity and water saturation as determined from well logs because it reflects only the critical water saturation. It was determined from reservoirs in which oil viscosity was approximately twice that of water and requires adjustment for low- or high-gravity oils.

**Timur's Model.** Timur<sup>22</sup> used a database of 155 sandstone samples from three oil fields (Fig. 14.19). The three sandstones exhibit varying degrees of sorting, consolidation, and ranges of porosity. Timur measured irreducible water saturation ( $S_{wi}$ ) using a centrifuge and then held  $k$  proportional to  $S_{wi}^{-2}$  in the general power-law relationship,

$$k = a \Phi^b S_{wi}^{-2} \dots \dots \dots (14.10)$$

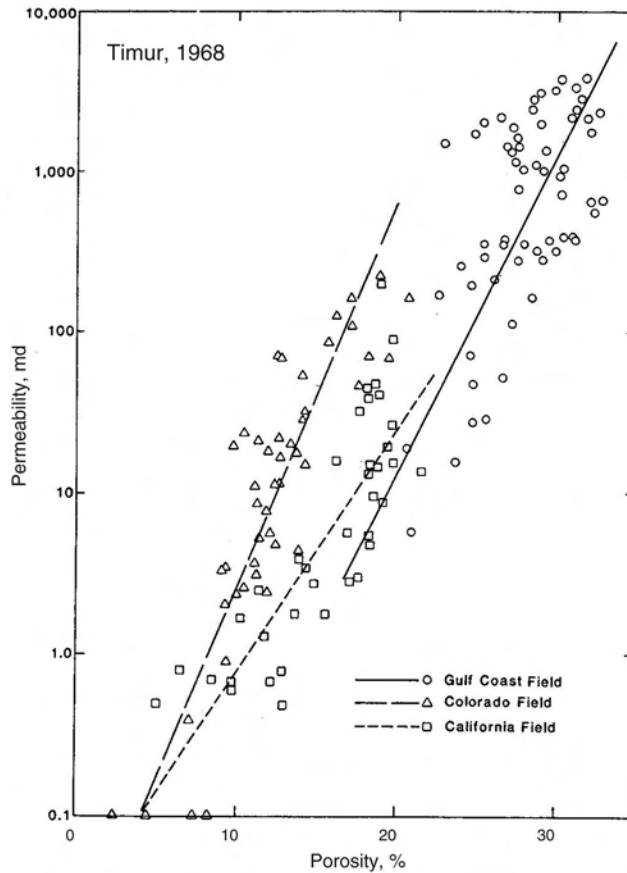


Fig. 14.19—Permeability/porosity data from three U.S. oil fields by Timur.<sup>22</sup>

Coefficients  $a$  and  $b$  were determined statistically. Timur's statistical results show that the exponent  $b$  can range between 3 and 5 and still give reasonable results. Results for  $b=4.4$  produced a fit somewhat better than other values; it was obtained by taking the logarithm of both sides of Eq. 14.6 and testing the correlation coefficient with respect to  $\Phi^b/S_{wi}^2$ . For  $b=4.4$ , the value of  $a$  is 0.136 if  $\Phi$  and  $S_{wi}$  are in percent and 8,581 if  $\Phi$  and  $S_{wi}$  are fractional values. There is no theoretical basis for the substitution of  $S_{wi}$  for specific surface area  $\Sigma$ , so although the form of Eq. 14.10 is similar to that of Eq. 14.5, it is strictly an empirical relationship. The effectiveness of Eq. 14.10 as a predictor of permeability is shown in Fig. 14.20, and its form on a  $\log_{10}(k)$ - $\Phi$  plot is shown in Fig. 14.21.

It is not easy to apply Eq. 14.10, which is based totally on core data, to an oil reservoir.<sup>37</sup> The  $S_{wi}$  core data used to establish Eq. 14.10 were obtained for a fixed value of capillary pressure ( $P_c$ ). In a reservoir,  $P_c$  varies with height, and because  $S_{wi}$  varies with  $P_c$ , it is necessary to assume a functional dependence of  $S_{wi}$  on  $P_c$ . There are also some practical difficulties in establishing the coefficients  $a$  and  $b$  in a reservoir in which the oil/water contact cuts across lithologies because of regional dip or structure. In particular, within the transition zone, only part of the water is irreducible ( $S_{wi}$ ); the remainder is movable. Thus, a log-based estimate of saturation immediately above the oil/water contact will overestimate  $S_{wi}$ .

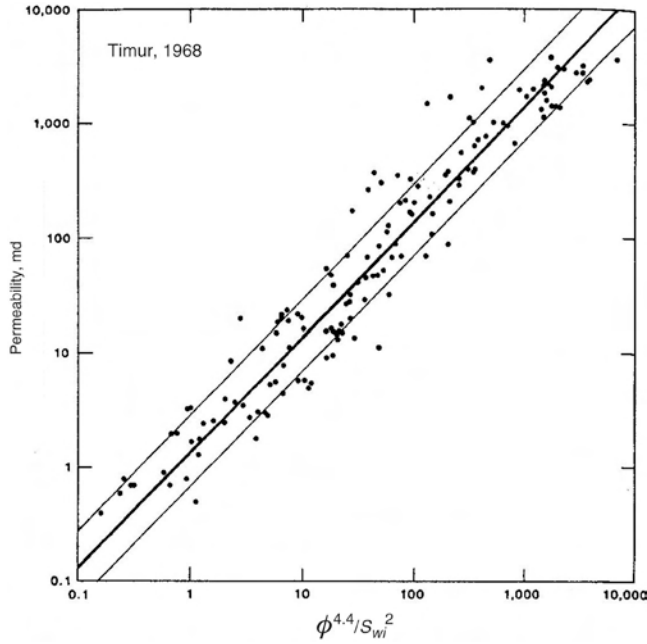


Fig. 14.20—Permeability data from three U.S. oil fields as a function of  $\Phi^{4.4}/S_{wi}^2$ , after Timur.<sup>22</sup> Two bounding lines represent the standard error band that includes 68% of the sample points.

**Dual-Water Model.** An algorithm discussed by Ahmed *et al.*<sup>38</sup> is attributed to Coates. An extension of Eq. 14.10 and Fig. 14.21, it assumes that permeability declines to zero as  $S_{wi}$  increases to fill the entire pore space:

$$k = [100\Phi_e^2(1 - S_{wi})/S_{wi}]^2 \dots\dots\dots (14.11)$$

A further refinement incorporates the presence of clay minerals and is based on the dual-water model. It requires log-based estimates of the total porosity ( $\Phi_t$ ) and either effective porosity ( $\Phi_e$ ) or bound water saturation ( $S_{bw}$ ). Effective porosity is defined as  $\Phi_e = \Phi_t(1 - S_{bw})$ . The fractional volume of bound water,  $V_{bw} = S_{bw}\Phi_t$ , is computed, and an estimate of a parameter  $V_{bi} = S_{wi}\Phi_t$  called the (fractional) bulk volume irreducible water in clean wet rock must also be provided. Then, computed as a function of depth is the total immovable water,

$$V_{wt} = V_{bi}(1 - S_{bw}) + V_{bw}, \dots\dots\dots (14.12)$$

and the permeability,

$$k = [100\Phi_e^2(\Phi_t - V_{wt})/V_{wt}]^2 \dots\dots\dots (14.13)$$

The algorithm of Eqs. 14.12 and 14.13 uses a pair of parameters,  $V_{bi}$  and  $V_{bw}$ , which in effect sweep out a broad region of the  $\log(k)$ - $\Phi$  crossplot (Fig. 14.22). For the solid curves,  $V_{bw}$  has been set to 0.0 as if the rock were entirely clay free. As irreducible water  $V_{bi}$  increases, the curves shift downward and to the right, into the regime populated by fine-grained rock. The dashed curve is drawn for  $V_{bw}$  and  $V_{bi}$  each equal to 0.05, thereby representing one of a

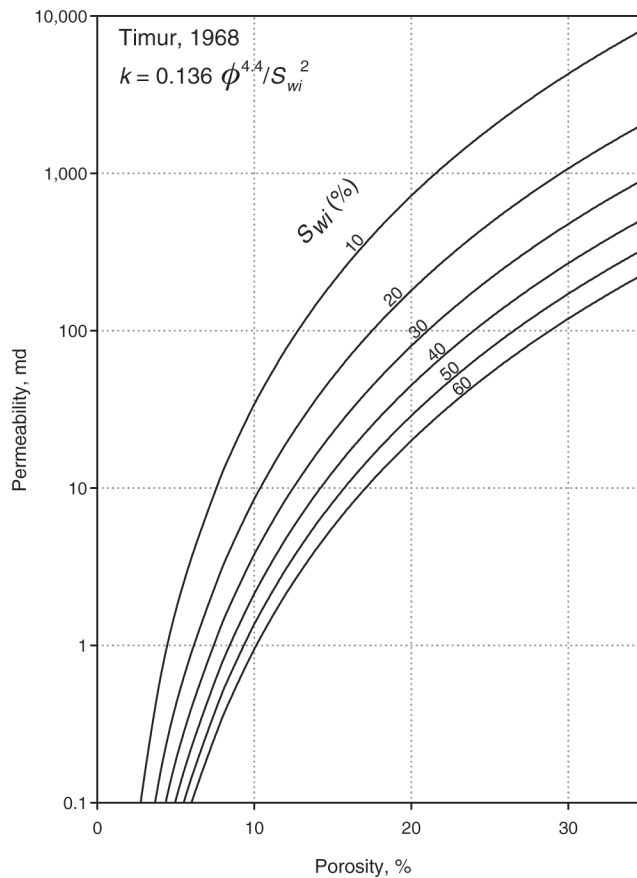


Fig. 14.21—Permeability/porosity relationship with irreducible water saturation as a parameter, after Timur.<sup>22</sup>

second family of curves for a fine-grained dirty sandstone. Note how  $S_{bw}$  increases with decreasing  $\Phi$ .

This algorithm produces reasonable results in sandstones if  $V_{bi}$  is chosen judiciously. One difficulty is choosing a value for  $V_{bi}$  in coarse-grained and gravel-bearing sandstones.

**“Tight” Sandstones.** Predicting permeability becomes much more difficult in formations with small grain size and an abundance of clay minerals. Such rocks are called “tight gas sands” or “submillidarcy reservoirs” (see example in Fig. 14.1). Kukul and Simons<sup>39</sup> show that the Timur equation produces  $k$  values much too high in such formations and establish some predictive equations that decrease the porosity by multiplying  $\Phi$  by  $1 - V_{cl}$ , where  $V_{cl}$  is the clay fraction. They show that the water saturation term  $S_{wi}$  is not so important in these high-clay rocks. Although their predictive equation is a welcome improvement, the scatter shows the difficulty in dealing with such low-porosity systems.

**Nuclear Magnetic Resonance.** Eq. 14.5a indicates that other measures of specific surface area could be correlated with permeability. A study by Sen *et al.*<sup>40</sup> provides laboratory data on 100 sandstone samples on exchange cation molarity ( $Q_v$ ), nuclear magnetic resonance (NMR) longitudinal decay time ( $t_1$ ), and pore-surface-area-to-pore-volume ratio ( $\Sigma_p$ ) from the gas adsorption method. Borgia *et al.*<sup>41</sup> provide data on  $\Sigma_p$  and  $t_1$  on 32 samples. Both studies include measurements of  $k$ ,  $\Phi$ , and formation factor ( $F$ ) on their samples. Both sample suites are made

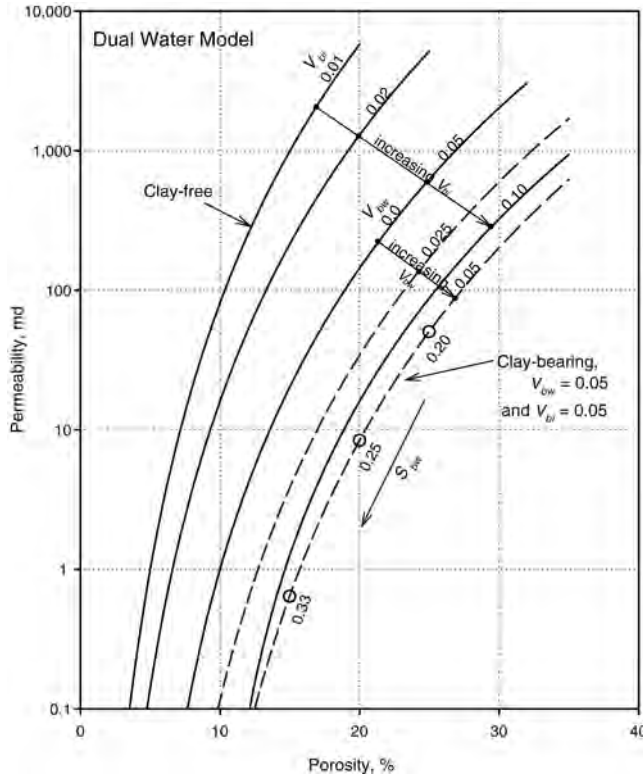


**Fig. 14.22—Permeability/porosity relationship based on the dual-water model incorporating irreducible ( $V_{bf}$ ) and bound water ( $V_{bw}$ ) as parameters. Four solid curves show effect of increasing  $V_{bf}$  with  $V_{bw}=0.0$ . Two dashed curves show effect of increasing  $V_{bw}$  with  $V_{bf}=0.05$ .**

up of samples from different formations, so the  $\log(k)-\Phi$  plots exhibit scatter, as shown by [Fig. 14.23](#).

Both groups of experimenters found that  $k$  correlated best with measures of specific surface when it formed a product with  $\Phi^m$  or  $\Phi^2$ . For example, Sen *et al.*<sup>40</sup> found  $k$  to be strongly correlated ( $R$  around 0.9) with  $(\Phi^m/\Sigma_p)^{2.08}$ , with  $(\Phi^m t_1)^{2.15}$ , and with  $(\Phi^m/Q_v)^{2.11}$ . Two of these correlations are shown as insets in [Fig. 14.23](#). Borgia *et al.*<sup>41</sup> did not incorporate  $m$  into their regression equations but found  $k$  to be best correlated with  $(\Phi^4/\Sigma_p^2)^{0.76}$  and with  $(\Phi^4 t_{12})^{0.72}$ . As an example of these statistical fits, the expression from Sen *et al.*,<sup>40</sup>

$$k = 0.794(\Phi^m t_1)^{2.15}, \dots\dots\dots (14.14)$$

where  $k$  is in millidarcies,  $t_1$  is in milliseconds, and  $\Phi$  is fractional porosity, is plotted in [Fig. 14.24](#). Because the porosity exponent is very close to that established by Timur ([Eq. 14.9](#)), the curves in [Fig. 14.24](#) are quite similar to those in [Fig. 14.21](#).

Later work showed that the transverse decay time  $t_2$ , which is a more practical parameter to detect with a logging tool than  $t_1$ , could also be used to estimate permeability (consult [References 21, 42, and 43](#) for further details on NMR):

$$k = c\Phi^4 t_{2gm}^2, \dots\dots\dots (14.15)$$

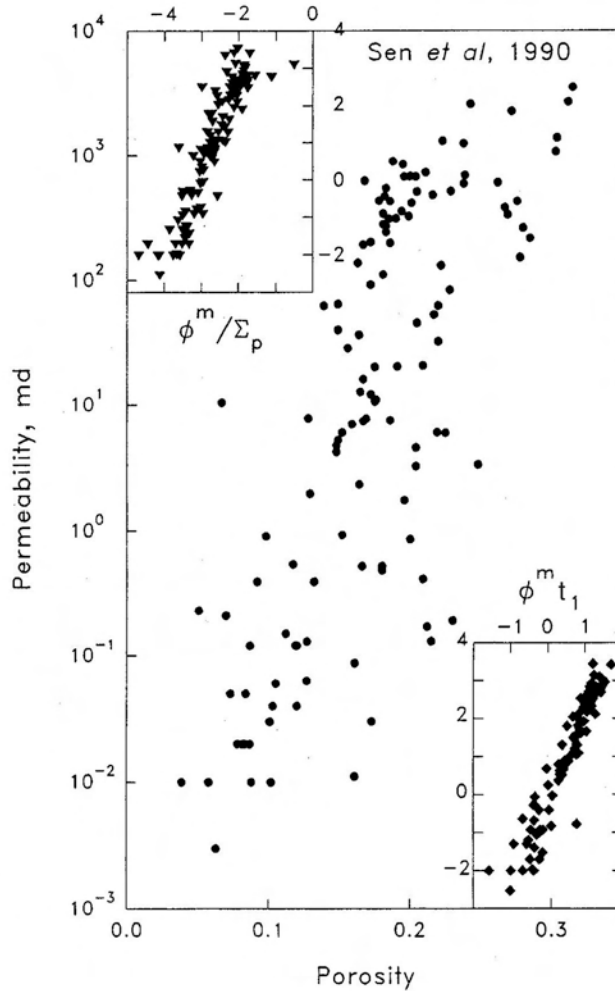


Fig. 14.23—Permeability/porosity data from Sen *et al.*<sup>40</sup> Inserts show  $\log(k)$  plotted against  $\log(\Phi^m/\Sigma_p)$  and against  $\log(\Phi^m t_1)$ .

where  $k$  is in millidarcies,  $t_{2gm}$  is the geometric mean of  $t_2$  in milliseconds, and  $c=4.5$  in sandstones and 0.1 in carbonates.<sup>43</sup> The value of  $k$  obtained from Eq. 14.15 is referred to as  $k_{SDR}$ . Better results are obtained if a cutoff can be selected for  $t_{2L}$  so that only the pores contributing to permeability are included. Kenyon<sup>43</sup> notes that the NMR measurement is inherently responsive to pore size, whereas permeability depends on pore throat size. He suggests that the experimentally determined  $\Phi^4$  dependence somehow accounts for the way in which the ratio (pore throat size to pore size) varies with porosity.

The Coates equation for estimating permeability is

$$k = c\Phi^4(V_{ffi}/V_{bvi})^2, \dots\dots\dots (14.16)$$

where  $k$  is in millidarcies,  $V_{bvi}$  is the bulk volume irreducible fluid fraction,  $V_{ffi}$  is the free fluid fraction and is equal to  $\Phi - V_{bvi}$ , and porosity  $\Phi$  is taken from the NMR tool.<sup>42,44</sup> Eq. 14.16 closely resembles Eq. 14.11, which is written in terms of irreducible water saturation;  $V_{bvi}$  is

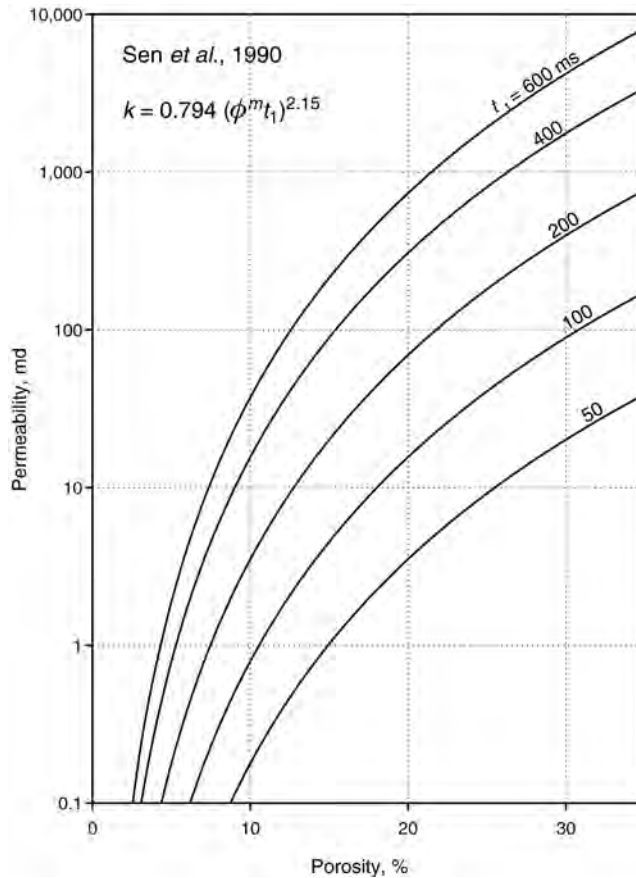


Fig. 14.24—Empirical relationship among permeability, porosity, and  $t_1$  from NMR measurement by Sen et al.<sup>40</sup>

computed from the portion of the  $t_2$  spectrum with the smallest times. Except for the porosity term  $\Phi^4$ , there is little obvious resemblance between Eqs. 14.15 and 14.16. However, Sigal<sup>45</sup> argues that a  $t_2$  cutoff time is implicit in Eq. 14.16 and that its value is incorporated in the constant  $c$ . Even so, the two equations are not equivalent because the two choices of  $t_2$  result in different weightings of the pore size distribution spectrum. Sigal relates the two choices of  $t_2$ , one explicit in Eq. 14.15 and the other implicit in Eq. 14.16, for different distributions of  $t_2$  and for several experimental data sets.

As Sigal<sup>45</sup> points out, the problem of selecting a value of  $t_2$  from NMR data is analogous to the problem of selecting a value of  $R$  from capillary pressure data (which is reviewed in the next section): One must capture the length scale appropriate to the estimation of permeability.

**Summary.** Timur's equation and its corresponding chart offer a viable method of permeability estimation in which porosity and irreducible water saturation can be estimated. Difficulties arise if there is uncertainty in  $S_{wi}$ , as there is within an extensive transition zone. The dual-water predictor is an interesting embellishment that can include a clay content parameter. Laboratory data show that, when combined with  $\Phi^m$ , specific surface area, cation exchange molarity, and NMR decay time all correlate well with  $k$ . Because it responds to the pore size spectrum, NMR is a particularly effective tool in obtaining log-based estimates of permeability.



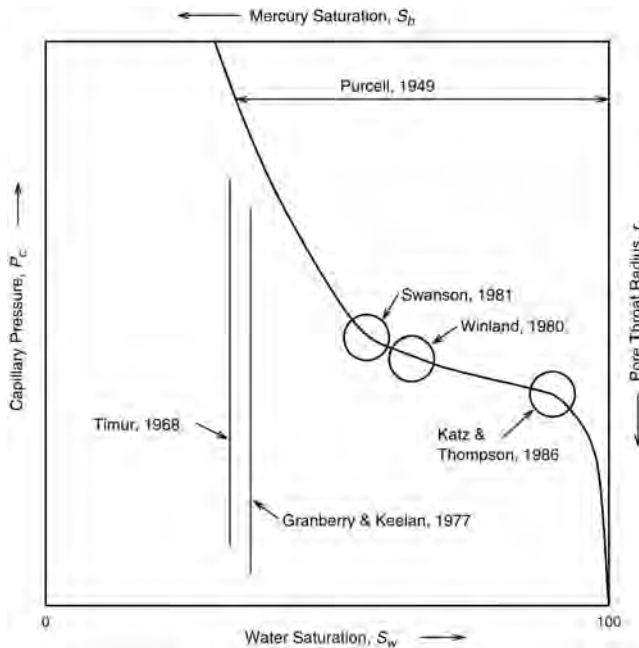


Fig. 14.25—Capillary pressure curve (idealized) showing measures used by different authors for determination of characteristic pore dimension.

**14.4.5 Models Based on Pore Dimension. Capillary Pressure and Pore Size.** Of course, the dimension of interconnected pores plays a major role in determining permeability (Eq. 14.5a). Thus, all the methods of estimating permeability discussed so far are indirect methods. A viable direct method requires both adequate theoretical underpinnings relating pore throat dimension to permeability and experimental determination of the critical pore dimension parameters. Many workers have made use of the capillary pressure curve, obtained experimentally by injecting mercury into a dried sample. As mercury pressure is increased, more mercury is forced into progressively smaller pores in the rock, and the resident pore fluid (air) is expelled. A length  $r$ , usually referred to as the pore throat radius, is related to the injection pressure by the Washburn equation,

$$P_c = 2\sigma\cos\theta/r, \dots\dots\dots (14.17)$$

where  $\sigma$  is the interfacial tension and  $\theta$  is the wetting angle. The injection process can be visualized by examining the idealized capillary pressure curve of Fig. 14.25. A finite pressure is required to inject mercury into a 100% water-saturated sample (right side of Fig. 14.25). At the first inflection point (entry pressure), mercury occupies only a small fraction of the pore volume containing the largest pores. Next, much of the pore space becomes filled with mercury with a comparatively slight increase in pressure (progressing from the circle labeled Katz and Thompson to the circle labeled Swanson in Fig. 14.25). Finally, large pressure increases are required to force more mercury into the smallest pores (steep curve to left of Swanson circle).

Many authors have linked capillary pressure curves to permeability. Purcell<sup>46</sup> derived an expression relating  $k$  to an integral of  $P_c^{-2}$  over the entire saturation span, achieving a good match with core data. The relationships established by Timur<sup>22</sup> and Granberry and Keelan,<sup>36</sup> discussed previously, are represented at low water saturation in Fig. 14.25. Contributions by

Swanson,<sup>18</sup> Winland,<sup>47</sup> and Katz and Thompson,<sup>48</sup> symbolized by the circles in Fig. 14.25, are reviewed next.

**Swanson’s Equation.** Swanson<sup>18</sup> provides a method of determining air and brine permeabilities from a single point on the capillary pressure curve. His regression relationships are based on permeability and capillary pressure data on 203 sandstone samples from 41 formations and 116 carbonates from 33 formations. His method picks the maximum ratio of mercury saturation to pressure,  $(S_b/P_c)_{\max}$ , from the capillary pressure curve, arguing that at this point all the connected space is filled with mercury and “this capillary pressure corresponds to pore sizes effectively interconnecting the total major pore system and, thus, those that dominate fluid flow.” From linear regression, Swanson obtains simple equations of the form,

$$k = a(S_b/P_c)_{\max}^c, \dots\dots\dots (14.18)$$

where the constants  $a$  and  $c$  depend on rock type (carbonate vs. sandstone) and fluid type (air or brine). For carbonates and sandstones combined,  $c=2.005$ . Because  $S_b$  is defined as the mercury saturation as percent of bulk volume, it must be proportional to  $\Phi(1-S_w)$ ; through Eq. 14.17,  $P_c$  can be linked with a pore throat radius  $r_{\text{apex}}$ . Thus, Swanson’s result shows that  $k$  is proportional to  $[\Phi(1-S_{wi})r_{\text{apex}}]^2$ , again demonstrating the dependence of  $k$  on the square of a pore throat size.

**Winland’s Equation and Pittman’s Results.** An empirical equation relating permeability, porosity, and a capillary pressure parameter is referred to as Winland’s equation.<sup>47,49</sup> Based on laboratory measurements on 312 samples, Winland’s regression equation is

$$\log r_{35} = 0.732 + 0.588 \log k - 0.8641 \log \Phi, \dots\dots\dots (14.19)$$

where  $r_{35}$  is the pore throat radius at 35% mercury saturation,  $k$  is air permeability, and  $\Phi$  is porosity in percent. A  $\log(k)\text{-}\Phi$  plot based on Eq. 14.19 and showing five characteristic lines for pore throat radius is shown in Fig. 14.26. Note that at a given porosity, permeability increases roughly as the square of the pore throat radius. And for a given throat size, the dependence of permeability on porosity is slightly less than  $\Phi^2$ . Kolodzie<sup>47</sup> states that a pore throat size of 0.5  $\mu\text{m}$  was used as a cutoff for reserves determinations, in preference to the use of  $k$  or  $\Phi$ . Hartmann and Coalson<sup>50</sup> also present Winland’s equation in the same format as Fig. 14.26. They state that  $r_{35}$  is a function of both entry size and pore throat sorting and is a good measure of the largest connected pore throats in a rock with intergranular porosity.

Martin *et al.*<sup>51</sup> used the  $r_{35}$  parameter, along with other petrophysical, geological, and engineering data, to identify flow units in five carbonate reservoirs. With Eq. 14.19,  $r_{35}$  can be computed from permeability and porosity measurements on core samples. Flow units are grouped by the size of pore throats using the designations of megaport, macroport, mesoport, and microport shown in Fig. 14.26. A completion analysis for the different  $r_{35}$  size ranges in a reservoir of medium thickness and medium gravity oil yielded the following: megaport, tens of thousands of barrels of oil per day; macroport, thousands; mesoport, hundreds; and microport, nonreservoir. After flow units are identified, well logs and sequence stratigraphy are used to identify zones with similar properties where no core data exist. The method works well in carbonates where flow is controlled by intergranular, intercrystalline, or interparticle pore space but not so well if fractures or vugs are present.

Pittman<sup>49</sup> sheds additional light on Winland’s equation, linking it to Swanson’s results. Pittman used a set of 202 sandstone samples from 14 formations on which  $k$ ,  $\Phi$ , and mercury injection data had been obtained. Using Eq. 14.17, he associated a pore size  $r_{\text{apex}}$  with the cap-

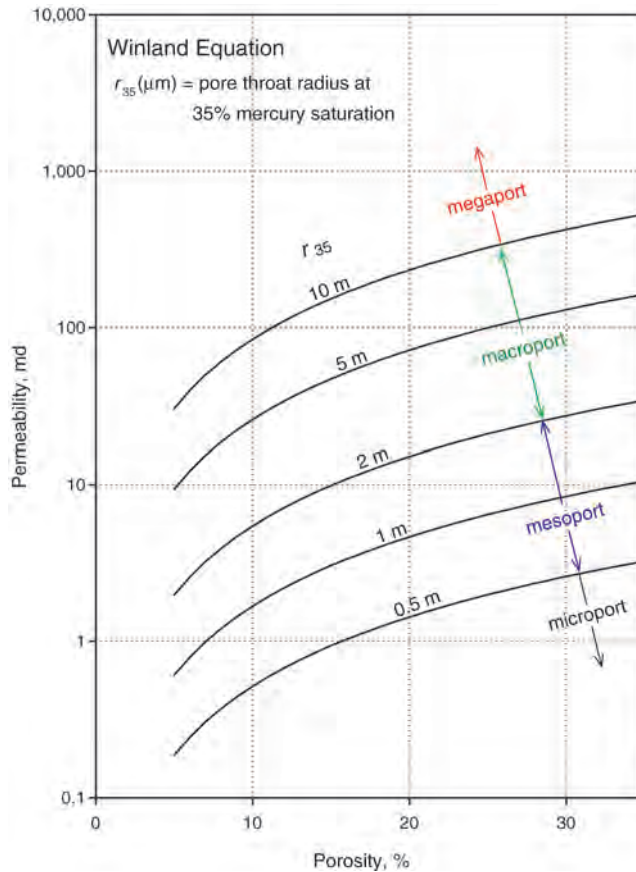


Fig. 14.26—Empirical model based on regression attributed to Winland, from Kolodzie.<sup>47</sup> Labels for four ranges of  $r_{35}$  are taken from Martin *et al.*<sup>51</sup>

illary pressure,  $P_c$ , determined by Swanson’s method and found that the mean value of  $r_{apex}$  has a mercury saturation of 36%. That is, on a statistical basis, the points denoted by circles labeled Swanson and Winland in Fig. 14.25 are practically identical, and the two methods are sampling the same fraction of the pore space.

Pittman<sup>49</sup> also established regression equations for pore aperture sizes ranging from 10% to 75% mercury saturation. His expressions have been rearranged and displayed in Table 14.1 to show the exponents of  $r$  and  $\Phi$  required to predict  $k$ . (Because  $r$  was used as the dependent variable in Pittman’s regressions, the coefficients in Table 14.1 differ somewhat from what would be obtained if  $k$  were the dependent variable; however the changes would not invalidate the point of this discussion.) Note that the  $r$  exponent decreases with increasing mercury saturation, while the  $\Phi$  exponent increases. That is, the porosity term contributes relatively less to  $k$  than does  $r$  for mercury saturation values <35%. In fact, Pittman noted that the porosity term was statistically insignificant for  $r_{10}$  through  $r_{35}$ .

**Katz and Thompson’s Equation.** Another investigation on the influence of pore structure on flow properties comes from Katz and Thompson<sup>48</sup> and Thompson *et al.*<sup>52</sup> They use percolation theory to derive a deceptively simple relationship,

$$k = (1/226)l_c^2 \sigma / \sigma_o, \dots\dots\dots (14.20a)$$

**TABLE 14.1—PREDICTIVE EQUATIONS FOR PERMEABILITY BASED ON REGRESSION EQUATIONS BY PITTMAN<sup>49</sup> AS A FUNCTION OF FRACTIONAL POROSITY AND PORE THROAT RADIUS AS MERCURY SATURATION VARIES FROM 10 TO 70%**

Saturation, %	Predictive Equation
10	$k = 4.19 r_{10}^{2.00} \phi^{0.770}$
20	$k = 5.59 r_{20}^{1.93} \phi^{0.584}$
30	$k = 13.9 r_{30}^{1.82} \phi^{0.768}$
40	$k = 52.3 r_{40}^{1.72} \phi^{1.17}$
50	$k = 405 r_{50}^{1.66} \phi^{1.93}$
60	$k = 2,820 r_{60}^{1.54} \phi^{2.57}$
70	$k = 53,400 r_{70}^{1.59} \phi^{3.69}$

where  $k$  is absolute permeability (same units as  $l_c^2$ ),  $\sigma$  is electrical conductivity of the rock, and  $\sigma_o$  is the conductivity of the saturant. The value of the constant, given as 1/226, is dependent on the geometry assumed for the pore space. They substantiate Eq. 14.20a with experimental data on 60 sandstone and carbonate samples with permeabilities ranging from <1 md to 5 darcies.

The parameter  $l_c$  in Eq. 14.20a represents a dimension of a very particular subset of pores: “The arguments suggest that permeability can be estimated by assuming that the effective pore size is the smallest pore on the connected path of pores containing the largest pores. We call that effective pore size  $l_c$ .” To obtain  $l_c$ , the pressure at the inflection point on a capillary pressure curve is converted to a diameter. The authors argue that the inflection point marks the pressure at which a sample is first filled continuously end to end with mercury and that the large pores first filled are those that control permeability.

The Katz and Thompson<sup>48</sup> equation and its characteristic curves are given in Fig. 14.27. To plot curves on  $\log(k)-\Phi$  plots, we assumed the simplest relation between formation factor and porosity (cementation exponent of 2.0),  $\sigma/\sigma_o = \Phi^2$ . Some data points from Katz and Thompson’s experiments are posted in Fig. 14.27 to indicate how well their measured  $l_c$  match the curves (This is not really a test of their model because they used formation factor in their correlations, not  $\Phi^2$ ). Their result is similar to that of Swanson’s and Winland’s equations: Permeability is closely proportional to the square of  $r\Phi$ .

To obtain compatibility with other worker’s expressions, we define a critical radius  $r_c = l_c/2$ , keeping both permeability and  $r_c^2$  in units of  $\mu\text{m}^2$ :

$$k = (4/226)r_c^2\sigma/\sigma_o \dots\dots\dots (14.20b)$$

Eq. 14.20b is identical in form to Eq. 14.5d, but the percolation concepts used to derive Eq. 14.20b are quite different from the geometrical arguments used to derive the Kozeny-Carman expression. The coefficient in Eq. 14.5d, which is  $\approx 0.4$ , is considerably greater than that (0.0177) in Eq. 14.20b. Consequently, the characteristic radius  $r_c$  is  $\approx 4.7$  times greater than the hydraulic radius,  $r_h$ . Although  $r_h$  is defined as the ratio of pore volume to pore surface area, it can be determined in a variety of ways, including the use of mercury injection. Conceptually, then, the Kozeny-Carman equation could also be represented by an extended horizontal line across Fig. 14.25; i.e., as a method that samples a broad spectrum of pore sizes.

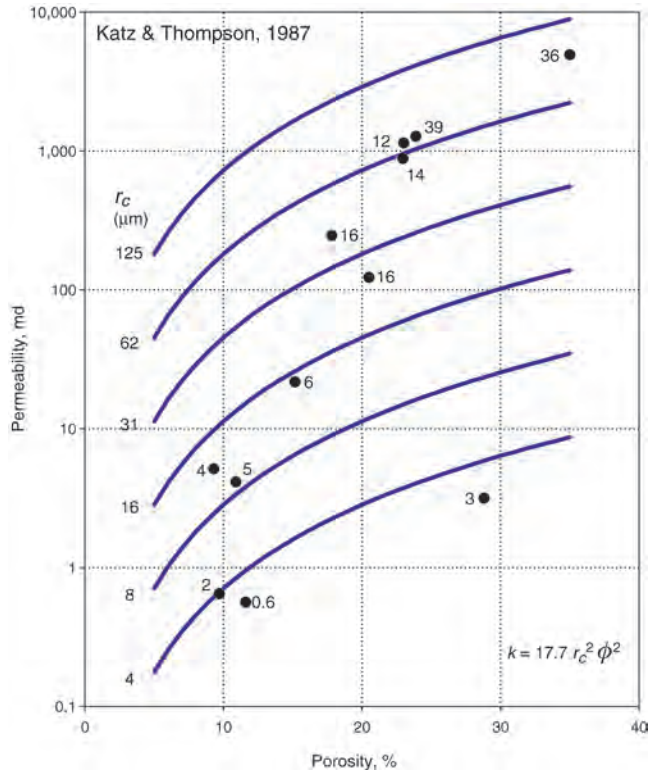


**Fig. 14.27—Permeability equation with critical pore-size radius ( $R_c$ ) as a parameter, from Katz and Thompson.<sup>48</sup> Values of  $r_c$  posted next to data points are from mercury injection tests.**

It is interesting to compare the Katz and Thompson model (Fig. 14.27) with Winland’s empirical equation (Fig. 14.26). The shapes of the curves are comparable; i.e., the models agree on the approximate  $\Phi^2$  dependence. The pore radii given by the Winland equation are smaller than comparable radii in the Katz and Thompson model. This is expected because the Winland equation requires a saturation of 35%, a criterion of greater injection pressure than that of Katz and Thompson. What is noteworthy is the general agreement between the two models regarding the form of the  $\log(k)$ - $\Phi$  relationship. They demonstrate that in the models invoking higher powers of  $\Phi$ , which we have shown in previous graphs are not well grounded physically, the higher powers of  $\Phi$  are required to compensate for lack of knowledge regarding the critical pore dimension. It does seem, however, that the empirical data that often show a “straight-line”  $\log(k)$ - $\Phi$  relationship contain some fundamental information regarding how the critical pore dimension relates to porosity.

**Flow Zone Indicator.** Amaefule and Altunbay<sup>53</sup> rearranged a version of the Kozeny-Carman equation (Eq. 14.5c) to obtain a parameter group named the flow zone indicator ( $I$ ),

$$I = 1 / \sqrt{(f\tau)\Sigma_g} = [0.0314\sqrt{(k/\Phi)}][(1 - \Phi)/\Phi], \dots\dots\dots (14.21)$$

where the factor 0.0314 allows  $k$  to be expressed in millidarcies. As can be seen from Eq. 14.21,  $I$  has the units of pore size, in micrometers, and can be computed from core measurements of  $k$  and  $\Phi$ , even though it is defined in terms of  $f$ ,  $\tau$ , and  $\Sigma_g$ , which are not easily measured. The choice of Eq. 14.5c over other forms of the Kozeny-Carman equation that use

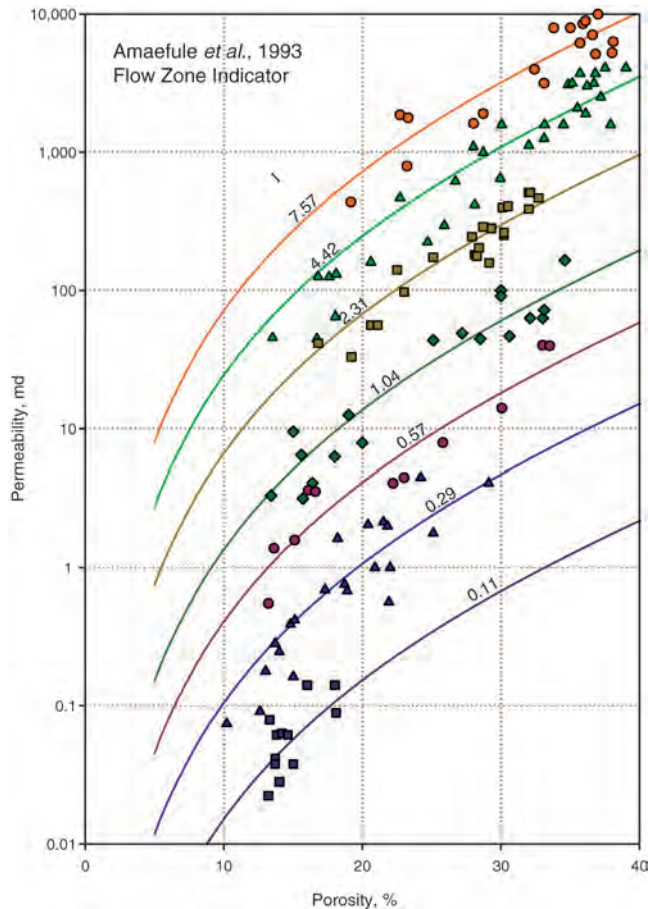


**Fig. 14.28—Zonation of permeability and porosity data based on a parameter called the flow zone indicator ( $I$ ), in  $\mu\text{m}$ . Data from southeast Asia and algorithm taken from Amaefule and Altunbay.<sup>53</sup>**

alternative definition of specific surface area (Eqs. 14.5a and 14.5b) seems a bit arbitrary and results in the particular combination of porosity terms used in Eq. 14.21.

Amaefule and Altunbay<sup>53</sup> use  $I$  to define zones called “hydraulic flow units” on a doubly logarithmic plot incorporating the terms in Eq. 14.21. For compatibility with other plots in this chapter, a plot in  $\log(k)$ - $\Phi$  coordinates is shown in Fig. 14.28. Each data point on a  $\log(k)$ - $\Phi$  plot has an  $I$  value that associates it with a nearby curve of constant  $I$  value. The difficult step is deciding where the boundaries between adjacent  $I$  bands should be positioned and how to compute a value of  $I$  from well logs in uncored wells. Options for doing so are described next.

### 14.5 Statistical Approaches and Reservoir Zonation

Having considered petrological controls on permeability/porosity patterns in Section 14.2 and various petrophysical (grain size, surface area, and pore size) models in Section 14.4, we now consider techniques for applying well logs and other data to the problem of predicting  $k$  or  $\log(k)$  in uncored wells. If the rock formation of interest has a fairly uniform grain composition and a common diagenetic history, then  $\log(k)$ - $\Phi$  patterns are simple, straightforward statistical prediction techniques can be used, and reservoir zonation is not required. However, if a field encompasses several lithologies, perhaps with varying diagenetic imprints resulting from vary-

ing mineral composition and fluid flow histories, then the  $\log(k)$ - $\Phi$  patterns are scattered, and reservoir zonation is required before predictive techniques can be applied.

A widely used statistical approach is multiple linear regression.<sup>54,55</sup> Linear regression techniques are popular for establishing predictors of geological variables because the methods are effective at predicting mean values, are fast computationally, are available in statistical software packages, and provide a means of assessing errors.

**14.5.1 Predictors With One or Two Input Variables.** When a straight-line relationship between  $\log(k)$  and  $\Phi$  exists, as it does in Figs. 14.5 and 14.6, the computation of a predictor for  $\log(k)$  by Eq. 14.3 is straightforward and merits little discussion. Curvature in the  $\log(k)$ - $\Phi$  relationship is treated by adopting a polynomial in  $\Phi$ . Increased accuracy is also afforded by dividing the field by area or vertically and computing regression coefficients for each area. In one area, curvature in the statistical predictor may be rather pronounced; in another, curvature may be absent.

**14.5.2 Predictors With Several Input Variables.** The quality of the predictor can often be enhanced by adding a variable such as gamma ray response or depth normalized to top of formation. As variables are added to Eq. 14.3, families of curves are required to present graphically the effect of combinations of variables. When one or two parameters are varied, the curves sweep out a large area on the  $\log(k)$ - $\Phi$  plot. Predictive power can be increased by adding other parameters. Predictive accuracy does not increase indefinitely as parameters are added but instead usually reaches a limit after several (anywhere from two to six) parameters are included in the regression (see Fig. 17 of Wendt *et al.*<sup>55</sup> for an example).

**14.5.3 Predictors Using Computed Parameters.** Computed logs such as shale volume and differences between porosities from different logs can be included as independent variables. In this way, petrological information can also be incorporated into the predictive relationships. A petrological parameter (cement or gravel) is first “predicted” from well logs using core observations as “ground truth.” The predicted petrological parameters can then be included in a relationship to estimate permeability.

As the complexity of the  $\log(k)$ - $\Phi$  plot increases (i.e., as the data deviate from a linear trend), more variables must be incorporated into the predictive model to maintain predictive accuracy, although instability can result from having too many variables. The better the understanding is of petrological controls on permeability, the more effective the predictor and its application will be. Other complications with regression methods, including underestimation of high-permeability zones and overestimation of low-permeability zones, are mentioned by various authors.<sup>54–56</sup> At some point, it becomes necessary to adopt a method of zoning the reservoir.

A database approach equivalent to an  $n$ -dimensional lookup table can also be used for predicting permeability within a field or common geology.<sup>56</sup> In this approach, the user must first select the logs or log-derived variables that offer sufficient discriminating power for permeability. One must also choose a suitable bin size for each variable on the basis of its resolution. Then, a database is constructed from the core permeability values and associated log values. Each  $n$ -dimensional bin or volume is bounded by incremental log values and contains mean and standard deviation values of permeability plus the number of samples. In application, permeability estimates are extracted from a bin addressed by the log values. An interpolation scheme is used to extract an estimate from an empty bin. Like the regression method, the database approach can be used only when adequate core data are available to build the model, and results generally cannot be transferred to other areas.

Fuzzy clustering techniques provide a means of determining the number of clusters (bins in the preceding paragraph) and their domains.<sup>57</sup> The term “fuzzy” indicates that a given input/output pair can belong (partially) to more than one cluster. Finol and Jing<sup>57</sup> applied the tech-

nique to a shaly sandstone reservoir in which permeability ranged from 0.05 to 2,500 md. Six clusters were defined. In each cluster, permeability is determined by

$$\log(k_i) = a_{i0} + a_{i1}\Phi + a_{i2}\log(Q_v), \quad i = 1, \dots, 6, \dots \quad (14.22)$$

where  $\Phi$  is porosity and  $Q_v$  is the cation exchange capacity per unit pore volume. The final determination of  $\log(k)$  is a weighted sum of the six  $\log(k_i)$ , with weights determined by the degree of membership of  $\Phi$  and  $\log(Q_v)$  in their respective clusters. An average correlation coefficient of 0.95 was obtained on test sets.<sup>57</sup> Implementation of Eq. 14.22 in uncored wells requires that  $Q_v$  be determined from a porosity log and requires an estimate of grain density and shale fraction ( $V_{sh}$ ).

Artificial neural networks are a third method of establishing a predictor specific to an area of interest. A back-propagation neural network is optimized on a training set in which the desired output (permeability at a given depth) is furnished to the network, along with a set of inputs chosen by the user. Rogers *et al.*<sup>58</sup> established a predictor for a Jurassic carbonate field using only porosity and geographic coordinates as inputs. For each value of permeability to be predicted, porosity values spanning the depth of the desired permeability value were provided as inputs, rather than a single porosity value at a single depth. Permeability values predicted by the neural network in test wells were generally closer to the core measurements than were the values predicted by linear regression.

## 14.6 Discussion

The best petrophysical models show that pore throat size  $r$  is a prime control on  $k$ . Yet,  $r$  is missing from example data sets (Figs. 14.5 through 14.11) and from the diagram summarizing diagenetic processes (Fig. 14.2). With the models, it is possible to consider what the range of pore sizes might have been when sediments were deposited and what the range is in the present state of consolidation. As an example, consider the samples in Fig. 14.5 from the Hosston formation. The uppermost vertical bar in Fig. 14.3 shows the range of grain size reported for the Hosston formation. The range of initial pore throat sizes (vertical hachured bar in Fig. 14.3) was computed from the present-day grain size using data from Beard and Weyl<sup>3</sup> (Fig. 14.4) to transform grain size to initial permeability, followed by application of the Katz-Thompson equation (Eq. 14.20) to obtain pore throat size from  $k$  and  $\Phi$ . Present-day pore throat sizes (lowermost solid bar in Fig. 14.3) were computed from present-day  $k$  and  $\Phi$  with the Katz-Thompson<sup>48</sup> equation (Eq. 14.20). From this exercise, one can see that the largest pore throat size has diminished from 250 (initial) to 45 (present day)  $\mu\text{m}$ , that the smallest present-day sizes are  $<2 \mu\text{m}$ , and that the range of pore throat size has broadened considerably on the logarithmic phi scale.

Expressions relating permeability  $k$  to porosity  $\Phi$  are summarized in Table 14.2. There, permeability is in millidarcies, and grain sizes ( $d$ ) and pore sizes ( $r$ ) are expressed in micrometers, so the coefficients may differ from the originating equation in the text. From these representative equations, it can be seen that (1) the predictive equations are simple in form, (2)  $k$  is related to a power of  $\Phi$  (except for the Krumbein and Monk<sup>26</sup> equation), and (3)  $k$  is related to the square of either a characteristic length or a measure of surface area.

We have seen that models relying on estimates of surface area, whether that estimate comes from irreducible water saturation, NMR, gas adsorption, or cation exchange data, require porosity raised to a power of  $\approx 4$ . How can surface-area models requiring a porosity power of 4 (Figs. 14.21 and 14.24) be reconciled with pore dimension models requiring a power of 2 (Figs. 14.26 and 14.27)? The answer lies in the pore-size distribution. Because most of the surface area is contributed by the smallest grains (pores), measures of surface area emphasize the small end of the pore-size spectrum. Yet, the small pores contribute least to permeability.



TABLE 14.2—EIGHT EQUATIONS RELATING PERMEABILITY TO FRACTIONAL POROSITY			
Class	Author	Equation Number	Equation
Sand pack	Krumbein and Monk <sup>26</sup>	6	$k=0.76d_g^2e^{-1.31\sigma}$
Grain-based models	Berg <sup>28</sup>	7b	$k=80.8d^2\phi^{5.1}e^{-1.385\phi}$
	Van Baaren <sup>30</sup>	8a	$k=10d_g^2\phi^{3.64+m}C^{-3.64}$
Surface-area models	Timur <sup>22</sup>	10	$k=8,581S_{wi}^{-2}\phi^{4.4}$
	Sen <i>et al.</i> <sup>40</sup>	14	$k=0.794t_1^{2.15}\phi^{m+2.15}$
Pore-size models	Kozeny-Carman <sup>19-21</sup>	5d	$k=400r_n^2\phi^m$
	Winland <sup>47</sup>	19	$k=49.4f_{35}^2\phi^{1.47}$
	Katz and Thompson <sup>48</sup>	20	$k=17.9r_c^2\phi^m$

Parameters are defined in the text, referenced by equation number. Grain diameters ( $d$ ) and pore throat radii ( $r$ ) are given in  $\mu\text{m}$ ; permeability is given in md.

The high ( $\approx 4$ ) power of porosity serves to unweight the contribution of the small pores. In the surface-area models, porosity serves a dual role, first as a measure of tortuosity and second as a measure of the pore-size distribution function.

A similar question arises with the grain size models. Both models by Berg<sup>28</sup> (Fig. 14.17) and Van Baaren<sup>38</sup> require a porosity power of  $\approx 5$ , multiplied by the square of a dominant grain size. Why is the porosity power so high? The probable reason is that the dominant grain size becomes a progressively poorer measure of dominant pore size as the spread in grain size increases and small grains (pores) become more abundant. Again, porosity serves as both a measure of tortuosity and a weighting factor to compensate for the presence of small pores at lower porosities. Moreover, the retention of a sorting term in Eqs. 14.7a and 14.8a is inadequate compensation for small pores, even though a sorting term is all that is needed in sized samples (Eq. 14.6).

Models incorporating an estimator of pore size (Eqs. 14.5d, 14.19, and 14.20 in Table 14.2) include porosity raised to a power of  $m$  ( $\approx 2$ ). Estimates of dominant or characteristic pore size are more effective at predicting  $k$  than estimates of grain size or surface area, so the higher exponent of porosity to compensate for the low end of the porosity spectrum is not required. Given a measure of  $r$  and  $\Phi$ , the more information that  $r$  contains regarding the large through-going pores, the lower the dependence on  $\Phi$  is. Indeed, the findings of Beard and Weyl,<sup>3</sup> Swanson,<sup>18</sup> Pittman,<sup>49</sup> and Katz and Thompson<sup>48</sup> all show that  $\Phi$  is not so important as a predictor of  $k$  as long as the dominant  $r$  is well specified. Conversely, using Pittman’s findings of Table 14.1, as  $r$  decreases below  $r_{\text{apex}}$ ,  $r$  becomes a progressively poorer estimator of the dominant  $r$ , and a higher exponent of  $\Phi$  is required to compensate for the inclusion of pore throats that do not contribute to flow.

The preceding considerations hold for predicting  $k$  on individual samples from a wide range of rock formations, whereas the first part of this chapter shows that  $\Phi$  can be a good predictor of  $k$  for samples from a given rock formation. Why is this? The pore-size models produce curves of constant pore size that transgress the steeper  $\log(k)$ - $\Phi$  data trends. The cutting of the  $\log(k)$ - $\Phi$  trends by the curves of constant pore size shows that porosity reduction is always accompanied by a reduction in characteristic pore size. As rocks from a common source are compacted and undergo diagenesis, pore space is reduced, and permeable pathways are progres-

sively blocked in a systematic way that maintains a consistent relationship between  $\Phi$  and  $r$ . Samples from different formations that have undergone different diagenetic processes follow different evolutionary paths in  $\log(k)$ - $\Phi$ - $r$  space and thus produce different trends on a  $\log(k)$ - $\Phi$  plot.

### 14.7 Practical Applications

The problem of predicting permeability has been reviewed by compiling data and predictive algorithms from the literature. Which approach should be used to estimate permeability from core and well log data? As a practical matter, it depends on what data are available from a given well or field:

1. In cases in which no core data are available, one can proceed by analogy using data developed in formations with geological properties similar to the one under study. Figs. 14.5 through 14.8 are examples of the types of analog data that one might use.

2. When porosity and grain size estimates are available, refer to Fig. 14.17. This chart appears to give good estimates for many consolidated rocks. Exceptions will exist, such as rocks containing illite in pore space and low-permeability formations such as those shown in Fig. 14.8.

3. In situations in which porosity and water saturation can be estimated, permeability can be estimated from Timur's<sup>22</sup> relationship (Eq. 14.10 and Fig. 14.21). In clay-bearing rocks, the dual-water relationship for permeability (Eqs. 14.12 and 14.13) is an interesting enhancement, but the user is required to provide estimates of both interstitial and bound water.

4. When NMR logs are available, one can make use of the permeability transforms developed for such logs. Laboratory determination of a  $t_2$  cutoff is advised.

5. Permeability is controlled by a pore dimension of a selected subset of the pore population and can be determined from capillary pressure by mercury injection (Figs. 14.26 and 14.27 and Eqs. 14.18 through 14.20). Mercury injection can be applied to determine the permeability of small or fragmented samples.

6. In field developments in which core data are abundant and a relatively simple (linear)  $\log(k)$ - $\Phi$  relation is the result of a fairly uniform lithology and uncomplicated diagenetic history, then one can turn to regression methods to predict  $k$  from well log estimates of  $\Phi$ .

7. In heterogeneous reservoirs, a high degree of scatter on a  $\log(k)$ - $\Phi$  plot requires that the reservoir be zoned before  $k$  can be estimated. One must choose a petrophysical parameter with which to zone the reservoir rocks. Various practitioners have used  $r_{35}$ , the flow zone indicator ( $I$ ), the square root of  $k/\Phi$ , and even  $k$  itself (note that each of these four parameters has the dimension of length or length squared). One must also choose a method of zoning or clustering; among the candidates are linear regression, neural networks, data binning, and fuzzy clustering. A good set of core data is required to establish the zones or clusters. After the method is tested, then well logs are used to compute a value of the zonation parameter. The more geological information that can be incorporated into the zonation procedure, the better. In fact, the breadth of petrophysical, well test, and geological data is probably more important than the particular zonation parameter or clustering methodology chosen. Complex reservoirs require complex methods.

8. Fractured reservoirs are a special and difficult case. Fracture permeability cannot be measured with core samples, so it is difficult to establish ground truth. Methods of estimating fracture permeability from fracture aperture and fracture density are tenuous because aperture varies throughout the fracture plane, some fractures are sealed with mineral deposits, and some are open. Combinations of techniques seem to work well. Examination of core can provide orientation and number of fractures, facies descriptions, and mineralization on fracture surfaces. Borehole images provide fracture number, orientation, and aperture. Flow (spinner) logs reveal zones of fluid flow into the wellbore. Sonic waveform logs show fracture location, and if conditions permit, permeability estimates can be extracted from Stoneley waves. Other well logs

provide porosity estimates. Well tests provide estimates of permeability over isolated intervals. Analysis of the state of stress can provide insight on fracture location and the probability of being open or closed. Analysis of complementary data sets can provide insights that cannot be obtained from isolated data sets.

In all cases, one must bear in mind that a permeability predictor will be unique to the field or formation for which it is developed. This unfortunate fact is a result of the multiple pathways that can be followed during burial and diagenesis, as seen in [Section 14.2](#).

### Nomenclature

$A$	=	area
$d$	=	grain diameter
$f$	=	shape factor
$F$	=	formation factor
$g$	=	gravitational acceleration
$I$	=	flow zone indicator
$k$	=	permeability
$K$	=	hydraulic conductivity
$l_c$	=	pore-space dimension
$m$	=	Archie cementation exponent
$M_i$	=	weight fraction of mineral component
$p$	=	pressure
$P_c$	=	capillary pressure
$q$	=	volumetric flow rate
$Q_v$	=	cation molarity
$r_h$	=	hydraulic radius
$r_{35}$	=	pore throat radius at 35% mercury saturation
$R$	=	pore throat dimension
$S_b$	=	mercury saturation
$S_{bw}$	=	bound water saturation
$S_{wi}$	=	irreducible water saturation
$S_{ciw}$	=	critical water saturation
$t_1$	=	NMR longitudinal decay time
$t_2$	=	NMR transverse decay time
$V_{ffi}$	=	free fluid fraction
$V_{bw}$	=	volume of bound water, fraction
$V_{bi}$	=	bulk volume irreducible water, fraction
$V_{cl}$	=	clay fraction
$V_{sh}$	=	shale fraction
$z$	=	elevation
$\theta$	=	wetting angle
$\mu$	=	dynamic viscosity
$\rho$	=	density
$\sigma_D$	=	standard deviation
$\sigma$	=	electrical conductivity of rock
$\sigma_o$	=	electrical conductivity of saturant
$\sigma$	=	interfacial tension
$\Sigma_p$	=	ratio of pore surface area to pore volume
$\Sigma_r$	=	ratio of pore surface area to rock volume

- $\Sigma_g$  = ratio of pore surface area to grain volume  
 $\Sigma$  = specific surface area  
 $\tau$  = tortuosity  
 $\Phi$  = porosity  
 $\Phi_t$  = total porosity  
 $\Phi_e$  = effective porosity

### Subscripts

- $e$  = effective  
 $l$  = liquid  
 $o$  = oil  
 $t$  = total  
 $w$  = water

---

### References

1. *RP 27, Recommended Practice for Determining Permeability of Porous Media*, API, Dallas, Texas (1956).
2. Bass, D.M. Jr.: "Properties of Reservoir Rocks," *Petroleum Engineering Handbook*, H.B. Bradley (ed.), Society of Petroleum Engineers, Richardson, Texas (1987) Chap. 26.
3. Beard, D.C. and Weyl, P.K.: "Influence of Texture on Porosity and Permeability of Unconsolidated Sand," *American Association of Petroleum Geologists Bull.* (1973) **57**, No. 2, 349.
4. Neuzil, C.E.: "How Permeable Are Clays and Shales?" *Water Resources Research* (1994) **30**, No. 2, 145.
5. Thomson, A.: "Petrography and Diagenesis of the Hosston Sandstone Reservoirs at Bassfield, Jefferson Davis County, Mississippi," *Trans., Gulf Coast Association of Geological Societies* (1978) 651.
6. Bloch, S.: "Empirical Prediction of Porosity and Permeability in Sandstones," *American Association of Petroleum Geologists Bull.* (1991) **75**, No. 7, 1145.
7. Bos, M.R.E.: "Prolific Dry Oil Production From Sands With Water Saturations in Excess of 50%: A Study of a Dual Porosity System," *Trans., 23rd Annual Logging Symposium, Society of Professional Well Log Analysts* (1982) paper BB.
8. Wilson, M.D.: "Inherited Grain-Rimming Clays in Sandstones From Eolian and Shelf Environments: Their Origin and Control on Reservoir Properties," *Origin, Diagenesis, and Petrophysics of Clay Minerals in Sandstones*, SEPM Special Publication No. 47 (1992) 213–225.
9. Stalder, P.J.: "Influence of Crystallographic Habit and Aggregate Structure of Authigenic Clay Minerals on Sandstone Permeability," *Geologie en Mijnbouw* (1973) **42**, No. 4.
10. Pallatt, N.: "The Relationship Between Permeability and the Morphology of Diagenetic Illite in Reservoir Rocks," *JPT* (December 1984) 2225.
11. Petty, D.M.: "Depositional Facies, Textural Characteristics, and Reservoir Properties of Dolomites in Frobisher-Alida Interval in Southwest North Dakota," *American Association of Petroleum Geologists Bull.* (1988) **72**, No. 10, 1229.
12. Mortensen, J., Engstrom, F., and Lind, I.: "The Relation Among Porosity, Permeability, and Specific Surface of Chalk From the Gorm Field, Danish North Sea," *SPERE* (1998) 245.
13. Lucia, F.J.: "Rock-Fabric/Petrophysical Classification of Carbonate Pore Space for Reservoir Characterization," *American Association of Petroleum Geologists Bull.* (1995) **79**, No. 9, 1275.
14. Klinkenberg, L.J.: "The Permeability of Porous Media to Liquids and Gases," *Drill. & Prod. Prac.* (1941) 200.
15. Jones, S.C.: "Using the Inertial Coefficient,  $\beta$ , To Characterize Heterogeneity in Reservoir Rock," paper SPE 16949 presented at the 1987 SPE Annual Technical Conference and Exhibition, Dallas, 27–30 September.

16. Jones, F.O. and Owens, W.W.: "A Laboratory Study of Low-Permeability Gas Sands," *JPT* (September 1980) 1631.
17. Jones, S.C.: "Two-Point Determinations of Permeability and PV vs. Net Confining Stress," *SPEFE* (1988) 235.
18. Swanson, B.F.: "A Simple Correlation Between Permeabilities and Mercury Capillary Pressures," *JPT* (December 1981) 2498.
19. Carman, P.C.: *Flow of Gases Through Porous Media*, Academic Press Inc., New York City (1956).
20. Amyx, J.W., Bass, D.M. Jr., and Whiting, R.L.: *Petroleum Reservoir Engineering*, McGraw-Hill Book Co., New York City (1960).
21. Hearst, J.R., Nelson, P.H., and Paillet, F.L.: *Well Logging for Physical Properties*, John Wiley & Sons, New York City (2000).
22. Timur, A.: "An Investigation of Permeability, Porosity, and Residual Water Saturation Relationships for Sandstone Reservoirs," *Log Analyst* (1968) **9**, No. 4, 8.
23. Paterson, M.S.: "The Equivalent Channel Model for Permeability and Resistivity in Fluid-Saturated Rock: A Re-appraisal," *Mechanics of Materials* (1983) **2**, 345–352.
24. Walsh, J.B. and Brace, W.F.: "The Effect of Pressure on Porosity and the Transport Properties of Rock," *J. Geophysical Research* (1984) **89**, No. B11, 9425.
25. Clennell, M.B.: "Tortuosity: A Guide Through the Maze," *Developments in Petrophysics*, M.A. Lovell and P.K. Harvey (eds.), Geological Society Special Publication No. 122 (1997) 299.
26. Krumbein, W.C. and Monk, G.D.: "Permeability as a Function of Size Parameters of Unconsolidated Sand," *Trans., AIME* (1943) **151**, 153.
27. Morrow, N.R., Huppler, J.D., and Simmons, A.B. III: "Porosity and Permeability of Unconsolidated, Upper Miocene Sands From Grain-Size Analysis," *J. of Sedimentary Petrology* (1969) **39**, No. 1, 312.
28. Berg, R.R.: "Method for Determining Permeability From Reservoir Rock Properties," *Trans., Gulf Coast Association of Geological Societies* (1970) **20**, 303.
29. Nelson, P.H.: Permeability-Porosity Relationships in Sedimentary Rocks, *Log Analyst* (May-June 1994) 35, No. 3, 38.
30. Van Baaren, J.P.: "Quick-Look Permeability Estimates Using Sidewall Samples and Porosity Logs," *Trans.*, 6th Annual European Logging Symposium, Society of Professional Well Log Analysts (1979).
31. Herron, M.M.: "Estimating the Intrinsic Permeability of Clastic Sediments From Geochemical Data," *Trans.*, 28th Annual Logging Symposium, Society of Professional Well Log Analysts (1987) paper HH.
32. Panda, M.N. and Lake, L.W.: "Estimation of Single-Phase Permeability From Parameters of Particle-Size Distribution," *American Association of Petroleum Geologists Bull.* (1994) **78**, No. 7, 1028.
33. Panda, M.N. and Lake, L.W.: "A Physical Model of Cementation and Its Effects on Single-Phase Permeability," *American Association of Petroleum Geologists Bull.* (1995) **79**, No. 3, 431.
34. Bryant, S., Cade, C., and Mellor, D.: "Permeability Prediction From Geologic Models," *American Association of Petroleum Geologists Bull.* (1993) **77**, No. 8, 1338.
35. Cade, C.A., Evans, I.J., and Bryant, S.L.: "Analysis of Permeability Controls: A New Approach," *Clay Minerals* (1994) **29**, 491.
36. Granberry, R.J., and Keelan, D.K.: "Critical Water Estimates for Gulf Coast Sands," *Trans., Gulf Coast Association of Geological Societies* (1977) 41.
37. Raymer, L.L.: "Elevation and Hydrocarbon Density Correction for Log-Derived Permeability Relationships," *Log Analyst* (1981) **22**, No. 3, 3.
38. Ahmed, U., Crary, S.F., and Coates, G.R.: "Permeability Estimation: The Various Sources and Their Interrelationships," *JPT* (1991) 578.
39. Kukal, G.C. and Simons, K.E.: "Log Analysis Techniques for Quantifying the Permeability of Submillidarcy Sandstone Reservoirs," *SPEFE* (1986) 609.
40. Sen, P.N. *et al.*: "Surface-To-Volume Ratio, Charge Density, Nuclear Magnetic Relaxation, and Permeability in Clay-Bearing Sandstones," *Geophysics* (1990) **55**, No. 1, 61.
41. Borgia, G.C. *et al.*: "Specific Surface and Fluid Transport in Sandstones Through NMR Studies," *SPEFE* (1992) 206.

42. Coates, G.R., Xiao, L., and Prammer, M.G.: *NMR Logging, Principles and Applications*, Halliburton Energy Services, Houston (1999).
43. Kenyon, W.E.: "Petrophysical Principles of Applications of NMR Logging," *Log Analyst* (1997) **38**, No. 2, 21.
44. Coates, G.R. *et al.*: "The Magnetic Resonance Imaging Log Characterized by Comparison With Petrophysical Properties and Laboratory Core Data," paper SPE 22723 presented at 1991 SPE Annual Technical Conference and Exhibition, Dallas, 6–9 October.
45. Sigal, R.: "Coates and SDR Permeability: Two Variations on the Same Theme," *Petrophysics* (2002) **43**, No. 1, 38.
46. Purcell, W.R.: "Capillary Pressures: Their Measurement Using Mercury and the Calculation of Permeability Therefrom," *Trans.*, AIME (February 1949) 39.
47. Kolodzie, S. Jr.: "Analysis of Pore Throat Size and Use of the Waxman-Smiths Equation to Determine OOIP in Spindle Field, Colorado," paper SPE 9382 presented at 1980 SPE Annual Technical Conference and Exhibition, Dallas, 21–24 September.
48. Katz, A.J. and Thompson, A.H.: "Quantitative Prediction of Permeability in Porous Rock," *Physical Review B* (1986) **34**, No. 11, 8179.
49. Pittman, E.D.: "Relationship of Porosity and Permeability to Various Parameters Derived From Mercury Injection—Capillary Pressure Curves for Sandstone," *American Association of Petroleum Geologists Bull.* (1992) **76**, No. 2, 191.
50. Hartmann, D.J. and Coalson, E.B.: "Evaluation of the Morrow Sandstone in Sorrento Field, Cheyenne County, Colorado," *Morrow Sandstones of Southeast Colorado and Adjacent Areas*, S.A. Sonnenberg *et al.* (eds.), Rocky Mountain Association of Geologists (1990) 91.
51. Martin, A.J., Solomon, S.T., and Hartmann, D.J.: "Characterization of Petrophysical Flow Units in Five Carbonate Reservoirs," *American Association of Petroleum Geologists Bull.* (1997) **81**, No. 5, 734.
52. Thompson, A.H., Katz, A.J., and Krohn, C.E.: "The Microgeometry and Transport Properties of Sedimentary Rock," *Advances in Physics* (1987) **36**, No. 5, 625.
53. Amaefule, J.O. and Altunbay, M.: "Enhanced Reservoir Description: Using Core and Log Data To Identify Hydraulic (Flow) Units and Predict Permeability in Uncored Intervals/Wells," SPE 26436 presented at the 1993 SPE Annual Technical Conference and Exhibition, Houston, 3–6 October.
54. Allen, J.R.: "Prediction of Permeability From Logs by Multiple Regression," *Trans.*, Society of Professional Well Log Analysts (1979).
55. Wendt, W.A., Sakurai, S., and Nelson, P.H.: "Permeability Prediction From Well Logs Using Multiple Regression," *Reservoir Characterization*, L.W. Lake and H.B. Carroll, Jr. (eds.), Academic Press, Inc., New York City (1986) 181-222.
56. Nicolaysen, R. and Svendsen, T.: "Estimating the Permeability for the Troll Field Using Statistical Methods Querying a Fieldwide Database," *Trans.*, Society of Professional Well Log Analysts (1991) paper QQ.
57. Finol, J. and Jing, X-D.D.: "Permeability Prediction in Shaly Formations: The Fuzzy Modeling Approach," *Geophysics* (2002) **67**, No. 3, 817.
58. Rogers, S.J. *et al.*: "Predicting Permeability From Porosity Using Artificial Neural Networks," *American Association of Petroleum Geologists Bull.* (1995) **79**, No. 12, 1786.
59. Lucia, F.J.: *Carbonate Reservoir Characterization*, Springer, Berlin (1999).

### SI Metric Conversion Factors

atm	× 1.013 250*	E+05	= Pa
cp	× 1.0*	E−03	= Pa·s
in.	× 2.54*	E+00	= cm
ft	× 3.048*	E−01	= m
psi	× 6.894 757	E+00	= kPa

\*Conversion factor is exact.

# Chapter 15

## Relative Permeability and Capillary Pressure

Richard L. Christiansen, Colorado School of Mines

### 15.1 Introduction

Reservoir engineers use relative permeability and capillary pressure relationships for estimating the amount of oil and gas in a reservoir and for predicting the capacity for flow of oil, water, and gas throughout the life of the reservoir. Relative permeabilities and capillary pressure are complex functions of the structure and chemistry of the fluids and solids in a producing reservoir. As a result, they can vary from place to place in a reservoir. Most often, these relationships are obtained by measurements, but network models are emerging as viable routes for estimating capillary pressure and relative permeability functions.

Before defining relative permeability and capillary pressure, let us briefly review the definition of permeability. Permeability represents the capacity for flow through porous material. It is defined by Darcy’s law (without gravitational effects) as

$$q = - \frac{kA}{\mu} \frac{\Delta P}{L} \dots\dots\dots (15.1)$$

Darcy’s law relates the flow rate  $q$  to the permeability  $k$ , cross-sectional area  $A$ , viscosity  $\mu$ , pressure drop  $\Delta P$ , and length  $L$  of the material. High permeability corresponds to increased capacity for flow. The dimensions of permeability are length squared, often expressed as darcies (1 darcy =  $0.987 \times 10^{-8}$  cm<sup>2</sup>), millidarcies, or micrometers squared. Some writers use “absolute permeability” or “intrinsic permeability” in place of permeability.

For multiple-phase flow, the following expressions define relative permeabilities, specifically written for oil and water flow (without gravitational effects) in the  $x$  direction:

$$q_o = - \frac{kk_{ro}A}{\mu_o} \frac{\partial p_o}{\partial x} \dots\dots\dots (15.2)$$

$$\text{and } q_w = - \frac{kk_{rw}A}{\mu_w} \frac{\partial p_w}{\partial x} \dots\dots\dots (15.3)$$

where  $k_{ro}$  and  $k_{rw}$  are the relative permeabilities of oil and water, respectively. Relative permeabilities are dimensionless functions that usually range between 0 and 1. Eqs. 15.2 and 15.3 allow for differences in the pressure in the oil and water phases. The difference in pressure between the two phases is the capillary pressure:

$$P_{cow} = p_o - p_w \dots\dots\dots (15.4)$$

Capillary pressure relationships are dimensional functions that range from large negative to large positive values. (Capillary pressure is often defined as the pressure of the less-dense phase minus the pressure of the more-dense phase.) Relative permeabilities and capillary pressures are usually viewed as functions of the saturation of phases in the porous sample—so, for oil/water flow in the absence of a gas phase, we have  $k_{ro}(S_w)$ ,  $k_{rw}(S_w)$ , and  $P_c(S_w)$ . Saturation is the fraction of pore space that is occupied by a phase. In the present example of oil/water flow,  $S_w + S_o = 1$ .

In some discussions, the products of permeability and relative permeability (e.g.,  $kk_{ro}$  and  $kk_{rw}$  in Eqs. 15.2 and 15.3) are termed the effective permeabilities. Effective permeability of oil at irreducible water saturation, or  $k_o(S_{wi})$ , is sometimes used to normalize relative permeabilities in place of absolute permeability. With this normalization,  $k_{ro}(S_{wi})$  equals 1. It is possible for water relative permeability to exceed 1 when  $k_o(S_{wi})$  is the normalizing factor. One must be very careful when using data to note whether absolute permeability or an effective permeability is used for normalizing.

The remainder of this chapter includes discussion of typical capillary pressure relationships and capillary pressure models, typical relative permeability relationships and relative permeability models, measurement of rock/fluid relationships, and trends in rock/fluid properties.<sup>1</sup>

**15.2 Observations of Capillary Pressure Relationships**

As defined in the Introduction, capillary pressure refers to the difference in pressure across the interface between two phases. With Laplace’s equation, the capillary pressure  $P_{cow}$  between adjacent oil and water phases can be related to the principal radii of curvature  $R_1$  and  $R_2$  of the shared interface and the interfacial tension  $\sigma_{ow}$  for the oil/water interface:

$$P_{cow} = p_o - p_w = \sigma_{ow} \left( \frac{1}{R_1} + \frac{1}{R_2} \right) \dots\dots\dots (15.5)$$

The relationship between capillary pressure and fluid saturation could be computed in principle, but this is rarely attempted except for very idealized models of porous media. Methods for measuring the relationship are discussed later in this chapter.

Fig. 15.1 shows a sketch of a typical capillary pressure relationship for gas invading a porous medium that is initially saturated with water; the gas/water capillary pressure is defined as  $P_{cgw} = p_g - p_w$ . For this example, water is the wetting phase, and gas is the nonwetting phase. As shown in Figs. 15.2 and 15.3, a wetting phase spreads out on the solid, and a nonwetting phase does not. Wettability of a solid with respect to two phases is characterized by the contact angle. Popular terminology for saturation changes in porous media reflects wettability: “drainage” refers to the decreasing saturation of a wetting phase, and “imbibition” refers to the increasing wetting-phase saturation. Thus, the capillary pressure relationship in Fig. 15.1 is for drainage—specifically primary drainage, meaning that the wetting phase (water) is decreasing from an initial value of 100%.

Gas does not penetrate the medium in Fig. 15.1 until the capillary pressure exceeds the threshold pressure  $P_{ct}$ , which depends on the size and shape of the pores and the wettability of the sample. As capillary pressure increases beyond this value, the saturation of the water contin-



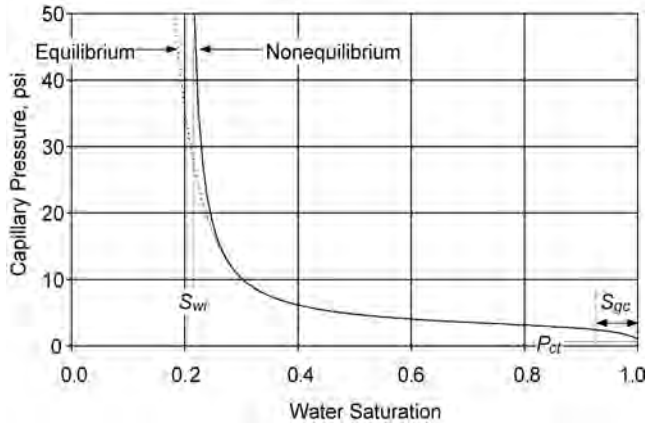


Fig. 15.1—A typical capillary pressure relationship for primary drainage of water with invasion of gas. Water is the wetting phase.

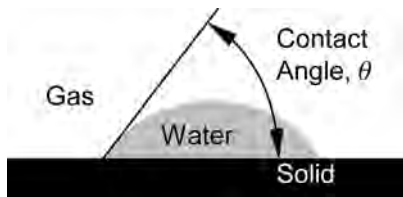


Fig. 15.2—Water = wetting phase. A drop of water spreading on a solid, with a contact angle less than 90°.

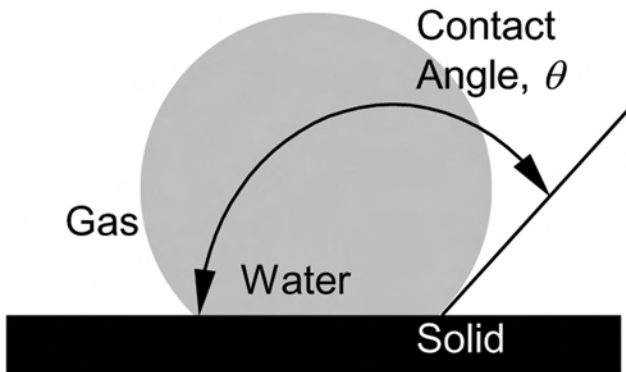
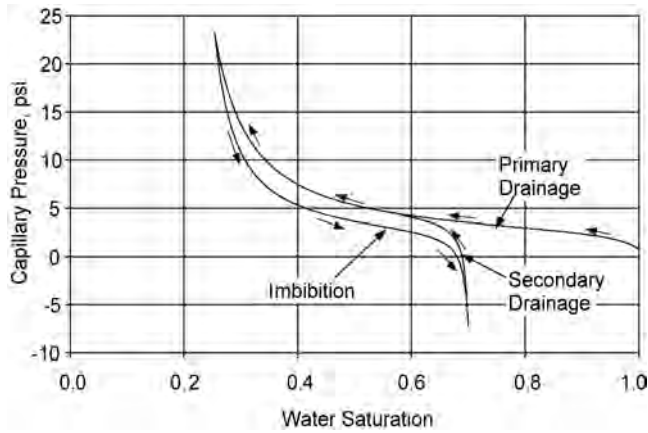


Fig. 15.3—Water = nonwetting phase. A drop of water resting on a solid, with a contact angle greater than 90°.

ues to decrease. It is generally believed that the gas cannot flow until its saturation is greater than a critical level  $S_{gc}$ , which is often 5 to 15% of the total pore volume. If gas is not mobile below  $S_{gc}$ , then the capillary pressure relationship between  $S_w = 1 - S_{gc}$  and  $S_w = 1$  in Fig. 15.1 is fictitious, as suggested by Muskat<sup>2</sup>—a detail largely ignored in later literature.

Below  $S_w = 1 - S_{gc}$ , the capillary pressure increases with decreasing water saturation, with water saturation approaching an irreducible level  $S_{wi}$  at very high capillary pressures. Morrow and Melrose<sup>3</sup> argue that capillary pressure measurements have not reached equilibrium if the



**Fig. 15.4—Primary drainage, imbibition, and secondary drainage for a gas/water system in which the water strongly wets the solid surface.**

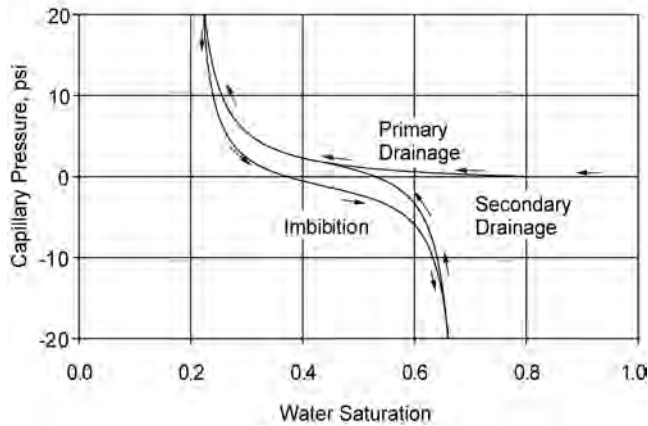


**Fig. 15.5—Primary drainage, imbibition, and secondary drainage for an oil/water system in which the oil and water wet the solid surface equally.**

capillary pressure trend asymptotically approaches an irreducible water saturation. As the water saturation decreases during a measurement, the capacity for flow of water rapidly diminishes, so the time needed for equilibration often increases beyond practical limitations. Hence, a difference develops between the measured relationship and the hypothetical equilibrium relationship, as shown in Fig. 15.1.

After completing measurements of capillary pressure for primary drainage, the direction of saturation change can be reversed, and another capillary pressure relationship can be measured—it is usually called an imbibition relationship. Imbibition is often analogous to the waterflooding process. The primary drainage and imbibition relationships generally differ significantly, as shown in Fig. 15.4 for a gas/water system. This difference is called capillary pressure hysteresis—the magnitude of capillary pressure depends on the saturation and the direction of saturation change. For imbibition of a strongly wetting phase, the capillary pressure generally does not reach zero until the wetting-phase saturation is large, as shown in Fig. 15.4. For a less strongly wetting phase, the capillary pressure reaches zero at a lower saturation, as shown in Fig. 15.5. Capillary pressure behavior for secondary drainage is also shown in Figs. 15.4 and 15.5.

**TABLE 15.1—A SUMMARY OF THE OBSERVATIONS OF WETTABILITY FROM TREIBER *ET AL.*<sup>5</sup>**

	<u>Total Reservoirs</u>	<u>Carbonate Reservoirs</u>	<u>Silicic Reservoirs</u>
Water-wet	27%	8%	43%
Intermediate-wet	7%	8%	7%
Oil-wet	66%	84%	50%

As shown in Figs. 15.4 and 15.5, the wettability of the porous material is an important factor in the shape of capillary pressure relationships. Wettabilities of reservoir systems are categorized by a variety of names. Some systems are strongly water-wet, while others are oil-wet or neutrally wet. Spotty (or “dalmation”) wettability and mixed wettability describe systems with nonuniform wetting properties, in which portions of the solid surface are wet by one phase, and other portions are wet by the other phase. Mixed wettability, as proposed by Salathiel,<sup>4</sup> describes a nonuniform wetting condition that developed through a process of contact of oil with the solid surface. Salathiel hypothesized that the initial trapping of oil in a reservoir is a primary drainage process, as water (the wetting phase) is displaced by nonwetting oil. Then, those portions of the pore structure that experience intimate contact with the oil phase become coated with hydrocarbon compounds and change to oil-wet.

The drainage and imbibition terminology for saturation changes breaks down when applied to reservoirs with nonuniform wettability. Rather than using drainage and imbibition to refer to the decreasing and increasing saturation of the wetting phase, some engineers define these terms to mean decreasing and increasing water saturation, even if water is not the wetting phase for all surfaces.

Treiber *et al.*<sup>5</sup> reported a study of wettabilities of 55 oil reservoirs. Twenty-five of the reservoirs were carbonate, and the others were silicic (28 sandstone, 1 conglomerate, and 1 chert). To characterize wettability, they used the following ranges for the oil/water/solid contact angle as measured through the water phase:

0 to 75° = water-wet

75 to 105° = intermediate-wet

105 to 180° = oil-wet

Their wettability results are listed in Table 15.1. At the time of publication in 1972, it was surprising to readers that two-thirds of the reservoirs were oil-wet. Previously, reservoirs were believed to be mostly water-wet. Treiber *et al.*<sup>5</sup> also observed that calcium sulfate is strongly water-wet; thus, carbonate reservoirs with some calcium sulfate grains may have microscopic variations in wettability—dalmation wettability, as described previously.

**15.2.1 Drainage and Imbibition for a Strongly Wet System.** An example of capillary pressure relationships during drainage and imbibition for an unconsolidated dolomite powder is shown in Fig. 15.6.<sup>6</sup> The wetting phase is water, and the nonwetting phase is decane. The imbibition curve remains above zero capillary pressure, similar to the typical form of Fig. 15.4.

**15.2.2 Heterogeneity.** Most naturally occurring porous media are heterogeneous, having laminations, fractures, vugs, and so forth. Such heterogeneities give rise to “bumps” in a capillary pressure relationship. An example of these bumps is shown in Fig. 15.7, as estimated with a simple model for a laminated material: the Brooks-Corey expression (Eq. 15.9 in the Capillary Pressure Models section of this chapter) for gas/oil capillary pressure was applied to rock consisting of alternate layers of two differing permeabilities. The permeabilities of the two layers differ by a factor of 4, and the threshold pressures differ by a factor of 2 (per the inverse-square-root proportionality to permeability that is suggested by Eq. 15.6 in the Capillary Pressure

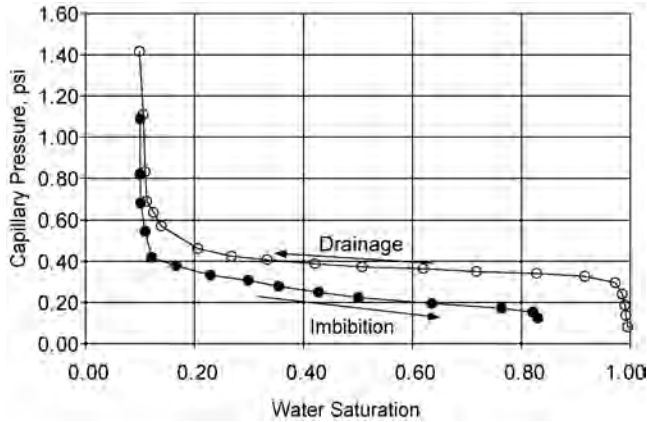


Fig. 15.6—Primary drainage and imbibition for unconsolidated dolomite powder (the lines merely connect the data). After Morrow *et al.*<sup>6</sup>

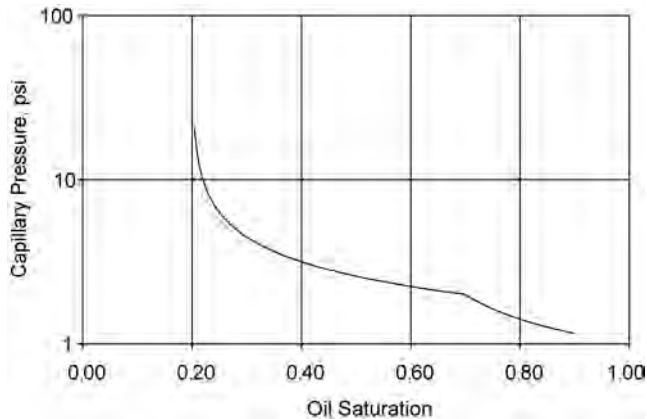


Fig. 15.7—A bump in a gas/oil capillary pressure relationship for a hypothetical heterogeneity.

Models section). The threshold pressure for the higher-permeability layer is 1 psi. The residual oil saturation is 0.20, and the exponent  $\lambda$  is 2 for both layers. All layers have the same thickness. Starting at 100% oil saturation, the oil first drains from the high-permeability layers; when the capillary pressure reaches the threshold pressure for the low-permeability layers, oil drains from those layers. The consequence is a bump in the capillary pressure relationship at oil saturation equal to approximately 0.70. Heterogeneities other than laminations can cause bumps. Any porous material that is a composite of two types of pore structure should demonstrate bumps. Similar bumps are often seen for actual rock, as demonstrated with the mercury capillary pressure data in Fig. 15.8.

**15.2.3 Wettability.** As reported by Bethel and Calhoun,<sup>7</sup> wettability affects the position of capillary pressure curves, as shown in Fig. 15.9 for displacement of oil (starting at  $S_o = 100\%$ ) by water from a glass-bead pack. The contact angles in the legend of Fig. 15.9 are as suggested by Bethel and Calhoun. The wettability moves from strongly water-wet at the top of the legend to strongly oil-wet at the bottom. With increasing oil wetness, the capillary pressure shifts upward, reflecting the increased pressure needed to push water into the pore spaces of

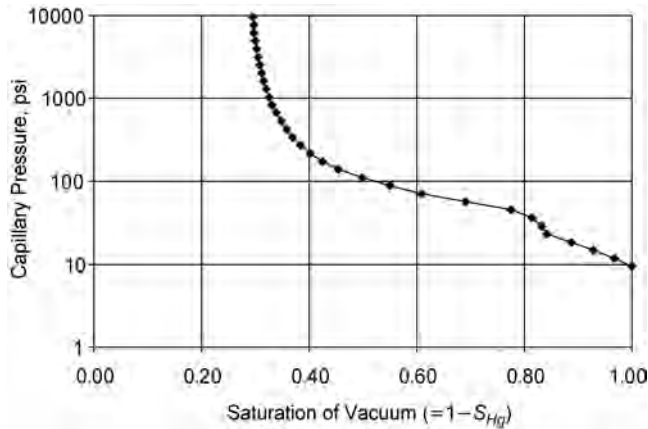


Fig. 15.8—A bump in a vacuum-mercury capillary pressure curve for a sample from the Williston basin.

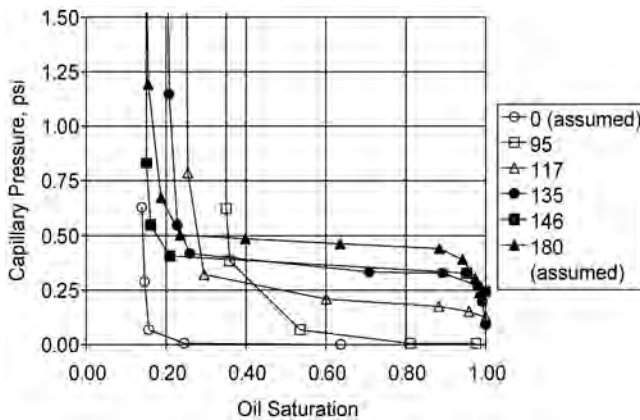


Fig. 15.9—Primary-drainage capillary pressures ( $P_c = p_w - p_o$ ) from Bethel and Calhoun.<sup>7</sup> These authors wrote capillary pressure as the negative of Eq. 4 because oil was the wetting phase for most of the tests. The legend gives contact angles measured through the water phase (in degrees).

the specimen. Fig. 15.9 also shows a variation in the residual oil saturation  $S_{or}$  with increasing wettability. When strongly water-wet,  $S_{or}$  is approximately 14%; when intermediate-wet,  $S_{or}$  rises to approximately 35%; and when strongly oil-wet,  $S_{or}$  returns to approximately 15%. Morrow<sup>8</sup> reports numerous examples of  $S_{or}$  between 6 and 10% for strongly oil-wet and intermediate oil-wet bead packs. For water-wet systems, the residual oil saturation is 14 to 16% for an unconsolidated sand with fairly uniform grain size, according to Chatzis *et al.*<sup>9</sup> These authors reported residual nonwetting saturations of 11% for clusters of smaller beads surrounded by larger beads. For larger beads surrounded by smaller beads, the residual nonwetting saturation rose to 36%.

Jerauld and Rathmell<sup>10</sup> report the imbibition and secondary-drainage data of Fig. 15.10 for a rock sample (permeability = 223 md, porosity = 0.257) from the Prudhoe Bay field, which they identify as a mixed-wet reservoir. As is typical of mixed-wet samples, the water saturation increases rapidly during imbibition for decreasing capillary pressure in the vicinity of zero. Sim-

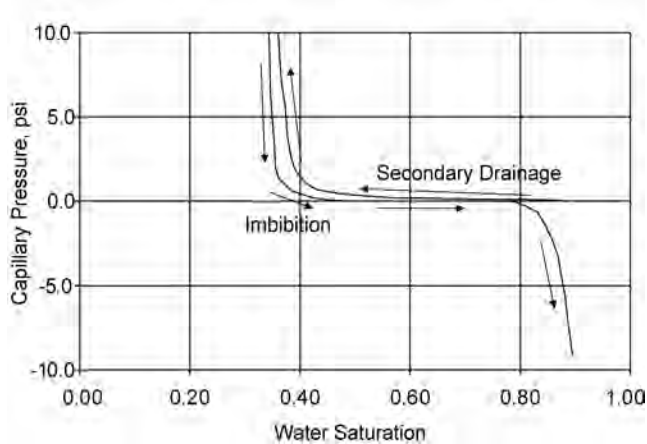


Fig. 15.10—Capillary pressure relationship for a mixed-wet sample from the Prudhoe Bay field (from Jerauld and Rathmell<sup>10</sup>).

ilarly, water saturation decreases rapidly during the secondary-drainage cycle for increasing capillary pressure just above zero.

### 15.3 Capillary Pressure Models

**15.3.1 Leverett  $j$ -Function.** Leverett and coworkers,<sup>11</sup> based on the evaluation of gas/water capillary pressure data for drainage and imbibition in unconsolidated sands, proposed the following definition:

$$P_{c_{gw}} = \sigma_{gw} \sqrt{\frac{\Phi}{k}} j(S_w). \dots\dots\dots (15.6)$$

The function  $j(S_w)$ , defined in Eq. 15.6, is known to many as the “Leverett  $j$ -function.” The  $j$ -function is obtained from experimental data by plotting  $\frac{P_{c_{gw}}}{\sigma_{gw}} \sqrt{\frac{k}{\Phi}}$  against  $S_w$ . The combination  $\sqrt{k/\Phi}$  is often considered an estimate of the mean hydraulic radius of pore throats. However, the directional dependence of permeability complicates this interpretation: Which permeability should be used? While permeabilities for just one direction are one answer, this choice is often not available.

The  $j$ -function has been used for correlating capillary pressure data for rocks with similar pore types and wettability, but with different permeabilities.<sup>12</sup> Applications include allotment of oil reserves during unitization negotiations. However, one should be very careful when correlating data with Eq. 15.6 to use permeabilities that are measured in the same direction. Perhaps some of the scatter typical of  $j$ -function correlations results from inconsistent directions of permeability measurement.

The proportionalities of Eq. 15.6 summarize an intuitive expectation for the relationship between capillary pressure, interfacial tension (IFT), and permeability that is widely used. Occasionally,  $\cos \theta$  is included adjacent to  $\sigma_{gw}$  in the definition of the  $j$ -function, although Leverett did not write it that way. While the contact angle should affect capillary pressure, the cosine function may not be the correct function to include in the definition of the  $j$ -function. Indeed, the dependence of capillary pressure on the contact angle could be quite complex. Neverthe-

less, the traditional procedure for adjusting capillary pressures for wettability uses the cosine function:

$$\frac{P_{c, \text{Condition 1}}}{P_{c, \text{Condition 2}}} = \frac{(\sigma \cos \theta)_{\text{Condition 1}}}{(\sigma \cos \theta)_{\text{Condition 2}}} \dots\dots\dots (15.7)$$

This procedure of Eq. 15.7 has been applied to the conversion of mercury capillary pressures to oil/water, gas/oil, and gas/water capillary pressures. The results are mixed: sometimes it works well, and sometimes it does not.

**15.3.2 Thomeer Model.** Thomeer<sup>13</sup> proposed a model of the following form for describing mercury-injection capillary pressure data:

$$P_c = P_{ct} e^{-G \left| \ln \left( S_{Hg} / S_{Hg\infty} \right) \right|} \dots\dots\dots (15.8)$$

in which  $S_{Hg}$  is the saturation of mercury. The Thomeer function has three parameters: the threshold pressure  $P_{ct}$ , the pore geometric factor  $G$ , and the mercury saturation at infinite capillary pressure  $S_{Hg\infty}$ . (Thomeer wrote Eq. 15.8 with bulk mercury saturation instead of mercury saturation. Bulk mercury saturation equals the product of porosity and mercury saturation. Bulk mercury saturation is appropriate for irregularly shaped samples as collected from drilling cuttings.) Thomeer related absolute permeability to the three parameters of Eq. 15.8.

**15.3.3 Brooks and Corey.** Brooks and Corey,<sup>14</sup> extending the earlier work of Corey,<sup>15</sup> suggested the following relationship for capillary pressure during primary drainage of oil from an oil-saturated porous medium during gas invasion:

$$P_{cgo} = P_{ct} \left( \frac{1 - S_{or}}{S_o - S_{or}} \right)^{1/\lambda} \dots\dots\dots (15.9)$$

$S_{or}$  is the residual oil saturation that remains trapped in the pore at high capillary pressure.  $P_{ct}$ , the threshold pressure, corresponds approximately to the pressure at which the gas phase is sufficiently connected to allow flow. Brooks and Corey related the parameter  $\lambda$  to the distribution of pore sizes. For narrow distributions,  $\lambda$  is greater than 2; for wide distributions,  $\lambda$  is less than 2. Eq. 15.9 should be representative of any primary-drainage process as long as the porous medium is homogeneous and strongly wetted by the drainage phase; that is, the contact angle measured through the wetting phase must be small.

Brooks and Corey provide no suggestions for estimating the residual oil saturation and the threshold pressure in Eq. 15.9. Typical values of residual oil saturation vary from 8 to 40%. Thomas *et al.*<sup>16</sup> suggested the following expression for roughly estimating gas/water threshold pressures of low-permeability (less than 1 md), water-saturated sandstones and limestones:

$$P_{c_{gwt}} = 7.37 k^{-0.43} \dots\dots\dots (15.10)$$

(0.43 is near to the 0.5 in the Leverett function). For this expression, the appropriate units are millidarcies for permeability  $k$  and psi for threshold pressure  $P_{c_{gwt}}$ . Eq. 15.10 should be applicable to fluid pairs other than gas and water if it is adjusted for IFT differences.

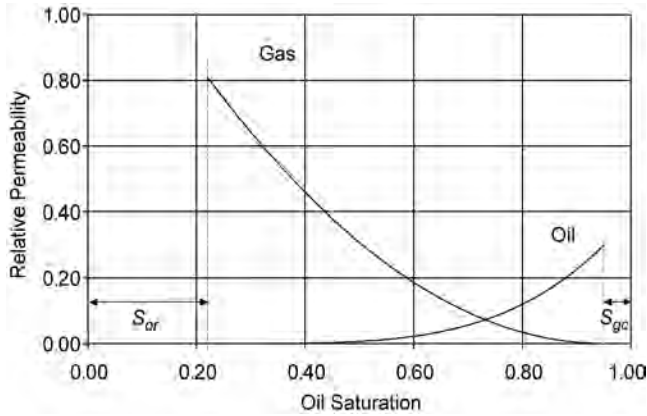


Fig. 15.11—Typical relative permeability behavior for a gas/oil system.

**15.3.4 Bentsen and Anli.** Bentsen and Anli<sup>17</sup> proposed the following expression for capillary pressure for a primary-drainage process in which a porous sample initially saturated with water is invaded by an oil phase:

$$P_{cow} = P_{ct} - P_{cs} \ln \left( \frac{S_w - S_{wi}}{1 - S_{wi}} \right) \dots \dots \dots (15.11)$$

$P_{cs}$  is a parameter with pressure units for controlling the shape of the capillary pressure function. Bentsen and Anli developed Eq. 15.11 following a qualitative argument. These authors reported a range of parameters for several rock/oil/water systems, but they did not suggest means for estimating those parameters.

**15.3.5 Alpak-Lake-Embid Model.** An interesting model was proposed by Alpak *et al.*<sup>18</sup> for representing both capillary pressure and relative permeability relationships. For capillary pressure, they suggested an expression that can be obtained by applying basic thermodynamic arguments to capillary pressure concepts. Their model relates capillary pressure to the change of oil/water interfacial area and water/solid interfacial area with water saturation. Alpak *et al.*<sup>18</sup> applied their model to drainage and imbibition data with fair success. Research in the years to come may show whether this approach to interpreting capillary pressure is useful.

## 15.4 Observations of Relative Permeability Relationships

As defined in the Introduction of this chapter, relative permeabilities are dimensionless functions of saturation with values generally ranging between 0 and 1. Figs. 15.11 and 15.12 show typical behavior for a gas/oil system. The semilog scale of Fig. 15.12 is convenient for reading the relative permeabilities less than 0.05. Although the curves are labeled “Gas” and “Oil” in these figures, the phase identity of a curve can be deduced without the labels. For example, the relative permeability that increases in the direction of increasing oil saturation must be the oil relative permeability. The endpoints of the relative permeabilities in Figs. 15.11 and 15.12 are defined by the critical gas saturation  $S_{gc}$  and the residual oil saturation  $S_{or}$ . Common names and symbols for some saturation endpoints are listed in Table 15.2.

**15.4.1 Hysteresis.** As is the case for capillary pressure, the relative permeabilities depend on the direction of saturation change, as shown schematically in Fig. 15.13. For this gas/oil system, hysteresis is much greater for the gas relative permeability. Usually, the hysteresis of the



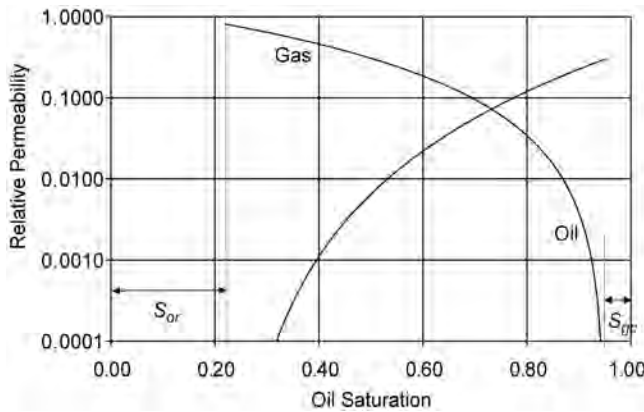


Fig. 15.12—Relative permeabilities of Fig. 15.11 on a logarithmic scale.

TABLE 15.2—TERMINOLOGY FOR SATURATION ENDPOINTS		
Saturation Endpoints	Common Names	Symbols
Remaining oil saturation after displacement by water or gas	Residual oil saturation	$S_{or}$
Minimum saturation of hydrocarbon condensate needed for flow	Critical condensate saturation	$S_{cc}$
Remaining water saturation after displacement by oil or gas	Irreducible water saturation	$S_{wi}$
Initial water saturation in a reservoir (this may equal $S_{wi}$ )	Connate water saturation	$S_{wc}$
Minimum saturation at which gas becomes mobile during a gas displacement	Critical gas saturation	$S_{gc}$
Remaining gas saturation after displacement by oil or water	Residual or trapped-gas saturation	$S_{gr}$ or $S_{gt}$

wetting phase (oil, in this example) is very small. The trapped-gas saturation  $S_{gt}$  that remains at the end of the imbibition process is a key feature of hysteresis.

Actual observations of hysteresis for water/oil systems are shown in Figs. 15.14 through 15.16. These three figures share some common characteristics. For example, one phase shows large hysteresis, while the other phase shows small hysteresis. Interestingly, the imbibition tracks in Figs. 15.15 and 15.16 are above the secondary-drainage trends. Jones and Roszelle<sup>19</sup> report large variations in  $k_{rw}$  and small variations in  $k_{ro}$  in what they consider to be a water-wet sample.

**15.4.2 Wettability.** Wettability affects the position of relative permeabilities, as shown in Fig. 15.17 (from Owens and Archer<sup>22</sup>). The authors measured oil/water relative permeabilities for varying wettabilities with a Torpedo sandstone sample. Wettability was controlled by the concentration of additives in the oil and water. Advancing contact angles were measured on a flat quartz surface.

Fig. 15.17 shows two important trends. With increasing wetting by the water, the intersection of the oil and water relative permeabilities shifts to the right, and the maximum  $k_{rw}$

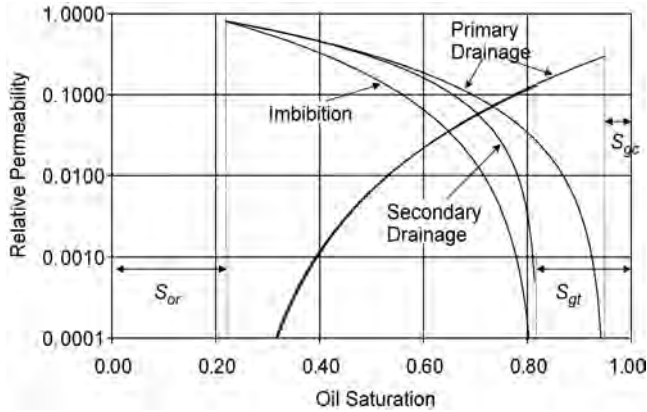


Fig. 15.13—Hysteresis behavior of relative permeabilities.

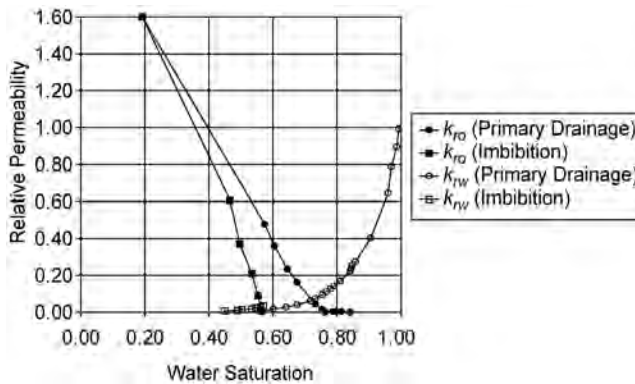


Fig. 15.14—Hysteresis for Nellie Bly sandstone, as reported by Geffen *et al.*<sup>20</sup>

decreases. Similar trends were documented by Morrow *et al.*<sup>23</sup> and by McCaffery and Bennion.<sup>24</sup> Reservoir engineers use these trends as indicators of wettability.

As mentioned previously, Treiber *et al.*<sup>5</sup> reported wettabilities for 55 oil-producing reservoirs. A rock was deemed water-wet if  $k_{rw}$  at  $S_{or}$  is less than 15% of  $k_{ro}$  at  $S_{wi}$ ; intermediate-wet if  $k_{rw}$  at  $S_{or}$  is between 15 and 50% of  $k_{ro}$  at  $S_{wi}$ ; and oil-wet if  $k_{rw}$  at  $S_{or}$  is greater than 50% of  $k_{ro}$  at  $S_{wi}$ .

In addition to the shape of the relative permeability relationships, the authors used connate water saturations, gas/oil and gas/water relative permeabilities, and contact-angle measurements to supplement their judgment of wettability. The judgments of Treiber *et al.*<sup>5</sup> relied heavily on the results of Schneider and Owens<sup>25</sup> and Owens and Archer.<sup>22</sup> Treiber *et al.*<sup>5</sup> emphasized that interpretation of wettability from relative permeability behavior is subject to large error because the relative permeabilities depend on connate water saturations and pore-size distribution in addition to wettability. Furthermore, the authors recognized that laminations and other heterogeneities can dramatically alter the relative permeability behavior and, hence, the interpretation of wettability. To prevent such mistaken interpretations, the authors selected rock samples with a high degree of homogeneity.

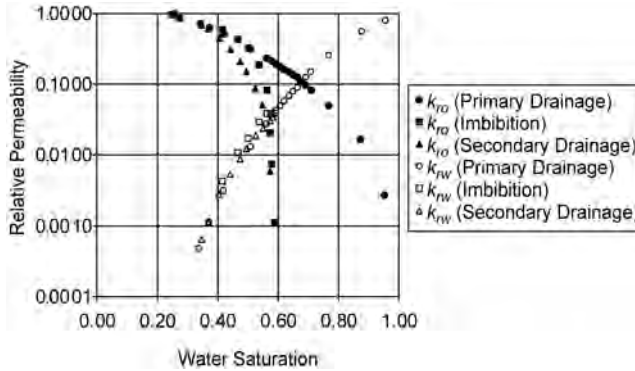


Fig. 15.15—Hysteresis for Berea sandstone as reported by Braun and Holland.<sup>21</sup>

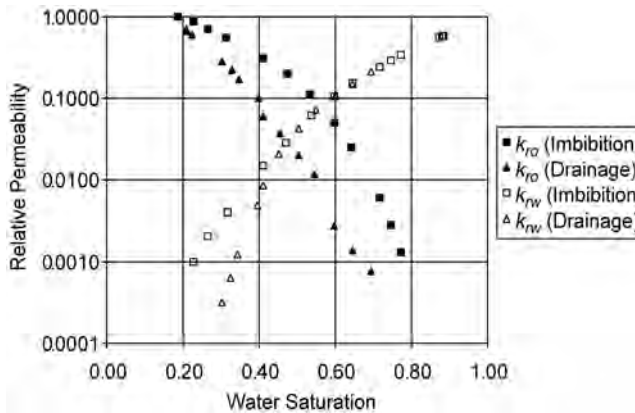


Fig. 15.16—Hysteresis for a mixed-wet sample from the Kingfish field (from Braun and Holland<sup>21</sup>).

**15.4.3 IFT.** Relative permeabilities change with decreasing IFT, especially when IFT falls below 0.1 dyne/cm<sup>2</sup>. The sensitivity of relative permeability to decreasing IFT is of great interest for enhanced-oil-recovery processes, such as miscible-gas processes and surfactant processes, and for the recovery of fluids from retrograde gas reservoirs.

The change in gas/oil relative permeabilities with decreasing gas/oil IFT as reported by Bardon and Longeron<sup>26</sup> is shown in Fig. 15.18. At very low IFT, the relative permeabilities approach an “X” shape, with endpoints close to oil saturations of 0 and 1, while at higher IFT, the relative permeabilities display more curvature and have endpoints more distant from the edges of the water-saturation scale. Significant changes in relative permeabilities are not usually observed until the IFT falls below approximately 0.1 dyne/cm<sup>2</sup>. Another example of the effect of IFT on relative permeabilities as reported by Haniff and Ali<sup>27</sup> is shown in Fig. 15.19. Asar and Handy<sup>28</sup> also reported on the changes in relative permeabilities for gas/condensate systems as the gas/condensate IFT decreased from approximately 10 to 0.01 dyne/cm<sup>2</sup>. Amaefule and Handy<sup>29</sup> reported relative permeabilities for low-IFT oil/water displacements.

**15.4.4 Endpoint Saturation Relationships.** Residual oil saturation, irreducible water saturation, trapped-oil and -gas saturations, and critical gas and condensate saturations are the most frequently encountered saturation endpoints. Residual oil, irreducible water, and trapped-gas and trapped-oil saturations all refer to the remaining saturation of those phases after extensive

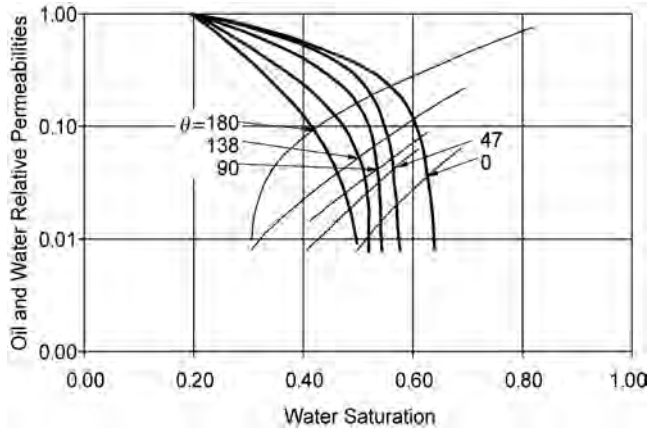


Fig. 15.17—Oil/water relative permeabilities for Torpedo sandstone with varying wettability (from Owens and Archer<sup>22</sup>). Contact angles measured through the water phase are shown in degrees. For all measurements, the water saturation was increasing, as it does in waterflooding.

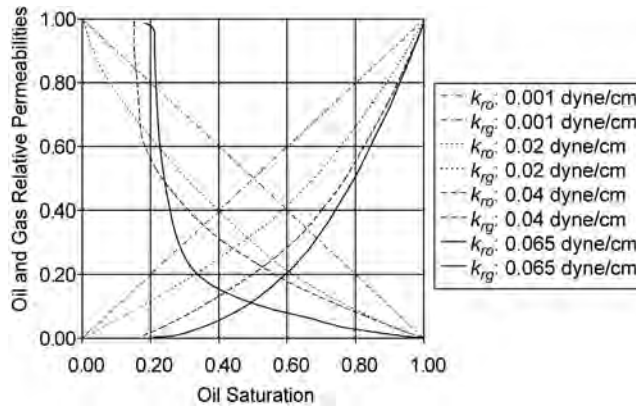


Fig. 15.18—Effect of reduced IFT on relative permeability (from Bardon and Longeron<sup>26</sup>).

displacement by other phases. Critical saturation, whether gas or condensate, refers to the minimum saturation at which a phase becomes mobile.

The endpoint saturation of a phase for a specific displacement process depends on the structure of the porous material, the wettabilities with respect to the various phases, the previous saturation history of the phases, and the extent of the displacement process (the number of pore volumes injected). The endpoint saturation also can depend on IFTs when they are very low, and on the rate of displacement when it is very high.

Results reported by Chatzis *et al.*<sup>9</sup> give general insight on the combined effects of wettability and porous structure on residual saturations. In tests with an unconsolidated sand of nonuniform grain size, the wetting phase (oil) was displaced by a nonwetting phase (air) from an initial saturation of 100% to a residual value. The authors observed residual wetting-phase saturations  $S_{wr}$  of 7 to 8%. They also found that heterogeneities in the porous medium can lead to  $S_{wr}$  greater or less than 7 to 8%, depending on the nature of the heterogeneities. Chatzis *et al.*<sup>9</sup> also reported residual nonwetting-phase (air) saturations  $S_{mwr}$  for displacements by a wetting phase (oil). They reported that  $S_{mwr}$  is approximately 14% for an unconsolidated sand of

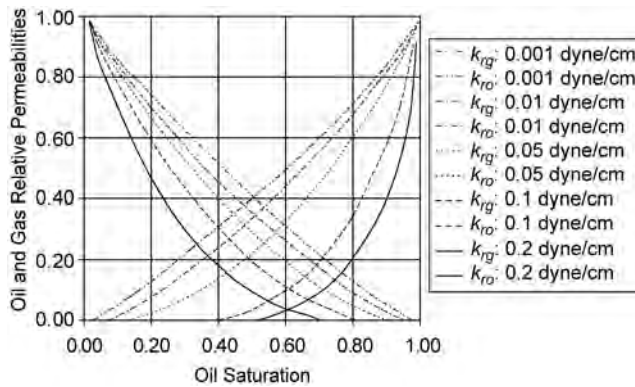


Fig. 15.19—Effect of reduced IFT on relative permeability (from Haniff and Ali<sup>27</sup>).

fairly uniform size. In tests on sandpicks of distributed grain size,  $S_{nwr}$  rose to an average of 16%. Chatzis *et al.*<sup>9</sup> also measured  $S_{nwr}$  for glass-bead packs consisting of lightly consolidated clusters of glass beads of one grain size distributed in unconsolidated glass beads of another size. They reported that  $S_{nwr}$  was 11% for clusters of smaller beads surrounded by larger beads. For larger beads surrounded by smaller beads,  $S_{nwr}$  rose to 36%. These results suggest two general conclusions. First, the residual saturation of a wetting phase is less than the residual saturation of a nonwetting phase. Second, the residual saturation of a nonwetting phase is much more sensitive to heterogeneities in the porous structure.

General conclusions on the effects of wettability are useful, but the diverse array of wetting alternatives suggests caution, especially in oil/water reservoir systems. This wide range of wetting possibilities is an obstacle to interpreting or predicting the effect of wettability on endpoint saturations. Indeed, conflicting results for different porous media are likely. For example, Jadhunandan and Morrow<sup>30</sup> report that residual oil saturation displays a minimum value for mixed-wet media as wettability shifts from water-wet to oil-wet—counter to the results of Bethel and Calhoun,<sup>7</sup> who reported a maximum for media of uniform wettability.

In the subsections below, specific relationships for endpoints of the oil, gas, and water phases are discussed.

**Critical Gas Saturation.** The critical gas saturation is that saturation at which gas first becomes mobile during a gasflood in a porous material that is initially saturated with oil and/or water. If, for example, the critical gas saturation is 5%, then gas does not flow until its saturation exceeds 5%. Values of  $S_{gc}$  range from zero to 20%.

**Critical Condensate Saturation.** Interest in the mobility of condensates in retrograde gas reservoirs developed in the 1990s, as it was observed that condensates could hamper gas production severely in some reservoirs, particularly those with low permeability. The trend of increasing critical condensate saturations with decreasing permeability, as summarized by Barnum *et al.*,<sup>31</sup> is reproduced in Fig. 15.20.

**Trapped, or Residual, Gas Saturation.** As shown in Fig. 15.21, the remaining gas saturation after a waterflood depends on the gas saturation before the waterflood. The relationship of Fig. 15.21 is often called a “trapping relationship.” The amount of gas that is trapped in gas reservoirs is of considerable economic significance. For example, in a gas reservoir, encroachment of the aquifer will lead to trapping of some portion of the gas.

Several correlations and summaries for residual gas saturation are found in the literature. Katz and Lee<sup>32</sup> provide a summary of residual gas saturations in a graphical form that is useful for estimates. According to the model presented by Naar and Henderson<sup>33</sup> for multiphase flow through rock, the trapped or residual gas saturation is one-half of its initial saturation; this Naar-

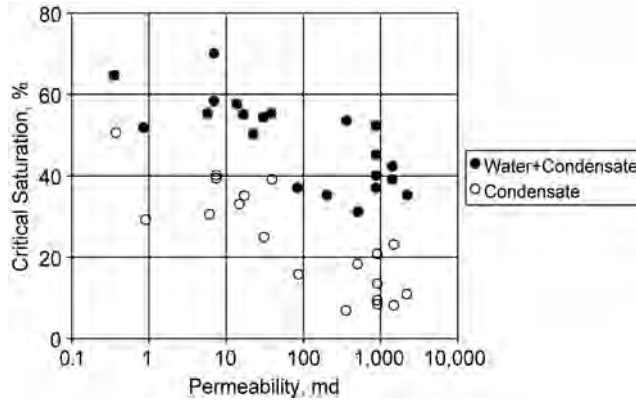


Fig. 15.20—Critical condensate saturations increase with decreasing permeability.<sup>31</sup>

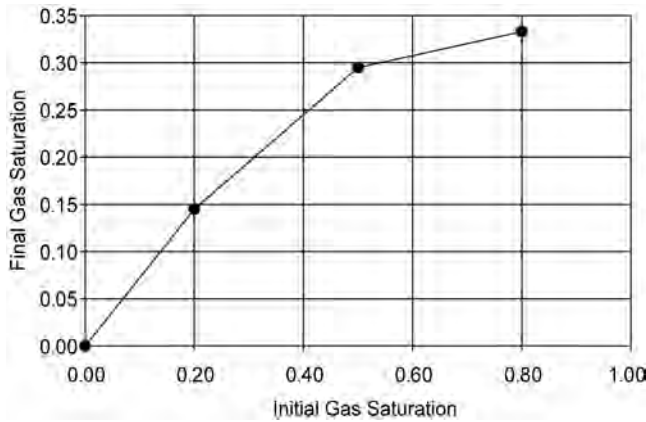


Fig. 15.21—Gas-trapping relationship for a sample ( $k=313$  md;  $\Phi=0.311$ ) from the Smackover formation in Texas (from Keelan and Pugh<sup>35</sup>).

Henderson rule is the simplest correlation for residual gas. Agarwal<sup>34</sup> correlated a large collection of residual gas saturations for consolidated and unconsolidated sandstones, for unconsolidated sands, and for limestones. The ranges of parameters in the correlations are summarized in Table 15.3. The correlations may be erroneous outside of these ranges. Three of the Agarwal correlations are listed below:

$$\text{Consolidated Sandstone : } S_{gr} = 0.8084 S_{gi} - 0.6387 S_{gi}^2 \dots\dots\dots (15.12)$$

$$\text{Unconsolidated Sandstone : } S_{gr} = -0.5126 S_{gi} + 2.61 \Phi S_{gi} - 0.2677 \Phi + 0.148. \dots\dots (15.13)$$

$$\text{Limestone : } S_{gr} = -0.5348 \Phi + 0.03356 \log_{10} k + 0.1546 S_{gi} + 0.144. \dots\dots\dots (15.14)$$

In these expressions, residual gas saturation  $S_{gr}$ , initial gas saturation  $S_{gi}$ , and porosity  $\Phi$  are fractional quantities, not percents. Permeability  $k$  is in millidarcies.

Land<sup>36</sup> suggested the following form for estimating trapped-gas saturation  $S_{gr}$  as a function of initial gas saturation  $S_{gi}$ :

**TABLE 15.3—RANGE OF PARAMETERS FOR THE AGARWAL<sup>34</sup> CORRELATIONS FOR RESIDUAL GAS SATURATION**

Type of Rock	No. of Data	Variable	Minimum	Maximum
Consolidated Sandstones	153	$\phi$ , fraction	0.144	0.2954
		$k$ , md	18	2440
		$S_{gi}$ , fraction	0.071	0.885
Limestones	86	$\phi$ , fraction	0.147	0.315
		$k$ , md	3.5	470
		$S_{gi}$ , fraction	0.473	0.794
Unconsolidated Sandstones	23	$\phi$ , fraction	0.28	0.34
		$k$ , md	750	3720
		$S_{gi}$ , fraction	0.103	0.62

$$\frac{1 - S_{wi}}{S_{gr}} - \frac{1 - S_{wi}}{S_{gi}} = C \dots\dots\dots (15.15)$$

To calculate  $C$ , a limited data set is needed, consisting of the maximum trapped-gas saturation  $S_{gr,max}$  for  $S_{gi} = 1 - S_{wi}$ . Then,

$$C = \frac{1 - S_{wi}}{S_{gr, max}} - 1 \dots\dots\dots (15.16)$$

Land<sup>37</sup> reported  $C = 1.27$  for four Berea sandstone samples.

**Residual Oil Relationships.** Residual oil saturations after waterflooding or gasflooding are clearly significant for oil recovery. Here, the dependence of residual oil saturation on initial oil saturation and capillary number for a waterflood will be considered.

The relationship between initial and residual oil saturation is termed the oil-trapping relationship. For strongly water-wet rocks, the oil-trapping relationship should be identical to the gas-trapping relationship. Indeed, because of this analogy and because it is easier to measure gas-trapping relationships, few oil-trapping relationships have been measured. A set of oil-trapping relationships reported by Pickell *et al.*<sup>38</sup> are shown in Fig. 15.22. Oil-trapping relationships are important for estimating reserves in transition zones. In conventional reservoir engineering, residual oil saturation refers to the remaining oil saturation after a displacement that starts near the maximum initial oil saturation, which generally equals one minus the initial water saturation.

In the remainder of this section, the dependence of residual oil saturation on capillary number is discussed for processes starting with initial oil saturation at a maximum value:  $S_o = 1 - S_{wi}$ . This topic has received much more attention in the literature than oil-trapping functions. The capillary number is the ratio of viscous forces to capillary forces. It is represented quantitatively with various expressions, as summarized by Lake.<sup>39</sup> These expressions are derived from the ratio of pressure drop in the water phase to the capillary pressure between the oil and water phases. A popular definition of the capillary number is as follows:

$$N_c = \frac{\mu_w v}{\sigma_{ow}}, \dots\dots\dots (15.17)$$

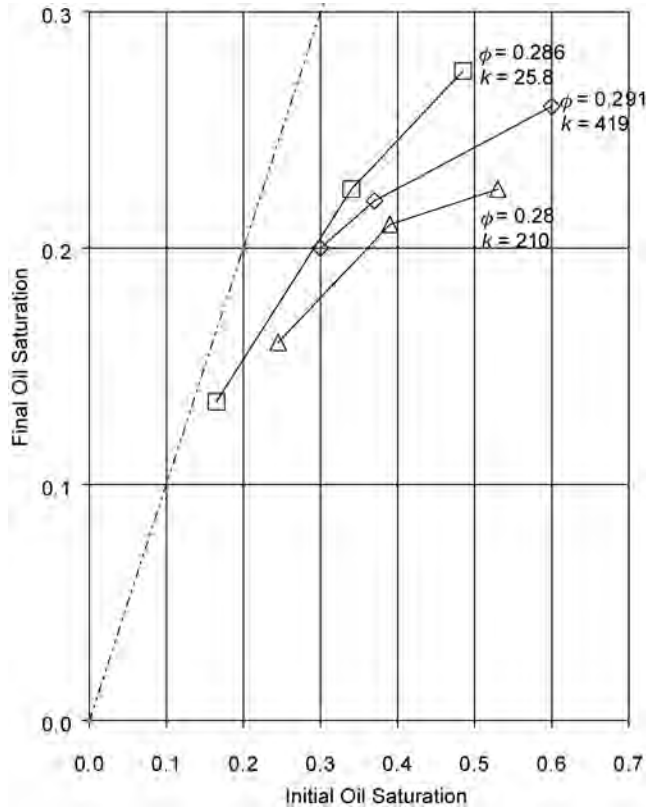


Fig. 15.22—Oil-trapping relationships for samples of Dalton sandstone.<sup>38</sup>

with  $v$  representing the velocity of the water. The capillary number is small (less than 0.00001) when capillary forces dominate the flow processes. The following example shows just how small capillary numbers can be.

**Example 15.1** Use the following quantities to estimate a capillary number for a waterflood with Eq. 15.17, where

$$\mu_w = 1 \text{ cp} = 0.01 \text{ g/cm/s}$$

$$v = 1 \text{ ft/D} = 30.48 \text{ cm}/(24 \times 3,600 \text{ s}) = 0.00035 \text{ cm/s}$$

$$\sigma_{ow} = 30 \text{ dynes/cm}$$

Therefore, the capillary number is as follows:

$$N_c = \frac{(0.01 \text{ g/cm/s})(0.00035 \text{ cm/s})}{(30 \text{ dynes/cm})} = 1.2 \times 10^{-7}.$$

Capillary forces do indeed dominate flow processes for waterfloods. Even in high-velocity regions, such as the vicinity of a well that is producing oil and water, the capillary number will remain very small.

Having defined the capillary number, the relationship between residual oil saturation and capillary number will be discussed next. As the capillary number for an oil-displacing process



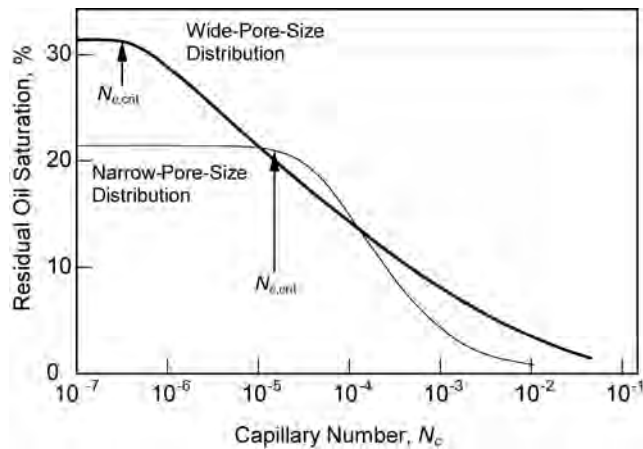


Fig. 15.23—Typical behavior of relationships for mobilization of residual oil (patterned after Figs. 3-17 and 3-18 of Lake<sup>43</sup>).

increases, residual oil saturation decreases in the manner sketched in Fig. 15.23. Above the “critical capillary number,” the rate of decrease of  $S_{or}$  is particularly rapid. The critical capillary number is  $10^{-5}$  to  $10^{-4}$  for porous media with fairly uniform pore sizes. With increasing distribution of pore sizes, the critical capillary number decreases, the  $S_{or}$  at low  $N_c$  increases, and the domain for decreasing  $S_{or}$  becomes broader. Extensive discussion of these relationships is available elsewhere.<sup>40</sup> King *et al.*<sup>41</sup> suggested centrifuge methods for measuring these relationships. Pope *et al.*<sup>42</sup> correlated residual phase saturation with a modified form of the capillary number, which was termed the “trapping number.” Adjusting a parameter in their correlation fits the effects of wetting on residual saturation.

**Residual (Irreducible) Water Saturation.** Residual, or irreducible, water saturation  $S_{wi}$  is the lowest water saturation that can be achieved by a displacement process, and it varies with the nature of the process—gas displacement or oil displacement. Also,  $S_{wi}$  varies with the extent of the displacement, as measured by pore volumes of oil or gas injected or by time allowed for drainage.

To be more specific, the results of Chatzis *et al.*<sup>9</sup> (discussed in the introduction to this section) can be extended to suggest irreducible water saturations of 7 to 9% for displacements in unconsolidated sand and glass beads that are water-wet. Furthermore,  $S_{wi}$  should increase slightly with increasing breadth of grain-size distribution. Significant variations in  $S_{wi}$  should occur when small clusters of consolidated media of one grain size are surrounded by media of another grain size. If the grains of the clusters are smaller than those of the surrounding media,  $S_{wi}$  increases; if the grains of the clusters are larger than those of the surrounding media,  $S_{wi}$  decreases.

The saturation of water in an oil or gas reservoir at discovery is called the connate water saturation, or  $S_{wc}$ . The connate water saturation and the irreducible water saturation can differ. If the reservoir processes that produced the connate water saturation can be replicated, then the  $S_{wi}$  for the replicated processes should be the same as  $S_{wc}$ .  $S_{wc}$  is significant for its connection to initial oil or gas saturation in a reservoir. For an oil reservoir,  $S_o = 1 - S_{wc}$ ; for a gas reservoir,  $S_g = 1 - S_{wc}$ . The connate water saturation will also affect initial oil or gas relative permeability and, hence, the economic viability of a reservoir. Bulnes and Fitting<sup>44</sup> concluded that low-permeability limestone reservoirs are more viable than sandstone reservoirs of the same permeability because the connate water saturation is lower in the limestones than in the sandstones; as a result, the relative permeabilities to oil are higher in the limestones than in the sandstones.

Salathiel<sup>4</sup> observed that the connate water saturations in carefully retrieved rock samples from some oil reservoirs are substantially lower than can be achieved when the rock is waterflooded and then oilflooded. He attributed this effect to the mixed-wettability condition. When the reservoir was first invaded by oil, the rock was water-wet, and low water saturations were obtained. However, the wettability of the rock surfaces that were now in contact with oil changed from water-wet to oil-wet as portions of the hydrocarbons adsorbed onto the solid surfaces. So, when such a rock is waterflooded and then oilflooded, the connate water saturation is not obtained because the water in the oil-wet portions of the rock becomes trapped.

**15.4.5 Temperature.** The effects of temperature on relative permeability have been studied primarily for applications to steamflooding and in-situ combustion. Mechanistically speaking, temperature can affect relative permeability by altering the IFT between flowing phases or by altering the wettability of the porous material. IFT between water and oil should decrease with increasing temperature, but to substantially influence relative permeability, the IFT would need to decrease to 0.1 dyne/cm<sup>2</sup> or less, according to the discussions in previous sections. Such reductions would be possible only at very high temperatures with light oils. Therefore, temperature-related IFT reductions could influence relative permeabilities for in-situ combustion processes, but they would not be important for typical steamflooding.

The influence of temperature on wettability and, hence, on relative permeability is more likely to be important for most applications. With increasing temperature, the wettability could shift either to more water-wet or more oil-wet conditions, depending on the reservoir fluids and the chemical composition of the porous medium.

Akin *et al.*<sup>45</sup> reviewed a wide variety of published studies of relative permeabilities for heavy oil and water at different temperatures. Some of the studies concluded that these relative permeabilities were unaffected by temperature changes, while other studies concluded the opposite. In the light of the previous paragraph, these contradictory observations in the literature are not surprising. However, Akin *et al.*<sup>45</sup> concluded that viscous instability—not wettability change—is the cause of most reported changes in relative permeability with increasing temperature.\* With increasing temperature, the viscosity of the heavy oil decreases, and the water/oil displacement process becomes more stable. The changing stability of the displacement (estimated with the expression of Peters and Flock<sup>46</sup>) causes the apparent relative permeabilities to change with temperature. Nevertheless, it is possible that relative permeabilities do change with temperature for some systems. As Akin *et al.*<sup>45</sup> conclude, further study of this subject is needed.

## 15.5 Relative Permeability Models

**15.5.1 Brooks-Corey and Related Models.** In 1954, Corey<sup>15</sup> combined predictions of a tube-bundle model with his empirical expression for capillary pressure to obtain expressions for gas and oil relative permeabilities. In 1964, Brooks and Corey<sup>47</sup> extended Corey's results using Eq. 15.9 for capillary pressure to obtain the following expressions for oil and gas relative permeabilities:

$$k_{ro} = \left( \frac{S_o - S_{or}}{1 - S_{or}} \right)^{\frac{2+3\lambda}{\lambda}} \dots\dots\dots (15.18)$$

\* Viscous instability results from displacement of a viscous (low-mobility) phase by a less-viscous (high-mobility) phase. The high-mobility phase is prone to bypass or "finger" through the low-mobility phase. With "viscous fingering," the displacement must be 2D or 3D rather than 1D. One-dimensional displacements are preferred for measurement of relative permeabilities.

$$\text{and } k_{rg} = \left( \frac{1 - S_o}{1 - S_{or}} \right)^2 \left[ 1 - \left( \frac{S_o - S_{or}}{1 - S_{or}} \right)^{\frac{2+\lambda}{\lambda}} \right] \dots\dots\dots (15.19)$$

Eqs. 15.18 and 15.19 apply to a porous material that is initially fully saturated with oil and then invaded by gas. These equations do not allow for nonzero critical gas saturation. For  $\lambda=2$ , Eqs. 15.18 and 15.19 reduce to the 1954 Corey expressions. Brooks and Corey related the parameter  $\lambda$  to the distribution of pore sizes. For narrow distributions,  $\lambda$  is greater than 2; for wide distributions,  $\lambda$  is less than 2. They reported that  $\lambda=7.30$  for an unconsolidated pack of glass beads of uniform diameter. For sandpicks with broader distributions of particle sizes,  $\lambda$  ranged from 1.8 to 3.7. For a particularly homogeneous consolidated sandstone, they reported  $\lambda =4.17$ .

The following “power-law” relationships are often used to describe oil, water, and gas relative permeabilities, respectively:

$$k_{ro} = k_{ro, \max} \left( \frac{S_o - S_{or}}{1 - S_{or} - S_{wc} - S_{gc}} \right)^{n_o}, \dots\dots\dots (15.20)$$

$$k_{rw} = k_{rw, \max} \left( \frac{S_w - S_{wc}}{1 - S_{or} - S_{wc} - S_{gc}} \right)^{n_w}, \dots\dots\dots (15.21)$$

$$\text{and } k_{rg} = k_{rg, \max} \left( \frac{S_g - S_{gc}}{1 - S_{or} - S_{wc} - S_{gc}} \right)^{n_g} \dots\dots\dots (15.22)$$

The exponents  $n_o$ ,  $n_w$ , and  $n_g$  range from 1 to 6. The maximum relative permeabilities,  $k_{ro, \max}$ ,  $k_{rw, \max}$ , and  $k_{rg, \max}$ , are between 0 and 1. These expressions are often referred to as modified Brooks-Corey relations, reflecting their similarity to the Brooks-Corey expression for oil relative permeability.

**15.5.2 A Model for Heterogeneous Rock.** In 1956, Corey and Rathjens<sup>48</sup> extended Corey’s earlier work to explain the effect of laminations on gas/oil relative permeability relations. They considered flow parallel and flow perpendicular to  $N$  laminations. For flow perpendicular to laminations,

$$k_{roT} = \frac{1}{k_T \sum_{i=1}^N \frac{f_i}{k_i k_{roi}}} \dots\dots\dots (15.23)$$

$$\text{and } k_{rgT} = \frac{1}{k_T \sum_{i=1}^N \frac{f_i}{k_i k_{rgi}}} \dots\dots\dots (15.24)$$

For flow parallel to laminations,

$$k_{roT} = \frac{1}{k_T} \sum_{i=1}^N f_i k_i k_{roi} \dots\dots\dots (15.25)$$

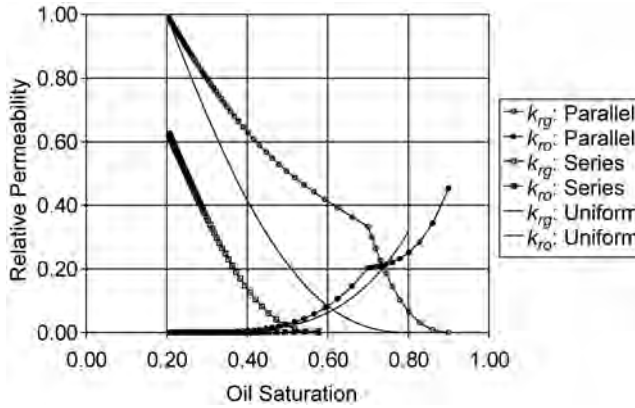


Fig. 15.24—Predictions of Eqs. 15.23 through 15.26 for flow parallel and perpendicular to laminations.

$$\text{and } k_{rgT} = \frac{1}{k_T} \sum_{i=1}^N f_i k_i k_{rgi} \dots\dots\dots (15.26)$$

In these expressions,  $k_i$  is the permeability of each layer;  $k_{roi}$  and  $k_{rgi}$  are oil and gas relative permeabilities for each layer, respectively;  $f_i$  is the fraction of total sample volume for each layer;  $k_T$  is the total permeability of the laminated materials; and  $k_{roT}$  and  $k_{rgT}$  are the resulting total relative permeabilities of the laminated materials. The predictions of Eqs. 15.23 through 15.26 for  $N = 2$  are shown in Fig. 15.24. The permeability of one region is one-fourth that of the other region. The relative permeabilities are given by Eqs. 15.18 and 15.19 with  $\lambda = 2$  and with  $S_{or} = S_{gc} = 0.20$ . Corey and Rathjens<sup>48</sup> noted two consequences of laminations: bumps in the relative permeability relationships and a shifting of the critical gas saturation. As shown in Fig. 15.24, the critical gas saturation shifts from 0.20 for the uniform sample to 0.10 for flow parallel to strata, and to 0.33 for flow perpendicular to laminations. Also, the relative permeability for flow perpendicular to laminations is much less than that parallel to laminations. As shown in Fig. 15.25, measured relative permeabilities for a sample of Berea outcrop sandstone with visually apparent laminations show the predicted trends. The Corey-Rathjens observations were used by Ehrlich<sup>49</sup> to explain the relative permeability behavior of vuggy and fractured samples.

**15.5.3 Chierici Model.** Chierici<sup>50</sup> proposed exponential expressions for fitting gas/oil relative permeabilities:

$$k_{ro} = \exp(-A S_{gN}^L) \dots\dots\dots (15.27)$$

$$\text{and } k_{rg} = \exp(-B S_{gN}^{-M}), \dots\dots\dots (15.28)$$

with gas saturation normalized as follows:  $S_{gN} = \frac{S_g - S_{gc}}{1 - S_{wi} - S_g}$ . His expressions for oil/water relative permeabilities are

$$k_{ro} = k_{ro, \max} \exp(-A S_{wN}^L) \dots\dots\dots (15.29)$$

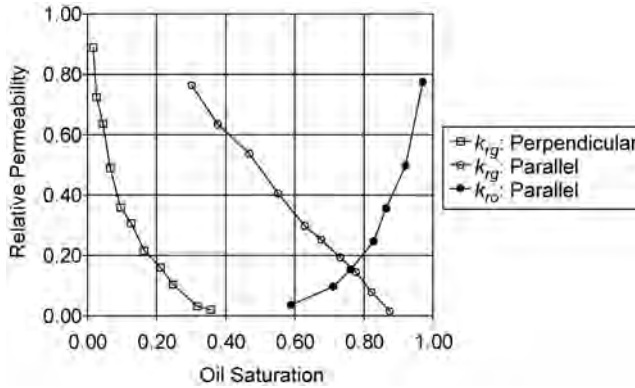


Fig. 15.25—Observed relative permeabilities parallel and perpendicular to stratification for a sample of Berea outcrop (from Corey and Rathjens<sup>48</sup>).

$$\text{and } k_{rw} = k_{rw, \max} \exp(-B S_{wN}^{-M}), \dots\dots\dots (15.30)$$

with water saturation normalized as follows:  $S_{wN} = \frac{S_w - S_{wi}}{1 - S_{or} - S_w}$ . The Chierici expressions were used in a recent discussion of three-phase relative permeabilities.<sup>51</sup>

**15.5.4 Correlations of Honarpour *et al.* and Ibrahim.** Other researchers have offered correlations for laboratory measurements of relative permeabilities. Honarpour *et al.*<sup>52</sup> suggest correlations for two sets of rock samples—sandstones and conglomerates and limestones and dolomites—with varying wettabilities. Ibrahim<sup>53</sup> reported a more extensive set of correlations. Such correlations are useful for understanding general trends and for preliminary estimates; however, they can be far from correct when applied to a specific formation.

**15.5.5 Hysteresis Models.** The effect of relative permeability hysteresis on reservoir performance can be significant for processes with variable directions of saturation change. For example, during coning of water toward an oil-producing well, the water saturation is increasing; however, if the production rate is decreased or set to zero, the water saturation can decrease. Hysteresis also can affect the performance of a waterflood if the relative production rate of a well in a pattern of producers is changed. To facilitate simulation of these processes, a number of models have been proposed for representing hysteresis effects on relative permeability and capillary pressure. The hysteresis models of Killough<sup>54</sup> and Carlson<sup>55</sup> are used in some commercial simulation software. Fayers *et al.*<sup>51</sup> proposed another model for incorporating hysteresis effects in reservoir simulation. These models extrapolate and interpolate from measured drainage and imbibition curves to generate “reasonable” estimates of relative permeabilities. Although these models may be satisfactory for preliminary estimates, many more experimental data on hysteresis of relative permeability and capillary pressure are needed.

**15.5.6 Carman-Kozeny Models.** Alpak *et al.*<sup>18</sup> used concepts from a model for capillary pressure to build a relative permeability model with the form of the Carman-Kozeny expression for permeability. (See Alpak *et al.*<sup>18</sup> for references to other related models.) The Alpak *et al.*<sup>18</sup> model relates relative permeabilities to the total surface area of the solid  $A_T$ , the oil/water interfacial area  $A_{ow}$ , the water/solid interfacial area  $A_{ws}$ , and the oil/solid interfacial area  $A_{os}$ :

$$k_{rw} = S_w^3 \frac{\tau}{\tau_w} \frac{A_T^2}{(A_{ow} + A_{ws})^2} \dots\dots\dots (15.31)$$

$$\text{and } k_{ro} = S_o^3 \frac{\tau}{\tau_o} \frac{A_T^2}{(A_{ow} + A_{os})^2} \dots\dots\dots (15.32)$$

This relative permeability model includes tortuosity relationships,  $\tau_w/\tau$  and  $\tau_o/\tau$ , that do not arise in the capillary pressure model of Alpak *et al.*<sup>18</sup> This interesting difference suggests that relative permeabilities cannot be estimated from capillary pressure information alone. Alpak *et al.*<sup>18</sup> suggested relationships for the tortuosity and the area functions. They used the model to fit relative permeability data for unconsolidated and consolidated media. Future research will test the merit of this approach to modeling relative permeability.

**15.5.7 Network Models.** The advent of computers led to the development of models that represent porous structure as 2D and 3D networks of flow channels. Analysis of these network models leads to capillary pressure and relative permeability relationships. The capacity of these models to represent real behavior has increased with improved descriptions of the displacement mechanisms.<sup>56</sup>

**15.5.8 Models for Three-Phase Relative Permeabilities.** Many reservoir processes, such as waterflooding below the bubblepoint pressure of the oil in place, involve simultaneous flow of three phases. To model these processes, three-phase relative permeabilities are mandatory. Measurements of three-phase relative permeabilities are much rarer than those for two-phase relative permeabilities, and there is more uncertainty in the reported three-phase data, as noted by Baker<sup>57</sup> in his 1988 review of three-phase correlations.

Current efforts in three-phase relative permeability studies are weighted toward identification of models for extrapolating two-phase relative permeability data to three-phase applications. Stone<sup>58</sup> started this trend in 1970 with a model that is now known as the Stone I model. In this model for water-wet porous media, the three-phase water relative permeability  $k_{rw,wog}$  depends only on water saturation and is identical to  $k_{rw,wo}$  measured in water/oil displacements:

$$k_{rw, wog}(S_w) = k_{rw, wo}(S_w) \dots\dots\dots (15.33)$$

Similarly, the three-phase gas relative permeability  $k_{rg,wog}$  depends only on gas saturation and is identical to  $k_{rg,go}$  measured in gas/oil displacements at irreducible water saturation.

$$k_{rg, wog}(S_g) = k_{rg, go}(S_g) \dots\dots\dots (15.34)$$

The equality of water and gas relative permeabilities in two- and three-phase flow, as described by Eqs. 15.33 and 15.34, is supported by much of the three-phase data in the literature for water-wet media. On the other hand, the three-phase oil relative permeability  $k_{ro,wog}$  depends nonlinearly on water and gas saturations:\*

\* The factors that contain  $k_{ro,wo}(S_{wo})$  in Eqs. 15.35 and 15.41 reflect normalization of relative permeabilities with respect to absolute permeability, as is the convention in this chapter. For a comparison of these normalized equations to data, see Ref. 59. Originally, Stone normalized with respect to oil permeability at irreducible water saturation. The Stone versions of Eqs. 15.35 and 15.41 can be recovered exactly by omitting the extra factors from Eqs. 15.35 and 15.41.

$$k_{ro, wog}(S_w, S_g) = \frac{1}{k_{ro, wo}(S_{wc})} S_o S \frac{k_{ro, wo}(S_w)}{(1 - S_{wS})} \frac{k_{ro, og}(S_g)}{(1 - S_{gS})}, \dots\dots\dots (15.35)$$

with the oil, water, and gas saturations scaled, respectively, as follows:

$$S_{oS} = \frac{S_o - S_{om}}{1 - S_{wc} - S_{om}} \quad \text{for } S_o \geq S_{om}, \dots\dots\dots (15.36)$$

$$S_{wS} = \frac{S_w - S_{wc}}{1 - S_{wc} - S_{om}} \quad \text{for } S_w \geq S_{wc}, \dots\dots\dots (15.37)$$

$$\text{and } S_{gS} = \frac{S_g}{1 - S_{wc} - S_{om}}. \dots\dots\dots (15.38)$$

According to Stone, the minimum oil saturation  $S_{om}$  should be in the range of  $\frac{1}{4} S_{wc}$  to  $\frac{1}{2} S_{wc}$ , and it should be less than or equal to the smaller of  $S_{orw}$  or  $S_{org}$ , the residual oil saturations for waterflooding and gasflooding, respectively. Fayers and Matthews<sup>59</sup> proposed the following expression for  $S_{om}$ :

$$S_{om} = \alpha S_{orw} + (1 - \alpha) S_{org}, \dots\dots\dots (15.39)$$

with  $\alpha = 1 - S_g / (1 - S_{wc} - S_{org})$ . Aleman, as reported by Baker,<sup>57</sup> proposed an alternative expression:

$$S_{om} = S_{orw} \left( \frac{S_w - S_{wc}}{1 - S_{owc} - S_{orw}} \right)^\alpha + S_{org} \left( \frac{S_g}{1 - S_{owc} - S_{orw}} \right)^\beta \dots\dots\dots (15.40)$$

To account for hysteresis effects in three-phase flow, Stone recommended use of the appropriate two-phase relative permeabilities. For example, in a water-wet system, if oil saturation is decreasing and gas and water saturations are increasing in the three-phase setting, then the following two-phase relative permeabilities should be used:  $k_{ro,wo}$  for decreasing oil saturation;  $k_{rw,wo}$  for increasing water saturation; and  $k_{rg,go}$  for increasing gas saturation.

In 1973, Stone<sup>60</sup> proposed another model, which has become known as the Stone II model. In this model, the three-phase water and gas relative permeabilities are again equal to those measured in two-phase flow, as expressed by Eqs. 15.33 and 15.34, while the oil relative permeability is as follows:

$$k_{ro, wog}(S_w, S_g) = k_{ro, wo}(S_{wc}) \left\{ \left[ \frac{k_{ro, wo}}{k_{ro, wo}(S_{wc})} + k_{rw, wo} \right] \left[ \frac{k_{ro, og}}{k_{ro, wo}(S_{wc})} + k_{rg, go} \right] - (k_{rw, wo} + k_{rg, go}) \right\} \dots\dots\dots (15.41)$$

The water/oil and the gas/oil relative permeabilities in Eq. 15.41 are functions of water saturation and gas saturation, respectively.

Baker<sup>57</sup> compared four versions of the Stone models and various other models to available data for three-phase relative permeabilities. He concluded that models based on linear interpolation from the two-phase relative permeabilities perform as well as the other models. As an example of linear interpolation models, Baker suggested the following saturation weighting of two-phase relative permeabilities:

$$k_{ro, wog} = \frac{(S_w - S_{wr}) k_{ro, wo} + (S_g - S_{gr}) k_{ro, go}}{(S_w - S_{wr}) + (S_g - S_{gr})}, \dots\dots\dots (15.42)$$

$$k_{rw, wog} = \frac{(S_o - S_{or}) k_{rw, ow} + (S_g - S_{gr}) k_{rw, gw}}{(S_o - S_{or}) + (S_g - S_{gr})}, \dots\dots\dots (15.43)$$

$$\text{and } k_{rg, wog} = \frac{(S_w - S_{wr}) k_{rg, gw} + (S_o - S_{or}) k_{rg, go}}{(S_w - S_{wr}) + (S_o - S_{or})}. \dots\dots\dots (15.44)$$

Blunt<sup>61</sup> showed how to extend this model to describe relative permeability of oil at very low saturations, often termed the “layer drainage” regime.

Another model for three-phase relative permeabilities and capillary pressures was proposed recently by Fayers *et al.*<sup>51</sup> The lasting value of this or any of the above-mentioned models, will be known only when more data become available for comparisons.

## 15.6 Measurement of Rock/Fluid Relationships

**15.6.1 Reliability of Measurements.** The reliability of measurements of relative permeabilities and capillary pressures is an important issue for reservoir engineering. Although there are many factors that influence reliability, the following three topics are emphasized here:

- Sampling of rocks for measurements.
- Measurement methods.
- Treatment of data from the measurements.

Proper sampling of rocks for measurements is most important for ensuring the reliability of relative permeability and capillary pressure data. If samples are obtained improperly, costly and reliable methods for measuring rock/fluid properties may no longer be necessary or suitable. The goal of sampling should be to avoid or minimize mechanical and chemical damage to the rock. Mechanical and chemical damage can occur during any of four steps in the sampling process: coring and core retrieval, shipping and storing, cutting samples from the core, and cleaning and preparing the sample. With all of these opportunities, some damage is inevitable.

It should be obvious that reliable data require good measurement methods and correct treatment of the data obtained. But defining “good” and “correct” requires some not-so-obvious understanding—a goal of this discussion is to touch on the important issues. Measurement of relative permeability and capillary pressure relationships is complicated, particularly because of the intertwining nature of these rock/fluid properties. Indeed, it is the deciphering of these complications that largely defines what is meant by “good” and “correct.”<sup>62</sup>

**15.6.2 Sample Handling and Preparation.** From cutting a core from a formation to final preparations of a specimen for testing, improper practices will alter the porous structure and wettability of rock samples, which in turn will alter the quality of measurements. The most appropriate procedures depend on the ultimate objective of sample analysis. If the sample is to



be used only for porosity and permeability measurement, wettability alterations during handling are not important. But for capillary pressure and relative permeability measurements with native-state wetting conditions, one must work to avoid contamination of the sample. Next, a distillation of industry experience with handling and preparation of samples is presented.

**Cutting a Core From a Formation.** Drilling fluids often contain oxygen, surfactants, polymers, clays, and other particulates in oil- or water-based slurries. To minimize contamination with drilling fluids, cores are sometimes cut with fresh formation oil, synthetic formation brines, or drilling fluids formulated to minimize invasion. Sometimes, the extent of invasion can be assessed later in the laboratory. Coring also can produce fractures in the rock, either by the mechanical stress of the drilling process, by relief of the in-situ mechanical and thermal stresses on the core as it travels to the surface, or by retrieval (often with a big hammer) from the core barrel at the surface.

**Shipping.** A variety of methods are used to ship core. Core has been shipped in containers filled with oil or water from the producing formation, it has been shipped in sealed polymeric bags with metallic barriers to oxygen permeation, and it has been shipped after wrapping with a metallic foil and a wax-coated fabric. Some core has been frozen immediately with dry ice or liquid nitrogen upon arrival at the surface, then shipped in a frozen condition to prevent oxidative and bacterial actions and to minimize evaporation of the water or oil.

**Sample Collection.** Selection of the locations in the core for taking samples is a critical step. For porosity and permeability testing, samples are usually collected at regular intervals (e.g., every foot). Sometimes, the most homogeneous samples are selected. Such a bias likely imposes an undesirable bias on the results. Selecting locations for sampling should follow a logical or a statistical thought process. For example, criteria for sample selection can include mineralogy, pore structure, homogeneity or heterogeneity, porosity, and permeability. Computerized tomography (CT) scanning can help the selection of samples without internal pebbles or fractures that might drastically affect the outcome of measurements. In general, the characteristics of a collected sample should represent a significant portion of the reservoir. After locations are chosen, collection can begin. Collecting a rock sample from the core generally entails a cutting action with diamond-coated saws and boring tools. The coolant for these cutting processes is a source of contamination. To reduce contamination, liquid nitrogen is sometimes used as a coolant, but most often kerosene or water is used—these coolants should be free of contaminants. For preserving water saturations in the sample, kerosene is a common choice for cooling. Excessive exposure of the core to air during sample collection can foster a shift of wettability from its native condition.

**Sample Cleaning and Preparation.** After collection from the core, rock samples are thoroughly cleaned in preparation for porosity, permeability, and other measurements. Cleaning by flushing the sample alternately with toluene, chloroform, acetone, and methanol (and mixtures of these) is common and often satisfactory. To preserve delicate clay structures in some samples, a cleaning process with miscible fluids and supercritical drying is sometimes used. Cleaning a sample with boiling solvent (such as toluene) in a reflux-extraction unit should be avoided. During such cleaning, water vaporizes, and any surface coated with water can become coated with high-molecular-weight hydrocarbons that are less soluble at elevated temperatures—this can impart a nearly permanent change in wettability.

**Final Preparations for Testing.** After suitable cleaning, the samples can be used in the clean condition for porosity, absolute permeability, and mercury capillary pressure measurements; alternatively, the condition of the samples can be returned to near reservoir condition by processes of flooding with brine and oil from the formation and aging in formation oil. Such restored-state samples can be suitable for capillary pressure and relative permeability measurements with reservoir fluids. Common practice includes centrifugation of brine-saturated samples in air to reduce the brine saturation to near reservoir levels. Some rock samples are not

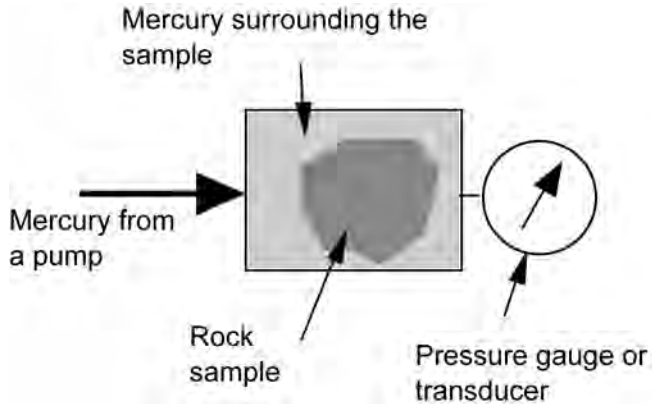


Fig. 15.26—To measure the mercury capillary pressure relationship, mercury is metered into an evacuated rock sample.

cleaned after collection from the core but are maintained instead in a preserved state by storing them in uncontaminated oil from the reservoir. Such samples are flooded with formation oil in preparation for measurements.

**15.6.3 Measuring Capillary Pressure Relationships.** Most methods for measuring capillary pressure may be grouped under three headings: mercury methods, porous-plate methods, and centrifuge methods. Each of these is discussed below. Vapor-pressure and gravity-equilibrium methods also have been used, but they are not discussed here. The literature offers few examples of capillary pressure measurements with overburden stress matching that in the reservoir. The magnitude of error caused by this omission will vary, of course, from reservoir to reservoir, but the meaning and significance of capillary pressure data without the appropriate overburden stress are questionable. Some commercial laboratories offer capillary pressure measurements with overburden stress.

**Mercury Methods.** In the mercury method, a sample of rock is evacuated, and the volume of mercury that enters the sample at increasing pressures is measured, as shown in Fig. 15.26. Mercury methods are especially suited for samples of irregular shape, such as those found in drill cuttings. Mercury methods are useful for investigating the porous structure of the sample. Complete mercury capillary pressure curves can be determined within an hour or so, depending on the permeability of the sample. To apply the proper overburden stress, a cylindrical sample could be mounted in a confining sleeve in a variation of the apparatus of Fig. 15.26. Some commercial laboratories offer mercury measurements with overburden stress.

Use of the mercury method was first documented in the petroleum literature by Purcell in 1949.<sup>63</sup> Purcell showed that mercury capillary pressure and air/water capillary pressure relationships could be correlated. He outlined a method for estimating permeability from mercury measurements. Rose and Bruce<sup>64</sup> proposed a relationship between a rock's threshold capillary properties and its permeability. Thomeer<sup>13</sup> proposed a correlation for estimating permeability from three parameters of the mercury capillary pressure curve, as mentioned previously. Swanson<sup>65</sup> proposed a correlation between permeability and the intersection of a 45° line with the mercury capillary pressure relationship plotted on a log-log scale.

**Porous-Plate Methods.** The porous-plate method can yield very accurate capillary pressure relationships. The following example describes the method. Consider a cylindrical rock sample that is first saturated with water. A flat face of the sample is then pressed against a flat porous plate (or membrane) in a chamber filled with gas, as shown in Fig. 15.27. The porous plate is

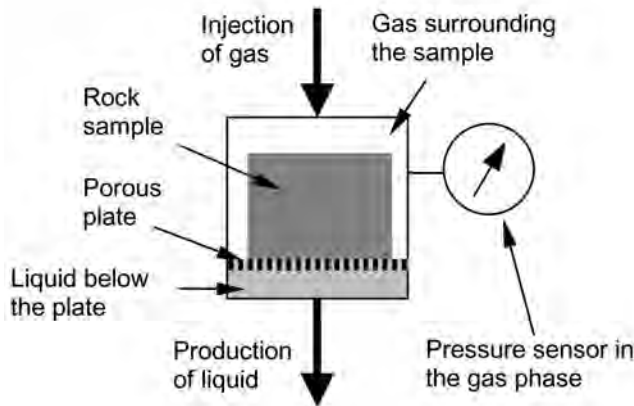


**Fig. 15.27—The difference in pressure between the gas and the liquid (at ambient pressure) must not exceed the threshold pressure of the porous plate.**

also saturated with water. Often, a moist tissue is placed between the sample and the plate to produce good capillary contact.

Then, pressure in the gas phase above the porous plate is increased by a small step, forcing gas to displace the water from the sample through the plate. When the displacement ceases, the difference in pressure between the gas surrounding the sample and the water on the lower side of the plate is the capillary pressure corresponding to the saturation of water remaining in the sample. After a measurement is completed, the pressure in the gas is increased again, forcing more gas into the sample. This process is repeated, increasing the capillary pressure in a series of steps, yielding the capillary pressure relationship for decreasing water saturation.

If the pressure in the gas is raised too far, the gas will penetrate through the porous plate, terminating the test. The highest capillary pressure that can be achieved with the porous-plate method equals the threshold pressure of the plate—that pressure at which gas can penetrate through the plate. The plate threshold pressure depends on the size of pores in the plates and the interfacial properties of the two fluids separated by the plate. The process of gas injection is often reversed before the capillary pressure reaches the threshold pressure of the plate. By decreasing the pressure in the gas in small steps, the capillary pressure relationship for increasing water saturation can be determined.

Porous-plate methods have been applied to gas/water systems, gas/oil systems, and oil/water systems using porous plates with suitable wettability to prevent penetration through the plate of the phase surrounding the rock sample. Considerable time may be needed to reach equilibrium with porous-plate methods—often a week or more at each displacement step for oil/water systems. Christoffersen and Whitson<sup>66</sup> provide an example of the porous-plate technology with automated control of gas/oil displacements. To reduce equilibration time, their system features a thin membrane in place of a porous plate. They could complete the measurements on a 5-md chalk sample in 14 days.

As suggested earlier, capillary pressure relationships should be measured with an applied overburden stress that approximates the stress in the reservoir. The apparatus of Fig. 15.27 does not provide specifically for overburden stress, but by confining a cylindrical sample in a rubber (or similarly flexible) sleeve, one can apply approximately the needed stress. The downside of applying stress with the sleeve is that much of the surface area of the sample is blocked, which slows the pace of the test.

**Centrifuge Methods.** Centrifuge methods are increasingly favored for measuring capillary pressures. Although not as quick as mercury measurements, centrifuge measurements are much

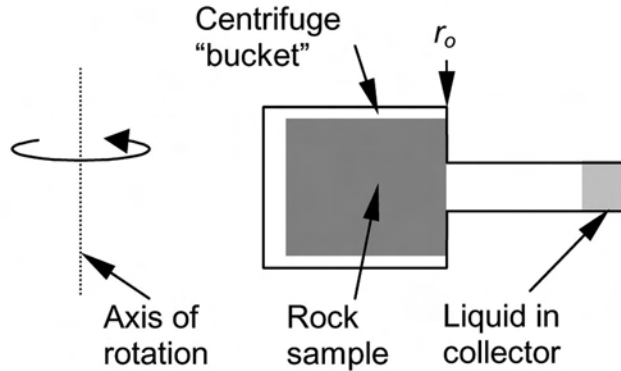


**Fig. 15.28**—In this sketch of a centrifuge test, the rock sample is surrounded by gas, and the produced liquid is accumulating in the collection tube.

faster than porous-plate methods. To measure a gas/oil capillary pressure relationship with the centrifuge method, a cylindrical sample is first saturated with oil; next, it is mounted in a centrifuge, as shown in Fig. 15.28, and is spun in steps of increasing spin rate. The centrifugal forces throw oil from the sample while pulling surrounding gas into the sample. The duration of each spin step must be sufficient for production of oil to cease.

The average saturation of oil in the sample at each spin rate may be calculated from the volume of oil that is produced to the collector relative to the porous volume of the sample. Because 4 to 24 hours are needed to reach equilibrium at each spin rate, most centrifuge data sets consist of eight or fewer spin rates. Ruth and Chen<sup>67</sup> recommend at least 15 spin rates for accurate evaluation of capillary pressure.

The capillary pressure distribution  $P_c(r)$  at each spin-rate step depends on the gas/oil density difference  $\Delta\rho$ , the spin rate  $\omega$ , and the dimensions of the sample relative to the axis of rotation:

$$P_c(r) = \frac{1}{2}\Delta\rho\omega^2(r_o^2 - r^2) \dots\dots\dots (15.45)$$

Here,  $r_o$  is the radius from the axis of rotation to the outside face of the sample (see Fig. 15.28), and  $r$  is the radial distance to any point in the sample. At each spin rate, the capillary pressure at the inside face of the sample (at  $r_i$ ) is

$$P_{ci} = \frac{1}{2}\Delta\rho\omega^2(r_o^2 - r_i^2) \dots\dots\dots (15.46)$$

The process for converting a set of average saturations and  $P_{ci}$  from centrifuge measurements to capillary pressure relationships can involve differentiation of the centrifuge data, as first described by Hassler and Brunner.<sup>68</sup> This differentiation process compounds any error in the original data. So, although the centrifuge method is faster than the porous-plate method, it is not as accurate.<sup>69</sup>

Many variations of the centrifuge method are found in the literature and in industry practice. For example, to measure water/oil capillary pressure for increasing water saturation, the bucket in Fig. 15.28 is reversed so that the rock is on the outside, surrounded by water; the oil that is displaced by the water segregates toward the axis of rotation. Means for applying overburden stress also have been included in centrifuge designs. Baldwin and Spinler<sup>70</sup> and Spinler

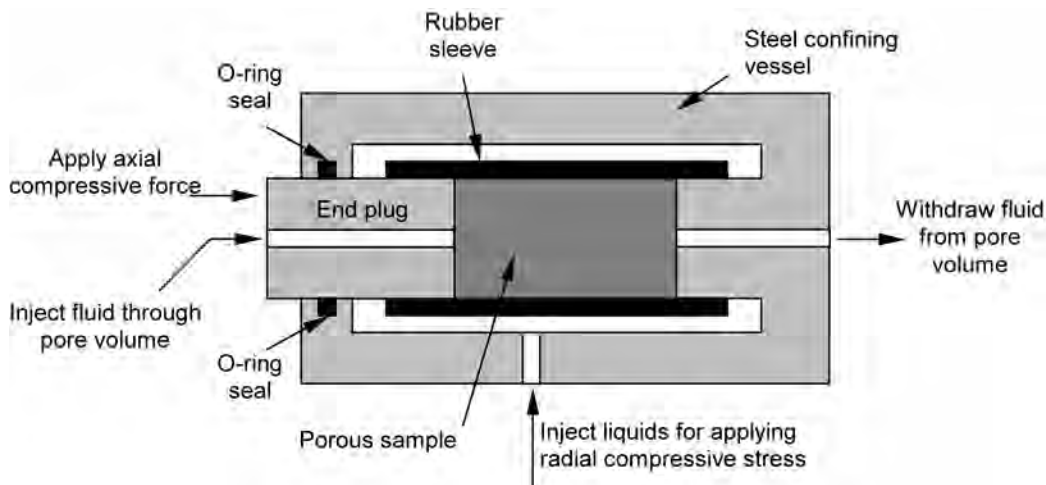


Fig. 15.29—Typical sample holder for relative permeability measurements.

*et al.*<sup>71</sup> used magnetic resonance imaging to obtain capillary pressure relationships by direct measurement of fluid saturations in a rock sample taken from a centrifuge test.

**15.6.4 Measurement of Relative Permeabilities.** There are many variations in methods for measuring relative permeabilities; only their general features will be discussed here. Usually, a cylindrical porous sample is mounted in a holder similar to that shown in Fig. 15.29. The cylindrical surfaces of the sample are sealed to prevent flow. The seal is accomplished in Fig. 15.29 with a rubber sleeve that also allows for application of a radial confining stress. Fluids are injected and produced from the sample through ports at each end. Often, additional ports are added for pressure measurement. In addition to the sample holder, other apparatus are needed to inject and collect fluids, measure pressures, apply confining pressure, measure saturations, and so forth. Some of these external features are shown in Fig. 15.30. Phase saturations can be estimated from the change in mass of the rock sample, the change of electrical conductivity, or the change of absorption of X-rays<sup>72</sup> or other radiation. Acoustic methods<sup>73</sup> and CT scanning<sup>74,75</sup> are also used. To measure the change in mass, the rock sample is quickly removed from the assembly, weighed, then returned to the assembly. Because this procedure could cause the saturation to change, in-situ techniques such as electrical conductivity or X-ray absorption have an advantage. Steady-state and unsteady-state methods for measuring relative permeabilities are discussed further in the subsections below.

**Steady-State Methods.** In steady-state methods, both phases (oil and water, gas and oil, or gas and water) are injected simultaneously at constant rates. Injection continues until a steady state is reached, as indicated by constant pressure drop and constant saturations. Four subcategories of the steady-state methods are introduced below.

**Multiple-Core Method.** In the multiple-core method, frequently called the Penn State method, a rock sample is sandwiched between two other rock samples to build a lengthened sample. The upstream and downstream rock samples distribute flow of the multiple phases over the cross section of the rock and reduce the influence of capillary end effects<sup>76</sup> on the central rock sample. Pressure drop is measured across the central sample while two fluid phases are pumped through the sample at constant flow rates. In some early applications of this method, the saturations in the central rock sample were measured by quickly removing the sample and measuring its mass.

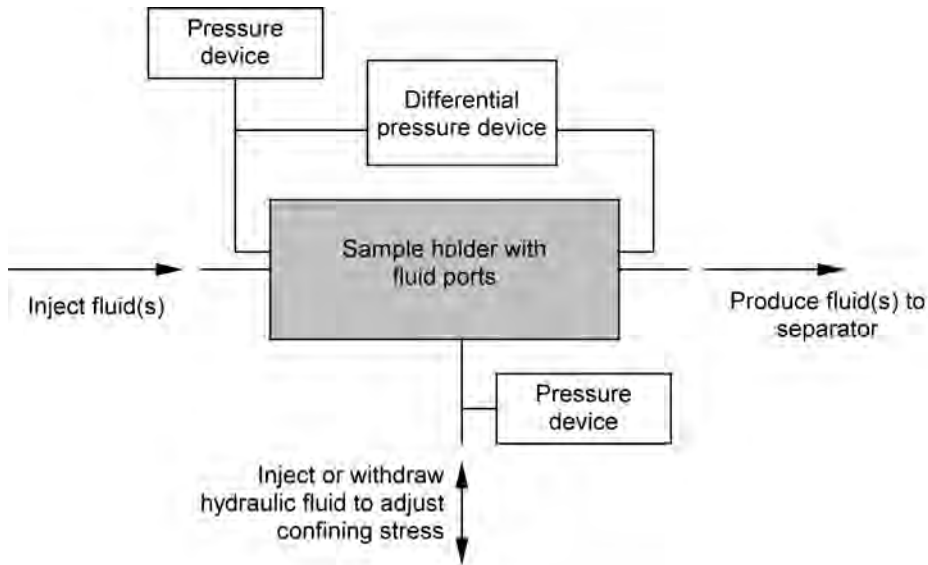


Fig. 15.30—Sample holder with auxiliary apparatus for managing and monitoring the displacement.

**High-Rate Method.** In the high-rate method, two fluid phases are injected into a rock sample at high and constant flow rate. The actual magnitude of rate that is required for this method will depend on the length of the rock sample as well as its capillary pressure properties. The injection rate must be sufficient so that capillary end effects are negligible. Of the steady-state methods, the high-rate subcategory is used most frequently.

**Stationary-Liquid Method.** In the stationary-liquid method, relative permeability of one highly mobile phase is measured in the presence of an essentially immobile second phase. Typically, the immobile phase is a liquid phase, while the mobile phase is usually gas. Because of the high mobility of gas, the liquid phase can be essentially immobile as long as the pressure gradient is small.

**Uniform-Capillary-Pressure Method.** In the uniform-capillary-pressure method, often called the Hassler<sup>77</sup> method, the capillary pressure between two flowing phases is kept uniform throughout a rock sample by keeping the pressure gradients in both phases equal. This is accomplished by incorporating porous plates or membranes at the entrance and exit faces of the porous sample (not shown in Fig. 15.29). The membranes allow passage of just one of the injected fluids, so the pressure drop in each flowing phase can be measured separately. Although the Hassler method is rarely used, measurement methods with selective membranes are frequently encountered in the literature.

**Unsteady-State Methods.** In unsteady-state methods, just one phase is injected at either a constant flow rate or a constant pressure drop. Throughout the injection, the pressure drop and production of phases are measured. Three subcategories are described next.

**High-Rate Methods.** For measurements with high-rate unsteady-state methods, the injection rate must be sufficient so that capillary spreading effects and capillary end effects can be eliminated. The injection and production data and the differential pressure data must be differentiated to obtain the relative permeabilities. These high-rate methods are used most frequently in the oil and gas industry. They provide results for the least cost and with the least delay in time. The quality of the results has been questioned, but there is evidence in the literature that the methods can give results equivalent to those obtained with other methods.

*Low-Rate Methods.* The enormous increase in computing power and its availability in the last 20 years has facilitated measurement of relative permeabilities in low-rate unsteady-state tests. These tests are preferred to high-rate tests for samples that have fines that become mobile at high rates. The test equipment is identical to that used for high-rate methods, but numerical models are used for interpreting the production and pressure-drop data. The low-rate methods are not widely used.

*Centrifuge Methods.* Relative permeabilities can be measured in centrifuge tests using the same apparatus as that described for measurements of capillary pressure (Fig. 15.28). Standard practice provides for measurement of the relative permeability of the lowest-mobility phase. To obtain this relative permeability, the production of one phase as a function of drainage time must be measured. Then, differentiation of the data per the algorithm devised by Hagoort<sup>78</sup> gives the relative permeability.

**15.6.5 Measurement of Endpoint Saturations.** Endpoint saturations are often valued more highly than capillary pressures and relative permeabilities for several reasons. First, the residual oil saturation for a waterflood defines the maximum amount of oil that can be recovered, so it is very useful for economics calculations. Irreducible water saturation is very useful for assessing the volume of oil in place in a reservoir. Furthermore, the endpoints can be measured more accurately than capillary pressure and relative permeability relationships. As such, some discussion of methods for measuring endpoint saturation is included here.

To measure residual oil saturations after a waterflood or gasflood, the apparatus of Figs. 15.29 and 15.30 can be used, but pressure-drop data are not needed—just the oil saturation at the end of the flood is required. As a result, residual oil saturations are much less costly to measure than relative permeabilities and capillary pressures. Still, care is needed to ensure proper wetting conditions for the measurements.

In principle, irreducible water saturation should be measured by oilflooding a rock sample that is initially saturated with water. (Of course, the wettability of the sample will influence the results, so care in handling and preparing the sample is important.) However, irreducible water saturations from such oilflooding are often greater than water saturations measured in retrieved cores from reservoirs. Therefore, alternative approaches have been explored. Satisfying estimates of  $S_{wi}$  have been obtained from mercury-injection tests, with the mercury representing the oil phase and the vapor phase in the test representing the displaced water phase.<sup>79</sup>

## 15.7 Trends and Cautions in Rock/Fluid Properties

At the conclusion of this discussion of capillary pressure and relative permeabilities, five important trends and cautions are worth emphasizing. Some of them were discussed in this chapter; others are offered as extrapolations from discussions of this chapter.

First, the need for accurate measurement of capillary pressure and relative permeability functions increases with the resolution of reservoir models. With low-resolution models, there is a need for algorithms to “upscale” permeabilities, relative permeabilities, and capillary pressures from the scale of measurement on a small sample of rock to the relatively huge size of blocks in reservoir models. The results of the averaging processes of upscaling are insensitive to the quality of measurements on small samples. The need for upscaling should diminish as increases in computer power permit higher-resolution models.

Second, to obtain accurate measurements of capillary pressure and relative permeabilities, tests with representative samples at representative conditions are critical. Much of the available data in our industry do not pass this standard.

Third, capillary end effects and viscous fingering have corrupted a significant portion of relative permeability data. If capillary pressure and relative permeabilities are available, the extent of this corruption for a sample can be assessed and sometimes corrected.

Fourth, we often interpret water/oil wettabilities from the shape of relative permeabilities. Such interpretations are particularly susceptible to error caused by the heterogeneity of the sample used for measurements. This susceptibility was conceded in the original literature on wettability interpretation, but it is not widely acknowledged.

Fifth, the quality of estimates of capillary pressure and relative permeability with network models is increasing. These models offer the hope of providing estimates for a large set of rock samples for any particular reservoir while avoiding the costs of measuring capillary pressure and relative permeability.

### Nomenclature

- $A$  = area perpendicular to flow,  $L^2$
- $A, B$  = parameters in Chierici functions
- $A_T$  = total surface area of a porous sample,  $L^2$
- $A_{ow}$  = area of oil/water interface in a porous sample,  $L^2$
- $A_{os}$  = area of oil/solid interface in a porous sample,  $L^2$
- $A_{ws}$  = area of water/solid interface in a porous sample,  $L^2$
- $C$  = parameter in the Land function
- $e$  = basis of natural logarithm (2.718...)
- $f_i$  = fraction of total sample volume occupied by layer  $i$  in a laminated sample
- $G$  = pore geometric factor in Thomeer function
- $j(S_w)$  = Leverett  $j$ -function
- $k$  = permeability,  $L^2$ , md
- $k_i$  = permeability of layer  $i$  in a laminated sample,  $L^2$ , md
- $k_T$  = total permeability in a laminated sample,  $L^2$ , md
- $k_{rg}$  = relative permeability for gas
- $k_{rgi}$  = relative permeability for gas in layer  $i$  of a laminated sample
- $k_{rg,max}$  = maximum relative permeability for gas in modified Brooks-Corey functions
- $k_{rg,go}$  = relative permeability for gas in gas/oil flow for three-phase models
- $k_{rg,gw}$  = relative permeability for gas in gas/water flow for three-phase models
- $k_{rg,wog}$  = relative permeability for gas in oil/water/gas flow for three-phase models
- $k_{rgo}$  = relative permeability for oil in layer  $i$  of a laminated sample
- $k_{rgT}$  = total relative permeability for gas in a laminated sample
- $k_{ro}$  = relative permeability for oil
- $k_{roi}$  = relative permeability for oil in layer  $i$  of a laminated sample
- $k_{ro,max}$  = maximum relative permeability for oil in modified Brooks-Corey functions
- $k_{ro,og}$  = relative permeability for oil in oil/gas flow for three-phase models
- $k_{ro,wo}$  = relative permeability for oil in oil/water flow for three-phase models
- $k_{ro,wog}$  = relative permeability for oil in oil/water/gas flow for three-phase models
- $k_{roT}$  = total relative permeability for oil in a laminated sample
- $k_{rw}$  = relative permeability for water
- $k_{rw,max}$  = maximum relative permeability for water in modified Brooks-Corey functions
- $k_{rw,gw}$  = relative permeability for water in gas/water flow for three-phase models
- $k_{rw,wo}$  = relative permeability for water in oil/water flow for three-phase models
- $k_{rw,wog}$  = relative permeability for water in oil/water/gas flow for three-phase models
- $L$  = length



- $L, M$  = parameters in Chierici functions  
 $n_g$  = gas exponent for modified Brooks-Corey functions  
 $n_o$  = oil exponent for modified Brooks-Corey functions  
 $n_w$  = water exponent for modified Brooks-Corey functions  
 $N$  = number of laminations  
 $N_c$  = capillary number  
 $P_c$  = capillary pressure, m/Lt<sup>2</sup>, psi  
 $P_{cgo}$  = capillary pressure between gas and oil phases, m/Lt<sup>2</sup>, psi  
 $P_{cow}$  = capillary pressure between oil and water phases, m/Lt<sup>2</sup>, psi  
 $P_{cgw}$  = capillary pressure between gas and water phases, m/Lt<sup>2</sup>, psi  
 $P_{cgwt}$  = threshold capillary pressure between gas and water phases, m/Lt<sup>2</sup>, psi  
 $P_{ci}$  = capillary pressure at inside face of sample in centrifuge test, m/Lt<sup>2</sup>, psi  
 $P_{ct}$  = threshold capillary pressure, m/Lt<sup>2</sup>, psi  
 $P_{cs}$  = shape parameter in Bentsen-Anli function, m/Lt<sup>2</sup>, psi  
 $p_g$  = pressure in the gas phase, m/Lt<sup>2</sup>, psi  
 $p_o$  = pressure in the oil phase, m/Lt<sup>2</sup>, psi  
 $p_w$  = pressure in the water phase, m/Lt<sup>2</sup>, psi  
 $\Delta P$  = pressure drop, m/Lt<sup>2</sup>, psi  
 $q$  = flow rate, L<sup>3</sup>/t  
 $q_o$  = flow rate of oil, L<sup>3</sup>/t  
 $q_w$  = flow rate of water, L<sup>3</sup>/t  
 $r$  = radius to a point in sample in centrifuge test, L  
 $r_i$  = radius to inside face of sample in centrifuge test, L  
 $r_o$  = radius to outside face of sample in centrifuge test, L  
 $R_1, R_2$  = principal radii of curvature, L  
 $S_{cc}$  = critical saturation of condensate  
 $S_g$  = saturation of gas  
 $S_{gc}$  = critical saturation of gas  
 $S_{gi}$  = initial saturation of gas  
 $S_{gN}$  = normalized gas saturation  
 $S_{gr}$  = residual saturation of gas  
 $S_{gr,max}$  = maximum residual or trapped gas saturation  
 $S_{gS}$  = scaled saturation of gas for Stone I model  
 $S_{gt}$  = trapped saturation of gas  
 $S_{Hg}$  = saturation of mercury  
 $S_{nwr}$  = residual saturation of nonwetting phase  
 $S_o$  = saturation of oil  
 $S_{om}$  = minimum saturation of oil for three-phase models  
 $S_{or}$  = residual saturation of oil  
 $S_{org}$  = residual saturation of oil for a gas/oil displacement  
 $S_{orw}$  = residual saturation of oil for a water/oil displacement  
 $S_{oS}$  = scaled saturation of oil for Stone I model  
 $S_w$  = saturation of water  
 $S_{wc}$  = critical saturation of water  
 $S_{wi}$  = irreducible or residual saturation of water

- $S_{wn}$  = normalized water saturation  
 $S_{wr}$  = residual saturation of water or wetting phase  
 $S_{wS}$  = scaled saturation of water for Stone I model  
 $v$  = velocity, L/t, cm/s  
 $x$  = position in the  $x$  direction, L  
 $\alpha$  = parameter in Eqs. 15.39 and 15.40  
 $\beta$  = parameter in Eq. 15.40  
 $\theta$  = contact angle, degrees  
 $\lambda$  = pore-size-distribution parameter in Corey functions  
 $\mu$  = viscosity, m/Lt, cp  
 $\mu_o$  = viscosity of oil, m/Lt, cp  
 $\mu_w$  = viscosity of water, m/Lt, cp  
 $\Delta\rho$  = density difference for fluids in centrifuge tests, m/L<sup>3</sup>  
 $\sigma_{gw}$  = gas/water interfacial tension, m/t<sup>2</sup>, dyne/cm  
 $\sigma_{ow}$  = oil/water interfacial tension, m/t<sup>2</sup>, dyne/cm  
 $\tau$  = tortuosity of porous sample  
 $\tau_o$  = tortuosity of oil phase in porous sample  
 $\tau_w$  = tortuosity of water phase in porous sample  
 $\Phi$  = porosity  
 $\omega$  = spin rate for centrifuge tests, 1/t ( $\omega = 2\pi \times \text{RPM} / 60$ )

---

## References

1. This chapter relies heavily on Christiansen, R.L.: *Two-Phase Flow through Porous Media*, KNQ Engineering, Littleton, Colorado (2001) Chaps. 1, 4, and 5.
2. Muskat, M.: "Calculation of Initial Fluid Distributions in Oil Reservoirs," *Trans.*, AIME (1949) **179**, 119.
3. Morrow, N.R. and Melrose, J.C.: "Application of Capillary Pressure Measurements to the Determination of Connate Water Saturation," in *Interfacial Phenomena in Petroleum Recovery*, N.R. Morrow (ed.), Marcel Dekker Inc., New York City (1991) 257–287.
4. Salathiel, R.A.: "Oil Recovery by Surface Film Drainage In Mixed-Wettability Rocks," *JPT* (October 1973) 1216; *Trans.*, AIME, **255**.
5. Treiber, L.E., Archer, D.L., and Owens, W.W.: "A Laboratory Evaluation of the Wettability of Fifty Oil-Producing Reservoirs," *SPEJ* (December 1972) 531; *Trans.*, AIME, **253**.
6. From Fig. 6 of Morrow, N.R., Cram, P.J., and McCaffery, P.G.: "Displacement Studies in Dolomite with Wettability Control by Octanoic Acid," *SPEJ* (August 1973) 221; *Trans.*, AIME, **255**.
7. Bethel, F.T. and Calhoun, J.C.: "Capillary Desaturation in Unconsolidated Beads," *Trans.*, AIME (1953) **198**, 197.
8. Morrow, N.R.: "Irreducible Wetting-Phase Saturations in Porous Media," *Chem. Eng. Sci.* (November 1970) **25**, No. 11, 1799.
9. Chatzis, I., Morrow, N.R., and Lim, H.T.: "Magnitude and Detailed Structure of Residual Oil Saturation," *SPEJ* (April 1983) 311.
10. Jerauld, G.R. and Rathmell, J.J.: "Wettability and Relative Permeability of Prudhoe Bay: A Case Study in Mixed-Wet Reservoirs," *SPEJ* (February 1997) 58.
11. Leverett, M.C.: "Capillary Behavior in Porous Solids," *Trans.*, Petroleum Division of AIME (1941) **142**, 152; see also Leverett, M.C., Lewis, W.B., and True, M.E.: "Dimensional-Model Studies of Oil-Field Behavior," *Trans.*, Petroleum Division of AIME (1942) **146**, 175.
12. Brown, H.W.: "Capillary Pressure Investigations," *Trans.*, AIME (1951) **192**, 67.
13. Thomeer, J.H.M.: "Introduction of a Pore Geometrical Factor Defined by the Capillary Pressure Curve," *JPT* (March 1960) 73; *Trans.*, AIME, **219**.

14. Brooks, R.H. and Corey, A.T.: "Hydraulic Properties of Porous Media," Hydrology Papers, No. 3, Colorado State U., Fort Collins, Colorado (1964).
15. Corey, A.T.: "The Interrelation Between Gas and Oil Relative Permeabilities," *Producers Monthly* (November 1954) **18**, 38.
16. Thomas, L.K., Katz, D.L., and Tek, M.R.: "Threshold Pressure Phenomena in Porous Media," *SPEJ* (June 1968) 174; *Trans.*, AIME, **243**.
17. Bentsen, R.G., and Anli, J.: "A New Displacement Capillary Pressure Model," *J. Cdn. Pet. Tech.* (July–September 1976) **15**, No. 3, 75. For further applications of the model, see Bentsen, R.G. and Anli, J.: "Using Parameter Estimation Techniques to Convert Centrifuge Data into a Capillary Pressure Curve," *SPEJ* (February 1977) 57; *Trans.*, AIME, **263**.
18. Alpak, F.O., Lake, L.W., and Embid, S.M.: "Validation of a Modified Carman-Kozeny Equation To Model Two-Phase Relative Permeabilities," paper SPE 56479 presented at the 1999 SPE Annual Technical Conference and Exhibition, Houston, 3–6 October.
19. Jones, S.C. and Roszelle, W.O.: "Graphical Techniques for Determining Relative Permeability From Displacement Experiments," *JPT* (May 1978) 807; *Trans.*, AIME, **265**.
20. Geffen, T.M. *et al.*: "Experimental Investigation of Factors Affecting Laboratory Relative Permeability Measurements," *Trans.*, AIME (1951) **192**, 99.
21. Braun, E.M. and Holland, R.F.: "Relative Permeability Hysteresis: Laboratory Measurements and a Conceptual Model," *SPEJ* (August 1995) 222.
22. Owens, W.W. and Archer, D.L.: "The Effect of Rock Wettability on Oil-Water Relative Permeability Relationships," *JPT* (July 1971) 873; *Trans.*, AIME, **251**.
23. Morrow, N.R., Cram, P.J., and McCaffery, P.G.: "Displacement Studies in Dolomite with Wettability Control by Octanoic Acid," *SPEJ* (August 1973) 221; *Trans.*, AIME, **255**.
24. McCaffery, F.G. and Bennion, D.W.: "The Effect of Wettability on Two-Phase Relative Permeabilities," *J. Cdn. Pet. Tech.* (October–December 1974) **13**, No. 4, 42.
25. Schneider, F.N. and Owens, W.W.: "Sandstone and Carbonate Two- and Three-Phase Relative Permeability Characteristics," *SPEJ* (March 1970) 75; *Trans.*, AIME, **249**.
26. Bardon, C. and Longeron, D.G.: "Influence of Very Low Interfacial Tensions on Relative Permeability," *SPEJ* (October 1980) 391.
27. Haniff, M.S. and Ali, J.K.: "Relative Permeability and Low Tension Fluid Flow in Gas Condensate Systems," paper SPE 20917 presented at the 1990 SPE Europec, The Hague, 22–24 October.
28. Asar, H. and Handy, L.L.: "Influence of Interfacial Tension on Gas/Oil Relative Permeability in a Gas-Condensate System," *SPEJ* (February 1988) 257.
29. Amaefule, J.O. and Handy, L.L.: "The Effect of Interfacial Tensions on Relative Oil/Water Permeabilities of Consolidated Porous Media," *SPEJ* (June 1982) 371.
30. Jadhunandan, P.P. and Morrow, N.R.: "Effect of Wettability on Waterflood Recovery for Crude-Oil/Brine/Rock Systems," *SPEJ* (February 1995) 40; *Trans.*, AIME, **299**.
31. Barnum, R.S. *et al.*: "Gas Condensate Reservoir Behavior: Productivity and Recovery Reduction Due to Condensation," paper SPE 30767 presented at the 1995 SPE Annual Technical Conference and Exhibition, Dallas, 22–25 October.
32. Katz, D.L. and Lee, R.L.: *Natural Gas Engineering*, McGraw-Hill Publishing Co., New York City (1990) 83–86.
33. Naar, J. and Henderson, J.H.: "An Imbibition Model—Its Application to Flow Behavior and the Prediction of Oil Recovery," *Trans.*, AIME (1961) **222**, 61.
34. Agarwal, R.G.: "Unsteady-State Performance of Water-Drive Gas Reservoirs," PhD thesis, Texas A&M U., College Station, Texas (1967) 46–59.
35. Keelan, D.K. and Pugh, V.J.: "Trapped-Gas Saturations in Carbonate Formations," *SPEJ* (April 1975) 149; *Trans.*, AIME, **259**.
36. Land, C.S.: "Calculation of Imbibition Relative Permeability for Two- and Three-Phase Flow From Rock Properties," *SPEJ* (June 1968) 149; *Trans.*, AIME, **243**.
37. Land, C.S.: "Comparison of Calculated with Experimental Imbibition Relative Permeability," *SPEJ* (December 1971) 419; *Trans.*, AIME, **251**.
38. Pickell, J.J., Swanson, B.F., and Hickman, W.B.: "Application of Air-Mercury and Oil-Air Capillary Pressure Data in the Study of Pore Structure and Fluid Distribution," *SPEJ* (March 1966) 55; *Trans.*, AIME, **237**.
39. Lake, L.W.: *Enhanced Oil Recovery*, Prentice Hall, Englewood Cliffs, New Jersey (1989) 71.

40. Green, D.W. and Willhite, G.P.: *Enhanced Oil Recovery*, Textbook Series, SPE, Richardson, Texas (1998) **6**, 18–27.
41. King, M.J. *et al.*: “Simultaneous Determination of Residual Saturation and Capillary Pressure Curves Utilizing the Ultracentrifuge,” paper SPE 15595 presented at the 1986 SPE Annual Technical Conference and Exhibition, New Orleans, 5–8 October.
42. Pope, G.A. *et al.*: “Modeling Relative Permeability Effects in Gas-Condensate Reservoirs With a New Trapping Model,” *SPEEE* (April 2000) 171.
43. Lake, L.W.: *Enhanced Oil Recovery*, Prentice Hall, Englewood Cliffs, New Jersey (1989).
44. Bulnes, A.C. and Fitting, R.U. Jr.: “An Introductory Discussion of the Reservoir Performance of Limestone Formations,” *Trans.*, AIME (1945) **160**, 179.
45. Akin, S., Castanier, L.M., and Brigham, W.E.: “Effect of Temperature on Heavy-Oil/Water Relative Permeabilities,” paper SPE 49021 prepared for presentation at the 1998 SPE Annual Technical Conference and Exhibition, New Orleans, 27–30 September.
46. Peters, E.J. and Flock, D.L.: “The Onset of Instability During Two-Phase Immiscible Displacement in Porous Media,” *SPEJ* (1981) 249. See also Peters, E.J. and Khataniar, S.: “The Effect of Instability on Relative Permeability Curves Obtained by the Dynamic-Displacement Method,” *SPEFE* (December 1987) 469.
47. Brooks, R.H. and Corey, A.T.: “Hydraulic Properties of Porous Media,” *Hydrology Papers*, No. 3, Colorado State U., Fort Collins, Colorado (1964).
48. Corey, A.T. and Rathjens, C.H.: “Effect of Stratification on Relative Permeability,” *Trans.*, AIME (1956) **207**, 358.
49. Ehrlich, R.: “Relative Permeability Characteristics of Vugular Cores—Their Measurement and Significance,” paper SPE 3553 presented at the 1971 SPE Annual Meeting, New Orleans, 3–6 October.
50. Chierici, G.L.: “Novel Relations for Drainage and Imbibition Relative Permeabilities,” *SPEJ* (June 1984) 275.
51. Fayers, F.J. *et al.*: “An Improved Three Phase Flow Model Incorporating Compositional Variance,” paper SPE 59313 presented at the 2000 SPE/DOE Improved Oil Recovery Symposium, Tulsa, 3–5 April.
52. Honarpour, M., Koederitz, L., and Harvey, A.H.: *Relative Permeability of Petroleum Reservoirs*, CRC Press, Boca Raton, Florida (1986) 16–41.
53. Ibrahim, M.N.M.: “Two-Phase Relative Permeability Prediction Using a Linear Regression Model,” PhD thesis, U. of Missouri-Rolla (1999).
54. Killough, J.E.: “Reservoir Simulation with History-Dependent Saturation Functions,” *SPEJ* (February 1976) 37; *Trans.*, AIME, **261**.
55. Carlson, F.M.: “Simulation of Relative Permeability Hysteresis to the Nonwetting Phase,” paper SPE 10157 presented at the 1981 SPE Annual Technical Conference and Exhibition, San Antonio, Texas, 5–7 October.
56. Fenwick, D.H. and Blunt, M.J.: “Network Modeling of Three-Phase Flow in Porous Media,” *SPEJ* (March 1998) 86; Fenwick, D.H. and Blunt, M.J.: “Three-Dimensional Modeling of Three Phase Imbibition and Drainage,” *Adv. Water Res.* (1998) **21**, No. 2, 121. See also Lerdahl, T.R., Øren, P.-E., and Bakke, S.: “A Predictive Network Model for Three-Phase Flow in Porous Media,” paper SPE 59311 presented at the 2000 SPE/DOE Improved Oil Recovery Symposium, Tulsa, 3–5 April.
57. Baker, L.E.: “Three-Phase Relative Permeability Correlations,” paper SPE 17369 presented at the 1988 SPE/DOE Enhanced Oil Recovery Symposium, Tulsa, 17–20 April.
58. Stone, H.L.: “Probability Model for Estimating Three-Phase Relative Permeability,” *JPT* (February 1970) 214; *Trans.*, AIME, **249**.
59. Fayers, F.J. and Matthews, J.D.: “Evaluation of Normalized Stone’s Methods for Estimating Three-Phase Relative Permeabilities,” *SPEJ* (April 1984) 224.
60. Stone, H.L.: “Estimation of Three-Phase Relative Permeability and Residual Oil Data,” *J. Cdn. Pet. Tech.* (October–December 1973) **12**, No. 4, 53.
61. Blunt, M.J.: “An Empirical Model for Three-Phase Relative Permeability,” paper SPE 56474 presented at the 1999 SPE Annual Technical Conference and Exhibition, Houston, 3–6 October.
62. Much more discussion of these topics is found in Chaps. 4–6 of [Ref. 1](#).

63. Purcell, W.R.: “Capillary Pressures—Their Measurement Using Mercury and the Calculation of Permeability Therefrom,” *Trans.*, AIME (1949) **186**, 39.
64. Rose, W. and Bruce, W.A.: “Evaluation of Capillary Character in Petroleum Reservoir Rock,” *Trans.*, AIME (1949) **186**, 127.
65. Swanson, B.F.: “A Simple Correlation Between Permeabilities and Mercury Capillary Pressures,” *JPT* (December 1981) 2498.
66. Christoffersen, K.R. and Whitson, C.H.: “Gas/Oil Capillary Pressure of Chalk at Elevated Pressures,” paper SPE 26673 presented at the 1993 SPE Annual Technical Conference and Exhibition, Houston, 3–6 October. A more compact version of this paper is found in *SPEFE* (September 1995) 153.
67. Ruth, D.W. and Chen, Z.A.: “Measurement and Interpretation of Centrifuge Capillary Pressure Curves—The SCA Survey Data,” *The Log Analyst* (September–October 1995) **36**, 21.
68. Hassler, G.L. and Brunner, E.: “Measurement of Capillary Pressures in Small Core Samples,” *Trans.*, AIME (1945) **160**, 114.
69. For details of the data-reduction process, see Chap. 4 of [Ref. 1](#).
70. Baldwin, B.A. and Spinler, E.A.: “A Direct Method for Simultaneously Determining Positive and Negative Capillary Pressure Curves in Reservoir Rock,” *J. Pet. Sci. and Eng.* (June 1998) **20**, Nos. 3–4, 161.
71. Spinler, E.A., Baldwin, B.A., and Graue, A.: “Simultaneous Measurement of Multiple Capillary Pressure Curves from Wettability and Rock Property Variations within Single Rock Plugs,” paper 9957 presented at the 1999 Intl. Symposium of the Soc. of Core Analysts, Golden, Colorado, 1–4 August.
72. Oak, M.J., Baker, L.E., and Thomas, D.C.: “Three-Phase Relative Permeability of Berea Sandstone,” *JPT* (August 1990) 1054; *Trans.*, AIME, **289**.
73. Islam, M.R. and Bentsen, R.G.: “A Dynamic Method for Measuring Relative Permeability,” *J. Cdn. Pet. Tech.* (January–February 1986) **25**, No. 1, 39.
74. MacAllister, D.J. *et al.*: “Application of X-Ray CT Scanning To Determine Gas/Water Relative Permeabilities,” *SPEFE* (September 1993) 184; *Trans.*, AIME, **295**.
75. DiCarlo, D.A., Sahni, A., and Blunt, M.J.: “Three-Phase Relative Permeability of Water-Wet, Oil-Wet, and Mixed-Wet Sandpacks,” *SPEJ* (March 2000) 82.
76. End effects were considered in detail first by Richardson, J.G. *et al.*: “Laboratory Determination of Relative Permeability,” *Trans.*, AIME (1952) **195**, 187. See Chaps. 3, 5, and 7 of [Ref. 1](#).
77. Hassler, G.L.: “Method and Apparatus for Permeability Measurements,” U.S. Patent No. 2,345,935 (1942). Also see Brownscombe, E.R., Slobod, R.L., and Caudle, B.H.: “Laboratory Determination of Relative Permeability: Parts 1 and 2,” *Oil & Gas J.* (9 February 1950) 68 and (16 February 1950) 98.
78. Hagoort, J.: “Oil Recovery by Gravity Drainage,” *SPEJ* (June 1980) 139.
79. Rathmell, J.J., Atkins, L.K., and Kralik, J.G.: “Application of Low Invasion Coring and Outcrop Studies to Reservoir Development Planning for the Villano Field,” paper 9902 presented at the 1999 Intl. Symposium of the Soc. of Core Analysts, Golden, Colorado, 1–4 August.

### SI Metric Conversion Factors

dyne × 1.0*	E – 02	= mN
ft × 3.048*	E – 01	= m
in. × 2.54*	E + 00	= cm
in. <sup>2</sup> × 6.451 6*	E + 00	= cm <sup>2</sup>
psi × 6.894 757	E + 00	= kPa

\*Conversion factor is exact.



## Chapter 16

### Petroleum Economics

John D. Wright, SPE, Norwest Questa Engineering Corp.

#### 16.1 Introduction

Economics drives the entire oil/gas producing industry. Almost every decision is made on the basis of an economic evaluation. Economic evaluations are also performed to determine reserves and the “standardized measure of value” for reporting purposes for publicly held companies. In many cases, the goal of the company is to make decisions that have the best chance of maximizing the present day profit. This chapter discusses economic evaluation under two conditions. First, techniques that assume we know the future parameters with certainty are discussed. Later, methods of handling the inherent uncertainty involved in oil/gas operations are discussed.

Having stated a company goal in terms of profit, it behooves us to examine the definition of profit. There are at least three ways to calculate profit, each with its own set of assumptions and rules and each leading to a different answer. The three models are the net cash flow model, the financial net income model, and the tax model.

In the simplest analysis, profit for a period is the revenue received during the period less the costs incurred during the period. Note that profit is defined for some time period, which can be arbitrarily long. In the oil/gas business the period is usually one month or one year. The amount of revenue received during the period is usually similar for all three models, especially for yearly periods. There might be some timing differences in revenue recognition, but they are usually relatively minor. The three models differ considerably in the timing of the costs. Costs can be further subdivided into expenses, which benefit only the current period, and investments, which benefit more than one period. The cash flow model assumes that 100% of both the investment and the expenses are recognized when they occur. The financial net income model attempts to match the revenue with the costs to produce that revenue. This leads to recognizing the expenses in the current period and recognizing the investment over a longer time period—often the life of the project. The total cost over the life of the project is the same in the cash flow model and the financial net income model, but the portion of the costs allocated to each time period is significantly different. The concept of spreading the investment over the productive life of the project leads to depreciation.

Accountants may use various types of depreciation to match the revenues with the costs required to generate the revenues. Two major types of depreciation are “units-of-production” and “straight-line” depreciation. Dividing the production for a period by the total volume to be

TABLE 16.1—EXAMPLE OF THREE TYPES OF DEPRECIATION

Initial Investment \$1,000,000				
Year	Annual Production, bbl	Units of Production Depreciation	Straight-Line Depreciation	7-year Modified Accelerated Cost Recovery System (MACRS) Depreciation
1	50,000	\$240,319	\$125,000	\$142,900
2	40,000	192,255	125,000	244,900
3	32,000	153,804	125,000	174,900
4	25,600	123,043	125,000	124,900
5	20,480	98,435	125,000	89,300
6	16,384	78,748	125,000	89,200
7	13,107	62,998	125,000	89,300
8	10,486	50,399	125,000	44,600
Total	208,057	\$1,000,000	\$1,000,000	\$1,000,000

produced and multiplying that fraction by the total investment yields the units-of-production depreciation for a period. This results in the investments being allocated on a \$/barrel basis. The straight-line method of depreciation allocates the investment on \$/unit time basis. **Table 16.1** shows an example of each of the different ways of allocating an investment including the modified accelerated cost recovery system (MACRS), which is currently used by the U.S. Internal Revenue Service for most oilfield investments.

The federal and state governments use the tax model to determine the amount of profit that a company has made for each year so that a portion of that profit can be extracted to pay for government services. The tax model allocates the investments to the period under consideration in yet another manner. The Internal Revenue Service publishes a somewhat arbitrary table of allocation factors for different types of investments. This table is called a depreciation schedule and is currently the MACRS table shown in **Table 16.1**. The term “depreciation” is used in both the financial net income model and the tax model, but the calculation method is very different.

## 16.2 Economic Model for Oil and Gas Property Evaluation

The cash flow model is the most common model used to evaluate oil/gas projects. Normally, only very large acquisitions are evaluated by examining the impact of the acquisition on the financial net income. The tax model is used only if an after-tax analysis is done.

Cash flows for the project are forecast for each year or each month until the well or project is no longer economical. Because of the ready availability of powerful computers, evaluations are usually done on a monthly basis, and the results are reported on an annual basis. Monthly calculations are more detailed but not necessarily more accurate. (There is often a tendency to consider more detailed calculations as being more accurate. The use of finer time increments does not necessarily lead to projections that are more in conformity with truth.)

Whether the calculations are done on a monthly or yearly basis, the same process is followed. The profit for each period is defined as net cash flow and, for a Royalty-Tax system such as that used in the U.S. and about one-half the other countries in the world, is calculated as shown schematically in **Fig. 16.1**, adapted from Thompson and Wright,<sup>1</sup> page 1-13. A sample calculation is shown in **Table 16.2**. The values in this table were calculated monthly and then accumulated on an annual basis. Several “terms of art” are used in the oil/gas business and are described next.



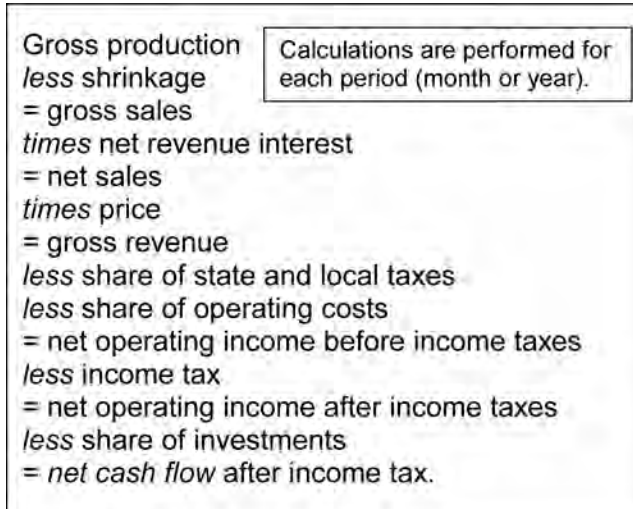


Fig. 16.1—Calculation of periodic net cash flow for a royalty tax system (like the U.S.), adapted from Thompson and Wright.<sup>1</sup>

TABLE 16.2—EXAMPLE MONTHLY NET CASH FLOW CALCULATION							
Example Well—Annual Summary of Monthly Net Cash Flows							
Days in Year = 365.25		Severance + <i>Ad valorem</i> Tax Rate = 10%					
Working Interest = 100%		Initial Operating Cost = \$2,000/month					
Net Revenue Interest = 85%							
Year	Gross production, bbl	Net production, bbl	Price, \$/bbl	Gross income, dollars	Severance & <i>Ad valorem</i> tax, dollars	Operating costs, dollars	Net operating income BFIT <sub>t</sub> , dollars
Total	50,080	42,568		773,541	77,354	110,818	585,369
0							
1	24,781	21,063	17.74	373,581	37,358	22,273	313,950
2	13,957	11,863	18.24	216,398	21,640	24,996	169,762
3	6,978	5,932	18.79	111,445	11,145	25,746	74,554
4	3,489	2,966	19.35	57,394	5,739	26,519	25,136
5	875	744	19.79	14,722	1,472	11,283	1,967

**16.2.1 Gross Production.** Gross production is the volume of oil/gas that is projected to be produced during the particular month or year being calculated. Gross production is one of the most important numbers entering the net cash flow calculation and, simultaneously, one of the most difficult to determine accurately. Much of the science and art of petroleum engineering is involved in estimating these numbers for future time periods.

**16.2.2 Shrinkage.** In the model defined in Fig. 16.1, “shrinkage” is used to reduce the volumes produced from a well to the volumes sold from a well. Usually the decline curves that are used to forecast future revenues are based on production rather than sales. If there is significant shrinkage, that should be taken into account before calculating the cash flows. Typical causes of shrinkage include lease use of gas for heater treaters or compressor fuel. Oil shrink-

**TABLE 16.2—EXAMPLE MONTHLY NET CASH FLOW CALCULATION  
(continued)**

Example Well—Annual Summary of Monthly Net Cash Flows						
	Annual Interest Rate:		10%	20%	34.30%	
	Monthly Interest Rate:		0.797%	1.531%	2.488%	
Year	Investments, dollars	Net cash flow BFIT, dollars	Cumulative net cash flow BFIT, dollars	Discounted net cash flow BFIT, dollars	Discounted net cash flow BFIT, dollars	Discounted net cash flow BFIT, dollars
Total	425,000	160,371		99,368	51,950	0
0	425,000	-425,000	-425,000	-425,000	-425,000	-425,000
1	0	313,951	-111,049	285,139	268,981	37,358
2	0	169,762	58,713	129,815	110,137	21,640
3	0	74,554	133,267	47,606	36,133	11,145
4	0	25,137	158,404	13,473	9,177	5,739
5	0	1,967	160,371	917	573	1,472

age might occur because of basic sediment and water (BS&W) corrections or because of temperature differences between the volume of oil measured at the tank and volume of oil measured at the refinery.

**16.2.3 Gross Sales.** Gross sales is the volume of oil/gas that is projected to be sold during the time period. If shrinkage is negligible, gross sales will equal gross production.

Typically, the people who drill and operate a well do not own the minerals they are extracting. For example, the U.S. Government, state governments, Indian tribes, or private citizens usually own minerals in the United States. In most other countries, the state usually owns the minerals. The producers lease the right to develop the minerals from the mineral owners. This leads to various kinds of interests in the property.

**16.2.4 Working Interest.** Working interest is a share of the costs. The total of all the working interests in a well must be equal to one. Along with the share of the costs comes a reduced (usually) share of the revenue. It is quite common for a company to own less than 100% of the working interest in a well or project. Owning smaller interests in many projects, called diversification, is one of the ways to manage the risk involved in drilling for oil/gas. Working interest may also change over time as a result of “oil field deals.” Sometimes one party will pay a disproportionate share of the costs to drill the first well on a prospect to earn a share of a lease held by some other oil company. As deals become more and more complex, it becomes very difficult to determine ownership. One method of answering the “who, what, when” question is discussed in [Ref. 1](#).

**16.2.5 Royalty.** Royalty is a share of the revenue free and clear of all costs of development and production. The royalty is paid to the owner of the mineral interest under the land associated with the well. In the United States, the mineral interest can be “severed” from the surface ownership so that the person who owns the surface may not have any interest in the minerals and may not receive any income from a well. In rare cases the owners of the working interest will own the minerals and, in that case, there is no royalty. Typical royalty rates in the U.S. range from 1/8 (12.5%) to 25% of the production. Royalties in other countries can range from zero to more than 30%. Some royalties, such as Alberta’s, increase with increasing production and price.

**16.2.6 Overriding Royalty.** Overriding royalty is the same as a royalty, except it does not come about because of ownership of the mineral interest. An “override” is a classic way for a lease broker or geologist to be compensated for buying leases or putting a deal together. Overrides may range from 1% of large deals to 7.5% of really “hot” or promising prospects.

**16.2.7 Net Revenue Interest.** For net revenue interest, the working interest owners pay all of the costs. Because the royalty and overriding royalty interest owners share in the production, but not in the costs, the working interest owners as a group receive less than 100% of the revenue. In many cases, the working interest owners receive around 80% of the gross revenues, although sometimes it might be as high as 87.5% or as low as 70% (or less). The share of the gross production from the well is referred to as “net revenue interest.” If there is a 12.5% royalty, a 7.5% overriding royalty, and you own a 50% working interest, then your net revenue interest is 40% (100% less 12.5% less 7.5% times 50%).

**16.2.8 Net Sales.** Net sales is the product of gross sales and net revenue interest. It is your share of the production after accounting for shrinkage, royalties, and splitting the proceeds with other working interest owners.

**16.2.9 Price.** Oil is usually priced in U.S.\$/barrel except in some countries where it is priced by the tonne. Gas is priced either in \$/million British Thermal Units (MMBtu) or by the cubic meter. Be careful to use the same volume units on the sales forecast and the price forecast. The price of oil/gas varies dramatically with time and less dramatically with the quality of the oil or gas. There are several “benchmark” crudes in the world, for which the price is reported on a daily basis. Benchmark crudes include Brent in the North Sea, Minas in Indonesia, Urals in Russia, Dubai in the Persian/Arabian Gulf, and others. The most commonly quoted number in the U.S. is West Texas Intermediate (WTI) delivered at Cushing, Oklahoma.

WTI is the underlying product for the New York Mercantile Exchange (NYMEX) futures prices. According to the NYMEX, “crude oil is the world’s most actively traded commodity. Over the past decade, the NYMEX division light, sweet (low-sulfur) crude-oil futures contract has become the world’s most liquid forum for crude oil trading, as well as the world’s largest volume futures contract trading on a physical commodity. Because of its excellent liquidity and price transparency, the contract is used as a principal international pricing benchmark.”<sup>2</sup> The physical specifications for WTI on the NYMEX are “crudes with 0.42% sulfur by weight or less, not less than 37°API gravity nor more than 42°API gravity.” Since 1992, the spot price of WTI has been as low as \$10.50/bbl in December 1998 and as high as more than \$36.00/bbl in the fall of 2000.

The actual price received by a producer is usually set for several days or one month at a time and may include a transportation charge, which reduces the effective price, or a bonus depending upon the supply and demand conditions in the local area. Many refiners are posting prices online, and these postings change rapidly. Conoco, for example, posted 147 different prices between January 1, 2001 and August 31, 2001, while Enron had 191 different prices in the same period. (Crude oil price postings are another indicator of the volatility of the oil/gas industry. When this chapter was first drafted in September 2001, the links to the postings were Conoco, Enron, Tosco, and Phillips. Since then, Enron went out of business, while Phillips purchased Tosco and then merged with Conoco.) Websites that have crude oil price bulletins for various companies are [www.conocophillips.com/buy/postings](http://www.conocophillips.com/buy/postings); [www.kochoil.com/crude.asp](http://www.kochoil.com/crude.asp); [www.shell.ca/code/prices/oilprices.html](http://www.shell.ca/code/prices/oilprices.html); and [seweb1.phillips66.com/crude/crudesupply.nsf](http://seweb1.phillips66.com/crude/crudesupply.nsf).

Projecting the future price of oil to use in an evaluation is quite difficult, and unfortunately, oil price is usually one of the most important factors in the evaluation. One popular, although not necessarily accurate, way of projecting future prices is to use a forward “strip” either from the NYMEX or from other crude oil traders. **Fig. 16.2** shows the NYMEX oil strip as of Septem-

Contract	Last	Open	High	Low	Most Recent Settle	Chg	Open Interest	Previous Day's Total Volume	Last Updated
Sep 2001	N/A	27.10	28.10	27.10	27.91*	0.73	631	0	8/30/01 17:00:50
Oct 2001	27.21	26.70	27.25	26.62	27.20	0.65	130,453	3,185	8/31/01 15:39:38
Nov 2001	27.40	26.85	27.40	26.75	27.35	0.62	61,640	27,410	8/31/01 13:38:27
Dec 2001	27.30	26.80	27.40	26.80	27.34	0.61	53,133	448	8/31/01 15:39:38
Jan 2002	27.06	26.49	27.10	26.49	27.04	0.59	25,497	206	8/31/01 15:39:38
Feb 2002	26.65	26.20	26.85	26.20	26.74	0.57	12,503	50	8/31/01 15:00:00
Mar 2002	26.22	25.96	26.22	25.93	26.45	0.55	10,103	905	8/31/01 13:38:28
Apr 2002	25.72	25.65	25.72	25.65	26.17	0.53	10,903	419	8/31/01 13:38:30
May 2002	25.38	25.38	25.45	25.38	25.89	0.51	7,758	169	8/31/01 13:38:30
Jun 2002	25.55	25.12	25.55	25.12	25.61	0.49	23,686	200	8/31/01 16:15:12
Jul 2002	N/A	24.88	24.88	24.88	24.88	-0.25	7,673	86	8/30/01 17:00:48
Aug 2002	N/A	24.65	24.65	24.65	24.65	-0.24	5,286	39	8/30/01 17:00:48
Sep 2002	24.85	24.80	24.85	24.80	24.88	0.46	10,945	25	8/31/01 15:00:00
Oct 2002	N/A	24.19	24.19	24.19	24.19	-0.24	6,133	205	8/30/01 17:00:51
Nov 2002	N/A	23.97	23.97	23.97	23.97	-0.24	4,884	330	8/30/01 17:00:51
Dec 2002	24.15	24.05	24.15	24.05	24.23	0.45	28,023	1,825	8/31/01 13:38:25
Dec 2003	N/A	22.32	22.32	22.32	22.32*	-0.21	11,412	0	8/30/01 17:00:53
Dec 2004	N/A	21.64	21.64	21.64	21.64*	-0.21	7,177	0	8/30/01 17:00:53
Dec 2005	N/A	21.26	21.26	21.26	21.26*	-0.21	4,936	0	8/30/01 17:00:54
Dec 2006	N/A	20.94	20.94	20.94	20.94*	-0.21	2,442	0	8/30/01 17:00:54

Fig. 16.2—NYMEX light sweet crude oil futures prices as of September 1, 2001 (after NYMEX<sup>2</sup>).

ber 1, 2001. A differential between the property being evaluated and the NYMEX is then applied to estimate prices at the property. More information can be obtained from the NYMEX website, which is [www.nymex.com](http://www.nymex.com).

Natural gas prices are also quoted at more than 50 market centers throughout the United States. Examples include Opal, Wyoming; Katy Hub, Texas; and the southern California border. Sabine Pipe Line Company's Henry Hub in Louisiana is the hub most often quoted. In April 1990 the NYMEX launched the world's first natural gas futures contract with Henry Hub as the physical delivery point. In October 1992, the NYMEX began trading options on natural gas futures, which allowed traders and speculators to "play" the market. The natural gas market is even more volatile than the oil market with prices as low as \$1.80 in early 1999 and over \$10 for a short time in December 2000. Future gas prices for use in an economic evaluation are often forecast in the same manner as previously described for oil. The Henry Hub future price from the NYMEX is adjusted for "basis" differential. Fig. 16.3 shows the NYMEX gas strip as of September 1, 2001.

The NYMEX trades in "paper barrels," in which the seller of a contract either has to purchase an offsetting contract or deliver a specified volume of a specified quality of hydrocarbon at a specified location. A contract on the NYMEX consists of 1,000 bbl of crude or 10,000 MMBtu of gas. The forward strip shows the month when the crude or natural gas will have to be delivered; the prices at which the contract traded during the day; the number of contracts

Contract	Last	Open	High	Low	Most Recent Settle	Chg	Open Interest	Previous Day's Total Volume	Last Updated
<u>Aug 2001</u>	N/A	3.280	3.360	3.060	3.167*	-0.003	10	0	8/30/01 19:02:08
<u>Sep 2001</u>	N/A	2.390	2.440	2.250	2.295	-0.120	8,233	53,285	8/30/01 17:04:55
<u>Oct 2001</u>	2.380	2.290	2.430	2.265	2.380	-0.015	81,659	36,813	8/31/01 13:36:14
<u>Nov 2001</u>	2.700	2.630	2.725	2.600	2.710	-0.010	41,009	11,465	8/31/01 13:36:15
<u>Dec 2001</u>	3.040	2.950	3.070	2.935	3.040	-0.005	35,628	4,493	8/31/01 13:36:15
<u>Jan 2002</u>	3.180	3.120	3.200	3.070	3.190	-0.005	40,923	167	8/31/01 16:20:14
<u>Feb 2002</u>	3.170	3.090	3.180	3.060	3.162	-0.005	26,155	30	8/31/01 15:00:14
<u>Mar 2002</u>	3.090	3.040	3.120	2.980	3.095	-0.002	24,602	1,757	8/31/01 13:36:17
<u>Apr 2002</u>	3.030	2.900	3.030	2.900	3.005	-0.002	32,537	4	8/31/01 15:00:14
<u>May 2002</u>	3.025	2.950	3.050	2.940	3.025	-0.002	19,342	331	8/31/01 13:36:17
<u>Jun 2002</u>	3.075	3.000	3.075	2.980	3.065	-0.004	12,421	209	8/31/01 13:36:18
<u>Jul 2002</u>	3.125	3.080	3.130	3.060	3.113	-0.004	11,310	119	8/31/01 13:36:18
<u>Aug 2002</u>	3.180	3.130	3.180	3.112	3.158	-0.004	22,616	298	8/31/01 13:36:19
<u>Sep 2002</u>	3.170	3.000	3.175	3.113	3.159	-0.004	13,140	4	8/31/01 15:00:15
<u>Oct 2002</u>	3.190	3.090	3.190	3.090	3.174	-0.004	22,124	3,602	8/31/01 13:36:19
<u>Nov 2002</u>	3.300	3.250	3.320	3.200	3.329	-0.004	13,006	381	8/31/01 13:36:21
<u>Dec 2002</u>	3.480	3.450	3.480	3.450	3.501	-0.004	10,961	230	8/31/01 13:36:21
<u>Dec 2003</u>	3.590	3.664	3.590	3.564	3.600	-0.004	2,749	15	8/31/01 13:36:26

Fig. 16.3—NYMEX Henry Hub natural gas futures prices as of September 1, 2001 (after NYMEX<sup>2</sup>).

“open” (open interest) where the obligation to deliver the commodity still exists; and the number of contracts traded during the previous day. Fig. 16.2 shows that on September 1, 2001 there were open interests for 130 million barrels of crude for October delivery. This volume represents more than one-half the crude oil produced in the United States during October 2001. More information on these contracts can be obtained at [www.nymex.com/jsp/index.jsp](http://www.nymex.com/jsp/index.jsp).

Many producers have chosen to use the NYMEX to “hedge” or set a price for their oil/gas in the future. This can be an effective strategy for managing risk, but it can also be extremely frustrating when gas is currently selling for \$8/MMBtu on the spot market and it was agreed months ago to sell gas today for \$2.80/MMBtu.

**16.2.10 State and Local Taxes.** In the U.S., most states levy a tax called a “severance” tax on all minerals extracted and sold from a property. This tax may range from 3 to 12.5% of the value of the minerals produced. Local taxing districts such as counties or taxing districts such as fire districts may also impose a tax on oil/gas production. This tax is often referred to as an *ad valorem* tax from the Latin for “according to value.” In most cases the assessed value of the property is multiplied by the mill levy of the taxing district just like the property tax on houses and buildings. The method of calculating assessed value varies considerably from state to state. The two most common methods of calculating assessed value are to use some fraction of the revenue received and to use some fraction of the calculated net present value of the projected production.<sup>3</sup> The methodology used varies widely from state to state and from time to time. Often, *ad valorem* taxes are approximated as a percentage of each owner’s revenue

when calculating net cash flow. The percentage can range from less than 5 to 20%. Indian tribes and cities in some states may also collect a severance tax on oil/gas produced within their borders. In most cases, each party pays their own severance and *ad valorem* taxes. In other words, the working interest owners only pay state and local taxes on their share of the production, and the royalty owners pay the tax on their share of the production.

In countries other than the U.S., it is not so common for local governments to impose a severance tax, but it does occur. An example is Argentina, where the provincial governments impose a sales tax ranging from 1 to 2%. In most cases there are numerous other taxes that may need to be taken into account such as road taxes, airport taxes, or stamp duties. The oil company usually attempts to negotiate an agreement that exempts them from all these taxes in return for a royalty or a share of the production. These negotiations are sometimes successful and sometimes not.

**16.2.11 Operating Costs.** Operating costs are those costs that are necessary to maintain production from the well. They would include direct expenses, such as electricity for a pumping unit motor; hot oil treatments; payments to a pumper to monitor and do minor repairs on the well; replacement of pumps or rods; fixing flow line leaks; plowing roads; and a myriad of other expenses associated with owning an interest in an oil/gas well. Direct expenses might range from \$250/well per month for a flowing gas well to \$3,000/well per month for an on-shore oil well producing a large amount of fluid. Offshore wells can have even higher operating costs.

Another component of operating costs is the Council of Petroleum Accountants Societies (COPAS) or fixed-rate overhead charge. (As stated from the COPAS website, “COPAS was created in 1961 to provide a forum for discussing and solving the more difficult problems related to accounting for oil/gas. These discussions frequently have resulted in the creation of guideline documents and educational materials. You can find these materials in the Products section of this site. COPAS has grown to 23 local Societies and over 2,700 members in the United States and Canada. COPAS has a strong emphasis in providing quality educational materials related to oil/gas accounting.”)<sup>4</sup> For producing wells this is a charge levied by the operator of the property to reimburse the operator for the costs of administering the payment of invoices, disbursement of monies, and filing of government forms associated with the lease. This charge is subject to negotiation between the operator and the non-operators in a property and can range from \$100/well per month to \$1,500/well per month or more. The accounting firm of Ernst & Young (E&Y) surveys operators for their costs of company operated wells annually. Even though the figures that E&Y solicit are internal numbers, they give an idea of what might be expected for COPAS charges. Their most recent report can be obtained from [www.ey.com/global/Content.nsf/US/Energy\\_Chemicals\\_Uilities\\_-\\_Annual\\_Fixed\\_Rate\\_Overhead\\_Survey](http://www.ey.com/global/Content.nsf/US/Energy_Chemicals_Uilities_-_Annual_Fixed_Rate_Overhead_Survey).

Operating costs in other countries can vary dramatically. In most cases the operating costs will include facilities to house expatriate workers and their dependents as well as other normal operating expenses. Depending on the situation, these costs can be very significant in the cash flow calculations.

**16.2.12 Net Operating Income.** Sometimes called “cash generated from operations” or other names, net operating income is the cash flow to the working interest owner after operating costs and state and local taxes have been paid, but before investments have been made. This represents the cash generated during the period that is available for investment.

**16.2.13 Income Tax.** Almost all federal governments including the United States Government and most state governments levy a tax on income. The calculation of these taxes can be fairly straightforward in countries such as Indonesia or extremely difficult, especially when a single

project is being evaluated for a reasonably large company in the U.S. Even when the appropriate software is available to aid in the evaluation, the input data necessary to accurately calculate income tax is often hard to obtain. For this reason and because income tax often has a relatively low impact on the final decision, it is common practice to calculate before federal income tax (BFIT) net cash flows when evaluating U.S. properties. Major oil companies are more likely to attempt to include the effects of income tax in their calculations, while independents seldom include it. The effect of using BFIT numbers on the ultimate decision is highly dependent on the individual case, but experience indicates that in the U.S. it seldom changes the decision.

**16.2.14 Investment.** Investments are costs that benefit future periods as opposed to operating costs that only benefit the current period. Examples include buying a lease, drilling a well, buying and installing a pumping unit, and building tank batteries. In all of these cases, the goods purchased are expected to help produce money far into the future.

**16.2.15 Net Cash Flow.** Net cash flow is the amount of money that flows into or out of the treasury during any one period. It is equal to the net operating income (either before or after income taxes) less the investments.

Each of these items is estimated for every future time period until the net operating income is no longer positive. At that time the well(s) is (are) usually assumed to be plugged and abandoned. There may be an additional expense at that time for abandonment costs, or the salvage value of the equipment may be equal to or greater than the abandonment costs.

### 16.3 Time Value of Money

Money has a time value. This means a dollar received today has more value to us than a dollar received far in the future. Other than a desire for instant gratification, there is a very rational reason for this phenomenon. If we have a dollar today, we can put it to work by making an investment and have more than a dollar at some future date. This concept of putting the money to work has important implications later in this section when discount rates are discussed.

Another important concept is the concept of equivalence between a current lump sum of money and a lump sum to be received in the future. Offering someone a choice between receiving \$100 today and receiving \$101 one year from today can demonstrate this. Most people will opt for the \$100 today. If we increase the amount of future money to \$115 or \$125 or perhaps \$200 and guarantee payment, there will be a point at which the future sum of money will become more attractive than the current \$100. The amount of future money necessary to sway the person to choose the future sum is dependent upon many things—the inflation rate, current opportunities to invest the \$100, and perceived risk, among others. No matter what the amount of money necessary to tip the scales, the concept that money has a time value is established.

In the case just discussed, if the person is indifferent to receiving \$125 one year from now or \$100 now, we say that the two sums are “equivalent.” This concept of equivalence is fundamental to the evaluation of all engineering projects. We are often faced with the choice of having a certain sum of money now or receiving various sums of money in the future. By determining the equivalence between money received today and money received in the future, we can make an informed decision.

In the previous example, making the choice is relatively simple. There are only two sums to compare, and the time period is one year. This is usually not the case in oil/gas property evaluations, so we need a mechanism to handle complex choices. The mechanism that works best is interest.

We can define interest as the amount of money that must be added to our current sum to make an equivalent future sum. The amount of interest necessary to create equivalence is dependent upon the period under consideration. We may be indifferent to receiving \$100 now,

\$112.50 six months from now, or \$125 one year from now. In that case, the \$12.50 or \$25.00 is the amount of interest. To easily compare all three alternatives, interest is compared as a rate. It may be expressed as 12.5% per six months or 25% per year. The interest rate is calculated by dividing the amount of interest paid per period by the principal amount at the beginning of the period. Often, interest rate is expressed on an annual basis such as 25% per annum.

For loans or bank deposits that exceed one year, the interest is usually compounded. That is, the interest earned during the first period is added to the original principal to form the principal for the second period. The compound interest concept will be used when calculating the equivalence between a sum of money today and future sums of money.

**16.3.1 Future Worth of a Lump Sum.** If we have a present sum of money,  $P$ , and we put it to work at a compound interest rate,  $i$ , we will have a future lump sum of money,  $F$ , at the end of  $n$  periods. The relationship between these parameters is expressed in equation form as

$$F = P(1 + i)^n \dots\dots\dots (16.1)$$

The term  $(1 + i)^n$  is called the single payment compound amount factor in many texts and is often tabulated.

**Example 16.1 Future Value.** \$1,000 is placed in a bank paying 12% per compounding period. How much money will be in the account after five periods?

$$\begin{aligned} F &= P(1 + i)^n \\ F &= \$ 1,000(1 + 0.12)^5 \\ F &= \$ 1,762. \end{aligned}$$

**16.3.2 Present Worth of Lump Sum.** Present worth of lump sum is by far the most important equation in discussing the time value of money. This one equation allows the creation of an equivalence between future projected net cash flows and current sums of money, which can then be compared to the amount to be invested to obtain those net cash flows.

If an amount,  $F$ , is going to be received  $n$  periods in the future, then its present value,  $P$ , can be calculated for a given interest rate,  $i$ , by rearranging Eq. 16.1.

$$P = \frac{F}{(1 + i)^n} \dots\dots\dots (16.2)$$

This is the inverse of the single payment compound amount formula. The justification for this formula lies in the equivalence concept. The sums  $P$  and  $F$  are equivalent to each other because  $P$  could be invested at  $i$  for  $n$  periods to become  $F$ . The term  $(1 + i)^{-n}$  is often referred to as the “single payment present worth factor” or “discount factor.” The value of  $n$  in the previous equations does not have to be an integer. Although there are some theoretical difficulties, it is quite practical to use a value of 2.5 for  $n$  to create an equivalence between a future lump sum received 2.5 periods in the future and a present lump sum. This technique is used quite often when calculating the present value of annual cash flow streams.



**Example 16.2 Present Value.** \$1,762 will be received five periods from now. What is the present value of this amount at an interest rate of 12% per period?

$$P = \frac{F}{(1+i)^n}$$

$$P = \frac{\$1,762}{(1+0.12)^5}$$

$$P = \$1,000.$$

When cash flows are calculated for several periods, as done in Fig. 16.1, Eq. 16.2 can be used repeatedly to find the equivalent present value of each of the future cash flows.

**16.3.3 Annuities and Loans.** There are a number of specialized equations that can be used when particular types of repetitive cash flows are projected. In particular, when the same cash flow,  $A$ , is received at the end of every period, the present value of the cash flow stream can be calculated from the equation,

$$P = \frac{A}{\left[ \frac{i}{(1+i)^n - 1} + i \right]} \dots\dots\dots (16.3)$$

Eq. 16.3 is often called the annuity equation because it can be rearranged to calculate the value of  $A$ , which is the amount of money one would receive at the end of every  $n$  period if one invested  $P$  at an interest rate of  $i$ . It is also used to calculate loan payments where  $P$  is the principal amount.

**Example 16.3 Loan.** What are the monthly payments on a \$100,000 loan with a term of 360 months (30 years) at an interest rate of 1% per month compounded monthly?

$$A = P \left[ \frac{i}{(1+i)^n - 1} + i \right] \dots\dots\dots (16.4)$$

$$A = \$100,000 \left[ \frac{0.01}{(1+0.01)^{360} - 1} + 0.01 \right]$$

$$A = \$1,028.61.$$

There are a number of other specialized equations, but they are of limited use in today's era of fast computers. See Thompson and Wright,<sup>1</sup> Chap. 2, for examples.

**16.3.4 Annual vs. Monthly Interest Rates.** Interest rates are normally expressed on an annual basis or *per annum*. As the previous equations show, when working with monthly cash flows, it is necessary to convert the annual interest rate to a monthly interest rate. There are two ways to do this: divide the annual interest rate by 12, or calculate the equivalent effective monthly interest rate. These two methods will result in different answers.

	APR	Length of Loan	Monthly Payment	Total Finance Charge	Total of Payments
Creditor A	14%	3 years	\$205.07	\$1,382.52	\$7,382.52
Creditor B	14%	4 years	\$163.96	\$1,870.08	\$7,870.08
Creditor C	15%	4 years	\$166.98	\$2,015.04	\$8,015.04

**Fig. 16.4—Comparison of monthly payments at different interest rates and terms from [www.federalreserve.gov/pubs/consumerhdbk/cost.htm](http://www.federalreserve.gov/pubs/consumerhdbk/cost.htm).**

Consumer lending groups use the divide-by-12 method to comply with the Truth-in-Lending Act. The Truth-in-Lending Act required disclosures from lenders, which include, among other things, the note interest rate, any points or origination costs, and most lender imposed fees, such as underwriting and processing fees. These fees are all rolled into the calculation of an annual percentage rate (APR) for the loan. As the name implies, this is an annual rate. Because most consumer loans are paid on a monthly basis, the monthly rate, used in Eq. 16.3 to determine the monthly payments, is obtained by dividing the annual rate by 12. Fig. 16.4 from the Federal Reserve website shows some sample monthly payments. The next example illustrates the calculation.

**Example 16.4** *Monthly Payment Calculation.*

- Loan principal = \$6,000.
- APR = 15%.
- Monthly interest rate = 15%/12 = 1.25%/month.
- Loan term = 4 years (48 months).

$$A = P \left[ \frac{i}{(1+i)^n - 1} + i \right]$$

$$A = \$ 6,000 \left[ \frac{0.0125}{(1 + 0.0125)^{48} - 1} + 0.0125 \right]$$

$$A = \$ 166.98.$$

The effective-monthly-rate method, although more complicated to calculate, has some advantages as discussed later in Sec. 16.5. In this method, the annual interest rate is converted to a monthly rate, which, when compounded 12 times, results in the annual interest rate. The derivation of the effective monthly interest rate begins with the relationship  $(1 + i) = (1 + i_m)^{12}$ .

Rearranging this equation gives

$$i_m = \frac{1}{(1+i)^{12}} - 1 \dots\dots\dots (16.5)$$

The divide-by-12 method leads to a higher monthly payment than the effective-monthly-rate method, as shown in the next example.

**Example 16.5** *Monthly Payments With Effective Monthly Interest Rates.* Using the data from Example Four, the effective monthly interest rate is calculated as

$$i_m = \frac{1}{(1+i)^{12}} - 1.$$

$$i_m = \frac{1}{(1+0.15)^{12}} - 1.$$

$$i_m = 0.01171.$$

The loan payment is then calculated.

$$A = P \left[ \frac{i}{(1+i)^n - 1} + i \right].$$

$$A = \$6,000 \left[ \frac{0.01171}{(1+0.01171)^{48} - 1} + 0.01171 \right].$$

$$A = \$164.12.$$

## 16.4 Key Economic Parameters

When the purpose of an economic analysis is to help make a decision, there are several key managerial indicators or economic parameters that are considered. Although there are many parameters that can be considered (see Thompson and Wright,<sup>1</sup> Chap. 3), the most common decision criteria are net present value, internal rate of return, and profit-to-investment ratio (both discounted and undiscounted). Each of these criteria is discussed next.

**16.4.1 Net Present Value.** Net present value is the sum of the individual monthly or yearly net cash flows after they have been discounted with Eq. 16.2. In Table 16.2, the three columns labeled “Discounted Net Cash Flow” show this calculation at annual discount rates of 10, 20, and 34.3%. The net present values (NPV) at these discount rates are \$99,368, \$51,950, and \$0, respectively. In this table, the NPV were calculated on a monthly basis using effective-monthly interest rates converted from annual rates with Eq. 16.5.

After the discounting method has been specified, there is still the question of what discount rate to use. The author recommends the company’s average investment opportunity rate (see Thompson and Wright,<sup>1</sup> pages 3-7 and 3-8 and Newendorp and Schuyler,<sup>5</sup> pages 9 through 12). The average investment opportunity rate is the interest rate that represents, on average, the return of the future investment opportunities available to the company. This is the rate at which the treasury will grow. An alternative interest rate is the weighted average cost of capital (WACC). This is an interest rate that, as the name indicates, is the average of the cost of each source of financing weighted by the fraction of the total financing that source represents. Sources of financing include debt, which has an explicit interest rate associated with it, and equity, which has an implicit cost associated with attracting and retaining investors. The average investment opportunity rate and the weighted average cost of capital are often very similar to each other and often much lower than the typical “hurdle rates” used in the industry.

The use of high discount rates to account for risk is not recommended. Much has been written about the fallacy of using high discount rates (see, for example, Capen<sup>6</sup>). Later sections of this chapter deal with decisions under uncertainty.

The decision criterion using net present value is very simple. For project screening, all projects with a positive NPV at the company average investment opportunity rate are acceptable. If the projects with a positive NPV perform as projected, they will return more to the treasury than the average company project will return. In the case of mutually exclusive alternatives, where choosing one alternative precludes choosing another, the alternative with the

highest NPV should be chosen. An example of mutually exclusive alternatives might be choosing between injecting CO<sub>2</sub> or high-pressure air as a secondary recovery method—only one or the other may be chosen, not both.

**16.4.2 Internal Rate of Return.** Internal rate of return (IRR) has been a popular managerial indicator since the 1950s, and it is still widely used today. IRR is defined as that interest rate which, when used in the calculation of NPV, causes the NPV to be zero. In [Table 16.2](#) that interest rate is 2.488% per month or 34.30% per year. Notice that, once again, we are using the effective monthly interest rate and, therefore, must use [Eq. 16.5](#) to convert to annual interest rate.

IRR can easily be used to screen projects. If the IRR is greater than the average investment opportunity rate, the project passes the screen. However, the unwary might be trapped in a situation where two mutually exclusive projects are being compared. Many evaluators have a tendency to think that the project with the larger IRR is the better project. This is not necessarily so. If IRR is used to compare two mutually exclusive projects, it is necessary to calculate the IRR on the incremental capital used for the project with the larger investment. Although this can lead to the correct decision, the procedure is tedious enough that it is easier to just compare NPVs at the average investment opportunity rate. Choosing the project with the higher NPV, at the average investment opportunity rate, leads to the same decision as calculating incremental IRR.

Under certain circumstances there may be more than one interest rate that will cause the NPV to be zero. This is referred to as multiple rates of return and occurs primarily in the evaluation of acceleration projects. As stated by Phillips,<sup>7</sup> an acceleration project is “one in which money is invested, not necessarily to show a profit but to decrease the time required to obtain the income from a project. In fact, acceleration projects will generally result in a net loss.” An example acceleration project might be a decision to downspace from 80 acres to 40 acres in a coalbed methane field. In this hypothetical case, virtually the same amount of gas is expected to be produced over a shorter time period, yet there is a large investment to drill the additional wells. When the infill project is evaluated on an incremental basis, the cash flow stream is negative then positive and then negative again, as shown in [Table 16.3](#). On an undiscounted basis, the project loses money. The only justification for doing the project (in this hypothetical case) is to “accelerate” the cash flows, so the company can invest them elsewhere.

The number of sign changes in the cash flow stream is the number of potential values for IRR. In [Table 16.3](#), there are two sign changes (negative to positive in year one and positive to negative in year six), so there are two values of IRR.

The key to evaluating acceleration projects is again to examine the NPV of the project at the company average investment opportunity rate. The rationale for accelerating the cash flows is to invest them elsewhere, so you must know what you are going to do with them (on average). If the NPV of the project is positive at the company average investment opportunity rate, then you can profitably invest the accelerated cash flows elsewhere. If the NPV is negative, you are better off not accelerating the cash flows. [Table 16.3](#) also illustrates how sensitive some of these projects can be to the company average investment opportunity rate. This project is only profitable at interest rates between 1.2 and 12.9%, as shown in columns E and F. The discounted net cash flow is zero at those interest rates. You would have to be very sure of the numbers to invest \$2,500,000 to return \$15,374 more than average projects.

Several years ago, a spirited discussion appeared in the literature sparked by E.L. Dougherty's paper on discounted cash flow rate of return.<sup>8</sup> This discussion presents a good analysis of different points of view.

**16.4.3 Discounted Profit-to-Investment Ratio.** Discounted profit-to-investment ratio has been touted by R.D. Seba<sup>9</sup> as “the only investment selection criterion you will ever need,” in his

TABLE 16.3—ANALYSIS OF AN ACCELERATION PROJECT

A (Year)	B (Net Cash Flow)	C (Cumulative Net Cash Flow)	D (Discounted Net Cash Flow at 12%/Annum Using Mid-Year Discounting)	E (Discounted Net Cash Flow at 1.2%/Annum Using Mid-Year Discounting)	F (Discounted Net Cash Flow at 12.9%/Annum Using Mid-Year Discounting)
0	-2,500,000	-2,500,000	-2,500,000	-2,500,000	-2,500,000
1	260,000	-2,240,000	245,677	258,471	244,681
2	1,000,000	-1,240,000	843,671	982,461	833,456
3	1,800,000	560,000	1,355,899	1,747,692	1,328,650
4	1,100,000	1,660,000	739,826	1,055,509	719,094
5	700,000	2,360,000	420,356	663,811	405,272
6	-800,000	1,560,000	-428,934	-749,744	-410,198
7	-500,000	1,060,000	-239,361	-463,095	-227,054
8	-400,000	660,000	-170,972	-366,132	-160,870
9	-300,000	360,000	-114,490	-271,378	-106,854
10	-400,000	-40,000	-136,298	-357,595	-126,178
Total	-40,000		15,374	0	0

paper of the same name. This paper and the various discussions of it present a good discussion of the method. Mechanically, profit-to-investment ratio is calculated by dividing the sum of either the net operating income or the net cash flow from a project by the sum of the investments. If undiscounted numbers are used, the result is an undiscounted profit-to-investment ratio; if discounted numbers are used, the result is a discounted profit-to-investment ratio. If net operating income is used in the numerator, a value of 1.0 is a breakeven value where the investment is just recovered. If net cash flow is used in the numerator, a value of 0.0 is a breakeven value. Either definition is appropriate for the numerator, as long as it is clearly stated which definition has been used.

Discounted profit-to-investment ratio at the company average investment opportunity rate is indeed a powerful selection and ranking tool, as stated by Seba. As a selection tool, all projects with a value greater than 1.0 (or 0.0) would be selected. In the presence of limited capital, the projects are ranked in decreasing order of discounted profit-to-investment ratio and selected until the capital available for investment is exhausted. This very simple tool results in the portfolio of projects that causes the treasury to grow at the fastest rate, if the projects perform as expected. Erdogan *et al.*<sup>10</sup> pointed out that “this approach maximizes expected value but ignores risk. In fact, funding projects with the highest discounted P/I will tend to produce a high-risk portfolio.” This is a valid criticism and is addressed at length in Sec. 16.8.

The example in Table 16.2 can be used to demonstrate the calculation of profit to investment ratio.

**Example 16.6** Profit-to-Investment Ratio from Table 16.2.

Total undiscounted net operating income = \$585,369.

Total undiscounted investment = \$425,000.

Total undiscounted net cash flow = \$160,371.

Total investment discounted at 10% = \$425,000 (because only one investment was made and that was at time 0).

Total net cash flow discounted at 10% = \$99,368.

Total net operating income discounted at 10% = \$99,368 + \$425,000 = \$524,368.

$$\text{Undiscounted profit-to-investment ratio} = \frac{\text{net operating income}}{\text{investment}} \dots\dots\dots (16.6)$$

$$\text{Undiscounted profit-to-investment ratio} = \frac{\$ 585,369}{\$ 425,000}$$

$$\text{Undiscounted profit-to-investment ratio} = 1.38.$$

Alternatively,

$$\text{undiscounted profit-to-investment ratio} = \frac{\text{net cash flow}}{\text{investment}} \dots\dots\dots (16.7)$$

$$\text{Undiscounted profit-to-investment ratio} = \frac{\$ 160,371}{\$ 425,000}$$

$$\text{Undiscounted profit-to-investment ratio} = 0.38.$$

Using discounted values,

$$\text{Discounted profit-to-investment ratio} = \frac{\text{discounted net operating income}}{\text{discounted investment}} \dots\dots\dots (16.8)$$

$$\text{Discounted profit-to-investment ratio} = \frac{\$ 524,368}{\$ 425,000}$$

$$\text{Discounted profit-to-investment ratio} = 1.23.$$

Again, alternatively,

$$\text{discounted profit-to-investment ratio} = \frac{\text{discounted net cash flow}}{\text{discounted investment}} \dots\dots\dots (16.9)$$

$$\text{Discounted profit-to-investment ratio} = \frac{\$ 99,368}{\$ 425,000}$$

$$\text{Discounted profit-to-investment ratio} = 0.23.$$

## 16.5 Recommended Practices for Economic Calculations

More than 70 different people have calculated the simple problem shown in [Table 16.2](#) in three phases. Phase One consisted of 30 runs with different programs during the 1990s. In Phase Two, the problem was run by 12 vendors of commercially available economic evaluation software in late 1999 and early 2000. Phase Three included runs by various oil company and vendor personnel during late 2000 and early 2001. In each phase, the problem statement was identical, except for the effective and production dates, which were always January 1 and February 1, respectively, of the year when the case was run. The problem is an evaluation of a drilling prospect assuming a single “time 0” investment, exponential decline, and escalating

prices and costs. The problem was originally designed to be solved by hand, so it has a five-year life.

There was a surprising diversity in the reported answers. For example, the NPV at 20% was expected to be \$51,950, yet the answers received ranged from about \$3,000 to almost \$100,000. In fact, the problem was solved 74 different times, which resulted in 68 different answers. (More details are available in Wright and Thompson.<sup>11</sup>) In 2000, a large project conducted by the Society of Petroleum Evaluation Engineers (SPEE) found that the differences arise from a combination of unstated assumptions; differences in interpretation of various parameters; different, but equally valid, treatment of factors such as discounting or escalation; and apparent misunderstanding of the problem statements. The results of that study indicated that there was a great need for standardization and communication regarding upstream economic calculation. To begin that communication process, the SPEE formed committees to draft recommended evaluation practices. Ten of those recommended evaluation practices were approved by the members attending the annual meeting of SPEE in June 2001 and are in the process of being approved by the SPEE membership as a whole. These recommended engineering practices (REP) address issues such as the elements of a report (REP 1) and how to discount cash flows (REP 5). The REPs are available on the SPEE website, which is [www.spee.org](http://www.spee.org). The SPEE REPs are not intended to be required practices but are suggested ways to present the problem when you do not have compelling reasons to do otherwise.

REP 5 on discounting is of particular interest in the context of this chapter. It is recommended that end-month discounting be used for calculations using monthly cash flows and that mid-year discounting be used for calculations using yearly cash flows. Additionally, it is recommended that the effective monthly interest rate, as defined by [Eq. 16.4](#), is used. When monthly cash flows are discounted using the effective monthly interest rate, the results are very similar to that obtained by discounting annual numbers using mid-year discounting.

## 16.6 Risk Analysis for Oil and Gas Property Evaluation

In the previous discussions, we assumed to know the model parameters with certainty. This is clearly not the case, so some method of handling uncertainty is appropriate. There have been a number of textbooks written on the subject, but one of the best is *Decision Analysis for Petroleum Exploration*, originally written in 1975 by Paul Newendorp and updated in 2000 by Newendorp and John Schuyler. The following discussion briefly covers some of the topics contained in their book.

**16.6.1 Risk and Uncertainty.** When making a decision in the oil/gas business, we are seldom certain of the results of that decision. This is both the curse and the attraction of the industry. Great fortunes can be made or squandered on the basis of a single decision. Some authors use the terms “risk” and “uncertainty” interchangeably, and some authors make a great distinction between them. We shall use the term uncertainty to express the concept that we do not know the outcome of a decision when we make it. We shall use the term risk to mean that in any decision we make, there is a possibility of an unpleasant outcome—losing money in the context of this chapter. Further, we will assume rational decision making.

The practice of “risk analysis” or “decision analysis” is a way to analyze the potential results of decisions objectively and consistently. Risk analysis does not eliminate dry holes or even bankruptcy, but applied properly it helps keep you in the game. One of the most important aspects of “playing the game” is to try to make sure you are in a winning game. Risk analysis can provide the information to keep you from playing a known losing game, such as being on the wrong side of the roulette wheel in a gambling casino, but it may not help you much if you are unknowingly playing a losing game while thinking you have a chance of winning. Judgment (and luck) still count.

A	B	C	D
Outcome	Probability of Outcome	Conditional Value of Outcome	B × C
Dry hole	0.10	1,000,000	100,000
Discovery	0.90	-100,000	-90,000
Total	1.00		10,000

**16.6.2 Expected Monetary Value Concept.** Expected monetary value (EMV) is the foundation of risk analysis as described in this chapter. Newendorp and Schuyler<sup>5</sup> (page 82) state that “the expected value concept is more nearly a strategy, or philosophy for consistent decision making than an absolute measure of profitability.” In applying the strategy, the decision maker should be playing a winning game, should have sufficient money for repeated trials, and should apply the concept consistently over a large number of decisions. Numerically, expected value is the return on average given repeated trials. That is, over the long haul, we would obtain an average result equal to the expected value. When making a decision, each alternative has an expected value associated with it. Having made a decision, there are a number of potential outcomes. The expected value of a decision alternative is obtained by summing the product of the probability of occurrence of a potential outcome and the payoff for each potential outcome. This is done for each decision alternative, and we then choose the one with the highest expected monetary value.

As an example, assume you have 100 prospects to drill: 10 prospects contain oil worth \$10 million (each), and 90 contain nothing but heartbreak and cost you \$100,000 (each) to drill and abandon. All numbers are net present values at the company average opportunity investment rate and, therefore, include the costs to drill and produce the oil. The costs include additional development wells. If you drill all 100 prospects, you will have a present-day profit of  $10 \times \$10$  million less  $90 \times \$100,000$  or \$1 million. This is certainly a winning game. [Now, if we could run a three-dimensional (3D) seismic survey to highgrade the prospects and only drill 20 wells to get our \$100 million of oil, we would be playing a winning game. That analysis is beyond the purview of this chapter but is a topic under the category of “decisions to purchase imperfect information.”] We can divide the \$1 million profit by the 100 wells we drilled and see that each well is worth \$10,000 on average. Let us use expected value to investigate the drilling of one well.

Out of 100 possible wells, ten will result in field discoveries. Therefore, the probability of success is 10%. If we are successful in discovering a field, the conditional value of that success is \$1 million. The probability of failure (dry hole) is 90%, and the conditional value of failure is -\$100,000. We can analyze this example in a table such as [Table 16.4](#). The expected value of the decision alternative is +\$10,000, found at the bottom of column D. This is the same value we calculated (on average) assuming we drilled all 100 prospects. So what happens if our model truly represents nature and we drill the well? We probably drill a dry hole and lose \$100,000. In fact, that will happen nine times out of ten (on average). This is where the repeated trials and consistent application previously mentioned come in. If we apply the same methodology a large number of times, the odds are in our favor, and we will prevail. We expect the odds to catch up with us somewhere around 30 trials.

In this table, we are modeling what we expect to find in nature. That model can be as simple as shown in [Table 16.4](#), or it can be excruciatingly complex with hundreds or even thousands of potential outcomes. However, simple or complex, some conditions must be met. First, the probabilities in column B must sum to exactly one. That means our model includes



all possible outcomes or states of nature. This may be uncomfortable at first, but it is necessary. Second, each conditional value for an outcome must include all costs to achieve that outcome and all revenues from that outcome. Third, the net present values must be calculated using the company average opportunity rate. We are always comparing a decision alternative with the “do nothing” alternative. If we “do nothing,” we are implicitly saying we are going to invest the money in average projects for the company, which will earn money at the company average opportunity rate. The expected monetary value (EMV) for that decision alternative is zero. In order for our analysis to make any sense at all, that rate must be used in calculating expected values.

Expected value theory assumes that the decision maker is impartial to money. This means that a gain of \$10,000 brings the same amount of positive “utility” as a loss of \$10,000 brings negative utility. If the gain of \$1 million does not bring ten times as much pleasure as the loss of \$100,000 brings pain, then the expected values should be expressed in a “currency” such as utility that linearizes the problem. Newendorp and Schuyler (Chap. 5) discuss utility theory as do others.<sup>12-14</sup> In practice, the decision maker is usually impartial to money because the individual decisions are small, relative to the size of the treasury, or can get that way by joint venturing with other companies.

EMV provides a means to screen projects, compare two mutually exclusive projects, and rank projects in the presence of uncertainty. When screening projects, all projects with positive EMVs pass the screen. When comparing mutually exclusive projects, choose the one with the largest EMV. When ranking projects, rank them by the EMV to expected investment ratio.

Ranking projects by EMVs to expected-investment ratio suffers from the same criticism that discounted profit-to-investment ratio suffers. Namely, this ranking may lead to the highest aggregate NPV, but it also leads to the highest risk portfolio. It may be possible to choose a different mix of projects that will significantly reduce the overall risk without significantly reducing the overall EMV. That is the goal of the emerging field of “portfolio analysis,” which is discussed in Sec. 16.8.

EMV calculations lend themselves to sensitivity analysis. It is a simple matter to change probabilities and/or payoffs and recalculate the results. One very enlightening graph is a plot of expected value vs. probability of success. For a two-outcome scenario (or a scenario that can be reduced to two outcomes), the relationship between EMV and probability of success is linear. You only need to know the NPV given failure and the NPV given success to prepare the plot. The plot for the example in Table 16.4 is shown in Fig. 16.5. Note that at a probability of success of 10%, the EMV is \$10,000. As the probability of success increases, the EMV increases rapidly, reaching \$450,000 per well at a 50% success ratio. The plot can be used to estimate the breakeven probability of success, which in this case is 9%. If the considered opinion of the explorationists is that the probability of success lies between 15 and 30%, the decision is easy. If the probability of success lies between 5 and 15%, more analysis may be indicated.

**16.6.3 Decision Trees.** Decision trees are useful tools to analyze a series of sequential decisions, although they can be used for single decisions as well. They are a way to graphically represent the principles discussed in the section about expected monetary value. Traditionally, decision trees are constructed with “time” flowing from left to right and are made up of “nodes” that are connected by “branches.” There are three types of nodes: decision nodes represented by squares, chance nodes represented by circles, and terminal nodes represented by triangles. Fig. 16.6 illustrates the previous sample EMV problem in a decision tree format.

The first square node shows two possible decisions: drill a well, or drop the acreage. In a real-world example, we may have more options, such as release the property, bring in a partner, and others, but that just adds to the number of branches emanating from the decision node. If we drop the acreage, we arrive at a terminal node, and it will cost us nothing. If there

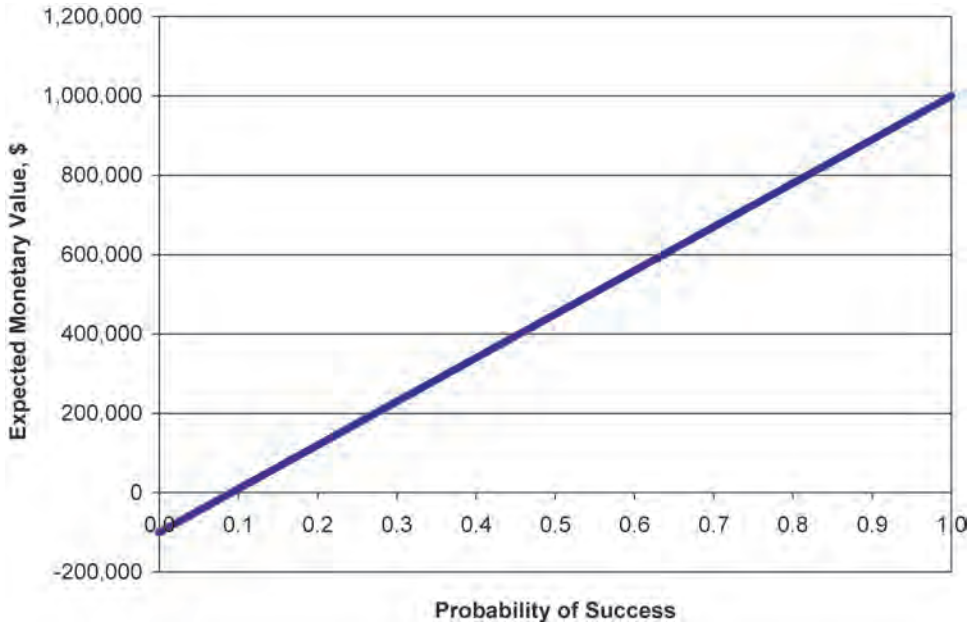


Fig. 16.5—Example of the effect of probability of success on expected monetary value.

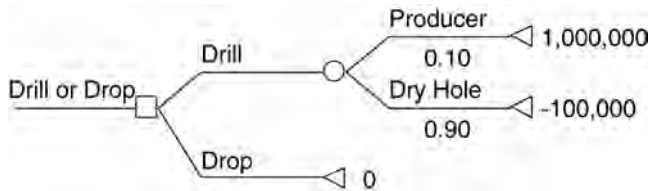


Fig. 16.6—Example decision tree.

were abandonment costs, they would be shown as negative numbers on that terminal node. The round chance node, if we drill, shows all the possible outcomes just like the decision table (Table 16.4). Notice that if we drill, the probabilities and payoffs are the same as those used in the EMV problem.

The probabilities attached to a chance node must sum to exactly 1.0. This means we believe we have modeled all the possible outcomes. If a two-outcome decision tree is too simple for your problem, as it probably should be, then you can add as many branches as you wish to the chance node. There are two options in assigning costs or payoffs to get to the terminal node. One is to only show the incremental costs (payoffs) to get from one node to another. The other is to show all the costs and payoffs from the root to the terminal node. The incremental method makes sensitivity runs easier, while the total cost/payoff method is often easier to explain. Done properly, both methods arrive at the same answer.

A decision tree is solved from right to left by “rolling” it back. The expected value of each chance node closest to the terminal nodes is determined just as shown in the expected value table (Table 16.4). The chance node may now be replaced with its expected value and the tree to the right “trimmed” to simplify the presentation. This procedure is repeated with the next line of chance nodes, if any, until a decision node is reached. At this node the decision rule is to make the decision with the highest EMV. Note that the highest EMV may still be negative

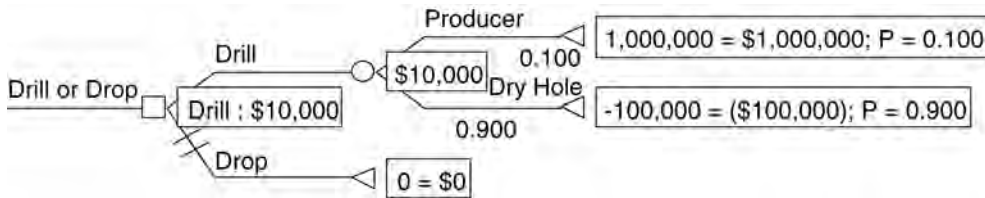


Fig. 16.7—Solved decision tree.

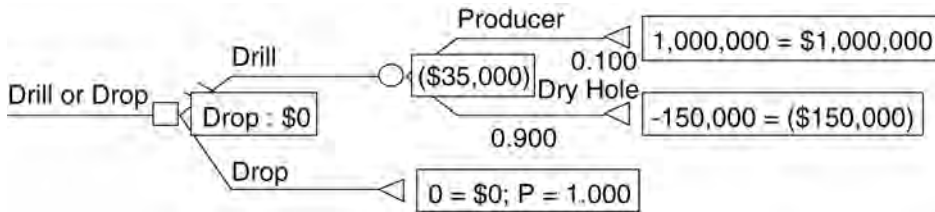


Fig. 16.8—Solved decision tree with dry-hole cost of \$150,000.

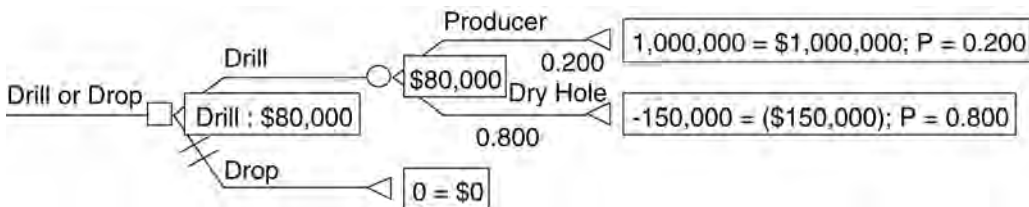


Fig. 16.9—Solved decision tree with dry-hole cost of \$150,000 and a probability of success of 20%.

but less negative than the alternatives. Again, the decision node can be replaced with the value of the highest EMV. The procedure is repeated until there is only one decision node remaining at the left side of the tree. The decision rule is to make the decision with the highest EMV.

The solved decision tree for the example is shown in Fig. 16.7. The chance node on the upper right, which had shown a 10% chance of a +\$1,000,000 outcome and a 90% chance of a -\$10,000 outcome has been replaced by the “certainty equivalent” of +\$10,000. (0.1 times +1,000,000 plus 0.9 times -100,000 equals +10,000.) Notice that the rejected decision alternative “drop” has two slashes through its branch. This is the traditional method of showing a rejected alternative. Once a decision tree has been solved, it is a simple matter to run sensitivity analyses. If we wish to evaluate the difference a \$150,000 dry hole cost has on our example, we could revise the terminal value for dry hole and resolve the decision tree. In that case, the expected value of the decision alternative drill is -\$35,000, and we should drop the lease without drilling. Fig. 16.8 shows the solved decision tree for that case. But what if the probability of success is really 20% with a \$150,000 dry-hole cost? Fig. 16.9 shows that the decision is now to drill with an EMV of \$80,000. This analysis can be continued as long as desired, and it is possible to plot sensitivities to any of the parameters.

Decision trees are quite useful for analyzing sequential decisions because all the possible courses of action can be laid out with probabilities and payoffs before the first decision is made. As the project proceeds, the tree can be modified to remove the decisions that have already been made and update the remaining decisions, probabilities, and payoffs. They can be as simple or as complex as desired and may even use Monte Carlo simulation to assign values

to the terminal points. Additional discussions can be found in Newendorp and Schulyer (Chap. 4), as well as many others.<sup>15,16</sup>

**16.6.4 Monte Carlo Simulation.** Monte Carlo Simulation is a calculation technique that uses distributions for uncertain input variables rather than single point estimates. It results in a distribution of potential outcomes with associated probabilities and has a number of advantages:

- The possibility to describe uncertainty in the input variables using distribution of possible values rather than a single average or most likely value.
- All of the parameters that are not known with certainty can be correctly modeled (limited by our ability to understand the distribution of the input values).
- It can be used to model any system or process that can be described with mathematical relationships.
  - The model can be very simple or extremely complex as necessary. With the current computer power available, it is possible to run very complex models in minutes or hours.
  - Any type of distribution can be used to describe a particular input variable.
  - It allows for the blending of the expertise of the entire company. Geologists can describe the uncertainty of geological parameters. Engineers can describe the uncertainty of engineering parameters.
  - The cost of doing a simulation model is typically small, especially in comparison to a pilot project.
  - The method lends itself to sensitivity analysis. It is easy to change one or more of the parameters and rerun the simulation.

There are also a number of pitfalls in Monte Carlo Simulation:

- It requires an attempt at quantifying uncertainty. Depending upon the corporate culture, it may be very difficult to accept that there is more than one possible answer.
- It requires expertise to build the computer model and debug it. This is true even with current available spreadsheet models.
- Like any computer calculation, it is subject to the garbage in/garbage out (GIGO) problem. If the input data distributions are wrong, the answers are almost sure to be wrong.
- There is a tendency to believe the answers because of the sophistication of the calculation technique.
  - It is sometimes difficult to convey the results of the simulation to management in a manner they can understand. Often, management is looking for *the* answer rather than a range of answers with associated probabilities of occurrence.

A Monte Carlo simulation study consists of the following steps:

1. Determine the objectives of the study. This is often a simple step with an answer such as “determine remaining reserves” or “determine whether or not to take this deal.” Occasionally, however, this can lead to intense discussions about the goals of the corporation and “what we are really about.” Normally, we try to use simulation to help make a decision. Keep the objective in mind as you design the study.
2. Determine the mathematical relationships between variables. Again, sometimes this can be very simple and sometimes the system being simulated can be extremely complex.
3. Separate variables that are known with certainty and variables that are subject to uncertainty. There is a real tendency to say, “We know so little about this variable that we can’t come up with a distribution, so let us just assume it is known.” An example might be a price forecast where there is so much uncertainty that we just use the current oil price and hold it constant. Of course, this is totally contrary to what we are trying to do. Important uncertain variables should always be simulated with a distribution. It is possible to simplify the problem and still get a valid result. At this stage, it would be appropriate to perform an analysis to see what variables have the greatest effect on the outcome. If a variable has little effect on the

outcome or decision, even if it is uncertain, then a cost-effective solution can be obtained by fixing the value of that variable and treating it as known.

4. Determine whether variables are independent or if partial (or full) dependencies or correlations exist. In some cases variables are independent of each other. For instance, in calculating volumetrics, the area of the trap almost never depends on the value of oil formation volume factor. However, the average water saturation often depends on the average porosity, and that relationship should probably be taken into account. A great deal of thought should be put into this stage of modeling. An example of dependencies between offshore gas fields is contained in the paper by van Elk *et al.*<sup>17</sup>

5. Choose distribution types and parameters for the independent variables. The types of distribution, which can be used in currently available simulation programs, are virtually unlimited. Examples include uniform distributions where any value of the input variable has the same chance of occurring as any other value, and triangular distributions where values close to the mode, or the most likely value, are much more likely to occur. Although the choice of the type of distribution may have a significant effect on the outcome, we often do not have sufficient data to discern a log-normal distribution from a triangular distribution with any degree of certainty. It is recommended that the distribution shape be chosen from theoretical considerations and the data we have used to determine parameters for that type of distribution.

6. Model total or partial dependencies. Dependencies and correlations can be modeled in a number of ways. One of the most popular methods uses the bounding envelope method, as described in Murtha,<sup>18</sup> and Newendorp and Schuyler (pages 436 through 457). This has the advantage of allowing the user to fully control the type of dependency at the expense of some programming effort. The other method uses the rank correlation coefficient available in commercially available software programs. (See Murtha, page 89.)

7. Perform the simulation. A number of software programs are available to perform the calculations. Some are add-ins to spreadsheet programs, and some are stand-alone programs. A simple example, shown later in this chapter, steps through the calculation method. Depending on the complexity of the problem and the effect of low probability events, it might be necessary to run as few as 1,000 passes or as many as 1,000,000 passes. Typically, 5,000 or 10,000 passes is sufficient.

8. Calculate the results and display the answers. The results are usually presented as tables and graphs such as histograms and cumulative frequency curves. Values of interest, such as the mean or expected value of the outcome, are reported. In economic evaluation, the user is also usually interested in the probability that the project will lose money or exceed a certain minimum rate-of-return, so these values are examined.

9. Perform a sensitivity analysis. Once the model has been set up and verified, it is relatively easy to alter some of the critical assumptions and see what effect that has on the outcomes. Assumptions can be examined in greater detail, especially assumptions that have the greatest effect and might cause a different decision to be made.

A simple example of the use of Monte Carlo simulation would be to use the hyperbolic decline equation to calculate remaining reserves. The equation is

$$\text{ERR} = \frac{q_i^n}{(1-n)D_i} (q_i^{1-n} - q_{el}^{1-n}) f \dots\dots\dots (16.10)$$

For the purposes of illustration, assume we have the deterministic or single-value estimates of the parameters:  $q_i = 100$  B/D,  $q_{el} = 5$  B/D,  $D_i = 0.6/\text{year}$ , and  $n = 0.3$ .

With these values the estimated remaining reserves (ERR) are calculated to be 76,231 bbl. However, if we do not know all the values with certainty, we can use Monte Carlo simulation to calculate the expected value for ERR, as well as a range of values and their associated prob-

Variable	Minimum	Most Likely	Maximum
$q_i$	90	100	110
$q_{ei}$	2	4	9
$D_i$	0.4	0.65	0.75
$n$	0	0.2	0.7

Name	Minimum Calculated or Sampled Value	Mean Calculated or Sampled Value	Maximum Calculated or Sampled Value	5% of Values are Less Than	5% of Values are Greater Than
ERR	44,131	79,088	183,078	57,027	111,288
$q_i$	90.11	100	109.88	93.16	106.83
$q_{ei}$	2.01	5	8.95	2.84	7.68
$D_i$	0.402	0.6	0.748	0.466	0.708
$n$	.00325	0.3	0.6974	.0836	0.5676

abilities. Let us assume that the uncertainty in all the values can be represented by triangular distributions and that the mean of the triangular distributions are the previously stated values. (The mean of a triangular distribution is the sum of the minimum, mode, and maximum values divided by three.) Let us also assume that the variables are independent; for instance,  $q_{ei}$  is not a function of  $q_i$ . An example set of distribution parameters is shown in [Table 16.5](#). When this set of distributions is run through a Monte Carlo Simulator 10,000 times, the results are shown in [Table 16.6](#).

There are several important results. Note first that the mean value of ERR from the Monte Carlo Simulation (79,088 bbl) is not the same as the deterministic value (76,231 bbl), even though the means for the inputs to the Monte Carlo simulation were the deterministic values. Also note that the value of ERR, using the “most likely” values for each variable (68,847 bbl), is also considerably different. These results occur because the nature of the equation for calculating ERR is complex; uncertain variables are raised to powers of other uncertain variables; and input distributions are not symmetrical.

The minimum and maximum values calculated for ERR are not particularly meaningful because they can vary considerably with the number of simulation passes. However, note that 90% of the values lie between 57,027 bbl and 111,288 bbl. This is a very wide range and gives an indication of the magnitude of uncertainty. [Table 16.7](#) contains the complete distribution of ERR as calculated in this simulation. If another set of calculations was run, the 0 and 100% numbers could change considerably, but the numbers near the center of the distribution would not change significantly. A second simulation run was made, as shown in [Table 16.7](#). In the “Pass 2” column, the median (50%) values vary by less than 0.2% and, in this case, even the 0 and 100% values do not change significantly from those in the “Pass 1” column.

If one were to decide to use the 10% value as the official value for remaining reserves, that value would be 59,903 bbl, which is 21% less than the value calculated deterministically. (The presentation of cumulative frequency shown here is a percentage less than presentation, which is quite common. If a percent greater than presentation is used, the table will show that 90% of the calculated values are greater than 59,903 bbl.) A graph of the data in the cumulative frequency table is shown in [Fig. 16.10](#).

Cumulative Frequency	Pass 1	Pass 2
	Estimated Remaining Reserves, bbl	Estimated Remaining Reserves, bbl
0%	44,131	44,071
5%	57,028	56,707
10%	59,903	59,874
15%	62,307	62,233
20%	64,444	64,451
25%	66,428	66,430
30%	68,387	68,280
35%	70,262	70,169
40%	71,963	72,064
45%	73,814	74,123
50%	75,978	76,110
55%	78,129	78,203
60%	80,441	80,407
65%	82,861	82,948
70%	85,671	85,802
75%	88,713	88,603
80%	92,162	92,066
85%	96,561	96,241
90%	102,550	102,143
95%	111,289	111,988
100%	183,078	184,589

Fig. 16.10 and its associated table are very common outputs from a Monte Carlo simulation. Another common output is a histogram in which the relative frequency of a particular range of outcomes is plotted, as shown in Fig. 16.11. The values plotted on the  $x$ -axis are the midpoints of the bars. The most common result of the calculation is a value between 75,000 and 85,000 bbl, which occurs about 26% of the time.

The sensitivity of the results to the various input parameters is often presented in one form of a “Tornado” diagram, such as Fig. 16.12. In these diagrams, the input parameter with the largest regression correlation coefficient is plotted at the top of the figure, and the other input parameters are plotted at the bottom in descending order; thus, resulting in a tornado shape. This same information can also be presented in tabular form, as shown in Table 16.8.

The regression correlation coefficient, reported by the commonly available Monte Carlo simulation software, is simply the square root of the  $r^2$  value from a linear fit of ERR to each of the input variables. In Table 16.8,  $n$  has a correlation coefficient of +0.73. The positive correlation coefficient means as  $n$  increases, ERR increases. The square of the correlation coefficient (0.53) means that 53 percent of the variability of ERR can be explained by the variation in  $n$ . Fig. 16.13 is a crossplot of ERR and  $n$ . The linear least squares fit of the data has an  $r^2$  of 0.53, which results in an  $r$  of 0.73, as shown in Fig. 16.12 and Table 16.8. Similarly,  $D_i$  has a large effect on ERR, as shown in Table 16.8. However, because the correlation coefficient is negative, increases in  $D_i$  result in decreases in ERR. The estimate of  $q_{el}$  has little effect on the remaining reserves for this example. Only 2% ( $-0.146^2$ ) of the variability in ERR is explained by the variability in  $q_{el}$ .

**16.6.5 Interpretation of Results.** One of the more important numbers is the mean or expected value of the distribution. We can make a decision with this number alone, just as we have done with EMV and decision trees. However, much more information is available, such as the probability of the project losing money (assuming EMV was calculated in the simulation) and the chances of the project making a large amount of money. Ideally, the entire cumulative fre-

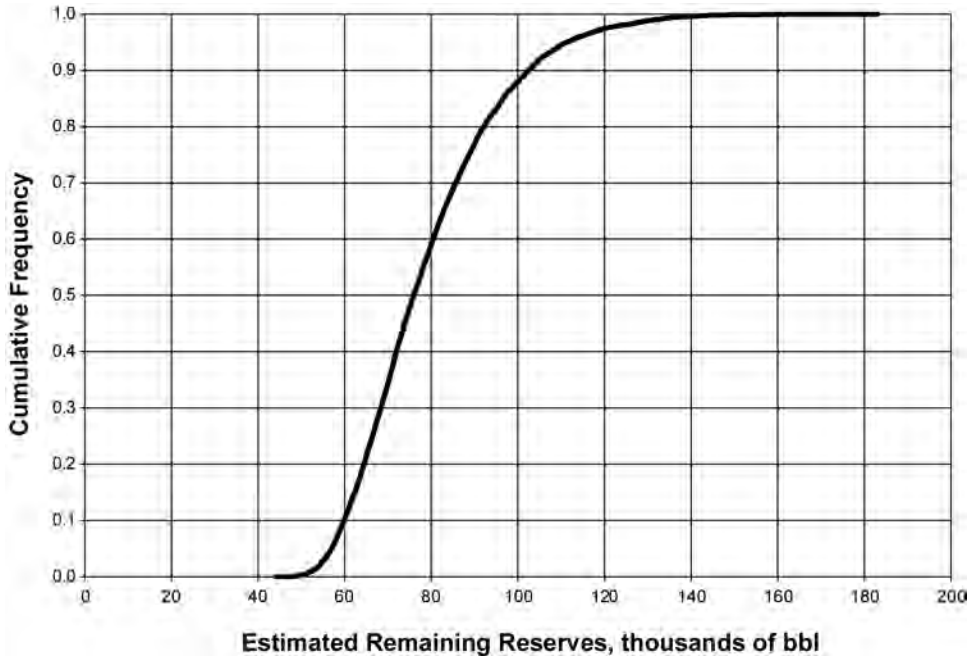


Fig. 16.10—Cumulative frequency of example estimated recoverable reserves.

quency graph should be presented and compared with other projects, so the decision maker can see the full spectrum of anticipated possibilities.

**16.6.6 Further Reading.** There are a number of good references on Monte Carlo simulation, including a paper by Murtha<sup>19</sup> and the text by Newendorp and Schuyler (Chap. 8). Another excellent reference is Chap. 10 on Risk Analysis and Decision Making in Vol. VI, *Emerging and Peripheral Technologies*.

## 16.7 The Next Frontier

There are two methods of advanced decision analysis that are slowly making their way into the petroleum project evaluation process. One of these is known as portfolio analysis, and the other is the real options analysis. The portfolio analysis quantifies the effect of interactions between projects, and the real options analysis attempts to value the fact that a company has several options in developing projects, such as the ability to abandon a project early or defer a decision to make an investment until the financial climate is more beneficial.

**16.7.1 Portfolio Analysis.** Portfolio analysis is based on the Nobel Prize-winning work of Harry Markowitz in the early 1950s<sup>20,21</sup> in which he showed that the variance in results from a portfolio of stocks could be reduced by choosing stocks with a negative correlation. If two stocks are correlated negatively, when one stock is down the other stock will be up, and the portfolio will grow with very few wild swings. This concept has been introduced into the petroleum literature by several authors<sup>22–30</sup> with some modifications. The following paragraphs from Brashear, Becker, and Faulder<sup>23</sup> give an overview of the methodology. (Superscripts denoting the references have been added by the current author.)

Harry Markowitz (1957)<sup>21</sup> demonstrated in the stock market that risk and return are usually correlated. Achieving higher yields generally necessitates taking greater risks. Further, he pointed out the risk-reducing effects



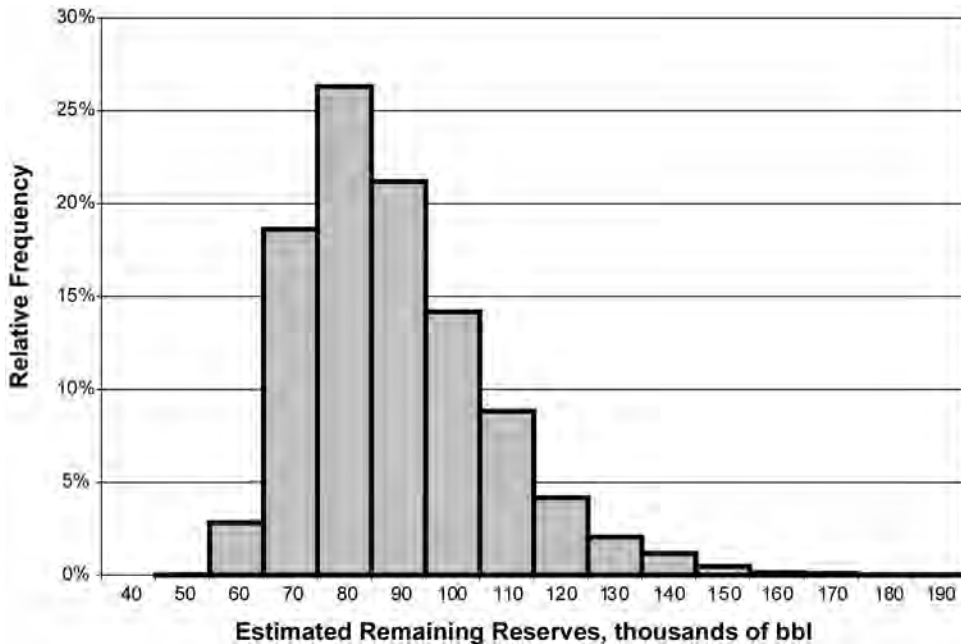


Fig. 16.11—Histogram of example estimated recoverable reserves.

of diversification were reduced if multiple investments are positively correlated but amplified if the investments are negatively correlated. He posited that a rational investor would seek the mix of investments (portfolios) for which no other combination would have a higher return without increased risk or lower risk without loss of return. He coined the phrase “efficient frontier” for the set of portfolios that meets these conditions. The choice of a single portfolio along this frontier depends on the decision-maker’s tolerance for risk.

David Hertz (1968)<sup>25</sup> extended these concepts from investments in financial assets to investments in “real” assets. An efficient frontier could be composed of capital projects that reflected both economic value and risk (measured by standard deviation). Newendorp<sup>26</sup> recognized Hertz’s work and speculated about a 2D display (expected value and expected loss) to illuminate individual project selections but did not propose a full portfolio optimization approach. Ball (1983)<sup>27</sup> applied Hertz’s insights specifically to the upstream oil business. This idea was later proposed also by Hightower and David (1991)<sup>28</sup> and Edwards and Hewitt (1993)<sup>29</sup> and updated by Howell *et al.* (1998),<sup>24</sup> Ball and Savage (1999)<sup>30</sup> and Brashear *et al.* (1999).<sup>31–33</sup>

While these conceptual advances were being made, increases in the speed of commonly available computers and the efficiency of the required solution algorithms have made the approach practical at field, division, and corporate levels.

The method is conceptually simple but computationally complex. The algorithm is a mathematical programming solution that evaluates all combinations of investments that yield a specific “target” expected value to define the one combination (portfolio) with the lowest risk at a given capital constraint. Other constraints can be added. The process is repeated for all other specific target values, each time finding the specific portfolio with the lowest risk. The locus of the minimum-risk points, the efficient frontier, is the set of all portfolios that satisfies the criterion that no increase in value is possible (given the constraints) without greater risk and no reduction in risk is possible without loss in value. Other algorithms find the maximum value at each risk level; either way the result is the same.

Fig. 16.14 is an example of the results of a portfolio analysis presented as a graph of reward vs. risk showing the efficient frontier. In some references, the axes are reversed. Reward is often represented by expected monetary value (EMV), while risk has several possible defini-

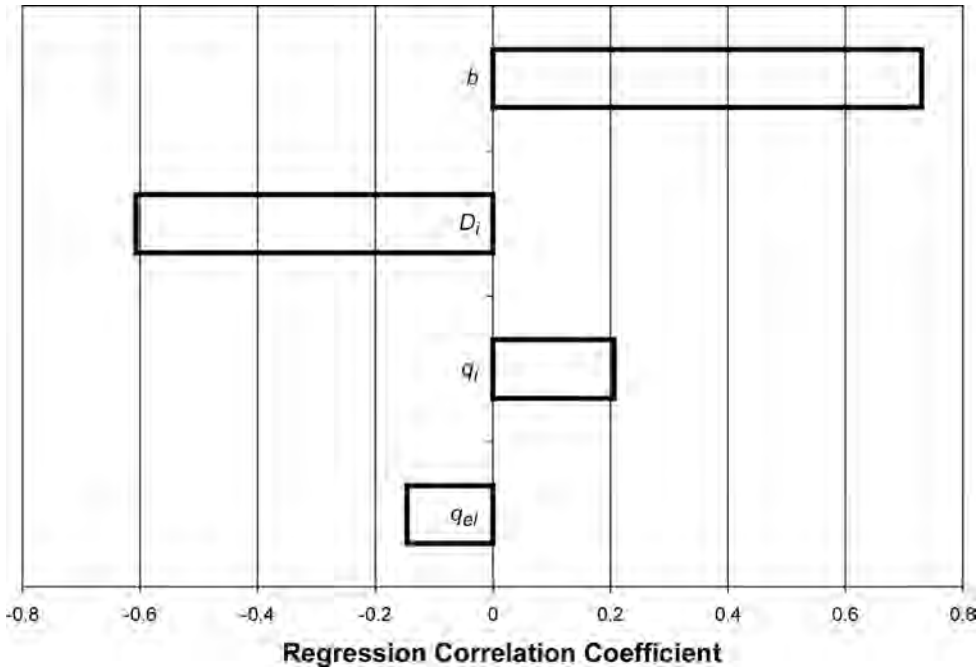


Fig. 16.12—Tornado diagram for estimated recoverable reserves.

Variable	Correlation Coefficient $r$
$n$	0.730
$D_i$	-0.607
$q_i$	0.206
$q_{ei}$	-0.146

tions. Markowitz used variance of the expected portfolio return as a metric for risk (or its square root, standard deviation). The petroleum industry is more concerned about downside risk, so oftentimes, semistandard deviation (the downside) or mean loss is used as a measure of risk. Whatever the metrics, the objective is to select a portfolio of projects that maximizes reward for an acceptable level of risk. A quantitative example is used to demonstrate the methodology.

**Table 16.9** contains the parameters for estimated distributions of net present value (NPV) for nine different projects (labeled A through I), along with the present value cost of each project and the ratio of EMV to investment. Net present value is the result of one possible outcome, while EMV is the expected value or average of all of the possible outcomes. In this example, the NPV is assumed to be normally distributed for each project. Using the ranking criterion from [Sec. 16.6.2](#), the projects are ranked in order of decreasing EMV to investment ratio and chosen until the budget is exhausted. For a budget of \$2,500 (which applies throughout the examples that follow), the project mix is I, D, G, and H, which results in an expected value of \$1,591. Correlation between the projects, such as those caused by oil price, rig rates,

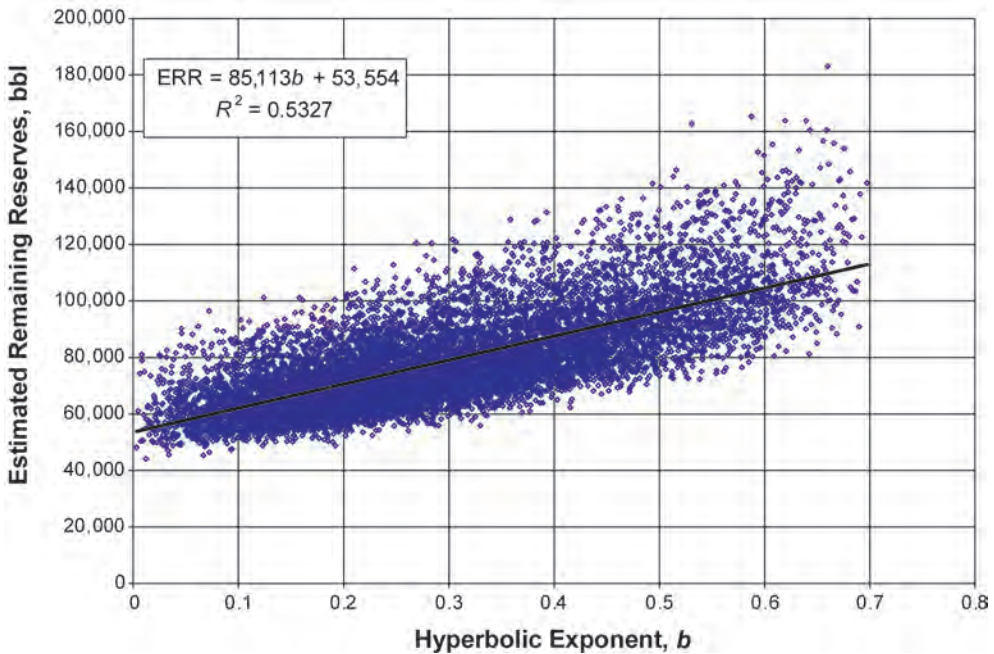


Fig. 16.13—Correlation of estimated recoverable reserves (ERR) with hyperbolic exponent, *b*.

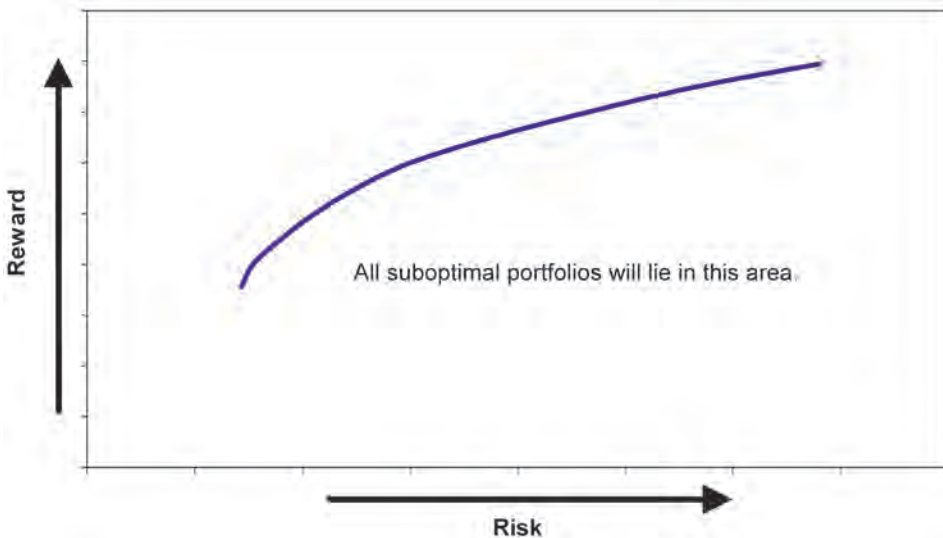


Fig. 16.14—Reward vs. risk diagram showing the efficient frontier.

geological concepts, or pipeline constraints, is ignored with this ranking method. Later in this section, correlations are included. While this portfolio has the highest EMV, it also has the highest risk, whether risk is defined as variance or as mean loss. For the purposes of illustration, the projects are assumed to be positively correlated, as shown in [Table 16.10](#). If risk is defined as variance or standard deviation, an analytical solution can be used to calculate the variance of the correlated projects.<sup>29</sup> When the efficient frontier is calculated with the methods

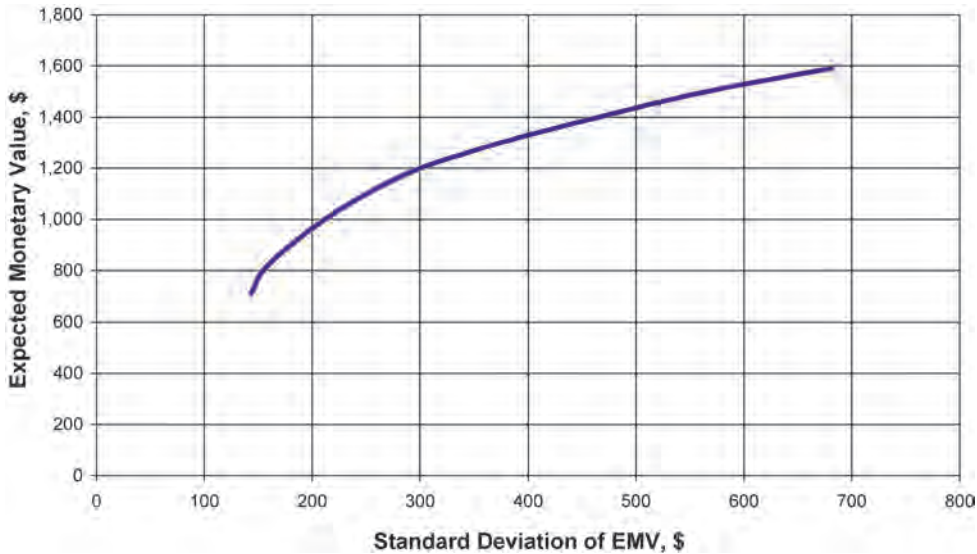


Fig. 16.15—Efficient frontier for example projects with standard deviation as risk for a \$2,500 budget.

shown by Winston,<sup>34</sup> the result is as shown in Fig. 16.15. The standard deviation of the expected returns can be reduced from \$681 to \$300, if the decision maker is willing to accept a reduction in expected results from \$1,591 to \$1,200. This might be a good trade because the company can still capture 75% ( $1,200/1,591$ ) of the expected value while reducing its exposure to variance by 56% ( $381/681$ ). Deviations about the mean for net present value at various levels of risk (defined as standard deviation about EMV) are shown in Fig. 16.16. There is about a 16% chance ( $-1$  standard deviation) that the NPV will be less than approximately \$900 for risk levels from \$300 to \$681. Notice that the less risky portfolios are very unlikely ( $<2.3\%$ ) to return less than about \$575 ( $-2$  standard deviations), while the most aggressive portfolio could return less than \$228. Of course, there is a corresponding decrease in the potential upside if a more conservative portfolio is chosen.

The optimal portfolio for each point on the efficient frontier can be calculated. Fig. 16.17 graphically illustrates the project mix for several points on the efficient frontier. At an expected value of \$1,200 (standard deviation of \$300), the project mix is 7% of A, 100% of D, 77.7% of E, 100% of F, 15.3% of G, and 100% of I. Project H, selected using EMV/investment, is not selected at all, while 100% of F was taken in which only two projects were ranked lower using EMV/investment. This is because F is almost a sure thing with a standard deviation of 22 about a mean of 147, while the return on H is quite uncertain with a standard deviation that exceeds its expected value.

This analysis assumes that a continuous range of interests from 0 to 100% is available in each project. For those instances in which the available interests are available only in increments such as 15, 25, 35, 50, 75, or 100%, the same methodology can be applied. However, the resulting efficient frontier will be jagged and discontinuous.

The effect of correlation between the projects is shown in Fig. 16.18. The highest EMV is independent of the correlation between the projects, but the variance (or standard deviation) for a given NPV is quite dependent on the correlation. If all projects are perfectly correlated ( $+1$ ), the standard deviation of the NPV at maximum EMV is \$950. If the projects are totally independent of each other (unlikely in the oil industry because of price, if nothing else), the standard deviation of NPV at maximum EMV is \$519. If the projects are all negatively correlated with correlation coefficients of  $-0.1$ , the standard deviation of NPV at maximum EMV is

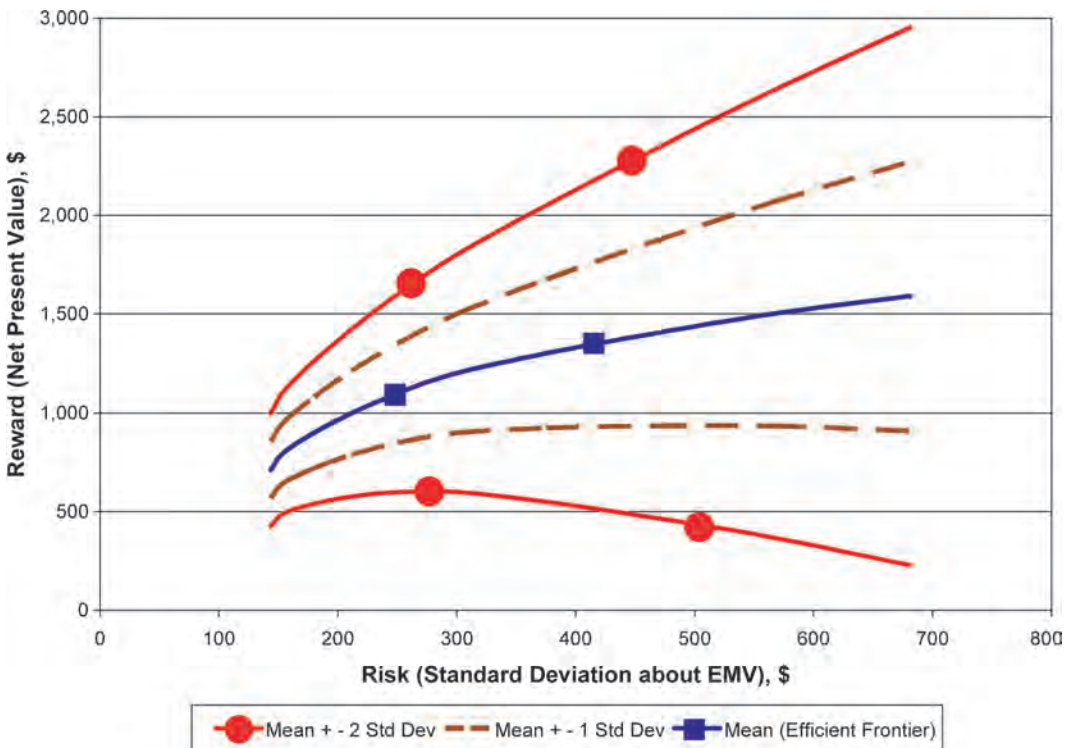


Fig. 16.16—Ranges of net present value for various levels of risk and a \$2,500 budget.

Project	Invest	EMV @ 10%	Std. Dev. of EMV	EMV @ 10%/ Invest
A	1,000	273	88	0.27
B	500	236	218	0.47
C	1,000	233	131	0.23
D	500	344	153	0.69
E	1,000	293	87	0.29
F	500	147	22	0.29
G	1,000	606	393	0.61
H	500	271	273	0.54
I	500	371	131	0.74

reduced to \$454. This illustrates the power of finding projects that are not correlated with each other or that have a negative correlation.

If the metric of risk is mean loss rather than variance, the calculations become more tedious. Ball and Savage<sup>30</sup> discuss the methodology and give an Internet link to a spreadsheet with a sample calculation. When their methodology is applied to the example (with the example correlation matrix), the results are as shown in Fig. 16.19. Again, the portfolio with the maximum EMV of \$1,591 has the highest risk. In this case, however, the decision maker can reduce the risk from \$277 to \$48 (83% reduction) with only a 25% reduction in EMV. The project selection, using mean loss as a metric of risk, is somewhat different. Now, we would

TABLE 16.10—CORRELATION COEFFICIENT MATRIX FOR EXAMPLE PROJECTS										
		Project								
		A	B	C	D	E	F	G	H	I
Project	A	1	0.46	0.50	0.44	0.17	0.22	0.19	0.44	0.31
	B	0.46	1	0.37	0.15	0.49	0.48	0.29	0.19	0.33
	C	0.50	0.37	1	0.36	0.20	0.47	0.48	0.49	0.17
	D	0.44	0.15	0.36	1	0.48	0.17	0.37	0.30	0.19
	E	0.17	0.49	0.20	0.48	1	0.34	0.18	0.26	0.19
	F	0.22	0.48	0.47	0.17	0.34	1	0.39	0.36	0.15
	G	0.19	0.29	0.48	0.37	0.18	0.39	1	0.22	0.37
	H	0.44	0.19	0.49	0.30	0.26	0.36	0.22	1	0.45
	I	0.31	0.33	0.17	0.19	0.19	0.15	0.37	0.45	1

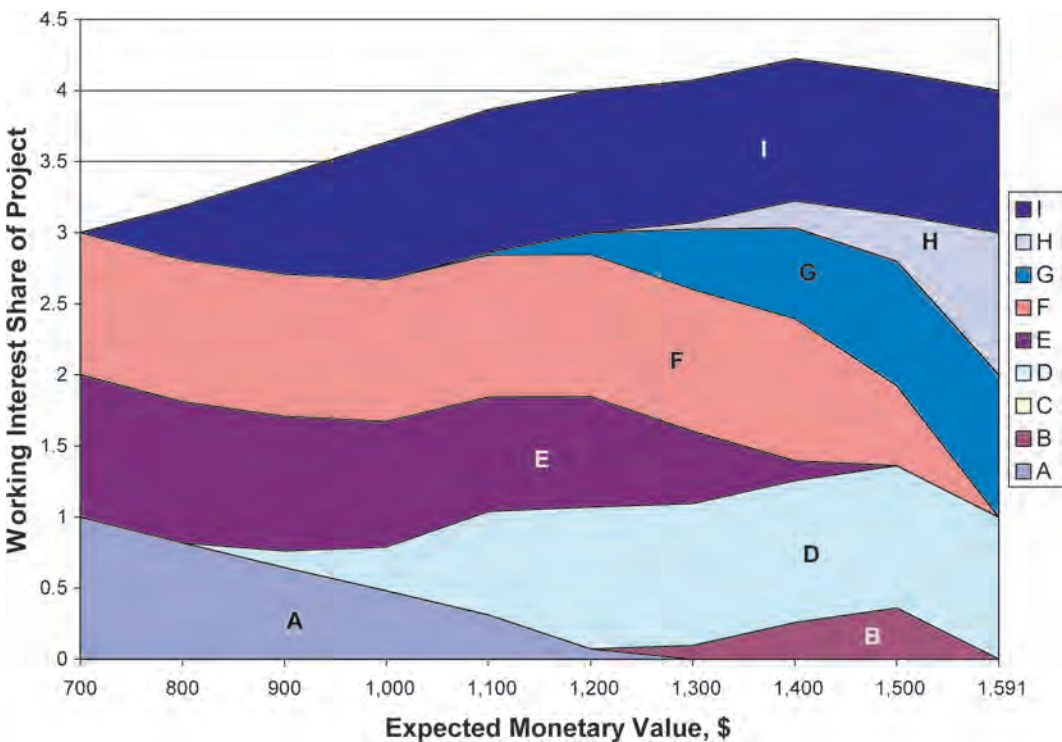


Fig. 16.17—Project mix on the efficient frontier using the example correlation matrix and a \$2,500 budget showing the working interest invested in Project A, Project B, etc. at each value of expected monetary value.

select 100% of D, 85% of E, 100% of F, 15% of G, and 100% of I. Metrics other than EMV can be managed as shown by Howell *et al.* They give an example of a “generic” E&P portfolio in which the metrics include earnings, production, net cash flow, and reserves.

A portfolio analysis has considerable value, but it is not easy to implement. Not only do we have to establish parameters describing the uncertainty on a project-by-project basis, we also have to determine the correlations between the various projects, which requires considerable skill. On a positive note, the computer capabilities currently available can certainly solve

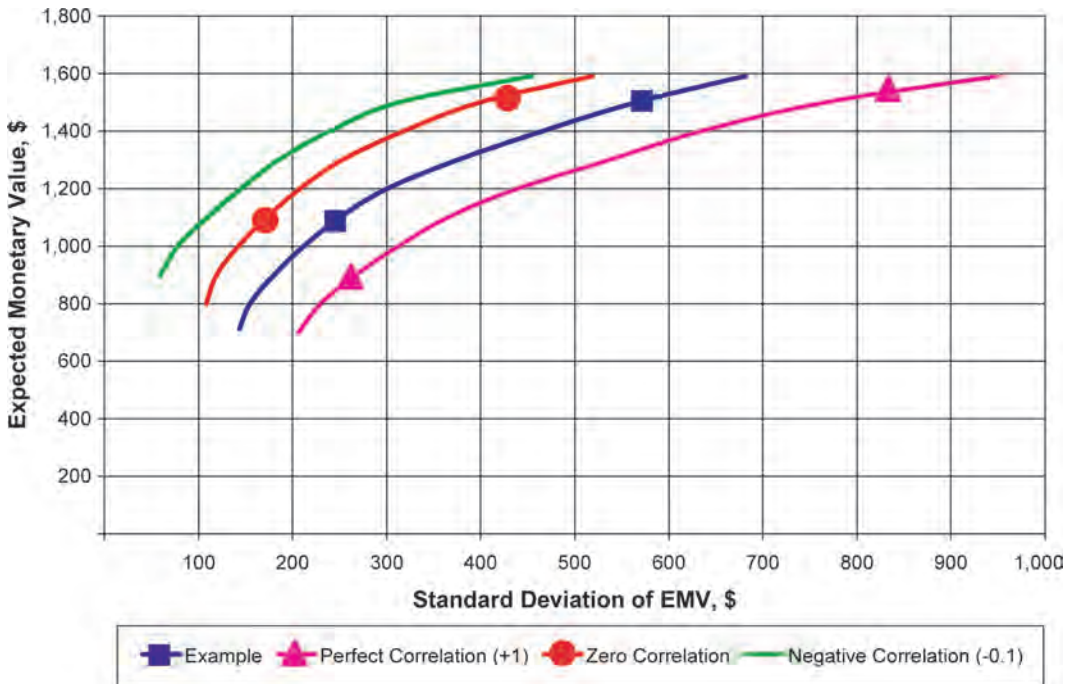


Fig. 16.18—The effect of different correlation matrices on the efficient frontier and a \$2,500 budget.

the problems once they are formulated. As more decision makers become educated in the methods, it is expected that portfolio analysis will become more common.

**16.7.2 Real Options.** In the last quarter-century, financial options such as “calls” and “puts” on publicly traded stocks have become an integral part of managing stock portfolios. The seminal work on financial options was done by Black and Scholes,<sup>35</sup> published in 1973, and Merton,<sup>36</sup> also published in 1973. Merton and Scholes shared the 1997 Nobel Prize in economics for their work. Black, Scholes, and Merton all worked on attempting to determine the value of an option. In recent years, the concepts of valuing options have been expanded from financial options to what are called “real” options in project evaluation.

Financial options include “calls” in which the owner of the option has the right, but not the obligation (thus, an option), to purchase a stock at a specified strike price. If the option can only be exercised at the end of a specified period of time, the option is referred to as a European option. If the owner of the option can exercise the option at any time up to the expiration date, the option is referred to as an American option. A financial put option is the right, but not the obligation, to sell a stock at a specified strike price. Again, there can be European put options that are exercisable only on a specific date or American put options that can be exercised anytime prior to the expiration date.

The proponents of real options valuation (ROV) or real options analysis (ROA) argue, for example, that “option pricing methods are superior to traditional DCF (discounted cash flow) approaches because they explicitly capture the value of flexibility.”<sup>37</sup> Copeland and Antikarov<sup>38</sup> even go so far as to assert, “...the net present value technique systematically undervalues everything because it fails to capture the value of flexibility.” There is a certain amount of irony in comparing the assertions of ROV proponents in which traditional methods undervalue everything with the assertions of portfolio analysis proponents in which “conventional treatments of

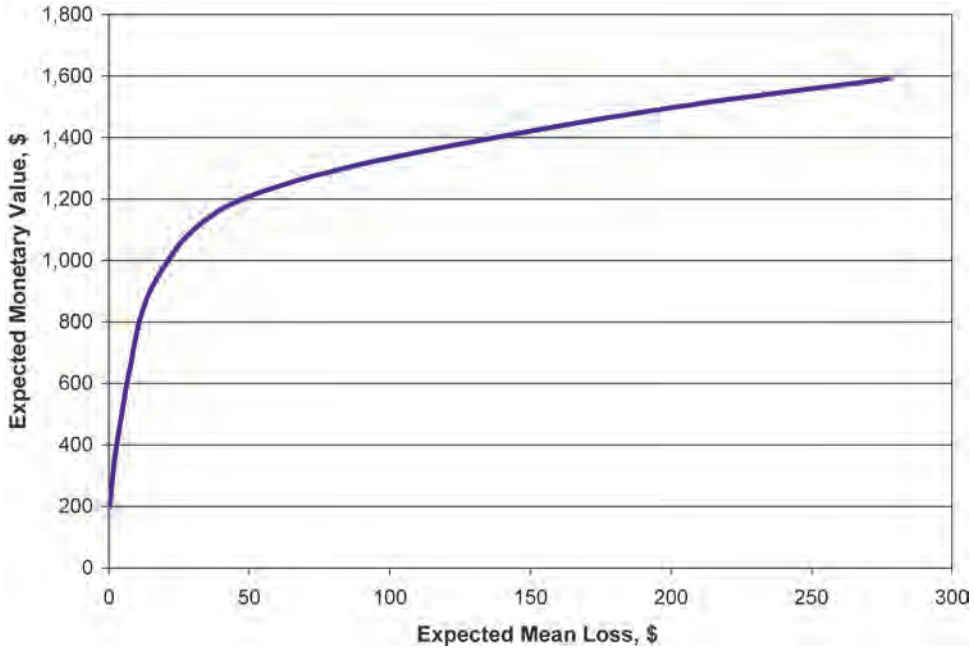


Fig. 16.19—The efficient frontier in which risk is defined as expected mean loss (\$2,500 budget).

uncertainty contribute to overestimation of returns...” (See Brashear, Becker, and Faulder,<sup>23</sup> page 21.)

There are many types of real options that can be modeled as calls and/or puts or combinations thereof. In the oil/gas production business, the option to develop a field is similar to a call option. The producer has the option to invest the development costs and receive the value of the reserves. An example of a put option is the case in which the producer has the ability to abandon or sell the property. A property sale differs from a stock put in that the price of the sale might be unknown, while the exercise price of a stock put is usually known with certainty. There are a number of other types of real options. Trigeorgis<sup>39</sup> lists several types of real options including the option to defer investment; the option to default during staged construction; the option to expand; the option to contract; the option to shut down and restart operations; the option to abandon for salvage value; the option to switch use; and the corporate growth option. Copeland, Koller, and Murrin (pages 400 through 402) list similar real options along with compound options, which are options on options, and “rainbow” options in which there are multiple sources of uncertainty. As they state, the exploration and development of natural resources is an example of a compound rainbow option. All of these various types of options can be valued if several parameters are known. The simplest place to begin is with a call option.

The most famous equation in option valuation is the Black-Scholes equation for a European call option. The following equations use the algebraic symbols of Black and Scholes rather than the more modern symbols.

$$w(x, t) = xN(d_1) - ce^{r(t-t^*)}N(d_2), \dots\dots\dots (16.11)$$

where  $N(d)$  is the cumulative normal density function and



$$d_1 = \frac{\ln(x/c) + \left(r + \frac{v^2}{2}\right)(t^* - t)}{v\sqrt{t^* - t}}, \dots\dots\dots (16.12)$$

and

$$d_2 = \frac{\ln(x/c) + \left(r - \frac{v^2}{2}\right)(t^* - t)}{v\sqrt{t^* - t}}. \dots\dots\dots (16.13)$$

In Eq. 16.11,  $w(x,t)$  is the value (at any time,  $t$ ) of the call option on a stock with a current price of  $x$ . The strike or exercise price is  $c$ ; the risk-free interest rate is  $r$ ; the maturity date is  $t^*$ ; and  $v^2$  is the variance rate of the return on the stock. The variance is one of the most important and interesting parts of the equation. Black and Scholes assume, among other things, that “the distribution of possible stock prices at the end of any finite interval is log-normal” and that the stock price on any day is independent of the price on the previous day. This assumption of a “random-walk” in stock price is premised on the existence of an efficient market in which the stock is fairly valued on any given day, and all the information available concerning the stock has been taken into account by the market.

While the Black-Scholes formula revolutionized the financial markets, it has had little direct application in the oil/gas business because the assumptions used in its development are not particularly appropriate for oil/gas properties. As Davis\* explains, “real options are different from financial options because the exercise price (in both calls and puts) is not known with certainty; exercise is not instantaneous; and the stochastic process for the underlying asset is not the same as it is for financial options. All of these aspects make the calculation of real option value considerably more complicated than calculating the value of a financial option.”

Lohrenz and Dickens<sup>40</sup> present a real-world oil/gas example using the Black Scholes formula in their comparison of option theory and discounted cash flow methods for an actual field in the offshore Gulf of Mexico. They discuss many options that are available during the “lifetimes of searchable, developable, and producible oil/gas assets.” In their analysis, they showed that the value of the development option (like a call option on a stock) increased dramatically (by a factor of greater than 3) as the variance in the oil/gas asset value increased from zero (perfect knowledge) to 1.0/year. They end their paper with the warning “...we should always temper results from uncertainty analyses [both option theory and decision trees] and their use with the understanding that the real world and its real uncertainties have not been captured—only modeled by necessarily flawed and incomplete practice and practitioners.” Another good example of the Black-Scholes model is presented by Copeland and Antikarov<sup>38</sup> (pages 106 through 110).

The mathematics and application of real options can quickly become very complex. The value of the asset underlying the option is assumed to vary in time in a stochastic manner. That means at least part of the price varies in a random and unpredictable fashion. Dixit and Pindyck<sup>41</sup> discuss several potential mathematical models for the price of the asset beginning on page 59 of their book. The most common of these in financial options is the Wiener or Brownian motion process. In this process, the change in value from one period to the next is assumed to follow a normal or log-normal distribution. (The standard assumption for stock prices is that the change in price over time is log-normally distributed.) This process is one of the underlying assumptions in the Black-Scholes model. As Dixit and Pindyck point out, the process has

---

\* Personal communication with Graham Davis, Colorado School of Mines, Golden, Colorado (2002).

some interesting properties—one being that all future values depend only on the current value and not on any historical value. In other words, there is no memory of past prices. One consequence of the assumptions in a Wiener process, as stated in Dixit and Pindyck (page 65), is that “the variance of the change in a Wiener process grows linearly with the time horizon” and that “over the long run its variance will go to infinity.” This is problematical when applying this process to the value of oil/gas properties. There is certainly an upper limit to the value of an oil/gas property no matter what the time frame. Those who lived through the “boom” in the late 1970s will remember the commonly accepted forecasts showing average annual oil prices of \$100/barrel or more before the end of the 21<sup>st</sup> century.

Dixit and Pindyck discuss a number of other potential mathematical models including “Brownian motion with drift” (a process with an increasing or decreasing trend and randomness superimposed), “mean-reverting processes,” and jump processes (sometimes called Poisson processes). When these processes are applied to value-an-option on an underlying asset of a second-order partial differential equation results. These equations, just like the diffusivity equation common in fluid flow in porous media, only have analytical solutions for certain simple boundary conditions (such as those used by Black and Scholes). The equations can be solved by a number of techniques including finite difference techniques, as those discussed by Trigeorgis (pages 305 through 320) or by a “binomial lattice” technique, as discussed by Copeland and Antikarov in Chap. 7 of their book where they present a spreadsheet model for a binomial lattice. Winston<sup>42,43</sup> presents a number of examples of valuing options using the Black-Scholes method and simulation. Winston's book contains a CD with spreadsheets for all examples. Trigeorgis (pages 320 through 329) presents a log-transformed binomial lattice approach and gives references to other approaches from polynomial approximation to numerical integration. Pickles and Smith<sup>44</sup> also discuss the binomial lattice method and present a numerical example for producing oil/gas properties.

Paddock, Siegel, and Smith<sup>45</sup> applied real option valuation techniques to 21 tracts in the federal lease sale number 62, held in 1980. This study is also used as an example for oil/gas in the text by Dixit and Pindyck (pages 396 through 403) and is cited by Trigeorgis as “the first empirical evidence that option values are better than DCF-based bids in valuing offshore oil leases.”

Valuing a developed reserve, even at a particular time, is quite difficult. Paddock, Siegel, and Smith used the work of Gruy, Garb, and Wood<sup>46</sup> to estimate developed reserve prices as one-third of crude oil prices. In practice, the value of developed reserves is highly dependent on the perceptions of future prices, as well as the level of operating costs and the fiscal terms. Johnston<sup>47</sup> (pages 13 and 14) estimates that “proved, developed, producing reserves are worth from one-half to two-thirds of the wellhead price times the contractor’s take.” The United States has a contractor’s take of about 50%, so producing reserves (in this case, working interest reserves) would be worth about one-fourth to one-third of the wellhead price using Johnston’s rule of thumb. If contractor’s take is lower, such as the approximately 10% contractor’s take in Venezuela, then, obviously, the working interest reserves would be worth much less. Data on actual transactions, as reported by Cornerstone Ventures, L.P.<sup>48</sup> for the period of 1991 through 1998, indicate that the median price of U.S. proved developed producing reserves, in the ground and net of royalty, during that time period ranged from \$4.08/bbl to \$5.26/bbl, while the yearly average spot price of oil (WTI) ranged from \$14.37/bbl to \$22.20/bbl. **Table 16.11**, from the Cornerstone “Annual Reserves Report,” shows the annual averages for WTI and the median price for oil-dominated transactions from 1991 to 1998. The ratio of the median price to the WTI price ranges from 19 to 28% with an average of about 25%. Paddock, Siegel, and Smith calculate a standard deviation for the “real (CPI deflated) refiner cost of imported crude oil” of 0.142/year. They then assumed that this standard deviation would apply to the change in value of the underlying asset (reserves in the ground). An analysis of

**TABLE 16.11—DATA ON OIL-DOMINATED TRANSACTIONS IN THE U.S.  
FROM 1991 THROUGH 1998**

Transaction Data for Oil-Dominated Transactions		
Year	Median \$/BOE for Acquisitions	WTI \$/bbl Average
1991	5.26	21.54
1992	4.36	20.58
1993	4.08	18.42
1994	3.88	17.19
1995	4.43	18.42
1996	4.20	22.20
1997	5.07	20.56
1998	4.09	14.37

Source: Cornerstone "Annual Reserves Report" (see Ref. 48).

the Cornerstone figures indicates that, for the period of 1991 through 1998, the standard deviation of the change in median acquisition price is 0.15/year on either a nominal basis or on a CPI adjusted basis. This is in remarkable agreement with that calculated by Paddock, Siegel, and Smith covering the period of 1974 through 1980. Pickles and Smith calculated a standard deviation of 0.22/year for the period of 1985 through 1989 based on quarterly median reserve prices as reported by Strevig and Associates, the predecessor to Cornerstone Ventures. These values for standard deviation would appear to be in good agreement, but one of the underlying assumptions is that property prices follow a Wiener or Brownian motion process.

One of the more disconcerting aspects of this assumption is the discussion of the underlying process for oil prices as discussed by Dixit and Pindyck (pages 403 through 405). They discuss a "unit root test" to determine "whether a price series is mean reverting or is a random walk." In their words, "this is a weak test that for short time series (for example, 30 years or less) will often fail to reject the hypothesis of a random walk, even if the series is in fact mean reverting." Considering the different processes underlying the price of oil/gas such as the Texas Railroad Commission in the 1950s and 1960s, the rise of OPEC's power in the 1970s, the Federal Power Commission's regulation of natural gas prices—all overlying the fundamental supply and demand relationship, it is difficult to imagine a meaningful process lasting much longer than 30 years. Dixit and Pindyck report that Wey\* used a 100-year series for the real price of crude oil and found that oil prices are mean reverting and not a random walk. They report that Wey shows "ignoring mean reversion can lead one to undervalue the reserve by 40 percent or more" when the development cost in \$/bbl is one-half the mean developed reserve price, while it will have little effect when the development cost is close to the developed reserve price.

Chorn and Carr<sup>49</sup> discuss option pricing principles and then apply those principles to the purchase of information. Their advice is to "purchase information that will impact the upcoming decisions, if the value increase justifies the cost of the information. Secondly, adhere rigorously to the converse, i.e., invest now or abandon the project if there is no information to be gained (or it's [sic] expense is too great) that will significantly change the project's outcome or impact the investment decision process." This is sound advice with or without real option analysis, but they show how real options can be used to value that information—a value which is often difficult to quantify.

Davidson<sup>50</sup> presented an excellent paper on benefits and difficulties with real options. He states that "the primary contribution of ROA is to produce a frame shift. Instead of thinking

\* Wey, L.: "Effects of Mean-Reversion on the Valuation of Offshore Oil Reserves and Optimal Investment Rules," unpublished undergraduate thesis, MIT, Cambridge, Massachusetts (May 1993).

about a project from a do-it or don't-do-it frame, ROA promotes thinking from a what-are-all-the-possibilities frame. The frame shift leads to a richer assessment of the opportunity.” He criticizes the approach by stating that “the ROA valuation methodology is not only inaccurate for E&P projects, it is needlessly complicated. The methodology leads to procedures and presentations that can inhibit insightful discussions for key assumptions and choices.” He then presents a method of getting the benefits of both real options analysis and present value analysis. Hooper and Rutherford<sup>51</sup> also discuss the benefits of real options in framing the problem and the questions.

Real options analysis is slowly working its way into the E&P business. The mathematics are daunting; the terminology is foreign; the underlying assumptions are shaky; and communicating the results in an easily understood manner is difficult, but the method does show promise. The breach between the theoreticians and the practitioners in the E&P business needs to be bridged. This breach is well illustrated by the following quote from Copeland and Antikarov's practitioner's guide<sup>38</sup> (page 164) in which they discuss compound options. “Exploration and development for natural resources (oil, natural gas, gold, copper, and coal) have multiple phases. Oil, for example, has sonic testing [sic] (2D and 3D), drilling, and development via construction of refineries [sic], pipelines, and storage facilities.” On the other hand, the frame shift mentioned by Davidson and Hooper and Rutherford is a real benefit. It remains to be seen how widely the process will be applied. In his book, Trigeorgis (page 375) lists ten points of future research. The first two (listed next) are very relevant.

- Analyzing more actual case applications and tackling real-life implementation issues and problems in more practical detail.

- Developing generic options-based user-friendly software packages with simulation capabilities that can handle multiple real options as a practical aid to corporate planners.

If these points are done, along with educating the managers, real options could become a useful tool.

## Nomenclature

$A$	= constant periodic payment
$b$	= hyperbolic exponent
$c$	= strike or exercise price
$d_1, d_2$	= intermediate variables
$D_i$	= initial decline rate, 1/year
$e$	= the base of natural logarithms, 2.718...
$f$	= factor to cause the time units to cancel, 365 days/year
$F$	= future lump sum of money
$i$	= the periodic interest rate
$n$	= the number of periods for interest calculations or the hyperbolic exponent for decline curve equations
$N(d)$	= cumulative normal density function
$P$	= present lump sum of money
$q_{el}$	= rate at the economic limit, B/D [ $\text{m}^3/\text{d}$ ]
$q_i$	= initial rate, B/D [ $\text{m}^3/\text{d}$ ]
$r$	= risk free interest rate
$R^2$	= the square of the sample correlation coefficient
$t^*$	= maturity date
$t$	= time
$\nu^2$	= variance rate of the return on the stock
$w(x, t)$	= value of a European call option at any time, $t$
$x$	= current price of the stock

## Subscripts

$m$  = monthly (when applied to the interest rate,  $i$ )

## References

1. Thompson, R.S. and Wright, J.D.: *Oil Property Evaluation*, Thompson-Wright Associates, Golden, Colorado (1985).
2. "Light Sweet Crude Oil," NYMEX, [www.nymex.com](http://www.nymex.com).
3. Olds, D.R.: "An Overview of Ad Valorem Taxes," paper SPE 26390 presented at the 1993 SPE Annual Technical Conference and Exhibition, Houston, 3–6 October.
4. "Home Page," COPAS, [www.copas.com](http://www.copas.com).
5. Newendorp, P.D. and Schuyler, J.R.: *Decision Analysis for Petroleum Exploration*, second edition, Planning Press, Aurora, Colorado (2000).
6. Capen, E.C.: "Property Evaluation—A Return to First Principles," paper SPE 68595 presented at the 2001 SPE Hydrocarbon Economics and Evaluation Symposium, Dallas, 2–3 April.
7. Phillips, C.E.: "The Appreciation of Equity Concept and Its Relationship to Multiple Rates of Return," *JPT* (February 1965) 159.
8. Dougherty, E.L.: "What Discounted Cash Flow Rate of Return Never Did Require," *JPT* (January 1986) 85.
9. Seba, R.D.: "The Only Investment Selection Criterion You Will Ever Need," paper SPE 16310 presented at the 1987 SPE Hydrocarbon Economics and Evaluation Symposium, Dallas, 2–3 March.
10. Erdogan, M. *et al.*: "Optimization of Decision Tree and Simulation Portfolios: A Comparison," paper SPE 68575 presented at the 2001 SPE Hydrocarbon Economics and Evaluation Symposium, Dallas, 2–3 April.
11. Wright, J.D. and Thompson, R.S.: "A Comparative Analysis of Twelve Economic Software Programs," paper SPE 68588 presented at the 2001 SPE Hydrocarbon Economics and Evaluation Symposium, Dallas, 2–3 April.
12. von Neumann, J. and Morgenstern, O.: *Theory of Games and Economic Behavior*, third edition, Princeton U. Press, Princeton, New Jersey (1953).
13. Smith, M.B.: "Parametric Utility Functions for Decisions Under Uncertainty," paper SPE 3973 presented at the 1972 SPE Annual Meeting, San Antonio, Texas, 8–11 October.
14. Akindele, F.M. and Shapiro, R.A.: "On The Use Of Probability Distribution Of Risky Investments," paper SPE 7455 presented at the 1978 SPE Annual Technical Conference and Exhibition, Houston, 1–3 October.
15. Magee, J.F.: "Decision Trees for Decision Making," *Harvard Business Review* (July/August 1964) **42**, No. 4, 126.
16. Magee, John F.: "How to Use Decision Trees in Capital Investment," *Harvard Business Review* (September/October 1964) **42**, No. 5, 79.
17. van Elk, J.F., Vijayan, K., and Gupta, R.: "Probabilistic Addition of Reserves—A New Approach," paper SPE 64454 presented at the 2000 SPE Asia Pacific Oil and Gas Conference and Exhibition, Brisbane, 16–18 October.
18. Murtha, J.A.: *Decisions Involving Uncertainty: A Risk Tutorial for the Petroleum Industry*, Palisade Corporation, Newfield, New York (2000).
19. Murtha, J.A.: "Monte Carlo Simulation: Its Status and Future," *JPT* (April 1997) 361.
20. Markowitz, H.: "Portfolio Selection," *J. of Finance* (March 1952) **7**, No. 1, 77.
21. Markowitz, H.M.: *Portfolio Selection and Efficient Diversification of Investments*, second edition, Blackwell Publishers, Inc., Malden, Massachusetts (1957).
22. Ball, B.C. Jr. and Savage, S.L.: "Holistic vs. Hole-istic E&P Strategies," *JPT* (September 1999) 74.
23. Brashear, J.P., Becker, A.B., and Faulder, D.D.: "Where Have All the Profits Gone?" *JPT* (June 2001) **20**, 70.
24. Howell, J.I. III *et al.*: "Managing E&P Assets from a Portfolio Perspective," *Oil & Gas J.* (November 1998) 54.

25. Hertz, D. B.: "Investment Policies That Pay Off," *Harvard Business Review* (January/February 1968) **46**, No. 1, 96.
26. Newendorp, P. and Schuyler, J.: *Decision Analysis for Petroleum Exploration*, second edition, Planning Press, Aurora, Colorado (2001) 562–566.
27. Ball, B.C.: "Managing Risk in the Real World," *European J. of Operational Research* (1983) **14**, 248.
28. Hightower, M.L. and David, A.: "Portfolio Modeling: A Technique for Sophisticated Oil and Gas Investors," paper SPE 22016 presented at the 1991 SPE Hydrocarbon Economics and Evaluation Symposium, Dallas, 11–12 April.
29. Edwards, R.A. and Hewett, T.A.: "Applying Financial Portfolio Theory to the Analysis of Producing Properties," paper SPE 26392 presented at the 1993 SPE Annual Technical Conference and Exhibition, Houston, 3–6 October.
30. Ball, B.C. and Savage, S.L.: "Portfolio Thinking: Beyond Optimization," *Pet. Eng. Intl.* (May 1999) 54.
31. Brashear, J.P. *et al.*: "Why Aren't More U.S. Companies Replacing Oil and Gas Reserves?" *Oil & Gas J.* (3 March 1997) 85.
32. Brashear, J.P. *et al.*: "How to Overcome Difficulties With Reserves Replacement," *Oil & Gas J.* (10 March 1997) 75.
33. Brashear, J.P. *et al.*: "Analytical Approaches for Reserves Replacement Planning," *Oil & Gas J.* (17 March 1997) 106.
34. Winston, W.: *Financial Models Using Simulation and Optimization*, Palisade Corporation, Newfield, New York (1998).
35. Black, F. and Scholes, M.: "The Pricing of Options and Corporate Liabilities," *J. of Political Economy* (May 1973) 637.
36. Merton, R.C.: "The Theory of Rational Option Pricing," *Bell J. of Economics & Management Science* (Spring 1973) **4**, 141.
37. Copeland, T., Koller, T., and Murrin, J.: *Valuation: Measuring and Managing the Value of Companies*, third edition, John Wiley & Sons, Inc., New York City (2000) 395.
38. Copeland, T. and Antikarov, V.: *Real Options: A Practitioner's Guide*, Texere, New York City (2001) 13.
39. Trigeorgis, L.: *Real Options: Managerial Flexibility and Strategy in Resource Allocation*, The MIT Press, Cambridge, Massachusetts (1996) 9–14.
40. Lohrenz, J. and Dickens, R. N.: "Option Theory for Evaluation of Oil and Gas Assets: The Upsides and Downsides," paper SPE 25837 presented at the 1993 SPE Hydrocarbon Economics and Evaluation Symposium, Dallas, 29–30 March.
41. Dixit, A.K. and Pindyck, R.S.: *Investment Under Uncertainty*, Princeton U. Press, Princeton, New Jersey (1994) 468.
42. Winston, W.: *Financial Models Using Simulation and Optimization*, second edition, Palisade Corporation, Newfield, New York (2000) 505.
43. Winston, W.: *Financial Models Using Simulation and Optimization II*, Palisade Corporation, Newfield, New York (2001) 382.
44. Pickles, E. and Smith, J. L.: "Petroleum Property Valuation: A Binomial Lattice Implementation of Option Pricing Theory," *The Energy J.* (1993) **14**, No. 2, 1.
45. Paddock, J.L., Siegel, D.R., and Smith, J.L.: "Option Valuation of Claims on Real Assets: The Case of Offshore Petroleum Leases," *Quarterly J. of Economics* (August 1988) **103**, No. 3, 479.
46. Gruy, H.J., Garb, F.A., and Wood, J.W.: "Determining the Value of Oil and Gas in the Ground," *World Oil* (March 1982) 105.
47. Johnston, D.: *International Petroleum Fiscal Systems and Production Sharing Contracts*, PennWell Publishing Co., Tulsa, Oklahoma (1994) 325.
48. "Annual Reserves Report," Cornerstone Ventures, L.P. (26 February 1999) **15**, No. 5, 3.
49. Chorn, L.G. and Carr, P.P.: "The Value of Purchasing Information To Reduce Risk in Capital Investment Projects," paper SPE 37948 presented at the 1997 SPE Hydrocarbon Economics and Evaluation Symposium, Dallas, 16–18 March.
50. Davidson, L.B.: "Practical Issues in Using Risk-Based Decision Analysis," paper SPE 71417 presented at the 2001 SPE Annual Technical Conference and Exhibition, New Orleans, 30 September–3 October.

51. Hooper, H.T. III and Rutherford, S.R.: "Real Options and Probabilistic Economics: Bridging the Gap," paper SPE 71408 presented at the 2001 SPE Annual Technical Conference and Exhibition, New Orleans, 30 September–3 October.

**SI Metric Conversion Factors**

acre	×	4.046 873		E + 03	= m <sup>2</sup>
°API		141.5/(131.5 + °API)			= g/cm <sup>3</sup>
bbl	×	1.589 873		E – 01	= m <sup>3</sup>
Btu	×	1.055 056		E + 00	= kJ





## Chapter 17

### International Oil and Gas Law

**Mark D. Bingham**, Davis Graham & Stubbs LLP, **Scot W. Anderson**, Davis Graham & Stubbs LLP, and **Dustin M. Ammons**, Chevron USA Inc.

#### 17.1 Introduction

The search for petroleum drives oil and gas companies from the familiar confines of their home countries out into the world. The worldwide scope of the exploration for the production of oil and gas has led to the rise of international and multinational petroleum companies—companies that are nominally based in a home country but operate throughout the world. Today, almost all major oil companies have a presence in most oil-producing regions, and many mid-size and smaller petroleum companies operate in more than one country.

Each host country has its own specific laws and regulations that apply to oil and gas development in that country. Still, it is possible to describe some common approaches and concepts that apply to international petroleum law. The United States has also passed certain laws that apply to the international operations of U.S. companies. This chapter describes some of the legal issues affecting international oil and gas development, as well as the laws that will apply to U.S. companies operating internationally.

#### 17.2 History of International Oil and Gas Development

Petroleum has been an internationally traded commodity since the late 1800s. International oil and gas development paralleled domestic development in the United States in the 1900s. In the early 1900s, Standard Oil Company of New Jersey held a near-monopoly on domestic oil supply and price. Specific judicial and legislative action by the United States government caused this monopoly to break up, and various large, integrated oil companies were formed, which participated in all petroleum industry segments from exploration to marketing. These major companies sought mineral development opportunities both domestically and abroad. At the same time, European oil companies also sought to capitalize on mineral development opportunities beyond their borders.<sup>1</sup> (For a highly readable account on the history of the international petroleum industry, see [Ref. 1.](#))

Initially, these major companies, from the United States and Europe, sought rights in oil from countries in the Middle East by means of concessions, which authorized the company to explore, develop, and market the oil from certain lands for a specified period of time. The concession area might have covered the entire country, such as Abu Dhabi or Kuwait; the concession period could have lasted decades, such as 75 years for Abu Dhabi and Kuwait or 66

years for Saudi Arabia; the concession might not have contained development obligations, as the concession might have been viewed as a transfer of the mineral rights for a term of years; and the developing company might have had unilateral control over all management and decisions associated with the concession.<sup>2</sup> These concessions were granted by the government or sovereign of the host country, who was often subject to strong internal or foreign political pressures. In exchange for granting the concession, the host country typically received an initial or bonus payment and a right to some fractional share of, or a royalty interest in the value of, the oil produced. In these early development years, produced natural gas was generally considered a waste byproduct and was vented or flared.

Although some host countries may have only granted limited or relatively short-lived concession agreements, others granted broadly scoped rights, which left the host country with little control over what might have been that country's most valuable single asset. In an effort to regain control over their mineral resources, countries such as Mexico, Saudi Arabia, and Iran resorted to expropriation and nationalization of the petroleum rights by Pemex, Saudi Aramco, and the national oil company of Iran, respectively. Other countries in the Middle East modified their concessions through renegotiated agreements to significantly change the balance of control over the mineral rights. In 1960, the formation of the Organization of Petroleum Exporting Countries (OPEC), an entity that represents the interests of numerous similarly situated oil exporting countries, helped facilitate further changes in contract rights and royalty benefits enjoyed by the member countries.

Today, the term "concession" has lost favor, as it implies that rights might have been conceded or given away, and some host country citizens might have considered their rights and interests to have been abused by the developing companies. Most host countries now issue licenses or leases similar in nature to those used in the United States, covering defined areas or "blocks" and allowing the host country a significantly greater amount of direct participation in the decisions affecting, and the capital costs associated with development of, its natural resources. The license or lease might be a nonexclusive right to conduct exploration operations or an exclusive right to conduct development and production operations. The developing company is commonly obligated to a yearly capital commitment, an established work program, and the relinquishment of undeveloped lands after a specified primary term. There may be multiple bonus payments at various development thresholds, the royalty percentage due the host country might vary based on production volumes and cost recovery factors, and the foreign company could be subject to various local taxes. Many countries have formed national oil companies that may have the right to participate for up to a 51% ownership share under licenses, or those countries may form a joint operating company with the developing company to be the licensee.

Alternatively, host countries may enter into "service agreements," which allow a foreign company to develop the petroleum resources in a specified area for a specified consideration, typically in the form of a share of the production stream taken in kind by the host country. Although the developing company bears all the financial risk, the host country generally does not transfer any mineral or property rights to the developing company, and the host country controls the development of its lands at the developing company's expense. These types of service contracts are common in countries such as Mexico, where there is a constitutional prohibition against the disposal of any of the national petroleum rights retained by the host country.

Today, produced natural gas has now evolved into a highly desirable commodity, particularly in areas accessed by gas transportation pipelines or liquefied natural gas (LNG) processing and transportation facilities. Today's international petroleum development agreements, whether in the form of licenses or service contracts, address the value attributable to natural gas and the obligations for its development and marketing.

### 17.3 Interests in Petroleum Properties

Over the years, host countries seeking the development of their natural resources have developed a variety of contractual and legal mechanisms to promote exploration and production. These approaches to the creation of interests in mineral development can be divided into four general categories: concessions and licenses, production sharing agreements, participation agreements, and service contracts.<sup>2,3</sup>

**17.3.1 Concessions and Licenses.** Some host countries grant mineral developers the exclusive right to explore, develop, and produce from petroleum properties. Such rights were first granted in the form of concessions. In their earliest form, concessions were granted by host countries to cover large areas and, sometimes, entire countries. The mineral developer had the unfettered right to explore or develop as it saw fit, and the host country retained only a royalty interest in the produced petroleum.

These broad concessions were seen to reserve too little control and revenue for the host country and are no longer used. Despite the demise of the early concessions, many countries, however, still grant oil producers exclusive rights to explore or develop petroleum properties, either through a more limited concession or a licensing process. Under either approach, the mineral title remains with the host country or its national oil company, and the development of the mineral resource is permissive. The title to oil and gas typically passes at the wellhead.

Unlike the broad grants of the first concessions, a modern concession or license typically covers a specific area or mineral property. If the area is not yet producing, the licensee will be required to conduct a work program, typically consisting of gathering or processing seismic data and drilling exploratory wells. A licensee is now required to relinquish areas within the license that are not explored or developed. Concessions and licenses typically run for a set number of years, subject to renewal if certain requirements are met.

Many of the original concessions were negotiated in the Middle East and North Africa, and some countries in these areas still offer concessions to petroleum developers. In Tunisia, for example, a producer may begin exploration under a research permit, which defines the area to be explored. This area can be granted as a concession, which requires a decree from the relevant ministry and the passage of a law by the Tunisian legislature. The concession might be withdrawn should the concession holder interrupt production or fail to pay the required royalties.

Licensing arrangements were developed after the advent and collapse of the earliest concessions. Under a licensing arrangement, the host country retains ownership and control of petroleum in place and grants the licensee the right to explore for and develop that resource. Licenses are used, for example, throughout the North Sea, and have been used in the United Kingdom since the 1960s. In the United Kingdom, the Department of Trade and Industry (DTI) selects tracts that it will offer in a licensing round. Any license awarded in that round will be governed by a standard form agreement, The Model License, which sets out the standard terms for the license. Prospective developers then submit proposed work programs for an area to be licensed. DTI then chooses the work program and licensee it wants to develop a specific area. The DTI may not award a license to the highest bidder, but rather looks to manage the development of resources in the U.K. continental shelf in the manner most advantageous to the host country.

The imposition of a work program has significant benefits for the host country, as it assures that its natural resources will be developed promptly. Even if an exploratory drilling program is unsuccessful, the results of seismic surveys, seismic analysis, and exploration drilling conducted throughout a country and its offshore areas will help the host country better define its mineral resources. In many circumstances, a petroleum producer will win a concession, license, or other mineral development right by bidding for the property with an extensive work commitment. This commitment can, however, lead to uneconomic results. A company might, for example, commit to conduct seismic surveys and drill two exploratory wells as part

of a licensing bid. If, after analyzing the seismic data and drilling the first hole, the company doubts the prospectivity of the license area, it is nonetheless committed to drill an additional well. A company may be loath to spend its exploration budget on a second well in a license area at that point. Mineral developers can negotiate alternatives to work program commitments in some circumstances.

In summary, a host country that uses a concession or license to promote mineral development grants the licensee or concessionaire an exclusive right to develop a specific area. That right is gained through certain commitments—e.g., to conduct a work program or to pay royalty—and can be lost if those commitments are not kept. As the area approaches production, the licensee may be required to relinquish portions of the license area that are outside the producing structure.

**17.3.2 Production Sharing Agreements.** The production sharing agreement was first developed in Indonesia in the 1960s. Production sharing arrangements are common throughout the world and are often favored by countries that lack the financial or technical capability to develop mineral resources. In a production sharing arrangement, the oil producer gains the right to conduct exploration and assumes the entire risk of exploration failure.

If, however, the developing company succeeds in finding petroleum and developing the resource, the host country takes a share of the oil produced. The developing company is allowed to retain some petroleum as reimbursement for its development costs (the “cost share”) and then receives a portion of the produced oil as its profit (the “profit share”). The host country typically retains the greater portion of produced petroleum, and many modern production-sharing agreements use a sliding scale, with the host country’s pro rata share increasing as more oil is produced. While the host country often takes the largest percentage of production, the terms can vary significantly, even within a country. Indonesia, for example, recognizes the cost and risk of development in “frontier areas” and awards contractors a higher percentage of the gross revenue from gas sales in those areas.

Because the host country is a beneficiary of the production from a property subject to a production sharing agreement, some agreements provide for tax relief. This relief may come in the form of a straightforward tax amnesty (perhaps limited in its duration) or through an obligation upon the host country to pay any taxes. The host country may also take a role in the management of the project. Many production-sharing arrangements require the host country’s national oil company to operate the field.

**17.3.3 Participation Agreements.** In participation agreements, petroleum properties are developed through a joint venture or similar arrangement between the host country and the developing company. In some instances, the host country and the developing company will create a new entity to be jointly owned. Other times, the host country and the developing company will create a contractual joint arrangement. The distinguishing characteristic of a participation agreement, in any event, is the cooperative development of petroleum properties by the host country and the developing company.

The joint entity or venture will be managed by both the host country and the developing company, but management control may be tilted toward one side or the other. Some participation agreements provide for the developing company to carry the host country financially, and fund exploration costs, for example. The developing company is then allowed to recoup these costs from future production.

**17.3.4 Service Agreements.** In some countries, the right to develop petroleum resources has been granted exclusively to a national oil company. In these countries, mineral developers enter into service agreements with the national oil company. The developing company might, for example, simply conduct drilling programs or build facilities in return for a fee. The contractor

then has no legal interest in the mineral property. Some service agreements allow the contractor to purchase and export produced petroleum, although these arrangements are often tied to the assumption of some exploration risk by the contractor. Some service companies take equity stakes in international petroleum projects, and, thus, the line between service arrangements and other mineral development arrangements can be blurred.<sup>4</sup> Some large developing companies disfavor service arrangements, as they wish to have an interest in the mineral property itself.

Mexico is an example of a host country that uses service contracts. Article 27 of the 1917 Constitution of Mexico, as amended 10 January 1934, grants the Mexican nation direct ownership of all hydrocarbons. In early December 2001, Mexico's "Multiple Services Contract" law and regulations were released in an effort to attract foreign developing companies to participate in exploration and production of Mexico's petroleum resources. Service contractors are paid in cash—not oil—and, therefore, will not be able to book reserves.

**17.3.5 Common Contractual Provisions.** Because the various mineral development agreements previously discussed are drafted by the host country, they tend to have provisions designed to protect host country interests or promote host country policies. The scope and nature of these provisions will vary from country to country and between the common types of mineral development agreements. Nonetheless, many mineral development contracts will include at least some of the following contractual requirements.

**Training.** Many contracts require the developing company to provide training to local workers or employees of the national oil company. The training obligation may be described with some particularity, but it is common for the obligation to come in the form of a fixed annual commitment for training expenses.

**Local Labor and Services.** Petroleum development contracts often require the mineral developer to use local labor, unless special skills are required, and to contract for services with local contractors. In some countries, there are companies owned by or affiliated with the host country or the national oil company that provide oilfield services. The mineral developer might be required to contract with that particular company, as opposed to a more general obligation to use local contractors. If the company uses expatriate personnel, the petroleum development arrangements may place limits on the number of expatriates, their roles and duties, and even the types of property that they can bring into the country.

**Domestic Marketing Obligation.** Some contracts require the petroleum producer to sell a specified percentage of its production in the domestic market. Under a production sharing contract, this domestic marketing obligation (DMO) might apply to the share left to the developing company after it has provided the host country with its share of production, thereby creating an even greater financial burden on the production from the mineral property. A DMO can have significant adverse effects on the economics of a mineral property, especially if the market for natural gas or oil is weak in the host country or if the payment for the domestically delivered petroleum is not in convertible currency. Also, a DMO might require the company to sell oil or gas into the domestic market at a discount to international open market prices.

**Data.** Some mineral development agreements require developing companies to provide copies of data, such as seismic surveys and drilling results, to the host country. Other agreements vest ownership of the data in the host country and provide a license to the oil company to use the data so long as the company maintains its concession, license, or contract in good standing.

**Local Office and Local Agent.** A contract or license may require the developing company to maintain a local office and to hire local residents to staff that office. Some mineral development arrangements require the developing company to be represented by a local agent.

**Choice of Law.** Many international petroleum agreements between mineral developers and host countries require that the contract be governed by the laws of the host country. As dis-

cussed in [Sec. 17.8](#), the use of an arbitration provision can help manage some of the adverse effects of the application of local law.

**Assignment and Transfer Limitations.** Mineral development agreements commonly require some sort of host country approval before all or part of a mineral interest can be transferred to a third party. These limitations can be significant, as petroleum developers often like to bring in partners to share the expense and risk of mineral development. In some cases, assignments or transfers can be approved by a ministry or department of the government (or perhaps a few such ministries). In the worst case, a transfer may require legislative approval, which can be difficult to achieve and very time consuming. Such approvals also often require publication or notice periods before they are official, which creates an additional element of risk in a commercial assignment of a mineral interest in a host country.

**Equipment.** Some development arrangements require the operator to transfer equipment used in mineral development to the host country or to its national oil company. The arrangements also typically place most of the burden of abandonment costs on the mineral developer, although the extent of that cost shift can vary.

**Insurance.** Many mineral development agreements require the operating company to carry insurance, and these clauses typically dictate that the insurance comply with host country requirements.

**Management.** Oil and gas development arrangements sometimes create a management role for the host country or its representatives. In a licensing arrangement like that in the United Kingdom, the government does not have a direct management role in field operations, but rather governs that development through regulations and license requirements. In other circumstances, such as the Indonesian production-sharing contract, the national oil company is the operator of the field and has significant management authority. Other arrangements adopt more moderate approaches. In Romania, for example, the standard Exploration and Production Sharing Agreement creates a Management Committee to govern field operations, and the seats are held equally by the national oil company and the producing companies. Committees such as this are commonly chaired by a host country governmental representative. If the management committee is responsible for approving budgets and annual work programs, the host country can gain considerable influence over operations in this manner. Also, some petroleum development arrangements require government approval of the operator of a field. This requirement can also hinder the free transfer of mineral interests.

**Foreign Exchange and Banking.** The petroleum development agreement may require the foreign developer to open and fund a local bank account. The agreement or local law may limit the ability of the company to convert local currency to other currency and might require that a local bank make the conversion. As noted, the foreign mineral developer may be required to receive some payments in local currency.

## 17.4 Considerations in Conducting Operations in International Projects

There are many complex considerations that must be addressed in each relationship between a host country and a foreign oil company. (For a general discussion of due diligence issues in international projects, see [Ref. 5](#).) The foreign oil company must recognize and adjust to the existence of the sovereign power of the host country and assume the political risk that its interests and investments might be expropriated, with or without compensation; that the government might be overthrown; or that significant security might be necessary to protect the foreign company's employees and assets. The foreign company must recognize that there is an increasing awareness by host countries of the need to conserve and protect the environment and to train its citizens to be skilled and competent in the industry. The foreign oil company must remain aware that relationships with host country officials should not involve bribery, favors, preferences, or other illegal actions. Many of these considerations are discussed in greater detail.

**17.4.1 Political Risk.** There are many risks associated with an international oil and gas development project. The modern commercial reality is that almost every development project will require capitalization and financing, with associated risks and obligations dictated by third parties who are outside the control of the company proposing the international project. Other risks include whether the project will be completed on time and within the anticipated budget. Further, there is the risk that the project, once completed, fails to perform as projected, or that the anticipated product markets do not evolve or that product prices do not reach the anticipated levels. To some degree, each of these risks can be managed by contractual protections. Certain risks cannot be controlled by such protections, however, and they include the political risks of expropriation, inconvertibility of currency, and political unrest.

Expropriation can include the outright nationalization of a developing company's projects, such as occurred in Mexico and Iran. Expropriation can occur by gradual nationalization through host country taxation or project participation. Expropriation can also occur indirectly by the refusal or mere failure, either through a lack of attention or by willful delay, on the part of the host country government, to issue required approvals or consents for development projects. This process is sometimes referred to as "creeping expropriation."

Currency risks arise when a project is financed in one currency and the resulting petroleum production is sold domestically in a different currency. If the currency standards between these differing markets erode or shift owing to various political and economic factors, the profitability or financial stability of a project can be abruptly undermined even though the accounting figures show the project to be on budget.

Political unrest can exist in violent circumstances such as wars, insurrections, or riots. Potentially more devastating, however, is the political unrest that arises when well-conceived projects and contracts cannot be enforced under applicable laws. Before investing in any host country, the developing company must evaluate the certainty, predictability and enforceability of any contract or relationship with a host country. Certainty can be evidenced by a long-standing constitution, well-established laws, and a reliable governing body. Predictability is evidenced by the host country's governmental application of its law in a manner that is consistent, evenhanded, and objective. There is little point in investing large amounts of money and time in a development project if the developing company has no means of ensuring that the host country government can either be required by a court to perform its obligations under the applicable contracts or to pay adequate compensatory damages.

Developing companies can mitigate political risks by obtaining financing through export credit agencies such as the U.S. Export/Import Bank and by obtaining political risk insurance from private companies or from quasigovernmental entities such as the Overseas Private Investment Corporation of the United States or the Multilateral Investment Guarantee Agency, which is a member of the World Bank Group. Host countries that do not have established or predictable ownership laws or procedures for enforcing rights, such as countries emerging from military dictatorships to market economies, pose special problems for insurers and for lenders seeking to protect their funds through mortgages or other liens on the producing lands. As a consequence, export credit agencies might impose strict limitations on the availability of financing and could impose stringent insurance coverage requirements. Political risk insurance can be expensive, and its coverage can be limited in scope to only certain events or risks such as expropriation, unavailability of foreign exchange, and war. On the other hand, these credit and insurance agencies will likely be committed to work with the host country government to bring political pressure to bear in order to protect their financial investments.

Other methods to mitigate political risk include joint venturing with host country nationals, good corporate citizenship in the host country, and contractual assurances from the host country in the mineral development agreement. Typical contractual assurances address the stability of the legal regime, waiver of sovereign immunity, effective dispute resolution in a neutral

forum, and the selection of a governing law that is consistent with the expectations of the parties. The developing company should seek for stability in the legal regime, including assurances that the government will not unilaterally modify the terms and conditions of the investment or change the tax or participation structure to the detriment of the developing company. A waiver of sovereign immunity will not only allow a developing company to force a host country to a legal forum, but it will also prevent the government of the host country from changing its laws to the detriment of the developing company.

Host countries generally will want contracts involving their government to be governed by the law of the host country and will want any dispute regarding those contracts to be resolved in courts located within the host country. Similarly, the developing companies tend to prefer the laws and courts of their respective countries. A reasonable compromise is to choose a neutral forum and governing law. Choice of law provisions are generally upheld so long as there is a reasonable connection between the transaction involved and the jurisdiction whose law is selected, and there is no evidence of unfair advantage from an equal bargaining perspective. Further discussion regarding choice of law and forums for dispute resolution can be found in [Sec. 17.8](#).

**17.4.2 Security.** Another form of political risk includes physical risks to employees and assets of the developing company by terrorism, kidnapping, or physical abuse. Developing companies typically have substantial financial and manpower commitments for the security of employees and assets. Fenced compounds, security cameras, and guards may be necessary to protect plant sites, equipment sites, well sites, storage yards, offices, and company employees located therein. “Company towns” help manage the interaction of the developing company employees with host company nationals in a controlled environment. Automobile drivers and bodyguards may be necessary to ensure the physical protection of company employees and their families outside these controlled environments. Also, some insurers offer kidnapping insurance to help mitigate that risk.

**17.4.3 Bribery and Corruption.** Bribery has many different, but similar, definitions. Some common definitions include: offering, giving, receiving, or soliciting something of value for the purpose of influencing the action of an official in the discharge of his or her official duties; money or favor given or promised to a person in a position of trust to influence his or her judgment or conduct; something that serves to induce or influence; and an advantage that one competitor secures over other competitors by secret and/or corrupt dealings.

There is generally little debate that bribery is unethical, but the determination of what constitutes bribery can be hotly contested. What might be business courtesies such as gifts or favors, consistent with local custom or practice, to some may be construed as a business inducement, bribery, or commercial influence that might or might not be considered unethical or illegal depending on the country where the business is conducted.

In 1977, the United States enacted the Foreign Corrupt Practices Act (FCPA) to impose severe penalties, including fines and imprisonment, on companies and personnel who bribe or otherwise attempt to influence officials of a host country. Almost all countries have adopted similar laws, but until recently, such laws might not have been strictly enforced, and in some host countries, it may continue to be an accepted practice to provide favors to governmental officials in return for special treatment.

The FCPA was enacted in response to embarrassing public disclosures of payments made by prominent U.S. companies to political officials in several countries to secure large orders for military equipment, where foreign government officials might have requested or suggested some special consideration in return for favorable purchase contracts. The breadth of the FCPA covers other overseas business opportunities including the oil and gas industry. Competition for exploration and production rights creates many potential FCPA problems for U.S. companies



conducting business abroad. Commonly, foreign investment laws impose limits on foreign ownership, which then requires the developing company to establish some form of a partnership with a company located in the host country. Government officials who could delay or prevent the award of exploration or production rights might feel less inclined to do so if they were “comfortable” with the developing company and its local partner by the suggestion or expectation of some form of inducement or payment.

The FCPA attempts to prevent corrupt practices by two methods: by mandating accounting standards for public companies, and by prohibiting payments from public companies to foreign political officials with knowledge of a corrupt purpose. Compliance with the accounting standards under the FCPA is monitored by the Securities and Exchange Commission. Enforcement of the FCPA falls under the responsibility of the U.S. Department of Justice.

A public company is one that has registered securities or that files reports in accordance with the Securities Exchange Act of 1934. Under the FCPA, public companies are required to maintain books and records in such a way that corrupt payments cannot be hidden within a company’s accounting system. The books and records must be kept in reasonable detail and must accurately and fairly reflect the transactions and disposition of assets of the company. The FCPA also precludes senior management of a public company from avoiding responsibility if corrupt payments are made. The transactions of the company must be executed in accordance with authorizations by the company’s management. Foreign subsidiaries of public companies must also comply with these requirements. Foreign affiliates that are owned 50 percent or less by the public company are only required to make “a good faith attempt” to cause the affiliate to follow the accounting standards.

The FCPA antibribery provisions make it unlawful for public companies or any shareholder, officer, director, employee, or agent thereof to: make use of the mails or other forms of interstate commerce corruptly in the furtherance of an offer, payment, promise or authorization of payment; support any foreign official, political party, or candidate for political office; influence any act or decision of that official or inducing that official to use influence to affect or influence any act of a foreign government or agency; assist a public company in directing business to any person or in obtaining or retaining business with any person. Each of these elements must be satisfied in order for a violation of the FCPA to exist. The fundamental notion of when an act is done corruptly can be difficult to determine. It is apparent, however, that a payment is corrupt if it is tendered with the intent to influence the recipient to misuse his or her official position to divert or obtain business wrongfully.<sup>6</sup>

Retaining a local influential person or agent to help secure a foreign contract is not a violation of the FCPA but rather might be a necessary reality in order to secure the contract. Corporate legal advisers are available to examine the facts and the relevant law to determine if an FCPA violation has or will occur. Some factors to be considered include determining if the host country has a reputation for bribery; if the agent’s commission is excessive or if it will be paid in cash; if the agent is related to a government official or if the government official has any ownership relationship with the agent; if it is illegal under the local law for the agent to act as an agent; if the agent has made statements suggesting that a particular amount of money is needed to secure the business opportunity; if the agent has suggested that any kind of false documentation be used; if the agent has refused to promise in writing to abide by the FCPA.<sup>7</sup>

Although other countries generally have not followed the United States by enacting laws similar to the FCPA to penalize corrupt payments made to government officials to secure business opportunities, the developing oil company should also keep in mind that many host countries have enacted laws to prevent such payments, and any of the actions previously discussed could result in a violation of the host country’s laws in addition to the FCPA.

**17.4.4 Indigenous Rights.** In a standard oil and gas lease in the United States, a large corporate or sophisticated landowner might sometimes be in a position of negotiating strength to

obtain lease provisions that limit or require certain activities occurring on the leased lands. It is rare for this control, however, to include proactive involvement, such as requiring the lessee to conduct certain operations. The large corporation or landowner rarely has any power greater than a veto right. International contracts, however, have a completely different balance of power—one that includes the obligation of integrating individuals in the management and labor force necessary to complete the project.

Host governments typically can exercise a considerable amount of control over all operations within the contract area. This control is commonly exercised through a body known as a joint management committee (JMC). A JMC is typically composed of representatives from the host country government and from the developing company. These representatives meet regularly in open sessions where minutes and approvals are recorded. JMC approvals range from the mundane issues of work programs and budgets to far-reaching and substantial issues affecting the project and the investment by the developing company. If the host country governmental representatives are not educated or experienced in the various subject matters addressed by the JMC, experts are routinely retained to advise the host country representatives. These host country representative positions create a substantial amount of goodwill and are prestigious for the local individual but can be a large financial expense for the developing company.

Another typical requirement of host countries dictates the use of local personnel and materials to perform the operations associated with the project. These provisions are rigidly applied and seriously monitored by host country governments. The requirement to use local materials and labor is commonly applied and administered through the procurement provisions of the mineral development agreement. JMC procurement personnel will play an active role in ensuring that local people are employed and service and supply contracts are given to local companies. Procurement requirements can raise quality concerns for the developing company, as it may fear it will be forced to use local companies or materials that are not suited for the intended job only because the local service or supply company owners are well connected with the host country government. The requirement for the use of local labor and supplies is so important to the host country, however, that the developing company must accept the inevitable and learn to work within the local system.

The salvage rights of a host country also can be burdensome for a developing company, particularly after considering the large investment cost of any development project. Host countries typically mandate that once a project reaches its economic life, all equipment and materials used in connection with the project will become the property of the host country, without any salvage value or consideration given to the developing company. This requirement can even apply to indirect materials and equipment used on the project such as boats, airplanes, helicopters, automobiles, seismic equipment, electronic equipment, and computers.

In addition to the objective of increasing production of petroleum from within its country, another main objective of host country governments is to obtain training of its nationals to perform necessary duties and to potentially take over the operation of projects within the borders of the country.

**17.4.5 Training Obligations.** Each work program of a mineral development agreement with a host country will include a training budget. These training obligations can be substantial and range from hundreds of thousands to millions of dollars on an annual basis. Important positions associated with the project that are staffed by the developing company are typically “seconded” early in the program with local trainees. This involves putting employees from the host country into operational positions for training under the developing company, while these “seconded” remain as employees of the national oil company. The developing company will be responsible for paying the secondees a salary and benefits comparable to that of the developing company’s staff.

**17.4.6 Necessary Relationships for Efficient and Economic Development.** The cost of a large foreign development can be so substantial that one developing company alone may not want to take on the risks, costs, or liabilities. Consequently, in addition to the relationships established between a developing company and the host country, there will likely be relationships between two or more developing companies that participate together in an operation in a host country to obtain, maintain, and maximize economic production from a large project. Such participation requires a joint operating agreement to establish and govern the relationship between the multiple developing companies. One company is designated as the operator and is given necessary authority to conduct all operations required under the host country mineral development agreement. Operating committees are commonly established to address and advise the operator on various technical or financial matters. The authority of the operator also may be limited by the working interest parties, who have the right to approve certain actions taken by the operator. Further, participation in certain operations may be optional, and provisions are necessary to govern these elections. International joint operating agreements can be on standardized form agreements or can be individually negotiated by the working interest parties and contain many of the same types of provisions found in joint operating agreements used in the United States for domestic oil and gas developments, as discussed in greater detail next.

## 17.5 Joint Operating Agreement

The exploration and development of oil properties is an enterprise fraught with risk. Consequently, mineral developers look to share the risks, costs, and rewards of exploration and production with other companies. The contractual arrangements between these coventurers can be quite complicated and result in all sorts of contracts. The foundation to these arrangements, however, is the joint operating agreement (JOA). (For a thorough discussion on the nature of operating agreements in the United Kingdom, see [Ref. 8.](#))

In international petroleum development, a JOA sets out the basic commercial relationship between two or more petroleum developers. The JOA will name one of the parties as the operator. The operator is responsible for day-to-day management of the exploration and development program. The other parties, the nonoperators, reimburse the operator for its costs on a pro rata basis relative to their respective ownership interests in the project. Many of the issues related to joint operating agreements arise in determining the respective rights of the operators and nonoperators.

A joint operating agreement will set out the percentage ownership interests held by the various parties, and each is responsible for its proportionate share of operating costs. The party with the highest participating interest is typically the operator, but this need not be the case.

The operator will develop proposed work programs and budgets, including Authorization for Expenditures (AFE). These programs are subject to approval by the parties to the JOA. Voting rights are established proportionately, and a proposed program or AFE can typically be approved by a specified voting percentage. If a party's interest in the property is high enough, it might have a blocking vote.

The JOA will usually include a set of accounting principles to be used by the operator in allocating costs and revenues among the parties to the JOA. The accounting principles will allow an objective determination of costs and expenses. The accounting principles sometimes allow the operator to pass through some overhead charges. These charges relate to the cost of corporate headquarters support for the field operations, and reflect home office charges rather than the charges directly arising from the field. Overhead might be determined on an allocation of corporate costs, or might be negotiated. Overhead charges are sometimes tied to a published index, which allows easy calculation of the costs, and which should reflect standard industry charges for services or the effect of inflation on such charges.

Many JOAs allow a party to "sole risk" a proposed project. One party may wish to drill an exploratory well, and the other parties refuse to authorize payment of the cost. If the votes are

insufficient to authorize the well, a party might pay for all those costs by itself, therefore taking on the sole risk for that well's success or failure. If the well leads to a discovery, the sole risk party gains, in return, the sole right to production from that discovery. The sole risk party will have the right to use field facilities for any resulting production. Some JOAs allow the nonparticipating parties to join in the new development, but only upon payment of a significant premium. The payment of a premium reflects the fact that these parties did not take on the risk of the initial expenditure and so should not be able to simply pay their pro rata share of the costs and gain the benefits accruing from the bold decision of the sole risk party.

JOAs may also create preemptive or preferential rights, allowing the parties to the JOA the right to purchase another participant's interest before it is sold to a third party. Preemptive rights can be quite restrictive—designed to assure that the existing participants can control future ownership—or relatively relaxed—simply requiring that a first offer be made to the JOA parties or that those parties have a right to negotiate for a purchase before a third party offer can be accepted.

A joint operating agreement typically includes a clause indemnifying the operator from some liabilities that would otherwise accrue to the operator in that role. The notion is that certain risks should be shared pro rata among the parties to the JOA, rather than borne entirely by the operator. Thus, the JOA will typically provide for a fairly broad indemnity of the operator, subject only to exceptions for affirmative acts or omissions of the operator, such as the operator's willful misconduct, willful default, or perhaps gross negligence. A merely negligent act of the operator, then, might create a liability that is shared pro rata by the parties to the JOA. Some JOAs define concepts like willful misconduct and attempt to limit willful acts to the acts of senior managers or other management employees of the operator. In doing so, the JOA shifts the risk of willful misconduct of lower level employees of the operator to the parties to the JOA, rather than the operator by itself. The indemnity provisions of a JOA and the definitions of willfulness can inspire lively debate in the course of negotiations.

## 17.6 Marketing Arrangements

The marketing of petroleum products is influenced by the nature of the petroleum produced and the location of the field. The market for oil and other liquids is quite different from the market for natural gas. Also, the transportation of oil and natural gas to the marketplace can pose significant commercial and technical issues. As a result, oil producers and energy buyers have developed sophisticated legal arrangements to address these issues.

**17.6.1 Oil Marketing.** Crude oil can be sold anywhere in the world, and the market price for oil is determined at any one of a number of hubs (central marketing points) throughout the world. Consequently, if an international oil producer can get the oil on a boat, the cargo can be sold into the world market. Local economics, therefore, have little effect on the market price for oil that reaches the marketplace. As noted, however, the producer may be required by its mineral development agreement to sell oil into the local market, or perhaps to sell a portion of its oil to the local government at a discount against the market price at a particular hub.

As discussed, it is common for producing properties to be owned or controlled by a number of parties, including foreign oil companies and national entities. Once oil is produced, the parties must determine who owns the oil and how it will be marketed. The parties operating a field typically enter into a lifting agreement, which describes the process for taking oil from the wellhead to the marketplace. It will also describe the process for determining the parties' ownership interest in that oil. Ownership of produced oil is typically proportional to the parties' field interests, but that proportional interest may vary from shipment to shipment. There are occasions, for example, in which one party will overlift (take more than its proportional share) and the other parties will underlift. While this practice is more common with gas agreements than with oil sales arrangements, the parties may enter into a balancing agreement,

which is designed to assure that each party takes its pro rata share of oil by the end of the life of the field.

Some international agreements also provide for the foreign oil company to market the oil on behalf of the local companies. The marketing of oil requires a knowledge of the markets and pricing mechanisms, and an oil company may be able to secure a fee or other consideration for providing this service. A sophisticated financial market has evolved around the petroleum market, and companies can trade in futures and derivatives if they choose. These financial instruments are typically used as market hedging devices and do not affect the direct sale of oil into the marketplace.

Where markets are well developed near the producing property, the oil company may be able to transport its oil to market through a pipeline. In some instances, the oil company may have an ownership interest in the pipeline, and indeed may have been required to contribute capital to the construction of the pipeline. In other cases, the pipeline might be owned by the government or a government controlled company, or perhaps another oil company or group of oil companies. Whatever the circumstance, the producing company will be required to pay a tariff to the pipeline company for the right to transport oil through the pipeline. Because pipelines often have a monopoly on transportation from a field or area, it is critical that the oil producer negotiate a tariff rate that remains certain throughout the producing life of the field. Tariffs may be indexed, which allows the tariff rate to vary over time, based on external and objective economic factors. The oil producer may have problems, however, if it is required to renegotiate the tariff rate after it has spent its capital in field development and must rely on the pipeline to get its oil to market. The tariff rate will certainly affect the economic return from a field.

**17.6.2 Gas Markets.** Unlike the market for oil, the market for natural gas is local. Natural gas can be marketed worldwide only by converting the gas to liquefied natural gas, which is discussed below. In all other circumstances, natural gas must be taken to market through pipelines and put to domestic or commercial use within the pipeline system.

When a mineral property produces natural gas, the mineral developer must address the vagaries and logistics of the local market. In some parts of the world, markets are well developed, and indeed have grown together. The United Kingdom market is an interesting example of how markets can develop over time. When gas was first produced on the U.K. continental shelf, all natural gas was purchased by a single quasigovernmental company. Gas was purchased under take or pay contracts designed to last the life of the field. Gas sellers were committed to sell every molecule of gas produced from the field to that buyer, and the amount of gas taken in any year would swing within a contractually specified range.

Over time, England opened its internal gas market and allowed other companies to buy and sell gas and use the onshore gas transportation system, subject to a uniform tariff for transportation cost. A sophisticated gas trading process immediately sprang up, and gas buyers and gas sellers would trade gas on the day, or buy or sell gas forward. The prior model for gas sales agreements, the long term take or pay contract, diminished in usefulness, as gas producers wanted the flexibility to manage and hedge the market risk of gas. Gas producers and trading companies would enter into master gas sales agreements, which provided standard terms and conditions for any gas sale. Each individual sale thereafter could be consummated over the telephone, and then confirmed by a fax, all pursuant to the master gas sales agreement. Gas producers moved from having every molecule of gas committed to a single buyer under a set of long term contracts to a diversified portfolio of gas sales arrangements designed to meet their commercial needs.

While England was opening its internal market, the European Union passed a gas directive designed to open the entire European common market. Simultaneously with this legal action, a group of companies built a gas pipeline interconnecting England and Europe. The interconnec-

tor pipeline created a new market for English gas and opened the U.K. market to European gas. While there are a number of logistical and political impediments to the complete opening of the European gas market, the trend is toward an open market, and the same trading and hedging markets that developed in England are now developing in Europe. Thus, gas sales arrangements are becoming more and more transnational in Europe. To add to the complication, existing or planned pipelines will allow the marketing of Algerian and Russian gas into Europe, which will further expand the borders of the gas marketplace.

For a mineral developer in Europe, the development of a natural gas field allows that producer to tap into a market that is becoming more and more open, which allows the developer to market its gas to a number of potential buyers and use futures and hedging to manage price risk.

In other parts of the world, however, the marketplace for natural gas is much less developed. The natural gas producer is likely to find itself in much the same position as the early gas developers in England—forced to sell gas to a single buyer at a set price. In these circumstances, a long-term contract provides some benefit to the gas producer. The field depletion contract allows the gas producer to recognize a set return on its investment, although the producer won't have the opportunity to take advantage of the risks and rewards of a vigorous market.

Where market opportunities exist, as in Europe, the various participants in a gas project may have different views of when to participate in the market. As a result, gas producers enter into complex gas allocation and gas-balancing arrangements, which are designed to allow maximum flexibility in taking gas on a given day, while assuring that each party has received its fair share of gas by the end of field life. A certain amount of gas must be used to operate producing fields and pipelines, and the allocation agreement assures that each party receives its proper share of the remainder. Balancing arrangements, as discussed, are put in place to allow a party to take extra gas on a day and then come back into balance over time. If a party has overproduced in the past, it might find that its pro rata share is reduced until its allocation comes back into balance, or at least closer to balance, with the other field owners.

**17.6.3 Liquefied Natural Gas.** Sometimes a natural gas find is too far from markets to allow the sale of gas through a pipeline. In these circumstances, the mineral developer may choose to convert the natural gas to liquefied natural gas (LNG).<sup>9</sup> The producer must develop facilities to cool and liquefy the LNG and then store the LNG in pressurized tanks. The LNG can then be placed on a ship and transported anywhere in the world. The problem, of course, is that this process is very expensive. Also, the end-buyer must have facilities designed to allow unloading of the LNG, which limits the market for this product. Thus, LNG development is used only where there are large quantities of natural gas available and local markets are insufficient to allow marketing of the gas. Algeria, for example, ships LNG to Turkey, even though there is a pipeline that allows some Algerian gas to enter the European market. Similarly, Indonesian LNG is sold to Japan, China, and India. Alaskan LNG projects are being developed for sales into existing and developing Pacific Rim markets. At present, LNG tends to be marketed under long-term single buyer contracts.

## 17.7 Abandonment

For many years, little attention was paid to the process or cost associated with the decommissioning or abandonment of oil and gas facilities, either by governments or commercial operators. The issues to abandonment and decommissioning are especially acute for offshore installations. The cost of decommissioning is quite high. The United Kingdom Offshore Operators Association (UKOOA) estimates the cost of decommissioning a small southern North Sea structure to be £30 million, with the cost of decommissioning a larger structure running as high as £200 million.<sup>10</sup> Consequently, oil and gas operators prefer to remove as little of an

offshore structure as possible, while environmental groups routinely advocate complete removal of facilities.

These issues received a great deal of attention when Shell Oil proposed abandoning the Brent Spar, a large floating oil storage and loading platform. Shell proposed scuttling the platform. The environmental organization Greenpeace decided that this approach to abandonment was inappropriate and focused a great deal of attention on the proposed decommissioning of the Brent Spar. As a result, Shell changed its proposed approach to decommissioning that facility at a significantly greater cost.

There are several international conventions and guidelines addressing the decommissioning of offshore oil and gas facilities. The United Nations, for example, passed the 1958 Geneva Convention on the continental shelf. Sec. 5(5) of that Convention calls for the complete removal of all offshore oil and gas facilities. This Convention, however, has had little effect on the regulation of offshore oil and gas facilities. Only approximately 38 countries are signatories to the Convention, and few countries with abandonment regulations require complete removal of offshore structures. In 1982, the United Nations Convention on the Law of the Seas (UNCLOS) was passed, effectively superceding the 1958 Convention. UNCLOS contemplates the partial removal of offshore facilities.<sup>11</sup>

In addition to these conventions, the International Maritime Organization (IMO) provides standards for the decommissioning of offshore platforms and installations. Under IMO guidelines, for example, structures in less than 100 meters of water must be completely removed. Structures in deeper water can be partially removed but must allow for 55 meters of open water above the abandoned portion of the facility.

The parties to most international oil and gas agreements have only recently been including provisions addressing abandonment of offshore facilities. Some joint operating agreements, for example, simply provide for an abandonment plan to be drafted five years before the end of field life, with some rules concerning the approval of that plan. Other JOA's now include provisions requiring the parties to contribute toward abandonment as the field begins to decline, with remedies specified if a party fails to meet the contribution standards in the agreement.

## 17.8 Dispute Resolution

The petroleum engineer should have a basic understanding of dispute resolution in international petroleum transactions to effectively evaluate particular projects, strategies, and agreements.<sup>12</sup> (For additional information on international dispute resolution, see [Ref. 12](#).) Disputes are inevitable during the course of long-term transactions, and international petroleum transactions are certainly no exception. Most contracts and operating agreements include dispute resolution provisions, which provide for choice of law, choice of forum, and the method for resolving disputes.<sup>13</sup> While litigation and various other types of alternative dispute resolution (ADR) may be used, including mediation, the preferred method, in international petroleum transactions, is arbitration. Of course, any discussion of dispute resolution, like dispute resolution itself, is of little substance without a discussion of whether judgments and arbitral awards can be enforced.

### 17.8.1 Choice of Law, Choice of Forum, and Contractual Dispute Resolution Provisions.

The primary consideration in any dispute resolution provision is the agreement among the parties about which jurisdiction's law shall govern and where disputes will be resolved. Choice of law and choice of forum provisions are generally recommended and indispensable because the absence of such provisions may relegate the parties to the uncertainties of a foreign legal system or to a body of law and panel of decision-makers ill prepared to resolve the complexities of international petroleum transactions and oil and gas law.

**Choice of Law.** An agreement about what substantive law applies to a given transaction is essential to resolving disputes about contract interpretation, performance, and remedies. Choice of law clauses are generally upheld during dispute resolution, but enforceability depends on

whether the parties are subject to arbitration or litigation. In arbitration, the choice of law agreed to by the parties is almost always given effect to resolve disputes concerning the substance of the transaction. If the dispute is litigated or otherwise submitted to a court in a particular jurisdiction, most courts have a distinct body of law governing conflict of laws, which provide varying results based upon the particular court's evaluation of the choice of law clause, the transaction, and the public policies of the particular jurisdiction.

Common law principles applied in United States courts generally provide that the law chosen by the parties of a contract shall apply unless the chosen jurisdiction has no substantial relationship to the parties or transaction and there is no reasonable basis for the parties' choice, or unless application of the chosen law violates a fundamental policy or interest of a host country that has a materially greater interest. Admittedly, litigation under such common law principles may not provide certainty in enforcing choice of law clauses. Because other legal systems might raise even more questions concerning enforceability, arbitration is often the preferred dispute resolution method.

**Choice of Forum.** Forum selection clauses allow parties to select a particular group or court to hear their dispute. In the context of arbitration or other forms of ADR, the choice of forum clause is often included within a particular arbitration or ADR clause or is incorporated by reference to the governing arbitration or ADR rules of a specific institution that prescribes the place of hearing and related procedures. In litigation, as with choice of law clauses, there is some uncertainty whether choice of forum clauses will be upheld in all jurisdictions.

The general rule in most western nations is that forum selection clauses are valid and the party resisting enforcement of the clause must show fraud or establish that the circumstances make enforcement unreasonable or unjust before the party can avoid the clause. Of course, fundamental public policy concerns may be considered by a particular jurisdiction, but in the context of disputes between parties from different nations, most western courts generally limit public policy exceptions to situations in which the contractual forum chosen either won't hear the dispute on a fair and impartial basis or physical danger is associated with the chosen forum.

**17.8.2 Arbitration and Alternative Dispute Resolution (ADR).** Arbitration and other ADR systems are particularly suited to the resolution of conflicts in international petroleum transactions.<sup>14</sup> (For a concise introduction to international arbitration and ADR, as well as an exhaustive list of references and links, see [Ref. 14.](#)) Litigation is considered more expensive and arguably leads to more adversarial relationships rather than relationships that facilitate long-term development and cooperation typically associated with the development of international petroleum projects. Depending upon the arbitration clause and arbitration forum used, arbitration can offer a quicker, confidential, and binding resolution. A variety of pre-arbitral methods, including mediation, provide nonbinding alternatives to parties who wish to avoid litigation and arbitration.

**International Arbitration.** Parties may agree to *ad hoc* or institutional arbitration. *Ad hoc* arbitration involves arbitration proceedings chosen by the parties themselves in accordance with mutually agreed-upon rules and procedures. This type of arbitration requires the parties to assume the responsibilities of administering and planning the entire arbitration without the supervision of an established institution. The parties can specifically reference and adopt the arbitration rules of other associations. The United Nations Commission on International Trade Law (UNCITRAL) established arbitration rules without an institution that oversees the proceedings so that parties could either use the UNCITRAL rules in their own *ad hoc* proceedings or require the institution chosen to apply such rules. In *ad hoc* arbitration, there is no quality control and oversight by a reputable institution. While *ad hoc* arbitral awards are also observed by most parties and enforceable under the same laws discussed next, international courts may be more likely to intervene than if the arbitration were before an established institution.



In international petroleum transactions, parties more often choose or resort to institutional arbitration before any one of the many public and private institutions. The most recognized and respected institutions are the International Chamber of Commerce (ICC), the London Court of International Arbitration (LCIA), the American Arbitration Association (AAA), and the International Centre for the Settlement of International Disputes (ICSID), although there are countless other regional, local and industry-specialized arbitration forums.<sup>15-17</sup> (For a thorough discussion of these institutions and for helpful Internet links to other institutions and resources, see [Refs. 15 through 17](#).) These institutions provide a sophisticated forum allowing parties to resolve conflicts under established rules and procedures before arbitrators adept at applying international law and understanding different legal systems.

In 1985, the United Nations General Assembly adopted the Model Law on International Commercial Arbitration drafted by UNCITRAL. The model law was created to provide a uniform and common law of arbitration throughout the world with the goal of resolving the many inherent conflicts among various national arbitration laws. UNCITRAL's model arbitration law has served as the basis for many national arbitration statutes throughout the world and even for some state statutes in the United States. Until the majority of nations fully adopt UNCITRAL's model law on arbitration, there will be differences among the nations in interpreting and applying the arbitration rules chosen by the parties or the rules of a particular institution.

The actual process of arbitration varies depending upon the arbitration clause included in a particular contract and the rules and procedures promulgated by the arbitral institution chosen. Whether engaged in *ad hoc* or institutional arbitration, parties must resolve numerous procedural issues, including selection of arbitrators, number of arbitrators, the language used in the arbitral proceedings, and the procedures used for discovery and fact gathering. Institutional arbitration has been criticized because it has taken on more characteristics of litigation, becoming costly and time-consuming, and certain arbitration associations may not provide the expertise and industry knowledge sufficient to resolve disputes concerning complex international petroleum transactions. Increasingly, parties have looked to other forms of ADR to resolve their disputes in less formal environments that accommodate quicker resolution and foster continued business relationships.

***International Mediation and Other ADR.*** Before litigating or arbitrating a dispute, many parties choose mediation, conciliation, minitrial and other pre-arbitral and prelitigation alternatives. International mediation, a popular alternative among eastern cultures, is a formal process in which parties submit their dispute to a mutually agreed-upon third party or to a particular mediation or ADR organization chosen by the parties. Various international organizations have developed the general procedural rules for mediation, including the ICC, UNCITRAL, and the Commercial Arbitration and Mediation Center for the Americas (CAMCA). Conciliation is considered a less formal alternative to mediation and, unlike mediation, is used less for the purpose of obtaining a final settlement and agreement between the parties, and more for the purpose of maintaining communication between the parties. Like mediation, general procedural guidelines have been promulgated by various international organizations (e.g., the ICC Rules of Optional Conciliation) which are designed to assist the conciliation process and assure impartiality, equity and justice.

Other nonbinding ADR alternatives include the use of pre-arbitral referees and minitrials, which allow neutral parties to narrow the issues and assess the facts and law governing their dispute and provides the parties with an unbiased view of their respective strengths and weaknesses. There are many ADR centers throughout the world and offered by many international organizations. Alternatives are less likely to be drafted into international petroleum contracts but are increasingly popular to avoid initiating the lengthy and binding methods of arbitration and litigation.

**17.8.3 Enforcement of Judgments and Arbitral Awards.** The enforcement of judgments and arbitral awards is the final step in a dispute resolution process and can often be more problematic than litigating or arbitrating the dispute itself. Enforcement efforts usually require bilateral and multilateral agreements among countries. Obtaining satisfaction upon a judgment or award often involves efforts under different legal systems with varying public policies that can be cited to avoid enforcement or limit the satisfaction sought.

There is no settled international law requiring enforcement of foreign judgments, although many nations are either parties to various enforcement conventions and regional agreements or base enforcement upon principals of international comity and reciprocity embodied in their own national laws. The first of two significant sessions for the Hague Conference on Private International Law occurred from 6 June 2001 to 22 June 2001 in pursuit of a new Convention on Jurisdiction and Foreign Judgments in Civil and Commercial Matters. A finalized convention on enforcement of judgments is not expected until after the second session of The Hague Conference on Private International Law scheduled for the beginning of 2003.

Enforcement of judgments varies, depending upon the legal system of particular nations. As discussed in [Sec. 17.9](#), there are many differences between the civil code and common law legal systems. Whereas civil code nations have specific national laws governing recognition and enforcement of foreign judgments, courts in common law countries, such as the United States, will evaluate applicable statutes and analyze each situation based upon developed common law principles affecting jurisdictions, notice and due process, and fraud. Most nations, including those that are parties to bilateral and multilateral conventions or enforcement of foreign judgments, have public policy exceptions that allow the jurisdiction to avoid enforcement. The lack of certainty in enforcement of judgments and the lengthy process often required for obtaining satisfaction are additional reasons for parties to choose arbitration or other forms of ADR.

Like judgments, enforcement of arbitral awards is subject to bilateral and multilateral agreements among nations, but owing to the long history of arbitration as a successful method of resolving international disputes, arbitral awards are generally observed around the world by private parties and governments or state-owned entities. Arbitral awards are automatically enforceable in most countries under the 1958 United Nations Convention on the Recognition and Enforcement of Foreign Arbitral Awards, also known as the New York Convention. Where arbitral awards cannot be enforced under the New York Convention, the particular host nation's own domestic laws and other bilateral and regional agreements might provide a mechanism for enforcement. For example, many Latin American countries are not signatories to the New York Convention; however, most of the nations in Latin America have established national arbitration laws or are bound by the Inter-American Convention on International Commercial Arbitration (Panama Convention).

The international agreements and laws affecting enforcement have simple requirements, usually that the arbitration agreement be reduced to writing, signed by all parties, and that the parties had notice of the proceeding and a reasonable opportunity to participate. Conventions, including the New York Convention, have been ratified by countries subject to various public policy exceptions peculiar to each jurisdiction. For instance, many countries governed by Islamic Law maintain an affirmative defense to arbitral awards where a Muslim was not the arbitrator or included among the panel of arbitrators. Even where arbitral awards are recognized in a given jurisdiction, satisfaction of the award by means of seizure of property can prove impossible. This is especially true for assets and property related to exploration and development of a nation's natural resources, which might be protected under international law and principles of sovereignty, discussed next.

## 17.9 International Law and Legal Systems

Disputes in international petroleum transactions often involve a host country or national oil company. Because governments are often in conflict with other governments or private parties, a variety of international law considerations must be addressed, including national sovereignty, international treaties and conventions, the type of legal system used in a particular nation, and whether certain domestic laws have extraterritorial application.<sup>18</sup>

**17.9.1 Sovereignty.** Sovereignty refers to the right of a nation to control the people or things within its boundaries. It is recognized among all nations of the world that sovereignty extends to the nation's natural resources. Notwithstanding trends toward privatization, much of the world's natural resources remain publicly owned or controlled by governmental entities. Based upon their sovereignty, nations are free to change their legal regimes and laws governing natural resources and have the power to expropriate the property of foreign nationals doing business in their country. Examination of such expropriations or takings by host nations of the property and contractual rights of foreign nationals is precluded by various doctrines of international law. The act of state doctrine, a doctrine derived from the principal of sovereignty, requires courts to refrain from reviewing the official acts of other nations affecting matters and resources within that nation's borders.

International law also recognizes the doctrine of sovereign immunity. Sovereign immunity prohibits a nation and its state-owned entities from being sued in the courts of other nations absent express and implied waiver of such sovereign immunity. Sovereignty does not grant the license to violate international law and may not protect a nation or its governmental entities from claims related to international commerce. In the context of expropriation, the trend in international law is toward an international consensus that property should not be taken for public purposes without just compensation. While the world community may be far from adopting the takings jurisprudence applied in the United States, where governments must pay compensation for acquiring private property for public uses, many treaties and trade organizations recognize the basic principle. International law presently requires application of the expropriating nation's own domestic compensation laws before other nations can take actions in response to the expropriation of a foreign company's property.

When a dispute between citizens or corporations and a national oil company concerns a breach of contract or similar claim other than expropriation, many nations recognize a restrictive theory of sovereign immunity. The restrictive theory holds that when a sovereign nation is engaged in essentially private transactions, such as commercial contracts, there is less risk of interfering with the integrity of the nation. Several nations have statutes that adopt the restrictive theory of sovereign immunity. The United States applies the Foreign Sovereign Immunities Act (FSIA), which allows courts to find an express or implied waiver of sovereign immunity. Generally waiver is construed very narrowly under the FSIA, although the grounds for finding waiver are broader where the national oil company or governmental entity is engaged in worldwide mineral development or are otherwise parties to operating agreements and private contracts other than concessions. Significant petroleum transactions involving governments often stipulate an express waiver of sovereign immunity, and such waivers are generally upheld. The United Kingdom follows a law similar to the FSIA, the State Immunity Act of 1978, and the European Union (EU) has adopted the European Convention on State Immunity and Additional Protocol.

Even though modern laws and international agreements are changing to put all parties, including governments, on equal footing with respect to commercial transactions, there are still obstacles to litigating matters concerning a nation's development of its own natural resources. In addition to the act of state doctrine previously discussed, many courts deny jurisdiction or refuse to adjudicate international petroleum disputes that raise a political question. In these in-

stances, courts may recognize that the dispute is already subject to trade agreements or national policies, or that such disputes are more appropriately addressed through diplomacy.

**17.9.2 Treaties and Conventions.** International law is the body of principles and customs that nations recognize as binding on their mutual relations with one another. International agreements, customs, and general principles are the primary sources of international law. Treaties, conventions, pacts, accords, and protocols are all international agreements.<sup>19</sup> (For a thorough listing of international agreements, including helpful links for treaty research, see [Ref. 19](#).) Treaties may be either bilateral, an agreement between two nations, or multilateral, an agreement among several nations. Once signed by the participating countries, the treaties serve as a source of international law to resolve international disputes. Conventions are similar to treaties, but the term refers to larger groups of participating nations, and ratification of a particular convention represents the legal obligation of a participating nation to apply the convention.

The major treaties and conventions include the Vienna Convention on the Law of Treaties, governing how treaties become binding; the United Nations Convention on Contracts for the International Sale of Goods (CISG), establishing rules governing the formation of contracts and contractual remedies similar to the Uniform Commercial Code used in the United States; and the United Nations Convention on the Law of the Sea (UNCLOS), which sets forth generally accepted doctrines used to resolve boundary disputes. Other effective and generally accepted conventions include the New York Convention, as discussed, and other dispute resolution conventions, including the Convention on the Settlement of Investment Disputes Between States and Nationals of Other States drafted by the International Centre for Settlement Investment Disputes. Still other treaties and conventions exist to assist parties in gathering evidence during disputes. The 1970 Hague Convention on the Taking of Evidence Abroad in Civil or Commercial Matters includes the framework for service of judicial documents, and the 1970 Hague Evidence Convention provides alternative methods of discovery and evidence gathering. The brevity of this introduction to international law precludes an exhaustive list of treaties and conventions, particularly regional agreements that may affect operations and commerce in particular regions of the world.

**17.9.3 Civil Law and Common Law Systems.** The resolution of disputes, enforcement of judgments and arbitral awards, and the application of international law are significantly influenced by the type of legal system used in a particular nation.<sup>20</sup> The domestic law of a given nation or of two or three nations may need to be considered in international petroleum development transactions if the actual development occurs within the boundaries of a single nation but involves various multinational foreign corporations. Except for the peculiarities of a few legal systems, such as Islamic law, legal systems are either based upon the common law or civil law. These systems have different origins and traditions, and their basic distinctions should be understood to effectively resolve disputes.

The primary distinction between the common law system and civil law system is the scope of the judiciary and origins of law. In common law jurisdictions, the common law is created by the judiciary to address specific facts and circumstances, and detailed opinions are written to build accepted rules and principles that become precedent to assist in resolving future disputes. Legislation is limited to address specific social and economic matters.

Civil law systems limit the judiciary's role to interpretation of legislation and legislative principles evidenced in very thorough and complete civil codes created to address all issues that may arise. Courts in civil law jurisdictions, unlike common law courts, are not bound by their own prior decisions or by precedents set by other courts. The systems include other differences affecting how evidence is admitted and trials are conducted. For example, common law courts allow extensive discovery prior to trial, including depositions and interrogatories or otherwise limit out-of-court statements not under oath. Civil law courts do not have such strict

evidentiary rules, and discovery mechanisms such as depositions and interrogatories are not used to resolve disputes.

An understanding of these legal systems is imperative for the most beneficial selection of a governing law and forum for any dispute under an international petroleum development transaction.

#### **17.9.4 Foreign Corrupt Practices Act and Extraterritorial Application of Domestic Laws.**

The United States and a few other nations have domestic laws that expressly apply to the foreign conduct of its citizens. The most notable example of extraterritorial application of domestic law is the United States Foreign Corrupt Practices Act (FCPA) discussed in [Sec. 17.4](#).<sup>6,7</sup> The FCPA was passed to prevent bribery of foreign officials and to protect businesses from having competitors gain an advantage by offering bribes, although the FCPA has been criticized for putting U.S. companies at a significant disadvantage relative to other nations that do not have a similar law governing the foreign conduct of its companies. By its express terms, the FCPA applies to all types of business entities organized under the laws of the United States, including U.S. citizen employees of foreign companies.

Other examples of domestic laws with extraterritorial application include the Sherman Antitrust Act, which purports to govern conduct outside of the United States and even conduct of foreign companies in an effort to prevent monopolies and cartels from affecting interstate commerce. The antitrust laws of the United States do not apply to foreign conduct where the alleged anticompetitive activities do not have a direct, substantial and reasonably foreseeable effect on commerce in the United States. Also, the U.S. Justice Department may decline to pursue such foreign conduct for reasons of international comity. The EU adheres to a similar antitrust law with extraterritorial application known as Articles 85 and 86 of the Treaty of Rome.

The United States also applies its antiboycott law to conduct abroad. The Export Administration Act prohibits conduct that furthers a boycott of countries friendly to the United States for both U.S. citizens and corporations. By its express terms, the act applies to foreign subsidiaries controlled in fact by a U.S. citizen or corporation, although practical application of the act has been limited to Arab boycotts of Israel.

Many nations have laws authorizing export controls and other economic sanctions. As is the case for many world leaders, the President of the United States has the authority to regulate international commerce and property transactions during any declared national emergency under the International Emergency Economic Powers Act. From time to time, this act has been used to prohibit corporate citizens of the United States from doing business in specific countries. Similar economic sanctions have been used by other nations, although such foreign policy controls are far less used than in decades past because much of the world community has recognized the benefits of eliminating restraints on free trade.

---

## **References**

1. Yergin, D.: *The Prize: The Epic Quest for Oil, Money and Power*, Simon and Schuster, New York City (1993).
2. Smith, E., et al.: *International Petroleum Transactions*, Rocky Mountain Mineral Law Foundation, Denver (1993) Chaps. 5–6.
3. Smith, E.: “Typical World Petroleum Arrangements,” *International Resources Law: A Blueprint for Mineral Development*, Rocky Mountain Mineral Law Foundation, Denver (1991) Chap. 9, 9–1.
4. Darbonne, N. and Haines, L.: “Service or Oil Company?” *Hart’s Oil and Gas Investor* (July 1998) **18**, 28.
5. Clark, P. and Bain, L.: “International Project Due Diligence—What the Lawyer Can Do to Really Protect the Client’s Deal,” *45 Rocky Mountain Mineral Law Institute* (1999) Chap. 15, 15–1.

6. Duncan, C.: "Comment: The 1998 Foreign Corrupt Practices Act: Moral Empiricism or Moral Imperialism," *Asian-Pacific Law and Policy J.* (2000) **1**, No. 2, 87.
7. Schuchat, F.: "How to Succeed in International Business and Comply with U.S. Laws Prohibiting Corrupt Payments, Without Losing Out to Foreign Competition," *International Resources Law: Today's Oil, Gas, and Mining Projects*, Rocky Mountain Mineral Law Foundation, Denver (1997) Chap. 7A, 1.
8. Taylor, M., Tyne, S., and Windsor, T.: *Taylor and Windsor on Joint Operating Agreements*, second edition, London Group U.K. Ltd., London (1992).
9. Weems, P.: "Overview of Issues Common to Structuring, Negotiating, and Documenting LNG Projects," *Intl. Energy Law and Taxation Review* (2000) **8**.
10. "Decommissioning," U.K. Offshore Operations Association, [www.ukooa.co.uk/issues](http://www.ukooa.co.uk/issues) (see Environment menu).
11. The United Nations, U.N. Convention on the Law of the Seas, Article 60 (3) 1982.
12. *Rocky Mountain Mineral Law Foundation Special Institute on International Energy and Minerals Arbitration*, Rocky Mountain Mineral Law Foundation, Westminster, Colorado (2002).
13. Bishop, R.: "Drafting for International Dispute Resolution: Mediation, Forum Selection, and Arbitration Clauses," *44 Rocky Mountain Mineral Law Institute* (1998) Chap. 8, 8–1.
14. "ASIL Guide to Electronic Resources for International Law," The American Society of International Law, [www.asil.org/resource/arb1.htm](http://www.asil.org/resource/arb1.htm).
15. American Arbitration Association, [www.adr.org](http://www.adr.org).
16. The London Court of International Arbitration, [www.lcia-arbitration.com](http://www.lcia-arbitration.com).
17. International Chamber of Commerce, [www.iccwbo.org](http://www.iccwbo.org).
18. Smith, E., *et al.*: *International Petroleum Transactions*, second edition, Rocky Mountain Mineral Law Foundation, Denver (2000) Chaps. 1–2.
19. "ASIL Guide to Electronic Resources for International Law," The American Society of International Law, [www.asil.org/resource/treaty1.htm](http://www.asil.org/resource/treaty1.htm).
20. Arkin, H.: "Dispute Resolution: A Comparative Analysis Under Differing Legal Systems," *International Resources Law II: A Blueprint for Mineral Development*, Rocky Mountain Mineral Law Foundation, Westminster, Colorado (1995) Chap. 11, 1.

# Chapter 18

## The 21st Century Energy Mix

John R. Fanchi, Colorado School of Mines

### 18.1 Introduction

Energy demand is expected to grow during the next century as more countries seek a better quality of life for their citizens. Increasing trends in population and consumption, price volatility, supply instability, and environmental concerns are changing the energy mix and energy strategies in the 21st century. The energy mix is the set of energy sources that are used to meet energy demand. Energy demand will be met by a global energy mix that is transitioning from a mix dominated by fossil fuels to a more balanced energy portfolio.

The emerging energy mix will rely on clean energy. Clean energy refers to energy that has little or no detrimental impact on the environment. The goal is sustainable development—the integration of social and environmental concerns into development activities that optimize economic profitability and value creation as the world undergoes the transition from nonrenewable fossil fuels to renewable fuels and a sustainable, secure energy infrastructure.

This chapter presents an overview of energy sources available for use in the 21st century. Following the overview, a prediction of the contribution of hydrocarbon oil and gas to the 21st century energy mix is presented. This prediction is only one possible scenario selected from the literature for analysis. The scenario assumes a gradual transition from the dominance of fossil fuels in the current energy mix to a more balanced energy portfolio. The projected energy portfolio for the 21st century is presented, and the implications for society and the emergence of an energy industry are discussed.

### 18.2 Energy Options

The literature contains several sources, such as [Refs. 1 through 10](#), that present a description of the energy sources that are available or are expected to be available during the 21st century. Today's energy options include fossil fuels, nuclear energy, solar energy, renewable fuels, and alternative sources.

Fossil fuels are the dominant energy source in the modern global economy, but environmental concerns are prompting changes to an energy supply that is clean. Natural gas is a source of relatively clean energy. Oil and gas fields are considered conventional sources of natural gas. Two unconventional sources of natural gas are coalbed methane and gas hydrates.

Coalbeds are an abundant source of methane. Miners historically have known the presence of methane gas in coal as a safety hazard, but it is now being viewed as a source of natural

gas. Coalbed methane exists as a sorbed monomolecular layer on the internal surface of the coal. Its composition is predominantly methane but can also include other constituents, such as ethane, carbon dioxide, nitrogen, and hydrogen. The gas, which is bound in the micropore structure of the coalbed, can diffuse into the natural fracture network when a pressure gradient exists between the matrix and the fracture network. The fracture network in coalbeds consists of microfractures called cleats. Gas subsequently flows through the microfractures to the production well. (See the chapter on gas properties and correlations in this section of the Handbook for more information about methane.)

Gas hydrates are chemical complexes that form when one type of molecule completely encloses another type of molecule in a lattice. In the case of gas hydrates, hydrogen-bonded water molecules form a cage-like structure in which mobile molecules of gas are absorbed or bound. Although gas hydrates occur throughout the world, difficulties in cost-effective production have hampered development of the resource. Gas hydrates generally are considered troublesome for oil- and gasfield operations because they can reduce the flow capacity of wells and pipelines, but their potential commercial value as a clean energy resource is changing the industry perception. Gas hydrates have the potential to be a significant gas resource because of the relatively large volume of gas contained in the gas-hydrate complex. (See the chapters on phase behavior of water systems and water hydration in this section of the Handbook for more information about gas hydrates.)

Currently, nuclear fission provides nuclear energy. Nuclear fission is the process in which a large, unstable nucleus decays into two smaller fragments. Fission depends on a finite supply of fissionable material. Nuclear fusion is the combination, or fusing, of two small nuclei into a single larger nucleus. Many scientists expect nuclear energy to be provided by nuclear fusion sometime during the 21st century. The sun supplies energy through fusion reactions. Attempts to harness and commercialize fusion energy have been unsuccessful so far because of the technical difficulties involved in igniting, containing, and controlling a fusion reaction. Fusion energy is expected to contribute significantly to the energy mix by the end of the 21st century, even though a prototype commercial-scale nuclear reactor is not expected to exist until 2015 at the earliest.<sup>11</sup> Both fission and fusion reactions release large amounts of energy, including significant volumes of waste heat that must be dissipated and controlled. The decay products of the fission process can be highly radioactive for a long period of time, while the byproducts of fusion are relatively safe. One of the fission products, the plutonium isotope with atomic number 239, is of special concern because it is a radioactive material with a half-life of 24,000 years, and it can be used for creating nuclear weapons.<sup>6</sup> Half-life is the time it takes half of the nuclei in the radioactive sample to decay. Fusion byproducts, in contrast, include the stable, naturally occurring isotope of helium with atomic number 4 and short-lived neutrons.<sup>6</sup>

Solar energy is available in three forms: passive, active, and electric. Active and passive solar energy generally are used for space conditioning, such as heating and cooling. Active solar energy technologies are typically mechanical devices, such as solar hot-water heaters, that collect and distribute solar energy. Passive solar heating integrates building design with environmental factors enabling the capture of solar energy. A simple example is south-facing windows in a house. Solar electric devices, such as photovoltaic cells, convert sunlight into electricity. Groups of photovoltaic cells can provide electricity in quantities ranging from a few milliwatts to several megawatts and can power devices ranging from calculators to power plants. To get an idea of the scale of these values, a large color TV requires approximately 1 kilowatt of power, while a power plant for a modern city requires approximately 3 gigawatts.<sup>12</sup>

Renewable fuels range from hydroelectric and wind to synfuels and biomass.<sup>1,3</sup> The kinetic energy of wind and flowing water are indirect forms of solar energy and are considered renewable. Wind turbines harness wind energy, and hydroelectric energy is generated by the flow of



water through a turbine. Both convert the mechanical energy of a rotating blade into electrical energy in a generator.

The oceans are another solar-powered source of energy.<sup>3,6</sup> Waves and tides can be used to drive electric generators. Temperature gradients in the ocean exist between warm surface water and cooler water below the surface. If the temperature gradient is large enough, it can be used to generate power with ocean thermal-energy-conversion power plants. Similarly, temperature gradients and steam generated by geothermal sources can drive electric generators as a source of energy.

Biomass refers to wood and other plant or animal matter that can be burned directly or can be converted into fuel.<sup>1,3,6</sup> Historically, wood has been a source of fuel. Technologies now exist to convert plants, garbage, and animal dung into natural gas. Methanol, or wood alcohol, is a volatile fuel that has been used in racecars for years. Ethanol, which can be produced from sugarcane, can be blended with gasoline to form a blended fuel (gasohol) and used in conventional automobile engines or used as the sole fuel source for modified engines. Synthetic fuels (synfuels) are fossil fuel substitutes created by chemical reactions with such basic resources as coal or biomass. Synfuels are used as substitutes for conventional fossil fuels such as natural gas and oil.

There are several ways to convert biomass into synfuels. Oils produced by plants such as rapeseed (canola), sunflowers, and soybeans can be extracted and refined into a synthetic diesel fuel that can be burned in diesel engines. Thermal pyrolysis and a series of catalytic reactions can convert the hydrocarbons in wood and municipal wastes into a synthetic gasoline.

One difficulty with the exploitation of biomass fuels is the potential impact on the fertility of the region. For example, excessive use of dung and crop residues for fuel, instead of fertilizer, can deprive the soil of nutrients needed for future crops.

Synthetic liquid hydrocarbon fuels can be produced from natural gas by a gas-to-liquids (GTL) conversion process that consists of the following three major steps<sup>13</sup>:

- Natural gas is partially oxidized with air to produce synthetic gas (syngas).
- The synthetic gas is reacted in a Fischer-Tropsch (F-T) reactor to polymerize it into liquid hydrocarbons of various carbon-chain lengths.
- The heavy fraction of the F-T products is separated and cracked back to transportation fuels in a hydrocracking reactor.

The F-T process produces a hydrocarbon mixture with a range of molecular weight components by reacting hydrogen and carbon monoxide in the presence of a catalyst. The primary product of the GTL process is a low-sulfur, low-aromatic, high-cetane diesel fuel.<sup>13</sup>

Alternative sources of energy include hydrogen fuel cells and cogeneration. Hydrogen can be used as fuel for a modified internal combustion engine or in a fuel cell. Fuel cells are electrochemical devices that directly convert hydrogen or hydrogen-rich fuels into electricity through a chemical process. Fuel cells do not need recharging or replacing and can produce electricity as long as they are supplied with fuel. Hydrogen and oxygen are fuel-cell fuels that can be produced by the electrolysis of water. Ausubel<sup>14</sup> has suggested that the potential of nuclear energy will be realized when nuclear energy can be used as a source of electricity and high-temperature heat for splitting water into its constituent parts.

The environmental acceptability of hydrogen fuel cells depends on how the hydrogen is produced. If a renewable energy source such as solar energy is used to generate electricity for electrolysis, vehicles powered by hydrogen fuel cells would be relatively clean. Hydrogen combustion emits water vapor, but it also emits NO<sub>x</sub> compounds. Nitrogen dioxide (x=2) contributes to photochemical smog and can increase the severity of respiratory illnesses. The shipping and storage of hydrogen are important unresolved issues that hinder the widespread acceptance and implementation of hydrogen fuel-cell technology.

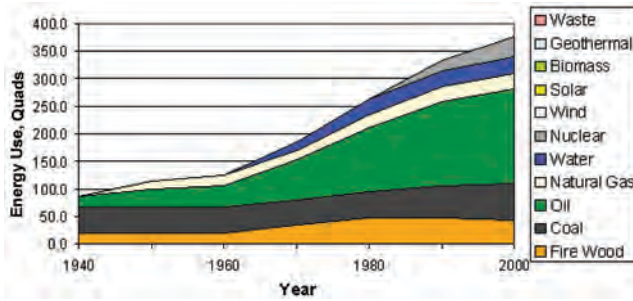


Fig. 18.1—Historical global energy consumption.

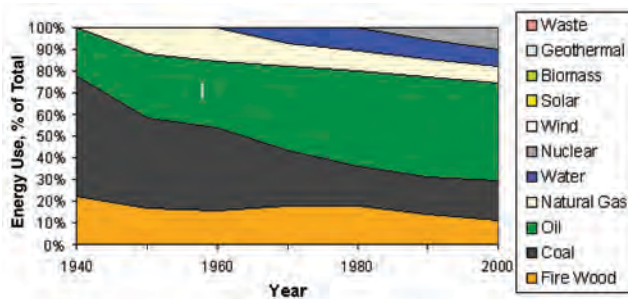


Fig. 18.2—Historical energy distribution as a percentage of total energy consumed.

Cogeneration is the simultaneous production of two or more sources of energy. The most common example of cogeneration is the simultaneous generation of electricity and useful heat. In this case, a fuel like natural gas can be burned in a boiler to produce steam. The steam drives an electric generator and is recaptured for heating or manufacturing. Cogeneration is most effective when the cogeneration facility is near the site where the excess heat can be used.

### 18.3 Energy Forecast

Several energy forecasts have appeared in the recent literature.<sup>13,15–21</sup> Although the assumptions, methods, and results presented in each of these predictions are debatable, they all show an energy infrastructure in transition. The trend in the 20th century has been a move away from fuels with many carbon atoms to fuels with few or no carbon atoms. This decarbonization process is discussed by Ford<sup>13</sup> and Ausubel.<sup>14</sup> Ausubel defines decarbonization as “the progressive reduction in the amount of carbon used to produce a given amount of energy.” Two energy forecasts are discussed here. One is a projection of world energy consumption through 2100, published by Schollnberger.<sup>15</sup> Schollnberger’s forecast of world oil production is compared with a projection that uses a different method.

Energy forecasts rely on projections of historical trends. **Figs. 18.1 and 18.2** are based on data presented by Schollnberger<sup>15</sup> and show the dominance of fossil fuels in the energy mix at the end of the 20th century. **Fig. 18.1** shows historical energy consumption in quads, a unit of energy that is often used in global energy discussions because it is comparable in magnitude to global energy values. One quad equals one quadrillion BTU, or  $10^{15}$  BTU. In SI units, one quad is approximately  $10^{18}$  J. Beginning at the bottom of **Fig. 18.1**, we see that firewood, coal, oil, natural gas, water, and nuclear energy were the major contributors to energy in the latter half of the 20th century.

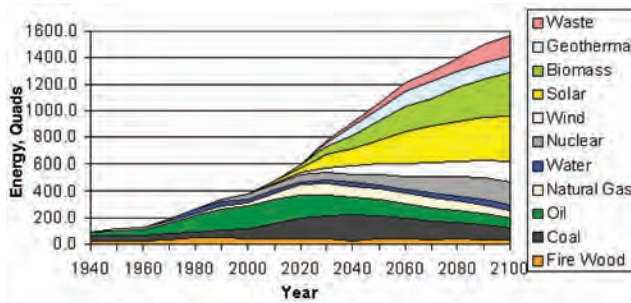


Fig. 18.3—Forecast of a 21st century energy portfolio under Scenario C.

Fig. 18.2 illustrates the dominance of fossil fuels in the energy mix at the end of the 20th century as a percent of total energy consumed. For example, oil accounted for approximately 22% of world energy consumed in 1940 and approximately 45% of world energy consumed in 2000. Schollnberger’s estimate for 2000 was a projection<sup>15</sup> from historical data that was complete through the end of 1996. According to the U.S. Energy Information Agency (EIA),<sup>16</sup> actual oil consumption was approximately 40% of world energy consumed in 2000. This shows that Schollnberger’s forecast overestimated oil consumption over a relatively short forecast of 4 years; however, Schollnberger’s focus was on long-term trends, not short-term forecasting. In addition, Schollnberger was more interested in the combined forecast of oil and gas consumption or demand because gas can be substituted for oil in many instances. If we combine oil and gas, Schollnberger forecast oil and gas consumption to be approximately 53% of world energy consumed in 2000, while EIA statistics show oil and gas consumption to be approximately 62% of world energy consumed. From this perspective, Schollnberger underestimated oil and gas consumption in 2000.

Schollnberger’s<sup>15</sup> forecasts were designed to cover the entire 21st century and predict the contribution of a variety of energy sources to the 21st century energy portfolio. Schollnberger<sup>15</sup> considered three forecast scenarios:

- A. “Another century of oil and gas” corresponding to continued high hydrocarbon demand.
- B. “The end of the internal combustion engine” corresponding to a low hydrocarbon demand scenario.
- C. “Energy mix” corresponding to a scenario with intermediate demand for hydrocarbons and an increasing demand for alternative energy sources.

Schollnberger views Scenario C as the most likely scenario. It is consistent with Smil’s observation<sup>22</sup> that, historically, the transition from one energy source to another has taken several generations. Leaders of the international energy industry have expressed a similar view that the energy mix is undergoing a shift from liquid fossil fuels to other fuel sources.<sup>23,24</sup>

There are circumstances in which Scenarios A and B could be more likely than Scenario C. For example, Scenario B would be more likely if environmental issues led to political restrictions on the use of hydrocarbons and an increased reliance on conservation. Scenario B would also be more likely if the development of a commercially competitive fuel cell for powering vehicles reduced the demand for hydrocarbons as a transportation fuel source. Failure to develop alternative technologies would make Scenario A, which assumes that enough hydrocarbons will be supplied to meet demand, more likely.

Scenario C shows that natural gas will gain importance as the economy shifts from a reliance on hydrocarbon liquid to a reliance on hydrocarbon gas. Eventually, renewable energy sources such as biomass and solar will displace oil and gas (see Fig. 18.3).

Society’s demand for petroleum fuels should continue at or above current levels for a number of years, but the trend seems clear (see Fig. 18.4). The global energy portfolio is undergo-

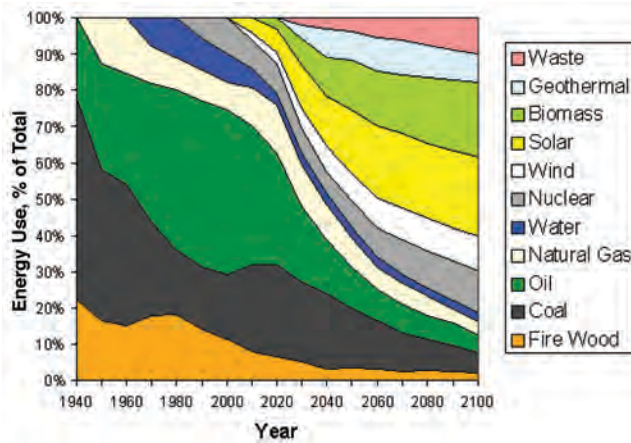


Fig. 18.4—Energy distribution as a percentage of total energy consumed under Scenario C.

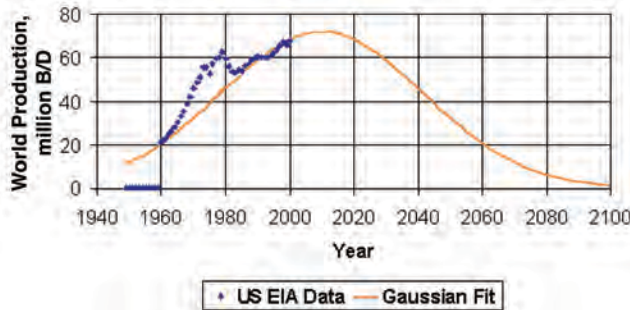


Fig. 18.5—Oil forecast with Gaussian curve.

ing a transition from an energy portfolio dominated by fossil fuels to an energy portfolio that includes a range of fuel types. Schollnberger's Scenario C presents one possible energy portfolio, and Fig. 18.4 illustrates the historical and projected energy consumption trends.

Schollnberger's forecast is based on demand. An alternative approach is to base the forecast on supply. Beginning with Hubbert,<sup>25</sup> several authors have noted that annual U.S. and world oil production approximately follows a bell-shaped (Gaussian) curve. Analyses of historical data typically predict that world oil production will peak in the first decade of the 21st century,<sup>17,20,21,26–30</sup> and that cumulative world oil production will range from 1.8 to 2.1 trillion barrels.<sup>21</sup> Note that Laherrère<sup>17,29,30</sup> used proprietary reserves data for non-U.S. fields from a consulting firm's database to prepare his forecasts.

Forecasts based on Gaussian fits to historical data can be checked readily with publicly available data. Fig. 18.5 shows a Gaussian curve fit of world oil production data from the U.S. EIA database. The fit is designed to match the most recent part of the production curve most accurately. This gives a match that is similar to Deffeyes.<sup>21</sup> The peak oil-production rate in Fig. 18.5 occurs in 2010, and cumulative oil production by year 2100 is a little less than 2.1 trillion barrels.

If a Gaussian fit of historical data is accepted as a reasonable method for projecting oil production, future oil-production rates can be estimated as a percentage of the oil-production rate in the year 2000. Fig. 18.6 shows this estimate. According to this approach, world oil

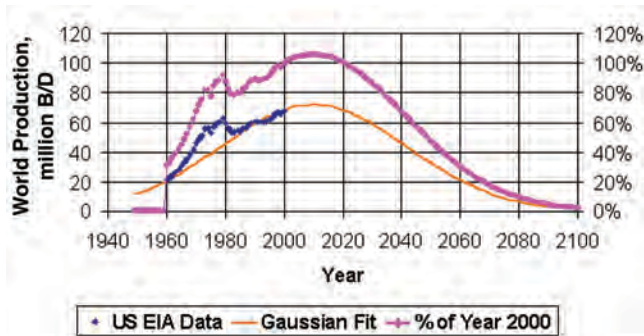


Fig. 18.6—Oil forecast as a percentage of oil consumed in 2000 with Gaussian curve.

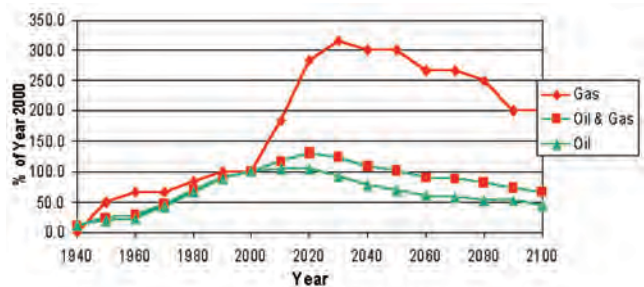


Fig. 18.7—Oil and gas forecast under Scenario C as a percentage of the amount consumed in 2000.

production will decline by the middle of the 21st century to 50% of the 2000 world oil-production rate. This forecast can be compared with Schollnberger’s Scenario C.

According to Scenario C, fossil fuel consumption will increase relative to its use today until about the middle of the 21st century, when it will begin to decline (see Fig. 18.7). By the end of the 21st century, fossil fuel consumption will be approximately 70% of what it is today. Gas consumption will be considerably larger, while oil consumption will decline to approximately one-half. This illustrates the range of uncertainty in existing forecasts. A more immediate test of forecast validity is the peak of world oil production.

Forecasts of the world oil-production peak tend to shift as more historical data is accumulated. Laherrère<sup>29</sup> points out that curve fits of historical data should be applied to activity that is “unaffected by political or significant economic interference, to areas having a large number of fields, and to areas of unfettered activity.” Furthermore, curve-fit forecasts work best when the inflection point (or peak) has passed.

### 18.4 Changing Industry Policy

One of the most pressing environmental concerns facing the world today is global climate change. A purported cause of adverse global climate change is the greenhouse effect. Increasing levels of carbon dioxide and other greenhouse gases such as methane in the atmosphere absorb infrared radiation rather than letting it escape into space. The resulting atmospheric heating is attributed to excessive emissions of carbon dioxide into the atmosphere. Although the evidence for global climate change and its implications for society are in dispute,<sup>31–35</sup> the petroleum industry is considering methods for mitigating the emission of greenhouse gases.

One way to reduce the emission of carbon dioxide into the atmosphere is to collect and store carbon dioxide in oil and gas reservoirs as part of a process known as CO<sub>2</sub> sequestration.

The goal of CO<sub>2</sub> sequestration, as stated by the U.S. Dept. of Energy, is to provide economically competitive and environmentally safe options to offset all projected growth in baseline emissions of greenhouse gases.<sup>36</sup> Carbon sequestration programs are designed to reduce the climatic greenhouse effect by collecting and storing carbon dioxide in nonatmospheric sites. Sequestration of greenhouse gases is part of the more general problem of sustainable development.<sup>37,38</sup>

The goal of sustainable development is to integrate social and environmental concerns into a development plan that optimizes economic profitability and value creation. One industry response to environmental and social concerns in the context of sustainable development<sup>38</sup> is the “triple bottom line.” The three components of sustainable development and the three goals of the triple bottom line are economic prosperity, social equity, and environmental protection. The focus of the triple bottom line is the creation of long-term shareholder value by recognizing that corporations are dependent on licenses provided by society to do business. In this regard, major energy companies<sup>39,40</sup> are undertaking the task of developing methods for determining the extent of greenhouse gas emissions that result from their activities. This positive step indicates the recognition by energy companies that environmental issues are legitimate resource management concerns.

One of the key elements of the triple bottom-line policy is the development and implementation of strategies that will enable the energy industry to meet future global energy needs and environmental objectives. Studies show that energy consumption correlates positively to quality of life,<sup>13,40</sup> with quality of life measured by such factors as infant mortality, literacy, life expectancy, and university attendance. Cassidy and Grossman<sup>1</sup> provide a good discussion of two diametrically opposed ethical positions that apply to the global distribution of energy.<sup>7</sup> Their discussion is outlined in the following section to illustrate some of the issues that may affect the business decisions of global energy industry organizations.

### **18.5 Ethical Issues in Energy Distribution**

According to Cassidy and Grossman,<sup>1</sup> future energy distribution will be affected by the distribution of energy between nations with a large per-capita energy base and those without. Traditional ethics would favor a policy of helping those nations without energy resources, but opinions differ on how to proceed. Two of the more important ethical positions being considered are “lifeboat ethics” and “spaceship ethics.”

Proponents of lifeboat ethics oppose the transfer of wealth by charitable means. In this view, the more developed industrial nations are considered rich boats and the less developed, overcrowded nations are poor boats. The rich boats should not give the poor boats energy because their help would discourage the poor boats from making difficult choices about issues such as population control and investment in infrastructure. Lifeboat ethics is a “tough love” position.

Proponents of spaceship ethics argue that everyone is a passenger on spaceship Earth. In this view, some passengers travel in first class while others are in steerage. A more equitable distribution of energy is needed because it is morally just and it will prevent revolts and social turmoil. Thus, the wealthy should transfer part of their resources to the poor for both moral and practical reasons. If the size of the resource is increased, the need for sacrifice will be lessened.

### **18.6 Implications for Engineers**

In an attempt to respond to market realities, some oil and gas companies and electric power companies are beginning to transform themselves into energy companies. The trend is expected to continue,<sup>13,15,41</sup> and these companies will be pioneers in the emerging energy industry.

Improvements in technology and an increasing reliance on information require a high level of technical expertise to acquire resources on behalf of society. To meet the technical demands,

Walesh<sup>42</sup> predicts that engineers will need periods of dedicated learning or retraining between periods of full-time employment throughout their careers. Engineers in energy companies will need to understand and appreciate the role of alternative energy components in the energy mix. They will need to be able to identify and solve problems in the acquisition and environmentally acceptable use of several energy components. This will give engineers additional flexibility and help them thrive in an energy industry that is evolving from an industry dominated by fossil fuels to an industry working with many energy sources.

## 18.7 Conclusions

Fossil fuel (e.g., coal, oil, and gas) was the fuel of choice during the last half of the 20th century. The 21st century will see a gradual transition from the dominance of fossil fuels in the current energy mix to a more balanced energy portfolio.<sup>43</sup> The goal is to integrate social and environmental concerns into a development plan that optimizes economic profitability and value creation as the world undergoes the transition from the use of nonrenewable fossil fuels to the use of renewable fuels and the creation of a sustainable, secure energy infrastructure.

## Acknowledgments

I would like to thank Ken Lerner, Don Williamson, and Wolfgang Schollnberger for their comments.

---

## References

1. Cassedy, E.S. and Grossman, P.Z.: *Introduction to Energy*, second edition, Cambridge U. Press., Cambridge, U.K. (1998).
2. Khartchenko, N.V.: *Advanced Energy Systems*, Taylor & Francis, Washington, DC (1998).
3. Ristinen, R.A. and Kraushaar, J.J.: *Energy and the Environment*, Wiley, New York (1999).
4. Thumann, A. and Mehta, D.P.: *Handbook of Energy Engineering*, fourth edition, Fairmont Press, Lilburn, Georgia (1997).
5. Selley, R.C.: *Elements of Petroleum Geology*, Academic Press, San Diego, California (1998).
6. Kraushaar, J.J. and Ristinen, R.A.: *Energy and Problems of a Technical Society*, second edition, Wiley, New York (1993).
7. Guyot, G.: *Physics of the Environment and Climate*, Wiley, New York (1998) 123–130.
8. Mihelcic, J.R.: *Fundamentals of Environmental Engineering*, Wiley, New York (1999).
9. Pielou, E.C.: *The Energy of Nature*, U. Chicago Press, Chicago (2001).
10. Fanchi, J.R.: *Energy: Technology and Directions for the Future*, Elsevier-Academic Press, Boston, Massachusetts (2004) Chap. 15.
11. Morrison, P. and Tsipis, K.: *Reason Enough to Hope*, MIT Press, Cambridge, Massachusetts (1998) 162–171.
12. Smil, V.: *General Energetics*, Wiley, New York (1991).
13. “Petroleum in the 21st Century,” *Oil & Gas J.* (13 December 1999) 3.
14. Ausubel, J.H.: “Where is Energy Going?” *The Industrial Physicist* (February 2000) 16.
15. Schollnberger, W.E.: “Projection’s of the World’s Hydrocarbon Resources and Reserve Depletion in the 21st Century,” *Houston Geological Soc. Bull.* (November 1998) 31.
16. “International Energy Outlook—2001,” report DOE/EIA-0484, Office of Integrated Analysis and Forecasting, U.S. DOE, Washington, DC (2001).
17. Laherrère, J.H.: “World Oil Supply—What Goes Up Must Come Down, But When Will It Peak?” *Oil & Gas J.* (1 February 1999) 57.
18. Campbell, C.J. and Laherrère, J.H.: “The End of Cheap Oil,” *Scientific American* (March 1998) 78.
19. Taylor, P.J.: “Modeling the U.S. Oil Industry: How Much Oil is Left?” *JPT* (May 1997) 502.
20. Al-Jarri, A.S. and Startzman, R.A.: “Worldwide Petroleum-Liquid Supply and Demand,” *JPT* (December 1997) 1329.

21. Deffeyes, K.S.: *Hubbert's Peak—The Impending World Oil Shortage*, Princeton U. Press, Princeton, New Jersey (2001) 147.
22. Smil, V.: *Energies*, MIT Press, Cambridge, Massachusetts (1999) 133–173.
23. Fletcher, S.: "Industry Leaders See Challenges Ahead for Energy Business," *Oil & Gas J.* (19 February 2001) 24.
24. Truly, R.H.: "How Will We Meet the Future: Transitions to New Energy Frontiers," Natl. Academy of Engineering Technical Symposium, 9 October 2001.
25. Hubbert, M.K.: "Nuclear Energy and the Fossil Fuels," *Proc.*, API Drilling and Production Practice, San Antonio, Texas (1956) 7–25.
26. Ivanhoe, L.F.: "Future World Oil Supplies: There Is a Finite Limit," *World Oil* (1995) 77.
27. Ivanhoe, L.F.: "Updated Hubbert Curves Analyze World Oil Supply," *World Oil* (1996) 91.
28. Campbell, C.J. and Laherrère, J.H.: "The End of Cheap Oil," *Scientific American* (March 1998) 83.
29. Laherrère, J.H.: "Learn Strengths, Weaknesses To Understand Hubbert Curves," *Oil & Gas J.* (17 April 2000) 63.
30. Laherrère, J.H.: letter in *Oil & Gas J.* (1 March 1999).
31. Weart, S.R.: "The Discovery of the Risk of Global Warming," *Physics Today* (January 1997) 34.
32. "CO<sub>2</sub> and Global Warming," *Oil & Gas J.* (4 September 2000) 29.
33. Gerhard, L.C. and Hanson, B.M.: "Ad Hoc Committee on Global Climate Issues: Annual Report," *AAPG Bulletin* (2000) **84**, 466.
34. Malin, C.B.: "Petroleum Industry Faces Challenge of Change in Confronting Global Warming," *Oil & Gas J.* (28 August 2000) 58.
35. Grossman, D.: "Dissent in the Maelstrom," *Scientific American* (November 2001) 38.
36. "Carbon Sequestration Research and Development," U.S. DOE, Washington, DC (December 1999), [www.ornl.gov/carbon\\_sequestration/](http://www.ornl.gov/carbon_sequestration/).
37. Whittaker, M.: "Emerging 'Triple Bottom Line' Model for Industry Weighs Environmental, Economic, and Social Considerations," *Oil & Gas J.* (20 December 1999) 23.
38. Bradley, A.S. and Hartog, J.J.: "Sustainable Development—Implementation Strategy for a Global E&P Business," *JPT* (October 2000) 66.
39. Brush, R.M. *et al.*: "Immiscible CO<sub>2</sub> Flooding for Increased Oil Recovery and Reduced Emissions," paper SPE 59328 presented at the 2000 SPE/DOE Improved Oil Recovery Symposium, Tulsa, Oklahoma, 3–5 April.
40. Skov, A.M.: "National Health, Wealth, and Energy Use," *JPT* (May 1999) 48.
41. Hamto, M.: "Fuel-Cell Technology to Provide Clean, Sustainable Energy," *JPT* (April 2000) 26.
42. Welsh, S.G.: *Engineering Your Future*, Prentice Hall, Englewood Cliffs, New Jersey (1995) 395.
43. Fanchi, J.R.: *Energy in the 21st Century*, World Scientific, Singapore (2005) Chap. 10.

### SI Metric Conversion Factors

Btu ×	1.055 056	E + 00	=kJ
kW-hr ×	3.6*	E + 06	=J
quad ×	1.055 056	E + 12	=J

\*Conversion factor is exact.



# AUTHOR INDEX

- A**  
Abdul-Majeed, G.H., 288, 316, 319, 329, 331  
Abou-Kassem, J.H., 227–228  
Adewumi, M.A., 414  
Agarwal, R.G., 742  
Ahmed, T.H., 276, 316, 319–320, 322  
Ahmed, U., 708  
Akin, S., 746  
Ali, M.A., 422–426  
Alikhan, A.A., 268, 276  
Almehaideb, R.A., 268, 280–281, 312–331  
Alpak, F.O., 736, 750–751  
Altunbay, M., 717–718  
Amaefule, J.O., 717–718  
Ammons, Dustin M., 809–830  
Anderson, Scot W., 809–830  
Andrade, E.N., 323, 325  
Anli, J., 736  
Antikarov, V., 799, 801, 804  
Archer, D.L., 737–738  
Asgarpour, S., 268, 311, 314, 316, 319  
Ashby, W.H., Jr., 481  
Asheim, H., 285  
Atkinson, B.K., 659  
Ausubel, J.H., 834  
Aziz, K., 228–229, 231, 238
- B**  
Baker, L.E., 751–752  
Baker, O., 286–288  
Baldwin, B.A., 756–757  
Ball, B.C., 797  
Barenblatt, G.E., 124, 126  
Barnum, R.S., 741  
Bass, D.M., Jr., 687  
Batzle, Michael L., 571–685, 687–726  
Beal, C., 279, 323, 325, 329, 331  
Beard, D.C., 689–690, 702–703, 705, 721  
Becher, P., 533  
Becker, A.B., 792–793, 800  
Beggs, H.D., 268, 279, 286, 310, 314–331  
Bennion, D.W., 738  
Bennison, T., 279, 324–325  
Bentsen, R.G., 736  
Berg, R.R., 703–704, 721  
Bergman, D.F., 324–328  
Bethel, F.T., 732, 741  
Bienlawski, Z.T., 645, 647  
Bingham, Mark D., 809–830  
Biot, M.A., 638–639, 656  
Birch, F., 571  
Black, F., 799–802  
Blumer, David J., 465–497  
Bobra, M., 544  
Borgia, G.C., 709  
Box, M.R.E., 693  
Brace, W.F., 657, 701–702  
Brashear, J.P., 792–793, 800  
Brooks, R.H., 731, 735–736, 746–747  
Brown, D.L., 592  
Brown, E.T., 645–651, 662  
Brown, G.G., 227  
Brown, R., 623  
Brown, T.S., 442  
Brulé, M.R., 266, 268, 284–285  
Brunner, E., 756  
Bryant, S., 705  
Buckley, J.S., 414, 427–429  
Budiansky, B., 638–639  
Burke, N.E., 411, 414  
Burnett, E.S., 224
- C**  
Cade, C., 705  
Calhoun, J.C., Jr., 320, 322, 732, 741  
Calingeart, G., 242–243  
Capen, E.C., 779  
Carlson, F.M., 749  
Carman-Kozeny models, 749–750  
Carmichael, R.S., 571  
Carr, N.L., 236–240  
Carr, P.P., 803  
Carslaw, H.S., 101  
Cassedy, E.S., 838  
Castagna, J.P., 571, 611  
Chatzis, I., 740–741, 745  
Chen, C.T., 593  
Chen, H.-Y., 123  
Chen, Z.A., 756  
Cheng, C.H., 633  
Chevallier, V., 407  
Chew, J., 280, 326, 328  
Chierici, G.L., 748–749  
Chorn, L.G., 803  
Chou, J.C.S., 479, 592  
Christiansen, Richard L., 727–765  
Christman, P.G., 268–269, 276, 313–314, 318–331  
Christoffersen, K.R., 755  
Cimino, R., 415  
Civan, F., 426  
Clark, S.P., 571  
Clark, V.A., 638  
Clementz, D.M., 427  
Coalson, E.B., 714  
Coates, G.R., 662, 708  
Colback, P.S.B., 659  
Cole, K.S., 638  
Cole, R.H., 638  
Collins, R.E., 424–426  
Collins, S.H., 427  
Connally, J.A., Jr., 280, 326, 328  
Cook, N.G., 595  
Copeland, T., 799, 801, 804  
Corbett, K., 654  
Corey, A.T., 731, 735–736, 746–747  
Costain, T.G., 414  
Coutinho, J.A.P., 447–449  
Cox, E.R., 242  
Crocker, M.E., 427  
Crump, K.S., 88
- D**  
Daubert, T.E., 260  
Davidson, L.B., 803–804  
Davis, D.S., 242–243  
Davis, Graham, 801  
de Boer, R.B., 414–415  
Deere, D.U., 662

DeFreitas, M.H., 652–653, 660  
 De Ghetto, G., 268, 276, 312, 314, 320–331  
 Denoo, S.A., 662  
 de Swaan-O, A., 124, 126  
 Dickens, R.N., 801  
 Dindoruk, B., 268–269, 276, 313–314, 318–331  
 Dirand, M., 407  
 Dixit, A.K., 801–803  
 Dobereiner, L., 652–653, 660–661  
 Dokla, M.E., 268, 271, 311, 314, 316, 319  
 Dorset, D.L., 407  
 Dorsey, N.E., 479  
 Dotson, C.R., 479  
 Drake, Edward, 465  
 Dranchuk, P.M., 227–228  
 Dubey, S.T., 423  
 Duffy, J., 613  
 Duhamel, J.M.C., 121  
 Dunning, J.D., 659  
 Dvorcik, J., 638–639

**E**

Eberhart-Phillips, D., 613  
 Egbogah, E.O., 323, 325  
 Elam, F.M., 310, 314–315, 319  
 Elsharkawy, A.M., 268, 276, 313–314, 317–331  
 Embid, S.M., 736  
 Erdogan, M., 781  
 Erickson, D.D., 442–443  
 Eshelby, J.D., 632  
 Euchner, J.A., 435, 452  
 Eustes, Alfred W., III, 1–43

**F**

Fanchi, John R., 45–76, 831–840  
 Farshad, F.F., 269, 274, 276, 311, 314, 317–322  
 Faulder, D.D., 792–793, 800  
 Fayers, F.J., 751–752  
 Federov, M.K., 592–593  
 Fettke, C.R., 466  
 Finol, J., 719–720  
 Firoozabadi, A., 289, 421  
 Fitzgerald, D.J., 280, 324–325  
 Flock, D.L., 746  
 Fotland, P., 409  
 Fu, J.C., 411

**G**

Garb, F.A., 802  
 Garrison, A.D., 466  
 Gassmann, F., 613  
 Gibbs, J.W., 333–337  
 Glasø, O., 261, 267, 271–274, 292, 310, 314–315, 319, 323, 325  
 Godbole, S.P., 417  
 Gordon, W.C., 466  
 Granberry, R.J., 706, 713  
 Gregory, A.R., 571, 616  
 Griggs, D.T., 659  
 Gringarten, A.C., 110, 114  
 Griswold, W.T., 465  
 Grossman, P.Z., 838  
 Gruesbeck, C., 424–426  
 Gruy, H.J., 802

**H**

Hall, K.R., 227  
 Hammami, A., 409–410, 415  
 Han, D.-H., 571–685

Hansen, J.H., 417, 442, 449  
 Hartmann, D.J., 714  
 Hasan, M., 270, 312, 314  
 Hasin, Z., 601–602  
 Hassler, G.L., 756  
 Hawkins, M.F., 481  
 Helgeson, H.C., 594  
 Henderson, J.H., 741–742  
 Herron, M.M., 705  
 Hirschberg, A., 401, 409, 411, 413–415, 421  
 Hoek, E., 645–651, 662  
 Hofmann, R., 571–685  
 Holm, L.W., 428  
 Honarpour, M., 749  
 Hooper, H.T., III, 804  
 Howell, J.I., III, 798  
 Huang, E.T.S., 428  
 Hubbert, M.K., 596  
 Hudson, J.A., 633  
 Huff, W.L., 659  
 Hurst, W., 94

**I**

Ibrahim, M.N.M., 749  
 Islam, M.R., 422–427

**J**

Jacobson, H.A., 271, 273, 292  
 Jaeger, J.C., 101, 642  
 Jamaluddin, A.K.M., 409  
 Jeager, J.C., 595  
 Jerauld, G.R., 733  
 Jessen, K., 371–396  
 Jing, X.-D.D., 719–720  
 Jizba, D.L., 652–655  
 Johns, R.T., 333–369  
 Johnston, D., 802  
 Jones, 470  
 Joshi, N.B., 402, 409–410  
 Jukerji, T., 620

**K**

Kamath, V.A., 422, 427–428  
 Kartoatmodjo, R.S.T., 268, 274, 276, 311–331  
 Katahara, K.W., 629, 671  
 Katz, A.J., 714–718, 721  
 Katz, D.L., 227–228, 525, 741  
 Kawanaka, S., 415  
 Kay, W.B., 224, 237  
 Kazemi, H., 124, 126  
 Keating, J.F., 452  
 Keelan, D.K., 706, 713  
 Keenan, J.H., 592  
 Kelgeson, H.C., 592  
 Kelvin, W.T., 101  
 Kesler, M.G., 243–244  
 Kestin, J., 484  
 Khairy, M., 313–314, 317, 319  
 Al-Khafaji, A.H., 279, 323, 325–331  
 Al-Khalsiy, K.M., 311, 314  
 Khan, S.A., 280, 326, 328–329, 331  
 Killough, J.E., 749  
 King, M.J., 745  
 Kirby, S.H., 659  
 Kirkham, D.H., 592, 594  
 Klimentos, T., 640  
 Kocabas, I., 426–427  
 Kohse, Bruce F., 397–464  
 Kokal, Sunil L., 173–215, 414, 533–570

Kolodzie, S., Jr., 714  
 Korringa, J., 623  
 Kouzel, B., 329–331  
 Krumbein, W.C., 702–703  
 Kuster, G.T., 633–634  
 Kwong, J.N.S., 361–364, 413–415, 417, 438, 443–444

**L**

Labedi, R.M., 280, 310, 314–315, 319–331  
 Lake, Larry W., 705, 736, 743, 839  
 Lama, R.D., 571  
 Land, C.S., 742  
 Lane, A.C., 466  
 Larner, Ken, 839  
 Larsen, L.L., 390  
 Lasater, J.A., 261, 267, 292, 310, 314  
 Lee, A.L., 237–238  
 Lee, B.I., 243–244  
 Lee, R.L., 741  
 Leontaritis, K.J., 401, 420, 426–427  
 Leung, P.K., 654, 657  
 Leverett, M.C., 734–735  
 Levitan, L.L., 313–314, 317, 319  
 Li, Y.-K., 417–418  
 Lin, E.C., 428  
 Lira-Galeana, C., 444–446  
 Loh, J., 526  
 Lohrenz, J., 801  
 Lucia, F.J., 695

**M**

Macary, S.M., 311, 314, 317, 319  
 McCaffery, F.G., 738  
 McCain, W.D., Jr., 478, 481, 483, 485–486  
 McKetta, J.J., 501  
 MacMillan, D.J., 416–417  
 Al-Maamari, R.S.H., 428–429  
 Makogon, Y.F., 528  
 Mansoori, G.A., 420  
 Marchin, L.M., 427  
 Al-Marhoun, M.A., 270–271, 274, 276, 310–311, 314–322  
 Markowitz, Harry, 792  
 Martin, A.J., 714  
 Martin, R.J., 657  
 Masliyah, J.H., 417  
 Mattar, L., 234  
 Matthews, J.D., 751  
 Mavko, G., 571, 620, 623  
 Mei, H., 441  
 Melrose, J.C., 427, 729  
 Meredith, P.G., 659  
 Merton, R.C., 799  
 Metcalfe, R.S., 386–387  
 Miller, R.P., 662  
 Millero, F.J., 593  
 Mindlin, R.D., 613  
 Minssieux, L., 422–423, 426  
 Monger, T.G., 411  
 Monk, G.D., 702–703  
 Morgenstern, N.R., 660–661  
 Morrow, N.R., 428, 703, 729, 733, 738, 741  
 Mortensen, J., 695  
 Munn, M.J., 465–466  
 Murphy, W.F., 638  
 Murrell, S.A.F., 647  
 Murtha, M., 313–314, 317, 319, 789  
 Muskat, M., 729

**N**

Naar, J., 741–742  
 Al-Najjar, H.S., 268, 311, 314, 316, 319  
 Nelson, Philip H., 687–726  
 Nelson, R.A., 661  
 Newendorp, Paul, 783, 785, 792  
 Newman, A.B., 110, 113–114, 116, 120  
 Ng, J.T.H., 323, 325  
 Nghiem, Long X., 397–464  
 Nichita, D.V., 446, 449  
 Nisle, R.G., 103  
 Nolen-Hoeksema, R.C., 620  
 Nor-Azian, N., 414  
 Novosad, Z., 414  
 Nur, A., 589–590, 608–609, 616, 638–639  
 Nye, J.F., 595

**O**

Obomanu, D.A., 310, 314–315, 319  
 O'Connell, R.J., 638–639  
 Okpobiri, G.A., 310, 314–315, 319  
 Omar, M.I., 268–269, 312, 314, 317, 319  
 Orr, F.M., Jr., 371–396  
 Osif, T.L., 479  
 Osman, M.E., 268, 271, 311, 314, 316, 319  
 Owens, W.W., 737–738  
 Owolabi, O.O., 264, 270–271, 310, 314–315, 319  
 Ozkan, Erdal, 77–172

**P**

Paddock, J.L., 802–803  
 Pan, H., 421, 445  
 Panda, M.N., 705  
 Parra-Ramirez, M., 412  
 Paterson, M.S., 701–702  
 Pauly, J., 448  
 Peck, R.B., 655  
 Pedersen, W.B., 432, 438, 440–441, 443–444, 449  
 Peng, D., 355, 357, 417–419, 441, 447  
 Peramanu, S., 411  
 Peters, E.J., 746  
 Petrosky, G.E., Jr., 269, 276, 311–331  
 Pickell, J.J., 743  
 Pindyck, R.S., 801–803  
 Piper, L.D., 229–230, 232–233, 237  
 Piro, G., 422–423  
 Pittman, E.D., 714–715, 721  
 Pitzer, K.S., 243, 481  
 Pope, G.A., 745  
 Potter, R.W., 592  
 Prausnitz, J.M., 433

**Q**

Qin, X., 427

**R**

Rafavich, F., 611  
 Raghavan, R., 124, 134  
 Ramey, H.J., Jr., 110, 114, 282, 284–286, 289  
 Ramirez-Jaramillo, E., 452  
 Rao, B.R., 589  
 Rao, K.S., 589  
 Rassamdana, H., 403, 410, 414  
 Rathjens, C.H., 747  
 Rathmell, J.J., 733  
 Raymer, L.L., 652  
 Reddy, S.R., 435  
 Redlich, O., 361–364, 413–415, 417, 438, 443–444  
 Riazi, M.R., 260, 289

Rich, J.L., 466  
 Ring, J.N., 427  
 Robinson, D.B., 355, 357, 417–419, 441, 447  
 Robinson, J.R., 279, 323, 325–326, 328  
 Rogers, P.S.Z., 481  
 Root, P.J., 124, 126  
 Rowe, A.M., 479, 592  
 Russell, W.L., 666  
 Ruth, D.W., 756  
 Rutherford, S.R., 804

**S**

Sahimi, M., 403  
 Salathiel, R.A., 731, 746  
 Salman, N.H., 316, 319  
 Savage, S.L., 797  
 Sayegh, S.G., 414  
 Schilthuis, R.J., 466  
 Schmidt, Z., 268, 274, 276, 311, 314–331  
 Schneider, F.N., 738  
 Scholes, M., 799–802  
 Schollnberger, W.E., 834–837, 839  
 Schuyler, John, 783, 785, 792  
 Scott, T.E., 616, 652–653  
 Seba, R.D., 780–781  
 Sengupta, M., 620  
 Al-Shammasi, A.A., 261, 274, 292, 313–314, 317, 319  
 Sheriff, R.E., 640  
 Shtrikman, S., 601–602  
 Siegel, D.R., 802–803  
 Simmons, G., 616  
 Sloan, E.D., 499–531  
 Smith, J.L., 802–803  
 Soave, G., 361–364, 413–415, 417, 438, 443–444  
 Al-Soof, N.B.A., 311, 314  
 Speight, J.G., 401–402  
 Spinler, E.A., 756–757  
 Srivastava, R.K., 411  
 Standing, M.B., 181, 227–228, 261, 276, 279, 292, 310, 314–325, 479  
 Stassner, J.E., 543  
 Stehfest, H., 88–89, 95  
 Steiger, R.P., 654, 657  
 Stenby, E.H., 448–449  
 Stewart, W.F., 224, 229–230  
 Stone, H.L., 751  
 Sutton, Robert P., 224, 226–227, 231, 237, 257–331  
 Swanson, B.F., 713–716, 721  
 Swerdloff, W., 286–288

**T**

Tanner, M.T., 640  
 Terzaghi, K., 615, 655  
 Thomas, F.B., 416  
 Thomas, L.K., 587, 735  
 Thomeer, J.H.M., 735  
 Thompson, A.H., 714–718, 721  
 Thompson, R.S., 768, 783  
 Thomsen, L., 635–636  
 Timur, A., 706–707, 713  
 Tittmann, B.R., 638  
 Todd, A.C., 268–269, 312, 314, 317, 319  
 Toksoz, N.M., 633–634  
 Torrey, P.D., 465  
 Towler, Brian F., 217–256  
 Treiber, L.E., 738  
 Trigeorgis, L., 800, 802, 804

Trube, A.S., 234  
 Truesdale, 470  
 Trujillo, D.E., 411  
 Tsonopoulos, C., 503, 506  
 Turner, W.R., 406  
 Turta, A.T., 422–423  
 Tutuncu, A.T., 638

**U**

Ujtai, 659  
 Ungerer, P., 449

**V**

Van Baaren, J.P., 704–705, 721  
 van der Waals, J.D., 355, 357–359  
 van Elk, J.F., 789  
 van Everdingen, A.F., 94  
 Vazquez, M.E., 268, 310, 314–315, 319–322, 329, 331  
 Velarde, J., 261, 313–314, 318–319  
 Vernik, L., 609  
 Vo-Thant, D., 639  
 Vutukuri, V.S., 571

**W**

Wahl, J.S., 671  
 Walesh, S.G., 839  
 Walsh, J.B., 632, 638, 701–702  
 Wang, J.X., 409, 414  
 Wang, S., 426  
 Wang, Z.J., 589–591, 611, 629  
 Warren, J.E., 124, 126  
 Wasman, M.H., 423  
 Watson, K.M., 260, 266–267  
 Wattenbarger, R.A., 452  
 Wehe, A.H., 501  
 Weingarten, J.S., 435, 452  
 Weyl, P.K., 689–690, 702–703, 705, 721  
 White, D.E., 466  
 Whitson, C.H., 260, 266, 268, 284–285, 755  
 Wichert, E., 228–229, 231, 238  
 Wiid, B.L., 659  
 Williams, John M., 173–215  
 Williamson, Don, 839  
 Wilson, M.D., 694  
 Wilson, W.D., 593  
 Winkler, K., 638  
 Winston, W., 802  
 Wojtanowicz, A.K., 423  
 Won, K.W., 416–417, 438, 449  
 Wood, J.W., 802  
 Wright, John D., 767–807  
 Wyllie, M.R., 593

**Y**

Yamamoto, T., 639  
 Yan, J., 422, 427–428  
 Yang, Z., 415  
 Yarborough, L., 227, 386–387  
 Yarranton, H.W., 417  
 Yeh, S.W., 422, 428  
 Yin, H.-Z., 608, 616

**Z**

Zarembo, V.I., 592–593  
 Zhang, J.-X., 661  
 Zhou, X., 417

# SUBJECT INDEX

## A

- abandonment, 822–823
  - Abu Dhabi, 809–810
  - acentric factor, 361
  - acetone, 753
  - acetylenes, 258
  - acoustic methods, 408, 757
  - activity coefficients
    - asphaltenes and, 412–413, 415–417
    - waxes and, 433–434, 437–438
  - adsorption, 423–424
  - ad valorem tax, 773–774
  - Alaska, 264, 694, 822
  - Alberta, 423, 770
  - algebra, 57–62
  - Algeria, 822
  - alkanes. *See* asphaltenes; waxes
  - alternative dispute resolution (ADR), 823–825
  - aluminum, 183–184
  - American Arbitration Association (AAA), 825
  - American Petroleum Institute (API)
    - API number, 588, 590–592
    - crude oil emulsions and, 537
    - fluid sampling and, 185–187, 191–199, 208, 214
    - gamma ray logs and, 668, 671
    - NYMEX and, 771
    - oil properties and, 259–260, 266, 268, 274
    - viscosity standards and, 277–281
  - American Society for Testing and Materials (ASTM), 197, 199, 212, 431, 537, 549
  - amplitude vs. offset (AVO), 611, 620
  - anhydrite, 573
  - anisotropy
    - parameter, 637
    - polar, 635
    - shear-wave splitting and, 634–635
    - 3D/2D conversion and, 144–146
    - vertical transverse isotropy and, 635–636
  - annual percentage rate (APR), 778
  - annuities, 777
  - apparent molecular weight, 220
  - arbitration, 824–826
  - Archie's Law, 573
  - arenites, 609–610
  - aromatics, 400–401. *See also* asphaltenes
  - artificial neural networks, 720
  - ASPEN, 517
  - asphaltene precipitation envelope (APE), 398
    - acoustic-resonance technique and, 408
    - electrical-conductance technique and, 408
    - EOS models and, 417–420
    - filtration technique and, 408
    - gravimetric technique and, 408
    - light-scattering technique and, 408–409
    - viscometric technique and, 409
  - asphaltenes, 258
    - activity coefficients and, 412–413, 415–417
    - adsorption and, 423–424
    - alkane correlation and, 403–404
    - APE measurement techniques and, 398, 408–409, 417–420
    - bubblepoint and, 414–415
    - carbon dioxide flooding and, 411–412
    - characteristics of, 400–403
    - colloidal model and, 420–421
    - cosolvents and, 429–430
    - crude oil emulsions and, 536
    - deposition and, 422–429
    - dipole moments and, 408
    - dispersion and, 401–402
    - equations of state models and, 417–420
    - Flory-Huggins model and, 413–417
    - fugacity and, 417–419
    - gas injection and, 398
    - heavy polar fraction and, 542–545
    - micellization model and, 420–422
    - nature of, 401–402
    - plugging and, 422–429
    - porosity and, 426
    - precipitation behavior and, 397–398, 408–430
    - primary depletion and, 397–398
    - reversibility process and, 409–411
    - rich-gas flooding and, 411–412
    - SARA classification and, 400–401, 403
    - stability of, 403
    - steric repulsion and, 542–543
    - supersaturation and, 415
    - thermodynamic models for, 412–422
    - wettability alteration and, 427–429
  - assignment limitations, 814
  - Athabasca, 411
  - atomic weight, 217
  - attenuation, 637–640
  - Austin chalk, 654–655
  - Authorization for Expenditures (AFE), 819
  - automatic titrators, 470
  - axial waves, 8
- ## B
- banking, 814–815
  - basic sediment and water (BS&W), 533, 536–537, 549–550, 560, 770
  - bending waves, 9
  - Benedict-Webb-Rubin (BWR) equation, 587–588
  - benzene, 258
  - Bessel functions, 82
    - Laplace transformations and, 90–92, 131, 135
    - modified, 84–86
    - order of, 83
    - solutions of, 83–84
  - binary phase diagrams, 373–376
  - biomass, 833
  - Biot's poroelastic term, 656
  - Black-Scholes equation, 800–802
  - boundary conditions
    - Bessel functions and, 82–86
    - classical linear oscillator and, 13–24
    - damping and, 11–34
    - diffusion and, 80–86, 101–110 (*See also* diffusion)
    - divergence and, 52–53, 79
    - fluid flow and, 47–48
    - Green's functions and, 100, 110–121, 123
    - initial boundary value problem (IBVP) and, 77–82, 90, 96
    - Laplace transformations and, 86–100
    - partial differential equations (PDEs) and, 48
    - second law of thermodynamics and, 341–344
    - skin-zone radius and, 95–100
    - source functions and, 104–108
  - bounds, 599–603

- boycotts, 829  
 Boyle's law, 218, 355  
 Bradford field, 465–466  
 Brent Spar, 823  
 bribery, 816–817  
 brines  
   crude oil emulsions and, 533, 536, 548–549  
     (see also crude oil emulsions)  
   density and, 592–594  
   fluid properties of, 592–594  
   glass containers and, 477  
   organic constituents and, 490–491  
   pH and, 548  
   porosity and, 592–594, 607–609  
   produced water and, 467, 474–475, 477, 480–482,  
     485–486, 490–491  
   rock strength measurement and, 665  
   sampling techniques and, 199–202, 753–754  
   saturated sandstone and, 608–609  
   surface tension and, 282–304  
   surfactant/polymer floods and, 384–386  
 Brownian motion, 803  
 bubblepoint, 180  
   asphaltenes and, 414–415  
   carbon dioxide and, 271, 273  
   correlations for, 261–270  
   gas gravity and, 268–269  
   gas-injection processes and, 386–394  
   hydrogen sulfide and, 273  
   produced water density and, 480–481  
   relative permeability and, 750–752  
   reservoir classification and, 381–384  
   supersaturation and, 415  
   surfactant/polymer floods and, 384–386  
   temperature and, 268–269  
   varying gas/oil ratio and, 261, 264–270  
 bulk-filtration apparatus, 432  
 bulk lubrication, 660–661  
 bulk modulus, 586, 591  
   anisotropy and, 634–637  
   attenuation and, 637–640  
   Biot's poroelastic term and, 656  
   bounds and, 599–603  
   cracked rock and, 632–634  
   Gassmann equations and, 619–629  
   in-situ stresses and, 616–618  
   porosity dependence and, 607–609  
   pressure and, 612–616  
   P waves and, 621  
   solid mineral, 629–632  
   stress-strain and, 597–599  
   S waves and, 621  
   temperature and, 618–619  
   velocity-porosity relations and, 609–612  
   Young's, 597  
 buoyancy, 466
- C**  
 calcite, 573  
 calculus  
   dependent variables, 1–2  
   derivatives, 3–5  
   differential equation, 1, 5–6, 11  
   independent variables, 1–2, 46–48  
   limits, 1–3  
   slope, 1–5  
 California, 772  
 Calingear-Davis equation, 242–243  
 Canada Mitsue crude oil, 428  
 canola, 833  
 capillary forces  
   electrophoresis (CE), 470  
   gas-injection processes and, 386–394  
   surfactant/polymer floods and, 384–386  
 capillary pressure, 713–714  
   Alpak-Lake-Embid model and, 736  
   Brooks-Corey model and, 735–736  
   capillary number and, 743–745  
   defined, 728  
   drainage and, 728, 731  
   heterogeneity and, 731–732  
   hypothetical equilibrium and, 729–730  
   imbibition and, 728, 731  
   interfacial tension and, 734–735, 746  
   Laplace's equation and, 728  
   Leverett j-function and, 734–735  
   measurement of, 754–757  
   relationships for, 728–734  
   temperature and, 746  
   Thomeer model and, 735  
   viscous fingering and, 759  
   wettability and, 728–734, 746  
 carbonates, 573, 575, 611–612, 694–695  
 carbon dioxide, 271, 273, 837–838  
 Carman-Kozeny models, 749–750  
 Cartesian coordinates, 1–2  
   diffusivity and, 80–81  
   initial boundary value problem (IBVP) and, 77–82  
   matrices and, 57–58  
   rotation of, 57–58  
   vectors and, 51  
 cementation, 574–575, 624, 705  
 centrifuge methods, 196, 755–757, 759  
 chalks, 654–655, 695  
 Charles' law, 218, 355  
 China, 822  
 chlorite, 576  
 chloroform, 753  
 choice of law, 823–824  
 civil law, 828–829  
 Clapeyron equation, 241–243, 435  
 classical linear oscillator (CLO)  
   pendulums and, 24–34  
   single degree of freedom (SDOF) and, 13–24  
   two degrees of freedom (2DOF) and, 24–34  
 Clausius-Clapeyron equation, 241–243, 435  
 clays, 582, 609, 624  
   bulk lubrication and, 660–661  
   diagenesis and, 662  
   porous minerals and, 573, 575  
   radioactive, 666–671  
   rock failure and, 653–655  
   rock strength measurement and, 662–666  
   single-phase permeability and, 691–692  
 clean energy, 831  
 cloud point, 431–432  
 coal, 465, 831–832, 834  
 coalescence, 540–541  
 cogeneration, 834  
 cohesion, 650  
 Cold Lake, 411  
 Commercial Arbitration and Mediation Center for the  
   Americas (CAMCA), 825  
 common law, 824, 828–829  
 compaction strength, 653  
 complementary error function, 50, 119  
 complex numbers, 59  
 compressibility, 590–591

- clay content and, 653–655
  - compaction strength and, 653
  - Coulomb-Navier failure and, 642–645
  - elasticity and, 8, 36–37, 603–640
  - first law of thermodynamics and, 338–341
  - gas properties and, 233–236
  - Gassmann equations and, 619–629
  - grain texture and, 661–662
  - Hoek-Brown relationships and, 645–651
  - ideal gas law and, 587
  - initial boundary value problem (IBVP) and, 79–82
  - isobaric, 356–357
  - isothermal, 233–236, 275–277, 320–322, 356–357, 590
  - log parameters and, 662–666
  - Mohr failure and, 645–651
  - oil properties and, 275–277, 320–322
  - phase behavior and, 356–357
  - pore fluid effects and, 655–661
  - principle of corresponding states and, 360–361
  - produced water and, 478–479
  - real fluid equation and, 356
  - rock strength measurement and, 662–666
  - source functions and, 102–103
  - supercompressibility and, 223
  - uniaxial, 595, 651–655, 662–663, 665
  - compressional (P) waves, 8–9, 36–37, 621, 629–630
  - computerized tomography (CT) scanning, 753, 757
  - concessions, 811–812
  - condensate water, 492
  - conductivity, 408, 484, 538, 687–688
  - connate water, 466, 470, 492
  - Conoco, 771
  - consumer price index (CPI), 802–803
  - continuity equation, 45–46
  - contracts, 813–814
  - convection, 48–50, 54–57
  - Convention on Jurisdiction and Foreign Judgments in Civil and Commercial Matters, 826
  - Convention on the Settlement of Investment Disputes Between States and Nationals of Other States, 828
  - Cornerstone Ventures, L.P., 802
  - corrosion, 471–472
  - corruption, 816–817, 829
  - Coulomb damping, 10–11
  - Coulomb-Navier failure, 642–645
  - Council of Petroleum Accountants Societies (COPAS), 774
  - Cox chart, 242
  - Cragoe's relationship, 266
  - creaming, 552–553
  - cricondentherm, 381–382
  - crossover tie line, 392
  - cross-polarized microscopy, 431
  - crude oil emulsions, 211, 258–261
    - agitation and, 551
    - API standards and, 537
    - appearance and, 536–537
    - asphaltenes and, 536, 542–545
    - ASTM standards and, 537, 549
    - basic sediment and water, 533, 536–537, 549–550, 560
    - brine composition and, 549
    - characteristics of, 536–540
    - color and, 536–537
    - definition of, 534
    - demulsification and, 550–560, 563–566
    - desalters and, 554, 556
    - difficulties from, 533
    - droplet size and, 535–538, 547
    - emulsion separation index (ESI) test and, 569–570
    - field treatment program and, 561–563
    - finely divided solids and, 536
    - free-water knockout drums and, 553–554
    - gravitational separation and, 554
    - heavy polar fraction in, 542–546
    - interfacial tension (IFT) and, 536–537, 539–540, 559–560
    - Karl-Fischer titration and, 537
    - occurrence of, 533–534
    - pH and, 548
    - production costs and, 533
    - production traps and, 554
    - retention time and, 551
    - retrofitting and, 552
    - rheology and, 538–540
    - salinity and, 533, 550, 554, 556
    - sampling and, 560–561
    - shear and, 551
    - solids and, 546–547
    - stability and, 540–550
    - steric repulsion and, 542–543
    - Stokes' Law and, 554
    - surface-active agents and, 536
    - surface films and, 540–541
    - temperature and, 547
    - three-phase separators and, 554
    - types of, 534–536
    - viscosity and, 538–540
    - waxes and, 536, 545–546
  - curl, 52–53
  - cutters, 453
- D**
- D'Alembert's principle, 13
  - Dalton's law, 221
  - damping
    - classical linear oscillator and, 13–24
    - Coulomb, 10–11
    - hysteretic, 11
    - single degree of freedom (SDOF) and, 13–24
    - two degrees of freedom (2DOF) and, 24–34
    - vibrating systems and, 9–11, 13–24
    - viscous, 10
  - Danian samples, 695
  - Darcy's law, 62–63, 73
    - diffusivity and, 80–82
    - Green's functions and, 112
    - initial boundary value problem (IBVP) and, 79–82
    - Laplace transformations and, 90
    - relative permeability and, 727
    - single-phase permeability and, 687–688
  - Darcy velocity field, 51
  - decane, 400
  - Decision Analysis for Petroleum Exploration* (Newendorp & Schuyler), 783
  - decision trees, 785–788
  - decommissioning, 822–823
  - deformation. *See* rock failure
  - degrees of freedom (DOF)
    - boundary conditions and, 11–34
    - continuous systems and, 7, 34–36
    - damping and, 11–34
    - discrete systems and, 6–7
    - dominant, 7
    - excitation/response functions and, 6–8
    - H<sub>2</sub>O+hydrocarbon systems and, 500–501
    - multiple, 34
    - pure fluid properties and, 350–364
    - single (SDOF), 9, 13–24
    - two (2DOF), 9–10, 24–34

- demulsification
    - aggregation and, 552
    - agitation and, 565
    - chemical approach to, 556–560
    - creaming and, 552–553
    - databases and, 566
    - destabilizing emulsions and, 550–552
    - efficiency factors and, 558
    - electrostatic coalescing and, 566
    - flocculation and, 552
    - mechanisms for, 552–553, 559–560
    - methods for, 553–560
    - optimization of, 563–566
    - overdosing and, 565
    - process evaluation and, 565–566
    - proper mixing and, 564–565
    - retention time and, 565–566
  - density, 219–220, 233, 277
    - API number and, 588, 590–592
    - Benedict-Webb-Rubin equation and, 587
    - brines and, 592–594
    - buoyant, 580
    - definition of, 577–578, 580
    - dry, 580
    - fluid properties and, 580, 585–594
    - Gassmann equations and, 619–629
    - grain, 580
    - initial boundary value problem (IBVP) and, 79–82
    - in-situ, 582–584
    - isotropic, 603–604
    - measurement techniques for, 584–585
    - oil properties and, 277
    - produced water and, 479–482
    - saturated, 580
    - seismic data and, 585
    - volume fraction and, 581–582
  - Department of Trade and Industry (DTI), 811
  - dependent variables, 1–2
  - deposition
    - adsorption and, 423–424
    - asphaltenes and, 258, 397–403, 408–429
    - produced water and, 471–472
    - scale, 471–472
    - waxes and, 398–400, 404–408, 430–453
    - wettability alteration and, 427–429
  - derivatives, 3–5
  - desalters, 554, 556
  - determinants, 61–62
  - dewpoint, 180
    - gas-injection processes and, 386–394
    - H<sub>2</sub>O+hydrocarbon systems and, 501–503, 508–514
    - reservoir classification and, 381–384
    - surfactant/polymer floods and, 386–394
  - diagenetic water, 492
  - diesel fuels, 407
  - diethylenetriaminepentamethylene phosphonic acid, 471
  - differential equations
    - chain rule, 4
    - continued, 4
    - derivatives, 3–5
    - L'Hopital's rule, 3
    - limits, 1–3
    - linear superposition rule, 4
    - multiple, 4
    - ordinary (ODE), 1, 5, 11
    - partial (PDE), 1, 5, 11
    - product rule, 4
    - quotient rule, 4
    - solutions, 5–6
  - differential-scanning calorimetry, 431
  - diffusion, 80–81
    - Bessel functions and, 82–86
    - Dirac delta function and, 101
    - Green's functions and, 100, 110–121, 123
    - Poisson's summation formula and, 106–107
    - source functions and, 101–110 (*see also* source functions)
    - waxes and, 450–451
  - dilatational waves, 8
  - diolefins, 258
  - Dirac delta function, 101, 125
  - direct hydrocarbon indicators (DHI), 620
  - discounted profit-to-investment ratio, 780–782
  - dispersion, 8–9
    - asphaltenes and, 401–402
    - attenuation and, 637–640
    - fluid flow and, 48–50, 54–57
    - velocity and, 637–640
    - waxes and, 451–452
  - dispute resolution, 815–816, 823–826
  - dissolution, 431
  - distortional waves, 8–9
  - divergence, 52–53, 79
  - dolomites, 573–576, 607, 692
  - domestic marketing obligation (DMO), 813
  - downhole sampling, 472–478
  - drainage, 728, 731
  - drilling-mud gas, 213
  - drillstem tests (DSTs)
    - fluid sampling and, 179, 187–188, 200
    - produced water and, 472–478
  - dual-water model, 708–709
  - Duhem's theorem, 335–336
- E**
- economic issues (*see also* international oil and gas law)
    - decision trees and, 785–788
    - discounted profit-to-investment ratio and, 780–782
    - estimated remaining reserves and, 789–791
    - expected monetary value and, 784–788, 791–799
    - gross production and, 769
    - gross sales and, 770
    - industrial importance of, 767–768
    - internal rate of return and, 780
    - investment and, 775 (*See also* investment)
    - joint operating agreements and, 819–820
    - Monte Carlo simulation and, 788–791
    - net cash flow and, 775
    - net operating income and, 774
    - net present value and, 779–780, 783
    - net revenue interest and, 771
    - net sales and, 771
    - operating costs and, 774
    - portfolio analysis and, 792–799
    - price and, 771–773
    - property evaluation and, 768–775, 783–792
    - real options and, 799–804
    - recommended calculation practices, 782–783
    - risk analysis and, 783–792
    - royalties and, 768, 770–771
    - shrinkage and, 769–770
    - taxes and, 773–775
    - time value of money, 775–779
    - working interest and, 770
  - eigenvectors, 61–62, 65–69
  - elasticity
    - attenuation and, 637–640
    - Biot's poroelastic term and, 656
    - cracked rock and, 632–634



- Gassman equations and, 619–629  
 mechanical failure and, 640–666  
 mineral properties and, 603–604  
 modulus of, 36–37  
 Newton's Second Law and, 604  
 porosity dependence and, 607–609  
 pressure and, 612–616  
 rock failure and, 640–666  
 temperature and, 618–619  
 velocity dispersion and, 637–640  
 velocity-porosity relations and, 609–612  
 waves and, 8, 36–37, 604–607
- electrical-conductance technique, 408, 484  
 electrostatic coalescing, 566  
 electrostatic grids, 556  
 emulsion separation index (ESI) test, 569–570  
 energy  
 equilibrium and, 344–350  
 first law of thermodynamics and, 338–341  
 fugacity criterion and, 346–347, 349–350  
 pure fluid properties and, 350–364  
 second law of thermodynamics and, 341–344
- energy demand  
 biomass and, 831–833  
 carbon dioxide sequestration and, 837–838  
 changing industrial policy and, 837–838  
 clean energy and, 831  
 coal and, 831–832, 834  
 cogeneration and, 834  
 distribution ethics and, 838  
 engineers and, 838–839  
 Fischer-Tropsch (F-T) reactor and, 833  
 forecasting of, 834–837  
 Gaussian analysis and, 836–837  
 nuclear energy and, 831–832  
 oceans and, 833  
 options for, 831–834  
 renewable fuels and, 831–833  
 solar energy and, 831–833
- enhanced oil recovery (EOR) processes  
 gas-injection, 386–394  
 multicontact miscibility and, 392–394  
 phase diagrams and, 371–372, 379, 384–394  
 surfactant/polymer floods and, 384–386
- Enron, 771  
 enthalpy  
 of fusion, 445  
 H<sub>2</sub>O+hydrocarbon systems and, 525  
 Joule-Thomson expansions and, 525  
 phase behavior and, 344–350  
 waxes and, 435–436, 439–440, 445–449
- entropy  
 equilibrium and, 344–350  
 second law of thermodynamics and, 341–344
- equations, mathematical  
 Alpak-Lake-Embid, 736  
 amplitude loss, 637–638  
 anisotropic, 636–637  
 annuities, 777  
 API number, 588  
 aspect ratio of cracked rock, 633  
 asphaltene precipitation, 403–404, 412–426  
 Benedict-Webb-Rubin, 587–588  
 Bentsen-Anli, 736  
 Bessel functions, 83–86  
 binary phase diagrams, 374  
 Biot's poroelastic term, 656  
 Black-Scholes, 800–801  
 Boyle's law, 218  
 Brooks-Corey, 735–736, 746–747  
 bubblepoint pressure, 261, 266, 310–313  
 Calingear-Davis, 242–243  
 capillary number, 743  
 capillary pressure, 713, 729, 734–736, 756  
 Carman-Kozeny, 750  
 Charles' law, 218  
 Chierici, 748–749  
 Clapeyron, 241–242  
 Clausius-Clapeyron, 435  
 clay/failure effects, 654–655  
 Coates, 711  
 cohesion, 650  
 compaction strength, 653  
 complementary error function, 50, 119  
 compressibility, 478–479, 587, 590–591, 652–655, 662, 665  
 compressional velocity, 613  
 compressive strength, 662, 664–665  
 continuity, 45–46  
 convection/dispersion, 48–50  
 coordinate rotation, 57–58  
 Coulomb damping, 10–11  
 Coulomb-Navier failure, 642–645  
 crude oil characterization, 260  
 crude oil emulsions, 539, 554  
 crushing strength, 661  
 D'Alembert's principle, 13  
 Darcy's law, 63, 687–688, 727  
 density, 481, 578, 580–582, 587–588, 592–593  
 derivatives, 3–5  
 diffusivity, 80–82  
 dual-water model, 708  
 effective stress, 655–656  
 elasticity, 604, 607, 656  
 equilibrium, 344–350  
 estimated remaining reserves, 789  
 expected monetary value, 784–785  
 finite difference method, 54–57  
 first law of thermodynamics, 338–341  
 flow zone indicator, 717  
 fluid flow, 45–72  
 formation volume factor (FVF), 233, 274, 315–318, 482–483  
 fractional shale volume, 670  
 future worth, 776  
 gamma function, 83  
 gamma ray index, 669–670  
 gas-oil ratio, 592  
 Gassmann's, 621–633  
 gas viscosity, 236–237  
 Green's functions, 110–121  
 H<sub>2</sub>O+hydrocarbon systems, 500, 503–506,  
 513, 516, 519–525  
 Herron, 705  
 Hoek-Brown, 646–651  
 Hooke's law, 13, 599  
 hysteretic damping, 11  
 ideal gas, 218, 355, 587  
 initial boundary value problem (IBVP), 77–82  
 interest rate, 778–779  
 internal friction angle, 643, 664  
 isobaric heat capacity, 593  
 isothermal compressibility, 234–235, 275–276, 320–321  
 isothermal velocity, 587, 589  
 Katz-Thompson, 715–716  
 Kozeny-Carman, 701–702  
 Krumbain-Monk, 703  
 K-value, 433–435, 438–441, 447–448  
 Langmuir isotherm, 423  
 Laplace, 86–100, 728

- Lee-Kesler, 243  
 Leverett *j*-function, 734–735  
 limits, 1–3  
 loans, 777–778  
 matrix, 57–62  
 mixing-line technique, 493  
 modulus of elasticity, 36–37  
 Mohr failure, 646–651  
 Newton's Second Law, 13, 18, 604  
 nonhydrocarbon gas effects, 271–273  
 nuclear magnetic resonance, 710–711  
 oil density, 277  
 permeability, 687, 696, 698–699, 701–717, 720  
 pH, 487–488  
 phase behavior, 334–335, 338–350, 354–366  
 phase rule, 372–373  
 Poisson's ratio, 598  
 Poisson's summation formula, 106–107  
 porosity, 578–580  
 power-law, 706  
 present value, 776–777  
 produced water, 478–489, 493  
 profit-to-investment ratio, 782  
 proportionality, 6  
 pseudopressure, 81  
 real fluid, 356  
 real-gas law, 223–231  
 real-gas pseudopotential, 241  
 redox potential, 489  
 relative permeability, 727, 742–743, 746–752  
 Reuss effective modulus, 601  
 rock strength, 662, 664–665  
 saturation gain function, 624, 629  
 Scatchard-Hildebrand, 436–437  
 shear velocity, 615  
 source functions, 100–108 (*see also* source functions)  
 stress-strain, 594, 596–602, 616–617, 642–651, 655  
 superposition, 6  
 surface tension, 282–300  
 Swanson, 714  
 Taylor's series, 54  
 ternary phase diagrams, 376, 378–379  
 Thomeer, 735  
 Timur, 706  
 transient fluid flow, 77–82 (*see also* transient analysis)  
 uniaxial compressive strength, 652–655, 662, 665  
 universal quasi-chemical, 448  
 Van Baaren, 704–705  
 van't Hoff, 435  
 vector analysis, 51–54  
 velocity, 588  
 velocity-attenuation, 637–639  
 vibration systems, 6, 10–37  
 viscosity, 280, 323–330, 485–486  
 viscous damping, 10  
 Voigt modulus, 601  
 Washburn, 713  
 wax precipitation, 432–452  
 Weinaug-Katz, 282  
 Wilson's, 448  
 Winland, 714  
 Young's modulus, 597
- equations, stoichiometric, 488  
 equations of state  
   accuracy of, 355  
   acentric factor and, 361  
   asphaltene precipitation models and, 417–421  
   Boyle's law, 355  
   Charles' law, 355  
   cubic, 357–364  
   equilibrium conditions and, 344–350  
   Flory-Huggins model and, 413–417  
   H<sub>2</sub>O+hydrocarbon systems and, 517  
   ideal gas and, 355  
   initial boundary value problem (IBVP) and, 79–82  
   in-situ fluids and, 366–367  
   Maxwell's, 362–363  
   mixture properties and, 364–366  
   Peng-Robinson, 355, 357, 417–419, 441, 447  
   phase behavior and, 344–350, 354–366  
   pressure-volume diagram and, 359–360  
   principle of corresponding states and, 360–361  
   pure solid fugacity and, 433–435  
   real fluid, 356  
   Soave-Redlich-Kwong, 361–364, 413–415, 417, 438, 443–444  
   solid-solution models and, 436–444  
   two-phase envelope calculation and, 363–364  
   van der Waals, 355, 357–359  
   vapor pressure and, 361–363  
   waxes and, 434–438, 442–444
- equilibrium  
   asphaltene precipitation models and, 412–422  
   capillary pressure and, 713–714, 727–762  
   Duhem's theorem and, 335–336  
   fugacity criterion and, 346–347, 349–350  
   gas-injection processes and, 386–394  
   H<sub>2</sub>O+hydrocarbon systems and, 499–528  
   inverse lever rule and, 374  
   mixture properties and, 364–366  
   multicomponent liquid/vapor systems and, 347–350  
   pH and, 486–489  
   phase behavior and, 333–350  
   phase diagrams and, 376–395  
   pore fluid effects and, 655–661  
   produced water and, 489–490  
   pure fluids and, 346–347, 350–364  
   radioactivity and, 666–671  
   redox potential and, 489–490  
   rock failure and, 640–666  
   second law of thermodynamics and, 341–344  
   single-component liquid/vapor systems and, 345–347  
   solid/liquid, 432–435  
   surfactant/polymer floods and, 384–386  
   waves and, 13  
   wax precipitation models and, 432–449
- equivoluminal waves, 8–9  
 Ernst & Young, 774  
 estimated remaining reserves (ERR), 789–791  
 ethane, 371  
 ethanol, 833  
 ethical issues, 838  
 ethylene glycol, 183  
 European Convention on State Immunity and Additional Protocol, 827  
 European Union, 821–822, 827, 829  
 excitation function, 6–8  
 expected monetary value (EMV), 791  
   concept of, 784–785  
   decision trees and, 785–788  
   portfolio analysis and, 792–799  
 Export Administration Act, 829  
 extraterritorial law, 829
- F**  
 Federal Power Commission, 803  
 feldspars, 573, 693  
 field-filtered samples, 474

- filtration technique, 408  
 finite difference method, 54–57  
 Fischer-Tropsch (F-T) reactor, 833  
 flexural waves, 9  
 flocculation, 552  
 Flory-Huggins model, 413–417, 436, 442  
 flowline sampling, 473  
 flow zone indicators, 717–718  
 fluid flow  
   Bessel functions and, 82–86  
   boundary conditions and, 47–48, 81–82  
   capillary pressure and, 713–714, 727–762  
   complementary error function and, 50  
   continuity equations and, 45–46  
   convection and, 48–50, 54–57  
   curl and, 52–53  
   Darcy's law and, 62–63, 73, 79–82  
   diffusion and, 80–86, 101–121  
   Dirac delta function and, 101, 125  
   dispersion and, 48–50, 54–57  
   divergence and, 52–53, 79  
   factors affecting, 277–281  
   first law of thermodynamics and, 338–341  
   flux and, 45–46, 54  
   formation testers and, 187–188  
   gradient and, 52–53  
   incompressible, 53–54  
   initial boundary value problem (IBVP) and, 77–82, 90, 96  
   in-situ characterization and, 366–367  
   Laplace transformations and, 86–100  
   mass conservation and, 45–46  
   matrices and, 57–62  
   Newtonian fluids and, 277  
   numerical methods and, 54–57  
   one-dimensional convection/dispersion equation and, 48–50  
   partial differential equations (PDEs) and, 45–50, 54–57  
   permeability tensor and, 62–74 (*see also* permeability)  
   pore fluid sensitivity and, 697–698  
   porous media and, 77–81  
   pure fluid properties and, 350–364  
   PVT analysis and, 218–219  
     (*see also* pressure/volume/temperature (PVT) analysis)  
   relative permeability and, 727–762  
   single-phase permeability and, 687–724  
   superposition and, 126, 128  
   Taylor's series and, 54  
   three-dimensional convection/dispersion equation and, 54  
   transient analysis and, 77–172 (*see also* transient analysis)  
   unsteady, 110–168  
   vector analysis and, 51–54  
   viscosity and, 277–281 (*see also* viscosity)  
   volumetric properties and, 350–364  
 fluid properties, 585  
   Benedict-Webb-Rubin equation and, 587  
   brines and, 592–594  
   gas and, 586–588 (*see also* gases)  
   Gassmann equations and, 619–629  
   heat capacity and, 587, 594  
   ideal gas law and, 586–587  
   measurement of, 752–759  
   oil properties and, 588–592 (*see also* oil)  
 fluid sampling, 215, 752–754  
   American Petroleum Institute (API) and, 185–187, 191–195, 198–199, 208, 214  
   American Society for Testing and Materials (ASTM) and, 197, 199, 212  
   asphaltic fluids and, 185, 211–212  
   backup and, 178  
   BS&W determination and, 197–198, 203, 211  
   carbon dioxide liberation and, 181, 188  
   certainty issues and, 173–174  
   cost optimization and, 173, 213–214  
   critical temperature and, 180  
   crude-oil emulsions and, 211, 533–570  
   data measurement/recording and, 202–205  
   dilution and, 177  
   documentation and, 178–179  
   downhole, 178, 185–189  
   drilling-mud gas and, 213  
   drillstem tests (DSTs) and, 179, 187–188, 200  
   equipment selection/preparation and, 183–184  
   error and, 173–175, 178, 185–187  
   formation testers and, 187–188  
   gas chromatography and, 207–208  
   gas/oil ratio (GOR) and, 174, 178, 181–183, 189–195, 202  
   hazards and, 210–211  
   isokinetic, 195–196  
   nonpressurized hydrocarbon procedures and, 196–199  
   oil-based mud (OBM) and, 174, 182, 188, 207  
   oilfield waters and, 176–178, 199–202  
   on-site measurements and, 212–213  
   phase behavior and, 173, 180  
   pressurized hydrocarbon procedures and, 184–196  
   PVT analysis and, 173  
   quality control and, 185–187, 205–210  
   recommended measurements for, 176–177  
   reservoir-fluid type, 180–181  
   saturation condition and, 180–181  
   Saybolt measurement and, 196  
   separator conditions and, 178, 182–183, 189–195  
   setting up program for, 174–180  
   slippage and, 182  
   surface-separator technique and, 178  
   tank of oil and, 196–199  
   temperature and, 182–183  
   thief and, 196  
   transfer to container and, 185–187, 191–195  
   troubleshooting and, 179–180  
   vapor space and, 187  
   water-cut measurements and, 213  
   waxy fluids and, 185, 211–212  
   well conditioning and, 181–183  
   wellhead, 178, 195  
 flux, 129  
   Bessel functions and, 82–86  
   convection/dispersion equation and, 48–50  
   Darcy's law and, 79–82  
   diffusivity and, 80–82  
   divergence and, 79  
   Green's functions and, 110–121  
   Laplace transformations and, 86–100, 121–168  
   mass conservation and, 45–46  
   source functions and, 101–110, 110–168  
     (*see also* source functions)  
   vector analysis and, 51–54  
 Ford Motor Company, 834  
 Foreign Corrupt Practices Act (FCPA), 816–817, 829  
 foreign exchange, 814–815  
 Foreign Sovereign Immunities Act (FSIA), 827  
 formation testers, 187–188  
 formation volume factor (FVF), 233  
   oil properties and, 257, 273–275, 285, 315–319  
   produced water and, 482–483  
   surface tension and, 285  
 formation water, 492  
 FORTRAN, 470  
 forum, 824  
 fossil water, 466

fracture. *See* rock failure  
 freefalling bodies, 1–5  
 free-water knockout drums, 553–554  
 frequency, 42  
   classical linear oscillator and, 13–24  
   damping and, 11–34  
   resonance and, 9–10  
   wave propagation and, 9–10  
 frontier areas, 812  
 fugacity, 346–347  
   asphaltenes and, 417–419  
   waxes and, 433–435  
 future worth, 776  
 fuzzy clustering techniques, 719–720

**G**

gamma function, 83  
 gamma rays, 585, 666–671, 705  
 garbage in/garbage out (GIGO) problems, 788  
 gases (*see also* phase behavior)  
   Amagat's law and, 221  
   apparent molecular weight and, 220  
   Benedict-Webb-Rubin equation and, 587  
   Boyle's law and, 218  
   Calingart-Davis equation and, 242–243  
   capillary pressure and, 713–714, 727–762  
   Charles' law and, 218  
   chromotography and, 207–208  
   Clapeyron equation and, 241–242  
   Cox chart and, 242  
   Dalton's law and, 221  
   density, 233  
   drilling-mud, 213  
   economic evaluation and, 768–775, 783–792  
   equilibrium, 218–219, 224  
   estimated remaining reserves and, 789–791  
   formation volume factor, 233  
   free-water knockout drums and, 553–554  
   gas gravity, 501, 525  
   heat capacity, 587  
   ideal, 217–218, 355, 586–587  
   inhibitors and, 516–517, 520–524  
   injection processes, 386–394  
   international law and, 809–829  
   isothermal compressibility and, 233–235  
   isothermal velocity and, 587  
   Klinkenberg effect and, 696–697  
   Lee-Kesler equation and, 243–244  
   marketing of, 821–822  
   mixtures and, 220–221  
   molecular weight and, 217  
   mole fraction and, 220  
   nonhydrocarbon gas effects and, 270–273  
   phase characterization of, 586–588  
   phase diagrams and, 376–395  
   physical constants and, 222  
   pressure/volume/temperature (PVT) analysis and, 218–219  
   produced water and, 466, 490  
   property evaluation and, 768–775, 783–792  
   pseudocritical, 223–233, 236–241  
   real, 222–223, 241  
   relative density and, 219–220  
   relative permeability and, 727–762  
   sequestration and, 837–838  
   slippage and, 182  
   specific gravity and, 219–221, 268–269  
   trapping relationship and, 741–742  
   vapor pressure and, 241–244  
   viscosity and, 236–241

gas-injection processes  
   asphaltenes and, 398  
   multicontact miscibility and, 392–394  
   phase diagrams and, 386–394  
 gasohol, 833  
 gas/oil ratio (GOR), 174, 178, 202  
   formation volume factor and, 273–275  
   oil properties and, 261 (*see also* oil)  
   separator sampling and, 189–195  
   solution, 273  
   surface tension and, 281–288  
   well conditioning and, 181–183  
 Gassmann equations, 632  
   fluid effects model and, 619–629  
   frequency effects and, 623  
   invalid assumptions in, 620  
   Kuster-Toksoz model and, 633–634  
   Reuss modulus and, 626  
   rock texture and, 624  
   seismic velocity changes and, 619–620  
   Voigt modulus and, 625  
 Gaussian analysis, 836–837  
 Geneva Convention, 823  
 GeoMark Research database, 261, 274, 276  
 geomechanics, 62  
 Gibbs energy  
   equilibrium and, 344–350  
   fugacity criterion and, 346–347, 349–350  
   H<sub>2</sub>O+hydrocarbon systems and, 517  
   mixture properties and, 364–366  
   phase rule and, 372–373  
   pure fluid properties and, 350–364  
   second law of thermodynamics and, 341–344  
   thermodynamic-micellization model and, 421–422  
   volumetric properties of pure fluids and, 350–364  
   wax models and, 447–449  
 Gibbs phase rule, 500–501, 512–513  
 glass containers, 184, 476–477  
 gradient, 52–53, 79  
 grain-to-grain stress, 574  
 gravimetric technique, 408  
 gravity  
   crude oil emulsions and, 554  
   gases and, 501, 525  
   settling and, 450  
 Green's functions, 100  
   Darcy's law and, 112  
   Laplace transformations and, 123  
   Newman's product method and, 110, 113–114, 116, 120  
   porosity and, 110–121  
   source functions and, 100  
   system dimension and, 113–114  
   unsteady flow and, 110–121  
 grids, 71–74  
 gross production, 769  
 gross sales, 770  
 Gulf Coast, 703, 706  
 Gulf of Mexico, 276, 415, 592, 671, 801  
 Gulf of Suez, 276  
 gypsum, 573

**H**

H<sub>2</sub>O+hydrocarbon systems  
   calculability and, 517–518  
   cooling curves and, 525  
   crystal structure and, 507–508  
   cubic structure and, 507  
   degrees of freedom (DOF) and, 500–501  
   dewpoint and, 501–503, 508–514

- equations of state and, 517
  - first law of thermodynamics and, 525
  - flowline blockages and, 527–528
  - formation conditions and, 517–527
  - Gibbs energy and, 517
  - Gibbs phase rule and, 500–501, 512–513
  - hexagonal structure and, 507
  - with hydrates, 506–527
  - without hydrates, 501–506
  - inhibitors and, 516–517, 520–524
  - MeOH/MEG injection amounts and, 520–524
  - phase behavior of, 499–528
  - pressure/temperature diagrams and, 508–517
  - pure condensates and, 514–515
  - solubility and, 501–506
  - stability and, 506–508
  - Hague Conference on Private International Law, 826
  - Hague Convention on the Taking of Evidence Abroad in Civil or Commercial Matters, 828
  - Hamilton's principle, 13
  - Hasin-Shtrikman technique, 601–602
  - heat capacity, 587, 594
  - heat transfer, 341–344
  - hematite, 573
  - Henry Hub, 772
  - heptadecane, 258
  - heptanes, 260–261, 401
  - Hertzian contact theory, 661
  - heterogeneity
    - capillary pressure and, 731–732
    - relative permeability and, 747–748
  - hexane, 400
  - high performance liquid chromatography (HPLC), 470
  - high-rate method, 758
  - Hoek-Brown relationships, 645–651, 662
  - homogeneity, 738
  - Hooke's law, 13, 599
  - host countries. *See* international oil and gas law
  - hydraulic fracturing, 397
  - hydrocarbons
    - aromatic, 258
    - asphaltenes and, 258, 397–403, 408–429
    - attenuation and, 637–640
    - biomass and, 833
    - classification of, 257–258
    - Fischer-Tropsch (F-T) reactor and, 833
    - fluid properties and, 585–594
    - gases and, 217–256, 222 (*see also* gases)
    - Gassmann equations and, 619–629
    - H<sub>2</sub>O+hydrocarbon systems and, 499–528
    - isomers and, 258
    - nonpressurized fluid sampling and, 196–199
    - oil and, 257–331 (*see also* oil)
    - paraffin, 257–258
    - pH and, 486–489
    - phase diagrams and, 376–395
    - physical constants and, 222
    - pressurized fluid sampling and, 184–196
    - produced water and, 465–494
    - pseudocritical properties and, 223–233
    - rock properties and, 573 (*see also* rock properties)
    - solubility and, 501–506
    - surface tension and, 289–403
    - surfactant/polymer floods and, 384–386
    - viscosity and, 277–281
    - waxes and, 398–400, 404–408, 430–453
  - hydrogen sulfide
    - bubblepoint and, 273
    - NACE specifications and, 471
    - phase diagrams and, 371
    - produced water and, 471, 478
  - hydrophilic-lipophilic balance (HLB), 557–558
  - hysteresis, 11, 736–737, 749
  - HYSYS, 517
- I**
- ideal gas, 217–218, 355
  - igneous rocks, 573
  - illite, 692
  - imaginary numbers, 59
  - imbibition, 728, 731
  - improved-oil-recovery (IOR) processes
    - asphaltenes and, 258, 397–403, 408–429
    - waxes and, 398–400, 404–408, 430–453
  - income tax, 774–775
  - independent variables, 1–2, 46–47
  - India, 822
  - indigenous rights, 817–818
  - Indonesia, 812, 822
  - inductively coupled plasma spectroscopy (ICP), 470, 475, 477–478
  - inhibitors, 516–517, 520–524, 536
  - initial boundary value problem (IBVP), 77–82, 90, 96
  - in-situ fluids and, 366–367
  - Institute of Petroleum, 537
  - insurance, 814
  - Inter-American Convention on International Commercial Arbitration, 826
  - interest, 770–771
    - loans and, 777–779
    - time value of money and, 775–778
    - Truth-in-Lending Act and, 778
  - interfacial tension (IFT), 484
    - capillary pressure and, 734–735, 746
    - crude oil emulsions and, 536–537, 539–540, 559–560
    - relative permeability and, 739
  - internal rate of return (IRR), 780
  - international arbitration, 824–825
  - International Centre for Settlement Investment Disputes, 828
  - International Centre for the Settlement of International Disputes (ICSID), 825
  - International Chamber of Commerce (ICC), 825
  - International Emergency Powers Act, 829
  - international oil and gas law
    - abandonment and, 822–823
    - arbitration and, 824–826
    - bribery and, 816–817
    - civil law and, 828–829
    - common law and, 828–829
    - concessions and, 811–812
    - contractual provisions and, 813–814
    - conventions and, 828
    - corruption and, 816–817, 829
    - dispute resolution and, 815–816, 823–826
    - extraterritorial laws and, 829
    - Foreign Corrupt Practices Act (FCPA), 816–817
    - frontier areas and, 812
    - historical perspective on, 809–810
    - indigenous rights and, 817–818
    - joint management committee and, 818
    - licenses and, 811–812
    - marketing agreements and, 820–822
    - monopolies and, 809
    - operations and, 814–820
    - participation agreements and, 812
    - political risk and, 815–816
    - production sharing agreements and, 812

- religion and, 826
- security issues and, 816
- services agreements and, 812–813
- sovereignty and, 827–828
- training obligations and, 818
- treaties and, 828
- UNCLOS and, 823
- worldwide production and, 809
- interstitial water, 492
- inverse lever rule, 374
- investment
  - decision trees and, 785–788
  - discounted profit-to-investment ratio and, 780–782
  - estimated remaining reserves and, 789–791
  - expected monetary value and, 784–788, 791–799
  - Foreign Corrupt Practices Act (FCPA) and, 816–817
  - internal rate of return and, 780
  - Monte Carlo simulation and, 787–792
  - net present value and, 779–780, 783
  - portfolio analysis and, 792–799
  - property evaluation and, 768–775, 783–792
  - real options and, 799–804
  - recommended practices for, 782–783
  - time value of money and, 775–778
  - uncertainty and, 783
  - weighted average cost of capital (WACC) and, 779
  - See also international oil and gas law
- ion chromatography (IC), 470
- ion selective electrodes, 470
- irrotational waves, 8
- Islamic Law, 826
- isobaric compressibility, 356–357
- isothermal compressibility, 590
  - coefficient of, 356–357
  - gas properties and, 233–236,
  - oil properties and, 275–277, 320–322
- isotopes, 666–671
- Israel, 829
- J**
- Japan, 822
- joint management committee (JMC), 818
- joint operating agreement (JOA), 819–820
- Joule-Thomson expansions, 525
- juvenile water, 466, 492
- K**
- kaolinite, 692–693
- Karl-Fischer titration, 537
- Katy Hub, 772
- kinetic theory
  - cooling curves and, 525
  - emulsion stability and, 540
  - first law of thermodynamics and, 338–341
  - ideal gas and, 217–218
  - rock failure and, 640–666
- Klinkenberg effect, 696–699
- Kozeny-Carman equation, 701–702, 705, 717–718
- Kuwait, 415, 809–810
- K-value equations, 433–435, 438–441, 447–448
- L**
- labor issues, 813
- Langmuir isotherm equation, 423
- Laplace transformations
  - applications and, 146–168
  - asymptotic forms and, 88–100
  - Bessel functions and, 90–92, 131, 135
  - capillary pressure and, 728
  - computational considerations and, 146–168
  - convolution and, 87
  - cylindrical reservoirs and, 130–137
  - Darcy's law and, 90
  - defined, 86
  - derivatives and, 87
  - Dirac delta function and, 125
  - domain function and, 88
  - Duhamel's theorem and, 121
  - Green's functions and, 123
  - infinite-slab reservoirs and, 129–130
  - initial boundary value problem (IBVP) and, 90, 96
  - integrals and, 87, 146–148
  - inverse, 88–100
  - limiting forms and, 146
  - line source solutions and, 92, 128–129
  - naturally fractured reservoirs and, 122–123
  - point source solutions and, 124–134
  - pressure distribution and, 91
  - ratio R and, 153–154
  - rectangular parallelepiped reservoirs and, 137–144
  - series F and, 150–153
  - series S and, 148–150
  - skin-zone radius and, 95–100
  - source functions and, 121–168
  - Stehfest algorithm and, 88–89, 95
  - superposition and, 126, 128
  - surface source solutions and, 128–129
  - 3D/2D anisotropy conversion and, 144–146
  - translation and, 87
  - volumetric source solutions and, 128–129
- Laplacian operators, 53
- lasers, 408–409, 470
- Lee-Kesler equation, 243–244
- legal issues. See international oil and gas law
- Leverett j-function, 734–735
- L'Hopital's rule, 3
- licenses, 811–812
- lifeboat ethics, 838
- light-scattering technique, 408–409, 470
- limestones, 473, 662–666, 745
- limits, 1–3
- linear superposition rule, 4
- liquids (see also phase behavior)
  - crude oil emulsions and, 533–570 (see also oil)
  - fluid properties and, 585–594
  - fugacity and, 433–435
  - H<sub>2</sub>O+hydrocarbon systems and, 499–528
  - phase diagrams and, 376–395
  - solid/liquid equilibrium and, 432–435
  - solid-solution models and, 436–444
  - solubility and, 501–506
  - stationary-liquid method and, 758
  - thermodynamic-micellization model and, 421–422
  - water and, 492 (see also water)
  - waxes and, 398–400, 404–408, 430–453
- liquefied natural gas (LNG), 810, 822
- lithology, 651, 664
- loans, 777–779
- local taxes, 773–774
- logging techniques, 584–585
- London Court of International Arbitration (LCIA), 825
- longitudinal waves, 9
- Louisiana, 772
- Lower Cretaceous Hosston formation, 692
- low-rate methods, 759
- M**
- Maastrichtian samples, 695
- magnetite, 573

- markets. See international oil and gas law
- mass conservation, 45  
 accumulation and, 46  
 equilibrium and, 344–350  
 first law of thermodynamics and, 338–341  
 initial boundary value problem (IBVP) and, 77–82  
 second law of thermodynamics and, 341–344
- mathematics  
 algebra, 57–62  
 calculus, 1–6, 11, 46–48  
 complex numbers, 59  
 D'Alembert's principle, 13  
 Darcy's law, 62–63, 73  
 dependent variables, 1–2  
 derivatives, 3–5  
 differential-equation solutions, 5–6  
 finite difference method, 54–57  
 fluid flow and, 45–76  
 Gaussian analysis, 836–837  
 Green's functions, 100, 110–121, 123  
 Hamilton's principle, 13  
 Hooke's law, 13  
 imaginary numbers, 59  
 independent variables, 1–2  
 inverse lever rule, 374  
 Laplace transformations, 86–100  
 L'Hopital's rule, 3  
 limits, 1–3  
 linear algebra, 57–62  
 linear superposition rule, 4  
 matrices, 57–62  
 Monte Carlo simulation, 787–792  
 Newton's Second Law, 13, 18  
 numerical methods and, 54–57  
 ordinary differential equations (ODEs), 1, 5, 11  
 partial differential equations (PDEs), 1, 5, 11  
 risk analysis and, 783–792  
 slope, 1–5  
 source functions, 100–168 (see also source functions)  
 Taylor's series, 54  
 transient analysis, 77–172 (see also transient analysis)  
 vector analysis, 51–54  
 vibration systems, 1–37
- matrices  
 Cartesian coordinates and, 57–58  
 coordinate transformation and, 68–69  
 Darcy's law and, 62–63  
 determinants and, 61–62  
 diagonalizing and, 62–69  
 diffusivity and, 81  
 eigenvectors and, 61–62, 66–69  
 fluid flow and, 57–62  
 inverse, 61  
 normalization and, 67  
 null, 60–61  
 operations of, 60–61  
 permeability tensors and, 62–74  
 properties of, 58–60  
 rotational transformation and, 69–74  
 similarity transformations and, 64–65  
 symmetric, 60
- Maxwell's equal area construction, 362–363
- mechanical vibration analysis, 12–13  
 continuous systems and, 34–36  
 geometric boundaries and, 36–37  
 SDOF system and, 13–24  
 2DOF system and, 24–34
- megapascals, 595
- mercury, 735, 754
- metamorphic rocks, 573
- meteoric water, 491
- methane, 337, 371, 400, 831–832
- methanol, 753, 833  
 $\text{H}_2\text{O}$ +hydrocarbon systems and, 516–517, 520–524
- Mexico, 810, 813
- micas, 573
- migration, 466
- minerals  
 bounds and, 599–603  
 clays and, 653–655  
 Gassmann equations and, 619–629  
 international oil and gas law and, 813–814  
 (see also international oil and gas law)  
 properties of, 603–604  
 radioactive, 666–671  
 rock failure and, 640–666 (see also rock properties)  
 royalties and, 768, 770–771  
 severance taxes and, 773–774  
 single-phase permeability and, 705
- mixing-line technique, 492–493
- mixtures, 220–221  
 asphaltenes and, 258, 397–403, 408–429  
 equations of state and, 364–366  
 fluid properties and, 585–594  
 gas-injection processes and, 386–394  
 gas viscosity and, 236–241  
 phase diagrams and, 376–395  
 rock properties and, 573–577  
 surfactant/polymer floods and, 384–386  
 volumetric properties of, 364–366  
 waxes and, 398–400, 404–408, 430–453
- mobile analyzers, 474–475
- Model License, 811
- Mohr circles, 642, 656
- Mohr failure, 645–651
- molar fraction, 545–546
- molar internal energy, 339  
 equilibrium and, 344–350  
 phase diagrams and, 376–395  
 pure fluid properties and, 350–364  
 second law of thermodynamics and, 341–344
- molecular weight, 271, 543  
 apparent, 220  
 ideal gas law and, 587  
 isothermal velocity and, 589–590  
 Klinkenberg effect and, 696–697
- mole fractions, 220, 283, 290  
 asphaltenes and, 542–545  
 crude oil emulsions and, 542–546  
 phase behavior and, 334–335  
 waxes and, 433–435
- monoethylene glycol (MEG), 516–517, 520–524
- monopolies, 809
- Monte Carlo simulation, 787–792
- mudstone, 653–654
- multicomponent activity coefficient models, 415–417
- Multiflash, 517
- Multilateral Investment Guarantee Agency, 815
- multiple-core method, 757
- Muslims, 826
- N**
- naphthenes, 258, 400
- National Association of Corrosion Engineers (NACE), 471
- National Institute of Standards and Technology (NIST), 217
- naturally-fractured-reservoir modeling, 62
- natural occurring radioactive materials (NORM), 666
- net cash flow, 775

net operating income, 774  
 net present value (NPV), 783  
   economic parameters and, 779–780  
   portfolio analysis and, 792–799  
 net revenue interest, 771  
 net sales, 771  
 network models, 750  
 neutron logs, 585  
 Newtonian fluids, 277  
 Newton's Second Law, 13, 18, 604  
 New York Convention, 826, 828  
 New York Mercantile Exchange (NYMEX), 771–773  
 nitric acid, 477–478  
 nitrogen, 371  
 nitrogen dioxide, 833  
 nodes, 7  
 nonane, 400  
 normalization, 67  
 North Dakota, 694  
 North Sea, 266, 407, 415, 418, 694–695, 811  
 North Slope, 694  
 nuclear energy, 831–832  
 nuclear magnetic resonance (NMR), 432, 585  
   laboratory determination and, 722  
   single-phase permeability and, 709–712, 722

**O**

oil (*see also* phase behavior)  
 API standards and, 259–260, 266, 268, 274, 590–592  
 asphaltenes and, 258, 397–403, 408–429  
   (*see also* asphaltenes)  
 bubblepoint pressure and, 261, 264–270, 310–314  
 bulk modulus and, 591  
 capillary pressure and, 713–714, 727–762  
 classification issues and, 257–258  
 coal oil and, 465  
 crude oil characterization and, 259–261  
 crude oil emulsions and, 533–570  
 density and, 277  
 economic evaluation and, 768–775, 783–792  
 enhanced oil recovery (EOR) processes and,  
   371–372, 379, 384–394  
 estimated remaining reserves and, 789–791  
 formation volume factor (FVF) and, 257, 273–275,  
   285, 315–319  
 gas-injection processes and, 386–394  
 international law and, 809–829  
 isothermal compressibility and, 275–277, 590–591  
 marketing of, 820–821  
 nonhydrocarbon gas effects and, 270–273  
 phase diagrams and, 376–395  
 produced water and, 465–494  
 property evaluation and, 768–775, 783–792  
 pseudocritical, 290–291  
 relative permeability and, 727–762  
 residual saturation and, 743–745  
 sequestration and, 837–838  
 solution gas/oil ratio and, 273  
 specific gravity and, 259–260, 277–281  
 surface tension and, 281–304  
 viscosity and, 277–281, 323–331  
 waxes and, 398–400, 404–408, 430–453  
 wettability and, 728–734, 737–738  
 whale oil and, 465  
 oil-based mud (OBM), 174, 182, 188, 207  
 Oil Creek, 465  
 Oklahoma, 771  
 olefins, 258  
 Oligocene-Miocene sandstones, 693

operating costs, 774  
 ordinary differential equations (ODEs), 1, 5, 11  
 Organization of Petroleum Exporting Countries (OPEC),  
   803, 810  
 organophosphonates, 471  
 outliers, 261  
 overriding royalties, 771  
 Overseas Private Investment Corporation, 815  
 ownership issues. *See* international oil and gas law  
 oxides, 489–490, 573

**P**

Pacific Rim, 822  
 Panama Convention, 826  
 paper barrels, 772–773  
 paraffins, 257–258, 278–279  
   petroleum fluid classification and, 400  
   waxes and, 398–400, 404–408, 430–453, 544  
 parallelepiped  
   boundary conditions and, 106–107  
   diffusion and, 106–107  
   rectangular reservoirs and, 137–144  
   source functions and, 106–107  
 partial differential equations (PDEs), 1, 5, 11  
   boundary conditions and, 47–48  
   continuity equation, 45–46  
   finite difference method, 54–57  
   fluid flow and, 45–50  
   independent variables and, 46–48  
   initial boundary value problem (IBVP) and, 77–82  
   Laplacian operators and, 53  
   one-dimensional convection/dispersion equation, 48–50  
   Poisson's summation formula and, 106–107  
   Taylor's series and, 54  
   three-dimensional convection/dispersion equation, 54  
   transient analysis and, 77 (*see also* transient analysis)  
 participation agreements, 812  
 Pascal measurement, 595  
 pendulums, 24–34  
 Pennsylvania, 258, 465–466  
 pentane, 258, 400–401  
 permeability  
   absolute, 727  
   capillary pressure and, 713–714  
   Darcy's law and, 79–82, 687–688  
   Green's functions and, 110–121  
   initial boundary value problem (IBVP) and, 79–82  
   intrinsic, 727  
   Laplace transformations and, 121–168  
   porosity and, 688  
   relative, 727–762 (*see also* relative permeability)  
   rock failure and, 640–666  
   single-phase, 687–724 (*see also* single-phase permeability)  
   source functions and, 104–168 (*see also* source functions)  
   upscale, 759  
 permeability tensors  
   channel sand and, 71–74  
   coordinate transformation and, 68–69  
   Darcy's law and, 62–63, 73  
   diagonalizing and, 62–69  
   eigenvectors and, 66–69  
   matrices and, 62–74  
   rotational transformation and, 69–74  
   similarity transformations and, 64–65  
 pH, 474–475, 486–489, 548  
 phase behavior, 173, 180  
   acentric factor and, 361  
   activity coefficients and, 412–413, 415–417, 433–434  
   compressibility and, 356–357



- description of, 333
- Duhem's theorem and, 335–336
- equations of state and, 344–350, 354–366
- equilibrium and, 333–350
- first law of thermodynamics and, 338–341
- fluid properties and, 585–594
- fugacity criterion and, 346–347
- Gibbs and, 333–336, 500–501
- H<sub>2</sub>O+hydrocarbon systems and, 499–528
- ideal gas and, 355
- in-situ fluids characterization and, 366–367
- mole fractions and, 334–335
- phase diagrams and, 371–395
- pressure-volume diagram and, 359–360
- principle of corresponding states and, 360–361
- real fluid equation and, 356
- retrograde condensation and, 375
- retrograde vaporization and, 375
- reversible thermodynamic systems and, 336–337
- second law of thermodynamics and, 341–344
- single-phase permeability and, 687–724
- stability and, 336–337
- surfactant/polymer floods and, 384–386
- two-phase envelope calculation and, 363–364
- vapor pressure and, 361–363
- volumetric properties of mixtures and, 364–366
- volumetric properties of pure fluids and, 350–364
- phase diagrams
  - binary, 373–375
  - cricondenterm and, 381–382
  - dilution plane and, 388–389
  - enhanced oil recovery (EOR) processes and, 371–372, 379, 384–394
  - gas-injection processes and, 386–394
  - inverse lever rule and, 374
  - multicontact miscibility and, 392–394
  - phase rule and, 372–373
  - quaternary, 380–381
  - reservoir fluid systems and, 381–384
  - single component, 371–372
  - surface tension and, 281–282
  - surfactant/polymer floods and, 384–386
  - ternary, 376–380
- plugging
  - adsorption and, 423–424
  - asphaltenes and, 422–429
  - porosity and, 426
  - wettability alteration and, 427–429
- point source solutions
  - bounded reservoirs and, 104–105
  - continuous, 103–104, 108–110
  - cylindrical reservoirs and, 130–137
  - diffusion and, 101–110
  - Green's functions and, 110–121
  - infinite reservoirs and, 103–104
  - infinite slab reservoirs and, 130–137
  - instantaneous, 103–108, 115
  - Laplace transformations and, 124–134
  - Newman's product method and, 110, 113
  - rectangular parallelepiped reservoirs and, 137–144
  - superposition and, 126, 128
  - system dimension and, 113–114
  - unsteady flow and, 110–168
- Poisson's ratio, 598, 617
- Poisson's summation formula, 106–107
- political risk, 815–816
- poly-acrylic polymers, 471
- polymer floods, 384–386
- porosity
  - asphaltenes and, 426
  - Biot's poroelastic term and, 656
  - brines and, 607–609
  - bulk lubrication and, 660–661
  - bulk modulus and, 586, 591 (*see also* bulk modulus)
  - capillary pressure and, 713–714, 727–762
  - chemical effects and, 659
  - crack, 580, 632–634
  - critical, 608, 628–629, 652
  - definition of, 578–580
  - delta function and, 110
  - dependence, 607–609
  - diffusion and, 101–110 (*see also* diffusion)
  - effective, 580, 655–658
  - fluid properties and, 585–594
  - fractional, 613–614
  - fracture, 580
  - Gassmann equations and, 619–629
  - Green's functions and, 110–121
  - ineffective, 580
  - initial boundary value problem (IBVP) and, 77–82
  - in-situ, 582–584
  - Laplace transformations and, 121–168
  - logging of, 584–585
  - measurement techniques for, 584–585
  - permeability and, 688
  - Reuss modulus and, 607, 626–628
  - rock failure and, 651–652, 655–662
  - rock strength measurement and, 662–666
  - sedimentary rocks and, 573–577
  - single-phase permeability and, 687–724
  - squirt-flow mechanisms and, 639
  - total, 580
  - transient analysis and, 77–82 (*see also* transient analysis)
  - transition, 651–652
  - velocity relations and, 609–612
  - Voigt modulus and, 599, 601, 607–608, 625–626
  - vuggy, 694
  - wettability and, 728–734
- porous-plate methods, 754–755
- portfolio analysis, 792–799
- potash, 666
- potassium-40, 666–668
- potential energy, 338–341, 525
- pour-point temperature, 431–432
- power of transmitted light (PTL), 408
- precipitation behavior
  - asphaltenes and, 397–398, 408–430
  - waxes and, 430–453
- present worth, 776–777
- pressure
  - capillary, 713–714, 727–762 (*see also* capillary pressure)
  - diffusion and, 80–86, 101–110
  - effective stress and, 655–658
  - effective vs. differential, 615
  - first law of thermodynamics and, 338–341
  - fluid sampling hazards and, 210
  - Green's functions and, 110–121
  - H<sub>2</sub>O+hydrocarbon systems and, 508–517
  - initial boundary value problem (IBVP) and, 79–82
  - in-situ density and, 582–584
  - Klinkenberg effect and, 696–699
  - Laplace transformations and, 86–100
  - minimum miscibility (MMP), 392
  - pore fluid effects and, 655–661
  - pseudopressure and, 81
  - P waves and, 621, 629–630
  - relative permeability and, 727–762
  - reversibility and, 409–410

- rock failure and, 640–666
  - second law of thermodynamics and, 341–344
  - single-phase permeability and, 698–700
  - skin-zone radius and, 95–100
  - source functions and, 101–110, 110–168
    - (see also source functions)
  - stress-strain and, 594–597
  - S waves and, 621, 629–630
  - vapor, 241–244, 361–363
  - waxes and, 399–400
  - well conditioning and, 181–183
  - pressure-volume diagram, 359–360
  - pressure/volume/temperature (PVT) analysis, 517
    - API number and, 588, 590
    - asphaltenes and, 258, 397–403, 408–429
    - bubblepoint and, 261, 264–270, 310–314
    - Calingeart-Davis equation and, 242–243
    - Clapeyron equations and, 241–242
    - Cox chart and, 242
    - cricondentherm and, 381–382
    - critical pressure, 218–219
    - critical temperature, 218–219
    - crude oil characterization and, 259–261
    - equilibrium and, 224
    - fluid sampling and, 173–174, 176, 209–210
      - (see also fluid sampling)
    - gas properties and, 217–256
    - gravimetric technique and, 408
    - heat capacity and, 594
    - ideal gas and, 217–218, 355
    - in-situ fluids and, 366–367
    - Lee-Kesler equation and, 243–244
    - light-scattering technique and, 408
    - mixture properties and, 364–366
    - oil properties and, 257–331
    - phase behavior and, 333–367 (see also phase behavior)
    - phase diagrams and, 376–395
    - pressure-volume diagram and, 359–360
    - principle of corresponding states and, 360–361
    - pseudocritical properties and, 223–233, 236–241
    - pseudopotential properties and, 241
    - pure fluid properties and, 350–364
    - real gases and, 223–233
    - recommended measurements for, 176–177
    - reservoir classification and, 381–384
    - surface tension and, 281–288
    - viscosity and, 277–281
    - waxes and, 398–400, 404–408, 430–453
  - price, 771–773
  - principle of corresponding states, 360–361
  - Process II, 517
  - produced water
    - brine and, 486
    - characterization of, 470–471
    - chemical analyses interpretation and, 491–492
    - chemical complexity of, 467
    - compressibility and, 478–479
    - connate water and, 466, 470
    - corrosion and, 471–472
    - crude oil emulsions and, 533–570
    - density and, 479–482
    - displacement effects and, 466–467
    - dissolved gases and, 490
    - economics of, 469–471
    - formation volume factor and, 482–483
    - handling costs and, 467
    - historical perspective on, 465–467
    - importance of, 467–468
    - irreducible water saturation and, 468
    - migration and, 466
    - mixing-line technique and, 492–493
    - organic constituents and, 490–492
    - pH and, 474–475, 486–489
    - polymer-gel water-shutoff treatments and, 467
    - primary production and, 468–469
    - redox potential and, 489–490
    - resistivity and, 484
    - salinity and, 480–482, 485
    - sampling of, 472–478
    - sands and, 465–466
    - scale deposition and, 471–472
    - sources of, 467–468
    - surface tension and, 484
    - suspended solids and, 494
    - temperature effects and, 468–469
    - viscosity and, 484–486
  - production downhole sampling, 185–189
  - production sharing agreements, 812
  - production traps, 554
  - property evaluation
    - economic models for, 768–775
    - gross production and, 769
    - gross sales and, 770
    - net operating income and, 774
    - net revenue interest and, 771
    - net sales and, 771
    - operating costs and, 774
    - price and, 771–773
    - risk analysis and, 783–792
    - royalties and, 768, 770–771
    - shrinkage and, 769–770
    - taxes and, 773–775
    - working interest and, 770
  - proportionality, 6
  - Prudhoe Bay field, 428, 733
  - pseudocritical properties
    - hydrocarbons and, 223–233
    - oil properties and, 290–291
    - surface tension and, 290–291
    - viscosity and, 236–241
  - pseudopotential properties, 241
  - pure fluids
    - acentric factor and, 361
    - cubic equations of state and, 357–364
    - equilibrium and, 344–350
    - fugacity criterion and, 346–347, 349–350
    - phase behavior models of, 354–364
    - pressure-volume diagrams and, 359–360
    - principle of corresponding states and, 360–361
    - volumetric properties of, 350–364
  - pure solids, 433–436
  - PVTsim, 517
  - pyrolysis, 833
- Q**
- quartz, 573, 576, 608–610, 692
  - quaternary phase diagrams, 380–381
- R**
- radioactivity, 666–671
  - radium, 667
  - rainbow options, 800
  - Rangely field, 386, 389–390, 412
  - real gases
    - deviation factor and, 224–225, 228–229
    - pseudocritical properties and, 224–233
    - pseudopotential properties and, 241
    - real-gas law and, 223–233

- supercompressibility and, 223
- real options, 799–804
- recommended engineering practices (REPs), 783
- redox potential, 489–490
- reflux-extraction units, 753
- relative density. *See* specific gravity
- relative permeability
  - Brooks-Corey model and, 746–747
  - bubblepoint and, 750–752
  - Carman-Kozeny models and, 749–750
  - centrifuge methods and, 755–757
  - Chierici model and, 7489
  - Darcy's law and, 727
  - endpoint saturation and, 736, 739–746, 759
  - heterogeneity and, 747–748
  - homogeneity and, 738
  - Honarpour model and, 749
  - hysteresis and, 736–737, 749
  - Ibrahim model and, 749
  - interfacial tension and, 739
  - measurement of, 752, 757–760
  - mercury methods and, 754
  - multiphase flow and, 727–728
  - network models and, 750
  - porous-plate methods and, 754–755
  - sample handling and, 752–754
  - steady-state methods and, 757–758
  - three-phase models and, 750–752
  - unsteady-state methods and, 758–759
  - wettability and, 737–738
- religion, 826
- renewable fuels, 831–833
- reservoirs (*see also* gas; oil)
  - asphaltenes and, 258, 397–403, 408–429
  - capillary pressure and, 713–714, 727–762
  - classification of, 381–384
  - cricondentherm and, 381–382
  - cylindrical, 130–137
  - estimated remaining reserves and, 789–791
  - fluid sampling and, 180–181 (*see also* fluid sampling)
  - gas-injection processes and, 386–394
  - Gassmann equations and, 619–629
  - Green's functions and, 110–121
  - infinite-slab, 129–130
  - Laplace transformations and, 121–168
  - mechanical failure and, 640–666
  - petroleum fluid classification and, 400–401
  - phase diagrams and, 376–395
  - produced water and, 465–494
  - property evaluation and, 768–775, 783–792
  - rectangular parallelepiped, 137–144
  - relative permeability and, 727–762
  - rock failure and, 640–666
  - sequestration and, 837–838
  - single-phase permeability and, 687–724
  - source functions and, 110–168 (*see also* source functions)
  - statistical approaches and, 718–720
  - surface tension and, 281–304
  - surfactant/polymer floods and, 384–386
  - trapping relationship and, 741–742
  - viscosity and, 277–281
  - waxes and, 398–400, 404–408, 430–453
  - well conditioning and, 181–183
  - wettability and, 728–734, 737–738
  - zonation and, 718–720
- resins, 258, 400–402, 545 (*see also* asphaltenes)
- resistivity, 408, 484
- resonance, 9–10
- response function, 6–8
- retrograde condensation, 375
- retrograde vaporization, 375
- Reuss modulus, 601, 607, 626–628
- rheology, 538–540
- risk analysis
  - decision trees and, 785–788
  - expected monetary value and, 784–785, 791–799
  - Monte Carlo simulation and, 788–791
  - portfolio analysis and, 792–799
  - uncertainty and, 783
- rock failure
  - bulk lubrication and, 660–661
  - catastrophic effects of, 640
  - chemical effects and, 659
  - clay content and, 653–655
  - cohesion and, 650
  - compaction strength and, 653
  - Coulomb-Navier, 642–645
  - curved envelopes and, 645–651
  - defined, 641
  - effective stress and, 655–658
  - grain size and, 661–662
  - Hoek-Brown relationships and, 645–651, 662
  - internal friction angle and, 643
  - log parameters and, 662–666
  - Mohr, 645–651
  - permanent deformation and, 640–641
  - pore fluid effects and, 655–661
  - porosity and, 655–662
  - radioactivity and, 666–671
  - rock strength measurement and, 662–666
  - uniaxial compressive strength and, 651–653
- rock properties
  - aggregates and, 573–577
  - Archie's Law and, 573
  - bounds and, 599–603
  - bulk modulus and, 586, 591, 607–640  
(*see also* bulk modulus)
  - capillary pressure and, 713–714, 727–762
  - classification issues and, 573–577
  - clays and, 573
  - deformation, 597–599
  - density, 577–585
  - elasticity, 594–640
  - empirical knowledge of, 571–572
  - fluid properties, 585–594
  - forward modeling and, 571
  - gamma ray characteristics, 666–671
  - Gassmann equations and, 619–629
  - Hasin-Shtrikman technique and, 601–602
  - limited data and, 572–573
  - measurement of, 752–759
  - mechanical failure, 640–666
  - as mineral/pore mixtures, 573–577
  - Newton's Second Law and, 604
  - organic mixtures and, 573–577
  - porosity, 577–585
  - relative permeability and, 727–762
  - rock strength measurement and, 662–666
  - rock types and, 573
  - sample handling and, 752–754
  - saturation gain function and, 624–625, 630–631
  - single-phase permeability and, 687–724
  - stress-strain, 594–640
- Roscoe surfaces, 656, 661
- Rotliegend sandstones, 694
- royalties, 768, 770–771
- Russia, 822

- S**
- Sabine Pipe Line Company, 772
- salinity, 480–482, 485–486
- crude oil emulsions and, 533, 550, 554, 556
  - desalters and, 554, 556
  - radioactivity and, 667
- sampling techniques, 752
- centrifuge methods, 755–757
  - cleaning and, 753
  - collection and, 753
  - core cutting and, 753
  - data corruption and, 759–760
  - endpoint saturations and, 759
  - mercury methods, 754
  - porous-plate methods, 754–755
  - preparation and, 753–754
  - shipping and, 753
  - steady-state methods, 757–758
  - unsteady-state methods, 758–759
  - viscous fingering and, 759
- sandpacks, 689–690
- sands, 465–466
- gridding of, 71–74
  - rock properties and, 573, 575, 584
- sandstones, 573, 618
- brine saturated, 608–609
  - capillary pressure and, 735–736 (see also capillary pressure)
  - compressional velocities and, 639–640
  - grain size and, 661–662
  - Hoek-Brown relationships and, 645–651
  - relative permeability and, 737, 742
    - (see also relative permeability)
  - rock strength measurement and, 662–666
  - shale and, 653–655
  - single-phase permeability and, 692–694, 709
  - solid mineral bulk modulus and, 629–632
  - tight, 709
  - uniaxial compressibility strength and, 652
  - velocity-porosity relations and, 609–612
- SARA (saturates, aromatics, resins, asphaltenes)
- classification, 400–401, 403, 430
- saturation, 400–401
- bulk mercury, 735
  - capillary number and, 743–745
  - capillary pressure and, 713–714, 727–762
  - critical condensate, 741
  - critical gas, 741
  - critical water, 706
  - endpoint, 736, 739–746, 759
  - gain function and, 624–625, 630–631
  - Gassmann equations and, 619–629
  - Kuster-Toksoz model and, 633–634
  - relative permeability and, 727–762
  - residual gas, 741–742
  - residual oil, 743–745
  - residual water, 745–746
  - sampling techniques and, 752–760
  - single-phase permeability and, 709–713
  - trapped gas, 741–742
- Saudi Arabia, 810
- Saybolt measurement, 196
- scalar fields, 51
- scale deposition, 471–472
- Scanning Electron Microscope (SEM), 574–575
- Scatchard-Hildebrand equation, 436–437
- Scott-Magat theory, 415
- scrapers, 453
- seawater, 492
- security issues, 816
- sedimentary rocks, 573–577
- Gassmann equations and, 619–629
- seismic data
- API number and, 588
  - brines and, 592–594
  - chemical effects and, 650
  - fluid properties and, 585–594
  - gas and, 586–588
  - Gassmann equations and, 619–629
  - oil and, 588–592
  - rock failure and, 640–666
- sequestration, 837–838
- services agreements, 812–813
- severance tax, 773–774
- shales, 576, 584, 653–655
- bulk lubrication and, 660–661
  - radioactivity and, 666–671
  - rock strength measurement and, 662–666
  - single-phase permeability and, 691–692
- shear (S) waves, 8–9, 451–452, 621, 629–630
- Shell Oil, 823
- shrinkage, 769–770
- silicates, 573
- silts, 576
- single carbon number (SCN) fractions, 430
- single-phase permeability
- applications of, 722–723
  - Berg's model and, 703
  - capillary pressure and, 713–714
  - carbonates and, 694–695
  - clays and, 691–692
  - core measurement corrections and, 696–701
  - Darcy's law and, 687–688
  - dual-water model and, 708–709
  - empirical trends and, 695–696
  - flow zone indicator and, 717–718
  - grain size and, 688–689, 695, 701–718, 721
  - Granberry-Keelan chart and, 706
  - Katz-Thompson equation and, 715–717
  - Klinkenberg effect and, 696–699
  - Kozeny-Carman equation and, 701–702
  - Krumbein-Monk equation and, 702–703
  - mineralogical factors and, 705
  - nuclear magnetic resonance and, 709–712
  - petrologic controls and, 688–696
  - petrophysical models for, 701–718
  - Pittman and, 714–715
  - pore dimension and, 713–718, 721
  - pore fluid sensitivity and, 697–698
  - predictors and, 719–720
  - pressure dependence and, 698–701
  - reservoir zonation and, 718–720
  - sandstones and, 692–694, 709
  - shales and, 691–692
  - statistical approaches and, 718–720
  - stress-strain and, 688
  - surface area and, 705–712
  - Swanson equation and, 714
  - Timur model and, 706–707
  - unconsolidated sandpacks and, 689–691, 705
  - Van Baaren's model and, 704–705
  - water saturation and, 705–712
  - Winland's equation and, 714–715
- skin-zone radius, 95–100
- slippage, 182
- slope, 1–5
- Smackover limestone water, 473
- smectite, 576
- Society of Petroleum Evaluation Engineers (SPEE), 783

- solar energy, 831–833
  - solids
    - basic sediment and water (BS&W), 533, 536–537, 549–550, 560, 770
    - cracked rock and, 632–634
    - crude oil emulsions and, 533–570
    - mineral bulk modulus and, 629–632
    - produced water and, 494
    - waxes and, 398–400, 404–408, 430–453
  - solid-solution models
    - EOS for liquid/vapor phases, 442–444
    - equation of state for liquid/vapor phases, 437–438
    - Flory-Huggins, 442
    - ideal, 441
    - internally consistent, 441
    - regular, 436–444
  - solubility, 501–506
  - source functions
    - applications and, 146–168
    - bounded reservoirs and, 104–108
    - compressibility and, 102–103
    - computational considerations and, 146–168
    - cylindrical reservoirs and, 130–137
    - diffusion and, 101–110
    - Dirac delta function and, 125
    - Duhamel's theorem and, 121
    - Green's functions and, 100
    - infinite reservoirs and, 103–104, 108–110, 130–137
    - integral and, 146–148
    - Laplace transformations and, 86–100, 121–168
    - limiting forms and, 146
    - Newman's product method and, 110, 113–114, 116, 120
    - point-source solutions and, 101–110, 124–128
    - Poisson's summation formula and, 106–107
    - ratio  $R$  and, 153–154
    - rectangular parallelepiped reservoirs and, 137–144
    - series  $F$  and, 150–153
    - series  $S$  and, 148–150
    - superposition and, 126, 128
    - system dimension and, 113–114
    - 3D/2D anisotropy conversion and, 144–146
    - unsteady-flow problems and, 110–121
  - sovereignty issues, 827–828
  - soybeans, 833
  - spaceship ethics, 838
  - specific gravity, 219–221
    - gas properties and, 268–269
    - viscosity and, 277–281
  - spherical coordinates
    - diffusion and, 101–110
    - Laplace transformations and, 124–128, 130–133
    - source functions and, 101–110, 124–128
  - split-stream sampling, 195–196
  - springs, 11
    - classical linear oscillator and, 13–24
  - squirt-flow mechanisms, 639
  - stable-isotope analysis, 474
  - Standard Oil Company, 809
  - state taxes, 773–774
  - stationary-liquid method, 758
  - steady-state measurements, 757–758
  - steric repulsion, 542–543
  - Stokes' Law, 554
  - Stoneley waves, 722–723
  - stress-strain
    - anisotropic, 595, 634–637
    - attenuation and, 637–640
    - biaxial, 595
    - Biot's poroelastic term and, 656
    - bounds and, 599–603
    - cohesion and, 650
    - cracked rock and, 632–634
    - definitions for, 594–597
    - deformation and, 597–599
    - effective, 655–658
    - elastic wave velocities and, 604–607
    - Gassmann equations and, 619–629
    - Hasin-Shtrikman technique and, 601–602
    - Hoek-Brown relationships and, 645–651
    - Hooke's law and, 599
    - hydrostatic, 595
    - in-situ, 616–618
    - Klinkenberg effect and, 696–699
    - lithostatic, 616–618
    - log parameters and, 662–666
    - mechanical failure and, 640–666
    - Newton's Second Law and, 604
    - Poisson's ratio and, 598
    - porosity dependence and, 607–609
    - pressure and, 594–597, 612–616
    - Reuss modulus and, 601, 626–628
    - rock failure and, 640–666
    - shear, 596, 640–666
    - single-phase permeability and, 688
    - temperature and, 618–619
    - tensile, 596
    - triaxial, 595
    - uniaxial, 595, 651–655, 662–663, 665
    - velocity dispersion and, 637–640
    - velocity-porosity relations and, 609–612
    - Voigt modulus and, 625–626
    - waves and, 9
    - Young's modulus and, 597
  - sulfate-reducing bacteria (SRB), 478
  - sulfates, 573
  - sunflowers, 833
  - supercompressibility, 223
  - superposition, 6, 126, 128
  - supersaturation, 415
  - surface-active agents, 536
  - surface area
    - dual-water model and, 708–709
    - Granberry-Keelan chart and, 706
    - nuclear magnetic resonance and, 709–712
    - single-phase permeability and, 705–713
    - tight sandstones and, 709
    - Timur model and, 706–707
  - surface bonding, 660–661
  - surface films, 540–541
  - surface tension
    - calculation of, 282–300
    - oil properties and, 281–304
    - phase behavior and, 281–282
    - produced water and, 474
    - pseudocritical properties and, 290–291
    - water-hydrocarbon, 289–304
  - surfactant floods, 384–386, 753
  - sustainable development, 831–833, 838
  - synthetic fuels, 833
- T**
- taxes, 773–775
  - Taylor's series, 54
  - Teflon, 184
  - temperature (*see also* pressure/volume/temperature (PVT) analysis)
    - Benedict-Webb-Rubin equation and, 587
    - capillary pressure and, 746

- crude oil emulsions and, 547
  - elasticity and, 618–619
  - fluid sampling and, 180, 182–183
  - of fusion, 435–436
  - H<sub>2</sub>O+hydrocarbon systems and, 508–517
  - hydrocarbon solubility and, 503–504
  - pour-point, 431–432
  - produced water and, 468–469
  - second law of thermodynamics and, 341–344
  - waxes and, 399, 406, 431–432, 450
  - tension, 8–9
  - ternary phase diagrams, 376–380
  - Texas, 428, 473, 689–690, 772, 803
  - thermal pyrolysis, 833
  - thermodynamics
    - asphaltene precipitation models and, 412–422
    - Benedict-Webb-Rubin equation and, 587
    - colloidal model and, 420–421
    - cooling curves and, 525
    - elasticity and, 618–619
    - first law of, 338–341, 525
    - fluid properties and, 585–594
    - heat capacity and, 587, 594
    - micellization model and, 421–422
    - phase behavior and, 333–367 (*see also* phase behavior)
    - pyrolysis and, 833
    - reversible systems and, 336–337
    - second law of, 341–344
    - solid/liquid equilibrium and, 432–435
    - state functions and, 337–338
    - wax precipitation models and, 432–449
  - thief, 196
  - thin-skin concept, 95–98
  - thorium, 666–668
  - three-phase separators, 554
  - time (*see also* velocity)
    - classical linear oscillator and, 13–24
    - crude oil emulsions and, 551
    - damping and, 11–34
    - expected monetary value and, 784–788
    - first law of thermodynamics and, 338–341
    - initial boundary value problem (IBVP) and, 77–82
    - interest and, 771
    - investment and, 782 (*see also* investment)
    - Laplace transformations and, 86–100
    - phase behavior and, 333–367
    - real options and, 799–804
    - reversible thermodynamic systems and, 336–337
    - 3D/2D anisotropy conversion and, 144–146
    - working interest and, 770
  - time value of money, 775–778
  - titrators, 470
  - toluene, 753
  - Torpedo sandstone, 737
  - torsion, 8–9, 13
  - training, 813, 818
  - transfer limitations, 814
  - transient analysis
    - Bessel functions and, 82–86
    - boundary conditions and, 81–82
    - Duhamel's theorem and, 121
    - Green's functions and, 100, 110–121, 123
    - initial boundary value problem (IBVP) and, 77–82
    - Laplace transformations and, 86–100
    - Newman's product method and, 110, 113–114, 116, 120
    - porous media and, 77–81
    - source functions and, 110–168 (*see also* source functions)
    - unsteady flow and, 110–168
  - transverse waves, 8–9
  - trapping relationship, 741–742
  - treaties, 828
  - Truth-in-Lending Act, 778
- U**
- uncertainty, 783
  - uniform-capillary-pressure method, 758
  - Uniform Commercial Code, 828
  - United Kingdom
    - international law and, 811, 814, 819, 821–822, 825
    - London Court of International Arbitration (LCIA), 825
  - United Kingdom Offshore Operators Association (UKOOA), 822–823
  - United Nations
    - Commission on International Trade Law (UNCITRAL), 824–825
    - Convention on Contracts for the International Sale of Goods (CISG), 828
    - Convention on the Law of the Seas (UNCLOS), 823, 828
    - Convention on the Recognition and Enforcement of Foreign Arbitral Awards, 826, 828
  - United States (*see also* international oil and gas law)
    - American Arbitration Association (AAA), 825
    - American Petroleum Institute (API), 588, 590–592 (*see also* American Petroleum Institute (API))
    - American Society for Testing and Materials (ASTM), 197, 199, 212, 431, 537, 549
    - Department of Energy, 838
    - Department of Justice, 817, 829
    - Energy Information Agency (EIA), 835
    - Export/Import Bank, 815
    - Geological Survey, 470
  - universal quasichemical (UNIQUAC) equation, 448
  - unsteady flow
    - Dirac delta function and, 125
    - Duhamel's theorem and, 121
    - Green's functions and, 110–121
    - Laplace transformations and, 121–168
    - Newman's product method and, 110, 113–114, 116, 120
    - source functions and, 110–168
    - superposition and, 126, 128
    - system dimension and, 113–114
  - unsteady-state measurements, 758–759
  - Upper Fox Hills Sandstone, 639–640
  - upper s(Voigt) limit, 599–603
  - upscaling, 62
  - uranium, 666–668
- V**
- van't Hoff equation, 435
  - vapors
    - multicontact miscibility and, 392–394
    - phase diagrams and, 376–395
    - retrograde vaporization and, 375
    - solid-solution models and, 436–444
    - pressure and, 241–244, 361–363
    - waxes and, 437–438
  - vectors
    - Cartesian coordinates and, 51
    - curl and, 52–53
    - Darcy velocity field and, 51
    - divergence and, 52–53
    - eigenvectors and, 61–62, 65–69
    - fluid flow and, 51–54
    - gradient and, 52–53
    - initial boundary value problem (IBVP) and, 77–82
    - scalar fields and, 51
  - velocity, 588
    - anisotropy and, 634–637

- attenuation and, 637–640
  - capillary number and, 743–745
  - compressional, 639–640
  - convection and, 48–50
  - damping and, 11–34
  - Darcy, 51, 687
  - dispersion and, 48–50, 637–640
  - elastic wave, 604–607
  - fluid flow and, 53–54
  - flux and, 54
  - Gassmann equations and, 619–629
  - initial boundary value problem (IBVP) and, 77–82
  - isothermal, 587, 589–590
  - kinetic theory and, 217–218
  - mineral properties and, 603–604 (see also rock properties)
  - molecular weight and, 589–590
  - Newton's Second Law and, 604
  - porosity relations and, 609–612
  - slippage and, 182
  - sonic, 586
  - waves and, 8–11
  - Venezuela, 802
  - vertical transverse isotropy (VTI), 635–636
  - vibrating systems
    - amplitude and, 42
    - boundary conditions and, 11–12
    - classical linear oscillator and, 13–24
    - continuous, 6–7, 34–36
    - damping and, 9–34
    - derivatives and, 3–5
    - deterministic, 6
    - differential-equation solutions and, 5–6
    - discrete, 6
    - equivalent springs and, 11
    - excitation/response functions and, 6–8
    - geometric boundaries and, 36–37
    - initial conditions and, 11–12
    - limits and, 1–3
    - linear, 6
    - mechanical analysis and, 12–13
    - multiple-degree-of-freedom, 34
    - Newton's Second Law and, 18
    - nodes and, 7
    - nonlinear, 6
    - pendulums and, 24–34
    - period, 42
    - random, 6
    - single-degree-of-freedom (SDOF), 9–10, 13–24
    - theory and, 6–8
    - two-degrees-of-freedom (2DOF), 9–10, 24–34
    - wave behavior and, 8–11, 36–37
  - Vienna Convention on the Law of Treaties, 828
  - viscometric technique, 409
  - viscosity
    - API standards and, 277–281
    - crude oil emulsions and, 538–540
    - Darcy's law and, 79–82
    - dead oil, 279–280
    - gas properties and, 236–241
    - initial boundary value problem (IBVP) and, 77–82
    - interfacial, 539–540
    - Newtonian fluids and, 277
    - oil properties and, 277–281, 323–331
    - produced water and, 484–486
    - Saybolt measurement and, 196
    - specific gravity and, 277–281
    - transient analysis and, 77–82 (see also transient analysis)
  - viscous damping, 10
  - Voigt modulus, 599, 601, 607–608, 625
  - volume (see also pressure/volume/temperature (PVT) analysis)
    - initial boundary value problem (IBVP) and, 77–82
    - mixtures and, 364–366
    - phase behavior and, 350–366
    - phase diagrams and, 376–395
    - pressure-volume diagram and, 359–360
    - pure fluids and, 350–364
    - shrinkage and, 769–770
    - single-phase permeability and, 687–724
  - volumetric source solutions, 128–129
- W**
- war, 815
  - Washburn equation, 713
  - Wasson field, 390
  - WATEQ model, 470
  - water (see also produced water)
    - basic sediment and water, 533, 536–537, 549–550, 560, 770
    - capillary number and, 743–745
    - condensate, 492
    - connate, 466, 470, 492
    - crude oil emulsions and, 533–570
    - desalters and, 554, 556
    - dewpoint and, 180, 381–394, 501–503, 508–514
    - diagenetic, 492
    - dissociation reaction and, 487
    - dual-water model and, 708–709
    - formation, 492
    - fossil, 466
    - free-water knockout drums and, 553–554
    - hydrocarbon systems and, 499–528
    - interstitial, 492
    - juvenile, 466, 492
    - meteoric, 491
    - pH and, 486–489
    - phase diagrams and, 376–395
    - residual saturation and, 745–746
    - sampling techniques and, 472–478
    - sea, 492
    - single-phase permeability and, 709–713
    - solubility and, 501–506
    - surface tension and, 289–403
    - suspended solids and, 494
    - wettability and, 728–734, 737–738
  - water-alternating-gas (WAG) processes, 428–429
  - water-cut measurements, 213
  - wave number, 42
  - waves
    - boundary conditions and, 11–34
    - classical linear oscillator and, 13–24
    - continuous, 34–36
    - D'Alembert's principle and, 13
    - damping and, 9–34
    - degrees of freedom (DOF) and, 9–10
    - dispersion and, 8–9
    - elastic, 8–9, 36–37
    - equilibrium and, 13
    - excitation/response function and, 6–8
    - frequency and, 9–10
    - geometric boundaries and, 36–37
    - Hamilton's principle and, 13
    - Hooke's law and, 13
    - lateral, 8–9
    - longitudinal, 8
    - Newton's Second Law and, 13, 18
    - nodes and, 7
    - propagation of, 8–9, 36–37
    - resonance and, 9–10
    - single degree of freedom (SDOF) and, 13–24

- standing, 7
  - Stoneley, 722–723
  - stress and, 9
  - transient, 7
  - two degrees of freedom (2DOF) and, 24–34
  - types of, 8–9
  - velocity and, 8–11
  - vibrating systems and, 6–37
  - wax-appearance temperature (WAT), 406, 431, 450
  - waxes
    - activity coefficients and, 433–434, 437–438
    - bulk-filtration apparatus and, 432
    - characteristics of, 400, 404–408
    - cloud point and, 431–432
    - cold finger technique and, 431
    - compositional analysis and, 430–431
    - cross-polarized microscopy and, 431
    - crude oil emulsions and, 536
    - crystal structure and, 405–406, 450, 452
    - cutters and, 453
    - deposition models and, 449–452
    - differential-scanning calorimetry and, 431
    - diffusion and, 450–451
    - dispersion and, 451–452
    - dissolution temperature and, 431
    - enthalpy and, 445–449
    - equations of state and, 434–438, 442–444
    - Flory-Huggins model and, 436, 442
    - Gibbs energy models and, 447–449
    - gravity settling and, 450
    - heavy polar fraction and, 545–546
    - K-value equations and, 433–435, 438–441, 447–448
    - light transmittance and, 431
    - multisolid models and, 444–447
    - PNA analysis and, 430–431
    - pour-point temperature and, 431–432
    - precipitation behavior and, 398–400, 430–453
    - pressure changes and, 399–400
    - produced, 465–494
    - pulse nuclear magnetic resonance and, 432
    - pure ideal solid model and, 435–436
    - pure solid fugacity and, 433–435
    - SARA classification and, 430
    - scrapers and, 453
    - solidification behavior and, 406–408
    - solid-liquid equilibrium and, 432–435
    - solid-solution models and, 436–444
    - temperature reduction and, 399
    - thermodynamic models for, 432–449
    - types of, 404–406
    - ultrasonic techniques and, 431
    - viscometric techniques and, 431
  - weighted average cost of capital (WACC), 779
  - Weinaug-Katz equation, 282
  - wellbores
    - asphaltenes and, 258, 397–403, 408–429
    - core measurement corrections and, 696–700
    - crude oil emulsions and, 533–570
    - Laplace transformations and, 86–100
    - sandface production rate and, 96
    - skin-zone radius and, 95–100
    - storage coefficient and, 96
    - transient analysis and, 77–172 (*see also* transient analysis)
    - unloading rate and, 96
    - waxes and, 398–400, 404–408, 430–453
  - well conditioning, 181–183
  - wellhead sampling, 195, 473
    - crude oil emulsions and, 533–570
    - isokinetic sampling and, 195–196
  - well-log analysis
    - flow zone indicators and, 717–718
    - Hoek-Brown relationships and, 645–651
    - rock strength measurement and, 662–666
    - single-phase permeability and, 687–724
    - Winland's equation and, 714–715
    - zonation and, 718–720
  - West Texas Intermediate (WTI), 771, 802
  - wettability
    - alteration and, 427–429
    - capillary pressure and, 728–734, 746
    - dalmation, 731
    - endpoint saturation and, 736, 739–746, 759
    - mixed, 731
    - relative permeability and, 737–738
  - Weyburn oil, 421
  - whale oil, 465
  - Wiener process, 802–803
  - Williston basin, 694
  - Wilson's equation, 448
  - Winland's equation, 714, 716
  - work
    - first law of thermodynamics and, 338–341
    - second law of thermodynamics and, 341–344
  - working interest, 770
  - World Bank, 815
  - Wyoming, 428, 772
- X**
- X-rays, 577
- Y**
- Young's modulus, 597, 661, 663
- Z**
- zeolites, 573
  - zonation, 718–720